Journal of Oncology

Role of DNA Damage/Oxidative Stress as Novel Biomarkers in Tumorigenesis

Lead Guest Editor: Muhammad Muddassir Ali
Guest Editors: Recep Liman and İbrahim Hakkı Cigerci

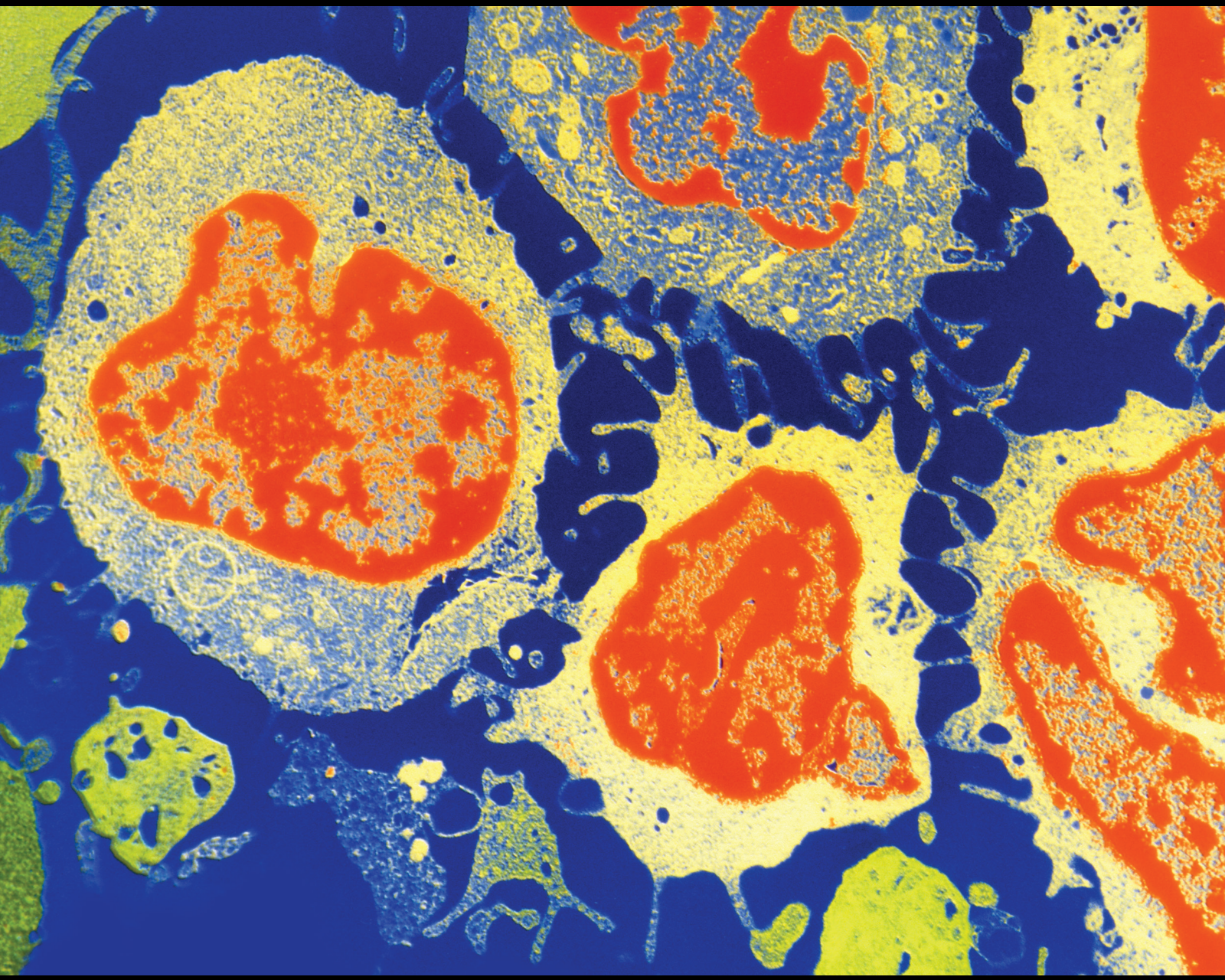

Role of DNA Damage/Oxidative Stress as Novel Biomarkers in Tumorigenesis

Journal of Oncology

Role of DNA Damage/Oxidative Stress as Novel Biomarkers in Tumorigenesis

Lead Guest Editor: Muhammad Muddassir Ali
Guest Editors: Recep Liman and İbrahim Hakkı Cigerci

Contents

Contents

Contents

Hindawi
Journal of Oncology
Volume 2023, Article ID 9850715, 1 page
https://doi.org/10.1155/2023/9850715

Retraction

Retracted: Deep Learning-Based Health Management Model Application in Extreme Myopia Eye Vision Monitoring and Risk Prediction

Journal of Oncology

Received 11 July 2023; Accepted 11 July 2023; Published 12 July 2023

This article has been retracted by Hindawi following an investigation undertaken by the publisher [1]. This investigation has uncovered evidence of one or more of the following indicators of systematic manipulation of the publication process:

(1) Discrepancies in scope
(2) Discrepancies in the description of the research reported
(3) Discrepancies between the availability of data and the research described
(4) Inappropriate citations
(5) Incoherent, meaningless and/or irrelevant content included in the article
(6) Peer-review manipulation

The presence of these indicators undermines our confidence in the integrity of the article's content and we cannot, therefore, vouch for its reliability. Please note that this notice is intended solely to alert readers that the content of this article is unreliable. We have not investigated whether authors were aware of or involved in the systematic manipulation of the publication process.

Wiley and Hindawi regrets that the usual quality checks did not identify these issues before publication and have since put additional measures in place to safeguard research integrity.

We wish to credit our own Research Integrity and Research Publishing teams and anonymous and named external researchers and research integrity experts for contributing to this investigation.

The corresponding author, as the representative of all authors, has been given the opportunity to register their agreement or disagreement to this retraction. We have kept a record of any response received.

References

[1] Z. Huang, X. Xu, and W. Cheng, "Deep Learning-Based Health Management Model Application in Extreme Myopia Eye Vision Monitoring and Risk Prediction," *Journal of Oncology*, vol. 2022, Article ID 4537021, 8 pages, 2022.

Hindawi
Journal of Oncology
Volume 2023, Article ID 9835164, 1 page
https://doi.org/10.1155/2023/9835164

Retraction

Retracted: Red Blood Cell Membrane-Camouflaged Gold Nanoparticles for Treatment of Melanoma

Journal of Oncology

Received 11 July 2023; Accepted 11 July 2023; Published 12 July 2023

This article has been retracted by Hindawi following an investigation undertaken by the publisher [1]. This investigation has uncovered evidence of one or more of the following indicators of systematic manipulation of the publication process:

(1) Discrepancies in scope
(2) Discrepancies in the description of the research reported
(3) Discrepancies between the availability of data and the research described
(4) Inappropriate citations
(5) Incoherent, meaningless and/or irrelevant content included in the article
(6) Peer-review manipulation

The presence of these indicators undermines our confidence in the integrity of the article's content and we cannot, therefore, vouch for its reliability. Please note that this notice is intended solely to alert readers that the content of this article is unreliable. We have not investigated whether authors were aware of or involved in the systematic manipulation of the publication process.

Wiley and Hindawi regrets that the usual quality checks did not identify these issues before publication and have since put additional measures in place to safeguard research integrity.

We wish to credit our own Research Integrity and Research Publishing teams and anonymous and named external researchers and research integrity experts for contributing to this investigation.

The corresponding author, as the representative of all authors, has been given the opportunity to register their agreement or disagreement to this retraction. We have kept a record of any response received.

References

[1] L. Zhao, H. Xie, and J. Li, "Red Blood Cell Membrane-Camouflaged Gold Nanoparticles for Treatment of Melanoma," *Journal of Oncology*, vol. 2022, Article ID 3514984, 11 pages, 2022.

Hindawi
Journal of Oncology
Volume 2023, Article ID 9832716, 1 page
https://doi.org/10.1155/2023/9832716

Retraction

Retracted: Analysis of Clinical Characteristics and Risk Factors of Postoperative Recurrence and Malignant Transformation of Low-Grade Glioma

Journal of Oncology

Received 11 July 2023; Accepted 11 July 2023; Published 12 July 2023

This article has been retracted by Hindawi following an investigation undertaken by the publisher [1]. This investigation has uncovered evidence of one or more of the following indicators of systematic manipulation of the publication process:

(1) Discrepancies in scope
(2) Discrepancies in the description of the research reported
(3) Discrepancies between the availability of data and the research described
(4) Inappropriate citations
(5) Incoherent, meaningless and/or irrelevant content included in the article
(6) Peer-review manipulation

The presence of these indicators undermines our confidence in the integrity of the article's content and we cannot, therefore, vouch for its reliability. Please note that this notice is intended solely to alert readers that the content of this article is unreliable. We have not investigated whether authors were aware of or involved in the systematic manipulation of the publication process.

Wiley and Hindawi regrets that the usual quality checks did not identify these issues before publication and have since put additional measures in place to safeguard research integrity.

We wish to credit our own Research Integrity and Research Publishing teams and anonymous and named external researchers and research integrity experts for contributing to this investigation.

The corresponding author, as the representative of all authors, has been given the opportunity to register their agreement or disagreement to this retraction. We have kept a record of any response received.

References

[1] C. Luo, Q. Luo, Y. Xu et al., "Analysis of Clinical Characteristics and Risk Factors of Postoperative Recurrence and Malignant Transformation of Low-Grade Glioma," *Journal of Oncology*, vol. 2022, Article ID 4948943, 11 pages, 2022.

Hindawi
Journal of Oncology
Volume 2023, Article ID 9815674, 1 page
https://doi.org/10.1155/2023/9815674

Retraction

Retracted: Screening of Key Prognosis Genes of Lung Adenocarcinoma Based on Expression Analysis on TCGA Database

Journal of Oncology

Received 11 July 2023; Accepted 11 July 2023; Published 12 July 2023

This article has been retracted by Hindawi following an investigation undertaken by the publisher [1]. This investigation has uncovered evidence of one or more of the following indicators of systematic manipulation of the publication process:

(1) Discrepancies in scope
(2) Discrepancies in the description of the research reported
(3) Discrepancies between the availability of data and the research described
(4) Inappropriate citations
(5) Incoherent, meaningless and/or irrelevant content included in the article
(6) Peer-review manipulation

The presence of these indicators undermines our confidence in the integrity of the article's content and we cannot, therefore, vouch for its reliability. Please note that this notice is intended solely to alert readers that the content of this article is unreliable. We have not investigated whether authors were aware of or involved in the systematic manipulation of the publication process.

Wiley and Hindawi regrets that the usual quality checks did not identify these issues before publication and have since put additional measures in place to safeguard research integrity.

We wish to credit our own Research Integrity and Research Publishing teams and anonymous and named external researchers and research integrity experts for contributing to this investigation.

The corresponding author, as the representative of all authors, has been given the opportunity to register their agreement or disagreement to this retraction. We have kept a record of any response received.

References

[1] Y. Shen, X. Tang, X. Zhou et al., "Screening of Key Prognosis Genes of Lung Adenocarcinoma Based on Expression Analysis on TCGA Database," *Journal of Oncology*, vol. 2022, Article ID 4435092, 13 pages, 2022.

Hindawi
Journal of Oncology
Volume 2023, Article ID 6037121, 14 pages
https://doi.org/10.1155/2023/6037121

Research Article

Hypoxia-Related lncRNA Prognostic Model of Ovarian Cancer Based on Big Data Analysis

Yu Zhang,[1] Jing Zhang,[1] Fei Wang,[1] and Le Wang[2]

[1]*Department of Gynecology, Shaanxi Provincial Peoples Hospital, Xi'an 710068, China*
[2]*Department of Neurology, Shaanxi Provincial Peoples Hospital, Xi'an 710068, China*

Correspondence should be addressed to Le Wang; wangle201209@163.com

Received 31 August 2022; Revised 26 September 2022; Accepted 3 October 2022; Published 7 April 2023

Academic Editor: Muhammad Muddassir Ali

Background. Hypoxia is regarded as a key factor in promoting the occurrence and development of ovarian cancer. In ovarian cancer, hypoxia promotes cell proliferation, epithelial to mesenchymal transformation, invasion, and metastasis. Long non-coding RNAs (lncRNAs) are extensively involved in the regulation of many cellular mechanisms, i.e., gene expression, cell growth, and cell cycle. *Materials and Methods*. In our study, a hypoxia-related lncRNA prediction model was established by applying LASSO-penalized Cox regression analysis in public databases. Patients with ovarian cancer were divided into two groups based on the median risk score. The survival rate was analyzed in the Cancer Genome Atlas (TCGA) and International Cancer Genome Consortium (ICGC) datasets, and the mechanisms were investigated. *Results*. Through the prognostic analysis of DElncRNAs (differentially expressed long non-coding RNAs), a total of 5 lncRNAs were found to be closely associated with OS (overall survival) in ovarian cancer patients. It was evaluated through Kaplan–Meier analysis that low-risk patients can live longer than high-risk patients (TCGA: $p = 1.302e - 04$; ICGC: $1.501e - 03$). The distribution of risk scores and OS status revealed that higher risk score will lead to lower OS. It was evaluated that low-risk group had higher immune score ($p = 0.0064$) and lower stromal score ($p = 0.00023$). *Conclusion*. It was concluded that a hypoxia-related lncRNA model can be used to predict the prognosis of ovarian cancer. Our designed model is more accurate in terms of age, grade, and stage when predicting the overall survival of the patients of ovarian cancer.

1. Introduction

Ovarian cancer is a type of malignant tumor that cannot be easily detected in the early stage and has a poor prognosis. There are many risk factors associated with its occurrence and development, i.e., family history of ovarian or breast cancer, obesity (BMI of 30 and above), genetic mutations, delayed menopause, fertility treatments, polycystic ovary syndrome, and smoking. The mortality rate of this type of tumor is ranked fifth among other female malignant tumors [1]. Due to the concealment of the incidence of ovarian cancer, more than half of the patients lost the opportunity for early diagnosis, which seriously affects its prognosis [2]. Surgery plus chemotherapy is a classic treatment for ovarian cancer. First-line maintenance therapy, including bevacizumab or PARP inhibitors, can prolong progression-free survival (PFS), which is different from OS [3, 4]. Therefore, it is necessary to explore more treatments to prolong the lifespan of ovarian cancer patients. At present, immunotherapy is the new major therapeutic tool of ovarian cancer. However, the effect of single immunotherapy for ovarian cancer is not obvious [5, 6].

When malignant tumors increase in their size, tumors gradually form a hypoxia environment, due to which the cancer cells undergo some adaptive changes, such as proliferation and angiogenesis [7]. The direct reaction of molecules to reverse hypoxia is to stabilize the HIFs. Otherwise, HIF can enhance cell viability and increase angiogenesis and cell invasion. HIF can help in the survival of cancer cells that can undergo apoptosis [8, 9]. Hypoxia can also alter the immune microenvironment of malignant tumors [10]. In ovarian cancer, hypoxia promotes cell

proliferation [11], epithelial to mesenchymal transformation, invasion, and metastasis [12]. The aforementioned phenomenon may lead to higher mortality of patients [13].

lncRNAs consist of more than 200 nucleotides and can interact with various kinds of biomolecules such as DNA, RNA, and proteins, which have attracted increasing attention. lncRNAs are extensively involved in the regulation of many important cellular processes, such as gene expression, dosage compensation, and regulation of the cell growth and cell cycle [14]. lncRNAs may play their role in the nucleus as well as in the cytoplasm. The lncRNAs can act as modulators to affect the protein-coding gene expression by regulating the transcriptional and post-transcriptional processes. As there is difference in expression of lncRNAs in various tissues, some of them have been identified for their implication in the pathogenesis of the diseases, such as tumor, neurological, cardiovascular, and orthopedic disease. Recent evidence suggests that lncRNAs precipitated the malignant phenotype of cancer through genomic or transcriptional changes. In addition to these changes, changing the immune environment may also promote the malignant phenotype [15, 16]. However, a study on hypoxia-related lncRNA in ovarian cancer is still need of the hour. Therefore, a hypoxia-related lncRNA model was established in our study. This model can be applied to pre-calculate the prognosis of ovarian cancer. More importantly, the immune status can be predicted by this model, which can act as a guiding tool for better clinical treatment.

2. Materials and Methods

2.1. Data Acquisition. TCGA database (TCGA-OV, 379 samples) (https://tcga-data.nci.nih.gov/tcga/) and the ICGC portal (OV-AU, 81 samples) (https://dcc.icgc.org) were used to extract the RNA sequence data. At the same time, the corresponding clinical features were also downloaded. One of the inclusion criteria of the study was that the patients must survive more than 30 days. The gene expression profiles of normal ovarian tissue as a controlled study were downloaded from the GTEx database (88 samples).

2.2. Obtention of Genes and lncRNAs That Are Related to Hypoxia. We downloaded 200 genes related to hypoxia (Table S1 *of GSEA)*. In TCGA database, using Pearson correlation ($|R| > 0.4$, $p < 0.001$), 1330 lncRNAs that have a relationship with hypoxia were selected. Then, the difference analysis was performed by a limma R package. To screen the hypoxia-related differentially expressed lncRNAs (DElncRNAs), we set the standard as (FDR) < 0.05 and $|\log2FC| \geq 1$.

2.3. Risk Scoring of Candidate Genes for Hypoxia-Related lncRNAs. To identify candidate genes for hypoxia-related lncRNAs from TCGA cohort, we analyzed OS by univariate Cox analysis. Firstly, we built the prognostic model using LASSO-penalized Cox regression analysis. The risk score was calculated using the following formula.

$$\text{RiskScore} = \sum(CoeCCL\text{lnc}RNACC \times \text{expressCConoCClncRNACC}). \quad (1)$$

Ovarian cancer patients were then categorized into two groups on the basis of median of TCGA cohort risk scores and named as high or low risk. PCA was performed with the "stats" R packages to explore the distribution of the groups. OS of the two groups was analyzed by Kaplan–Meier analysis. ROC curves with "survival ROC" R package were plotted for 1/3/5 years. Cox regression was utilized to predict the independent values. The above analyses were carried out simultaneously in TCGA and ICGC datasets. After that, the nomogram including risk, grade, stage, and age was set up by the "rms" R package. Finally, we plotted the correction curve to evaluate the difference between the predicted values and actual values.

2.4. GSEA. GSEA between the two groups was performed in the gene set with the parameter kegg.v7.4.symbols.gmt. To detect the significantly enriched pathways, the criterion was $p < 0.05$ and FDR < 0.05.

2.5. Immunity Analysis. The following methods were used to calculate the immune penetration status between TCGA project samples, including XCell, TIMER, QUANTISEQ, EPIC, CiberSort-ABS, and CiberSort. All these methods are in silico techniques that were used to integrate the advantages of gene enrichment. These are deconvolution techniques to reanalyze the data in comprehensive way [17, 18]. Meanwhile, we compared the TME scores between the two risk groups by the "ggpubr" R package.

2.6. Division of Clusters by Risk Model. Using the "Consensus Cluster Plus" R package, two molecular subgroups were grouped based on the prognostic model in ovarian cancer patients. Kaplan–Meier survival analysis, PCA, and tSNE were performed. In addition, analysis of immune-related indexes including immune infiltration cells and TME scores was carried out between the two molecular subgroups.

3. Results

3.1. Hypoxia-Related lncRNAs in Ovarian Cancer. In ovarian cancer, we identified 1330 hypoxia-related lncRNAs. The network of the hypoxia-related genes and lncRNAs is presented in Figure 1(a). There were a total of 145 hypoxia-related DElncRNAs, of which 111 lncRNAs were downregulated, and 34 were upregulated (Table S2). Through the prognostic analysis of DElncRNAs, a total of 5 lncRNAs were found closely associated with OS of ovarian cancer patients, serving as candidate lncRNAs for modeling (Figure 1(b)).

3.2. Evaluation of Prognostic Role of Hypoxia-Related lncRNAs by Risk Model. We constructed a risk model including 5 lncRNAs (DNM3OS, AC073046.1, AC083799.1, C6orf223, and

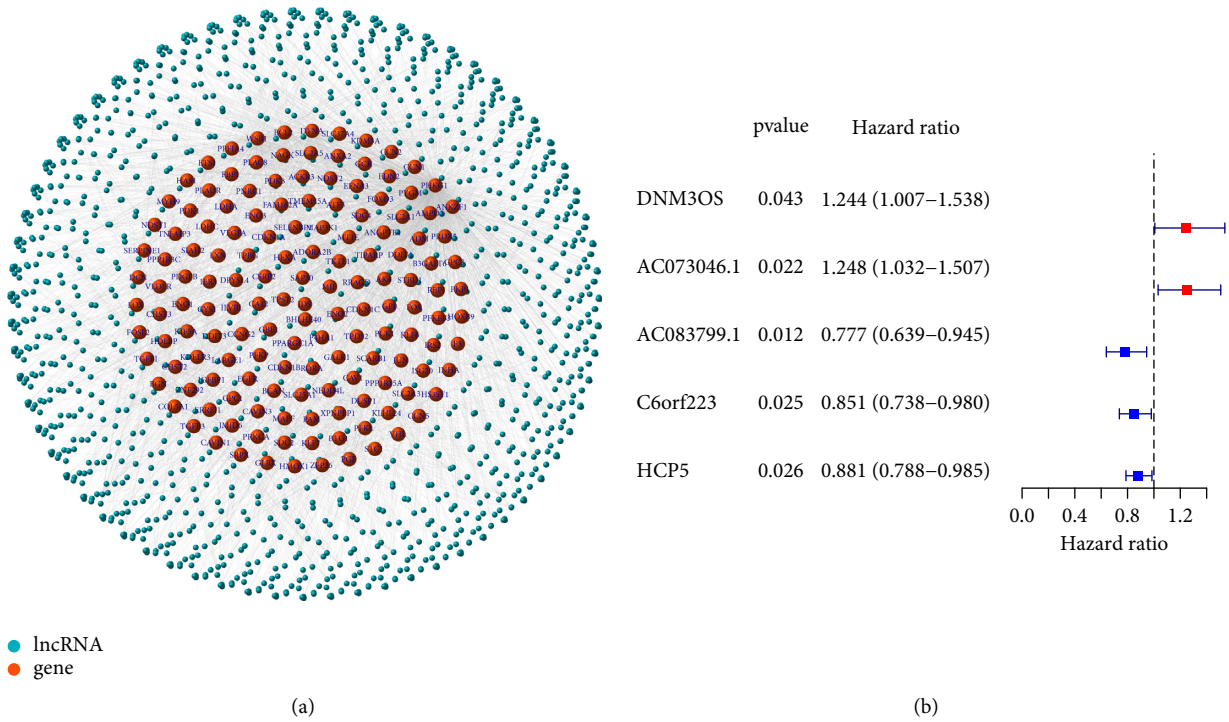

Figure 1: (a) The network of the hypoxia-related genes and lncRNAs. (b) DElncRNAs related to prognosis.

HCP5) in TCGA cohort. The formula we used to calculate the risk score is risk score = DNM3OS × 0.152 + AC073046.1 × 0.126-AC083799.1 × 0.184-C6orf223 × 0.097-HCP5 × 0.082. After calculations, we evaluated revisions to the risk models established in TCGA and ICGC databases. Kaplan–Meier analysis showed that low-risk patients can live longer than high-risk patients (TCGA: $p = 1.302e - 04$; ICGC: $1.501e - 03$) (Figures 2(a) and 2(b)). At the same time, we analyzed the OS time of patients in different clinical groups in TCGA dataset. There was no significant difference in OS time when patients were diagnosed with stage I-II or grade 1-2 ($p = 0.765, 0.651$). But, significant differences were observed in OS time for the stage III-IV group ($p < 0.001$), G3 group ($p < 0.001$), under 60 years ($p = 0.033$), and over 60 years ($p = 0.003$) (Figures 2(c)–2(h)).

In ROC curve analysis, the one-year AUC in TCGA cohort was 0.652, while the 3- and 5-year AUCs were 0.641 and 0.613, respectively (Figures 3(a) and 3(c)). The value of AUC in the ICGC cohort was calculated as 0.707, 0.626, and 0.626, respectively (Figures 3(b) and 3(d)). We also found that the model was more accurate in terms of age, grade, and stage when predicting the OS. The distribution of risk scores and OS status indicated that a higher risk score will lead to a lower OS (Figures 3(e)–3(h)).

When univariate Cox regression analysis was performed, core risk showed its association to OS. The HR value of TCGA cohort was 2.714 (95% CI = 1.652–4.458, $p > 0.001$). For the ICGC cohort, the HR value was 3.248 (95% CI = 1.189–8.869), and the p value was 0.022. (Figures 4(a) and 4(b)). Different from univariate analysis, multivariate analysis demonstrated an independent role of the risk score in predicting OS in the both cohorts. For TCGA cohort, the HR value was 2.574, 95% CI was 1.560 to 4.248, and the p value was 0.001. For the ICGC cohort, the HR value was 3.404 (95% CI = 1.123–10.324, $p = 0.030$) (Figures 4(c) and 4(d)). PCA verified that the predictive model could divide ovarian cancer patients into two different groups in two datasets (Figures 4(e) and 4(f)).

Finally, we used other factors including risk, grade, age, and stage to predict 1-/3-/5-year OS (Figure 5(a)). Calibration chart was used to judge whether the result of the nomogram is accurate (Figure 5(b)).

3.3. Cancer-Related Pathways Are Enriched. In the high-risk group, the pathways enriched in cancer-related pathways were adherens junction, TGF-beta, Wnt, Notch, GnRH signaling pathway, and glycerophospholipid metabolism. In the low-risk group, the pathways were enriched in oxidative phosphorylation, antigen processing, antigen presentation, graft-versus-host disease, metabolism related to glutathione, allograft rejection, and protein export (Figure 6).

3.4. Immune Scoring of Risks Groups Evaluated by GSEA. We further analyzed the immune status of the two groups with different risks in TCGA database. More M1 macrophages, myeloid dendritic, activated NK, and CD8 + T cells were detected in the low-risk group, while fewer cancer-associated fibroblasts (CAFs) and neutrophils were detected in the low-risk group (Figure 7(a), Supplementary 1). The low-risk group had a higher immune score ($p = 0.0064$) and a lower stromal score ($p = 0.00023$). However, the ESTIMATE score did not show significant differences between the two risk groups (Figures 7(b)–7(d)).

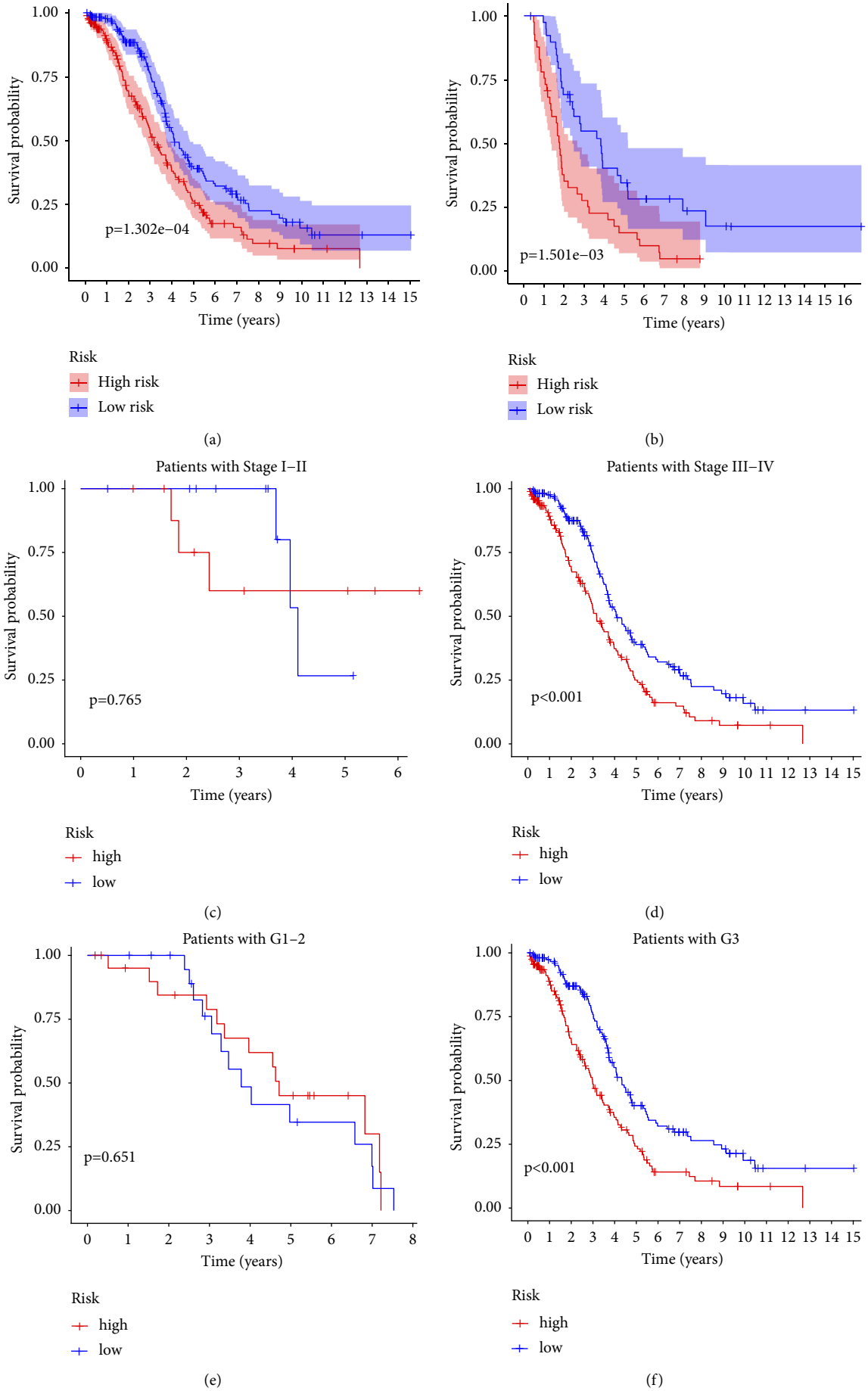

Figure 2: Continued.

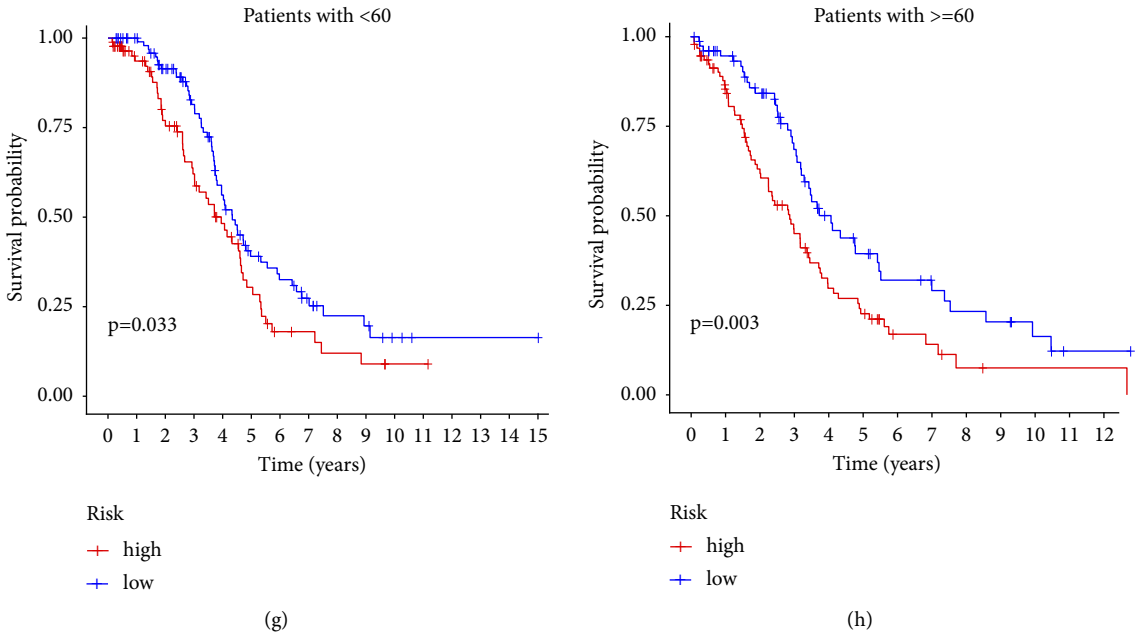

Figure 2: Kaplan–Meier analysis in TCGA cohort (a) and ICGC cohort (b). Kaplan–Meier analysis of the OS time in different clinical groups in TCGA cohort ((c, d) stage; (e, f) grade; (g, h) age).

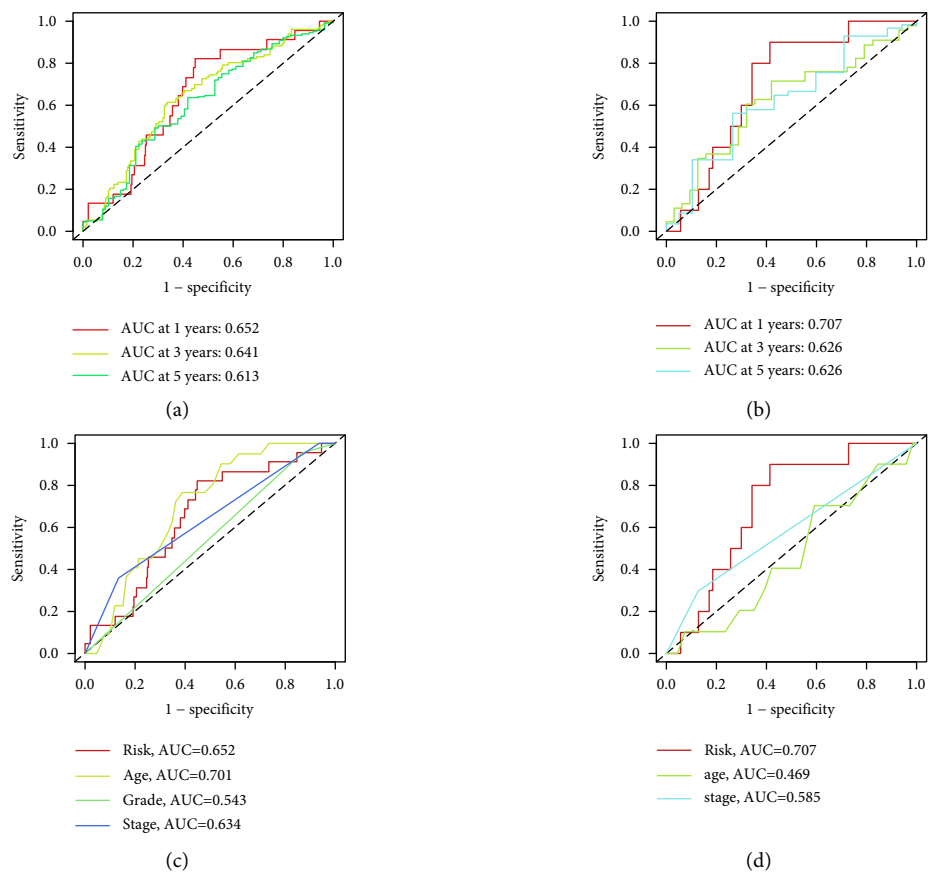

Figure 3: Continued.

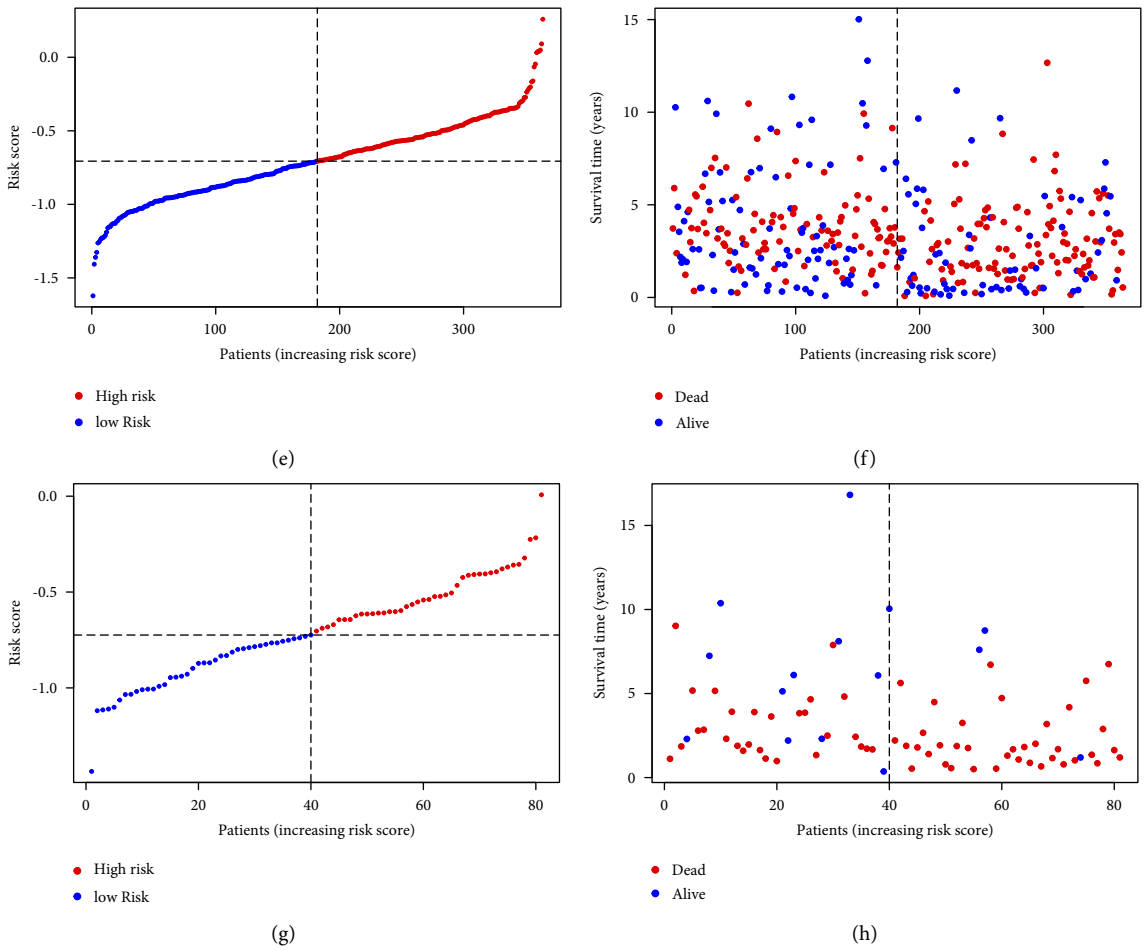

Figure 3: (a, b) ROC curve analysis of 1/3/5 years (a) in TCGA cohort (b) in ICGC cohort, (c, d) ROC curve analysis of risk sore and other clinicopathological features in (c) TCGA cohort, (d) ICGC cohort, (e) distribution of risk scores, (f) survival status, in the TCGA database, distribution of (g) risk scores, and (h) survival status in the ICGC database.

3.5. Analyses Related to Molecular Subtype. Based on this hypoxia-related lncRNA model, we redivided ovarian cancer patients into two clusters (Figure 8(a)). The OS of cluster1 patients was shorter than cluster2 patients (Figure 8(b)). Most of the patients of cluster2 were in the low-risk group, while most patients of cluster1 were in the high-risk group (Figure 8(c)). PCA and tSNE2 clearly showed that patients can be grouped as two completely various subgroups (Figures 8(d) and 8(e)).

Cluster1 showed lower stromal score ($p = 0.0071$) (Figure 9(a)), lower immune score ($p = 1.2e - 14$) (Figure 9(b)), and lower ESTIMATE score ($p = 7.7e - 09$) (Figure 9(c)).

The heatmap of immune cells was drawn by using the following methods, including TIMER, CIBERSORT, CIBERSORT-ABS, QUANTISEQ, MCPCOUNTER, XCELL, and EPIC. All the graphs are presented in Figure 10.

4. Discussion

Ovarian cancer is a malignant disease that cannot be cured completely. Surgery, chemotherapy, and targeted therapy are the most commonly used methods for its treatment nowadays, but the prognosis remains poor [19, 20]. Many research studies have evaluated that hypoxia-related lncRNAs are involved in the progression of various cancers. Hypoxic regions are commonly found in solid tumors, and the appearance of these regions often harms the progression of tumors and triggers tumor immunosuppression and may affect the therapeutic response. However, the underlying mechanism is not fully understood. In our study, hypoxia-related lncRNA was selected as the standard to subgroup patients with various risks. Patients in different groups have different prognoses and different immune statuses. This model can help the clinicians to classify and individualize the treatment of ovarian cancer patients and inspire researchers to gain insight into the important role of hypoxia-related lncRNAs in ovarian cancer.

Hypoxia can change the repair mechanism of DNA [21], promote tumorigenesis [22] and metastasis [23, 24], and lead to the development of cancer stem cells [25, 26], which are resistant to chemotherapy and radiotherapy [27, 28]. Therefore, the relationship between hypoxia and cancer needs further study, including hypoxia-related coding genes and non-coding genes. However, it is reported that DNA damage is not induced by hypoxia; instead this hypoxia leads

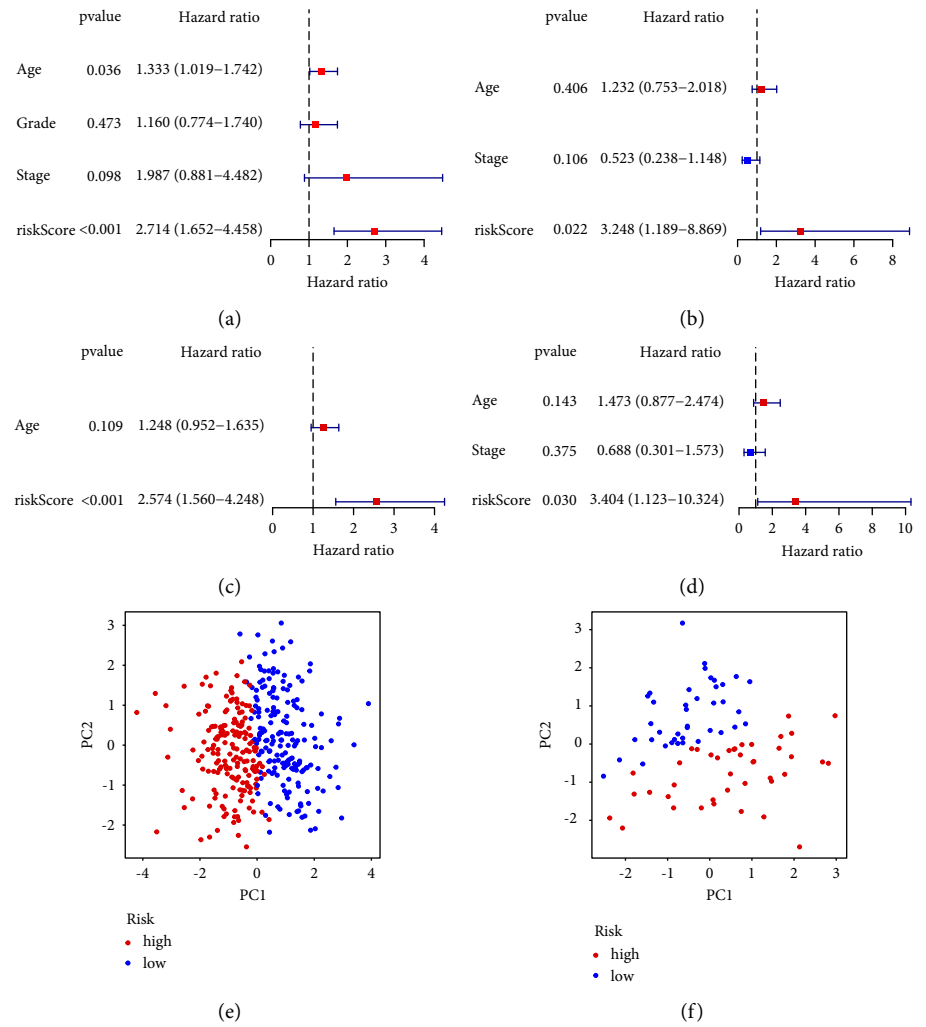

Figure 4: (a) Univariate Cox regression analysis in TCGA database. (b) Regression analysis in ICGC database. Multivariate Cox regression analysis in (c) TCGA database and (d) ICGC database. PCA in (e) TCGA dataset or (f) ICGC dataset.

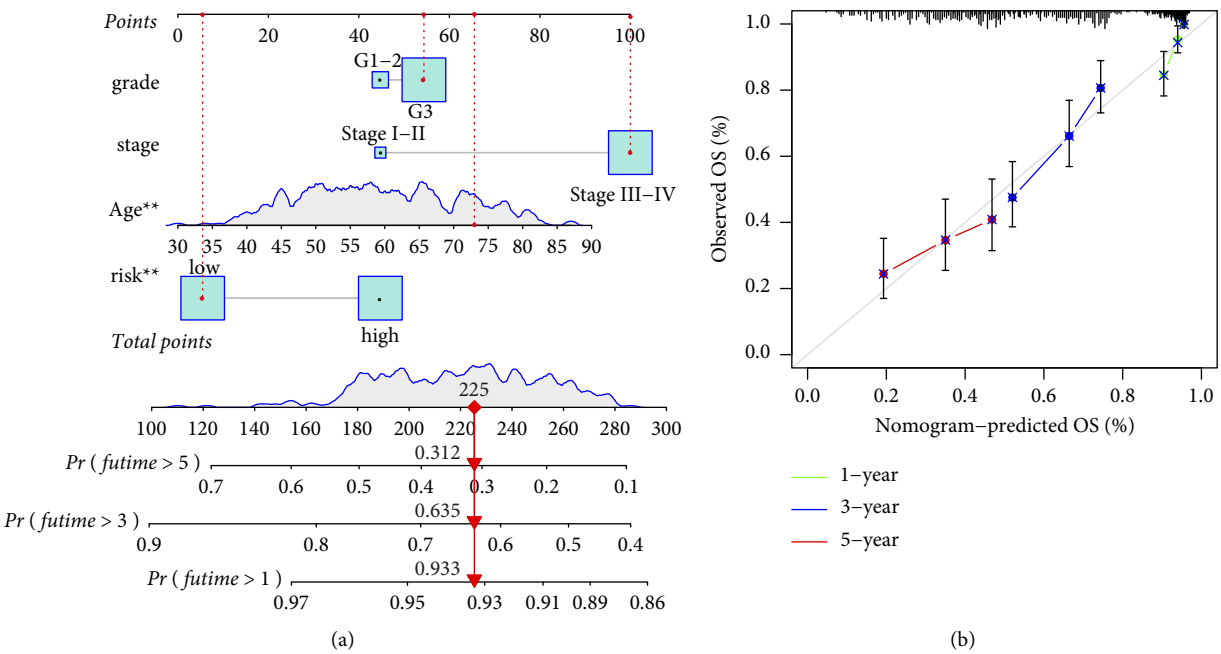

Figure 5: (a) Construction of nomogram including the prognostic hypoxia-related lncRNA signature and clinicopathological features. (b) The correction curve predicted the value of the nomogram in predicting prognosis.

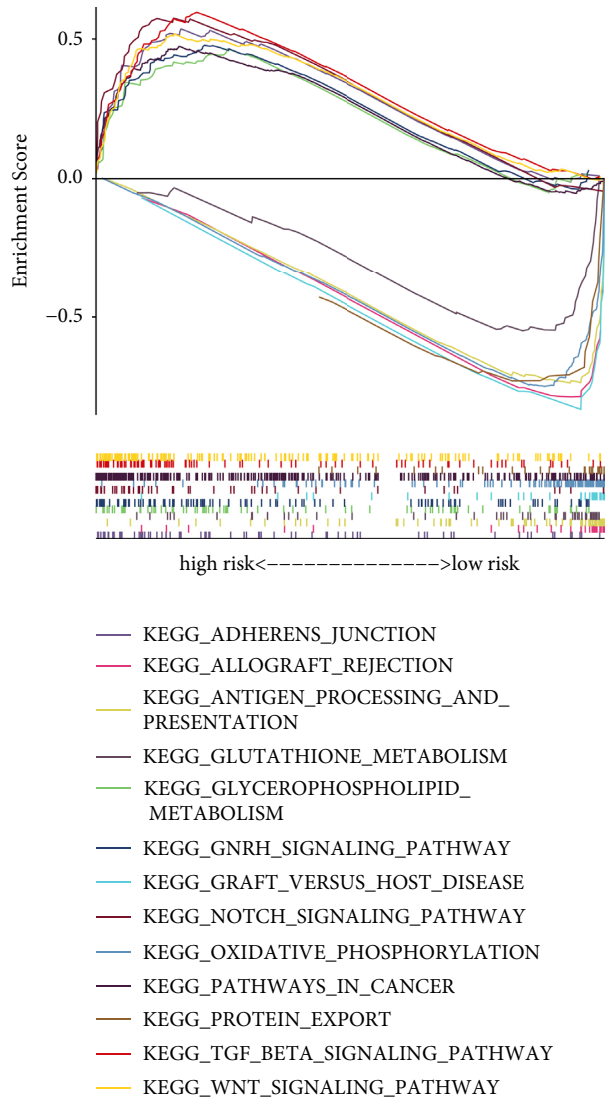

Figure 6: GSEA of the prognostic hypoxia-related lncRNA signature.

to some genomic instabilities [21]. The modeling of hypoxia-related lncRNA to stratify patients with malignant tumors has been a concern by some scholars. For example, related research has been carried out on hepatocellular cancer and renal cell cancer [29, 30]. In our study, a prognostic model consisting of five lncRNA was constructed, including DNM3OS, AC073046.1, AC083799.1, C6orf223, and HCP5. DNM3OS was overexpressed in ovarian cancer and facilitated ovarian cancer progression, and its high expression might lead to a poor prognosis [31]; the conclusion is similar to our research. At the same time, the role of DNM3OS in other malignant tumors has been confirmed. Tumor-associated mesenchymal stem cells can target DNM3OS, leading to the progression of hepatocellular cancer [32]. In retinoblastoma, the DNM3OS-miR-134-5p-SMAD6 axis can promote cell proliferation, migration, and the EMT process [33]. DNM3OS can also promote tumor progression in gastric cancer [34] and oral cancer [35]. HCP5 has been studied in several kinds of tumors, including ovarian [36], esophageal [37], gastric [38], and colorectal cancer [39]. It has been demonstrated that HCP5 can target miR-525-5p/PRC1 signaling pathway and can target the Wnt/beta-catenin pathway [36]. Other types of lncRNAs are presented for the first time, through our study.

In the high-risk group, enriched Wnt, Notch, TGF-beta, and tumor-related pathways were found. It has been regarded as one of the leading factors of high mortality in the high-risk group. Wnt/beta-catenin pathway played an important role in ovarian cancer cells' carcinogenesis, stemness, and resistance ability against chemotherapy [40]. The hyperactivation of the Wnt signaling pathway mediated some drug resistance in ovarian cancer, such as olaparib [41]. The synergistic effect of Wnt and Notch signaling pathway can promote the proliferation of cancer cells and further increase the migration of cancer cells [42]. Studies have shown that the Notch pathway is closely related to angiogenesis and chemotherapy resistance of ovarian cancer [43, 44]. The Notch signal pathway was regarded as the characteristic of enriched ovarian cancer stem cells induced by hypoxia [45]. TGFβ pathway also facilitates epithelial-

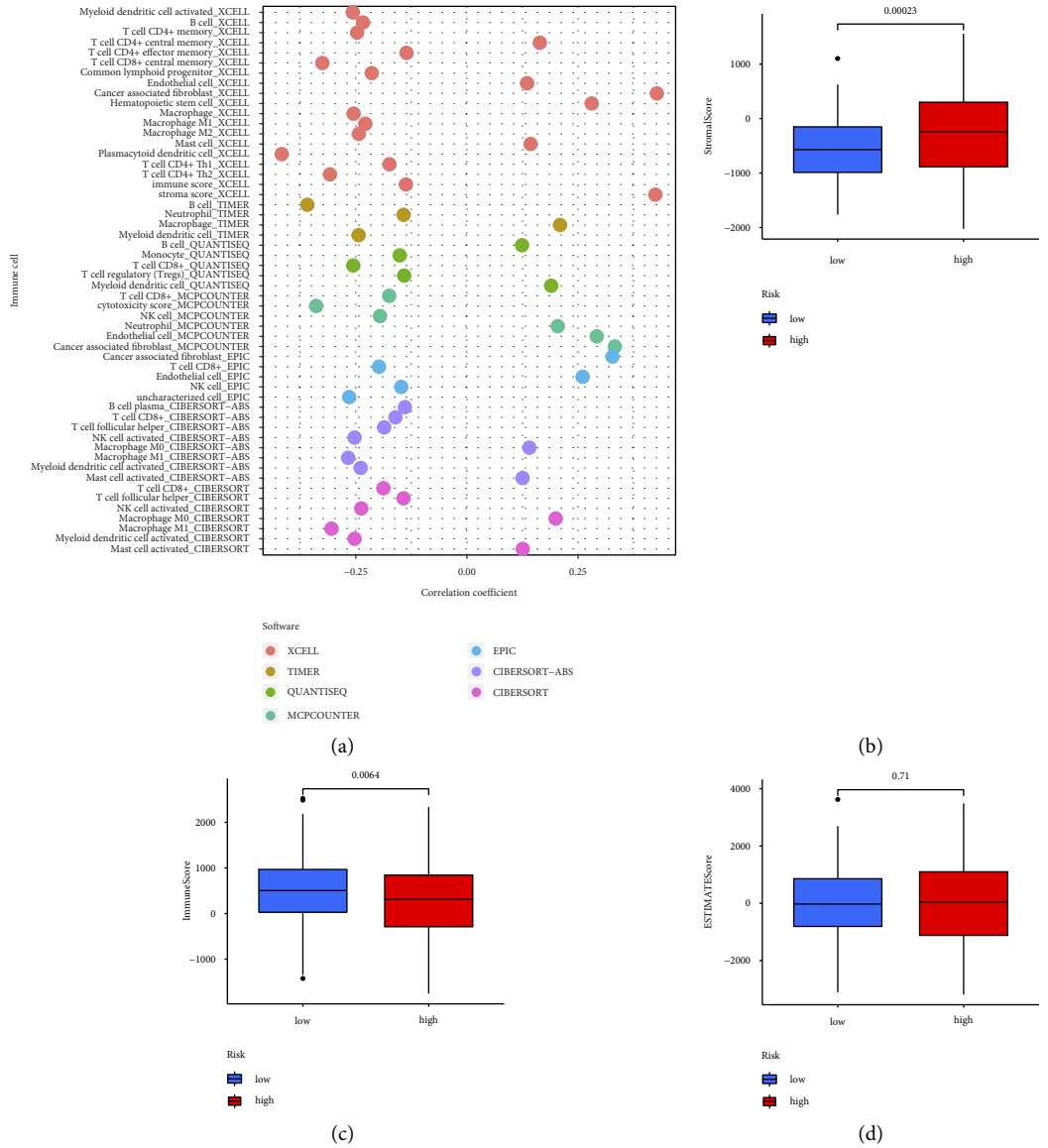

Figure 7: (a) The immune infiltration status of the risk model. (b, c, d) TME scores in different risk groups.

mesenchymal transition (EMT) of epithelial ovarian cancer (EOC) [46].

Hypoxia can promote the development of malignant tumors, including ovarian cancer. At the same time, ascites can also induce hypoxia [47]. One reason is that the function of anti-tumor immune cells is inhibited in a hypoxia environment [10]. Therefore, the immune environment of the two groups was compared. More M1 macrophages, myeloid dendritic cells, activated NK cells, and CD8 + T cells were detected in the low-risk group, while less cancer-associated fibroblasts (CAFs) and neutrophils were detected in the low-risk group. M1 macrophages have an anti-tumor effect, while M2 macrophages can promote tumor [48]. M2 macrophages were also closely related to the progression of cancer cells [49]. We found higher M1/M2 values in the low-risk group, which did not differ from previous findings, and patients with higher M1/M2 values lived longer [50]. Dendritic cells can activate T cells such as CD4+ and CD8+ cells to fight tumors by presenting an antigen [51, 52]. Other studies have shown that NK cells had abilities that could lead to ovarian cancer cell death, and they often co-infiltrate with CD8 + T cells [53]. CD8 + T cells are quite important in anti-tumor immunity, and further, we can predict patients' OS [54]. In ovarian cancer, CAF may lead to deterioration and drug resistance of the ovarian cancer [55]. Regarding the former research, ovarian tumors are generally regarded as cold tumors, which pose a challenge to the treatment. The immune activity of patients in the low-risk group tends to be "hot" and may be sensitive to immunotherapy, which provides new opportunities for patients.

lncRNAs play many roles in cancer diagnosis and treatment, but the most important role of these RNAs is to control gene expression and regulate many important biological processes in the body, such as proliferation, genome stability,

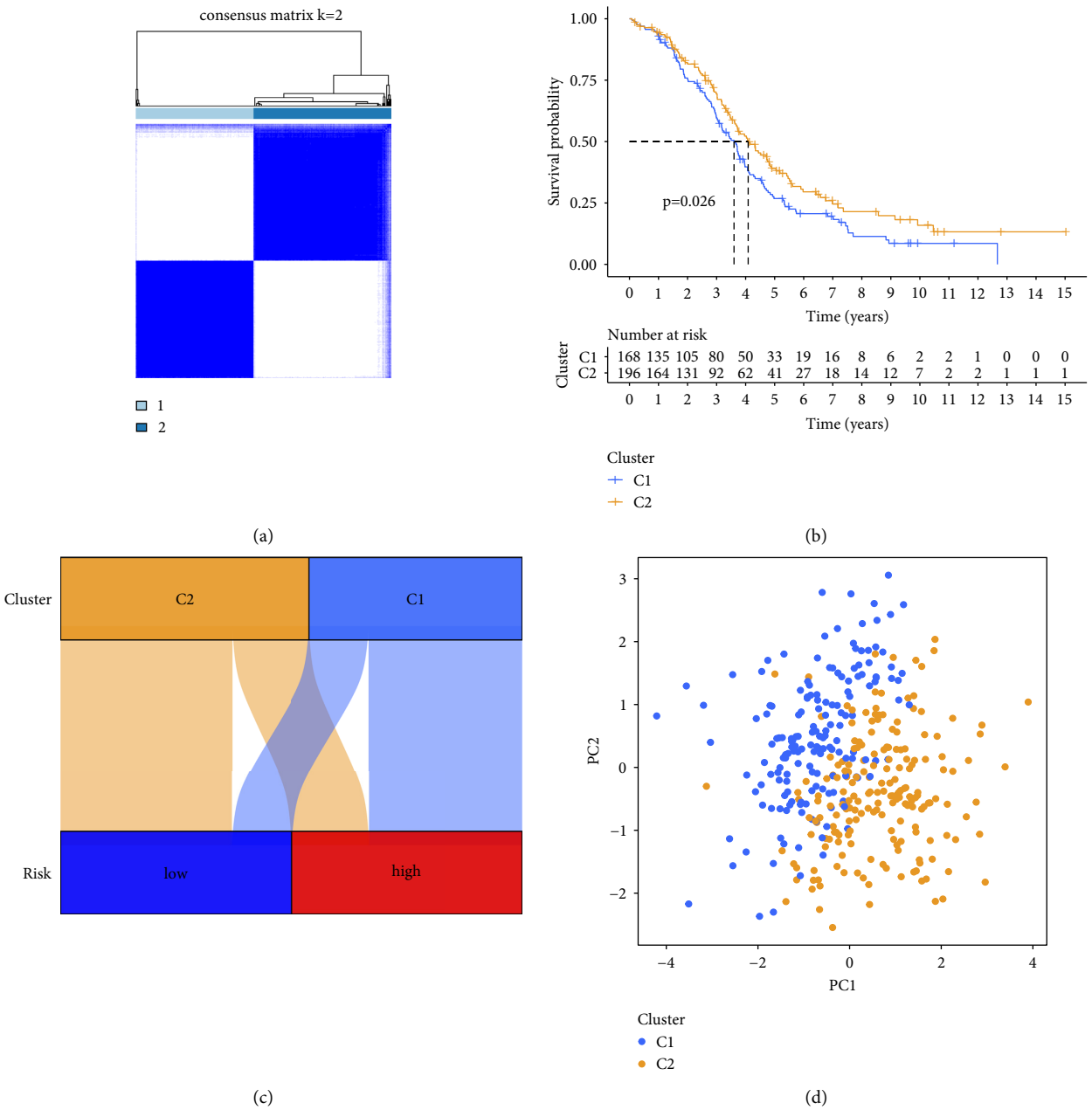

Figure 8: Continued.

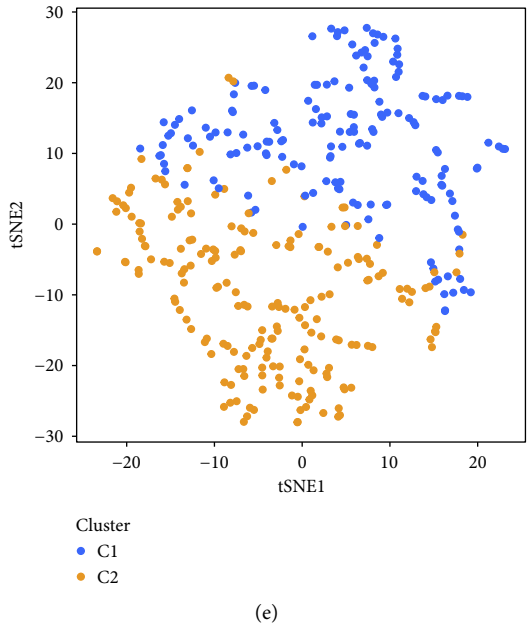

(e)

Figure 8: (a) Molecular subgroups according to according to the prognostic model. (b) Kaplan–Meier survival analysis of the two clusters. (c) The relationship between clusters and risk groups. PCA (d) and tSNE2 (e) of the two clusters.

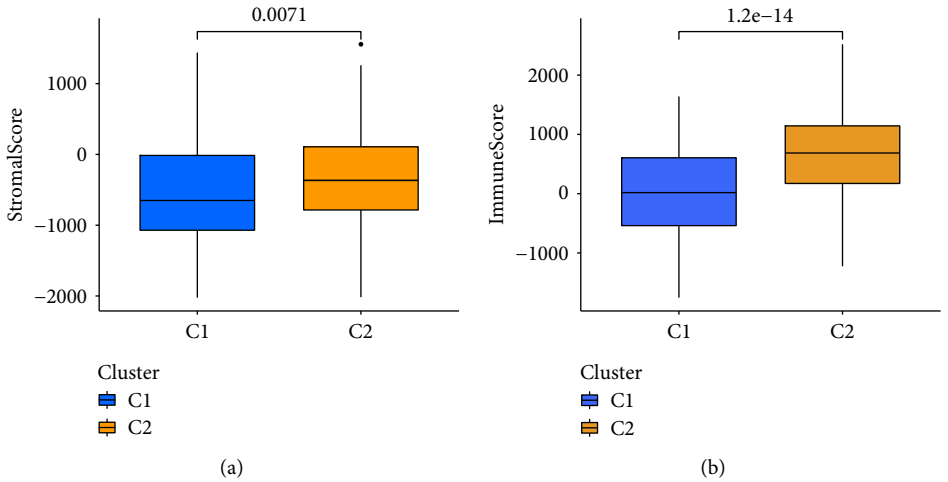

(a) (b)

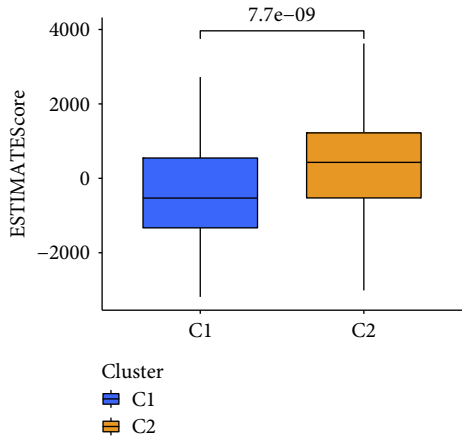

(c)

Figure 9: TME scores of the two clusters. (a) Stromal score of C1 and C2. (b) Immune score of C1 and C2. (c) ESTIMATE score of both clusters.

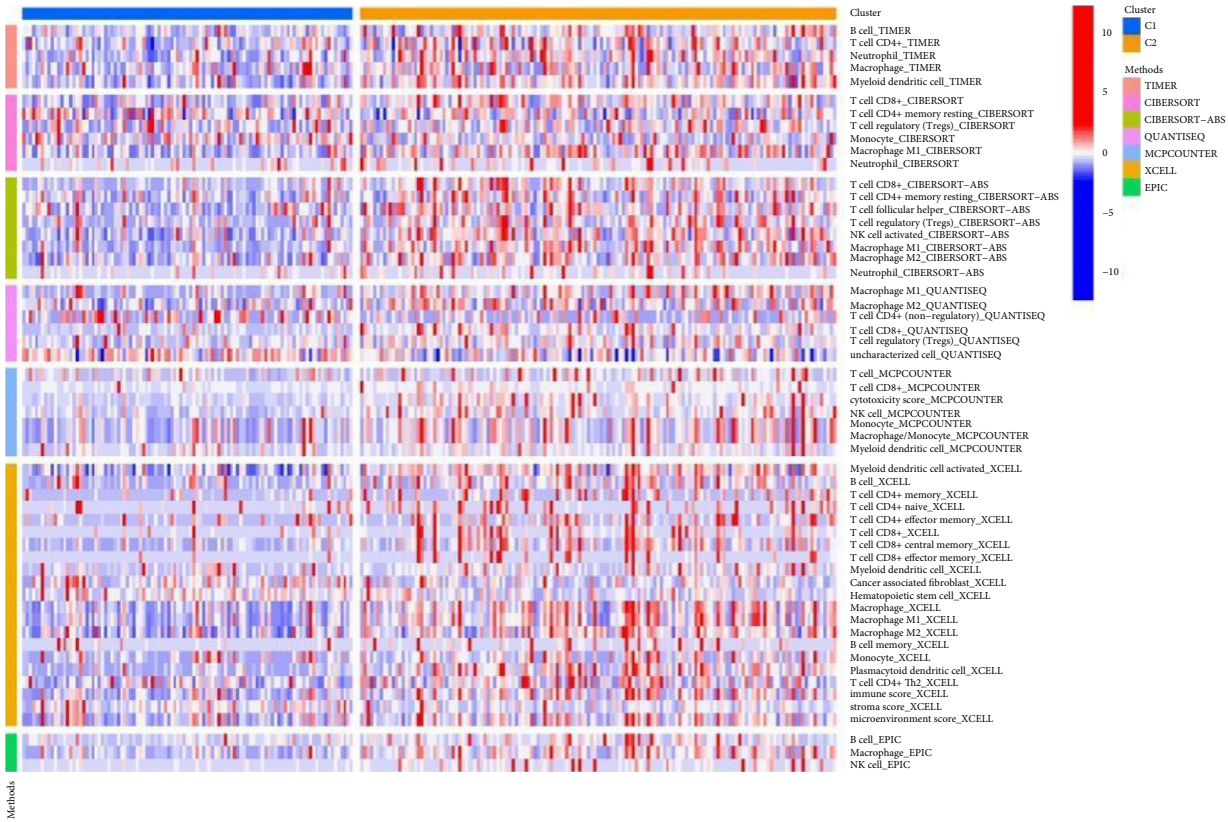

Figure 10: The heatmap of immune infiltration of the two clusters.

apoptosis, pyrolysis, autophagy, and immunity, and dysregulation of these functions contributes to the progression of many tumors. We can conclude that the model is verified in the external dataset; the model can be further stratified through analysis of patients with different clinicopathological characteristics, which can provide more accurate guidance for clinical treatment. The limitation of study is that there is no experimental verification of lncRNA in the model. The reason is that it is impossible to accumulate enough fresh tissue specimens for survival analysis in a short period.

5. Conclusion

It was concluded the hypoxic microenvironment is closely related to the occurrence and development of ovarian cancer. Our established hypoxia-related lncRNA model can be applied to pre-calculate the prognosis of ovarian cancer. In addition, the immune status can be predicted using this model. Our result indicates that the hypoxia-related lncRNA model can serve as a guiding tool for better clinical treatment of ovarian cancer.

Data Availability

TCGA database can be found at https://tcga-data.nci.nih.gov/tcga/, and the ICGC database can be found at https://dcc.icgc.org.

Conflicts of Interest

The authors declare that they have no conflicts of interest.

Authors' Contributions

LW designed the study. YZ and JZ collected and integrated the data. YZ, JZ, and FW performed the data analysis. YZ drafted the manuscript. JZ, FW, and LW critically reviewed the manuscript. All authors have read and agreed to the published version of the manuscript.

Acknowledgments

This study was supported by the Natural Science Foundation of Shaanxi Province (nos. 2021JQ-913 and 2021JQ-912), the Science and Technology Development Incubator Foundation of Shaanxi Provincial People's Hospital (no. 2022YJY-45), and the Scientific and Technological Talents Support Program of Shaanxi Provincial People's Hospital (no. 2022JY-33).

Supplementary Materials

Table S1: 200 hypoxia-related genes were downloaded from Gene Set Enrichment Analysis (hallmark-hypoxia). Table S2: 145 hypoxia-related DElncRNAs (differentially expressed lncRNAs). Supplementary 1 (a, b): correlation between

immune infiltrating cells and risk score. (*Supplementary Materials*)

References

[1] R. L. Siegel, K. D. Miller, and A. Jemal, "Cancer statistics," *CA: A Cancer Journal for Clinicians*, vol. 69, no. 1, pp. 7–34, 2019.

[2] S. S. Buys, E. Partridge, A. Black, and T. Chen, "Effect of screening on ovarian cancer mortality: the prostate, lung, colorectal and ovarian (PLCO) cancer screening randomized controlled trial," *JAMA*, vol. 305, no. 22, pp. 2295–2303, 2011.

[3] A. González-Martín, B. Pothuri, I. Vergote et al., "Niraparib in patients with newly diagnosed advanced ovarian cancer," *New England Journal of Medicine*, vol. 381, no. 25, pp. 2391–2402, 2019.

[4] I. Ray-Coquard, P. Pautier, S. Pignata et al., "Olaparib plus bevacizumab as first-line maintenance in ovarian cancer," *New England Journal of Medicine*, vol. 381, no. 25, pp. 2416–2428, 2019.

[5] J. Hamanishi, M. Mandai, T. Ikeda et al., "Safety and antitumor activity of anti-PD-1 antibody, nivolumab, in patients with platinum-resistant ovarian cancer," *Journal of Clinical Oncology*, vol. 33, no. 34, pp. 4015–4022, 2015.

[6] E. Ghisoni, M. Imbimbo, S. Zimmermann, and G. Valabrega, "Ovarian cancer immunotherapy: turning up the heat," *International Journal of Molecular Sciences*, vol. 20, no. 12, p. 2927, 2019.

[7] X. Jing, F. Yang, C. Shao et al., "Role of hypoxia in cancer therapy by regulating the tumor microenvironment," *Molecular Cancer*, vol. 18, no. 1, p. 157, 2019.

[8] L. Iommarini, A. M. Porcelli, G. Gasparre, and I. Kurelac, "Non-canonical mechanisms regulating hypoxia-inducible factor 1 alpha in cancer," *Frontiers Oncology*, vol. 7, p. 286, 2017.

[9] D. Singh, R. Arora, P. Kaur, B. Singh, R. Mannan, and S. Arora, "Overexpression of hypoxia-inducible factor and metabolic pathways: possible targets of cancer," *Cell & Bioscience*, vol. 7, no. 1, p. 62, 2017.

[10] L. Chen, A. Endler, and F. Shibasaki, "Hypoxia and angiogenesis: regulation of hypoxia-inducible factors via novel binding factors," *Experimental & Molecular Medicine*, vol. 41, no. 12, pp. 849–857, 2009.

[11] A. Y. S. Law and C. K. C. Wong, "Stanniocalcin-2 is a HIF-1 target gene that promotes cell proliferation in hypoxia," *Experimental Cell Research*, vol. 316, no. 3, pp. 466–476, 2010.

[12] Y. Yang, S. Yin, S. Li, Y. Chen, and L. Yang, "p>Stanniocalcin 1 in tumor microenvironment promotes metastasis of ovarian cancer</p>," *OncoTargets and Therapy*, vol. 12, pp. 2789–2798, 2019.

[13] R. Osada, A. Horiuchi, N. Kikuchi et al., "Expression of hypoxia-inducible factor 1α, hypoxia-inducible factor 2α, and von Hippel–Lindau protein in epithelial ovarian neoplasms and allelic loss of von Hippel-Lindau gene: nuclear expression of hypoxia-inducible factor 1α is an independent prognostic factor in ovarian carcinoma," *Human Pathology*, vol. 38, no. 9, pp. 1310–1320, 2007.

[14] C. Klec, F. Prinz, and M. Pichler, "Involvement of the long noncoding RNA NEAT1 in carcinogenesis," *Mol Oncol*, vol. 13, no. 1, pp. 46–60, 2019.

[15] M. K. Atianand, D. R. Caffrey, and K. A. Fitzgerald, "Immunobiology of long noncoding RNAs," *Annual Review of Immunology*, vol. 35, no. 1, pp. 177–198, 2017.

[16] Y. G. Chen, A. T. Satpathy, and H. Y. Chang, "Gene regulation in the immune system by long noncoding RNAs," *Nature Immunology*, vol. 18, no. 9, pp. 962–972, 2017.

[17] T. Li, J. Fan, B. Wang et al., "TIMER: a web server for comprehensive analysis of tumor-infiltrating immune cells," *Cancer Research*, vol. 77, no. 21, pp. 108–e110, 2017.

[18] D. Aran, A. J. Butte, and A. J. Butte, "Cell: digitally portraying the tissue cellular heterogeneity landscape," *Genome Biology*, vol. 17, no. 1, pp. 175–214, 2016.

[19] D. K. Armstrong, R. D. Alvarez, J. N. Bakkum-Gamez et al., "Ovarian cancer, version 2.2020, NCCN clinical practice guidelines in oncology," *Journal of the National Comprehensive Cancer Network*, vol. 19, no. 2, pp. 191–226, 2021.

[20] S. Morand, M. Devanaboyina, H. Staats, L. Stanbery, and J. Nemunaitis, "Ovarian cancer immunotherapy and personalized medicine," *International Journal of Molecular Sciences*, vol. 22, no. 12, p. 6532, 2021.

[21] A. R. Kaplan and P. M. Glazer, "Impact of hypoxia on DNA repair and genome integrity," *Mutagenesis*, vol. 35, no. 1, pp. 61–68, 2020.

[22] M. Tafani, B. Pucci, A. Russo et al., "Modulators of HIF1α and NFkB in cancer treatment: is it a rational approach for controlling malignant progression?" *Frontiers in Pharmacology*, vol. 4, p. 13, 2013.

[23] G. Fluegen, A. Avivar-Valderas, Y. Wang et al., "Phenotypic heterogeneity of disseminated tumour cells is preset by primary tumour hypoxic microenvironments," *Nature Cell Biology*, vol. 19, no. 2, pp. 120–132, 2017.

[24] A. Chen, J. Sceneay, N. Gödde et al., "Intermittent hypoxia induces a metastatic phenotype in breast cancer," *Oncogene*, vol. 37, no. 31, pp. 4214–4225, 2018.

[25] T. Muinao, H. P. Deka Boruah, and M. Pal, "Diagnostic and Prognostic Biomarkers in ovarian cancer and the potential roles of cancer stem cells - an updated review," *Experimental Cell Research*, vol. 362, pp. 1–10, 2018.

[26] C. Corrò and H. Moch, "Biomarker discovery for renal cancer stem cells," *The Journal of Pathology: Clinical Research*, vol. 4, no. 1, pp. 3–18, 2018.

[27] K. Graham and E. Unger, "Overcoming tumor hypoxia as a barrier to radiotherapy, chemotherapy and immunotherapy in cancer treatment," *International Journal of Nanomedicine*, vol. 13, pp. 6049–6058, 2018.

[28] Y. Kato, M. Yashiro, Y. Fuyuhiro et al., "Effects of acute and chronic hypoxia on the radiosensitivity of gastric and esophageal cancer cells," *Anticancer Research*, vol. 31, no. 10, pp. 3369–3375, 2011.

[29] P. Tang, W. Qu, T. Wang et al., "Identifying a hypoxia-related long non-coding RNAs signature to improve the prediction of prognosis and immunotherapy response in hepatocellular carcinoma. Carcinoma," *Frontiers in Genetics*, vol. 12, p. 785185, Article ID 785185, 2021.

[30] H. Chen, Y. Pan, X. Jin, and G. Chen, "Identification of a four hypoxia-associated long non-coding RNA signature and establishment of a nomogram predicting prognosis of clear cell renal cell carcinoma," *Frontiers Oncology*, vol. 11, p. 713346, Article ID 713346, 2021.

[31] L. He and G. He, "DNM3OS facilitates ovarian cancer progression by regulating miR-193a-3p/MAP3K3 Axis," *Yonsei Medical Journal*, vol. 62, no. 6, pp. 535–544, 2021.

[32] W. Wang, Q. Wang, D.-B. Huang et al., "Tumor-associated mesenchymal stem cells promote hepatocellular carcinoma metastasis via a DNM3OS/KDM6B/TIAM1 axis," *Cancer Letters*, vol. 503, pp. 19–31, 2021.

[33] H. Wang and X. Ji, "SMAD6, positively regulated by the DNM3OS-miR-134-5p axis, confers promoting effects to cell proliferation, migration and EMT process in retinoblastoma," *Cancer Cell International*, vol. 20, no. 1, p. 23, 2020.

[34] S. Wang, B. Ni, Z. Zhang et al., "Long non-coding RNA DNM3OS promotes tumor progression and EMT in gastric cancer by associating with Snail," *Biochemical and Biophysical Research Communications*, vol. 511, no. 1, pp. 57–62, 2019.

[35] X. Fang, Z. Tang, H. Zhang, and H. Quan, "Long non-coding RNA DNM3OS/miR-204-5p/HIP1 axis modulates oral cancer cell viability and migration," *Journal of Oral Pathology & Medicine*, vol. 49, no. 9, pp. 865–875, 2020.

[36] L. Wang, M. He, L. Fu, and Y. Jin, "Role of lncRNAHCP5/microRNA-525-5p/PRC1 crosstalk in the malignant behaviors of ovarian cancer cells," *Experimental Cell Research*, vol. 394, no. 1, p. 112129, Article ID 112129, 2020.

[37] Y. Guo, L. Wang, H. Yang, and N. Ding, "Knockdown long non-coding RNA HCP5 enhances the radiosensitivity of esophageal carcinoma by modulating AKT signaling activation," *Bioengineered*, vol. 13, no. 1, pp. 884–893, 2022.

[38] M. Gao, L. Liu, Y. Yang, M. Li, Q. Ma, and Z. Chang, "LncRNA HCP5 induces gastric cancer cell proliferation, invasion, and EMT processes through the miR-186-5p/wnt5a Axis under hypoxia," *Frontiers in Cell and Developmental Biology*, vol. 9, p. 663654, Article ID 663654, 2021.

[39] N. Bai, Y. Ma, J. Zhao, and B. Li, "<p>Knockdown of lncRNA HCP5 Suppresses the Progression of Colorectal Cancer by miR-299-3p/PFN1/AKT Axis</p&gt," *Cancer Management and Research*, vol. 12, pp. 4747–4758, 2020.

[40] M. Koni, V. Pinnarò, and M. F. Brizzi, "The Wnt signalling pathway: a tailored target in cancer," *International Journal of Molecular Sciences*, vol. 21, no. 20, p. 7697, 2020.

[41] T. M. Yamamoto, A. McMellen, Z. L. Watson et al., "Activation of Wnt signaling promotes olaparib resistant ovarian cancer," *Molecular Carcinogenesis*, vol. 58, no. 10, pp. 1770–1782, 2019.

[42] S. Bocchicchio, M. Tesone, and G. Irusta, "Convergence of Wnt and Notch signaling controls ovarian cancer cell survival," *Journal of Cellular Physiology*, vol. 234, no. 12, pp. 22130–22143, 2019.

[43] J. A. Perez-Fidalgo, B. Ortega, S. Simon, E. P. Samartzis, and S. Boussios, "NOTCH signalling in ovarian cancer angiogenesis," *Annals of Translational Medicine*, vol. 8, no. 24, p. 1705, 2020.

[44] M. Akbarzadeh, S. Akbarzadeh, and M. Majidinia, "Targeting Notch signaling pathway as an effective strategy in overcoming drug resistance in ovarian cancer," *Pathology, Research & Practice*, vol. 216, no. 11, p. 153158, Article ID 153158, 2020.

[45] E. J. Seo, D. K. Kim, I. H. Jang et al., "Hypoxia-NOTCH1-SOX2 signaling is important for maintaining cancer stem cells in ovarian cancer," *Oncotarget*, vol. 7, no. 34, pp. 55624–55638, 2016.

[46] A. Kumari, Z. Shonibare, M. Monavarian et al., "TGFβ signaling networks in ovarian cancer progression and plasticity," *Clinical & Experimental Metastasis*, vol. 38, no. 2, pp. 139–161, 2021.

[47] B. A. Runyon, "Patients with deficient ascitic fluid opsonic activity are predisposed to spontaneous bacterial peritonitis," *Hepatology*, vol. 8, no. 3, pp. 632–635, 1988.

[48] Y.-c Huang and Z. P Feng, "The good and bad of microglia/macrophages: new hope in stroke therapeutics therapeutics," *Acta Pharmacologica Sinica*, vol. 34, no. 1, pp. 6-7, 2013.

[49] X. Yuan, J. Zhang, D. Li et al., "Prognostic significance of tumor-associated macrophages in ovarian cancer: a meta-analysis," *Gynecologic Oncology*, vol. 147, no. 1, pp. 181–187, 2017.

[50] M. Zhang, Y. He, X. Sun et al., "A high M1/M2 ratio of tumor-associated macrophages is associated with extended survival in ovarian cancer patients," *Journal of Ovarian Research*, vol. 7, no. 1, p. 19, 2014.

[51] A. M. Dudek, S. Martin, A. D. Garg, and P. Agostinis, "Immature, semi-mature, and fully mature dendritic cells: toward a DC-cancer cells interface that augments anticancer immunity," *Frontiers in Immunology*, vol. 4, p. 438, 2013.

[52] T. R. Mempel, S. E. Henrickson, and U. H. Von Andrian, "T-cell priming by dendritic cells in lymph nodes occurs in three distinct phases," *Nature*, vol. 427, no. 6970, pp. 154–159, 2004.

[53] J. S. Hoogstad-van Evert, R. Bekkers, N. Ottevanger, J. H. Jansen, L. Massuger, and H. Dolstra, "Harnessing natural killer cells for the treatment of ovarian cancer," *Gynecologic Oncology*, vol. 157, no. 3, pp. 810–816, 2020.

[54] G. Zhang, Q. Xu, X. Zhang et al., "Spatial cytotoxic and memory T cells in tumor predict superior survival outcomes in patients with high-grade serous ovarian cancer," *Cancer Medicine*, vol. 10, no. 12, pp. 3905–3918, 2021.

[55] W. Sun and S. Fu, "Role of cancer-associated fibroblasts in tumor structure, composition and the microenvironment in ovarian cancer," *Oncology Letters*, vol. 18, no. 3, pp. 2173–2178, 2019.

Hindawi
Journal of Oncology
Volume 2023, Article ID 4643792, 19 pages
https://doi.org/10.1155/2023/4643792

Research Article

Prediction of the Prognosis of Clear Cell Renal Cell Carcinoma by Cuproptosis-Related lncRNA Signals Based on Machine Learning and Construction of ceRNA Network

Zhiliang Xiao,[1] **Menglei Zhang**,[2] **Zhenduo Shi**,[3] **Guanghui Zang**,[3] **Qing Liang**,[3] **Lin Hao**,[3] **Yang Dong**,[3] **Kun Pang**,[3] **Yabin Wang**,[1] **and Conghui Han**[1,3]

[1]*School of Medicine, Jiangsu University, Zhenjiang, China*
[2]*Department of Obstetrics and Gynecology, The First Affiliated Hospital of Nanchang University, Nanchang, China*
[3]*Department of Urology, The Affiliated School of Clinical Medicine of Xuzhou Medical University, Xuzhou Central Hospital, Xuzhou, China*

Correspondence should be addressed to Conghui Han; 100338@yzpc.edu.cn

Received 8 September 2022; Revised 26 October 2022; Accepted 24 November 2022; Published 13 March 2023

Academic Editor: Muhammad Muddassir Ali

Background. Clear cell renal cell carcinoma's (ccRCC) occurrence and development are strongly linked to the metabolic reprogramming of tumors, and thus far, neither its prognosis nor treatment has achieved satisfying clinical outcomes. *Methods*. The Cancer Genome Atlas (TCGA) and Gene Expression Omnibus (GEO) databases, respectively, provided us with information on the RNA expression of ccRCC patients and their clinical data. Cuproptosis-related genes (CRGS) were discovered in recent massive research. With the help of log-rank testing and univariate Cox analysis, the prognostic significance of CRGS was examined. Different cuproptosis subtypes were identified using consensus clustering analysis, and GSVA was used to further investigate the likely signaling pathways between various subtypes. Univariate Cox, least absolute shrinkage and selection operator (Lasso), random forest (RF), and multivariate stepwise Cox regression analysis were used to build prognostic models. After that, the models were verified by means of the C index, Kaplan–Meier (K-M) survival curves, and time-dependent receiver operating characteristic (ROC) curves. The association between prognostic models and the tumor immune microenvironment as well as the relationship between prognostic models and immunotherapy were next examined using ssGSEA and TIDE analysis. Four online prediction websites-Mircode, MiRDB, MiRTarBase, and TargetScan-were used to build a lncRNA-miRNA-mRNA ceRNA network. *Results*. By consensus clustering, two subgroups of cuproptosis were identified that represented distinct prognostic and immunological microenvironments. *Conclusion*. A prognostic risk model with 13 CR-lncRNAs was developed. The immune microenvironment and responsiveness to immunotherapy are substantially connected with the model, which may reliably predict the prognosis of patients with ccRCC.

1. Introduction

CCRCC is the most prevalent subtype of renal malignancy, accounting for nearly 70% of all cases [1]. In addition, it exhibits higher rates of recurrence, metastasis, and mortality when compared to chromophobe cell renal carcinoma (cRCC) and papillary renal cell carcinoma (pRCC) [2, 3]. Due to the insidious nature of ccRCC, 30% of patients have metastases when they are first diagnosed [4]. Currently, partial or radical nephrectomy is the best treatment option for nonmetastatic ccRCC patients, but this procedure has a postoperative recurrence rate that can range from 20 to 40%, which has a substantial impact on patient prognosis [5]. In addition, radiation and chemotherapy frequently have poor results for patients with metastatic ccRCC, and drug resistance brought on by prolonged medication frequently results in a terrible prognosis. Despite the fact that immunotherapies such as programmed death-1 (PD-1) and programmed death ligand 1 (PD-L1) have been employed in the treatment of ccRCC recently and have demonstrated

some therapeutic results, some patients still do not respond well to this course of action [6, 7].

According to previous research, copper can induce tumor angiogenesis, which aids in the progression of cancer, as well as be directly linked to the occurrence and growth of a variety of malignancies [8–10]. Besides that, certain outcomes have been attained previously based on the use of copper ion chelators in the therapy of cancer [11, 12]. The key to pathological and physiological processes is cell death, and cuproptosis is the most recent type of death that differs from previous cell deaths such as apoptosis [13], necrosis [14], and ferroptosis [15]. According to the research, iron-sulfur cluster protein loss and fatty acylated protein aggregation are induced by copper binding to tricarboxylic acid (TCA) cycle fatty acyl proteins, which results in death from toxic protein stress [16]. In this regard, it is worth noting that studies have shown that the occurrence and development of ccRCC frequently involve reprogramming of the TCA cycle. This is primarily accomplished by affecting the upregulation of the VHL/HIF pathway, which results in the inhibition of the TCA cycle, thereby promoting the occurrence and development of ccRCC [17–19]. In view of this, the cuproptosis theory may provide a novel approach to the therapy of ccRCC.

Long noncoding RNA (LncRNA) is a subclass of noncoding RNAs that can take part in and control a number of pathophysiological processes. lncRNA is a noncoding RNA whose biological function is more than 209 bases long. Similar to coding genes, lncRNAs can be chromatin reprogrammed. Dysregulation and posttranscriptional regulation of enhancers are widely involved in biological, physiological, and pathological processes. As a newly discovered class of RNA molecules, several lncRNAs have been identified as biomarkers of cancer, which control tumor proliferation, immune evasion, cell death resistance, and regional or distant metastasis. Therefore, lncRNA represents an important improvement in our understanding of copper worm disease and evidence that lncRNA is a therapeutic target that can induce GC copper Fibrobacteres. However, the specific role of lncRNA in the adjustment of aeruginosa is largely unknown. By controlling metabolic reprogramming, lncRNA can regulate carcinogenesis [20]. Additionally, studies have shown that lncRNAs play a variety of roles in the development of ccRCC, including upregulating lncRNA PVT1 and activating the HIF2α pathway to promote the growth and progression of ccRCC cells, as well as lncRNA HCG18, which promotes ccRCC migration and transfer by modulating the miR-152-3/RAB14 axis [21, 22]. LncRNA can also be used to predict the progression of ccRCC [23, 24]. In a recent study, it was found that CRGS is linked to immune infiltration and the immune checkpoint PD-1, which can help predict how well ccRCC patients would fare and offer new information about how to treat the disease [25]. Nevertheless, there is still a lack of knowledge about the mechanism of action of CR-lncRNA in ccRCC, particularly its influence on prognosis. This study investigated the function of CR-lncRNA in ccRCC and developed a new prognostic model based on CR-lncRNA, which may offer fresh perspectives for future studies on ccRCC and patient-specific management.

The proposed CR-lncRNA-based prognostic model includes the following advantages. (1) Due to the discrete Fourier transform data, its main information components are concentrated in the low-frequency part of the frequency domain, and the high-frequency part is mainly secondary information or noise. Therefore, the lengthening lncRNA sequence can be truncated into a fixed-length vector by intercepting the fixed-length part of the low frequency. (2) Two traditional convolutional models were used vgg16_bn build task models with Resnet18. Firstly, to adapt the data dimension, the commonly used two-dimensional convolution and pooling are adjusted to one-dimensional convolution and pooling. At the same time, since the label data are a twenty-four-dimensional data, the task model is extended to a multioutput model. LncRNA tissue-specific analysis was performed on multiple output regression, multiple output classification, and multilabel classification, respectively.

2. Methods and Materials

2.1. Data Collection. A recent significant study investigated the cuproptosis subtypes and built a predictive model to improve the prognosis of patients with CRC. Gene expression data were downloaded from the TCGA database to identify distinct molecular subtypes using a nonnegative matrix factorization algorithm [16]. Samples with a survival time of less than 30 days were disregarded as we downloaded the gene expression profile data, clinical information data, mutation data, and copy number variation (CNV) data of ccRCC from the TCGA official website. Finally, 71 normal samples and 511 tumor samples were comprised. The GEO database provided the CRGS gene expression profile in ccRCC. Gene count values were employed for differential analysis, and for downstream analysis, count values were converted to log2 (TPM +1) values.

2.2. Analysis of Genetic Mutation Data of CRGS. The TCGA Kidney Renal Clear Cell Carcinoma (TCGA-KIRC) cohort was used to investigate the differences in CRGS expression between normal and malignant samples. These discrepancies in gene expression were then re-examined in the GSE53757 and GSE40435 cohorts. We further confirmed them using the immunohistochemistry results of proteins in the Human Protein Atlas (HPA) database to assess their alterations in protein expression. The location of these genes on different chromosomes was visualized using the "RCircos" package, the "maftools" package was used to plot the mutational landscape of these genes, and finally, univariate COX regression analysis and log-rank test were performed to investigate the impact of these genes on the prognosis of ccRCC patients.

2.3. Consensus Clustering Analysis Based on CRGS. Using the "ConsensusClusterPlus" R package, we performed unsupervised clustering of the ccRCC samples based on the expression patterns of the 19 CRGS. To ensure the stability of the clusters, 1000 random repeated samplings were carried out on 80% of the samples and all genes. The Euclidean

distance clustering algorithm was selected. The appropriate number of clusters was established through using cumulative distribution function (CDF) and intra-group correlation. To confirm the discriminating of various subtypes, principal component analysis (PCA) was utilized. The variations in survival among various subtypes were then shown using K-M survival curves, and the log-rank test was used to determine whether the differences were statistically significant.

2.4. Identification of Molecular Characteristics, Immune Infiltration Characteristics, and Immunotherapeutic Response Based on Different Subtypes. The "GSVA" package was used to study the pathways implicated in various subtypes through gene set variation analysis (GSVA). To further investigate the differences in immune infiltration features across distinct subtypes, the infiltration abundance of diverse immune cells in different subtypes was estimated using the single sample genes enrichment analysis (ssGSEA) algorithm of the aforementioned R package. The tumor immune dysfunction and exclusion (TIDE) approach, which was developed in recent years, can be used to anticipate whether immunotherapy will benefit tumor patients. This research thorough investigation of hundreds of distinct tumor expression profiles looked for indicators to predict whether patients would respond to immune checkpoint blockade (ICB) therapy, i.e., a higher TIDE score indicates a lower likelihood of responding to immunotherapy [26]. The website it created (https://tide.dfci.harvard.edu/) was subsequently used to forecast the immunotherapy response in patients from different subtypes. The results of the analysis were visualized using the R packages "tinyarray," "pheatmap," and "ggplot2." Statistical significance was set at a P-value <0.05.

2.5. Differential Analysis of mRNA, lncRNA, and MicroRNA. The three approaches of "Edger," "DESeq2," and "limma" were utilized to produce the overlapping mRNAs, lncRNAs, and microRNAs (miRNAs), which were then employed as the differential genes. $|\text{Log2fold change}| > 1$ and false discovery rate (FDR) < 0.05 were the screening criteria thresholds for the approaches described above.

2.6. WGCNA Identifies Cuproptosis-Related Modules. The "WGCNA" R package was used to conduct the WGCNA analysis of the lncRNAs from the ccRCC samples. According to the scale-free network criteria, the best soft threshold was chosen. The modules with distances of less than 0.25 were then combined, and the minimum number of genes for the modules was set at 30. The modules having the strongest association with cuproptosis were chosen for further analysis after a correlation analysis between the modules and cuproptosis phenotypic data was completed.

2.7. Construction and Evaluation of Prognostic Risk Scoring Models. The R package "Caret" was used to first randomly divide the ccRCC samples in the TCGA queue into training and test sets in a ratio of 7 : 3. The training set and test set are used to train and test the model, respectively, to create a stable model. After intersecting the differential lncRNA of the ccRCC with the lncRNA in the module most associated with cuproptosis discovered by the aforementioned WGCNA, a univariate Cox regression analysis and log-rank test were carried out. Subsequently, lncRNAs with a P value <0.05 obtained by both of the above two test methods were considered as candidate lncRNAs. We selected characteristic genes using two machine learning approaches, namely, Lasso regression and RF, to avoid the overfitting of the model. A well-known machine learning technique called lasso regression decreases the dimensionality of high-dimensional data by assigning each feature a penalty coefficient that makes the coefficient of unimportant features 0 and therefore eliminates collinearity across features. Is frequently employed to tune the COX proportional hazards model (CPH) [27]. Studies have proven that RF can also be used to model survival analyses, and a minimal depth (MD) strategy has also been developed to identify key prognostic characteristics, and recent studies have pointed out that tree-based machine learning methods outperform deep learning in dealing with tabular data [28–30]. The overlapping lncRNAs chosen by the two machine learning methods above were subjected to multivariate stepwise Cox regression analysis, and the best CPH model was found according to the Akaike information criterion (AIC) criteria, which states that the smaller the AIC value, the better the model's performance [31]. The performance and precision of the model in the training set were assessed by using the time-dependent ROC curve and the C-index, and the performance of the risk score as an independent prognostic indicator was confirmed utilizing univariate and multivariate Cox regression analysis. In order to more thoroughly assess the performance of our prognostic model, we gathered a number of lncRNA-based prognostic risk scoring models developed based on the TCGA-KIRC cohort in recent years, computed the time-dependent ROC curve and C index of the lncRNA model based on the entire TCGA-KIRC cohort, and compared them with our developed prognostic model [32–37].

2.8. Construction of Competing Endogenous RNA (ceRNA) Network. We predicted the target miRNAs of these lncRNAs by applying the mircode website (https://mircode.org/download.php) based on the overlapping lncRNAs identified by the aforementioned univariate Cox analysis and log-rank test. The resulting target miRNAs were crossed with the differential miRNAs and then submitted to miRDB (https://mirdb.org/), miRTarBase (https://mirtarbase.cuhk.edu.cn/), and targets can (https://www.targetscan.org/). The target mRNAs of the aforementioned miRNAs were predicted by the three websites in turn. The final target mRNAs were chosen based on predictions made simultaneously by the three websites' predicted targets. We created a lncRNA-miRNA-mRNA ceRNA network in the Cytoscape based on the above predicted results.

2.9. Functional Enrichment Analysis. Using the LNCSEA online platform (https://bio.liclab.net/LncSEA/), the functional enrichment analysis of the aforementioned prognostic CR-lncRNAs was carried out [38]. Functional enrichment annotation of CR-lncRNA target miRNAs was performed using the miEAA online tool (https://ccb-compute2.cs.uni-saarland.de/mieaa2/) [39]. In order to investigate the probable biological pathways of patients in different risk groups, we simultaneously performed gene set enrichment analysis (GSEA) on patients in high- and low-risk groups using the R package "clusterProfiler." The adjusted *P*value <0.05 and *q* value <0.05 were used to identify statistically significant enriched pathways.

2.10. Immunotherapy Response Prediction and Drug Sensitivity Analysis. ICB therapy has now been proven to be beneficial for some tumor patients, although the majority of patients do not gain from it, which may be partially attributed to tumor heterogeneity and varied immune checkpoint expression. In order to determine whether patients might benefit from immunotherapy, we compared the immune checkpoint expression between high- and low-risk patients. We then used the TIDE website to estimate the immunotherapy response for ccRCC patients in different risk groups. Sensitive anticancer drugs were examined using the "pRRophetic" R package for two risk groups. The Wilcoxon rank test was used to analyze differences between various risk groups, and a *P* value lower than 0.05 was regarded as statistically significant.

2.11. Statistical Analysis. R software was used to perform all analyses (version 4.1.2). The association analysis of two categorical variables and the sample rate (composition ratio) of two or more groups were both compared using the chi-square test. To determine whether there were any differences in the distribution of measurement data or grade data between the two groups, a Wilcoxon rank-sum test was utilized. The Kruskal–Wallis test was used for nonparametric comparisons when there were three or more groups. For correlation testing in the correlation analysis, Spearman, and distance correlation tests were employed. The statistical significance was defined as a *P* value of 0.05, where * denotes *P* value <0.05, ** denotes *P* value <0.01 and *** denotes *P* value <0.001, and ns denotes no statistical significance.

3. Results

3.1. Landscape of Genetic Mutations in CRGS. The 19 CRGS were acquired through recent significant scientific discoveries [16]. Following that, differential analysis of the previously mentioned genes in the TCGA cohort revealed that, with the exception of LIPT1, LIPT2, and ATP7A, which revealed no statistically significant differences, the expression of the majority of CRGS differed significantly between normal and tumor samples and most of them were downregulated (Figure 1(a)). Next, the expression levels of these CRGS were checked again in the two GEO cohorts, GSE40435 and GSE53757, and although the results were slightly different from the TCGA cohort, the general results were similar (Figures 1(b) and 1(c)). It is common knowledge that proteins carry out the majority of biological processes in humans. To this end, we further assessed the variance in these genes protein expression in the HPA database between tumor and normal tissues. The outcomes demonstrated that most genes expressed differently at the protein level as well (Figure 1(f)). The findings from the K-M survival curve were similar to those from the univariate Cox analysis, with the exception that CDKN2A and GCSH were risk factors, whereas the remaining genes were protective (Figure 1(d)). The somatic mutation rate of each CRGS was incredibly low, and just 23 (6.44%) of 357 ccRCC samples showed genetic alterations, according to our analysis of somatic mutations in these genes (Figure 1(e)). Figure 1(f) demonstrates that the majority of CRGS have low CNV frequencies. The frequency of copy number deletions is almost 9% for only PDHB. On the chromosome, CRGS is located, as shown in Figure 1(c). We hypothesized that the genetic variation in ccRCC is largely stable because both somatic mutations and CNV frequencies had very small sample sizes. Of course, additional elements such as methylation and histone modifications might also be at work. According to the aforementioned findings, CRGS has a significant impact on the prognosis of ccRCC patients as well as the occurrence and progression of cancer.

3.2. Identification of Molecular Subtypes Based on CRGS. We used the "ConsensusClusterPlus" R package, a consensus clustering method based on a machine learning algorithm, to perform unsupervised clustering of ccRCC patients-based on the expression levels of the 19 CRGS. Finally, as shown in Figures 2(a) and 2(b), we were able to distinguish the cuproptosis molecules into two optimum clusters, A and B, each of which had 335 and 176 samples, respectively. Based on the abovementioned results, we can infer that patients in clusters A and B reflect two distinct cuproptosis phenotypes, with cluster A presenting the activating subtype of cuproptosis and cluster B representing the suppressing subtype. The PCA results demonstrated good discrimination between the two distinct subtypes (Figure 2(c)). A subsequent study of survival analysis revealed that patients in cluster A had significantly higher overall survival (OS) than those in cluster B (Figure 2(d)). For the two subtypes, GSVA analysis identified separate underlying biological processes and pathways (Figure 2(e)). The pathways DNA repair, Myc targets, Reactive Oxygen Species pathway, and Kras Signaling pathway, which are typically linked to tumor development and tumor immune inflammation, were significantly enriched in patients in cluster B compared with patients in cluster A. Therefore, the reason that cluster B patients have a poor prognosis may be due to the activation of the aforementioned pathways. However, the spermatogenesis, pancreas beta cells, heme metabolism, and androgen response of patients in cluster A

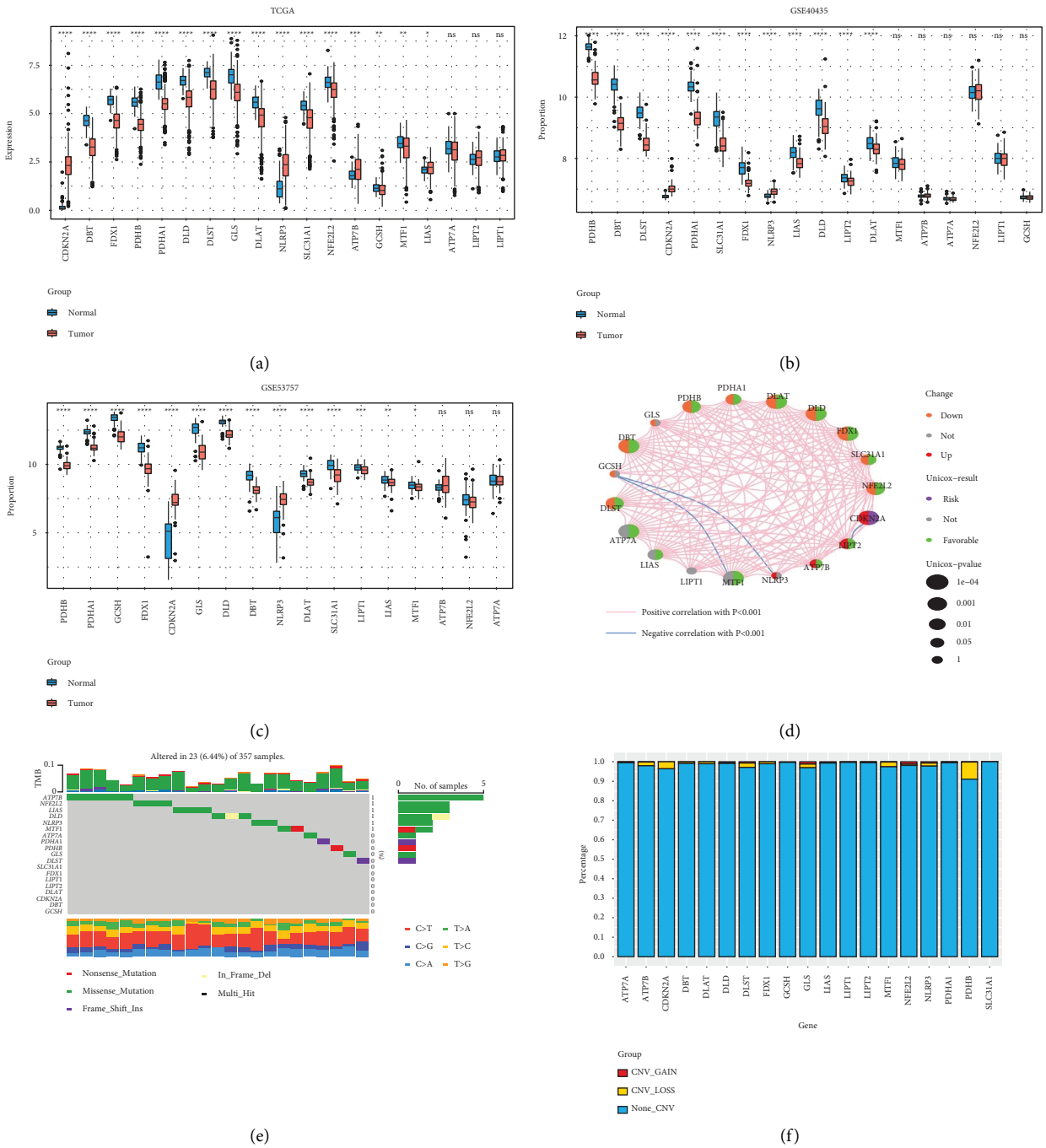

Figure 1: Identification of 19 CRGS and their genetic mutational landscape. (a) Differential expression of CRGS in the TCGA cohort; (b) differential expression of CRGS in the GSE40435 cohort; (c) differential expression of CRGS in the GSE53757 cohort; (d) co-expression network between CRGS; (e) mutation frequency of CRGS; (f) copy number variation frequency of CRGS. $^{*}P$ value <0.05, $^{**}P$ value <0.01, $^{***}P$ value <0.001, $^{****}P$ value <0.0001.

were significantly enriched. In light of the variations in the biological pathways mentioned above, we investigated the immune infiltration traits of the two subtypes. As can be seen in Figure 2(f), cluster A had a larger concentration of infiltrating neutrophil, mast, and eosinophil cells, whereas cluster B had a higher concentration of infiltrating activated CD8 T cells, CD4 T cells, activated B cells, and myeloid-derived suppressor cells (MDSC) cells. Then, using the TIDE website, we predicted whether certain patient subgroups would respond to immunotherapy. According to Figure 2(g), patients in cluster A had lower TIDE scores, making them more likely to benefit from immunotherapy. Figure 2(h) compares the immunotherapy responses of different patient subgroups (cluster A, 89% vs. cluster B, 72%). Our findings imply that therapeutic regimens developed for cuproptosis may be a potential anticancer target in ccRCC patients and may improve ccRCC patients' responsiveness to immunotherapy.

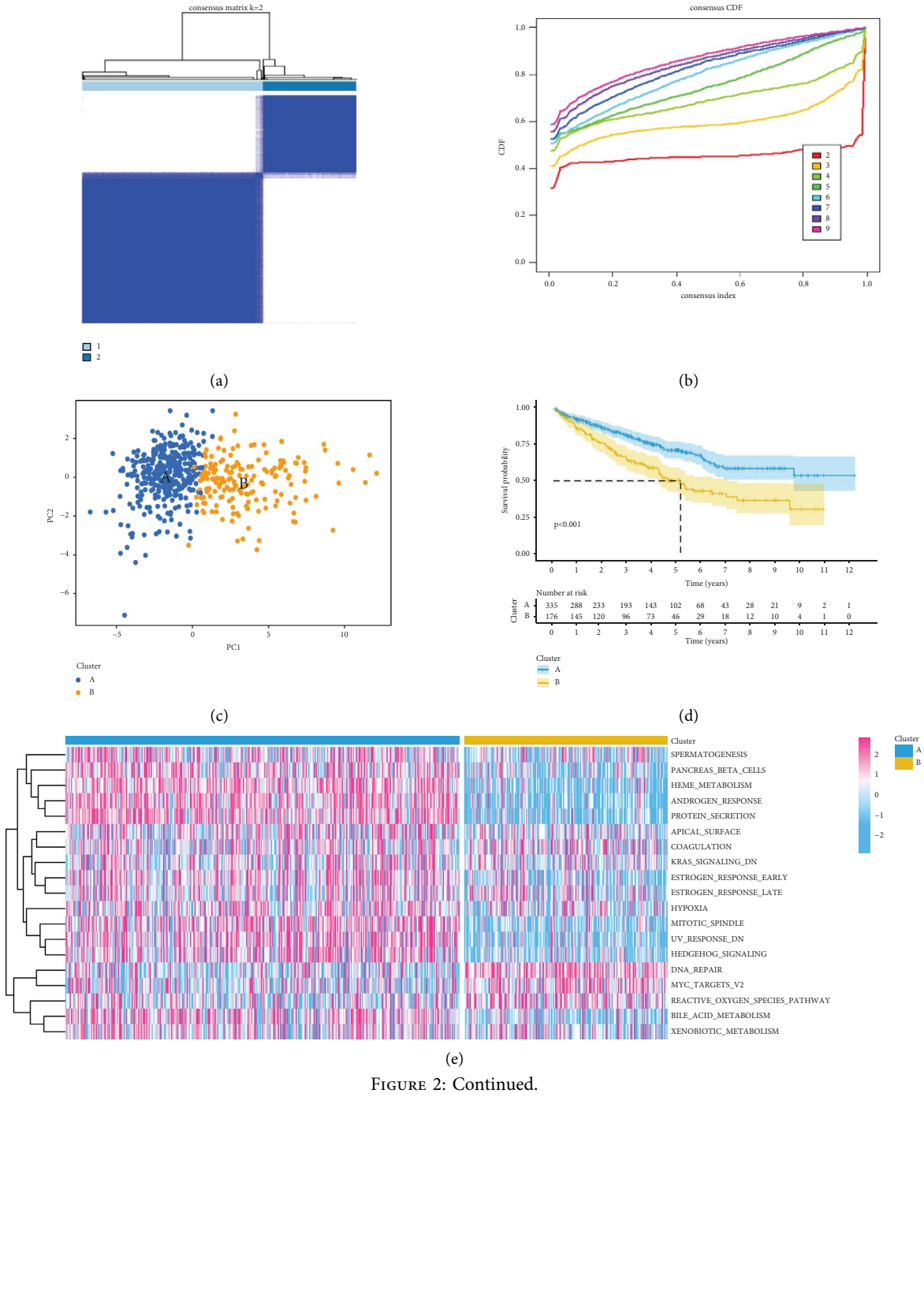

Figure 2: Continued.

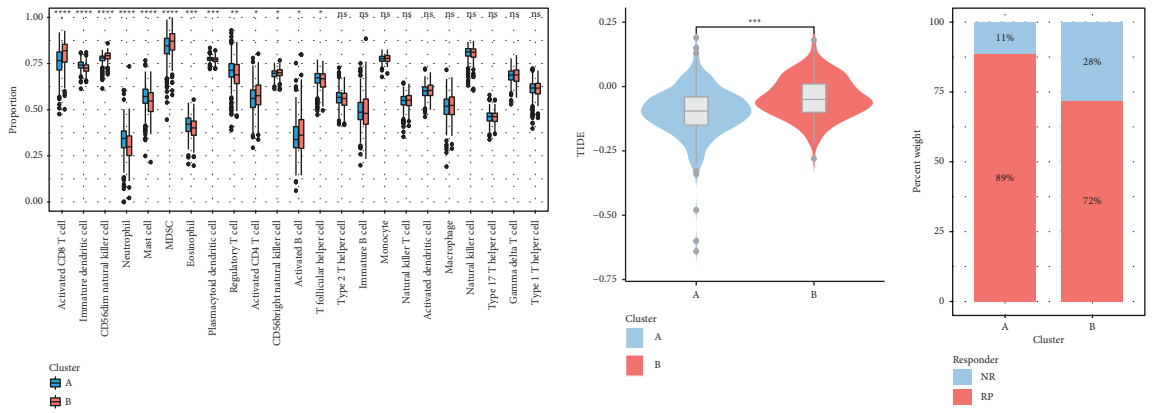

(f) (g) (h)

FIGURE 2: Consensus cluster analysis, immune infiltration analysis, and immunotherapy response analysis based on 19 CRGS. (a) Consensus clustering-based on CRGS; (b) cumulative distribution function plot; (c) PCA analysis between two cuproptosis clusters; (d) survival analysis between two cuproptosis clusters; (e) GSVA analysis; (f) differences between 23 immune cells in different cuproptosis clusters; (g) differences in TIDE scores among different cuproptosis clusters; and (h) differences in immunotherapy response among different cuproptosis clusters. $^{*}P$ value <0.05, $^{**}P$ value <0.01, $^{***}P$ value <0.001, $^{****}P$ value <0.0001.

3.3. Identification of CR-lncRNAs. As master regulators of gene expression, lncRNAs have been implicated in a number of malignancies in recent years. A notable illustration is PCAT-1 dysregulation, which is strongly linked to the development of prostate cancer [40]. Additionally, lncRNAs can be employed independently to forecast tumor prognosis, tumor progression, and disease diagnosis [41, 42]. Therefore, we retrieved the lncRNA expression profiles of ccRCC patients from the TCGA database and, after deleting the lncRNAs that were barely expressed, acquired 9024 lncRNAs for WGCNA analysis. The WGCNA network was built using the one-step method, and Figure 3(a) shows that there were no outlier samples discovered and that the samples were well clustered. The ideal soft threshold of 3 was identified using the scale-free topology fitting index of 0.85 and network connectivity as the standard (Figure 3(b)). A hierarchical clustering dendrogram that obtained 10 modules is shown in Figure 3(c). As can be seen from Figure 3(d), the blue, green, and magenta modules are all significantly associated with tumor and cuproptosis, but the blue module has the strongest correlation with tumor ($r = -0.5$, $P < 0.001$). As a result, we chose the lncRNAs identified in the blue modules to further develop the prognostic molecular characteristics of ccRCC patients.

3.4. Construction and Validation of Prognostic Risk Scoring Model. We eventually discovered 4229 overlapping mRNAs, 2287 overlapping lncRNAs, and 181 overlapping miRNAs using the three methods of "EdgeR," "DESeq2," and "limma" for gene differential analysis. The differential lncRNAs were intersected with the 1033 lncRNAs in the blue module above to provide 630 overlapping lncRNAs as candidate lncRNAs. Subsequently, univariate Cox regression analysis and the log-rank test yielded 116 lncRNAs with prognostic significance (P value <0.05). Figure 4(a) displays the optimum parameter (λ) interval for Lasso regression using 10-fold cross-validation. When we selected the λ value with the smallest mean error, we got 33 lncRNAs (Figure 4(b)). The relationship between the number of trees and the error rate in the RF algorithm is illustrated in Figure 4(c), along with the characteristic genes the algorithm identified. It is clear that as the tree expands, the error rate curve gradually flattens out, showing that the number of trees chosen was sound. The MD approach yielded a threshold of 7.9681, and using this threshold, we were able to derive 44 significant eigengenes (Figure 4(d)). By intersecting the lncRNAs produced by the previous two approaches, we identified 23 potential lncRNAs (Figure 4(e)). Based on the aforementioned potential lncRNAs, a multivariate stepwise CPH model was created, and with an AIC = 1234.71, we were able to generate the ideal CPH model for 13 lncRNA combinations in the training set (Figure 4(f)).

The expression of lncRNA in the aforementioned model and the regression coefficient obtained by multivariate stepwise Cox regression analysis were used to generate the risk score for each patient. The following is the calculating formula: risk score = (−0.3586 ∗ AC007637.1 exp) + (−0.2050 ∗ LINC00113 exp) + (−0.5718 ∗ AL162377.1 exp) + (−1.1979 ∗ AL353803.2 exp) + (−0.5197 ∗ PSMG3-AS1 exp) + (1.3177 ∗ TFAP2A-AS2 exp) + (0.5387 ∗ AC007881.3 exp) + (1.5752 ∗ LINC01460 exp) + (0.9538 ∗ LCMT1-AS1 exp) + (0.9434 ∗ HMGA2-AS1 exp) + (2.0661 ∗ AC007993.3 exp) + (2.1685 ∗ AC117382.2 exp) + (−0.3046 ∗ AC008556.1 exp). Based on the median risk score, patients were separated into high- and low-scoring groups. The risk score's area under the curve (AUC) at one year, three years, and five years is 0.800, 0.793, and 0.819, respectively, according to the ROC curve of the training set (Figure 5(a)). The ROC curve of the test set also displays greater accuracy, with AUCs exceeding 0.75 at one year, three years, and five years (Figure 5(d)). The C index, which was 0.77 in the training set (Figure 5(b)) and 0.71 in the validation set (Figure 5(e)), both of which were considerably higher than the remaining clinicopathological variables, also showed that the model had great consistency. In the training

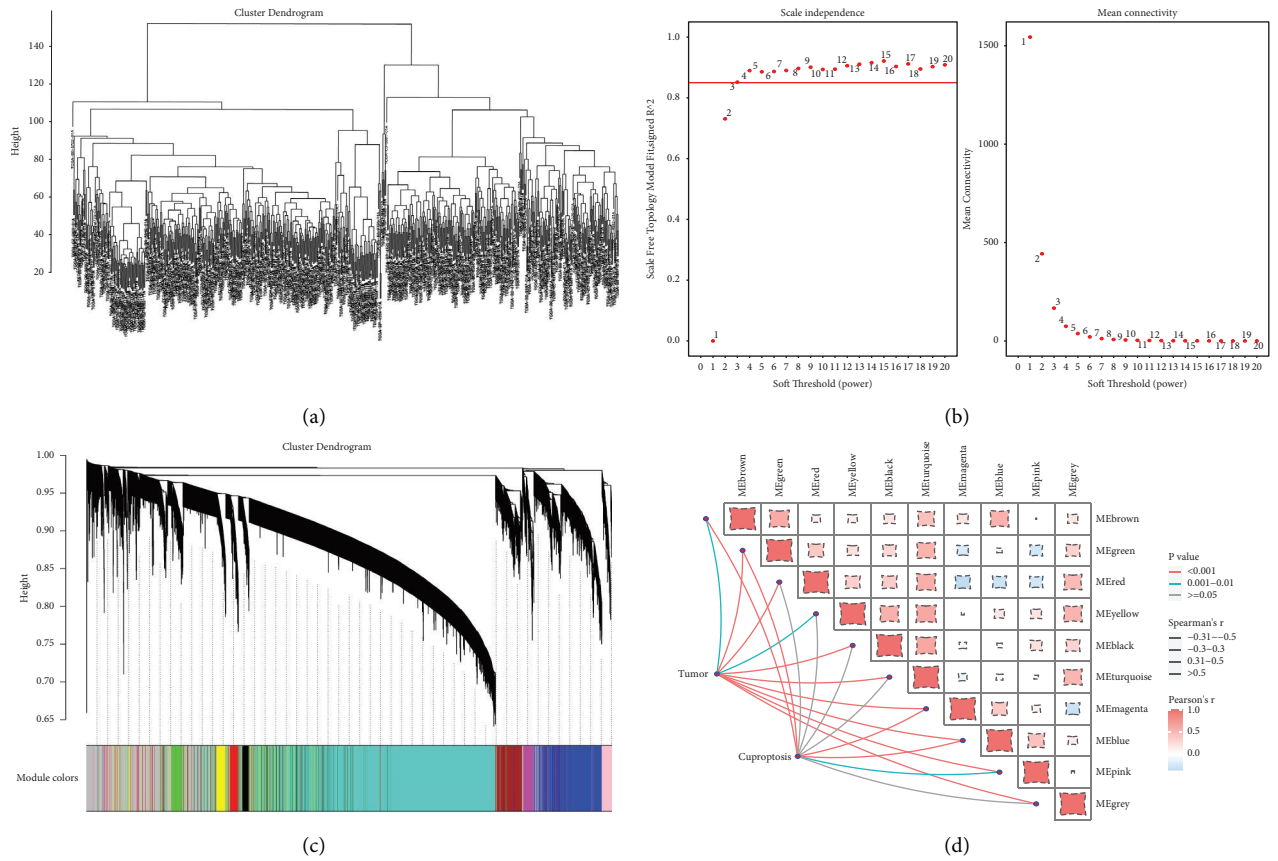

Figure 3: Weighted correlation network analysis. (a) Cluster analysis of all samples in the TCGA cohort; (b) analysis of network topology for various soft thresholding powers. The left panel shows the scale-free fit index (y-axis) as a function of the soft thresholding power (x-axis). The right panel displays the mean connectivity (degree, y-axis) as a function of the soft-thresholding power (x-axis); (c) clustering dendrogram of different similarity genes-based on topological overlap; and (d) the module-traits associations diagram. Each grid corresponds to a module, the color of the grid represents the size of the correlation between different modules, the thickness of the lines represents the size of the correlation between modules and phenotypes, and the color of the lines represents the size of the P value of the correlation test between modules and phenotypes.

and test sets, the OS of patients in the high-score grouping was considerably lower than that in the low-risk category (Figures 5(c) and 5(f), P value <0.001). Additionally, the prognostic risk model we created performs better than some current models when comparing the two indicators of AUC and the C index (Figure 5(g)). The results above show that the prognostic risk score model based on 13 CR-lncRNAs can precisely predict the prognosis of ccRCC patients.

3.5. Correlation of Prognostic Risk Scoring Models with Clinical Pathological Features. The association between risk scores and clinicopathological characteristics was also demonstrated by our investigation. As observed in Figure 6(a), grade and stage vary among various risk groups even if risk scores are really not related to age and gender. Furthermore, a greater risk score was significantly correlated with both a higher grade and stage (Figure 6(b)). Likewise, the outcomes of patients in the high-risk group were considerably worse than those in the low-risk group in all clinical subgroups, according to the findings of the subsequent survival analysis (Figure 6(c)). The risk score was also revealed to be an independent prognostic factor in ccRCC patients by univariate and multivariate Cox regression analysis (Figures 6(d) and 6(e)). In light of the aforementioned findings, the prognostic risk score model, which is made up of 13 CR-lncRNAs, is a very promising biomarker that can not only accurately predict the prognosis of ccRCC patients but also assess their clinical progression.

3.6. Correlation of Prognostic Models with Tumor Immune Microenvironment and Immunotherapy Responses. The ssGSEA analysis suggests that the immune infiltration features of the patients in the two risk groups varied. While patients in the low-risk group had higher rates of neutrophil, immature dendritic cell, and mast cell infiltration, patients in the high-risk group had higher rates of activated CD4 T cell, activated CD8 T cell, and MDSC infiltration (Figure 7(a)). It was further revealed by PCA analysis that the two patient groups represented various immune cell infiltration microenvironments (Figure 7(b)). The majority of immunological checkpoints were more strongly expressed in the high-risk group, whereas PD-L1 and PD-L2 expression were

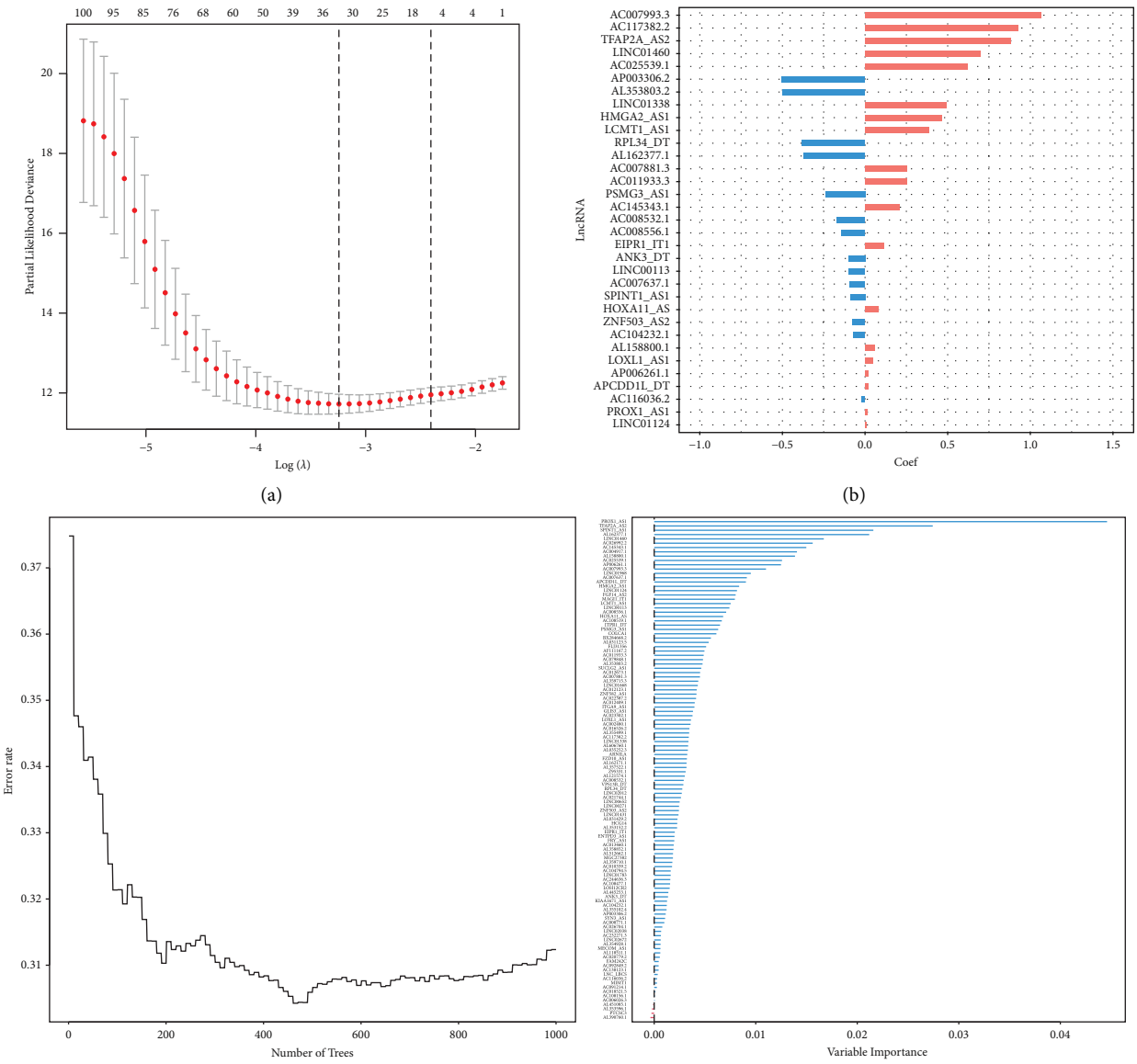

Figure 4: Continued.

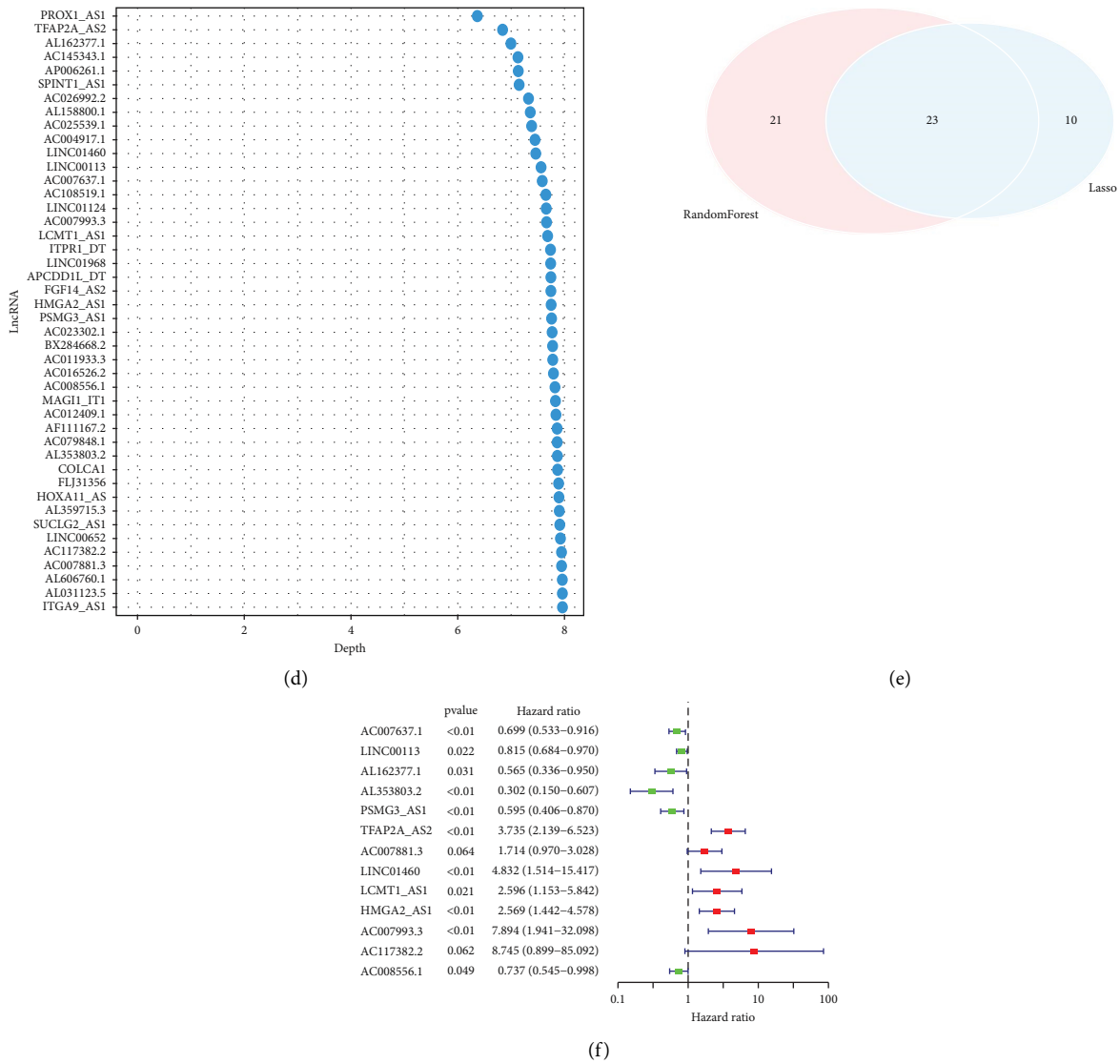

Figure 4: Construction of a prognostic risk scoring model. (a) Tuning parameter map for lasso regression based on 10-fold cross-validation; (b) the selected lncRNAs and their regression coefficients based on lambda with the smallest mean error of lasso regression; (c) prognostic feature lncRNAs selected based on the random forest algorithm; (d) prognostic signature lncRNAs selected based on the MD method; (e) venn diagram showing overlapping lncRNAs obtained by the lasso algorithm and random forest algorithm; (f) forest plot showing 13 CR-lncRNAs obtained by multivariate stepwise COX regression analysis.

more prominent in the low-risk group (Figure 7(c)). According to the current understanding, immunotherapy has a greater chance of helping tumor patients the more PD-L1 is expressed. Additionally, because the majority of immune checkpoints are significantly expressed in the high-risk group, it is more likely to produce immunosuppression, which will cause the cancer to advance in those people. We next used the TIDE online tool to predict immunotherapy responses for patients in the two groups once more. The findings demonstrated that the low-risk group had lower TIDE scores than the high-risk group (Figure 7(d)). Moreover, Figures 7(e) and 7(f) show that better immunotherapy outcomes are significantly correlated with lower risk scores. Therefore, we can conclude that immunotherapy is more likely to be beneficial for patients in the low-risk group. Together, the prognostic risk score model may be helpful in identifying patients' TIME and forecasting their response to immunotherapy.

3.7. Construction of ceRNA Networks. It is generally known that miRNA can influence mRNA expression via binding to mRNA. As a ceRNA, lncRNA can also control the expression of mRNA by competitively binding to miRNA, influencing the occurrence and progression of cancer. To learn more about the regulatory role of CR-lncRNA at the gene level, we firstly predicted the target miRNAs of the aforementioned prognostic CR-lncRNAs using the website miRcode, yielding 23 differential miRNAs (Figure 8(a)). The target miRNAs identified above were then used to predict the target mRNAs via the miRDB, miRTarBase, and TargetScan websites, and a total of 174 differentially overlapping

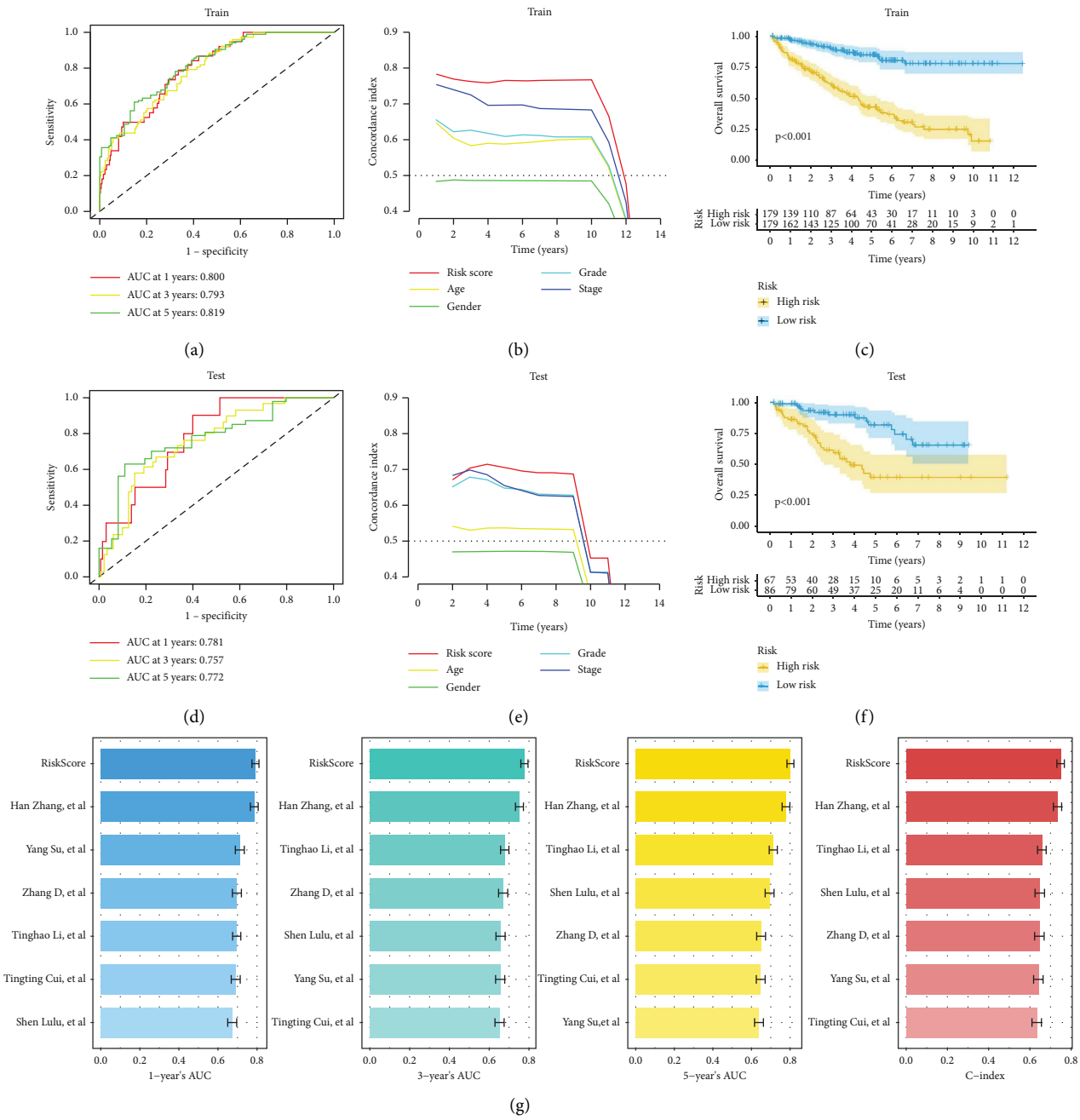

Figure 5: Evaluation and validation of prognostic risk scoring models. (a–c) Time-dependent ROC curves, C index, and K-M survival analysis in the training set; (d–f) time-dependent ROC curves, C index, and K-M survival analysis in the test set; (g) comparison of AUC values and C-index of different prognostic risk score models.

mRNAs were discovered (Figure 8(b)). We created a lncRNA-miRNA-mRNA ceRNA network based on the results above (Figure 8(c)).

3.8. Functional Enrichment Annotation. We discovered that the aforementioned prognostic CR-lncRNAs were considerably enriched in cell proliferation, metastasis, stemness, and EMT as well as being significantly related with a variety of immune cells by enrichment analysis (Figures 9(a) and 9(b)). The miRNA enrichment analysis revealed that the aforementioned miRNAs were significantly enriched in pathways involved in the development of cancer and immune inflammation, including the p53 signaling pathway, the JAK-STAT signaling pathway, the expression of PD-L1, the PD-1 checkpoint pathway in cancer, the chemokine signaling pathway, and other pathways (Figure 9(c)). The underlying biological pathways in patients in the high-risk and low-risk groups were then further investigated using GSEA analysis. According to the findings, the IL-6/JAK/STAT3 signaling, E2f targets, and epithelial-mesenchymal transition (EMT) pathways were considerably enriched in

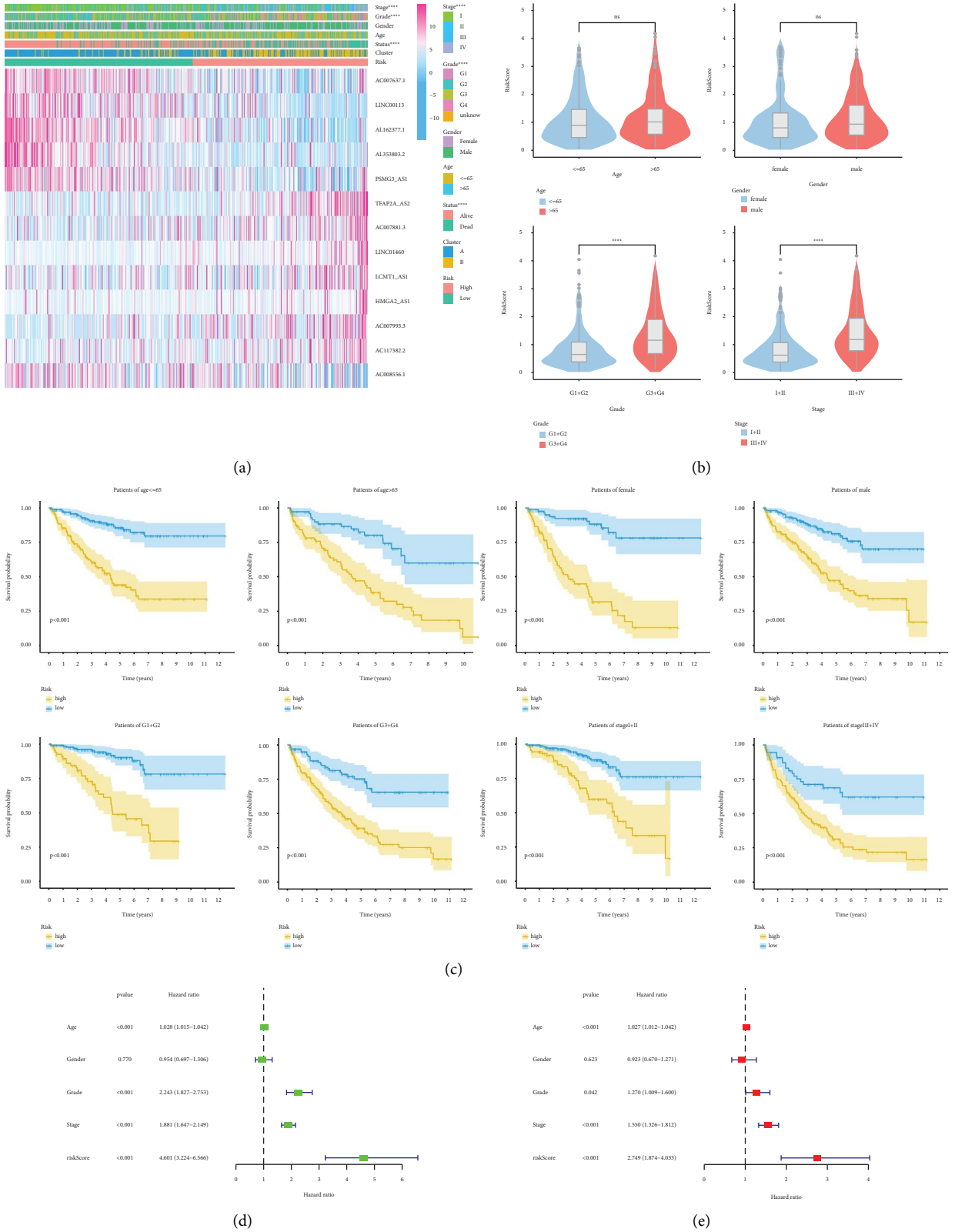

Figure 6: Association of prognostic risk score models with clinicopathological variables. (a) Heatmap of clinical correlations for prognostic models; (b) differences in risk scores between different clinical subgroups; (c) differences in overall survival among patients in different risk groups in different clinical subgroups; (d) univariate COX regression analysis of risk scores and clinicopathological variables; (e) multivariate COX regression analysis of risk scores and clinicopathological variables. $^{*}P$ value <0.05, $^{**}P$ value <0.01, $^{***}P$ value <0.001, $^{****}P$ value <0.0001.

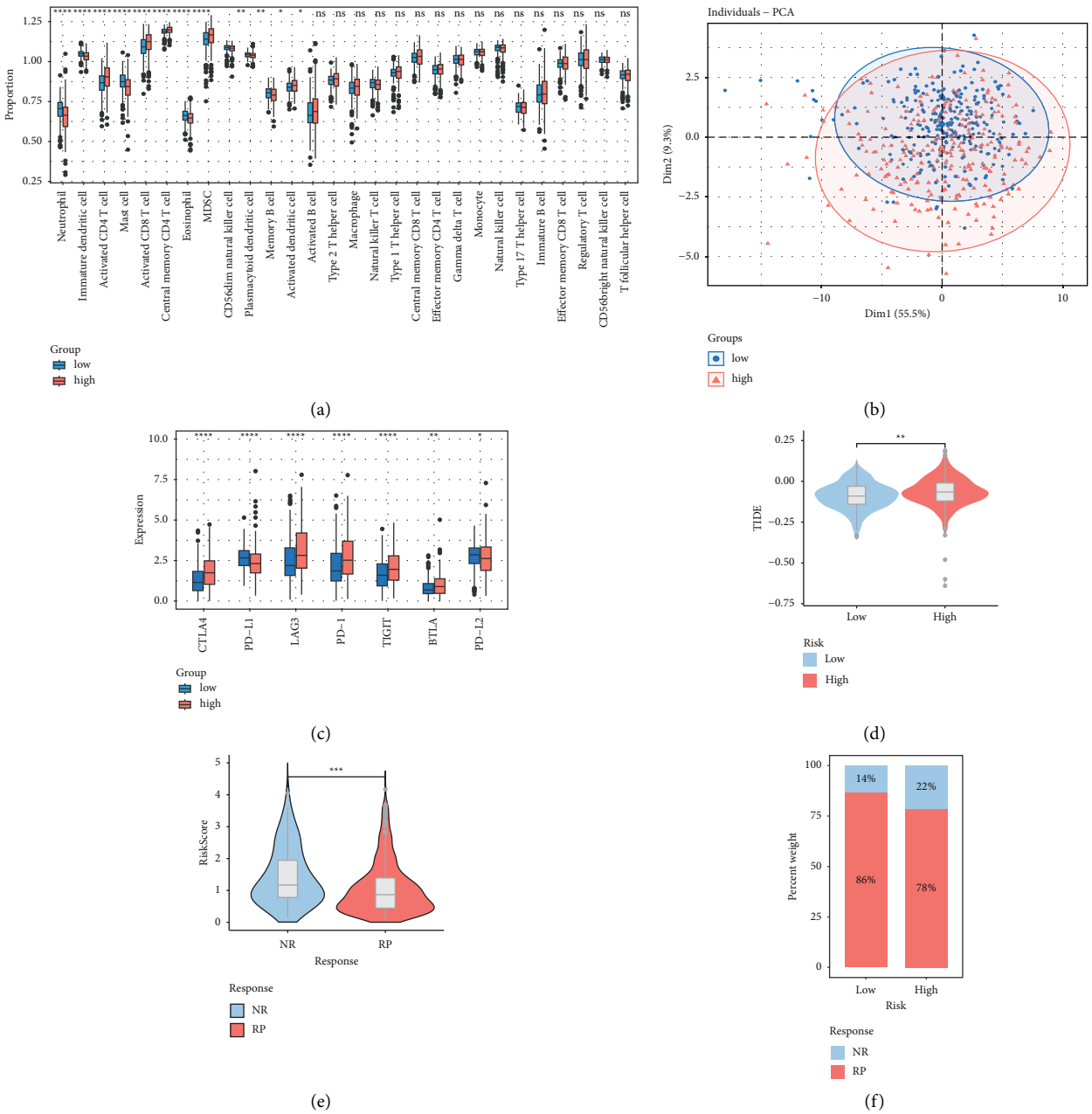

FIGURE 7: Correlation of prognostic risk score models with immune infiltration and response to immunotherapy. (a) Differences in immune cell infiltration between patients in high and low-risk groups; (b) PCA analysis reveals distinct immune microenvironments between different risk groups; (c) differences in the expression of immune checkpoints between high and low-risk groups; (d) differences in TIDE scores between high and low-risk groups; (e-f) differences in immunotherapy response between high and low-risk groups. $^{*}P$ value <0.05, $^{**}P$ value <0.01, $^{***}P$ value <0.001, $^{****}P$ value <0.0001.

the high-risk group. Patients in the low-risk group, on the contrary side, had significantly higher levels of pathways such oxidative ylation, protein metabolism, fat acid metabolism, and androgen response (Figure 9(d)).

3.9. Sensitivity Analysis of Antitumor Drugs. With the use of the "pRRophetic" R package, we acquired 6 potentially sensitive medications to help further direct the individualized treatment of ccRCC patients. Results showed that in the high-risk group, acadesine (AICAR), all-trans retinoic acid (ATRA), palbociclib (PD-0332991), and cisplatin were more sensitive, whereas in the low-risk group, GSK1904529A and KIN001102 were more sensitive (Figure 10).

4. Discussion

Using the TCGA and GEO datasets, this study investigated the expression differences of CRGS at the gene level between normal tissue and tumor samples, and further confirmed the

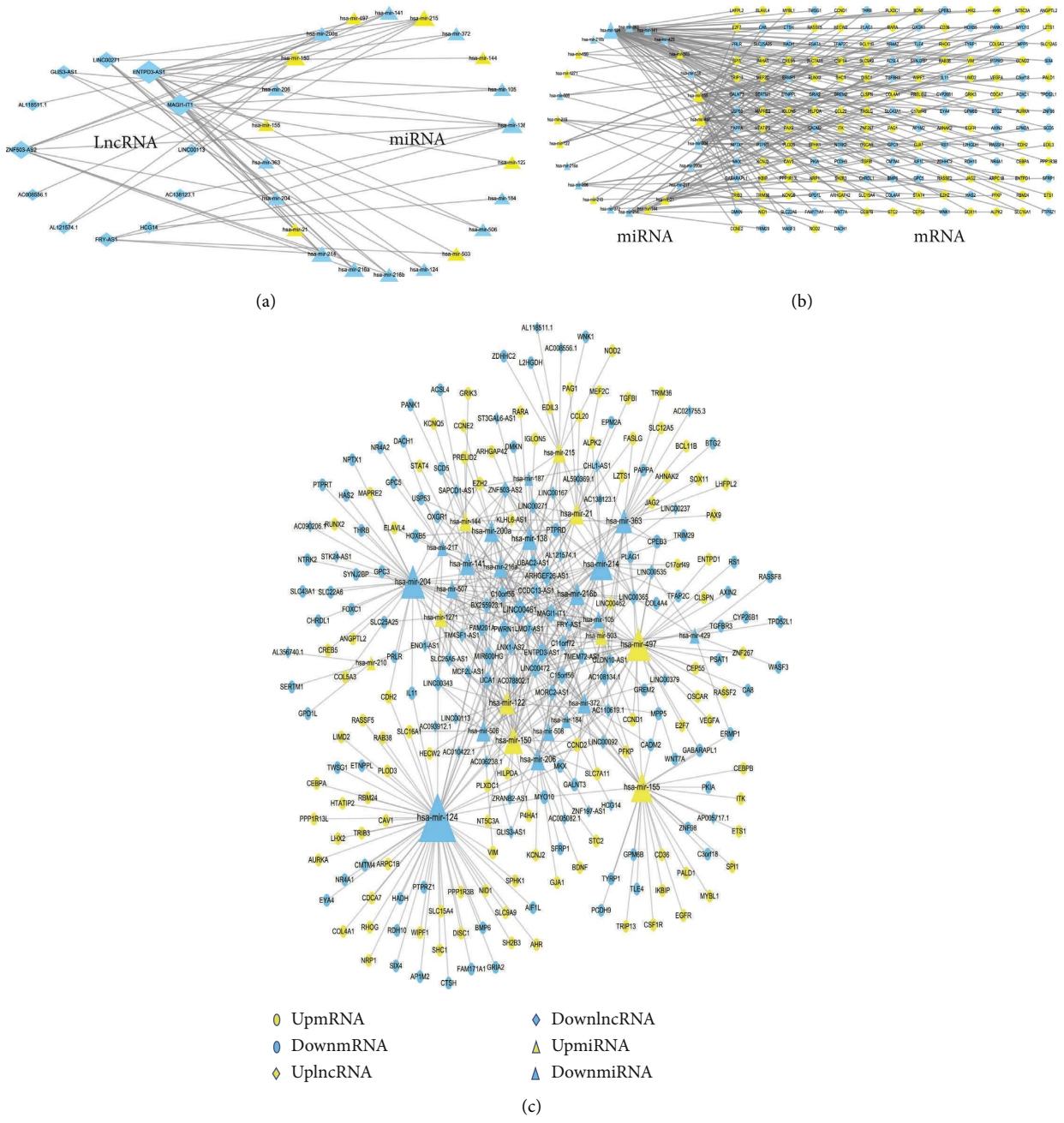

Figure 8: Construction of the ceRNA network. (a) Interaction network diagram between lncRNA and miRNA; (b) interaction network diagram between mRNA and miRNA; (c) ceRNA network diagram of lncRNA-miRNA-mRNA. Yellow means upregulation, blue means downregulation.

expression variations of CRGS at the protein level in the HPA datasets. In ccRCC, the majority of CRGS were lowly expressed, and a survival study afterward indicated that most CRGS were protective genes in ccRCC patients. In addition, the genetic mutation data analysis confirmed that the genetic mutation of the above genes in ccRCC is relatively rare. The two subtypes of cuproptosis clusters were then established by consensus clustering-based on the expression of 19 CRGS, and further analysis proved that the subtype with high CRGS expression was substantially associated with higher survival. These findings imply that cuproptosis might be a therapeutic target for people with ccRCC. It is interesting to note that there were significant differences between the TIME of the two subtypes, with the subtype considerably downregulated in CRGS having a larger abundance of cytotoxic T lymphocytes (CTLs) infiltration but also more MDSC infiltration. It is well recognized that MDSC influence immunosuppressive tolerance through a variety of methods as significant elements of the milieu that suppresses the immune response to cancer. Numerous studies have proven that MDSC, in particular, suppress the T-cell immunological response by creating a lot of reactive

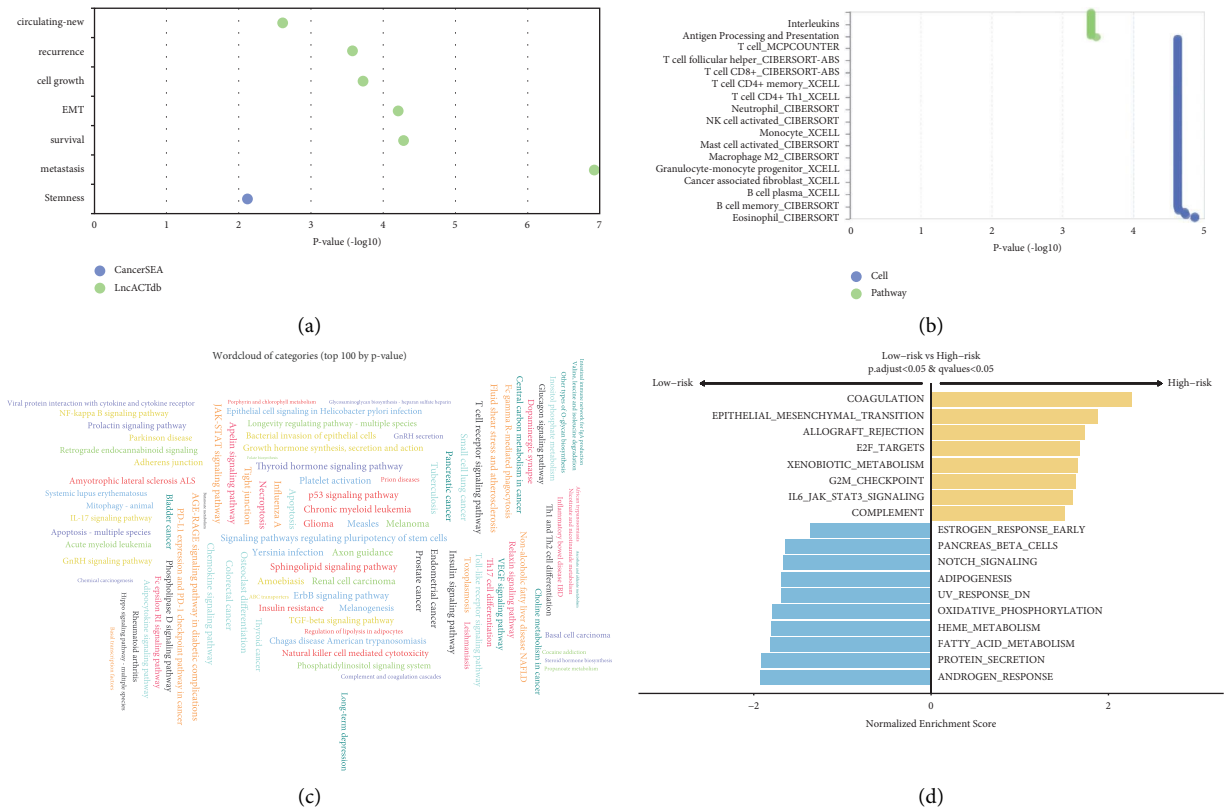

FIGURE 9: Functional enrichment analysis. (a-b) lncRNA enrichment analysis entry; (c) miRNA enrichment analysis entries; (d) GSEA enrichment analysis entries for high- and low-risk groups.

oxygen species (ROS) [43–45]. Also, MDSCs have been linked to a number of tumor-related events, including angiogenesis, treatment resistance, and metastasis [46]. This may also explain why cluster B subtypes have lower survival rates and higher CTLs infiltration. Notably, subsequent GSVA analysis also supported the finding that patients with the cluster B subtype had substantial ROS PATHWAY enrichment. The outcomes of the TIDE online tool also revealed that patients with the cluster B subtype responded to immunotherapy less favorably. The statistics shown above clearly demonstrate that cuproptosis is highly related to the prognosis and immunotherapy of patients with ccRCC, opening up new research directions.

LncRNA, which acts as master regulator of gene expression, has been linked to a number of cancers and can be used independently to predict a patient's prognosis and make a diagnosis of the disease [40–42]. By using WGCNA, we were able to recognize CR-lncRNA. Subsequently, prognostic characteristic genes were further screened using univariate Cox regression analysis, log-rank test, LASSO regression, and RF. Finally, using multiple stepwise Cox regression, an optimal prognostic risk score model made up of 13 CR-lncRNAs was constructed. The model has strong predictive performance and consistency, as indicated by the ROC curve and the C index. Furthermore, it was discovered that the CR-lncRNA-based prognosis models developed using WGCNA and various machine learning algorithms were typically superior to some current models when compared to some lncRNA-based prognostic models developed in the TCGA-KIRC cohort in recent years.

Besides that, we investigated the relationship between predictive risk scores and clinicopathological characteristics and discovered that there was a substantial relationship between risk scores and clinicopathological variables in ccRCC. Furthermore, studies showed a significant positive correlation between the risk score and the tumor's aggressiveness, with the greater the risk score, the higher the tumor grade and stage. Subsequent analysis of immune checkpoint expression and immune infiltration analysis confirmed that, except for PD-L1 and PD-L2, the remaining immune checkpoints were more highly expressed in the high-risk group, and the infiltration abundance of MDSC was also higher. This demonstrates that patients with higher risk scores are more likely to produce an immunosuppressive microenvironment, enabling tumor cells to elude the immune system's surveillance and promoting the growth and development of malignancies. Furthermore, evidence that patients with greater risk scores had a worse response to immunotherapy came from the TIDE study. We conducted the GSEA analysis to investigate the mechanism underlying this difference. Pathways including EMT and IL6 Jak Stat3 Signaling were discovered to be considerably enriched in the high-risk group. Studies have already shown that activating the EMT pathway can promote tumor cell infiltration, tumor migration, and metastasis. It can also cause the formation of an immunosuppressive microenvironment, which helps

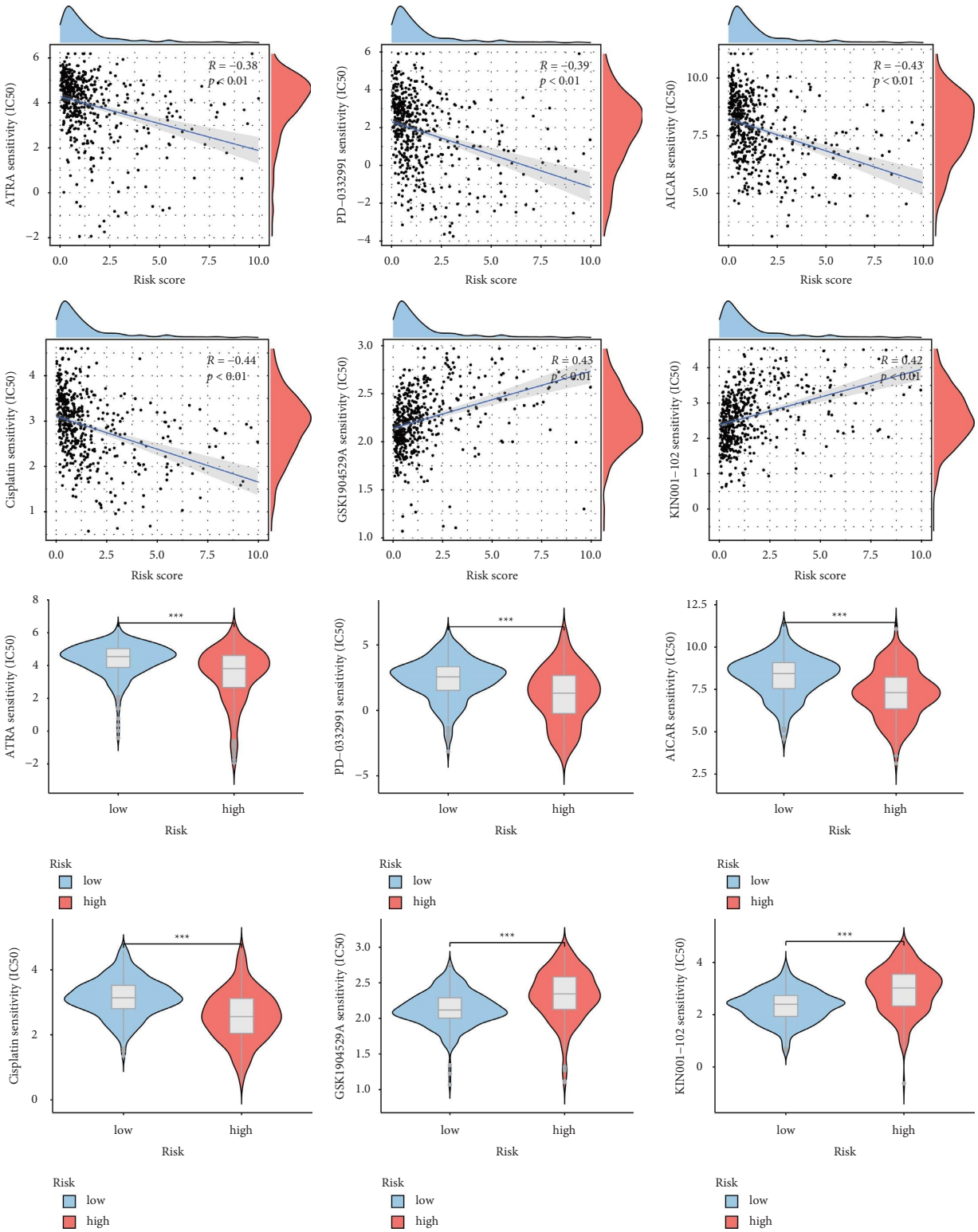

Figure 10: 6 potential antitumor drugs-based on prognostic risk score model. *P value <0.05, **P value <0.01, ***P value <0.001.

tumor cells to escape the immune system [47, 48]. Meanwhile, the IL-6/JAK/ STAT3 Signaling pathway is overactivated in many forms of cancer, and it is implicated in driving cancer cell proliferation, invasion, and metastasis, as well as interacting with TIME to inhibit antitumor immune responses [49]. Moreover, it has been shown that the Stat3 transcription factor in the Stat3 signaling pathway can increase the expression of S100A8 and S100A9, preventing dendritic cell (DC) differentiation and stimulating the accumulation of MDSC, which in turn mediates the

immunosuppressive effects [50]. According to the results above, there may be a connection between the activation of the aforementioned pathways and the differences in TIME and immunotherapy responses amongst different risk subgroups.

We developed a lncRNA-miRNA-mRNA ceRNA network to more thoroughly elucidate the regulatory role of CR-lncRNA at the gene level. Following enrichment analysis, it was discovered that the aforementioned lncRNAs and miRNAs were strongly linked to tumor development, metastasis, prognosis, cell proliferation, and TIME. AICAR, ATRA, PD-0332991, Cisplatin, GSK1904529A, and KIN001-102 were among the six possible anticancer medications that were tested using drug sensitivity analysis. And research has shown that ATRA can enhance the survival of tumor-specific CD8 T cells and upregulated MHC I expression in tumor cells to function as antitumor immunity [51–53]. Additionally, it can also promote MDSC differentiation and maturation, which in turn lowers their population, triggering the immune system to inhibit tumor growth [54]. A highly selective CDK4/6 inhibitor known as PD-0332991 has been shown to have antiproliferative effects in a variety of malignancies, including renal cell carcinoma and liver cancer [55, 56].

This study has some relative merits overall. First off, the CR-lncRNA-based prognostic model created by the WGCNA and several machine learning algorithms can successfully predict the prognosis of ccRCC patients. It offers greater prediction performance and consistency when compared to several other lncRNA-based models already in use. Significant relationships between the model, TIME, and immunotherapy were also discovered in the final research. There are, however, some restrictions-based on bioinformatics analysis, and multicenter prospective studies are still required for validation in the latter phase, which is also the main objective of our future research work.

5. Conclusion

We explore the potential function of CRGS in ccRCC after a thorough investigation. Based on CR-lncRNA, a model for prognostic risk scoring was developed. This model can distinguish TIME, predict the effectiveness of immunotherapy, and provide great and independent prognostic performance in ccRCC patients, allowing for more personalized treatment. For upcoming ccRCC research, it offers fresh perspectives and ideas.

Data Availability

The datasets used to support the findings of this study are publicly available in the GEO database (https://www.ncbi.nlm.nih.gov/geo/) and TCGA database (https://portal.gdc.cancer.gov/).

Conflicts of Interest

The authors declare that they have no conflicts of interest.

Acknowledgments

This work was supported by the Medical Innovation Team Project of Jiangsu Province [grant no. CXTDA-2017048]; the Jiangsu Provincial Key Research and Development Program [grant nos. BE2020758 and BE2019637]; the Key Project of Xuzhou Science and Technology [grant nos. KC19075 and KC21184]; and the Xuzhou Clinical Medicine Expert Team Project [grant no 2018TD004], the Xuzhou Medical Outstanding Talents (Xuzhou Health Education Research [2017] No. 22).

References

[1] R. L. Siegel, K. D. Miller, and A. Jemal, "Cancer statistics," *CA: A Cancer Journal for Clinicians*, vol. 65, no. 1, pp. 5–29, 2015.

[2] J. C. Cheville, C. M. Lohse, H. Zincke, A. L. Weaver, and M. L. Blute, "Comparisons of outcome and prognostic features among histologic subtypes of renal cell carcinoma," *The American Journal of Surgical Pathology*, vol. 27, no. 5, pp. 612–624, 2003.

[3] P. E. Teloken, R. H. Thompson, S. K. Tickoo et al., "Prognostic impact of histological subtype on surgically treated localized renal cell carcinoma," *The Journal of Urology*, vol. 182, no. 5, pp. 2132–2136, 2009.

[4] B. C. Leibovich, C. M. Lohse, P. L. Crispen et al., "Histological subtype is an independent predictor of outcome for patients with renal cell carcinoma," *The Journal of Urology*, vol. 183, no. 4, pp. 1309–1316, 2010.

[5] N. K. Janzen, H. L. Kim, R. A. Figlin, and A. S. Belldegrun, "Surveillance after radical or partial nephrectomy for localized renal cell carcinoma and management of recurrent disease," *Urologic Clinics of North America*, vol. 30, no. 4, pp. 843–852, 2003.

[6] A. Bex, L. Albiges, B. Ljungberg et al., "Updated European association of urology guidelines for cytoreductive nephrectomy in patients with synchronous metastatic clear-cell renal cell carcinoma," *European Urology*, vol. 74, no. 6, pp. 805–809, 2018.

[7] L. Albiges, T. Powles, M. Staehler et al., "Updated European association of urology guidelines on renal cell carcinoma: immune checkpoint inhibition is the new backbone in first-line treatment of metastatic clear-cell renal cell carcinoma," *European Urology*, vol. 76, no. 2, pp. 151–156, 2019.

[8] T. Atakul, S. O. Altinkaya, B. I. Abas, and C. Yenisey, "Serum copper and zinc levels in patients with endometrial cancer," *Biological Trace Element Research*, vol. 195, no. 1, pp. 46–54, 2020.

[9] A. Gupte and R. J. Mumper, "Elevated copper and oxidative stress in cancer cells as a target for cancer treatment," *Cancer Treatment Reviews*, vol. 35, no. 1, pp. 32–46, 2009.

[10] V. L. Goodman, G. J. Brewer, and S. D. Merajver, "Copper deficiency as an anti-cancer strategy," *Endocrine-Related Cancer*, vol. 11, no. 2, pp. 255–263, 2004.

[11] J. C. Juarez, O. Betancourt, S. R. Pirie-Shepherd et al., "Copper binding by tetrathiomolybdate attenuates angiogenesis and tumor cell proliferation through the inhibition of superoxide dismutase 1," *Clinical Cancer Research*, vol. 12, no. 16, pp. 4974–4982, 2006.

[12] G. Khan and S. Merajver, "Copper chelation in cancer therapy using tetrathiomolybdate: an evolving paradigm," *Expert Opinion on Investigational Drugs*, vol. 18, no. 4, pp. 541–548, 2009.

[13] B. A. Carneiro and W. S. El-Deiry, "Targeting apoptosis in cancer therapy," *Nature Reviews Clinical Oncology*, vol. 17, no. 7, pp. 395–417, 2020.

[14] R. Weinlich, A. Oberst, H. M. Beere, and D. R. Green, "Necroptosis in development, inflammation and disease," *Nature Reviews Molecular Cell Biology*, vol. 18, no. 2, pp. 127–136, 2017.

[15] S. J. Dixon, K. M. Lemberg, M. R. Lamprecht et al., "Ferroptosis: an iron-dependent form of nonapoptotic cell death," *Cell*, vol. 149, no. 5, pp. 1060–1072, 2012.

[16] Y. Huang, D. Yin, and L. Wu, "Identification of cuproptosis-related subtypes and development of a prognostic signature in colorectal cancer," *Scientific Reports*, vol. 12, no. 1, pp. 1–10, 2022.

[17] W. M. Linehan, L. S. Schmidt, D. R. Crooks et al., "The metabolic basis of kidney cancer," *Cancer Discovery*, vol. 9, no. 8, pp. 1006–1021, 2019.

[18] The Cancer Genome Atlas Research Network, "Comprehensive molecular characterization of clear cell renal cell carcinoma," *Nature*, vol. 499, no. 7456, pp. 43–49, 2013.

[19] H. I. Wettersten, O. A. Aboud, P. N. Lara, and R. H. Weiss, "Metabolic reprogramming in clear cell renal cell carcinoma," *Nature Reviews Nephrology*, vol. 13, no. 7, pp. 410–419, 2017.

[20] Y. T. Tan, J. F. Lin, T. Li, J. J. Li, R. H. Xu, and H. Q. Ju, "LncRNA-mediated posttranslational modifications and reprogramming of energy metabolism in cancer," *Cancer Communications*, vol. 41, no. 2, pp. 109–120, 2021.

[21] M. X. Zhang, L. Z. Zhang, L. M. Fu et al., "Positive feedback regulation of lncRNA PVT1 and HIF2α contributes to clear cell renal cell carcinoma tumorigenesis and metastasis," *Oncogene*, vol. 40, no. 37, pp. 5639–5650, 2021.

[22] Y. Yang, P. Gong, D. Yao, D. Xue, and X. He, "LncRNA HCG18 promotes clear cell renal cell carcinoma progression by targeting miR-152-3p to upregulate RAB14," *Cancer Management and Research*, vol. 13, pp. 2287–2294, 2021.

[23] S. Zhang, F. Zhang, Y. Niu, and S. Yu, "Aberration of lncRNA LINC00460 is a promising prognosis factor and associated with progression of clear cell renal cell carcinoma," *Cancer Management and Research*, vol. 13, pp. 6489–6497, 2021.

[24] M. Li, B. Yin, M. Chen et al., "Downregulation of the lncRNA ASB16-AS1 decreases LARP1 expression and promotes clear cell renal cell carcinoma progression via miR-185-5p/miR-214-3p," *Frontiers in Oncology*, vol. 10, Article ID 617105, 2020.

[25] Z. Bian, R. Fan, and L. Xie, "A novel cuproptosis-related prognostic gene signature and validation of differential expression in clear cell renal cell carcinoma," *Genes*, vol. 13, no. 5, p. 851, 2022.

[26] P. Jiang, S. Gu, D. Pan et al., "Signatures of T cell dysfunction and exclusion predict cancer immunotherapy response," *Nature Medicine*, vol. 24, no. 10, pp. 1550–1558, 2018.

[27] H. R. Frost and C. I. Amos, "Gene set selection via LASSO penalized regression (SLPR)," *Nucleic Acids Research*, vol. 45, no. 12, Article ID e114, 2017.

[28] H. Ishwaran, U. B. Kogalur, X. Chen, and A. J. Minn, "Random survival forests for high-dimensional data," *Statistical Analysis and Data Mining: The ASA Data Science Journal*, vol. 4, no. 1, pp. 115–132, 2011.

[29] C. Strobl, J. Malley, and G. Tutz, "An introduction to recursive partitioning: rationale, application, and characteristics of classification and regression trees, bagging, and random forests," *Psychological Methods*, vol. 14, no. 4, pp. 323–348, 2009.

[30] L. Grinsztajn, E. Oyallon, and G. Varoquaux, "Why do tree-based models still outperform deep learning on tabular data?," 2022, https://arxiv.org/abs/2207.08815.

[31] H. Akaike, "A new look at the statistical model identification," *IEEE Transactions on Automatic Control*, vol. 19, no. 6, pp. 716–723, 1974.

[32] D. Zhang, S. Zeng, and X. Hu, "Identification of a three-long noncoding RNA prognostic model involved competitive endogenous RNA in kidney renal clear cell carcinoma," *Cancer Cell International*, vol. 20, no. 1, p. 319, 2020.

[33] Y. Su, T. Zhang, J. Tang et al., "Construction of competitive endogenous RNA network and verification of 3-key LncRNA signature associated with distant metastasis and poor prognosis in patients with clear cell renal cell carcinoma," *Frontiers in Oncology*, vol. 11, Article ID 640150, 2021.

[34] T. Li, H. Tong, J. Zhu et al., "Identification of a three-glycolysis-related lncRNA signature correlated with prognosis and metastasis in clear cell renal cell carcinoma," *Frontiers of Medicine*, vol. 8, Article ID 777507, 2021.

[35] S. Lulu, H. Hualing, Z. Shan, C. Dianxi, L. Yiqing, and L. Qin, "Establishing a prognostic model based on three genomic instability-related LncRNAs for clear cell renal cell cancer," *Clinical Genitourinary Cancer*, vol. 20, no. 4, pp. e317–e329, 2022.

[36] H. Zhang, C. Qin, H. W. Liu, X. Guo, and H. Gan, "An effective hypoxia-related long non-coding RNAs assessment model for prognosis of clear cell renal carcinoma," *Frontiers in Oncology*, vol. 11, Article ID 616722, 2021.

[37] T. Cui, J. Guo, and Z. Sun, "A computational prognostic model of lncRNA signature for clear cell renal cell carcinoma with genome instability," *Expert Review of Molecular Diagnostics*, vol. 22, no. 2, pp. 213–222, 2022.

[38] J. Chen, J. Zhang, Y. Gao et al., "LncSEA: a platform for long non-coding RNA related sets and enrichment analysis," *Nucleic Acids Research*, vol. 49, no. 1, pp. 969–980, 2021.

[39] C. Backes, Q. T. Khaleeq, E. Meese, and A. Keller, "miEAA: microRNA enrichment analysis and annotation," *Nucleic Acids Research*, vol. 44, no. 1, pp. W110–W116, 2016.

[40] J. R. Prensner, M. K. Iyer, O. A. Balbin et al., "Transcriptome sequencing across a prostate cancer cohort identifies PCAT-1, an unannotated lincRNA implicated in disease progression," *Nature Biotechnology*, vol. 29, no. 8, pp. 742–749, 2011.

[41] R. A. Gupta, N. Shah, K. C. Wang et al., "Long non-coding RNA HOTAIR reprograms chromatin state to promote cancer metastasis," *Nature*, vol. 464, no. 7291, pp. 1071–1076, 2010.

[42] J. B. de Kok, G. W. Verhaegh, R. W. Roelofs et al., "DD3(PCA3), a very sensitive and specific marker to detect prostate tumors," *Cancer Research*, vol. 62, no. 9, pp. 2695–2698, 2002.

[43] C. A. Corzo, M. J. Cotter, P. Cheng et al., "Mechanism regulating reactive oxygen species in tumor-induced myeloid-derived suppressor cells," *The Journal of Immunology*, vol. 182, no. 9, pp. 5693–5701, 2009.

[44] X. Chen, M. Song, B. Zhang, and Y. Zhang, "Reactive oxygen species regulate T cell immune response in the tumor microenvironment," *Oxidative Medicine and Cellular Longevity*, vol. 2016, Article ID 1580967, 10 pages, 2016.

[45] S. Nagaraj, K. Gupta, V. Pisarev et al., "Altered recognition of antigen is a mechanism of CD8+ T cell tolerance in cancer," *Nature Medicine*, vol. 13, no. 7, pp. 828–835, 2007.

[46] D. I. Gabrilovich, "Myeloid-derived suppressor cells," *Cancer immunology research*, vol. 5, no. 1, pp. 3–8, 2017.

[47] A. Dongre and R. A. Weinberg, "New insights into the mechanisms of epithelial-mesenchymal transition and implications for cancer," *Nature Reviews Molecular Cell Biology*, vol. 20, no. 2, pp. 69–84, 2019.

[48] S. Terry, P. Savagner, S. Ortiz-Cuaran et al., "New insights into the role of EMT in tumor immune escape," *Molecular oncology*, vol. 11, no. 7, pp. 824–846, 2017.

[49] D. E. Johnson, R. A. O'Keefe, and J. R. Grandis, "Targeting the IL-6/JAK/STAT3 signalling axis in cancer," *Nature Reviews Clinical Oncology*, vol. 15, no. 4, pp. 234–248, 2018.

[50] P. Cheng, C. A. Corzo, N. Luetteke et al., "Inhibition of dendritic cell differentiation and accumulation of myeloid-derived suppressor cells in cancer is regulated by S100A9 protein," *Journal of Experimental Medicine*, vol. 205, no. 10, pp. 2235–2249, 2008.

[51] Y. Guo, K. Pino-Lagos, C. A. Ahonen et al., "A retinoic acid--rich tumor microenvironment provides clonal survival cues for tumor-specific CD8(+) T cells," *Cancer Research*, vol. 72, no. 20, pp. 5230–5239, 2012.

[52] N. Bhattacharya, R. Yuan, T. R. Prestwood et al., "Normalizing microbiota-induced retinoic acid deficiency stimulates protective CD8(+) T cell-mediated immunity in colorectal cancer," *Immunity*, vol. 45, no. 3, pp. 641–655, 2016.

[53] W. Yin, Y. Song, Q. Liu, Y. Wu, and R. He, "Topical treatment of all-trans retinoic acid inhibits murine melanoma partly by promoting CD8(+) T-cell immunity," *Immunology*, vol. 152, no. 2, pp. 287–297, 2017.

[54] N. Mirza, M. Fishman, I. Fricke et al., "All-trans-retinoic acid improves differentiation of myeloid cells and immune response in cancer patients," *Cancer Research*, vol. 66, no. 18, pp. 9299–9307, 2006.

[55] J. Bollard, V. Miguela, M. Ruiz de Galarreta et al., "Palbociclib (PD-0332991), a selective CDK4/6 inhibitor, restricts tumour growth in preclinical models of hepatocellular carcinoma," *Gut*, vol. 66, no. 7, pp. 1286–1296, 2017.

[56] J. E. Logan, N. Mostofizadeh, A. J. Desai et al., "PD-0332991, a potent and selective inhibitor of cyclin-dependent kinase 4/6, demonstrates inhibition of proliferation in renal cell carcinoma at nanomolar concentrations and molecular markers predict for sensitivity," *Anticancer Research*, vol. 33, no. 8, pp. 2997–3004, 2013.

Hindawi
Journal of Oncology
Volume 2023, Article ID 9931419, 17 pages
https://doi.org/10.1155/2023/9931419

Research Article

Identification and Validation of a m5C RNA Modification-Related Gene Signature for Predicting Prognosis and Immunotherapeutic Efficiency of Gastric Cancer

Li Song,[1] **Shouguo Wang**,[1] **Qiankun Li**,[2] **Yao Lu**,[2] **Rungong Yang**,[2] **and Xianqi Feng**[1]

[1]*Academy of Advanced Interdisciplinary Studies, Qilu University of Technology, (Shandong Academy of Sciences), Jinan, Shandong 250353, China*
[2]*Department of Tissue Repair and Regeneration, the First Medical Center of Chinese PLA General Hospital, Beijing 100853, China*

Correspondence should be addressed to Xianqi Feng; qlu-xianqifeng@qlu.edu.cn

Received 17 August 2022; Revised 15 September 2022; Accepted 20 September 2022; Published 8 March 2023

Academic Editor: İbrahim Hakkı Cigerci

Background. 5-methylcytosine (m5C) is a major site of RNA methylation modification, and its abnormal modification is associated with the development of gastric cancer (GC). This study aimed to explore the value of m5C-related genes on the prognosis of GC patients through bioinformatics. *Methods*. First, m5C-related genes were obtained by nonnegative matrix factorization (NMF) analysis and differentially expressed analysis. The m5C-related model was established and validated in distinct datasets. Moreover, a differential analysis of risk scores according to clinical characteristics was performed. The enrichment analysis was carried out to elucidate the underlying molecular mechanisms. Furthermore, we calculated the differences in immunotherapy and chemotherapy sensitivity between the high- and low-risk groups. Finally, we validated the expression levels of identified model genes by quantitative real-time polymerase chain reaction (qRT-PCR). *Results*. A total of five m5C-related subtypes of GC patients in the TCGA database were identified. The m5C-related model was constructed based on APOD, ASCL2, MFAP2, and CREB3L3. Functional enrichment revealed that the m5C-related model might involve in the cell cycle and cell adhesion. Moreover, the high-risk group had a higher abundance of stromal and immune cells in malignant tumor tissues and a lower tumor purity than the low-risk group. The patients in the high-risk group were more sensitive to chemotherapy and had better sensitivity to CTLA4 inhibitors. Furthermore, qRT-PCR results from our specimens verified an over-expression of ASCL2, CREB3L3, and MFAP2 in the cancer cells compared with the normal cells. *Conclusion*. A total of five GC subtypes were identified, and a risk model was constructed based on m5C modification.

1. Introduction

GC is the fifth most common malignancy worldwide and the third leading cause of global cancer-related mortality [1, 2]. Although clinical and surgical conditions improved significantly, the 5-year survival rate for GC patients remains very low, as more than 80% of patients are diagnosed at an advanced stage [3, 4]. Now, surgical resection is still the most effective treatment for early GC. Besides, chemotherapy, radiotherapy, immunotherapy, and molecular targeted therapy also play essential roles in the prognosis for GC [5, 6]. However, the mechanism of GC progression and metastasis is still unclear, and the prognosis leading to metastasis, recurrence, and advanced GC is not yet satisfactory. Therefore, it is urgent to study the mechanism of GC progression to develop new therapeutic strategies.

RNA modifications, such as N6 methyladenosine (m6A), play a visible role in epigenetic gene regulation and cell function and are closely related to many human diseases such as cancer, neurological diseases, and immune disorders [7–11]. As another important RNA modification, m5C has attracted more and more attention, and like m6A, m5C has its methyltransferase, demethylase, and binding proteins [12]. Members of the NOP2/Sun domain family 1-7

(NSUN1-7) and DNA methyltransferase (DNMT) homolog DNMT2 act as m5C writers in mammals and catalyze methylation at the C5 site of RNA [13, 14]. In contrast, TET2 oxidizes m5C to 5-hmC and then removes the methyl group [15, 16]. Subsequently, the Aly/REF output factor (ALYREF) and Y-box binding protein 1 (YBX1), which are characterized by readers, recognize and bind the m5C motif and then perform different biological functions [17, 18]. In addition, these regulatory factors are known to be synergistically involved in multiple tumor progressions with m5C modification. Chen et al. [19] found TRDMT1, an RNA methyltransferase known to methylate tRNA, is a writer of RNA m5C at sites of DNA damage and contributes to the resistance of cancer cells to radiotherapy and PARP inhibitors. Breast tumors expressing low levels of TRDMT1 are more responsive to radiotherapy. Du et al. [20] analyzed the clinical relevance of m5C regulators in pan-cancer. Liu et al. [21] wrote that the RNA m5C modification and its regulators have been shown to be involved in the progression of various cancers, including hepatocellular carcinoma, bladder cancer, glioblastoma multiforme, breast cancer, and head and neck carcinoma, indicating that RNA m5C might play an important role in tumorigenesis and progression.

In the present study, the effect of m5C on the prognosis of GC patients was explored by bioinformatics methods, which identified five m5C-related subtypes and mined four m5C-related genes as biomarkers, and based on the relationship of the prognosis model, patient survival, therapies, and the role of m5C in GC were demonstrated roundly.

2. Materials and Methods

2.1. Data Source. GC-related datasets were obtained from The Cancer Genome Atlas (TCGA) database (https://portal.gdc.cancer.gov/) and the Gene Expression Omnibus (GEO) database (https://www.ncbi.nlm.nih.gov/gds). The TCGA-GC dataset contains 32 normal cases and 373 cancer cases. The 345 cancer samples that have complete survival data were split into a training set (242 cases) and a testing set (103 cases) according to a ratio of 7 : 3. The *t*-test was used to compare the different characteristics between patients in training and testing sets. The results are shown in Table 1. Moreover, the GSE15459 dataset containing 192 cancer cases was obtained from the GEO database as a validation set. The 13 m5C RNA regulators (NOP2, NSUN2, NSUN3, NSUN4, NSUN5, NSUN6, NSUN7, DNMT1, TRDMT1, DNMT3A, DNMT3B, TET2, and ALYREF) were obtained from the previous literature [22].

2.2. Identification of m5C-Related Subtypes. 373 GC samples from the TCGA database and the expression of 13 m5C RNA genes from the previous study were used for the nonnegative matrix factorization (NMF) analysis (R language, Version 0.23.0) [23] to identify m5C-related subtypes for GC patients. Then, overall survival (OS) and disease-specific survival (DSS) analyses of different subtypes were performed to screen the two subtypes with the most significant prognostic differences. These two subtypes were then used in subsequent analyses. Moreover, the clinical characteristics of the two subtypes were analyzed, and the results were visualized by ggplot2 (R package, Version 3.3.5) [24]. The immune cell infiltration of the two subtypes was calculated using the ssGSEA algorithm in the GSVA (R package) based on 24 immune cell types [25] and the MCPcounter algorithm by immunedeconv (R package, Version 2.0.4) based on 8 immune cell types and 2 stromal cell types.

2.3. Construction and Validation of an m5C-Related Model. The edgeR (R package) (Version 4.1) is used to perform differential expression analysis [26, 27]. $P < 0.05$ and $|\log2FC| > 1$ were considered as a difference. The DEGs between the two subtypes with the most significant differences were detected, and the DEGs between the GC samples ($n = 373$) and para-cancerous samples ($n = 32$) in the TCGA dataset were also screened. By overlapping DEGs selected above, the DEm5CRGs were finally screened. Then, Cox regression analyses and the LASSO algorithm were adopted to construct the risk signature. The threshold was $P < 0.05$. The risk score of each sample was calculated by the following formula: risk score $= h0(t) \times \exp(\beta_1 X_1 + \beta_2 X_2 + \ldots \beta_n X_n)$. The $h0(t)$ was the baseline hazard function, and the β was the regression coefficient. GC patients in the training set were split into high- and low-risk groups based on the median risk score. At last, R package Survminer and survival ROC were used to plot the Kaplan–Meier (KM) and ROC curves to evaluate the risk model in the training set, and then the testing and validation sets were used to validate [28, 29].

2.4. Differential Analysis of Risk Values in Clinical Characteristics. The stratification survival analysis was performed to confirm whether the risk model could apply in different clinicopathological characteristics (including age, gender, radiotherapy, and chemotherapy). Meanwhile, the clinicopathological data were involved in variance analysis to investigate differences between clinicopathological features and risk values.

2.5. Construction of a Nomogram. The risk score and clinicopathological data were merged into Cox regression analyses to detect the independent prognosis factors. Then, the selected independent prognostic factors were integrated to establish a nomogram. Furthermore, the calibration curves and the decision curve analysis (DCA) were plotted to assess the nomogram.

2.6. Difference Analysis and GSEA. The DEGs between high- and low-risk groups were detected by the "limma" package. $P < 0.05$ and $|\log_2^{FC}| > 1$ were considered as a difference. R package clusterProfiler (Version 4.0.2) was selected to perform GO enrichment and KEGG pathway analyses on these DEGs. Moreover, to further explore the related signaling pathways and potential biological mechanisms, R package clusterProfiler (Version 3.18.1) [30] was adopted to perform GSEA enrichment analysis. The significance

Table 1: Characteristics of patients in the training set and the testing set from the TCGA-GC cohort.

Characteristics	*n*	Training set	Testing set	*P* value
Total cases	148	102	46	
Age				
≤60	65	43	22	
>60	83	59	24	0.074
Metastasis				
M0	139	96	43	
M1	9	6	3	0.627
Node				
N0	30	20	10	
N1	46	31	15	
N2	32	23	9	
N3	40	28	12	**0.002**
Stage grouping				
Stage I	7	4	3	
Stage II	49	32	17	
Stage III	77	56	21	
Stage IV	15	10	5	0.310
Tumor				
T1	1	1	0	
T2	27	16	11	
T3	80	60	20	
T4	40	25	15	0.330
Treatment type				
Pharmaceutical therapy	86	58	28	
Radiation and pharmaceutical therapy	61	44	17	
Radiation therapy	1	0	1	0.385
Gender				
Female	51	35	16	
Male	97	67	30	0.250

Statistical significance is shown in bold.

thresholds for GSEA were $|NES| > 1$, $q < 0.25$, and NOM $P < 0.05$.

2.7. Analysis of Immunotherapy and Chemotherapy. The immune cell infiltration situations of the sample are inferred by the ESTIMATE and the CIBERSORT algorithms, and differences were analyzed between the high- and low-risk groups from the training set [31]. The tumor purity of the two groups was assessed using ABSOLUTE software. The expression of targeted immune checkpoints and the sensitivity to immunotherapy were analyzed in the two groups, and the prediction of susceptibility to PD-1 and CTLA4 inhibitors was analyzed in the two groups using the SubMap algorithm. We used oncoPredict (Version 0.2) in R language to analyze the sensitivity of commonly used chemotherapy drugs of GC samples [32].

2.8. Expression Validation of Prognostic lncRNAs. GC cell lines (MKN-27, MKN-45, and SMU-1) and human immortalized normal gastric cells CES-1 were obtained from CyberKang (Shanghai) Biotechnology Co., Ltd. and maintained in complete RPMI-1640 and DMEM medium (Welgene, Inc., Gyeongsan-si, Korea) at 37°C in a humidified 5% CO2 incubator. The prognostic gene expression levels were vilified by qRT-PCR. All cells were lysed with the TRIzol Reagent (cat.:356281), and total RNA was isolated. The RNA was reverse-transcribed to cDNA using the Script RT I First strand cDNA SynthesisAll-in-OneTMFirst-Strand cDNA Synthesis Kit (cat: G33330-50) before qRT-PCR. PCR was conducted in a BIO-RAD CFX96 Touch TM PCR detection system (Bio-Rad Laboratories, Inc., USA). The detailed forward and reverse primers are shown in supplementary table 1. All primers were synthesized by Servicebio (Servicebio, Wuhan, China). The experiment was repeated in triplicate on independent occasions.

2.9. Statistical analyses. The Wilcoxon test was used to perform a different comparison between the two groups. Associations between risk scores and gene function or related pathways were calculated by Pearson correlation.

3. Results

3.1. Identification of m5C-Related Subtypes. NMF analysis finally identified five m5C-related subtypes (Figures S1 and 1(a)). OS and DSS analyses showed that survival differences between group3 and group4 were the most significant ($P < 0.05$; Figure S2). The distribution features of the clinical characteristics and the infiltration of immune cell types in group3 and group4 are shown (Figures 1(b) and 1(c)). The two groups were quite different in 5-cell concentrations (Figure 1(d)). Nine 5mC genes were significantly different between them (Figure 1(e)).

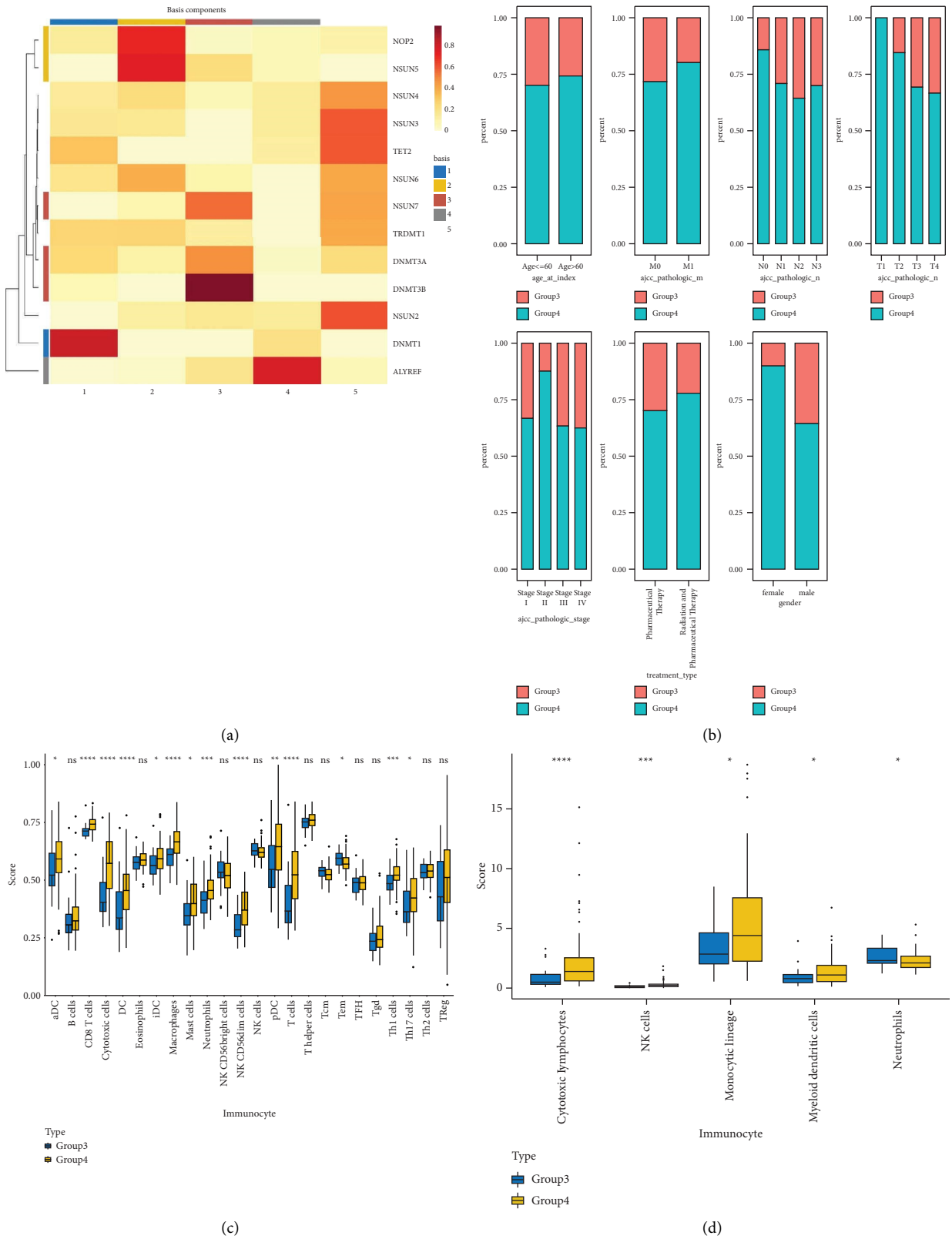

Figure 1: Continued.

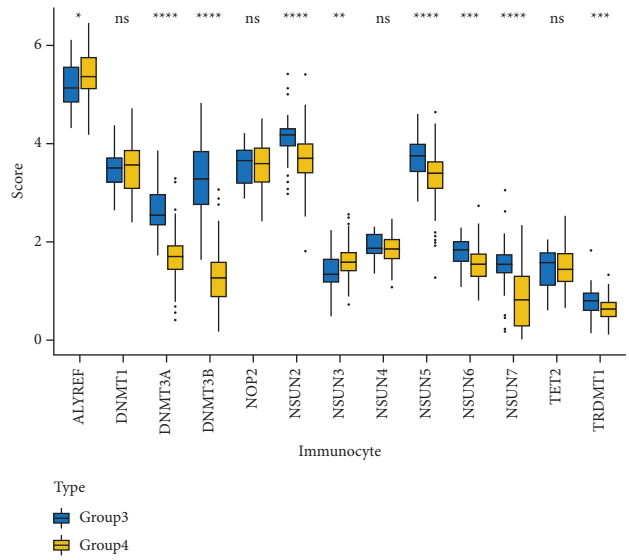

(e)

Figure 1: Identification of five m5C-related subtypes. (a) The heat map of m5C gene expression, the abscissa is the sample classification group, the ordinate is 13 m5C genes, and the lighter color indicated the smaller P value. (b) Differences in clinical features (age, AJCC pathologicM, AJCC _pathologic_N, AJCC _pathologic_T, AJCC _pathologic_stage, treatment_type, and gender) between subtypes. (c) Immune cell infiltration ssGSEA analysis of subtypes with significant survival differences. (d) Immune cell infiltration MCPcounter analysis of subtypes with significant survival differences. (e) the m5C gene expression pattern of significant survival differential subtypes. Group 1–5: 5 different subtypes by the rank value analyzed by NMF. * represent $P < 0.05$, ** represent $P < 0.01$, *** represent $P < 0.001$, **** represent $P < 0.0001$.

3.2. Construction and Validation of an m5C-Related Model. In group3 and group4, 377 DEGs (245 up, 132 down) were identified (Figure 2(a)). In contrast, a total of 1196 DEGs (748 up and 448 down) were identified from normal and GC samples (in the TCGA dataset) (Figures 2(b)–2(d)). Finally, 102 DEm5CRGs were extracted from the intersection (Figure 2(e)). Cox regression (univariate) analysis showed that 8 DEm5CRGs were related to OS ($P < 0.05$; Table 2). Subsequently, a model involving 4 DEm5CRGs (APOD, ASCL2, MFAP2, CREB3L3) was constructed by LASSO and Cox regression (multivariable) analysis (Table 3 and Figure 2(f)). Then, the risk score of each sample was calculated with the following equation: risk score = 0.0807 × expAPOD + (0.1439) × expASCL2 + 0.1296 × expMFAP2 + 0.1091 × expCREB3L3, and the samples were grouped according to the median risk score. The high scores patients had a shorter OS (Figure 2(g)). The AUCs were 0.628, 0.695, and 0.641 (1, 3, and 5 years) (Figure 2(h)). The results showed that MFAP2, APOD, and CREB3L3 were highly expressed in the high score group, while ASCL2 was low. Similarly, the 103 GC (testing set) cases were split into high- ($n = 52$) and low-score ($n = 51$) groups, and the 192 GC cases (validation set) were split into high- ($n = 96$) and low-score ($n = 96$) groups. Results are consistent with the training set (Figures S(3a) and (3b)). The AUCs of the testing set were 0.670, 0.658, and 0.869 (1, 3, 5-year) (Figure S3(c)), and the AUCs of the validating set were 0.627, 0.671, and 0.700 (for 1, 3, 5-year OS) (Figure S3(d)).

The risk scores, patient survival status, survival time, and gene expression pattern are shown in Figures S4(a)–S4(c).

3.3. Differential Analysis of Risk Values. To implore the clinicopathological characteristics and the survival of cases in the two groups, a hierarchical analysis of the km curve in the TCGA cases was performed. High score patients younger than 60 years old or whose pathological stage were T3 or T4 had a worse prognosis (Figure 3). Differences analysis between clinicopathological features and risk values showed that M0 and M1 and Stage II, Stage III, and Stage IV had significant differences (Figure S5).

3.4. Construction of a Nomogram. Score and treatment type were associated with GC cases prognosis and were the factor that were independent prognostic (Figures 4(a) and 4(b)). Then, the nomogram model was constructed to predict the survival of GC patients (Figure 4(c)). The calibration curves (C-index = 0.6547) and DCA curves of the nomogram were also plotted (Figures 4(d) and 4(e)).

3.5. Difference Analysis and GSEA. A total of 151 DEGs (139 up and 12 down) were identified (Figures 5(a) and 5(b)).

The main enriched cellular functions and KEGG pathway of DEGs between high- and low-risk groups are extracellular matrix organization, complement and coagulation cascades, ECM-receptor interaction, and so on (Figures 5(c) and 5(d)).

The results of GSEA analysis showed that the expression of focal adhesion, etc. were up-regulated (Figures 5(e) and 5(f)).

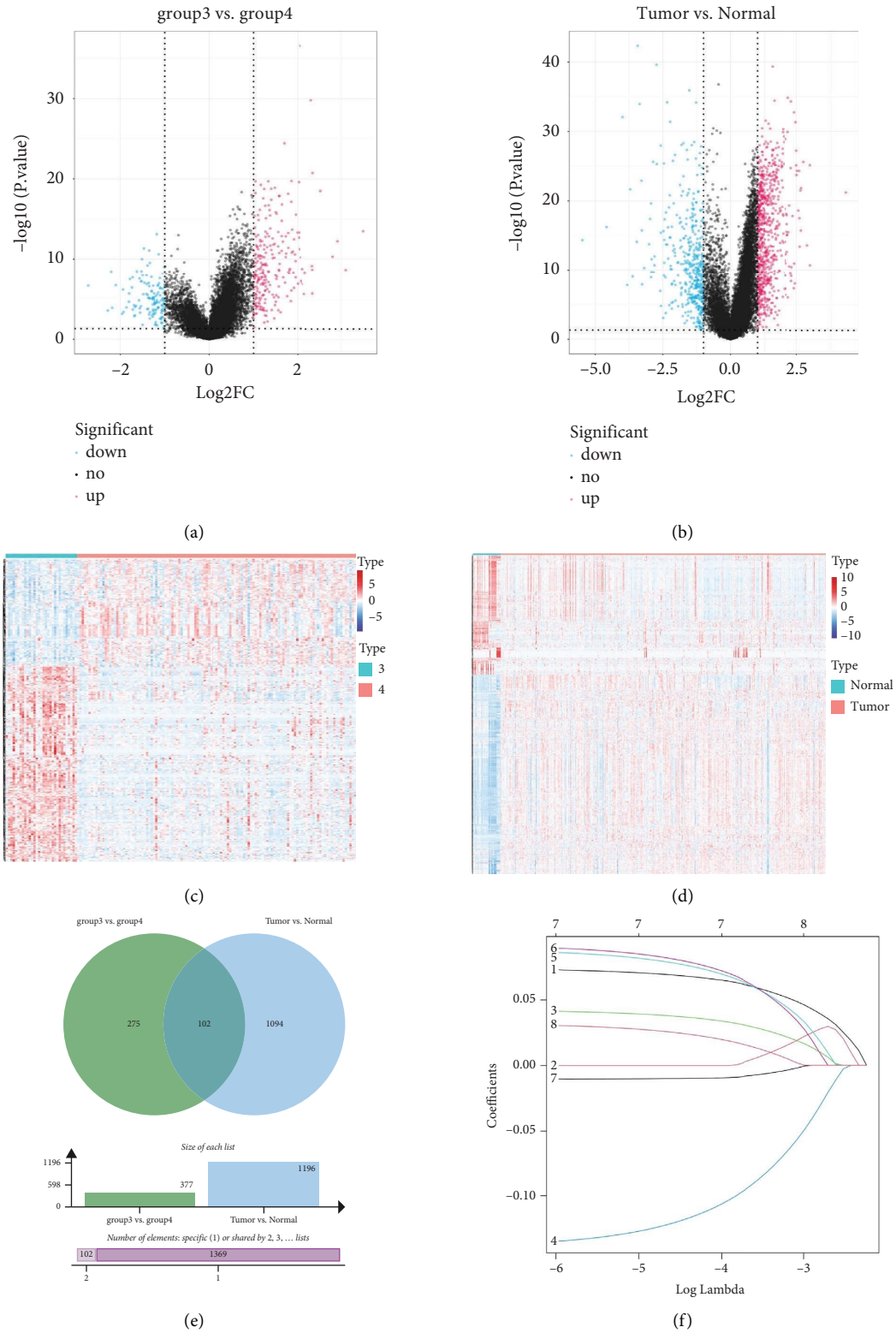

Figure 2: Continued.

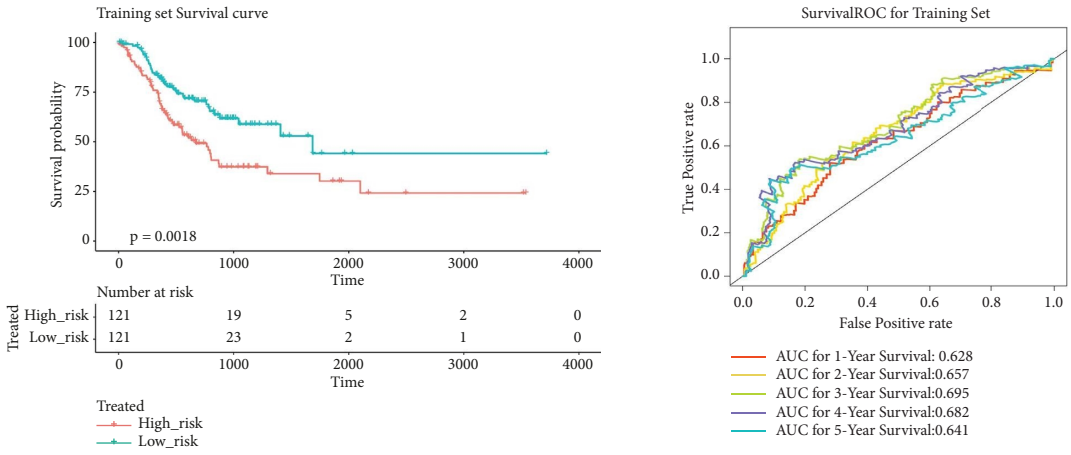

(g) (h)

Figure 2: Construction of an m5C-related risk model. (a) The volcano map of DEGs of two subtypes of survival differences in GC. The abscissa represents $\log2^{FC}$, and the ordinate represents −log10 (adjust. *P* value). Red: upregulation; blue: downregulation. (a) The volcano map of DEGs between GC and normal samples from the TCGA database. Red: upregulation; blue: downregulation. (c) The heat map of DEGs of two subtypes. (d) The heat map of DEGs between normal and GC samples. (e) The venn diagram of DEGs in (a) and (b). (f) Screening characteristic genes by LASSO regression analysis. The abscissa is log (Lambda), and the ordinate is the coefficient of the gene. (g) The KM survival curve of high-andlow-risk groups in the training set. (h) The ROC curve and AUC for four DEm5CRGs.

Table 2: Cox regression (univariate) analysis 8 DEm5CRGs related to OS ($P < 0.05$).

Variable	HR	Lower 95% CI	Upper 95% CI	*P* value
APOD	1.1320	1.0342	1.2390	0.007148
GAMT	1.2210	1.0477	1.4229	0.010569
FKBP10	1.1510	1.0105	1.3111	0.034305
ASCL2	0.8947	0.8045	0.9949	0.039988
MFAP2	1.1789	1.0068	1.3804	0.040913
CREB3L3	1.1468	1.0051	1.3085	0.041760
PLEKHS1	0.8649	0.7516	0.9954	0.042918
AGT	1.1425	1.0013	1.3036	0.047765

CI: confidence interval.

Table 3: Cox regression (multivariable) analysis 4 DEm5CRGs as biomarkers.

Variable	coef	HR	Lower 95% CI	Upper 95% CI	*P* value
ASCL2	−0.1439	0.8659	0.7746	0.968	0.01136
APOD	0.0807	1.0840	0.9808	1.198	0.11401
CREB3L3	0.1091	1.1153	0.9691	1.284	0.12800
MFAP2	0.1296	1.1384	0.9601	1.350	0.13573

CI: confidence interval.

3.6. Analysis of Immunotherapy and Chemotherapy. The stromal score, the immune score, and the ESTIMATE composite score were obtained, and there were differences in the ESTIMATE composite score and the stromal score between high- and low-risk groups (Figure 6(a); $P < 0.0001$). The high-risk group has lower tumor purity (Figure 6(b)). There are eight immune cell (macrophages M1, mast cells resting, etc.) abundances that differ between high- and low-risk groups (Figure 6(c)). The results of the correlation analysis between the risk score and immune cell abundance suggest that the abundance of monocytes, mast cells resting, and T cells CD4 memory resting was positively correlated with a risk score and the abundance of NK cells resting, T cells follicular helper, and T cells CD4 memory activated was negatively correlated with the risk score (Figure 6(d)).

The immune checkpoint PD-L1 expression levels differed significantly between high- and low-risk groups (Figure 7(a)). The expression of routine immune checkpoints in high- and low-risk groups is shown in supplementary table 2. The high-risk group was more sensitive to the overall immune checkpoint and had better sensitivity to CTLA4 inhibitors (Figure 7(b)).

Among 198 commonly used drugs for the treatment of GC, 182 species showed significant differences between high- and low-risk groups, and most high-risk groups were more sensitive to these drugs than low-risk groups (Figure 7(c)).

3.7. Expression Validation of Prognostic lncRNAs. The qRT-PCR results from our specimens verified an over-expression of ASCL2, CREB3L3, and MFAP2 in GC cells compared with the human immortalized normal gastric cells (Figure 8).

4. Discussion

It is well known that GC is one of the leading causes of cancer-related deaths globally [33]. Although significant advancements in the treatments for GC have been acquired in recent years, the overall prognosis of GC patients is still poor [34]. m5C, in which the methyl group is attached to the fifth position of the cytosine ring, is catalyzed by RNA methyltransferase. m5C modification has also been closely related to cancer progression [35]. Meanwhile, bioinformatic studies have shown that m5C regulators could be

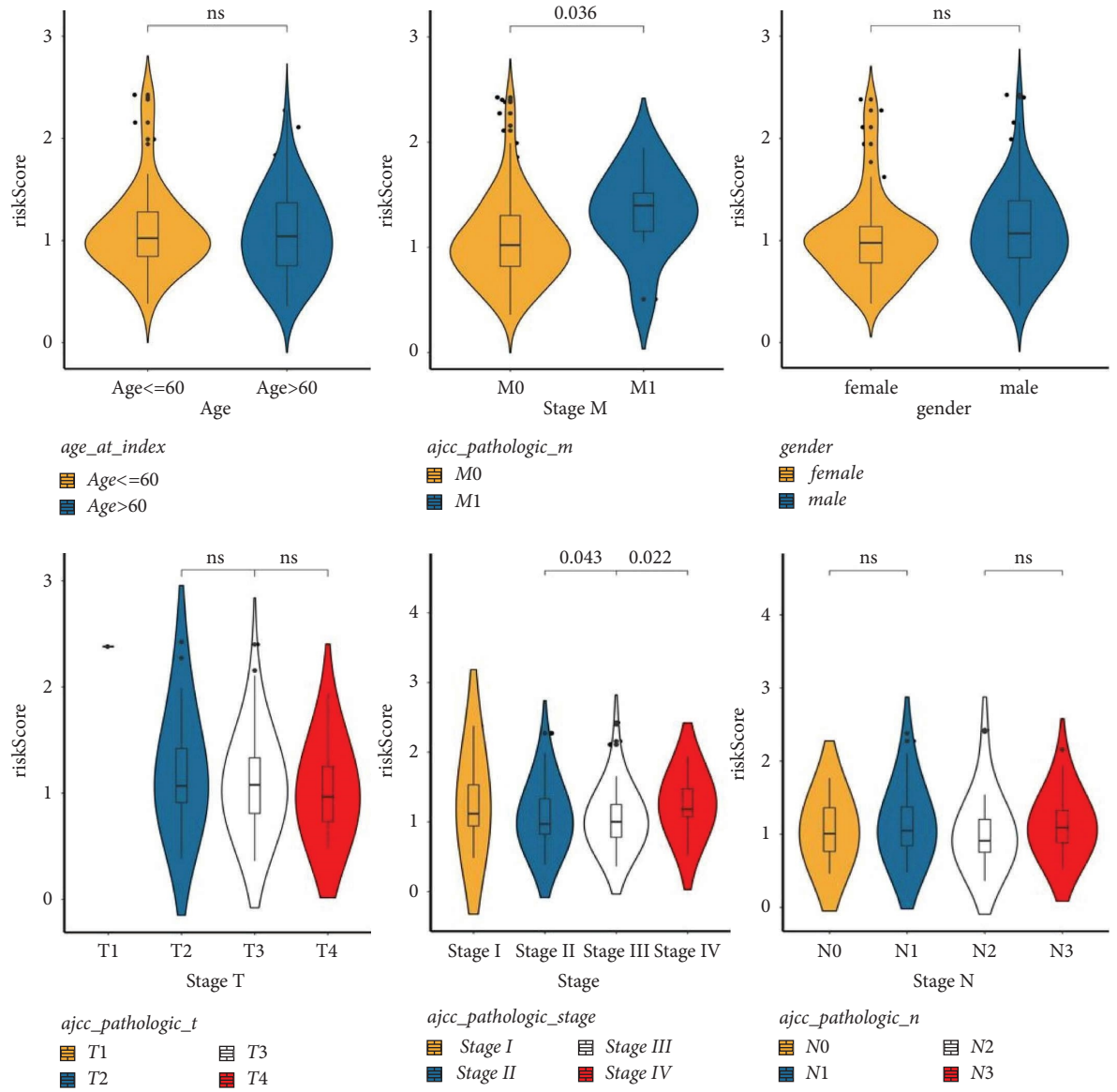

Figure 3: Analysis of differences in risk values in clinical features. The violin plot showed the analysis of differences in risk values under clinical characteristics, the abscissa represents different clinical traits, and the ordinate represents risk value scores.

used as a prognostic factor for lung adenocarcinoma (LUAD), head and neck squamous cell carcinoma (NHSCC), and hepatocellular carcinoma (HCC) [36–38].

With the development of molecular biology and clinical treatment with precision therapy, researchers have been exploring new prognostic markers of GC at the molecular level. Zhu et al. [3] revealed the expression, prognostic value, potential functional networks, protein interactions, and immune infiltration of MTFR2 (mitochondrial fission regulator 2) in GC, concluding that MTFR2 may be a potential prognostic marker and therapeutic target for GC patients. Zhu et al. [34] explored the association between VEGFR-2 and the prognosis of GC. They showed that the high expression of VEGFR-2 as well as the VEGFR-2 rs1870377 A > T genetic polymorphism may be prognostic factors for patients with resected GC. Zu et al. [39] considered that the preoperative prealbumin level was an independent prognostic factor for GC patients, and it is essential to predict the prognosis of patients with GC. Here, we established a prognosis model for GC based on five m5C-related subtypes and four DEm5CRGs (APOD, ASCL2, MFAP2, and CREB3L3) as biomarkers, employing 405 GC samples about second-generation sequencing data, clinical information, and copy gene variation information from the TCGA database, and at last, verifying the four biomarkers in GC cells compared with the human immortalized normal gastric cells by the RT-qPCR method, which is usually missing in bioinformatic analysis.

The four m5C-related genes based on 2 m5C-related subtypes affect the occurrence and development of cancer. Firstly, APOD (apolipoprotein D) is a lipocalin that participates in various cellular processes, including

Variable	HR	lower 95%CI	upper 95%CI	pvalue
riskScore	2.4276	1.4524	4.0574	0.0007142
treatment_type	0.4604	0.2682	0.7904	0.0049089
ajcc_pathologic_m	2.1865	0.8679	5.5083	0.0970152
gender	1.5554	0.8516	2.8408	0.1506272
ajcc_pathologic_stage	1.3132	0.8975	1.9215	0.1606363
ajcc_pathologic_n	1.1581	0.9048	1.4823	0.2438130
age_at_index	1.0030	0.9773	1.0294	0.8195461
ajcc_pathologic_t	1.0244	0.7099	1.4784	0.8974057

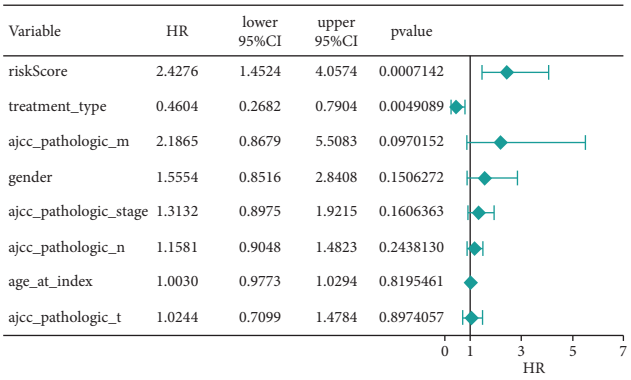

(a)

Variable	HR	lower 95%CI	upper 95%CI	pvalue
riskScore	2.5592	1.5136	4.3271	0.0004537
treatment_type	0.4383	0.2534	0.7582	0.0031777

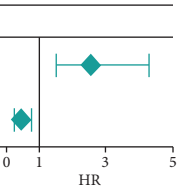

(b)

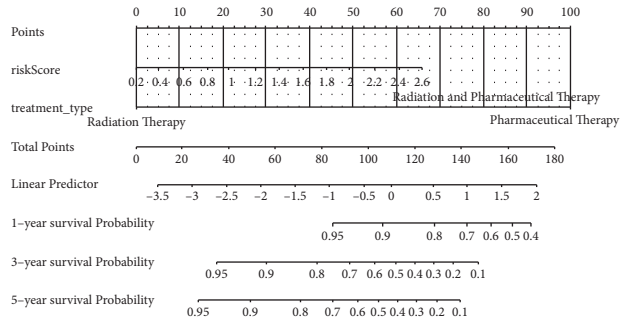

(c)

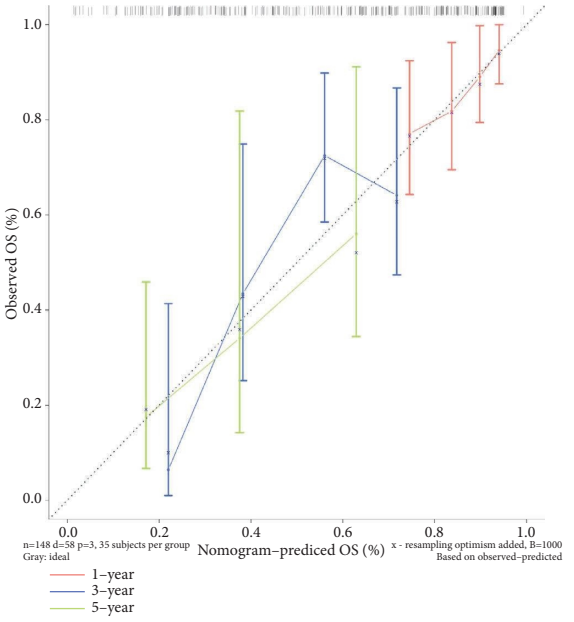

(d)

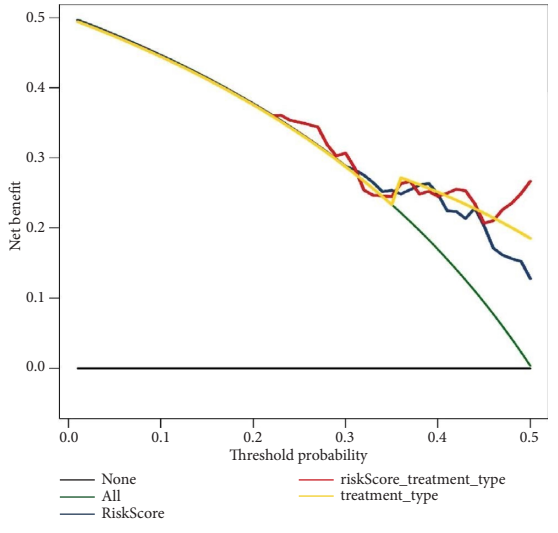

(e)

Figure 4: Establishment and validation of the prognosis model. (a) The forest map of univariate COX-independent prognosis. The hazard Ratio (HR) is the risk ratio. The lower 95% CI and the upper 95% CI are the 95% confidence intervals of risk values. (b) The forest map of multivariate COX-independent prognosis. (c) Nomograms for risk models and treatment types. (d) The correction curve of 1–5 years of clinical characteristics ($P < 0.05$). (e) The decision-making curve of 1–5 years of clinical characteristics ($P < 0.05$).

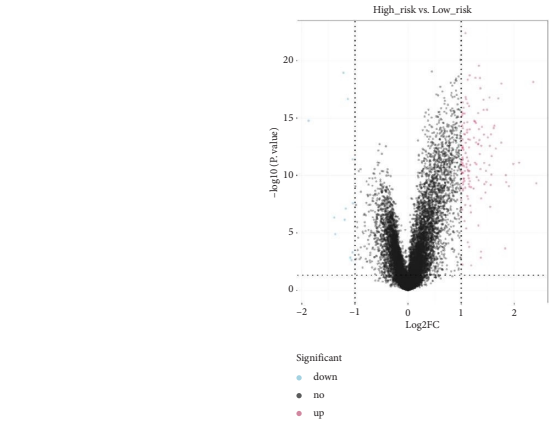

(a)

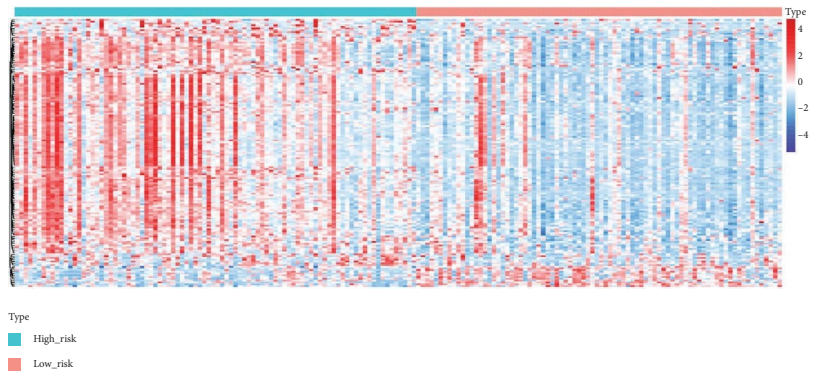

(b)

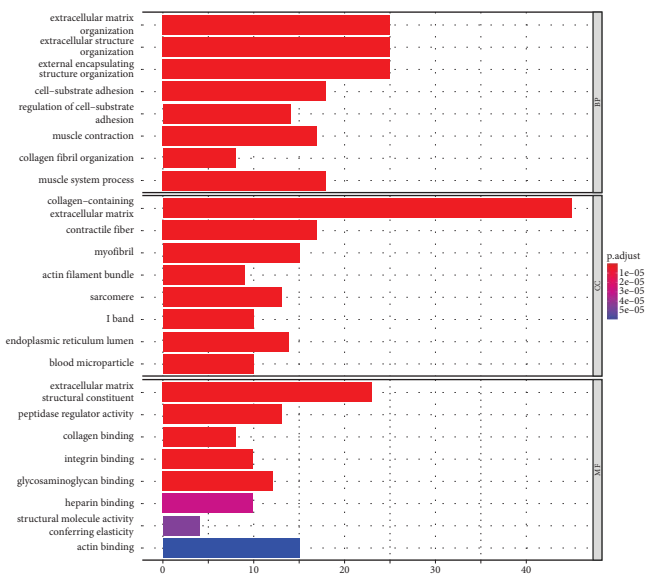

(c)

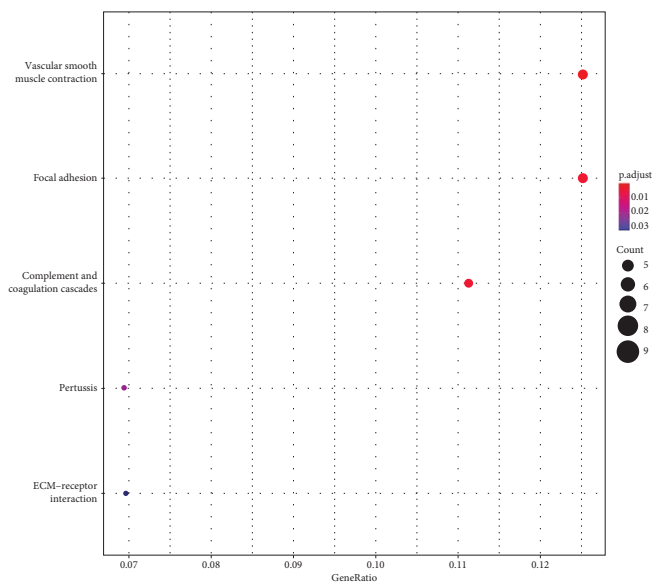

(d)

Figure 5: Continued.

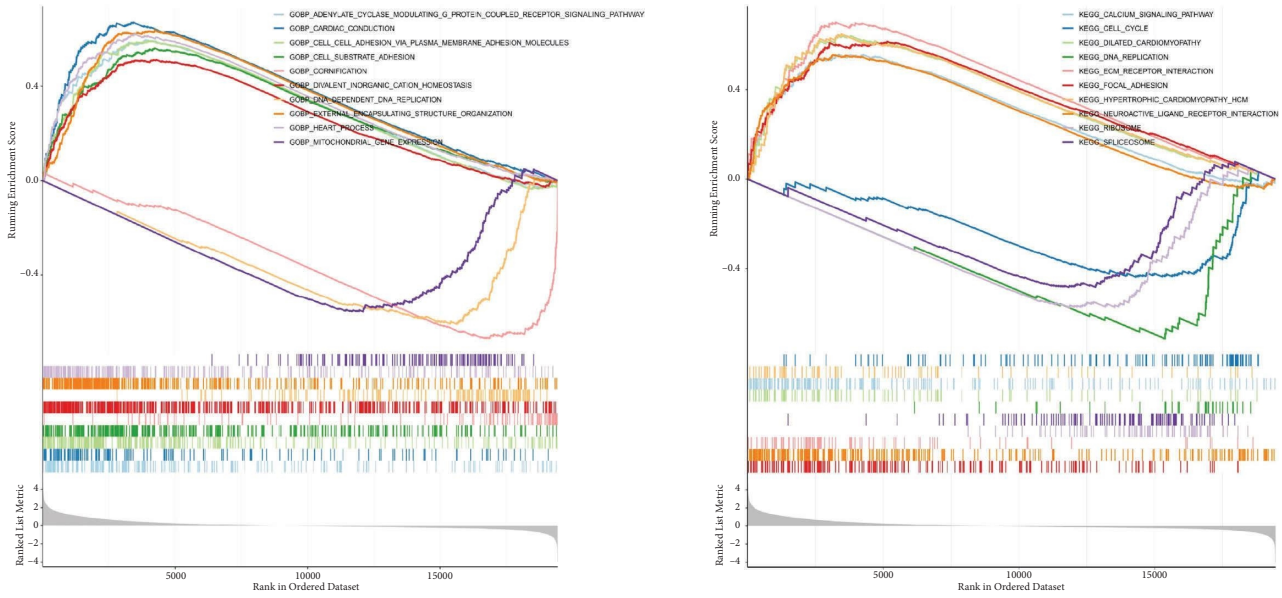

(e) (f)

Figure 5: Differences analysis and the GO and KEGG pathway enrichment analysis of the 151 DEGs. (a) The volcano map of the DEGs, including 139 up-related genes (red) and 12 down-related genes (blue). (b) The heat map of the DEGs. (c) The top 8 terms are enriched in the GO systems, including extracellular matrix organization, extracellular structure organization, and external encapsulating structure organization. (d) KEGG enrichment analysis of DEGs, including 5 KEGG pathway, complement and coagulation cascades, vascular smooth muscle contraction, focal adhesion, pertussis, and ECM-receptor interaction. (e) GSEA enrichment analysis in high- and low-risk groups GO enrichment analysis. (f) GSEA enrichment analysis in high- and low-risk groups KEGG pathway analysis.

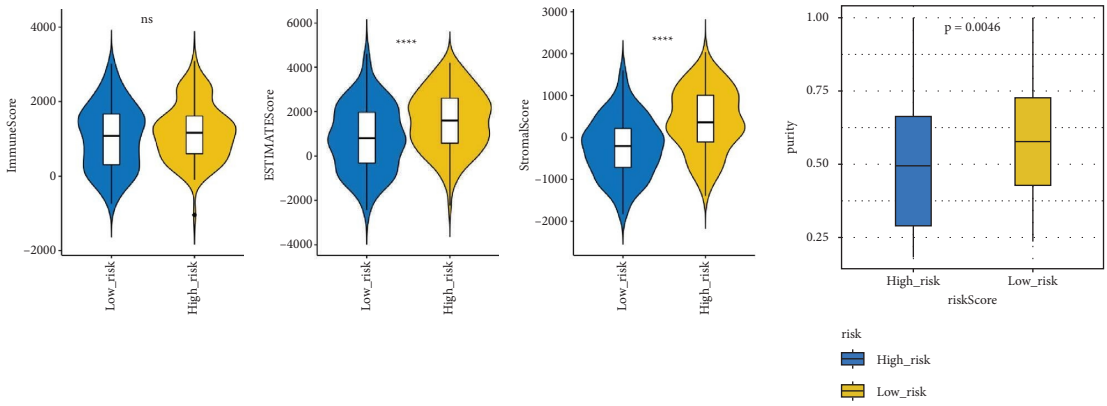

(a) (b)

Figure 6: Continued.

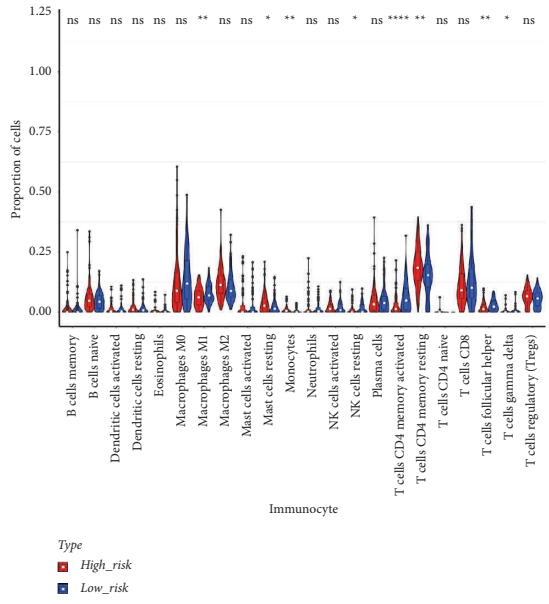

(c)

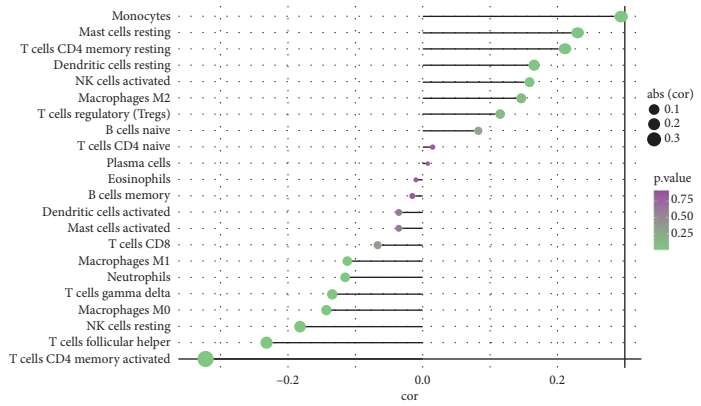

(d)

Figure 6: Treatment analysis of the high- and low-risk groups. (a) ESTIMATE difference scores for the high- and low-risk groups, based on the ESTIMATE comprehensive score and the matrix score. (b) Differences analysis in tumor purity between the high- and low-risk groups, having a significantly lower tumor purity of the high-risk group. (c) Immune cells proportion in the high- and low-risk groups, targeting tumor-infiltrating immune cells in each sample. (d) The lollipop chart depicting the correlation analysis of the risk value and immune cells.

cytoprotection, and is a biomarker positively correlated with the prognosis of breast and prostate cancer [40]. APOD was also reported to be the prognostic factor of GC. Patients with high expression of APOD might have a shorter OS time, correlating with worse prognosis [41]. Second, ASCL2 (Achaete-scute homolog 2) is an essential helix-loop-helix transcription factor and a cancer stem cell marker, and specific reports have revealed that ASCL2 promotes cell proliferation and migration in colon cancer [42, 43]. In the meantime, ASCL2 also serves an essential role in the growth of GC. It was able to downregulate the expression level of miR223, contribute to EMT (the epithelial-mesenchymal transition), and promote gastric tumor metastasis, which indicated that ASCL2 might serve as a therapeutic target in the treatment of GC [44]. Third, MFAP2 (microfibril-associated protein 2) plays a vital role in the regulation of the integrin signal pathway in cancer cell-ECM (extracellular matrix) interaction. The intracellular form of MFAP2 can induce the transcription of integrin $\alpha 4$ in human osteosarcoma cell line SAOS-2 in vascular development [45]. Scholars also validated that MFAP2 was up-regulated in GC tissue, and it was implicated in the malignant behavior of GC cells, such as proliferation, migration, and invasion [46]. The fourth biomarker is CREB3L3, a member of the basic leucine zipper family and the AMP-dependent transcription factor family. It can link to acute inflammatory response and hepatocellular carcinoma [47]. Dewaele et al. illustrated that EWSR1-CREB3L3 gene fusion is associated with a mesenteric sclerosing epithelioid fibrosarcoma [48]. In GC, CREB3L3 is related to the OS derived from univariate and multivariate Cox regression analysis and is highly expressed in cancer tissues [49]. In a word, the four biomarkers can affect the occurrence and development of cancer in various degrees, including GC, and the guiding significance is great to analyze the relationship between the prognosis model and the survival of GC patients.

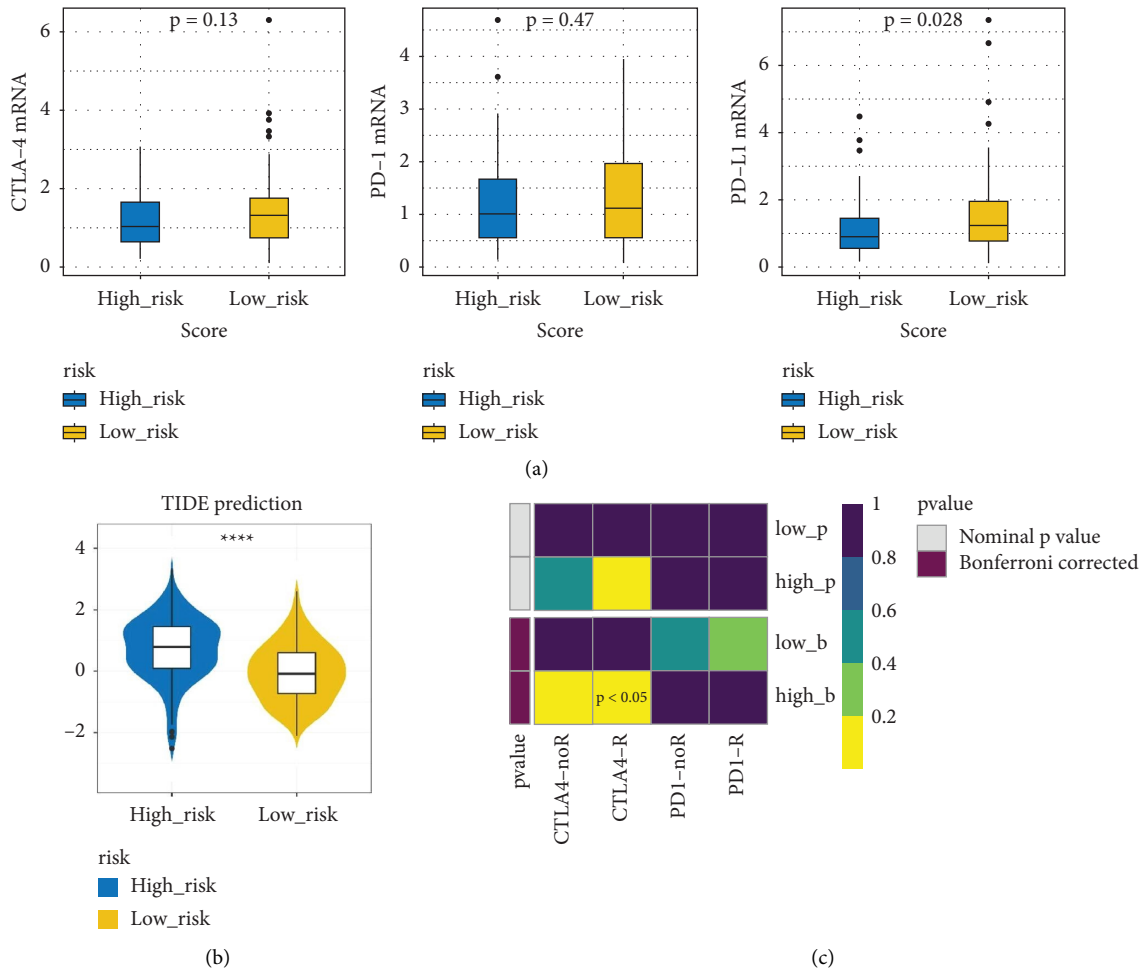

Figure 7: The TIED score and sensitivity scores of high- and low-risk groups. (a) Differences analysis of PD-1, PD-L1, and CTLA-4 in the high- and low-risk groups, basing on the TIED score of targeted immune checkpoints. (b) Sensitivity scores to whole immune checkpoints in high-low risk groups. (c) Sensitivity of the high- and low-risk groups predicted by the SubMap algorithm; R for immunotherapy responders and noR for immunotherapy nonresponders. $P < 0.05$, corrected by Bonferroni, was considered statistically significant.

Moreover, GO and KEGG function analysis indicated that DEGs among the four gene biomarkers were closely correlated with biological processes and signaling pathways, such as ECM organization, extracellular structure organization, external encapsulating structure organization, complement and coagulation cascades, vascular smooth muscle contraction, and focal adhesion.

The m5C locus has been reported to be involved in a variety of biological processes, including structural stability and metabolism of RNA, tRNA recognition, and stress response [8]. A recent study has shown that in human urothelial cell carcinoma of the bladder, m5C regulators bound to the 3′UTR of oncogene mRNA, stabilizing its expression, thereby promoting cancer progression [50]. Yang et al. [17] found that NSUN2 (NOP2/Sun domain family, member 2; MYC-induced SUN domain-containing protein, Misu) was the main enzyme catalyzing m5C formation, while the Aly/REF export factor (ALYREF, an mRNA transport adaptor, also named THOC4) functioned as a specific mRNA m5C-binding protein regulating mRNA export. In addition, $p57^{Kip2}$ was an important downstream gene regulated by NSUN2 in GC. $p57^{Kip2}$ is the recently found CDK inhibitor of the Cip/Kip family and has been involved in many biological processes, including cell cycle control, differentiation, apoptosis, tumorigenesis, and development, which is in accordance with GO terms and KEGG pathways of 4 m5C-related genes [51, 52]. Previous studies found that the expression level of NSUN2 was negatively correlated with $p57^{Kip2}$, and the ability of NSUN2 to knockdown cells proliferation was enhanced after $p57^{Kip2}$ silencing in GC. It revealed another regulatory mechanism that NSUN2 plays an oncogenic role by repressing $p57^{Kip2}$ expression in GC. The cause may be NSUN2 destabilizing the $p57^{Kip2}$ mRNA relying on its methyltransferase activity and m5C modifications in the 3′-untranslated region (UTR) of $p57^{Kip2}$ mRNA [53].

It has been reported that m5C modification is involved in immune microenvironment regulation, and the tumor immune microenvironment plays a role in the effect of m5C regulators on patient prognosis [54]. ALYREF, the Aly/REF nuclear export factor, functions as an m5C reader; its expression levels were significantly associated with immune infiltrating cells, such as

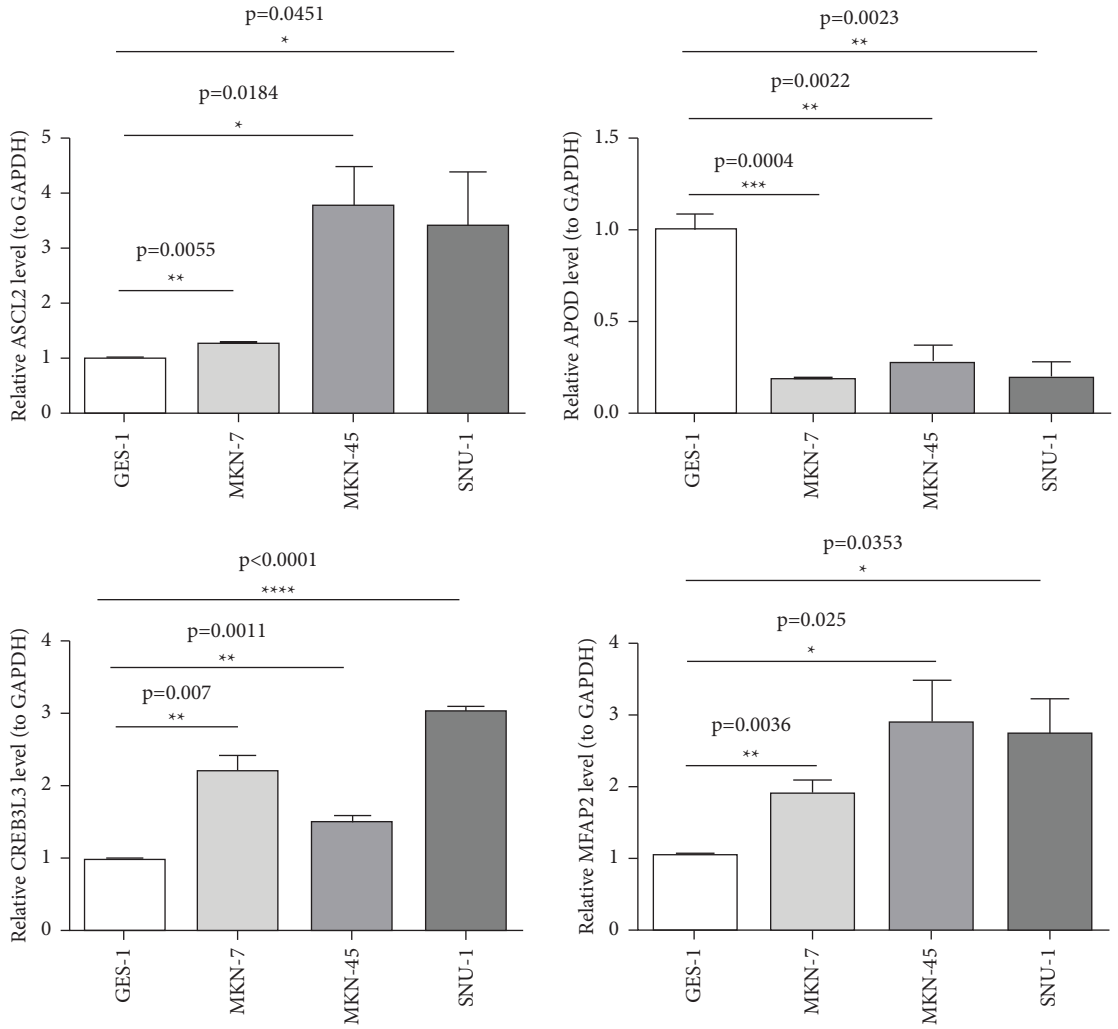

Figure 8: mRNA expression levels of the four prognostic genes in the GC cells and human immortalized normal gastric cells.

B cells, macrophages, NK cells, and dendritic cells [55]. In an eight-lncRNAm5C-related prognostic signature, monocytes, memory B cells, activated mast cells, and naïve CD4 T cells presented a significant differences in high- and low-risk groups [56]. In the present study, significant differences existed in 5 types immune infiltrating cells obtained by the MCP counter algorithm, including NK cells, monocytic lineage, myeloid dendritic cells, cytotoxic lymphocytes, and neutrophils, which have similarities with previous studies.

5. Conclusion

Four DEm5CRGs were identified as biomarkers of the prognostic model in GC using three cohort profile datasets and integrated bioinformatics analysis. The expression pattern and prognostic value of m5C genes in GC were determined, and a novel m5C gene-based risk scoring system was established to predict the clinical outcomes of GC patients. It was found that m5C genes can reliably predict the OS of GC patients, providing a new target for the treatment of GC. However, to provide patients with a better prognosis and find the ideal individualized and targeted therapy, further prospective trials to test clinical efficacy are necessary.

Data Availability

The datasets generated and/or analyzed during the current study are available in the TCGA database (https://portal.gdc.cancer.gov/) and GEO database (https://www.ncbi.nlm.nih.gov/geo/).

Ethical Approval

All the obtained data were used according to the GEO and TCGA data access policies, as well as publication guidelines.

Conflicts of Interest

The authors declare that there are no conflicts of interest.

Authors' Contributions

All authors made positive contributions to the conception and design of the bioinformatic analysis. The literature collection was conducted by Li Song, Xianqi Feng, ShouguoWang, and Rungong Yang. Data acquisition and analysis and figure illustration were completed by Li Song, Qiankun

Li, and Yao Lu. Li Song wrote the first draft of the manuscript. All authors commented on and revised previous versions of the manuscript. All authors read the final manuscript and approved the submission.

Acknowledgments

This work was supported by the National Natural Science Foundation of China (no. 81901971).

Supplementary Materials

Supplementary Figure 1: determination of the k value using the NMF rank survey with multiple parameters. Supplementary Figure 2: OS and DSS analyses of different subtypes. (a) Overall survival (OS) curves for 5 different subtypes. (b) Disease-specific survival (DSS) curves for 5 different subtypes. $P < 0.05$ showed statistically significant. Supplementary Figure 3: validation of the m5C-related risk model. (a) The KM survival curve of the high- and low-risk group in the validation set. (b) The KM survival curve of high- and low-risk group in the testing set. (c) The ROC curve and AUC for four signatures in the validation set. (d) The ROC curve and AUC of four signature in the test set. Supplementary Figure 4: the risk score, survival time, survival status, and expression of the four signatures in the training set (a), validation set (b), and testing set (c). Supplementary Figure 5: KM survival stratification analyses between high- and low-risk GC samples with clinicopathological data. Supplementary Table 1: the primer sequences for qRT-PCR. Supplementary Table 2: the detailed information for TIDE analysis. (*Supplementary Materials*)

References

[1] H. Sung, J. Ferlay, R. L. Siegel et al., "Global cancer statistics 2020: GLOBOCAN estimates of incidence and mortality worldwide for 36 cancers in 185 countries," *CA: A Cancer Journal for Clinicians*, vol. 71, no. 3, pp. 209–249, 2021.

[2] M. Zhu, P. Zhang, S. Yu et al., "Targeting ZFP64/GAL-1 axis promotes therapeutic effect of nab-paclitaxel and reverses immunosuppressive microenvironment in gastric cancer," *Journal of Experimental & Clinical Cancer Research*, vol. 41, no. 1, p. 14, 2022.

[3] H. Zhu, G. Wang, H. Zhu, and A. Xu, "MTFR2, a potential biomarker for prognosis and immune infiltrates, promotes progression of gastric cancer based on bioinformatics analysis and experiments," *Journal of Cancer*, vol. 12, no. 12, pp. 3611–3625, 2021.

[4] L. Zong, M. Abe, Y. Seto, and J. Ji, "The challenge of screening for early gastric cancer in China," *The Lancet*, vol. 388, no. 10060, p. 2606, 2016.

[5] I. V. Zurlo, M. Schino, A. Strippoli et al., "Predictive value of NLR, TILs (CD4+/CD8+) and PD-L1 expression for prognosis and response to preoperative chemotherapy in gastric cancer," *Cancer Immunology, Immunotherapy*, vol. 71, no. 1, pp. 45–55, 2022.

[6] K. Zou, S. Yang, L. Zheng, C. Yang, and B. Xiong, "Efficacy and safety of target combined chemotherapy in advanced gastric cancer: a meta-analysis and system review," *BMC Cancer*, vol. 16, no. 1, p. 737, 2016.

[7] I. A. Roundtree, M. E. Evans, T. Pan, and C. He, "Dynamic RNA modifications in gene expression regulation," *Cell*, vol. 169, no. 7, pp. 1187–1200, 2017.

[8] B. S. Zhao, I. A. Roundtree, and C. He, "Post-transcriptional gene regulation by mRNA modifications," *Nature Reviews Molecular Cell Biology*, vol. 18, no. 1, pp. 31–42, 2017.

[9] N. Pinello, S. Sun, and J. J. L. Wong, "Aberrant expression of enzymes regulating m6A mRNA methylation: implication in cancer," *Cancer Biology & Medicine*, vol. 15, no. 4, pp. 323–334, 2018.

[10] T. Lence, J. Akhtar, M. Bayer et al., "m^6A modulates neuronal functions and sex determination in *Drosophila*," *Nature*, vol. 540, no. 7632, pp. 242–247, 2016.

[11] J. Tong, G. Cao, T. Zhang et al., "m^6A mRNA methylation sustains treg suppressive functions," *Cell Research*, vol. 28, no. 2, pp. 253–256, 2018.

[12] O. K. Zahid, B. S. Zhao, C. He, and A. R. Hall, "Quantifying mammalian genomic DNA hydroxymethylcytosine content using solid-state nanopores," *Scientific Reports*, vol. 6, no. 1, p. 29565, 2016.

[13] R. Reid, P. J. Greene, and D. V. Santi, "Exposition of a family of RNA m5C methyltransferases from searching genomic and proteomic sequences," *Nucleic Acids Research*, vol. 27, no. 15, pp. 3138–3145, 1999.

[14] M. G. Goll, F. Kirpekar, K. A. Maggert et al., "Methylation of $tRNA^{Asp}$ by the DNA methyltransferase homolog dnmt2," *Science*, vol. 311, no. 5759, pp. 395–398, 2006.

[15] Q. Shen, Q. Zhang, Y. Shi et al., "Tet2 promotes pathogen infection-induced myelopoiesis through mRNA oxidation," *Nature*, vol. 554, no. 7690, pp. 123–127, 2018.

[16] M. Schapira, "Structural chemistry of human RNA methyltransferases," *ACS Chemical Biology*, vol. 11, no. 3, pp. 575–582, 2016.

[17] X. Yang, Y. Yang, B. F. Sun et al., "5-methylcytosine promotes mRNA export-NSUN2 as the methyltransferase and ALYREF as an m^5C reader," *Cell Research*, vol. 27, no. 5, pp. 606–625, 2017.

[18] X. Chen, A. Li, B. F. Sun et al., "5-methylcytosine promotes pathogenesis of bladder cancer through stabilizing mRNAs," *Nature Cell Biology*, vol. 21, no. 8, pp. 978–990, 2019.

[19] H. Chen, H. Yang, X. Zhu et al., "m 5 C modification of mRNA serves a DNA damage code to promote homologous recombination," *Nature Communications*, vol. 11, no. 1, p. 2834, 2020.

[20] E. Du, J. Li, F. Sheng et al., "A pan-cancer analysis reveals genetic alterations, molecular mechanisms, and clinical relevance of m 5 C regulators," *Clinical and Translational Medicine*, vol. 10, no. 5, p. e180, 2020.

[21] T. Liu, X. Hu, C. Lin et al., "5-methylcytosine RNA methylation regulators affect prognosis and tumor microenvironment in lung adenocarcinoma," *Annals of Translational Medicine*, vol. 10, no. 5, p. 259, 2022.

[22] X. Li and Y. Meng, "Expression and prognostic characteristics of m 5 C regulators in low-grade glioma," *Journal of Cellular and Molecular Medicine*, vol. 25, no. 3, pp. 1383–1393, 2021.

[23] R. Gaujoux and C. Seoighe, "A flexible R package for non-negative matrix factorization," *BMC Bioinformatics*, vol. 11, no. 1, p. 367, 2010.

[24] H. Wickham, *ggplot2: Elegant Graphics for Data Analysis*, Springer, New York, NY, USA, 2016.

[25] S. Hänzelmann, R. Castelo, and J. Guinney, "GSVA: gene set variation analysis for microarray and RNA-seq data," *BMC Bioinformatics*, vol. 14, no. 1, p. 7, 2013.

[26] M. D. Robinson, D. J. McCarthy, and G. K. Smyth, "edgeR: a Bioconductor package for differential expression analysis of digital gene expression data," *Bioinformatics*, vol. 26, no. 1, pp. 139-140, 2010.

[27] D. J. McCarthy, Y. Chen, and G. K. Smyth, "Differential expression analysis of multifactor RNA-Seq experiments with respect to biological variation," *Nucleic Acids Research*, vol. 40, no. 10, pp. 4288–4297, 2012.

[28] T. M. Therneau and P. M. Grambsch, *Modeling Survival Data: Extending the Cox Model*, Springer, New York, NY, USA, 2000.

[29] A. Kassambara, M. Kosinski, and P. Biecek, "Survminer: Drawing Survival Curves using 'ggplot2'," 2020, https://CRAN.R-project.org/package=survminer.

[30] T. Wu, E. Hu, S. Xu et al., "clusterProfiler 4.0: a universal enrichment tool for interpreting omics data," *Innovation*, vol. 2, no. 3, Article ID 100141, 2021.

[31] H. Hackl, P. Charoentong, F. Finotello, and Z. Trajanoski, "Computational genomics tools for dissecting tumour-immune cell interactions," *Nature Reviews Genetics*, vol. 17, no. 8, pp. 441–458, 2016.

[32] D. Maeser, R. F. Gruener, and R. S. Huang, "oncoPredict: an R package for predicting invivo or cancer patient drug response and biomarkers from cell line screening data," *Briefings in Bioinformatics*, vol. 22, no. 6, Article ID bbab260, 7 pages, 2021.

[33] R. Shridhar, K. Almhanna, S. E. Hoffe et al., "Increased survival associated with surgery and radiation therapy in metastatic gastric cancer," *Cancer*, vol. 119, no. 9, pp. 1636–1642, 2013.

[34] X. Zhu, Y. Wang, W. Xue et al., "The VEGFR-2 protein and the VEGFR-2 rs1870377 A>T genetic polymorphism are prognostic factors for gastric cancer," *Cancer Biology & Therapy*, vol. 20, no. 4, pp. 497–504, 2019.

[35] J. Pan, Z. Huang, and Y. Xu, "m5C-related lncRNAs predict overall survival of patients and regulate the tumor immune microenvironment in lung adenocarcinoma," *Frontiers in Cell and Developmental Biology*, vol. 9, Article ID 671821, 2021.

[36] J. Sun, Z. Zhang, S. Bao et al., "Identification of tumor immune infiltration-associated lncRNAs for improving prognosis and immunotherapy response of patients with non-small cell lung cancer," *Journal for ImmunoTherapy of Cancer*, vol. 8, no. 1, Article ID e000110, 2020.

[37] M. Xue, Q. Shi, L. Zheng, Q. Li, L. Yang, and Y. Zhang, "Gene signatures of m5C regulators may predict prognoses of patients with head and neck squamous cell carcinoma," *American Journal of Tourism Research*, vol. 12, no. 10, pp. 6841–6852, 2020.

[38] Y. He, X. Yu, J. Li, Q. Zhang, Q. Zheng, and W. Guo, "Role of m5C-related regulatory genes in the diagnosis and prognosis of hepatocellular carcinoma," *American Journal of Tourism Research*, vol. 12, no. 3, pp. 912–922, 2020.

[39] H. Zu, H. Wang, C. Li, and Y. Xue, "Preoperative prealbumin levels on admission as an independent predictive factor in patients with gastric cancer," *Medicine (Baltimore)*, vol. 99, no. 11, Article ID e19196, 2020.

[40] M. Wu, Q. Li, and H. Wang, "Identification of novel biomarkers associated with the prognosis and potential pathogenesis of breast cancer via integrated bioinformatics analysis," *Technology in Cancer Research and Treatment*, vol. 20, Article ID 153303382199208, 16 pages, 2021.

[41] X. Guo, X. Liang, Y. Wang et al., "Significance of tumor mutation burden combined with immune infiltrates in the progression and prognosis of advanced gastric cancer," *Frontiers in Genetics*, vol. 12, Article ID 642608, 2021.

[42] A. M. Jubb, S. Chalasani, G. D. Frantz et al., "Achaete-scute like 2 (ascl2) is a target of Wnt signalling and is upregulated in intestinal neoplasia," *Oncogene*, vol. 25, no. 24, pp. 3445–3457, 2006.

[43] R. Zhu, Y. Yang, Y. Tian et al., "Ascl2 knockdown results in tumor growth arrest by miRNA-302b-related inhibition of colon cancer progenitor cells," *PLoS One*, vol. 7, no. 2, Article ID e32170, 2012.

[44] Q. Zuo, J. Wang, C. Chen et al., "ASCL2 expression contributes to gastric tumor migration and invasion by down-regulating miR223 and inducing EMT," *Molecular Medicine Reports*, vol. 18, no. 4, pp. 3751–3759, 2018.

[45] F. Segade, N. Suganuma, J. C. Mychaleckyj, and R. P. Mecham, "The intracellular form of human MAGP1 elicits a complex and specific transcriptional response," *The International Journal of Biochemistry & Cell Biology*, vol. 39, no. 12, pp. 2303–2313, 2007.

[46] L. W. Yao, L. L. Wu, L. H. Zhang et al., "MFAP2 is over-expressed in gastric cancer and promotes motility via the MFAP2/integrin$\alpha 5\beta 1$/FAK/ERK pathway," *Oncogenesis*, vol. 9, no. 2, p. 17, 2020.

[47] T. Debniak, R. J. Scott, R. A. Lea et al., "Founder mutations for early onset melanoma as revealed by whole exome sequencing suggests that this is not associated with the increasing incidence of melanoma in Poland," *Cancer Research and Treatment*, vol. 51, no. 1, pp. 337–344, 2019.

[48] F. Dong, B. J. Quade, P. Dal Cin, and V. Y. Jo, "Expanding the spectrum of translocations in sclerosing epitheloid fibrosarcoma: a new case with EWSR1-CREB3L3 fusion," *Genes Chromosomes & Cancer*, vol. 57, no. 12, pp. 675–677, 2018.

[49] G. Fang, J. Fan, Z. Ding et al., "Prognostic and predictive value of transcription factors panel for digestive system carcinoma," *Frontiers in Oncology*, vol. 11, Article ID 670129, 2021.

[50] K. Chen, Z. Wei, Q. Zhang et al., "WHISTLE: a high-accuracy map of the human N6-methyladenosine (m6A) epitranscriptome predicted using a machine learning approach," *Nucleic Acids Research*, vol. 47, no. 7, p. e41, 2019.

[51] Y. Yan, J. Frisén, M. H. Lee, J. Massagué, and M. Barbacid, "Ablation of the CDK inhibitor p57Kip2 results in increased apoptosis and delayed differentiation during mouse development," *Genes & Development*, vol. 11, no. 8, pp. 973–983, 1997.

[52] P. Zhang, N. J. Liégeois, C. Wong et al., "Altered cell differentiation and proliferation in mice lacking $p57^{KIP2}$ indicates a role in Beckwith-Wiedemann syndrome," *Nature*, vol. 387, no. 6629, pp. 151–158, 1997.

[53] L. Mei, C. Shen, R. Miao et al., "RNA methyltransferase NSUN2 promotes gastric cancer cell proliferation by repressing p57 Kip2 by an m 5 C-dependent manner," *Cell Death & Disease*, vol. 11, no. 4, p. 270, 2020.

[54] R. Wang, Y. Guo, P. Ma et al., "Comprehensive analysis of 5-Methylcytosine (m 5 C) regulators and the immune microenvironment in pancreatic adenocarcinoma to aid

immunotherapy," *Frontiers in Oncology*, vol. 12, Article ID 851766, 2022.

[55] C. Xue, Y. Zhao, G. Li, and L. Li, "Multi-Omic analyses of the m 5 C regulator ALYREF reveal its essential roles in hepatocellular carcinoma," *Frontiers in Oncology*, vol. 11, Article ID 633415, 2021.

[56] H. Zhou, M. Meng, Z. Wang et al., "The role of m5C-related lncRNAs in predicting overall prognosis and regulating the lower grade glioma microenvironment," *Frontiers in Oncology*, vol. 12, Article ID 814742, 2022.

Hindawi
Journal of Oncology
Volume 2023, Article ID 9346621, 21 pages
https://doi.org/10.1155/2023/9346621

Research Article

Microdissecting the Hypoxia Landscape in Colon Cancer Reveals Three Distinct Subtypes and Their Potential Mechanism to Facilitate the Development of Cancer

Pingfei Tang, Yueming Wu, Chaojun Zhu, Qingyuan Li, and Side Liu

Guangdong Provincial Key Laboratory of Gastroenterology, Department of Gastroenterology, Nanfang Hospital, Southern Medical University, Guangzhou 510515, China

Correspondence should be addressed to Side Liu; sideliu@smu.edu.cn

Received 9 September 2022; Revised 9 October 2022; Accepted 25 November 2022; Published 7 March 2023

Academic Editor: Muhammad Muddassir Ali

Background. Hypoxia contributes to tumor progression and confers drug resistance. We attempted to microdissect the hypoxia landscape in colon cancer (CC) and explore its correlation with immunotherapy response. *Materials and Methods*. The hypoxia landscape in CC patients was microdissected through unsupervised clustering. The "xCell" algorithms were applied to decipher the tumor immune infiltration characteristics. A hypoxia-related index signature was developed via the LASSO (least absolute shrinkage and selection operator) Cox regression in The Cancer Genome Atlas (TCGA)-colon adenocarcinoma (COAD) cohort and validated in an independent dataset from the Gene Expression Omnibus (GEO) database. The tumor immune dysfunction and exclusion (TIDE) algorithm was utilized to evaluate the correlation between the hypoxia-related index (HRI) signature and immunotherapy response. Quantitative reverse transcription polymerase chain reaction (qRT-PCR) and western blotting were performed to verify the mRNA expression levels of five key genes. The Cell Counting Kit-8 (CCK-8) assay and flow cytometry were performed to examine the cell viability and cell apoptosis. *Results*. Patients were classified into hypoxia-high, hypoxia-median, and hypoxia-low clusters in TCGA-COAD and verified in the GSE 17538 dataset. Compared with the hypoxia-low cluster, the hypoxia-high cluster consistently presented an unfavorable prognosis, higher immune scores, and stromal scores and elevated infiltration levels of several critical immune and stromal cells. Otherwise, we also found 600 hypoxia-related differentially expressed genes (HRDEGs) between the hypoxia-high cluster and the hypoxia-low cluster. Based on the 600 HRDEGs, we constructed the HRI signature which consists of 11 genes and shows a good prognostic value in both TCGA-COAD and GSE 17538 (AUC of 6-year survival prediction >0.75). Patients with low HRI scores were consistently predicted to be more responsive to immunotherapy. Of the 11 HRI signature genes, RGS16, SNAI1, CDR2L, FRMD5, and FSTL3 were differently expressed between tumors and adjacent tissues. Low expression of SNAI1, CDR2L, FRMD5, and FSTL3 could induce cell viability and promote tumor cell apoptosis. *Conclusion*. In our study, we discovered three hypoxia clusters which correlate with the clinical outcome and the tumor immune microenvironment in CC. Based on the hypoxia cluster and HRDEGs, we constructed a reliable HRI signature that could accurately predict the prognosis and immunotherapeutic responsiveness in CC patients and discovered four key genes that could affect tumor cell viability and apoptosis.

1. Introduction

Colon cancer (CC) is the fifth most frequent malignant disease with 1,148,515 new cases diagnosed in 2020 and accounting for 576,858 cancer-associated deaths around the world [1]. The 5-year survival probability for colorectal cancer ranges from 90% in early-stage patients to 14% in distant-stage patients [2]. The American Joint Committee on Cancer (AJCC) staging is a critical assessment system for the treatment management of CC [3], and patients with stage III or high-risk stage II may need to undergo a combination treatment of curative resection and adjuvant therapy [4]. However, most of the distant-stage patients miss the radical surgical opportunity and die due to metastasis or recurrence.

Owing to the tumor heterogeneity and diverse molecular pattern, patients with the same AJCC stage exhibit tremendous survival differences. Thus, it is imperative to conduct in-depth microdissection and develop new prognostic biomarkers for patients with CC.

Hypoxia is a specific hallmark of solid tumors, owing to the unrestricted growth and abnormal vascularization during the tumor progression [5]. Hypoxia promotes the tumor metastatic cascade, including invasion, migration, and distant metastasis [6]. The hypoxia-inducible factor (HIF)-1α pathway contributes greatly to the modulation of hypoxia-related downstream gene expression and pathway activity in cancer cells under hypoxic conditions [7]. Hypoxia also promotes the epithelial-to-mesenchymal transition (EMT) process and facilitates the invasion of CC cells by activation of HIF1A, whereas treatment with HIF1A-specific small interfering RNAs (siRNAs) suppresses these processes [8]. Our previous study [9] has constructed a hypoxia-related long noncoding RNAs signature that is tightly associated with the prognosis and drug sensitivity in patients with hepatocellular carcinoma. The HIF-1α signaling pathway also confers drug resistance under hypoxic stress in colorectal carcinoma [10, 11]. Hence, we speculate that the hypoxic exposure level in tumor tissues probably has a critical impact on the prognosis and treatment effectiveness of CC.

Over the past decade, immunotherapeutic treatment based on immune checkpoint inhibitors (ICIs) has resulted in revolutionary long-term benefits in the therapy of several cancer types [12]. ICIs such as anti-PD-1 (programmed cell death 1) and anti-PD-L1 (programmed cell death 1 ligand 1) have achieved a durable response in a subset of microsatellite instability-high (MSI-H) patients [12], whereas the MSI-L/MSS (MSI-low/microsatellite stability) patients who constitute the majority of CC patients have not obtained satisfactory benefits from ICI treatment. Interestingly, hypoxia has been reported to affect tumor plasticity, heterogeneity, and the immune resistance phenotype [13]. Hypoxia not only recruits myeloid-derived suppressive cells (MDSCs), cancer-associated fibroblasts (CAFs), and regulatory T cells (Tregs) to induce tumor immunosuppression [14] but also augments the expression level of immune checkpoints such as PD-L1 to promote tumor immune evasion [15]. Hence, targeting the hypoxic microenvironment may improve the efficacy of cancer immunotherapy [16]. Nevertheless, there is still a deficiency in comprehensive delineation of the interplay among hypoxia, tumor immune infiltrating patterns, and immunotherapy response in patients with CC.

In the current study, we discovered the hypoxia cluster in CC patients using unsupervised clustering based on two publicly available datasets (TCGA-COAD and GSE17538) and investigated the intrinsic correlation between hypoxia and the tumor immune microenvironment by the xCell algorithm and TIDE. Additionally, we developed a reliable hypoxia-related index (HRI) prognostic signature that exhibited good performance in predicting clinical prognosis and immunotherapy response in two independent datasets by the LASSO cox regression model. Finally, *in vitro* experiments were supplied to explore the results at the cell level. Our findings may deepen the understanding of the hypoxia role in the tumor microenvironment and provide beneficial information for immunotherapy in CC.

2. Materials and Methods

2.1. Data Preprocessing. The fragments per kilobase per million mapped reads (FPKM) profiles of the level-3 sequencing transcriptomic data in TCGA-COAD cohort were obtained from TCGA database (https://portal.gdc.cancer.gov/). We subsequently converted the FPKM values into the log2-transformed TPM (transcripts per million) values for further analysis. The corresponding detailed clinical parameters were publicly acquired from the cBioPortal database [17] (https://cbioportal.org).

Another publicly available, independent microarray dataset, GSE17538, was downloaded from the Gene Expression Omnibus database (https://www.ncbi.nlm.nih.gov/geo/). The TCGA-COAD cohort consisted of 402 primary CC samples and 39 adjacent normal tissues. Only 348 patients with complete clinical data and overall survival (OS) time of ≥1 month and 39 normal samples were used as the discovery cohort. The GSE17538 dataset was composed of two subsets, GSE17536 (177 CC patients) and GSE17537 (55 CC patients), and the nonbiological batch was corrected using the "ComBat" function via the R "sva" package. In total, 210 patients with CC in GSE17538 with complete clinical and histopathological grade information were enrolled as the independent validation cohort. Detailed information on all enrolled patients in the previous two datasets is listed in Supplemental Table 1 (Table S1).

2.2. Microdissecting the Hypoxia-Specific Cluster of CC. The "HALLMARK_HYPOXIA" gene set ("h.all.v7.2.symbols.gmt") includes 200 hypoxia-specific genes (Table S2), which have been demonstrated to typically represent the biological process under hypoxia conditions and was gathered from the molecular signatures database (MsigDB) [18]. TCGA-COAD cohort (348 patients) and GSE17538 dataset (210 patients) were assigned into different groups by the unsupervised clustering method according to the expression of the previous 200 hypoxia-specific genes, respectively, via the "km" method in the R "ConsensusClusterPlus" package. Survival analysis for hypoxia-specific clusters was performed by the R "survival" package, and the survival difference among these clusters was determined by the log-rank test.

2.3. Gene Set Variation Analysis (GSVA). Overall, 50 hallmark gene sets (h.all.v7.2.symbols.gmt) were downloaded from the MSigDB database [18]. In addition, 13 typical metabolic pathways (Table S3) associated with "GLYCOLYSIS," "OXIDATIVE_PHOSPHORYLATION," and "CITRATE_CYCLE_TCA_CYCLE" were curated from the MSigDB database. The activity differences of these hallmark pathways and metabolic pathways among different hypoxia-

specific clusters were explored by GSVA [19], which can calculate a specific pathway score for each sample using an unsupervised nonparametric algorithm.

2.4. Identifying Hypoxia-Related Differentially Expressed Genes (HRDEGs). Analysis of differentially expressed genes (DEGs) between the 348 COAD cancer samples and 39 adjacent normal samples in TCGA-COAD cohort was carried out by the "limma" package, according to the standard of the absolute value of log2 (fold change) greater than 1 and an adjusted p value less than 0.05. With the same method and criteria, DEGs between the hypoxia-high and hypoxia-low clusters were further examined. HRDEGs were defined as the intersection of the previous two gene lists.

2.5. Development of the HRI Signature. A univariable Cox regression model was applied to screen the prognostic HRDEGs in TCGA-COAD cohort. The LASSO penalty Cox regression model, which can avoid overfitting and select the most contributive variables through tuning the penalty parameter, was employed to develop the optimal HRI signature using the "glmnet" package [20]. The final HRI score formula is defined as follows: $\text{risk score} = \sum_{k=1}^{n} expk * coefk$, where k is the sequence number of the prognostic gene in the HRI signature, exp$k$ represents the corresponding gene expression of each patient, and coef$k$ represents the corresponding LASSO coefficient.

2.6. Evaluation and Validation of the Prognostic Capability of the HRI Signature. HRI scores of CC patients in TCGA--COAD cohort (discovery dataset) and GSE17538 (validation dataset) were calculated using the previous formula. Patients in each dataset were assigned to the HRI high- or low-risk group according to their respective median HRI scores. Survival analysis for each dataset was carried out by the "survival" package, and the survival differences were determined by the log-rank test. Time-dependent receiver operating characteristic (ROC) curves were drawn to evaluate the performance for prognosis prediction using the "timeROC" package. Multivariable Cox regression was conducted to determine whether the HRI signature was independent of other clinical parameters (age, sex, AJCC stage, and histopathological grade) in prognostic prediction.

2.7. Single Sample Gene Set Enrichment Analysis (GSEA). The gene list of critical immune function pathways (Table S4) was collected from the previous studies [21]. Single-sample GSEA (ssGSEA) [22], a particular kind of GSEA that can calculate the relative score for a predefined gene list at a single sample level, was utilized to calculate the relative scores of the previous immune function pathways using the "GSVA" package in R.

2.8. Analyzing the Immune Landscape of Hypoxia-Specific Clusters. The "xCell" algorithm, which can effectively infer immune and stromal cell abundance from the mixture transcriptomic profiles [23], was applied to comprehensively delineate the tumor immune microenvironment (TIME).

2.9. Evaluating the HRI Predictive Ability of Immunotherapy Response. The tumor immune dysfunction and exclusion (TIDE) algorithm, which can calculate the TIDE scores representing the dysregulation of tumor immune escape for tumor samples and function as a representative biomarker to predict responsiveness to immune checkpoint blockade [24], was employed to examine the HRI predictive capability of immunotherapy response in CC patients.

2.10. Quantitative Reverse Transcription Polymerase Chain Reaction (qRT-PCR). Thirty pairs of clinical samples (including tumors and corresponding adjacent normal samples) of patients diagnosed with CC were gathered at Nanfang Hospital of Southern Medical University. The samples were immediately preserved at −80°C postcollection after surgical resection until RNA extraction. All patients gave informed consent for sample collection and usage. The present research was supported by the Institutional Ethical Committee Board of Nanfang Hospital (NFEC-201809-K3). Total RNA from 30 pairs of clinical tissues was isolated using an RNAex Pro Reagent (Accurate Biology, China). qRT-PCR reactions were performed using the Evo M-MLV RT Premix for qPCR (Accurate Biology, China) and SYBR® Green Premix Pro Taq HS qPCR Kit (Accurate Biology, China). GAPDH was utilized as the internal standard, and each sample was analyzed in triplicate. All PCR primer sequences are presented in Table S5. *Relative quantification of mRNA expression levels of RGS16, SNAI1, CDR2L, FRMD5, and FSTL3 was analyzed via the* $2^{-\Delta\Delta Ct}$ *method.*

2.11. Cell Culture and Cell Transfection. Human colon cell line HCT116 was obtained from ATCC. Then, the cells were cultured in DMEM with 10% FBS at 37°C in 5% CO_2.

The plasmid and scramble were purchased from Biosystems (General Biosystems, Anhui, China). siRNA and siRNA scramble were obtained from the GenePharma Corporation (Shanghai, China). According to the introduction, all siRNA and vectors were transfected using a lipofectamine 3000 transfection kit (Invitrogen, USA). qRT-PCR was performed to test the transfection efficiency.

2.12. Western Blot. Proteins were extracted using RIPA (CWBIO, China), subjected to SDS-PAGE gel electrophoresis, and then transferred to a nitrocellulose membrane, incubated with primary antibodies, and incubated overnight at 4°C. The secondary antibody was then incubated for 1 h at room temperature. Immobilon ECL substrate was used for signal detection and image acquisition.

2.13. CCK-8 Assay. The Cell Counting Kit-8 (CCK-8, ImmunoWay Biotechnology Company, Plano, TX, USA) assay was used to monitor cell proliferation. In brief, the cells

transfected with siRNA or plasmid were placed on 96-well plates and cultured for 24 h, 48 h, 72 h, and 96 h. Then, the OD450 value was detected using the Thermo Scientific Varioskan Flash spectrophotometer (Thermo Scientific, Finland).

2.14. Flow Cytometry. Stably transfected tumor cells were placed in 6-well plates, 3×10^5 cells per well. The purified tumor cells were adjusted to 1×10^6/L. The apoptosis rate of tumor cells was evaluated by flow cytometry (FACScan, BD Bioscience) with an Annexin-V-FITC/PI apoptosis kit (ads5001; Absin, Shanghai, China).

2.15. Statistical Analysis. Numerical variable differences with normal distribution were determined using Student's *t*-test or analysis of variance for two or more groups, respectively. The Wilcoxon rank-sum test or Kruskal–Wallis test were performed to determine the numerical variable differences with nonnormal distribution for two or more groups, respectively. Categorical variable differences were examined via the chi-square test. Spearman correlation analysis was conducted to investigate the correlation between the continual variables. Univariate Cox and LASSO penalty Cox regression analyses were utilized to perform survival analyses. Survival differences were examined by the Kaplan–Meier curve and log-rank test. A two-tailed p value of <0.05 was set to indicate statistical significance. For multiple testing, the p value was corrected by the Benjamini–Hochberg method. We utilized R software (version 3.6.3) to perform all the statistical analyses.

3. Results

3.1. The Discovery of Hypoxia-Related Cluster Using Unsupervised Clustering. In total, 348 patients with complete clinical information in TCGA-COAD cohort were categorized into three different clusters by unsupervised clustering (Figure 1(a) and Figures S1A-S1B). Clusters 1, 2, and 3 consisted of 82, 182, and 84 patients, respectively. The detailed lists are shown in Table S6. The principal component analysis confirmed a clear distinction among the three clusters (Figure 1(c)). To clarify the relationship between the clusters and hypoxia, the HIF1A messenger RNA (mRNA) expression, which represents the mRNA level of the master regulator HIF-1α under hypoxic conditions, was compared among the three clusters. Notably, cluster 3 possessed the highest HIF1A mRNA level, while cluster 1 exhibited the lowest HIF1A mRNA level (Figure 1(d)). GSVA further showed that cluster 3 had the highest activity in the "HALLMARK_HYPOXIA" pathway, whereas cluster 1 displayed the lowest pathway activity (Figure 1(e)). These results demonstrated that the previous three clusters were strongly correlated with hypoxia exposure in CC tissues. Henceforth, we defined clusters 3, 2, and 1 as the hypoxia-high, hypoxia-median, and hypoxia-low subtypes, respectively. Survival analysis revealed a significant OS difference among the three hypoxia-specific clusters (global p value = 0.045, Figure 1(f)). The hypoxia-high subtype had the poorest OS outcome compared with the hypoxia-low (p = 0.031) and hypoxia-median (p = 0.046) subtypes.

To further verify the hypoxic landscape in CC, the independent microarray dataset GSE17538 was explored using the same unsupervised clustering method. Notably, 210 patients with complete clinical characteristics in GSE17538 were likewise classified into three different clusters (Figures 1(b), S1C-S1D, and 1(g)), with detailed lists shown in Table S7), namely, cluster 1 (77 patients), cluster 2 (68 patients), and cluster 3 (65 patients). Similarly, cluster 3 had the highest level of HIF1A mRNA expression and the activity of the "HALLMARK_HYPOXIA" pathway, while cluster 1 exhibited the lowest level for the previous two indices (Figures 1(h) and 1(i)). Thus, we also defined clusters 3, 2, and 1 in GSE17538 as the hypoxia-high, hypoxia-median, and hypoxia-low subtypes, respectively. In addition, there was a significant OS difference among the three clusters (global p value = $1.35e-04$, Figure 1(j)). The hypoxia-high cluster showed the poorest OS outcome compared with the hypoxia-low (p value $3.22e-05$) and hypoxia-median (p value 0.019) clusters. The previous results confirmed that the hypoxia exposure landscape is closely correlated with the clinical outcomes in patients with CC.

3.2. Distinct Molecular Patterns among the Hypoxia-Specific Clusters. Owing to the close relationship between hypoxia-specific clusters and clinical outcomes, we continued to explore the underlying molecular mechanisms. GSVA results for the hallmark gene sets showed that the relative activities of several tumor aggression-associated pathways, including "EPITHELIAL_MESENCHYMAL_TRANSITION," "ANGIOGENESIS," "MYOGENESIS," "APICAL_JUNCTION," "APICAL_SURFACE," "HYPOXIA," and "IL6_JAK_STAT3_SIGNALING," were elevated in the hypoxia-high group compared with those in the hypoxia-low group in both TCGA-COAD and GSE17538 datasets (Figures 2(a) and 2(b)).

3.3. Identification of HRDEGs. In total, 1756 DEGs (1748 upregulated and 8 downregulated genes, Figure 3(a)) between the hypoxia-high and hypoxia-low clusters (|log2FC| greater than 1 and adjusted p value less than 0.05) were identified. Using the same criteria, we acquired 2745 DEGs (1442 upregulated and 1303 downregulated genes, Figure 3(b)) between the tumor tissues and adjacent normal samples. Furthermore, 600 overlapping genes for the previous two gene lists (Figure 3(c), detailed lists shown in Table S8) were categorized as HRDEGs. Gene Ontology (GO) function enrichment analysis demonstrated that these HRDEGs were predominantly enriched in several biological process (BP) terms, including "extracellular matrix organization," "positive regulation of cell adhesion," and "cell-substrate adhesion" (Figure 3(d)). KEGG pathway analysis further showed a strong linkage between the HRDEGs and the following pathways: "cytokine-cytokine receptor interaction," "PI3K–Akt signaling pathway," and "focal adhesion" (Figure 3(e)). These enriched terms were closely

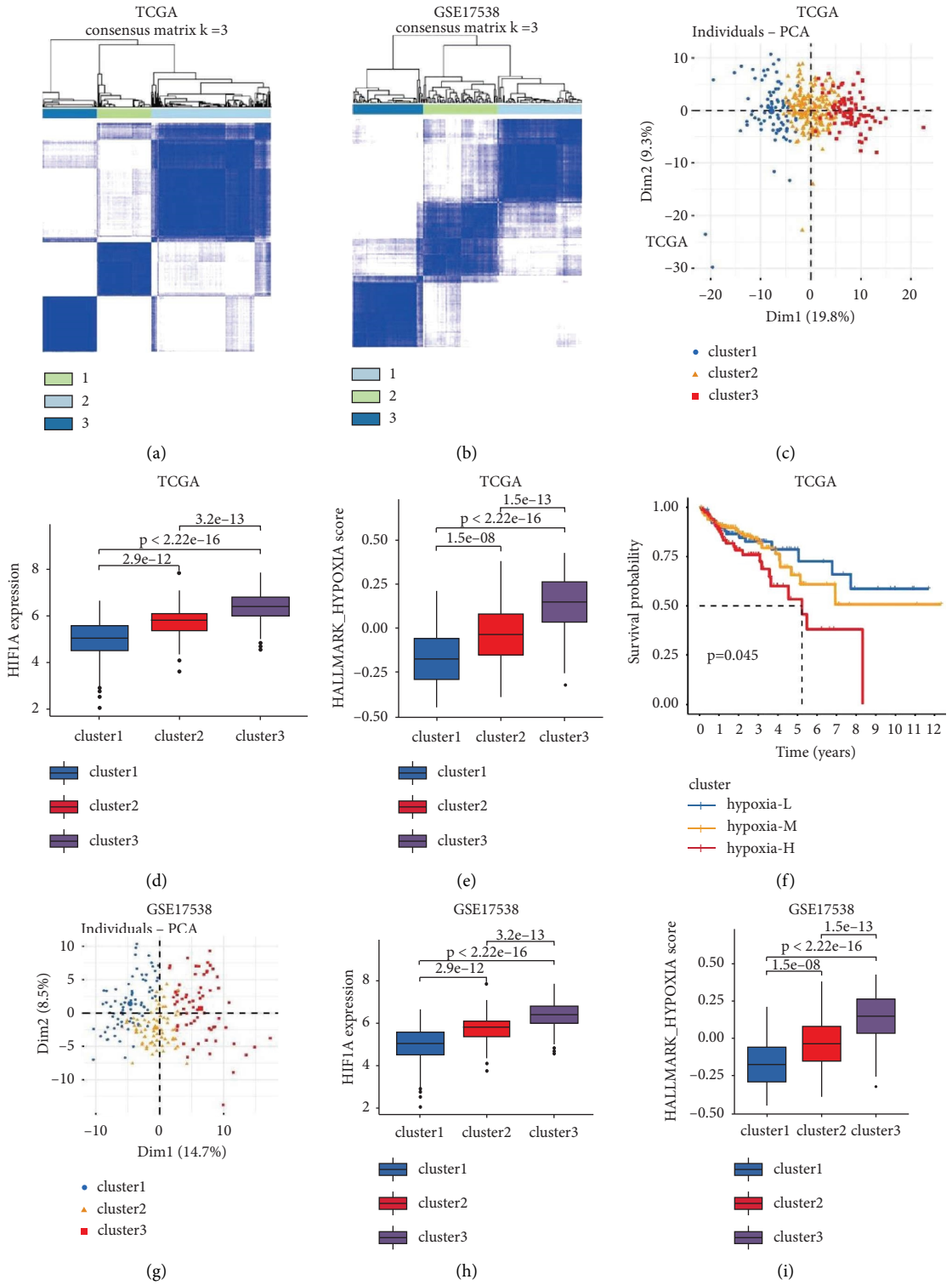

Figure 1: Continued.

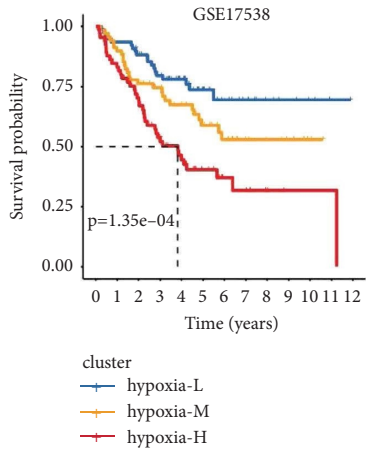

(j)

Figure 1: Microdissection of the hypoxia landscape in TCGA-COAD cohort and GSE17538 cohort. Consensus matrix plot of unsupervised clustering in TCGA-COAD cohort (a) and GSE17538 cohort (b), when $k = 3$ representing the optimal cluster number. (c) and (g) PCA plot of hypoxia-specific clusters. Comparison of HIF1A expression (d) and (h), HALLMARK_HYPOXIA pathway score (e) and (i), and the survival difference (f) and (j) among hypoxia-specific clusters. COAD: colon adenocarcinoma. PCA: principal component analysis. Hypoxia-L: hypoxia-low; hypoxia-M: hypoxia-median; hypoxia-H: hypoxia-high. OS: overall survival.

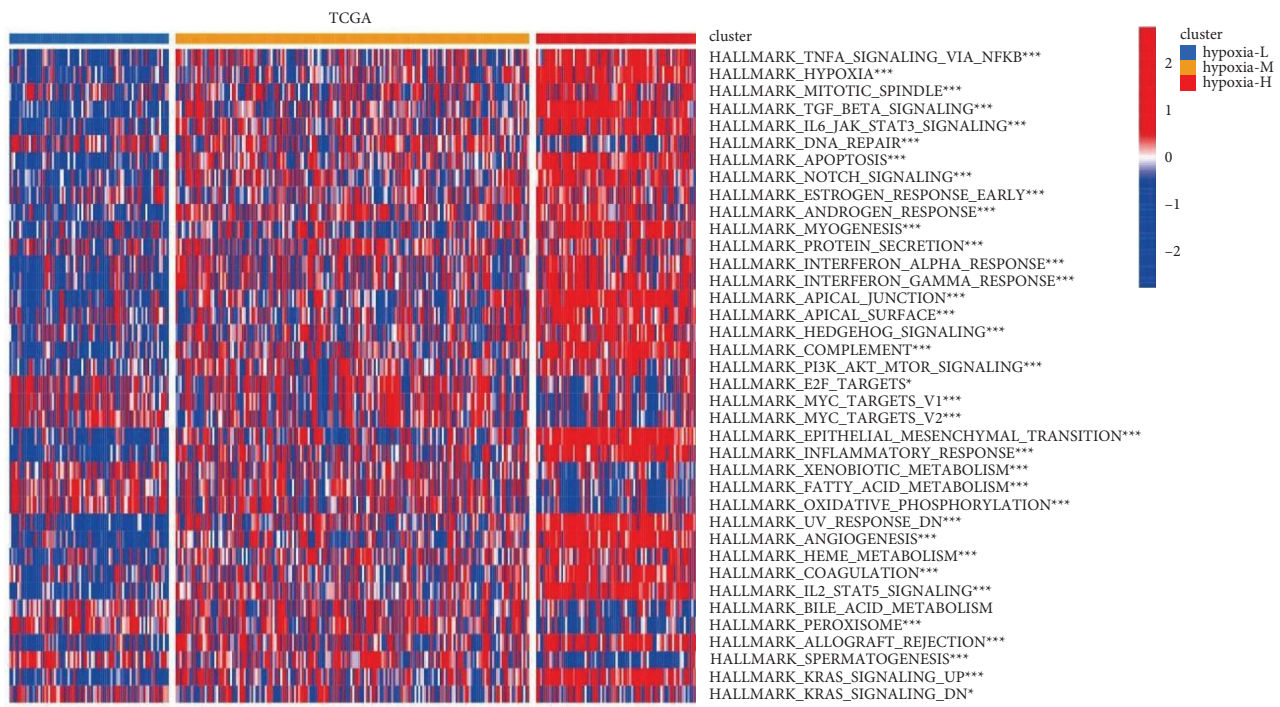

(a)

Figure 2: Continued.

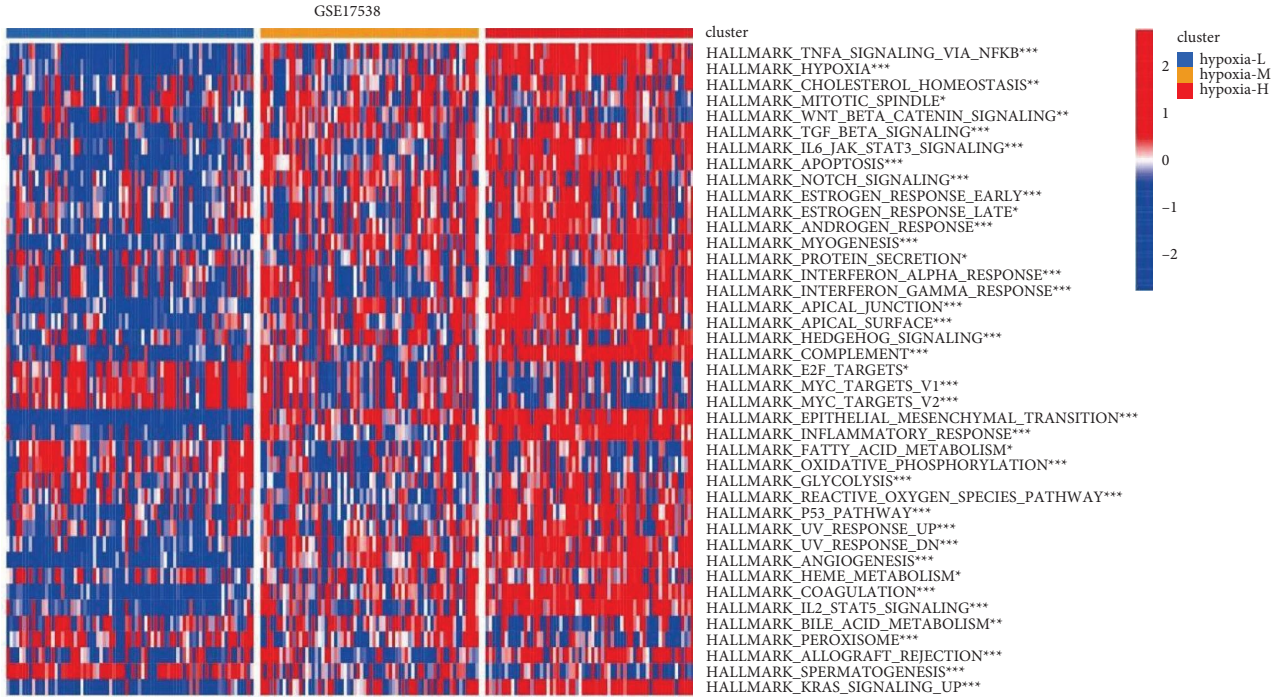

(b)

Figure 2: The distinct molecular pattern among the hypoxia-specific clusters. Comparison of the relative activities of the hallmark gene sets among hypoxia-specific clusters in TCGA-COAD (a) and GSE 17538 (b). COAD: colon adenocarcinoma. Hypoxia-L: hypoxia-low; hypoxia-M: hypoxia-median; hypoxia-H: hypoxia-high. $^{***}p < 0.001$; $^{**}p < 0.01$; $^{*}p < 0.05$.

associated with extracellular signal communication and cancer cell invasion, indicating that our defined HRDEGs probably participated in the tumor progression.

3.4. Development of HRI Signature. TCGA-COAD cohort with 348 patients was utilized as the discovery cohort to construct an HRI signature. The univariate Cox regression model yielded 22 prognostic genes out of the aforementioned 600 HRDEGs (Figure 4(a)). LASSO penalty Cox regression selected the optimal HRI signature according to the "lambda. min" standard, which represents the lambda (tuning parameter) with minimal cross-validation error. Ultimately, 11 selected optimal prognostic HRDEGs were incorporated to develop the HRI score signature (Figures S2A-S2B, detailed gene list shown in Table S9). The final HRI calculation formula was as follows (detailed formula development is described in the "Methods" section): HRI = (−0.140) ∗ CD177 expression + 0.045 ∗ CP expression + 0.006 ∗ RGS16 expression + 0.013 ∗ PGM5 expression + 0.206 ∗ SNAI1 expression + 0.010 ∗ CALB2 expression + 0.041 ∗ OSBPL1A expression + 0.043 ∗ CDR2L expression + 0.012 ∗ FRMD5 expression + 0.096 ∗ FSTL3 expression + 0.069 ∗ TUBB2B expression. The HRI scores for CC patients in TCGA-COAD cohort were calculated using the previous HRI calculation formula (Table S10). Patients were assigned into the HRI high- or low-risk groups based on the median HRI score. Survival analysis uncovered that the HRI high-risk group exhibited a significantly poorer OS outcome than the low-risk group ($p = 6.321e - 06$, Figure 4(b)). Time-dependent ROC curves showed that the areas under the curve (AUCs) of 1-, 3-, 5-, and 6-year survival predictions were 0.682, 0.699, 0.768, and 0.753, respectively (Figure 4(c)), indicating good prognostic prediction. To further validate the reliability of the signature, the HRI scores for 210 patients in the validation cohort GSE17538 were calculated using the same formula (Table S11). Because the data type of dataset GSE17538 (microarray data) was different from that of the TCGA-COAD cohort (sequencing data), we classified all patients in GSE17538 into HRI high-risk or low-risk groups according to the median HRI score of the dataset GSE17538. Similarly, the HRI high-risk group possessed a poorer OS prognosis than the low-risk counterpart ($p = 7.956e - 06$, Figure 4(d)). The AUCs for 1-, 3-, 5-, and 6-year survival predictions were 0.647, 0.645, 0.716, and 0.754, respectively (Figure 4(e)). These results verified the robustness and reliability of the HRI signature in different platform datasets.

Subsequently, we investigated the relationship between HRI scores and HIF1A mRNA expression. Notably, the HRI high-risk group consistently showed higher HIF1A expression than the low-risk counterpart in both TCGA--COAD (Figure 4(f)) and GSE17538 (Figure 4(g)), demonstrating that the HRI scores indeed reflected the hypoxic exposure level in CC tissues.

3.5. Correlation between the HRI Signature and Clinical Parameters. Owing to the remarkable impact of the HRI scores on the patient's clinical outcomes, we investigated the

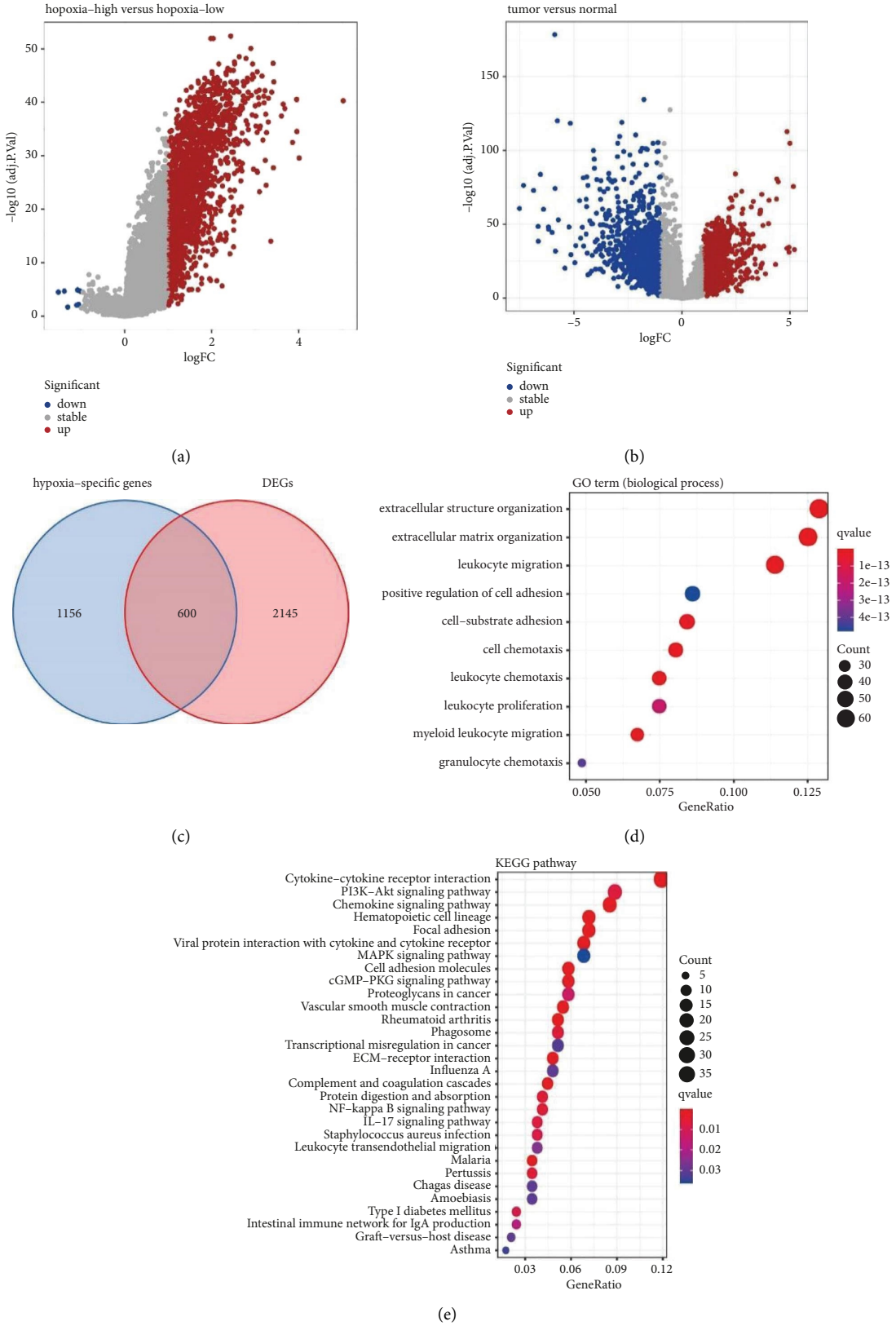

Figure 3: Identification of the hypoxia-related differentially expressed genes (HRDEGs) in TCGA-COAD cohort. (a) Volcano plot of hypoxia-specific genes between hypoxia-high and hypoxia-low clusters. (b) Volcano plot of differentially expressed genes (DEGs) between tumor and adjacent normal tissues. (c) Venn diagram of HRDEGs. Bubble plots for GO (d) and KEGG (e) functional annotation of the 600 HRDEGs. GO: gene ontology. KEGG: Kyoto encyclopedia of genes and genomes.

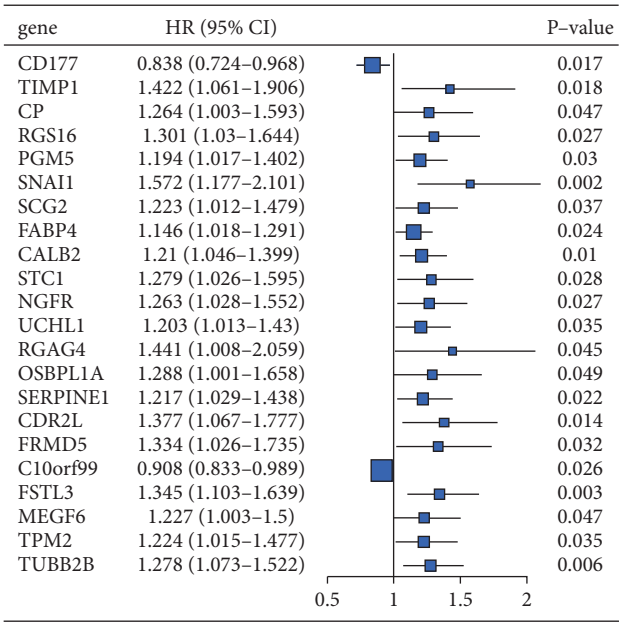

(a)

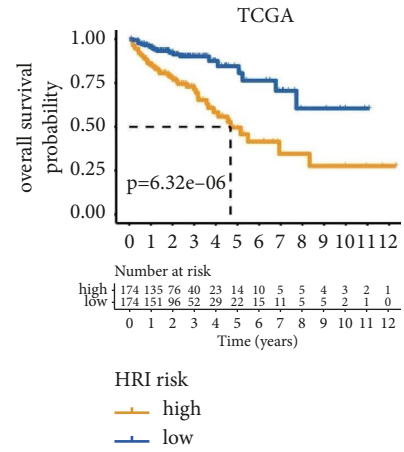

(b)

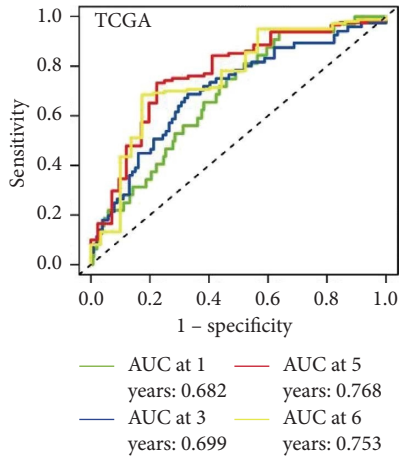

(c)

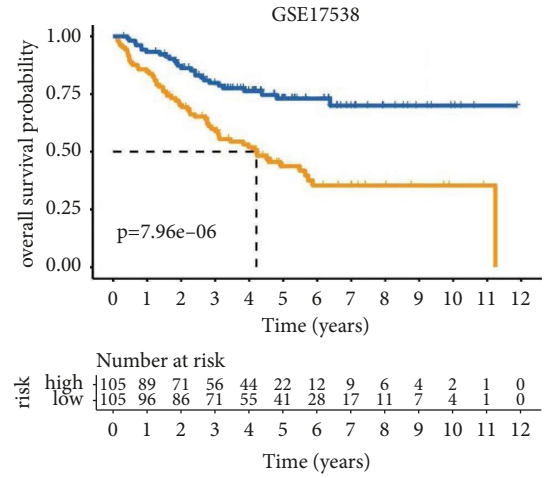

(d)

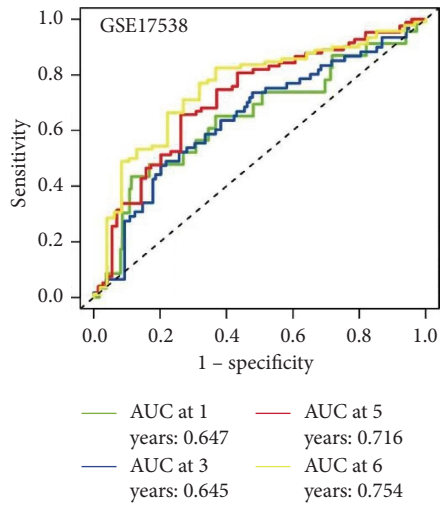

(e)

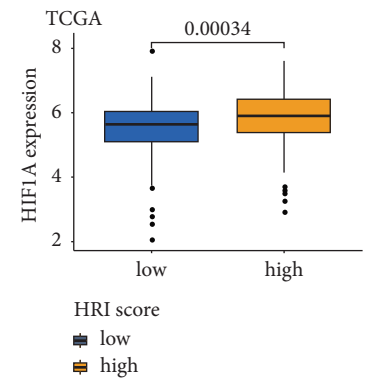

(f)

Figure 4: Continued.

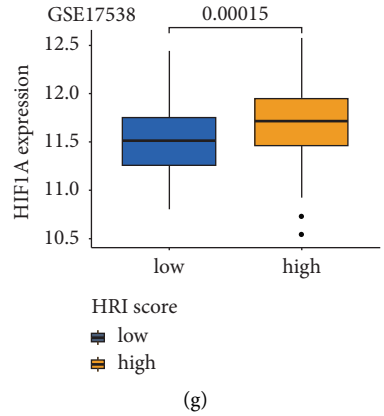

(g)

Figure 4: Development of the HRI signature. (a) Forest plot of twenty-two prognostic genes obtained by univariate Cox regression. Kaplan–Meier curves and the log-rank test p value for TCGA-COAD (b) and GSE17538 (d) datasets. The AUCs of the time-dependent ROC curves for TCGA-COAD (c) and GSE17538 (e) datasets. Comparison of HIF1A mRNA expression between HRI high-risk and low-risk groups in TCGA-COAD (f) and GSE17538 (g). AUC: area under the curve. ROC: receiver operating characteristic.

correlation between HRI scores and several critical clinical parameters. Results for TCGA-COAD cohort indicated that patients with T3-4, M1, N2, stage III-IV, and "Vascular Invasion" possessed higher HRI scores than patients with T1-2, M0, N0, stage I-II, and "nonvascular invasion," respectively (Figures 5(a)–5(e)). Furthermore, patients with stage III-IV, histopathological grade 3, and recurrence in GSE17538 had elevated HRI scores compared with patients with stage I-II, grade 1 or 2, and nonrecurrence, respectively (Figures S3A–S3C). Additionally, patients with high HRI scores had poorer disease-free survival outcomes in TCGA-COAD ($p = 9.12e - 05$, Figure 5(f)) and poorer recurrence-free survival outcomes in GSE17538 ($p = 0.006$, Figure S3D) than patients with low HRI scores.

To identify the independent predictive ability of the HRI signature, a multivariable Cox regression model was further performed on the TCGA-COAD and GSE17538 datasets. The results indicated that age, AJCC stage, and HRI scores were independent prognostic predictors after adjusting for other clinical parameters such as sex in TCGA-COAD cohort (Figure 5(g)). Similarly, stage and HRI risk scores were consistently independent of age, sex, and histopathological grade in GSE17538 (Figure S3E). The previous evidence demonstrated that the HRI signature can act as an independent indicator of prognosis in CC.

3.6. Different Molecular Patterns, TIME, and Immunotherapy Response between the High- and Low-Risk Groups. To further explore the underlying molecular mechanism, we investigated the different molecular patterns and TIME between the two HRI risk groups. GSEA results displayed that several critical hallmark pathways, including "APICAL_JUNCTION," "APICAL_SURFACE," "ANGIOGENESIS," "HYPOXIA," "EPITHELIAL_MESENCHYMAL_TRANSITION," and "P53_PATHWAY," were substantially enriched in the high-risk group in both TCGA-COAD (Figure S4A) and GSE17538 (Figure S4C) datasets. Furthermore, KEGG pathways such as "ADHERENS_JUNCTION," "FOCAL_ADHESION," and "PATHWAYS_IN_CANCER" were significantly enriched in the group with high HRI scores in both TCGA-COAD (Figure S4B) and GSE17538 (Figure S4D) datasets. These results suggest that hypoxia contributes to tumor aggression through the abovementioned oncogenic pathways. The "xCell" algorithm revealed that the high-risk group holds a higher abundance of macrophages, fibroblasts, and endothelial cells and higher stroma scores and microenvironment scores than the low-risk group in TCGA-COAD (Figure 6(a)). The high-risk group in GSE17538 possessed a higher infiltrating level of macrophages and higher immune scores and microenvironment scores than the low-risk counterpart (Figure S5A). The ssGSEA results displayed that the high-risk group consistently possessed higher scores in several critical immune pathways such as "check–point" and "T_cell_co–inhibition" than the low-risk group in both TCGA-COAD (Figure 6(b)) and GSE17538 (Figure S5B) cohorts. Moreover, the mRNA expression level of PD-L1 (CD274) was significantly elevated in the HRI high-risk group compared with the low counterpart in both TCGA-COAD (Figure 6(c)) and GSE17538 (Figure S5C) cohorts, suggesting distinct immune infiltration characteristics between the two groups.In addition, compared with the hypoxia-low cluster, the hypoxia-high clusterconsistently presented higher immune scores, stromal scores, and elevatedinfiltration levels of several critical immune and stromal cells (endothelialcells, fibroblasts, macrophages, dendritic cells, CD8+ T cells, CD4+ memory Tcells, B cells, and monocytes) in both TCGA-COAD and GSE17538 (Figure S7A-B). Theabove evidence demonstrated that elevated hypoxia exposure levels in CC tissuescorrelated with higher stromal and immune cell infiltration.

Using the TIDE algorithm, we estimated the TIDE scores for CC patients in the TCGA-COAD (Table S12) and GSE17538 (Table S13), respectively. Patients in the HRI high-risk group possessed higher TIDE scores than the corresponding low-risk patients in both TCGA-COAD (Figure 6(d)) and GSE17538 (Figure S5D). Moreover, HRI

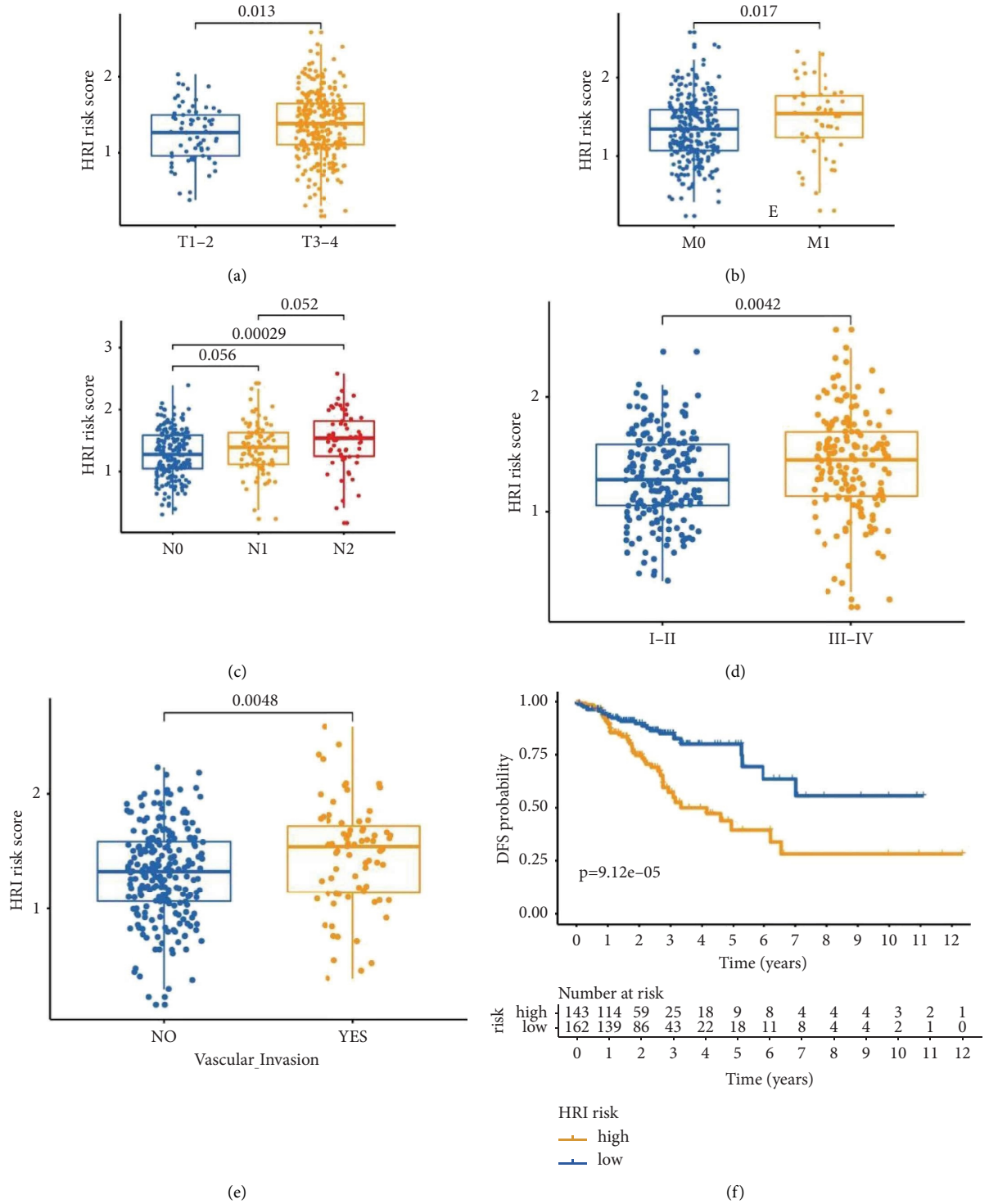

Figure 5: Continued.

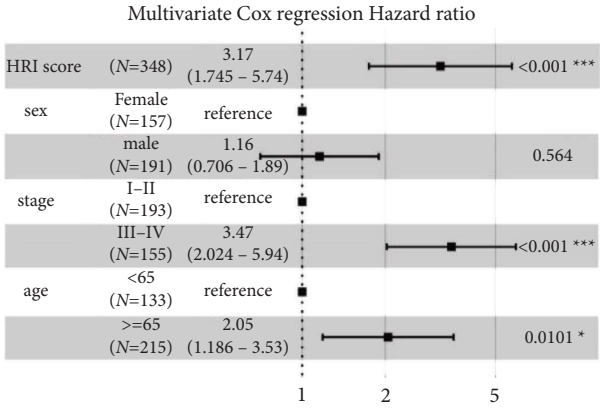

(g)

Figure 5: Correlation between the HRI score and clinical parameters in TCGA-COAD cohort. Comparison of HRI scores between different clinical subgroups, including T (a), M (b), N (c), stage (d), and vascular invasion (e). Disease-free survival (DFS) difference between HRI high-risk and low-risk groups (f). Forest plot for multivariate Cox regression analysis in TCGA-COAD (g). HRI: hypoxia-related index. $^{***}p < 0.001$; $^{**}p < 0.01$; $^{*}p < 0.05$.

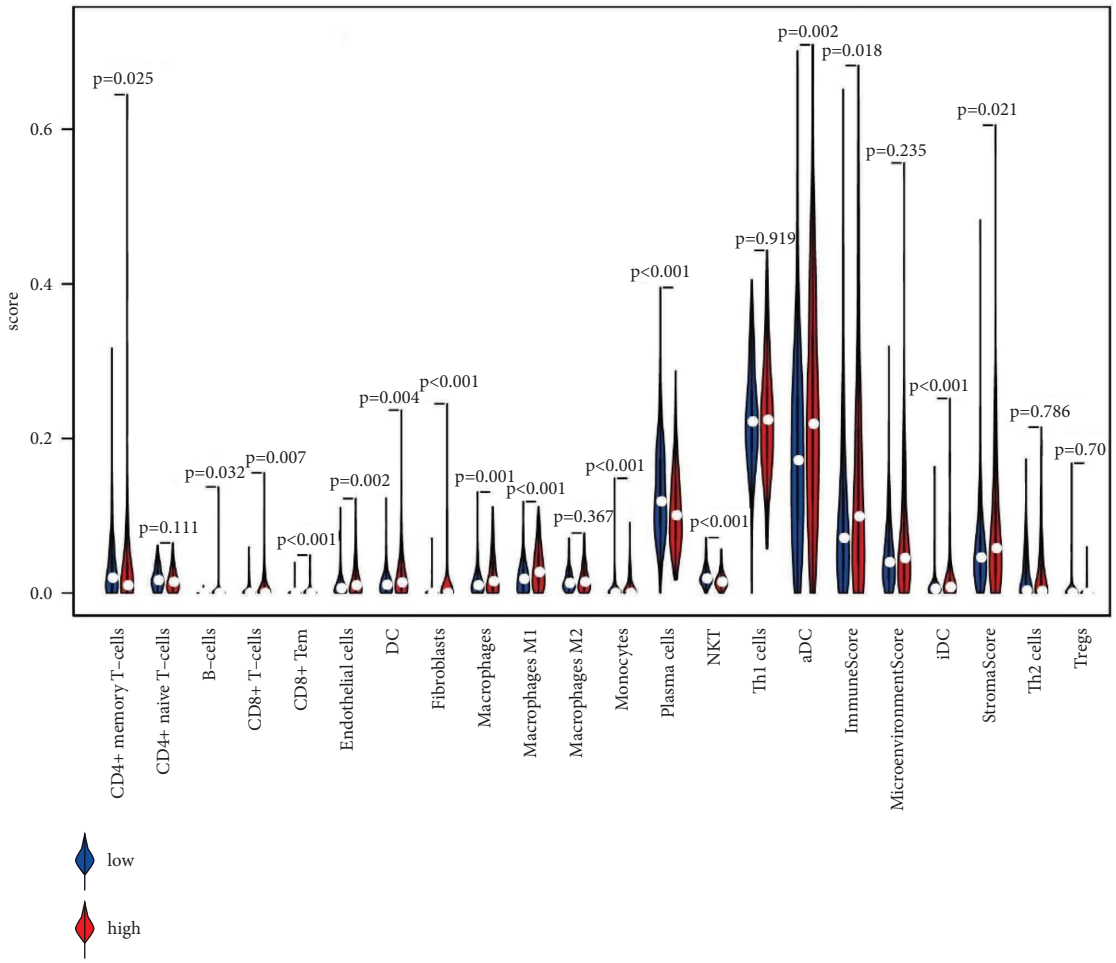

(a)

Figure 6: Continued.

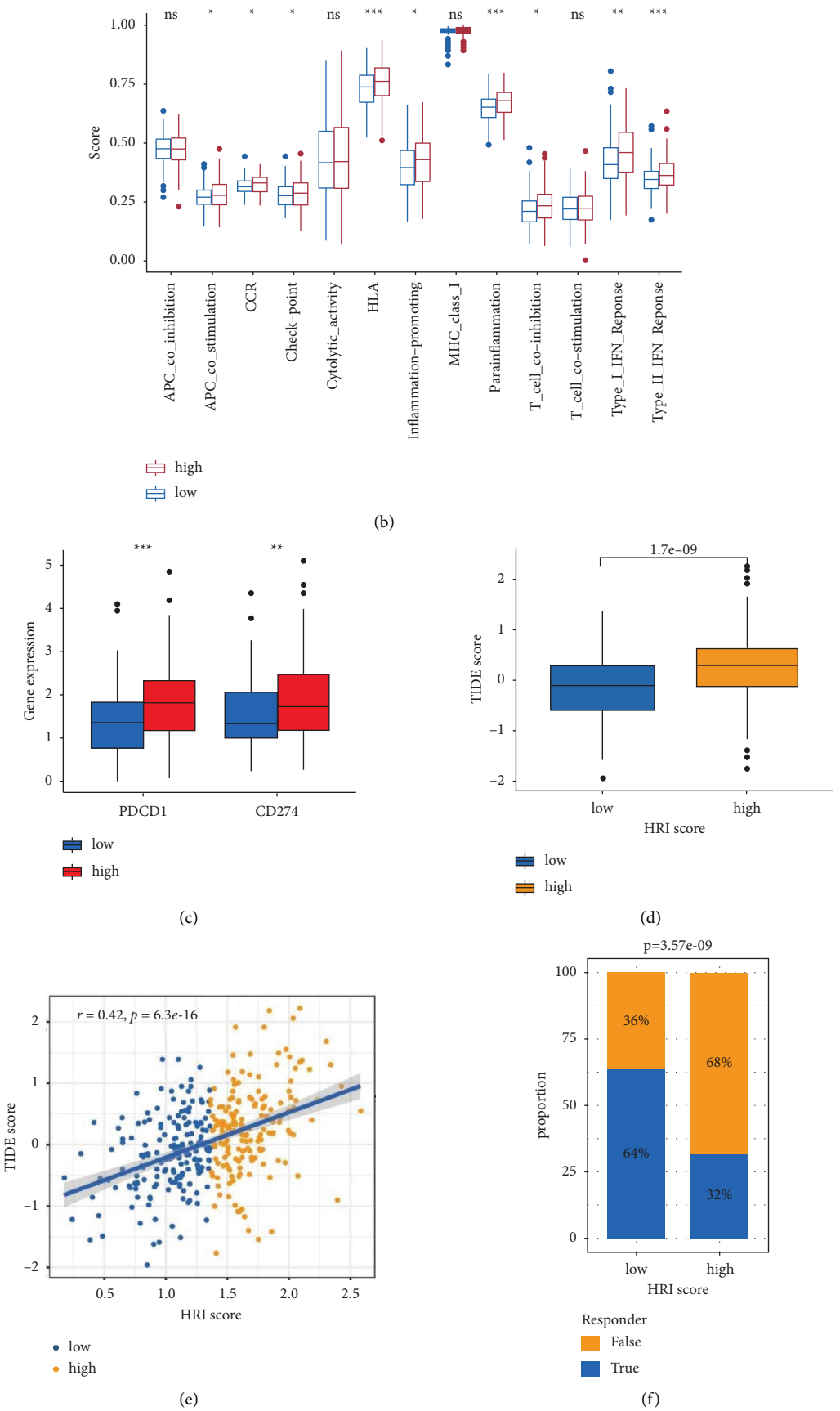

Figure 6: The distinct immune infiltration patterns in TCGA-COAD cohort. Comparison of the immune infiltration level (a), immune pathway activity (b), and immune checkpoint expression level (c) between HRI high-risk and low-risk groups. Comparison of TIDE scores between HRI high-risk and low-risk groups in TCGA-COAD (d). Correlation between TIDE scores and HRI scores in TCGA-COAD (e). Comparison of responder proportion predicted by the TIDE algorithm in TCGA-COAD (f). TIDE: tumor immune dysfunction and exclusion. HRI: hypoxia-related index. *** $p < 0.001$; ** $p < 0.01$; * $p < 0.05$; ns, no significance.

scores consistently displayed a positive correlation with the TIDE scores in TCGA-COAD (Figure 6(e)) and GSE17538 (Figure S5E), indicating that higher HRI scores represent greater immune evasion and immunotherapeutic resistance. Accordingly, the low-risk group was predicted to have a significantly higher ratio of immunotherapeutic responders than the high-risk group in both TCGA-COAD (Figure 6(f)) and GSE17538 (Figure S5F). The previous results demonstrated that HRI scores representing hypoxia levels in CC tissues have the potential to predict the immunotherapy response.

3.7. Correlation Analysis of MSI Status with HRI Signature. The MSI status information for CC patients in the TCGA-COAD cohort was curated from TCIA (The Cancer Immunome Atlas) database (https://tcia.at/home) [25]. There were 335 CC patients with complete MSI status in our TCGA-COAD dataset, including 46 MSI-H, 64 MSI-L, and 210 MSS (microsatellite stability), and 15 indeterminate cases, respectively. The chi-square test revealed a statistically significant difference in the constitutive proportion of MSI status between the two HRI risk groups ($p = 0.019$, Figure S6A). The HRI high-risk group presented an elevated ratio of MSI-H (17%) and MSI-L (25%) cases compared with the low-risk counterpart (11% and 15% of MSI-H and MSI-L cases, respectively). Subsequently, we stratified CC patients into different subgroups according to their MSI status and performed a subgroup survival analysis. Notably, patients with high HRI scores consistently exhibited poorer OS prognosis than those in the HRI low-risk group, irrespective of MSI status (Figures S6B–S6D).

3.8. Validating the mRNA Expression of Five Key Genes by qRT-PCR. The HRI signature consisted of 11 HRDEGs, namely, CD177, CP, RGS16, PGM5, SNAI1, CALB2, OSBPL1A, CDR2L, FRMD5, FSTL3, and TUBB2B. Among the HRI prognostic signatures, CD177 was the only protective factor, and the other 10 genes were all risk factors for prognostic prediction in CC. The mRNA expression levels of RGS16, SNAI1, CDR2L, FRMD5, and FSTL3 were higher in tumor samples than that in adjacent normal tissues in TCGA-COAD cohort (Figure 7(a)), suggesting that these five key genes participate in the progression of CC. Thus, we experimentally investigated their mRNA expression levels in 30 pairs of clinical samples by qRT-PCR. The results demonstrated that RGS16 (Figure 7(b)), SNAI1 (Figure 7(c)), CDR2L (Figure 7(d)), FRMD5 (Figure 7(e)), and FSTL3 (Figure 7(f)) consistently exhibited significantly higher relative mRNA expression levels in CC tumor samples than in paired adjacent normal tissues.

3.9. The Validation Experiment In Vitro. To further determine the influence of the previously selected differentially expressed genes (RGS16, SNAI1, CDR2L, FRMD5, and FSTL3) on cell proliferation and apoptosis, we interfered with the expression of five differential genes and detected the cell proliferation and apoptosis levels. First, we tested the transfection level of the disruptor or plasmid. The results showed that the expression of mRNA (Figure 8(a)) and protein levels (Figure 8(b)) in the siRNA group was induced, while the pLenti group could significantly upregulate the expression of mRNA and protein levels of genes. Subsequently, we detected the cell activity by CCK-8 experiment. The results showed that the expression of RGS16 had no significant effect on cell proliferation and apoptosis (Figures 9(a) and 10(a)), while the high expression of SNAI1, CDR2L, FRMD5, and FSTL3 could promote the proliferation of cancer cells and inhibit the apoptosis of cancer cells, but inhibiting their expression could inhibit the proliferation of cancer cells and promote the apoptosis of cancer cells (Figures 9(b)–9(e) and 10(b)–10(e)).

4. Discussion

CC ranks the fifth most frequent malignant disease worldwide, and advanced-stage cases are associated with high mortality [2]. Thus, it is urgent to identify novel prognostic predictors and targeted biomarkers. Hypoxia in the tumor microenvironment is a specific hallmark of solid tumors [5] and contributes to the tumor metastatic cascade [6]. Several studies have constructed different hypoxia-related gene signatures for predicting the clinical outcomes of colorectal cancer [26–28]. However, these studies mainly aimed to establish a prognostic signature for CC patients and lacked comprehensive microdissection of the hypoxia landscape and its correlation with immunotherapy in CC. Compared with the previously published literature, we identified three hypoxia-specific clusters and developed a novel HRI prognostic signature. As far as we know, this is the first comprehensive investigation of the correlation of the hypoxia landscape with metabolic reprogramming, TIME, and immunotherapeutic response prediction in CC.

The hypoxic tumor microenvironment in solid tumors maintains a selective pressure for tumor cells to adapt to the hypoxia response and promotes their invasion, migration, and dissemination [6]. Moreover, the HIF-1α pathway plays a pivotal role in the modulation of hypoxia-related downstream gene expression and biological processes in cancer cells under hypoxic conditions [7]. Hence, we classified the CC patients into three different clusters based on the expression levels of the 200 genes in the "HALLMARK_HYPOXIA" gene set and verified the relationship between the clusters and the HIF1A mRNA expression level. Hypoxia stress can decrease the expression of DUSP2 and increase cancer stemness and tumor growth in CC cells [29]. Hypoxia may promote EMT, invasion, and migration of CC cells by activation of HIF1A, whereas treatment with HIF1A-specific siRNAs suppresses these processes [8]. In agreement with the findings of the abovementioned studies, the hypoxia-high cluster in our study possessed a higher HIF1A mRNA expression and elevated relative scores in tumor aggression-associated pathways including "EPITHELIAL_MESENCHYMAL_TRANSITION" and "ANGIOGENESIS." Accordingly, the hypoxia-high cluster had

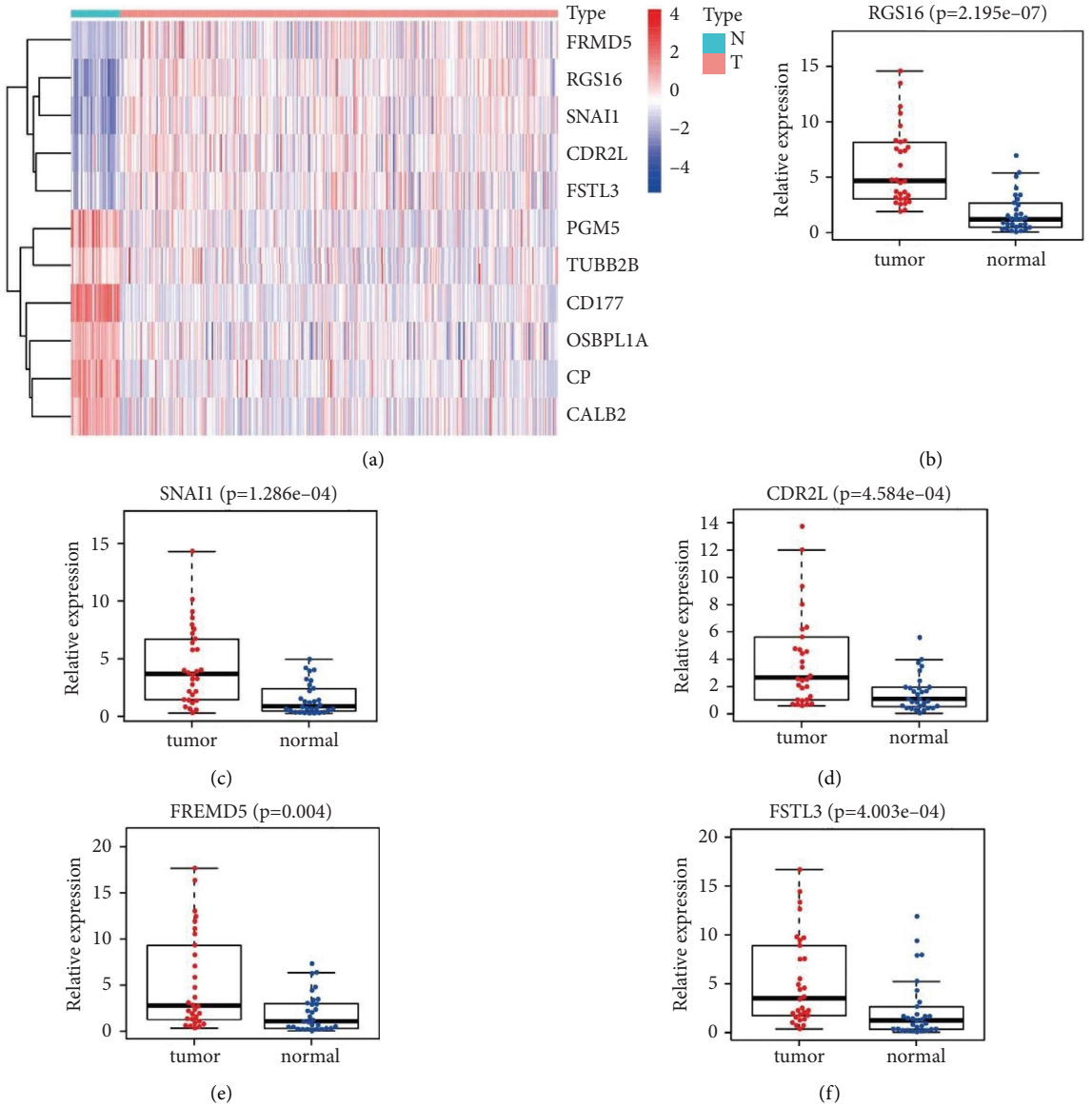

Figure 7: Verification of the mRNA expression levels of the five key genes in HRI signature by qRT-PCR. (a) Heatmap of the mRNA expression levels of all eleven genes in HRI signature in TCGA-COAD cohort. Comparison of relative mRNA expression levels of RGS16 (b), SNAI1 (c), CDR2L (d), FRMD5 (e), and FSTL3 (f) between 30 pairs of CC tumor and adjacent normal tissues using the qRT-PCR experiment. HRI: hypoxia-related index. qRT-PCR: quantitative reverse transcription polymerase chain reaction. N: normal; T: tumor; CC: colon cancer.

more CC patients with "Vascular_Invasion" and "Recurred/Progressed."

Cancer cells undergo metabolic reprogramming to reconcile themselves to hypoxic stress [30]. The HIF-1α pathway contributes greatly to metabolism alteration via glycolysis stimulation and oxidative phosphorylation (OXPHOS) suppression under hypoxic conditions during tumor development [14]. Upon hypoxic conditions, pancreatic ductal adenocarcinoma cells exhibited elevated HIF1A and HIF2A expression levels, increased expression of carbonic anhydrase 9, and activated glycolysis [31]. Our study also showed similar results in both TCGA-COAD and GSE17538 datasets. This phenomenon may be because of the cancer cells' metabolic plasticity and metabolic heterogeneity, depending on the complex tumor microenvironment [32].

Hypoxia stress also impacts TIME by inducing an immune suppression or immune evasion phenotype [33]. The local hypoxic microenvironment recruits immunosuppressive cells, such as MDSCs, tumor-associated macrophages, and CAFs, and upregulates immune checkpoint expression to induce antitumor resistance [15]. CAFs at the invasive front of tumor tissues boost tumor progression and metastasis in CC [34]. In our study, the hypoxia-high cluster consistently had a higher immune score, stromal score, and estimate score than the hypoxia-low cluster. Furthermore, macrophages and fibroblasts showed elevated infiltrating levels in the hypoxia-high group, supporting a positive

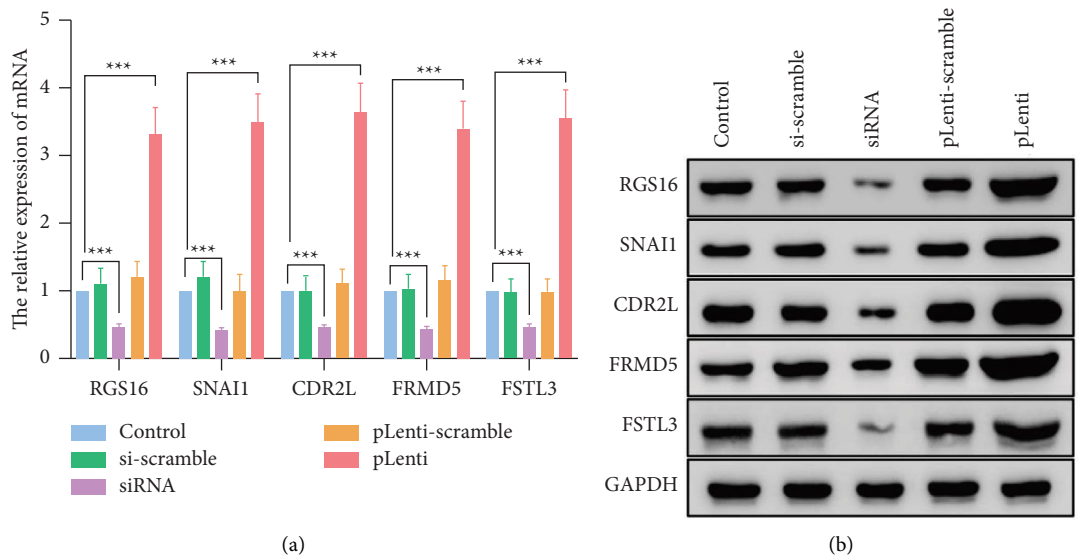

FIGURE 8: Transfection efficiency. Comparison of relative mRNA expression levels of RGS16, SNAI1, CDR2L, FRMD5, and FSTL3 of tumor cell line using the qRT-PCR experiment (a) and western blot experiment (b). *** $p < 0.001$; ** $p < 0.01$; * $p < 0.05$.

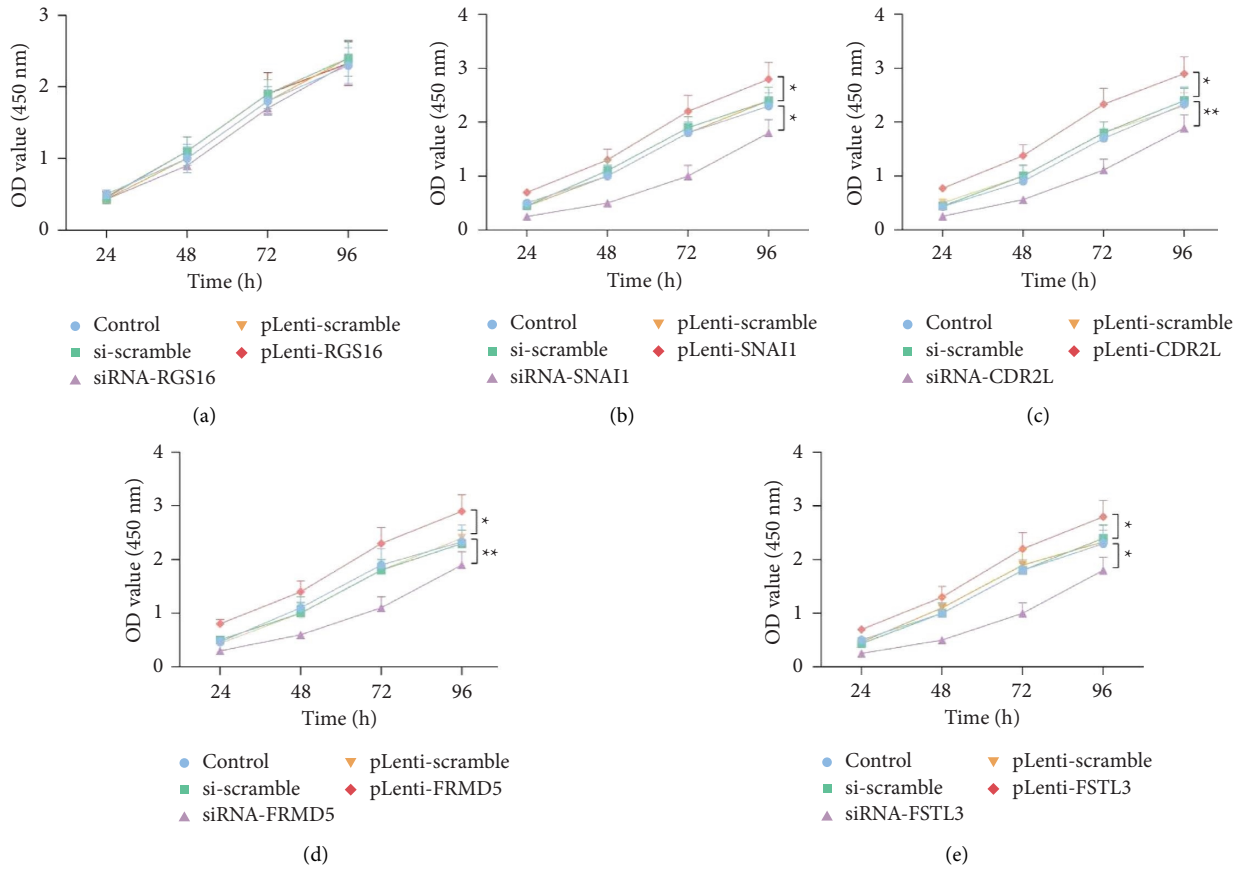

FIGURE 9: The CCK-8 assay. The effect of expression of RGS16 (a), SNAI1 (b), CDR2L (c), FRMD5 (d), and FSTL3 (e) on cell viability was examined using the CCK-8 assay. *** $p < 0.001$; ** $p < 0.01$; * $p < 0.05$.

correlation between hypoxia and tumor immune dysfunction. Accordingly, we speculate that the poor clinical outcomes of the patients in the hypoxia-high group partly depend on the immune suppression or evasion mechanism.

To further examine the clinical applicability, we developed a reliable HRI prognostic signature that is strongly correlated with critical clinical characteristics (T, N, M, AJCC stage, and tumor histological grade). Hypoxia-treated

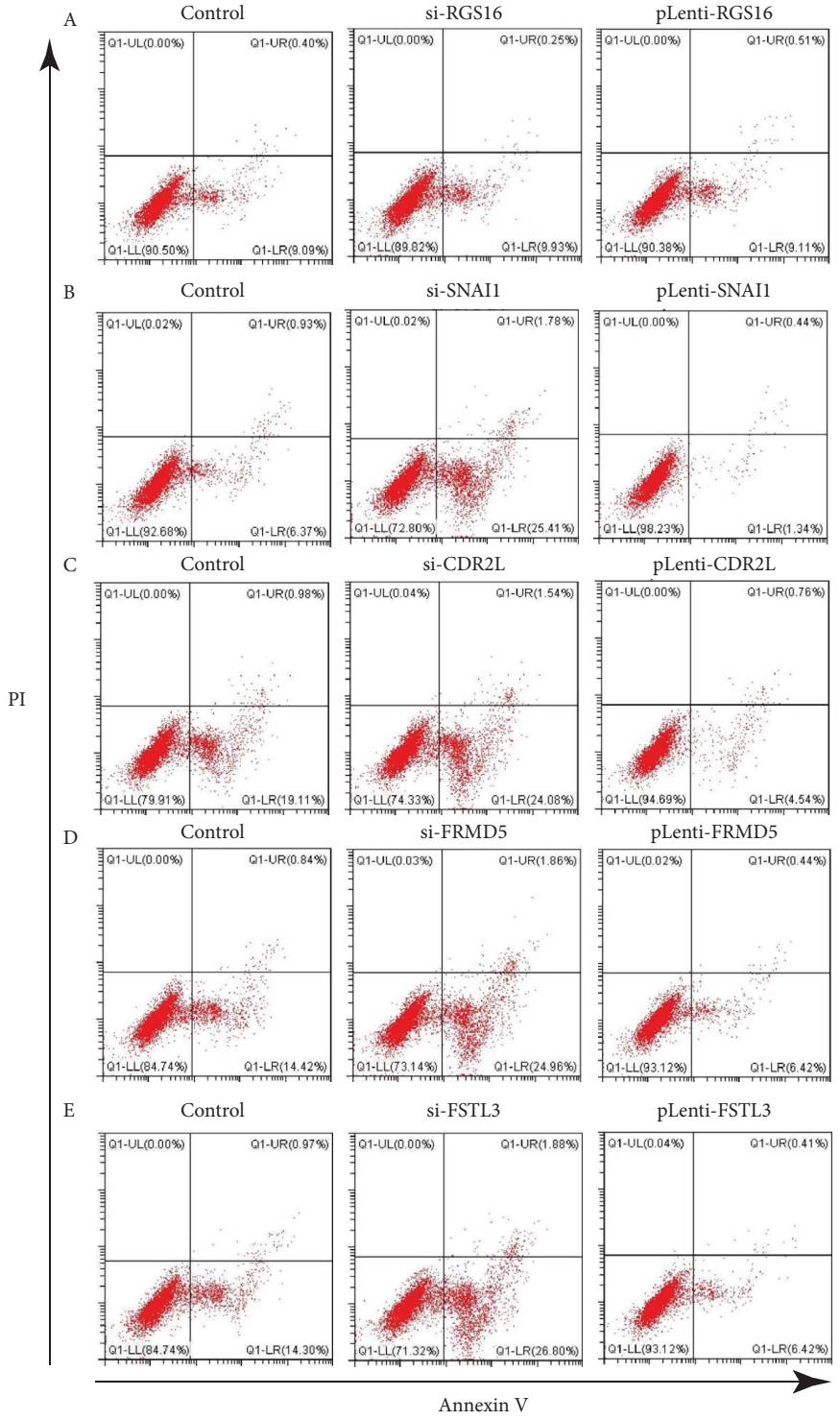

Figure 10: The flow cytometry assay. The effect of expression of RGS16 (a), SNAI1 (b), CDR2L (c), FRMD5 (d), and FSTL3 (e) on cell viability was examined using the flow cytometry assay.

CC cells have been reported to strengthen the metastatic ability of normoxic cancer cells [35]. HIF-1α is a master regulator of the hypoxia-response process of tumor cells under hypoxic conditions [7]. Hypoxia can promote EMT, invasion, and migration of CC cells by the activation of HIF1A [8]. In our study, the high HRI score group consistently possessed a higher HIF1A expression level than the low-risk counterpart, indicating the effectiveness of the HRI score to reflect hypoxia exposure in CC tumor tissues. Additionally, patients with M1, N2, T3–4, stage 3–4, and tumor grade 3 had higher HRI risk scores than those with M0, N0, T1–2, stage 1–2, and grade 1, respectively. This

further demonstrated that the HRI signature was strongly related to tumor progression and metastasis in CC.

Immunotherapy involving anti-PD-1/PD-L1 has resulted in revolutionary therapeutic benefits for various cancer types, and MSI-H status has proven to be an effective predictor of immunotherapeutic efficacy [36]. However, MSI-L/MSS patients, who represent most CC patients, have not acquired a satisfactory response from immunotherapy. High tumor mutational burden (TMB) in tumors is linked to favorable clinical outcomes; however, the TMB varies markedly among different cancer types, and there is a lack of a well-defined standard of high TMB [37]. Our study demonstrated that the HRI signature is positively correlated with the TIDE score, which represents the immune dysfunction and exclusion of tumor samples, and patients with a low HRI score are predicted to be more responsive to immunotherapy. The previous evidence suggests that the HRI score has the potential to be a complementary measure to MSI-H status and TMB in the personalized management of immunotherapy. Hypoxia gene sets were reported to be enriched in nonresponding pre-anti-PD-1 tumor samples with melanoma [38]. In agreement with these studies, CC patients with a high HRI score representing severe hypoxia exposure are predicted to have a lower response to immunotherapy. As targeting the hypoxic microenvironment may ameliorate the effects of cancer immunotherapy [16], we speculate that these patients with high HRI scores may acquire greater efficacy of immunotherapy in combination with antihypoxia drugs.

The HRI signature consists of 11 HRDEGs, and we focused on the 5 key genes (RGS16, SNAI1, CDR2L, FRMD5, and FSTL3), which exhibited elevated expression levels in tumor tissues and are prognostic risk factors for CC. RGS16 has already been reported to possess a higher expression level in colorectal cancer tissue than in the corresponding normal tissue and serves as an unfavorable prognostic marker [39]. Overexpression of SNAI1 (also known as SNAIL) is linked to increased stemness and decreased radiation sensitivity in CC cells [40]. A previously published study [41] reported the FRMD5 is a novel downstream gene targeted by the β-catenin/TCF7L2 complex in CC cells. CDR2L is widely present in ovarian cancer tissues and is abundantly expressed in testicular and prostate cancer tissues [42]. Knockdown of FSTL3 remarkably inhibited the aggression phenotype of lung cancer cells [43]. In the subsequent cell activity and apoptosis experiments, we found that the low expression of SNAI1, CDR2L, FRMD5, and FSTL3 could reduce the activity of cancer cells and increase the apoptosis rate of cancer cells. But RGS16 does not exhibit similar functions. According to previous literature reports, high expression of SNAI1 can promote the invasion ability of cancer cells [44], low expression of FRMD5 can weaken the metastatic ability of cancer cells [45, 46], and low expression of FSTL3 also has similar functions [47, 48]. The reason why RGS16 has no similar function may be that its mechanism of affecting prognosis is different from other genes. According to previous reports, the population with low expression of RGS16 presents a better prognosis than the population with high expression [39]. Therefore, RGS16 may affect the prognosis of patients by regulating the activity of immune cells and has no direct impact on the activity and apoptosis rate of cancer cells [49]. Collectively, these five key genes may act as oncogenic genes that contribute to the progression of CC, and their molecular mechanism is worth further studying to explore new therapeutic targets.

Nevertheless, there are still several limitations to our study. The HRI signature was identified in TCGA-COAD cohort and validated in another independent dataset, but these public datasets are mostly attributed to retrospective studies and may induce indispensable biases to some extent. Thus, prospective research will be required at a future date. Furthermore, although the HRI score is demonstrated to have a reliable predictive capability of immunotherapy response in CC by bioinformatical analysis, well-designed clinical trials should be performed to further prove its clinical effectiveness.

5. Conclusion

In conclusion, we discover three hypoxia clusters (hypoxia-H, hypoxia-L, and hypoxia-M) which correlate with the clinical outcome and the tumor immune microenvironment in CC. Furthermore, we found 600 HRDEs. Based on the 600 HRDEGs, we constructed a reliable HRI signature that could accurately predict the prognosis and immunotherapeutic responsiveness in CC patients. Finally, we discover five key genes which are differently expressed between tumors and adjacent tissues. Of them, four genes could affect tumor cell viability and apoptosis.

Data Availability

The expression profiles of GSE17538 were downloaded from the Gene Expression Omnibus (GEO) database (https://www.ncbi.nlm.nih.gov/geo/), and the expression profile of The Cancer Genome Atlas Colon Adenocarcinoma (TCGA-COAD) project was downloaded from TCGA database (https://portal.gdc.cancer.gov/).

Ethical Approval

This research work was approved by the Institutional Ethical Committee Board of Nanfang Hospital (NFEC-201809-K3).

Conflicts of Interest

The authors declare that they have no conflicts of interest.

Authors' Contributions

Pingfei Tang and Yueming Wu have contributed equally to this work.

Acknowledgments

This work was supported by the National Natural Science Foundation of China (grant no. 12026605) and the Guangdong Science and Technology Project (grant no. 2017B020209003). The authors acknowledge The Cancer Genome Atlas (TCGA) database and Geo Expression Omnibus (GEO) database for publicly providing these meaningful datasets involved in the present study.

Supplementary Materials

The following are available supplementary materials: Figure S1: microdissection of the hypoxia landscape in TCGA-COAD cohort and GSE17538. (A) Consensus CDF curve and (B) delta area curve, when $k = 3$ represents the optimal cluster number in TCGA-COAD cohort. (C) Consensus CDF curve and (D) delta area curve, when $k = 3$ represents the optimal cluster number in the GSE17538 cohort; Figure S2: construction of the hypoxia-related index signature. (A) The tuning parameters of the LASSO penalty Cox regression. (B) Cross-validation of the LASSO regression model, the left vertical dashed line means the "lambda. min" standard. LASSO: least absolute shrinkage and selection operator; Figure S3: correlation between the HRI score and clinical parameters in GSE17538. Comparison of HRI scores between different clinical subgroups, including stage (A), grade (B), and recurrence (C). Recurrence-free survival (RFS) difference between HRI high-risk and low-risk groups (D). Forest plot for multivariate Cox regression analysis in GSE17538 (E). HRI: hypoxia-related index. $^{***}p < 0.001$; $^{**}p < 0.01$; $^{*}p < 0.05$; Figure S4: GSEA results of TCGA-COAD cohort and GSE17538 dataset. The significantly enriched pathway in the HRI high-risk group versus the low-risk group for hallmark gene sets (A) and KEGG pathways (B) in TCGA-COAD cohort. The significantly enriched pathway in the HRI high-risk group versus the low-risk group for hallmark gene sets (C) and KEGG pathways (D) in the GSE17538 dataset. GSEA: gene set enrichment analysis. HRI: hypoxia-related index. KEGG: Kyoto Encyclopedia of Genes and Genomes; Figure S5: the distinct immune infiltration patterns in GSE17538. Comparison of the immune infiltrating level (A), immune pathway activity (B), and immune checkpoint expression level (C) between HRI high-risk and low-risk groups. Comparison of TIDE scores between HRI high-risk and low-risk groups in GSE17538 (D). Correlation between TIDE scores and HRI scores in GSE17538 (E). Comparison of responder proportion predicted by the TIDE algorithm in GSE17538 (F). TIDE: tumor immune dysfunction and exclusion. HRI: hypoxia-related index. $^{***}p < 0.001$; $^{**}p < 0.01$; $^{*}p < 0.05$; ns, no significance; Figure S6: relationship between HRI scores and MSI status in TCGA-COAD. (A) Comparison of distribution difference of MSI status between HRI high-risk and low-risk groups. Survival differences between HRI high-risk and low-risk groups according to MSI status, including MSI-H (B), MSI-L (C), and MSS (D). HRI: hypoxia-related index. MSI: microsatellite instability. MSS: microsatellite stability; Figure S7. The distinct tumor immune infiltration pattern from the "xCell" algorithm. Comparison of the tumor immune infiltration level among hypoxia-specific clusters in TCGA--COAD (A) and GSE17538 (B). hypoxia-L: hypoxia-low; hypoxia-M:hypoxia-median; hypoxia-H: hypoxia-high. $^{***}p < 0.001$; $^{**}p < 0.01$; $^{*}p < 0.05$; ns, no significance; Table S1: clinicopathological characteristics of patients enrolled in the present study; Table S2: the detailed gene list of the HALLMARK_HYPOXIA gene set; Table S3: the detailed gene list of 13 metabolic pathway gene sets; Table S4: the detailed gene list of 13 immune function pathway gene sets; Table S5: the primer sequences used in the present study; Table S6: clinical parameters of 348 patients in TCGA--COAD cohort; Table S7: clinical parameters of 210 patients in the GSE17538 dataset; Table S8: the detailed gene list of the 600 hypoxia-related differentially expressed genes; Table S9: the optimal model of LASSO Cox regression; Table S10: HRI risk scores of 348 patients in TCGA-COAD cohort; Table S11: HRI risk scores of 210 patients in the GSE17538 dataset; Table S12: TIDE scores of 348 patients in TCGA-COAD cohort; Table S13: TIDE scores of 210 patients in GSE17538. (*Supplementary Materials*)

References

[1] H. Sung, J. Ferlay, R. L. Siegel et al., "Global cancer statistics 2020: GLOBOCAN estimates of incidence and mortality worldwide for 36 cancers in 185 countries," *CA: A Cancer Journal for Clinicians*, vol. 71, no. 3, pp. 209–249, 2021.

[2] R. L. Siegel, K. D. Miller, A. Goding Sauer et al., "Colorectal cancer statistics, 2020," *CA: A Cancer Journal for Clinicians*, vol. 70, no. 3, pp. 145–164, 2020.

[3] M. B. Amin, F. L. Greene, S. B. Edge et al., "The Eighth Edition AJCC Cancer Staging Manual: continuing to build a bridge from a population-based to a more "personalized" approach to cancer staging," *CA: A Cancer Journal for Clinicians*, vol. 67, no. 2, pp. 93–99, 2017.

[4] A. B. Benson, A. P. Venook, M. M. Al-Hawary et al., "NCCN guidelines insights: colon cancer, version 2.2018," *Journal of the National Comprehensive Cancer Network*, vol. 16, no. 4, pp. 359–369, 2018.

[5] D. M. Gilkes, G. L. Semenza, and D. Wirtz, "Hypoxia and the extracellular matrix: drivers of tumour metastasis," *Nature Reviews Cancer*, vol. 14, no. 6, pp. 430–439, 2014.

[6] E. B. Rankin and A. J. Giaccia, "Hypoxic control of metastasis," *Science (New York, NY, USA)*, vol. 352, no. 6282, pp. 175–180, 2016.

[7] G. N. Masoud and W. Li, "HIF-1α pathway: role, regulation and intervention for cancer therapy," *Acta Pharmaceutica Sinica B*, vol. 5, no. 5, pp. 378–389, 2015.

[8] H. Li, M. Rokavec, L. Jiang, D. Horst, and H. Hermeking, "Antagonistic effects of p53 and HIF1A on microRNA-34a regulation of PPP1R11 and STAT3 and hypoxia-induced epithelial to mesenchymal transition in colorectal cancer cells," *Gastroenterology*, vol. 153, no. 2, pp. 505–520, 2017.

[9] P. Tang, W. Qu, T. Wang et al., "Identifying a hypoxia-related long non-coding RNAs signature to improve the prediction of prognosis and immunotherapy response in hepatocellular carcinoma," *Frontiers in Genetics*, vol. 12, Article ID 785185, 2021.

[10] K. Xu, Y. Zhan, Z. Yuan et al., "Hypoxia induces drug resistance in colorectal cancer through the HIF-1α/miR-338-5p/

IL-6 feedback loop," *Molecular Therapy*, vol. 27, no. 10, pp. 1810–1824, 2019.

[11] Y. A. Tang, Y. F. Chen, Y. Bao et al., "Hypoxic tumor microenvironment activates GLI2 via HIF-1α and TGF-β2 to promote chemoresistance in colorectal cancer," *Proceedings of the National Academy of Sciences of the United States of America*, vol. 115, no. 26, pp. E5990–E5999, 2018.

[12] M. F. Sanmamed and L. Chen, "A paradigm shift in cancer immunotherapy: from enhancement to normalization," *Cell*, vol. 175, no. 2, pp. 313–326, 2018.

[13] R. Abou Khouzam, H. V. Goutham, R. F. Zaarour et al., "Integrating tumor hypoxic stress in novel and more adaptable strategies for cancer immunotherapy," *Seminars in Cancer Biology*, vol. 65, pp. 140–154, 2020.

[14] C. Riera-Domingo, A. Audigé, S. Granja et al., "Immunity, Hypoxia, and Metabolism-the Ménage à Trois of Cancer: implications for Immunotherapy," *Physiological Reviews*, vol. 100, no. 1, pp. 1–102, 2020.

[15] A. Lequeux, M. Z. Noman, M. Xiao et al., "Impact of hypoxic tumor microenvironment and tumor cell plasticity on the expression of immune checkpoints," *Cancer Letters*, vol. 458, pp. 13–20, 2019.

[16] B. Wang, Q. Zhao, Y. Zhang et al., "Targeting hypoxia in the tumor microenvironment: a potential strategy to improve cancer immunotherapy," *Journal of Experimental and Clinical Cancer Research*, vol. 40, no. 1, p. 24, 2021.

[17] E. Cerami, J. Gao, U. Dogrusoz et al., "The cBio cancer genomics portal: an open platform for exploring multidimensional cancer genomics data," *Cancer Discovery*, vol. 2, no. 5, pp. 401–404, 2012.

[18] A. Liberzon, C. Birger, H. Thorvaldsdóttir, M. Ghandi, J. P. Mesirov, and P. Tamayo, "The molecular signatures database hallmark gene set collection," *Cell systems*, vol. 1, no. 6, pp. 417–425, 2015.

[19] S. Hänzelmann, R. Castelo, and J. Guinney, "GSVA: gene set variation analysis for microarray and RNA-seq data," *BMC Bioinformatics*, vol. 14, no. 1, p. 7, 2013.

[20] N. Simon, J. Friedman, T. Hastie, and R. Tibshirani, "Regularization paths for cox's proportional hazards model via coordinate descent," *Journal of Statistical Software*, vol. 39, no. 5, pp. 1–13, 2011.

[21] Y. He, Z. Jiang, C. Chen, and X. Wang, "Classification of triple-negative breast cancers based on Immunogenomic profiling," *Journal of Experimental and Clinical Cancer Research*, vol. 37, no. 1, p. 327, 2018.

[22] M. Yi, D. V. Nissley, F. Mccormick, and R. M. Stephens, "SSGSEA score-based Ras dependency indexes derived from gene expression data reveal potential Ras addiction mechanisms with possible clinical implications," *Scientific Reports*, vol. 10, no. 1, Article ID 10258, 2020.

[23] D. Aran, Z. Hu, and A. J. Butte, "XCell: digitally portraying the tissue cellular heterogeneity landscape," *Genome Biology*, vol. 18, no. 1, p. 220, 2017.

[24] P. Jiang, S. Gu, D. Pan et al., "Signatures of T cell dysfunction and exclusion predict cancer immunotherapy response," *Nature Medicine*, vol. 24, no. 10, pp. 1550–1558, 2018.

[25] H. Choudhry and A. L. Harris, "Advances in hypoxia-inducible factor Biology," *Cell Metabolism*, vol. 27, no. 2, pp. 281–298, 2018.

[26] Y. Zhang, F. Yang, X. Peng et al., "Hypoxia constructing the prognostic model of colorectal adenocarcinoma and related to the immune microenvironment," *Frontiers in Cell and Developmental Biology*, vol. 9, Article ID 665364, 2021.

[27] J. H. Lee, S. Jung, W. S. Park et al., "Prognostic nomogram of hypoxia-related genes predicting overall survival of colorectal cancer-Analysis of TCGA database," *Scientific Reports*, vol. 9, no. 1, p. 1803, 2019.

[28] Y. F. Zou, Y. M. Rong, Y. X. Tan et al., "A signature of hypoxia-related factors reveals functional dysregulation and robustly predicts clinical outcomes in stage I/II colorectal cancer patients," *Cancer Cell International*, vol. 19, no. 1, p. 243, 2019.

[29] P. C. Hou, Y. H. Li, S. C. Lin et al., "Hypoxia-induced downregulation of DUSP-2 phosphatase drives colon cancer stemness," *Cancer Research*, vol. 77, no. 16, pp. 4305–4316, 2017.

[30] D. Samanta and G. L. Semenza, "Metabolic adaptation of cancer and immune cells mediated by hypoxia-inducible factors," *Biochimica et biophysica acta. Reviews on cancer*, vol. 1870, no. 1, pp. 15–22, 2018.

[31] P. C. Mcdonald, S. C. Chafe, W. S. Brown et al., "Regulation of pH by carbonic anhydrase 9 mediates survival of pancreatic cancer cells with activated KRAS in response to hypoxia," *Gastroenterology*, vol. 157, no. 3, pp. 823–837, 2019.

[32] N. T. Moldogazieva, I. M. Mokhosoev, and A. A. Terentiev, "Metabolic heterogeneity of cancer cells: an interplay between HIF-1, GLUTs, and AMPK," *Cancers*, vol. 12, no. 4, p. 862, 2020.

[33] X. Jing, F. Yang, C. Shao et al., "Role of hypoxia in cancer therapy by regulating the tumor microenvironment," *Molecular Cancer*, vol. 18, no. 1, p. 157, 2019.

[34] M. Paauwe, M. J. A. Schoonderwoerd, R. F. Helderman et al., "Endoglin expression on cancer-associated fibroblasts regulates invasion and stimulates colorectal cancer metastasis," *Clinical Cancer Research*, vol. 24, no. 24, pp. 6331–6344, 2018.

[35] Y. Mi, L. Mu, K. Huang et al., "Hypoxic colorectal cancer cells promote metastasis of normoxic cancer cells depending on IL-8/p65 signaling pathway," *Cell Death and Disease*, vol. 11, no. 7, p. 610, 2020.

[36] D. Bruni, H. K. Angell, and J. Galon, "The immune contexture and Immunoscore in cancer prognosis and therapeutic efficacy," *Nature Reviews Cancer*, vol. 20, no. 11, pp. 662–680, 2020.

[37] R. M. Samstein, C. H. Lee, A. N. Shoushtari et al., "Tumor mutational load predicts survival after immunotherapy across multiple cancer types," *Nature Genetics*, vol. 51, no. 2, pp. 202–206, 2019.

[38] W. Hugo, J. M. Zaretsky, L. Sun et al., "Genomic and transcriptomic features of response to anti-PD-1 therapy in metastatic melanoma," *Cell*, vol. 165, no. 1, pp. 35–44, 2016.

[39] N. Miyoshi, H. Ishii, M. Sekimoto, Y. Doki, and M. Mori, "RGS16 is a marker for prognosis in colorectal cancer," *Annals of Surgical Oncology*, vol. 16, no. 12, pp. 3507–3514, 2009.

[40] Y. Zhu, C. Wang, S. A. Becker et al., "miR-145 antagonizes SNAI1-mediated stemness and radiation resistance in colorectal cancer," *Molecular Therapy*, vol. 26, no. 3, pp. 744–754, 2018.

[41] C. Zhu, K. Yamaguchi, T. Ohsugi et al., "Identification of FERM domain-containing protein 5 as a novel target of beta-catenin/TCF7L2 complex," *Cancer Science*, vol. 108, no. 4, pp. 612–619, 2017.

[42] M. Raspotnig, M. Haugen, M. Thorsteinsdottir et al., "Cerebellar degeneration-related proteins 2 and 2-like are present in ovarian cancer in patients with and without Yo antibodies,"

Cancer Immunology, Immunotherapy, vol. 66, no. 11, pp. 1463–1471, 2017.

[43] L. Gao, X. Chen, Y. Wang, and J. Zhang, "Up-regulation of FSTL3, regulated by lncRNA DSCAM-AS1/miR-122-5p Axis, promotes proliferation and migration of non-small cell lung cancer cells," *OncoTargets and Therapy*, vol. 13, pp. 2725–2738, 2020.

[44] Z. Pan, J. Cai, J. Lin et al., "A novel protein encoded by circFNDC3B inhibits tumor progression and EMT through regulating Snail in colon cancer," *Molecular Cancer*, vol. 19, no. 1, p. 71, 2020.

[45] X. Mao, S. K. Tey, F. C. F. Ko et al., "C-terminal truncated HBx protein activates caveolin-1/LRP6/β-catenin/FRMD5 axis in promoting hepatocarcinogenesis," *Cancer Letters*, vol. 444, pp. 60–69, 2019.

[46] A. M. Gawel, M. Ratajczak, E. Gajda et al., "Analysis of the role of FRMD5 in the Biology of papillary thyroid carcinoma," *International Journal of Molecular Sciences*, vol. 22, no. 13, p. 6726, 2021.

[47] F. Sun, P. Sun, X. Yang, L. Hu, J. Gao, and T. Tian, "Inhibition of FSTL3 abates the proliferation and metastasis of renal cell carcinoma via the GSK-3β/β-catenin signaling pathway," *Aging (Albany NY)*, vol. 13, no. 18, pp. 22528–22543, 2021.

[48] Z. T. Dai, Y. Xiang, X. Y. Zhang et al., "Regulation of follistatin-like 3 expression by miR-486-5p modulates gastric cancer cell proliferation, migration and tumor progression," *Aging*, vol. 13, no. 16, pp. 20302–20318, 2021.

[49] Y. Wang, H. Fu, Y. Jiang, B. Zhou, and P. Chen, "Novel circularRNA circ-0047078 promotes pancreatic ductal adenocarcinoma progression through mircoRNA miR-11181- Chemokine (C-X-C motif) Ligand 12/Melanoma Cell Adhesion Molecule/Regulator of G-protein signaling 16 pathway," *Molecular Biology Reports*, vol. 49, no. 9, pp. 8761–8775, 2022.

Hindawi
Journal of Oncology
Volume 2023, Article ID 5355269, 15 pages
https://doi.org/10.1155/2023/5355269

Research Article

Single-Cell and Transcriptome-Based Immune Cell-Related Prognostic Model in Clear Cell Renal Cell Carcinoma

Guanlin Wu,[1] **Weiming Guo**,[2] **Shuai Zhu**,[3] **and Gang Fan**[3,4]

[1]*School of Clinical Medicine, Shanghai University of Medicine & Health Sciences, Shanghai 201318, China*
[2]*The 2nd Affiliated Hospital of South China University, Hengyang 421001, China*
[3]*Department of Urology, The Affiliated Cancer Hospital of Xiangya School of Medicine of Central South University, Hunan Cancer Hospital, Changsha 410013, Hunan, China*
[4]*Department of Urology, Huazhong University of Science and Technology Union Shenzhen Hospital, The 6th Affiliated Hospital of Shenzhen University Health Science Center, Shenzhen 518060, China*

Correspondence should be addressed to Gang Fan; gang.fan.med@qq.com

Received 6 August 2022; Revised 26 September 2022; Accepted 11 October 2022; Published 7 March 2023

Academic Editor: Muhammad Muddassir Ali

Traditional studies mostly focus on the role of single gene in regulating clear cell renal cell carcinoma (ccRCC), while it ignores the impact of tumour heterogeneity on disease progression. The purpose of this study is to construct a prognostic risk model for ccRCC by analysing the differential marker genes related to immune cells in the single-cell database to provide help in clinical diagnosis and targeted therapy. Single-cell data and ligand-receptor relationship pair data were downloaded from related publications, and ccRCC phenotype and expression profile data were downloaded from TCGA and CPTAC. Based on the DEGs of each cluster acquired from single-cell data, immune cell marker genes, and ligand-receptor gene data, we constructed a multilayer network. Then, the genes in the network and the genes in TCGA were used to construct the WGCNA network, which screened out prognosis-associated genes for subsequent analysis. Finally, a prognostic risk scoring model was obtained, and CPTAC data showed that the effectiveness of this model was good. A nomogram based on the predictive model for predicting the overall survival was established, and internal validation was performed well. Our findings suggest that the predictive model built and based on the immune cell scRNA-seq will enable us to judge the prognosis of patients with ccRCC and provide more accurate directions for basic relevant research and clinical practice.

1. Introduction

RCC is a typical type of malignant tumour of the urinary system. According to the most recent report on cancer statistics, the number of newly diagnosed cases has climbed to 65,000 annually in the United States, resulting in around 15,000 fatalities annually, making it the sixth most prevalent tumour [1]. Clear cell renal cell carcinoma (ccRCC) accounts for around 80% of renal cancer pathological types, and its survival results were poorer than other subtypes of kidney tumours (such as papillary renal cell carcinoma and chromophobe renal cell carcinoma) [2]. Nearly 20% of ccRCC cases progress to an advanced stage at the beginning of diagnosis, and the five-year overall survival (OS) rate of metastatic cases dropped to about 10% [3]. With the development of immunotherapy, radiotherapy, and surgical intervention, combined strategies have greatly promoted carcinoma control. However, the actual clinical efficacy still needs to be improved, and 30% of patients with local ccRCC inevitably experience cancer-related progression and recurrence [4]. Recently, although targeted therapy has been shown to prolong the survival time of patients with metastases, the median survival time is still less than 3 years [5]. In addition, drug resistance and economic burden are unavoidable major problems in clinical practice [6]. Therefore, exploring the molecular mechanism of ccRCC pathogenesis and new therapeutic targets is still a challenging issue.

A crucial aspect of carcinoma is its comprehensive heterogeneity, which can cause individuals to react

differently to the same treatment. Despite many efforts to clarify tumour heterogeneity, so far, the understanding of it is still mainly limited to the level of tumour cells [7]. Previously, it has also been proved that stromal cells and tumour-infiltrating immune cells exhibit heterogeneity [8]. Similarly, the tumour microenvironment (TME) is gradually regarded as a potential solution for drug treatment targets [9]. In addition to anti-PD-1/PD-L1 or anti-CTLA-4 treatment strategies, tumour-associated macrophages (TAMs) [10] and cancer-associated fibroblasts (CAFs) [11] have also been previously reported as potential strategies for cancer treatment research. ROS is also an important factor in cancer treatment, it causes structural proteins to oxidise, which disables the proteolytic process. These reactions change how an enzyme works or how proteins are created. The latter could have a wide range of functional impacts downstream, including inhibition of binding and enzymatic activity, an increase or decrease in cellular uptake, inactivation of DNA repair enzymes, and a reduction in the fidelity of damaged DNA polymerases during DNA replication [12]. The successful implementation of these treatment plans requires a deeper insight of intratumoural heterogeneity.

It is obviously impossible to analyse intratumoural heterogeneity at the cellular level since traditional bulk RNA sequencing is predicated on the idea that every gene is expressed equally in each cell. However, through the application of single-cell RNA sequencing (scRNA-seq), it is possible to conduct single-cell transcriptome analysis. The latest progress in scRNA-seq has facilitated the transcriptional classification of many malignant tumour cell types, including breast cancer, lung cancer, and pancreatic ductal adenocarcinoma [13, 14]. Moreover, scRNA-seq is expected to have clinical utility in refractory cancer cases and is a noninvasive method for monitoring circulating cancer cells, analysing intratumoural heterogeneity, and sensitively estimating recurrent tumours [15].

We conducted a series of bioinformatics analyses using data from other publications about scRNA-seq in order to investigate the intratumour heterogeneity in ccRCC. We combined these analyses with ligand-receptor network analysis, immune cell multilayer network analysis, and weighted gene co-expression network analysis (WGCNA) to identify hub genes for creating an immune cell-related prognostic model. It would have several potential targets for ccRCC therapy. Moreover, we also investigated the prognostic value of immune cell clusters by correlating the scRNA-seq data with the data from The Cancer Genome Atlas (TCGA) and Clinical Proteomic Tumor Analysis Consortium (CPTAC) datasets. Our work will help elucidate the biology of ccRCC and promote the improvement of clinical diagnosis and treatment strategies for patients with ccRCC.

2. Methods

2.1. Raw Data Acquisition. ccRCC single-cell transcriptome data was downloaded from a database published by Young et al. [16]. The datasets of RNA sequencing profiles and the related patient clinical traits of ccRCC were downloaded from TCGA (https://portal.gdc.cancer.gov/) and CPTAC (https://cptac-data-portal.georgetown.edu/study-summary/S050), separately. Ligand and receptor data for building the multilayer network were acquired from [17].

2.2. Data Processing. For single-cell data, "limma," "Seurat," "dplyr," and "magrittr" R packages were used for analysis. Data filtering criteria included the following: (1) the number of genes in the data sample was controlled between 200 and 5,000; (2) the number of gene sequences was mainly distributed between 0 and 20,000; and (3) the percentage of mitochondria was controlled below 5%. Then, the log was taken for standardisation, and the first 2,000 genes with the larger coefficient of variation between cells were selected for analysis. Next, principal component analysis (PCA) dimensionality reduction was performed, the data were standardised before dimensionality reduction, and finally, significant dimensions were selected for subsequent analysis. Since the form of data downloaded from TCGA is log2-(data + 1), log processing is not necessary and the standardisation was done directly. Before standardisation, the data must be processed using log2-(data + 1) after being retrieved from the CPTAC database. The "limma" R package was used to carry out the standardisation.

2.3. Cell Type Recognition and Clustering Analysis. The recognition of different cell types was based on the "limma," "Seurat," "dplyr," and "magrittr" R packages. We used the 20 principal components (PCs) selected in the previous step to perform TSNE clustering. Subsequently, the cell type was annotated through the "singleR" R package. In order to facilitate the display of subsequent results, we have annotated both subpopulations and single cells.

2.4. Identification of Differentially Expressed Genes in Each Cluster. We used several R packages, including "limma," "Seurat," "dplyr," and "magrittr" to analyse the genes contained in each cluster. The FindAllMarkers algorithm was used to screen and calculate the differentially expressed genes (DEGs) in each cluster. The screening standard is $|\log FC| > 0.5$, and the P value after correction is <0.05.

2.5. Immune Cell Function Status Analysis. We used "GSVA" and "GSEABase" R packages to conduct functional status analysis on samples annotated by single cell, and we referred to the marker genes of immune cell functional status provided by the CancerSEA (https://biocc.hrbmu.edu.cn/CancerSEA/home.jsp) database to clarify the functional status of DEGs in immune cells.

2.6. Immune Cell Marker Gene Expression Analysis. The marker genes of immune cells in kidney cancer tissues were obtained from the CellMarker (https://bio-bigdata.hrbmu.edu.cn/CellMarker/) database. In addition, marker genes associated with macrophages and monocytes were acquired from [18]. The expression levels of these marker genes were analysed and displayed through a heat map.

2.7. Construction of Ligand-Receptor and Immune Cell Multilayer Networks. The construction of the ligand-receptor network was carried out using the "igraph" R package. To make sure that the ligand genes and associated receptor genes were all included in the gene set taken in union, we first took the intersection of the genes in the ligand-receptor table provided in the literature [17] and the differential genes in all immune cell clusters and the marker genes of all included immune cells. Then, we obtained the data for transcription factors and their target genes from the TRRUST (https://www.grnpedia.org/trrust/) database and combined it with the data for ligand-receptor network genes, which is the intersection of the transcription factors' target genes and network genes.

2.8. Weighted Gene Co-Expression Network Analysis. Through the WGCNA algorithm [19], the genes in the immune cell multifactor network were used to construct a co-expression network to find the key modules related to OS and OS time. An appropriate soft threshold value was determined by an R software package (https://www.r-project.org/) to implement according to the WGCNA algorithm. The gradient method was used to test different power values (ranging from 1 to 20) in both the scale independence degree and the module's average connectivity. The most suitable power value could be fixed when the independence degree was above 0.9, as well as when the average connectivity degree was relatively higher [20, 21]. The WGCNA algorithm was also implemented in the construction of scale-free gene co-expression networks. Meanwhile, the corresponding gene sequencing information in each module was extracted. To assess modular feature associations, correlations between module eigengenes (MEs) and clinical features were applied. MEs are the most important components in the PCA of each gene module. The determination of relevant modules needs to be based on the calculation of the correlation strength between MEs and clinical features. The correlation was assessed by gene significance (GS = lgP), where the P value was derived from the linear regression analysis of gene expression and clinical information. The key module takes the highest correlation coefficient among all modules, which was selected out for the next step [22].

2.9. Key Module Functional Enrichment Analysis. The sequencing information of genes in the key modules from WGCNA was utilized by using the "clusterProfiler" R package to perform gene ontology (GO) and Kyoto Encyclopedia of Genes and Genomes (KEGG) pathway analyses. Among them, GO is to annotate biological processes (BPs), molecular functions (MFs), and cellular components (CCs). The criterion for screening in GO term is P value <0.05. The screening criteria for the KEGG pathway are minGSSize = 5, maxGSSize = 500, and qvalueCutoff = 0.05.

2.10. Selection of Candidate Prognostic Related Genes. Univariate Cox regression analysis was performed through the "survival" R package to screen prognostic characteristic genes from the previous OS-related WGCNA key modules. When the P value is less than 0.05, that is, when the differential expression of these genes has a significant impact on the patient's OS, these genes can be regarded as potential prognostic related genes. Data in this step were from ccRCC cancer samples in TCGA.

2.11. Construction, Evaluation, and Validation of Disease Prognosis Risk Model. For the candidate prognostic related genes, combined with their expression in TCGA, univariate Cox regression analysis was used to obtain genes with more significant risk. Then, LASSO dimensionality reduction with 1,000 iterations was performed to screen out redundant genes to obtain more precise prognostic related genes with high hazard ratio (HR) to construct a risk prognosis model. The following formula was used to calculate the risk score for each patient by using a linear combination of specific features that were weighted by their respective coefficients from LASSO:

$$\text{risk score} = \sum_{i=1}^{n} \exp_i * \beta_i, \tag{1}$$

where n is the number of prognostic genes, $\exp_i$ is the expression value of the i-th gene, and β_i is the regression coefficient of the i-th gene in the LASSO algorithm. According to the risk score of each patient given by the model, the median was taken as the cutoff value, and the samples were divided into high and low risk groups. The time-dependent receiver operating characteristic (ROC) curve was used to evaluate the predictive ability of the model's 1-, 3-, and 5-year survival periods. The survival curves of the high and low risk groups were also analysed. The CPTAC dataset was taken as the external validation database to verify the prognostic risk model.

2.12. Construction and Assessment of a Predictive Nomogram. Nomograms are widely used to predict the prognosis of cancer patients, mainly because they can simplify statistical prediction models into a single numerical estimate of OS probability tailored to individual patient conditions. In this study, the prognostic model was used to construct a nomogram to assess the probability of OS in patients with ccRCC at one, three, and five years. Subsequently, discrimination and calibration were carried out. The discrimination of the nomogram was calculated by the bootstrap method using the consistency index (C-index), with 1,000 resamples. The value of the C-index is between 0.5 and 1.0, where 1.0 means that the results of the model can be correctly distinguished and 0.5 means random chance. The calibration curve of the nomogram is evaluated graphically by plotting the relationship between the predicted probability of the nomogram and the observed rate. Overlapping with the reference line indicates that the model is exactly the same. In addition, we also compared the predictive accuracy between nomogram built only with risk score and nomogram combined with all factors using ROC analysis.

3. Results

3.1. Pretreated Data. The single-cell data of the downloaded ccRCC were preprocessed as described in the Methods

section, and we obtained 30,092 cells in total. In addition, we found that the correlation between the sequencing depth and the detected genes was 0.95, indicating that the deeper the sequencing depth was, the more the genes were detected. Subsequently, we selected 2,000 genes with large variances for PCA analysis. The differences of all 20 PCs were extremely significant, indicating that the theoretical value and the actual value are quite different which can be used for subsequent analysis.

There were 607 samples in the KIRC expression profile data of TGCA, of which 72 were paracancerous samples, 535 were cancer samples, and one sample had incomplete clinical information which was then removed. Finally, the data of 534 ccRCC tumour tissue samples were used for subsequent relative analysis. Among the data downloaded from the CPTAC database, there were 110 cancer samples and 75 paracancerous samples. Only 103 cancer samples contained clinical information. As a result, the data of these 103 samples were eventually used for analysis.

3.2. ccRCC Heterogeneity. For cluster analysis of single-cell data, we obtained a total of 23 subgroup clusters. After annotating by cell type, we found that immune cells were mainly concentrated in subgroups 0, 1, 2, 3, 4, 5, 6, 7, 9, 12, 13, 15, 16, 18, and 22 (Figure 1, Supplementary Table 1). Specifically, CD8+ T cells were distributed in clusters 0, 2, 3, 7, 12, and 18. NK cells were only annotated in cluster 1. Monocytes assembled in clusters 4, 5, 13, and 22. Clusters 6, 9, and 15 were annotated to macrophages. B cells annotated only cluster 16.

3.3. Differentially Expressed Genes and Functional Enrichment in Different Immune Cell Subgroups. We performed differential expression analysis on the genes in 23 clusters obtained in the above step and displayed the first five genes in each cluster (Figure 2(a), Supplementary Table 2). According to the results of gene differential expression, we analysed the functional status of the annotated immune cell clusters. In each immune cell type, the enrichment degree of hypoxia and quiescence was relatively high. Besides the enrichment levels of EMT, invasion and stemness in B cells were also relatively high (Figures 2(b)–2(f)).

3.4. Identification of Immune Cell Marker Gene Expression. A total of 42 immune cell marker genes related to ccRCC were downloaded from the CellMarker database [18] and subjected to differential expression analysis. The results are shown in the heat map (Figure 2(g)).

3.5. Ligand-Receptor Network. In order to construct the ligand-receptor network, we first took the union of the differential genes of all immune cell clusters and the marker genes of all these immune cells. Afterwards, we intersected them with the ligand-receptor relationship pairs downloaded from [17]. Finally, a total of 981 pairs of ligand-receptor relationships were obtained (Figure 3(a), Supplementary Table 3).

3.6. Immune Cell Multifactor Network Based on Ligand-Receptor Network Combined with Transcription Factors. Intersecting genes in 981 ligand-receptor relationship pairs with transcription factor target genes, we obtained 7,987 immune cell multifactor network relationship pairs (Supplementary Table 4). Then, 966 genes were obtained by intersecting the 973 genes contained in the network and the genes in TCGA dataset about ccRCC (Supplementary Table 5). Because there are many relationship pairs, Figure 3(b) only shows a network diagram of partial genes.

3.7. Co-Expression Network. The construction of co-expression modules included 966 genes from the immune cell multifactor network. The appropriate scale-free power value was screened out as 4 (Figure 4(a)). All constructed modules are painted with different colours, and the cluster trees of genes are also shown in Figure 4(b). The black and magenta modules were chosen as the key modules, since they had the highest correlations with OS and OS time of ccRCC (Figures 4(c) and 4(d)). The correlations between MEs and clinic traits are shown in Figure 4(e). There were 53 genes in these two modules (Supplementary Table 6). For a deeper understanding about the biofunctions of these modules, genes in these modules were carried out to conduct GO and KEGG pathway analyses by using the "clusterProfiler" R package. According to the P value of each term, the top terms in the GO and KEGG pathways were extracted out and visualized (Figures 4(f)–4(i)).

3.8. Prognostic Risk Scoring Model. Using the "survival" *R* package to perform univariate Cox regression analysis on the 53 genes contained in the key modules of WGCNA, 28 genes with P value <0.05 were obtained. Figures 5(a)–5(d) show the survival analysis results of four genes among them. Then, the 28 genes with significant prognostic differences were subjected to LASSO regression analysis. We adopted the Cox proportional hazard model (family = "Cox") to calculate the HR and P values of these genes (Figure 5(e)) and then randomly simulated 1,000 times (maxit = 1000) to find the

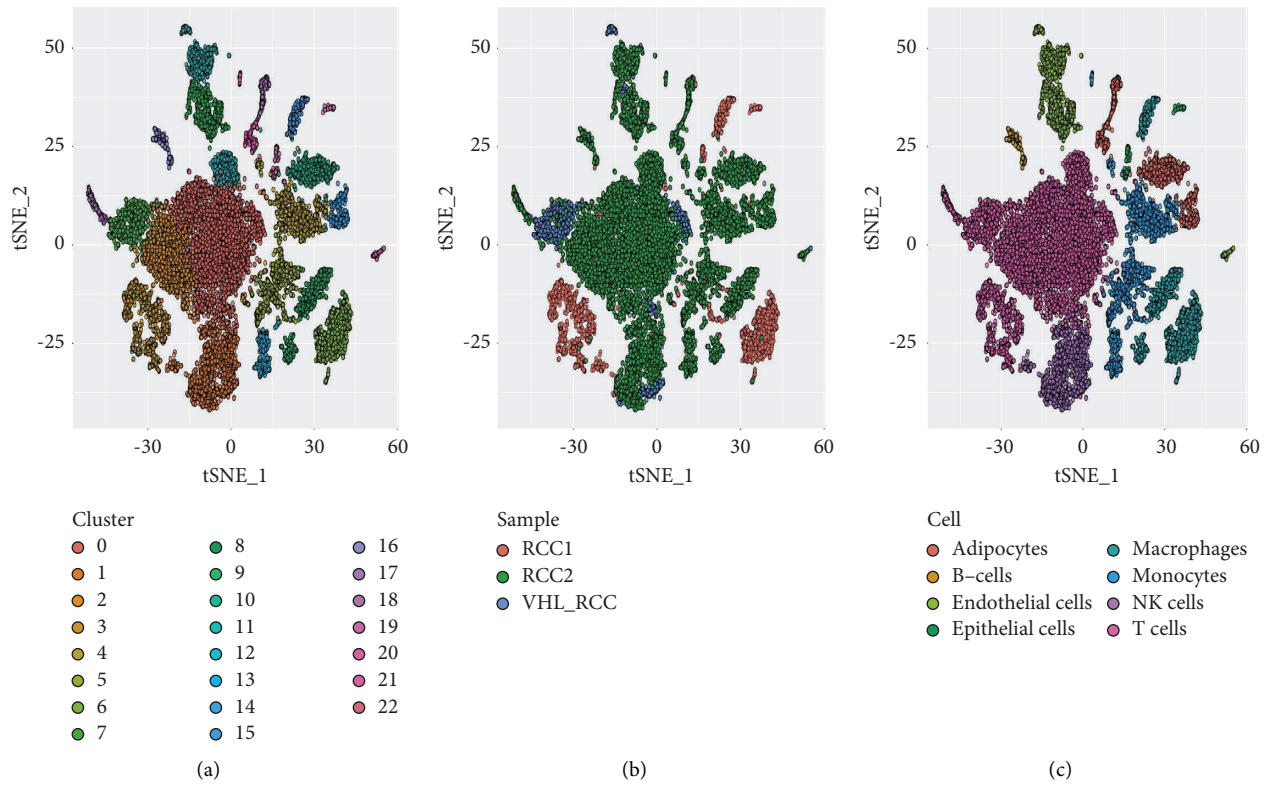

Figure 1: Cell clustering. (a) Clustering of single-cell subpopulations. (b) The distribution of samples in clusters. (c) Annotation for all cell types.

most suitable λ value in LASSO regression (Figure 5(f)). Finally, "lambda.min" was used to screen out 16 genes for constructing a risk scoring model from these 28 genes (Figure 5(g)).

$$\begin{aligned}\text{Risk score} = {} & \text{PAX2} * (-0.00104) + \text{NFKBIZ} * 0.11197 + \text{TEAD4} * 0.212538 + \text{HIPK2} * (-0.09059) + \text{CD14} * 0.051547 \\ & + \text{COL1A1} * 0.084915 + \text{NRG1} * (-0.10501) + \text{GPR182} * (-0.30944) + \text{ITGA6} * (-0.08147) + \text{HDAC1} \\ & * 0.225345 + \text{HOXA9} * 0.078825 + \text{E2F5} * 0.436804 + \text{APP} * (-0.14625) + \text{FGF1} * (-0.27736) + \text{L1CAM} \\ & * 0.149607 + \text{DDR1} * (-0.11874).\end{aligned} \tag{2}$$

3.9. Prognostic Model Prediction Effectiveness Evaluation and External Dataset Verification. In the evaluation of the predictive efficacy of the prognosis model, Kaplan–Meier (KM) survival analysis was performed on the high and low risk groups, and the difference was significant (Figure 5(h)). Moreover, in its ROC curve, the one-year AUC value was 0.794, the three-year AUC value was 0.746, and the five-year AUC value was 0.763 (Figure 5(j)). In the external CPTAC dataset, KM survival analysis was performed on the high and low risk groups, and the difference was also significant (Figure 5(i)). In addition, the one-year AUC value in its ROC curve was 0.783, and the three-year AUC value was 0.762 (Figure 5(k)). Because the external data do not have five-year survival data, only one-year and three-year ROC analysis was performed.

3.10. Predictive Nomogram. For the purpose of building a clinically applicable method to estimate the survival possibility of patients with ccRCC, we developed a nomogram to predict the probability of 1-, 3-, and 5-year OS based on the data in TCGA. The predictors of the nomogram included age, gender, T, N, M, grade, risk score, and stage (Figure 6(a)). The C-index for the model for evaluation of OS was 0.799. The visual calibration chart was used to evaluate the performance of the nomogram. When the angle of the line is 45°, it represents the best prediction result. Thus, our calibration chart indicated that the nomogram has a good predictive ability (Figures 6(b)–6(d)). The AUC values of the nomograms combined with all factors were greater than the nomograms built only with risk score in spite of the fact that their values were all more than 0.7. This indicated that the

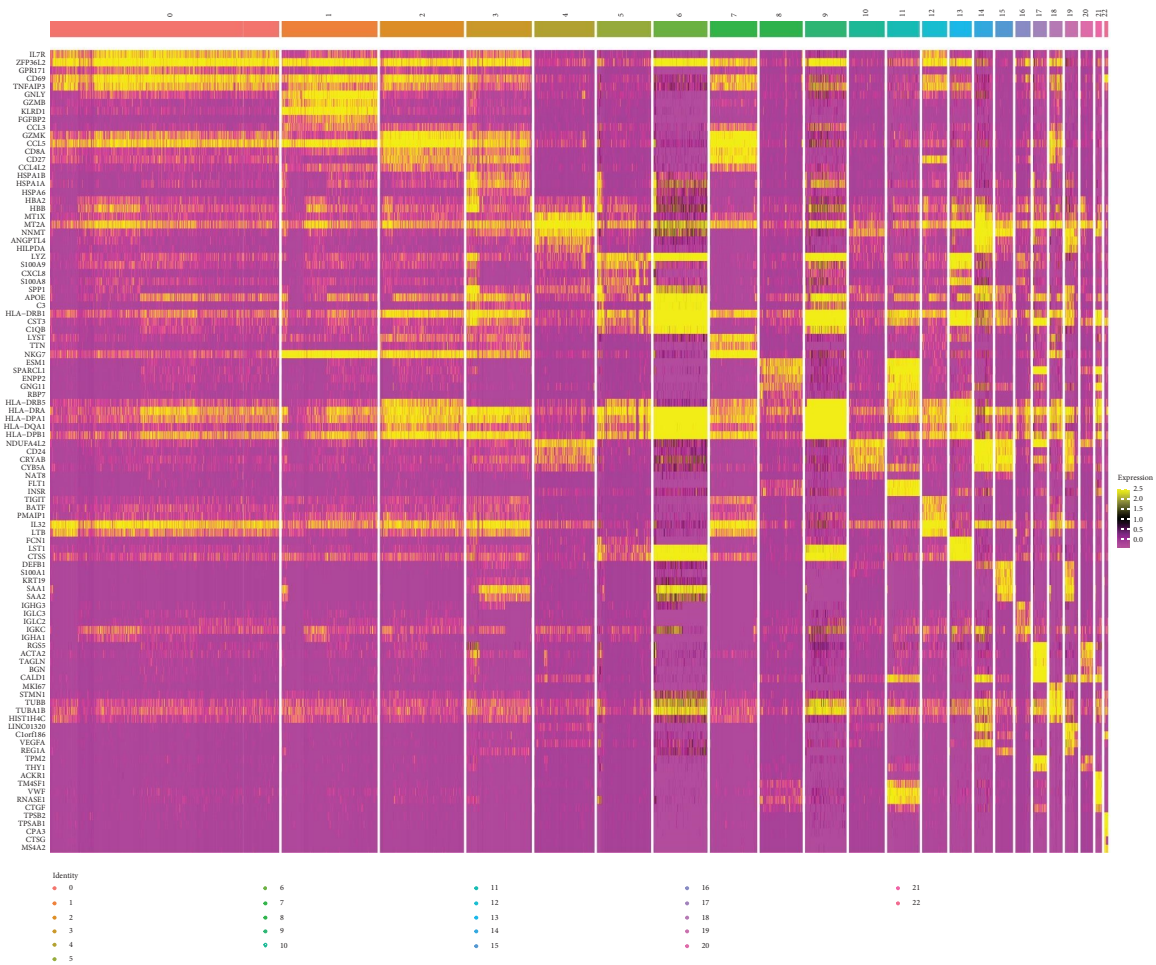

(a)

(b)

(c)

(d)

Figure 2: Continued.

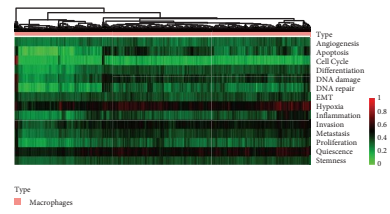

(e)

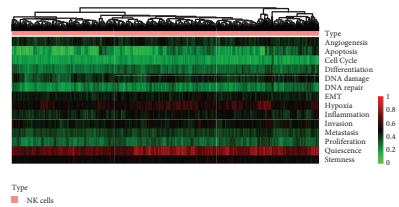

(f)

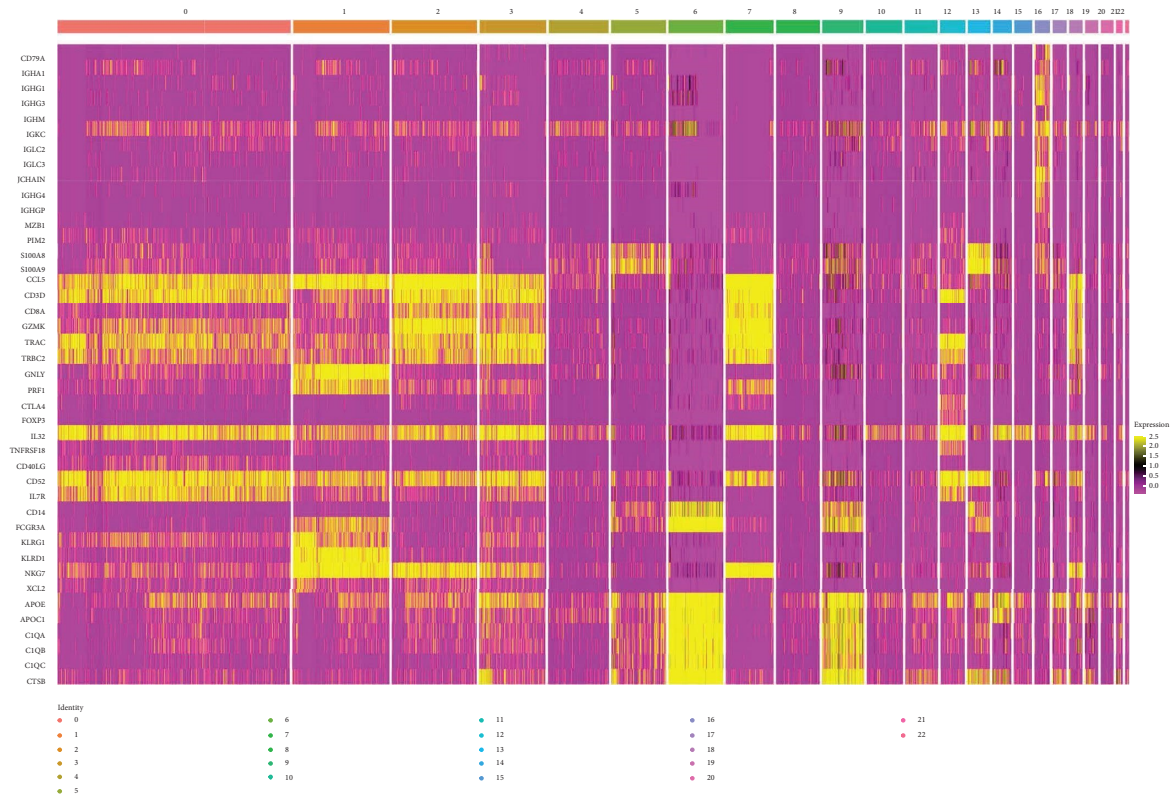

(g)

Figure 2: (a) Heat map of the top five differential genes in each cluster. (b) B cell functional status analysis. (c) T cell functional status analysis. (d) Monocyte functional status analysis. (e) Macrophage functional status analysis. (f) NK cell functional status analysis. (g) Heat map of immune cell marker genes.

predictive precision of the nomogram combined with all factors was better (Figures 6(e)–6(g)).

4. Discussion

The emergence of next-generation sequencing (NGS) has provided a feasible and cost-effective way to determine the transcriptional landscape of human cancers, including both bulk and single-cell resolution with unprecedented base-pair precision [23–25]. It has been established that cancer is attributed to dysregulated evolution [26, 27] in acquiring inheritable genetic/epigenetic traits [28–30]. However, the presence of tumour heterogeneity poses substantial challenges in the diagnosis and treatment of tumours [31–34]. Tumour heterogeneity exerts a vital role in various aspects (e.g., intertumour, intratumour, and intermetastasis heterogeneity, interdisease and interpatient heterogeneity, epigenetic and metabolic heterogeneity, TME heterogeneity, and tumour-intrinsic genetic heterogeneity)

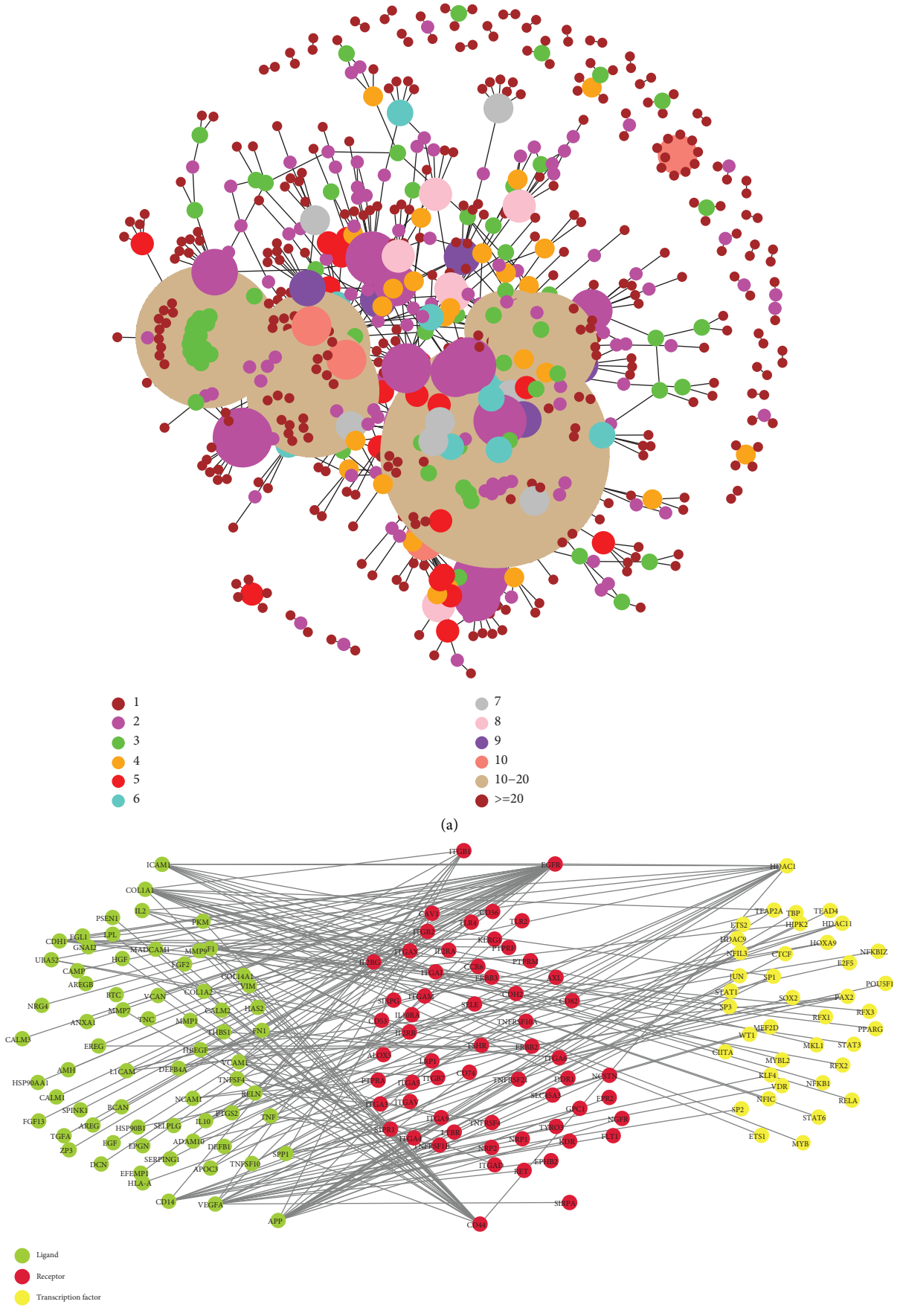

Figure 3: (a) Ligand-receptor interaction network diagram (different colours and sizes represent different numbers of node connections). (b) Multilayer network diagram (green is the ligand gene, red is the receptor gene, and yellow is the transcription factor).

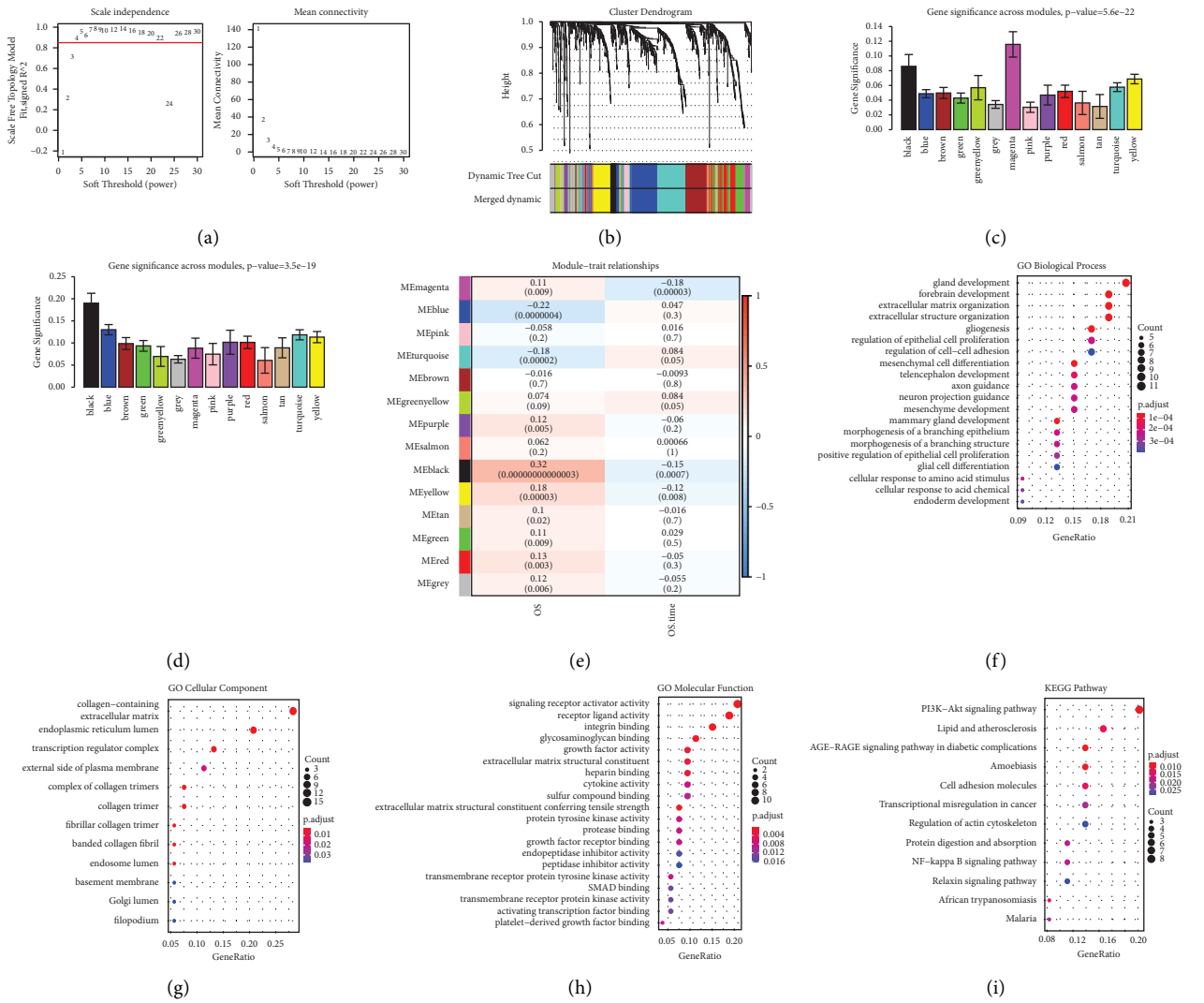

Figure 4: WGCNA and functional analysis in black and magenta modules. (a) Schematic diagram of threshold screening and determination. (b) Clustering dendrogram of all genes from last step. (c) Correlations of OS time with mean gene significance and errors in all modules. (d) Correlations of OS with mean gene significance and errors in all modules. (e) Heat map of the correlations between MEs and OS traits. (f) BP term in GO. (g) CC term in GO. (h) MF term in GO. (i) KEGG pathway analysis.

[35, 36, 36–38]. A landmark paper has demonstrated that ccRCC is a heterogeneous disease with marked genetic intermetastases and intratumour heterogeneity (G-IMH and G-ITH) [39]. Further studies have elucidated whether somatic mutation landscape and genetic heterogeneity influence the clinical outcomes of ccRCC tumour management [40]. Because of this, we adopted a series of bioinformatics methods to use the ccRCC single-cell data in published articles and the ccRCC-related data in public databases to study whether immune cell-related genes can construct a predictive prognostic model for patients with ccRCC, which may be helpful for further understanding of the intratumour heterogeneity of ccRCC, and provide corresponding support for related basic research and clinical applications in the future.

Since there are many genes used to annotate a certain cell, it is usually difficult to determine which of these genes are critical. As a result, we built some networks, hoping to better find key genes related to our target clinical traits to construct a risk prediction model. Researchers have traditionally been concerned with a few or linear pathways between different cells. Identifying the signalling network of communication within different cell types is invaluable in the diagnosis and treatment of ccRCC tumours. Furthermore, a complete network of cell-cell signalling includes not only intercellular signalling pathways but also intracellular signalling transduction and gene expression [41]. Thus, a complete network of molecular signalling mechanisms is required to show the interaction between the TME and related cell types. A study has proved a potential scRNA-seqtranscriptome-based multilayer network approach, which can be considered as a useful technique to identify the interplay between the TME and tumour cells, further predicting the prognostic and predictive signatures of

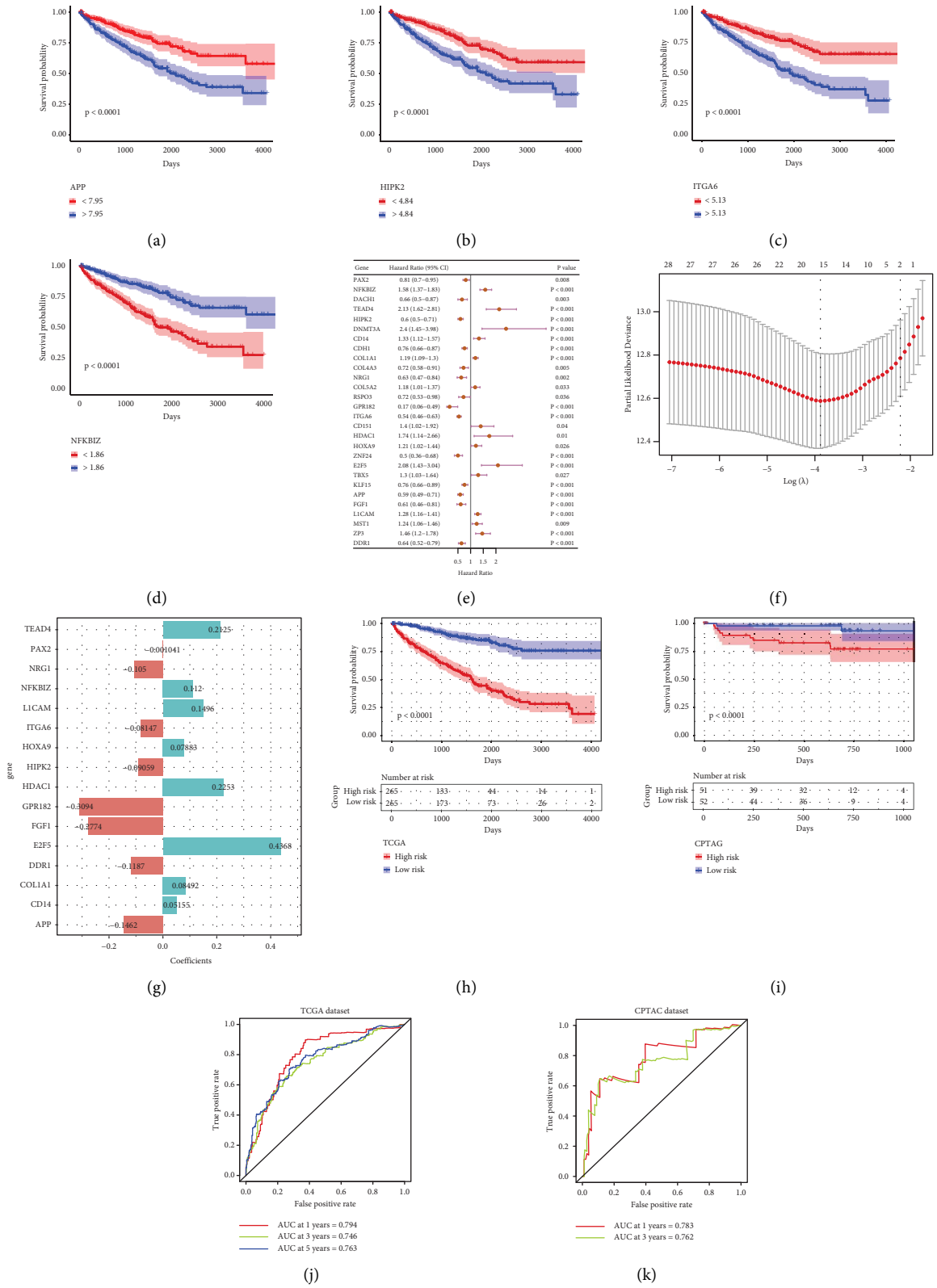

FIGURE 5: Construction and assessment of disease prognosis risk model. (a–d) Survival analysis of four genes among the candidate genes used to construct the risk prediction model. (e) Forest plot for univariate regression analysis of 28 genes. (f) Selection of appropriate λ value through LASSO regression analysis. (g) Scoring chart of risk model constructed by 16 genes. (h, j) Evaluation of predictive effectiveness of risk prognostic model. (i, k) Use of the data in the CPTAC database as an external dataset for verification.

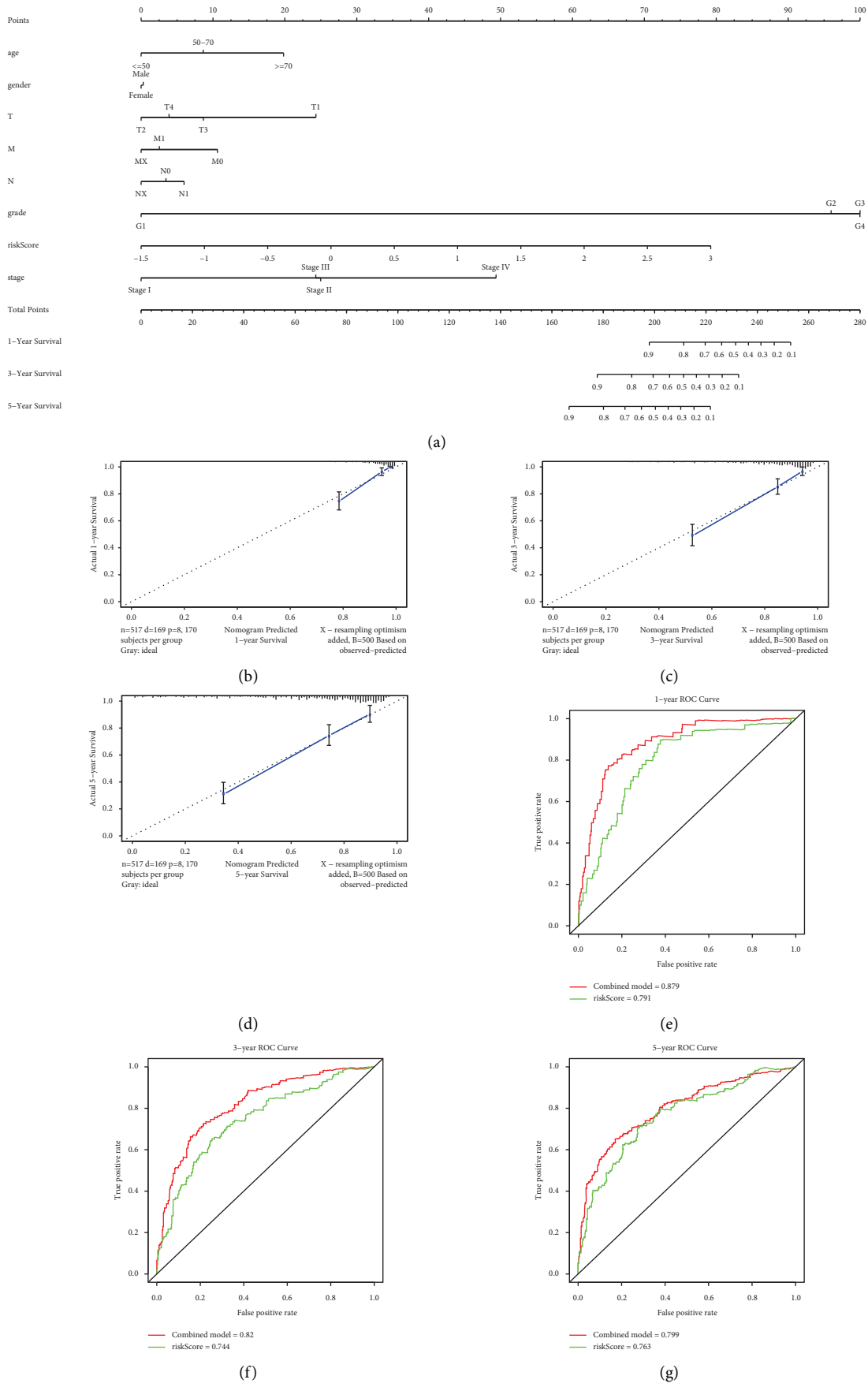

Figure 6: (a) Nomogram predicting 1-, 3-, and 5- year OS for patients with ccRCC. (b–d) The calibration curve for predicting 1-, 3-, and 5-year OS for patients with ccRCC. (e–g) Time-dependent ROC curve analysis evaluates the accuracy of the nomograms.

cancer patients [17]. In addition to the multilayer network, we also applied the WGCNA algorithm to explore the hub genes in key modules associated with the OS and OS time. The WGCNA algorithm explores the relationship between co-expression modules and clinical traits, which provides an opportunity to identify the hub genes in a module but not a downstream gene; thus, it possesses the distinct advantage of making the results more reliable and higher in biological significance [42]. In our study, we found all the genes related to the immune cells in the ccRCC samples through multilayer networks, then divided these genes into multiple modules using the WGCNA method, and used the genes in the modules with the strongest correlation with OS and OS time as the candidate genes for risk scoring model construction. Through the survival difference analysis of the genes in the key modules of the WGCNA algorithm, the genes with significant prognostic significance were found and the genes used to construct the risk prediction model were confirmed after LASSO dimensionality reduction processing. Subsequently, we verified the feasibility and effectiveness of the model for assessing the prognosis of patients with ccRCC through nomogram, which also showed that the immune cells in ccRCC do have an impact on the prognosis of patients.

Some genes in the prognostic risk scoring model have been proven to exert various effects on the regulation of certain tumours or diseases. Previous study has found that an imbalance of APP may be involved with the negative correlation between cancer and Alzheimer's disease [43]. As a vital target in the TLR signalling pathway, CD14 exerts a dual effect on oncogenesis, which can initiate several tumour-related signalling pathways or alter the immune microenvironment in the tumour [44]. COL1A1 was considered to be associated with the pathogenesis of COL1A1-PDGFB fusion uterine sarcoma [45]. It was reported that DDR1 is involved in the development of cancer and fibrotic diseases [46]. Regulating E2F5 is of great significance in maintaining genome stability and the cell cycle [47]. Study has shown that if certain signal mutations cause the destruction of FGF1, it is likely to give rise to cancer [48]. The dysregulation of HDAC1, a chromatin modifier, may cause harmful effects on cell fate and function, which could lead to cancer [49]. HIPK2, a multitalented protein, utilizes its kinase activity to regulate several pathways to limit the proliferation and differentiation of tumour cells and induce positive responses to therapies [50]. Since they are susceptible to ROS, proteins are typically the target of increased free radical production. ROS lead to the oxidation of structural proteins, which shuts down the proteolytic mechanism. These reactions alter the way proteins are built or how an enzyme functions. The latter could have many different downstream functional effects, such as inhibition of enzymatic and binding activities, an increase or decrease in cellular absorption, inactivation of DNA repair enzymes, and a decrease in the fidelity of damaged DNA polymerases in DNA replication [12]. HOXA9, a homeodomain-containing transcription factor, exerts a vital role in the proliferation of hematopoietic stem cells and is commonly negatively affected in acute leukaemias [51]. Recent study has shown that ITGA6 can be a useful biomarker for early detection of colorectal cancer cells in a noninvasive assay and as a prognostic factor [52]. L1CAM has been found in various types of human cancers, which indicates a bad prognosis [53]. NFKBIZ is a psoriasis susceptibility gene that encodes the functions of TRAF6 signalling players, especially in terms of positive and regulatory immune controls by interactions between immune cells and epithelial cells [54]. Oncogenic gene fusion involving NRG1 contributes to the activation of ErbB-mediated pathways, representing a potential target for tumour management [55]. PAX2 has been found in epithelial tumours of the kidney and the female genital tract [56]. TEAD4 binds with YAP, TAZ, VGLL, and other transcription factors to modulate various tumour-related processes, including tumour cell proliferation, cell survival, tissue regeneration, and stem cell maintenance, in cancer via its transcriptional output [57]. The above-reported functions and mechanisms of these genes could help elucidate their correlations with ccRCC and provide reliable evidence for further determination of diagnostic and therapeutic methods.

Although our study only used published data and information in public databases and did not directly use clinical samples for experimental testing and analysis, it is still sufficient to show that the data obtained through single-cell sequencing is able to provide an effective support to predict the prognosis of patients with ccRCC. Additionally, our research can also provide ideas for clinical diagnosis and treatment. For example, the genes in the risk prediction model we have established are more likely to become marker genes for clinical screening of ccRCC or therapeutic targets for metastatic ccRCC. Furthermore, our methods and results would enhance theoretical assistance for other researchers to explore other cancers related to tumour heterogeneity in the future.

5. Conclusion

Cancer has been proven to be caused by dysregulated evolution [27] that results in the acquisition of heritable genetic or epigenetic characteristics. However, the occurrence of tumour heterogeneity creates significant difficulties for both tumour identification and treatment. ccRCC is a heterogeneous disease with marked genetic intermetastases and intratumour heterogeneity (G-IMH and G-ITH). The purpose of this study is to determine whether immune cell-related genes can be used to build a predictive prognostic model for patients with ccRCC.

In our study, we used multilayer networks to identify all the immune cell-related genes in the ccRCC samples. We then used the WGCNA method to separate these genes into various modules, and we used the genes in the modules with the strongest correlation with OS and OS time as the candidate genes for risk scoring model construction. Following

all steps as detailed in result and discussion section, we then used a nomogram to validate the viability and efficacy of the model for determining a patient's prognosis for ccRCC, which also demonstrated that the immune cells in ccRCC do affect the prognosis of patients.

In a nutshell, our results indicate that the immune cell scRNA-seq predictive model will help us to assess the prognosis of patients with ccRCC and provide more precise guidelines for basic related research and clinical management. As a result, it may help to further our understanding of the intratumour heterogeneity of ccRCC and support future basic research and clinical applications.

Abbreviations

RCC:	Renal cell carcinoma
ccRCC:	Clear cell renal cell carcinoma
OS:	Overall survival
TME:	Tumour microenvironment
TAMs:	Tumour-associated macrophages
CAFs:	Cancer-associated fibroblasts
scRNA-seq:	Single-cell RNA sequencing
WGCNA:	Weighted gene co-expression network analysis
TCGA:	The Cancer Genome Atlas
CPTAC:	Consortium for Clinical Proteome Cancer Analysis
PCA:	Principal component analysis
PC:	Principal component
DEGs:	Differentially expressed genes
MEs:	Module eigengenes
GO:	Gene ontology
KEGG:	Kyoto Encyclopedia of Genes and Genomes
BP:	Biological process
MF:	Molecular function
CC:	Cellular component
HR:	Hazard ratio
ROC:	Receiver operating characteristic
C-index:	Concordance index
KM:	Kaplan–Meier
NGS:	Next-generation sequencing.

Data Availability

The data and materials can be obtained by contacting the corresponding author.

Consent

Not applicable.

Disclosure

A preprint has previously been published [58].

Conflicts of Interest

The authors declare that there are no conflicts of interest.

Authors' Contributions

GW designed the research plan, analysed datasets, and wrote the manuscript. WG and SZ provided meaningful discussion on key points. GF gave guidance in whole study and revised the manuscript. All authors have read and approved the final manuscript.

Acknowledgments

Thanks to the assistance of Mugu Inc (Beijing) in bioinformatics. This study was sponsored by the Guangdong Medical Research Foundation (A2021375).

Supplementary Materials

Supplementary Table 1: Notes on cell clustering. Supplementary Table 2: Differential genes in each cell cluster. Supplementary Table 3: Ligand-receptor relationship pair. Supplementary Table 4: Immune cell multifactor network relationship pair. Supplementary Table 5: Intersection genes in immune cell multifactor network relationship pair and TCGA. Supplementary Table 6: Genes in black and magenta models of WGCNA. (*Supplementary Materials*)

References

[1] R. L. Siegel, K. D. Miller, and A. Jemal, "Cancer statistics," *CA: A Cancer Journal for Clinicians*, vol. 68, no. 1, pp. 7–30, 2018.

[2] A. A. Hakimi, M. H. Voss, F. Kuo et al., "Transcriptomic profiling of the tumor microenvironment reveals distinct subgroups of clear cell renal cell cancer: data from a randomized phase III trial," *Cancer Discovery*, vol. 9, no. 4, pp. 510–525, 2019.

[3] T. J. Mitchell, S. Turajlic, A. Rowan et al., "Timing the landmark events in the evolution of clear cell renal cell cancer: TRACERx renal," *Cell*, vol. 173, no. 3, pp. 611–623, 2018.

[4] D. Miao, C. A. Margolis, W. Gao et al., "Genomic correlates of response to immune checkpoint therapies in clear cell renal cell carcinoma," *Science*, vol. 359, no. 6377, pp. 801–806, 2018.

[5] B. Greef and T. Eisen, "Medical treatment of renal cancer: new horizons," *British Journal of Cancer*, vol. 115, no. 5, pp. 505–516, 2016.

[6] Y. C. T. Shih, C. R. Chien, Y. Xu, I. W. Pan, G. L. Smith, and T. A. Buchholz, "Economic burden of renal cell carcinoma in the US: Part II--an updated analysis," *PharmacoEconomics*, vol. 29, no. 4, pp. 331–341, 2011.

[7] A. P. Patel, I. Tirosh, J. J. Trombetta et al., "Single-cell RNA-seq highlights intratumoral heterogeneity in primary glioblastoma," *Science*, vol. 344, no. 6190, pp. 1396–1401, 2014.

[8] E. Papalexi and R. Satija, "Single-cell RNA sequencing to explore immune cell heterogeneity," *Nature Reviews Immunology*, vol. 18, no. 1, pp. 35–45, 2018.

[9] A. Albini and M. B. Sporn, "The tumour microenvironment as a target for chemoprevention," *Nature Reviews Cancer*, vol. 7, no. 2, pp. 139–147, 2007.

[10] A. Mantovani, F. Marchesi, A. Malesci, L. Laghi, and P. Allavena, "Tumour-associated macrophages as treatment targets in oncology," *Nature Reviews Clinical Oncology*, vol. 14, no. 7, pp. 399–416, 2017.

[11] C. J. Hanley, M. Mellone, K. Ford et al., "Targeting the myofibroblastic cancer-associated fibroblast phenotype through inhibition of NOX4," *Journal of the National Cancer*

Institute: Journal of the National Cancer Institute, vol. 110, no. 1, pp. 109–120, 2018.

[12] P. Palozza, G. Calviello, S. Serini et al., "β-Carotene at high concentrations induces apoptosis by enhancing oxy-radical production in human adenocarcinoma cells," *Free Radical Biology and Medicine*, vol. 30, no. 9, pp. 1000–1007, 2001 May 1.

[13] J. Peng, B. F. Sun, C. Y. Chen et al., "Single-cell RNA-seq highlights intra-tumoral heterogeneity and malignant progression in pancreatic ductal adenocarcinoma," *Cell Research*, vol. 29, no. 9, pp. 725–738, 2019.

[14] W. Chung, H. H. Eum, H. O. Lee et al., "Single-cell RNA-seq enables comprehensive tumour and immune cell profiling in primary breast cancer," *Nature Communications*, vol. 8, no. 1, Article ID 15081, 2017.

[15] N. E. Navin, "The first five years of single-cell cancer genomics and beyond," *Genome Research*, vol. 25, no. 10, pp. 1499–1507, 2015.

[16] M. D. Young, T. J. Mitchell, F. A. Vieira Braga et al., "Single-cell transcriptomes from human kidneys reveal the cellular identity of renal tumors," *Science*, vol. 361, no. 6402, pp. 594–599, 2018.

[17] J. Zhang, M. Guan, Q. Wang, J. Zhang, T. Zhou, and X. Sun, "Single-cell transcriptome-based multilayer network biomarker for predicting prognosis and therapeutic response of gliomas," *Briefings in Bioinformatics*, vol. 21, no. 3, pp. 1080–1097, 2020.

[18] A. Vishwakarma, B. Nicholas, S. C. Michael et al., "Mapping the immune landscape of clear cell renal cell carcinoma by single-cell RNA-seq," Article ID 824482, 2019,https://www.biorxiv.org/content/10.1101/824482v1.

[19] P. Langfelder and S. Horvath, "WGCNA: an R package for weighted correlation network analysis," *BMC Bioinformatics*, vol. 9, no. 1, p. 559, 2008.

[20] L. Chen, L. Yuan, Y. Wang et al., "Co-expression network analysis identified FCER1G in association with progression and prognosis in human clear cell renal cell carcinoma," *International Journal of Biological Sciences*, vol. 13, no. 11, pp. 1361–1372, 2017.

[21] G. Wu, P. Xia, S. Yan, D. Chen, L. Xie, and G. Fan, "Identification of unique long non-coding RNAs as putative biomarkers for chromophobe renal cell carcinoma," *Personalized Medicine*, vol. 18, no. 1, pp. 9–19, 2021.

[22] M. D. Xia, R. R. Yu, and D. M. Chen, "Identification of hub biomarkers and immune-related pathways participating in the progression of antineutrophil cytoplasmic antibody-associated glomerulonephritis," *Frontiers in Immunology*, vol. 12, Article ID 809325, 2021.

[23] M. R. Stratton, "Exploring the genomes of cancer cells: progress and promise," *Science*, vol. 331, no. 6024, pp. 1553–1558, 2011.

[24] N. Navin, J. Kendall, J. Troge et al., "Tumour evolution inferred by single-cell sequencing," *Nature*, vol. 472, no. 7341, pp. 90–94, 2011.

[25] I. Tirosh, B. Izar, S. M. Prakadan et al., "Dissecting the multicellular ecosystem of metastatic melanoma by single-cellRNA-seq," *Science*, vol. 352, no. 6282, pp. 189–196, 2016.

[26] P. C. Nowell, "The clonal evolution of tumor cell populations," *Science*, vol. 194, no. 4260, pp. 23–28, 1976.

[27] L. R. Yates and P. J. Campbell, "Evolution of the cancer genome," *Nature Reviews Genetics*, vol. 13, no. 11, pp. 795–806, 2012.

[28] B. Vogelstein and K. W. Kinzler, "The path to cancer --Three strikes and you're out," *New England Journal of Medicine*, vol. 373, no. 20, pp. 1895–1898, 2015.

[29] M. Gerlinger, N. McGranahan, S. M. Dewhurst, R. A. Burrell, I. Tomlinson, and C. Swanton, "Cancer: evolution within a lifetime," *Annual Review of Genetics*, vol. 48, no. 1, pp. 215–236, 2014.

[30] G. H. Heppner, "Tumor heterogeneity," *Cancer Research*, vol. 44, no. 6, pp. 2259–2265, 1984.

[31] A. Marusyk, V. Almendro, and K. Polyak, "Intra-tumour heterogeneity: a looking glass for cancer?" *Nature Reviews Cancer*, vol. 12, no. 5, pp. 323–334, 2012.

[32] R. A. Burrell, N. McGranahan, J. Bartek, and C. Swanton, "The causes and consequences of genetic heterogeneity in cancer evolution," *Nature*, vol. 501, no. 7467, pp. 338–345, 2013.

[33] A. A. Alizadeh, V. Aranda, A. Bardelli et al., "Toward understanding and exploiting tumor heterogeneity," *Nature Medicine*, vol. 21, no. 8, pp. 846–853, 2015.

[34] D. L. Longo, "Tumor heterogeneity and personalized medicine," *New England Journal of Medicine*, vol. 366, no. 10, pp. 956-957, 2012.

[35] M. Jamal-Hanjani, S. A. Quezada, J. Larkin, and C. Swanton, "Translational implications of tumor heterogeneity," *Clinical Cancer Research*, vol. 21, no. 6, pp. 1258–1266, 2015.

[36] M. H. Voss and J. J. Hsieh, "Therapeutic guide for mTOuRing through the braided kidney cancer genomic river," *Clinical Cancer Research*, vol. 22, no. 10, pp. 2320–2322, 2016.

[37] P. L. Bedard, A. R. Hansen, M. J. Ratain, and L. L. Siu, "Tumour heterogeneity in the clinic," *Nature*, vol. 501, no. 7467, pp. 355–364, 2013.

[38] N. Andor, T. A. Graham, M. Jansen et al., "Pan-cancer analysis of the extent and consequences of intratumor heterogeneity," *Nature Medicine*, vol. 22, no. 1, pp. 105–113, 2016.

[39] M. Gerlinger, A. J. Rowan, S. Horswell et al., "Intratumor heterogeneity and branched evolution revealed by multiregion sequencing," *New England Journal of Medicine*, vol. 366, no. 10, pp. 883–892, 2012.

[40] J. J. Hsieh, B. J. Manley, N. Khan, J. Gao, M. I. Carlo, and E. H. Cheng, "Overcome tumor heterogeneity-imposed therapeutic barriers through convergent genomic biomarker discovery: a braided cancer river model of kidney cancer," *Seminars in Cell & Developmental Biology*, vol. 64, pp. 98–106, 2017.

[41] X. Sun, J. Su, J. Bao et al., "Cytokine combination therapy prediction for bone remodeling in tissue engineering based on the intracellular signaling pathway," *Biomaterials*, vol. 33, no. 33, pp. 8265–8276, 2012.

[42] W. C. Chou, A. L. Cheng, M. Brotto, and C. Y. Chuang, "Visual gene-network analysis reveals the cancer gene co-expression in human endometrial cancer," *BMC Genomics*, vol. 15, no. 1, p. 300, 2014.

[43] F. Galvao, K. C. Grokoski, B. B. da Silva, M. L. Lamers, and I. R. Siqueira, "The amyloid precursor protein (APP) processing as a biological link between Alzheimer's disease and cancer," *Ageing Research Reviews*, vol. 49, pp. 83–91, 2019.

[44] Z. Wu, Z. Zhang, Z. Lei, and P. Lei, "CD14: biology and role in the pathogenesis of disease," *Cytokine & Growth Factor Reviews*, vol. 48, pp. 24–31, 2019.

[45] S. Croce, I. Hostein, and W. G. McCluggage, "*NTRK* and other recently described kinase fusion positive uterine sarcomas: a review of a group of rare neoplasms," *Genes Chromosomes & Cancer*, vol. 60, no. 3, pp. 147–159, 2021.

[46] Y. C. Yeh, H. H. Lin, and M. J. Tang, "Dichotomy of the function of DDR1 in cells and disease progression,"

Biochimica et Biophysica Acta (BBA) - Molecular Cell Research, vol. 1866, no. 11, Article ID 118473, 2019.

[47] C. Dominguez-Brauer, P. M. Brauer, Y. J. Chen, J. Pimkina, and P. Raychaudhuri, "Tumor suppression by ARF: gatekeeper and caretaker," *Cell Cycle*, vol. 9, no. 1, pp. 86–89, 2010.

[48] X. Jiang, M. Skibba, C. Zhang, Y. Tan, Y. Xin, and Y. Qu, "The roles of fibroblast growth factors in the testicular development and tumor," *Journal of Diabetes Research*, vol. 2013, pp. 1–8, 2013.

[49] A. Laugesen and K. Helin, "Chromatin repressive complexes in stem cells, development, and cancer," *Cell Stem Cell*, vol. 14, no. 6, pp. 735–751, 2014.

[50] G. D'Orazi, C. Rinaldo, and S. Soddu, "Updates on HIPK2: a resourceful oncosuppressor for clearing cancer," *Journal of Experimental & Clinical Cancer Research*, vol. 31, no. 1, p. 63, 2012.

[51] C. T. Collins and J. L. Hess, "Role of HOXA9 in leukemia: dysregulation, cofactors and essential targets," *Oncogene*, vol. 35, no. 9, pp. 1090–1098, 2016.

[52] J. F. Beaulieu, "Integrin $\alpha 6\beta 4$ in colorectal cancer: expression, regulation, functional alterations and use as a biomarker," *Cancers*, vol. 12, no. 1, p. 41, 2019.

[53] P. Altevogt, K. Doberstein, and M. Fogel, "L1CAM in human cancer," *International Journal of Cancer*, vol. 138, no. 7, pp. 1565–1576, 2016.

[54] T. Dainichi, R. Matsumoto, A. Mostafa, and K. Kabashima, "Immune control by TRAF6-mediated pathways of epithelial cells in the EIME (epithelial immune microenvironment)," *Frontiers in Immunology*, vol. 10, p. 1107, 2019.

[55] J. Laskin, S. Liu, K. Tolba et al., "NRG1 fusion-driven tumors: biology, detection, and the therapeutic role of afatinib and other ErbB-targeting agents," *Annals of Oncology*, vol. 31, no. 12, pp. 1693–1703, 2020.

[56] N. G. Ordonez, "Value of PAX2 immunostaining in tumor diagnosis: a review and update," *Advances in Anatomic Pathology*, vol. 19, no. 6, pp. 401–409, 2012.

[57] M. Chen, B. Huang, L. Zhu, K. Chen, M. Liu, and C. Zhong, "Structural and Functional Overview of TEAD4 in Cancer Biology," *OncoTargets and Therapy*, vol. 13, pp. 9865–9874, 2020.

[58] G. Wu, L. Miao, Y. Weifeng et al., "Integrated analysis of single-cell and transcriptome based RNA-seq multilayer network and WGCNA for construction and validation of an immune cell-related prognostic model in clear cell renal cell carcinoma," p. 2021, 2022, https://www.biorxiv.org/content/10.1101/2021.10.15.464475v1.

Hindawi
Journal of Oncology
Volume 2023, Article ID 4738586, 11 pages
https://doi.org/10.1155/2023/4738586

Research Article

METTL14 Regulates PLAGL2/β-Catenin Signaling Axis to Promote the Development of Nonsmall Cell Lung Cancer

Qianhui Zhou,[1] Xihua Lai,[2] Yan Gao,[1] Quefei Chen,[1] Yuzhu Xu,[1] and Yi Liu[1]

[1]*Department of Respiratory and Critical Care Medicine, Zhuzhou Central Hospital, Zhuzhou 412000, Hunan, China*
[2]*Department of Cardiovascular Surgery, Zhuzhou Central Hospital, Zhuzhou 412000, Hunan, China*

Correspondence should be addressed to Yi Liu; hui648934631@126.com

Received 5 September 2022; Revised 14 October 2022; Accepted 28 January 2023; Published 23 February 2023

Academic Editor: Recep Liman

N6-methyladenosine (m6A) is an abundant eukaryotic mRNA modification involved in regulating the formation and metastasis of nonsmall cell lung cancer (NSCLC). We collected clinical NSCLC tissue and paracarcinoma tissue. Then methyltransferase-like 14 (METTL14), pleomorphic adenoma gene like-2 (PLAGL2), and β-catenin expressions were assessed using quantitative real-time PCR and western blot. PLAGL2, and β-catenin (nuclear) expressions were increased in NSCLC tissues. Cell proliferation, migration, invasion, and death were examined. PLAGL2 could activate β-catenin signaling to affect cell proliferation and migration abilities. RNA immunoprecipitation assay was operated to identify m6A modification levels of PLAGL2 after knockdown and overexpression of METTL14. PLAGL2 was regulated by METTL14-mediated m6A modification. Knockdown of METTL14 repressed cell proliferation, migration, and invasion, and promoted cell death. Interestingly, these effects were reversed when PLAGL2 was overexpressed. Finally, tumor formation in nude mice was performed to verify the role of the METTL14/PLAGL2/β-catenin signaling axis. Tumor formation in nude mice demonstrated METTL14/PLAGL2/β-catenin axis promoted NSCLC development *in vivo*. In brief, METTL14 promoted NSCLC development by increasing m6A methylation of PLAGL2 to activate β-catenin signaling. Our research provided essential clues for in-depth comprehension of the mechanism of NSCLC occurrence and development and also provided the basis for NSCLC treatment.

1. Introduction

Nonsmall cell lung cancer (NSCLC) accounts for 85% of all lung cancer incidence [1]. While it affects the quality of patients' life, it also increases the global economic burden. Due to a large number of mutations and general heterogeneity in this type of cancer, the use of traditional therapies has been challenging [2]. Small molecule tyrosine kinase inhibitors and immunotherapy have brought unprecedented survival benefits to selected patients. But overall cure rate and survival rate of NSCLC are still low [3]. At present, molecular-targeted therapy has also made great progress in the NSCLC treatment field [4]. Therefore, it is particularly essential to investigate the internal mechanism of NSCLC and provide potential scientific clues for subsequent treatment of NSCLC.

N6-methyladenosine (m6A) is an abundant eukaryotic mRNA modification and a common transcriptome modification in cancer. It was recently found to be involved in the regulation of NSCLC formation and metastasis [5]. Methyltransferase-like 14 (METTL14) is a core component of the m6A methyltransferase complex, and METTL14-induced abnormal m6A levels are related to tumorigenesis, proliferation, metastasis, and invasion [6]. METTL14 regulated various cancer occurrences and development, including breast cancer [7], colorectal cancer [8], and endometrioid epithelial ovarian cancer [9]. In NSCLC, knockdown of METTL14 inhibited Twist-mediated activation of AKT signaling to suppress NSCLC malignancy. This revealed METTL14 might be a potential therapeutic target for NSCLC [10]. As a writer of m6A methylation modification, METTL14 could promote the methylation modification of mRNA, thereby affecting its protein expression [11, 12]. Pleomorphic adenoma gene like-2 (PLAGL2) is the zinc finger protein transcription factor. It is overexpressed in many malignant tumors (gastric cancer, colorectal cancer, and breast cancer) and could facilitate

tumor proliferation, migration, and invasion [13–15]. Overexpression of PLAGL2 has been implicated in lung cancer [16]. We predicted m6A modification of PLAGL2 and METTL14 acting on PLAGL2 by RMBase and m6A2Target. However, METTL14 and PLAGL2 mechanism in NSCLC remains to be investigated.

β-catenin is the complete structural component of cadherin-based and adherent junctions [17]. Abnormal β-catenin activating in nuclear is related to many human cancers [18]. Furthermore, METTL14 attenuated cardiac ischemia-reperfusion injury via activating Wnt/β-catenin in an m6A-dependent manner, which provided a new therapeutic target for ischemic heart disease [19]. In addition, related studies have shown PLAGL2 could regulate β-catenin and its downstream pathways and promote tumor genesis and development [14, 20]. However, there have been no studies of PLAGL2 with β-catenin in NSCLC.

In our research, we hypothesized METTL14 promoted PLAGL2 expression by increasing m6A methylation modification of PLAGL2, activating β-catenin signaling, thereby affecting NSCLC development. To this end, we collected clinical NSCLC tissue and paracarcinoma tissue for relevant testing. METTL14/PLAGL2/β-catenin role was also investigated *in vivo* and *in vitro* to investigate whether METTL14 regulated PLAGL2/β-catenin signaling axis to promote the development of NSCLC. Our research provided essential clues for an in-depth comprehension of the mechanism of NSCLC occurrence and development and also provided the basis for NSCLC treatment.

2. Materials and Methods

2.1. Collection of Clinical Samples. Tumor tissue and paracarcinoma tissue samples from NSCLC patients by iconography, serological or histopathological examination in Zhuzhou Central Hospital from November 2020 to August 2021 were collected. Clinical samples were divided into two groups: the NSCLC group ($n = 5$) and the paracarcinoma tissues group ($n = 5$). This study was approved by the Medical Ethics Committee of Zhuzhou Central Hospital (ZZCHEC2021092-01). The research was conducted according to the World Medical Association Declaration of Helsinki. All the information about the study will be fully explained to the subjects by the researchers. All the participants provided informed consent before sampling.

2.2. Cell Culture and Treatment. NSCLC cell A549 (ZQ0003) was obtained from Zhongqiao Xinzhou Biotech (Shanghai, China). It was cultured in DMEM high glucose medium with 10% FBS and 1% double antibodies. PLAGL2 and METTL14 were knocked down and overexpressed in A549 cells, and divided into NC (sh-PLAGL2 NC + oe-PLAGL2 NC), sh-PLAGL2 (sh-PLAGL2+ oe-PLAGL2 NC), and oe-PLAGL2 (sh-PLAGL2 NC + oe-PLAGL2) groups; NC (sh-METTL14 NC + oe-METTL14 NC), sh-METTL14 (sh-METTL14+ oe- METTL14 NC), and oe-METTL14 (sh-METTL14 NC + oe-METTL14) groups. To further study PLAGL2 and β-catenin function, we performed interference PLAGL2 and overexpression of β-catenin. The subgroups were sh-NC, sh-PLAGL2, sh-PLAGL2 + oe-NC, and sh-PLAGL2 + oe-β-catenin groups. Next, to verify METTL14 and PLAGL2's influence on NSCLC development, METTL14 was knocked down, and PLAGL2 was overexpressed. The subgroups were sh-NC, sh-METTL14, sh-METTL14 + oe-NC, and sh-METTL14 + oe-PLAGL2 groups. sh-PLAGL2, oe-PLAGL2, sh-METTL14, oe-METTL14, oe-β-catenin, and their control were provided in GenePharma (Shanghai, China). Cell transfection was performed according to Lipofectamine 3000 (L3000015, Invitrogen, USA) kit.

2.3. Hematoxylin-Eosin (HE) Staining. HE staining was performed to assess the pathological status of the tumor and paracarcinoma tissues [21]. The slices were placed in xylene. Each grade of ethanol was placed for 5 min. After dyeing with hematoxylin for 3 min, they were returned to blue with PBS. Eosin was dyed 5 s. Gradient alcohol (95–100%) was dehydrated. After taking them out, they were placed in xylene, sealed with neutral gum, and observed under the microscope (BA210T, Motic).

2.4. Quantitative Real-Time PCR (qRT-PCR). In simple terms, total RNA was extracted through Trizol and reverse transcribed into cDNAs through cDNA reverse transcription kit (CW2569, CoWin Biosciences, Beijing, China). Ultra SYBR Mixture (CW2601, CoWin Biosciences, Beijing, China) was performed to evaluate the expression on ABI 7900 system. Using β-actin and U6 as reference genes, gene levels were calculated by $2^{-\Delta\Delta Ct}$. Primer sequences were as follows: METTL14-F: GTAGCACAGACGGGGACTTC, METTL14-R: TTGGTCCAACTGTGAGCCAG; PLAGL2-F: ACAATGCACCGCACAATGGC, PLAGL2-R: AAACAA TCTCTTCACCGCGCTC;β-catenin-F: ATTCTTGGCTAT TACGACAGACT,β-catenin-R: AGCAGACAGATAGCA CCTT;β-actin-F: ACCCTGAAGTACCCCATCGAG,β-actin-R: AGCACAGCCTGGATAGCAAC.

2.5. Western Blot (WB). RIPA kit (P0013B, Beyotime, Shanghai, China) extracted total protein from cells and tissues. Proteins were quantified according to the BCA protein assay kit (#7780, Cell Signaling Technology, USA) and isolated by 10% SDS-PAGE electrophoresis. Electrotransfer transferred the protein to the nitrocellulose filter membrane. The membrane was sealed with 5% skim milk to bind to nonspecific cells and incubated with primary antibody at 4°C overnight. For primary antibodies, METTL14 (26158-1-AP, 1 : 3000, Proteintech, USA), PLAGL2 (11540-1-AP, 1 : 300, Proteintech, USA), β-catenin (51067-2-AP, 1 : 1000, Proteintech, USA), PCNA (10205-2-AP, 1 : 1500, Proteintech, USA), and β-actin (60008-1-Ig, 1 : 5000, Proteintech, USA) were used. Then secondary antibodies were incubated. β-actin or PCNA acted as internal reference, and

Odyssey Infrared Imaging System (Li-COR Biosciences, USA) assessed the protein bands.

2.6. RNA Immunoprecipitation (RIP) Assay. RIP lysis was first prepared. A549 cells were lysed with RIP lysis buffer and then incubated with RIP immunoprecipitation buffer containing magnetic beads coupled to antibodies against Ago2 (CST, USA) or anti-rabbit IgG (negative control, CST, USA). Precipitated RNA was evaluated by qRT-PCR. Total RNA was used as input controls. The primer sequences were PLAGL2-F: TCAGCTCCCTCCAAAATACCAG, PLAGL2-R: CTCCGCCAGAAAACTATCCAC.

2.7. Immunofluorescence (IF). Cells were treated with slices, fixed with 4% paraformaldehyde. Slices were added 0.3% triton, permeated at 37°C. Slices were sealed with 5% BSA at 37°C. Cell slices were dropped with the appropriate dilution of primary antibody β-catenin (51067-2-AP, 1 : 100, Proteintech, USA). Then we added appropriate anti-rabbit-IgG-labeled fluorescent antibody and incubated them at 37°C for 90 min. DAPI working solution was nucleated for 10 min at 37°C, and then cells were sealed with buffer glycerol and observed under the fluorescence microscope.

2.8. Plate Clone Formation Assay. Cells were removed from each group at the exponential growth stage. Cells in each group were inoculated with 200 cells in each well in 6-well plates containing 1 mL culture medium restored to room temperature. Cells were placed in the 5% CO_2, 37°C, and saturated humidity incubator for 2 to 3 weeks, during which the liquid was appropriately changed. We discarded the culture medium, carefully soaked PBS twice, and added 4% paraformaldehyde (1 mL) to fix the cells. We removed the fixing solution and added 1 mL of dye solution to the working solution to stain. After decolorization, the absorbance (OD) value at 550 nm was assessed by using the enzyme-plate reader.

2.9. Trypan Blue Staining. Cells were collected after digestion with trypsin and EDTA. We centrifuged collected cells at 1500 g for 1 min, discarded the supernatant, and resuspended cells with 1 mL or an appropriate cell suspension depending on the number of cells. Trypan blue staining was performed according to previous reports [22].

2.10. Wound Healing Assay. Cells were digested with trypsin to form single cell suspension and inoculated on 6-well culture plates (5×10^5 cells per well). Cells were cultured in a 5% CO_2 incubator at 37°C for 24 h until cells were covered with six-well plates. We scratched with a horizontal line perpendicular to the back of the six-hole plate. Serum-free DMEM medium (D5796, Sigma, USA) was added. Scratches at 0 h were photographed and taken under the inverted biological microscope (DSZ2000X, Cnmicro, China) after incubation for 24 and 48 h.

2.11. Transwell Assay. Cell invasion assays were applied in the Transwell chamber (3428, Corning, USA) with a matrix gel (354262, BD, USA). Cells were digested with trypsin into a single cell suspension and suspended in serum-free medium to 2×10^6 cells/mL. The upper chamber was inoculated with 100 μL cells, and the lower chamber was inoculated with 10% FBS complete medium (500 μL). After being cultured in a 37°C incubator for 48 h, they were washed in the upper chamber with PBS. We fixed them with paraformaldehyde and removed the film. We dyed the film with crystal violet (0.1%) for 5 min. Upper outdoor surface cells were observed under the inverted microscope (DSZ2000X, Cnmicro, China). After decolorization by soaking in acetic acid, the number of cells was counted [23].

2.12. In Vivo Tumorigenesis. Twenty BALB/c nude mice (4–6 weeks) were randomly assigned to sh-NC, sh-METTL14, sh-METTL14+oe-NC, and sh-METTL14+oe-PLAGL2, with 5 mice in each group. Mice were raised under sterile conditions of ambient room temperature of 26–28°C, the humidity of 40–60%, and alternating day and night for 10 h/14 h. The Mice were fed sterile food and water. After 1 week of adaptive feeding, A549 cells that transfected with sh-NC, sh-METTL14, oe-NC, and oe-PLAGL2 were subcutaneously injected. The cell concentration was 5×10^6/mL, and 200 μL was injected [24, 25]. The formation of the transplanted tumor was observed, and tumors with a diameter $\geq$0.5 cm were considered tumor formation. Tumor volume was calculated. After the experiment was completed, we euthanized the mice under animal ethics. The mice were sacrificed with 150 mg/kg sodium pentobarbital.

2.13. Statistical Analysis. GraphPad Prism 8.0 software was applied for statistical analysis. Data were expressed as mean ± standard deviation (SD). First, normality and homogeneity of variance tests were performed. When the test conformed to the normal distribution and the variance was homogeneous, Student's t-test was used between the two groups. Comparisons among multiple groups were conducted by one-way analysis of variance (ANOVA), followed by Tukey's post hoc test. $P < 0.05$ indicated the difference was statistically significant.

3. Results

3.1. PLAGL2 Level Was Elevated in NSCLC Tissues. First, HE staining assessed the pathological status. Compared with paracarcinoma tissues, NSCLC tissues had larger nuclei, larger nucleoplasmic ratio, more obvious histopathological atypia, and unclear tissue structure (Figure 1(a)). Subsequently, PLAGL2 expression was measured by qRT-PCR. Compared with paracarcinoma tissues, PLAGL2 expression

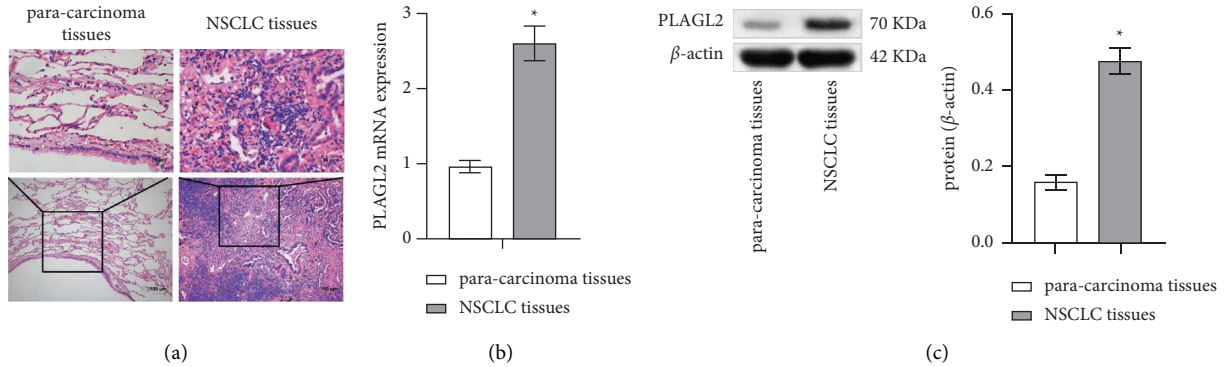

Figure 1: PLAGL2 level was elevated in NSCLC tissues. (a) HE staining assessed the pathological status. (b) PLAGL2 mRNA expression. (c) PLAGL2 protein expression. Student's t-test was used between the two groups. $^{*}P < 0.05$ vs. paracarcinoma tissues.

was elevated in NSCLC tissues (Figure 1(b)). PLAGL2 expression was further verified by WB, and WB results were consistent with the trend of qRT-PCR (Figure 1(c)).

3.2. PLAGL2 Activated β-catenin Signaling to Affect Cell Proliferation and Migration. Through a literature search, we found PLAGL2 regulated β-catenin and its downstream pathways and promoted tumor genesis and development [14, 20]. Therefore, we wanted to investigate PLAGL2's role in β-catenin. First, β-catenin (total) and β-catenin (nuclear) expressions were evaluated by WB. β-catenin (nuclear) level was promoted in NSCLC tissues than paracarcinoma tissues, but β-catenin (total) was not significantly different (Figure 2(a)). Subsequently, PLAGL2 was knocked down and overexpressed in A549 cells. PLAGL2 level in the sh-PLAGL2 group was repressed, and that in the oe-PLAGL2 group was increased than the NC group, indicating that PLAGL2 was successfully knocked down and overexpressed. At the same time, β-catenin expression was repressed in the sh-PLAGL2 group and accelerated in the oe-PLAGL2 group compared with the NC group (Figure 2(b)). WB further verified that β-catenin (nuclear) expression was inhibited in the sh-PLAGL2 group and accelerated in the oe-PLAGL2 group compared with the NC group. β-catenin (total) showed no significant difference (Figure 2(c)). IF further demonstrated β-catenin location. Compared with the NC group, β-catenin in the oe-PLAGL2 group showed nuclear transfer (Figure 2(d)). Then we performed interference with PLAGL2 and overexpression of β-catenin. PLAGL2 level was repressed in sh-PLAGL2 group than sh-NC. β-catenin expression was elevated in the sh-PLAGL2 + oe-β-catenin group compared with the sh-PLAGL2 + oe-NC group, indicating that we successfully interfered with PLAGL2 and overexpressed β-catenin (Figure 2(e)). Plate clone formation and wound healing assays showed that the number of clones and migration were repressed in the sh-PLAGL2 group than the sh-NC group. After β-catenin was overexpressed, the number of clones and migration increased (Figures 2(f) and 2(g)). This suggested that PLAGL2 activated β-catenin signaling to influence cell proliferation and migration.

3.3. PLAGL2 Signaling Was Regulated by METTL14-Mediated m6A Modification. First, we predicted m6A modification of PLAGL2 by RMBase and predicted METTL14 acted on PLAGL2 via m6A2Target. Therefore, we knocked down and overexpressed METTL14 to explore the mechanism of METTL14 and PLAGL2. METTL14 level in the sh-METTL14 group was suppressed and that in the oe-METTL14 group was increased than the NC group, indicating that METTL14 was successfully knocked down and overexpressed. In addition, PLAGL2 expression was repressed in the sh-METTL14 group, and accelerated in the oe-METTL14 group compared with the NC group (Figure 3(a)). Then we used RIP to identify the m6A modification of PLAGL2 after knockdown and overexpression of METTL14. The results revealed the m6A modification of PLAGL2 was repressed in the sh-METTL14 group and accelerated in the oe-METTL14 group than the NC group (Figure 3(b)). Collectively, PLAGL2 signaling was regulated by METTL14-mediated m6A modification.

3.4. METTL14 Regulated PLAGL2 Signaling to Affect NSCLC Cell Function. Next, to verify METTL14 and PLAGL2's influence on NSCLC development deeply, METTL14 was knocked down, and PLAGL2 was overexpressed. qRT-PCR showed METTL14 level was repressed in the sh-METTL14 than the sh-NC. In the sh-METTL14 + oe-PLAGL2 group, PLAGL2 expression was increased compared with the sh-METTL14 + oe-NC group. This indicated METTL14 was knocked down successfully, and PLAGL2 was successfully overexpressed (Figure 4(a)). WB showed decreased expressions of METTL14, PLAGL2, and β-catenin (nuclear) in the sh-METTL14 than in the sh-NC. PLAGL2 and β-catenin (nuclear) expressions were elevated in the sh-METTL14 + oe-PLAGL2 compared with the sh-METTL14 + oe-NC. β-catenin (total) showed no significant difference (Figure 4(b)). Cell function experiments showed knockdown of METTL14 reduced cell proliferation, migration, and invasion and facilitated cell death (cell viability decreased). After PLAGL2 was overexpressed, cell proliferation, migration, and invasion were increased, and cell

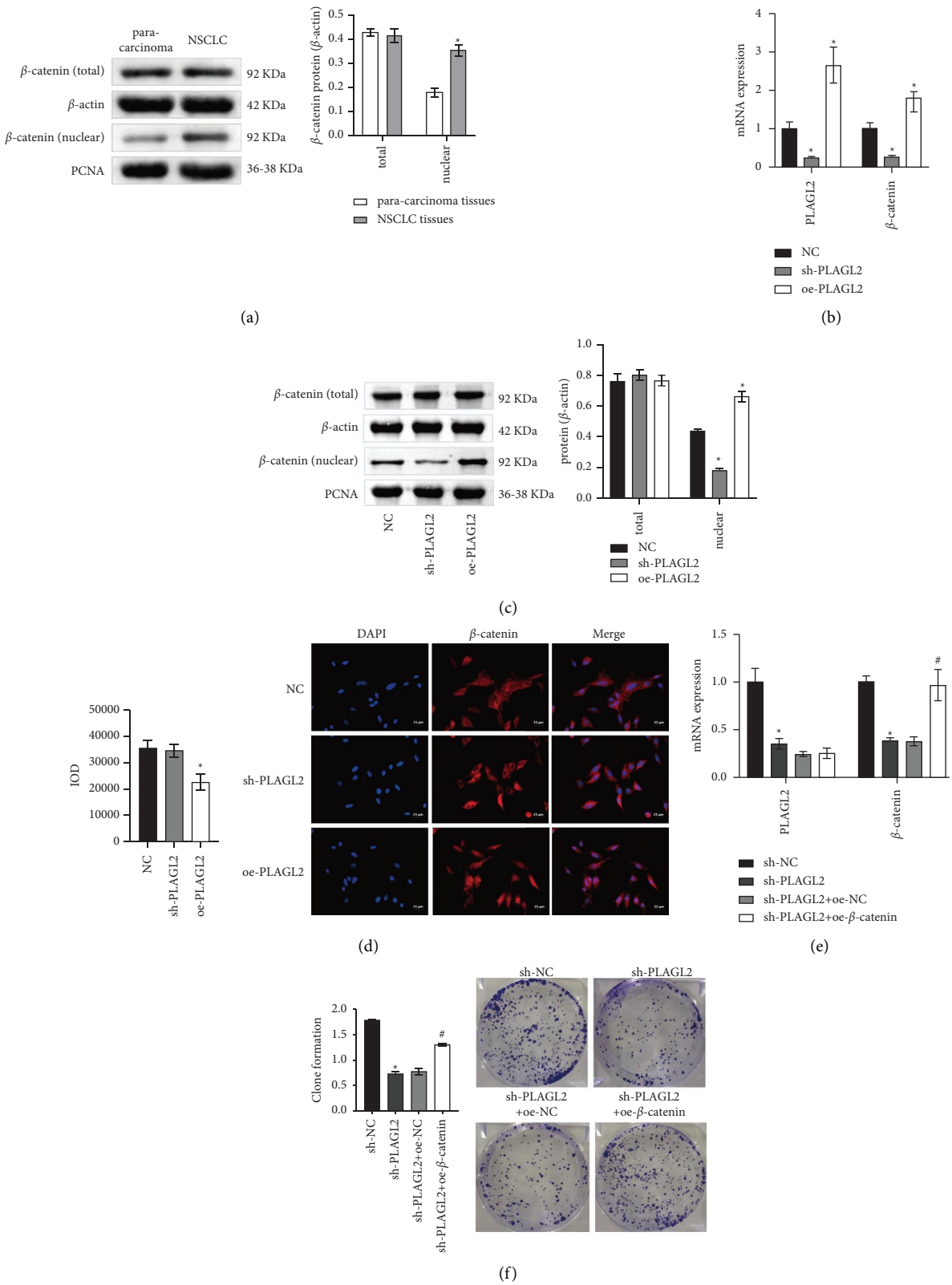

Figure 2: Continued.

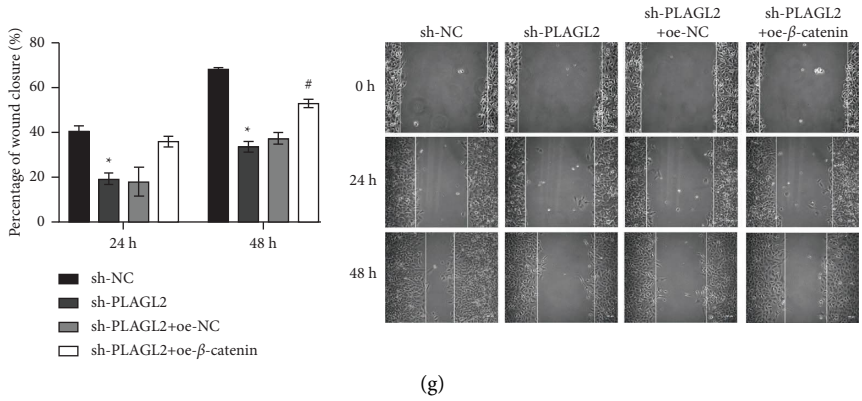

(g)

Figure 2: PLAGL2 activated β-catenin signaling to influence cell proliferation and migration. (a) β-catenin (total) and β-catenin (nuclear) protein expressions in NSCLC tissues. $^{*}P < 0.05$ vs. paracarcinoma tissues. (b) PLAGL2 and β-catenin mRNA expressions. (c) β-catenin (total) and β-catenin (nuclear) protein expressions in cells. (d) IF detection of β-catenin localization. $^{*}P < 0.05$ vs. NC. (e) PLAGL2 and β-catenin mRNA expressions. (f) Plate clone formation assay to evaluate cell proliferation. (g) Cell migration was tested by wound healing assay. Student's t-test was used between the two groups. Comparisons among multiple groups were conducted by one-way analysis of variance (ANOVA), followed by Tukey's post hoc test. $^{*}P < 0.05$ vs sh-NC, $^{\#}P < 0.05$ vs sh-PLAGL2 + oe-NC.

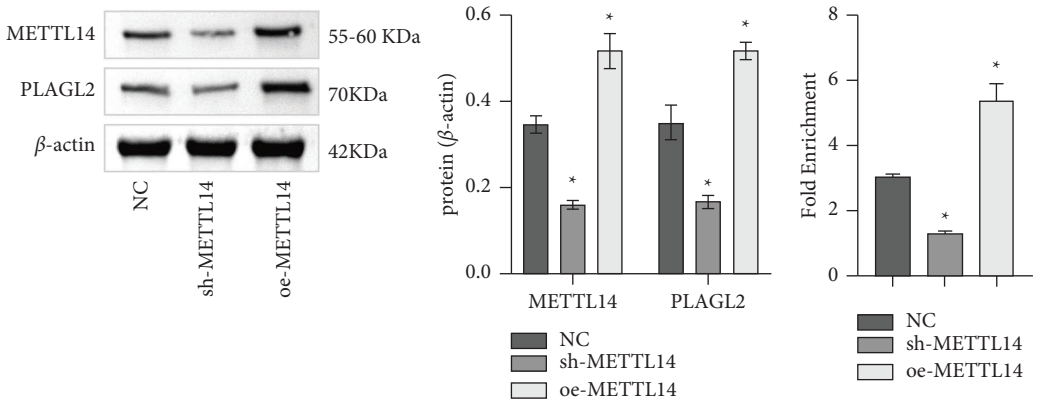

(a) (b)

Figure 3: PLAGL2 signaling was regulated by METTL14-mediated m6A modification. (a) METTL14 and PLAGL2 expressions were detected by WB. (b) RIP identified m6A modification levels of PLAGL2 after knockdown and overexpression of METTL14. Comparisons among multiple groups were conducted by one-way analysis of variance (ANOVA), followed by Tukey's post hoc test. $^{*}P < 0.05$ vs. NC.

death was suppressed (cell viability increased) (Figures 4(c)–4(f)).

3.5. METTL14/PLAGL2/β-Catenin Axis Promoted NSCLC Development In Vivo. To further validate METTL14/PLAGL2/β-catenin function, we performed *in vivo* experiments. Knockdown of METTL14 reduced tumor volume and weight. Tumor volume and weight increased after PLAGL2 was overexpressed (Figures 5(a) and 5(b)). Compared with sh-NC, METTL14 expression was decreased in sh-METTL14. In comparison with sh-METTL14 + oe-NC, PLAGL2 was elevated in sh-METTL14 + oe-PLAGL2, indicating METTL14 was successfully knocked down and PLAGL2 was successfully overexpressed. Besides, β-catenin expression was inhibited after the knockdown of METTL14. After PLAGL2 was overexpressed, β-catenin expression increased (Figure 5(c)). WB also showed decreased expressions of METTL14, PLAGL2, and β-catenin (nuclear) in sh-METTL14 compared to sh-NC. PLAGL2 and β-catenin (nuclear) expressions were elevated in sh-METTL14 + oe-PLAGL2 than sh-METTL14+oe-NC. β-catenin (total) showed no significant difference (Figure 5(d)). All in all, METTL14/PLAGL2/β-catenin axis promoted NSCLC development *in vivo*.

4. Discussion

NSCLC is one of the most devastating cancers, with high mortality worldwide [26]. New treatment options for NSCLC

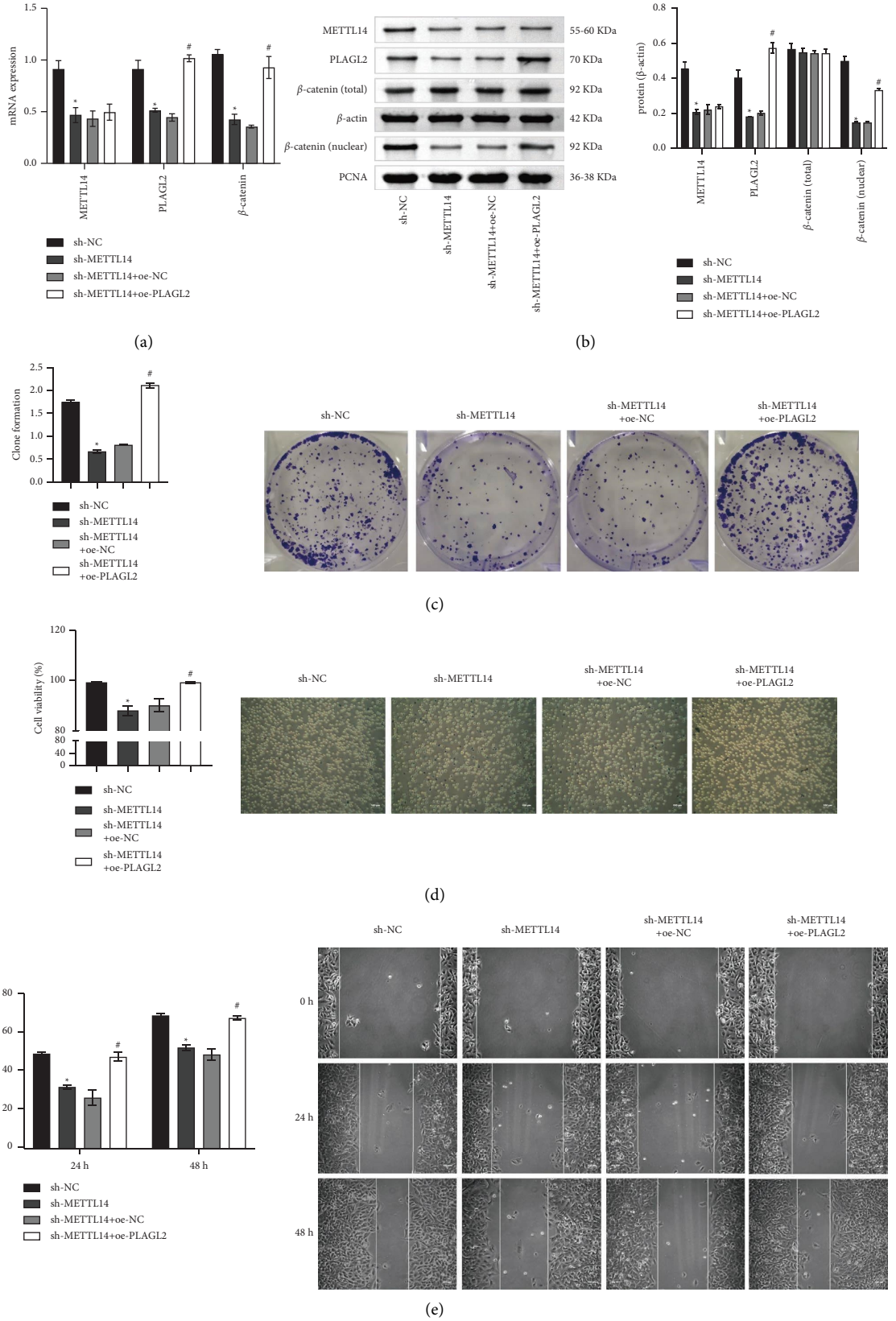

Figure 4: Continued.

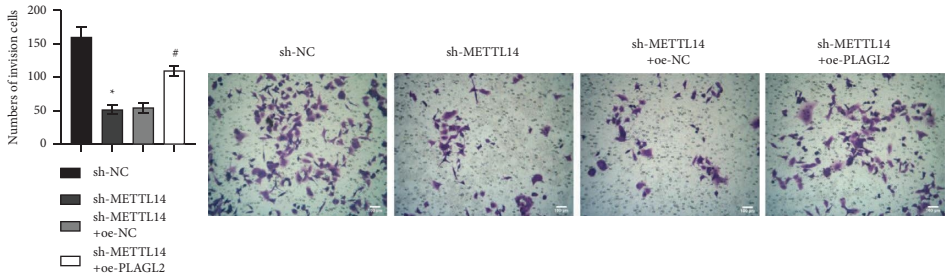

(f)

Figure 4: METTL14 regulated PLAGL2 signaling to affect NSCLC cell function. (a) METTL14, PLAGL2, and β-catenin mRNA expressions. (b) METTL14, PLAGL2, β-catenin (total), and β-catenin (nuclear) protein expressions. (c) Plate clone formation assay to measure cell proliferation. (d) Trypan blue staining to detect cell death (cell viability). (e) Cell migration was monitored by wound healing assay. (f) Cell invasion was determined by Transwell assay. Comparisons among multiple groups were conducted by one-way analysis of variance (ANOVA), followed by Tukey's post hoc test. $^{*}P < 0.05$ vs. sh-NC, $^{\#}P < 0.05$ vs. sh-METTL14 + oe-NC.

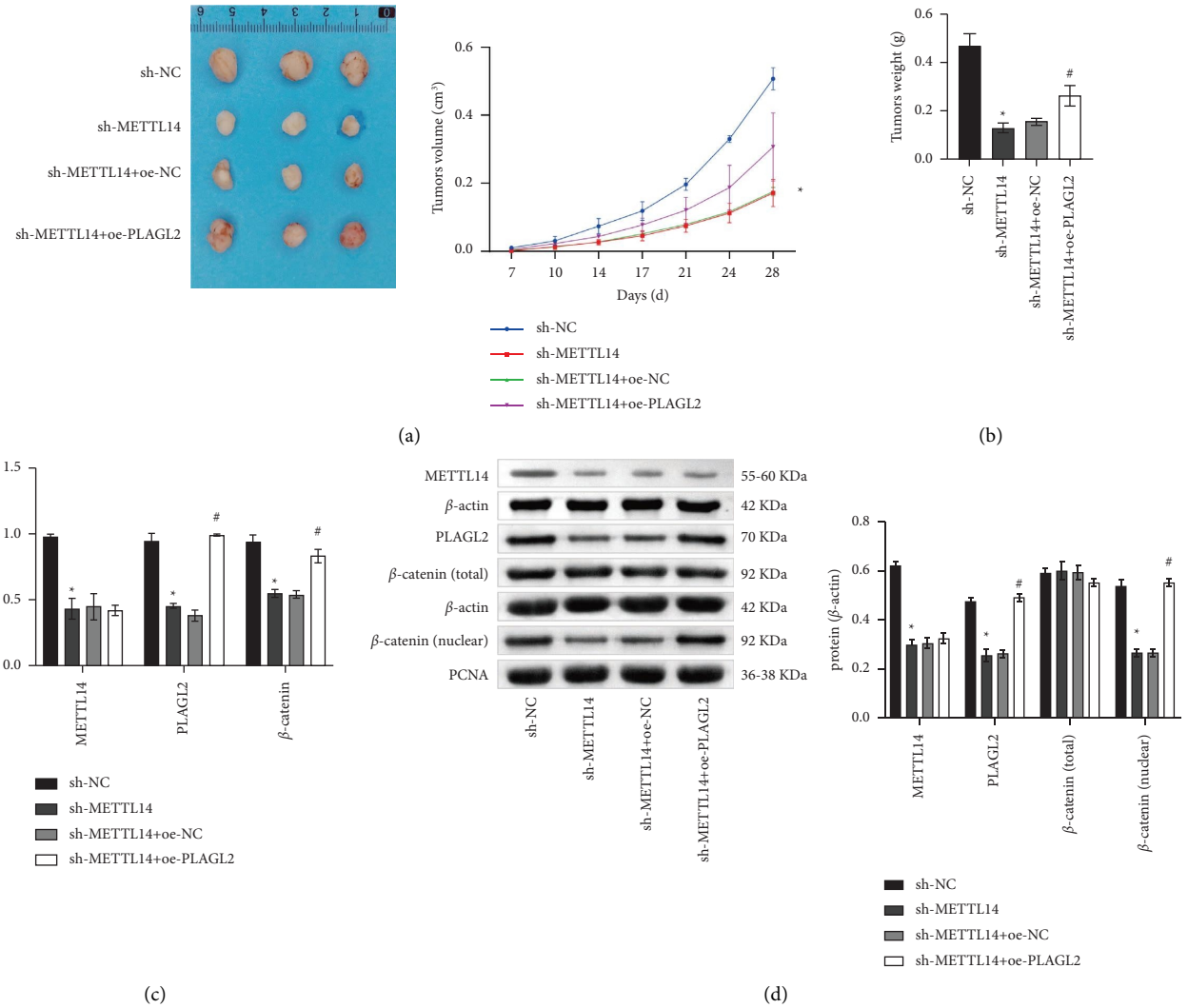

Figure 5: METTL14/PLAGL2/β-catenin axis promoted NSCLC development *in vivo*. (a) Tumor images and tumor volume. (b) Tumor weight. (c) METTL14, PLAGL2, and β-catenin mRNA expressions. (d) METTL14, PLAGL2, β-catenin (total), and β-catenin (nuclear) protein expressions. Comparisons among multiple groups were conducted by one-way analysis of variance (ANOVA), followed by Tukey's post hoc test. $^{*}P < 0.05$ vs. sh-NC, $^{\#}P < 0.05$ vs. sh-METTL14 + oe-NC.

have become available through extensive in-depth genomic studies to improve preclinical disease patterns and identify specific toxicity of targeted therapies [27]. In our research, we collected clinical NSCLC and paracarcinoma tissues and investigated METTL14/PLAGL2/β-catenin's role *in vivo* and *in vitro*. Our results demonstrated METTL14 promoted NSCLC development by increasing m6A methylation of PLAGL2 to activate β-catenin signaling. There has been no reported research on the related mechanism of the METTL14/PLAGL2/β-catenin axis in NSCLC, which is also our innovation of study.

Researchers believed PLAGL2 was overexpressed in different malignant tumors, and it could facilitate tumor proliferation, migration, invasion, and self-renewal [28]. We also found that PLAGL2 expression was elevated in NSCLC tissues. Wu et al. reported PLAGL2 facilitated β-catenin expression and nuclear translocation by inhibiting β-catenin phosphorylation level [20]. Liu et al. showed that lncRNA HCP5 could activate Wnt/β-catenin/Cyclin D1 signal through PLAGL2 in multiple myeloma [29]. In addition, PLAGL2 may be a very upstream key molecule regulating epithelial-mesenchymal transition and participated in Wnt/β-catenin signaling in colorectal adenocarcinoma [30]. These studies suggest that PLAGL2 may play an important role in cancer by modulating β-catenin signaling. In this study, we revealed β-catenin (nuclear) level was elevated in NSCLC tissues than paracarcinoma tissues. Moreover, PLAGL2 activated β-catenin signaling to influence cell proliferation and migration, suggesting that PLAGL2 played an important role in NSCLC by regulating β-catenin signaling. This is also the first time we have reported the study of PLAGL2 and β-catenin signaling in NSCLC.

m6A is the enzyme that plays a vital role in mRNA splicing, translation, and stabilization [31]. It regulates biological metabolism, cell differentiation and cycle, and responses to heat shock stress and cancer [32]. METTL14 is a well-known RNA m6A that plays a vital role in tumor growth by controlling RNA work [33]. Previous studies have reported that METTL14 can increase m6A modification of pri-miR-19a and promote mature miR-19a processing, thereby facilitating atherosclerotic vascular endothelial cell proliferation and invasion [34]. m6A regulator METTL14 has been reported to be differentially expressed between TP53-mutant and wild-type NSCLC [35]. But the mechanism of METTL14-mediated m6A modification with PLAGL2 is still unclear. We found that PLAGL2 signaling was regulated by METTL14-mediated m6A modification. Furthermore, METTL14 regulated PLAGL2 signaling to affect NSCLC cell function. This is also our first report of METTL14-mediated m6A modification and PLAGL2 in NSCLC. Through *in vivo* experiments, we further validated METTL14/PLAGL2/β-catenin axis promoted NSCLC development.

However, our study has some limitations. To verify whether PLAGL2 signaling was regulated by METTL14-mediated m6A modification, we should first apply RIP to identify whether PLAGL2 was modified by m6A and then use RIP to identify the m6A modification of PLAGL2 after knockdown and overexpression of METTL14. However, due to time and financial constraints, we directly used RIP to identify the m6A modification of PLAGL2 after the knockdown and overexpression of METTL14. Although our results also confirmed that PLAGL2 signaling was regulated by METTL14-mediated m6A modification, the results need to be proved step by step. In the future, we will further verify whether PLAGL2 was modified by m6A. Furthermore, the mechanism of METTL14 and the m6A methylation modification of PLAGL2 *in vivo* and the signaling pathways involved need to be further explored.

In conclusion, we demonstrated increased PLAGL2 and β-catenin (nuclear) expressions in NSCLC tissues. Furthermore, we conducted a preliminary exploration of the mechanisms involved in METTL14/PLAGL2/β-catenin. We found METTL14/PLAGL2/β-catenin axis promoted NSCLC development *in vitro* and *in vivo* experiments. Our research provides important clues for an in-depth comprehension of the mechanism of NSCLC occurrence and development and also provides a reference for NSCLC treatment.

Data Availability

The data used to support the findings of this study are available from the corresponding author upon request.

Ethical Approval

The study was approved by the Ethics Committee of Zhuzhou Central Hospital (ZZCHEC2021092-01). The research was conducted according to the World Medical Association Declaration of Helsinki. All the information about the study will be fully explained to the subjects by the researchers. All the participants provided informed consent before sampling. This study was approved by the Animal Ethics Committee of the Second Xiangya Hospital of Central South University (2022760). All experimental procedures were conducted in accordance with institutional guidelines for the use of experimental animals.

Conflicts of Interest

The authors declare that they have no conflict of interest.

Authors' Contributions

Qianhui Zhou and Xihua Lai designed the study. Qianhui Zhou and Yan Gao wrote the manuscript. Quefei Chen and Yi Liu revised the manuscript. Qianhui Zhou, Xihua Lai, and Yuzhu Xu participated in the material collection. All authors read and approved the final manuscript.

Acknowledgments

This work was supported by the Regulation of MIR486-5P on PLAGL2 Gene Expression in Nonsmall Cell Lung Cancer (2019–004), and the Natural Science Foundation of Hunan Province (2022JJ50105).

References

[1] R. L. Siegel, K. D. Miller, and A. Jemal, "Cancer statistics," *CA: A Cancer Journal for Clinicians*, vol. 65, no. 1, pp. 5–29, 2015.

[2] J. Kaur, J. Elms, A. L. Munn, D. Good, and M. Q. Wei, "Immunotherapy for non-small cell lung cancer (NSCLC), as a stand-alone and in combination therapy," *Critical Reviews in Oncology*, vol. 164, Article ID 103417, 2021.

[3] R. S. Herbst, D. Morgensztern, and C. Boshoff, "The biology and management of non-small cell lung cancer," *Nature*, vol. 553, no. 7689, pp. 446–454, 2018.

[4] T. Nagano, M. Tachihara, and Y. Nishimura, "Molecular mechanisms and targeted therapies including immunotherapy for non-small cell lung cancer," *Current Cancer Drug Targets*, vol. 19, no. 8, pp. 595–630, 2019.

[5] X. Mu, Q. Zhao, W. Chen et al., "IL-37 confers anti-tumor activity by regulation of m6A methylation," *Frontiers in Oncology*, vol. 10, Article ID 526866, 2020.

[6] Q. Guan, H. Lin, L. Miao et al., "Functions, mechanisms, and therapeutic implications of METTL14 in human cancer," *Journal of Hematology and Oncology*, vol. 15, no. 1, p. 13, 2022.

[7] T. Sun, Z. Wu, X. Wang et al., "LNC942 promoting METTL14-mediated m(6)A methylation in breast cancer cell proliferation and progression," *Oncogene*, vol. 39, no. 31, pp. 5358–5372, 2020.

[8] X. Chen, M. Xu, X. Xu et al., "METTL14-mediated N6-methyladenosine modification of SOX4 mRNA inhibits tumor metastasis in colorectal cancer," *Molecular Cancer*, vol. 19, no. 1, p. 106, 2020.

[9] Z. Ma, Q. Li, P. Liu, W. Dong, and Y. Zuo, "METTL3 regulates m6A in endometrioid epithelial ovarian cancer independently of METTl14 and WTAP," *Cell Biology International*, vol. 44, no. 12, pp. 2524–2531, 2020.

[10] F. Yang, W. Q. Yuan, J. Li, and Y. Q. Luo, "Knockdown of METTL14 suppresses the malignant progression of non-small cell lung cancer by reducing Twist expression," *Oncology Letters*, vol. 22, no. 6, p. 847, 2021.

[11] D. Jian, Y. Wang, L. Jian et al., "METTL14 aggravates endothelial inflammation and atherosclerosis by increasing FOXO1 N6-methyladeosine modifications," *Theranostics*, vol. 10, no. 20, pp. 8939–8956, 2020.

[12] L. Du, Y. Li, M. Kang et al., "USP48 is upregulated by Mettl14 to attenuate hepatocellular carcinoma via regulating SIRT6 stabilization," *Cancer Research*, vol. 81, no. 14, pp. 3822–3834, 2021.

[13] L. Wu, N. Zhao, Z. Zhou et al., "PLAGL2 promotes the proliferation and migration of gastric cancer cells via USP37-mediated deubiquitination of Snail1," *Theranostics*, vol. 11, no. 2, pp. 700–714, 2021.

[14] N. Li, D. Li, Y. Du et al., "Overexpressed PLAGL2 transcriptionally activates Wnt6 and promotes cancer development in colorectal cancer," *Oncology Reports*, vol. 41, no. 2, pp. 875–884, 2019.

[15] B. Xu, X. Zhang, S. Wang, and B. Shi, "MiR-449a suppresses cell migration and invasion by targeting PLAGL2 in breast cancer," *Pathology, Research and Practice*, vol. 214, no. 5, pp. 790–795, 2018.

[16] Y. S. Yang, M. C. W. Yang, and J. C. Weissler, "Pleiomorphic adenoma gene-like 2 expression is associated with the development of lung adenocarcinoma and emphysema," *Lung Cancer*, vol. 74, no. 1, pp. 12–24, 2011.

[17] T. Valenta, G. Hausmann, and K. Basler, "The many faces and functions of β-catenin," *The EMBO Journal*, vol. 31, no. 12, pp. 2714–2736, 2012.

[18] J. Xue, Y. Chen, Y. Wu et al., "Tumour suppressor TRIM33 targets nuclear β-catenin degradation," *Nature Communications*, vol. 6, no. 1, p. 6156, 2015.

[19] P. Pang, Z. Qu, S. Yu et al., "Mettl14 attenuates cardiac ischemia/reperfusion injury by regulating wnt1/β-catenin signaling pathway," *Frontiers in Cell and Developmental Biology*, vol. 9, Article ID 762853, 2021.

[20] L. Wu, Z. Zhou, S. Han et al., "PLAGL2 promotes epithelial-mesenchymal transition and mediates colorectal cancer metastasis via β-catenin-dependent regulation of ZEB1," *British Journal of Cancer*, vol. 122, no. 4, pp. 578–589, 2020.

[21] D. Xia, Z. Chen, and Q. Liu, "Circ-PGC increases the expression of FOXR2 by targeting miR-532-3p to promote the development of non-small cell lung cancer," *Cell Cycle*, vol. 20, no. 21, pp. 2195–2209, 2021.

[22] F. W. Xie, Y. H. Peng, W. W. Wang et al., "Influence of UGT1A1 gene methylation level in colorectal cancer cells on the sensitivity of the chemotherapy drug CPT-11," *Biomedicine and Pharmacotherapy*, vol. 68, no. 7, pp. 825–831, 2014.

[23] J. S. Wu, S. R. Sheng, X. H. Liang, and Y. L. Tang, "The role of tumor microenvironment in collective tumor cell invasion," *Future Oncology*, vol. 13, no. 11, pp. 991–1002, 2017.

[24] G. Liang, W. Meng, X. Huang et al., "miR-196b-5p-mediated downregulation of TSPAN12 and GATA6 promotes tumor progression in non-small cell lung cancer," *Proceedings of the National Academy of Sciences of the United States of America*, vol. 117, no. 8, pp. 4347–4357, 2020.

[25] T. Yang, H. Li, T. Chen, H. Ren, P. Shi, and M. Chen, "LncRNA MALAT1 depressed chemo-sensitivity of NSCLC cells through directly functioning on miR-197-3p/p120 catenin Axis," *Molecular Cell*, vol. 42, no. 3, pp. 270–283, 2019.

[26] Z. X. Wu, J. Li, S. Dong, L. Lin, C. Zou, and Z. S. Chen, "Tepotinib hydrochloride for the treatment of non-small cell lung cancer," *Drugs Today (Barc)*, vol. 57, no. 4, pp. 265–275, 2021.

[27] F. Valentino, G. Borra, P. Allione, and L. Rossi, "Emerging targets in advanced non-small-cell lung cancer," *Future Oncology*, vol. 14, no. 13, pp. 61–72, 2018.

[28] W. Hu, S. Zheng, H. Guo et al., "PLAGL2-EGFR-HIF-1/2α signaling loop promotes HCC progression and erlotinib insensitivity," *Hepatology*, vol. 73, no. 2, pp. 674–691, 2021.

[29] Q. Liu, R. Ran, M. Song et al., "LncRNA HCP5 acts as a miR-128-3p sponge to promote the progression of multiple myeloma through activating Wnt/β-catenin/cyclin D1 signaling via PLAGL2," *Cell Biology and Toxicology*, vol. 38, no. 6, pp. 979–993, 2021.

[30] Y. P. Wang, P. T. Guo, Z. Zhu et al., "Pleomorphic adenoma gene like-2 induces epithelial-mesenchymal transition via Wnt/β-catenin signaling pathway in human colorectal adenocarcinoma," *Oncology Reports*, vol. 37, no. 4, pp. 1961–1970, 2017.

[31] Z. Lin, Y. Niu, A. Wan et al., "RNA m(6) A methylation regulates sorafenib resistance in liver cancer through FOXO3-mediated autophagy," *The EMBO Journal*, vol. 39, no. 12, Article ID e103181, 2020.

[32] H. Zhou, K. Yin, Y. Zhang, J. Tian, and S. Wang, "The RNA m6A writer METTL14 in cancers: roles, structures, and applications," *Biochimica et Biophysica Acta (BBA) - Reviews on Cancer*, vol. 1876, no. 2, Article ID 188609, 2021.

[33] Q. Yao, L. He, X. Gao et al., "The m6A methyltransferase METTL14-mediated N6-methyladenosine modification of PTEN mRNA inhibits tumor growth and metastasis in

stomach adenocarcinoma," *Frontiers in Oncology*, vol. 11, Article ID 699749, 2021.

[34] B. Y. Zhang, L. Han, Y. F. Tang et al., "METTL14 regulates M6A methylation-modified primary miR-19a to promote cardiovascular endothelial cell proliferation and invasion," *European Review for Medical and Pharmacological Sciences*, vol. 24, no. 12, pp. 7015–7023, 2020.

[35] Z. Zhao, J. Wan, M. Guo et al., "Expression and prognostic significance of m6A-related genes in TP53-mutant non-small-cell lung cancer," *Journal of Clinical Laboratory Analysis*, vol. 36, no. 1, Article ID e24118, 2022.

Hindawi
Journal of Oncology
Volume 2023, Article ID 6017852, 12 pages
https://doi.org/10.1155/2023/6017852

Research Article

OLFML2A Overexpression Predicts an Unfavorable Prognosis in Patients with AML

Xuan Lu,[1] Ying Li,[1] Yan Yang,[2] Wanchuan Zhuang,[3] Xingxing Chai ,[3] and Chen Gong [4]

[1]*School of Life Sciences, Hefei Nomal University, Hefei, Anhui 230031, China*
[2]*Fudan University Affiliated Pudong Medical Center, Shanghai 201301, China*
[3]*Department of Hematology, Lianyungang Second People's Hospital, Lianyungang, Jiangsu 222000, China*
[4]*Department of Geriatric Medicine, Lianyungang Second People's Hospital, Lianyungang, Jiangsu 222000, China*

Correspondence should be addressed to Xingxing Chai; chaixx@hbut.edu.cn and Chen Gong; gcgc214@163.com

Received 29 August 2022; Revised 13 September 2022; Accepted 21 September 2022; Published 22 February 2023

Academic Editor: İbrahim Hakkı Cigerci

Background. Acute myeloid leukemia (AML) is a malignant clonal disease of the myeloid hematopoietic system. Clinically, standard treatment options include conventional chemotherapy as well as hematopoietic stem cell transplantation. Among them, chemotherapy has a remission rate of 60% to 80% and nearly 50% relapse in consolidation therapy. Some patients have a poor prognosis due to the presence of unfavorable factors such as advanced age, hematologic history, poor prognosis karyotype, severe infection, and organ insufficiency, which cannot tolerate or are not suitable for standard chemotherapy regimens, and scholars have tried to find new treatment strategies to improve this situation. In the pathogenesis and treatment of leukemia, epigenetics has received attention from experts and scholars. *Objective*. To investigate the relationship between OLFML2A overexpression and AML patients. *Methods*. From The Cancer Genome Atlas, researchers used the data of OLFML2A gene to analyze and study the pan-cancer using R language and then divided the high and low levels of this protein into two groups to study its relationship with the clinical characteristics of the disease. The relationship between the high levels of OLFML2A and various clinical features of the disease was studied with emphasis on the relationship between the high levels of OLFML2A and various clinical features of the disease. A multidimensional Cox regression analysis was also performed to study the factors affecting patient survival. The correlation between OLFML2A expression and immune infiltration through the immune microenvironment was analyzed. The researchers then conducted a series of studies to analyze the data collected in the study. The focus was on the relationship between the high levels of OLFML2A and immune infiltration. Gene ontology analysis was also performed to study the interactions between the different genes associated with this protein. *Results*. According to the pan-cancer analysis, OLFML2A was differentially expressed in different tumors. More importantly, the analysis of OLFML2A in the TCGA-AML database revealed that OLFML2A was highly expressed in AML. The researchers found that the high levels of OLFML2A were associated with different clinical features of the disease, and that the expression of the protein was different in different groups. Those patients with the high levels of OLFML2A were found to have substantially longer survival times compared to those with low-protein levels. *Conclusions*. The OLFML2A gene is able to act as a molecular indicator involved in the diagnosis, prognosis, and immune process of AML. It improves the molecular biology prognostic system of AML, provides help for the selection of AML treatment options, and provides new ideas for future biologically targeted therapy of AML.

1. Introduction

Acute myeloid leukemia (AML) is a malignant disease of the hematological system with strong biological and clinical heterogeneity. Currently, patients are generally stratified according to their cytogenetic and molecular biological findings to predict their treatment outcome [1]. In practice, we have found that the prognosis of patients graded according to the current risk stratification system still has some variability in treatment outcome and survival time for patients in the same risk stratum, suggesting that we should have a more detailed stratification prognosis system. In

recent years, studies have found that AML is associated with multiple mutated genes, suggesting that the development of leukemia may be the result of accumulation of mutations in multiple genes [2, 3]. In recent years, with the widespread use of high-throughput sequencing, i.e., second-generation sequencing technology, the role of leukemia-related mutated genes in diagnosis and treatment has been gradually highlighted [4]. Applying sequencing technology, we have successively discovered a variety of mutated genes related to the development and treatment of AML, and a large number of studies of these genes in AML have also emerged.

The OLFML2A (olfactomedin-like 2A) gene is located on chromosome 9q33.3 and encodes a protein also known as "photomedin-1," which belongs to the OLFM (Olfactomedin, OLFM) family IV [5]. Olfactomedin, an exocrine glycoprotein secreted by the epithelial cells of the olfactory organ and deposited in large quantities on its surface, was discovered in 1991 and was the first member of the OLFM family [6]. More than half of the OLFM family proteins are expressed in the neural tissue [7]. A large body of evidence suggests that OLFM family proteins play an important regulatory role in neurogenesis, neural crest formation, intercellular adhesion, tumor development, and cell cycle regulation [8, 9]. Related studies have shown that the OLFM family proteins are key regulatory molecules of cellular signaling pathways such as the Wnt signaling pathway [10, 11]. There is increasing evidence that the OLFM family proteins play important roles in the normal tissue development and disease development, e.g., myocilin and olfactomedin 2 are key molecules in the development of glaucoma [12], and OLFM4 is associated with the development of common malignancies such as gastric and pancreatic cancers [13, 14].

OLFML2A is a member of OLFM family IV, which contains at least eight exons spanning 37.7 kb and encodes a protein with an olfactomedin structural domain at the C-terminus and a unique serine/threonine region that distinguishes it from other proteins in the family, two to three potential glycosylation sites at the N-terminus, and homodimers or oligomers with disulfide bonds. Northern-blot of different tissue specimens from mice showed that OLFML2A transcription products were not found in the brain tissue [15]. OLFML2A is an exocrine glycoprotein that binds specifically to chondroitin sulphate-E (CS-E) and heparin [16]. CS-E binds to a number of heparin-binding growth factors, including midkine, Pleiotrophin, several FGFs, and HB-EGF. Specific binding of OLFML2A to CS-E may promote the local action of growth factors bound to CS-E. To date, the specific functions of the OLFML2A gene and its encoded protein remain unknown, and its role in the development of AML has not been reported in the literature.

Based on this, from The Cancer Genome Atlas, researchers analyzed the data using OLFML2A gene data, analyzed and studied pan-cancer using R language, and then divided the high and low levels of the protein into two groups in order to study its relationship with the clinical features of the disease. Finally, it was concluded that the OLFML2A gene, as a molecular indicator, can be involved in the diagnosis, prognosis, and immune process of AML and has the potential to be a reliable prognostic assessment indicator W and a potential therapeutic boot point for AML patients.

2. Methods

2.1. Preprocessing of Raw Data. We collected TCGA-AML expression profiles and clinical information from TCGA Genomic Data Commons Data Portal (https://portal.gdc.cancer.gov/). We excluded the insufficient cases or missing data in the later information processing. The genomic expression information of OLFML2A was calculated from the TCGA database by high-throughput sequencing. Because all information was publicly available, no ethical approval was required.

2.2. Pan-Cancer Analysis. Pan-cancer analysis was performed through the TIMER2 (Tumor Immunology Estimation Resource, version 2) network (https://timer.cistrome.org/) 16 to observe differences in OLFML2A expression in tumors and nearby normal tumor tissue or particular tumor subtypes in the TCGA program.

2.3. Gene Expression Analysis. We studied the correlation between different tissue characteristics and OLFML2A expression through the Wilcoxon rank-sum test.

2.4. Survival and Clinical Statistical Analysis. The association of OLFML2A with clinical features and overall survival was evaluated using the log-rank tests, Kaplan–Meier survival curves, and one-way Cox analysis. The correlation between high and low OLFML2A expression and clinical features was researched in this study (age, grade, BM blasts, cytogenetic risk, FLT3 mutation, IDH R132 mutation, IDH R140 mutation, NPM1 mutation, PB blasts, RAS mutation, and WBC count) between OLFML2A mutations. In addition, OLFML2A was split into high and low expression groups. The OLFML2A expression was judged in relation to overall survival by confirming the high and low OLFML2A expression based on the median. We applied survROC software to measure the accuracy of risk scores on prognosis using time-dependent subject operating characteristic (ROC) curves. We conducted univariate and multivariate analyses of risk scores after adjusting for age, sex, race, BM blasts, PB blasts, Cytogenetic risk, and FAB classifications. In addition, we analyzed the expression of OLFML2A with different clinicopathological features, and we investigated the association of OLFML2A expression with BM cells, cytogenetic risk, FAB classification, IDH1 R132 mutation, IDH1 R132 mutation, NPM1 mutation, and race.

2.5. Construction of Nomograms. Since the development of nomograms, they have been used to forecast cancer prognosis. This method uses a statistical method to score various factors, such as age, gender, and the TNM stage. It can then produce a total score that provides a personalized estimate of the likelihood of the disease returning. In the study, the

researchers used nomograms to predict the likelihood of patients with cancer returning. The R package rms generated them. The nomograms were then validated by implementing a series of calibration curves. Subsequently, we utilized the *c*-index to estimate nomogram accuracy.

2.6. Immunological Analysis. The researchers then performed a series of studies to analyze the data collected from the studies. They first used a computer program known as the CIBERSORT deconvolution to determine the relative composition of immune cells in each sample. Then, they performed an immune differential analysis to study the two groups' immune cell content differences.

2.7. Gene Ontology (GO) and Kyoto Encyclopedia of Genes and Genomes (KEGG). The cluster profile package was used for GO and KEGG enrichment analysis and underlying biological pathways that were likely to adjust the cancer development. They were also able to identify promising signals that could be linked to the disease.

3. Results

3.1. OLFML2A Had a High Expression in Multiple Cancer Tissues. To detect the differential expression of OLFML2A, we first investigated OLFML2A gene expression in 33 human cancers in TCGA using the TIMER database. Compared with normal samples, OLFML2A had higher expression in 27 cancers, including LUSC, BLCA, DLBC, BRCA, CESC, GBM, COAD, ESCA, KIPR, HNSC, KIRC, LGG, LAML, LUAD, READ, LIHC, PAAD, OV, PRAD, STAD, CHOL, PCPG, SKCM, TGCT, THYM, UCEC, and UCS, shown in Figure 1(a). By comparing the expression of OLFML2A gene in AML and normal samples, OLFML2A had a large overexpression in AML (as shown in Figure 1(b); $P < 0.001$).

3.2. The Difference in Clinical Characteristics. We grouped high and low OLFML2A gene expression, and the correlation between OLFML2A gene expression and clinical features were explored. We incorporated age, grade, BM blasts, cytogenetic risk, FLT3 mutation, IDH R132 mutation, IDH R140 mutation, NPM1 mutation, PB blasts, RAS mutation, and WBC count for picture mapping. After analyzing the data collected from the studies, the researchers concluded that the high levels of the OLFML2A were different from the low levels of the protein. They also noted that the difference was significant when it came to age, BM blasts, and FLT3 mutations ($P < 0.05$; Figure 2).

3.3. The Prognosis and Diagnosis of OLFML2A Value. Compared with high-risk patients, according to Kaplan–Meier survival curves, the survival of low OLFML2A expression patients was longer (log-rank test; $P < 0.001$) (Figure 3(b)). Figure 3(a) shows 0.977, indicating the area under the curve (AUC) value.

3.4. The Difference in Clinicopathological Feature. Through the analysis between OLFML2A expression and different clinicopathological characteristics, it could be seen that there was a relationship between OLFML2A expression and FAB classifications, BM blasts, IDH1 R132 mutation, IDH1 R132 mutation, cytogenetic risk, NPM1 mutation, and race (Figure 4 and Tables 1 and 2). In addition, univariate and multifactorial Cox regression analyses presented that an independent risk factor for AML was OLFML2A expression (Table 3).

3.5. Construction of the Nomogram. We constructed a prognostic nomogram in LUAD to predict the 1-, 3-, and 5 year survival probabilities of individuals by gender, race, age, WBC, BM blasts, PB blasts, cytogenetic risk, FLT3 mutation, IDH R132 mutation, IDH R140 mutation, IDH R172 mutation, RAS mutation, NPM1 mutation, PB blasts, and OLFML2A (Figure 5).

OLFML2A expression was positively correlated with iDC, macrophages, NK CD56dim cells, Tem, TFH, TGD, TH1 cells, TH17 cells, iDC, macrophages, NK CD56dim cells, Tem, TFH, TGD, TH1 cells, and TH17 cells ($P < 0.05$; Figure 6).

3.6. GO and KEGG. We performed GO analysis on OLFML2A. CC terms contain "focal adhesion," "cell-substrate adherence junction," "cell-substrate junction," "coated vesicle membrane," and "transport vesicle". BP terms include "positive regulation of dephosphorylation," "regulation of autophagy," "sterol metabolic process," "positive regulation of phosphatase activity," and "platelet activation,". MF terms were associated with "O-acyltransferase activity," "ubiquitin binding," "phosphatase activator activity," "phosphatidic acid binding," and "protein phosphatase activator activity". KEGG analysis shows that OLFML2A is associated with numerous pathways, including "Aldosterone synthesis and secretion," "cGMP-PKG signaling pathway," "Melanogenesis," "Adrenergic signaling in cardiomyocytes," and "Parathyroid hormone synthesis secretion and action" (Figure 7).

4. Discussion

Acute myeloid leukemia (AML) is a common aggressive hematologic malignancy characterized by impaired leukocyte maturation and excessive proliferation of hematopoietic stem cells, which can spread to other organs such as the central nervous system, skin, and gums. Due to impaired normal hematopoietic function, AML patients often present with anemia, bleeding, and severe infections [3]. In the past two decades, genomic, transcriptomic, and epigenomic studies of AML have made great progress. The latest 2017 European Leukemia Network (ELN) risk stratification guidelines combining cytogenetic abnormalities and genetic mutations have been widely used to predict the prognosis of AML patients [4]. Furthermore, based on these advances, several drugs have been approved for the treatment of AML, such as sorafenib for FMS-like tyrosine kinase 3 (FLT3)

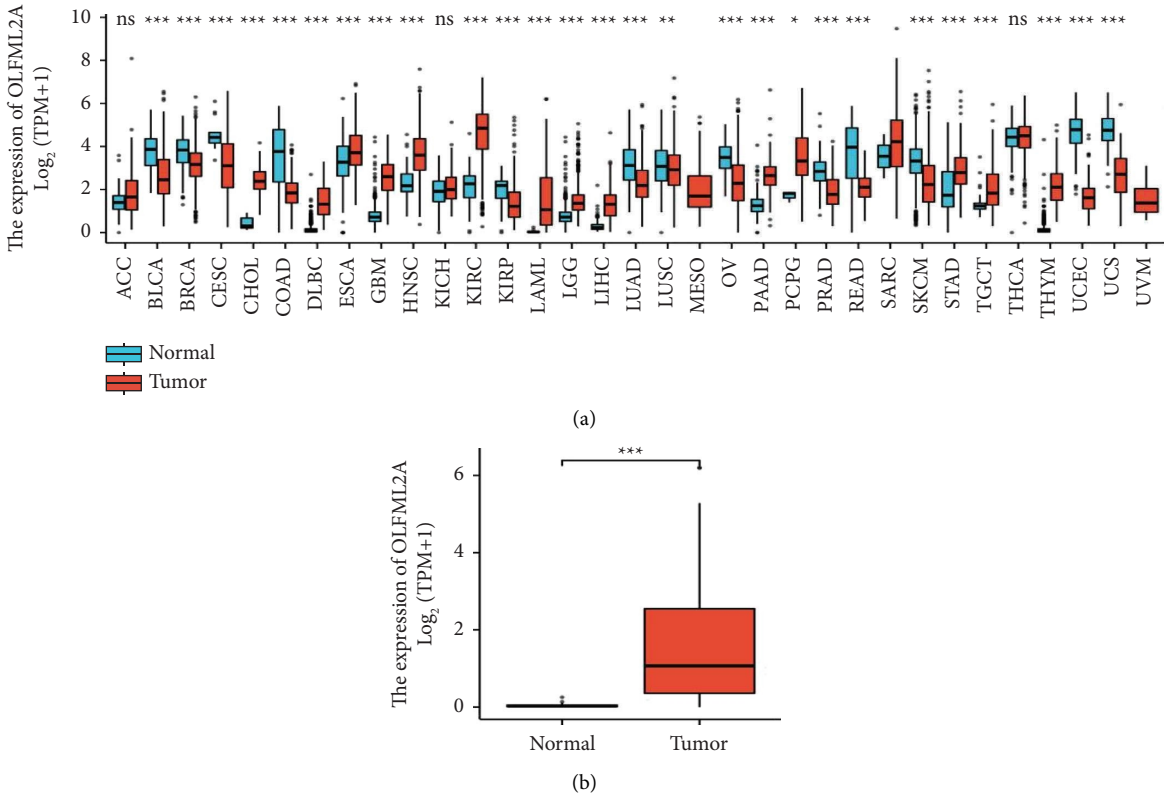

Figure 1: The higher expression of OLFML2A was displayed in AML from the TCGA database.

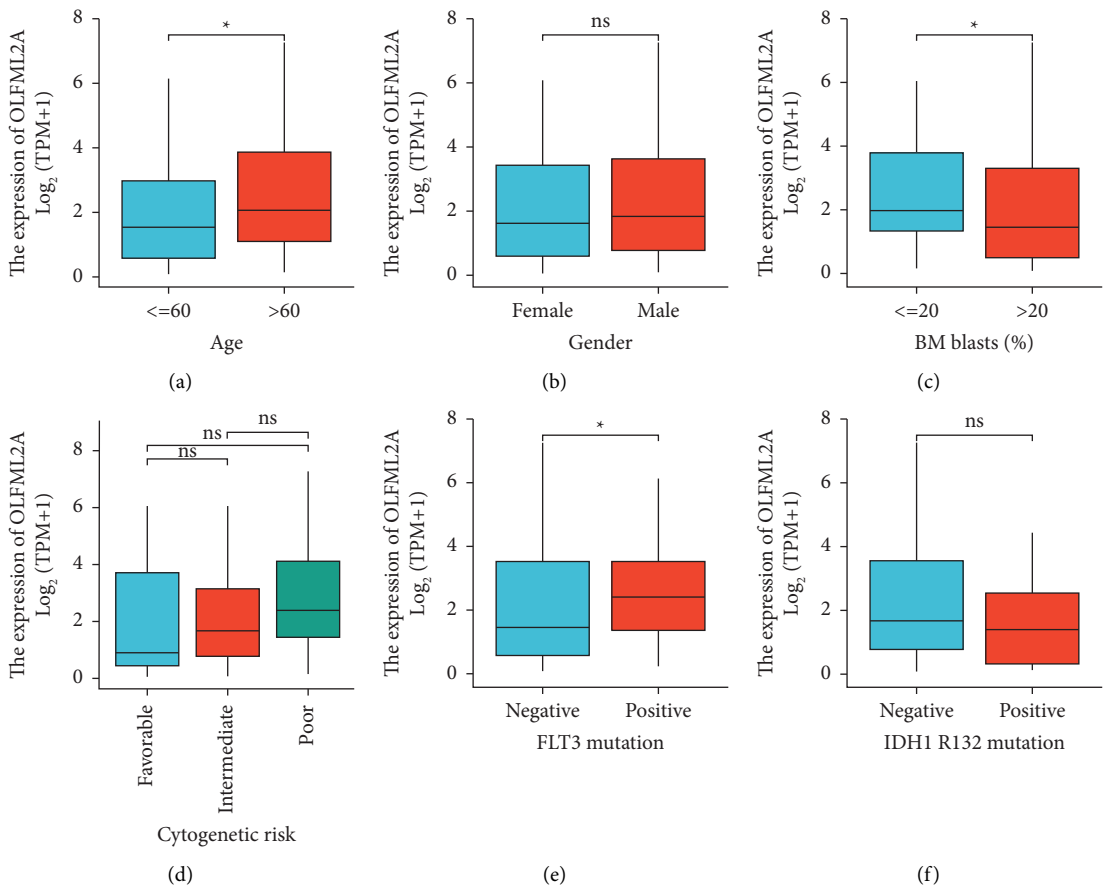

Figure 2: Continued.

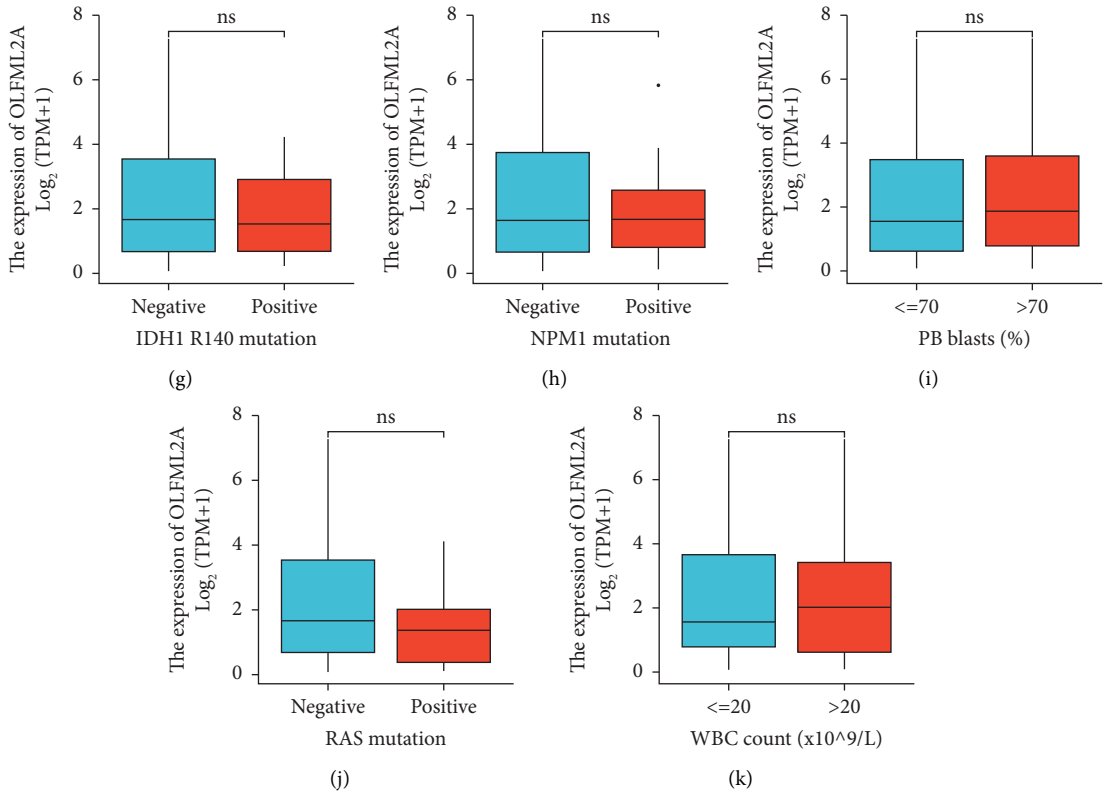

Figure 2: Association between OLFML2A expression and clinical characteristics in the TCGA database.

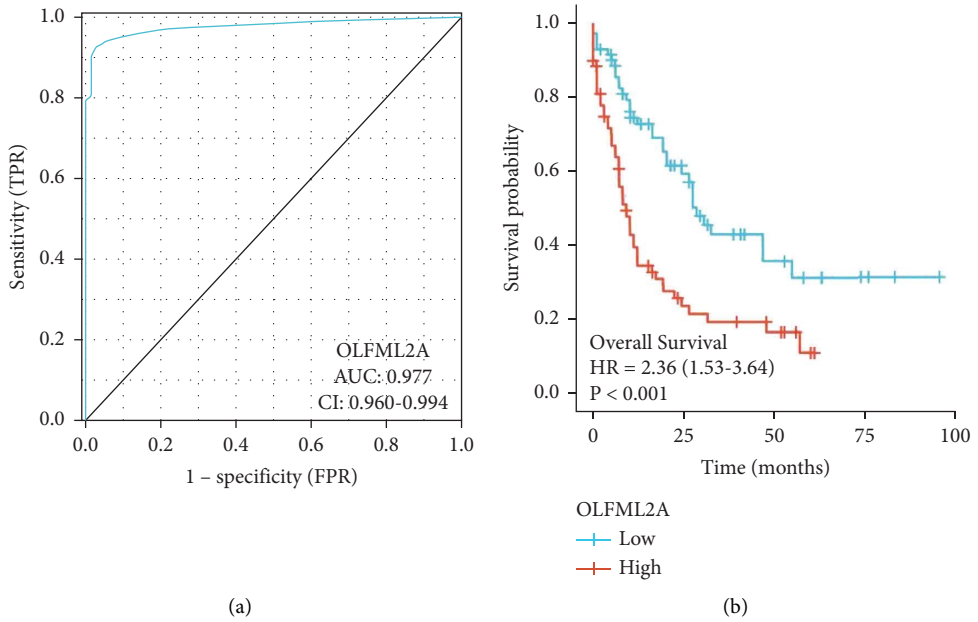

Figure 3: The prognosis and diagnosis of OLFML2A value in TCGA-AML.

mutations and Evonib for isocitrate dehydrogenase 1 and 2 (IDH1 and IDH2) mutations [17]. However, most patients with AML who receive chemotherapy relapse [18]. The next step in the approach to treat AML may be to uncover the molecular pathways involved in AML progression, chemotherapeutic efficacy, and relapse, with particular emphasis on the potential role of proteins in AML. There is growing evidence that proteins play an important role in the pathogenesis of cancer, including AML [19].

OLFML2A is an abnormal protein that can be found in various tissues such as the breast, colon, ovary, and liver [1]. Researchers have also found that high levels of this protein

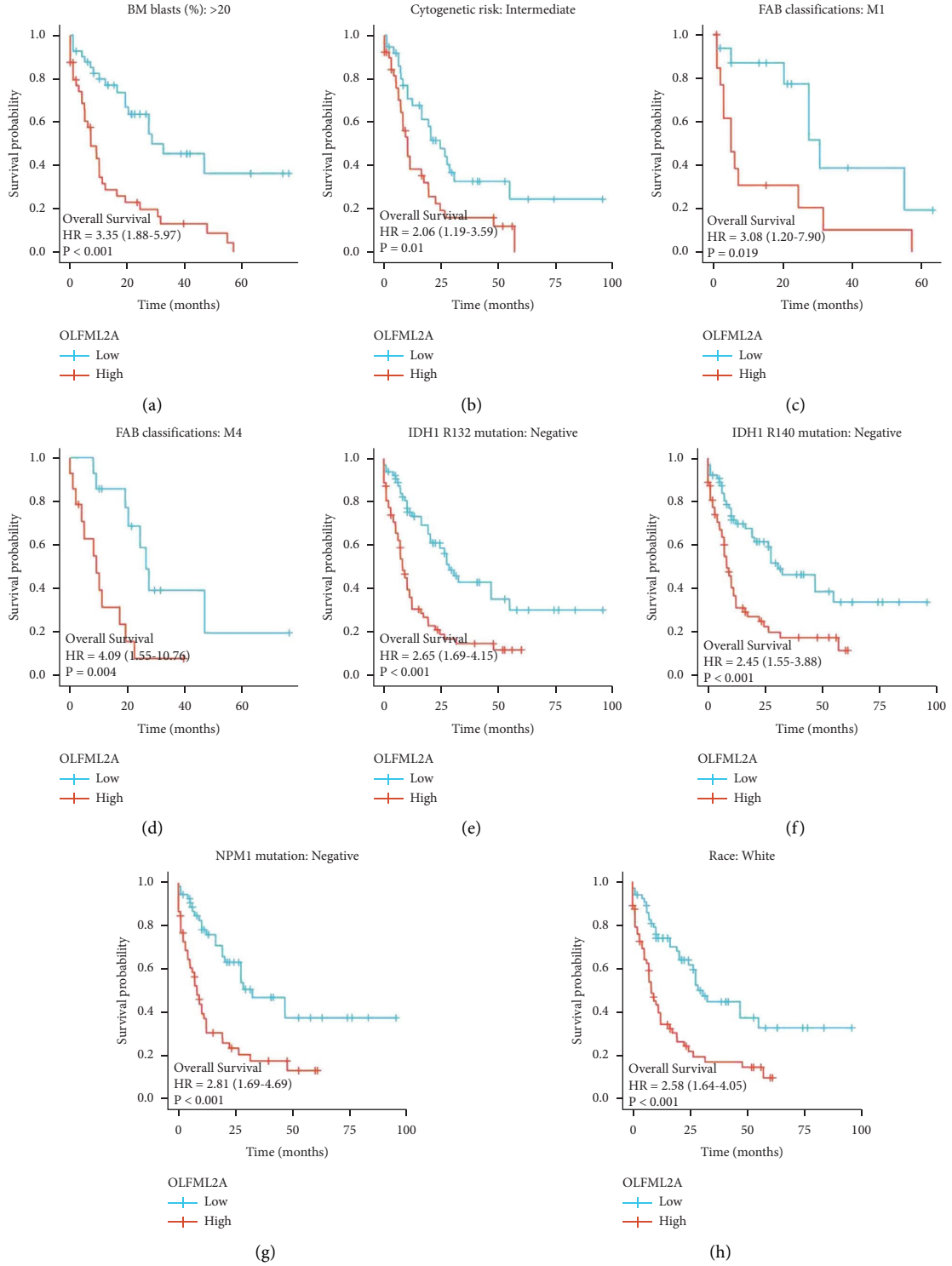

Figure 4: Analysis between OLFML2A expression and different clinicopathological features.

are detrimental to patients with acute lymphoblastic leukemia. The researchers hypothesized that the presence of OLFML2A in these patients could help to predict the likelihood of their cancer recurrence. They noted that the high levels of this protein could be a target for novel cancer treatments. In a previous study, researchers found that the presence of OLFML2A in breast cancer cells could hinder the development and metastasis of cancer cells [20]. The knockdown of OLFML2A in glioma cells inhibits the Wnt/β-catenin signaling pathway, which leads to upregulation of amyloid precursor protein (APP) expression and a decrease in the degree of stable β-catenin, resulting in having reduced MYC, CD44, and CSKN2A2 expression, thereby inhibiting cell proliferation and promoting apoptosis [21, 22].

Table 1: Association analysis between OLFML2A expression levels and clinicopathologic features in the TCGA-AML database.

Characteristic	Low expression of OLFML2A	High expression of OLFML2A	*P* value
n	75	76	
Gender, *n* (%)			1.000
Female	34 (22.5%)	34 (22.5%)	
Male	41 (27.2%)	42 (27.8%)	
Race, *n* (%)			1.000
Asian	0 (0%)	1 (0.7%)	
Black or African American	6 (4%)	7 (4.7%)	
White	67 (45%)	68 (45.6%)	
Age, *n* (%)			0.211
≤60	48 (31.8%)	40 (26.5%)	
>60	27 (17.9%)	36 (23.8%)	
WBC count ($\times 10^9$/L), *n* (%)			0.191
≤20	43 (28.7%)	34 (22.7%)	
>20	32 (21.3%)	41 (27.3%)	
BM blasts (%), *n* (%)			0.444
≤20	27 (17.9%)	33 (21.9%)	
>20	48 (31.8%)	43 (28.5%)	
PB blasts (%), *n* (%)			0.372
≤70	39 (25.8%)	33 (21.9%)	
>70	36 (23.8%)	43 (28.5%)	
Cytogenetic risk, *n* (%)			0.035
Favorable	21 (14.1%)	10 (6.7%)	
Intermediate	40 (26.8%)	42 (28.2%)	
Poor	13 (8.7%)	23 (15.4%)	
FAB classifications, *n* (%)			0.278
M0	6 (4%)	9 (6%)	
M1	17 (11.3%)	18 (12%)	
M2	23 (15.3%)	15 (10%)	
M3	7 (4.7%)	8 (5.3%)	
M4	14 (9.3%)	15 (10%)	
M5	4 (2.7%)	11 (7.3%)	
M6	2 (1.3%)	0 (0%)	
M7	1 (0.7%)	0 (0%)	
Cytogenetics, *n* (%)			0.014
Normal	32 (23.7%)	37 (27.4%)	
+8	7 (5.2%)	1 (0.7%)	
Del (5)	0 (0%)	1 (0.7%)	
Del (7)	3 (2.2%)	3 (2.2%)	
Inv (16)	8 (5.9%)	0 (0%)	
t (15; 17)	5 (3.7%)	6 (4.4%)	
t (8; 21)	4 (3%)	3 (2.2%)	
t (9; 11)	0 (0%)	1 (0.7%)	
Complex	7 (5.2%)	17 (12.6%)	
FLT3 mutation, *n* (%)			0.005
Negative	59 (40.1%)	43 (29.3%)	
Positive	14 (9.5%)	31 (21.1%)	
IDH1 R132 mutation, *n* (%)			0.579
Negative	67 (45%)	69 (46.3%)	
Positive	8 (5.4%)	5 (3.4%)	
IDH1 R172 mutation, *n* (%)			0.245
Negative	72 (48.3%)	75 (50.3%)	
Positive	2 (1.3%)	0 (0%)	
IDH1 R140 mutation, *n* (%)			0.745
Negative	67 (45%)	70 (47%)	
Positive	7 (4.7%)	5 (3.4%)	
RAS mutation, *n* (%)			1.000
Negative	71 (47.3%)	71 (47.3%)	
Positive	4 (2.7%)	4 (2.7%)	
NPM1 mutation, *n* (%)			1.000
Negative	59 (39.3%)	58 (38.7%)	
Positive	16 (10.7%)	17 (11.3%)	

Table 2: Logistic analysis of the relationship between OLFML2A expression and the clinicopathological features in the TCGA-AML database

Characteristics	Total (*N*)	Odds ratio (OLFML2A)	*P* value
Gender (male vs. female)	151	1.024 (0.539–1.948)	0.941
Race (White vs. Asian and Black or African American)	149	0.761 (0.239–2.305)	0.630
Age (>60 vs. ≤60)	151	1.600 (0.836–3.090)	0.158
WBC count (×10⁹/L) (>20 vs. ≤20)	150	1.620 (0.853–3.106)	0.142
BM blasts (%) (>20 vs. ≤20)	151	0.733 (0.379–1.408)	0.352
PB blasts (%) (>70 vs. ≤70)	151	1.412 (0.745–2.692)	0.292
Cytogenetic risk (intermediate and poor vs. favorable)	149	2.575 (1.140–6.156)	0.027
FAB classifications (M1&M2&M3&M4&M5&M6&M7 vs. M0)	150	0.657 (0.210–1.923)	0.448
Cytogenetics (+8&del (5) &del (7) &inv (16) &t (15; 17) &t (8; 21) &t (9; 11) &complex vs. normal)	135	0.814 (0.413–1.600)	0.551
FLT3 mutation (positive vs. negative)	147	3.038 (1.467–6.541)	0.003
IDH1 R132 mutation (positive vs. Negative)	149	0.607 (0.176–1.912)	0.402
IDH1 R140 mutation (positive vs. negative)	149	0.684 (0.194–2.245)	0.533
RAS mutation (positive vs. negative)	150	1.000 (0.228–4.378)	1.000
NPM1 mutation (positive vs. negative)	150	1.081 (0.498–2.357)	0.844

Table 3: Univariate and multivariate Cox regression analysis of factors associated with OS in TCGA-AML.

Characteristics	Total (*N*)	HR (95% CI) univariate analysis	*P* value univariate analysis	HR (95% CI) multivariate analysis	*P* value multivariate analysis
Gender	140				
Female	63	Reference			
Male	77	1.030 (0.674–1.572)	0.892		
Race	138				
Asian and Black or African American	11	Reference			
White	127	1.200 (0.485–2.966)	0.693		
Age	140				
≤60	79	Reference			
>60	61	3.333 (2.164–5.134)	<0.001	2.859 (1.819–4.494)	<0.001
WBC count (×10⁹/L)	139				
≤20	75	Reference			
>20	64	1.161 (0.760–1.772)	0.490		
BM blasts (%)	140				
≤20	59	Reference			
>20	81	1.165 (0.758–1.790)	0.486		
PB blasts (%)	140				
≤70	66	Reference			
>70	74	1.230 (0.806–1.878)	0.338		
Cytogenetic risk	138				
Favorable	31	Reference			
Intermediate	76	2.957 (1.498–5.836)	0.002	2.031 (1.003–4.113)	0.049
Poor	31	4.157 (1.944–8.893)	<0.001	2.506 (1.134–5.535)	0.023
FAB classifications	139				
M0	14	Reference			
M1&M2&M3&M4&M5&M6&M7	125	1.033 (0.517–2.062)	0.927		
OLFML2A	140				
Low	71	Reference			
High	69	2.362 (1.534–3.639)	<0.001	2.198 (1.409–3.429)	<0.001

Furthermore, by exploring the significance of OLFML2A expression in many clinical parameters, we found an association between OLFML2A and AML survival and clinical features. This study performed an immune cell infiltration analysis to gain insight into the role of OLFML2A. From The Cancer Genome Atlas, researchers used OLFML2A gene data to analyze the data. Pan-cancer was analyzed and studied using the R language. They then divided the high and low levels of the protein into two groups to study their relationship with clinical features of the disease. The researchers then conducted a series of studies to analyze the data collected from the study. They focused on the relationship between the high levels of OLFML2A and various clinical features of the disease. They also performed a multidimensional Cox regression analysis to examine the factors that affect patient survival. We analyzed the correlation between OLFML2A expression and immune

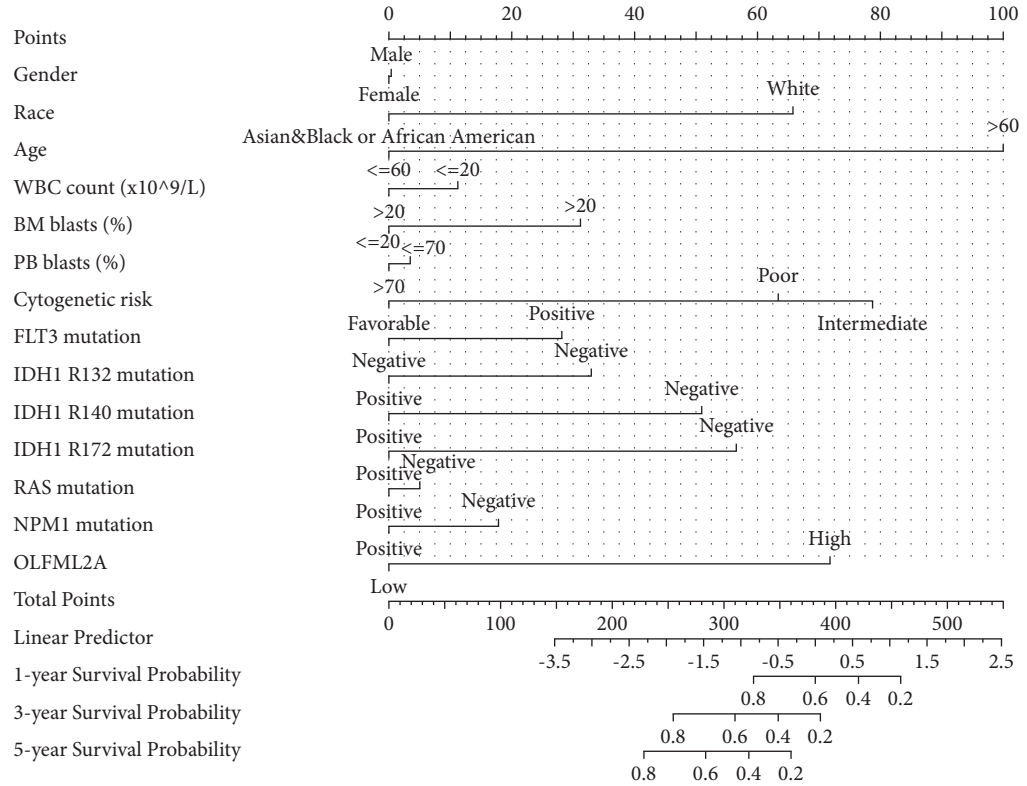

Figure 5: Nomogram for predicting the probability of 1-, 3-, and 5 years OS in TCGA Tumor immune microenvironment.

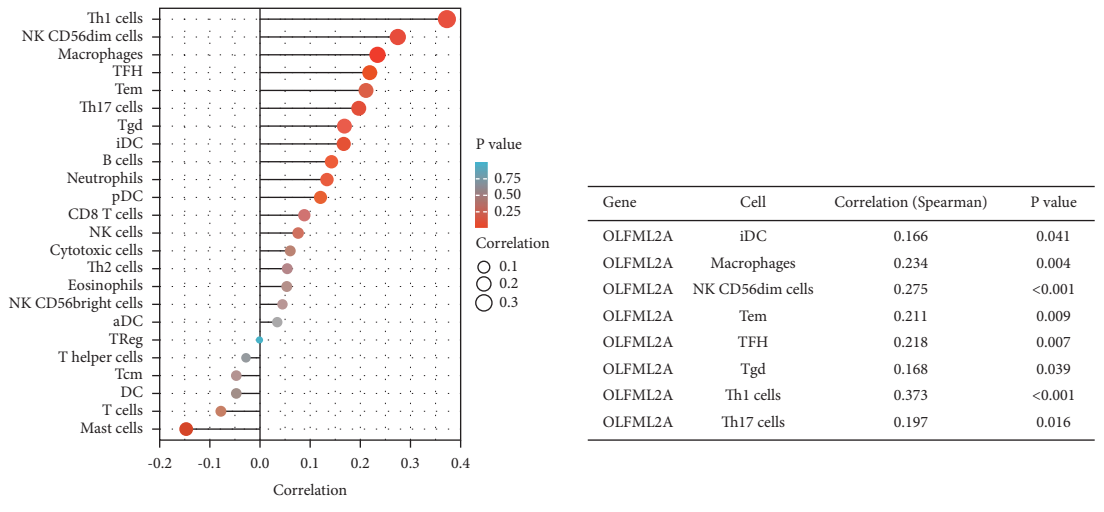

Gene	Cell	Correlation (Spearman)	P value
OLFML2A	iDC	0.166	0.041
OLFML2A	Macrophages	0.234	0.004
OLFML2A	NK CD56dim cells	0.275	<0.001
OLFML2A	Tem	0.211	0.009
OLFML2A	TFH	0.218	0.007
OLFML2A	Tgd	0.168	0.039
OLFML2A	Th1 cells	0.373	<0.001
OLFML2A	Th17 cells	0.197	0.016

(a)

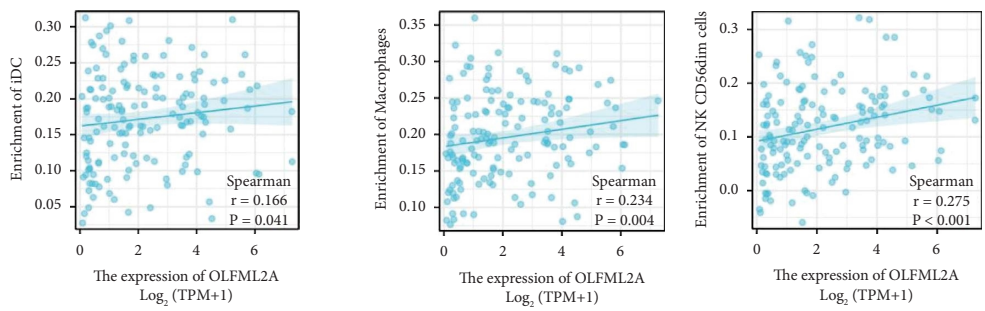

(b) (c) (d)

Figure 6: Continued.

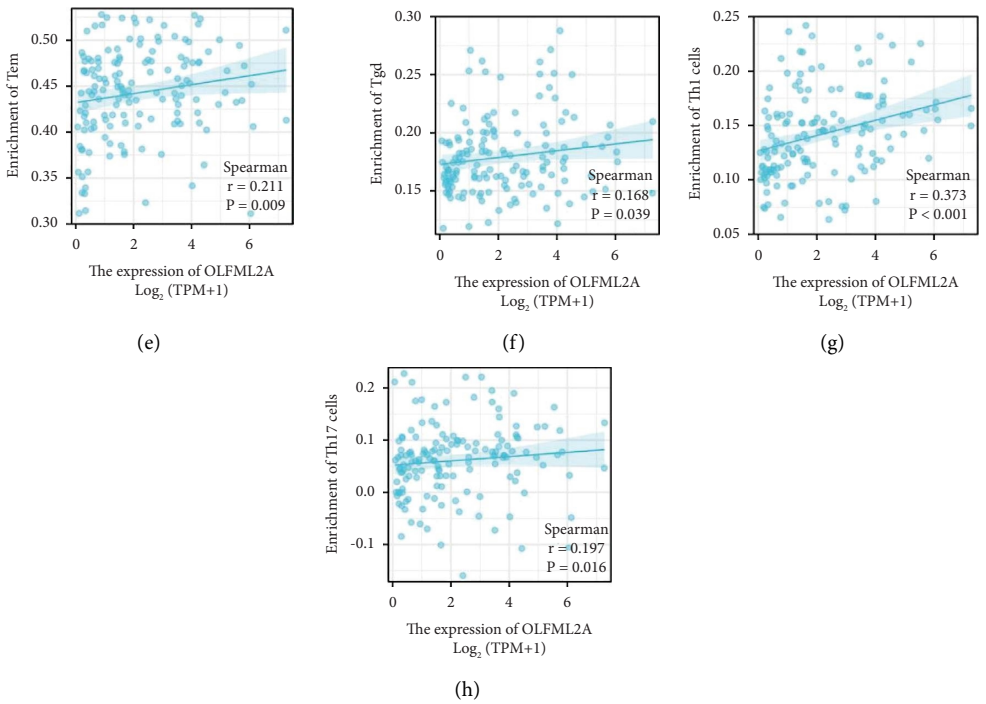

Figure 6: Relationship analysis between OLFML2A expression and immune infiltration in the AML microenvironment.

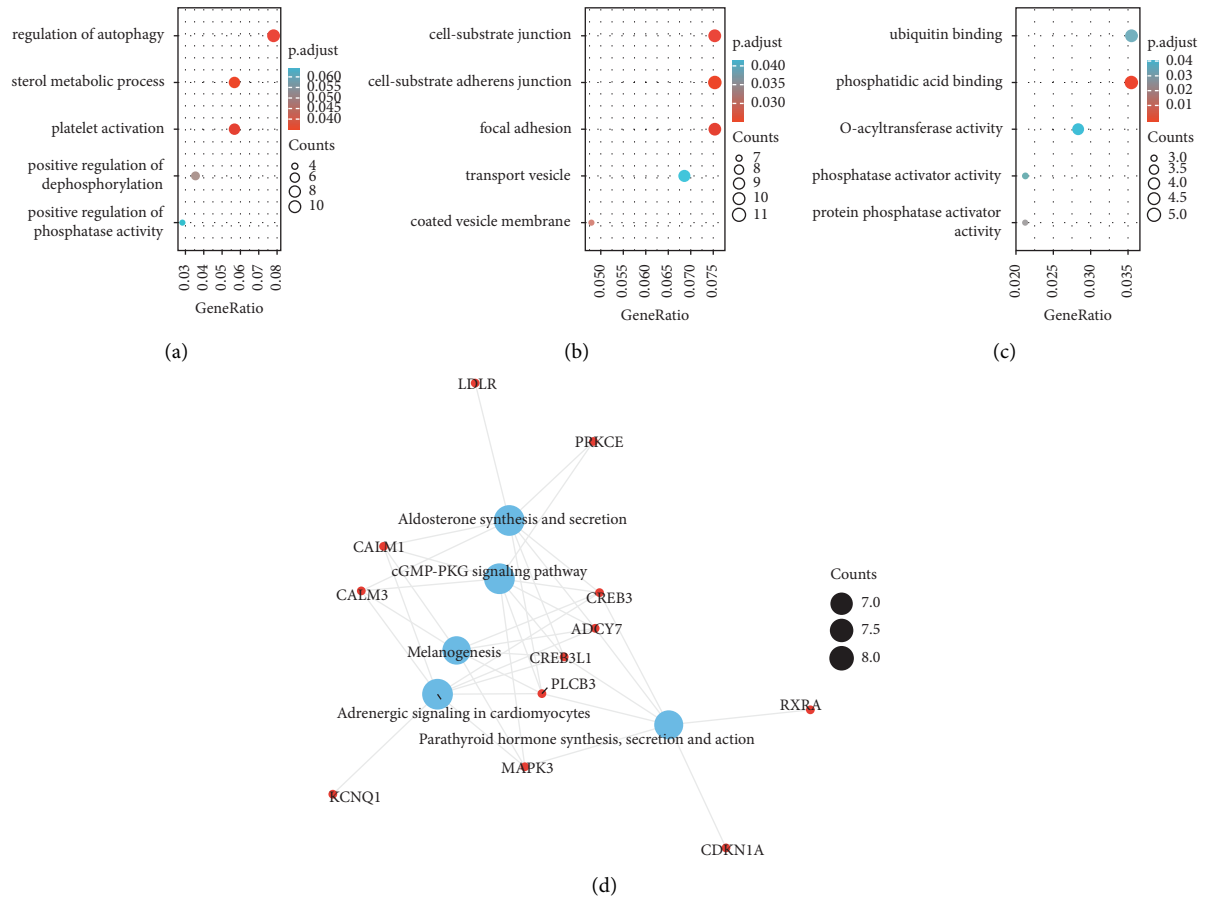

Figure 7: GO and KEGG enrichment analysis of OLFML2A associated genes in the TCGA-AML database.

infiltration in the immune microenvironment. The researchers then conducted a series of studies to analyze the data collected from the study. They focused on the relationship between the high levels of OLFML2A and immune infiltration. They also performed gene ontology analysis to examine the interaction between different genes associated with the protein. OLFML2A was differentially expressed in a variety of tumors based on pan-cancer analysis, including the brain cell counting system, DLBC, ESCA, BRCA, CHOL, LGG, COAD, lipocytes, Kipres, GBM, chronic cell count, oligosaccharide nucleic acid, oligos nucleic acid, adipocyte leukocyte leukemia, adipocyte count enzyme, hyaluronidase, cycloplasmic carcinoma, growth hormone, paclitaxel leukocyte leukemia, prostaglandin, cerebroside leukocyte acid, goitre, and auscocis. In addition, the analysis of OLFML2A in the TCGA-AML database revealed that OLFML2A is highly expressed in AML. The researchers found that high OLFML2A levels were associated with different clinical features of the disease. They also noted that protein expression was different in different groups. Patients with the high levels of OLFML2A were found to survive longer compared to those with low-protein levels. The researchers found that the high levels of OLFML2A were associated with various clinical features of the disease. They also noted that the protein was expressed differently in different groups. Some of these clinical features include BM primitive cells, cytogenetic risk, and IDH1 R132 mutations. Using columnar line graphs, it was possible to predict patient survival based on OLFML2A levels. A relationship was also found between this protein and the growth of acute lymphoblastic leukemia. In the immune microenvironment, the researchers discussed the positive correlation between OLFML2A and various immune cell activities. In parallel, we completed a GO analysis. The CC terminology encompasses "encapsulated vesicle membrane," "cell-matrix junction," "focal adhesion," "focal adhesion," and "cell-matrix junction." BP terms include "autophagy regulation," "positive regulation of phosphatase activity," "sterol metabolic process," and "phosphorylation."

5. Conclusion

The OLFML2A gene is able to act as a molecular indicator involved in the diagnosis, prognosis, and immune process of AML. It improves the molecular biology prognostic system of AML, provides help for the selection of AML treatment options, and provides new ideas for future biologically targeted therapy of AML.

Data Availability

The experimental data used to support the findings of this study are available from the corresponding author upon request.

Disclosure

Xuan Lu and Ying Li are common first authors.

Conflicts of Interest

The authors declare that they have no conflicts of interest regarding this work.

Acknowledgments

This study was supported by Lianyungang City Health Commission Project: Lianyungang City Health Commission project (202119); Lianyungang Science and Technology Plan Project: Correlation of total imaging load of cerebral small vessel disease with cognitive dysfunction and APOE gene polymorphism (SF2126); Jiangsu Provincial Health Commission Geriatric Health Project: Correlation between serum Ninjurin-1 level, ApoE gene polymorphism, and total imaging load of Cerebral Small Vessel Diseases in elderly patients with atrial fibrillation (LKM2022067).

References

[1] S. Ma, L. Duan, H. Dong et al., "OLFML2A downregulation inhibits glioma proliferation through suppression of Wnt/β-catenin signaling," *Frontiers in Oncology*, vol. 11, Article ID 717917, 2021.

[2] R. L. Siegel, K. D. Miller, and A. Jemal, "Cancer statistics, 2020," *CA: A Cancer Journal for Clinicians*, vol. 70, no. 1, pp. 7–30, 2020.

[3] C. Lv, L. Sun, Z. Guo et al., "Circular RNA regulatory network reveals cell–cell crosstalk in acute myeloid leukemia extramedullary infiltration," *Journal of Translational Medicine*, vol. 16, no. 1, pp. 361–415, 2018.

[4] K. H. Bai, S. Y. He, L. L. Shu et al., "Identification of cancer stem cell characteristics in liver hepatocellular carcinoma by WGCNA analysis of transcriptome stemness index," *Cancer Medicine*, vol. 9, no. 12, pp. 4290–4298, 2020.

[5] J. J. Cornelissen and D. Blaise, "Hematopoietic stem cell transplantation for patients with aml in first complete remission," *Blood*, vol. 127, no. 1, pp. 62–70, 2016.

[6] C. Röllig, "Diagnosis and treatment of acute myeloid leukemia: the updated 2018 onkopedia guideline," *Internist, Der*, vol. 60, no. 3, pp. 257–272, 2019.

[7] Leukemia and Lymphoma Group, "Chinese society of hematology, Chinese medical association (2017) Chinese guidelines for diagnosis and treatment of adult acute myeloid leukemia (not APL) (2017)," *Chinese Journal of Hematology*, vol. 38, pp. 177–182, 2017.

[8] M. S. Tallman, E. S. Wang, J. K. Altman et al., "Acute myeloid leukemia, version 3. 2019, NCCN clinical practice guidelines in oncology," *Journal of the National Comprehensive Cancer Network*, vol. 17, no. 6, pp. 721–749, 2019.

[9] M. Othus, F. R Appelbaum, S. H. Petersdorf et al., "Fate of patients with newly diagnosed acute myeloid leukemia who fail primary induction therapy," *Biology of Blood and Marrow Transplantation*, vol. 21, no. 3, pp. 559–564, 2015.

[10] M. A. Hossain, T. A. Asa, M. M. Rahman et al., "Network-based genetic profiling reveals cellular pathway differences between follicular thyroid carcinoma and follicular thyroid adenoma," *International Journal of Environmental Research and Public Health*, vol. 17, no. 4, p. 1373, 2020.

[11] M. Patel, S. Patel, N. Mangukia et al., "Ocimum basilicum miRNOME revisited: a cross kingdom approach," *Genomics*, vol. 111, no. 4, pp. 772–785, 2019.

[12] E. Estey, "Why are there so few randomized trials for patients with primary refractory acute myeloid leu-kemia," *Best Practice & Research Clinical Haematology*, vol. 29, no. 4, pp. 324–328, 2016.

[13] F. Marofi, H. S. Rahman, Z. M. J. Al-Obaidi et al., "Novel CAR T therapy is a ray of hope in the treatment of seriously ill AML

patients," *Stem Cell Research & Therapy*, vol. 12, no. 1, pp. 465–523, 2021.

[14] J. E. Megías-Vericat, D. Martínez-Cuadrón, M. Á. Sanz, and P. Montesinos, "Salvage regimens using conventional chemotherapy agents for relapsed/refractory adult AML patients: a systematic literature review," *Annals of Hematology*, vol. 97, no. 7, pp. 1115–1153, 2018.

[15] D. C. Perez-Ibave, R. Gonzalez-Alvarez, M. de la Luz Martinez-Fierro et al., "Olfactomedin-like 2 A and B (OLFML2A and OLFML2B) expression profile in primates (human and baboon)," *Biological Research*, vol. 49, no. 1, p. 44, 2016.

[16] C. Wu, M. Chen, Q. Zhang, L. Yu, J. Zhu, and X. Gao, "Genomic and GeneChip expression profiling reveals the inhibitory effects of amorphophalli rhizoma in TNBC cells," *Journal of Ethnopharmacology*, vol. 235, pp. 206–218, 2019.

[17] J. Greiner, M. Götz, D. Bunjes, S. Hofmann, and V. Wais, "Immunological and clinical impact of manipulated and unmanipulated DLI after allogeneic stem cell transplantation of AML patients," *Journal of Clinical Medicine*, vol. 9, no. 1, p. 39, 2019.

[18] D. A. Sallman, A. S. Asch, M. M. Al Malki et al., "The first-in-classanti-CD47 antibody magrolimab (5F9) in combination with azacitidine is effective in MDS and AML patients: ongoing phase 1b results," *Blood*, vol. 134, p. 569, 2019.

[19] D. Fumagalli, A. Blanchet-Cohen, D. Brown et al., "Transfer of clinically relevant gene expression signatures in breast cancer: from Affymetrix microarray to Illumina RNA-Sequencing technology," *BMC Genomics*, vol. 15, no. 1, p. 1008, 2014.

[20] M. Sébert, M. Passet, A. Raimbault et al., "Germline DDX41 mutations define a significant entity within adult MDS/AML patients," *Blood*, vol. 134, no. 17, pp. 1441–1444, 2019.

[21] H. A. Knaus, S. Berglund, H. Hackl et al., "Signatures of CD8+ T cell dysfunction in AML patients and their reversibility with response to chemotherapy," *JCI insight*, vol. 3, no. 21, Article ID e120974, 2018.

[22] A. M. Zeidan, R. Wang, X. Wang et al., "Clinical outcomes of older patients with AML receiving hypomethylating agents: a large population-based study in the United States," *Blood advances*, vol. 4, no. 10, pp. 2192–2201, 2020.

Hindawi
Journal of Oncology
Volume 2023, Article ID 9220547, 13 pages
https://doi.org/10.1155/2023/9220547

Research Article

Identification of Prognostic Aging-Related Genes Associated with Immune Cell Infiltration in Glioblastoma

Xiaopeng Zhu,[1,2] Xun Chen,[2,3] Zhao Liu,[4] Bihui Yang,[5] Yuxiang Zhou,[1] Sian Pan,[6] Yongkai Huang,[1] Deqing Han,[1] Yiqian Zeng ,[2,4] and Chao Liu [1]

[1]*Department of Neurosurgery, Zhuzhou Central Hospital, Zhuzhou, China*
[2]*Department of Trauma Center, Zhuzhou Central Hospital, Zhuzhou, China*
[3]*Department of Hepatobiliary Surgery, Zhuzhou Central Hospital, Zhuzhou 412000, Hunan Province, China*
[4]*Department of Critical Care Medicine, Zhuzhou Central Hospital, Zhuzhou, China*
[5]*Department of Hematology, Zhuzhou Central Hospital, Zhuzhou, China*
[6]*Department of Rehabilitation Medicine, Zhuzhou Central Hospital, Zhuzhou, China*

Correspondence should be addressed to Yiqian Zeng; 124137816@qq.com and Chao Liu; 1832546464@qq.com

Received 24 September 2022; Revised 21 October 2022; Accepted 25 November 2022; Published 21 February 2023

Academic Editor: Muhammad Muddassir Ali

Background. Aging is recognized as a main tumor risk factor, and thus aging has become a field of interest in the tumor research field. Glioblastoma multiforme represents the most typical primary malignant intracranial tumor, particularly in the elderly. However, the association between aging-related genes (AGs) and GBM prognosis remains unknown. As a result, the primary goal of this study was to determine the association among AGs and the prognosis of GBM. *Methods*. A total of 307 human AGs were downloaded from the HAGR database, while the expression profiles of GSE4290 and GSE4412 were obtained from the GEO database. Furthermore, data on GBM expression profiles were obtained from the Chinese Glioma Genome Atlas (CGGA) database. The DEAGs that were differentially expressed among the AG and GBM gene expression profiles derived from GSE4290 were then identified, followed by functional analysis of the DEAGs. The survival-related AGs were then screened using univariate Cox regression analysis , which was used to build and validate a prognostic risk model. Furthermore, the ESTIMATE and CIBERSORT algorithms were utilized to explore the association between the survival-related AGs and the tumor immune microenvironment. *Results*. In entire, 29 DEAGs were identified in the GSE4290. This was monitored by the construction of the prognosis risk model using four DEAGs from the CGGA training set, including C1QA, CDK1, EFEMP1, and IGFBP2. Next, the risk model was confirmed in the CGGA experiment set and the GSE 4412 dataset. Results showed that C1QA, CDK1, EFEMP1, and IGFBP2 levels were remarkably higher in the high-risk score groups, and they had a good association with immune and stromal scores. *Conclusion*. A robust prognostic risk model was constructed and validated using four AGs, including C1QA, CDK1, EFEMP1, and IGFBP2, which had a close relationship with the immune microenvironment of GBM. This study offers a new reference to further explore the pathogenesis of GBM and recognize new and more effective GBM treatments.

1. Introduction

Glioblastoma multiforme (GBM) represents the most typical primary malignant intracranial tumor, particularly in the elderly [1]. The standard first-line treatment for GBM at this time involves the most extensive surgical resection along with radiotherapy and adjuvant chemotherapy [1–3]. Although considerable efforts have been made in the dealing of GBM in current years, the prognosis is still poor [4]. A previous study reported that the median survival time is only about one year, and about 5% of people survive for five years overall [5]. The patients' age has been measured as a major prognostic factor for clinical outcomes [6]. Recent statistics indicate that the percentage of elderly patients with GBM is up to 25%, which can be attributed to the gradual expansion of the digits in advanced aging patients [6]. However, the exact molecular pathogenesis of GBM in elderly patients has not yet been fully elucidated. As a result, more research on

this disease is needed to predict therapeutic efficacy and guide clinical treatment decisions.

Notably, ageing is recognized as a major tumor risk factor, and thus ageing has become a focus in tumor research [7]. Many studies indicate that aging and aging-related diseases are mainly regulated by AGs which can suppress tumors through modulation of tumor cell senescence but may also enhance tumor enlargement, invasion, and metastasis [7]. However, the association between AGs and GBM prognosis has received little attention. Furthermore, there is no clear relationship between inflammation and tumor immunity in GBM. To address the essential issue of genomic erosion, a sophisticated network of DNA damage response (DDR) systems has been developed.

Cell-cycle checkpoint pathways, damage tolerance mechanisms, and DNA repair mechanisms are a few of them [8].

The HAGR is an important database for human aging-related gene expression studies. The value of AGs as prognostic factors for GBM patients was assessed in this research. The aging-related gene expression profiles were obtained from HAGR, while the GBM expression profiles were derived from the CGGA database. The main aim of this study was to elucidate the association between AGs and the prognosis of GBM by constructing a prognostic risk model. Meanwhile, the study also investigated the effects of AGs on GBM-related inflammation and immunity.

2. Methods

2.1. Acquisition of Data. All gene expression profiles were obtained from three public databases: the HAGR (HAGR, https://genomics.senescence.info/genes/), the GEO S (GEO, https://www.ncbi.nlm.nih.gov/gds), and the (CGGA) database (CGGA, https://www.cgga.org.cn/). A total of 307 human AGs was downloaded from the HAGR, and the GEOquery package was used to access the expression profiles of GSE4290 and GSE4412 from the GEO database. The GSE4290 dataset contained 81 GBM samples, while the GSE4412 dataset contained 85 GBM samples and was used as an independent verification group. Moreover, the GBM appearance profile statistics were downloaded from the CGGA database. An entire set of 406 GBM samples with continuation information were acquired from the CGGA database and randomly allocated into two groups using a 7 : 3 ratio: the GBM training set ($n = 284$) and the GBM test set ($n = 122$). R software (version 3.6.3, https://www.r-project.org/) was utilized to analyze the data.

2.2. Analysis of Differentially Expressed AGs (DEAGs). The R package limma was used to identify the DEAGs between the AGs and the GBM gene expression profiles derived from GSE4290. $|\text{LogFC}| > 1.5$ and false finding rate ($\text{FDR} < 0.05$) were set as the cut-off value. Finally, the DEAGs were visualized by a volcano plot using the ggpolt2 R package.

2.3. GO and KEGG Pathway Analyses. Pathway enrichment analyses using the gene ontology (GO) and KEGG databases were conducted using the cluster Profiler R package with a cut-off criterion of p value and FDR value <0.05 to investigate the gene function of the DEAGs. Biological processes (BP), cellular components (CC), and molecular functions make up the three categories that make up GO (MF).

2.4. Construction of a Prognostic Gene Signature. To further screen DEAGs related to survival, univariate cox regression evaluation was used. Notably, the candidate prognostic genes were chosen using the 0.05 p value threshold. Next, in the CGGA training set, LASSO regression analysis was used. The risk score was designed using the regression coefficient of each gene according to the following formula:

$$\text{Risk score} = \sum_{k=1}^{n} \text{coefficient}(\text{gene}_k) * \text{Exp}_k. \quad (1)$$

In the above formula, "n" indicates the number of the selected prognostic genes, "gene_k" is the kth selected genes, "coefficient" represents the estimated regression coefficient of genes from the multivariate Cox regression analysis, and "Exp_k" indicates the expression value of the kth selected genes. The GBM training set retrieved from the CGGA database was then dichotomized into a high-risk and low-risk groups according to the median risk score. A heatmap was used to show the relationship between candidate genes and risk scores, and Kaplan–Meier (KM) survival analysis and receiver operating characteristic (ROC) curve analysis were used to evaluate the risk score model's predictive power.

2.5. Gene Set Variation Analysis. The nonparametric, unsupervised technique for enriching gene sets is called gene set variation analysis (GSVA). The CGGA dataset was subjected to GSVA using the GSVA R package to score the high-risk and low-risk groups in order to compare the signaling pathway activity between the two groups. In addition, gene-set enrichment analysis was used to pinpoint changes in gene expression at the pathway level in order to evaluate the biological utility of the risk model. The Molecular Signatures Database v7.0 was used for running GSVA within the hallmark gene sets.

2.6. Evaluation of Immune Scores and Immune Cell Infiltration. The ESTIMATE algorithm and the estimate R package were used to determine the immune and stromal scores for GBM samples. In addition, we imputed the composition of immune cell infiltration in GBM through the CIBERSORT algorithm. It is worth noting that CIBERSORT provides a tool that is able to quantify the abundance of cell types in complex tissues using gene expression data [9].

2.7. Statistical Analysis. R version 3.6.3 was utilized to conduct the statistical investigation. While survival statistics were conducted using the Kaplan–Meier curve and log-rank test, differences in the distribution of the Chi-square test or

Fisher's exact tests were used to compare categorical data. The association between prognostic AGs and survival in GBM patients was also examined using univariate and multivariate Cox regression analysis. ROC curves were applied to validate the diagnostic value of the risk model, and the correlation between variables was determined using Spearman's rank correlation test. $p < 0.05$ was recognized to be statistically significant.

3. Results

3.1. Analysis of DEAGs in GBM Samples. In entire, 307 human AGs were downloaded from the HAGR, and the AGs were recognized using the gene expression profile of GSE4290. The GSE4290 contained 29 DEAGs, of which 22 were upregulated and 7 were downregulated, according to the results. In order to see the DEAGs, a volcano plot was used (Figure 1(a)).

3.2. Functional Analysis of DEAGs. The biological functions and association of DEAGs in GSE4290 were explored using GO and KEGG pathway analysis. Figure 2(b) shows the top 30 KEGG enrichment terms. Functional analysis indicated that the DEAGs were enriched in cellular senescence, microRNAs in cancer, cell cycle, and other diverse tumor-associated pathways. Figure 2(a) shows the top 10 improved GO terms, including BP, CC, and MF. Notably, aging and cell aging were significantly developed in the GO BP terms. These results suggest that the DEAGs are intimately related with aging and tumor.

3.3. Identification of a Prognostic Risk Model in the CGGA Training Set. The univariate Cox regression analysis method was used to analyze the expression of the 29 DEAGs identified from the CGGA training set to assess the prognostic value of DEAGs in GBM (Figures 1(c) and 1(d)). Results represented in the forest plot showed that four DEAGs were significantly associated with the survival time, including C1QA, CDK1, EFEMP1, and IGFBP2 (Figure 1(b)). Regarding that, LASSO regression was utilized to develop a prognostic risk technique for the four survival-associated DEAGs. The resulting formula was used to analyze the prognostic risk score:

$$\text{Risk score} = 0.143 * \text{C1QA} + 0.223 * \text{CDK1} + 0.118 * \text{EFEMP1} + 0.152 * \text{IGFBP2}. \quad (2)$$

Based on their median risk scores, the patients in the CGGA training set were then categorised as high-risk or low-risk. Patients in the low-risk group had better overall survival (OS) than those in the high-risk group, according to the results of the survival analysis ($p < 0.001$, Figure 3(a)). The AUC (area under the ROC curve) of the prognostic model was 0.747, 0.843, and 0.837 for the 1-, 3-, and 5-year OS, respectively, indicating a robust performance for survival prediction (Figure 3(b)). Figure 4(a) shows the risk plot for both high- and low-risk score groups, patient survival data, and gene expression information for the risk genes.

3.4. Verification of the Prognostic Risk Model in the Validation Datasets. The prognostic risk method was tested using CGGA test data to further validate its stability and reliability. Similarly, the GBM test set of the CGGA database was specified into either high-risk ($n = 61$) or low-risk ($n = 61$) groups. The K-M survival curve suggested that the overall survival (OS) of patients in the low-risk set was superior compared to those in the high-risk group ($p < 0.001$, Figure 3(c)). The AUC for the GBM test set was 0.681, 0.785, and 0.738 for the 1-, 3-, and 5-year OS, respectively, indicating great performance for survival prediction (Figure 3(d)). Figure 4(b) shows the risk distribution, patient survival status, and gene expression data of the risk genes in the CGGA test. Furthermore, the stability and reliability of the prognostic risk model were validated using an independent dataset, the GSE4412 dataset retrieved from the GEO database. The same risk model was applied, and the GBM test set obtained from the GEO was split into two groups: high-risk ($n = 43$) and low-risk ($n = 42$). Results showed significant differences in the overall survival (OS) of patients between the low-risk group and the high-risk group ($p < 0.001$, Figure 3(e)). Moreover, the AUC was 0.725, 0.808, and 0.793 for the 1-, 3-, and 5-year OS, respectively (Figure 3(f)). The corresponding risk distribution, patient survival status, and gene expression data of the risk genes in the GSE4412 test set are displayed in Figure 4(c).

3.5. GSVA of Risk Score-Related Signaling Pathways. GSVA was conducted to assess potential functional enrichment in the high-risk and low-risk groups in the CGGA dataset. Figure 5 shows the top 10 signaling pathways developed in the high-risk group, including angiogenesis, coagulation, epithelial-mesenchymal transition, hypoxia, IL-6/JAK/STAT3 signaling, provocative response, interferon-gamma response, and beta signaling. Most of them are common signaling pathways in the tumor immune microenvironment, metabolism, and progression.

3.6. Association between the Risk Score and Tumor Immunity. The immune and stromal scores in the CGGA and GSE4412 datasets, respectively, were computed using the ESTIMATE algorithm to clarify the association between the risk score and the immune/stromal score. The low-risk group had better immune scores than the high-risk group, according to the findings (Figures 6(a) and 7(a)). Moreover, Spearman's rank test results showed significant positive correlations among the risk score and immune score in CGGA and GSE4412 samples (Figures 6(b) and 7(b)). Meanwhile, the

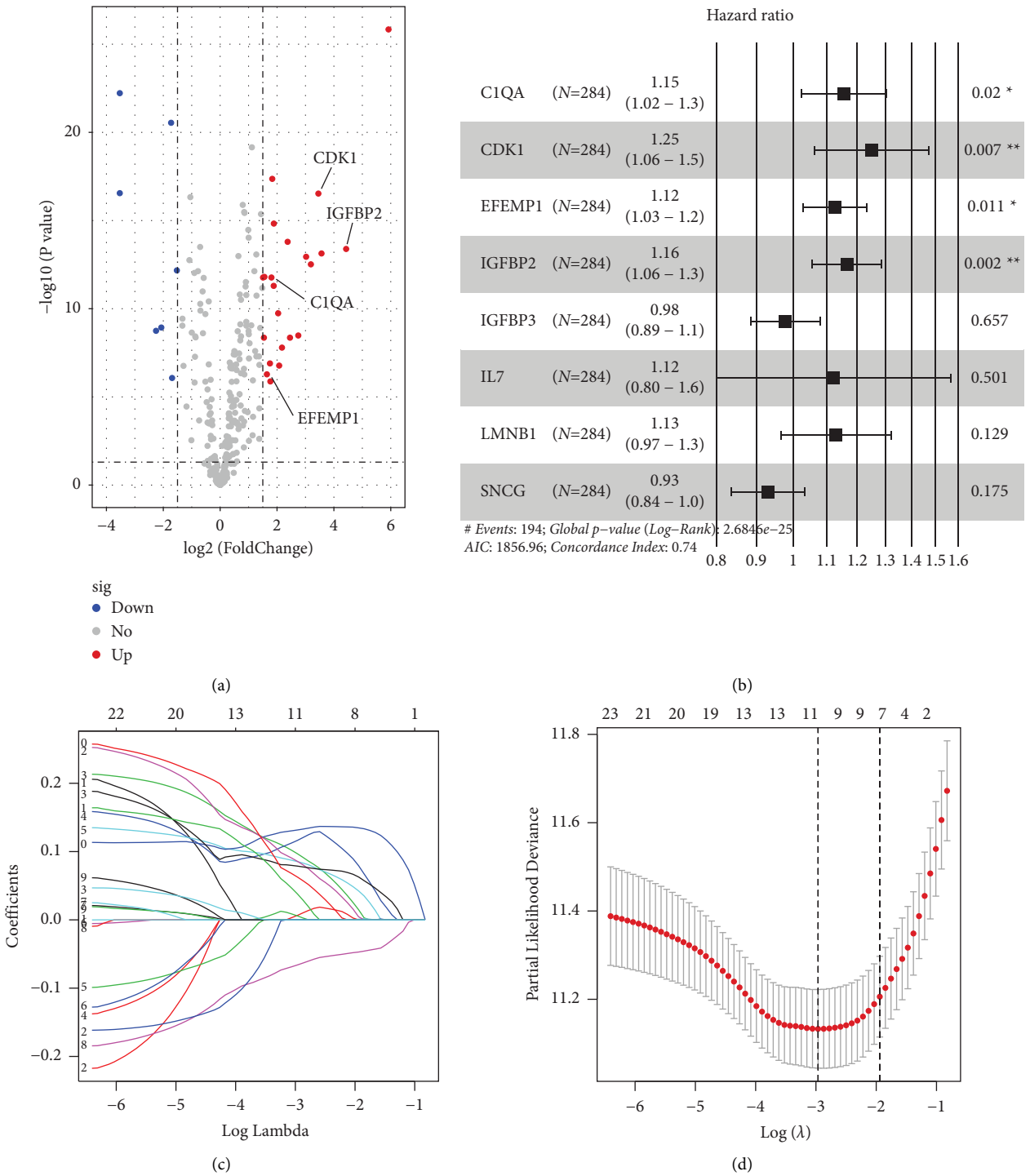

Figure 1: Identification of DEAGs related to GBM and 4 AGs of prognostic risk models in GBM patients. (a) 22 upregulated and 7 downregulated DEAGs in volcano plot (FDR < 0.05 and |logFC| > 1). (b) Forest plot for the characteristics of 4 risk DEAGs in the prognostic risk models. (c) LASSO coefficient profiles of candidate prognostic-related AGs. The coefficient profile plot was generated versus the log (λ). (d) Partial likelihood deviance map for the LASSO coefficient profiles.

risk score also had a significantly positive association with the stromal score and ESTIMATE score in CGGA and GSE4412 samples (Figures 6(c), 6(d), 7(c), and 7(d)). Considering that immune cells include many different subtypes, CIBERSORT was used to deconvolute the composition fraction of immune cells in the CGGA dataset. In order to evaluate the relevance, the proportions of immune cells in the low-risk and high-risk groups were compared. According to the findings, the low-risk group had a higher percentage of naive $CD4^+$ T cells, regulatory T cells

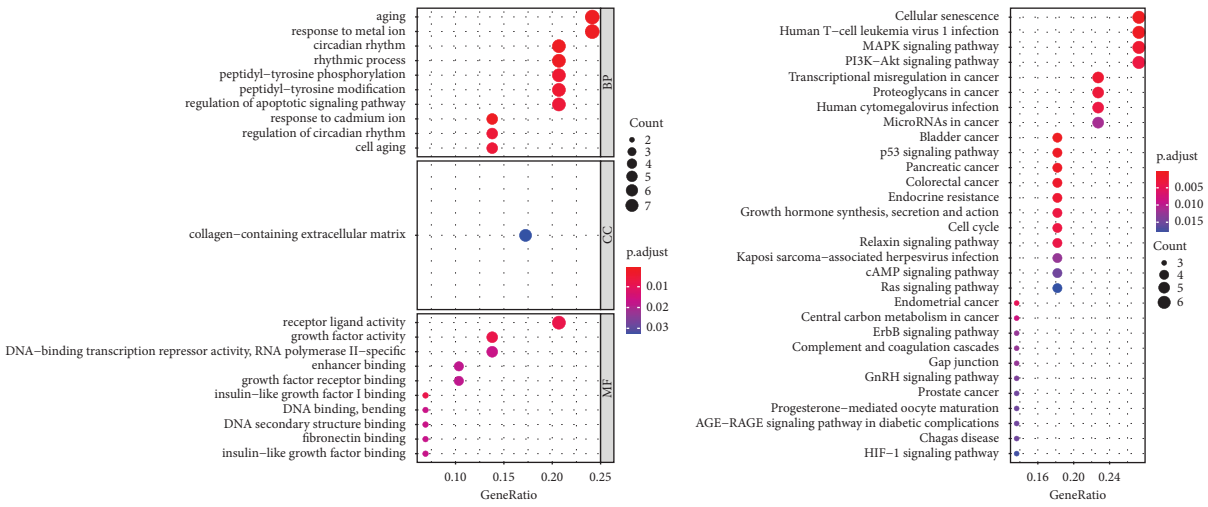

Figure 2: Functional enrichment analysis of DEAGs of the GSE4290 dataset. (a) The top 10 enrichment GO terms of BP, CC, and MF for DEAGs. (b) The top 30 enrichment pathways from KEGG pathway analysis for DEAGs.

(Tregs), gamma delta T cell monocytes, and activated mast cells than the high-risk group did (Figure 7(e)). Instead, fewer neutrophils, follicular helper T cells, M0 and M1 macrophages, and stimulated NK cells were present in the low-risk group compared to the high-risk group.

4. Discussion

Aging is a complex natural procedure, which involves aging-related immune remodeling and dysfunction [10]. It is worth noting that the incidence of tumors increases significantly with age, which can be attributed to a decline in immune function [11]. To date, the technique of aging in GBM has not yet been fully illuminated, and there are no corresponding studies in such patients [7]. Therefore, studies should be conducted to determine the role of AGs in GBM and explore the association of AGs with the prognosis of GBM.

This study identified the relationship between 29 DEAGs (Figures 1(a) and 1(b)) and GBM prognosis, and assembled a risk model with four DEAGs, including C1QA, CDK1, EFEMP1, and IGFBP2 to predict GBM prognosis. Following that, the model's prognostic value was determined using training and independent validation cohorts, with the results demonstrating a valid and robust performance for survival prediction. C1QA, CDK1, EFEMP1, and IGFBP2 were all significantly upregulated in high-risk score groups, which means that these patients have a worse prognosis.

The C1QA gene, which encodes the C1q protein in macrophages, dendritic cells, and THP1 cells, has been implicated in the aging response and is involved in some neurodegenerative diseases [12]. Interestingly, increased gene expression of C1QA has been proven to cause a high inflammatory state in the brain of people with psychosis [13]. In addition, a previous study concluded that increased C1QA expression may facilitate tumor progression and contribute towards an adverse outcome [8]. CDK1 participates in the regulation of the G2/M phase of the cell cycle [14]. Furthermore, CDK1 is frequently overexpressed in many human malignant tumor tissues, and it has been investigated as a PB for a variety of tumors. Over-expression of CDK1 in glioma and GBM cells contributes to glioma cell senescence escape and growth [15]. As a result, CDK1 has been proposed as a promising therapeutic target. Previous research has found that EFEMP1, also known as fibulin-3, is involved in ageing, age-related diseases, and tumor formation [16, 17]. EFEMP1 knockout mice aged faster and lived shorter lives. However, previous research on the role of EFEMP1 in GBM has been inconsistent. On the one hand, some studies have shown that it has an antitumor effect by inhibiting glioma growth [18]. On the other hand, some studies found that over-expression of EFEMP1 may enhance glioma growth and contribute to resistance through the influence of multiple oncogenic waving pathways, such as Notch, AKT, and EGFR waving pathways [19, 20]. Results obtained in this study are consistent with the latter conclusion. However, this shows that more studies are essential to clarify the function of EFEMP1 in the pathogenesis of GBM. It has been informed that IGFBP-2 appearance is expressively increased after 50 years of age [21]. Moreover, several studies have indicated that there is an expressively positive correlation between IGFBP-2 concentrations and mortality in healthy elderly populations [22, 23]. Over-expression of IGFBP-2 has also been found in GBM and many other types of human tumors [24–26]. Unfortunately, the high expression of IGFBP-2 was strongly associated with a significant shortening of survival, which is consistent with the results of this study [27, 28]. Therefore, most of the existing studies propose using IGFBP-2 as a biomarker or potential novel target for GBM treatment [29, 30].

For the first time, a GBM prognostic risk model based on four AGs was developed in this study. Subsequent GSVA analysis disclosed that the risk genes' signaling pathways are elaborated in immunomodulatory and inflammatory

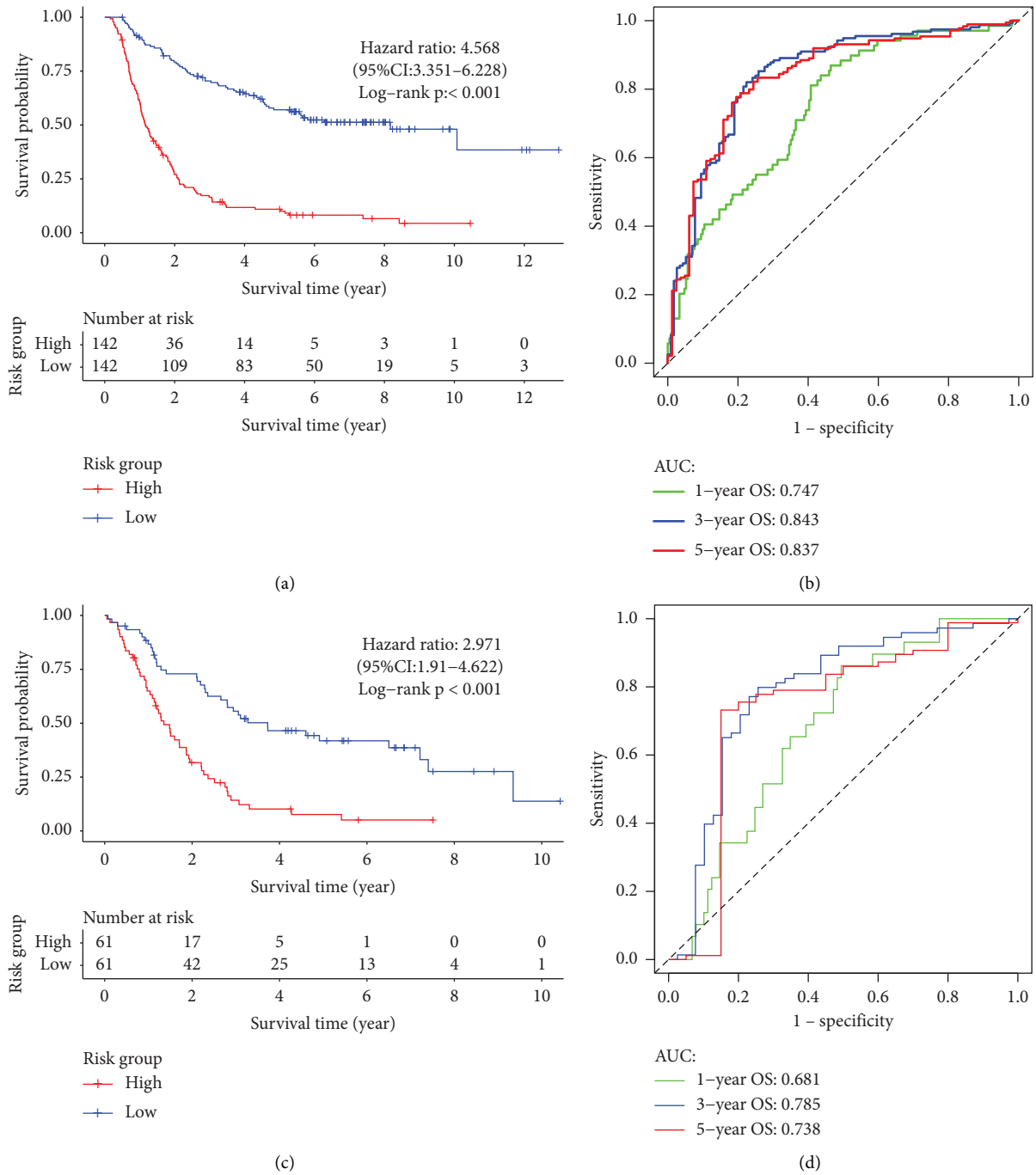

Figure 3: Continued.

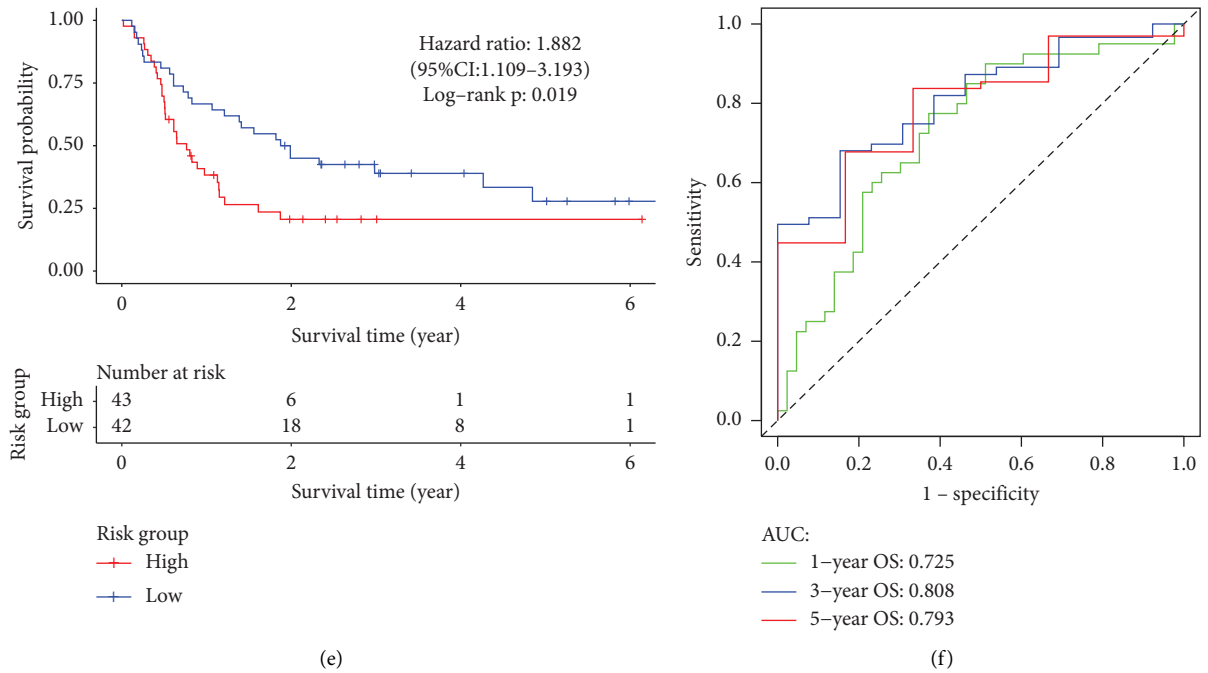

Figure 3: Identification and verification of the prognostic risk model in GBM. (a) Kaplan–Meier survival analysis of high-risk and low-risk groups in the CGGA training set. (b) Time-dependent ROC curves for 1-, 3-, and 5-y OS in the CGGA training set. (c, e) Kaplan–Meier survival analysis of high-risk and low-risk groups in the CGGA test set and GEO test set, respectively. (d, f) Time-dependent ROC curves for 1-, 3-, and 5-y OS in the CGGA test set and GEO test set, respectively.

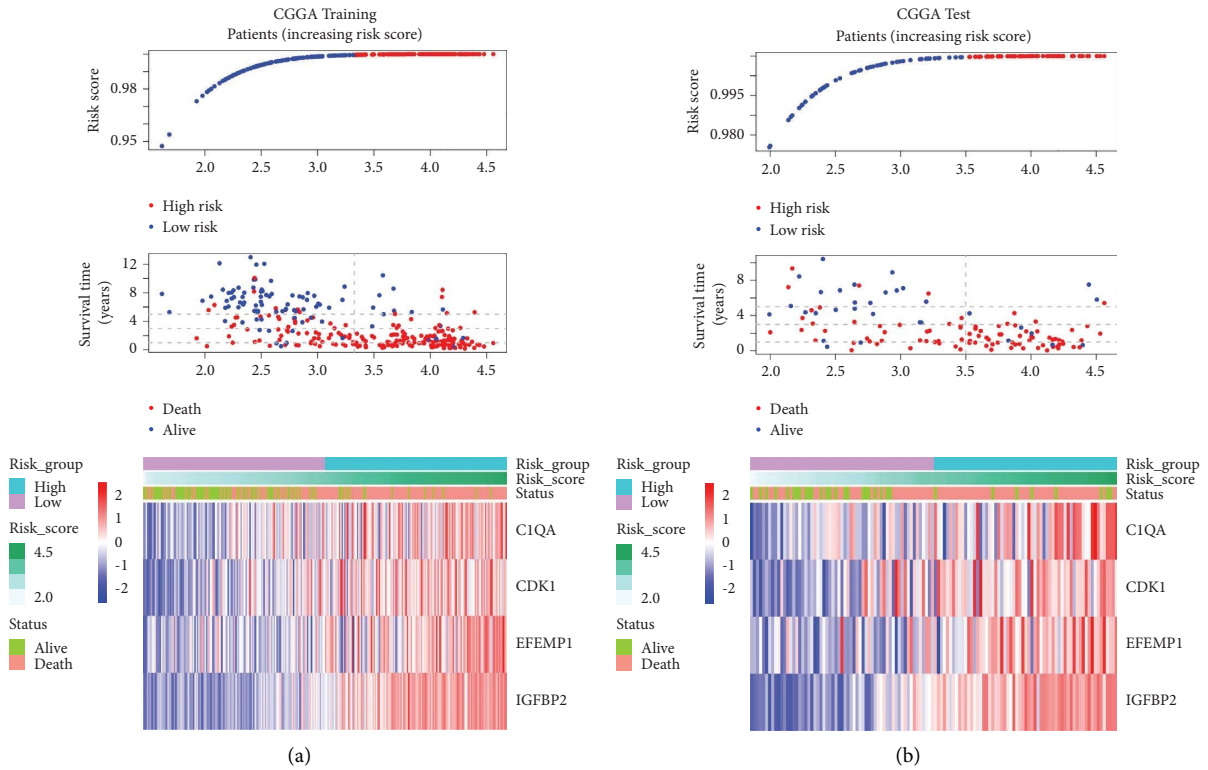

Figure 4: Continued.

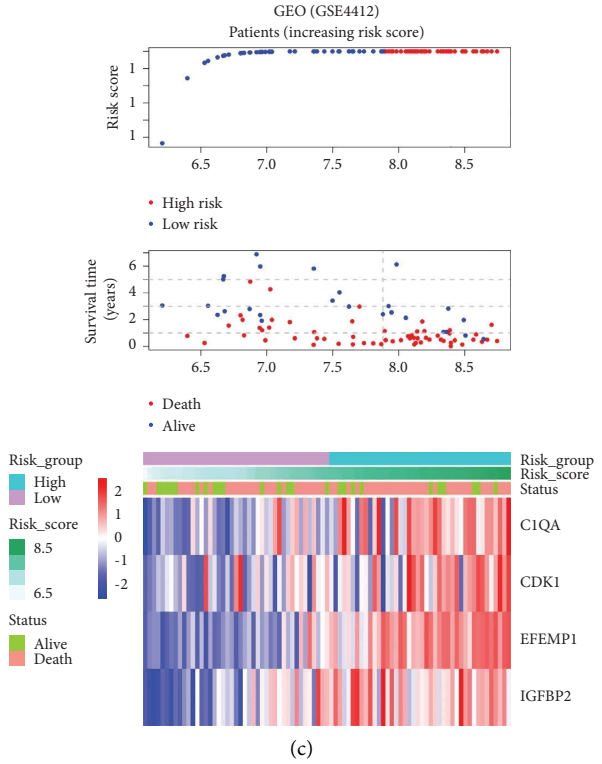

(c)

Figure 4: Prognosis and expression of risk genes of the high-risk and low-risk GBM patients. (a) Risk plot distribution, survival status, and risk gene expression in the CGGA training set. (b) Risk plot distribution, survival status, and expression of the risk genes in the CGGA test set. (c) Risk plot distribution, survival status, and expression of the risk genes in the GEO test set.

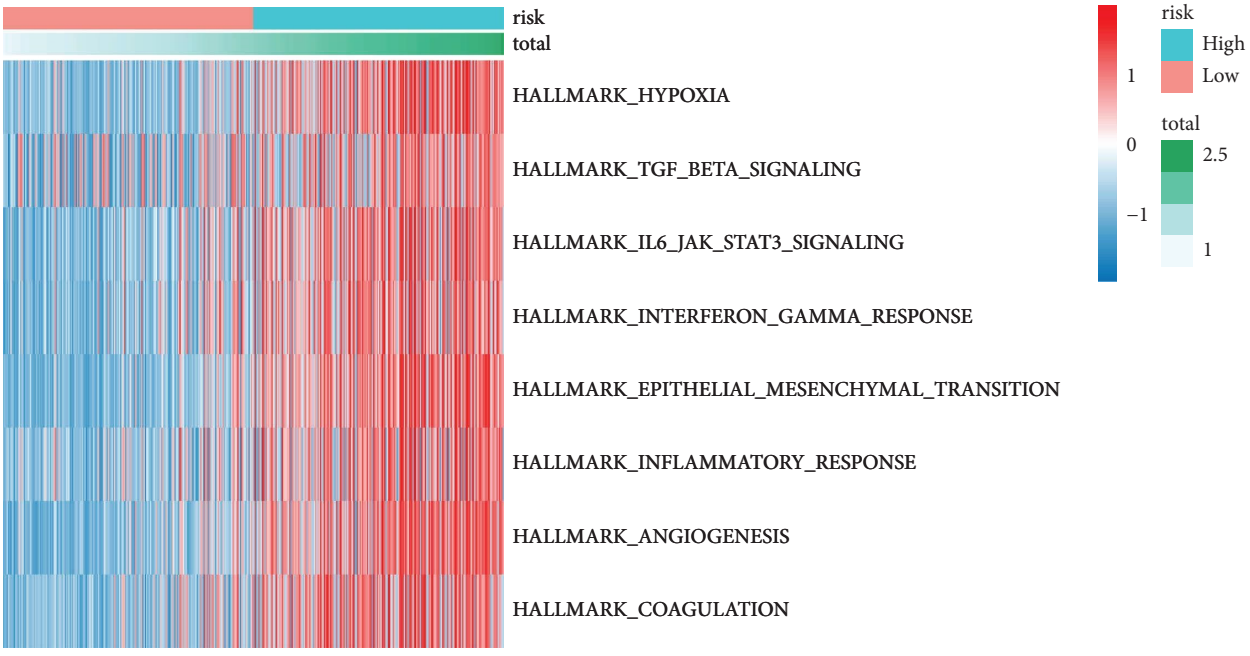

Figure 5: The top 10 enriched pathways of the risk gene in high-risk and low-risk groups through GSVA.

responses. The results strongly suggested a relationship between the risk genes and the GBM immune microenvironment. Based on the above findings, we further explored the relationship among the risk score and immune score and deconvoluted the conformation fraction of immune cells in the CGGA data set and GSE4412 data set. The immune and

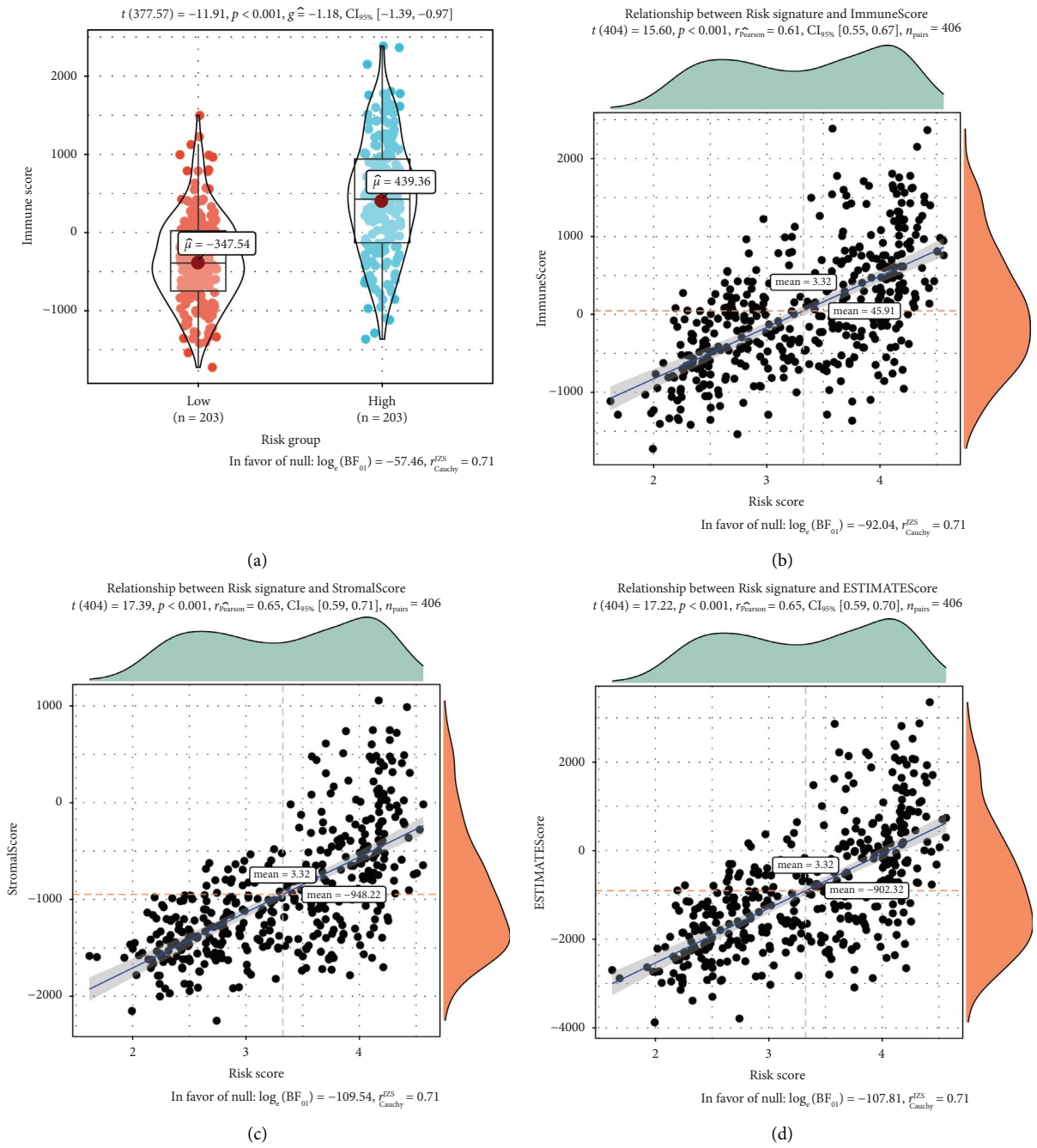

Figure 6: Correlation between the risk score and tumor immunity in the CGGA data set. (a) Comparisons of the immune scores in high-risk and low-risk GBM patients. (b) Association among the risk score and the immune score in GBM samples. (c) Association among the risk score and the stromal score in GBM samples. (d) Association among the risk score and the ESTIMATE score in GBM samples.

stromal scores were found to be positively associated with the risk score. This implies that the higher the immune and stromal scores, the greater the immune cell infiltration and the worse the prognosis. Recent studies have proposed that the immune score serves as an important prognostic factor of GBM. Furthermore, this study analyzed the GBM data using the CIBERSORT algorithm in order to investigate the compositional differences of 22 immune cell types based on the risk model. The findings showed that the high-risk group's NK cells, M0 macrophages, M1 macrophages, and neutrophils were activated by the infiltration of follicular helper T cells and suggested a poor prognosis. On the other hand, the infiltration of naive $CD4^+$ T cells, regulatory T cells (Tregs), gamma-delta T cells, monocytes, and activated mast cells in the low-risk group suggested a relatively good prognosis in GBM patients.

Notably, macrophages are the most abundant tumor immune infiltration cell types in human GBM. Macrophages have two main phenotypes, M1 and M2, which are differentiated from untreated macrophages (M0). Several

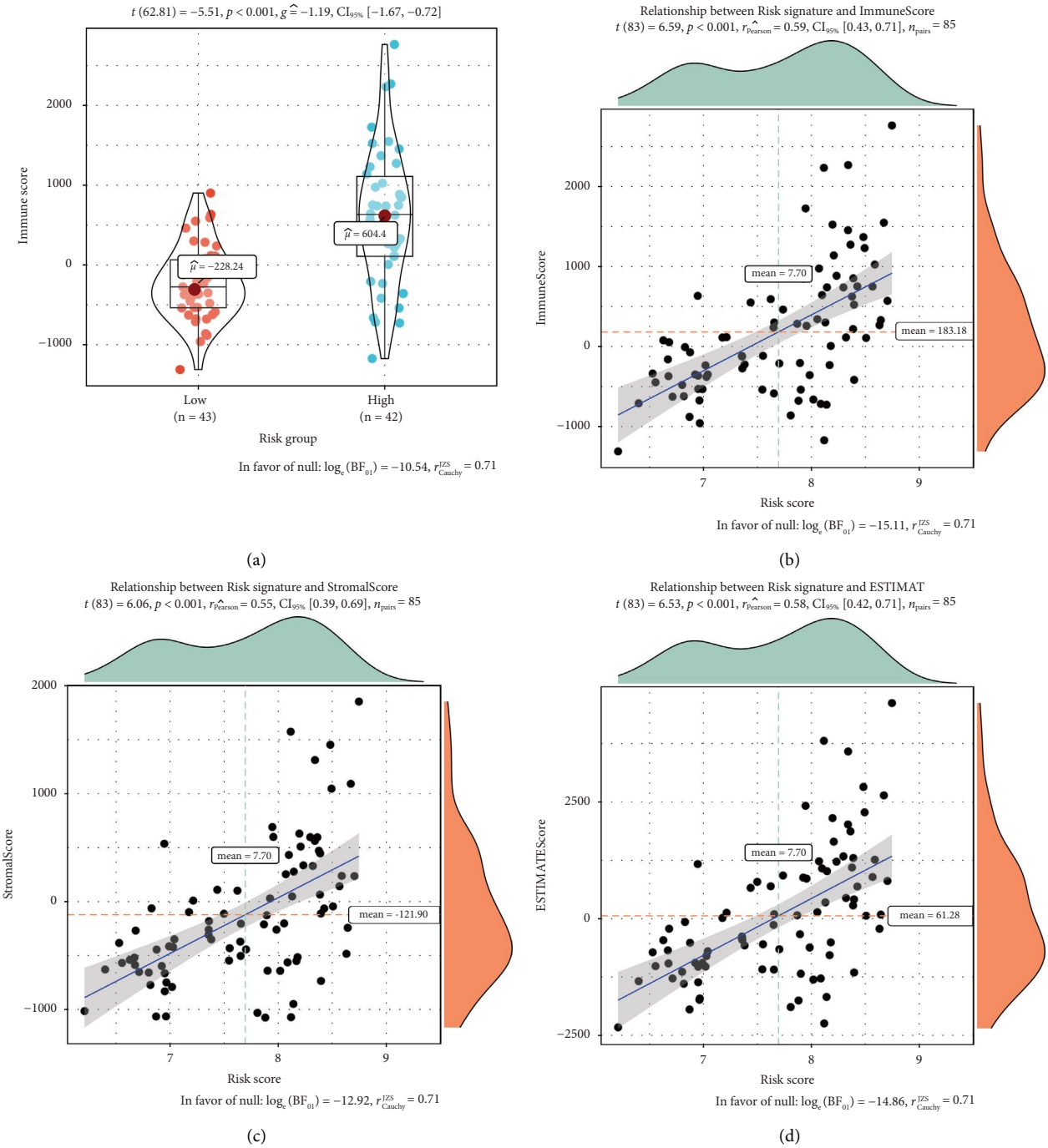

Figure 7: Continued.

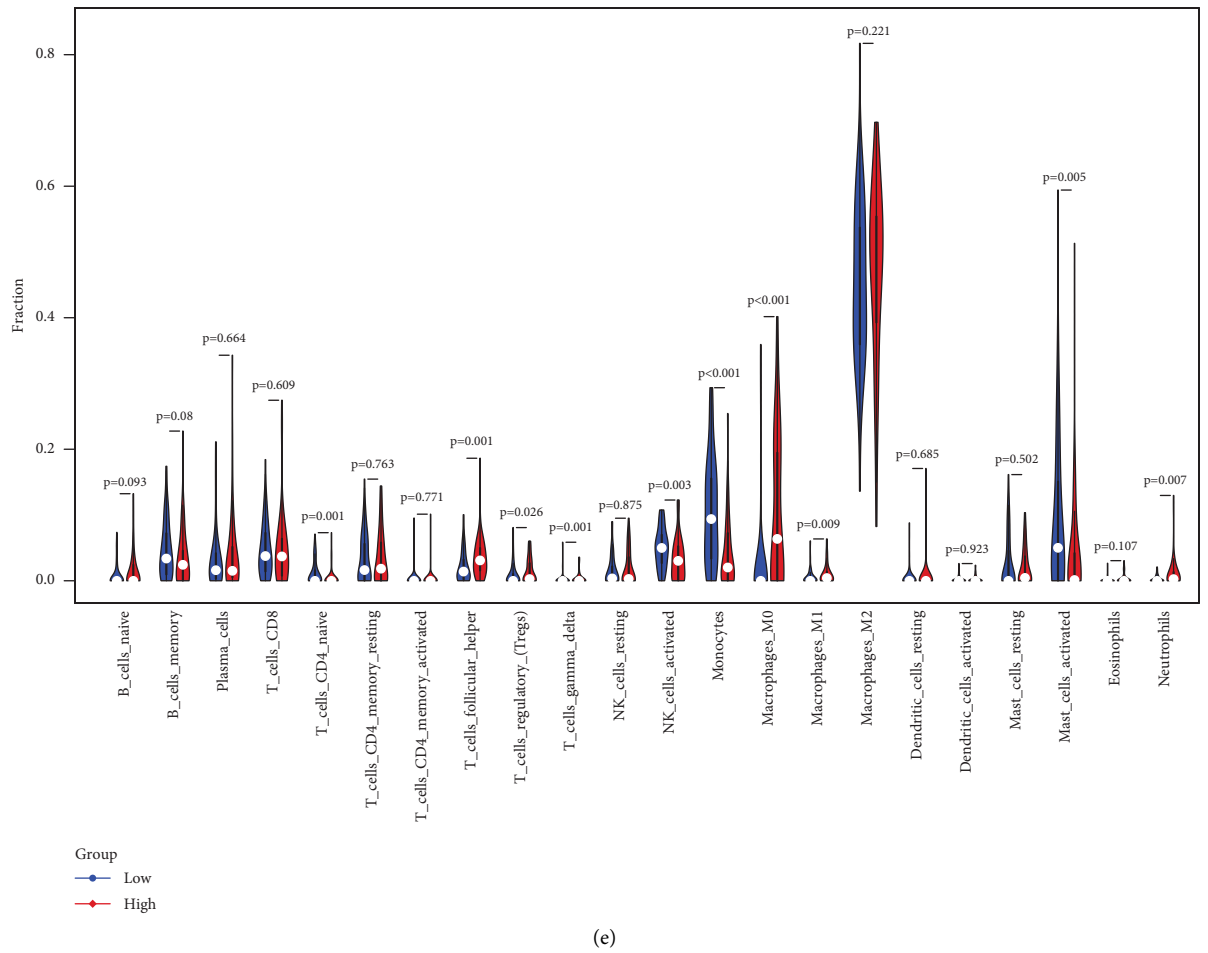

(e)

Figure 7: Correlation between the risk score and tumor immunity in the GSE4412 data set. (a) Comparisons of the immune scores in high-risk and low-risk GBM patients. (b) Association among the risk score and the immune score in GBM samples. (c) In GBM samples, there is an association between the risk score and the stromal score. (d) Association among the risk score and the ESTIMATE score in GBM samples. (e) Comparisons of the fractions of 22 types of immune cells among the high-risk and low-risk groups in the CGGA data set.

previous studies indicate that M1 macrophages can perform antitumorigenic functions, whereas M0 and M2 macrophages can perform protumorigenic functions [12, 31, 32]. Despite the fact that M1 macrophages have proinflammatory and antitumor effects, a previous study found that they were inversely related to survival in GBM patients [33]. This study has shown that the proportion of M0 and M1 macrophages was significantly higher in the high-risk group than in the low-risk group. Therefore, more comprehensive and in-depth studies should be conducted to elucidate the mechanism of action of macrophages in GBM.

The role of monocytes and mast cells in tumor development and progression has previously been established. Nonetheless, the interactions of monocytes and mast cells in the tumor microenvironment are complex and contradictory [34, 35]. This study has shown that monocytes and activated mast cells were significantly lower in the high-risk group. NK cells are capable of directly killing tumor cells [36]. Although it has great cytotoxicity, the proportion of NK cells was low in the GBM immune microenvironment [37]. Interestingly, a previous study found that NK cell deficiency in GBM improves prognosis, which is in line with our results [38]. With regard to T cells, $CD4^+$ T cells seem to play a dual role in tumor immunity, while follicular helper T cells and gamma-delta T cells are relatively good prognostic signatures. The results obtained in this study are in accordance with the above-mentioned conclusions, with the exception of follicular helper T cells [39–42]. Accumulating evidence suggests that regulatory T cells are involved in immunosuppression and are associated with tumor escape and tumor progression, which is unfavorable for the outcome [43, 44]. Therefore, this discrepancy with our results should be explored more intensively. Overall, the occurrence and development of GBM involve a complex immune microenvironment [45], and thus more research is needed to explore the complex tumor immune relationships.

This study had some limitations as well. Although there was a correlation among the four AGs and the tumor immune microenvironment, further experimental verification is needed to assess the robustness of the prognostic risk model. Future studies should investigate how the four genes are elaborated in the regulation of tumor immunity.

In conclusion, a robust prognostic risk model was constructed and validated using four AGs, including C1QA, CDK1, EFEMP1, and IGFBP2, which had a close relationship with the immune microenvironment of GBM. This study offers a new reference to further explore the pathogenesis and identify new and more effective GBM treatments.

Data Availability

The data used to support the findings of this study are available from the corresponding author upon reasonable request.

Additional Points

Reporting Checklist. The authors have completed the TRIPOD reporting checklist.

Ethical Approval

The authors are accountable for all aspects of the work in ensuring that questions related to the accuracy or integrity of any part of the work are appropriately investigated and resolved.

Conflicts of Interest

All authors have completed the ICMJE uniform disclosure form. The authors declare that they have no conflicts of interest.

Authors' Contributions

XZ and XC completed the drawing of the picture and the writing part of the content. XZ and XC contributed equally to this work. ZL, BY, YZ, SP, YH, and DH provided support for content writing and data analysis. YZ and CL conceived and supervised the writing of this article.

Acknowledgments

This work was supported by the Scientific Research Project (2019) of Health Commission of Hunan (B2019200), Natural Science Foundation of Hunan Province (2022JJ31024), and Science and Technology Project of Zhuzhou (2020-006).

References

[1] A. P. Becker, B. E. Sells, S. J. Haque, and A. Chakravarti, "Tumor heterogeneity in glioblastomas: from light microscopy to molecular pathology," *Cancers*, vol. 13, 2021.

[2] R. Chen, M. Smith-Cohn, A. L. Cohen, and H. Colman, "Glioma subclassifications and their clinical significance," *Neurotherapeutics*, vol. 14, no. 2, pp. 284–297, 2017.

[3] C. Hanna, T. A. Lawrie, E. Rogozińska et al., "Treatment of newly diagnosed glioblastoma in the elderly: a network meta-analysis," *Cochrane Database of Systematic Reviews*, vol. 3, Article ID Cd013261, 2020.

[4] F. Di Cintio, M. Dal Bo, L. Baboci, E. De Mattia, M. Polano, and G. Toffoli, "The molecular and microenvironmental landscape of glioblastomas: implications for the novel treatment choices," *Frontiers in Neuroscience*, vol. 14, Article ID 603647, 2020.

[5] Q. T. Ostrom, N. Patil, G. Cioffi, K. Waite, C. Kruchko, and J. S. Barnholtz-Sloan, "CBTRUS statistical report: primary brain and other central nervous system tumors diagnosed in the United States in 2013-2017," *Neuro-Oncology*, vol. 22, no. Supplement_1, pp. iv1–iv96, 2020.

[6] M. Ferguson, G. Rodrigues, J. Cao, and G. Bauman, "Management of high-grade gliomas in the elderly," *Seminars in Radiation Oncology*, vol. 24, no. 4, pp. 279–288, 2014.

[7] A. Calcinotto, J. Kohli, E. Zagato, L. Pellegrini, M. Demaria, and A. Alimonti, "Cellular senescence: aging, cancer, and injury," *Physiological Reviews*, vol. 99, no. 2, pp. 1047–1078, 2019.

[8] L. H. Chen, J. F. Liu, Y. Lu, Xy He, C. Zhang, and Hh Zhou, "Complement C1q (C1qA, C1qB, and C1qC) may Be a potential prognostic factor and an index of tumor microenvironment remodeling in osteosarcoma," *Frontiers Oncology*, vol. 11, Article ID 642144, 2021.

[9] B. Chen, M. S. Khodadoust, C. L. Liu, A. M. Newman, and A. A. Alizadeh, "Profiling tumor infiltrating immune cells with CIBERSORT," *Methods in Molecular Biology*, vol. 1711, pp. 243–259, 2018.

[10] C. L. Brinkmeyer-Langford, J. Guan, G. Ji, and J. J. Cai, "Aging shapes the population-mean and -dispersion of gene expression in human brains," *Frontiers in Aging Neuroscience*, vol. 8, p. 183, 2016.

[11] M. Fane and A. T. Weeraratna, "How the ageing microenvironment influences tumour progression," *Nature Reviews Cancer*, vol. 20, no. 2, pp. 89–106, 2020.

[12] M. I. Fonseca, S. H. Chu, M. X. Hernandez et al., "Cell-specific deletion of C1qa identifies microglia as the dominant source of C1q in mouse brain," *Journal of Neuroinflammation*, vol. 14, no. 1, p. 48, 2017.

[13] T. D. Purves-Tyson, K. Robinson, A. M. Brown et al., "Increased macrophages and C1qA, C3, C4 transcripts in the midbrain of people with schizophrenia," *Frontiers in Immunology*, vol. 11, p. 2002, 2020.

[14] J. Wang, B. Li, C. Wang, Y. Luo, M. Zhao, and P. Chen, "Long noncoding RNA FOXD2-AS1 promotes glioma cell cycle progression and proliferation through the FOXD2-AS1/miR-31/CDK1 pathway," *Journal of Cellular Biochemistry*, vol. 120, no. 12, Article ID 19784, 2019.

[15] Z. Song, Y. Pan, G. Ling et al., "Escape of U251 glioma cells from temozolomide-induced senescence was modulated by CDK1/survivin signaling," *Am J Transl Res*, vol. 9, no. 5, pp. 2163–2180, 2017.

[16] P. J. McLaughlin, B. Bakall, J. Choi et al., "Lack of fibulin-3 causes early aging and herniation, but not macular degeneration in mice," *Human Molecular Genetics*, vol. 16, no. 24, pp. 3059–3070, 2007.

[17] M. Tasaki, M. Ueda, Y. Hoshii et al., "A novel age-related venous amyloidosis derived from EGF-containing fibulin-like extracellular matrix protein 1," *The Journal of Pathology*, vol. 247, no. 4, pp. 444–455, 2019.

[18] Y. Hu, P. D. Pioli, E. Siegel et al., "EFEMP1 suppresses malignant glioma growth and exerts its action within the tumor extracellular compartment," *Molecular Cancer*, vol. 10, no. 1, p. 123, 2011.

[19] D. Lei, F. Zhang, D. Yao, N. Xiong, X. Jiang, and H. Zhao, "MiR-338-5p suppresses proliferation, migration, invasion,

and promote apoptosis of glioblastoma cells by directly targeting EFEMP1," *Biomedicine & Pharmacotherapy*, vol. 89, pp. 957–965, 2017.

[20] S. Zhang, Z. Ye, X. Song et al., "Association of EFEMP1 gene polymorphisms with the risk of glioma: a hospital-based case-control study in a Chinese Han population," *Journal of the Neurological Sciences*, vol. 349, no. 1-2, pp. 54–59, 2015.

[21] Z. Li and F. Picard, "Modulation of IGFBP2 mRNA expression in white adipose tissue upon aging and obesity," *Hormone and Metabolic Research*, vol. 42, no. 11, pp. 787–791, 2010.

[22] D. Hu, L. Pawlikowska, A. Kanaya et al., "Serum insulin-like growth factor-1 binding proteins 1 and 2 and mortality in older adults: the Health, Aging, and Body Composition Study," *Journal of the American Geriatrics Society*, vol. 57, no. 7, pp. 1213–1218, 2009.

[23] M. Sunderić, N. Mihailović, and O. Nedić, "Protein molecular forms of insulin-like growth factor binding protein-2 change with aging," *Experimental Gerontology*, vol. 58, pp. 154–158, 2014.

[24] Y. Lin, T. Jiang, K. Zhou et al., "Plasma IGFBP-2 levels predict clinical outcomes of patients with high-grade gliomas," *Neuro-Oncology*, vol. 11, no. 5, pp. 468–476, 2009.

[25] Y. Liu, F. Li, Y. T. Yang et al., "IGFBP2 promotes vasculogenic mimicry formation via regulating CD144 and MMP2 expression in glioma," *Oncogene*, vol. 38, no. 11, pp. 1815–1831, 2019.

[26] S. S. Patil, R. Railkar, M. Swain, H. S. Atreya, R. R. Dighe, and P. Kondaiah, "Novel anti IGFBP2 single chain variable fragment inhibits glioma cell migration and invasion," *Journal of Neuro-Oncology*, vol. 123, no. 2, pp. 225–235, 2015.

[27] J. Cai, Q. Chen, Y. Cui et al., "Immune heterogeneity and clinicopathologic characterization of IGFBP2 in 2447 glioma samples," *OncoImmunology*, vol. 7, no. 5, Article ID e1426516, 2018.

[28] C. Song, F. Shen, Y. Liu, J. Zhang, and S. Wei Song, "IGFBP2 promotes neural stem cell maintenance and proliferation differentially associated with glioblastoma subtypes," *Brain Research*, vol. 1704, pp. 174–186, 2019.

[29] T. Li, M. E. Forbes, G. N. Fuller, J. Li, X. Yang, and W. Zhang, "IGFBP2: integrative hub of developmental and oncogenic signaling network," *Oncogene*, vol. 39, no. 11, pp. 2243–2257, 2020.

[30] L. M. Moore, K. M. Holmes, S. M. Smith et al., "IGFBP2 is a candidate biomarker for Ink4a-Arf status and a therapeutic target for high-grade gliomas," *Proceedings of the National Academy of Sciences of the United States of America*, vol. 106, no. 39, pp. 16675–16679, 2009.

[31] Q. Guo, X. Xiao, and J. Zhang, "MYD88 is a potential prognostic gene and immune signature of tumor microenvironment for gliomas," *Frontiers Oncology*, vol. 11, Article ID 654388, 2021.

[32] Y. Tian, Y. Ke, and Y. Ma, "High expression of stromal signatures correlated with macrophage infiltration, angiogenesis and poor prognosis in glioma microenvironment," *PeerJ*, vol. 8, Article ID e9038, 2020.

[33] M. B. Pereira, L. R. C. Barros, P. A. Bracco et al., "Transcriptional characterization of immunological infiltrates and their relation with glioblastoma patients overall survival," *OncoImmunology*, vol. 7, no. 6, Article ID e1431083, 2018.

[34] S. J. Galli and M. Tsai, "Mast cells: versatile regulators of inflammation, tissue remodeling, host defense and homeostasis," *Journal of Dermatological Science*, vol. 49, no. 1, pp. 7–19, 2008.

[35] M. Prosniak, L. A. Harshyne, D. W. Andrews et al., "Glioma grade is associated with the accumulation and activity of cells bearing M2 monocyte markers," *Clinical Cancer Research*, vol. 19, no. 14, pp. 3776–3786, 2013.

[36] M. G. Morvan and L. L. Lanier, "NK cells and cancer: you can teach innate cells new tricks," *Nature Reviews Cancer*, vol. 16, no. 1, pp. 7–19, 2016.

[37] I. Golán, L. Rodríguez de la Fuente, and J. A. Costoya, "NK cell-based glioblastoma immunotherapy," *Cancers*, vol. 10, 2018.

[38] S. Wu, W. Yang, H. Zhang et al., "The prognostic landscape of tumor-infiltrating immune cells and immune checkpoints in glioblastoma," *Technology in Cancer Research and Treatment*, vol. 18, Article ID 153303381986994, 2019.

[39] A. J. Gentles, A. M. Newman, C. L. Liu et al., "The prognostic landscape of genes and infiltrating immune cells across human cancers," *Nature Medicine*, vol. 21, no. 8, pp. 938–945, 2015.

[40] C. Gu-Trantien and K. Willard-Gallo, "PD-1(hi)CXCR5(-) CD4(+) T(FH) cells play defense in cancer and offense in arthritis," *Trends in Immunology*, vol. 38, no. 12, pp. 875–878, 2017.

[41] S. Ning, J. Wu, Y. Pan, K. Qiao, L. Li, and Q. Huang, "Identification of CD4+ conventional T cells-related lncRNA signature to improve the prediction of prognosis and immunotherapy response in breast cancer," *Frontiers in Immunology*, vol. 13, Article ID 880769, 2022.

[42] K. I. Woroniecka, K. E. Rhodin, P. Chongsathidkiet, K. A. Keith, and P. E. Fecci, "T-Cell dysfunction in glioblastoma: applying a new framework," *Clinical Cancer Research*, vol. 24, no. 16, pp. 3792–3802, 2018.

[43] C. Banissi, F. Ghiringhelli, L. Chen, and A. F. Carpentier, "Treg depletion with a low-dose metronomic temozolomide regimen in a rat glioma model," *Cancer Immunology, Immunotherapy*, vol. 58, no. 10, pp. 1627–1634, 2009.

[44] L. Vandenberk and S. W. Van Gool, "Treg infiltration in glioma: a hurdle for antiglioma immunotherapy," *Immunotherapy*, vol. 4, no. 7, pp. 675–678, 2012.

[45] M. L. Broekman, S. L. N. Maas, E. R. Abels, T. R. Mempel, A. M. Krichevsky, and X. O. Breakefield, "Multidimensional communication in the microenvirons of glioblastoma," *Nature Reviews Neurology*, vol. 14, no. 8, pp. 482–495, 2018.

Hindawi
Journal of Oncology
Volume 2023, Article ID 2311231, 11 pages
https://doi.org/10.1155/2023/2311231

Research Article

Tumor Suppressor miR-613 Alleviates Non-Small Cell Lung Cancer Cell via Repressing M2 Macrophage Polarization

Mingjun Yang,[1] **Wen Zhou**,[1] **Mingming Xu**,[1] **Xiao Han**,[1] **Yanyan Shi**,[1] **Min Shi**,[1] **and Zhipeng Wang**[2]

[1]*Department of Cardiothoracic Surgery, Affiliated Hospital of Nantong University, No. 20, Xisi Road, Nantong, Jiangsu 226001, China*
[2]*Department of Thoracic Surgery, Haimen People's Hospital, No. 1201, Beijing Road, Nantong, Jiangsu 226001, China*

Correspondence should be addressed to Mingjun Yang; ymj851117@ntu.edu.cn

Received 24 August 2022; Revised 10 October 2022; Accepted 24 November 2022; Published 16 February 2023

Academic Editor: İbrahim Hakkı Cigerci

Background. Non-small cell lung cancer (NSCLC) is a crucial crux of cancer-related death, and M2 macrophage polarization facilitates NSCLC development. MicroRNA-613 (miR-613) is a tumor suppressor. This research aimed to clarify the miR-613 function in NSCLC and its impact on M2 macrophage polarization. *Methods.* miR-613 expressions in NSCLC tissues and cells were evaluated using quantitative real-time PCR. For miR-613 function in NSCLC, cell proliferation analysis, cell counting kit-8, flow cytometry, western blot, transwell, and wound-healing were conducted. Meanwhile, the miR-613 impact on M2 macrophage polarization was assessed by the NSCLC models. *Results.* miR-613 was lessened in NSCLC cells and tissues. It was corroborated that miR-613 overexpression retrained NSCLC cell proliferation, invasion, and migration but facilitated cell apoptosis. Moreover, miR-613 overexpression restrained NSCLC development by repressing M2 macrophage polarization. *Conclusion.* Tumor suppressor miR-613 ameliorated NSCLC by restraining M2 macrophage polarization.

1. Introduction

Lung cancer is a malignant tumor worldwide with high frequency in morbidity and mortality [1]. Nearly, 85% of lung cancer is non-small-cell lung cancer (NSCLC) [2, 3]. Although multiple progress has been achieved in NSCLC treatment, the effect is unsatisfactory [4, 5]. Thus, there is an urgent need to better understand NSCLC pathogenesis and identify novel therapeutic targets to alleviate NSCLC.

In search for more effective intervention methods for NSCLC, the importance of targeting the tumor microenvironment (TME) has gradually attracted wide attention [6, 7]. TME forms of cancer and stromal cells containing macrophages, and endothelial cells [8, 9]. As one of the pivotal components of TME, tumor-associated macrophages (TAMs) are major coordinators of immune cells [10]. TAMs mainly include M1 and M2, and M2 macrophages accelerate tumorigenesis [11, 12]. Crucially, accumulated studies demonstrate that M2 macrophages drive proliferation, migration, invasion, and other malignant phenotypes of NSCLC, thereby aggravating NSCLC [13, 14]. Nevertheless, the definite mechanism of M2 macrophages facilitating the NSCLC occurrence is not fully clarified.

MicroRNAs (miRNAs) are highly conserved small noncoding RNAs [15], exert pivotal functions in various human malignancies, and are promising targets for tumor therapy [16, 17]. Recently, increasing miRNAs have been confirmed to mediate the NSCLC process. For instance, miR-130a mediates macrophage polarization in NSCLC, and miR-130a loss is interrelated to NSCLC-poor prognosis and increased tumor stage [18]; miR-4319 knockdown accelerates NSCLC tumor progression by accelerating M2 macrophage polarization, which might supply promising strategies for NSCLC treatment [19].

miR-613 is a widely functional miRNA in various tumors. It has been reported that miR-613 slows down the process of cervical squamous cell cancer by targeting LETM1 [20]. miR-613 can regulate gastric cancer progression by

regulating reactive oxygen species (ROS) production, glutathione content (GSH), and superoxide dismutase (SOD) activity [21]. miR-613 represses cell migration and invasion in esophageal squamous cell carcinoma via mediating G6PD to inactivate the STAT3 signaling pathway [22]. miR-613 induces NSCLC cell sensitivity to cisplatin by targeting GJA1 [23]. However, it remains unknown whether miR-613 mediates M2 macrophage polarization in NSCLC.

The current research confirmed the low expression of miR-613 in NSCLC tissues and cells. On this basis, this study attempted to further investigate whether miR-613 participated in the NSCLC regulation by mediating M2 macrophage polarization.

2. Materials and Methods

2.1. Samples. NSCLC and adjacent normal tissues ($n = 20$ for each) were gathered from patients at Affiliated Hospital of Nantong University and stored with liquid nitrogen for the follow-up research. Informed consent was signed by all patients before performing surgery. The present research was permitted by the Ethics Committee.

2.2. Cell Culture. Normal human lung cell lines HLF-A was from Procell (Wuhan, China), NSCLC cells HCC827, H1299, H1650, and A549 were from the American Type Culture Collection (ATCC, Maryland, USA), and THP-1 cells were from ATCC.

HLF-A cells were put in minimum essential medium (Thermo Fisher Scientific, Waltham, Massachusetts, USA) containing 1% penicillin, 10% FBS, and streptomycin (Gibco, New York, USA). NSCLC cells HCC827, H1299, and H1650 were put in RPMI-1640 with 10% FBS. THP-1 cells were put in RPMI-1640 with 10% FBS and 0.05 mM 2-mercaptoethanol. A549 cells were grown in ATCC-formulated F-12K (ATCC) containing 10% FBS. All cells were cultivated at 37°C, 5% CO_2.

For macrophage induction, THP-1 cells were differentiated into macrophages by treatment with phorbol 12-myristate 13-acetate (150 nM, Sigma-Aldrich, St Louis, USA) for 1 d [24]. The cells were developed with 20 ng/mL IL-4 (MedChemExpress, New Jersey, USA) for 48 h to achieve M2 macrophages [13].

2.3. Cell Transfection. miR-613 mimic and NC-mimic were obtained from Ribobio (Guangzhou, China). H1650 cells and M2 macrophages (1×10^6) were placed in six-hole plates and cultured overnight, followed by cell transfection with miR-613 mimic or NC-mimic after 24 h using Lipofectamine 2000 following the manufacturer's protocols.

2.4. Co-Culture System. Transwell inserts with 0.4 μM aperture from Corning (New York, USA) were applied as a co-culture system. THP-1 cells (2×10^5) were placed in Transwell inserts and handled with 20 ng/mL IL-4 for 2 d to differentiate to M2 macrophages, and the miR-613 mimic was transfected into M2 macrophages. Afterward, the upper chambers were transferred into Petri dishes with H1650 cells and co-cultured for 24 h.

2.5. RNA Extraction. Total RNA was extracted in a TRIzol reagent (Beyotime, Shanghai, China) as per standard procedure, and then, RNA content and quality were evaluated via detecting optical density (A260, A280, and A230).

2.6. Quantitative Real-Time PCR. cDNA was synthesized with A cDNA synthesis kit (Thermo Fisher Scientific) and one step PrimeScript miRNA cDNA synthesis kit (TaKaRa, Dalian, China), referring to manufacturers' protocol. Real-time was run on ABI 7300 real-time qPCR system (ABI company) with SYBR green PCR kits (Thermo Fisher Scientific). For the miR-613 expression analysis, qRT-PCR was conducted with TaqMan microRNA assay. U6 and β-actin were internal references. The relative level was tested through $2^{-\Delta\Delta CT}$ [25]. Table 1 lists all primer sequences.

2.7. Cell Counting Kit-8 (CCK-8) Assay. H1650 cells treated differently (1×10^3) were inoculated in plates with 96 holes. The plates were placed in the incubator and incubated for 24 h, 48 h, or 72 h (at 37°C, 5% CO_2). Then, the cells were handled for 1.5 h at 37 °C using 10 μL CCK-8 solution (Beyotime). Afterward, cell viability was assessed with a microplate reader (Bio-Rad, California, USA).

2.8. Cell Proliferation. The proliferation of H1650 cells was determined using EdU Cell Proliferation Kits (Ribobio) following a standard procedure. H1650 cells (1×10^3) were placed in 96-well plates and cultured for one day. EdU (50 μM) was incubated with cells for two hours. Cells were then fastened with 4% paraformaldehyde (Solarbio, Beijing) and dyed by Hoechst 33342 and an Apollo reaction cocktail. The images were obtained by fluorescence microscopy (Olympus, Tokyo, Japan). The percentage of positive cells was counted and calculated using ImageJ2X (Rawak Software Inc.).

2.9. Flow Cytometry. The apoptosis condition of H1650 cells was assessed via FITC Annexin V Apoptosis Detection Kit I (BD Biosciences, New Jersey, USA). After H1650 cells were harvested, the cells were resuspended, handled for 20 min with FITC Annexin V at 37°C, and further handled for 20 min with propidium iodide (PI) in the dark. H1650 cell apoptosis was tested with a FACSCalibur Flow Cytometer (BD Biosciences).

2.10. Western Blot. RIPA lysis buffer (Solarbio) was adopted to extract total proteins following protocol. After protein content was tested by BCA assay kits (Abcam), the same amount of protein was segregated with SDS-PAGE (Thermo Fisher Scientific) before transferring it onto PVDF membranes (Millipore, Massachusetts). Then, membranes were fostered for one hour with 5% skimmed milk and further treated at 4°C overnight with primary antibodies containing

Table 1: Primer sequence used in qRT-PCR.

Gene name	Primer sequence (5′-3′)
miR-613	Forward: GTGAGTGCGTTTCCAAGTGT Reverse: TGAGTGGCAAAGAAGGAACAT
Arg-1	Forward: AGGCGCTGTCATCGATTTCT Reverse: TGGAGTCCAGCAGACTCAAT
CD206	Forward: CTCTGTTCAGCTATTGGACGC Reverse: CGGAATTTCTGGGATTCAGCTTC
iNOS	Forward: GCGCTCTAGTGAAGCAAAGC Reverse: AGTGAAATCCGATGTGGCCT
CD86	Forward: CTTTGCTTCTCTGCTGCTGT Reverse: GGCCATCACAAAGAGAATGTTAC
β-actin	Forward: CTCCATCCTGGCCTCGCTGT Reverse: GCTGTCACCTTCACCGTTCC
U6	Forward: CTCGCTTCGGCAGCACA Reverse: AACGCTTCACGAATTTGCGT

anti-Bax (Abcam, 1 : 1000, ab32503), anti-Bcl2 (Abcam, 1 : 1000, ab32124), anti-β-actin (Abcam, 1 μg/mL, ab8226), and anti-cleaved-caspase-3 (Abcam, 1 : 500, ab32042). Subsequently, these membranes were incubated with secondary antibodies (Abcam). Proteins were visualized using an electrochemiluminescence system (Solarbio) and were evaluated by ImageJ2X (Rawak Software Inc.).

2.11. Wound-Healing Assay. H1650 cells were fostered to 50% confluence in six-hole plates; the 1% double-antibody serum-free medium was replaced. Then, the plate surface was lightly scratched by 200 μL pipette tips and put into a 37°C 5% CO_2 incubator for culture. After scratching with an inverted optical microscope (Olympus), H1650 cell migration was monitored at 0 h and 48 h. The migration area was measured using ImageJ2X (Rawak Software Inc.), and the mobility was calculated.

2.12. Transwell Analysis. For cell migration analysis, H1650 cells (5×10^4) were suspended in a FBS-free medium (100 μL) and transferred onto an upper chamber (Corning, Cambridge) with noncoated membranes. Lower chambers were filled with standard medium (Thermo Fisher Scientific). After incubating for 24 h, the cells on the membrane upper surface were removed and stained cells on the membrane lower surface with crystal violet (0.1%, Solarbio).

For cell invasion analysis, Matrigel chambers were conducted. After H1650 cells were harvested, they were resuspended in a serum-free medium and transferred to hydrated matrix chambers (50 μL). The bottom chambers were put in RPMI-1640 (500 μL) containing 10% FBS. On the next day, cells on the upper surface were scraped and stained infiltrating cells on the lower surface by 0.1% crystal violet (Solarbio). All cells were counted with 3–5 random fields. Then, we use ImageJ2X (Rawak Software Inc.) to quantify.

2.13. Enzyme-Linked Immunosorbent Assay. IL-10 and TGF-β levels in M2 macrophage culture supernatant were tested with enzyme-linked immunosorbent assay with IL-10 ELISA Kit (Thermo Fisher Scientific) and TGF-β ELISA Kit (Spbio, Wuhan, China), referring to manufacturer's instructions.

2.14. In Vivo Assay. C57BL/6 mice (5 weeks old) were from Vital River Laboratory Animal Technology (Beijing, China).

Macrophages with different treatments were co-cultured with H1650 cells. H1650 cells were grouped: H1650+$M^{NCmimic}$, H1650+$M^{IL\text{-}4+NCmimic}$ and H1650+$M^{IL\text{-}4+miR\text{-}613mimic}$. The mice were subcutaneously injected with the abovementioned H1650 cells (5×10^5) [13]. The tumor volumes were tested with a vernier caliper. Three weeks after inoculation, sacrificed all mice with an intraperitoneal injection of pentobarbital sodium (100 mg/kg), gathered and weighed tumor tissues for subsequent studies.

2.15. TUNEL and Ki-67 Staining. TUNEL kit (Beyotime) was applied for TUNEL staining following instructions. Xenograft tissues were fastened in 4% paraformaldehyde, embedded in paraffin, and deparaffinized and rehydrated. Followed by the antigen retrieval, sections (5 μm) were incubated for 1.5 h with a 50 μL TUNEL mix at 37°C, washed, and DAPI (2 μg/mL) was added for nuclei staining, followed by washing using PBS and observing under a fluorescence microscope (OLYMPUS).

For Ki-67 staining, the abovementioned sections were handled by anti-Ki-67 (Abcam, 1 μg/mL, ab15580) at 4°C and handled by secondary antibodies (Abcam, biotin conjugated goat polyclonal vector, 1 : 250) and observed with a microscope. Mean intensities for positive Ki-67 expression were determined with Image software. Randomly selected the percentage of Ki-67 positive staining from five fields.

2.16. Statistical Analysis. Data are measured as mean ± standard deviation. Statistically significant differences were evaluated with one-way or two-way ANOVA or an unpaired student's *t*-test followed by a Tukey's post-test. $P < 0.05$ was statistical significance.

3. Results

3.1. miR-613 Is Lessened in NSCLC. To clarify the miR-613 function in NSCLC, we determined the miR-613 level in NSCLC tissues and found a decreased miR-613 level in NSCLC tissues (Figure 1(a)). Meanwhile, miR-613 dropped in NSCLC cells HCC827, H1299, H1650, and A549 compared with normal human lung cell lines HLF-A, and the decrease was most notable in H1650 cells (Figure 1(b)), which shows that the differential expression of miR-613 is most obvious in H1650 cells. Therefore, we selected H1650 cells for subsequent experiments. In summary, our study confirmed that miR-613 is lowly expressed in NSCLC tissues and cells, which suggests that miR-613 may be a potential therapeutic target for NSCLC.

3.2. miR-613 Overexpression Advances NSCLC Cell Apoptosis and Represses Cell Proliferation. Due to the decreased miR-613 in H1650 cells being most remarkable, H1650 cells were

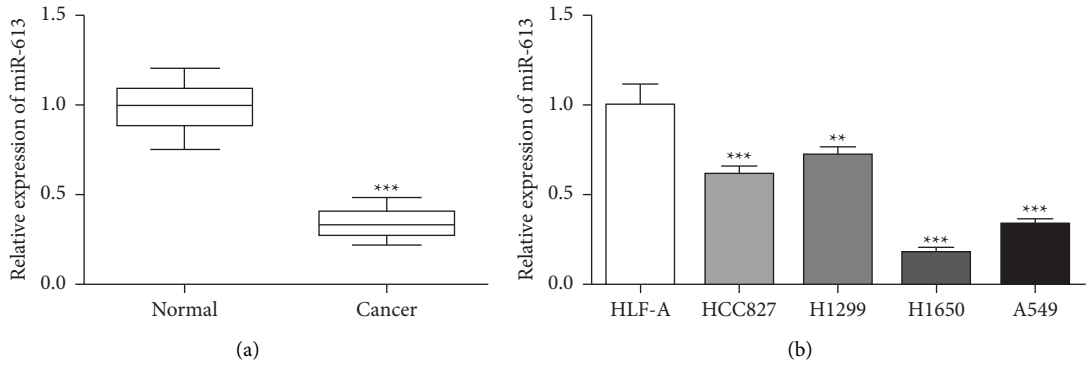

Figure 1: miR-613 expression in non-small cell lung cancer tissues and cells. (a) After harvesting twenty pairs of NSCLC and adjacent normal tissues, the miR-613 expression was tested in NSCLC and control groups using quantitative real-time PCR (qRT-PCR). (b) qRT-PCR analysis for miR-613 expression in human lung cell lines HLF-A and NSCLC cells HCC827, H1299, H1650, and A549. $^{**}P < 0.01$ *vs.* HLF-A. $^{***}P < 0.001$ *vs.* Normal or HLF-A.

selected to verify the miR-613 function in NSCLC development. After transfecting the miR-613 mimic into H1650 cells, CCK-8 results corroborated that the miR-613 overexpression reduced the H1650 cell viability (Figure 2(a)). Meanwhile, the H1650 cell proliferation was weakened after the transfection of the miR-613 mimic (Figure 2(b)). By contraries, flow cytometry analysis expounded that the miR-613 overexpression enhanced the H1650 cell apoptosis (Figure 2(c)). Bax, Bcl-2, and cleaved-caspase-3 were apoptosis-related proteins [26]. As displayed in Figure 2(d), Bax and cleaved-caspase-3 were elevated after miR-613 mimic transfection, while the Bcl-2 was decreased. Overall, the miR-613 overexpression restrained NSCLC cell proliferation and accelerated cell apoptosis.

3.3. miR-613 Overexpression Weakens NSCLC Cell Invasion and Migration. Subsequently, we continued to evaluate miR-613 impact on NSCLC cell invasion and migration. As exhibited in Figure 3(a), miR-613 mimic repressed H1650 cell migration, and this conclusion was further validated by Transwell analysis (Figure 3(b)). Meanwhile, the H1650 cell invasion was restrained after the miR-613 overexpression (Figure 3(c)). To sum up, the miR-613 overexpression restrained NSCLC cell invasion and migration.

3.4. miR-613 Represses the M2 Macrophage Polarization. Previous studies authenticate that M2 macrophage polarization accelerates NSCLC progression [27, 28]. Thus, we attempted to clarify whether miR-613 had an inhibitory effect on M2 macrophage polarization. After THP-1 cells were induced to differentiate into macrophages, a miR-613 mimic was transfected into IL-4-induced M2 macrophages. miR-613 mimic transfection efficiency in M2 macrophages was verified, and miR-613 was lowly expressed in M2 macrophages (Supplementary Figure 1). Arg-1, CD206 are M2 macrophage markers, iNOS, CD86 are M1 macrophage markers [29]. We found that Arg-1 and CD206 were elevated, while iNOS and CD86 were decreased after IL-4 treatment, and these trends were partially reversed by miR-613 mimic transfection (Figure 4(a)).

M2 macrophages usually excrete anti-inflammatory factors such as TGF-β and IL-10 [30]. Thus, we further evaluated the TGF-β and IL-10 levels in the cell culture supernatant. ELISA results clarified that the IL-10 and TGF-β contents were elevated after IL-4 treatment, while miR-613 mimics partially reversed this trend (Figure 4(b)). The abovementioned experimental results illustrated that miR-613 restrained the M2 macrophage polarization.

3.5. miR-613 Restrains NSCLC Cell Growth by Reducing M2 Macrophage Polarization. We further determined whether miR-613 regulated the NSCLC cell growth by repressing M2 macrophage polarization. Macrophages with different treatments (as in Figure 4) were co-cultured with H1650 cells. Figure 5(a) presents a schematic diagram of the co-culture system. CCK-8 assay authenticated that co-culture of M2 macrophages increased H1650 cell viability, while this increase was partially inverted after the miR-613 was overexpressed in M2 macrophages (Figure 5(b)). The same trend was discovered in the H1650 cell proliferation analysis (Figure 5(c)). On the contrary, the co-culture of M2 macrophages weakened H1650 cell apoptosis, while the miR-613 overexpression partially reversed this effect (Figure 5(d)). Meanwhile, the co-culture of M2 macrophages accelerated H1650 cell migration, while this trend was partially inverted after the miR-613 was overexpressed in M2 macrophages, and the Transwell assay further confirmed this finding (Figures 5(e)–5(f)). Moreover, we further evaluated the H1650 cell invasion, and the results expounded that the co-culture of M2 macrophages facilitated H1650 cell invasion, while the miR-613 overexpression partially reversed this effect (Figure 5(g)). In summary, miR-613 restrained NSCLC cell growth by reducing M2 macrophage polarization.

3.6. miR-613 Represses Tumor Growth via Restraining M2 Macrophage Polarization in Vivo. We further evaluated the *in vivo* function of miR-613. As displayed in

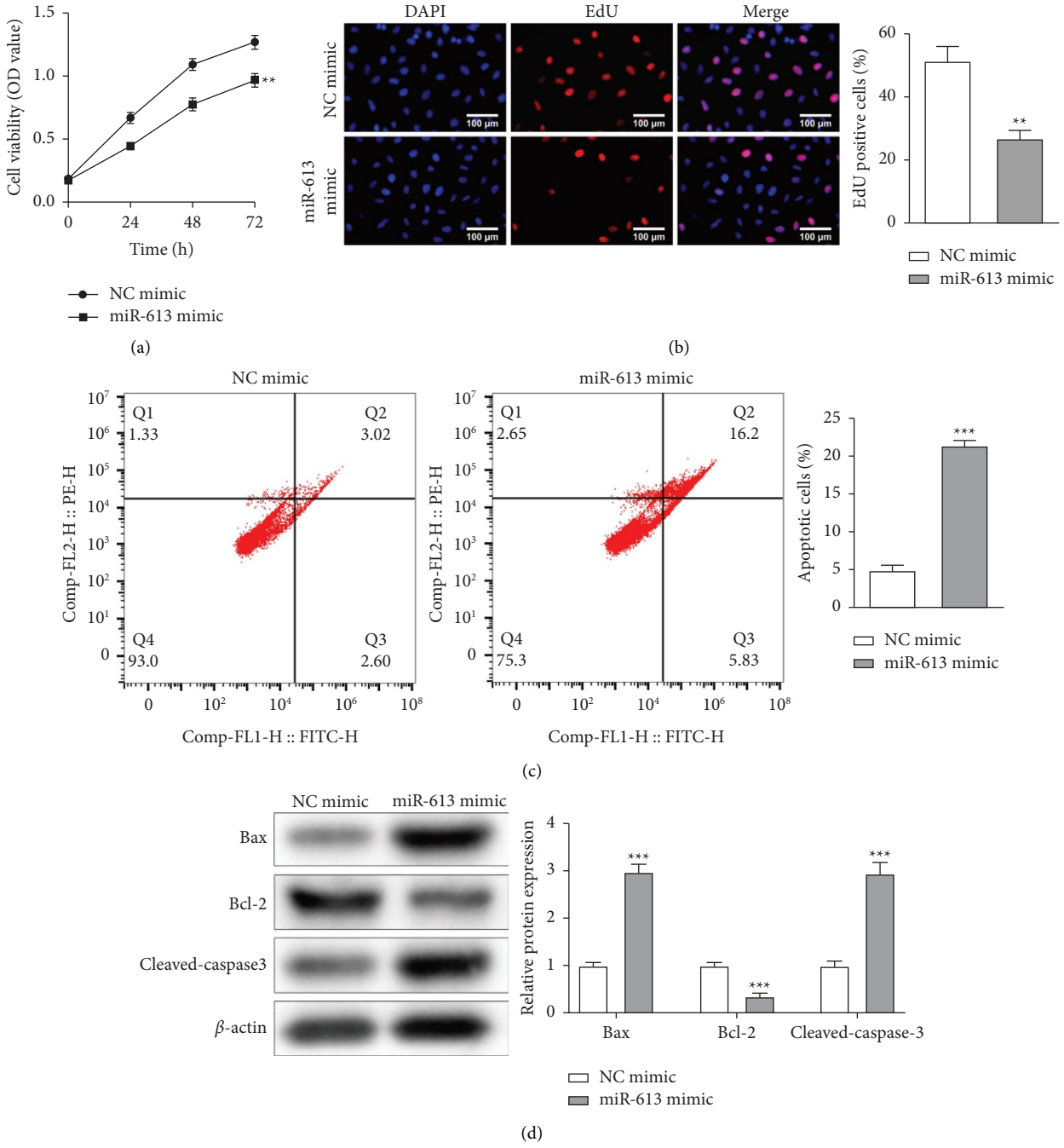

Figure 2: Analysis of miR-613 on NSCLC cell proliferation and apoptosis. miR-613 mimic was transfected into H1650 cells. (a) Evaluation of H1650 cell viability by cell counting kit-8 (CCK-8). (b) Edu method was conducted to assess H1650 cell proliferation (scale bar: 100 μm). (c) H1650 cell apoptosis was determined by flow cytometry. (d) The levels of apoptosis-related proteins Bax, Bcl2, and cleaved caspase-3 were tested by Western blot. $^{**}P < 0.01$, $^{***}P < 0.001$ *vs.* NC-mimic. NC: negative control.

Figures 6(a) and 6(b), the co-culture of M2 macrophages facilitated tumor growth, but this trend was inverted in part after the miR-613 was overexpressed in M2 macrophages. Meanwhile, Ki67 staining confirmed that the co-culture of M2 macrophages accelerated the proliferation, and the miR-613 overexpression partially reversed this trend (Figure 6(c)). On the contrary, TUNEL staining demonstrated that the co-culture of M2 macrophages restrained the apoptosis, while this restraint was partially reversed after the miR-613 was overexpressed in M2 macrophages (Figure 6(c)). Furthermore, miR-613 was decreased after co-culture of M2 macrophages, and this decrease was partially reversed by miR-613 overexpression (Figure 6(d)). These data confirmed miR-613 overexpression restrained tumor growth by repressing M2 macrophage polarization.

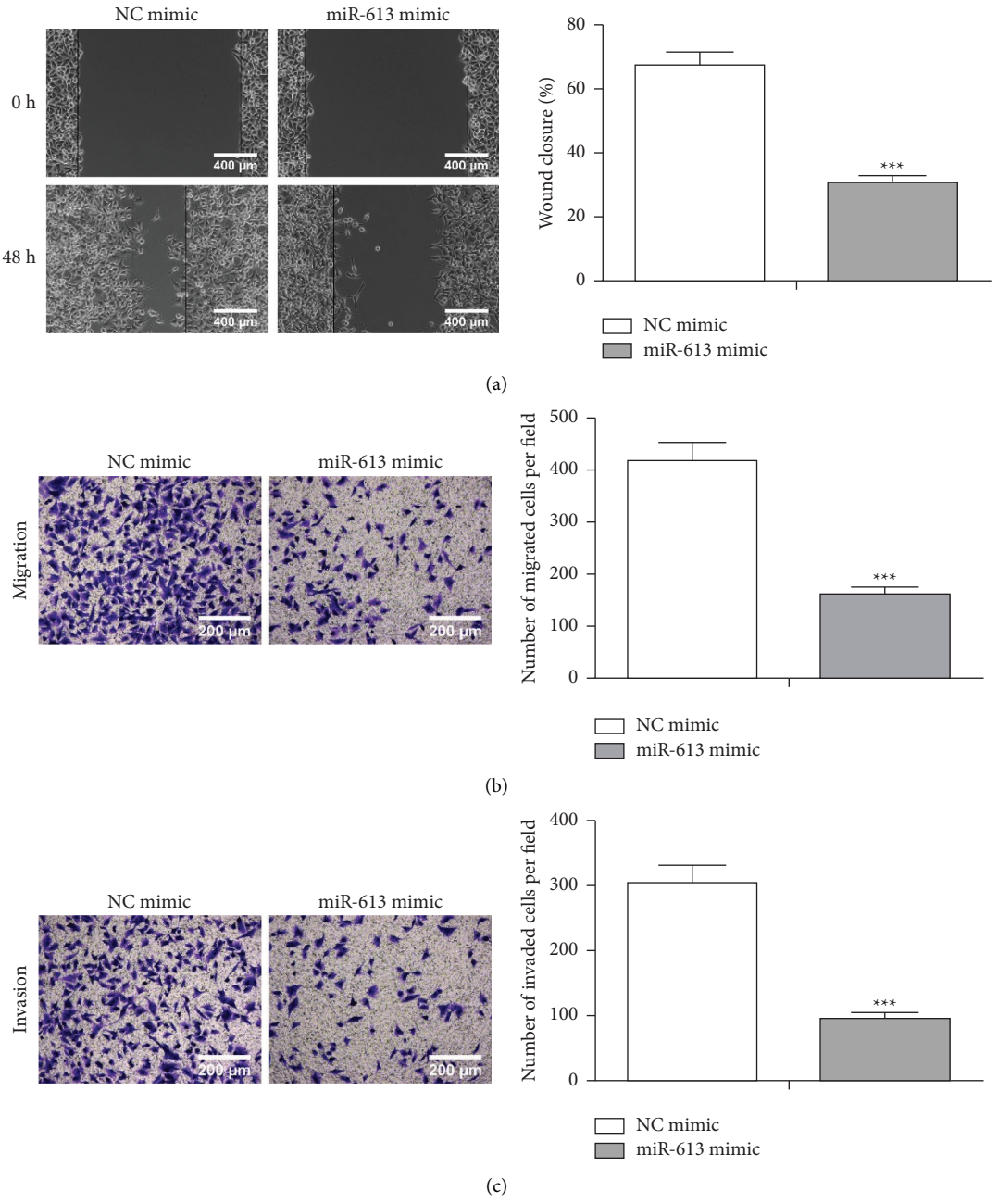

Figure 3: Regulation of miR-613 on NSCLC cell migration and invasion. miR-613 mimic and NC-mimic were transfected into H1650 cells. Wound-healing (a) (scale bar: 400 μm) and Transwell analyses (b) (scale bar: 200 μm) were conducted to evaluate H1650 cell migration. (c) The H1650 cell invasion was assessed using Transwell (scale bar: 200 μm). $^{***}P < 0.001$ *vs.* NC-mimic.

4. Discussion

The high global mortality rate from NSCLC is a major issue and the challenges of cancer-related treatment [31]. Various miRNAs are pivotal regulatory molecules in NSCLC [7, 32]. Similarly, our study authenticated that miR-613 was lessened in NSCLC. Furthermore, our research demonstrated that miR-613 overexpression restrained NSCLC cell proliferation, migration, invasion, and enhanced apoptosis. Meanwhile, we confirmed that miR-613 overexpression restrained NSCLC growth by repressing M2 macrophage polarization. The completion of this research might provide promising biomarkers for NSCLC treatment.

Accumulated evidence suggests that miR-613 is interrelated to various tumor genesis and development. For instance, miR-613 is lowly expressed in colorectal cancer and has diagnostic and prognostic functions in colorectal cancer [33]; miR-613 represses hepatocellular carcinoma cell dedifferentiation through the SOX9 signaling, which provides novel therapeutic targets for hepatocellular carcinoma [34]. It has been authenticated that miR-613 initiates NSCLC cell cycle arrest via regulating CDK4 [35]. Similarly, we verified

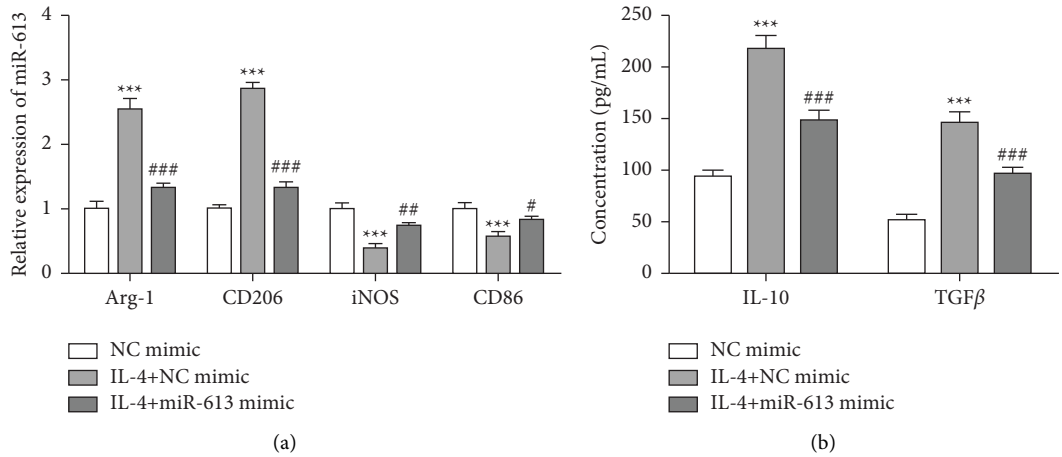

Figure 4: miR-613 regulates the M2 macrophage polarization. After differentiating THP-1 cells into macrophages with 24 h treatment of 150 nM phorbol 12-myristate 13-acetate, the cells were fostered for 48 h with 20 ng/mL IL-4 to achieve the M2 macrophages, and miR-613 mimic was transfected into M2 macrophages. (a) The expressions of Arg-1 and CD206 (markers for M2 macrophages) and iNOS and CD86 (markers for M1 macrophages) were measured using qRT-PCR. (b) The IL-10 and TGF-β levels in cell culture supernatant were tested by enzyme-linked immunosorbent assay (ELISA). $^{***}P < 0.001$ *vs.* NC-mimic. $^{\#}P < 0.05$, $^{\#\#}P < 0.01$, $^{\#\#\#}P < 0.001$ *vs.* IL-4+NC-mimic.

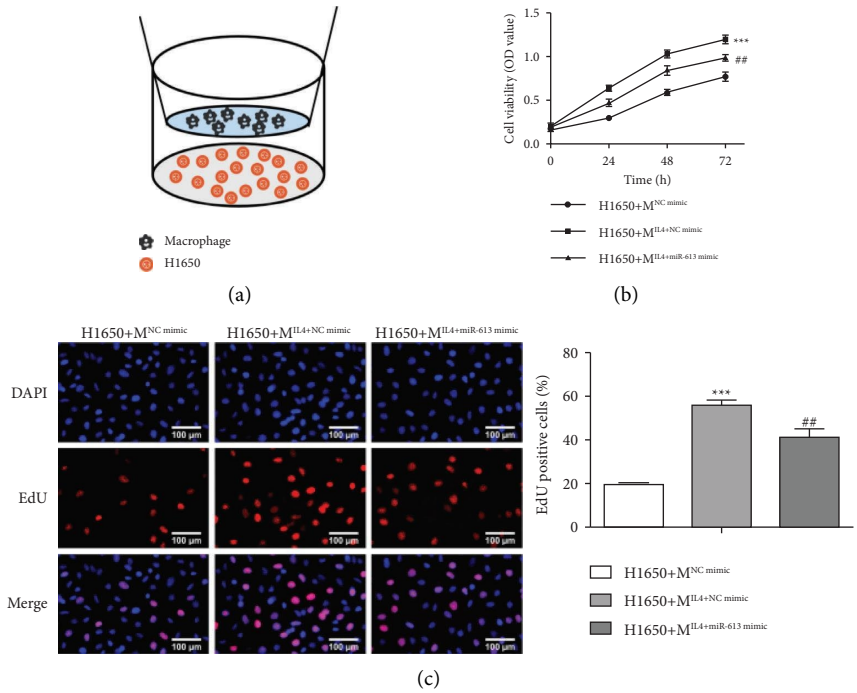

Figure 5: Continued.

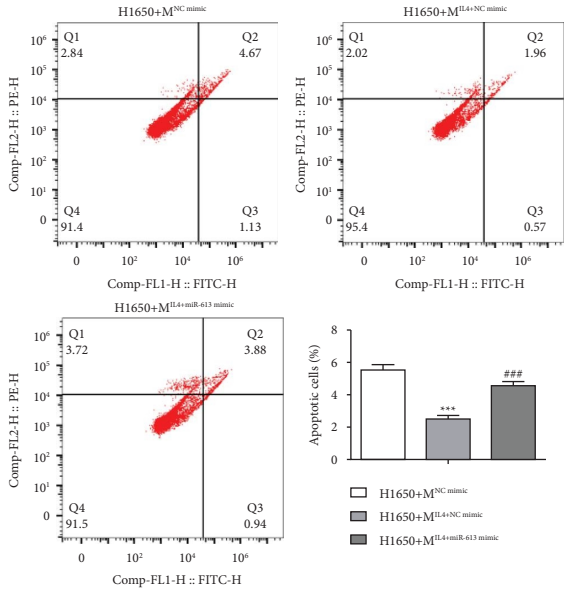

(d)

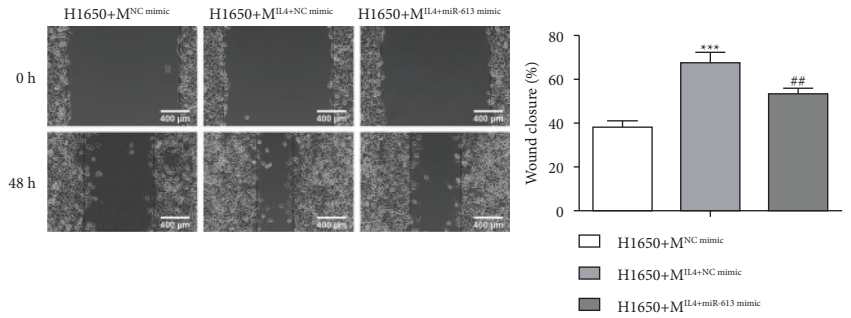

(e)

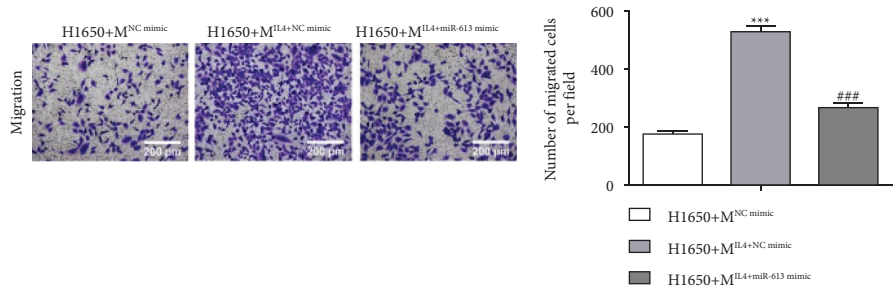

(f)

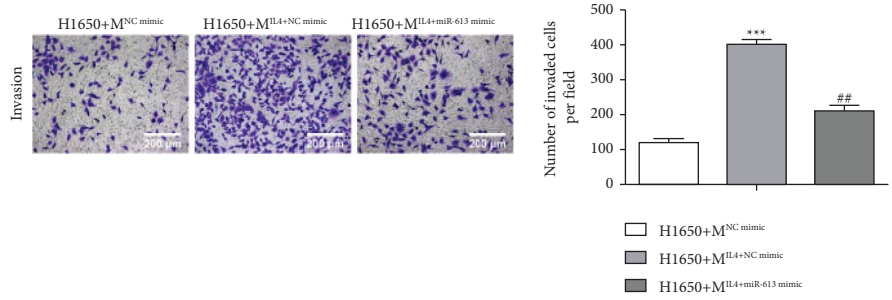

(g)

FIGURE 5: miR-613 regulates NSCLC cell growth by repressing M2 macrophage polarization. Macrophages with different treatments (as in Figure 4) were co-cultured with H1650 cells. H1650 cells were grouped: H1650+$M^{NCmimic}$, H1650+$M^{IL\text{-}4+NCmimic}$ and H1650+$M^{IL\text{-}4+miR\text{-}613mimic}$. (a) The schematic diagram of the co-culture system. (b) CCK-8 was conducted to assess H1650 cell viability. (c) Evaluation of H1650 cell proliferation by the Edu method (scale bar: 100 μm). (d) Detection of H1650 cell apoptosis by flow cytometry. (e and f) H1650 cell migration was tested using Transwell (scale bar: 200 μm) and wound-healing analyses (scale bar: 400 μm). (g) H1650 cell invasion was measured by Transwell (scale bar: 200 μm). $^{***}P < 0.001$ *vs.* H1650+$M^{NCmimic}$. $^{\#\#}P < 0.01$, $^{\#\#\#}P < 0.001$ *vs.* H1650+$M^{IL\text{-}4+NCmimic}$.

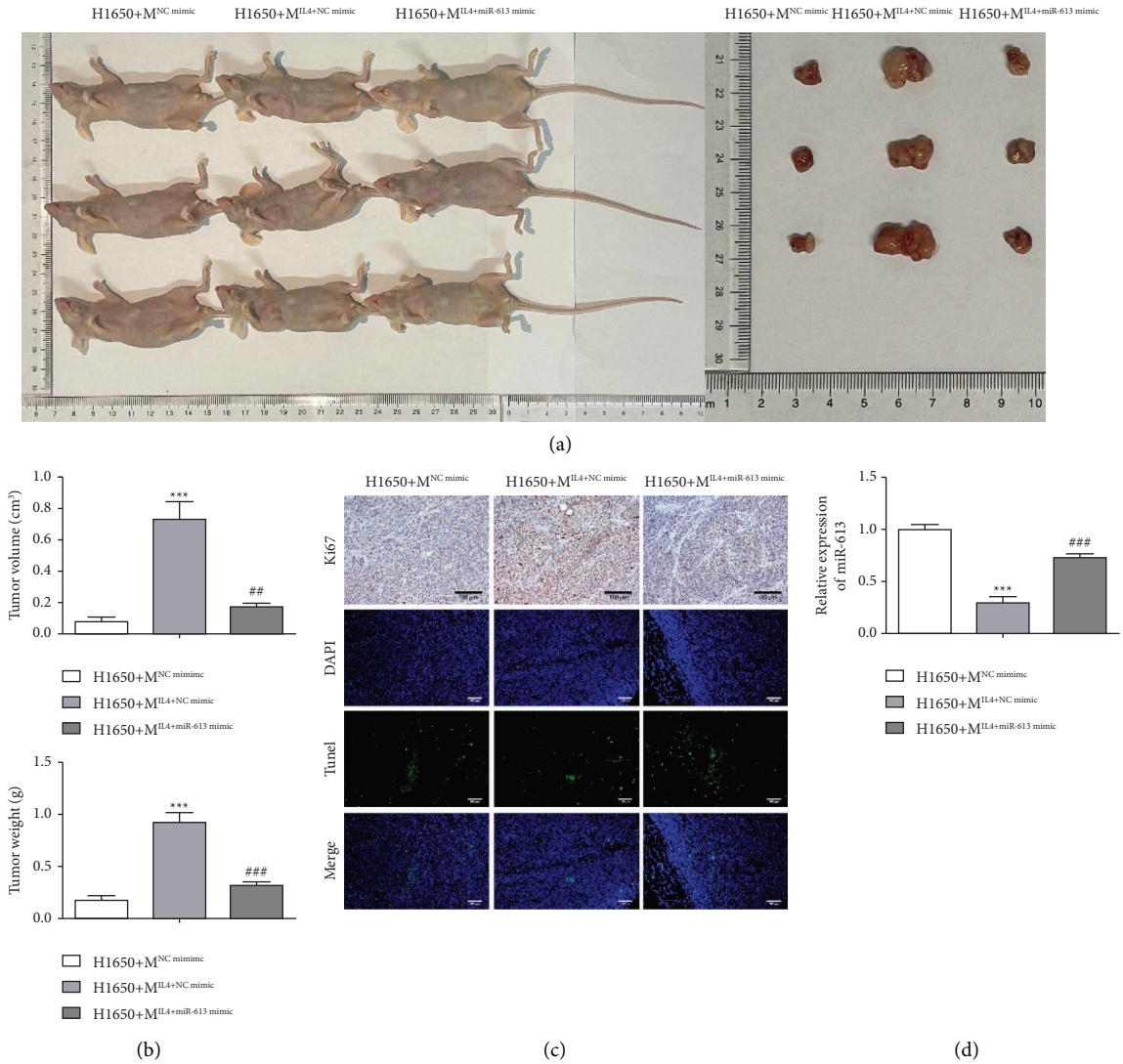

FIGURE 6: miR-613 influences tumor growth by reducing the M2 macrophage polarization *in vivo*. Macrophages with different treatments (as in Figure 4) were co-cultured with H1650 cells. H1650 cells were grouped: H1650+$M^{NCmimic}$, H1650+$M^{IL\text{-}4+\ NCmimic}$ and H1650+$M^{IL\text{-}4+miR\text{-}613mimic}$. The C57BL/6 mice were subcutaneously injected with the above H1650 cells (5×10^5 cells). (a, b) Analysis of the tumor weight. (c) The proliferation and apoptosis were analyzed by Ki-67 staining and TUNEL staining (scale bar: 100 μm). (d) miR-613 expression in tumors by qRT-PCR. $^{***}P < 0.001$ *vs.* H1650+$M^{NCmimic}$. $^{\#\#}P < 0.01$, $^{\#\#\#}P < 0.001$ *vs.* H1650+$M^{IL\text{-}4+NCmimic}$.

that miR-613 was lessened in NSCLC cells and tissues. Simultaneously, we further confirmed that the transfection of miR-613 mimic advanced cell apoptosis and weakened NSCLC cell proliferation, migration, and invasion through various gain-of-function assays, which was similar to a previous conclusion [36].

Previous reports state that macrophages with carcinogenic functions in tumor environments are considered as TAMs and typically exhibit an M2 phenotype [37, 38]. Increasing studies authenticate that M2 macrophages are interrelated to multiple tumors development. For instance, Sousa et al. confirmed that the high number of M2 macrophages is relevant to rapid proliferation and poor prognosis of human primary breast tumors [39]; Yamaguchi et al. clarified that the peritoneal TAMs polarization into M2 phenotype facilitates the gastric cancer tumor growth, prompting that intraperitoneal TAMs is a promising target for gastric cancer [40]. Recently, the pivotal function of M2 macrophage polarization in NSCLC has attracted widespread attention from researchers. M2 macrophages activate the ERK1/2/Fra-1/slug pathway through epithelial-mesenchymal transformation to accelerate the malignant development of NSCLC [41]. Puerarin reduces the M2 macrophage metastasis and polarization of NSCLC transplant-tumor-associated macrophages by inactivating MEK/ERK 1/2 signaling, thereby alleviating NSCLC [42]. Considering the critical functions of miR-613 and M2 macrophages in NSCLC, this study attempted to clarify whether miR-613 alleviated NSCLC by mediating M2 macrophage polarization. As expected, our experimental data revealed that miR-613 restrained NSCLC growth through repressing M2 macrophage polarization.

However, there are still some limitations in this study, and although, we found that miR-613 regulated NSCLC development by inhibiting M2 macrophage polarization, whether miR-613 would regulate NSCLC development by regulating downstream gene targets or oxidative stress response to inhibit M2 macrophage polarization still needs further investigation.

In general, we confirmed miR-613 overexpression enhanced apoptosis and restrained NSCLC cell proliferation, migration, and invasion. Meanwhile, miR-613 overexpression restrained NSCLC growth by repressing M2 macrophage polarization, which provides novel insights and strategies for treating NSCLC.

Data Availability

The data used to support the findings of this study of the study are available from the corresponding author upon reasonable request.

Ethical Approval

The experimental protocol was established, according to the ethical guidelines of the Helsinki Declaration. All programs about animal are approved by the Animal Ethics Committee of Affiliated Hospital of Nantong University.

Consent

All patients signed an informed consent form before performing surgery and the study was approved by the Ethics Committee of Affiliated Hospital of Nantong University.

Conflicts of Interest

The authors declare that they have no conflicts of interest.

Authors' Contributions

MJY and WZ conceived and designed the study. MMX, XH, and YYS conducted most of the experiments. MS and ZPW analyzed the data. MJY performed the literature search and data extraction. MJY drafted the manuscript. MJY and WZ finalized the manuscript. All authors read and approved the final manuscript. Mingjun Yang and Wen Zhou contributed equally to this work.

Acknowledgments

This work was supported by Nantong Science and Technology Planning Project (MS12021095).

Supplementary Materials

Supplementary Figure 1 Analysis of the miR-613 expression in M2 macrophages. After THP-1 cells were treated with 150 nM PMA for 24 h to be differentiated into macrophages, the cells were incubated with 20 ng/mL IL-4 for 48 h to achieve M2 macrophages, and miR-613 mimic was transfected into M2 macrophages. The miR-613 expression in M2 macrophages was determined using qRT-PCR. $^{***}P < 0.001$ vs. control. $^{\#\#\#}P < 0.001$ vs. IL-4+NC-mimic. (*Supplementary Materials*)

References

[1] I. Toumazis, M. Bastani, S. S. Han, and S. K. Plevritis, "Risk-Based lung cancer screening: a systematic review," *Lung Cancer*, vol. 147, pp. 154–186, 2020.

[2] R. A. de Mello, N. M. Neves, H. Tadokoro, G. A. Amaral, P. Castelo-Branco, and V. A. Zia, "New target therapies in advanced non-small cell lung cancer: a review of the literature and future perspectives," *Journal of Clinical Medicine*, vol. 9, no. 11, p. 3543, 2020.

[3] R. Ye, R. Tang, S. Gan et al., "New insights into long non-coding RNAs in non-small cell lung cancer," *Biomedicine & Pharmacotherapy*, vol. 131, Article ID 110775, 2020.

[4] M. Liao and L. Peng, "MiR-206 may suppress non-small lung cancer metastasis by targeting CORO1C," *Cellular and Molecular Biology Letters*, vol. 25, no. 1, p. 22, 2020.

[5] D. Kauffmann-Guerrero, K. Kahnert, and R. M. Huber, "Treatment sequencing for anaplastic lymphoma kinase-rearranged non-small-cell lung cancer," *Drugs*, vol. 81, no. 1, pp. 87–100, 2021.

[6] A. Lin, T. Wei, H. Meng, P. Luo, and J. Zhang, "Role of the dynamic tumor microenvironment in controversies regarding immune checkpoint inhibitors for the treatment of non-small cell lung cancer (NSCLC) with EGFR mutations," *Molecular Cancer*, vol. 18, no. 1, p. 139, 2019.

[7] S. S. Lee and Y. K. Cheah, "The interplay between MicroRNAs and cellular components of tumour microenvironment (TME) on non-small-cell lung cancer (NSCLC) progression," *Journal of Immunology Research*, vol. 2019, Article ID 3046379, 12 pages, 2019.

[8] M. De Palma, D. Biziato, and T. V. Petrova, "Microenvironmental regulation of tumour angiogenesis," *Nature Reviews Cancer*, vol. 17, no. 8, pp. 457–474, 2017.

[9] S. J. Turley, V. Cremasco, and J. L. Astarita, "Immunological hallmarks of stromal cells in the tumour microenvironment," *Nature Reviews Immunology*, vol. 15, no. 11, pp. 669–682, 2015.

[10] T. Chanmee, P. Ontong, K. Konno, and N. Itano, "Tumor-associated macrophages as major players in the tumor microenvironment," *Cancers*, vol. 6, no. 3, pp. 1670–1690, 2014.

[11] F. B. A. Dessouki, R. C. Kukreja, and D. K. Singla, "Stem cell-derived exosomes ameliorate doxorubicin-induced muscle toxicity through counteracting pyroptosis," *Pharmaceuticals*, vol. 13, no. 12, p. 450, 2020.

[12] Y. Lin, J. Xu, and H. Lan, "Tumor-associated macrophages in tumor metastasis: biological roles and clinical therapeutic applications," *Journal of Hematology & Oncology*, vol. 12, no. 1, p. 76, 2019.

[13] H. Li, N. Huang, W. Zhu et al., "Modulation the crosstalk between tumor-associated macrophages and non-small cell lung cancer to inhibit tumor migration and invasion by ginsenoside Rh2," *BMC Cancer*, vol. 18, no. 1, p. 579, 2018.

[14] R. Sumitomo, T. Hirai, M. Fujita, H. Murakami, Y. Otake, and C. L. Huang, "M2 tumor-associated macrophages promote tumor progression in non-small-cell lung cancer," *Experimental and Therapeutic Medicine*, vol. 18, no. 6, pp. 4490–4498, 2019.

[15] R. Narayanan and G. Schratt, "miRNA regulation of social and anxiety-related behaviour," *Cellular and Molecular Life Sciences*, vol. 77, no. 21, pp. 4347–4364, 2020.

[16] S. Sur, R. Steele, X. Shi, and R. B. Ray, "miRNA-29b inhibits prostate tumor growth and induces apoptosis by increasing bim expression," *Cells*, vol. 8, no. 11, p. 1455, 2019.

[17] M. Wu, G. Wang, W. Tian, Y. Deng, and Y. Xu, "MiRNA-based therapeutics for lung cancer," *Current Pharmaceutical Design*, vol. 23, no. 39, pp. 5989–5996, 2018.

[18] L. Lin, H. Lin, L. Wang, B. Wang, X. Hao, and Y. Shi, "miR-130a regulates macrophage polarization and is associated with non-small cell lung cancer," *Oncology Reports*, vol. 34, no. 6, pp. 3088–3096, 2015.

[19] Z. Li, C. Feng, J. Guo, X. Hu, and D. Xie, "GNAS-AS1/miR-4319/NECAB3 axis promotes migration and invasion of non-small cell lung cancer cells by altering macrophage polarization," *Functional Integrative Genomics*, vol. 20, no. 1, pp. 17–28, 2020.

[20] H. Ji and N. J. Hu, "MiR-613 blocked the progression of cervical cancer by targeting LETM1," *European Review for Medical and Pharmacological Sciences*, vol. 24, no. 12, pp. 6576–6582, 2020.

[21] H. Ying, Y. Jin, Y. Guo et al., "Long non-coding RNA NUT family member 2A-antisense RNA 1 sponges microRNA-613 to increase the resistance of gastric cancer cells to matrine through regulating oxidative stress and vascular endothelial growth factor A," *Aging (Albany NY)*, vol. 14, no. 12, pp. 5153–5162, 2022.

[22] X. Su, C. Gao, X. Feng, and M. Jiang, "miR-613 suppresses migration and invasion in esophageal squamous cell carcinoma via the targeting of G6PD," *Experimental and Therapeutic Medicine*, vol. 19, no. 4, pp. 3081–3089, 2020.

[23] J. Luo, Y. Jin, M. Li, and L. Dong, "Tumor suppressor miR-613 induces cisplatin sensitivity in non-small cell lung cancer cells by targeting GJA1," *Molecular Medicine Reports*, vol. 23, no. 5, p. 385, 2021.

[24] X. Tian, Y. Wu, Y. Yang et al., "Long noncoding RNA LINC00662 promotes M2 macrophage polarization and hepatocellular carcinoma progression via activating Wnt/β-catenin signaling," *Molecular Oncology*, vol. 14, no. 2, pp. 462–483, 2020.

[25] K. J. Livak and T. D. Schmittgen, "Analysis of relative gene expression data using real-time quantitative PCR and the $2-\Delta\Delta CT$ method," *Methods*, vol. 25, no. 4, pp. 402–408, 2001.

[26] H. Fu, J. Zhang, and M. Huang, "Topiroxostat ameliorates oxidative stress and inflammation in sepsis-induced lung injury," *Zeitschrift für Naturforschung C*, vol. 75, no. 11-12, pp. 425–431, 2020.

[27] W. Ren, J. Hou, C. Yang et al., "Extracellular vesicles secreted by hypoxia pre-challenged mesenchymal stem cells promote non-small cell lung cancer cell growth and mobility as well as macrophage M2 polarization via miR-21-5p delivery," *Journal of Experimental & Clinical Cancer Research*, vol. 38, no. 1, p. 62, 2019.

[28] L. Cao, X. Che, X. Qiu et al., *Cancer Management and Research*, vol. 11, pp. 6125–6138, 2019.

[29] D. Zhu, T. K. Johnson, Y. Wang et al., "Macrophage M2 polarization induced by exosomes from adipose-derived stem cells contributes to the exosomal proangiogenic effect on mouse ischemic hindlimb," *Stem Cell Research & Therapy*, vol. 11, no. 1, p. 162, 2020.

[30] Y. Bi, J. Chen, F. Hu, J. Liu, M. Li, and L. Zhao, "M2 macrophages as a potential target for antiatherosclerosis treatment," *Neural Plasticity*, vol. 2019, Article ID 6724903, 21 pages, 2019.

[31] L. Shi, B. Zhang, X. Sun et al., "MiR-204 inhibits human NSCLC metastasis through suppression of NUAK1," *British Journal of Cancer*, vol. 111, no. 12, pp. 2316–2327, 2014.

[32] J. F. Sui, "MiRNA-30 play an important role in non-small cell lung cancer (NSCLC)," *Clinical Laboratory*, vol. 66, no. 4, 2020.

[33] M. N. Eldaly, F. M. Metwally, W. G. Shousha, A. S. El-Saiid, and S. S. Ramadan, "Clinical potentials of miR-576-3p, miR-613, NDRG2 and YKL40 in colorectal cancer patients," *Asian Pacific Journal of Cancer Prevention*, vol. 21, no. 6, pp. 1689–1695, 2020.

[34] Z. Q. Zheng, Z. X. Li, G. Q. Zhou et al., "Long noncoding RNA FAM225A promotes nasopharyngeal carcinoma tumorigenesis and metastasis by acting as ceRNA to sponge miR-590-3p/miR-1275 and upregulate ITGB3," *Cancer Research*, vol. 79, no. 18, pp. 4612–4626, 2019.

[35] D. Li, D. Q. Li, D. Liu, and X. J. Tang, "MiR-613 induces cell cycle arrest by targeting CDK4 in non-small cell lung cancer," *Cellular Oncology*, vol. 39, no. 2, pp. 139–147, 2016.

[36] D. Li, D. Meng, and R. Niu, "Exosome-Reversed chemoresistance to cisplatin in non-small lung cancer through transferring miR-613," *Cancer Management and Research*, vol. 12, pp. 7961–7972, 2020.

[37] J. Kim and J. S. Bae, "Tumor-associated macrophages and neutrophils in tumor microenvironment," *Mediators of Inflammation*, vol. 2016, Article ID 6058147, 11 pages, 2016.

[38] Y. Yuan, Y. C. Jiang, C. K. Sun, and Q. M. Chen, "Role of the tumor microenvironment in tumor progression and the clinical applications (Review)," *Oncology Reports*, vol. 35, no. 5, pp. 2499–2515, 2016.

[39] S. Sousa, R. Brion, M. Lintunen et al., "Human breast cancer cells educate macrophages toward the M2 activation status," *Breast Cancer Research*, vol. 17, no. 1, p. 101, 2015.

[40] T. Yamaguchi, S. Fushida, Y. Yamamoto et al., "Tumor-associated macrophages of the M2 phenotype contribute to progression in gastric cancer with peritoneal dissemination," *Gastric Cancer*, vol. 19, no. 4, pp. 1052–1065, 2016.

[41] Z. Guo, J. Song, J. Hao et al., "M2 macrophages promote NSCLC metastasis by upregulating CRYAB," *Cell Death and Disease*, vol. 10, no. 6, p. 377, 2019.

[42] H. Kang, J. Zhang, B. Wang et al., "Puerarin inhibits M2 polarization and metastasis of tumor-associated macrophages from NSCLC xenograft model via inactivating MEK/ERK 1/2 pathway," *International Journal of Oncology*, vol. 50, no. 2, pp. 545–554, 2017.

Hindawi
Journal of Oncology
Volume 2023, Article ID 3077180, 12 pages
https://doi.org/10.1155/2023/3077180

Research Article

The Role of Nomogram Based on the Combination of Ultrasound Parameters and Clinical Indicators in the Degree of Pathological Remission of Breast Cancer

Huangjing Chen,[1] Hongyan Qian,[2] Guifang Chen,[1] Pengfei Zhu,[3] Chunjuan Sun,[3] Xiaotian Wu,[3] and Ying He[3]

[1]*Medical College of Nantong University, Nantong 226361, Jiangsu, China*
[2]*Key Laboratory of Cancer Research Center Nantong, Tumor Hospital Affiliated to Nantong University, Nantong 226006, Jiangsu, China*
[3]*Department of Ultrasound, Tumor Hospital Affiliated to Nantong University, Nantong 226006, Jiangsu, China*

Correspondence should be addressed to Ying He; cxh701023@163.com

Received 21 September 2022; Revised 17 October 2022; Accepted 27 January 2023; Published 16 February 2023

Academic Editor: İbrahim Hakkı Cigerci

Background. The mortality rate of breast cancer (BC) ranks first among female tumors worldwide and presents a trend of younger age, which poses a great threat to women's health and life. Neoadjuvant chemotherapy (NAC) for breast cancer is defined as the first step of treatment for breast cancer patients without distant metastasis before planned surgical treatment or local treatment with surgery and radiotherapy. According to the current NCCN guidelines, patients with different molecular types of BC should receive neoadjuvant chemotherapy (NAC), which can not only achieve tumor downstaging, increase the chance of surgery, and improve the breast-conserving rate. In addition, it can identify new genetic pathways and drugs related to cancer, improve patient survival rate, and make new progress in breast cancer management. *Objective*. To explore the role of the nomogram established by the combination of ultrasound parameters and clinical indicators in the degree of pathological remission of breast cancer. *Methods*. A total of 147 breast cancer patients who received neoadjuvant chemotherapy and elective surgery in the Department of Ultrasound, Nantong Cancer Hospital, from May 2014 to August 2021 were retrospectively included. Postoperative pathological remission was divided into two groups according to Miller–Payne classification: no significant remission group (NMHR group, $n = 93$) and significant remission group (MHR group, $n = 54$). Clinical characteristics of patients were recorded and collected. The multivariate logistic regression model was used to screen the information features related to the MHR group, and then, a nomogram model was constructed; ROC curve area, consistency index (C-index, CI), calibration curve, and H-L test were used to evaluate the model. And the decision curve is used to compare the net income of the single model and composite model. *Results*. Among 147 breast cancer patients, 54 (36.7%) had pathological remission. Multivariate logistic regression showed that ER, reduction/disappearance of strong echo halo, Adler classification after NAC, PR + CR, and morphological changes were independent risk factors for pathological remission ($P < 0.05$). Based on these factors, the nomogram was constructed and verified. The area under the curve (AUC) and CI were 0.966, the sensitivity and specificity were 96.15% and 92.31%, and the positive predictive value (PPV) and negative predictive value (NPV) were 87.72% and 97.15%, respectively. The mean absolute error of the agreement between the predicted value and the real value is 0.026, and the predicted risk is close to the actual risk. In the range of HRT of about 0.0~0.9, the net benefit of the composite evaluation model is higher than that of the single model. H-L test results showed that $\chi^2 = 8.430$, $P = 0.393 > 0.05$. *Conclusion*. The nomogram model established by combining the changes of ultrasound parameters and clinical indicators is a practical and convenient prediction model, which has a certain value in predicting the degree of pathological remission after neoadjuvant chemotherapy.

1. Introduction

Breast cancer (BC) has the highest mortality rate among female tumors worldwide, with an incidence rate of about 23%, posing a great threat to women's health and life [1, 2]. Neoadjuvant chemotherapy (NAC) is an important part of comprehensive therapy for BC patients with different molecular types, which can not only achieve tumor downstaging, increase the chance of surgery, and improve the breast-conserving rate. In addition, new genetic pathways and drugs related to cancer can be identified to improve the survival rate of patients and make new progress in BC management [3–7]. At present, the WHO and Response Evaluation Criteria In Solid Tumors (RECIST) are the most tumors used in clinical evaluation of NAC tumors [8–9], and all of them have their own advantages. The gold standard for NAC response has always been pathological assessment [10], including residual cancer burden (RCB) [11] and Miller-Payne score system [12]. Relevant data show that the pathological complete remission rate is 3% to 30% [13], not all patients are sensitive to NAC, and some patients may gradually develop drug resistance during chemotherapy, which limits the clinical efficacy of drugs and leads to treatment failure. Some patients (less than 5%) may progress during neoadjuvant therapy and even lose the opportunity to receive surgery [14]. Therefore, it is more and more important to accurately monitor and evaluate the efficacy of NAC and to observe the sensitivity of patients with advanced breast cancer to chemotherapy drugs, so as to realize individualized treatment and improve the breast-conserving rate and survival period of patients [15]. Imaging examination can not only evaluate the efficacy, pathological status, and prognosis of NAC but also help to select the most appropriate surgical method. Multiple imaging evaluation methods, including magnetic resonance imaging (MRI), computed tomography (CT), positron emission tomography (PET-CT), mammography (MM), and ultrasound (US), have been widely used around the world. Current studies generally believe that MRI is more objective than the US, and its characteristics of tomography make the lesion display more accurately and have advantages in predicting the degree of pathological remission and prognosis of the primary lesion. However, due to the high cost, it has not been fully popularized around the world, especially in developing countries [16–19]. At the same time, some studies have shown that breast cancer patients with ER negative before NAC and high expression of Ki67 are more sensitive to chemotherapy and benefit more after chemotherapy, which may be sensitive factors to predict the efficacy of chemotherapy [20, 21]. Studies have shown that many changes will occur in ultrasound images of patients with pcR after NAC, such as PR and CR in clinical efficacy evaluation, attenuation and disappearance of posterior echo, elevation of internal echo, narrowing or disappearance of strong echo halo around the tumor, all of which are effective related indicators of tumor NAC [22]. In order to develop a clinical applicable, cost-effective, and easy to promote the new approach, this study will be commonly used two-dimensional gray-scale ultrasound, color Doppler flow imaging (CDFI), and clinical common testing of immunohistochemical and serum index together, to develop and validate based on ultrasonic features and clinical pathology nomogram, and to predict the postoperative pathological remission after NAC. Based on the changes of various parameters in the MHR group after the end of NAC, we believe that the changes in these ultrasound parameters most intuitively reflect the changes of tumors during the entire process of NAC and are closely related to the degree of pathological remission. The aim of this study was to explore the role of the nomogram established by the combination of ultrasound parameters and clinical indicators in the degree of pathological remission of breast cancer.

2. Materials and Methods

2.1. Basic Information. This study retrospectively collected 147 breast cancer patients who underwent neoadjuvant chemotherapy and elective surgery in the Ultrasound Department of Nantong Cancer Hospital from May 2014 to August 2021. Inclusion criteria were as follows: ① female; ② primary breast cancer, confirmed by ultrasound biopsy and in line with the diagnostic criteria of "Chinese Society of Clinical Oncology Breast Cancer Guideline version 2021: updates and interpretations" [23]; ③ TNM stage II to III, no disease distant metastases to contralateral or other organs. Exclusion criteria were as follows: ① patients who have received other related treatments before neoadjuvant chemotherapy; ② patients with multiple lesions and malignant tumors of other organs; ③ patients with incomplete clinical and imaging data; ④ the chemotherapy cycle is not within 4–8 cycles (Figure 1). This study has passed the ethics approval of the Medical Ethics Committee of Nantong Cancer Hospital, and patients' informed consent forms are exempted due to the retrospective nature of this study.

2.2. Methods

2.2.1. Data Collection. Demographic and clinical data of patients were collected, including age, gender, menopause, history of childbearing and breastfeeding, family history of breast cancer (referring to immediate family members, including mothers, daughters, and sisters who have breast cancer), lymph node metastasis, and NAC course of treatment, NAC treatment plan, and breast cancer pathological type and stage.

2.2.2. Ultrasound Image Acquisition and Evaluation. Before and after neoadjuvant chemotherapy, 2D gray-scale ultrasound and color Doppler examination were performed. Ultrasound-related parameters were collected, including diameter, morphology, aspect ratio, hyperechoic halo, calcification, tumor boundary, internal echo of the mass, posterior echo, Adler grade, and RI resistance index before and after NAC treatment.

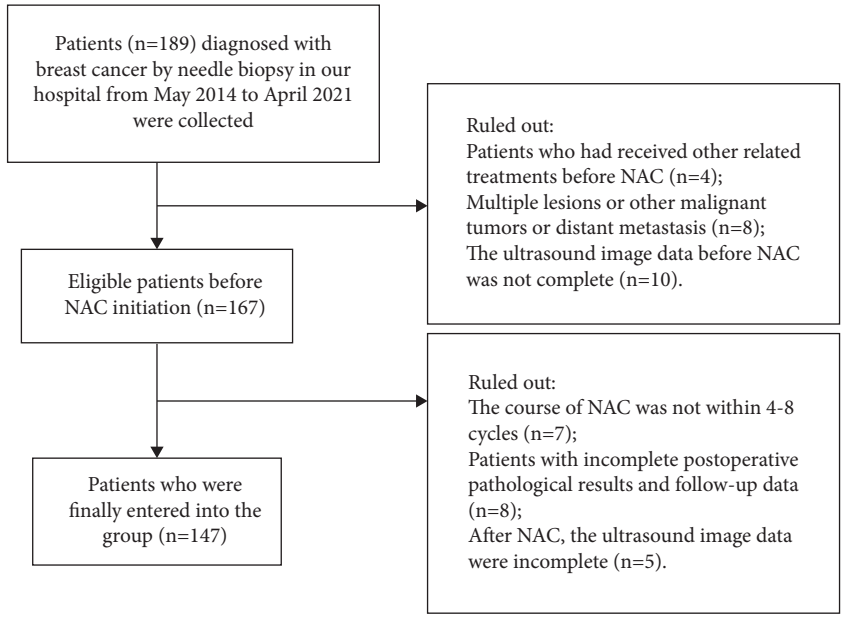

Figure 1: Flowchart of the study.

Diameter is defined as the maximum diameter line. According to the efficacy evaluation criteria for solid tumors, the efficacy was divided into four parts by the change of focal diameter; complete response (CR) : all target lesions disappear and no new lesions appear; partial response (PR): the total baseline longest diameter of all target lesions was reduced by ≥30%; progression disease (PD): the total baseline maximum diameter of all target lesions increased by ≥20%; and stable disease (SD): the total length of baseline diameter of all target lesions decreased but did not reach PR or increased but did not reach PD. CR and PR were considered to have significant therapeutic effects, while SD and PD were not.

Morphological change observation whether the morphology becomes regular was defined as the shape of the mass becomes more regular after the end of NAC, which can be described by geometric shapes, with fewer lobulations and no angular protrusions.

Aspect ratio: an aspect ratio <1 indicates that the long axis of the lump is parallel to the skin and an aspect ratio >1 indicates that the front and rear diameter is greater than the horizontal diameter. The aspect ratio changes the anterior and posterior diameter and horizontal meridian of the mass change.

Calcification changes refer to the increase in the number of strong echo spots in the mass on two-dimensional gray-scale ultrasound images compared with that before NAC.

Tumor boundary changes refer to the fuzzy, angular, minute lobulation, and burr of the original sharp and clear tumor edges after the end of NAC.

Internal echogenicity: compared with the glandular tissue of the breast to determine the echogenicity of the mass, it can be classified as very low, low, mixed, or isoechoic. Echogenicity refers to the increased echogenicity of the mass compared to that before the onset of NAC.

Posterior echo attenuation is defined as the contrast between the echo in the depth of the tumor and the tissue echo at the same depth in the area around the tumor on the same section, which is lower than the tissue echo at the same depth in the surrounding area. It is generally believed that posterior echo attenuation can represent malignant signs. Similar ones are said to have no change in rear echo. The change of the posterior echo was located as an enhancement of the posterior echo compared to the ultrasound image before the NAC began.

Adler grading observes the distribution and richness of blood flow, finds the section with the most abundant blood flow, calculates the number of blood vessels, and defines the blood flow characteristics according to the semiquantitative grading of Adler: Level 0: no blood flow in the lesion; Level I: a small amount of blood flow, with 1 or 2 punctured or thin rod blood flow; Grade II: moderate blood flow, one major blood vessel can be seen, its length is close to or beyond the radius of the lesion or 3~4 punctured or fine rod-shaped blood vessels; Grade III: abundant blood flow, visible more than 4 blood vessels or interconnected, intertwined into a network. The definition of Alder grading change is whether grading decreases after NAC.

Resistance index (RI) is the ratio of the difference between peak systolic and end diastolic velocity to peak systolic velocity, reflecting the distal resistance index of the vessel. RI was measured before and after NAC treatment to determine whether RI decreased.

2.2.3. Collection and Evaluation of Immunohistochemical and Serum Indicators. The biopsy specimen of the breast mass was fixed and sent to the pathology department for immunohistochemistry. The results of immunohistochemical staining were evaluated by two senior pathologists, respectively, in a double-blind method with reference to the

staining evaluation criteria proposed by Fromowitz et al. The percentage of positive cells in tumor cells was calculated to evaluate the status of ER (estrogen receptor), PR (progesterone receptor), proliferative nuclear antigen KI67, and human epidermal growth factor receptor C-erbb-2. ER, PR ≥1% was defined as ER, PR positive; Her-2 (0~+) was determined as negative, her-2 (3+) was determined as positive, and HER-2(2+) was determined by fluorescence in situ hybridization. K-67 ≥ 20% was highly expressed.

After the first admission, 3 ml fasting venous blood was collected from the subjects in the morning before NAC, and the levels of CEA (carcinoembryonic antigen), sugar antigen CA153, sugar antigen CA125, and sugar antigen 50CA50 were determined by electrochemiluminescence immunoassay. After the treatment of NAC, the above indicators were tested again, and the results of the two tests were recorded.

2.3. Grouping and Evaluation. The outcome of this study was the degree of postoperative pathological remission after NAC. The degree of postoperative pathological remission was evaluated according to Miller–Payne's modified grading criteria for pathological response. Grade I: no change or slight change in tumor cells, no overall reduction, or no significant change; Grade II: the number of tumor cells decreased by <30%; Grade III: tumor cells reduced by 30%~90%; Grade IV: reduction of tumor cells >90%, with only small clusters or widely dispersed residual cells; Grade V: no malignant cells in the tumor site, only fibrotic stroma. Grade I to III were nonmajor histological response (NMHR) groups, and grade IV to V were major histological response (MHR) groups.

2.4. Statistical Methods. SPSS 26.0 (Statistical Product and Service Solutions) and R Studio software were used for statistical analysis, Shapiro–Wilk test was used to test the normality of the data, and measurement data subject to normal distribution were expressed as mean ± standard deviation (mean ± SD). Measurement data that do not obey normal distribution are described by quartile M (P25, P75); enumeration data were described by [n(%)]; two independent samples t-test was used to compare the measurement data of the two groups with normal distribution, and Mann–Whitney U test was used to compare the measurement data of the two groups. The chi-square test was used for the comparison, and the variables with $P < 0.05$ in the univariate analysis results were used as independent variables in the multivariate analysis and were included in the multivariate logistic regression model analysis. The predicted probability of disease and the actual situation were plotted on the ROC curve, and the area under the curve was calculated. The independent risk factors were introduced into R Studio to establish a nomogram model for individualized prediction of disease, and the Bootstrap self-sampling method was used to conduct internal validation of the nomogram model. To measure the degree of discrimination of the model, the Hosmer–Lemeshow test is used to evaluate the model and the calibration curve to measure the degree of calibration of the model and used the decision curve to compare the net returns of the composite model and the single model.

3. Results

3.1. Baseline Data. From May 2014 to August 2021, a total of 189 candidates from Nantong Cancer Hospital were collected, and a total of 147 candidates met the inclusion criteria, including 93 in the NMHR group and 54 in the MHR group. The age of the NMHR group was greater than that of the MHR group ($P = 0.009$). The rate of treatment ≥6 periods in the MHR group was higher than that in the NMHR group ($P = 0.015$). The MHR group and NMHR group had different treatment regimens ($P < 0.001$). The positive rate of ER in the NMHR group was higher than that in the MHR group ($P < 0.001$). The positive rate of PR in the NMHR group was higher than that in the MHR group ($P < 0.001$). The positive rate of Ki67 was higher than that in the NMHR group ($P = 0.010$) as shown in Table 1.

3.2. Comparative Analysis of Differences between Ultrasound and Serum Indexes before and after Treatment. Table 2 shows that the hyperechoic halo rate of the MHR group before treatment was higher than that of the NMHR group ($P < 0.001$); the posterior echo attenuation rate of the NMHR group before treatment was higher than that of the MHR group ($P = 0.013$); MHR was displayed before and after treatment; Adler grades were different between the MHR group and NMHR group (both $P < 0.001$); RI and CA153 in the NMHR group were higher than those in the MHR group before treatment ($P < 0.001$ and $P = 0.003$, respectively). After treatment, the hyperechoic halo rate of the NMHR group was higher than that of the MHR group ($P < 0.001$); the diameter, RI, CEA, and CA153 of the NMHR group were higher than those of the MHR group after treatment ($P < 0.001$, $P < 0.001$, $P = 0.003$ and $P = 0.006$) as shown in Table 2.

3.3. Comparative Analysis of the Changes in Ultrasound Parameters between the NMHR Group and the MHR Group. Table 3 shows that in the MHR group, the diameter changes reaching PR + CR, regular morphological changes, narrowing/disappearance of hyperechoic halos, clear borders, posterior echo changes, decreased blood flow grade, and decreased RI were higher than those of the NMHR group (all $P < 0.05$) as shown in Table 3.

3.4. Multivariate Analysis of the Degree of Pathological Remission. The results of single-factor analysis of $P < 0.05$ variables as a multifactor analysis of the independent variable have a diameter change, shape change rules, strong echo halo narrow/disappear, boundary clear, rear echo change, blood flow and RI level lower eight indicators, binary classification multivariable logistic regression analysis, screening method of the independent variables selection method step by step forward. The results show that ER, narrowing/disappearance of strong echo halo, Adler

Table 1: Basic demographic data of patients.

Demographic indicators		NMHR ($n = 93$)	MHR ($n = 54$)	P
Age (years)		57.0 (49.0, 63.5)	52.5 (48.0, 57.0)	0.009
Whether menopause	No	49 (52.7)	33 (61.1)	0.322
	Yes	44 (47.3)	21 (38.9)	
History of birth and lactation	No	6 (6.5)	0 (0.0)	0.141
	Yes	87 (93.5)	54 (100.0)	
Family history	No	91 (97.8)	54 (100.0)	0.278
	Yes	2 (2.2)	0 (0.0)	
Lymph node metastasis	No	22 (23.9)	14 (25.9)	0.785
	Yes	70 (76.1)	40 (74.1)	
Period of treatment	<6 issues	39 (41.9)	12(22.2)	0.015
	≥6 periods	54 (58.1)	42 (77.8)	
Program	TAC	47 (50.5)	20 (37.0)	<0.001
	TCbHP	2 (2.2)	13 (24.1)	
	AT	11 (11.8)	8 (14.8)	
	TP	4 (4.3)	5 (9.3)	
	AC	8 (8.6)	1 (1.9)	
	TC	21 (22.6)	7 (13.0)	
Pathological type	Catheter	80 (86.0)	45 (83.3)	0.728
	Leaflet	6 (6.5)	3 (5.6)	
	Myeloid	4 (4.3)	2 (3.7)	
	Unknown	3 (3.2)	4 (7.4)	
ER	Feminine	32 (35.2)	39 (75.0)	<0.001
	Positive	59 (64.8)	13 (25.0)	
PR	Feminine	51 (56.0)	46 (88.5)	<0.001
	Positive	40 (44.0)	6 (11.5)	
CerbB-2	Feminine	7 (7.6)	3 (5.6)	0.893
	Positive	85 (92.4)	51 (94.4)	
Ki67	Feminine	20 (22.2)	3 (5.8)	0.010
	Positive	70 (77.8)	49 (94.2)	

classification after NAC, PR + CR, and morphological change rule enter the model. The response rate of ER positive was 0.176 times that of negative (OR = 0.176, 95%CI: 0.046~0.663). The remission rate of hyperechoic halo narrowing/disappearance was 10.661 times that of no narrowing/disappearing echogenic halo (OR = 10.661, 95% CI: 2.608~43.568). Each time Adler increased by one grade, and the remission rate became 0.129 times the original (OR = 0.129, 95% CI: 0.050~0.333). The remission rate of PR + CR positive was 5.846 times that of negative (OR = 5.846, 95% CI: 1.077~31.742). The remission rate of the morphological change rule was 6.223 times that of the rule (OR = 6.223, 95% CI: 1.696~22.824) as shown in Table 4.

3.5. Establishment of the Nomogram Model. According to the risk factors screened out from the multivariate logistic regression analysis results, a nomogram model for predicting the degree of remission was established. After adding the specific scores of the five variable indicators, the total score is obtained, and the specific probability value of the patient's remission can be obtained by the corresponding probability line, as shown in Figure 2.

3.6. Evaluation of Nomograms. The area under the curve (AUC) was 0.996 (95%CI: 0.921–0.989), the sensitivity was 96.15%, and the specificity was 92.31%. PPV and NPV were 87.27% and 97.15%, respectively (Table 5 and Figure 3). The nomogram model was internally validated by Bootstrap self-sampling for 2000 times, and the resulting C-index for predicting remission rate was 0.966, indicating a good resolution (Figure 4(a)). The calibration curve results show that the average absolute error of coincidence between the predicted value and the real value is 0.026, and the predicted risk is close to the actual risk, indicating that the predicted coincidence is high. In the HRT range of approximately 0.0–0.9, the net benefit rate of the composite evaluation model was higher than that of the simple model (Figure 4(b)). The results of the Hosmer–Lemeshow test showed that $= 8.430$, $P = 0.393 > 0.05$, indicating that through the HL test, there was no significant difference between the predicted value and the true value.

3.7. Typical Case Application. In the nomogram, by summing the scores of these 5 variables and locating them on a total subscale, the predicted probability of the degree of postoperative pathological response of the patient can be obtained. For example, Figures 5(a) and 5(b) are the ultrasound images of a 56-year-old female breast cancer patient before and after NAC, ER positive (0 points), the disappearance of hyperechoic halo after NAC (38 points), Alder grade 0 (100 points) points), the diameter change

Table 2: Comparative analysis of differences in ultrasound and serum indexes between the NMHR group and MHR group.

Index		Before therapy			After treatment		
		NMHR ($n = 93$)	MHR ($n = 54$)	P	NMHR ($n = 93$)	MHR ($n = 54$)	P
Form	Rule	3 (3.2)	1 (1.9)	0.622	5 (5.4)	3 (5.8)	1.000
	Irregular	90 (96.8)	53 (98.1)		88 (94.6)	49 (94.2)	
Direction	Level	83 (89.2)	51 (94.4)	0.442	85 (91.4)	46 (92.0)	1.000
	Vertical bit	10 (10.8)	3 (5.6)		8 (8.6)	4 (8.0)	
Strong echo halo	None	59 (63.4)	18 (33.3)	<0.001	66 (71.0)	52 (96.3)	<0.001
	Have	34 (36.6)	36 (66.7)		27 (29.0)	2 (3.7)	
Calcification	None	43 (46.2)	23 (42.6)	0.668	22 (23.7)	16 (32.0)	0.281
	Have	50 (53.8)	31 (57.4)		71 (76.3)	34 (68.0)	
Boundary	Clear	53 (57.0)	22 (40.7)	0.057	22 (23.7)	7 (13.0)	0.116
	Not clear	40 (43.0)	32 (59.3)		71 (76.3)	47 (87.0)	
Echo	Very low	16 (17.2)	5 (9.4)	0.412			0.662
	Low	74 (79.6)	44 (83.0)		69 (75.0)	35 (70.0)	
	Mix	2 (2.2)	3 (5.7)		3 (3.3)	1 (2.0)	
	Wait for an echo	1 (1.1)	1 (1.9)		20 (21.7)	14 (28.0)	
Rear echo attenuation	None	64 (68.8)	47 (87.0)	0.013	49 (52.7)	32 (59.3)	0.440
	Have	29 (31.2)	7 (13.0)		44 (47.3)	22 (40.7)	
Adler	Level 0	0 (0.0)	2 (3.7)	<0.001	10 (10.8)	38 (70.4)	<0.001
	Level 1	13 (14.0)	29 (53.7)		27 (29.0)	14 (25.9)	
	Level 2	46 (49.5)	22 (40.7)		38 (40.9)	2 (3.7)	
	Level 3	34 (36.6)	1 (1.9)		18 (19.4)	0 (0.0)	
Diameter		3.60 (2.40,5.05)	3.00 (2.08,4.80)	0.164	2.30 (1.40,4.00)	1.00 (0.70,1.80)	<0.001
RI		0.74 (0.68,0.80)	0.62 (0.60,0.68)	<0.001	0.68 (0.61,0.76)	0.00 (0.00,0.51)	<0.001
CEA		2.71 (1.68,5.71)	2.34 (1.41,5.18)	0.436	2.60 (1.60,3.81)	1.85 (1.28,3.07)	0.003
CA125		16.23 (10.74,25.22)	14.11 (10.29,24.74)	0.674	14.41 (10.67,19.52)	13.97 (10.19,17.27)	0.210
CA153		18.49 (12.22,28.50)	12.70 (7.95,21.83)	0.003	20.47 (15.73,28.55)	15.65 (12.48,23.61)	0.006
CA50		5.40 (2.61,11.00)	4.95 (2.70,9.65)	0.629	7.35 (4.30,11.25)	6.80 (3.90,11.20)	0.591

reached PR (28 points), and the morphological changes were more regular (30 points). The final total score is 196. The probability of predicting the degree of pathological remission as MHR was more than 90%, and the final MP grade was 5, which belonged to the MHR group.

Figures 5(c) and 5(d) are the ultrasound images of a 63-year-old female breast cancer patient before and after NAC, ER negative (28 points), hyperechoic halo narrowing after NAC (38 points), Alder grade 1 (66 points) points), the diameter change reached PR (28 points), and the morphological changes were not obvious (0 points). The final total score is 160. Judging from the experience of two senior physicians, this patient has a low probability of achieving MHR, but the model shows that the probability of predicting MHR is more than 70%, and the final MP grade is 4, which belongs to the MHR group. This shows that the model has a good predictive ability.

4. Discussion

Imaging examinations can not only evaluate the efficacy, pathological status, and prognosis of NAC but also help to choose the most appropriate surgical approach. Current research generally believes that magnetic resonance imaging (MRI) is more objective than ultrasound (Ultrasound, US). The degree of remission and prognosis has advantages, but due to the high cost, it has not been fully popularized in all parts of the world, especially in developing countries [16–19]. At the same time, some studies have shown that breast cancer patients with negative ER before NAC and high expression of Ki67 are more sensitive to chemotherapy and benefit more after chemotherapy, and the two may be sensitive factors for predicting the efficacy of chemotherapy [24, 25]. Some studies have shown that many changes will occur in the ultrasound images of patients who achieve pcR after NAC, such as clinical efficacy assessment achieves PR and CR, posterior echo attenuation disappears, internal echo increases, and the hyperechoic halo around the tumor narrows or disappears, and these are the relevant indicators of tumor NAC effective [26]. Different breast cancer patients have different sensitivities to neoadjuvant chemotherapy, and ultrasound diagnosis is an important means to assess the efficacy of neoadjuvant chemotherapy early and formulate individualized treatment plans for patients. Many studies have shown that the nomogram can be considered as an effective tool for predicting the degree of pathological remission after NAC [27, 28]. However, few studies have developed models for predicting NAC efficacy based on ultrasound and clinical indicators. In order to develop a new method that is clinically applicable, cost-effective, and easy to promote, this study combined commonly used two-dimensional gray-scale ultrasound and color Doppler ultrasound with immunohistochemical and serum markers commonly detected in clinics.

In this study, not only the ultrasound images before and after NAC were included but also the changes in parameters

Table 3: Comparative analysis of the changes in ultrasound parameters between the NMHR group and the MHR group.

Variables and their classification		NMHR ($n = 93$)	MHR ($n = 54$)	P value
PR + CR	None	48 (51.6)	6 (11.1)	<0.001
	Have	45 (48.4)	48 (88.9)	
Morphology rules	None	64 (68.8)	9 (16.7)	<0.001
	Have	29 (31.2)	45 (83.3)	
Change of direction	None	81 (87.1)	46 (85.2)	0.745
	Have	12 (12.9)	8 (14.8)	
Hyperechoic halo narrows/disappears	None	86 (92.5)	20 (37.0)	<0.001
	Have	7 (7.5)	34 (63.0)	
Increased number of calcifications	None	54 (58.1)	40 (74.1)	0.051
	Have	39 (41.9)	14 (25.9)	
Clear boundaries	None	65 (69.9)	29 (53.7)	0.049
	Have	28 (30.1)	25 (46.3)	
Echo becomes high	None	73 (78.5)	36 (66.7)	0.114
	Have	20 (21.5)	18 (33.3)	
Rear echo change	None	70 (75.3)	32 (59.3)	0.042
	Have	23 (24.7)	22 (40.7)	
Decreased blood flow	None	49 (52.7)	10 (18.5)	<0.001
	Have	44 (47.3)	44 (81.5)	
RI decreased	None	38 (40.9)	1 (1.9)	<0.001
	Have	55 (59.1)	53 (98.1)	

Table 4: Multivariate analysis of the degree of pathological remission.

Variable	Multiactor		
	OR	95% CI	P
ER (control: negative)	0.176	0.046~0.663	0.010
Hyperechoic halo narrows/disappears (control: negative)	10.661	2.608~43.568	0.001
NAC after Adler (control: grade 0)	0.129	0.050~0.333	<0.001
PR + CR (control: negative)	5.846	1.077~31.742	0.041
Morphology rules (control: negative)	6.223	1.696~22.824	0.006

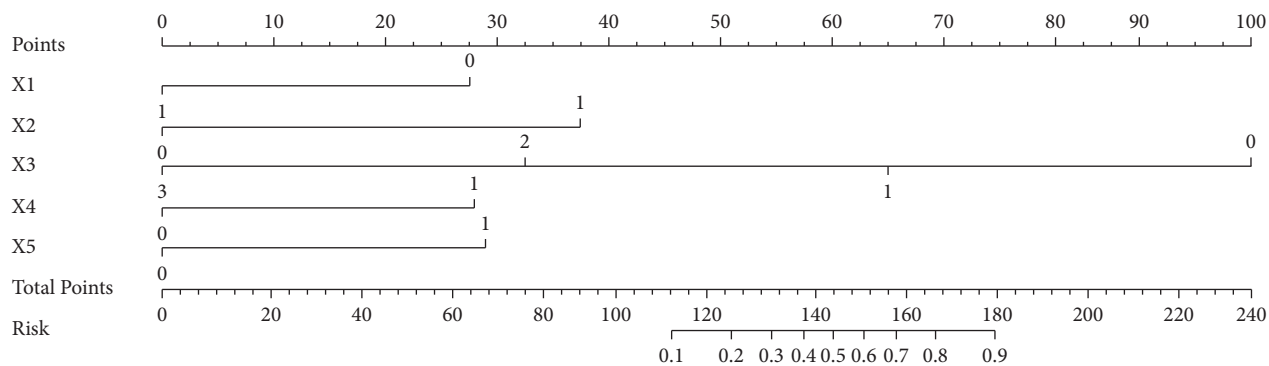

Figure 2: Nomogram predicting postoperative remission rate.

between them were analyzed. We believe that the changes in ultrasound parameters during treatment can more directly reflect the degree of pathological remission of NAC. Therefore, the pretreatment, posttreatment, changes in ultrasound image parameters, and commonly used clinical indicators are all incorporated into the nomogram-based prediction model for the degree of postoperative pathological remission after NAC, and these indicators are easy to obtain in daily clinical work. This means that ER(−), hyperechoic halo narrowing/disappearance, post-NAC Adler grade, PR + CR, and morphological changes are more likely to achieve significant responses. Based on the risk factors (ER, narrowing/disappearance of strong echo halo, Adler classification after NAC, PR + CR, and morphological change rule) selected from the results of multifactor logistic regression analysis, a line chart model was established to predict the remission degree. Evaluation of the model found that the nomogram performed well, and the AUC/C index under the

Table 5: ROC analysis of emission degree and prediction probability.

Variable	AUC	Standard error	*P* value	95% CI	PPV (%)	NPV (%)
Prediction probability	0.996	0.059	<0.001	0.921 ~ 0.989	87.72	97.15

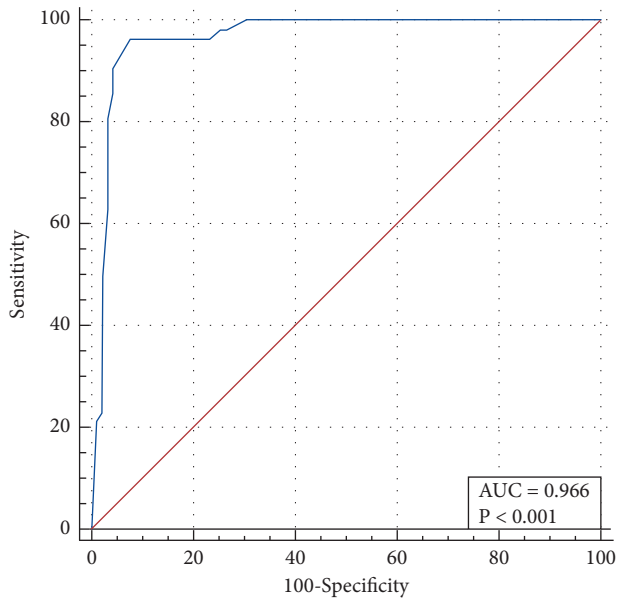

Figure 3: ROC analysis.

ROC curve reached a respectable 0.96. Sensitivity and specificity were 96.15% and 92.31%, both satisfactory. PPV and NPV were 87.27% and 97.15%, respectively. This means that the nomogram performed well. It is helpful to clarify the independent risk factors of postoperative pathological remission and to provide guidance for the choice of subsequent treatment. The predicted values obtained by the nomogram are in good agreement with the actual observed values. The results showed that the mean absolute error of the agreement between the predicted value and the true value was 0.026, and the predicted risk was close to the actual risk, indicating that the degree of agreement for predicting postoperative pathological remission was high.

The emerging deep learning representation of ultrasound image features, based on pre-NAC and post-NAC ultrasound images, uses deep learning radiomics to establish a pCR prediction model, which can provide an effective diagnostic reference for clinical routine pCR identification [29, 30]. Studies have shown that during the whole process of preoperative NAC treatment, ultrasound can dynamically observe the changes in the tumor and evaluate the effectiveness of NAC, so that the treatment plan can be changed in time when it is ineffective [31]. In the nomogram established by some scholars, it was also found that diameter reduction after NAC was an important dependent factor for predicting pCR, and the characteristics of ultrasound images and the changes between these characteristics were related to pCR [32, 33]. The change in diameter after the end of NAC, i.e., whether PR and CR are achieved, is the most important feature and also occupies an important position in the nomogram constructed in our study.

Many studies have found that the Adler grade, RI, and PI of the lesions after effective chemotherapy are lower than those before chemotherapy [34]. There are also studies showing that CR is a valid and valuable surrogate prognostic factor for survival after treatment [35]. The results of this study show that the blood flow grade after NAC is an independent influencing factor of MHR. Previous studies have shown that two-dimensional gray-scale ultrasound features, including hyperechoic halos, and tumor morphology are closely related to the diagnosis of breast cancer. The disappearance of the hyperechoic halo in the nomogram and the changes in tumor morphology were considered to be associated with a significant degree of pathological remission.

5. Limitations and Prospects

5.1. Limitations

(1) Since this is a single-center retrospective study, the exact parameters regarding the machine setup were not initially available. Furthermore, even for the same type of machine, the settings of different institutions may differ to some extent; therefore, it is difficult to assess whether the type of machine affects the parameters of the image and the performance of the prediction model.

(2) There is a lack of prospective validation to determine the influence of sonographers on the future performance of the model.

(3) The sonographer's judgment is subject to a certain degree. The evaluation of various characteristics of breast tumor ultrasonic images is qualitative and depends on the doctor's experience.

(4) The sample size contained is insufficient, and the obtained results may be biased. Moreover, the follow-up time is short, which can be used as a reference for evaluating the short-term prognosis of breast cancer NAC, and multisample and long-term follow-up studies are still needed for long-term prognosis. Furthermore, additions and improvements are needed.

5.2. Prospects

(1) This study developed a predictive model for the degree of pathological remission after NAC based on pre- and post-NAC ultrasound images and the changes in parameters between them and obtained good performance in an internal validation cohort. This model can provide an effective reference for evaluating the degree of pathological remission after routine surgery.

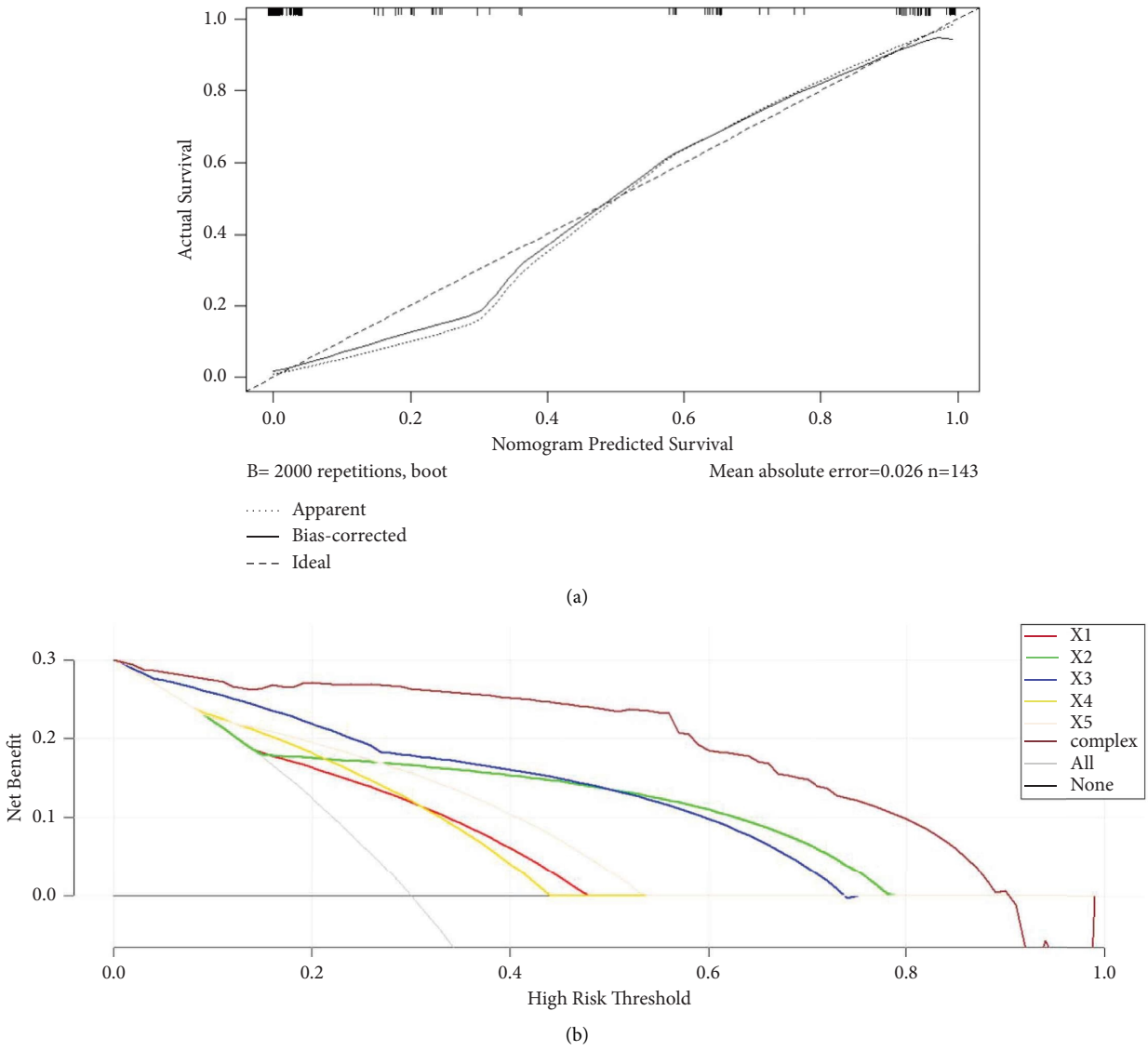

Figure 4: Calibration curve (a) and decision curve (b) of the nomogram model for predicting remission rate.

(2) In the future, we hope to continue prospective studies of ultrasound using and comparing the effectiveness of this method in various molecular subtypes of breast cancer and larger sample sizes. At the same time, more factors were introduced into the nomogram, such as serum change percentage, lymph node metastasis status, and hope to predict the response before NAC administration, which will be the focus of our future research. This operation needs to be continuously accumulated and improved in practical applications, which will also be the direction of the next research work.

(3) In the future, we hope to continue prospective studies with ultrasound to use and compare the effectiveness of this method in various molecular subtypes of breast cancer with larger sample sizes.

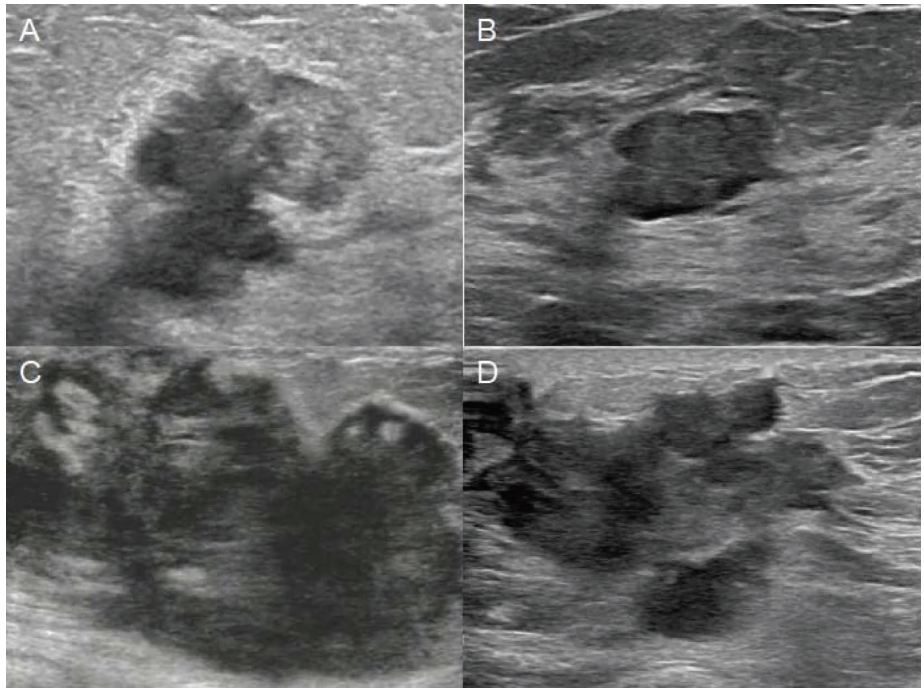

Figure 5: Ultrasound images of two patients who received NAC and belonged to the MHR group. (a, c) Images before NAC. (b, d) Images after NAC ends.

6. Conclusions

In conclusion, this study developed a predictive model for the degree of pathological remission after NAC based on US images before and after NAC, and the nomogram established by the combination of changes in ultrasound parameters and clinical indicators showed satisfactory efficiency, which means that the nomogram is a reliable method to predict the degree of postoperative pathological remission after NAC. It should be further explored in the future to give full play to the combination of changes in ultrasound image parameters and clinical indicators to better show the predictive value of US in predicting postoperative pathological remission [3].

Data Availability

The data used to support the findings of this study are available from the authors upon request.

Disclosure

Huangjing Chen and Hongyan Qian are the co-first authors.

Conflicts of Interest

The authors declare that they have no conflicts of interest.

Authors' Contributions

Huangjing Chen and Hongyan Qian contributed equally to this study.

Acknowledgments

The present study was supported by the Nantong Science and Technology Bureau (grant no. JC2020025), by the Health Committee of Nantong (grant no. MB2020021), and by the Clinical Medicine Special Program from Nantong University (grant no. 2019JY017).

References

[1] H. Sung, J. Ferlay, R. L. Siegel et al., "Global cancer statistics 2020: GLOBOCAN estimates of incidence and mortality worldwide for 36 cancers in 185 countries," *CA: A Cancer Journal for Clinicians*, vol. 71, no. 3, pp. 209–249, 2021.

[2] X. Wang, C. Wang, J. Guan, B. Chen, L. Xu, and C. Chen, "Progress of breast cancer basic research in China," *International Journal of Biological Sciences*, vol. 17, no. 8, pp. 2069–2079, 2021.

[3] W. J. Gradishar, M. S. Moran, J. Abraham et al., "NCCN Guidelines® insights: breast cancer, version 4.2021," *Journal of the National Comprehensive Cancer Network*, vol. 19, no. 5, pp. 484–493, 2021.

[4] M. Golshan, C. T. Cirrincione, W. M. Sikov et al., "Impact of neoadjuvant chemotherapy in stage II-III triple negative breast cancer on eligibility for breast-conserving surgery and breast conservation rates: surgical results from CALGB 40603 (Alliance)," *Annals of Surgery*, vol. 262, no. 3, pp. 434–439, 2015.

[5] L. M. De La Cruz, E. S. McDonald, R. Mick et al., "Anti-HER2 CD4+ T-helper type 1 immune response is superior to breast MRI for assessing response to neoadjuvant therapy in patients with HER2-positive breast cancer," *Annals of Surgical Oncology*, vol. 24, no. 4, pp. 1057–1063, 2017.

[6] A. Taghizadeh Kermani, S. Hosseini, A. Fanipakdel et al., "A randomized clinical trial on the antitumoral effects of low molecular weight heparin in the treatment of esophageal cancer," *Journal of Cellular Physiology*, vol. 234, no. 4, pp. 4191–4199, 2019.

[7] D. Fazilat-Panah, S. Vakili Ahrari Roudi, A. Keramati et al., "Changes in cytokeratin 18 during neoadjuvant chemotherapy of breast cancer: a prospective study," *Iranian journal of pathology*, vol. 15, no. 2, pp. 117–126, 2020.

[8] M. Blonski, J. Pallud, C. Gozé et al., "Neoadjuvant chemotherapy may optimize the extent of resection of World Health Organization grade II gliomas: a case series of 17 patients," *Journal of neuro-oncology*, vol. 113, no. 2, pp. 267–275, 2013.

[9] H. Watanabe, M. Okada, Y. Kaji et al., "New response evaluation criteria in solid tumours-revised RECIST guideline," *Cancer & chemotherapy*, vol. 36, no. 13, pp. 2495–2501, 2009.

[10] S. V. Liu, L. Melstrom, K. Yao, C. A. Russell, and S. F. Sener, "Neoadjuvant therapy for breast cancer," *Journal of Surgical Oncology*, vol. 101, no. 4, pp. 283–291, 2010.

[11] W. F. Symmans, F. Peintinger, C. Hatzis et al., "Measurement of residual breast cancer burden to predict survival after neoadjuvant chemotherapy," *Journal of Clinical Oncology*, vol. 25, no. 28, pp. 4414–4422, 2007.

[12] K. N. Ogston, I. D. Miller, S. Payne et al., "A new histological grading system to assess response of breast cancers to primary chemotherapy: prognostic significance and survival," *The Breast*, vol. 12, no. 5, pp. 320–327, 2003.

[13] A. S. Caudle, A. M. Gonzalez-Angulo, K. K. Hunt et al., "Predictors of tumor progression during neoadjuvant chemotherapy in breast cancer," *Journal of Clinical Oncology*, vol. 28, no. 11, pp. 1821–1828, 2010.

[14] Breast Cancer Expert Committee of National Cancer Quality Control Center, Breast Cancer Expert Committee of China Anti-Cancer Association, and Cancer Drug Clinical Research Committee of China Anti-Cancer Association, "Breast cancer expert committee of China anti-cancer association; cancer drug clinical research committee of China anti-cancer association," [guidelines for clinical diagnosis and treatment of advanced breast cancer in China (2020 edition)," *Zhonghua zhong liu za zhi [Chinese journal of oncology]*, vol. 42, no. 10, pp. 781–797, 2020.

[15] Early Breast Cancer Trialists' Collaborative Group Ebctcg, "Long-term outcomes for neoadjuvant versus adjuvant chemotherapy in early breast cancer: meta-analysis of individual patient data from ten randomised trials," *The Lancet Oncology*, vol. 19, no. 1, pp. 27–39, 2018.

[16] S. Sheikhbahaei, T. J. Trahan, J. Xiao et al., "FDG-PET/CT and MRI for evaluation of pathologic response to neoadjuvant chemotherapy in patients with breast cancer: a meta-analysis of diagnostic accuracy studies," *The Oncologist*, vol. 21, no. 8, pp. 931–939, 2016.

[17] Y. L. Gu, S. M. Pan, J. Ren, Z. X. Yang, and G. Q. Jiang, "Role of magnetic resonance imaging in detection of pathologic complete remission in breast cancer patients treated with neoadjuvant chemotherapy: a meta-analysis," *Clinical Breast Cancer*, vol. 17, no. 4, pp. 245–255, 2017.

[18] A. Amioka, N. Masumoto, N. Gouda et al., "Ability of contrast-enhanced ultrasonography to determine clinical responses of breast cancer to neoadjuvant chemotherapy," *Japanese Journal of Clinical Oncology*, vol. 46, no. 4, pp. 303–309, 2016.

[19] Y. Ma, S. Zhang, J. Li, J. Li, Y. Kang, and W. Ren, "Comparison of strain and shear-wave ultrasounic elastography in predicting the pathological response to neoadjuvant chemotherapy in breast cancers," *European Radiology*, vol. 27, no. 6, pp. 2282–2291, 2016.

[20] C. A. Parise and V. Caggiano, "Risk of mortality of node-negative, ER/PR/HER2 breast cancer subtypes in T1, T2, and T3 tumors," *Breast Cancer Research and Treatment*, vol. 165, no. 3, pp. 743–750, 2017.

[21] A. A. Hashmi, K. A. Hashmi, M. Irfan et al., "Ki67 index in intrinsic breast cancer subtypes and its association with prognostic parameters," *BMC Research Notes*, vol. 12, no. 1, p. 605, 2019.

[22] A. Rix, M. Piepenbrock, B. Flege et al., "Effects of contrast-enhanced ultrasound treatment on neoadjuvant chemotherapy in breast cancer," *Theranostics*, vol. 11, no. 19, pp. 9557–9570, 2021.

[23] J. B. Li and Z. F. Jiang, "Chinese society of clinical Oncology breast cancer guideline version 2021: updates and interpretations," *Zhonghua Yixue Zazhi*, vol. 101, no. 24, pp. 1835–1838, 2021.

[24] T. Iwamoto, Y. Kajiwara, Y. Zhu, and S. Iha, "Biomarkers of neoadjuvant/adjuvant chemotherapy for breast cancer," *Chinese Clinical Oncology*, vol. 9, no. 3, p. 27, 2020.

[25] G. Kanyılmaz, B. Benli Yavuz, M. Aktan, M. Karaağaç, M. Uyar, and S. Fındık, "Prognostic importance of ki-67 in breast cancer and its relationship with other prognostic factors," *European journal of breast health*, vol. 15, no. 4, pp. 256–261, 2019.

[26] J. Fei, G. Q. Wang, Y. Y. Meng et al., "Breast cancer subtypes affect the ultrasound performance for axillary lymph node status evaluation after neoadjuvant chemotherapy: a retrospective analysis," *Japanese Journal of Clinical Oncology*, vol. 51, no. 10, pp. 1509–1514, 2021.

[27] S. Y. Kim, N. Cho, Y. Choi et al., "Factors affecting pathologic complete response following neoadjuvant chemotherapy in breast cancer: development and validation of a predictive nomogram," *Radiology*, vol. 299, no. 2, pp. 290–300, 2021.

[28] J. Zhang, L. Xiao, S. Pu, Y. Liu, J. He, and K. Wang, "Can we reliably identify the pathological outcomes of neoadjuvant chemotherapy in patients with breast cancer? Development and validation of a logistic regression nomogram based on preoperative factors," *Annals of Surgical Oncology*, vol. 28, no. 5, pp. 2632–2645, 2021.

[29] M. Jiang, C. L. Li, X. M. Luo et al., "Ultrasound-based deep learning radiomics in the assessment of pathological complete response to neoadjuvant chemotherapy in locally advanced breast cancer," *European Journal of Cancer*, vol. 147, pp. 95–105, 2021.

[30] H. Cui, D. Zhao, P. Han et al., "Predicting pathological complete response after neoadjuvant chemotherapy in advanced breast cancer by ultrasound and clinicopathological features using a nomogram," *Frontiers in Oncology*, vol. 11, Article ID 718531, 2021.

[31] L. Song, L. Li, B. Liu et al., "Diagnostic evaluations of ultrasound and magnetic resonance imaging in mammary duct

ectasia and breast cancer," *Oncology Letters*, vol. 15, no. 2, pp. 1698–1706, 2018.

[32] Y. Wang, J. Li, Y. Xia et al., "Prognostic nomogram for intrahepatic cholangiocarcinoma after partial hepatectomy," *Journal of Clinical Oncology*, vol. 31, no. 9, pp. 1188–1195, 2013.

[33] K. Touijer and P. T. Scardino, "Nomograms for staging, prognosis, and predicting treatment outcomes," *Cancer*, vol. 115, no. 13, pp. 3107–3111, 2009.

[34] A. Kumar, V. Srivastava, S. Singh, and R. C. Shukla, "Color Doppler ultrasonography for treatment response prediction and evaluation in breast cancer," *Future Oncology*, vol. 6, no. 8, pp. 1265–1278, 2010.

[35] H. Wang and X. Mao, "Evaluation of the efficacy of neoadjuvant chemotherapy for breast cancer," *Drug Design, Development and Therapy*, vol. 14, pp. 2423–2433, 2020.

Hindawi
Journal of Oncology
Volume 2023, Article ID 3937352, 14 pages
https://doi.org/10.1155/2023/3937352

Research Article

SLC9A1 Binding mTOR Signaling Pathway-Derived Risk Score Predicting Survival and Immune in Clear Cell Renal Cell Carcinoma

Dengshuang Wu,[1,2] Zhipeng Xu ,[1,3] and Jianning Wang [1,3]

[1]*Department of Urology, Shandong Provincial Qianfoshan Hospital, Cheeloo College of Medicine, Shandong University, Jinan, Shandong, China*
[2]*Department of Urology, Qingdao Municipal Hospital, Qingdao 266011, Shandong, China*
[3]*Department of Urology, The First Affiliated Hospital of Shandong First Medical University and Shandong Provincial Qianfoshan Hospital, Shandong Medicine and Health Key Laboratory of Organ Transplantation and Nephrosis, Shandong Institute of Nephrology, Jinan, China*

Correspondence should be addressed to Zhipeng Xu; scofield_xzp@163.com and Jianning Wang; docjianningwang@163.com

Received 26 September 2022; Revised 18 October 2022; Accepted 27 January 2023; Published 13 February 2023

Academic Editor: Muhammad Muddassir Ali

Objective. Clear cell renal cell carcinoma (ccRCC) is one of the common renal cell carcinomas (RCC) with a high risk of recurrence. Considering that SLC9A1 is involved in various cellular physiological processes and probably mediates the course of mTOR signaling in tumors, this study constructed a risk model for SLC9A1 combined with mTOR signaling in ccRCC, aiming at better predicting the prognosis of patients. *Methods*. ccRCC expression matrices were downloaded from TCGA and ICGC databases to compare the expression of SLC9A1 in TCGA, and qRT-PCR was adopted to validate the SLC9A1 expression in different RCC cells and normal kidney cells. The CIBERSORT and ESTIMATE algorithms were used to assess samples for immunity. mTOR signaling-associated genes were downloaded from the KEGG website, and then the genes were adopted to screen genes associated with SLC9A1 expression and mTOR signaling pathway colleagues, based on which univariate COX regression and lasso regression Cox analyses were conducted to construct a ccRCC prognostic risk model. ROC curves and nomograms were used to assess the validity of the models. *Results*. ccRCC tumor samples showed lower SLC9A1 expression than normal samples, as also evidenced by qRT-PCR. The SLC9A1 expression was highly correlated with tumor immunity. Totally, 564 key genes associated with both SLC9A1 expression and mTOR signaling were screened out, and the risk model consisting of 11 gene signatures was constructed in ccRCC based on the 564 genes. Since patients at a high risk had poorer survival outcomes, the high-risk group presented poorer immunotherapy outcomes. Moreover, a higher clinical grade of patients suggested a higher risk score. The risk score can serve as one independent prognostic factor for the prognosis prediction of ccRCC patients. *Conclusion*. An extremely promising prognostic indicator for ccRCC based on SLCA9A1 and mTOR signaling has been constructed to provide reference for clinical treatment.

1. Introduction

Renal cell carcinoma (RCC) is one of the most common solid tumors of the adult kidney [1]. Among its subtypes, clear cell renal cell carcinoma (ccRCC) is the major one, with a high rate of occurrence (accounting for 80–90% of all cases) and relapse risk [2, 3]. Moreover, about 30% of patients presented distant metastasis during initial diagnosis [4]. Although the treatment of ccRCC has achieved great progress in recent years, especially immunotherapy, which has been considered an effective therapeutic method for advanced patients [5–7], cancer-specific morbidity and mortality continue to rise, and drug resistance persists unfortunately worldwide [8, 9]. The prognostic staging

system currently does not provide adequate guidance for treatment and cannot accurately predict clinical outcomes [10, 11]. Accordingly, it is urgent to identify the efficient prognostic model of ccRCC patients.

SLC9A1, also named Na/H exchanger 1 (NHE1) [12], belongs to the NHE exchanger family [13]. As a membrane protein, SLC9A1 exists in many mammalian cell types and is involved in intracellular pH (pHi) regulation [14, 15]. Many physiological processes are dependent on SLC9A1, including cell proliferation, cell volume regulation, cellular immunity, and cell death [16]. Furthermore, prior research has revealed that potential downstream impacts of mTOR on cell growth, survival, and tumorigenesis were under medication by SLC9A1 [17]. Reportedly, in gastric cancer, hepatocellular carcinoma (HCC), ovarian cancer, and gliomas, SLC9A1 favors tumorigenesis and predicts poor prognosis [13, 18, 19]. In breast cancer, SLC9A1 acts as a facilitator in tumor invasiveness [20]. Based on these findings, SLC9A1 protein has emerged as an important marker for tumorigenesis and prognosis, whereas the potential role of SLC9A1 in ccRCC has not been fully understood.

This study analyzed the SLC9A1 expression in ccRCC and its association with immunity. A prognostic risk model was established on the basis of SCL9A1 as well as mTOR signaling in ccRCC, with the purpose of finding possible prognostic markers in ccRCC and providing a theoretical basis for prognostic prediction of patients.

2. Materials and Methods

2.1. Cell Strains and Reagents. Human RCC cell strains (786-O, A498, OS-RC-2, ACHN, 769-P, Caki-1, and Caki-2) and human normal renal cells (293T and HK-2) were provided by American Type Culture Collection (ATCC, Rockville, MD, and the States). A498, ACHN, and HK-2 were incubated in MEM (Invitrogen, 11090-081). 786-O, 769-P, and OS-RC-2 were subjected to incubation in RPMI-1640 (Gibco, 11875500BT). Caki-1 and Caki-2 were subjected to incubation in Mccoy 5A (Gibco, 12330031). 293T was cultured in DMEM (Gibco, 11995500BT). The medium were supplemented with 10% fetal bovine serum (Gibco, the States). All the cell strains were maintained in an incubator (37°C, 5% CO_2).

2.2. RNA Isolation and Quantitative Real-Time PCR (qRT-PCR). Total RNA was extracted from cells through TRIzol reagent (Invitrogen). First-strand cDNA was generated from 1 μg total RNA using Hifair® II 1st Strand cDNA Synthesis Kit (11119ES60) from Yeasen (Shanghai, CN). qRT-PCR was conducted three times with a SYBR Green premix qPCR kit (Accurate Biotechnology, Changsha, Hunan, CN, AG11701). Sequences of primers for qRT-PCR were provided as follows: SLC9A: forward: 5′-ACCACGAGAACG CTCGATTG-3′, reverse: 5′-ACGTGTGTGTAGTCGATG CC-3′. GAPDH: forward: 5′- GGAGCGAGATCCCTCCAA AAT-3′, reverse: 5′-GGCTGTTGTCATACTTCTCATGG-3′. The specific experimental procedures were carried out in strict accordance with the kit instructions. Gene expression was measured and normalized relative to the GAPDH level using the $2^{-\Delta\Delta Ct}$ method.

2.3. Data Collection and Processing. Expression matrices for 526 ccRCC samples and 72 normal ones were acquired from The Cancer Genome Atlas (TCGA, https://portal.gdc.cancer.gov/repository) database and filtered for samples with missing clinical and survival information, with gene expression as the mean value. Data about mutation data and copy number variation for ccRCC were also obtained from TCGA. Additionally, ninety-one primary renal cell cancer samples with complete prognostic and clinical information in the International Cancer Genome Consortium (ICGC, https://dcc.icgc.org/) were screened, and their expression profiles were downloaded.

2.4. Tumor Immunity. The relative proportions of the 22 immune cell compositions in the expression matrix were assessed using CIBERSORT, and $p < 0.05$ was used for subsequent comparisons. In addition, immune scores in tumor samples were calculated using the ESTIMATE algorithm, outputting scores for immune, stromal, and ESTIMATES.

2.5. Screening for SLC9A1 and mTOR-Related Genes and Gene Sets. The mTOR pathway-related genes were acquired from the official website of the Kyoto Encyclopedia of Genes and Genomes (KEGG, https://www.genome.jp/kegg/), and sample mTOR pathway scores were calculated using the ssGSEA algorithm. The correlation between gene sets and genes was calculated, respectively, on the basis of the Hmisc package rcorr function of the R language, and the correlated gene sets were screened by $|\text{cor}| > 0.25$ and $p < 0.001$.

2.6. Enrichment Analysis. Gene ontology (GO) enrichment analysis was conducted to explore the possible biological functions of the relevant genes in biological processes, cellular components, and molecular functions through the cluster Profiler package in R. A separate KEGG pathway enrichment analysis was performed to search for potential mechanisms.

2.7. Construction and Validation of the Prognostic Risk Model. Prognostic significance of genes was calculated by single and multifactor Cox analyses performed with the survival package. $p < 0.05$ was the selection criterion for screening for subsequent analyses. Candidate genes were subjected to lasso regression analysis using the R package glmnet for screening for prognosis-associated gene signatures, and models were constructed by 10-fold cross-validation.

$$\text{Risk score (patient)} = \sum_{i=1}^{n} \text{expression}_{\text{gene } i} \times \text{cofficient}_{\text{Gene } i}. \quad (1)$$

The median risk score was defined with the R package survminer, and samples were classified according to the risk level. Kaplan–Meier (K–M) curves were drawn through the

R package time ROC to predict the prognostic classification efficiency of the risk score.

Module genes were extracted from published articles [21–23], and the c-index of these models was calculated and compared by the survcomp package.

2.8. Immunotherapy. The online software Tumor Immune Dysfunction and Exclusion (TIDE, https://tide.dfci.harvard.edu/) is used to assess the potential clinical effects of samples in immunotherapy.

2.9. Nomogram. The rms package was used along with the risk score and clinical characteristics to create nomogram that quantify the prognostic risk and likelihood of survival for patients at 1, 3, and 5 years. Moreover, usefulness of the model is also assessed by performing a decision curve analysis (DCA).

2.10. Statistical Analyses. With R software (3.6.1) and GraphPad Prism (9), statistical analyses were conducted, and the ggplot2 package was adopted for visualization. The correlation between gene expression and the pathway score was determined through Spearman correlation analysis and compared between the groups using the Wilcox test, $p < 0.05$.

3. Results

3.1. SLC9A1 Is Lowly Expressed in ccRCC. The overall flowchart is shown in Supplementary Figure 1. Comparison of TCGA expression profiles revealed lowly expressed SLC9A1 in ccRCC tumor tissues as compared with normal paracancerous tissues (Figure 1(a)). Moreover, qRT-PCR results revealed downregulated SLC9A1 in RCC cell strains as compared with normal kidney cell strains (Figure 1(b)). Next, we sorted out the mutation information of SLC9A1 through the SNV data of TCGA, and 2 samples had mutations in SLC9A1 gene, while 524 samples did not have mutations. As shown in Figure 1(c), gene expression in samples without SLC9A1 mutation was higher than that of the sample with SLC9A1 mutation, but there was no significant difference (maybe because of the too small sample size). Then, based on the CNV data of TCGA, the samples were divided into amplification, deletion, and diploid groups based on the CNV mutation of SLC9A1. We found that the samples without CNV mutation in SLC9A1 were significantly higher (Figure 1(d)).

3.2. Relationship between the Expression of SLC9A1 and Immunity. We found that some immune cells' scores expressed differently depending on the SLC9A1's expression level (Figure 2(a)). The immune scores of the tumor samples showed that the highly expressed group of SLC9A1 had higher immune infiltration than the lowly expressed one (Figure 2(b)). Correlation analysis revealed a positive association between SLC9A1 expression and the immune score (Figure 2(c)). On the other hand, we also examined the correlation of the SLC9A1 expression with 22 types of immune cell scores. Among them, there was a positive correlation between SLC9A1 expression and score about Macrophages M0, T regulatory cells (Tregs), etc., and a negative correlation between it and cells, scores such as NK cells activated (Figure 2(d)). We extracted the genes of immune-related pathways, and the expression of some genes (e.g., IL6 and MMP9) in immune-related pathways also increased with the increased expression of SLC9A1 (Figure 2(e)).

3.3. Relationship between the SLC9A1 and mTOR Pathway and Gene Set Enrichment Analysis. The Spearman correlation analysis revealed positive association of SLC9A1 expression with the mTOR signaling pathway scores of the patients calculated by the ssGSEA method (Figure 3(a)). Further analysis screened 1502 genes positively associated with SLC9A1 expression, 1077 ones negatively associated with it, 3061 genes with positive association with the mTOR signaling pathway score, and 1611 ones with negative association with the score. By overlapping analysis, 564 genes were found to be associated with both SLC9A1 and mTOR (Figure 3(b)). Meanwhile, enrichment analysis of 564 related genes was conducted and the genes were found to be associated with actin filament-related biological processes, phagocytosis, and the cGMP-PKG signaling pathway (Figure 3(c)).

3.4. Construction and Validation of the ccRCC Prognostic Risk Model. We identified 39 genes mostly associated with the prognosis in both TCGA and ICGA datasets of ccRCC through univariate Cox regression analysis. Supplementary Table 1 presents the results of the one-way Cox analysis for the 564 genes in both TCGA and the ICGC datasets. Then, Lasso regression was performed to further reduce model genes for model optimization. The change trajectory of every independent variable was analyzed as shown in Figures 4(a) and 4(b). According to the results, with the gradual increase of lambda, the number of independent variable coefficients close to 0 also increased gradually. We used 10-fold cross-validation for model establishment. The confidence interval under every lambda was analyzed, and when lambda = 0.0344, the model is optimal. For this reason, we chose eleven genes with lambda = 0.0344 as the target genes. The risk score was calculated using the following formula:

$$\begin{aligned}\text{Risk score} = {} & 0.158 * \text{COL6A2} - 0.218 * \text{EXTL3} + 0.357 * \text{HEATR6} - 0.276 * \text{HSPG2} - 0.015 * \text{MAML3} \\ & + 0.389 * \text{PPP1R18} + 0.316 * \text{RCC2} + 0.173 * \text{SEMA7A} + 0.022 * \text{SERPINH1} - 0.484 * \text{TLN1} + 0.177 * \text{TM9SF4}.\end{aligned} \tag{2}$$

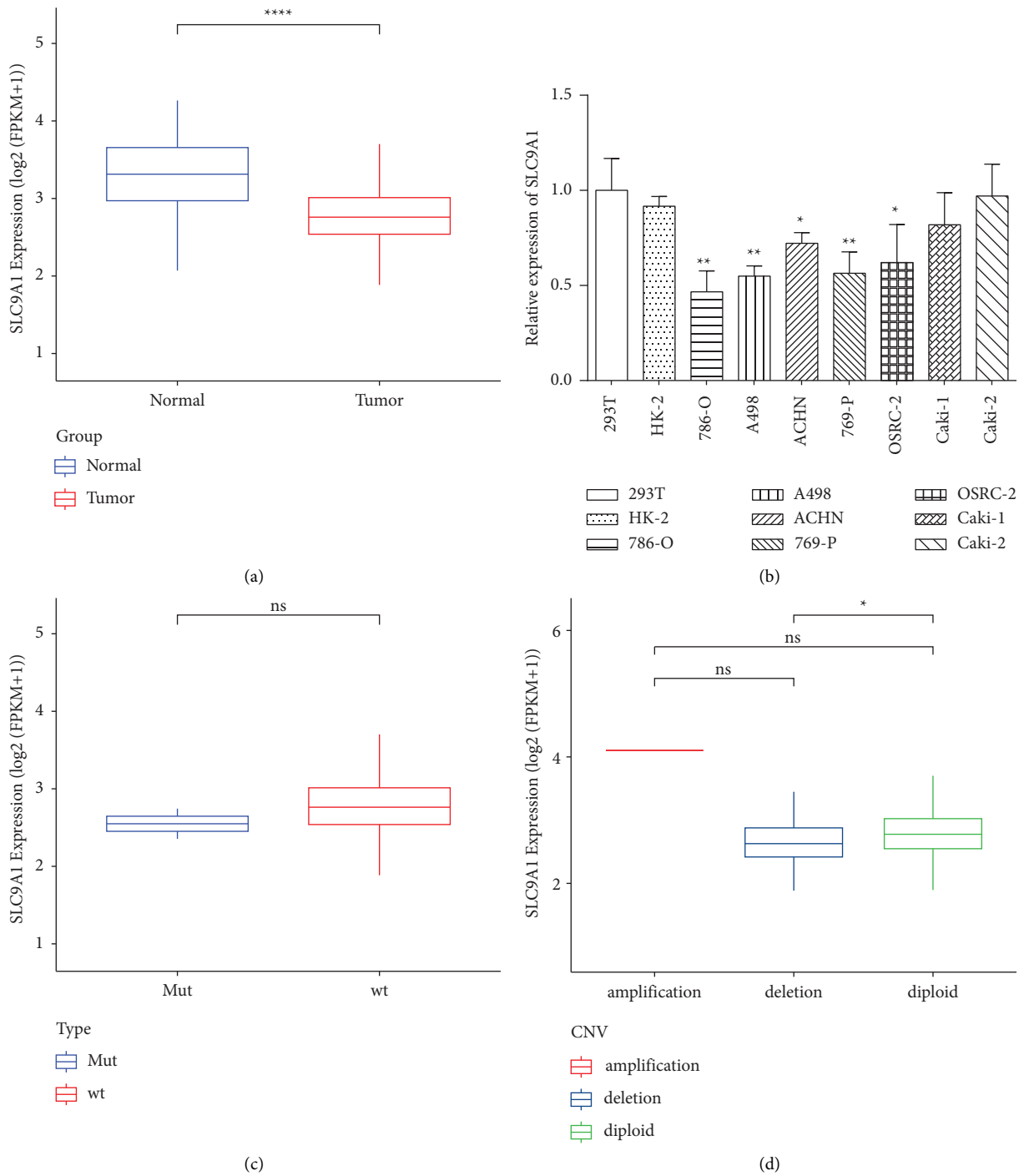

Figure 1: SLC9A1 is lowly expressed in ccRCC samples. (a) Expression of SLC9A1 in ccRCC cancer tissues and normal tissues in TCGA database. (b) qRT-PCR analysis of SLC9A1 in RCC cells vs. human normal renal cells (293T and HK-2). (c) Comparison of SLC9A1 expression between samples with or without SNV mutation. (d) Comparison of SLC9A1 expression between samples with or without CNV mutation. Note: SNV: single nucleotide variants; CNV: copy number variation. $^{*}p < 0.05$, $^{**}p < 0.01$, $^{***}p < 0.001$, and $^{****}p < 0.0001$.

The expression of these 11 genes in cancer and normal paracancerous tissues is described in detail in Supplementary Figure 2. Next, we used TCGA dataset as the training dataset and calculated the risk score of every sample through the expression of 11 genes. The ROC curve assisted in evaluating the accuracy of OS estimates derived from the prognostic risk model. The classification efficiency of 1–5 year prognosis prediction was analyzed, and the area under curve (AUC) in 1–5 years reached above 0.7. In addition, the patients were assigned to a high- or low- risk group in the light of the mean value of the risk score. The K–M survival curve showed a notably worse overall survival (OS) in the high-risk group than that in the other group (Figures 4(c) and 4(d)). The same method was used to

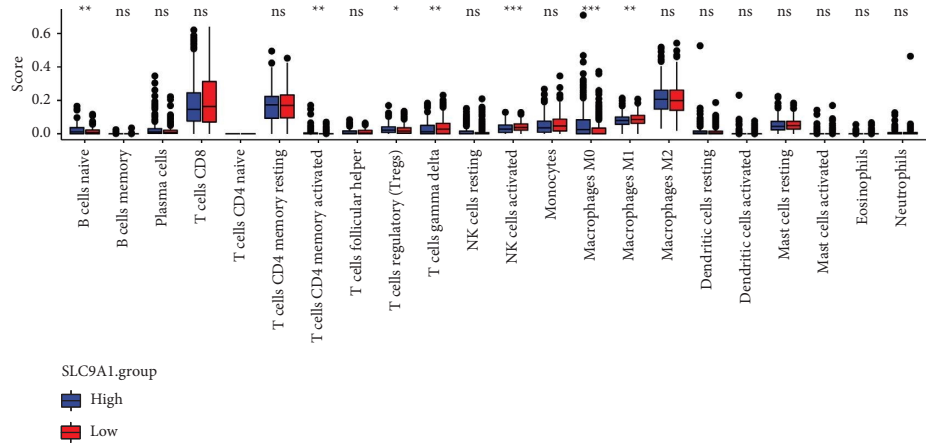

(a)

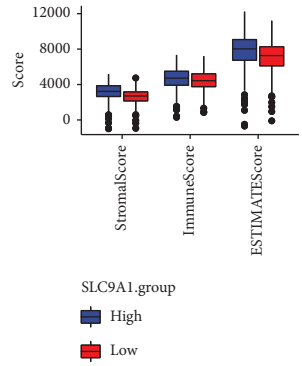

(b)

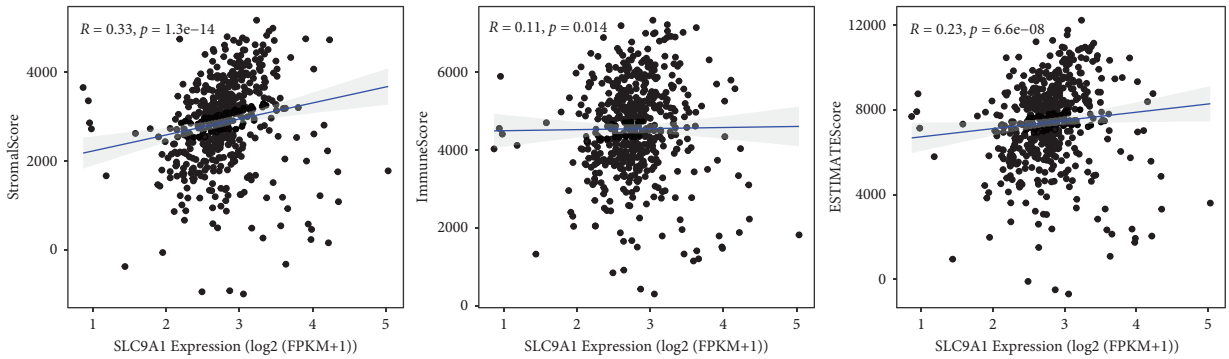

(c)

Figure 2: Continued.

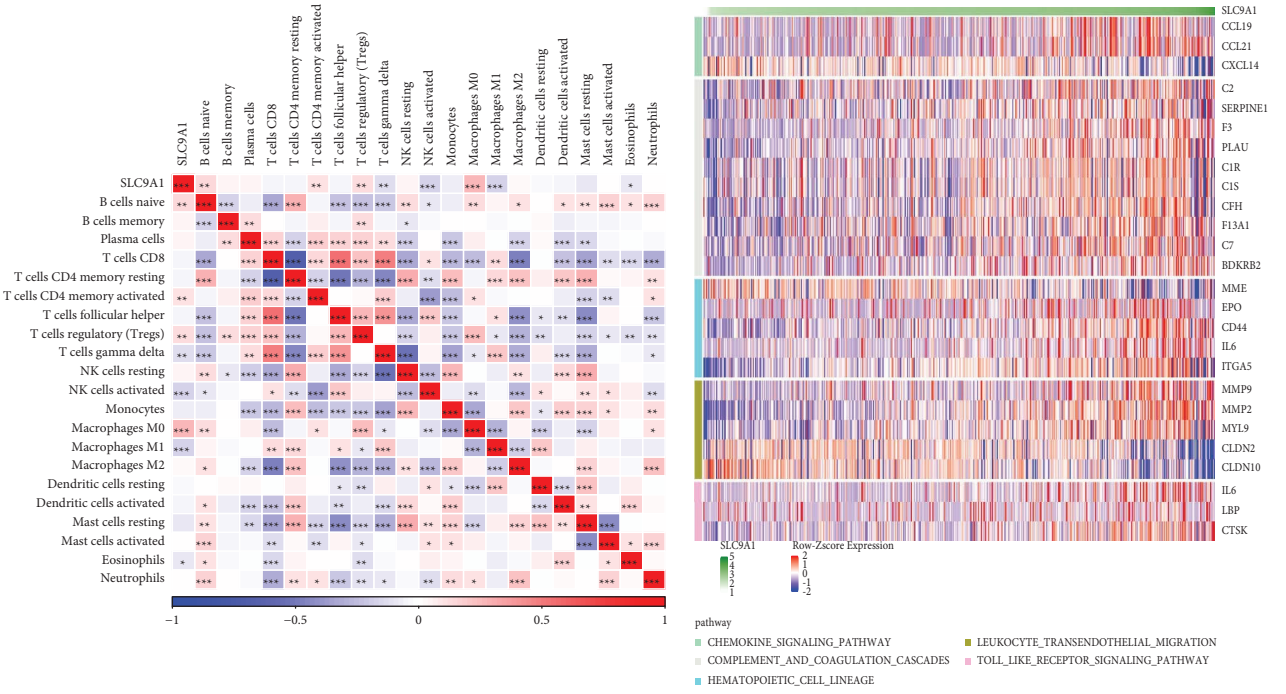

(d) (e)

Figure 2: Expression of SLC9A1 correlates with the immune score and promotes immune cell infiltration. (a) Comparison of 22 types of immune cell scores with high and low expression of SLC9A1. (b) Comparison of immune cell infiltration between high and low expression of SLC9A1. (c) Correlation between the expression of SLC9A1 and the immune score. (d) Correlation between the expression of SLC9A1 and 22 immune cell scores. (e) A heatmap of the correlation between SLC9A1 and the expression of immune-related pathway genes. $^{*}p < 0.05$, $^{**}p < 0.01$, and $^{***}p < 0.001$.

validate the ICGC dataset, and the similar results were observed (Figures 4(e) and 4(f)). Compared with the previous studies, our model is superior as shown in Supplementary Figure 3.

3.5. Association of the Prognostic Risk Model with Clinicopathological Characteristics. The differences in risk scores were compared for different clinicopathological characteristics, as shown in Figures 5(a)–5(f). The higher risk scores were significantly associated with higher TNM, histological grade, and advanced clinical staging. The risk score increases with T, M, and N stage, clinical stage, and histopathological grade.

3.6. Relationship between the Prognostic Risk Model and Immune Infiltration. We calculated scores for TCGA cohort samples at different risk levels in terms of 22 immune cells (Figure 6(a)), and the higher risk group had higher immune cell scores in some cells including CD8 T cells. Additionally, we also found higher immune scores in the high-risk group (Figure 6(b)). Immune checkpoint inhibitor therapy has gradually become the dominant method of systemic ccRCC treatment options [6]. Hence, the immune checkpoint genes in the high- and low-risk groups were analyzed, and the result showed significant differences in some immune checkpoint genes (Figure 6(c)). Next, as shown in Figure 6(d), the high-risk group got a higher TIDE score than the low-risk group, which indicated that the high-risk group was more likely to have immune escape and less likely to benefit from immunotherapy.

3.7. Establishment and Validation of a Nomogram for Prediction of OS. Univariate and multivariate Cox regression analyses of the risk score and clinicopathological characteristics revealed that M stage, age, and the risk score were significant prognostic factors (Figures 7(a) and 7(b)). For quantifying the risk assessment and survival probability of ccRCC patients, we combined the risk score with other clinicopathological features to establish a nomogram (Figure 7(c)). Moreover, the results suggest that the risk score had the strongest influence on survival prediction. Furthermore, the calibration curve was adopted to evaluate the prediction accuracy of the model. It can be observed that the predicted calibration curves of the three calibration points at 1, 3, and 5 years were nearly coincident with the standard curve, which suggests the good performance of the nomogram (Figure 7(d)). From the results of decision curve analysis (DCA), the risk score and nomogram provided notably higher benefits than the extreme curves. In contrast to other clinicopathological characteristics, both the nomogram and the risk score exhibited the most powerful survival prediction ability (Figures 7(e) and 7(f)). These data demonstrate that our prognostic risk model is reliable and effective at predicting the prognosis of ccRCC patients.

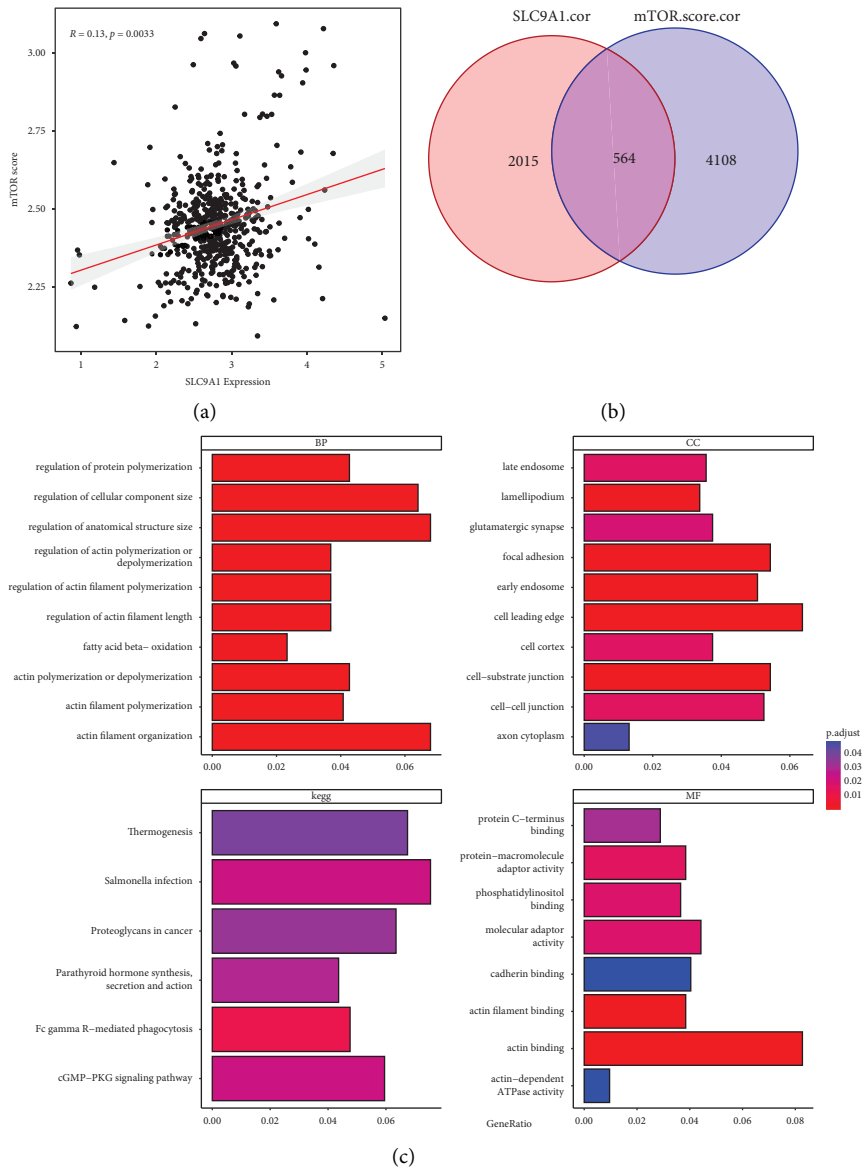

Figure 3: The expression of SLC9A1 combined with the expression of the mTOR signal pathway score. (a) Scatter plot of correlation between the expression of SLC9A1 and the mTOR signaling pathway score. (b) The Venn diagram shows 564 genes from both TCGA and ICGC gene sets. (c) Go and KEGG enrichment analysis of the 564 genes from both TCGA and ICGC gene sets. Note: GO: gene ontology; BP: biological process: CC: cellular components; MF: molecular functions.

4. Discussion

SLC9A1 expression and potential function are becoming increasingly important in various cancers. For instance, tumor tissues showed significantly higher SLC9A1 expression than normal tissues in HCC and revealed that SLC9A1 expression can serve as a crucial prognostic factor for immunotherapy against HCC [24]. By contrast, as a novel prognostic biomarker in colorectal cancer, a lower level of SLC9A1 mRNA expression was observed [25]. According to analysis of TCGA data and qRT-PCR analysis in this study, SLC9A1 was downregulated in ccRCC. Prior research has shown that cell proliferation, motility, survival, and metabolism are all under control by the mTOR signaling pathway, and SLC9A1 may contribute to mTOR's tumor-promoting effects [17, 26, 27]. The mTOR inhibitors have been approved as a therapeutic option for metastatic ccRCC [28]. Given this, this relationship between SLC9A1 and the mTOR pathway in ccRCC is worth investigating. By analyzing genes related to prognosis step by step using Cox regression, Lasso regression, K–M survival analysis, and multi-cox regression, we constructed a prognosis gene panel with eleven genes having a prognostic risk score model (including COL6A2, EXTL3, HEATR6, HSPG2, MAML3, PPP1R18, RCC2, SEMA7A, SERPINH1, TLN1, and TM9SF4). Additionally, the prognostic risk model was used to determine the risk scores for TCGA cohort and ICGC cohort patients, and a high- and low-risk subgroup

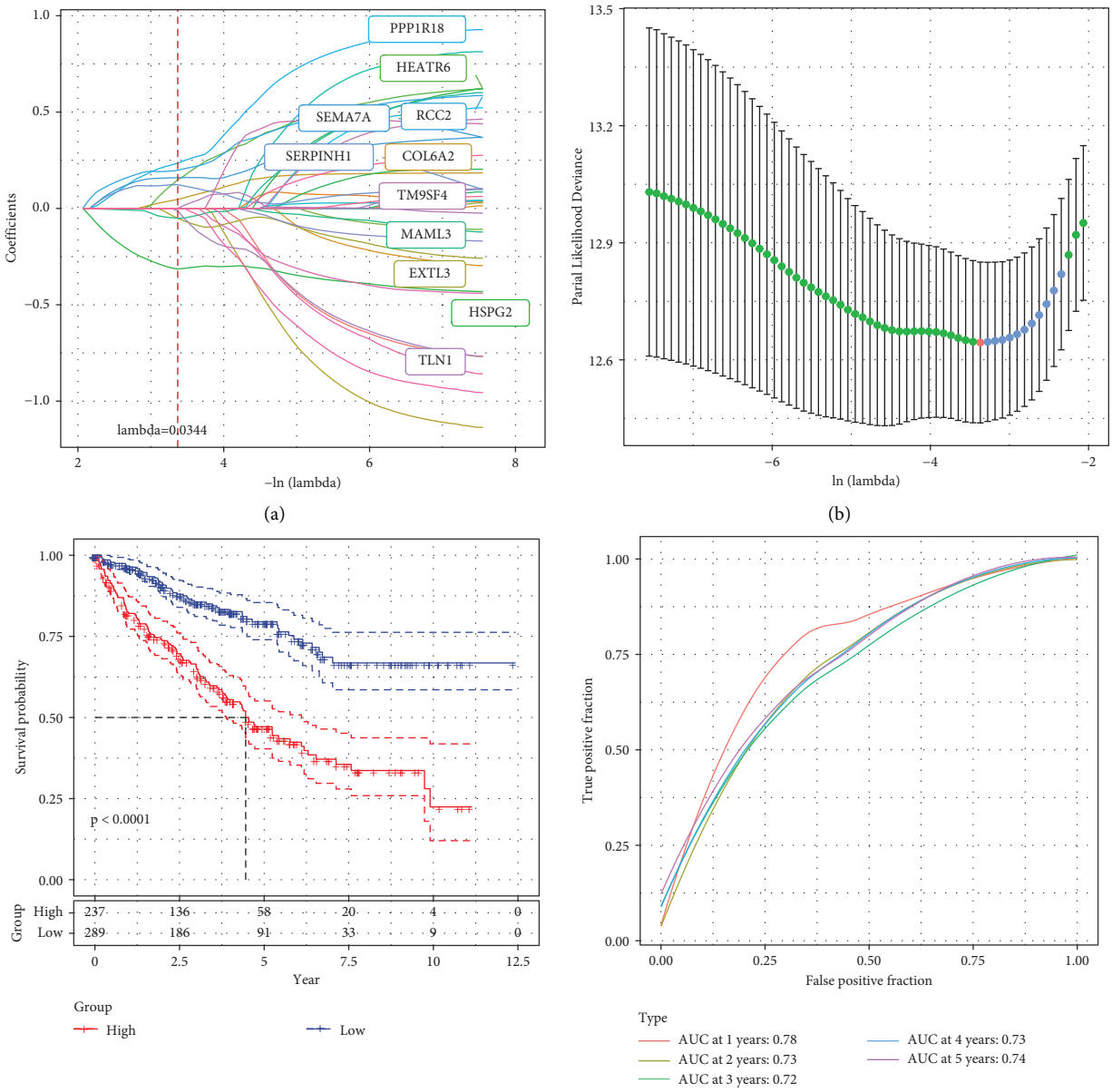

Figure 4: Continued.

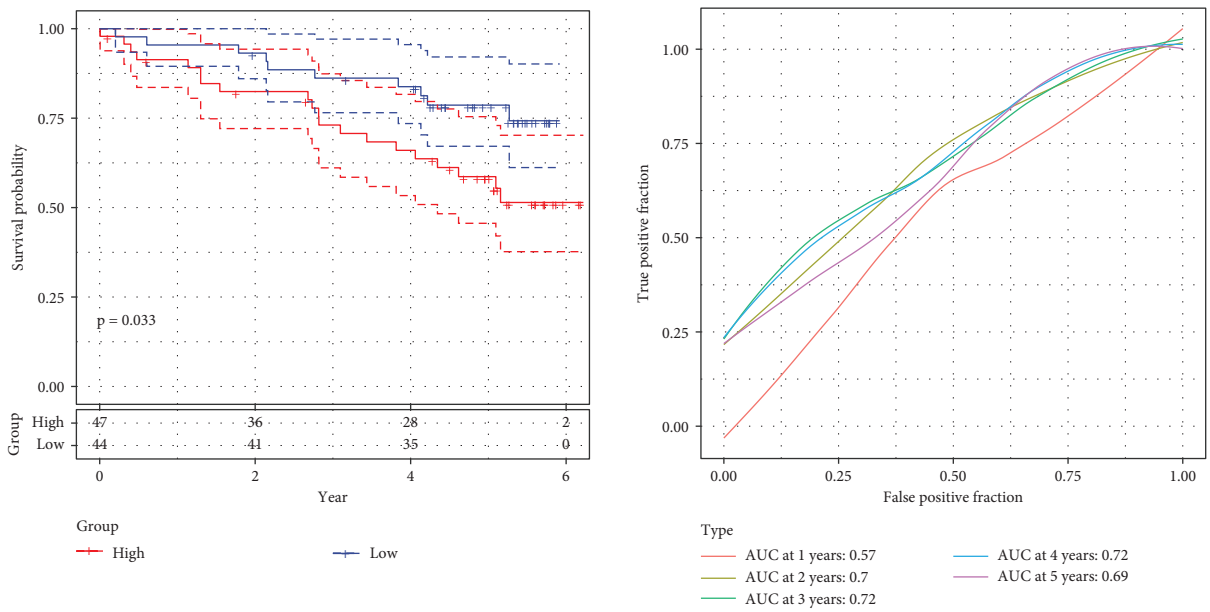

(e) (f)

Figure 4: Construction of the prognostic risk model in TCGA cohort and ICGC cohort. (a) The trajectory of each gene coefficient with lambda. (b) 10-fold cross-validation was used to find the best values for the penalty parameter. (c) The Kaplan–Meier (K–M) survival curve showed patients in the high- and low-risk group in TCGA dataset. (d) The prognostic signature's ROC curve at 1, 2, 3, 4, and 5 years in TCGA dataset. (e) The K–M survival curve showed that patients in the high- and low-risk group in the ICGC dataset. (f) The prognostic signature's ROC curve at 1, 2, 3, 4, and 5 years in the ICGC dataset.

for ccRCC patients was identified. Based on the K–M survival analysis and ROC curve, the eleven genes exhibited effective and reliable predictive abilities in the training set, with a significantly shorter OS in high-risk patients than that in low-risk ones. Furthermore, the association of the prognostic risk model with clinicopathological characteristics was verified. The results revealed association of the risk score with clinicopathological characteristics. The risk Score and other clinicopathological characteristics were combined to establish a nomogram, and the calibration curve showed the effectiveness of the nomogram. We also used DCA to evaluate the models, and the results showed that the constructed prognostic risk model is strong and generalizable.

In liver HCCs, SLC9A1 was strongly related with immune cell infiltration [24]. SLC9A1 blockade boosts immunity to glioma tumors by restoring oxidative stress in myeloid cells [29]. During this research, we found that the highly expressed group of SLC9A1 had higher immune infiltration in tumor samples and was closely associated with multiple immune cell scores. Alternatively, SLC9A1 participated in partial immune-related signaling pathways. Immune cell infiltrating tumors play an important prognostic role [30]. Therefore, we explored the immune signatures of the prognostic risk model. According to the results, the high-risk group presented a stronger immune cell infiltration and got a higher TIDE score, which indicated that the group was less likely to benefit from immunotherapy. These results may spark novel ideas for research, diagnosis, and treatment of ccRCC.

Eleven genes, COL6A2, EXTL3, HEATR6, HSPG2, MAML3, PPP1R18, RCC2, SEMA7A, SERPINH1, TLN1, and TM9SF4, were selected as important prognostic markers. COL6A2 is a member of the Collagen VI family and widely expressed in various cancers and promotes cancer progression. COL6A2 was also positively associated with an increased risk in the model of the current study (coefficient > 0). Zhong et al. found an up-regulation of COL6A2, which could be a factor in poor prognosis in metastatic ccRCC [31]. Exostosin-like glycosyltransferase 3 (EXTL3), belonging to the EXT family, takes a crucial part in predicting the prognosis of various cancers and immune deficiencies [32], but its role in ccRCC remains unknown. HEAT repeat containing 6 (HEATR6) is part of a highly expressed breast cancer amplicon. Prior research indicated that endometrial tumors from African-American women express elevated levels of HEATR6 [33]. There are few research studies of HEATR6 in ccRCC. A recent study showed that heparan sulfate proteoglycan 2(HSPG2) participates in tumor and stromal cell binding to the extracellular matrix of ccRCC, and HSPG2 showed the strongest binding to FN1, COL6, and COL12 in all cells [34]. Zhang et al. confirmed that silencing MAML3 suppresses the proliferation of gastric cancer by acting as a transcriptional coactivator in the Notch signaling pathway [35]. Genetic alterations in MAML3 and the Notch pathway in which it resides also appear to give a better prognosis for patients with ccRCC [36]. As a biomarker for immunotherapy, protein phosphatase 1 regulatory subunit 18 (PPP1R18) serves as an oncogenic role in ccRCC and was significantly related with immunity [37]. The

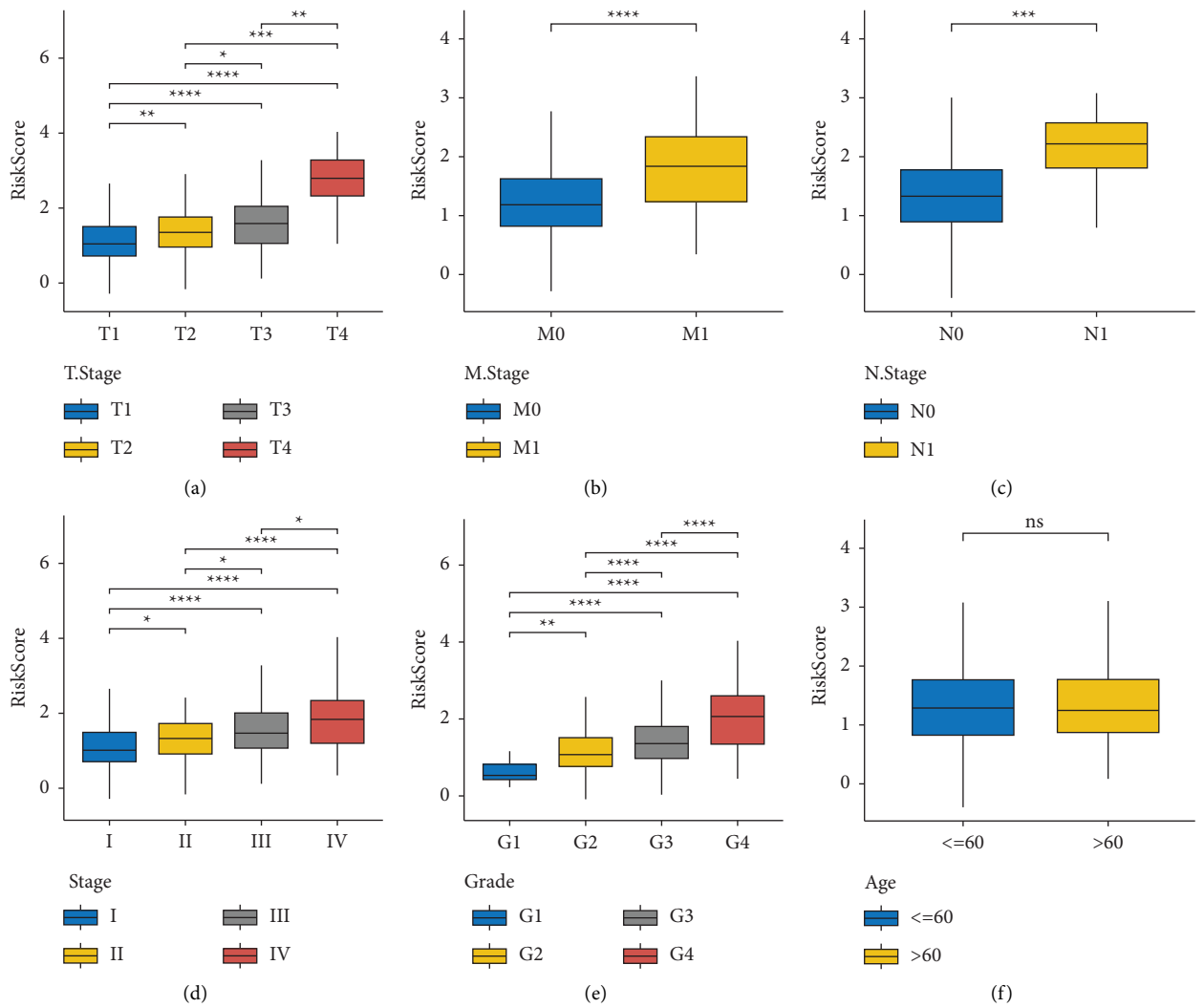

Figure 5: Comparison of the risk score for different clinicopathological characteristics. (a) T stage. (b) M stage. (c) N stage. (d) Clinical stage. (e) Histopathological grade. (f) Age. $^{*}p < 0.05$, $^{**}p < 0.01$, $^{***}p < 0.001$, and $^{****}p < 0.0001$.

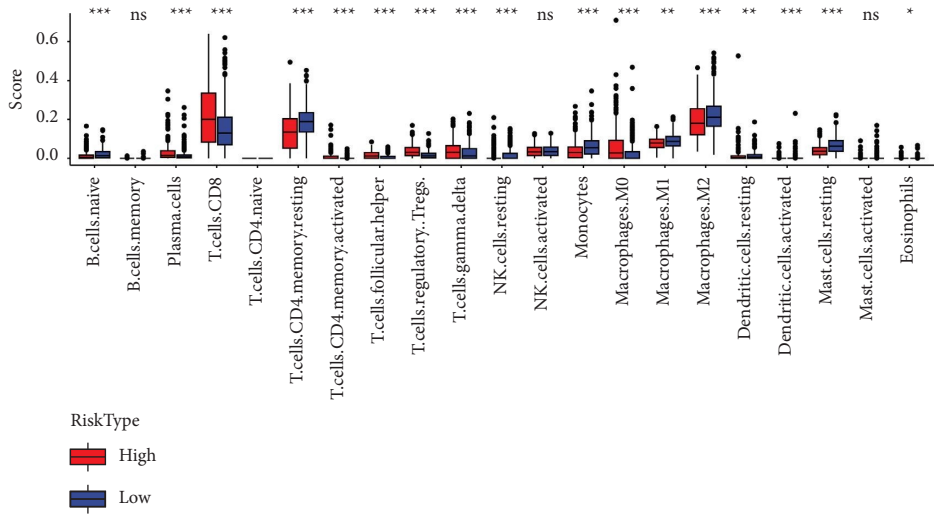

(a)

Figure 6: Continued.

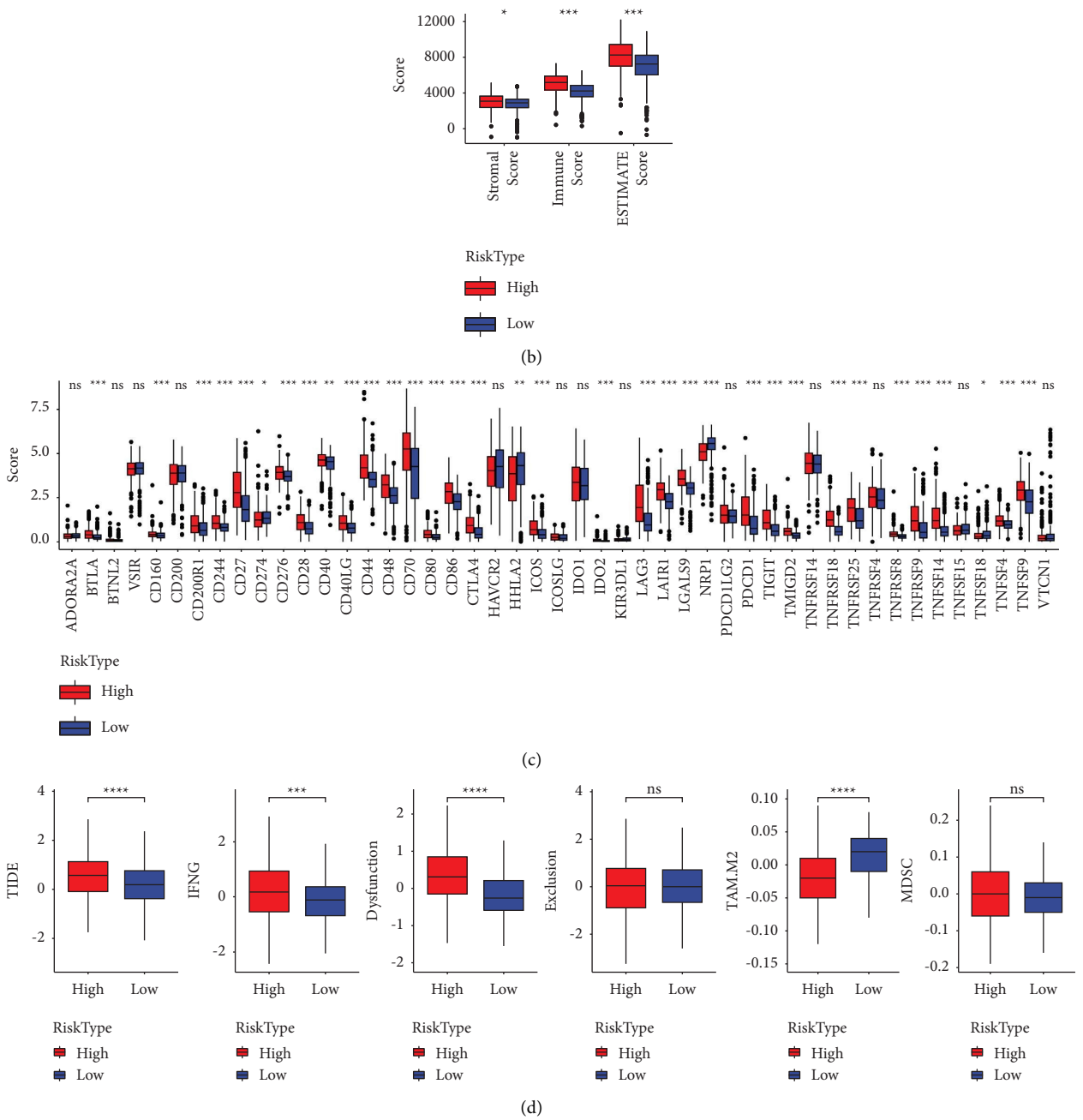

Figure 6: Comparison of immunological characteristics of different risk groups and differences of 22 immune cell scores (a), stromal, immune, and ESTIMATE scores (b) of the high- and low-risk groups in TCGA cohort. (c) Immune checkpoint genes differentially expressed in different risk groups in TCGA cohort. (d) The TIDE analysis results of different risk groups in TCGA cohort. $^{*}p < 0.05$, $^{**}p < 0.01$, $^{***}p < 0.001$, and $^{****}p < 0.0001$.

literature confirmed that chromosome condensation 2 (RCC2) was an oncogene and took a crucial part in promoting the proliferation of lung adenocarcinoma, esophageal squamous cell carcinoma, and acute myeloid leukemia [38]. The GPI-anchored semaphorin 7A (SEMA7A) affects inflammatory diseases, and Wang et al. found association of a high SEMA7A level with poor outcomes in ccRCC [39]. Serpin peptidase inhibitor clade H member 1 (SERPINH1), also known asHSP47, belongs to the serpin superfamily. The level of SERPINH1 is significantly elevated at the four TNM stages of ccRCC tissues and strongly correlates with unfavorable clinical outcomes [40]. The talin 1 (TLN1) receptor mediates cell adhesion, regulates integrin signaling, and promotes metastasis in various cancers, such as prostate, colon, and oral cancer [41]. According to Guazzi et al., transmembrane 9 superfamily 4 (TM9SF4) is a highly specific cancer biomarker that can be adopted to detect and stage gastrointestinal cancers [42], and its role in ccRCC remains unclear. The results of the present study show that these 11 genes are related with the prognosis of ccRCC

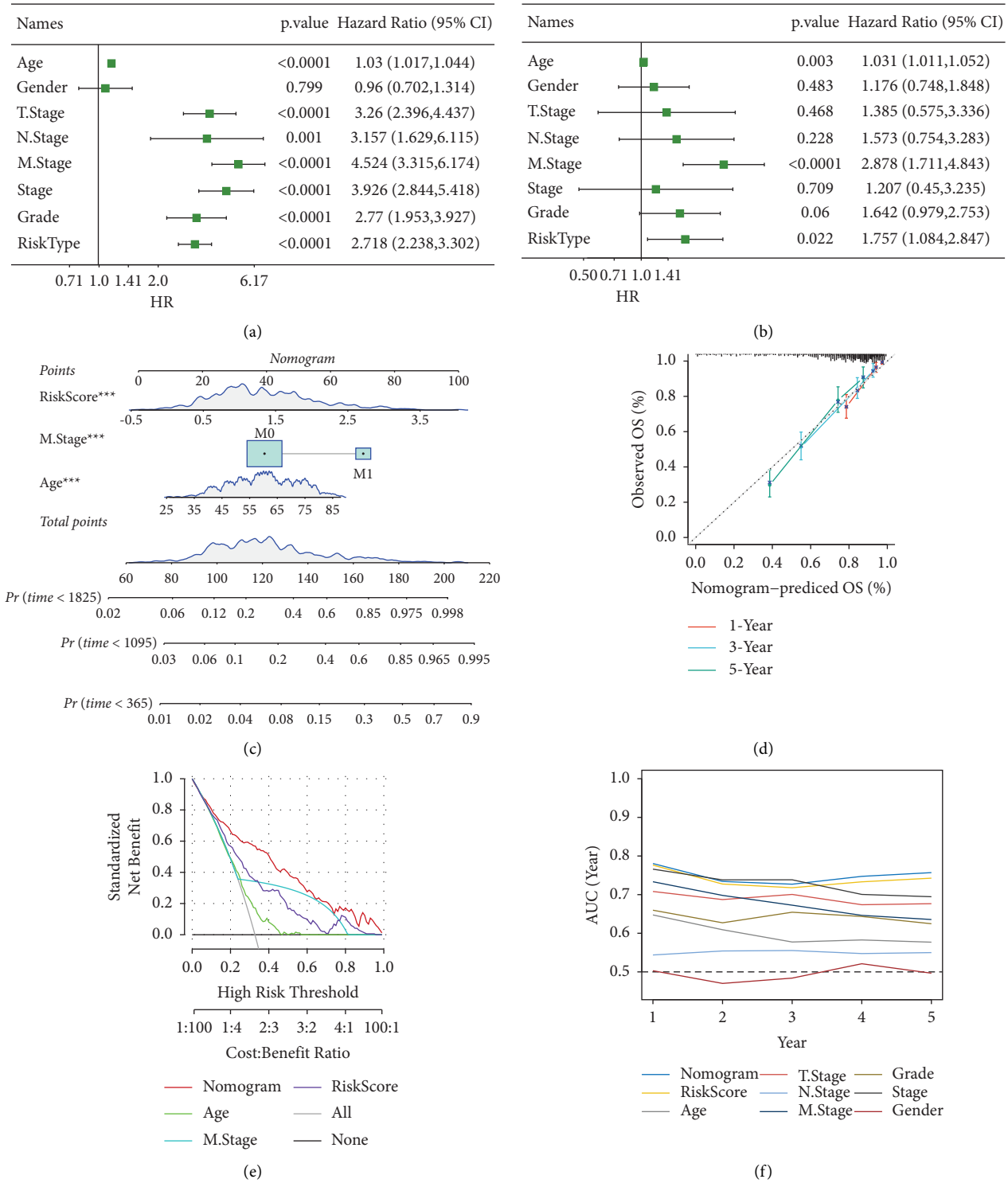

Figure 7: Construction of a nomogram and verification that the risk score has a powerful survival prediction ability. Univariate (a) and multivariate (b) Cox regression analysis of the risk score and clinicopathological characteristics in ccRCC patients. (c) The development of a nomogram based on the risk score and clinicopathological characteristics. (d) The calibration curve of the nomogram in 1, 3, and 5 years. (e) Decision curve of the nomogram. (f) Compared with other clinicopathological features, the nomogram and the risk score exhibited the more powerful capacity for survival prediction.

patients, but the exact mechanism still involves a huge network of gene regulation, which needs further exploration.

Because of the sample specificity of ccRCC, the dataset that could be selected for this study was small. Further validation of how SLC9A1 mediates mTOR signaling in ccRCC through ex vivo experimental data will be the direction of our subsequent studies. We also expect more scholars to explore this direction and more relevant datasets in the future for early validation of this risk model in a clinical cohort.

5. Conclusion

In summary, we have constructed a risk model consisting of 11 genes based on SLCA9A1 and mTOR signaling-related genes in ccRCC, which has great potential for prognostic assessment in ccRCC. The model can guide clinical immunotherapy to accurately identify high-risk patients for early clinical intervention.

Data Availability

The bioinformatic data were used to support this study and are available at TCGA and GEO databases. These prior datasets are cited at relevant places within the text as references.

Conflicts of Interest

The authors declare that they have no conflicts of interest.

Acknowledgments

This study was supported by the National Natural Science Foundation of China (Grant no. 81902601).

Supplementary Materials

Supplementary Figure 1: the overall flowchart for this work. Supplementary Figure 2: expression of 11 genes in cancer and adjacent tissues. Supplementary Figure 3: comparison with models in previously published studies. Supplementary Table 1: results of the univariate COX analysis of 564 genes in TCGA dataset and the ICGC dataset. (*Supplementary Materials*)

References

[1] D. J. Clark, S. M. Dhanasekaran, F. Petralia et al., "Integrated proteogenomic characterization of clear cell renal cell carcinoma," *Cell*, vol. 180, no. 1, p. 207, 2020.

[2] Y. Wang, R. Cong, S. Liu, B. Zhu, X. Wang, and Q. Xing, "Decreased expression of METTL14 predicts poor prognosis and construction of a prognostic signature for clear cell renal cell carcinoma," *Cancer Cell International*, vol. 21, no. 1, p. 46, 2021.

[3] H. Moch, A. L. Cubilla, P. A. Humphrey, V. E. Reuter, and T. M. Ulbright, "The 2016 WHO classification of tumours of the urinary system and male genital organs—Part A: renal, penile, and testicular tumours," *European Urology*, vol. 70, no. 1, pp. 93–105, 2016.

[4] C. Zhu, Z. Song, Z. Chen et al., "MicroRNA-4735-3p facilitates ferroptosis in clear cell renal cell carcinoma by targeting SLC40A1," *Analytical Cellular Pathology*, vol. 2022, Article ID 4213401, 12 pages, 2022.

[5] C. M. Diaz-Montero, B. I. Rini, and J. H. Finke, "The immunology of renal cell carcinoma," *Nature Reviews Nephrology*, vol. 16, no. 12, pp. 721–735, 2020.

[6] Y. F. Liu, Z. C. Zhang, S. Y. Wang et al., "Immune checkpoint inhibitor-based therapy for advanced clear cell renal cell carcinoma: a narrative review," *International Immunopharmacology*, vol. 110, Article ID 108900, 2022.

[7] W. Xu, M. B. Atkins, and D. F. Mcdermott, "Checkpoint inhibitor immunotherapy in kidney cancer," *Nature Reviews Urology*, vol. 17, no. 3, pp. 137–150, 2020.

[8] H. Sung, J. Ferlay, R. L. Siegel et al., "Global cancer statistics 2020: GLOBOCAN estimates of incidence and mortality worldwide for 36 cancers in 185 countries," *CA: A Cancer Journal for Clinicians*, vol. 71, no. 3, pp. 209–249, 2021.

[9] A. Deleuze, J. Saout, F. Dugay et al., "Immunotherapy in renal cell carcinoma: the future is now," *International Journal of Molecular Sciences*, vol. 21, no. 7, p. 2532, 2020.

[10] P. C. Barata and B. I. Rini, "Treatment of renal cell carcinoma: current status and future directions," *CA: A Cancer Journal for Clinicians*, vol. 67, no. 6, pp. 507–524, 2017.

[11] T. K. Choueiri, S. Halabi, B. L. Sanford et al., "Cabozantinib versus sunitinib as initial targeted therapy for patients with metastatic renal cell carcinoma of poor or intermediate risk: the alliance A031203 CABOSUN trial," *Journal of Clinical Oncology*, vol. 35, no. 6, pp. 591–597, 2017.

[12] Mammalian Gene Collection Mgc Program Team, E. A. Feingold, L. H. Grouse, J. G. Derge, R. D. Klausner, and F. S. Collins, "Generation and initial analysis of more than 15,000 full-length human and mouse cDNA sequences," *Proceedings of the National Academy of Sciences of the United States of America*, vol. 99, no. 26, pp. 16899–16903, 2002.

[13] R. Xie, H. Wang, H. Jin, G. Wen, B. Tuo, and J. Xu, "NHE1 is upregulated in gastric cancer and regulates gastric cancer cell proliferation, migration and invasion," *Oncology Reports*, vol. 37, no. 3, pp. 1451–1460, 2017.

[14] M. Mazzocchi, G. Di Giusto, M. Porta et al., "Na+/H+ exchanger isoform 1 activity in AQP2-expressing cells can be either proliferative or anti-proliferative depending on extracellular pH," *Journal of Physiology & Biochemistry*, vol. 76, no. 1, pp. 37–48, 2020.

[15] M. J. Hovde, D. E. Bolland, A. Armand et al., "Sodium hydrogen exchanger (NHE1) palmitoylation and potential functional regulation," *Life Sciences*, vol. 288, Article ID 120142, 2022.

[16] P. G. Valles, V. Bocanegra, A. Gil Lorenzo, and V. V. Costantino, "Physiological Functions and Regulation of the Na+/H+Exchanger [NHE1] in Renal Tubule Epithelial Cells," *Kidney & Blood Pressure Research*, vol. 40, no. 5, pp. 452–466, 2015.

[17] D. W. Good, T. George, and B. A. Watts, "Nerve growth factor inhibits Na+/H+ exchange and HCO3- absorption through parallel phosphatidylinositol 3-Kinase-mTOR and ERK pathways in thick ascending limb," *Journal of Biological Chemistry*, vol. 283, no. 39, pp. 26602–26611, 2008.

[18] C. Sanhueza, J. Araos, L. Naranjo et al., "NHE1 promote cell proliferation in ovarian cancer: a role of hypoxia-inducible factors.: IGCS-0038 06. Ovarian cancer[J]," *International Journal of Gynecological Cancer*, vol. 25, no. Suppl 1, pp. 55-56, 2015.

[19] X. Guan, L. Luo, G. Begum et al., "Elevated Na/H exchanger 1 (SLC9A1) emerges as a marker for tumorigenesis and prognosis in gliomas," *Journal of Experimental & Clinical Cancer Research*, vol. 37, no. 1, p. 255, 2018.

[20] X. Li and L. Fliegel, "Permissive role of Na+/H+ exchanger isoform 1 in migration and invasion of triple-negative basal-like breast cancer cells," *Molecular and Cellular Biochemistry*, vol. 477, no. 4, pp. 1207–1216, 2022.

[21] K. Li, Y. Li, Y. Lyu et al., "Development of a phagocytosis-dependent gene signature to predict prognosis and response to checkpoint inhibition in clear-cell renal cell carcinoma," *Frontiers in Immunology*, vol. 13, Article ID 853088, 2022.

[22] Z. Li, G. Du, R. Zhao et al., "Identification and validation of a hypoxia-related prognostic signature in clear cell renal cell carcinoma patients," *Medicine (Baltimore)*, vol. 100, no. 39, Article ID e27374, 2021.

[23] Y. Chen, Y. Liang, Y. Chen, S. Ouyang, K. Liu, and W. Yin, "Identification of prognostic metabolism-related genes in clear cell renal cell carcinoma," *JAMA Oncology*, vol. 2021, Article ID 2042114, 13 pages, 2021.

[24] Y. T. Zhou, H. Chen, M. Ai et al., "Type-1 Na+/H+ exchanger is a prognostic factor and associate with immune infiltration in liver hepatocellular carcinoma," *Life Sciences*, vol. 278, Article ID 119613, 2021.

[25] X. Zhou, M. Jiang, Z. Liu et al., "Na^+/H^+-Exchanger family as novel prognostic biomarkers in colorectal cancer," *JAMA Oncology*, vol. 2021, Article ID 3241351, 22 pages, 2021.

[26] G. Y. Liu and D. M. Sabatini, "mTOR at the nexus of nutrition, growth, ageing and disease," *Nature Reviews Molecular Cell Biology*, vol. 21, no. 4, pp. 183–203, 2020.

[27] D. Mossmann, S. Park, and M. N. Hall, "mTOR signalling and cellular metabolism are mutual determinants in cancer," *Nature Reviews Cancer*, vol. 18, no. 12, pp. 744–757, 2018.

[28] H. Guo, P. German, S. Bai et al., "The PI3K/AKT pathway and renal cell carcinoma," *Journal of Genetics and Genomics*, vol. 42, no. 7, pp. 343–353, 2015.

[29] M. N. Hasan, L. Luo, D. Ding et al., "Blocking NHE1 stimulates glioma tumor immunity by restoring OXPHOS function of myeloid cells," *Theranostics*, vol. 11, no. 3, pp. 1295–1309, 2021.

[30] G. Wieers, N. Demotte, D. Godelaine, and P. Van der Bruggen, "Immune suppression in tumors as a surmountable obstacle to clinical efficacy of cancer vaccines," *Cancers*, vol. 3, no. 3, pp. 2904–2954, 2011.

[31] T. Zhong, Z. Jiang, X. Wang et al., "Key genes associated with prognosis and metastasis of clear cell renal cell carcinoma," *PeerJ*, vol. 10, Article ID e12493, 2022.

[32] P. Chang, S. Chen, X. Chang, J. Zhu, Q. Tang, and L. Ma, "EXTL3 could serve as a potential biomarker of prognosis and immunotherapy for prostate cancer and its potential mechanisms," *European Journal of Medical Research*, vol. 27, no. 1, p. 115, 2022.

[33] M. D. Kessler, N. W. Bateman, T. P. Conrads, G. L. Maxwell, J. C. Dunning Hotopp, and T. D. O'Connor, "Ancestral characterization of 1018 cancer cell lines highlights disparities and reveals gene expression and mutational differences," *Cancer*, vol. 125, no. 12, pp. 2076–2088, 2019.

[34] K. H. Bond, T. Chiba, K. P. H. Wynne et al., "The extracellular matrix environment of clear cell renal cell carcinoma determines cancer associated fibroblast growth," *Cancers*, vol. 13, no. 23, p. 5873, 2021.

[35] Q. Zha, X. Wu, J. Zhang et al., "Hsa_circ_0007967 promotes gastric cancer proliferation through the miR-411-5p/MAML3 axis," *Cell Death & Disease*, vol. 8, no. 1, p. 144, 2022.

[36] C. Feng, Z. Xiong, H. Jiang, Q. Ding, Z. Fang, and W. Hui, "Genetic alteration in notch pathway is associated with better prognosis in renal cell carcinoma," *BioFactors*, vol. 42, no. 1, pp. 41–48, 2016.

[37] Y. Wang, S. Liu, Y. Chen, B. Zhu, and Q. Xing, "Survival prognosis, tumor immune landscape, and immune responses of PPP1R18 in kidney renal clear cell carcinoma and its potentially double mechanisms," *World Journal of Oncology*, vol. 13, no. 1, pp. 27–37, 2022.

[38] N. Zhang, Y. Shen, H. Li et al., "The m6A reader IGF2BP3 promotes acute myeloid leukemia progression by enhancing RCC2 stability," *Experimental and Molecular Medicine*, vol. 54, no. 2, pp. 194–205, 2022.

[39] Y. Wang, C. Li, X. Qi et al., "A comprehensive prognostic analysis of tumor-related blood group antigens in pan-cancers suggests that SEMA7A as a novel biomarker in kidney renal clear cell carcinoma," *International Journal of Molecular Sciences*, vol. 23, no. 15, p. 8799, 2022.

[40] Y. Qi, Y. Zhang, Z. Peng et al., "SERPINH1 overexpression in clear cell renal cell carcinoma: association with poor clinical outcome and its potential as a novel prognostic marker," *Journal of Cellular and Molecular Medicine*, vol. 22, no. 2, pp. 1224–1235, 2018.

[41] Y. Zhang, L. Sun, H. Li et al., "Binding blockade between TLN1 and integrin beta1 represses triple-negative breast cancer," *Elife*, vol. 11, 2022.

[42] P. Guazzi, D. Zocco, S. Isajevs et al., "TM9SF4 expression in tumor tissues: a novel diagnostic biomarker for gastrointestinal tumors," *Translational Cancer Research*, vol. 9, no. 11, pp. 6652–6659, 2020.

Hindawi
Journal of Oncology
Volume 2023, Article ID 7097909, 11 pages
https://doi.org/10.1155/2023/7097909

Research Article

M6A Promotes Colorectal Cancer Progression via Regulating the miR-27a-3p/BTG2 Pathway

Wenjun Liu,[1] Zilang Zhang,[2] Xitu Luo,[3] Kai Qian,[4] Baojun Huang,[1] Jianzhong Deng,[2] and Chengyu Yang[1]

[1]*The First Department of General Surgery, The Third Affiliated Hospital of Guangzhou Medical University, Guangzhou 510000, China*
[2]*Department of Anorectal Surgery, The First People's Hospital of Foshan, Foshan, Guangdong 528000, China*
[3]*The First Department of General Surgery, The First People's Hospital of FoShan, Foshan, Guangdong 528000, China*
[4]*Department of Vascular Surgery, Nanfang Hospital, Southern Medical University, Guangzhou 510000, China*

Correspondence should be addressed to Jianzhong Deng; jjwuvascular1@tom.com and Chengyu Yang; yangchengyu@gzhmu.edu.cn

Received 30 August 2022; Revised 2 October 2022; Accepted 24 November 2022; Published 10 February 2023

Academic Editor: Recep Liman

Long noncoding (lnc) RNAs regulate cancer progression. However, the importance of lncRNAs and how they are regulated in colorectal cancer (CRC) are unclear. We aim to evaluate the function of lncRNA ADAMTS9-AS2 in CRC and its fundamental mechanism. Levels of ADAMTS9-AS2, miR-27a-3p, and B-cell translocation gene 2 (BTG2) were measured by qPCR. Cell viability was analyzed by CCK-8 and colony formation. Migration and invasion were tested by transwell assay. The interactions among ADAMTS9-AS2, miR-27a-3p, BTG2, and YTHDF2 were analyzed by luciferase test, immunoblotting, RNA pull-down, or RNA immunoprecipitation (RIP). An animal model was adopted to assess ADAMTS9-AS2's function. Overexpressing ADAMTS9-AS2 inhibited cell migration, invasion, colony formation capacity, and proliferation *in vitro*. The direct targeting of miR-27a-3p by ADAMTS9-AS2 abrogated the latter's effect in CRC cells. BTG2 was identified a target of miR-27a-3p, and silencing BTG2 weakened miR-27a-3p's effect. Knocking down ADAMTS9-AS2 abolished sh-YTHDF2's inhibitory effect on cell proliferation and invasion. Finally, overexpressing ADAMTS9-AS2 restrained xenograft growth. M6A reader YTHDF2-mediated degradation of ADAMTS9-AS2 promotes colon carcinogenesis via miR-27a-3p/BTG2 axis.

1. Introduction

Colorectal cancer (CRC) is a leading gastrointestinal system's malignancy, and a major reason of tumor-related deaths globally due to increased morbidity. Given the unclear symptoms of early CRC, almost 60% are diagnosed at the advanced stage [1]. A key reason for CRC death is tumor recurrence and metastasis, which is closely linked to migration [2]. Hence, it is critical to better understand CRC's progression and metastasis.

Long noncoding RNAs (lncRNAs) regulate gene expression through various mechanisms [3]. Several lncRNAs have been identified in recent years that regulate tumor progression. A study reported that lncRNA HOTAIRM1 promoted thyroid cancer cells' growth and invasiveness [4]. Furthermore, data showed that the lncRNA FGD5-AS1 promoted chemoresistance of CRC cells [5]. ADAMTS9 is a tumor suppressor, and its antisense RNA 2 (ADAMTS9-AS2) transcript is a lncRNA that may impede tumor progression and metastasis [6]. Wang et al. reported that ADAMTS9-AS2 suppressed gastric tumor cell growth via regulating the expression of SPOP [7]. However, ADAMTS9-AS2's function in CRC is elusive.

N6-methyladenosine (m6A) is a common mRNAs modification [8]. m6A readers, such as YTHDF2, recognize m6A-containing mRNAs to regulate their stability [9]. There is evidence that aberrant m6A modification affects tumorigenesis. For instance, reduced m6A methylation in EC cells

suppressed PHLPP2, and increased the positive regulator mTORC2 [10].

MicroRNAs (miRNAs) modulate gene expression through interaction with mRNA's 3′UTR [11]. Data demonstrated that miR-27a-3p promotes CRC cell proliferation and motility [12]. It is also a biomarker for various malignancies and inhibits the tumor suppressor BTG2 [13]. LncRNAs can bind miRNAs as sponges and relieve the inhibitory effect of the latter on target mRNAs. Kong et al. reported that the lncRNA MCF2L-AS1 enhanced CRC cells' EMT via regulating miR-105-5p/RAB22A [14].

Among malignant tumors, the incidence and mortality of lung cancer have always been among the top in the world. Lung cancer is histopathologically divided into non-small-cell lung cancer (NSCLC) and small cell lung cancer. About 85% of lung cancer patients have non-small-cell lung cancer. Advances in the diagnosis and treatment have helped to improve the survival of cancer patients; However, the 5-year survival rate for NSCLC was 17.7. In addition, about 85% of patients with NSCLC are diagnosed at advanced stages. Therefore, further study of the pathogenesis of NSCLC, identification of new therapeutic targets, and prognostic biomarkers are the key to improve patient survival.

In this study, through bioinformatics analysis, the authors first found that RMRP may play an important role in NSCLC. Further studies showed that m6A modification improved the stability of methylated RMRP transcripts by reducing the rate of RNA degradation. In addition, RMRP can promote cell proliferation, migration, and invasion. Mechanistically, RMRP promotes TGFBR1 transcription by recruiting YBX1 to the TGFBR1 promoter. Here, we investigated the function of ADAMTS9-AS2 in CRC progression, and its regulatory influence of m6A modification. Data demonstrated that the novel ADAMTS9-AS2/miR-27a-3p/BTG2 ceRNA regulatory network might regulate CRC progression.

2. Materials and Methods

2.1. Patient Samples. Seventy-eight paired tumor and adjacent colorectal tissues from CRC patients who underwent surgical resection between February, 2016, and February, 2019, at the 1st People's Hospital of Foshan were included. Patients underwent no radio- or chemotherapy. Informed consents were received. This research has the approval from Ethics Committee of Nanfang Hospital.

2.2. Cell Culture and Transfection. Human CRC cells (LoVo, RKO, SW480, HCT116, and HT-29) and normal colon mucosa cells (NCM460) purchased from ATCC were kept in RPMI-1640 with 10% FBS (Gibco) at 37°C. The pcDNA3.1-ADAMTS9-AS2, pcDNA3.1-FTO and pcDNA3.1-YTHDF2 plasmids, the small interfering RNAs (siRNAs) specific for BTG2 (si-BTG2) and ADAMTS9-AS2 (si-ADAMTS9-AS2), and short hairpin (sh) RNA for YTHDF2 (sh-YTHDF2) were obtained from GenePharma (Suzhou). Hsa-miR-27a-3p mimics/inhibitors/negative control (NC) were obtained from GenePharma. Lipo2000 was adopted for transfections.

2.3. RT-qPCR. RNAs were isolated using TRIzol (Invitrogen), and cDNA was synthesized with a kit (Takara). qPCR was done with SYBR-Green Mix (ABI). The expression change was calculated by $2^{-\Delta\Delta Cq}$ [15]. Primers are shown as follows:

2.4. Methylated RNA Immunoprecipitation (MeRIP) Assay. Methylated RNA immunoprecipitation (MeRIP) is based on the principle of specific antibody specific binding to methylated modified bases and on the basis of RNA immunoprecipitation enrichment of methylated modified fragments, and then through high-throughput sequencing, the results were obtained by studying the RNA regions where methylation occurred on a transcriptome scale. m6A abundance was tested by EpiQuik. m6A RNA methylation quantitative kit (Biovision) was used for the m6A abundance test for the EpiQuik assay. In brief, 250 ng RNA was probed with m6A antibodies. The immunoprecipitation was reverse-transcribed to cDNA, then m6A-lncRNA levels were measured by qRT-PCR.

2.5. Immunoblotting. Proteins were isolated by RIPA buffer (Thermo), resolved by 8% SDS-PAGE, and blotted to PVDF membranes (Thermo). After blocking, membranes were probed with anti-YTHDF2 (1 : 3,000; ab220163), anti-BTG2 (1 : 2,000; ab244260), and anti-GAPDH (1 : 5000; ab8245) antibodies at 4°C. After washing, blots were probed with the 2nd antibody.

2.6. CCK-8 Analysis. Cells were cultured for 24, 48, 72, and 96 h; then, 10 μl CCK-8 was provided and kept for 2 h. OD470 was recorded with a plate reader.

2.7. Transwell Assay. Transwell inserts (8 m, Costar, Corning) with (invasion assay) or without (migration assay) Matrigel (Matrigel Basement Membrane Matrix, Corning) coating were placed in 24-well plates. Cells were cultured in top chambers without serum at a concentration of 0.1 million cells/well (invasion) or 0.5×105 cells/well (migration), and bottom chambers were loaded with RPMI-1640 (10% FBS). Two days later, cells on the top surface were discarded, while cells traveled through membranes were fixed and counted.

2.8. Colony Formation Assay. Cells were cultured (2×10^3 cells/well) for 8 days. Colonies were fixed by 3.8% PFA, stained with hematoxylin, air-dried, and counted.

2.9. Luciferase Reporter Assay. The potential miRNAs that bind to ADAMTS9-AS2 were predicted using DIANA-LncBase Predicted v2, and its downstream target of the candidate miRNAs was predicted by TargetScan. The

pmirGLO-ADAMTS9-AS2-wild-type (WT) or pmirGLO-ADAMTS9-AS2-mutant (MUT) reporter plasmids (Sangon Bio) and hsa-miR-27a-3p mimic/inhibitor/NC were cotransfected to CRC cells. Luciferase activity was detected 2 days later (Promega). Cells were cotransfected with WT- or MUT-pmirGLO-BTG2 and miR-27a-3p mimic/inhibitor/NC.

2.10. RNA Immunoprecipitation (RIP) Assay. EZ-Magna RIP kit was used. Cells were broken using RIPA buffer and probed with anti-YTHDF2, anti-IgG or anti-Ago2 antibodies, or NC IgG (Abcam, USA). Precipitated RNA was measured by qPCR.

2.11. RNA Pull-Down Assay. Lysates of SW480 and HCT116 were incubated with biotin-labeled ADAMTS9-AS2 probe (RiboBio) and streptavidin-coupled magnetic beads. Proteins in the complex pulled down by ADAMTS9-AS2 were analyzed by immunoblotting.

2.12. Xenograft Growth Assay. SW480-ADAMTS9-AS2 or control cells were seeded to female BALB/c nude mice. Tumors were monitored every week. Four weeks later, tumors were collected. Expressions of ADAMTS9-AS2, miR-27a-3p, and BTG2 were detected.

2.13. Data Analysis. SPSS 22.0 was adopted for analyzing data (mean ± SD). Comparisons between two or more groups were done by *t*-test or ANOVA. $P < 0.05$ was designated as significant.

3. Results

3.1. ADAMTS9-AS2 Is Decreased in CRC. Levels of ADAMTS9-AS2 in the CRC and normal colon tissues were analyzed using microarray data downloaded from TCGA database. The heatmap revealed that ADAMTS9-AS2 was drastically downregulated in CRC tissues (Figure 1(a)). In the GEPIA datasets as well, ADAMTS9-AS2 in CRC was considerably decreased than normal colon tissues (Figure 1(b)). Furthermore, patients with lower ADAMTS9-AS2 showed a shorter overall survival (OS) (Figure 1(c)). To verify the in silico data, we analyzed 78 pairs of CRC and adjacent tissues, CRC cells, and colon epithelial cells. ADAMTS9-AS2 was sharply suppressed in the CRC tissue (Figure 1(d)) and cell (Figure 1(e)). Thus, ADAMTS9-AS2 is downregulated in CRC and portends a poor prognosis.

3.2. The Effects of ADAMTS9-AS2 Are Partially Returned When Targeted miR-27a-3p Is Highly Expressed on CRC Cells. Bioinformatics analysis suggested that ADAMTS9-AS2 binds to miR-27a-3p via complementary base pairing (Figure 2(a)), which was proved by the luciferase assay. The luciferase activity was reduced in HCT116/SW480 cotransfected with miR-27a-3p mimic and pmirGLO-ADAMTS9-AS2-WT, whereas ADAMTS9-AS2-MUT showed no effect. In contrast, the luciferase activity was increased in cells cotransfected with miR-27a-3p inhibitor and pmirGLO-ADAMTS9-AS2-WT but not ADAMTS9-AS2-MUT (Figure 2(b)). The RIP assay further showed significantly higher enrichment of ADAMTS9-AS2 in miR-27a-3p mimic (Figures 2(c) and 2(d)). miR-27a-3p was upregulated in CRC tissues (Figure 2(e)). pcDNA3.1-ADAMTS9-AS2 transfection strikingly downregulated miR-27a-3p, which was partially reversed by miR-27a-3p (Figures 2(f) and 2(g)). CCK-8 and colony formation proved that pcDNA3.1-ADAMTS9-AS2-inhibited cell growth was diminished after miR-27a-3p (Figures 2(h) and 2(i)). The inhibitory effect on cell migration (Figure 2(j)) and invasion (Figure 2(k)) caused by pcDNA3.1-ADAMTS9-AS2 were alleviated by miR-27a-3p.

3.3. Knockdown of BTG2 Relieved miR-27a-3p-Silencing-Induced Effects on CRC Cells. We next identified BTG2 as a miR-27a-3p's target by analyzing 3′-UTR in the Starbase v3.0 database (Figure 3(a)). Transfecting miR-27a-3p and BTG2 3′ UTR-WT suppressed luciferase activity, while no difference was detected in BTG2 3′ UTR-MUT treatment. Transfecting miR-27a-3p inhibitor and BTG2-WT also increased the luciferase activity, whereas no difference was found in BTG2 3′ UTR-MUT treatment (Figure 3(b)). The RIP assay revealed greater enrichment of BTG2 in miR-27a-3p mimic (Figures 3(c) and 3(d)). In addition, BTG2 protein levels were downregulated in CRC tissues (Figure 3(e)). We then overexpressed BTG2 in cells transfected miR-27a-3p, and demonstrated BTG2 reversed miR-27a-3p's effects in cell growth (Figure 3(f)) and colony-forming capacity (Figure 3(g)). Furthermore, miR-27a-3p enhanced the migration (Figure 3(h)) and invasion (Figure 3(h)) and invasion of the CRC cells (Figure 3(i)), which was abrogated by BTG2. Furthermore, overexpressing ADAMTS9-AS2 upregulated BTG2 mRNA in HCT116 and SW480 cells, which was counteracted by miR-27a-3p mimic and siRNA-mediated BTG2 knockdown. Consistent with this, inhibiting miR-27a-3p also upregulated BTG2 mRNA in the CRC cell lines and was neutralized by si-BTG2 (Figure 3(j)). Taken together, ADAMTS9-AS2 may regulate BTG2 levels in CRC cells through an indirect interaction with miR-27a-3p.

3.4. YTHDF2 Enhanced the Degradation of m6A-ADAMTS9-AS2 in CRC Cells. The m6A demethylase FTO was overexpressed in the CRC cell lines. We therefore hypothesized that FTO may affect ADAMTS9-AS2 expression levels in CRC cells by altering its methylation status. As illustrated in Figure 4(a), overexpressing FTO in the SW480 and HCT116 cells significantly reduced m6A-ADAMTS9-AS2 levels. Furthermore, the hypomethylation of ADAMTS9-AS2 was related to a significant increase in its expression levels (Figure 4(b)), indicating that ADAMTS9-AS2 is regulated by m6A modification. In comparison to IgG immunoprecipitation, a RIP experiment demonstrated a higher concentration of ADAMTS9-AS2 in YTHDF2 immunoprecipitation (Figures 4(c) and 4(d)). RNA pull-down indicated that the complex pulled down by ADAMTS9-AS2 contained an

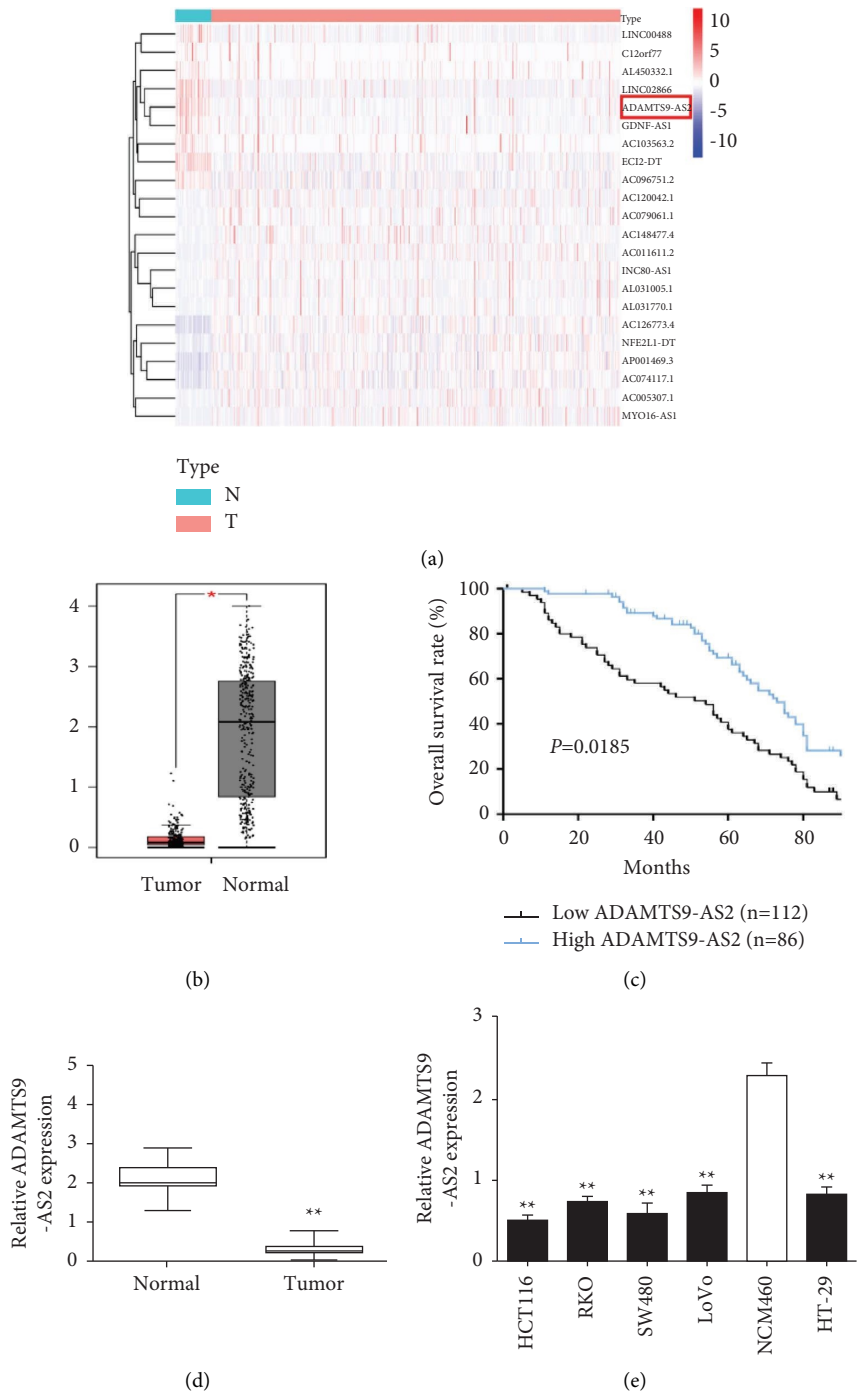

Figure 1: ADAMTS9-AS2 was decreased in CRC. (a) Heatmap of the lncRNA expression. (b) ADAMTS9-AS2 levels from TCGA datasets. (c) Kaplan–Meier analysis of ADAMTS9-AS2 levels and OS. (d) The level of ADAMTS9-AS2. (e) ADAMTS9-AS2 levels in CRC cells. $^{*}P < 0.05$ and $^{**}P < 0.01$.

Table 1: Oligonucleotide sequences.

Name	Sequence (5′-3′)
ADAMTS9-AS2	F: TCTGTTGCCCATTTCCTACC
	R: CCCTTCCATCCTGTCTACTCTA
miR-27a-3p	F: CTAATCGTGTTCACAGTGGCTAAG
	R: TATGGTTTTGACGACTGTGTGAT
BTG2	F: GCGCGGGCTCTTCCTCTTTG
	R: AAGGAAGGCTGGAAGAGTGC
GAPDH	F: TGTTCGTCATGGGTGTGAAC
	R: ATGGCATGGACTGTGGTCAT
U6	F: GCATCTGCAACACTTATCCTATAAT
	R: CGATTCGCGCATATGCTTGTGAT

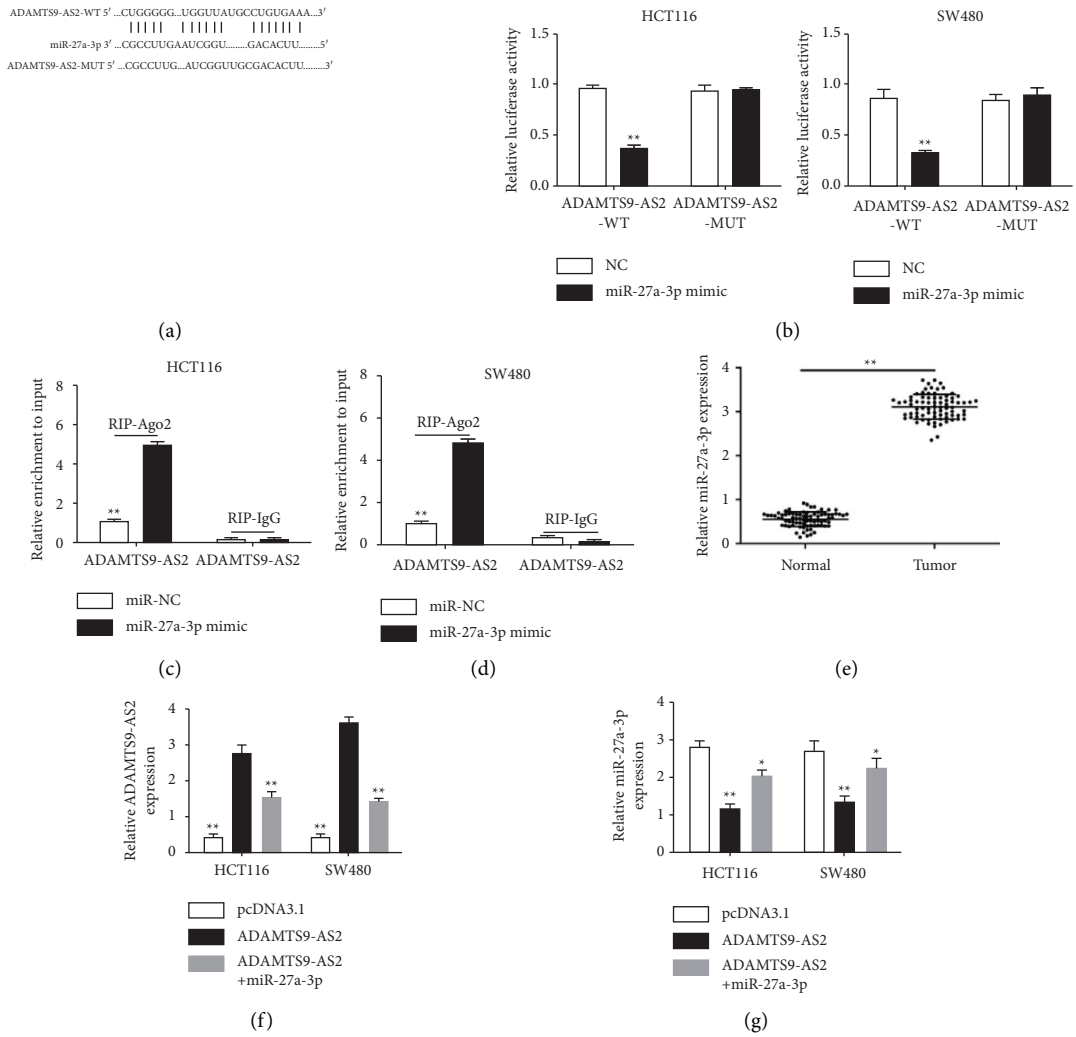

Figure 2: Continued.

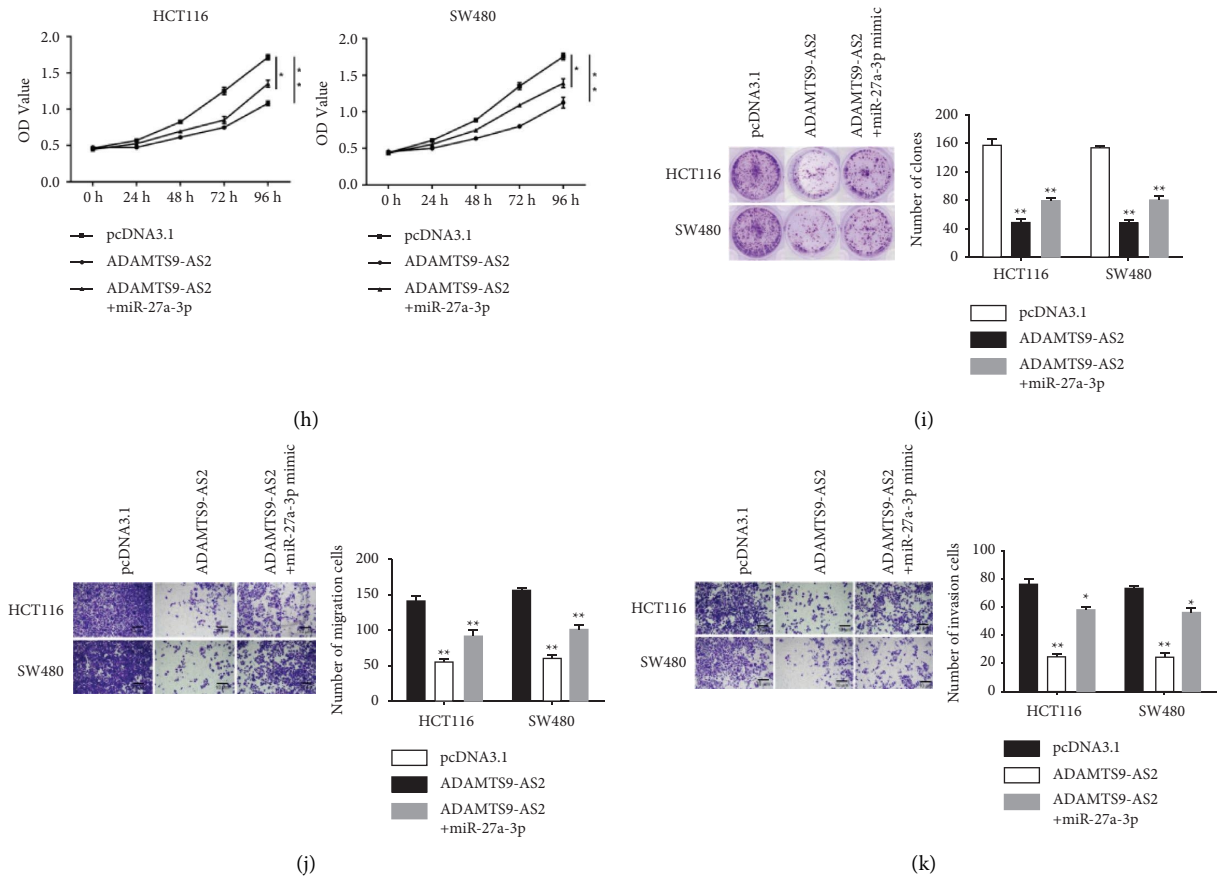

Figure 2: ADAMTS9-AS2-targeted miR-27a-3p returned the effects of ADAMTS9-AS2 on CRC cells. (a) miRNA target of ADAMTS9-AS2. (b–d) ADAMTS9-AS2 interaction with miR-27a-3p. (e) miR-27a-3p in CRC tissues. (f, g) Levels of ADAMTS9-AS2 and miR-27a-3p. (h, i) CCK-8 and clone formation. (j, k) Cell migration and invasion. $^{*}P < 0.05$ and $^{**}P < 0.01$.

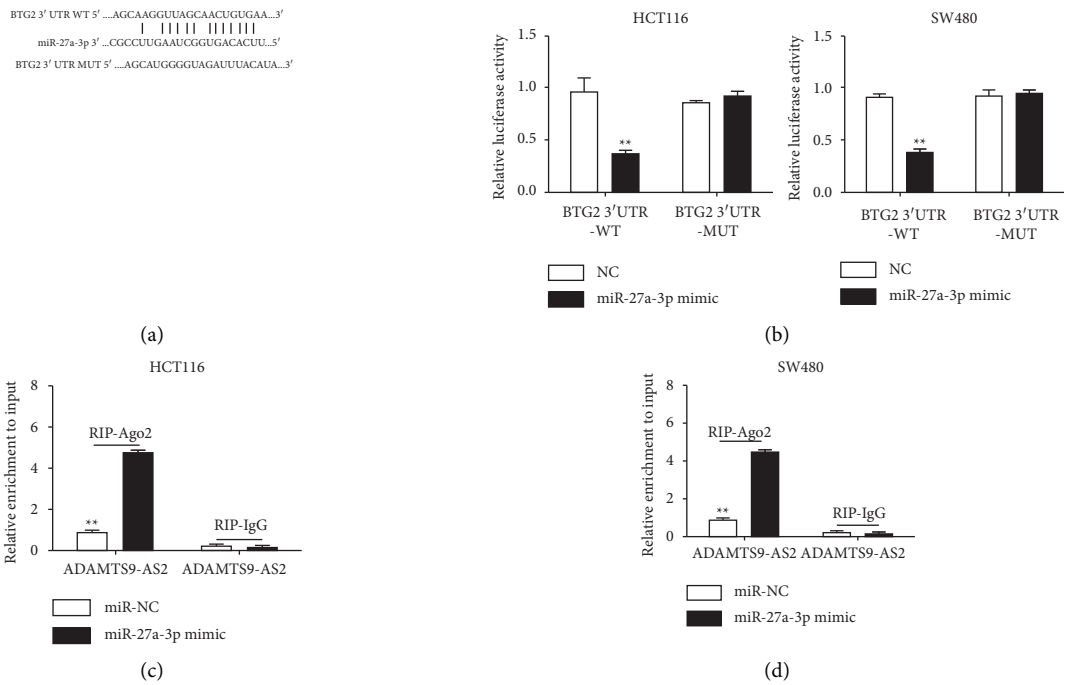

Figure 3: Continued.

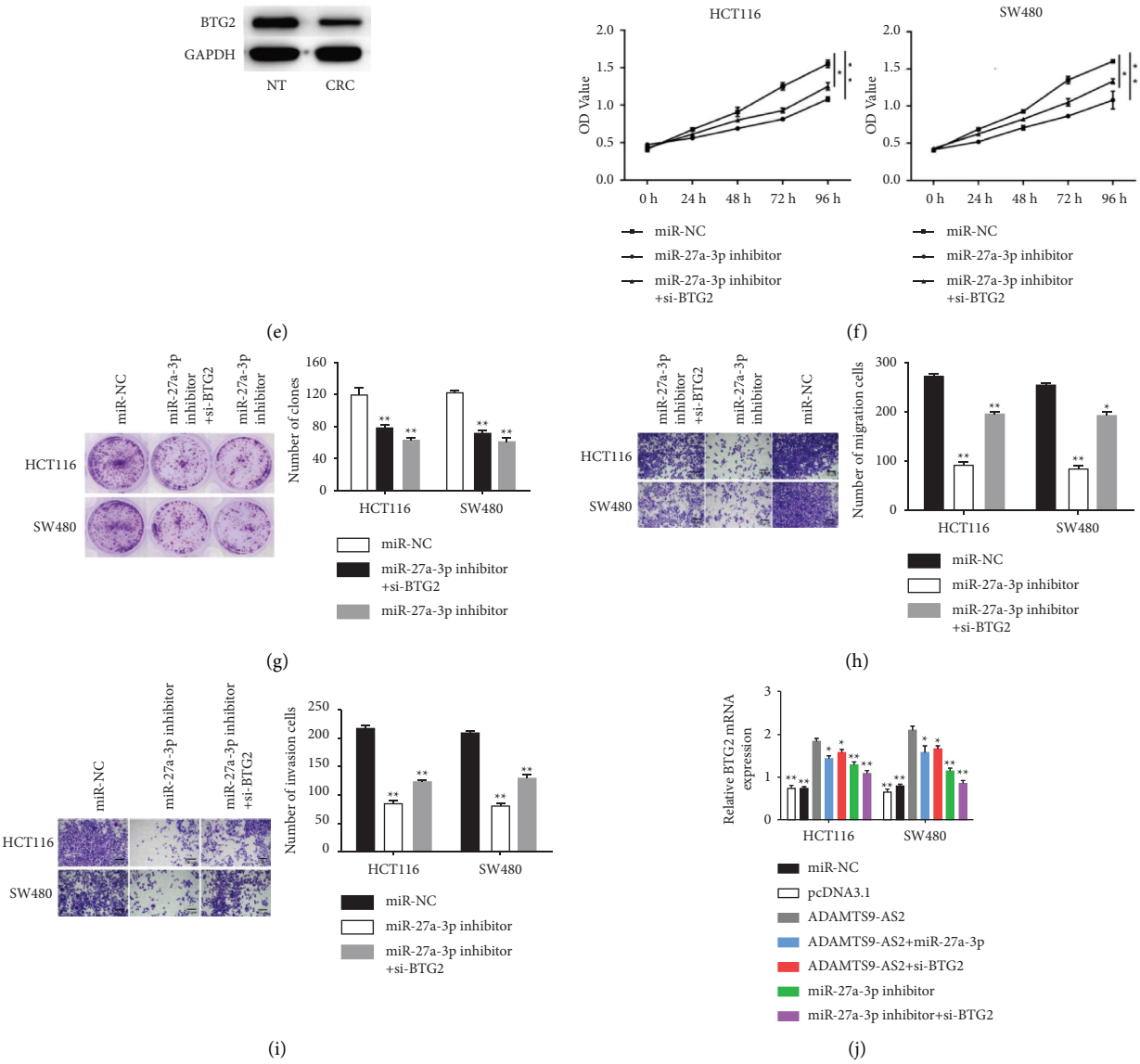

FIGURE 3: Targeting BTG2 by miR-27a-3p returned miR-27a-3p's inhibition on CRC cells. (a) miR-27a-3p's mRNA target. (b–d) Interaction of ADAMTS9-AS2 and miR-27a-3p. (e) BTG2 levels in CRC tissues. (f, g) CCK-8 and clone formation. (h, i) Cell migration/invasion assay. (j) BTG2 levels after transfection. $^{*}P < 0.05$ and $^{**}P < 0.01$.

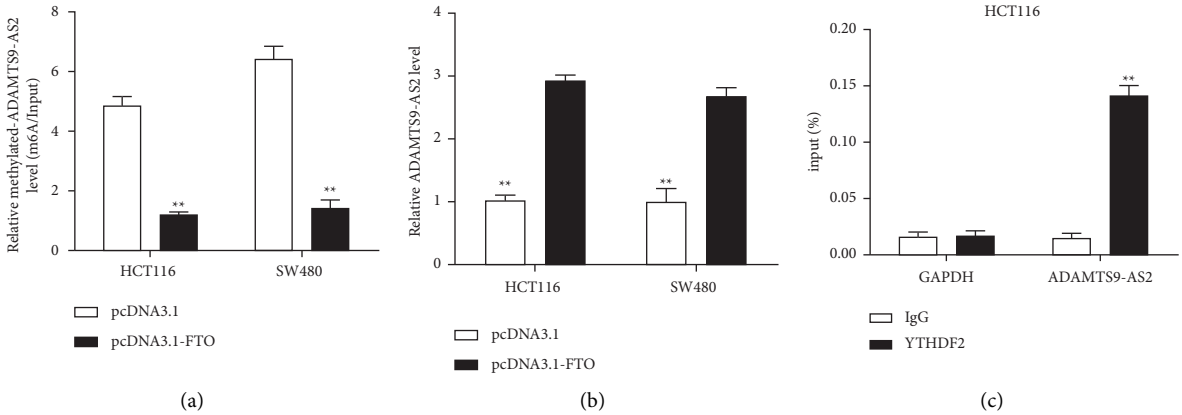

FIGURE 4: Continued.

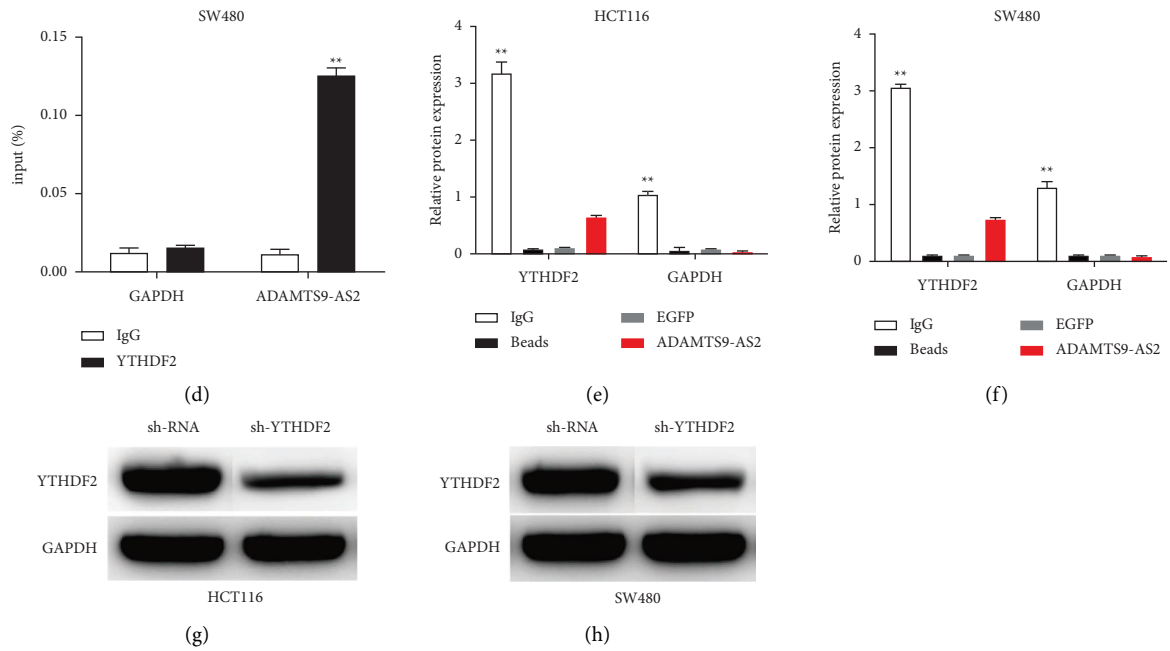

Figure 4: YTHDF2 increased degradation of m6A-methylated ADAMTS9-AS2 in CRC cells. FTO or pcDNA were transfected to HCT116 and SW480. (a) The enrichment of m6A-modified ADAMTS9-AS2 was measured using a MeRIP-qPCR experiment. (b) ADAMTS9-AS2 levels. (c, d) The endogenous combination of ADAMTS9-AS2 and YTHDF2 was measured by RIP and qPCR. (e, f) RNA pull-down confirmed that YTHDF2 recognized ADAMTS9-AS2. (g, h) Western blotting revealed sh-YTHDF2 transfection effectiveness. $^{*}P < 0.05$ and $^{**}P < 0.01$.

abundance of YTHDF2 protein (Figures 4(e) and 4(f)). The results revealed that YTHDF2 recognized ADAMTS9-AS2. YTHDF2 knockdown effectively reduced ADAMTS9-AS2 degradation (Figures 4(g) and 4(h)).

3.5. YTHDF2 Silencing Inhibited CRC Cells by Preventing the Degradation of Methylated ADAMTS9-AS2. To assess YTHDF2's function in CRC, we silenced it in cells overexpressing ADAMTS9-AS2. sh-YTHDF2's promotive effect on ADAMTS9-AS2 level was inhibited by si-ADAMTS9-AS2 (Figure 5(a)). YTHDF2 knockdown inhibited cell growth (Figure 5(b)), colony formation (Figure 5(c)), and invasion (Figure 5(d)), and the malignant phenotype was rescued by ADAMTS9-AS2 silencing.

3.6. ADAMTS9-AS2 Prevents Tumor Growth. The suppressive effects of ADAMTS9-AS2 on CRC growth was also evaluated by establishing xenografts. The CRC cells overexpressing ADAMTS9-AS2 showed less tumor volume (Figures 6(a) and 6(b)) and weight (Figure 6(c)) compared to controls, indicating that ADAMTS9-AS2 suppressed tumor growth. The ADAMTS9-AS2 levels were reduced in the tumor tissues (Figure 6(d)). Moreover, the overexpression of ADAMTS9-AS2 upregulated BTG2 (Figure 6(e)) and downregulated miR-27a-3p in CRC (Figure 6(f)).

4. Discussion

Increasing evidence shows that aberrant lncRNAs are linked to the development of CRC. For example, ENO1-IT modulates KAT7 histone acetyltransferase and consequently altered CRC biological function [16]. Furthermore, LINC00265 is upregulated in CRC, and its knockdown in mice significantly reduced colorectal carcinogenesis [17]. We found that ADAMTS9-AS2 was decreased in the CRC samples in TGCA database, and associated with the worse survival rate. ADAMTS9-AS2 (Ensembl, ENSG00000241684) has been linked to several tumor-associated genes in multiple cancers. For example, ADAMTS9-AS2 was increased in TMZ-resistant glioblastoma cells to enhance chemoresistance by upregulating the FUS/MDM2 axis [18]. We also demonstrated that ADAMTS9-AS2 decreased in CRC. Decreased ADAMTS9-AS2 was linked to poor differentiation, lymph node metastases, and advanced TNM staging. Overexpressing ADAMTS9-AS2 in CRC cells inhibited their malignant potential *in vitro*. Thus, ADAMTS9-AS2 is a potential marker for the CRC prognosis and may function as a tumor suppressor.

The hypothesis that ceRNA (competitive endogenous RNA), proposed by Pier Paolo Pandolfi's group at Harvard Medical School in 2011, is a mode of regulating gene expression. Transcripts that share miRNA-binding sites compete to bind the same miRNA, thereby regulating each other's expression levels. Based on ceRNA hypothesis, lncRNAs regulate mRNAs post-transcriptionally by competitively binding to miRNAs containing response regions [19, 20]. For instance, lncRNA UCA1 sponges miR-143 and upregulates MYO6, thereby promoting CRC [21]. Likewise, UICLM promotes CRC metastasis by upregulating ZEB2 via its sponging action on miRNA-215 [22]. A previous study showed that miR-27a-3p was upregulated in CRC, and silencing it decreased cell growth [12].

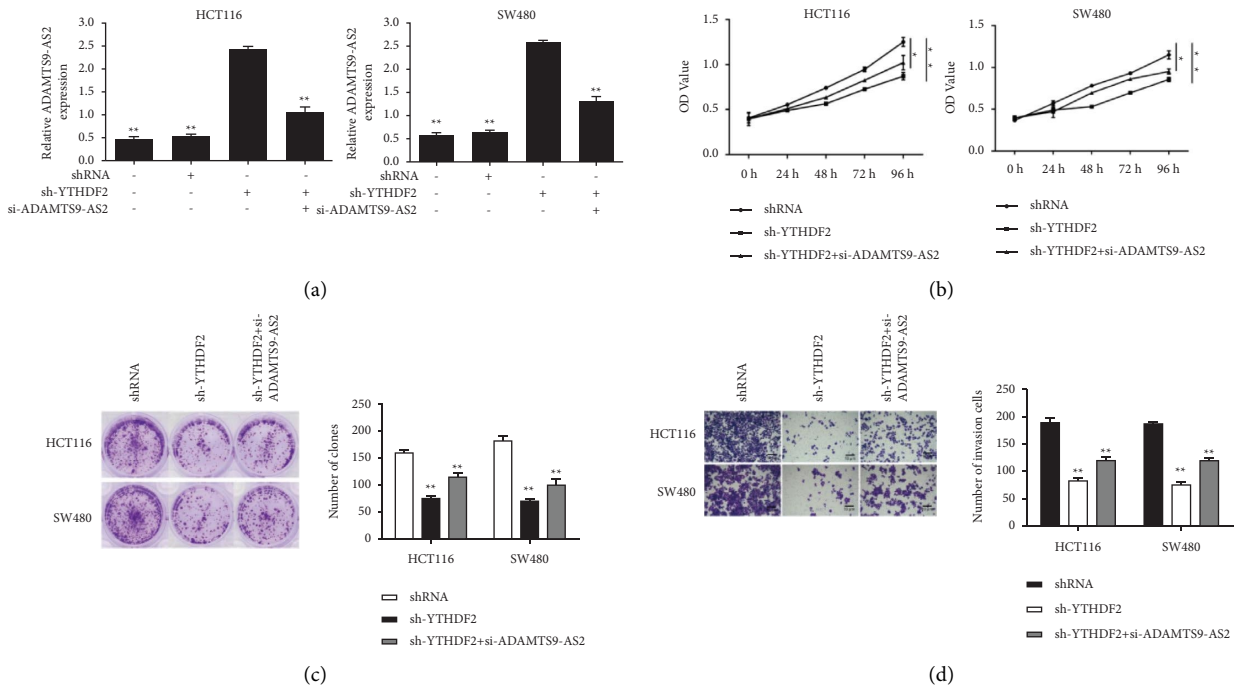

Figure 5: YTHDF2 knockdown suppressed growth and invasion of CRC cells by reducing m6A-modified ADAMTS9-AS2 degradation. (a) Levels of ADAMTS9-AS2. (b, c) Cell proliferation and colony formation assay. (d) Cell invasion assay. $^{*}P < 0.05$ and $^{**}P < 0.01$.

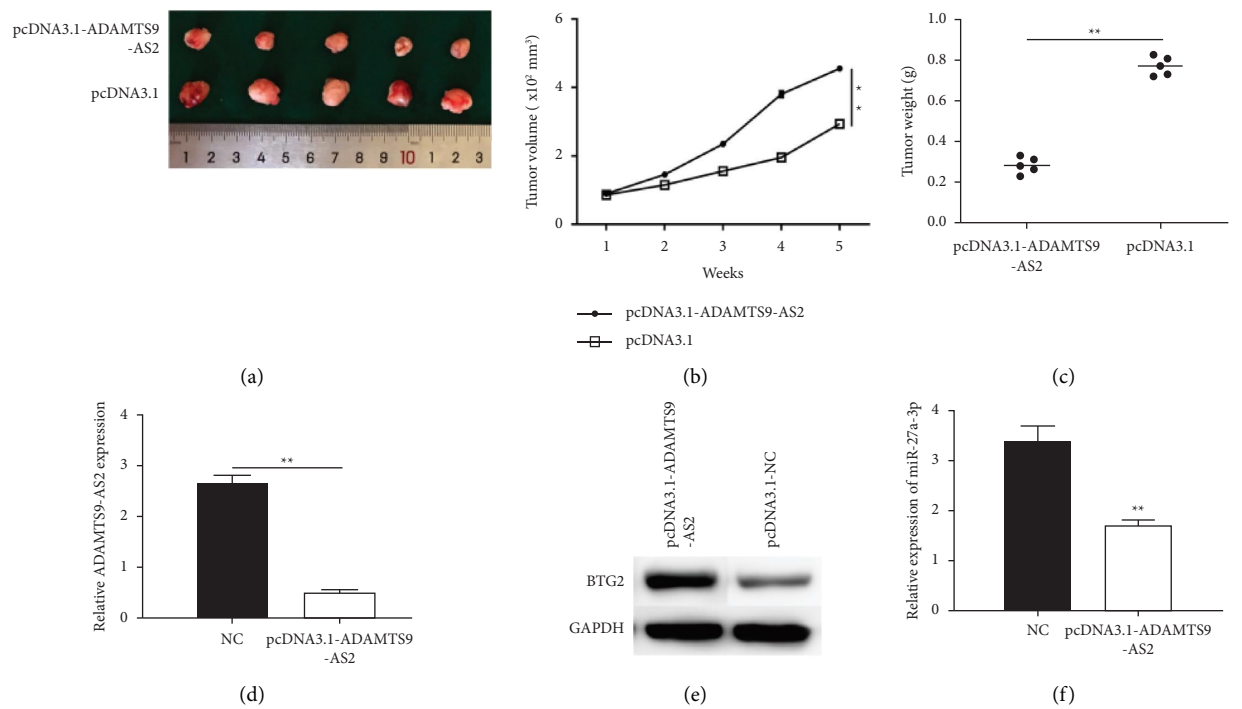

Figure 6: ADAMTS9-AS2 overexpression retarded tumor growth. SW480-pcDNA-ADAMTS9-AS2 or control cells were inoculated to nude mice for four weeks. (a, b) Tumor volume. (c) Tumor weight. (d) ADAMTS9-AS2 levels. (e) BTG2 protein levels. (f) miR-27a-3p levels in xenografts. $^{*}P < 0.05$ and $^{**}P < 0.01$.

BTG2 was proved as a miR-27a-3p's target by the luciferase assay and RIP assay. BTG2 regulates cell division, DNA repair, transcriptional control, and mRNA stability [23]. BTG2 was decreased in different cancers. For instance, BTG2 decrease promoted breast cancer's metastasis [24]. Likewise, miR-6875-3p affects cancer cells' invasiveness via BTG2 [25].

We revealed that BTG2 was decreased in CRC, and its silencing abrogated miR-27a-3p's pro-oncogenic effects. Given the abundance of m6A modification in eukaryotic mRNAs, it has received considerable attention as a regulatory factor in cancer and other pathological and developmental states.

Studies demonstrated that m6A binding protein YTHDF2 destabilized EGFR via binding to m6A site, and inhibited hepatocellular carcinoma cells [26]. YTHDF2 also regulates the stability of lncRNAs and mRNA during cancer development. Another study revealed that YTHDF2 inhibited lncRNA GAS5 in cervical cancer cells by promoting its degradation [27]. Consistent with this, hypermethylation of ADAMTS9-AS2 increased its degradation through the recruitment of YTHDF2. These findings show that aberrant m6A modification of ADAMTS9-AS2 is reliant on YTHDF2. Knocking down YTHDF2 inhibited CRC cell proliferation and invasion by restoring ADAMTS9-AS2 expression, implying that YTHDF2 may have an oncogenic role in CRC.

5. Conclusions

Our data indicated miR-27a-3p as a direct target of ADAMTS9-AS2 for the first time. Overexpression of ADAMTS9-AS2 downregulated miR-27a-3p. miR-27a-3p was increased in HT-29/SW480, and its overexpression ameliorated its inhibitory effects of elevated ADAMTS9-AS2. The results indicated that ADAMTS9-AS2 may inhibit CRC through regulating miR-27a-3p. In summary, ADAMTS9-AS2 is downregulated in CRC, and its overexpression inhibited growth and invasion of CRC cells. Mechanistically, ADAMTS9-AS2 functions as a ceRNA against miR-27a-3p, which upregulates BTG2. Furthermore, aberrant m6A modification was associated with the decreased levels of ADAMTS9-AS2 in CRC. The YTHDF2/ADAMTS9-AS2/miR-27a-3p/BTG2 modulatory network is a novel pathway participated in CRC development, and ADAMTS9-AS2 may function as a novel therapeutic target.

Data Availability

The experimental data used to support the findings of this study are available from the corresponding authors upon request.

Disclosure

Wenjun Liu and Zilang Zhang are the co-first authors.

Conflicts of Interest

The authors declare that they have no conflicts of interest regarding this work.

Authors' Contributions

WJL and LXT supervised the project. WJL, KQ, BJH, and JZD carried out experiments. ZLZ and CYY collected data and performed analysis. WJL and LXT wrote and edited the manuscript. Wenjun Liu and Zilang Zhang contributed equally to this paper.

Acknowledgments

The present study received support from Natural Science Foundation of Guangdong (2018A0303130312).

References

[1] H. Sung, J. Ferlay, R. L. Siegel et al., "Global cancer statistics 2020: GLOBOCAN estimates of incidence and mortality worldwide for 36 cancers in 185 countries," *CA: A Cancer Journal for Clinicians*, vol. 71, no. 3, pp. 209–249, 2021.

[2] S. M. Qaderi, B. Galjart, C. Verhoef et al., "Disease recurrence after colorectal cancer surgery in the modern era: a population-based study," *International Journal of Colorectal Disease*, vol. 36, no. 11, pp. 2399–2410, 2021.

[3] A. Sanchez Calle, Y. Kawamura, Y. Yamamoto, F. Takeshita, and T. Ochiya, "Emerging roles of long non-coding RNA in cancer," *Cancer Science*, vol. 109, no. 7, pp. 2093–2100, 2018.

[4] C. Li, X. Chen, T. Liu, and G. Chen, "lncRNA HOTAIRM1 regulates cell proliferation and the metastasis of thyroid cancer by targeting Wnt10b," *Oncology Reports*, vol. 45, no. 3, pp. 1083–1093, 2020.

[5] X. Xie, X. Pan, W. Zhang, and J. An, "A context hierarchical integrated network for medical image segmentation," *Computers & Electrical Engineering*, vol. 101, Article ID 108029, 2022.

[6] J. Song, A. Ye, E. Jiang et al., "Reconstruction and analysis of the aberrant lncRNA-miRNA-mRNA network based on competitive endogenous RNA in CESC," *Journal of Cellular Biochemistry*, vol. 119, no. 8, pp. 6665–6673, 2018.

[7] F. Wang, C. Tang, D. Xu et al., "LncRNA ADAMTS9-AS2 suppresses the proliferation of gastric cancer cells and the tumorigenicity of cancer stem cells through regulating SPOP," *Journal of Cellular and Molecular Medicine*, vol. 24, no. 8, pp. 4830–4838, 2020.

[8] X. Y. Chen, J. Zhang, and J. S. Zhu, "The role of m(6)A RNA methylation in human cancer," *Molecular Cancer*, vol. 18, no. 1, p. 103, 2019.

[9] W. Zhao, X. Qi, L. Liu, S. Ma, J. Liu, and J. Wu, "Epigenetic regulation of m(6)A modifications in human cancer," *Molecular Therapy - Nucleic Acids*, vol. 19, pp. 405–412, 2020.

[10] J. Liu, M. A. Eckert, B. T. Harada et al., "m(6 A mRNA methylation regulates AKT activity to promote the proliferation and tumorigenicity of endometrial cancer," *Nature Cell Biology*, vol. 20, no. 9, pp. 1074–1083, 2018.

[11] X. Xie, X. Pan, F. Shao, W. Zhang, and J. An, "Mci-net: multiscale context integrated network for liver ct image segmentation," *Computers & Electrical Engineering*, vol. 101, Article ID 108085, 2022.

[12] W. Liu, K. Qian, X. Wei et al., "miR-27a promotes proliferation, migration, and invasion of colorectal cancer by targeting FAM172A and acts as a diagnostic and prognostic biomarker," *Oncology Reports*, vol. 37, no. 6, pp. 3554–3564, 2017.

[13] X. Xie, W. Zhang, H. Wang et al., "Dynamic adaptive residual network for liver CT image segmentation," *Computers & Electrical Engineering*, vol. 91, Article ID 107024, 2021.

[14] W. Kong, H. Li, L. Xie et al., "LncRNA MCF2L-AS1 aggravates the malignant development of colorectal cancer via targeting miR-105-5p/RAB22A axis," *BMC Cancer*, vol. 21, no. 1, p. 1069, 2021.

[15] K. J. Livak and T. D. Schmittgen, "Analysis of relative gene expression data using real-time quantitative PCR and the 2−ΔΔCT method," *Methods*, vol. 25, no. 4, pp. 402–408, 2001.

[16] J. Hong, F. Guo, S. Y. Lu et al., "*F. nucleatum* targets lncRNA ENO1-IT1 to promote glycolysis and oncogenesis in colorectal cancer," *Gut*, vol. 70, no. 11, pp. 2123–2137, 2021.
[17] Y. Zhu, L. Gu, X. Lin et al., "LINC00265 promotes colorectal tumorigenesis via ZMIZ2 and USP7-mediated stabilization of *β*-catenin," *Cell Death & Differentiation*, vol. 27, no. 4, pp. 1316–1327, 2020.
[18] Y. Yan, Z. Xu, X. Chen et al., "Novel function of lncRNA ADAMTS9-AS2 in promoting temozolomide resistance in glioblastoma via upregulating the FUS/MDM2 ubiquitination Axis," *Frontiers in Cell and Developmental Biology*, vol. 7, p. 217, 2019.
[19] M. Cesana, D. Cacchiarelli, I. Legnini et al., "A long noncoding RNA controls muscle differentiation by functioning as a competing endogenous RNA," *Cell*, vol. 147, no. 4, pp. 947–369, 2011.
[20] Y. Tay, J. Rinn, and P. P. Pandolfi, "The multilayered complexity of ceRNA crosstalk and competition," *Nature*, vol. 505, no. 7483, pp. 344–352, 2014.
[21] A. Yang, X. Liu, P. Liu et al., "LncRNA UCA1 promotes development of gastric cancer via the miR-145/MYO6 axis," *Cellular and Molecular Biology Letters*, vol. 26, no. 1, p. 33, 2021.
[22] D. L. Chen, Y. X. Lu, J. X. Zhang et al., "Long non-coding RNA UICLM promotes colorectal cancer liver metastasis by acting as a ceRNA for microRNA-215 to regulate ZEB2 expression," *Theranostics*, vol. 7, no. 19, pp. 4836–4849, 2017.
[23] A. D. Boiko, S. Porteous, O. V. Razorenova, V. I. Krivokrysenko, B. R. Williams, and A. V. Gudkov, "A systematic search for downstream mediators of tumor suppressor function of p53 reveals a major role of BTG2 in suppression of Ras-induced transformation," *Genes & Development*, vol. 20, no. 2, pp. 236–252, 2006.
[24] H. Jinghua, Z. Qinghua, C. Chenchen et al., "MicroRNA miR-92a-3p regulates breast cancer cell proliferation and metastasis via regulating B-cell translocation gene 2 (BTG2)," *Bioengineered*, vol. 12, no. 1, pp. 2033–2044, 2021.
[25] Y. Xie, J. Du, Z. Liu, D. Zhang, X. Yao, and Y. Yang, "MiR-6875-3p promotes the proliferation, invasion and metastasis of hepatocellular carcinoma via BTG2/FAK/Akt pathway," *Journal of Experimental & Clinical Cancer Research*, vol. 38, no. 1, p. 7, 2019.
[26] L. Zhong, D. Liao, M. Zhang et al., "YTHDF2 suppresses cell proliferation and growth via destabilizing the EGFR mRNA in hepatocellular carcinoma," *Cancer letters*, vol. 442, pp. 252–261, 2019.
[27] J. Shen, X. P. Feng, R. B. Hu et al., "N-methyladenosine reader YTHDF2-mediated long noncoding RNA FENDRR degradation promotes cell proliferation in endometrioid endometrial carcinoma," *Laboratory Investigation*, vol. 6, pp. 775–784, 2021.

Hindawi
Journal of Oncology
Volume 2023, Article ID 8457112, 9 pages
https://doi.org/10.1155/2023/8457112

Research Article

LncRNA CASC2 Regulate Cell Proliferation and Invasion by Targeting miR-155/SOCS1 Axis in Hepatocellular Carcinoma

Ye Yuan,[1] **Jiaxin Ye**,[1] **Xujing Zhang**,[2] **and Zhisu Liu**[1]

[1]*Department of Hepatic and Gall Surgery, Zhongnan Hospital of Wuhan University, Wuchang, Wuhan 430000, China*
[2]*Health Examination Center, Wuhan Third Hospital, Tongren Hospital of Wuhan University, Wuchang, Wuhan 430000, China*

Correspondence should be addressed to Zhisu Liu; liuzhisu123@sina.com

Received 30 August 2022; Revised 8 October 2022; Accepted 12 October 2022; Published 10 February 2023

Academic Editor: Muhammad Muddassir Ali

Long noncoding RNAs (lncRNAs) have been reported to be involved in the development and progression of various human malignancies. However, the role of lncRNA CASC2 in hepatocellular carcinoma (HCC) remains mostly unknown. The aim of this study was to investigate the potential roles and underlying mechanisms of CASC2 in HCC progression. We found that CASC2 expressions were downregulated in HCC tissue samples and cell lines. The clinical assays revealed that lower levels of CASC2 were associated with the TNM stage, lymph node metastasis, and a poorer prognosis specific to HCC patients. Overexpression of CASC2 inhibited the proliferating, migratory, and invasion capacity of HCC cells. Bioinformatics analysis and the luciferase reporter assay revealed that CASC2 worked as a molecular sponge for miR-155. And CASC2 could upregulate SOCS1 expression by inhibiting miR-155 expression in HCC cells. Furthermore, SOCS1 inhibition partially inverses the suppression effect of cell proliferation, migration, and invasion regulated by CASC2 in Huh7 and HepG2 cells. Taken together, our findings identified CASC2 as a tumor suppressor to inhibit HCC development by regulating the miR-155/SOCS1 axis, and CASC2 might be a potential therapeutic target of HCC for future clinical treatment.

1. Introduction

Hepatocellular carcinoma (HCC) is one of the most prevalent malignant tumors with a high morbidity and mortality rate worldwide. Due to the lack of diagnostic biomarkers and other methods for detecting HCC in the early stages, many HCC patients are diagnosed at an advanced stage, and some effective interventions like surgery and liver transplantation are not suitable to conduct [1]. Although there are more and more advances in therapy for treating HCC, such as surgical operation, radiotherapy, and molecularly targeted therapy, the 5-year survival rate of HCC patients still remains dismal [2]. Tumor metastasis and recurrence after surgery are the main reasons which lead to the poor prognosis [3]. Hence, it is urgent to investigate the underlying molecular mechanisms of HCC and explore novel therapeutic targets to improve the diagnosis and prognosis of HCC patients.

Long noncoding RNAs (lncRNAs) are a class of noncoding RNAs longer than 200 nucleotides and have no protein-coding capacity. In recent years, accumulating studies have shown lncRNAs play an essential role in a broad range of cellular mechanisms like transcriptional activation, intranuclear trafficking, and epigenetic modifications [4]. It has been reported that lncRNAs are differently expressed in many cancers and play essential roles in tumorigenesis by regulating oncogenes or tumor suppressor genes, which prompts growing interest in the potential clinical application as therapeutic targets of tumors. Some well-studied lncRNAs such as HOX Transcript Antisense RNA (HOTAIR), X-Inactive Specific Transcript (XIST), and Nuclear Enriched Abundant Transcript1 (NEAT1) [5–7] demonstrated to participate in tumor progression, including regulating cell proliferation, cell cycle, apoptosis, and metastasis.

LncRNA Cancer Susceptibility Candidate 2 (CASC2) was first found in endometrial cancer in 2004 and could inhibit endometrial cancer carcinogenesis, which serves as a tumor suppressor [8]. Recent studies indicate that CASC2 is expressed at low in many human malignancies including

cervical cancer, pancreatic cancer, and thyroid cancer [9–11]. In gastric cancer, CASC2 acts as a tumor suppressor, and overexpression of CASC2 could inhibit proliferation, colony formation, migration, and invasion of cancer cells [12]. Moreover, CASC2 was found downregulated in malignant melanoma, and low CASC2 expression was correlated with tumor size, TNM stage, and poor overall and disease-free survival (DFS) of malignant melanoma patients [13]. CASC2 also acts as a ceRNA for miR-18a-regulated STAT3 expression and inhibits the proliferative and metastatic capability of colorectal cancer cells [14]. And it is reported that CASC2 may affect cell growth and apoptosis of HCC cells through different mechanisms [15]. However, the involvement of CASC2 in the regulation of HCC pathogenesis remains largely unknown.

In this study, we confirmed the low expression of CASC2 in HCC tissues and cell lines and explored the regulatory effect of CASC2 on cell proliferation, migration, and invasion. Furthermore, we revealed that CASC2 could serve as the miR-155 sponge and promote the expression of suppressor of cytokine signaling 1 (SOCS1). Our findings suggest that CASC2 might inhibit the progression of HCC by regulating the miR-155/SOCS1 axis.

2. Materials and Methods

2.1. Clinical Specimens. 42 pairs of HCC tissues and adjacent normal tissues were obtained from Zhongnan Hospital of Wuhan University between May 2018 and October 2019. All samples were immediately frozen in liquid nitrogen after surgery and stored at −80°C. The specimens were confirmed by two senior independent pathologists, and tumor staging was performed following the tumor node metastasis (TNM) staging method of UICC and AJCC 2008. Subjects were excluded if they exhibited any evidence of other malignancies or any other type of liver disease. And all HCC patients were free from human immunodeficiency virus (HIV), hepatitis virus and any other viral infections. All patients did not receive radiotherapy, chemotherapy, or any other antitumor therapy before surgery. This study was approved by the ethics committee of Zhongnan Hospital of the Wuhan University. Written informed consents were obtained from all participants before the study.

2.2. Cell Culture. Human HCC cell lines (HepG2, Huh7, SMMC-7721, and QGY-7701) and the normal liver cell line LO2 were obtained from the American Type Culture Collection (ATCC, Manassas, VA, USA). The cells were cultured using Roswell Park Memorial Institute 1640 (RPMI 1640) medium (Gibco, Rockville, MD, USA) supplemented with 10% fetal bovine serum (Gibco, Rockville, MD, USA), 100 U/ml penicillin, and 100 U/ml streptomycin. All cells were in a humidified incubator at 37°C and 5% CO_2.

2.3. Cell Transfection. MiR-155 mimics and miR-con were obtained from RiboBio (Guangzhou, China), and 100 pmol miR-155 mimics were transfected into each well, respectively. Plasmids with the pcDNA3.1 vector (Invitrogen, Carlsbad, CA, USA) containing CASC2 and SOCS1 overexpression sequences were constructed, and 2 μg plasmid were transfected into each well. Transfection of HCC cells was conducted using Lipofectamine 3000 (Thermo Fisher Scientific, Waltham, MA, USA) following the manufacturer's instructions. Cells were harvested after 48 h transfection for subsequent experiments.

2.4. qRT-PCR Assay. Total RNA was extracted from HCC tissues, adjacent tissues, and HCC cells using TRIzol reagent (Invitrogen, Carlsbad, CA, USA). Then the reverse transcription kit (Invitrogen, Carlsbad, CA, USA) was used to reverse-transcribe the RNA into cDNA. The QRT-PCR assay was performed using the SYBR Green Real-Time Kit (TaKaRa, Tokyo, Japan) and real-time PCR system (Applied Biosystems 7500, Foster City, CA, USA) according to the manufacturer's guidelines. U6 was used to normalize the relative expression of CASC2 and miR-155, and GAPDH was used to normalize the relative expression of SOCS1. The relative fold changes of target genes were evaluated by the $2^{-\Delta\Delta Ct}$ method. lncRNA CASC2 forward, 5′-GCT CGG ACG AAG ATT GGA GA-3′ and reverse, 5′-ATA AGG TCA GTA ATG AGA ACT GC-3'; U6 forward, 5′-CTC CTT GTA AGC ATT GAG T-3′ and reverse, 5′-AAC AGG CAG TTT ACG CGC TC-3'; GAPDH forward, 5′-AGT GTC ACC GTT CAG CCC TTG-3′ and reverse, 5′-ACC AAG TTG CAA CAG GTC AAG-3′.

2.5. CCK-8 Assay. The Cell Counting Kit 8 (CCK-8) assay (Solarbio, Beijing, China) was used to detect cell proliferation ability. Approximately 1×10^4 Huh7 cells were seeded in each well of 96-well plates overnight at 37°C. 10 μl of CCK-8 reagent was added to each well after incubation. After incubating for another 2 h at 37°C, the absorbance at 450 nm was determined by a microplate reader (Enspire, USA), and all results were recorded.

2.6. Transwell Assay. Transwell assays were used to evaluate the cell migration and invasion abilities. For the migration assay, 1×10^5 cells were suspended in 500 μl serum-free RPIM-1640 medium and seeded into the upper chamber (Corning, Corning, NY, USA), and 700 μl RPIM-1640 containing 10% Fetal Bovine Serum(FBS) was added to the lower chamber. After 24 h incubation at 37°C, the cells on the lower surface were fixed with paraformaldehyde, stained with 0.2% crystal violet, and then imaged and enumerated with an inverted microscope (Nikon, Tokyo, Japan). For invasion assay, the upper chamber was coated with Matrigel (BD, Franklin Lakes, NJ, USA) before cells seeded, and the other steps were the same as for migration assay.

2.7. Luciferase Reporter Assay. The potential complementary sequences of CASC2 and miR-155 were predicted using StarBase (https://starbase.cysu.edu.cn/). Sequences of wild-type (Wt) or mutant-type (Mut) CASC2 or 3′UTR of SOCS1 were synthesized and cloned into the commercial pmirGLO reporter vectors (ThermoFisher, Waltham, MA, USA). The

vectors were cotransfected with miR-155 mimics or miR-NC into 239T cells with Lipofectamine 2000. Subsequently, the luciferase assays were performed using the dual-luciferase reporter assay system (Promega, Madison, WI, USA) after 24 h of transfection, according to the manufacture's protocols.

2.8. Western Blot Analysis. Radioimmunoprecipitation assay (RIPA) lysis buffer (Beyotime, Shanghai, China) was used to extract the total proteins from HCC tissues and cell lines, and the protein concentrations were quantified by bicinchoninic acid (BCA) assay (Pierce, Rockford, IL, USA). 50 μg of total proteins were separated using 10% sodium dodecyl sulfate-polyacrylamide gel electrophoresis (SDS-PAGE) and transferred to a polyvinylidene fluoride (PVDF) membrane (Millipore, Billerica, MA, USA). After incubating with nonfat milk for 2 h at room temperature to block the membrane, the PVDF membrane was incubated with primary antibody (Abcam, Cambridge, MA, USA) at 4°C overnight, and then they were incubated with secondary antibody. Finally, proteins were visualized using diaminobenzidine (DAB) chromogenic kit (Solarbio, Beijing, China), and the intensity of bands was quantified using Image J software (NIH, Bethesda, MD, USA).

2.9. Statistical Analysis. All data were analyzed using the statistical product and service solutions (SPSS) 22.0 software (IBM, Armonk, NY, USA) and presented as the mean ± standard deviation ($\overline{x} \pm s$). The Student's t-test was used to analyze the significance of the difference between two groups. The Spearman's correlation analysis was used to analyze correlation among genes. $P < 0.05$ was considered as statistically significant difference.

3. Results

3.1. CASC2 is Highly Expressed and Affect the Clinical Progress of HCC. Quantitative real-time PCR was used to identify the expression of CASC2 in HCC tissues and cells. The results showed that CACS2 was significantly decreased in HCC tissues compared to adjacent normal tissues (Figure 1(a)). Similarly, we also found the expression of CASC2 was distinctly low-regulated in HCC cell lines (HepG2, Huh7, SMMC-7721, QGY-7701) compared to normal liver cell LO2 (Figure 1(b)). Then the 42 patients were divided into 2 groups depending on the median value of CASC2 expression (low CASC2 group $n = 21$; high-CASC2 group $n = 21$). As the results showed, low expression of CASC2 presented a positive correlation with an advanced TNM stage (Figure 1(c)) and positive lymph node metastasis (Figure 1(d)). To explore whether CASC2 may influence the survivals of HCC patients, Kaplan–Meier assays were performed, and the results showed that patients with high-CASC2 expression possessed longer overall survival (OS) and disease-free survival (DFS) compared to the low-CASC2 group ($P < 0.05$). Furthermore, univariate analyses showed that CASC2 expression, TNM stage, and lymph node metastasis were significantly associated with OS and DFS. Moreover, multivariate analyses revealed that CASC2 expression was an independent prognostic indicator of HCC patients regarding OS and DFS (Table 1), suggesting CASC2 might be a promising biomarker of prognosis.

3.2. Overexpression of CASC2 Inhibits HCC Cell Proliferation, Migration, and Invasion in HCC Cells. To validate the biological role of CASC2 in HCC cells, the Huh7 and HepG2 cell lines were chosen for functional experiments due to their low CASC2 expression. As shown in Figure 2(a), the expression of CASC2 in Huh7 and HepG2 cell lines were significantly upregulated after cell transfection. The CCK-8 assay demonstrated that overexpression of CASC2 significantly suppressed the proliferative abilities of Huh7 and HepG2 cells (Figure 2(b)). Furthermore, the colony formation assay showed that overexpression of CACS2 significantly decreased the number and size of cell colonies (Figure 2(c)). Transwell migration and invasion assays revealed that after CASC2 was overexpressed, the number of cells penetrating the inserts was significantly decreased, indicating that CASC2 could obviously inhibit the migratory and invasive capabilities of Huh7 and HepG2 cells (Figures 2(d) and 2(e)).

3.3. CASC2 Is a ceRNA and Functions as a Molecular Sponge for miR-155. To reveal the underlying molecular mechanism of CASC2 in regulating HCC cells, the bioinformatics analysis website StarBase 2.0 was adopted to predict the downstream target of CASC2. The results showed there was a binding sequence between CASC2 and miR-155 (Figure 3(a)). Dual-luciferase reporter assay indicated that miR-155 mimics could weaken the luciferase activities when transfected with the Wt-CASC2. However, miR-155 mimics did not reduce the luciferase activities when transfected with the Mut-CASC2, which indicated that CASC2 could bind to miR-155 directly (Figure 3(b)). In addition, we observed the distinct increase in miR-155 expression in 4 HCC cell lines (Figure 3(c)). We also found that overexpression of CASC2 inhibit the level of miR-155 in Huh7 cells markedly (Figure 3(d)). Moreover, miR-155 was upregulated in HCC tissues compared to adjacent normal tissues (Figure 3(e)). Pearson's correlation analysis was used to analysis the relationship between the expression of CASC2 and miR-155 in HCC specimens. The results showed the expression of CASC2 was negative correlated with miR-155 (Figure 3(f)). Taken together, our findings indicated that CASC2 acted as a competing endogenous RNA to sponge miR-155 in HCC cells.

3.4. SOCS1 Acts as a Target Gene regarding miR-155. We also used StarBase 2.0 to predict the potential target genes of miR-155 and found that suppressor of cytokine signaling 1 (SOCS1) might serve as a candidate target of miR-155 with high scores (Figure 4(a)). A dual-luciferase reporter assay indicated that miR-155 mimics could significantly weaken the luciferase activities of the vector carrying SOCS1 (Wt) 3′UTR instead of a mutant-type in Huh7 cell (Figure 4(b)),

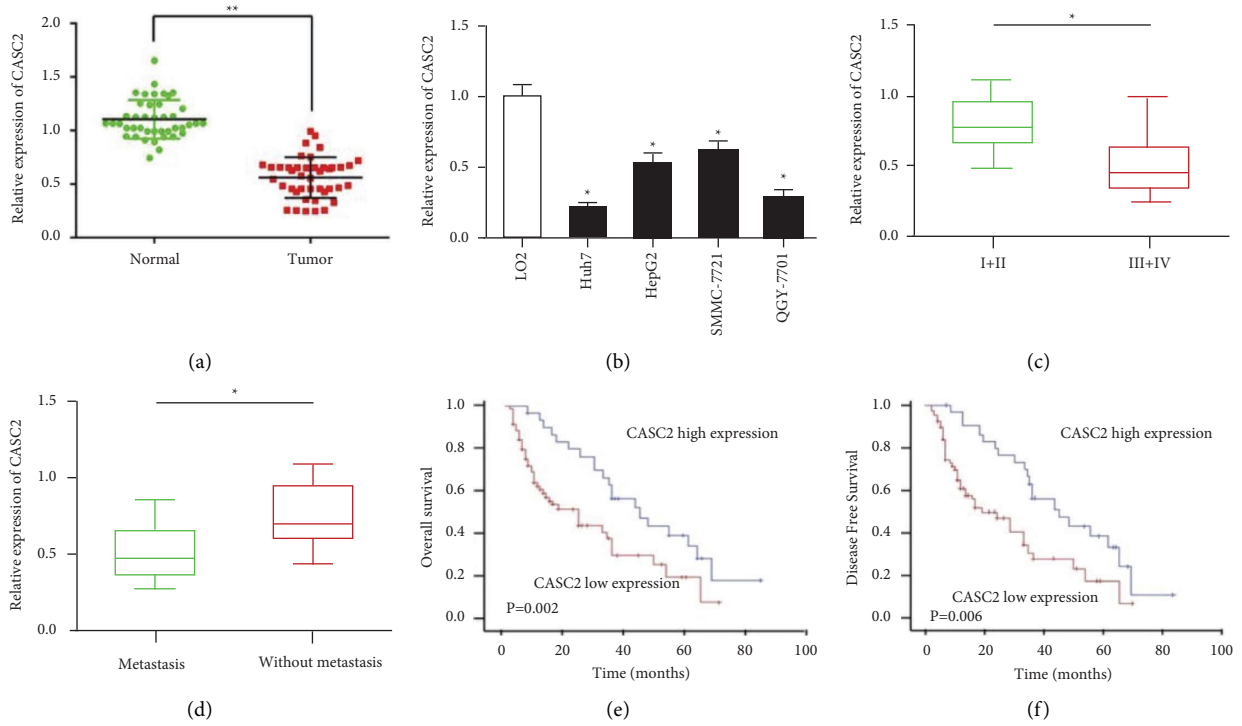

Figure 1: CASC2 was downregulated in HCC and correlated with clinical parameters. (a) The expression of CASC2 in HCC samples. (b) Relative CASC2 expression in four HCC cell lines and normal liver cell line. (c) Relative CASC2 expression in HCC tissues with different TNM stages. (d) Relative CASC2 expression in HCC tissues with or without metastasis. (e)-(f) Kaplan-Meier assays for OS and DFS curves according to CASC2 expression levels. $^{*}P < 0.05$, $^{**}P < 0.01$.

Table 1: Univariate and multivariate analyses for correlation of CASC2 expression with OS of HCC patients.

Variable	Univariate Cox's regression analysis		Multivariate Cox's regression analysis	
	Hazard ratio (95% CI)	*P* value	Hazard ratio (95% CI)	*P* value
CASC2 expression (high vs. low)	1.237 (0.775–2.044)	0.008	1.879 (0.711–2.425)	0.004*
Sex (male vs. female)	2.432 (1.337–3.212)	0.304	—	—
Age (<60 years vs. ≥60 years)	2.099 (1.225–3.108)	0.112	—	—
Tumor size (≥5 cm vs. <5 cm)	0.974 (0.582–1.706)	0.284	—	—
TNM staging (I~II vs. III~IV)	1.262 (0.897–1.981)	0.016	1.765 (0.892–2.241)	0.012*
Differentiation (poor vs. good/moderate)	1.417 (0.692–2.288)	0.492	—	—
Lymph node metastasis (yes vs. No)	1.696 (1.125–2.198)	0.005	1.233 (1.108–2.491)	0.002*

P value was acquired by Cox proportional hazards regression. *Statistically significant ($P < 0.05$).

indicating that miR-155 could bind the 3′UTR of SOCS1 mRNA. Moreover, the mRNA and protein expression of SOCS1 were significantly downregulated in the miR-155stably-overexpressing Huh7 cells compared with control group (Figure 4(c)). Besides, as revealed by the expressing correlation analysis, SOCS1 expression was negative correlated with miR-155 (Figure 4(d)), and positive correlated with CASC2 (Figure 4(e)) in HCC specimens. A rescue assay was conducted to clarify whether CASC2 regulates the biological function of HCCs cell through the miR-155/SOCS1 axis. We transfected CASC2-NC, CASC2-OE, and CASC2-OE + si-SOCS1 into Huh7 cells. The CCK-8 assay demonstrated that SOCS1 knockdown partially inverses the suppression effect of cell proliferation regulated by CASC2. Meanwhile, the transwell assays demonstrated that SOCS1 inhibition led to increased cell migration and invasion of Huh7 cells. Overall, these findings indicated that CASC2 may display the biological activity through regulating the miR-155/SOCS1 axis in HCC.

4. Discussion

During recent years, increasing evidence revealed that lncRNAs involve in clinical progression of many tumors including HCC. Several lncRNAs have been reported to play a vital role in regulating the tumorigenesis and cancer progression of HCC. He et al. [16] demonstrated that lncRNA maternally expressed gene 3 (MEG3) was downregulated in HCC and inhibited cell proliferation in vitro and tumor growth in vivo. Yang et al. [17] found that overexpression of HOTAIR could improve the carcinogenic activity of HCC cells and inhibit cell apoptosis. MALAT1

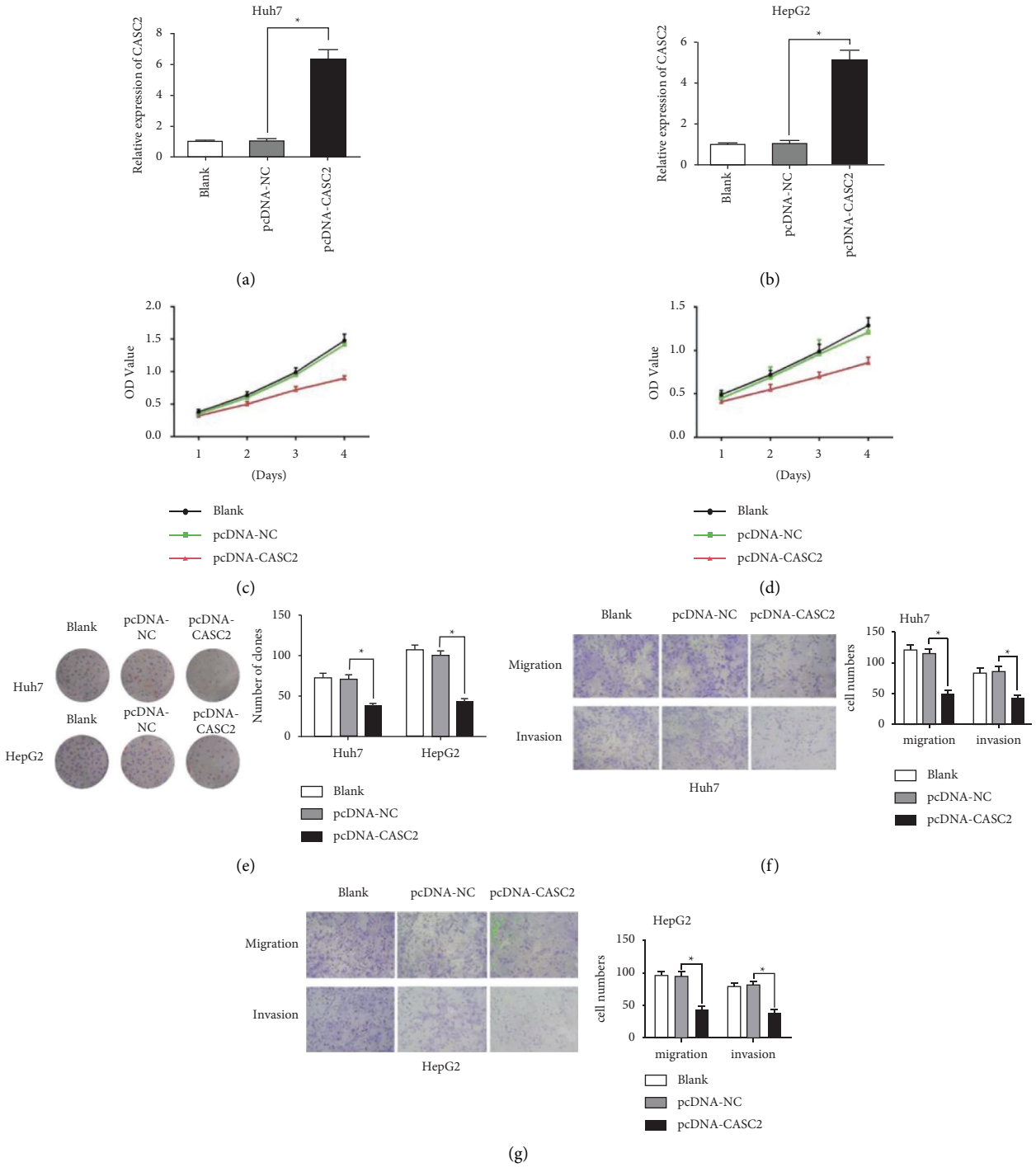

FIGURE 2: Biological functions of CASC2 on HCC cell proliferation, migration and invasion. (a) CASC2 expression in Huh7 and HepG2 cells were measured after transfected with pcDNA-NC or pcDNA-CASC2. (c)-(d) Growth curve of Huh7 and HepG2 cells by CCK-8 assays. (e) Colony formation of Huh7 and HepG2 cells. (f)-(g) The changes of migration and invasion ability in Huh7 and HepG2 cells after transfection. $^{*}P < 0.05$, $^{**}P < 0.01$.

was reported to promote the growth activity and invasiveness of HCC cells. Further research showed MALAT1 served as an oncogene by sponging miR-204 and releasing SIRT1 [18]. Besides, CTBP1-AS2 was associated with the occurrence and progression of HCC. Many studies previously demonstrated that CASC2 could function as a tumor suppressor in human cancers [19]. Jiang et al. [20] revealed that CASC2 could obviously inhibit the glioma cell proliferation and the growth of tumor xenografts in vivo by targeting miR-21. Wang et al. [21] found CASC2 repressed epithelial-mesenchymal transition (EMT) process of HCC cells by regulating the miR-367/FBXW7 axis. There is

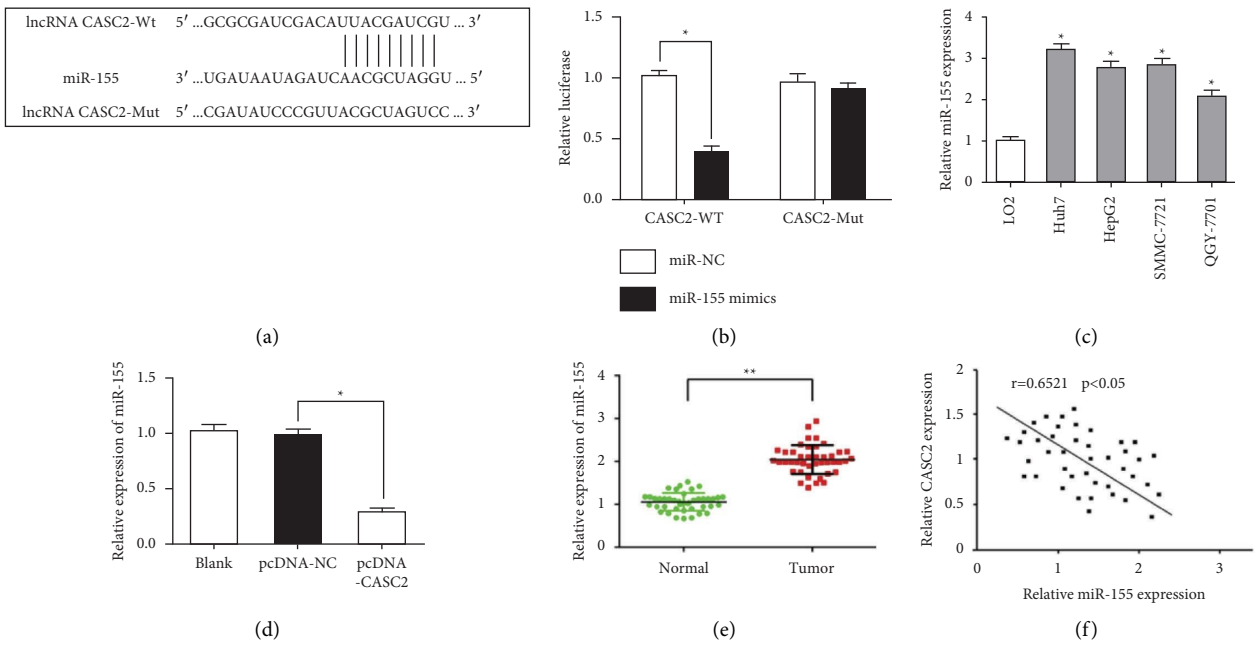

Figure 3: (a) The binding sites between CASC2 and miR-155 were predicted by StarBase 2.0. (b) Dual-luciferase reporter assays were conducted to confirm that CASC2 could target miR-155 directly. (c) The expression of miR-155 was detected by RT-qPCR in HCC cells. (d) Overexpression of CACS2 suppressed the expression of miR-155. (e) The expression of miR-155 was detected by RT-PCR assays. (f) The correlation analysis between CASC2 and miR-155 expression in HCC samples. $^{*}P < 0.05$, $^{**}P < 0.01$.

however limited investigation regarding the development effects and mechanisms by which CASC2 exerts on HCC.

In our study, we found that lncRNA CASC2 was significantly downregulated in HCC tissues compared with adjacent normal tissues and lowly expressed in four HCC cell lines. Then we analyzed the correlation between CASC2 expression and clinicopathological parameters of HCC patients and found that CASC2 were closely associated with TNM stage and lymph nodes metastasis. CASC2 expression was higher at a lower TNM stage compared to a higher TNM stage, and low expression of CASC2 presented a positive lymph node metastasis. Furthermore, Kaplan–Meier assays were performed to explore the prognostic value of CASC2 expression for HCC patients. The analysis indicated that HCC patients with higher expression of CASC2 have a longer OS and DFS than patients with low expression. A cox regression analysis showed that CASC2 expression was an independent prognostic indicator of HCC patients. These results showed that CACS2 might be a potential biomarker for the diagnosis and prognosis prediction of HCC. In order to investigate the biological function of CASC2 in HCC, CASC2 was overexpressed in Huh7 and HepG2 cells by cell transfection. We found that overexpression of CASC2 remarkably inhibited the proliferation, migration, and invasion of Huh7 and HepG2 cells, determined by CCK-8 and Transwell experiments, which indicated the tumor suppressor role of CASC2 in HCC.

MiRNAs are an abundant class of small, noncoding RNAs, which have been identified as important regulators of many biological process. It has been reported that lncRNAs can regulate miRNA expression by acting as competing endogenous RNA (ceRNA) [22]. In recent years, miRNAs were determined to regulate protein-coding gene expression by suppressing mRNA translation or reducing mRNA stability. And many miRNAs are identified to affect cancer phenotype by inhibiting the expression of oncogenes or tumor suppressors [23]. MiR-155 has been implicated in many human cancers, and aberrant expression of miR-155 displays an oncogenic feature. It is reported that miR-155 directly targets and inhibits many genes such as ATG5, SOCS3, SHIP1, and BCL2, which are involved in DNA damage response, cell cycle, hypoxia, inflammation, and tumorigenesis [24–26]. For instance, miR-155 is highly expressed in breast cancer, and high expression levels of miR-155 are associated with tumor subtype, metastasis, and poor survival rate of breast cancer patients [27]. Liu et al. [28] revealed that miR-155 could regulate the expression of PTEN, SOCS6, and SOCS1 protein by targeting the 3′ UTR of their mRNA directly, and inhibition miR-155 decreased cell proliferation and migration in cell lines H1299 and A549. Ahmadvand et al. [29] found that miR-155 is highly expressed in patients with diffuse large B cell lymphoma and directly inhibits HGAL expression.

To further investigate the underlying mechanisms of CASC2, we determined the potential miRNA of CASC2 with StarBase 2.0, and the results showed there was a binding sequence between CASC2 and miR-155. As shown in the luciferase reporter assay, the activity of luciferase in WT-CASC2 was distinctly inhibited by miR-155, which indicated that CASC2 could directly bound to miR-155. Then, we observed the distinct increase in miR-155 expression in 4 HCC cell lines, and found that overexpression of CASC2 could inhibit the level of miR-155 in Huh7 cells markedly. Also, we found that miR-155 was upregulated in HCC

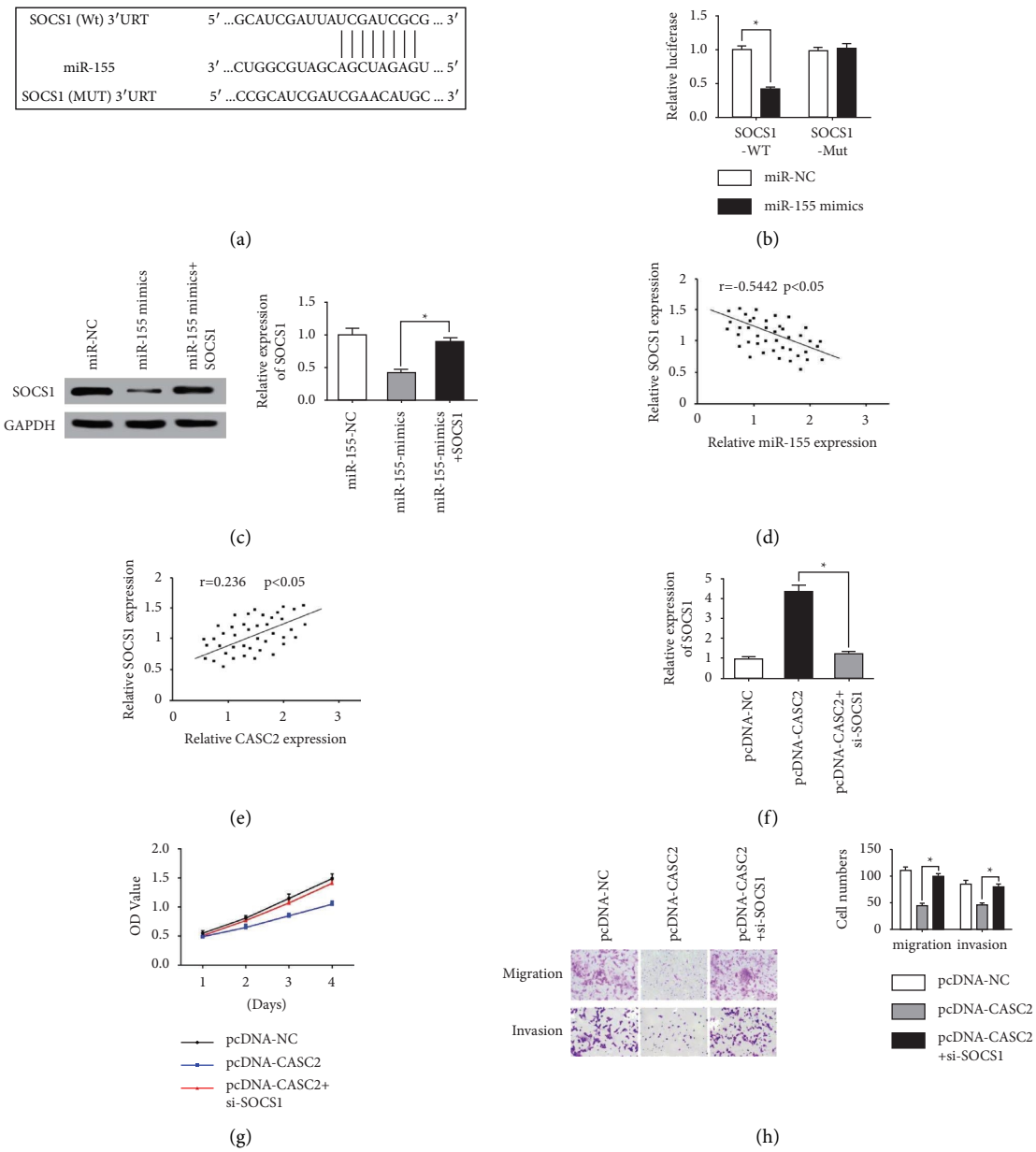

FIGURE 4: (a) The binding sites between SOCS1 and miR-155 were predicted by StarBase 2.0. (b) Dual-luciferase reporter assays were conducted to confirm that Mir-155 could target SOCS1 directly. (c) The mRNA and protein expressions of SOCS1 after transfection. (d) The correlation analysis between SOCS1 and miR-155 expression in HCC samples. (e) The correlation analysis between SOCS1 and CASC2 expression in HCC samples. (f) Protein expression changes of SOCS1 after transfection. (g) Growth curve of Huh7 cells by CCK-8 assays after co-transfection. (h) The determination of the effects of SOCS1 on the migration and invasion. $^{*}P < 0.05$, $^{**}P < 0.01$.

tissues, and correlation analysis presented a negative correlation between CASC2 and miR-155 expression in HCC tissues. Taken together, CASC2 may exhibit its tumor suppressor roles by acting as a competing endogenous RNA to sponge miR-155.

Growing studies have reported that SOCS1 displayed a displayed a dysregulated expression in gastric cancer, HCC, breast cancer and pancreatic cancer [30–32]. In this study, we found that SOCS1 was predicted as a candidate target of miR-155, and dual-luciferase reporter assays confirmed the direct targeting by miR-155 over SOCS1. Furthermore, SOCS1 was low-expressed in HCC tissue samples and cell lines and exhibited a negative relationship with miR-155 and a positive relation with CASC2 in HCC samples. The mRNA and protein levels of SOCS1 were significantly upregulated compared with the control group after miR-155 was overexpressed in Huh7. Finally, we performed rescue experiments, finding that SOCS1 inhibition partially inverses the suppression effect of cell proliferation regulated by CASC2. And transwell assays showed that SOCS1 knockdown led to increased cell migration and invasion of Huh7 cells. Functionally, these

results confirmed that CASC2 could function as a tumor suppressor by acting as a ceRNA to bind to miR-155 and downregulate the expression of SOCS1.

In conclusion, our findings uncovered that CASC2 could act as a tumor suppressor gene and inhibit cell proliferation, migration, and invasion through binding to miR-155, thus increasing the expression of its target gene SOCS1, demonstrating the ceRNA function of CASC2. In our study, we have partially elucidated the role of the CASC2/miR-155/SOCS1 axis in HCC development.

Data Availability

The datasets used and analyzed during the current study are available from the corresponding author on reasonable request.

Conflicts of Interest

The authors declare that there are no conflicts of interest.

Authors' Contributions

Ye Yuan and Jiaxin Ye contributed equally to this work.

Acknowledgments

This work is supported by Wuhan Health Research Fund (wx21q44).

References

[1] A. Ozakyol, "Global epidemiology of hepatocellular carcinoma (HCC epidemiology)," *Journal of Gastrointestinal Cancer*, vol. 48, no. 3, pp. 238–240, 2017.

[2] T. Couri and A. Pillai, "Goals and targets for personalized therapy for HCC," *Hepatology International*, vol. 13, no. 2, pp. 125–137, 2019.

[3] F. Pinero, M. Dirchwolf, and M. G. Pessoa, "Biomarkers in hepatocellular carcinoma: diagnosis, prognosis and treatment response assessment," *Cells*, vol. 9, no. 6, p. 1370, 2020.

[4] Y. H. Lin, "Crosstalk of lncRNA and cellular metabolism and their regulatory mechanism in cancer," *International Journal of Molecular Sciences*, vol. 21, no. 8, p. 2947, 2020.

[5] D. Cheng, J. Deng, B. Zhang et al., "LncRNA HOTAIR epigenetically suppresses miR-122 expression in hepatocellular carcinoma via DNA methylation," *EBioMedicine*, vol. 36, pp. 159–170, 2018.

[6] Z. Dong, J. Yang, F. Zheng, and Y. Zhang, "The expression of lncRNA XIST in hepatocellular carcinoma cells and its effect on biological function," *J Buon*, vol. 25, no. 5, pp. 2430–2437, 2020.

[7] S. Chen and X. Xia, "Long Noncoding RNA NEAT1 Suppresses Sorafenib Sensitivity of Hepatocellular Carcinoma Cells via Regulating miR-335-C-Met," *Journal of cellular physiology*, vol. 234, no. 9, 2019.

[8] S. Ghafouri-Fard, S. Dashti, and M. Taheri, "The role of long non-coding RNA CASC2 in the carcinogenesis process," *Biomedicine & Pharmacotherapy*, vol. 127, Article ID 110202, 2020.

[9] X. W. Wang and W. Zhang, "Long non-coding RNA cancer susceptibility candidate 2 inhibits the cell proliferation, invasion and angiogenesis of cervical cancer through the MAPK pathway," *European Review for Medical and Pharmacological Sciences*, vol. 23, no. 8, pp. 3261–3269, 2019.

[10] Y. Feng, W. Zou, C. Hu et al., "Modulation of CASC2/miR-21/PTEN pathway sensitizes cervical cancer to cisplatin," *Archives of Biochemistry and Biophysics*, vol. 623-624, pp. 20–30, 2017.

[11] X. Xiong, H. Zhu, and X. Chen, "Low expression of long noncoding RNA CASC2 indicates a poor prognosis and promotes tumorigenesis in thyroid carcinoma," *Biomedicine & Pharmacotherapy*, vol. 93, pp. 391–397, 2017.

[12] J. Zhou, H. Huang, S. Tong, and R. Huo, "Overexpression of long non-coding RNA cancer susceptibility 2 inhibits cell invasion and angiogenesis in gastric cancer," *Molecular Medicine Reports*, vol. 16, no. 4, pp. 5235–5240, 2017.

[13] Z. Wang, X. Wang, H. Zhou, X. Dan, L. Jiang, and Y. Wu, "Long non-coding RNA CASC2 inhibits tumorigenesis via the miR-181a/<italic>PLXNC1</italic> axis in melanoma," *Acta Biochimica et Biophysica Sinica*, vol. 50, no. 3, pp. 263–272, 2018.

[14] W. Dai, L. Mu, Y. Cui et al., "Long noncoding RNA CASC2 enhances berberineinduced cytotoxicity in colorectal cancer cells by silencing BCL2," *Molecular Medicine Reports*, vol. 20, no. 2, pp. 995–1006, 2019.

[15] J. Sun, H. Xu, Z. Lei et al., "The lncRNA CASC2 modulates hepatocellular carcinoma cell sensitivity and resistance to TRAIL through apoptotic and non-apoptotic signaling," *Frontiers in Oncology*, vol. 11, Article ID 726622, 2021.

[16] J. H. He, Z. P. Han, J. M. Liu et al., "Overexpression of long non-coding RNA MEG3 inhibits proliferation of hepatocellular carcinoma Huh7 cells via negative modulation of miRNA-664," *Journal of Cellular Biochemistry*, vol. 118, no. 11, pp. 3713–3721, 2017.

[17] L. Yang, X. Peng, Y. Li et al., "Long non-coding RNA HOTAIR promotes exosome secretion by regulating RAB35 and SNAP23 in hepatocellular carcinoma," *Molecular Cancer*, vol. 18, no. 1, p. 78, 2019.

[18] Z. H. Hou, X. W. Xu, X. Y. Fu, L. D. Zhou, S. P. Liu, and D. M. Tan, "Long non-coding RNA MALAT1 promotes angiogenesis and immunosuppressive properties of HCC cells by sponging miR-140," *American Journal of Physiology - Cell Physiology*, vol. 318, no. 3, pp. C649–C663, 2020.

[19] M. Wang and H. Zhao, "LncRNA CTBP1-AS2 promotes cell proliferation in hepatocellular carcinoma by regulating the miR-623/cyclin D1 Axis," *Cancer Biotherapy and Radiopharmaceuticals*, vol. 35, no. 10, pp. 765–770, 2020.

[20] C. Jiang, F. Shen, J. Du et al., "Upregulation of CASC2 sensitized glioma to temozolomide cytotoxicity through autophagy inhibition by sponging miR-193a-5p and regulating mTOR expression," *Biomedicine & Pharmacotherapy*, vol. 97, pp. 844–850, 2018.

[21] Y. Wang, Z. Liu, B. Yao et al., "Long non-coding RNA CASC2 suppresses epithelial-mesenchymal transition of hepatocellular carcinoma cells through CASC2/miR-367/FBXW7 axis," *Molecular Cancer*, vol. 16, no. 1, p. 123, 2017.

[22] Y. Bai, J. Long, Z. Liu et al., "Comprehensive analysis of a ceRNA network reveals potential prognostic cytoplasmic lncRNAs involved in HCC progression," *Journal of Cellular Physiology*, vol. 234, no. 10, pp. 18837–18848, 2019.

[23] S. Y. Sathipati and S. Y. Ho, "Novel miRNA signature for predicting the stage of hepatocellular carcinoma," *Scientific Reports*, vol. 10, no. 1, Article ID 14452, 2020.

[24] Q. Yu, X. P. Xu, X. M. Yin, and X. Q. Peng, "miR-155-5p increases the sensitivity of liver cancer cells to adriamycin by

regulating ATG5-mediated autophagy," *Neoplasma*, vol. 68, no. 1, pp. 87–95, 2021.

[25] X. Feng, J. Bao, C. Song et al., "Functional role of miR155 in physiological and pathological processes of liver injury (Review)," *Molecular Medicine Reports*, vol. 24, no. 4, p. 714, 2021.

[26] L. N. Dagan, X. Jiang, S. Bhatt, E. Cubedo, K. Rajewsky, and I. S. Lossos, "miR-155 regulates HGAL expression and increases lymphoma cell motility," *Blood*, vol. 119, no. 2, pp. 513–520, 2012.

[27] M. Abtin, M. R. Alivand, M. S. Khaniani, M. Bastami, M. Zaeifizadeh, and S. M. Derakhshan, "Simultaneous downregulation of miR-21 and miR-155 through oleuropein for breast cancer prevention and therapy," *Journal of Cellular Biochemistry*, vol. 119, no. 9, pp. 7151–7165, 2018.

[28] F. Liu, D. Song, Y. Wu, X. Liu, J. Zhu, and Y. Tang, "MiR-155 inhibits proliferation and invasion by directly targeting PDCD4 in non-small cell lung cancer," *Thoracic Cancer*, vol. 8, no. 6, pp. 613–619, 2017.

[29] M. Ahmadvand, M. Eskandari, H. Pashaiefar et al., "Over expression of circulating miR-155 predicts prognosis in diffuse large B-cell lymphoma," *Leukemia Research*, vol. 70, pp. 45–48, 2018.

[30] H. F. Pasha, R. H. Mohamed, and M. I. Radwan, "RASSF1A and SOCS1 genes methylation status as a noninvasive marker for hepatocellular carcinoma," *Cancer Biomarkers*, vol. 24, no. 2, pp. 241–247, 2019.

[31] J. Ding, K. Xu, S. Sun et al., "SOCS1 blocks G1-S transition in hepatocellular carcinoma by reducing the stability of the CyclinD1/CDK4 complex in the nucleus," *Aging (Albany NY)*, vol. 12, no. 4, pp. 3962–3975, 2020.

[32] Q. Qian, Y. Lv, and P. Li, "SOCS1 is associated with clinical progression and acts as an oncogenic role in triple-negative breast cancer," *Journal of international union of biochemistry and molecular biology Life*, vol. 70, no. 4, pp. 320–327, 2018.

Hindawi
Journal of Oncology
Volume 2023, Article ID 9667920, 6 pages
https://doi.org/10.1155/2023/9667920

Research Article

Long Non-Coding RNA HOTAIR Promotes Human Osteosarcoma Proliferation, Migration through Activation of the Wnt/b-Catenin Signaling Pathway

Hang Li, Shijian Fu, and Wenbo Wang

Orthopedics Department, The First Affiliated Hospital of Harbin Medical University, Harbin 150081, Heilongjiang, China

Correspondence should be addressed to Wenbo Wang; wangwenbo@54dr.net.cn

Received 26 September 2022; Revised 12 October 2022; Accepted 24 November 2022; Published 7 February 2023

Academic Editor: Muhammad Muddassir Ali

LncRNA HOTAIR exhibited different effects in human cancers. However, the role of HOTAIR was not reported in osteosarcoma. This study aimed to explore the function of HOTAIR in osteosarcoma. Firstly, we examined HOTAIR expression in breast cancer tissues by the RT-qPCR assay and examined HOTAIR protein expression via immunocytochemistry, to chemical assay, and Western blot. Then, for further exploring the function of HOTAIR, we also examined it by CCK-8 and transwell assays. Downregulation of HOTAIR was detected in osteosarcoma, which predicted poor prognosis of patients with osteosarcoma. Moreover, cell migration, invasion, and proliferation were suppressed by HOTAIR overexpression in osteosarcoma. Furthermore, LPR5 was a direct target of HOTAIR, which was upregulated in osteosarcoma. Especially, the upregulation of LPR5 could impair the suppressive effect of HOTAIR in breast cancer. HOTAIR was found to negatively regulate the EMT and Wnt/β-cadherin pathways in osteosarcoma. HOTAIR repressed the progression of osteosarcoma via regulating LPR5 and suppressing the Wnt/β-cadherin pathway. Our findings will provide a positive reference for studying the function of HOTAIR in osteosarcoma.

1. Introduction

Osteosarcoma (OS) is caused by bone cells' abnormal differentiation and proliferation. According to epidemiological data, the incidence of OS is around 0.2–3/100000 per year [1]. In children and teenagers with a high rate of malignancy, it is the most prominent primary bone tumor. OS usually shows a high tendency to metastatic spread [2]. OS is also associated with procedures that may require them: chemotherapy and radiology [3, 4]. However, in recent years, the survival rate of patients with OS accompanied by distant metastases has not been significantly improved [5, 6], the effect of chemotherapy has not been significantly improved, and the treatment of OS is still controversial. Therefore, new therapeutic targets need to be found to provide clinical treatment options to improve the survival rate.

Long noncoding RNAs (LncRNAs) are a family of 200 nt length RNA molecules [7, 8]. While proteins cannot be encoded, lncRNAs can participate in multiple levels of gene expression regulation, including epigenetic, transcriptional, and post-transcriptional modification, thus taking part in a variety of in vivo pathophysiological processes, including cancer proliferation and invasion [9, 10]. Gene expression analysis suggests LncRNA HOTAIR is situated at human chromosome 12q13 and consists of 5 short exons and 1 long exon within the antisense strand of the HOXC gene cluster [11]. HOTAIR is a typical molecular occurrence of epigenetic malignancy that has been shown to have great importance in the production and prediction of different tumors. New research suggests that HOTAIR is a chromatin regulation system that routinely controls tumor metabolism, proliferation, etc. [12–14]. A number of studies indicate that HOTAIR could bind these genes to the repressive polycomb complex 2 (PRC2) directly and silently [11]. In addition, HOTAIR may also interact with the LSD1/REST complex and H3K4 histone demethylation. HOTAIR knock-out can prevent invasion and metastasis of the breast tumor. The production of HOTAIR by improving the epithelial-

mesenchymal transformation in gastric cancer was shown to facilitate cellular invasion and migration. HOTAIR is reported to be involved in Wnt/β-catenin signaling through directly decreasing HIF-1 expression.

Therefore, in this study, we selected the human osteosarcoma cell line SAOS-2 and the human osteoblast cell line OB3. We applied RT-qPCR Western blot to our cells. In addition, we analyzed the lncRNA HOTAIR expression and its interaction with LPR5, attempting to establish a connection between HOTAIR and LPR5 in OS. Our findings indicate that HOTAIR and LRP5 expressions are upregulated, and levels of LRP5 expression have a positive correlation with HOTAIR in OS tissues and cell lines.

2. Methods

2.1. Cell Lines and Culture. Human osteosarcoma cell line SAOS-2 and human osteoblast cell line OB3 were purchased from the ScienCell Research Laboratories and the American Type Culture Collection (ATCC) (Manassas, VA, USA).

2.2. RT-qPCR. The TRIzol reagent was used to extract complete RNA (Sangon Biotech, Shanghai, China). For the qRT-PCR experiment, 2 μg of complete RNA for reverse transcript and cDNA synthesis is used with TransScript ® II Reverse Transcriptase (TransGen Biotech Co,, Beijing, China). Quantitative, real-time PCR experiments have been carried out with PerfectStartTM Green qPCR SuperMix (TransGen Biotech Co., Beijing, China). The results were normalized to GAPDH, a gene with constitutive expression. The PCR primers are for HOTAIR forward, 5′-GGTAGA AAAAGCAACCACGAAGC-3′; for HOTAIR reverse, 5′-ACATAAACCTCTGTCTGTGAGTGCC-3′; and for GAPDH, 5′-TGTTCGTCATGGGTGTGAA-3′ (forward) and 5′-ATGGCATGGACTGTGGTCAT-3′ (reverse). Using the 2-Ct process, the relative MFI2 and FOXP4 expression levels were identified and normalized.

2.3. Western Blot. A complete protein was extracted for 30 minutes, and the protein concentration was measured using a BCA protein measuring kit (Thermo Scientific, MA, USA). The Mammalian Complete Protein Extraction Kit (TransGen Biotech Co., Beijing, China) was used on ice. The corresponding numbers of total proteins, which were transferred to 0.22 μm polyvinylidene fluoride (PVDF) membranes (Millipore, Billerica, MA, USA.) and incubated with LRP5 (1 : 1000) or GAPDH (1 : 1500) anticorps are 12 per cent SDS-polyacrylamide gel electrophoresis (SDS-PAGE). The manufacturer's (Beyotime) identification of enhanced chemiluminescence (CEL) and the quantified densitometry of the band amplitude (Quantity One software; Bio-Rad, Hercules, CA) as proteins measured.

2.4. siRNA Transfection. As previously defined, the pENTR-shHOTAIR vector was constructed (Liu et al., 2014). In brief, Genepharmacy Technology (China) synthesized unique oligonucleotides targeting HOTAIR: sense, 5′-GATCCG CCACATGAACGCCCAGAGATTTTCAAGAGAAAT CTCTGGGCGTTCATGTGGTT TTTTG-3′; antisense, 5′-AATTCAAAAAACCACATGAACGCCCAGAGATTT CTCTTGAAAATCTCTGGGCGTTCATGTGGC G-3′. The pENTR-shHOTAIR plasmids and empty vectors were then transfected into U2OS cells, and G418 (400 μg/ml) was chosen for the HOTAIR overexpression subclones. To validate the upregulation of HOTAIR, real-time PCR was conducted.

2.5. Cell Viability Assay. The manufacturers' instructions using a cell counting kit-8 (CCK-8) (Dojindo, Kumamoto, Japan) observed the cell viability of siRNA Duplex osteomarcoma cells at 24 h, 48 h, and 72 h. Briefly, 1 to 104 cells were placed on 96-well tissue culture plate for 24, 48, and 72 hours. OS cells were subsequently treated with CCK-8 for 1 hour at 37°C. OS cells were used to measure 450 nm of absorption with a microplate reader, Thermo Plate (Rayto Life and Analytical Research, Co., Ltd.).

2.6. MTT Assay. The MTT test determined the cell proliferation effect of HOTAIR. In short, 2–10^3 cells/button were sown on 96-well plates and cultivated periodically. At the specified timepoints, the 10 mg MTT solution (5 mg/ml; Sigma-Aldrich) was used for each well, and the reaction was completed with 200 μl DMSO 2 hours later. The absorbance on a microplate reader was estimated at 570 nm. The experiment was repeated atleast three times.

2.7. Transwell Assay. The researchers used 24-well transwells with 8 μm pores (Corning Costar, Inc., Corning, NY, USA) and conducted migration and invasion assays, respectively. In the migration assay, the upper transwell chamber was filled with a noncoated membrane with 2–10^4 OS cells suspended in a 100 μl serum-free culture medium. The upper chamber for the invasion procedure was replaced with 3 to 10^4 OS cells plated without FBS in 100 μl of the required culture medium. In the samples, 500 μl culture medium containing 20 percent FBS was found in the lower culture chamber. In a wet climate, the cells were cultivated for 24 hours at 37°C and 5% CO_2. Set to 100 percent methanol for 30 minutes, 0.5% violet (Sigma, St. Louis, MO, USA) cells have been dyed over a 20-minute span, and a phase-contrast microscope (Olympus, Tokyo, China) has been compared.

3. Result

3.1. LncRNA HOTAIR Expression was Increased in OS Tissue. Figure 1 shows that HOTAIR expression was increased in OS tissues. Figure 1(a) shows the expression of HOTAIR in the tissues of OS. Figure 1(b) shows that high HOTAIR expression was detected in OS cell lines. First, in OS tissue and normal tissue using RT-qPCR, lncRNA expression was studied. It was shown that lncRNA HOTAIR expression was higher than in normal tissue. Similarly, high HOTAIR expression was also observed in the OB-3 and SAOS-2 tumor cell lines.

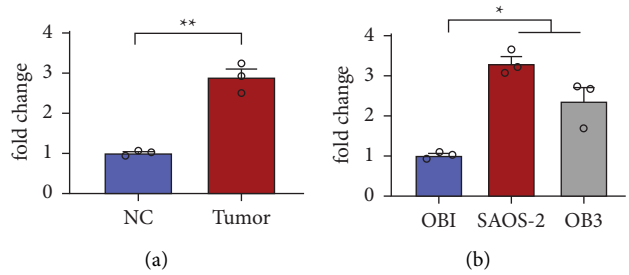

Figure 1: HOTAIR expression was increased in OS tissues. $^{*}P < 0.05$, $^{**}P < 0.01$.

3.2. HOTAIR Downregulation Prevented OS Cell Proliferation. The knockdown experiment was conducted to demonstrate the effect of HOTAIR on the proliferation of OS cells. Figures 2(a) and 2(b) show the HOTAIR expression in normal OB-3, SAOS-2 cell lines, and siRNA knockdown cell lines, and the expression of HOTAIR in OS cell lines is successfully knocked down. The cell proliferation was measured in the cell lines OB-3 and SAOS-2 by the CCK-8 assay. As shown in Figures 2(c) and 2(d), in the CCK-8 assay, we observed that in two OS cell lines, declining HOTAIR expression substantially suppressed cell proliferation. A central role of HOTAIR in the proliferation of OS was indicated by the findings.

3.3. HOTAIR Downregulation Inhibited the Invasion and Migration of OS Cells. Figures 3(a) and 3(b) show the representative images of the cell invasion results of HOTAIR knockdown on OB-3 and SAOS-2 cells. It was used to compare cell invasiveness before and after HOTAIR knockdown by transwell assay. Figures 3(c) and 3(d) show the quantification of outcomes for OS cell lines in cell invasion and migration assays. As shown in Figures 3(c) and 3(d), the downregulation of HOTAIR inhibited the migration of OS cell lines OB3 and SAOS-2 in the transwell migration assay.

3.4. Protein LPR5 was Positively Correlated with HOTAIR Expression. LRP5, which is a part of the LDL receptor family, comprises the VLDL receptor and the apolipoprotein E receptor 2. LRP5, which is a coreceptor of Wnt, is situated between Frizzled and Kremen receptors on the osteoblast membrane. Figure 4(a) shows the protein expression of LRP5 in osteosarcoma tissues detected by WB. It has been demonstrated that LPR5 is a potential oncogenic protein in OS. Figure 4(b) shows the quantification of the results for LPR5 expression in osteosarcoma tissues ($^{*}P < 0.05$). To explore whether there is any relationship between the expression of LPR5 and HOTAIR, we examined the correlation between HOTAIR and LPR5 expression. Figure 4(c) shows that the expression of HOTAIR and LPR5 has a positive correlation. As shown in Figure 4(c), we found a positive correlation between the two expressions. HOTAIR knockdown reduced the expression of LPR5 (Figure 4(d)). It suggested that the possible mechanism by which HOTAIR promotes cancer growth is the regulation of LPR5 expression.

4. Discussion

A number of lncRNAs have played a significant part in essential cellular processes in previous research, for example, gene expression regulation, and post-transcriptional modification [10, 15]. LncRNA expression is increasingly known to be implicated in pathological advancements such as the growth of human cancer, culminating in unchecked proliferation [10, 16]. An increased understanding of the biological role of lncRNA can also provide new approaches for human OS diagnosis and treatment. OS has been the most common bone cancer in the younger crowd, like children and young adults. It has remained poorly treated and has a poor prognosis [17]. Wnt is the secreted protein that causes tumor growth and skeletal development [18]. It includes 10 Frizzled receptors and 19 Wnt ligands, as well as LRP5, LRP6, and two low-density lipoprotein receptor-related protein (LRP) coreceptors [19]. As Wnt ligands were connecting to LRP5/6, the carboxyl end of Lrp5/6 was phosphorylated, and a binding position for Axin was formed [20]. It leads to the b-catenin level increased in the cytoplasm and nucleus [21, 22]. Ultimately, this leads to abnormal gene expression and tumor formation. It has been demonstrated that the expression of LRP5 is a common event in OS [23].

Despite numerous studies, the molecular mechanisms of OS proliferation and metastasis have remained unclear [24]. With the deepening understanding of lncRNA, it has been recognized that lncRNA is involved in every aspect of human physiology and pathology, which may be related to the molecular mechanism of proliferation and metastasis of OS. Earlier research found HOTAIR participates in multiple tumor forming and metastasis pathways [25]. In esophageal squamous cell cancer, HOTAIR knockdown may reduce the ability of cells to proliferate, migrate, and invade the extracellular matrix [26]. In gastric cancer, HOTAIR expression is upregulated to promote the proliferation of gastric cancer cells [27]. In human OS tissues, HOTAIR expression was substantially upregulated. The role of HOTAIR in the incidence and invasion of OS has been explored in this report.

Our findings found that HOTAIR downregulation prevented OS cell proliferation. CCK-8 and transwell assay findings indicated that HOTAIR knockdown by RNA interference greatly decreased cell proliferation, migration, and invasion in OS cells. To sum up, we demonstrated that HOTAIR and LRP5 expressions were upregulated, and levels of LRP5 expression were positively correlated with HOTAIRs in OS tissues and cell lines. However, there are

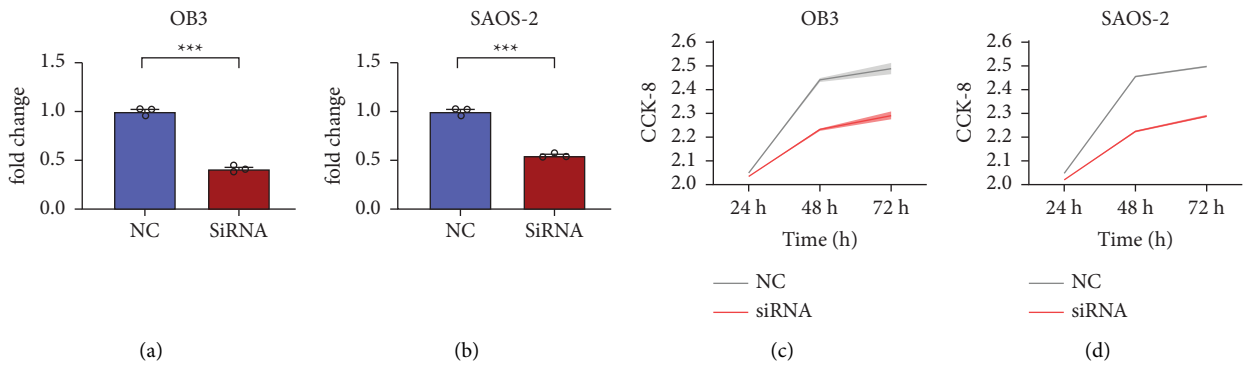

Figure 2: Downregulation of HOTAIR inhibited the progression of OS. $P < 0.05$, $^{**}P < 0.01$, and $^{***}P < 0.001$.

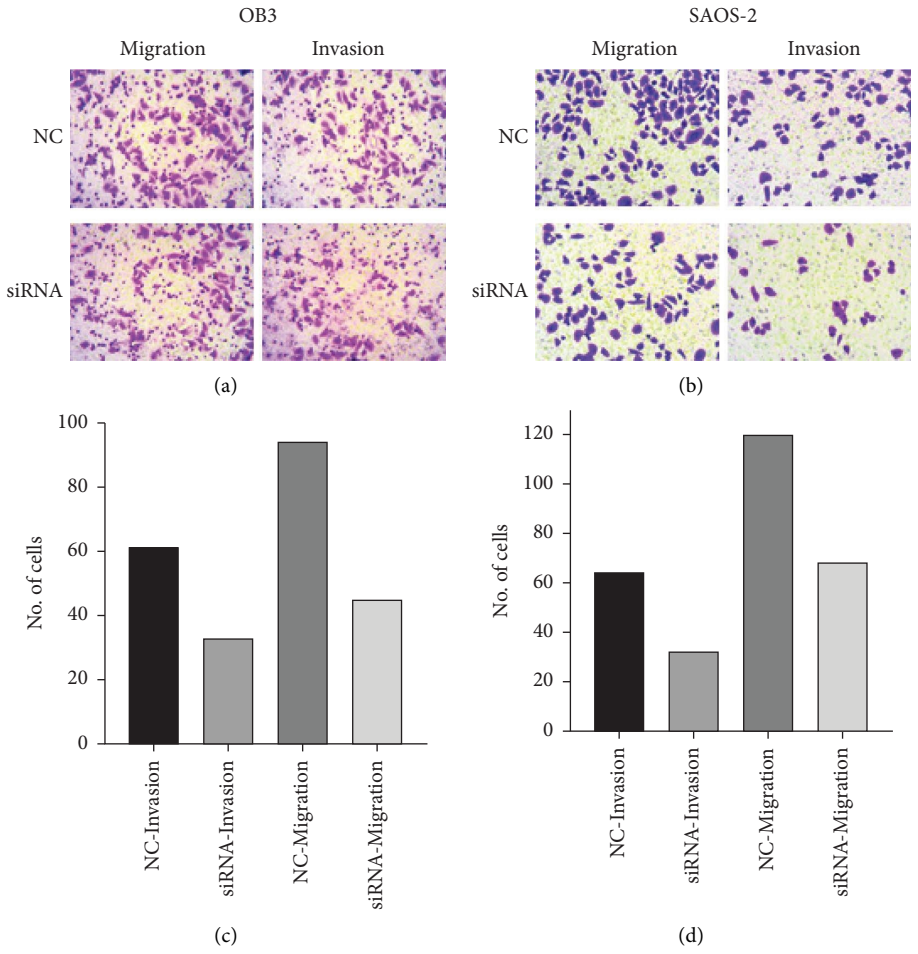

Figure 3: Downregulation of HOTAIR has prevented OS cell migration and invasion.

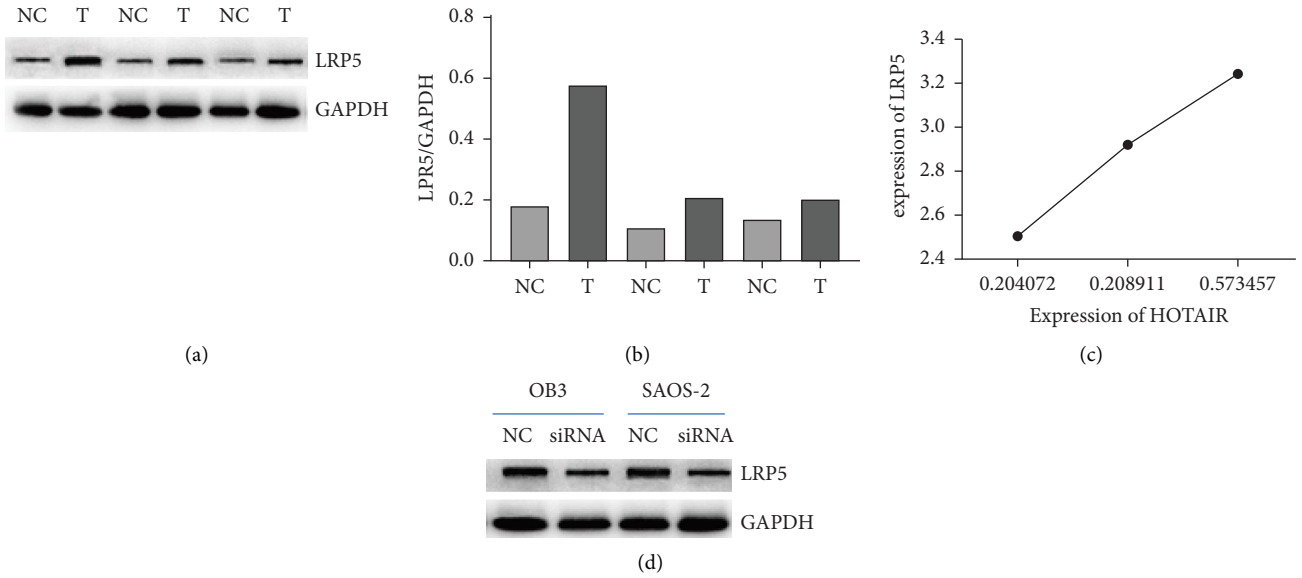

Figure 4: LPR5 was upregulated in osteosarcoma tissues.

still some limitations in our study, such as limited data. In the future, we need to collect more data for more in-depth data analysis, which will greatly improve the reliability and scientificness of our results.

Data Availability

The datasets used and/or analyzed during the current study are available from the corresponding author on reasonable request.

Conflicts of Interest

The authors declare that they have no conflicts of interest.

References

[1] L. Mirabello, R. J. Troisi, and S. A. Savage, "Osteosarcoma incidence and survival rates from 1973 to 2004: data from the surveillance, epidemiology, and end results program," *Cancer*, vol. 115, no. 7, pp. 1531–1543, 2009.

[2] D. D. Moore and H. H. Luu, "Osteosarcoma," *Cancer Treatment and Research Communications*, Elsevier, Amsterdam, Netherlands, 2014.

[3] S. S. Bielack, B. Kempf-Bielack, G. Delling et al., "Prognostic factors in high-grade osteosarcoma of the extremities or trunk: an analysis of 1,702 patients treated on neoadjuvant cooperative osteosarcoma study group protocols," *Journal of Clinical Oncology*, vol. 20, no. 3, pp. 776–790, 2002.

[4] S. A. Eccles and D. R. Welch, "Metastasis: recent discoveries and novel treatment strategies," *Lancet*, vol. 369, no. 9574, pp. 1742–1757, 2007.

[5] S. Iwata, T. Nakamura, C. L. Gaston et al., "Diaphyseal osteosarcomas have distinct clinical features from metaphyseal osteosarcomas," *European Journal of Surgical Oncology*, vol. 40, no. 9, pp. 1095–1100, 2014.

[6] M. W. Joo, S. H. Shin, Y. K. Kang et al., "Osteosarcoma in asian populations over the age of 40 years: a multicenter study," *Annals of Surgical Oncology*, vol. 22, no. 11, pp. 3557–3564, 2015.

[7] T. R. Mercer, M. E. Dinger, and J. S. Mattick, "Long noncoding RNAs: insights into functions," *Nature Reviews Genetics*, vol. 10, no. 3, pp. 155–159, 2009.

[8] J. Cao, "The functional role of long non-coding RNAs and epigenetics," *Biological Procedures Online*, vol. 16, no. 1, p. 42, 2014.

[9] L. Ma, V. B. Bajic, and Z. Zhang, "On the classification of long non-coding RNAs," *RNA Biology*, vol. 10, no. 6, pp. 925–933, 2013.

[10] C. P. Ponting, P. L. Oliver, and W. Reik, "Evolution and functions of long noncoding RNAs," *Cell*, vol. 136, no. 4, pp. 629–641, 2009.

[11] J. L. Rinn, M. Kertesz, J. K. Wang et al., "Functional demarcation of active and silent chromatin domains in human HOX loci by noncoding RNAs," *Cell*, vol. 129, no. 7, pp. 1311–1323, 2007.

[12] X. hua Liu, Z. li Liu, M. Sun, J. Liu, Z. x Wang, and W. De, "The long non-coding RNA HOTAIR indicates a poor prognosis and promotes metastasis in non-small cell lung cancer," *BMC Cancer*, vol. 13, no. 1, p. 464, 2013.

[13] Z. Yang, L. Zhou, L. M. Wu et al., "Overexpression of long non-coding RNA HOTAIR predicts tumor recurrence in hepatocellular carcinoma patients following liver transplantation," *Annals of Surgical Oncology*, vol. 18, no. 5, pp. 1243–1250, 2011.

[14] M. C. Tsai, O. Manor, Y. Wan et al., "Long noncoding RNA as modular scaffold of histone modification complexes," *Science*, vol. 329, no. 5992, pp. 689–693, 2010.

[15] S. U. Schmitz, P. Grote, and B. G. Herrmann, "Mechanisms of long noncoding RNA function in development and disease," *Cellular and Molecular Life Sciences*, vol. 73, no. 13, pp. 2491–2509, 2016.

[16] P. Kapranov, J. Cheng, S. Dike et al., "RNA maps reveal new RNA classes and a possible function for pervasive transcription," *Science*, vol. 316, no. 5830, pp. 1484–1488, 2007.

[17] M. S. Isakoff, S. S. Bielack, P. Meltzer, and R. Gorlick, "Osteosarcoma: current treatment and a collaborative pathway to

success," *Journal of Clinical Oncology*, vol. 33, no. 27, pp. 3029–3035, 2015.

[18] C. Y. Logan and R. Nusse, "The wnt signaling pathway in development and disease," *Annual Review of Cell and Developmental Biology*, vol. 20, no. 1, pp. 781–810, 2004.

[19] Z. G. Li, J. Yang, E. S. Vazquez et al., "Low-density lipoprotein receptor-related protein 5 (LRP5) mediates the prostate cancer-induced formation of new bone," *Oncogene*, vol. 27, pp. 596–603, 2008.

[20] B. T. MacDonald and X. He, "Frizzled and LRp5/6 receptors for wnt/β-catenin signaling," *Cold Spring Harbor Perspectives in Biology*, vol. 4, no. 12, Article ID a007880, 2012.

[21] K. Tamai, X. Zeng, C. Liu et al., "A mechanism for wnt coreceptor activation," *Molecular Cell*, vol. 13, no. 1, pp. 149–156, 2004.

[22] B. T. MacDonald, K. Tamai, and X. He, "Wnt/beta-catenin signaling: components, mechanisms, and diseases," *Developmental Cell*, vol. 17, no. 1, pp. 9–26, 2009.

[23] C. Adamopoulos, A. N. Gargalionis, E. K. Basdra, and A. G. Papavassiliou, "Deciphering signaling networks in osteosarcoma pathobiology," *Experimental Biology and Medicine*, vol. 241, no. 12, pp. 1296–1305, 2016.

[24] L. Mirabello, R. J. Troisi, and S. A. Savage, "Osteosarcoma incidence and survival rates from 1973 to 2004: data from the surveillance, epidemiology, and end results program," *Cancer*, vol. 115, 2009.

[25] X. He, W. Bao, X. Li et al., "The long non-coding RNA HOTAIR is upregulated in endometrial carcinoma and correlates with poor prognosis," *International Journal of Molecular Medicine*, vol. 33, no. 2, pp. 325–332, 2014.

[26] X. Li, Z. Wu, Q. Mei et al., "Long non-coding RNA HOTAIR, a driver of malignancy, predicts negative prognosis and exhibits oncogenic activity in oesophageal squamous cell carcinoma," *British Journal of Cancer*, vol. 109, no. 8, pp. 2266–2278, 2013.

[27] M. Hajjari, M. Behmanesh, M. Sadeghizadeh, and M. Zeinoddini, "Up-regulation of HOTAIR long non-coding RNA in human gastric adenocarcinoma tissues," *Medical Oncology*, vol. 30, no. 3, p. 670, 2013.

Hindawi
Journal of Oncology
Volume 2023, Article ID 4640563, 13 pages
https://doi.org/10.1155/2023/4640563

Research Article

Identification of Prognostic Markers of DNA Damage and Oxidative Stress in Diagnosing Papillary Renal Cell Carcinoma Based on High-Throughput Bioinformatics Screening

Le Li,[1] **XuKai Liu**,[2] **Yong Wen**,[3] **Pan Liu**,[1] **and Ting Sun**[1]

[1]*Department of Emergency, Zhuzhou Hospital Affiliated to Xiangya School of Medicine, Central South University, Zhuzhou 412007, China*
[2]*Department of Neurosurgery, Zhuzhou Hospital Affiliated to Xiangya School of Medicine, Central South University, Zhuzhou 412007, China*
[3]*Department of Neurosurgery, The First People's Hospital of Changde City, Changde 415000, China*

Correspondence should be addressed to Pan Liu; liupan85@126.com and Ting Sun; 815151258@qq.com

Received 11 September 2022; Revised 8 November 2022; Accepted 24 November 2022; Published 4 February 2023

Academic Editor: Muhammad Muddassir Ali

Purpose. Papillary renal cell carcinoma (pRCC) is the second most common histological subtype of adult kidney tumors, with a poor prognosis due to limited understanding of the disease mechanism. Herein, we have performed high-throughput bioinformatic screening to explore and identify potential biomarkers of DNA damage and oxidative stress for pRCC. *Methods*. RNA sequencing data related to pRCC were downloaded from the TCGA database, and differentially expressed genes (DEG) were identified by a wide variety of clustering and classification algorithms, including self-organized maps (SOM), artificial neural networks (ANN), support vector machines (SVM), fuzzy logic, and hyphenated techniques such as neuro-fuzzy networks. Then DAVID and STRING online biological information tools were used to analyze functional enrichment of the regulatory networks of DEG and construct a protein-protein interaction (PPI) network, and then the Cytoscape software was used to identify hub genes. The importance of key genes was assessed by the analysis of the Kaplan–Meier survival curves using the R software. Lastly, we have analyzed the expression of hub genes of DNA damage and oxidative stress (BDKRB1, NMUR2, PMCH, and SAA1) in pRCC tissues and adjacent normal tissues, as well as the relationship between the expression of hub genes in pRCC tissues and pathological characteristics and prognosis of pRCC patients. *Results*. A total of 1,992 DEGs for pRCC were identified, with 1,142 upregulated ones and 850 downregulated ones. The DEGs were significantly enriched in activities including DNA damage and oxidative stress, chemical synaptic transmission, an integral component of the membrane, calcium ion binding, and neuroactive ligand-receptor interaction. cytoHubba in the Cytoscape software was used to determine the top 10 hub genes in the PPI network as BDKRB2, NMUR2, NMU, BDKRB1, LPAR5, KNG1, LPAR3, SAA1, MCHR1, PMCH, and NCAPH. Furthermore, the expression level of hub genes BDKRB1, NMUR2, PMCH, and SAA1 in pRCC tissues was significantly higher than that in the adjacent normal tissues. Meanwhile, the expression level of hub genes BDKRB1, NMUR2, PMCH, and SAA1 in pRCC tissues was significantly positively correlated with tumor stage, lymph node metastasis, and the histopathology grade of pRCC. In addition, high expression levels of hub genes BDKRB1, NMUR2, PMCH, and SAA1 were associated with a poor prognosis for patients with pRCC. Univariate and multivariate analyses showed that the expression of hub genes BDKRB1, NMUR2, PMCH, and SAA1 were independent risk factors for the prognosis of patients with pRCC. *Conclusion*. The results of this analysis suggested that BDKRB1, NMUR2, PMCH, and SAA1 might be potential prognostic biomarkers and novel therapeutic targets for pRCC.

1. Introduction

Renal cell carcinoma (RCC), also known as kidney cancer, is derived from renal tubular epithelial cells and is the most common solid tumor of the kidney, accounting for 3% of adult malignant tumors [1]. It is a heterogeneous group of cancers arising from renal tubular epithelial cells that encompasses 85% of all primary renal neoplasms. Papillary renal cell carcinoma (pRCC) is the second most common histological subtype after clear cell renal cell carcinoma (ccRCC), and 10–15% of RCC histological types are papillary renal cell carcinoma [2]. There are two subtypes of pRCC, type I (basophilic) and type II (acidophilic), and type I has a better prognosis than type II [3]. Most research studies on kidney cancer has focused on ccRCC, and the related studies have shown that compared with ccRCC patients, pRCC patients typically have a lower stage and grade of tumor as well as longer overall survival [4]. The molecular mechanism of pRCC has not been clearly defined. With poor sensitivity to radiotherapy and chemotherapy, surgery is the preferred method for treatment of pRCC, but some patients are prone to metastasis and relapse after surgery. With continued advances in molecular medicine in recent years, the study of the occurrence, development, and metastasis mechanisms of pRCC can help to guide clinical diagnosis and treatment.

The cancer genome atlas (TCGA) project is a joint project of the National Cancer Institute and the National Human Genome Research Institute and aims to apply high-throughput genome analysis technology and to improve the ability to prevent, diagnose, and treat cancer. The cancer genome atlas (TCGA) research network includes analysis of a large number of human tumors to discover molecular aberrations at the DNA, RNA, protein, and epigenetic levels [5]. In this study, TCGA data were used to investigate genes that are deferentially expressed in pRCC. To mine the key genes related to pRCC occurrence and development, we conducted differential gene enrichment (Gene Ontology, GO) analysis and KEGG pathway enrichment analysis, constructed PPI interaction networks, screened hub genes, and performed survival analysis.

2. Materials and Methods

2.1. Data Collection. The published transcriptome data related to papillary renal cell carcinoma were downloaded from TCGA (https://cancergenome.nih.gov/). The data included 289 papillary renal cell carcinoma samples and 32 normal kidney tissues.

2.2. Identification of DEGs. We have performed the edgeR software package in R language (version 3.5.3, https://www.r-project.org/) and a wide variety of clustering and classification algorithms, including self-organized maps (SOM), artificial neural networks (ANN), support vector machines (SVM), fuzzy logic, and hyphenated techniques such as neuro-fuzzy networks to standardize the data and analyze differential expression. Genes with $|\log FC| > 2.0$ and FDR <0.05 were considered differentially expressed genes. To visualize the data graphically, the ggplot2 software package was used.

2.3. GO and KEGG Pathway Analysis. The DAVID database (DAVID; https://david.ncifcrf.gov) was used to perform annotation, visualization, and integrated discovery on the genes identified as significantly differently expressed [6]. Using DAVID, GO analysis was performed, including the analysis of cellular components (CC), molecular functions (MF), and biological process (BP) terms. A value of $P < 0.05$ was considered statistically significant. The Kyoto Encyclopedia of Genes and Genomes (KEGG) (https://www.genome.jp/kegg/) is a knowledge base for systematic analysis of gene functions, linking genomic information with higher order functional information [7]. An adjusted P value <0.05 was considered statistically significant.

2.4. Hub Genes Selection and Analysis of Modules from PPI Networks. The STRING database (http://string-db.org) aims to provide a critical assessment and integration of protein-protein (PPI) interactions [8]. STRING was used to analyze the selected differentially expressed genes and construct a PPI network. Then, cytoHubba in Cytoscape software (version 3.7.2) was used to screen the top 10 hub genes in the PPI network [9].

2.5. Survival Analyses of Hub Genes. The expression profiles and clinical data of 289 pRCC samples were downloaded from TCGA (http://tcga-data.nci.nih.gov) for the survival analysis of hub genes. The Kaplan–Meier method was used for the survival analysis, and log-rank P values were calculated. A log-rank P value <0.05 was considered statistically significant.

2.6. Clinical Specimens. A total of 60 paired pRCC samples and adjacent normal renal specimens were collected from Zhuzhou Central Hospital between June 2016 and June 2021. Inclusion criteria for specimen collection: (1) Postoperative pathology examination confirmed pRCC; (2) the patients with neither radiotherapy nor chemotherapy; (3) complete follow-up data were available; (4) the patients understood the purpose and requirements of the study, agreed to participate in the study, and signed a written informed consent, which was reviewed and approved by the Ethics Committee of Zhuzhou Central Hospital.

2.7. Total RNA Isolation and Quantitative Real-Time Polymerase Chain Reaction (qRT-PCR). The RNA was isolated by TRIzol® reagent (Ambion; USA) from pRCC tissues according to the manufacturer's protocols. And cDNA was reversely transcribed by PrimeScript RT reagent kit (Takara, China). We conducted RT-qPCR on an ABI 7500 RT-PCR system using the SYBR Premix Ex TaqII Kit (Takara, China). All quantifications were normalized to the level of glyceraldehyde phosphate dehydrogenase (GAPDH) in the reaction.

rimers of

BDKRB1 was Forward (5′–3′) CAC-TGT-CCT-ACC-GTC-TTT-GTCT,

Reverse (5′–3′) CGC-AAA-TCT-TGG-TAG-GTG-GT;

NMUR2 forward (5′–3′) GGC-AAG-GCC-ATG-TGT-AAG-ATC,

Reverse (5′–3′) GTA-AAA-CGA-CGG-CCAG;

PMCH forward (5′–3′) CAC-TGT-CCT-GAC-CGT-CTT-TGT-CT,

Reverse (5′–3′) CCA-TAT-GCC-TGT-GGA-GTG-GAA;

SAA1 forward (5′–3′) ACC-TGA-GGA-GCC-CCA,

Reverse (5′–3′) TCT-GCT-CCT-GGC-AGG-CC.

The comparative threshold cycle (CT) method, which compares the differences in CT values between common reference RNA and target gene RNA, was used to obtain the relative fold changes in gene expression. The expressions were calculated by $2^{-\Delta\Delta ct}$ method. Each experiment was performed in triplicate and repeated three times.

2.8. Statistical Analysis. SPSS 24.0 software was used for statistical analysis, and GraphPad Prism 7.0 software was used for analysis and mapping. All measurement data in the form of mean ± standard deviation (SD), according to two groups and multiple groups of measuring data comparison using Student's *t*-tests and one-way ANOVA. The relationship between the RNA expression levels of hub genes BDKRB1, NMUR2, PMCH, and SAA1 in the patients with pRCC tissue samples and the clinical pathological characteristics of patients with pRCC was analyzed through Pearson's Chi-squared test, and the relationship between the expression of hub genes BDKRB1, NMUR2, PMCH, and SAA1 and the prognosis of pRCC patients was analyzed by Kaplan–Meier survival analysis and the Cox proportional hazard model. $P < 0.05$ was considered to be significantly different.

3. Results

3.1. Identification of DEGs. The data for 289 cases of papillary renal cell carcinoma and 32 cases of normal kidney tissue were downloaded from TCGA and used for this study. The data were normalized and logarithmized, probes without corresponding gene annotation information were removed, and repeated probes were removed to finally get the expression profiles of 17,894 genes and 321 samples. Using the edgeR software package, with |logFC|> 2.0 and FDR <0.05 as the screening conditions for differentially expressed genes, a total of 1,992 DEGs were screened for pRCC, including 1,142 upregulated genes and 850 downregulated genes. Using these selected genes, a volcano map (Figure 1) was generated, and the top 50 gene heat maps with the most significant differences were selected (Figure 1(b)).

3.2. GO Term and KEGG Pathway Analyses. In order to better understand the relationships between DEGs and pRCC, we input all DEGs into the online tool DAVID to perform GO analysis. The results revealed that, for GO BP analysis, the DEGs of pRCC were mainly enriched in excretion, epidermis development, ion transmembrane transport, chemical synaptic transmission, chloride transmembrane transport, ion transport, and potassium ion transmembrane transport. For GO CC analysis, DEGs were mainly enriched in integral component of plasma membrane, extracellular region, extracellular space, plasma membrane, apical plasma membrane, anchored component of membrane, proteinaceous extracellular matrix, integral component of membrane, and basolateral plasma membrane. For GO analysis, DEGs were mainly enriched in calcium ion binding, heparin binding, sequence-specific DNA binding, transporter activity, and carbohydrate binding. The GO analysis findings are shown in Figure 2 and Table 1.

We next performed KEGG pathway analysis to analyze the pathways at the functional level. The results showed that DEGs were mainly enriched in neuroactive ligand-receptor interaction, calcium signaling pathway, gastric acid secretion, bile secretion, and pancreatic secretion. The KEGG pathways associated with enriched DEGs associated with pRCC are presented in Figure 2(b) and Table 2.

3.3. Identification of Hub Genes and Analysis of Modules from PPI Networks. The STRING database was used to construct PPI networks for DEGs related to the pathogenesis of papillary renal cell carcinoma. We used the MCODE in Cytoscape software to obtain the main PPI network (Figure 2(c)), and then used cytoHubba in Cytoscape software to identify the top 10 hub genes in the PPI network (Figure 2(c)): recombinant bradykinin receptor B2 (BDKRB2), neuromodulin U receptor 2 (NMUR2), neuromodulin U (NMU), recombinant bradykinin receptor B1 (BDKRB1), lysophosphatidic acid receptor 5 (LPAR5), Kininogen-1 (KNG1), lysophosphatidic acid receptor 3(LPAR3), serum amyloid A1 (SAA1), melanin-concentrating hormone receptor 1 (MCHR1), and precursor melanin-concentrating hormone (PMCH). These 10 hub genes are presented in Figure 2(c).

3.4. Survival Analysis of Hub Genes. Expression data for a total of 289 pRCC samples were downloaded from TCGA. The 10 hub genes were grouped by expression levels, and the data were used to conduct survival analyses. Increased expression levels of BDKRB1, NMUR2, PMCH, and SAA1 were associated with a worse survival rate for pRCC patients (Figure 3).

3.5. The Expression of Hub Genes BDKRB1, NMUR2, PMCH, and SAA1 in pRCC Tissues and Adjacent Normal Tissues of pRCC Patients. We selected 120 tissue samples (including 60 pRCC tissues and 60 normal adjacent tissues) to analyze the expression of hub genes BDKRB1, NMUR2, PMCH, and SAA1 in pRCC tissues by qRT-PCR. The results showed that the expression of hub genes BDKRB1, NMUR2, PMCH, and SAA1 in pRCC tissues was significantly higher than that in the normal adjacent tissues (Figures 4(a), 4(c), 4(e), and 4(g)). To further investigate the correlation between hub genes BDKRB1, NMUR2, PMCH, and SAA1 expression and pathological features of pRCC, the above samples were divided into high (above the mean) and low (below the mean) hub genes expression

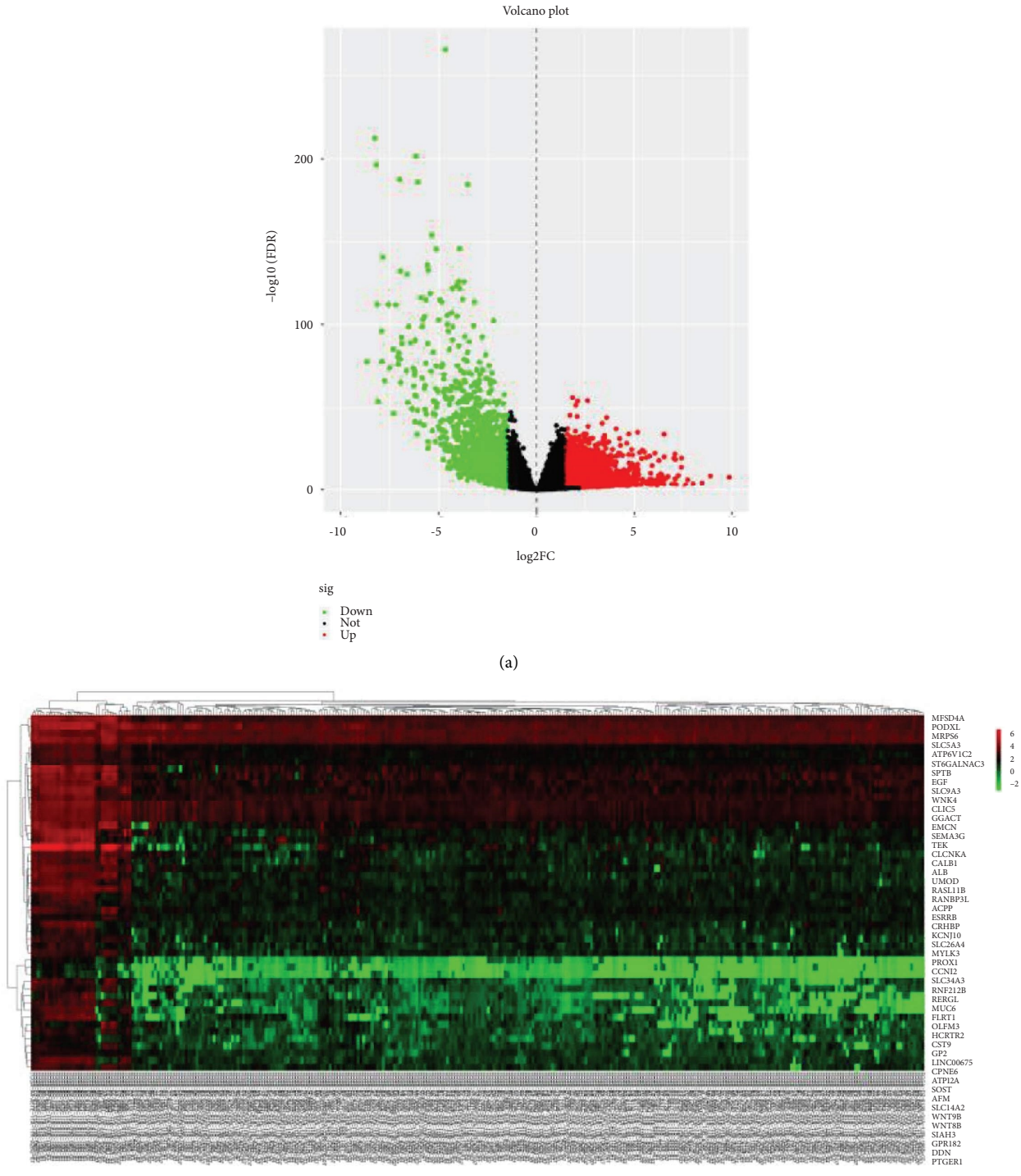

Figure 1: Identification of DEGs in papillary renal cell carcinoma. (a) Volcano plot of the DEGs (|logFC| >2.0 and FDR <0.05 were as the screening conditions). (b) Heatmaps of the top 50 DEGs in papillary renal cell carcinoma and normal kidney tissue. Red indicates that the expression of genes is relatively upregulated, green indicates that the expression of genes is relatively downregulated.

groups. Subsequently, the Chi-square test was used to analyze the relationship between hub genes BDKRB1, NMUR2, PMCH, and SAA1 expression level and pathological characteristics of pRCC patients, and the results showed that the expression level of hub genes BDKRB1, NMUR2, PMCH, and SAA1 expression in pRCC tissues were significantly positively correlated with tumor stage, lymph node metastasis, and histopathological grade of pRCC patients (Figures 4(b), 4(d), 4(f), and 4(h)), while the relationship with gender and age of patients was not statistically significant (Tables 3–6).

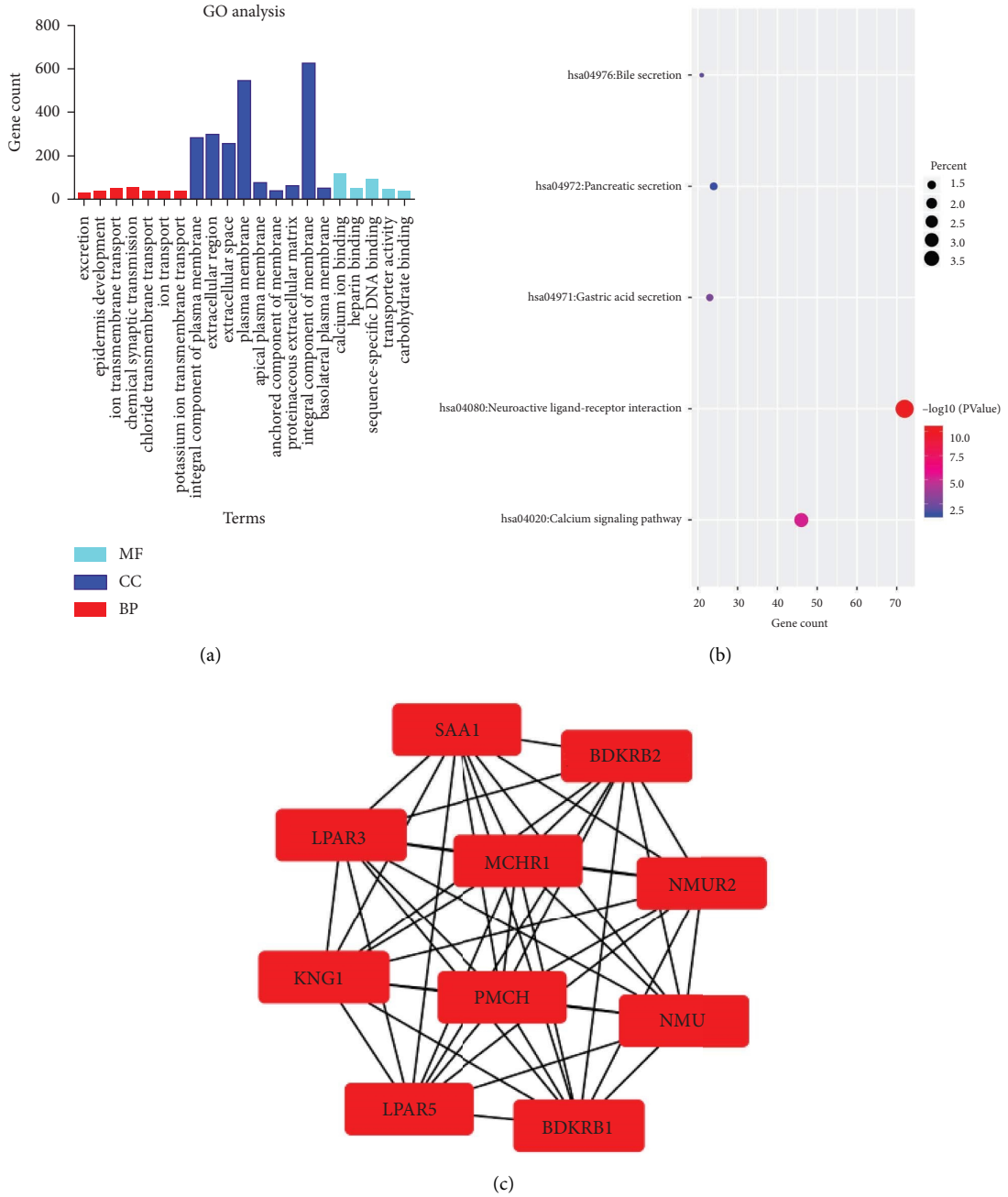

Figure 2: The pathway analyses of DEGs in pRCC. (a) GO enrichment analysis of DEGs in pRCC. GO, Gene Ontology; CC, cellular component; MF, molecular function; BP, biological process. (b) KEGG pathway analysis of DEGs in pRCC. (c) The top 10 hub genes selected from the PPI network.

3.6. Relationship between Hub Genes BDKRB1, NMUR2, PMCH, and SAA1 Expression and Prognosis of Patients with pRCC. The Kaplan–Meier survival analysis was used to study the relationship between hub genes BDKRB1, NMUR2, PMCH, and SAA1 expression and prognosis of patients with pRCC. The results showed that the overall survival rate of patients with high hub genes BDKRB1, NMUR2, PMCH, and SAA1 expression was significantly lower than that of patients with low hub genes BDKRB1, NMUR2, PMCH, and SAA1 expression (Figure 5). Then we conducted the COX proportional risk model analysis. The univariate and multivariate analyses showed that the expression of hub genes BDKRB1, NMUR2, PMCH, and SAA1 were independent risk factor for prognosis in patients with pRCC (Tables 7–10).

4. Discussion

Most patients with pRCC have no obvious symptoms or signs at the time of diagnosis, but the disease is often found by B-ultrasound or CT examination during a physical examination. Very few patients exhibit the typical triad signs of

Table 1: Gene ontology analysis of DEGs associated with pRCC.

Category	Term	Description	Count	P value
BP	GO:0007588	Excretion	18	$4.00E-05$
BP	GO:0008544	Epidermis development	27	$2.31E-04$
BP	GO:0034220	Ion transmembrane transport	47	$4.69E-04$
BP	GO:0007268	Chemical synaptic transmission	51	$7.34E-04$
BP	GO:1902476	Chloride transmembrane transport	26	0.005783318
BP	GO:0006811	Ion transport	31	0.011414198
BP	GO:0071805	Potassium ion transmembrane transport	29	0.034687627
CC	GO:0005887	Integral component of plasma membrane	279	$2.76E-27$
CC	GO:0005576	Extracellular region	293	$8.03E-23$
CC	GO:0005615	Extracellular space	252	$8.22E-21$
CC	GO:0005886	Plasma membrane	543	$1.13E-10$
CC	GO:0016324	Apical plasma membrane	69	$2.70E-08$
CC	GO:0031225	Anchored component of membrane	37	2.04e − 07
CC	GO:0005578	Proteinaceous extracellular matrix	61	$2.45E-06$
CC	GO:0016021	Integral component of membrane	620	$3.43E-05$
CC	GO:0016323	Basolateral plasma membrane	44	$6.86E-05$
MF	GO:0005509	Calcium ion binding	119	$8.07E-06$
MF	GO:0008201	Heparin binding	41	$2.33E-05$
MF	GO:0043565	Sequence-specific DNA binding	89	$1.82E-04$
MF	GO:0005215	Transporter activity	43	0.002430787
MF	GO:0030246	Carbohydrate binding	40	0.017062891

Table 2: KEGG pathway analysis of DEGs associated with pRCC.

Category	Term	Description	Count	P value
KEGG	hsa04080	Neuroactive ligand-receptor interaction	72	$4.38E-11$
KEGG	hsa04020	Calcium signaling pathway	46	$5.31E-06$
KEGG	hsa04971	Gastric acid secretion	23	0.002127995
KEGG	hsa04976	Bile secretion	21	0.012213919
KEGG	hsa04972	Pancreatic secretion	24	0.046905158

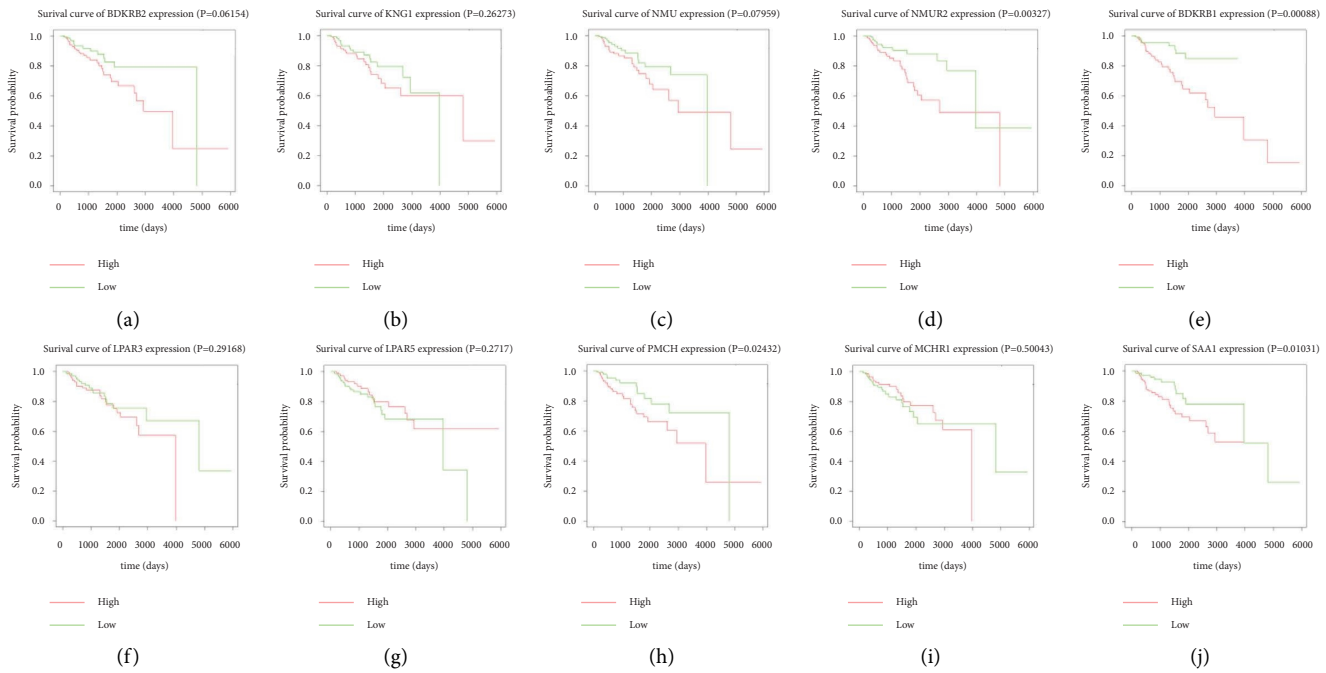

Figure 3: The prognostic values for the 10 hub genes for overall survival of patients with pRCC. (a) Kaplan-Meier plot for BDKRB2, $P = 0.06154$; (b) Kaplan-Meier plot for KNG1, $P = 0.26273$; (c) Kaplan-Meier plot for NMU, $P = 0.07959$; (d) Kaplan-Meier plot for NMUR2, $P = 0.00327$; (e) Kaplan-Meier plot for BDKRB1, $P = 0.00088$; (f) Kaplan-Meier plot for LPAR3, $P = 0.29168$; (g) Kaplan-Meier plot for LPAR5, $P = 0.2717$; (h) Kaplan-Meier plot for PMCH, $P = 0.02432$; (i) Kaplan-Meier plot for MCHR1, $P = 0.50043$; (j) Kaplan-Meier plot for SAA1, $P = 0.01031$. A value of $P < 0.05$ was considered statistically significant.

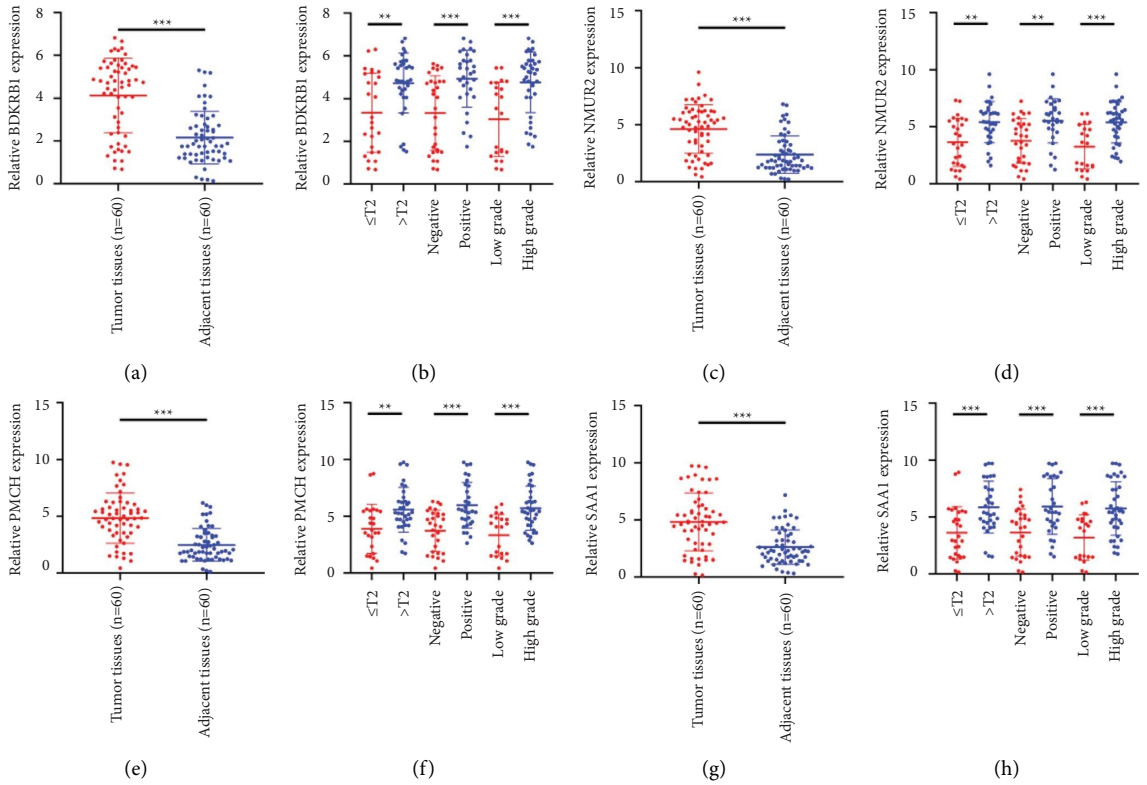

Figure 4: The expression of hub genes BDKRB1 (a), NMUR2 (b), PMCH (c), and SAA1 (d) in pRCC tissues and adjacent normal tissues, as well as the relationship between the expression of hub genes in pRCC tissues and pathological characteristics of pRCC patients (e–h).

Table 3: The relationship between BDKRB1 expression level in pRCC and pathology features of pRCC patients ($n = 60$).

Characteristics	BDKRB1		Chi-squared test	P value
	Low no. cases	High no. cases		
All patients	($n = 23$)	($n = 37$)		
Gender			0.035	0.852
Male	13	20		
Female	10	17		
Age (years)			0.012	0.914
≤60	9	15		
>60	14	22		
Tumor stage			7.274	0.007
≤T2	15	11		
>T2	8	26		
Lymph-node metastasis			5.711	0.017
Negative	16	14		
Positive	7	23		
Pathology grade			6.332	0.012
Low grade	13	9		
High grade	10	28		

kidney cancer: hematuria, abdominal mass, and lumbar pain, and the patients that do exhibit these signs typically have advanced disease. The overall prognosis of pRCC is better than that of ccRCC, but pRCC prognosis is significantly worse than that of ccRCC when pRCC invades the renal vein and/or the inferior vena cava [10]. There is currently no specific treatment for pRCC, and surgical treatment is the first choice in clinical practice. The prognosis of advanced patients is poor, a pRCC is insensitive to radiotherapy and chemotherapy. Therefore, the study of the mechanisms of pRCC development and metastasis will help improve clinical diagnosis and treatment.

In this study, bioinformatics technology was used to mine pRCC transcriptomic data downloaded from TCGA. A

Table 4: The relationship between NMUR2 expression level in pRCC and pathology features of pRCC patients ($n = 60$).

Characteristics	NMUR2		Chi-squared test	P value
	Low no. cases	High no. cases		
All patients	($n = 25$)	($n = 35$)		
Gender			1.009	0.315
Male	14	15		
Female	11	20		
Age (years)			0.156	0.693
≤60	12	15		
>60	13	20		
Tumor stage			6.251	0.012
≤T2	16	11		
>T2	9	24		
Lymph-node metastasis			7.096	0.008
Negative	18	13		
Positive	7	22		
Pathology grade			6.898	0.009
Low grade	14	8		
High grade	11	27		

Table 5: The relationship between PMCH expression level in pRCC and pathology features of pRCC patients ($n = 60$).

Characteristics	PMCH		Chi-squared test	P value
	Low no. cases	High no. cases		
All patients	($n = 30$)	($n = 30$)		
Gender			0.067	0.795
Male	17	16		
Female	13	14		
Age (years)			0.278	0.598
≤60	13	11		
>60	17	19		
Tumor stage			4.344	0.037
≤T2	17	9		
>T2	13	21		
Lymph-node metastasis			6.667	0.01
Negative	20	10		
Positive	10	20		
Pathology grade			7.177	0.007
Low grade	16	6		
High grade	14	24		

Table 6: The relationship between SAA1 expression level in pRCC and pathology features of pRCC patients ($n = 60$).

Characteristics	SAA1		Chi-squared test	P value
	Low no. cases	High no. cases		
All patients	($n = 31$)	($n = 29$)		
Gender			0.012	0.913
Male	17	15		
Female	15	14		
Age (years)			0.63	0.427
≤60	15	17		
>60	16	12		
Tumor stage			8.21	0.004
≤T2	20	8		
>T2	11	21		
Lymph-node metastasis			4.312	0.038
Negative	19	10		
Positive	12	19		
Pathology grade			9.121	0.003
Low grade	17	5		
High grade	14	24		

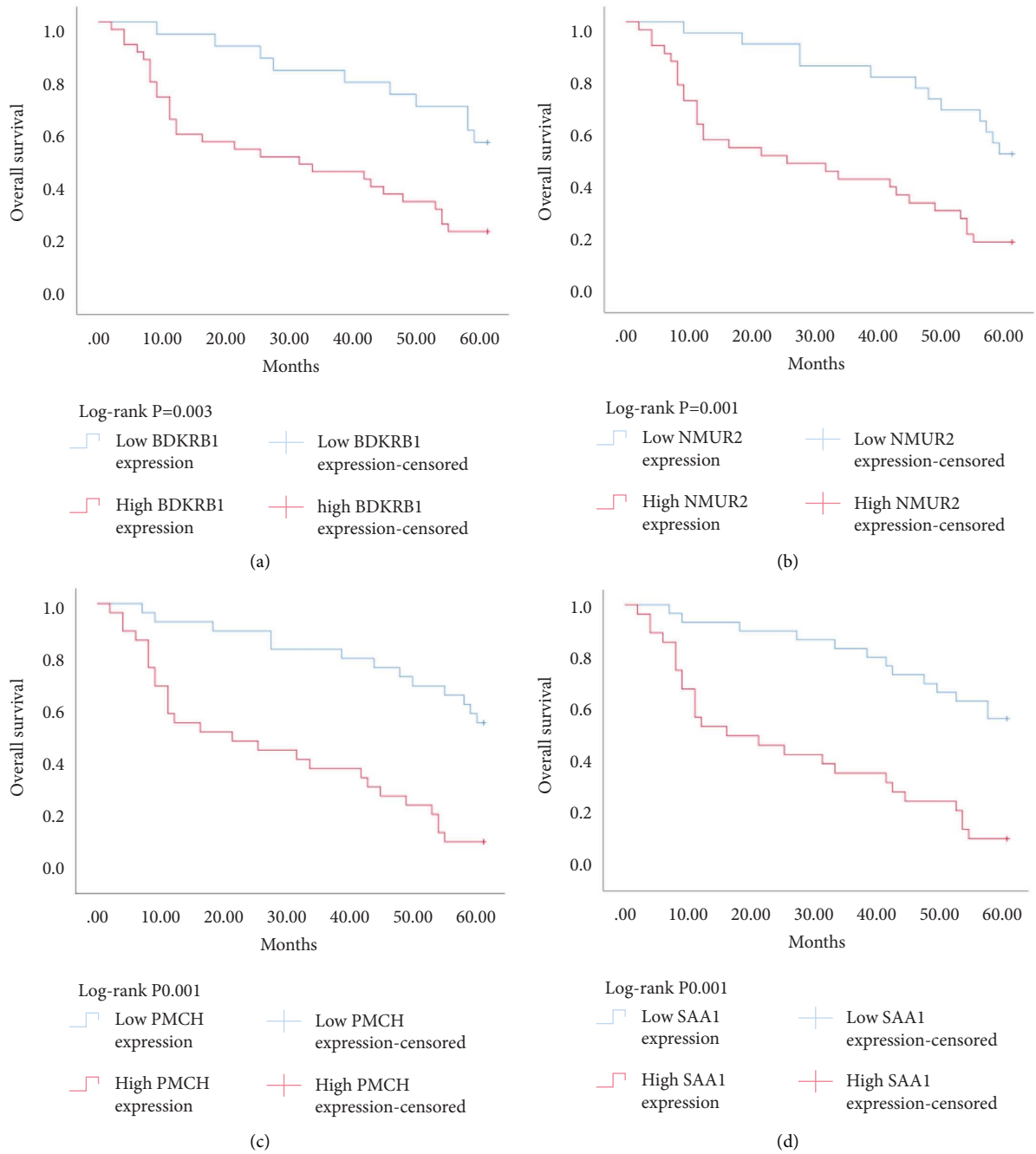

Figure 5: Relationship between hub genes BDKRB1 (a), NMUR2 (b), PMCH (c), and SAA1 (d) expression and prognosis of patients with pRCC.

total of 1,992 DEGs were identified, including 1,142 upregulated genes and 850 downregulated genes. We performed GO and KEGG pathway enrichment analyses to explore interactions between DEGs. The GO analysis revealed that 1,992 DEGs were significantly enriched in 21 terms, including excretion, epidermis development, ion transmembrane transport, chemical synaptic transmission, chloride transmembrane transport, ion transport, potassium ion transmembrane transport, integral component of plasma membrane, extracellular region, extracellular space, plasma membrane, apical plasma membrane, anchored component of membrane, proteinaceous extracellular matrix, integral component of membrane, basolateral plasma membrane, calcium ion binding, heparin binding, sequence-specific DNA binding, transporter activity, and carbohydrate binding. In addition, the KEGG pathway analysis revealed that 1,992 DEGs were significantly enriched in five pathways, including neuroactive ligand-receptor interaction, calcium signaling pathway, gastric acid secretion, bile secretion, and pancreatic secretion. According to the STRING results, we constructed the PPI network. Then hub genes were selected with a high degree

Table 7: Univariate and multivariate analysis of overall survival in patients with pRCC ($n = 60$).

Variable for overall survival	Univariate analysis			Multivariate analysis		
	HR	95% CI	P	HR	95% CI	P
Gender			0.108			
Male vs. female	0.581	0.3–1.126				
Ages (years)			0.134			
≤60 vs. >60	1.659	0.855–3.218				
Pathology grade			0.403			
Low grade vs. high grade	1.331	0.681–2.603				
Tumor stage			0.03			0.716
≤T2 vs. >T2	2.11	1.076–4.137		1.616	0.806–3.239	
Lymph-node metastasis			0.012			0.111
Negative vs. positive	2.31	1.2–4.448		1.743	0.880–3.450	
BDKRB1 expression			0.005			0.065
Low vs. high	2.829	1.366–5.858		2.082	0.957–4.532	

Abbreviations: HR, hazard ratio; CI, confidence interval.

Table 8: Univariate and multivariate analysis of overall survival in patients with pRCC ($n = 60$).

Variable for overall survival	Univariate analysis			Multivariate analysis		
	HR	95% CI	P	HR	95% CI	P
Gender			0.727			
Male vs. female	1.118	0.598–2.089				
Ages (years)			0.308			
≤60 vs. >60	1.386	0.74–2.598				
Pathology grade			0.489			
Low grade vs. high grade	1.254	0.661–2.38				
Tumor stage			0.007			0.086
≤T2 vs. >T2	2.461	1.278–4.739		0.548	0.276–1.089	
Lymph-node metastasis			0.012			0.209
Negative vs. positive	2.252	1.198–4.234		0.652	0.335–1.270	
NMUR2 expression			0.002			0.021
Low vs. high	2.95	1.488–5.847		0.432	0.212–0.882	

Abbreviations: HR, hazard ratio; CI, confidence interval.

Table 9: Univariate and multivariate analysis of overall survival in patients with pRCC ($n = 60$).

Variable for overall survival	Univariate analysis			Multivariate analysis		
	HR	95% CI	P	HR	95% CI	P
Gender			0.16			
Male vs. female	0.629	0.329–1.201				
Ages (years)			0.107			
≤60 vs. >60	1.716	0.89–3.31				
Pathology grade			0.49			
Low grade vs. high grade	1.259	0.654–2.423				
Tumor stage			0.131			
≤T2 vs. >T2	0.608	0.318–1.16				
Lymph-node metastasis			0.02			0.373
Negative vs. positive	0.468	0.246–0.889		0.732	0.368–1.456	
PMCH expression			0			0.001
Low vs. high	0.256	0.13–0.507		0.289	0.139–0.601	

Abbreviations: HR, hazard ratio; CI, confidence interval.

of interaction in the PPI network, including BDKRB2, NMUR2, NMU, BDKRB1, LPAR5, KNG1, LPAR3, SAA1, MCHR1, and PMCH. Further analysis of survival related to the expression of these hub genes revealed that BDKRB1, NMUR2, PMCH, and SAA1 are the key genes for the development of pRCC.

One hub gene, BDKRB1, is a well-established tumor suppressor gene, which is frequently mutated in familial breast and ovarian cancers. The gene product of BDKRB1 functions in a number of cellular pathways that maintain genomic stability, including DNA damage-induced cell cycle checkpoint activation, DNA damage repair, protein

Table 10: Univariate and multivariate analysis of overall survival in patients with pRCC ($n = 60$).

Variable for overall survival	Univariate analysis			Multivariate analysis		
	HR	95% CI	*P*	HR	95% CI	*P*
Gender			0.381			
Male vs. female	0.75	0.393–1.429				
Ages (years)			0.572			
≤60 vs. >60	1.202	0.635–2.275				
Pathology grade						
Low grade vs. high grade	1.335	0.683–2.609	0.399			
Tumor stage			0.016			0.209
≤T2 vs. >T2	0.443	0.228–0.861		0.639	0.318–1.284	
Lymph-node metastasis			0.036			0.333
Negative vs. positive	0.497	0.259–0.956		0.714	0.361–1.413	
SAA1 expression			0			0.004
Low vs. high	0.261	0.132–0.516		0.332	0.158–0.7	

Abbreviations: HR, hazard ratio; CI, confidence interval.

ubiquitination, chromatin remodeling, as well as transcriptional regulation and apoptosis. In this study, we found the role of BRCA1 in tumor suppression and DNA damage response, including DNA damage-induced cell cycle checkpoint activation and DNA damage repair. The other hub gene KNG1 (Kininogen-1) is expressed at low level in glioma cells. KNG1 can exert antiangiogenic properties and inhibit the proliferation of endothelial cells [11]. Previous work showed that KNG1 can be used as a serum biomarker for colorectal cancer [12]. Overexpression of the KNG1 inhibited proliferation and induces apoptosis of glioma cells [11]. In this study, KNG1 expression was downregulated in pRCC, which may be associated with the viability and angiogenesis of pRCC, but the analysis revealed no statistical impact of expression of this gene on survival, suggesting further investigation into the relationship between this gene and pRCC is required. Lysophosphatidic acid (LPA) is an extracellular biological lipid that interacts with G protein-coupled LPA receptors (LPAR1 to LPAR6) [13]. The lysophosphatidic acid receptor-3 (LPAR3) mediates viability among malignant cells and aggressiveness among certain tumors [14]. LPAR3 has been characterized as the major promoter of long-term viability in melanoma cells [15]. Other studies found that increased expression of LPAR3 increases malignancy in breast and ovarian cancers in vivo [16, 17]. In this study, LPAR3 was identified as a downregulated gene in pRCC. It was reported with the involvement of LPA5 in the activation of tumor progression in pancreatic cancer cells [13]. Bradykinin (BK) is produced in the inflammatory tissue microenvironment, where it acts in cell proliferation, leukocyte activation, cell migration, and endothelial cell activation [18]. BDKRB1 and BDKRB2 belong to the rhodopsin family of G protein-coupled receptors. The activation of BDKRB1 leads to the activation of macrophages, dendritic cells, and other cells in the tumor microenvironment, which have angiogenic properties and is related to the proliferation of malignant tumors [19]. BDKRB1 contributes to interleukin-8 production and glioblastoma migration [20]. Wang et al. reported that inhibition of BDKRB2, but not the B1 receptor, attenuated bradykinin-mediated invasion and migration in colorectal cancer cells and inhibited ERK1/2 activation and IL-6 production [21]. Thus, the identification of inhibitors against BDKRB1 may be a reasonable strategy to suppress pRCC. Neuromodulin U (NMU) activates the G protein-coupled receptor NMUR2, and NMU signaling interacts with several cancer-related pathways, including the WNT receptor cascade, resulting in increased activation of WNT/planar cell polarity (PCP) effector RAC1, which promotes tumor cell invasion and metastasis [22]. NMUR2 is a receptor that enhances NMU-mediated cell motility and invasion in human pancreas and endometrial cancer cells [23, 24]. Hub genes NMU and NMUR2 have not previously been reported to play roles in pRCC. PMCH encodes the 165 aa prohormone promelanin-concentrating hormone (PMCH), which is proteolytically processed into several peptides, including the oncogenic peptide melanin-concentrating hormone (MCH) [25]. In this study we found that increased expression of PMCH was associated with poor survival in patients with pRCC, suggesting PMCH may be a potential diagnostic biomarker or predictor of prognosis. Human serum amyloid A (SAA) is a high-density lipoprotein (HDL)-related lipoprotein with major roles in the regulation of inflammation and cholesterol transport [26]. Human serum amyloid A (SAA) has been widely regarded as an accurate and sensitive indicator of inflammation, which can be synthesized by the liver and cancer cells [27]. SAA1 regulates cell adhesion and migration and binding to laminin by inducing cytokine expression [28]. A previous study reported a relationship between increased SAA1 concentration and poor prognosis and distant metastasis in ccRCC patients [29].

In conclusion, bioinformatics analysis was used to identify DEGs that may be involved in the development or progression of the pRCC. This study identified several genes that may be involved in the pathology of papillary renal cell carcinoma. BDKRB1, NMUR2, PMCH, and SAA1 may contribute to the occurrence and development of papillary renal cell carcinoma. This identification of specific biological functions that may be involved in the mechanism of pRCC development provides new clues and directions for efforts to develop future treatments for papillary renal cell carcinoma.

Data Availability

All data generated or analyzed during this study are included within this article.

Conflicts of Interest

The authors declare that they have no conflicts of interests.

Authors' Contributions

Le Li and XuKai Liu designed the manuscript. Pan Liu and Ting Sun transcribed the whole article. Yong Wen downloaded the data for analysis. All authors read and approved the final version of the submitted manuscript. Le Li, XuKai Liu, and Yong Wen contributed equally to this work.

Acknowledgments

This work was supported by Hunan Natural Science Foundation (2021JJ50068).

References

[1] R. L. Siegel, K. D. Miller, and A. Jemal, "Cancer statistics, 2020," *CA: A Cancer Journal for Clinicians*, vol. 70, no. 1, pp. 7–30, 2020.

[2] H. Moch, A. L. Cubilla, P. A. Humphrey, V. E. Reuter, and TM. Ulbright, "The 2016 WHO classification of tumours of the urinary system and male genital organs—Part A: renal, penile, and testicular tumours," *European Urology*, vol. 70, no. 1, pp. 93–105, 2016.

[3] G. Pignot, C. Elie, S. Conquy et al., "Survival analysis of 130 patients with papillary renal cell carcinoma: prognostic utility of type 1 and type 2 subclassification," *Urology*, vol. 69, no. 2, pp. 230–235, 2007.

[4] A. Kaldany, D. J. Paulucci, M. Kannappan et al., "Clinicopathological and survival analysis of clinically advanced papillary and chromophobe renal cell carcinoma," *Urologic Oncology: Seminars and Original Investigations*, vol. 37, no. 10, pp. 727–734, 2019.

[5] J. N. Weinstein, E. A. Collisson, G. B. Mills et al., "The cancer genome atlas pan-cancer analysis project," *Nature Genetics*, vol. 45, no. 10, pp. 1113–1120, 2013.

[6] D. W. Huang, B. T. Sherman, and R. A. Lempicki, "Systematic and integrative analysis of large gene lists using DAVID bioinformatics resources," *Nature Protocols*, vol. 4, no. 1, pp. 44–57, 2009.

[7] M. Kanehisa, M. Furumichi, M. Tanabe, Y. Sato, and K. Morishima, "KEGG: new perspectives on genomes, pathways, diseases and drugs," *Nucleic Acids Research*, vol. 45, no. D1, pp. D353–d361, 2017.

[8] D. Szklarczyk, A. Franceschini, S. Wyder et al., "STRING v10: protein–protein interaction networks, integrated over the tree of life," *Nucleic Acids Research*, vol. 43, no. D1, pp. D447–D452, 2015.

[9] N. T. Doncheva, J. H. Morris, J. Gorodkin, and LJ. Jensen, "Cytoscape StringApp: network analysis and visualization of proteomics data," *Journal of Proteome Research*, vol. 18, no. 2, pp. 623–632, 2019.

[10] T. Kondo, E. Ikezawa, T. Takagi et al., "Negative impact of papillary histological subtype in patients with renal cell carcinoma extending into the inferior vena cava: single-center experience," *International Journal of Urology*, vol. 20, no. 11, pp. 1072–1077, 2013.

[11] J. Xu, J. Fang, Z. Cheng et al., "Overexpression of the Kininogen-1 inhibits proliferation and induces apoptosis of glioma cells," *Journal of Experimental & Clinical Cancer Research*, vol. 37, no. 1, p. 180, 2018.

[12] J. Wang, X. Wang, S. Lin et al., "Identification of kininogen-1 as a serum biomarker for the early detection of advanced colorectal adenoma and colorectal cancer," *PLoS One*, vol. 8, no. 7, Article ID e70519, 2013.

[13] S. Ishii, M. Hirane, K. Fukushima, A. Tomimatsu, N. Fukushima, and T. Tsujiuchi, "Diverse effects of LPA4, LPA5 and LPA6 on the activation of tumor progression in pancreatic cancer cells," *Biochemical and Biophysical Research Communications*, vol. 461, no. 1, pp. 59–64, 2015.

[14] C. C. Byrnes, W. Jia, A. A. Alshamrani, S. S. Kuppa, and MM. Murph, "miR-122-5p expression and secretion in melanoma cells is amplified by the LPAR3 SH3–binding domain to regulate Wnt1," *Molecular Cancer Research*, vol. 17, no. 1, pp. 299–309, 2019.

[15] W. Jia, S. K. Tran, C. A. Ruddick, and MM. Murph, "The Src homology 3 binding domain is required for lysophosphatidic acid 3 receptor-mediated cellular viability in melanoma cells," *Cancer Letters*, vol. 356, no. 2, pp. 589–596, 2015.

[16] S. Yu, M. M. Murph, Y. Lu et al., "Lysophosphatidic acid receptors determine tumorigenicity and aggressiveness of ovarian cancer cells," *Journal of the National Cancer Institute*, vol. 100, no. 22, pp. 1630–1642, 2008.

[17] S. Liu, M. Murph, N. Panupinthu, and GB. Mills, "ATX-LPA receptor axis in inflammation and cancer," *Cell Cycle*, vol. 8, no. 22, pp. 3695–3701, 2009.

[18] P. L. da Costa, P. Sirois, I. F. Tannock, and R. Chammas, "The role of kinin receptors in cancer and therapeutic opportunities," *Cancer Letters*, vol. 345, no. 1, pp. 27–38, 2014.

[19] M. Gao, Z. Zhang, J. Sun, B. Li, and Y. Li, "The roles of circRNA–miRNA–mRNA networks in the development and treatment of osteoporosis," *Frontiers in Endocrinology*, vol. 5, no. 13, Article ID 945310, 2022.

[20] Y. S. Liu, J. W. Hsu, and H. Y. Lin, "Bradykinin B1 receptor contributes to interleukin-8 production and glioblastoma migration through interaction of STAT3 and SP-1 (J)," *Neuropharmacology*, pp. 144143–144154, 2019.

[21] G. Wang, Y. Ye, X. Zhang, and J. Song, "Bradykinin stimulates IL-6 production and cell invasion in colorectal cancer cells," *Oncology Reports*, vol. 32, no. 4, pp. 1709–1714, 2014.

[22] S. Garczyk, N. Klotz, S. Szczepanski et al., "Oncogenic features of neuromedin U in breast cancer are associated with NMUR2 expression involving crosstalk with members of the WNT signaling pathway," *Oncotarget*, vol. 8, no. 22, pp. 36246–36265, 2017.

[23] K. Ketterer, B. Kong, D. Frank et al., "Neuromedin U is overexpressed in pancreatic cancer and increases invasiveness via the hepatocyte growth factor c-Met pathway," *Cancer Letters*, vol. 277, no. 1, pp. 72–81, 2009.

[24] T. Y. Lin, F. J. Wu, C. L. Chang, Z. Li, and C. W. Luo, "NMU signaling promotes endometrial cancer cell progression by modulating adhesion signaling," *Oncotarget*, vol. 7, no. 9, pp. 10228–10242, 2016.

[25] H. Sandig, J. McDonald, J. Gilmour, M. Arno, T. H. Lee, and DJ. Cousins, "Human Th2 cells selectively express the orexigenic peptide, pro-melanin-concentrating hormone," *Proceedings of the National Academy of Sciences of the United States of America*, vol. 104, no. 30, pp. 12440–12444, 2007.

[26] G. H. Sack Jr., "Serum amyloid A (SAA) proteins (J)," *Subcellular Biochemistry*, pp. 94421–94436, 2020.

[27] J. Zhou, J. Sheng, Y. Fan et al., "Association between serum amyloid A levels and cancers: a systematic review and meta-analysis," *Postgraduate Medical Journal*, vol. 94, no. 1115, pp. 499–507, 2018.

[28] C. Paret, Z. Schon, A. Szponar, and G. Kovacs, "Inflammatory protein serum amyloid A1 marks a subset of conventional renal cell carcinomas with fatal outcome," *European Urology*, vol. 57, no. 5, pp. 859–866, 2010.

[29] F. Oz Atalay, B. Aytac Vuruskan, and H. Vuruskan, "Significance of amyloid A immunoexpression in the prognosis of renal cell carcinoma," *Apmis*, vol. 124, no. 4, pp. 257–262, 2016.

Hindawi
Journal of Oncology
Volume 2023, Article ID 1083423, 12 pages
https://doi.org/10.1155/2023/1083423

Research Article

Polypeptide N-Acetylgalactosaminyltransferase 14 (GALNT14) as a Chemosensitivity-Related Biomarker for Osteosarcoma

Qiong Xi[1] and Jinqi Ma[2]

[1]*Department of Pediatrics, The Third Xiangya Hospital of Central South University, Changsha, China*
[2]*Department of Blood Transfusion, The Third Xiangya Hospital of Central South University, Changsha, China*

Correspondence should be addressed to Jinqi Ma; 601237@csu.edu.cn

Received 13 August 2022; Revised 21 October 2022; Accepted 24 November 2022; Published 2 February 2023

Academic Editor: İbrahim Hakkı Cigerci

Purpose. Osteosarcoma is the most common primary bone tumor. Polypeptide N-acetylgalactosaminyltransferase 14 (GALNT14), a member of the N-acetylgalactosaminyltransferase family, has been considered to be associated with various cancers. However, its role in osteosarcoma remains unknown. Here, we aimed to explore the expression and potential mechanism of GALNT14 in osteosarcoma through bioinformatics analysis and in vitro experiments. *Methods*. We investigated GALNT14 expression in osteosarcoma using GEO, the TIMER database, and clinical samples. Protein-protein interaction (PPI) network analysis on GALNT14 was performed by STRING. TARGET was used to identify differentially expressed genes (DEGs) between high and low GALNT14 expression. The correlation between GALNT14 and cuproptosis-related genes in osteosarcoma was analyzed by R language. The prognostic significance of GALNT14 was examined by Kaplan–Meier survival analysis. Additionally, we inhibited GALNT14 function in an osteosarcoma cell line by transfecting siRNA and subsequently explored the effect on drug sensitivity by CCK-8, clonogenic assay, and flow cytometry. *Results*. GALNT14 was significantly elevated in osteosarcoma tissue, osteosarcoma cell lines, and metastatic osteosarcoma. PPI analysis revealed that GALNT14 was associated with MUC7, MUC13, MUC5AC, C1GALT1, MUC15, MUC16, MUC1, MUC4, MUC21, and MUC17. In the high GALNT14 expression group, we discovered 81 upregulated DEGs and 73 downregulated DEGs. Functional enrichment analysis of DEGs showed significant enrichment in the Wnt, TGF-β, Hippo, PI3K signaling pathways and cell adhesion molecules. Expression of cuproptosis-related genes was closely related in osteosarcoma, and GALNT14 expression was significantly positively correlated with FDX1, a key regulator of cuproptosis. Kaplan–Meier survival showed that GALNT14 was linked to poor overall survival and disease-free survival in osteosarcoma. *In vitro* experiments suggested that GALNT14 was associated with chemotherapy resistance in osteosarcoma. *Conclusion*. We identified a GALNT family gene, GALNT14, that was highly expressed in osteosarcoma. This gene was closely associated with metastasis, progression, cuproptosis-related genes, and chemosensitivity of osteosarcoma, and showed correlation with poor overall survival and disease-free survival in osteosarcoma.

1. Introduction

Osteosarcoma, the most prevalent primary bone cancer, mostly occurs in children and adolescents, with the second highest incidence among older adults [1]. Multiagent chemotherapy combined with surgical resection is the standard treatment for patients with localized disease, and it results in long-term survival rates of approximately 70% [2]. Metastasis contributes to more than 90% of all cancer-related deaths, including osteosarcoma [3]. The lung is the site of more than 75% of osteosarcoma metastases, and most deaths from osteosarcoma are attributed to lung metastases. It is well understood how tumor cell dispersion and metastatic colonization of distant sites physically occur [4]. Whole-genome sequencing has elucidated many genes responsible for the metastatic progression of osteosarcoma. However, the underlying mechanisms are not well defined. Understanding the underlying mechanisms of the progression and metastasis of osteosarcoma may help to improve the prognosis.

The enzymes that make up the N-acetylgalactosaminyltransferase (GALNT) family add an N-acetylgalactosamine (GalNAc) to a threonine or serine residue of a mucin-type protein to start the process of O-glycosylation [5]. Thomsen-nouvelle (Tn) antigens, which are well-knowncancer-associated molecules, are synthesized largely as a result of this process [6]. There are 20 members in the GALNT family, ranging from GALNT1 to GALNT14 and from GANLTL1 to GANLTL6 [5]. The modification of O-glycosylation by GALNTs may impact a variety of biological functions associated with cancer, including tumor development, proliferation, and migration [7].

The GALNT14 gene, which is over 228 kb in length, is located on chromosome 2p23.1. The 552-amino acid type II membrane protein GALNT14 has a catalytic domain, a transmembrane domain, a stem region, and an N-terminal cytoplasmic domain [6]. GALNT14 has been found in various human tissues since it was first discovered in the gastric cancer cell line MKN45 in 2003 [8]. Further, the roles of GALNT14 in many malignancies have been identified, including the modification of migration characteristics, transformation of tissue invasiveness, and change in apoptotic signaling [9]. Clinically, GALNT14 has been proposed as a biomarker for anticancer therapy and prognosis [9]. However, the function of GALNT14 in osteosarcoma is still unclear.

In this study, we analyzed the expression of GALNT14 in osteosarcoma using expression data found in public databases. Then protein-protein interaction (PPI) analysis, GO/KEGG enrichment analysis, and correlation analysis of cuproptosis-related genes preliminarily revealed the potential function of GALNT14. Finally, we assessed the significance of GALNT14 in chemosensitivity and prognosis in osteosarcoma.

2. Methods

2.1. Differential Expression Analysis. The microarray transcriptome data were collected from three osteosarcoma datasets (GSE12865, GSE11414, and GSE21257) in the Gene Expression Omnibus (GEO, https://www.ncbi.nlm.nih.gov/geo) database. The three datasets contained samples from osteosarcoma tumor samples and normal human osteoblasts, osteosarcoma and human osteoblast cell lines, and osteosarcoma patients who developed metastases or not, respectively. GEO2R was used for GALNT14 expression analysis [10]. The Tumor Immune Estimation Resource (TIMER, https://cistrome.shinyapps.io/timer/) is a trustworthy and practical database that offers extensive gene expression data for a variety of cancer types. Using the DiffExp module of the TIMER database, we assessed the levels of GALNT14 in adjacent normal tissues and cancerous tissues across cancers [11].

2.2. Functional Enrichment Analysis. With online PPI data obtained from the STRING database (https://cn.string-db.org/) [12], we examined the GALNT14 PPI network.

Gene expression data of 98 osteosarcoma patients were obtained from the Therapeutically Applicable Research to Generate Effective Treatments (TARGET, https://ocg.cancer.gov/programs/target) database, an open database for childhood cancers. To examine the mRNA that differed in expression between groups (high GALNT14 expression vs. low GALNT14 expression), we used the limma package in the R programming language. The criterion for the differential expression of mRNAs was established as "adjusted $p < 0.05$ and Log2 (fold change) > 1 or Log2 (fold change) ≤1."

The differential expression data were evaluated by functional enrichment in order to better support the underlying function of GALNT14. Gene Ontology (GO) is a popular approach for annotating genes with functions, particularly molecular function (MF), biological pathways (BP), and cellular components (CC). The Kyoto Encyclopedia of Genes and Genomes (KEGG) enrichment analysis is a useful tool for learning about gene functions and related high-level genome functional data. The ClusterProfiler package (version: 3.18.0) in R was used to examine the GO function and the enriched KEGG pathway of possible targets in order to better understand the carcinogenesis of GALNT14. The boxplot was created using the R package ggplot2. The heatmap was created using the R software's pheatmap package [13].

2.3. The Correlations among Cuproptosis-Related Genes and GALNT14. The cuproptosis-related genes (CDKN2A, FDX1, DLD, DLAT, LIAS, GLS, LIPT1, MTF1, PDHA1, and PDHB) [14] and GALNT14 expression data were obtained from the TARGET database. A parametric (Pearson) or nonparametric (Spearman) test method was employed for the correlation analysis based on the data normality test. Next, the correlations between cuproptosis-related genes and GALNT14 were displayed via the R software package heatmap. The R software package circlize (version 0.4.12) was used to display the chord diagram. The correlation between quantitative variables without a normal distribution was described using Spearman's correlation analysis. Statistics were considered significant for p values < 0.05.

2.4. Kaplan–Meier Survival Analysis of GALNT14. The gene expression and clinical information of 98 individuals with osteosarcoma were retrieved from the TARGET database. The difference in overall survival (OS) and disease-free survival (DFS) between the high GALNT14 expression group and the low GALNT14 expression group was compared using the log-rank test. p values and the hazard ratio (HR) with a 95% confidence interval (CI) were calculated for Kaplan–Meier curves using log-rank testing and univariate Cox proportional hazards regression. All analyses were performed in R version 4.0.3. Statistics were considered significant if $p < 0.05$.

2.5. Clinical Tissues and Cell Culture. Normal human osteoblasts and osteosarcoma tumor samples were obtained from healthy donors or patients with osteosarcoma at Third Xiangya Hospital. Fresh tissues were preserved with liquid

nitrogen. All patients provided informed consent. Human osteosarcoma cell lines MG-63 and U-2 osteosarcoma were purchased from the American Type Culture Collection (ATCC; Manassas, VA, United States). Cell culture was performed based on the recommended protocols. Osteosarcoma cell lines were transfected with siRNA (5′-CCA UCC AGA AGG GCA AUA UTT-3′ (sense) and 5′- AUA UUG CCC UUC UGG AUG GTT-3′ (antisense)) using LipofectamineTM 3000 (Invitrogen, MA, United States) [15].

2.6. Cell Viability Assay and Clonogenic Assay. The cell counting kit-8 (CCK-8) assay was used to determine the viability of the cells. 96-well plates were seeded with MG-63 or U-2 osteosarcoma cells. Following adhesion, the cells were given the indicated concentrations and times of cisplatin or doxorubicin. Each well was then filled with 10 μl of CCK-8 reagent, and each was cultured at 37°C for 1 hour. The optical density of the cell lysates at 450 nm was measured in order to calculate the relative number of surviving cells.

For colony formation assays, MG-63 or U-2 osteosarcoma cells were seeded at 500 cells/well in 6-well plates and treated with various concentrations of cisplatin or doxorubicin for 14 days. After that, cells were fixed with 4% paraformaldehyde, followed by three washes in PBS and two washes in ddH_2O.

2.7. Extraction of RNA and qPCR. Using the usual TRIzol (Invitrogen, United States) RNA extraction technique, total RNA was isolated from the cells. Using a DNA/RNA GeneQuant Calculator, the quantity of RNA samples was determined by UV absorbance at 260–280 nm (Amersham Biosciences, Piscataway, NJ, USA). Using the PrimeScript RT Reagent Kit, reverse transcription was carried out (Takara, China). Real-time qPCR was carried out with the use of the Brilliant II SYBR Green RT-qPCR kit. For RT-PCR, the following primers were utilized: GALNT14 (474 bp): sense 5′-ACCTGGACACCT TCACCTACAT-3′, antisense 5′- CCAATCTGCTCTCAACATTCC-3′; GAPDH (230 bp): sense 5′- CTCTCTGCTCCTCCTGTTCGACAG-3′, antisense 5′- GTGGAATCATATTGGAACATGT -3′.

2.8. Flow Cytometry. Apoptosis was measured using Annexin V/PI double-staining (KeyGEN BioTECH, China). Briefly, cells were incubated with the required conditions and then washed with PBS and trypsinized to get a single cell suspension. Next, 10^5 cells/ml of suspension was suspended in 100 μL binding buffer and stained with Annexin V/PI in the dark for 30 min. The analysis was performed with FACSVerse (BD Biosciences) and FlowJo software (Tree Star, United States).

2.9. Statistical Analyses. Each result was independently verified by at least three separate experiments, and all data were displayed as mean ± standard deviation (SD). To determine whether differences were statistically significant, two-sided Student's *t*-tests or analysis of variance tests were utilized. Statistics were considered to be significant at $p < 0.05$.

3. Results

3.1. GALNT14 Expression in Osteosarcoma and Pan-Cancer. GSE12865 provided the expression profiles of osteosarcoma tumor samples and normal human osteoblasts. As shown in Figure 1(a), GALNT14 expression was significantly elevated in osteosarcoma ($p = 0.002$). We also observed upregulation of GALNT14 in the osteosarcoma cell line U2OS compared to GALNT14 expression in the human osteoblast cell line HOB ($p < 0.001$) (Figure 1(b)). Furthermore, osteosarcoma at the metastatic stage showed an increased GALNT14 level compared to that at the nonmetastatic stage ($p = 0.004$) (Figure 1(c)). The levels of GALNT14 across cancers were examined using the TIMER database. Compared with adjacent normal tissues, GALNT14 presented with a significantly higher expression in the tumor tissues of bladder urothelial carcinoma, cholangiocarcinoma, head and neck squamous cell carcinoma, kidney renal clear cell carcinoma, kidney renal papillary cell carcinoma, lung adenocarcinoma, lung squamous cell carcinoma, and uterine corpus endometrial carcinoma. However, kidney chromophobe, liver hepatocellular carcinoma, and prostate adenocarcinoma had lower GALNT14 expression than adjacent normal tissues (Figure 1(d)). All the *p* values of pan-cancer analysis were summarized in Supplementary Table 1.

3.2. PPI and Differentially Expressed Genes Associated with GALNT14. We used the STRING database to analyze the GALNT14 PPI network and revealed a link between GALNT14 and MUC7, MUC13, MUC5AC, C1GALT1, MUC15, MUC16, MUC1, MUC4, MUC21, and MUC17 (Figure 2(a)). We analyzed differentially expressed genes associated with GALNT14 levels using the osteosarcoma expression profile from the TARGET database, which contains the largest sample size of osteosarcoma. Differentially expressed genes were represented by a heatmap and a volcano plot (Figures 2(b) and 2(c)). In the high GALNT14 expression group, we discovered 81 upregulated genes and 73 downregulated genes. The functional enrichment analysis showed significant enrichment in pathways related to tumorigenesis and progression, such as the Wnt, TGF-β, Hippo, and PI3K signaling pathways. In addition, we also observed the enrichment of cell adhesion molecules, which may be closely related to tumor metastasis (Figure 3).

3.3. GALNT14 Was Associated with Cuproptosis-Related Genes in Osteosarcoma. We analyzed the correlation of the expression of GALNT14 and 10 cuproptosis-related genes by using the TARGET osteosarcoma dataset. As shown in Figure 4(a) and Supplementary Table 2, the expression levels of genes associated with cuproptosis were strongly correlated with osteosarcoma. Then the relationship between GALNT14 and cuproptosis-related genes was displayed separately. GALNT14 expression was significantly

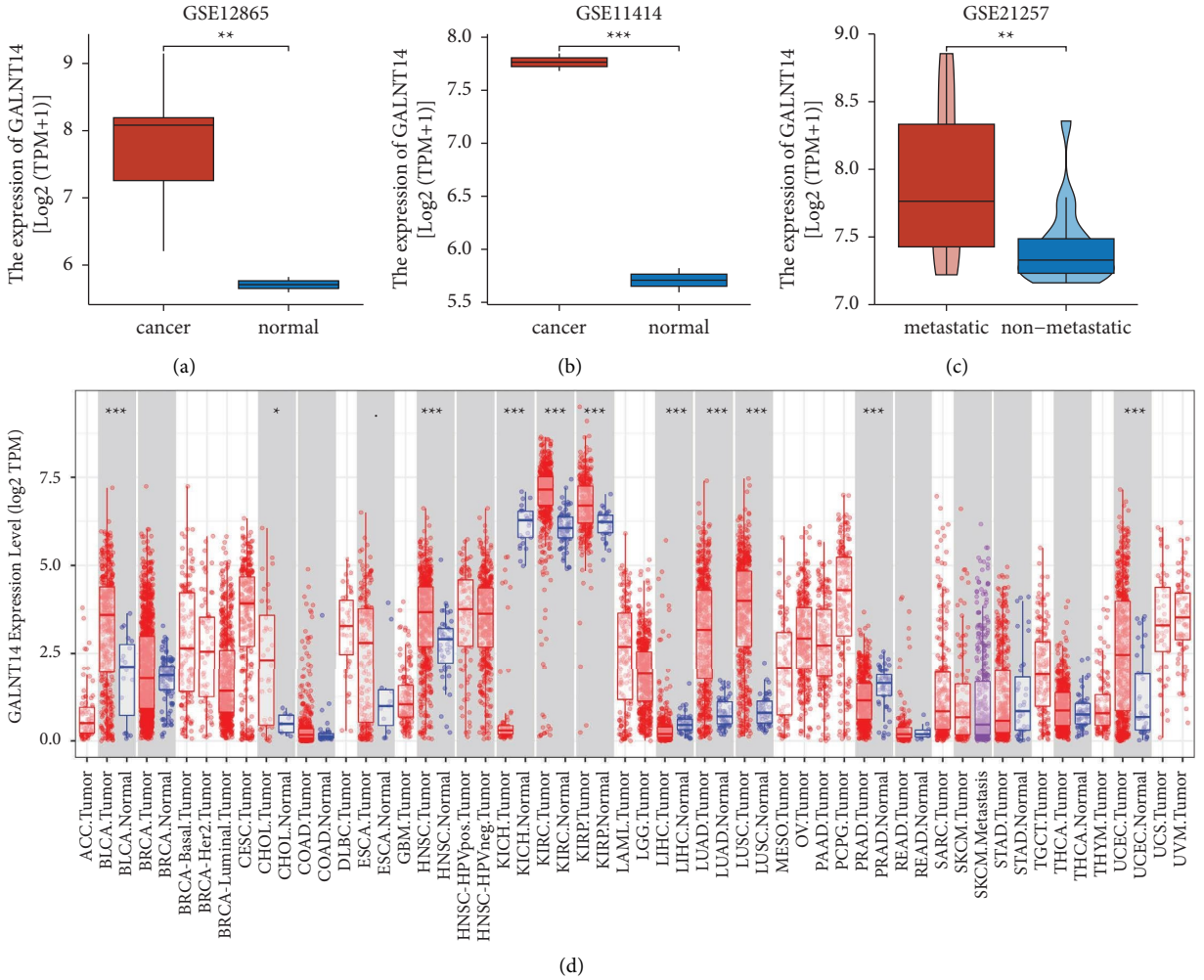

Figure 1: GALNT14 expression in osteosarcoma and pan-cancer. (a) GALNT14 expression data in an osteosarcoma from GSE12865. (b) GALNT14 expression data in osteosarcoma cell line from GSE11414. (c) GALNT14 expression data in metastatic osteosarcoma from GSE21257. (d) GALNT14 pan-cancer expression in TIMER. $^{**}p < 0.01$, $^{***}p < 0.001$.

positively correlated with FDX1 ($R = 0.33$, $p < 0.001$), a key regulator of copper ionophore-induced cell death (Figure 4(b)). Additionally, there was some association between DLAT and GALNT14 expression ($R = 0.17$, $p = 0.103$). The gene expression distributions are displayed in a dot plot (Figure 4(c))..

3.4. GALNT14 Was Associated with Poor OS and DFS in Osteosarcoma. We first performed a detailed analysis of the impact of GALNT14 on OS in osteosarcoma. The correlation between gene expression and survival time and status is depicted in Figure 5(a); high GALNT14 expression was associated with poor OS in osteosarcoma. Kaplan–Meier survival curves also demonstrated this trend ($p = 0.0305$, HR = 2.074, 95% CI (1.071, 4.016)) (Figure 5(b)). In addition, GALNT14 was also associated with poor DFS in osteosarcoma ($p = 0.00416$, HR = 2.41, 95% CI (1.32, 4.398)) (Supplementary Figure 1 and Figure 5(c)).

3.5. GALNT14 Was Related to Chemosensitivity in Osteosarcoma. First, we measured the expression of GALNT14 in normal human osteoblasts, drug-sensitive osteosarcoma, and drug-resistant osteosarcoma by RT-qPCR. As shown in Figure 6(a), the expression of GALNT14 was increased in osteosarcoma compared with normal osteoblasts, especially in drug-resistant osteosarcoma. Then, we explored the effect of GALNT14 on drug sensitivity in vitro. A siRNA was used to inhibit the expression of GALNT14 in the osteosarcoma cell lines MG-6 and U-2 (Figure 6(b)). We found that inhibition of GALNT14 improved sensitivity to the chemotherapeutics cisplatin and doxorubicin in MG-6 and U-2 cell lines by detecting cell proliferation with CCK-8 (Figure 6(c)), and consistent trends were also observed in the clonogenic assay (Figure 6(d)). In addition, as shown in Figure 7, flow cytometry revealed that inhibition of GALNT14 resulted in an increased rate of apoptosis after cisplatin or doxorubicin treatment.

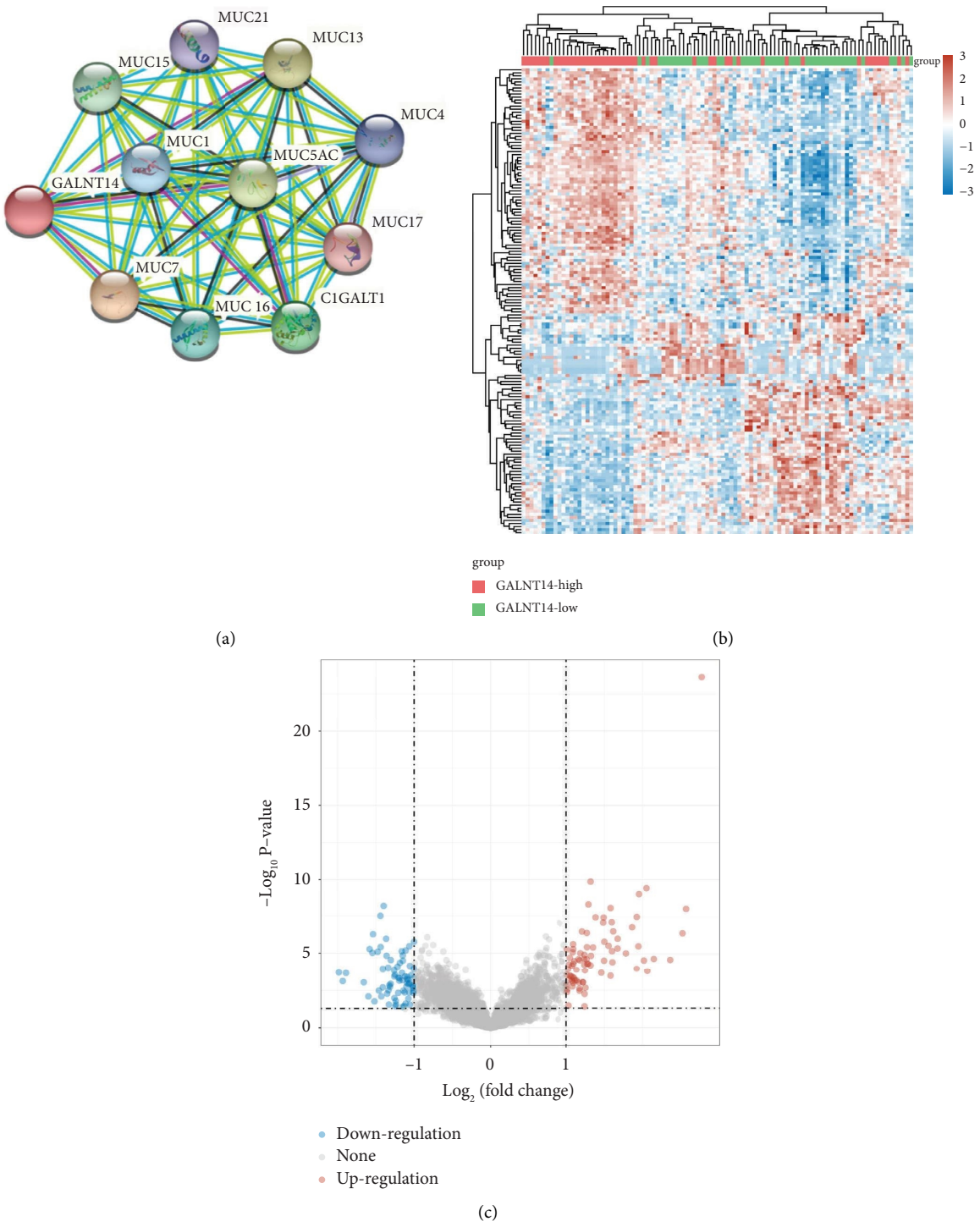

Figure 2: GALNT14 PPI network and coexpression genes in osteosarcoma. (a) PPI network of GALNT14. Differentially expressed genes associated with GALNT14 level showing in heatmap (b) and volcano plot (c).

4. Discussion

The association between GALNT14 expression and cancer characteristics has been studied in multiple tumors. For example, GALNT14 was found to be overexpressed in most breast cancer tissues and associated with lung metastasis [16, 17]. Overexpression of GALNT14 was also found in ovarian cancer [15, 18]. In summary, previous reports have suggested abnormal expression of GALNT14 in cancer and metastatic tissues. Our study revealed for the first time the expression of GALNT14 in osteosarcoma. Consistently, increased expression of GALNT14 was identified in osteosarcoma. GALNT14 expression was also elevated in metastatic osteosarcoma compared to the nonmetastatic stage.

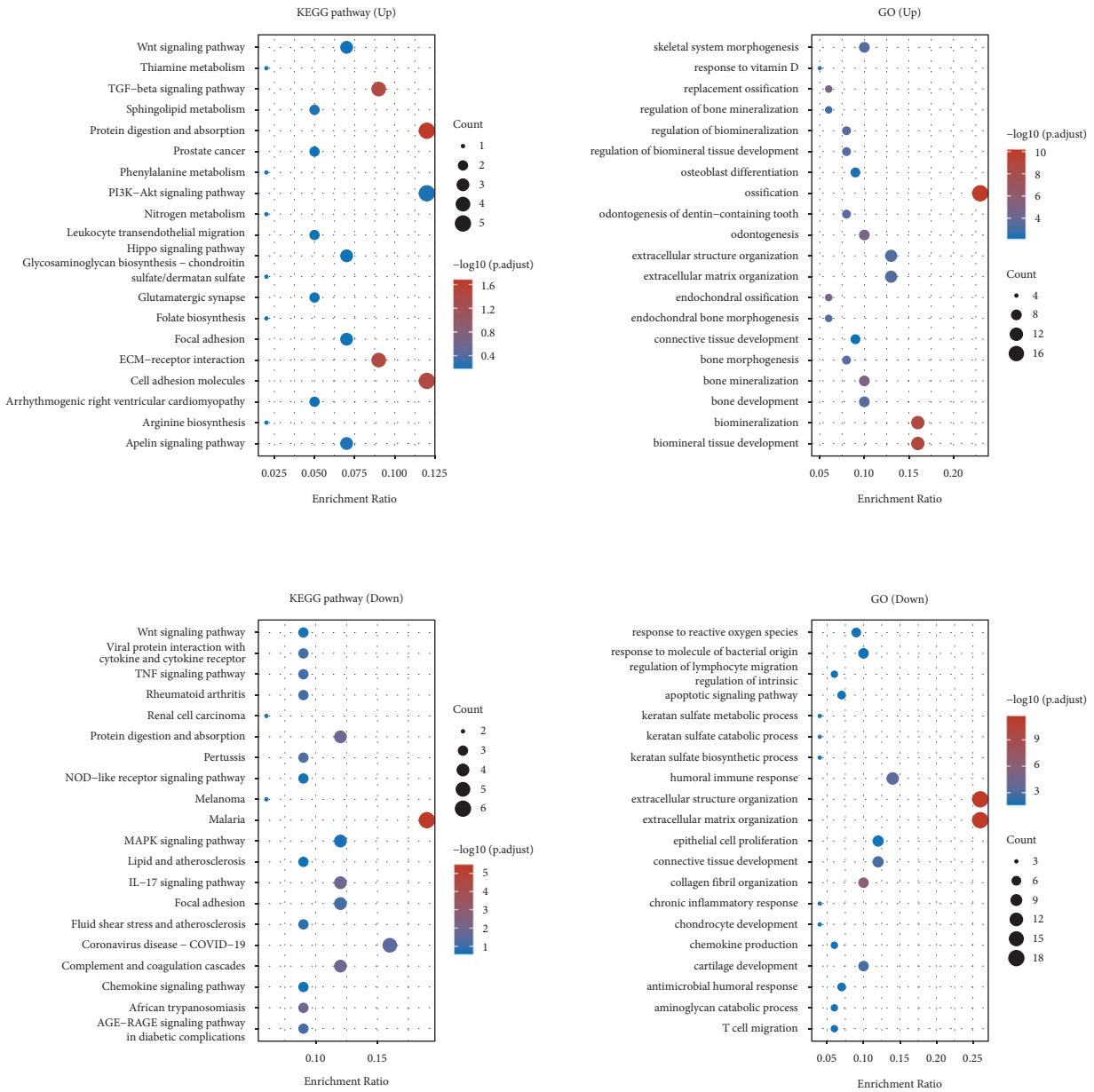

Figure 3: GO and KEGG enrichment analysis of genes associated with GALNT14 levels in osteosarcoma.

Our results support the potential application of GALNT14 as a predictive biomarker for the diagnosis and metastasis of osteosarcoma.

Previous studies have suggested the significance of GALNT14 for the metastasis of a wide variety of cancers [19–21]. In this study, in addition to aberrant expression in metastatic osteosarcoma, GALNT14 was also found to interact with mucins (except for C1GALT1) by PPI analysis. Altered mucin glycosylation patterns during malignant transformation have been considered to promote cancer cell differentiation, proliferation, invasion, and metastasis [22]. Additionally, we observed that multiple cancer-related pathways were enriched through functional enrichment analysis of genes associated with GALNT14 levels, such as the Wnt, TGF-β, Hippo, and PI3K signaling pathways. The Wnt signaling pathway is one of the key cascades regulating development and has also been tightly associated with osteosarcoma [23]. TGF-βs have been considered to exhibit protumoral and promigratory effects on osteosarcoma [24]. The Hippo signaling pathway shows a close relationship with osteosarcoma and is a potential therapeutic target in the future [25]. These results reveal the underlying mechanism by which GALNT14 promotes tumorigenesis and metastasis in osteosarcoma.

The elimination of superfluous and damaged cells is achieved by the vital process of cell death. Apoptosis, necroptosis, and ferroptosis are a few examples of programmed and nonprogrammed cell death that have been uncovered in previous research [26]. Recently, abnormal copper ion elevations have been linked to a previously

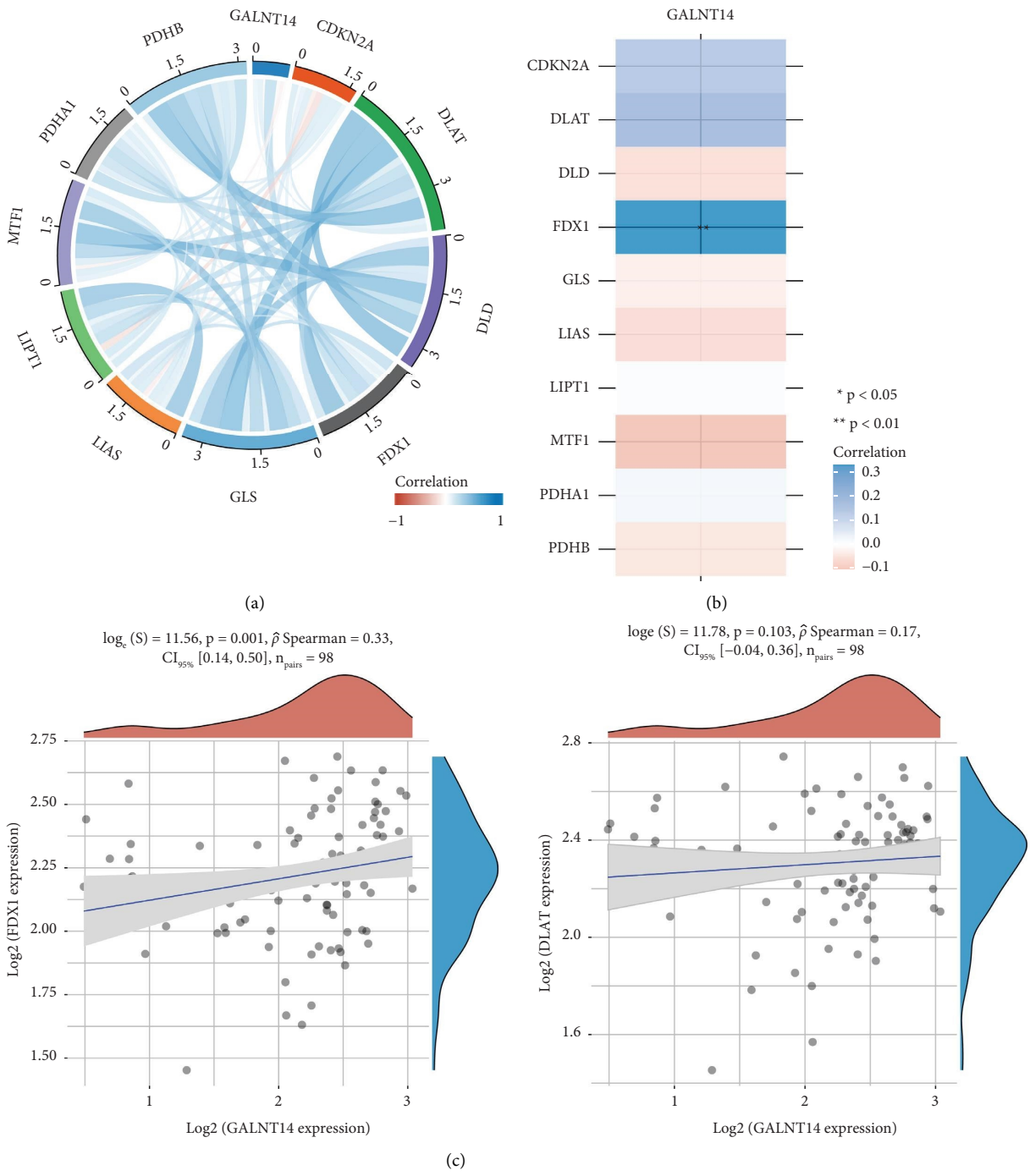

Figure 4: Correlation between GALNT14 and cuproptosis-related genes in osteosarcoma. (a) The correlation of expression of GALNT14 and 10 cuproptosis-related genes. (b) The correlation between GALNT14 and cuproptosis-related genes in osteosarcoma. (c) The correlation between GALNT14, FDX1, and DLAT in osteosarcoma.

unidentified death pathway called cuproptosis [27]. Therefore, significant interest has developed in the association of cuproptosis-related genes with osteosarcoma. Our results showed that the expression of multiple cuproptosis-related genes was closely correlated with osteosarcoma. In addition, GALNT14 is also closely associated with the expression of FDX1, a key gene in cuproptosis. In summary, our results suggest a possible novel mechanism of GALNT14 involvement in osteosarcoma cell proliferation and death.

Prognostic significance is currently a hot topic in oncology research. Multiple genes have been determined to be associated with the prognosis of osteosarcoma, and some prognostic models have been established [28, 29]. However, the prognostic significance of GALNT14 in osteosarcoma remains unknown. Previous studies have reported an association between GALNT14 and the prognosis of a variety of cancers, including gastric cancer, cholangiocarcinoma, ovarian cancer, and breast cancer [18, 21, 30, 31]. Our

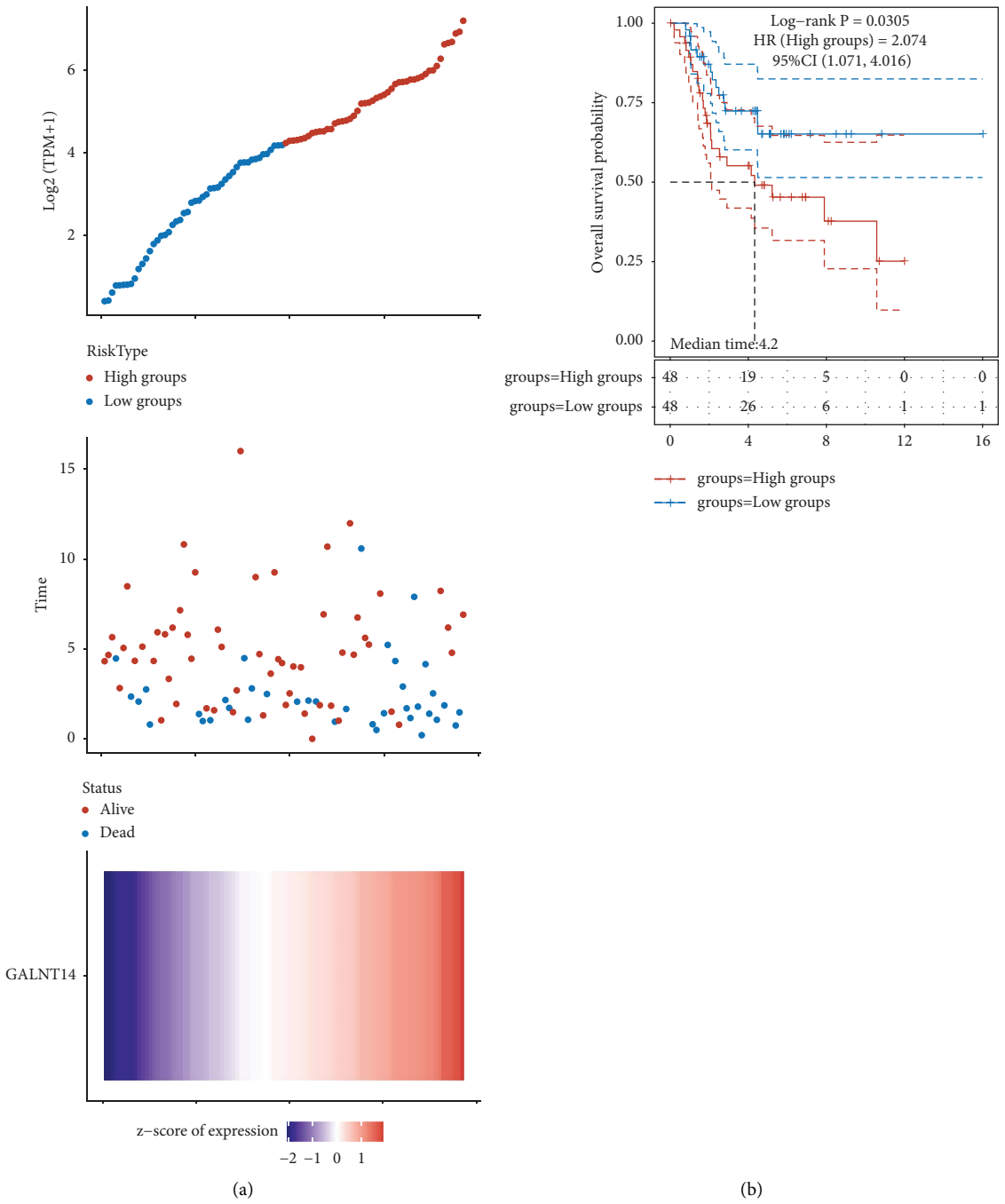

Figure 5: Continued.

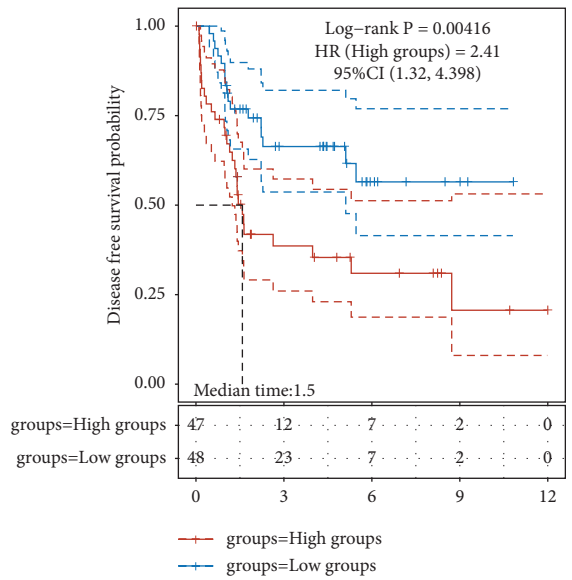

(c)

Figure 5: The OS significance of GALNT14 in osteosarcoma. (a) The gene expression, survival time, and OS survival status of the TARGET dataset. The top scatterplot represents gene expression from low to high. The scatter plot distribution represents the gene expression of different samples corresponding to the survival time and survival status. The bottom figure is the gene expression heatmap. (b) OS Kaplan–Meier survival analysis. (c) DFS Kaplan–Meier survival analysis. OS, overall survival; DFS, disease-free survival.

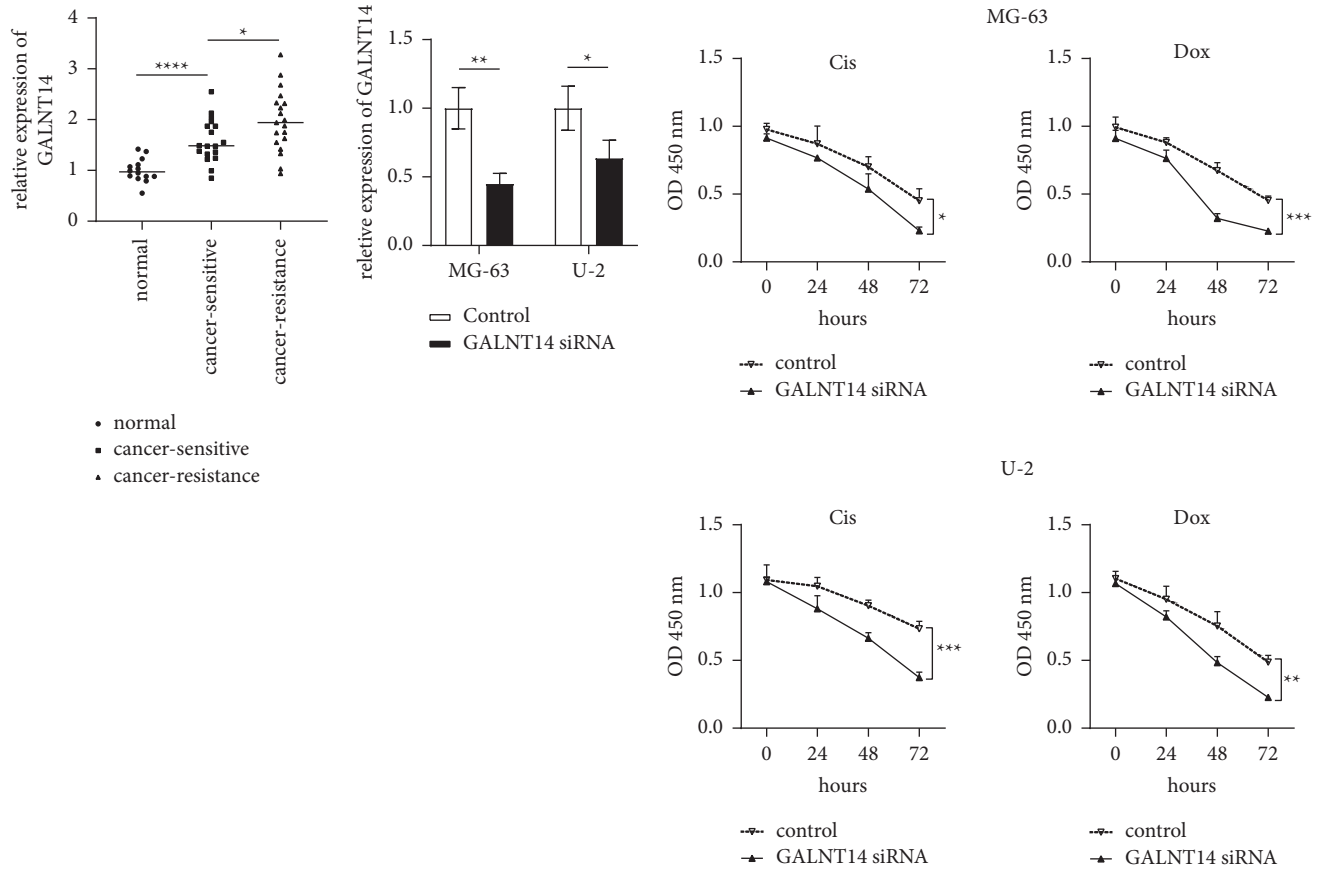

(a) (b) (c)

Figure 6: Continued.

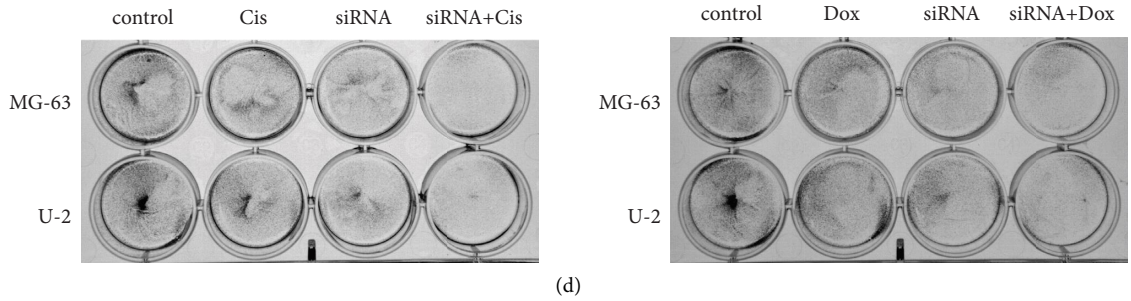

Figure 6: Interfering with GALNT14 expression promoted the inhibitory effect of cisplatin and doxorubicin on the proliferation of osteosarcoma cell lines. (a) The expression of GALNT14 in normal human osteoblasts, drug-sensitive osteosarcoma, and drug-resistant osteosarcoma. (b) GALNT14 siRNA transfection in osteosarcoma cell lines MG-63 and U-2. (c) MG-63 and U-2 OS cells were treated with Cis (20 μmol/L) or Dox (0.2 μg/mL) for 24 h. Then, cell viability was determined at 24 h, 48 h, and 72 h by the CCK-8 assay. (d) MG-63 or U-2 OS cells were seeded in six-well plates and treated with Cis (5 μmol/L) and Dox (0.05 μg/mL). The plates were imaged at 14 days to assess clones. Cis, cisplatin; Dox, doxorubicin. $^{*}p < 0.05$, $^{**}p < 0.01$, $^{***}p < 0.001$, $^{****}p < 0.0001$.

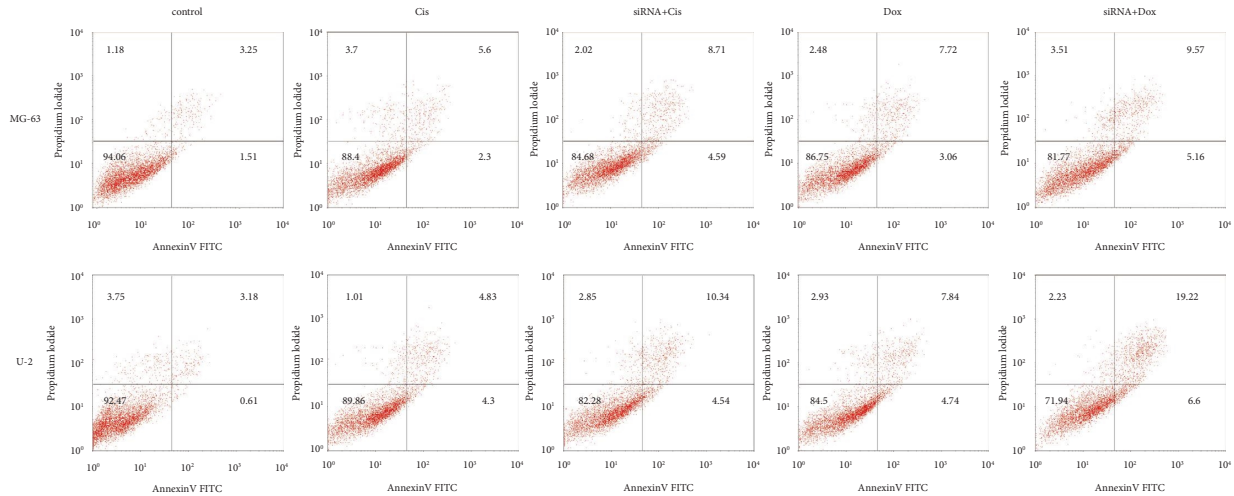

Figure 7: Interfering with GALNT14 expression promotes the apoptotic effect of cisplatin and doxorubicin on osteosarcoma cell lines. MG-63 and U-2 OS cells were treated with Cis (20 μmol/L) or Dox (0.2 μg/mL) for 24 h. Then, apoptosis was determined by flow cytometry. Cis, cisplatin; Dox, doxorubicin.

research revealed a strong correlation between high GALNT14 expression and poor OS and DFS in osteosarcoma. This finding indicates the potential of GALNT14 as a prognostic biomarker for osteosarcoma.

Through an extensive repertoire of resistance mechanisms, tumors elude targeted cancer therapy. This is also one of the main reasons for the poor prognosis of tumors. Osteosarcoma is a kind of disease that is particularly resistant to chemotherapy. This disease, according to clinical trials, only responds to high doses of chemotherapy and rapidly acquires resistance [32, 33]. Chemotherapy resistance in osteosarcoma potentially correlates to drug build-up in the cell, DNA damage repair, intracellular detoxification, signal transduction, apoptosis, the tumor microenvironment, and immunity [34]. GALNT14 serves as an emerging marker for predicting therapeutic outcomes in multiple tumors [9], and it has also been identified to be related to paclitaxel resistance in lung adenocarcinoma [35]. Here, we reveal for the first time the significance of GALNT14 in the chemosensitivity of osteosarcoma.

There are some limitations to this study. For example, the molecular interaction of GALNT14 and the mechanism of GALNT14 on drug sensitivity need further experimental verification. In conclusion, we identified a GALNT family gene, GALNT14, that was highly expressed in osteosarcoma. GALNT14 was closely associated with metastasis, progression, cuproptosis-related genes, and the chemosensitivity of osteosarcoma. Finally, the poor prognostic significance of GALNT14 in osteosarcoma was also elucidated. This discovery is anticipated to offer fresh perspectives on osteosarcoma diagnosis and therapy.

Data Availability

The data used to support the findings of this study are included within the article.

Conflicts of Interest

The authors declare that they have no conflicts of interest.

Acknowledgments

This study was supported by the Natural Science Foundation of Hunan Province (Grant number: 2021JJ31017).

Supplementary Materials

Supplementary Figure 1: the gene expression, survival time, and DFS survival status of the TARGET dataset. The top scatterplot represents gene expression from low to high. The scatter plot distribution represents the gene expression of different samples corresponding to the survival time and survival status. The bottom figure is the gene expression heatmap. Supplementary Table 1: p values of GALNT14 expression in pan-cancer analysis. Supplementary Table 2: the expression levels of cuproptosis-related genes were strongly correlated in osteosarcoma. (*Supplementary Materials*)

References

[1] L. Mirabello, R. J. Troisi, and S. A. Savage, "Osteosarcoma incidence and survival rates from 1973 to 2004: data from the surveillance, epidemiology, and end results program," *Cancer*, vol. 115, no. 7, pp. 1531–1543, 2009.

[2] S. S. Bielack, B. Kempf-Bielack, G. Delling et al., "Prognostic factors in high-grade osteosarcoma of the extremities or trunk: an analysis of 1, 702 patients treated on neoadjuvant cooperative osteosarcoma study group protocols," *Journal of Clinical Oncology*, vol. 20, no. 3, pp. 776–790, 2002.

[3] S. Valastyan and R. A. Weinberg, "Tumor metastasis: molecular insights and evolving paradigms," *Cell*, vol. 147, no. 2, pp. 275–292, 2011.

[4] A. F. Chambers, A. C. Groom, and I. C. MacDonald, "Dissemination and growth of cancer cells in metastatic sites," *Nature Reviews Cancer*, vol. 2, no. 8, pp. 563–572, 2002.

[5] E. P. Bennett, U. Mandel, H. Clausen, T. A Gerken, T. A Fritz, and L. A Tabak, "Control of mucin-type O-glycosylation: a classification of the polypeptide GalNAc-transferase gene family," *Glycobiology*, vol. 22, no. 6, pp. 736–756, 2012.

[6] K. G. Ten Hagen, T. A. Fritz, and L. A. Tabak, "All in the family: the UDP-GalNAc:polypeptide N-acetylgalactosaminyltransferases," *Glycobiology*, vol. 13, no. 1, pp. 1R–16R, 2003.

[7] E. M. Beaman and S. A. Brooks, "The extended ppGalNAc-T family and their functional involvement in the metastatic cascade," *Histology & Histopathology*, vol. 29, no. 3, pp. 293–304, 2014.

[8] H. Wang, K. Tachibana, Y. Zhang et al., "Cloning and characterization of a novel UDP-GalNAc:polypeptide N-acetylgalactosaminyltransferase, pp-GalNAc-T14," *Biochemical and Biophysical Research Communications*, vol. 300, no. 3, pp. 738–744, 2003.

[9] W. R. Lin and C. T. Yeh, "GALNT14: an emerging marker capable of predicting therapeutic outcomes in multiple cancers," *International Journal of Molecular Sciences*, vol. 21, no. 4, p. 1491, 2020.

[10] S. Davis and P. S. Meltzer, "GEOquery: a bridge between the gene expression Omnibus (GEO) and BioConductor," *Bioinformatics*, vol. 23, no. 14, pp. 1846-1847, 2007.

[11] T. Li, J. Fan, B. Wang et al., "TIMER: a web server for comprehensive analysis of tumor-infiltrating immune cells," *Cancer Research*, vol. 77, no. 21, pp. e108–e110, 2017.

[12] D. Szklarczyk, A. L. Gable, D. Lyon et al., "STRING v11: protein-protein association networks with increased coverage, supporting functional discovery in genome-wide experimental datasets," *Nucleic Acids Research*, vol. 47, no. D1, pp. D607–D613, 2019.

[13] M. E. Ritchie, B. Phipson, D. Wu et al., "Limma powers differential expression analyses for RNA-sequencing and microarray studies," *Nucleic Acids Research*, vol. 43, no. 7, p. e47, 2015.

[14] Z. Bian, R. Fan, and L. Xie, "A novel cuproptosis-related prognostic gene signature and validation of differential expression in clear cell renal cell carcinoma," *Genes*, vol. 13, no. 5, p. 851, 2022.

[15] R. Wang, C. Yu, D. Zhao, M. Wu, and Z. Yang, "The mucin-type glycosylating enzyme polypeptide N-acetylgalactosaminyltransferase 14 promotes the migration of ovarian cancer by modifying mucin 13," *Oncology Reports*, vol. 30, no. 2, pp. 667–676, 2013.

[16] K. H. Song, M. S. Park, T. S. Nandu, S. Gadad, S. C. Kim, and M. Y. Kim, "GALNT14 promotes lung-specific breast cancer metastasis by modulating self-renewal and interaction with the lung microenvironment," *Nature Communications*, vol. 7, no. 1, Article ID 13796, 2016.

[17] C. Wu, X. Guo, W. Wang et al., "N-Acetylgalactosaminyl-transferase-14 as a potential biomarker for breast cancer by immunohistochemistry," *BMC Cancer*, vol. 10, no. 1, p. 123, 2010.

[18] R. Sheta, M. Bachvarova, M. Plante et al., "Altered expression of different GalNActransferases is associated with disease progression and poor prognosis in women with high-grade serous ovarian cancer," *International Journal of Oncology*, vol. 51, no. 6, pp. 1887–1897, 2017.

[19] M. Y. Kim, "Role of GALNT14 in lung metastasis of breast cancer," *BMB Reports*, vol. 50, no. 5, pp. 233-234, 2017.

[20] O. S. Kwon, H. Lee, H. J. Kong et al., "Correction to: connectivity map-based drug repositioning of bortezomib to reverse the metastatic effect of GALNT14 in lung cancer," *Oncogene*, vol. 40, no. 10, p. 1921, 2021.

[21] K. H. Liang, T. S. Yeh, R. C. Wu, C. N. Yeh, and C. T. Yeh, "GALNT14 genotype is associated with perineural invasion, lymph node metastasis and overall survival in resected cholangiocarcinoma," *Oncology Letters*, vol. 13, no. 6, pp. 4215–4223, 2017.

[22] R. Bhatia, S. K. Gautam, A. Cannon et al., "Cancer-associated mucins: role in immune modulation and metastasis," *Cancer and Metastasis Reviews*, vol. 38, no. 1-2, pp. 223–236, 2019.

[23] K. Matsuoka, L. Bakiri, L. I. Wolff et al., "Wnt signaling and Loxl2 promote aggressive osteosarcoma," *Cell Research*, vol. 30, no. 10, pp. 885–901, 2020.

[24] A. Lamora, J. Talbot, M. Mullard, B. Brounais-Le Royer, F. Redini, and F. Verrecchia, "TGF-Beta signaling in bone remodeling and osteosarcoma progression," *Journal of Clinical Medicine*, vol. 5, no. 11, p. 96, 2016.

[25] E. Rothzerg, E. Ingley, B. Mullin, W. Xue, D. Wood, and J. Xu, "The Hippo in the room: targeting the Hippo signalling pathway for osteosarcoma therapies," *Journal of Cellular Physiology*, vol. 236, no. 3, pp. 1606–1615, 2021.

[26] P. Lei, T. Bai, and Y. Sun, "Mechanisms of ferroptosis and relations with regulated cell death: a review," *Frontiers in Physiology*, vol. 10, p. 139, 2019.

[27] P. Tsvetkov, S. Coy, B. Petrova et al., "Copper induces cell death by targeting lipoylated TCA cycle proteins," *Science*, vol. 375, no. 6586, pp. 1254–1261, 2022.

[28] S. Bakhshi and V. Radhakrishnan, "Prognostic markers in osteosarcoma," *Expert Review of Anticancer Therapy*, vol. 10, no. 2, pp. 271–287, 2010.

[29] G. Wu and M. Zhang, "A novel risk score model based on eight genes and a nomogram for predicting overall survival of patients with osteosarcoma," *BMC Cancer*, vol. 20, no. 1, p. 456, 2020.

[30] T. H. Chen, W. R. Lin, C. Lee et al., "Prognostic stratification of advanced gastric signet ring cell carcinoma by clinico-pathological factors and GALNT14 genotype," *Journal of Cancer*, vol. 9, no. 19, pp. 3540–3547, 2018.

[31] K. Milde-Langosch, D. Schutze, L. Oliveira-Ferrer et al., "Relevance of βGal–βGalNAc-containing glycans and the enzymes involved in their synthesis for invasion and survival in breast cancer patients," *Breast Cancer Research and Treatment*, vol. 151, no. 3, pp. 515–528, 2015.

[32] C. M. Hattinger, M. Fanelli, E. Tavanti et al., "Advances in emerging drugs for osteosarcoma," *Expert Opinion on Emerging Drugs*, vol. 20, no. 3, pp. 495–514, 2015.

[33] X. Yang, P. Yang, J. Shen et al., "Prevention of multidrug resistance (MDR) in osteosarcoma by NSC23925," *British Journal of Cancer*, vol. 110, no. 12, pp. 2896–2904, 2014.

[34] I. Lilienthal and N. Herold, "Targeting molecular mechanisms underlying treatment efficacy and resistance in osteosarcoma: a review of current and future strategies," *International Journal of Molecular Sciences*, vol. 21, no. 18, p. 6885, 2020.

[35] J. Pu, J. Shen, Z. Zhong, M. Yanling, and J. Gao, "KANK1 regulates paclitaxel resistance in lung adenocarcinoma A549 cells," *Artificial Cells, Nanomedicine, and Biotechnology*, vol. 48, no. 1, pp. 639–647, 2020.

Hindawi
Journal of Oncology
Volume 2023, Article ID 9815674, 1 page
https://doi.org/10.1155/2023/9815674

Retraction

Retracted: Screening of Key Prognosis Genes of Lung Adenocarcinoma Based on Expression Analysis on TCGA Database

Journal of Oncology

Received 11 July 2023; Accepted 11 July 2023; Published 12 July 2023

This article has been retracted by Hindawi following an investigation undertaken by the publisher [1]. This investigation has uncovered evidence of one or more of the following indicators of systematic manipulation of the publication process:

(1) Discrepancies in scope
(2) Discrepancies in the description of the research reported
(3) Discrepancies between the availability of data and the research described
(4) Inappropriate citations
(5) Incoherent, meaningless and/or irrelevant content included in the article
(6) Peer-review manipulation

The presence of these indicators undermines our confidence in the integrity of the article's content and we cannot, therefore, vouch for its reliability. Please note that this notice is intended solely to alert readers that the content of this article is unreliable. We have not investigated whether authors were aware of or involved in the systematic manipulation of the publication process.

Wiley and Hindawi regrets that the usual quality checks did not identify these issues before publication and have since put additional measures in place to safeguard research integrity.

We wish to credit our own Research Integrity and Research Publishing teams and anonymous and named external researchers and research integrity experts for contributing to this investigation.

The corresponding author, as the representative of all authors, has been given the opportunity to register their agreement or disagreement to this retraction. We have kept a record of any response received.

References

[1] Y. Shen, X. Tang, X. Zhou et al., "Screening of Key Prognosis Genes of Lung Adenocarcinoma Based on Expression Analysis on TCGA Database," *Journal of Oncology*, vol. 2022, Article ID 4435092, 13 pages, 2022.

Hindawi
Journal of Oncology
Volume 2022, Article ID 4435092, 13 pages
https://doi.org/10.1155/2022/4435092

Research Article

Screening of Key Prognosis Genes of Lung Adenocarcinoma Based on Expression Analysis on TCGA Database

Youfeng Shen,[1] Xiaoqing Tang,[2] Xiaoqin Zhou,[2] Yuanxue Yi,[1] Yuan Qiu,[3] Jian Xu,[1,4] and Xingzhong Tian[5]

[1]*Chongqing Precision Medical Industry Technology Research Institute, Chongqing 400000, China*
[2]*Department of Laboratory Medicine, Nanan People's Hospital, Chongqing 400060, China*
[3]*Department of Laboratory Medicine, Kaizhou District People's Hospital, Chongqing 405400, China*
[4]*College of Laboratory Medicine, Chongqing Medical University, Chongqing 400000, China*
[5]*The Fifth Hospital of Zhangjiakou, China*

Correspondence should be addressed to Jian Xu; jimxj@foxmail.com and Xingzhong Tian; 402809170@qq.com

Received 29 July 2022; Revised 3 September 2022; Accepted 16 September 2022; Published 26 December 2022

Academic Editor: Muhammad Muddassir Ali

Objective. The data of lung adenocarcinoma- (LUAD-) related gene expression profiles were mined from the Cancer Genome Atlas (TCGA) database using bioinformatics methods and potential biomarkers related to the occurrence, development, and prognosis of LUAD were screened out to explore the key prognostic genes and clinical significance. *Methods*. Following the LUAD gene expression profile data that were initially exported from the TCGA database, R software DESeq2 was employed to analyze the difference between the expression profiles of LUAD and normal tissues. The R package "clusterProfiler" was subsequently utilized to perform gene ontology (GO) and Kyoto Encyclopedia of Genes and Genomes (KEGG) pathway analyses of the differential genes. A protein-protein interaction (PPI) network was constructed via the String database, and cytohubba, a plugin of Cytoscape, was applied to screen hub genes using the MCC algorithm. The Gene Expression Profile Data Interactive Analysis (GEPIA) was used to analyze expressions of 10 candidate genes in LUAD samples and healthy lung samples, and the selected genes were employed for survival analysis. *Results*. A total of 1,598 differential genes were identified through differential analyses and data mining, with 1,394 genes upregulated and 204 downregulated. A total of 10 hub genes CCNA2, CDC20, CCNB2, KIF11, TOP2A, BUB1, BUB1B, CENPF, TPX2, and KIF2C were obtained using the cytohubba plugin. The results of the GEPIA analysis indicated that compared with normal lung tissue, the mRNA expression level of the described hub genes in LUAD tissue was significantly increased ($P < 0.05$). Survival analysis revealed that these genes had a significant impact on the overall survival time of LUAD patients ($P < 0.05$). *Conclusion*. The previously described key genes related to LUAD identified in the TCGA database may be used as potential prognostic biomarkers, which will contribute to further comprehension of the occurrence and development of LUAD and provide references for its diagnosis and treatment.

1. Introduction

Lung cancer has become the most common malignant tumor worldwide and the leading cause of cancer-related death, which is usually closely associated with a poor prognosis. According to the latest report of the Global Cancer Statistics Center, lung cancer has the highest incidence and mortality among all male patients with malignant tumors, while the incidence of lung cancer in female patients is lower than that of breast cancer and colon cancer, and the mortality rate is second only to that of breast cancer [1]. Lung adenocarcinoma (LUAD) is the most common pathological type of non-small-cell lung cancer, accounting for 85% of the incidence of lung cancer [2, 3]. In recent years, it has been characterized by rapid onset, younger age, high mortality, and poor prognosis. Therefore, it is increasingly

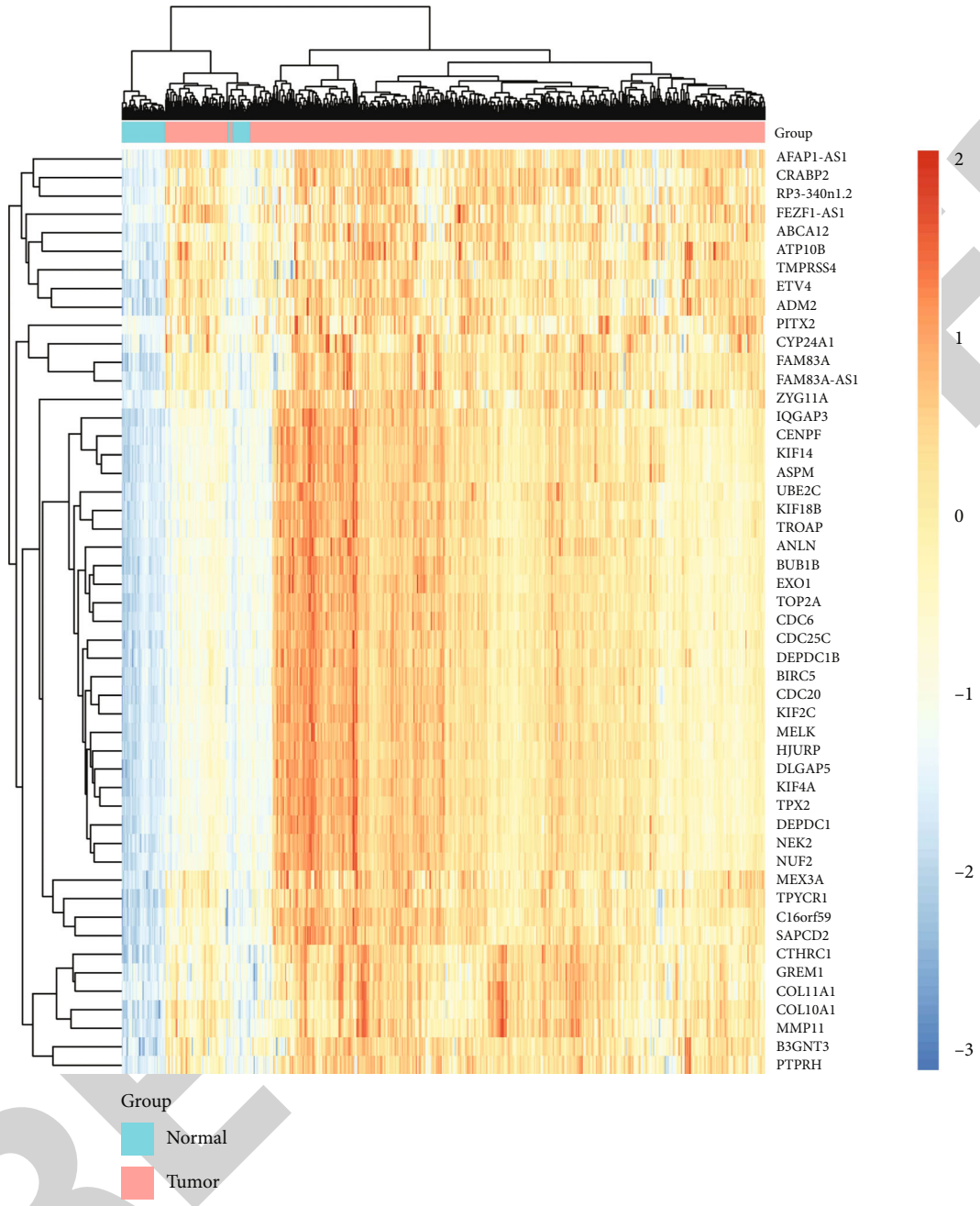

(a)

Figure 1: Continued.

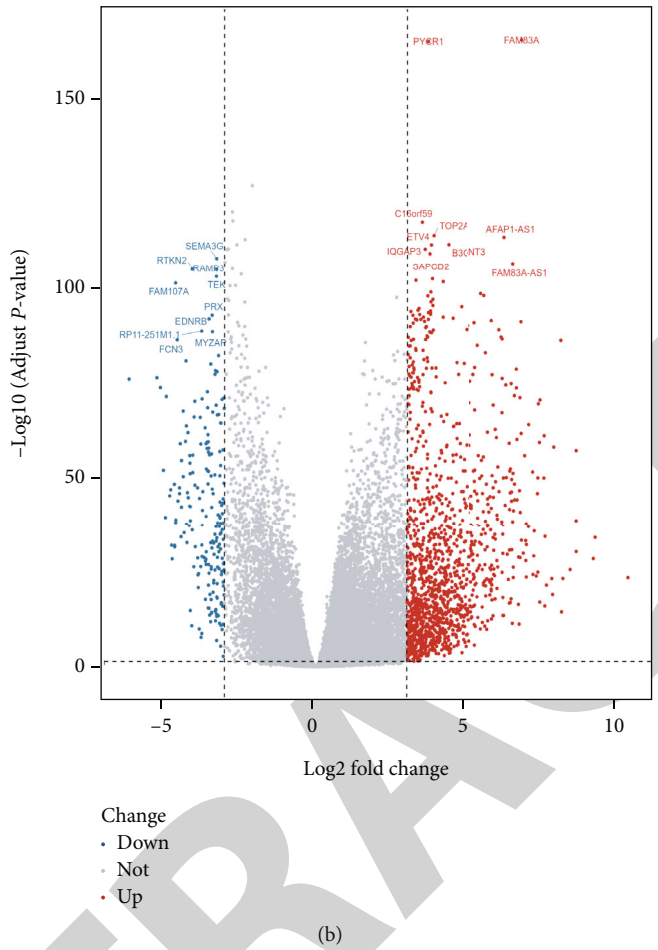

(b)

Figure 1: Heat map and volcano map of differentially expressed genes. (a) Heat map of the top 50 genes with the most significant differences. (b) Volcano map of differential genes (red dots: significantly upregulated genes, blue dots: significantly downregulated genes, gray dots: genes with no significant differences).

important to explore new prognostic genes for LUAD in the era of precision medicine.

The Cancer Genome Atlas (TCGA) is currently the largest tumor gene expression profile database in the world, including clinical sample data and genomic data of a variety of tumors, which promotes the discovery of de novo markers [4]. Based on TCGA studies, it was found that ZNF695 may be indirectly associated with proliferation in lung cancer. In LUAD, ZNF695 expression was significantly higher in bronchial and magnolia mRNA isoforms, exhibiting overrepresentation of growth and proliferation pathways, respectively [5]. RRM2 is upregulated in LUAD, and high RRM2 expression is associated with clinical progression and is considered an independent risk factor for OS in LUAD patients [6].

In this study, based on the TCGA database, the bioinformatics method was applied to screen and integrate the expression profile data of LUAD, analyze and find differential genes, and perform functional enrichment analysis, PPI network construction, key gene screening, survival analysis, etc. This provides a theoretical basis for further screening of prognostic genes in LUAD.

2. Material and Methods

2.1. Data Acquisition. "Lung cancer" was used as the keyword to search in TCGA (https://portal.gdc.cancer.gov/) database, and the data category was selected as "transcriptome profiling". Publicly available genomic data on LUAD were downloaded, including 551 samples, of which 497 were LUAD-associated and 54 were normal samples. The clinical information of 486 cases including gender, survival status, survival time, race, and pathological stage were obtained for subsequent analysis.

2.2. Method

2.2.1. Data Processing and Screening of Differentially Expressed Genes. After removing the repeated genes in the downloaded original data and the genes with 0 expressions in the multiple copies, differential analysis and screening of differentially expressed genes were undertaken using the R software package DESeq2. The selection criteria are as follows: $|\log 2(\text{FoldChange})| > 3$ and correct after P values (false discovery rate, FDR) <0.05. The top

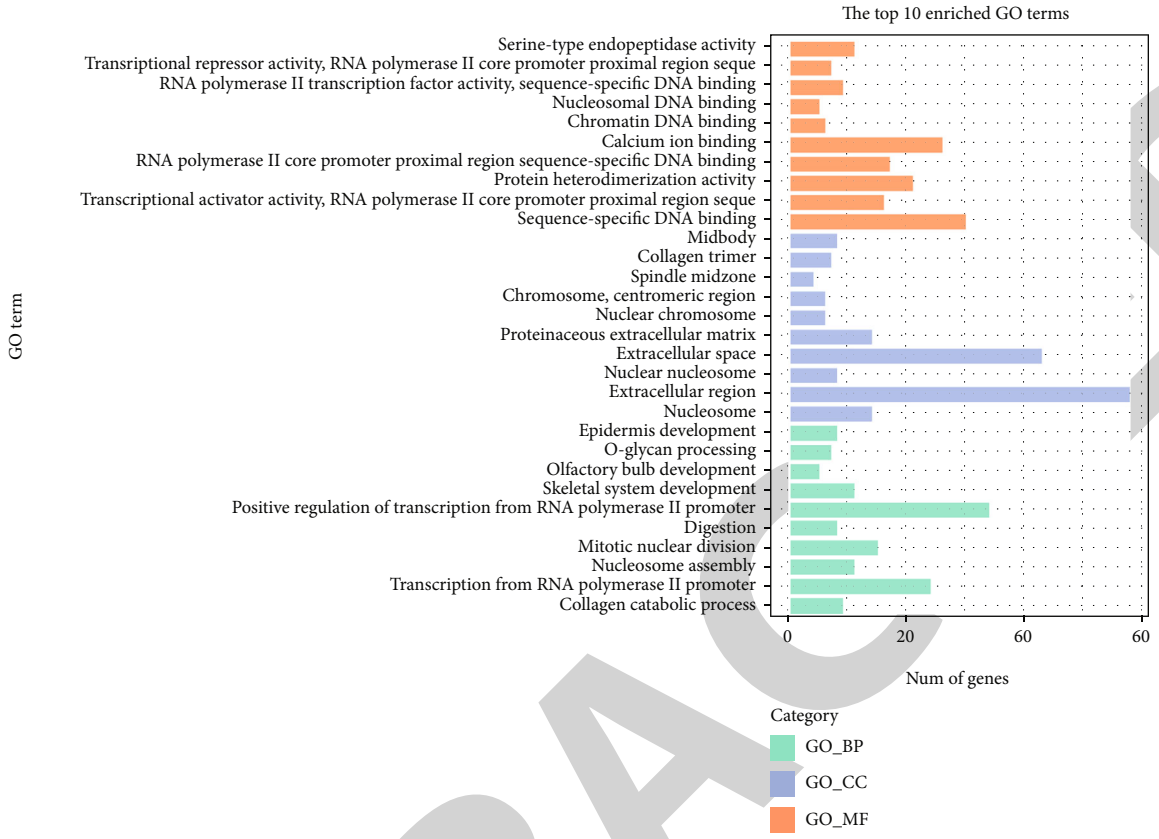

(a)

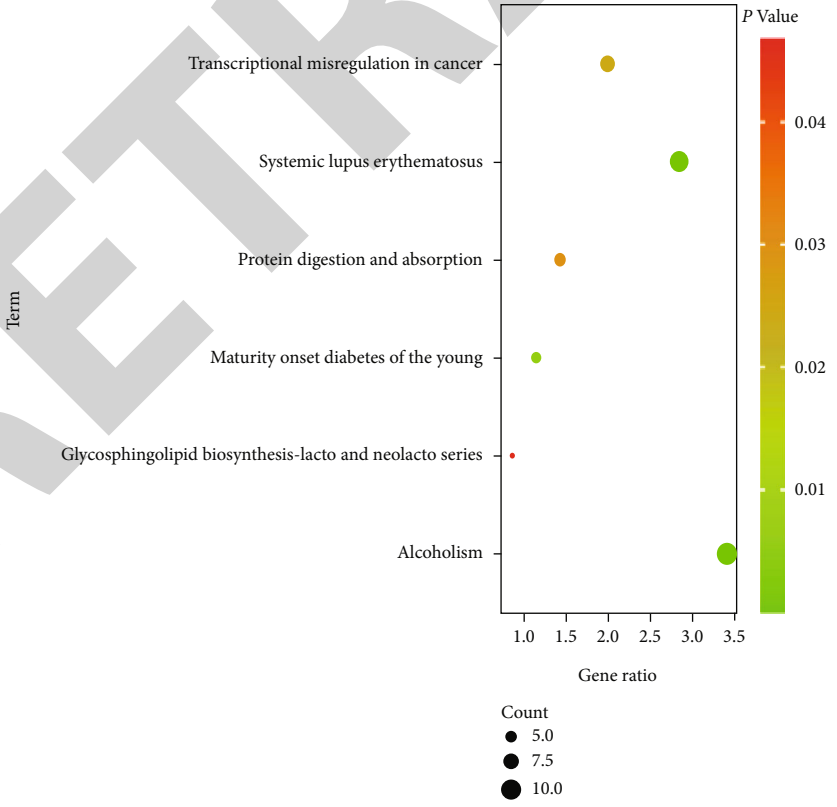

(b)

Figure 2: Continued.

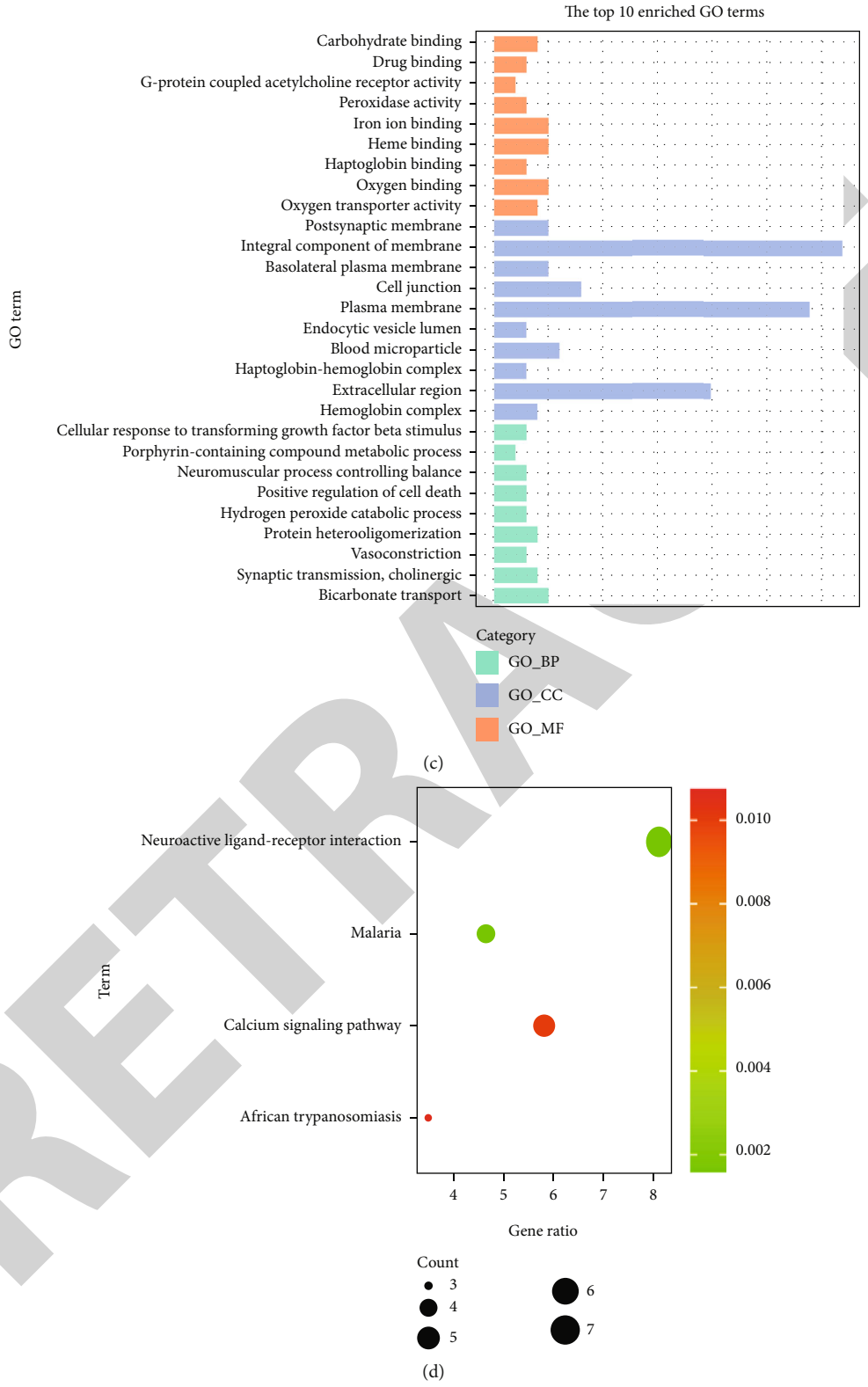

Figure 2: GO and KEGG enrichment analysis of differential genes. (a) GO enrichment analysis of 1394 upregulated genes. (b) KEGG enrichment analysis of 1394 upregulated genes. (c) GO enrichment analysis of 204 downregulated genes. (d) KEGG enrichment analysis of 204 downregulated genes.

50 cluster heat map of differential genes between normal samples and tumor samples was drawn using the R software package PheATMap. The R package GGPubR and GGThemes were used to draw the volcano map to observe the relationship between differential change times and FDR.

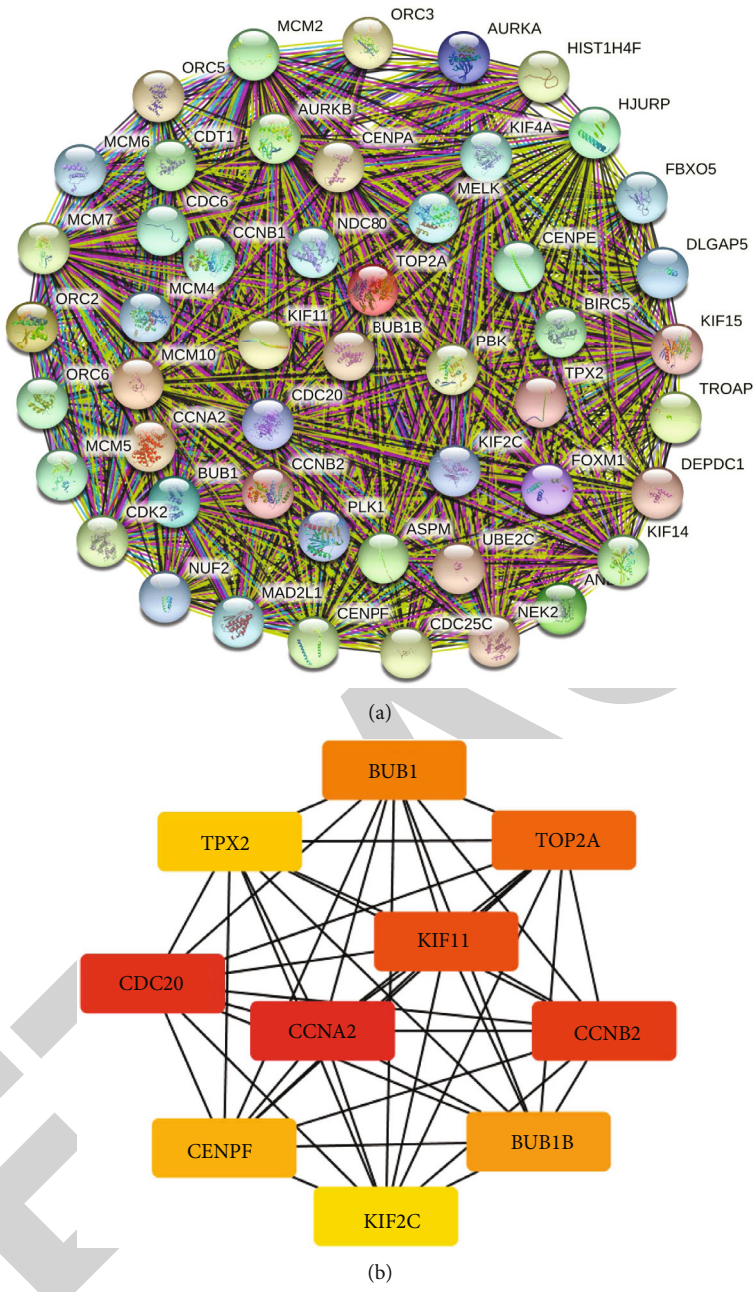

Figure 3: Screening of top 10 hub genes based on PPI network. (a) Top 50 gene-protein interaction network diagram. (b) MCC algorithm was used to screen the top 10 central genes.

2.2.2. GO and KEGG Enrichment Analysis of Differential Genes. Based on the R4.1.1 environment, four R packages (clusterProfiler, Stringr, org.hs.eg.db, and ggploT2) were performed using gene function analysis, including Biological process (BP), Cellular components (CC) and Molecular function (MF), and pathway analysis based on KEGG. The screening criterion is as follows: FDR < 0.05. The top 10 results of significantly enriched BP, CC, MF, and KEGG pathways were selected and graphed.

2.2.3. Protein Interaction Network Construction and Hub Gene Screening. The STRING Database (https://string-db.org/) is an online analytical tool for identifying known proteins or predicting protein-protein interactions. The selected differential genes were imported into the database for protein-protein interaction (PPI) analysis, and the confidence score threshold was set to 0.9. The PPI network results were then imported into Cytoscape 3.6.1 in TSV format for visualization. The top 10 genes were screened from the PPI network as hub genes using the MCC method in the Cytohubba plugin of Cytoscape.

2.2.4. Expression of 10 Hub Genes in LUAD. Using GEPIA (http://gepia.cancer-pku.cn/index.html) online analysis website ("Datasets" select "LUAD", "Matched normal data" select "TCGA normal and the Genotype-Tissue Expression

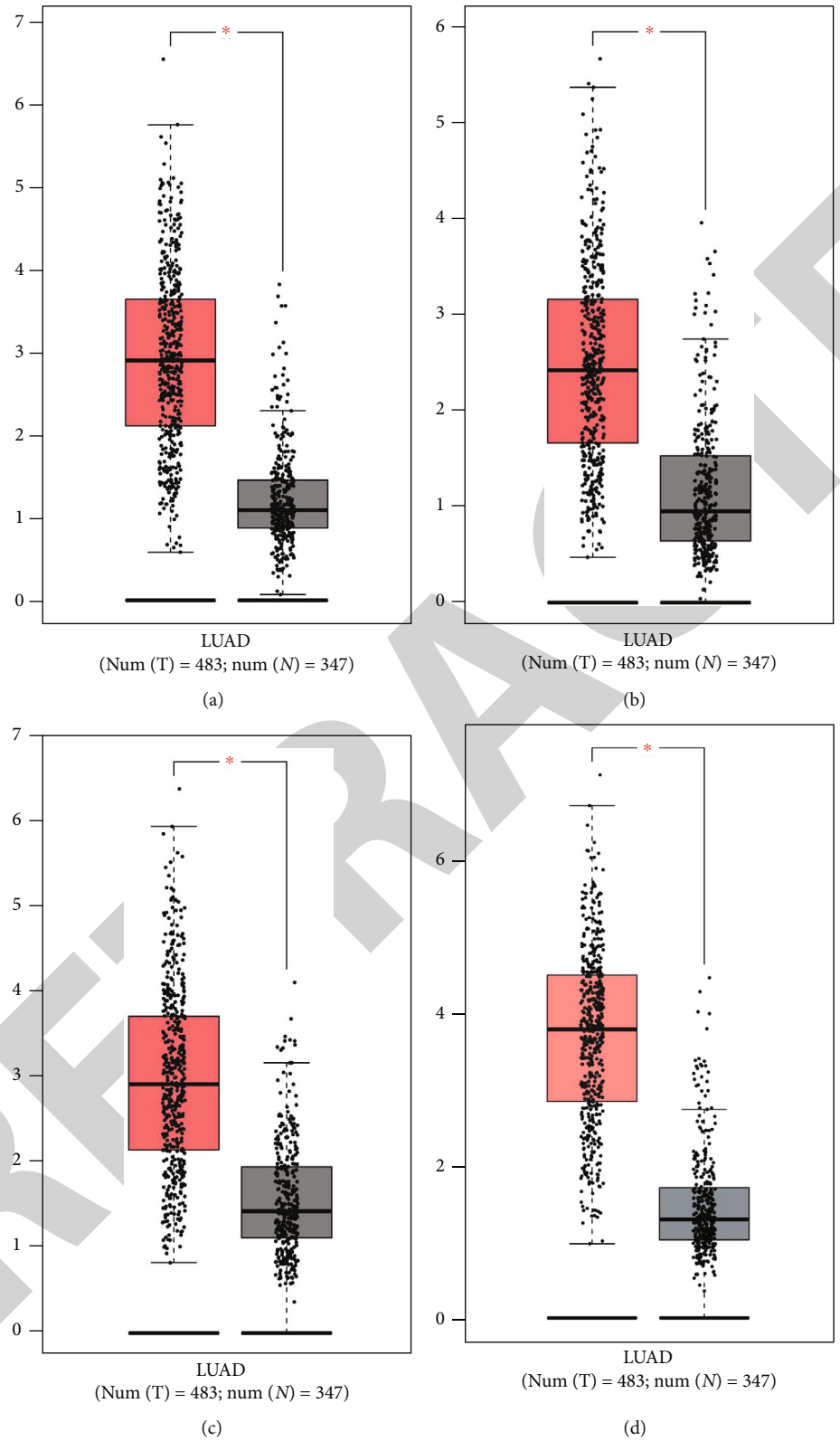

Figure 4: Continued.

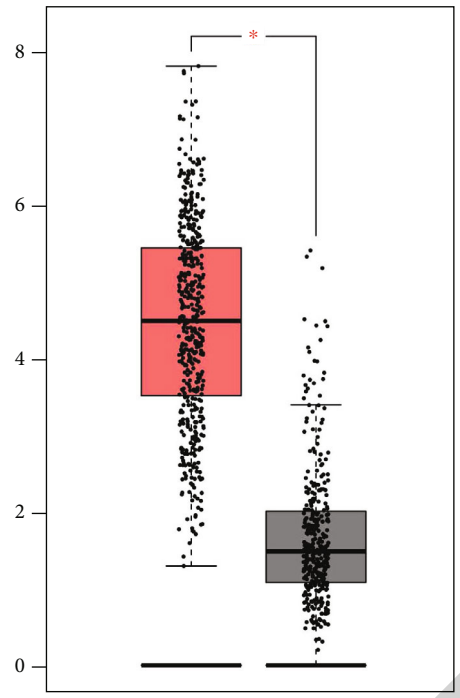

(e)

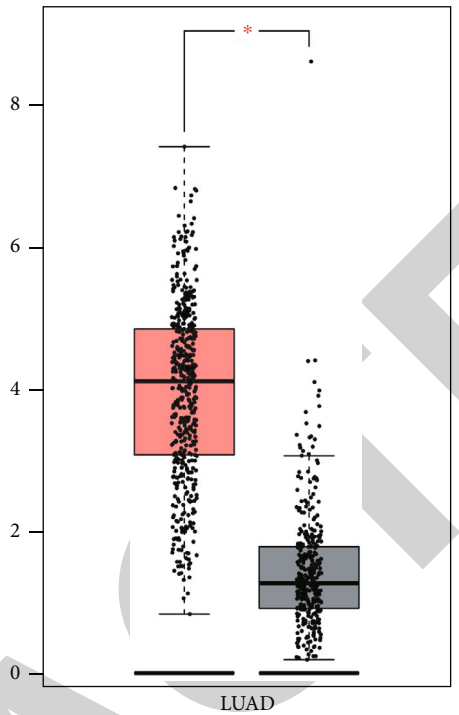

(f)

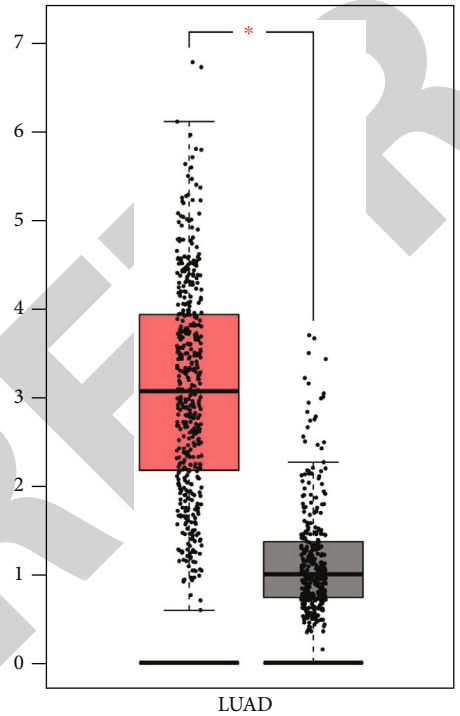

(g)

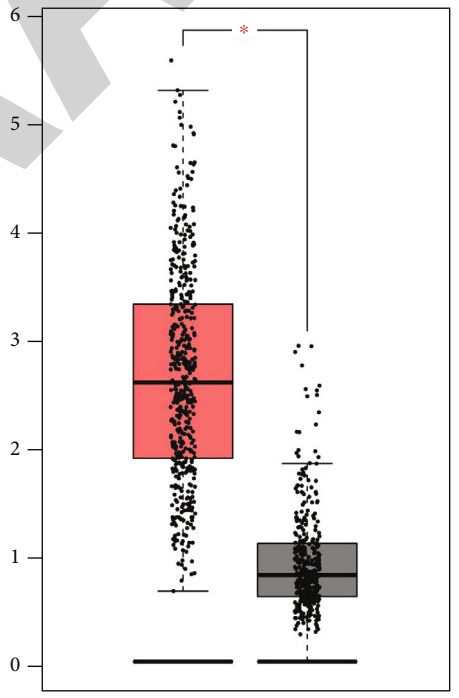

(h)

Figure 4: Continued.

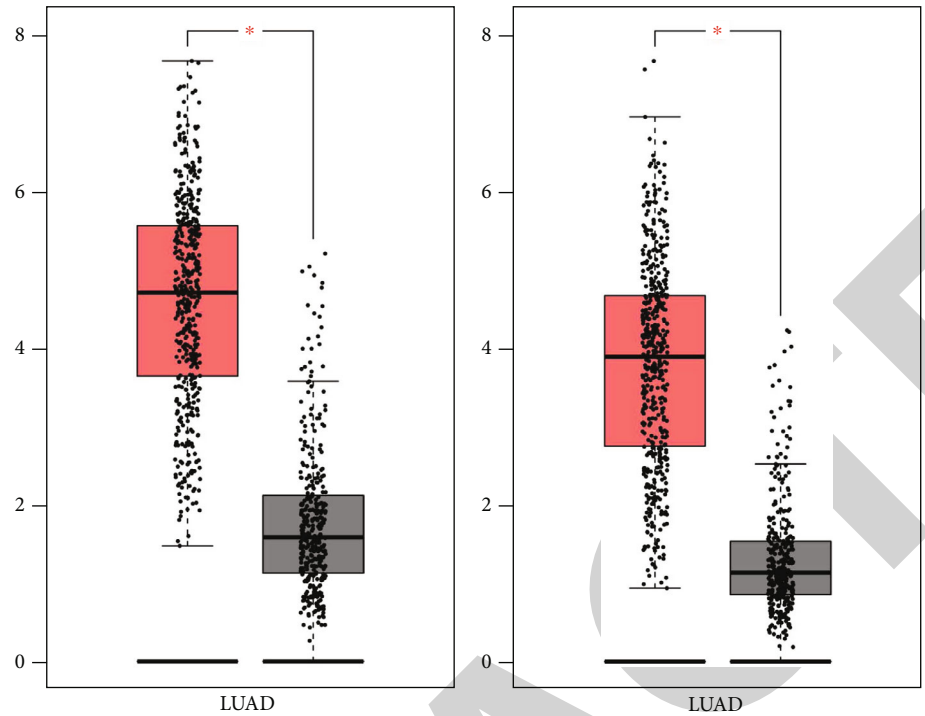

Figure 4: Expression levels of 10 hub genes in lung adenocarcinoma. (a–j) BUB1, BUB1B, CCNA2, CCNB2, CDC20, CENPF, KIF2C, KIF11, TOP2A, and TPX2 (Red: lung adenocarcinoma tissue, Grey: normal lung tissue.). ∗ represents $P < 0.05$, the difference is significant.

(GTEx) data"), the expression of 10 candidate genes in LUAD tumor samples and normal lung samples were analyzed and compared.

2.2.5. Survival Analysis of Key Genes. Based on R 4.1.1 environment, Survival package and SurvMiner package were used for survival analysis, Kaplan-Meier survival curve construction, and to estimate and screen the prognostic markers. The log-rank test was used to evaluate the survival difference between the expression level of key genes and the overall survival rate of lung adenocarcinoma patients, and $P < 0.05$ was considered statistically significant.

3. Result

3.1. Screening of Differentially Expressed Genes in LUAD. In this study, a total of 551 LUAD-related patient data were downloaded, collated, and analyzed from the TCGA database, including 497 tumor samples and 54 normal samples. DESeq2 R package was used for differential analysis, and a total of 1598 differential genes were screened, including 1397 upregulated genes and 204 downregulated genes. A heat map of the top 50 genes with the most significant differences (Figure 1(a)) and a volcano plot of the 1,598 differential genes (Figure 1(b)) were plotted.

3.2. Functional Enrichment Analysis of Differential Genes. R software was used for GO and KEGG enrichment analysis of 1,394 upregulated genes and 204 downregulated genes, respectively. The GO results of 1,394 upregulated genes showed that they were mainly involved in the positive regulation of RNA polymerase II transcription, mitotic mitosis, nucleosome assembly, and other biological processes, but they were also involved in the extracellular region, extracellular space, protein extracellular matrix, nucleosome, and other cytological components. It also plays the molecular biological functions of serine endothase activity, calcium ion binding, nucleosome binding, chromatin binding, and so on (Figure 2(a)). KEGG enrichment results showed that the pathways involved mainly protein digestion and absorption, tumor transcription dysregulation, and amino acid biosynthesis, etc. (Figure 2(b)). The 204 downregulated genes were mainly involved in biological processes such as oxygen transport, synaptic transmission, and cell response to TGF-β stimulation. It also participates in cytological components such as hemoglobin-haptoglobin complex, lateral basement plasma membrane, extracellular space, and cell-cell junction. It also plays molecular biological functions such as oxygen transporter activity, haptoglobin binding, iron binding, peroxidase activity, and G-protein-coupled acetylcholine receptor activity (Figure 2(c)). KEGG enrichment results also showed that the pathways involved mainly neural ligand-receptor interaction, calcium signaling pathway, PI3K-Akt signaling pathway, etc. (Figure 2(d)).

3.3. Protein Interaction Network Construction and Central Gene Screening. A PPI interaction network was constructed for LUAD-related differentially expressed genes based on String database. The MCC algorithm in Cytoscape plug-in CytoHubba was used to screen the top 50 genes in the PPI

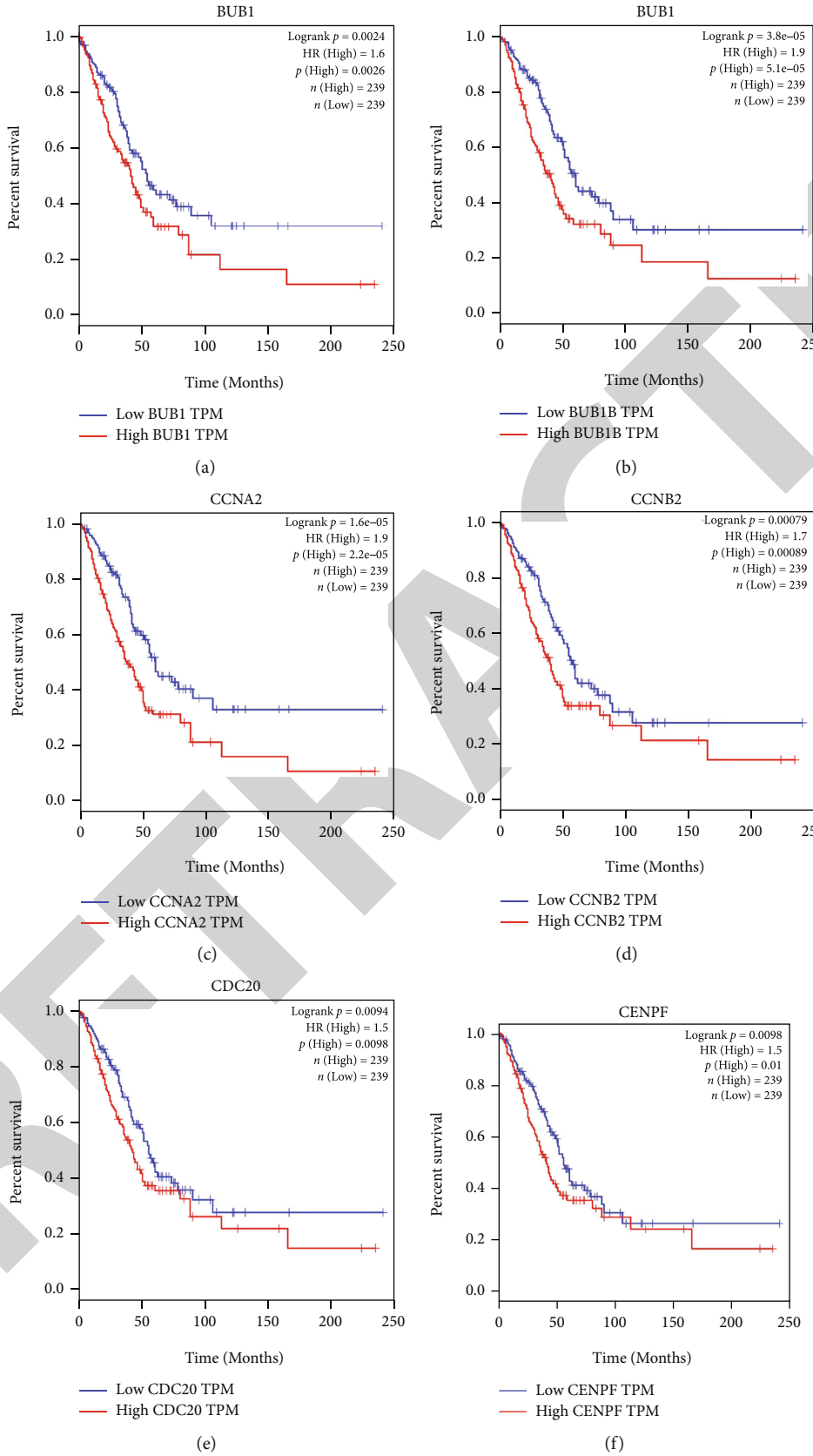

Figure 5: Continued.

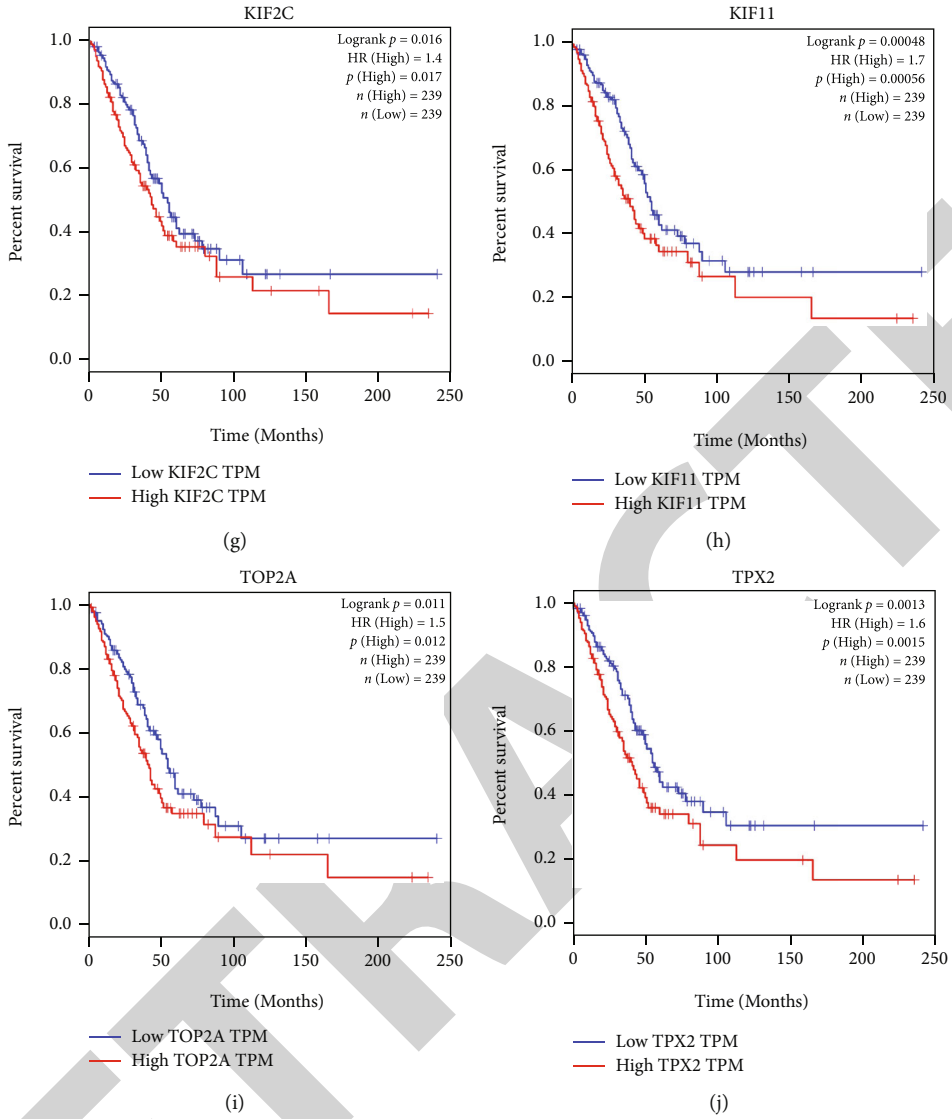

Figure 5: Overall survival analysis of 10 hub genes. (a–j) BUB1, BUB1B, CCNA2, CCNB2, CDC20, CENPF, KIF2C, KIF11, TOP2A, and TPX2.

network to construct the protein interaction network diagram (Figure 3(a)). The top 10 genes were selected as central genes, which were *CCNA2*, *CDC20*, *CCNB2*, *KIF11*, *TOP2A*, *BUB1*, *BUB1B*, *CENPF*, *TPX2*, and *KIF2C* (Figure 3(b).

3.4. GEPIA Analysis of the Expression of 10 Hub Genes in Lung Adenocarcinoma. Compared with normal lung tissue, the mRNA expression levels of 10 hub genes (*CCNA2*, *CDC20*, *CCNB2*, *KIF11*, *TOP2A*, *BUB1*, *BUB1B*, *CENPF*, *TPX2*, and *KIF2C*) in LUAD tissues were significantly increased ($P < 0.05$, Figure 4).

3.5. Survival Analysis of Key Genes. The survival of 10 hub genes screened from PPI network was analyzed using R software, and the Kaplan-Meier survival curve was drawn. Log-rank test revealed that these genes had a significant effect on the overall survival of patients with LUAD ($P < 0.05$, Figure 5). Therefore, it can be concluded that these genes play an important role in the occurrence and development of LUAD.

4. Discussion

Based on the TCGA database, this study used bioinformatics methods to explore the key genes related to the development and prognosis of LUAD. A total of 551 LUAD-related gene expression profiles were screened, including 497 LUAD samples and 54 normal samples. A total of 1598 differentially expressed genes were identified, including 1394 upregulated genes and 204 downregulated genes. The information on biological functions and regulated pathways involved in these differential genes were analyzed by clusterProfiler R package. GO analysis showed that it was mainly involved in the positive regulation of RNA polymerase II transcription, mitotic mitosis, nucleosome assembly, oxygen transport, synaptic transmission, and other biological processes. At the same time, they also participate in the extracellular space, extracellular matrix of proteins, nucleosomes, and other cytological components and participate in some protein binding. KEGG pathway analysis showed that this differentially expressed gene was mainly involved in neural

active ligand-receptor interaction, amino acid biosynthesis, calcium ion signaling pathway, PI3K-Akt signaling pathway, etc. The differential gene PPI interaction network was constructed through the String database, combined with the MCC algorithm in Cytohubba plug-in Cytoscape, and 10 key genes were finally identified, namely CCNA2, CDC20, CCNB2, KIF11, TOP2A, BUB1, BUB1B, CENPF, TPX2, and KIF2C. The GEPIA database is a visual big data analysis platform for cancer based on two well-known transcriptome databases, which are TCGA and GTEx. GEPIA database was used to analyze the expression of each gene in normal and cancer cells. Survival and SurvMiner of R package analyzed the influence of each gene on the overall survival rate of LUAD patients and further verified the accuracy of key gene screening.

Cyclin A2 (CCNA2) and cyclin B2 (CCNB2) belong to the cyclin family and are key regulators of a cell cycle [7]. They have been shown to be significantly overexpressed in a variety of cell cycles and are associated with the development and recurrence of lung cancer, breast cancer, colorectal cancer, and other cancers [8–12]. CDC20, a class of proteins encoding periodic kinases, belongs to the cell division cycle gene family. It has been reported that it is likely to be an oncogenic protein, which is overexpressed in a variety of poorly differentiated tumor cells, including lung cancer, colorectal cancer, breast cancer and bladder cancer, and is associated with their poor prognosis [13–16].

KIF11, a kinesin superfamily gene, is a spindle motor protein encoded by kinesin Eg5 gene and involved in the formation of mitotic spindles [17]. Ling et al. found that the overexpression of KIF11 in lung cancer was related to advanced pathological grade and lymph node metastasis, suggesting that KIF11 may be an effective target for lung cancer prevention and treatment [18]. DNA topoisomerase II Alpha (TOP2A) is encoded by TOP2A gene, which controls and changes the topological state of DNA during transcription and is involved in mitosis of various malignant tumor cells. It has been reported that TOP2A overexpression is closely related to the proliferation, invasion, and interference of NSCLC [19]. BUB1 is a serine/threonine protein kinase encoded by the human BUB1 gene, which plays a key role in centromere binding and spindle checkpoint activation during mitosis. Jiang et al. showed that phosphorylation of CDC20 may help BUB1 to achieve effective regulation of cell cycle [20]. BUB1B, an enzyme encoded by BUB1B gene, is significantly overexpressed in lung cancer, bladder cancer, gastric cancer, colon cancer, liver cancer, and other tumors and plays an important role in the occurrence and development of tumors [21]. Centromere Protein F(CENPF) is a key protein in cell cycle regulation. Previous studies have shown that overexpression of CENPF may be closely related to the occurrence, development, and prognosis of prostate cancer, liver cancer, breast cancer, and other malignant tumors, but its effect on LUAD is rarely reported [22]. Targeting Xenopus kinesin-like protein 2 (TPX2), a microtubule-associated protein involved in spindle assembly, plays a vital role in the induction of peripheral assembly and growth in M phase, and is also overexpressed in a variety of human tumors to promote tumorigenesis develop. It has been reported that TPX2 overexpression is associated with a poor prognosis of NSCLC, suggesting that TPX2 may become a prognostic gene [23]. KIF2C, a mitotic centromere-associated kinesin, is involved in microtubule depolymerization and chromosome segregation and regulates mitosis and cell cycle. Abnormal expression of KIF2C can lead to chromosome misalignment in S phase, chromosome misseparation in G2 phase, and stimulate the occurrence and development of tumors [24].

This study provides a basis for the treatment of LUAD, but it lacks validation from relevant in vivo and in vitro experiments, so the next step of work will be to conduct experiments to validate the mechanism of these hub genes with a view to providing new directions for clinical treatment.

5. Conclusion

In summary, 10 key genes related to the occurrence, development, and prognosis of LUAD were screened out based on the TCGA database. *CCNA2*, *CDC20*, *CCNB2*, *KIF11*, *TOP2A*, *BUB1*, *BUB1B*, *CENPF*, *TPX2* and *KIF2C* were significantly overexpressed in LUAD as well as plays an important role in the LUAD cell cycle. These results suggest that these genes have great potential in the subsequent prevention, treatment, and prognosis of LUAD, which can provide a certain reference value for the diagnosis and drug treatment of LUAD.

Data Availability

All data, models, and code generated or used during the study appear in the submitted article.

Conflicts of Interest

The authors declare that they have no conflicts of interests.

Authors' Contributions

Shen Youfeng and Tang Xiaoqing contributed equally to this study.

Acknowledgments

This study is self funded by the 2019 Municipal Science and Technology plan project (1921080D).

References

[1] R. L. Siegel, K. D. Miller, and A. Jemal, "Cancer statistics, 2020," *CA: a Cancer Journal for Clinicians*, vol. 70, no. 1, pp. 7–30, 2020.

[2] R. S. Herbst, D. Morgensztern, and C. Boshoff, "The biology and management of non-small cell lung cancer," *Nature*, vol. 553, no. 7689, pp. 446–454, 2018.

Hindawi
Journal of Oncology
Volume 2022, Article ID 6184631, 18 pages
https://doi.org/10.1155/2022/6184631

Research Article

Ginsenoside Rg1 Inhibits High Glucose-Induced Proliferation, Migration, and Angiogenesis in Retinal Endothelial Cells by Regulating the lncRNA SNHG7/miR-2116-5p/SIRT3 Axis

Liping Xue,[1] Min Hu,[1] Juanjuan Li,[2] Yadi Li,[1] Qin Zhu,[1] Guanglong Zhou,[1] Xiaofan Zhang,[1] Yuan Zhou,[1] Jieying Zhang,[1] and Peng Ding[3]

[1]*Department of Pediatric Ophthalmology, The Affiliated Hospital of Yunnan University, The Second People's Hospital of Yunnan, The Affiliated Ophthalmology Hospital of Yunnan University, Kunming 650021, Yunnan, China*
[2]*Department of Ophthalmology, The Affiliated Hospital of Yunnan University, The Second People's Hospital of Yunnan, The Affiliated Ophthalmology Hospital of Yunnan University, Kunming 650021, Yunnan, China*
[3]*Department of Neurosurgery, The First Affiliated Hospital of Kunming Medical University, Kunming 650032, Yunnan, China*

Correspondence should be addressed to Peng Ding; dingp1210@163.com

Received 12 July 2022; Revised 22 August 2022; Accepted 26 August 2022; Published 3 December 2022

Academic Editor: Recep Liman

Background. Diabetic retinopathy (DR), including retinal angiogenesis and endothelial cell proliferation and migration, is a serious complication in diabetic patients. It has been reported that ginsenoside Rg1 can prevent retinal damage. However, the mechanism by which Rg1 prevents retinal damage is unknown. Therefore, the aim of the present study was to investigate the mechanism by which Rg1 inhibits high glucose-induced complications through the regulation of the lncRNA SNHG7/miR-2116-5p/SIRT3 axis. *Methods*. Under high glucose (HG) conditions, human retinal endothelial cells (HRECs) were cultured to simulate a DR environment, and Rg1 was added after 48 h. Negative control (NC), miR-2116-5p mimic, si-SNHG7, pc-DNA SIRT3, and miR-2116-5p inhibitor were transfected into HRECs, and CCK-8 assay was used to detect the cell viability. Angiogenesis and transwell assays were used to evaluate angiogenesis and cell migration, respectively. qRT–PCR and Western blot were used to detect the expression of related genes and proteins. Luciferase reporter assays and bioinformatics were used to analyze the target binding sites of miR-2116-5p to lncRNA SNHG7 and SIRT3. *Results*. The proliferation, migration and angiogenesis of HRECs were induced by HG. As expected, HG upregulated miR-2116-5p and VEGF expression but downregulated lncRNA SNHG7 and SIRT3 expression. Importantly, Rg1 inhibited HG-induced HREC proliferation, migration, and angiogenesis by upregulating the lncRNA SNHG7, and miR-2116-5p had a target regulatory relationship with both lncRNA SNHG7 and SIRT3. *Conclusion*. Rg1 inhibits HG-induced proliferation, migration, angiogenesis, and VEGF expression in retinal endothelial cells through the lncRNA SNG7/miR-2116-5p/SIRT3 axis. This finding provides theoretical evidence for the clinical application of Rg1 in DR.

1. Introduction

Numerous studies have shown that diabetes causes various complications (diabetic nephropathy, diabetic retinopathy (DR) and cardiovascular disease), which have become the main cause of morbidity and mortality of diabetes [1]. Type 2 diabetes can lead to serious neurovascular complications, leading to visual impairment and blindness, and DR is one of the main causes [2]. The basic pathological changes in DR include the selective loss of pericytes, capillary basement membrane thickening, microangioma formation, endothelial cell proliferation, and retinal detachment due to neovascularization [3]. The first barrier to monitoring blood glucose changes is the retinal endothelium. The existing evidence suggests that a high concentration of glucose can lead to increasing numbers and migration of retinal endothelial cells, which is a key step in the occurrence of DR [4]. Although some new drugs and vitreoretinal microsurgery have been used in clinical DR treatment, the incidence of DR has dramatically increased in recent decades [5, 6].

Therefore, further revealing the etiology of DR is important for improving the available treatment methods [7, 8]. Ginsenoside Rg1 (Rg1) is a component of ginsenoside, which mainly exists in ginseng medicinal materials. Rg1 can quickly relieve fatigue, delay aging, stimulate the central nervous system, inhibit platelet aggregation, and improve learning and memory [9]. Rg1 has also been shown to be useful in the treatment of myocardial infarction [10], diabetic limb infarction [11], and ischemic necrosis of the skin [12]. Rg1 promotes neovascularization after myocardial infarction, diabetic limb infarction, skin ischemic necrosis, and neonatal hypoxic encephalopathy [13]. Experimental studies have shown that Rg1 has strong antioxidant and blood glucose-lowering activities [14, 15]. Rg1 can promote angiogenesis and enhance endothelial progenitor cell angiogenesis. Moreover, Rg1 can improve endoplasmic reticulum stress-induced apoptosis in diabetic cardiomyopathy induced by streptozotocin (STZ) [16]. Rg1 prevents retinal damage by inhibiting retinal cell apoptosis [17]. Moreover, experimental studies have shown that ginsenoside Rg1 plays a role in promoting vascular regeneration and enhancing endothelial progenitor cell angiogenesis [18].

LncRNAs have been shown to affect the progression mechanisms of DR through various methods [19]. In human retinal endothelial cells, HG-induced angiogenesis can be inhibited by the lncRNA SNHG7 through the miR-543/SIRT1 cascade [20]. Whether SNHG7 participates in the regulation of vascular growth in DR and whether it promotes angiogenesis in human retinal endothelial cells (HRECs) remain unclear. Notably, in the pathogenesis of DR, miRNAs also play an indispensable role. There have been reports of the abnormal expression of miRNAs in the retina of diabetic rats induced by STZ [21, 22]. In addition, it has been shown that miR-3197 and miR-2116-5p are immensely upregulated in DR patients and are effective diagnostic markers of DR [23].

As a conservative nicotinic adenine dinucleotide-dependent (NAD-dependent) deacetylase, sirtuins consist of seven isomers [24]. In addition, sirtuin-3 (SIRT3), a core member of the sirtuin family, is located on the mitochondrial membrane. SIRT3 can deacetylate the target protein, which plays an important role in antioxidation, biosynthesis, and energy metabolism of mitochondria [25]. For example, under the mediation of SIRT3, autophagy-related proteins can be acetylated, thus affecting autophagy [26]. SIRT3 is necessary for coronary angiogenesis and glycolysis [27]. In type 2 diabetic mice, retinal dysfunction may be related to the loss of SIRT3 and SIRT5 [28] because SIRT3 may promote autophagy by downregulating the expression of angiogenesis-related genes in retinal endothelial cells [29]. In addition, in a rat model of diabetes and retinopathy, the expression of autophagy-related proteins was promoted by the overexpression of SIRT3, while VEGF was inhibited [30]. These findings suggest that SIRT3 is a key therapeutic target for DR.

In the present study, StarBase website prediction suggested that miR-2116-5p has target binding sites for both the lncRNA SNHG7 and SIRT3, implying that miR-2116-5p, lncRNA SNHG7, and SIRT3 may act as an axis. Therefore, we investigated the mechanism by which ginsenoside Rg1 inhibits retinal endothelial cell lesions induced by high glucose by regulating the lncRNA SNHG7/miR-2116-5p/SIRT3 axis.

2. Methods

2.1. Animal Breeding and Modeling. In total, 120 healthy male SD rats of SPF class (Animal Experiment Center of Kunming Medical University), weighing 200 ± 25 g, were utilized, and all rats had no pathological changes in the anterior and anterior segments of the eyes after the examination. The blood glucose levels were within the normal range as detected by a blood glucose meter after tail vein collection. The rats were randomly divided into 3 groups (40/group): normal rats group (NC); DR rats (Model); Rg1-treated DR rats group (Rg1). The rats were acclimatized and housed for 1 week before the experiment, and they were fed and watered ad libitum. The rats in the diabetic group were fasted for 12 h before modeling and weighed before the experiment. In the diabetic group, freshly prepared STZ in buffer (55 mg/kg; Sigma–Aldrich, Germany) was injected once into the left lower abdominal cavity, and the rats ate and drank normally after the injection. After the rats were injected with STZ for 48 h, the blood glucose and body weight were measured. Additionally, in the diabetic rat models, blood glucose >16.7 mmol/L, polyuria, and polyphagia were considered. The blood glucose and body weight of the rats were observed once every 2 weeks. In the Rg1 group, gavage was started on the day of modeling, and 0.5 mL (12–5 g/ml) of Rg1 solution (Solarbio, Beijing, China) was given by gavage every day, while the same dose of saline was given to the model and NC groups. The rats were sacrificed 8 weeks after modeling, and fresh retinal specimens were removed and preserved for the relevant assays. The experimental scheme of this study was approved by the Animal Ethics Committee of Kunming Medical University and fully met the requirements of the National Institutes of Health Laboratory Animal Care Guide.

2.2. Cell Culture and Transfection. HRECs (American Type Culture Collection, Inc.) were cultured at 37°C with saturated humidity for two days before passaging. Before adding 1 mL of trypsin, the cells were washed with PBS 3 times, which covered the entire cell layer. The cells were observed under an inverted microscope until they shrank into a round shape, and then, 10% fetal bovine serum was added to neutralize trypsin. The samples were centrifuged at 1000 rpm for 5 min to collect the cells. Ten percent fetal bovine serum was added, and the cells were inoculated in 75 cm^2 culture flasks at 10 mL/bottle (10^4 cells/ml). A concentration of 5 mM glucose is a normal glucose condition, and 25 mM is a high glucose condition. The cells were incubated with 25 mM glucose for 48 h before adding 10 μM Rg1, followed by incubation for 48 h for the subsequent experiments. Using Lipofectamine™ 2000

(Med Chem Express, USA), the negative control (NC), si-SNHG7, miR-2116-5p mimic, miR-2116-5p inhibitor, and pc-DNA SIRT3 were transfected into HRECs.

2.3. HE Staining of Retinal Tissue. For the HE staining, rat retinal sections were routinely dewaxed and washed with ddH_2O for 10 s. Subsequently, hematoxylin staining solution was used to treat the rat retinal sections for 10 min, and the sections were washed with ddH_2O, subjected to 1% hydrochloric acid alcohol fractionation for 10 s, washed with ddH_2O, returned to blue in warm water for 1 min, subjected to eosin staining solution for 30 s, washed with water for 10 s, subjected to gradient alcohol dehydration, cleared with xylene, sealed with neutral gum and observed for the detection of inflammatory cell infiltration under a microscope.

2.4. Immunohistochemistry. After the glass slide was baked at 65°C for 2 h, it was placed in xylene for 10 minutes. The rat retinal sections were incubated in the following ethanol gradient (5 min per solution): 100%, 95%, 80% and distilled water. In a wet room, citric acid buffer was used to treat the slices, and hydrogen peroxide (3%) was used to remove endogenous peroxidase (25°C, 10 min). The sections were blocked with 5% bovine serum at 37°C for 30 min and then incubated with an anti-SIRT3 antibody (1 : 200) for 12 h at 4°C. The sections were incubated with goat anti-rabbit (IgG, 1 : 100) for 30 min at 37°C after washing the slices with PBS buffer. 3,3′-diaminobenzidine (DAB) was used to observe the sections, and a light microscope was used to acquire the images.

2.5. Cell Viability Assay. In total, 5×10^4 cells/well were inoculated into a 96-well plate, 10 μL CCK-8 solution (Sangon, Shanghai, China) was added, and the cells were incubated for 4 h at 25°C. The OD value was measured at 450 nm.

2.6. Angiogenesis Experiments. Cells were inoculated into a 24-well plate at 37°C, and Matrigel (Sigma–Aldrich, Germany) was added to each well and allowed to harden for 30 min. HRECs were inoculated at a density of 1.2×10^5 cells/well on top of the Matrigel-coated wells and cultured in a sterile incubator at 100% humidity, 37°C and 5% CO_2 for 6 h. An inverted microscope was used to observe the tube lumen and acquire the images. Image-Pro Plus software was used to calculate the number of Matrigel tubule formations in the field of view and the tube formation capacity.

2.7. Transwell Experiment. Cells were collected from each group 48 h after transfection and washed, and serum-free DMEM was used to adjust the cell concentration to 1×10^5 cells/mL. In 24-well Transwell plates (Corning, USA), 200 μL of cell suspension was added to the upper chamber, and in the lower chamber, 500 μL of DMEM containing 10% fetal bovine serum was added. After culturing for 24 h, the unstained cells were wiped off, while the stained cells were stained with crystal violet for 20 min. An inverted microscope was used to observe the cells, and five randomly selected visual fields were imaged and counted.

2.8. qRT-PCR Experiments. The total RNA was extracted from tissues and cells using a Total RNA Extractor (Sangon Biotech). A cDNA synthesis kit (Vazyme, Nanjing, China) was used to reverse transcribe 2 μg mRNA into cDNA, which was then diluted 10 times. One microliter of the prepared cDNA was used for qPCR, and the U6 or GAPDH gene was used as the reference gene. All primers (Table 1) used in this study were designed with Premier 5.0. The two-step reaction conditions for PCR were as follows: predenaturation (maintained at 95°C for 5 min), maintenance at 95°C for 10 s, annealing (30 s) and extension (30 s). Both annealing and extension were cycled 40 times. The confidence of the PCR results was assessed by the dissociation curve and cycle threshold (CT) values. The results were calculated by the $2^{-\Delta\Delta Ct}$ method after repetition at least 3 times.

2.9. Western Blot Assay. Proteins were extracted from retinal tissue utilizing RIPA lysis buffer (Sangon Biotech, Shanghai), and a BCA assay (Sangon Biotech, Shanghai) was used to determine the total protein content. 10% SDS–PAGE gel was used to separate the total proteins, which were then transferred to PVDF membranes by a constant current flow at 200 mA. Subsequently, the PVDF membranes were incubated with antibodies (Abcam, USA) for 12 h at 4°C. The PVDF membranes were washed with TBS buffer and incubated with secondary antibodies at 25°C for 1 h. After washing the membranes three times, chemiluminescent reagents were added, and the bands were analyzed for grayscale values using ImageJ software. Each experiment was repeated 3 times independently.

2.10. Bioinformatics and Dual Luciferase Gene Reporter Analysis. In this study, StarBase (http://starbase.sysu.edu.cn/) was used to predict the binding sites of miRNAs and lncRNAs. The dual-luciferase reporter vectors containing WT and mutant-type binding sites for SNHG7 or SIRT3 sequences were constructed by a rapid cloning kit (Vazyme, Nanjing, China) and named WT-SNHG7 or WT-SIRT3 and MUT- SNHG7 or SIRT3, respectively. Subsequently, WT-SNHG7 or WT-SIRT3 and MUT-SNHG7 or SIRT3 vectors were transfected into HRECs (Chinese Academy of Sciences Culture Collection) with NC mimic or miR-29b-3p mimic. After transfection for 48 h, a dual luciferase reporter assay was used to detect luciferase activity.

2.11. Statistical Analysis. GraphPad Prism 8 software was used to analyze and prepare graphs of the experimental data. In this study, the results are shown as the mean ± standard deviation (SD). As expected, two groups and multiple groups of data were analyzed by unpaired Student's *t*-test and one-way analysis of variance, followed by Tukey's post-hoc test. The *P* value representing statistical significance was 0.05.

Table 1: Primer sequences.

Target	Sequence
SNHG7	Forward: 5′-GCCCTGCAGCCTCGC-3′ Reversed: 5′-CAGCGGCGCCTCCTC-3′
miR-2116-5p	Forward: 5′-GGGTTCTTAGCATAGGAGGTC-3′ Reversed: 5′-GAATCGAGCACCAGTTACGCAATG-3′
SIRT3	Forward: 5′- CAATGTCGCTCACTACTTCCTT-3′ Reversed: 5′- CGTCAGCCCGTATGTCTTC-3′
U6	Forward: 5′-CTCGCTTCGGCAGCACA-3′ Reversed: 5′-AACGCTTCACGAATTTGCGT-3′
GAPDH	Forward: 5′-AATCCCATCACCATCTTCCA-3′ Reversed: 5′-TGGACTCCACGACGTACTCA-3′

3. Results

3.1. Effect of Rg1 on the Expression of SIRT3, the lncRNA SNHG7, and miR-2116-5p in the Retina of DR Rats. The effect of Rg1 on the expression of SIRT3, the lncRNA SNHG7 and miR-2116-5p in the retina of DR rats was investigated. Compared with the control group, the detection of blood glucose values in the different treatment groups revealed that the model group rats had significantly higher blood glucose after the STZ injection, and the blood glucose level was higher than 16.7 mmol/L, demonstrating a successful diabetic model. In contrast, the treatment group had significantly lower blood glucose (Figure 1(a)). Compared with the control group, SNHG7 and SIRT3 were significantly lower in the model group, and the expression of both SNHG7 and SIRT3 increased after the Rg1 treatment as shown by qRT-PCR (Figures 1(b) and 1(d)). As expected, compared with the control group, the expression of miR-2116-5p was significantly higher in the model group, and the expression of miR-2116-5p was significantly lower after the Rg1 treatment (Figure 1(c)). The HE staining results showed that the control rats had a clear and continuous inner boundary membrane and only a few vascular endothelial cells in the vitreous near the inner retinal boundary membrane. The model rats showed edema on the retinal surface, and the number of vascular endothelial cells was considerably increased. Moreover, the rats in the Rg1-treated group had a clear and continuous inner boundary membrane, reduced edema and decreased vascular endothelial cells (Figure 1(e)). Compared to the control group, SIRT3 was significantly reduced in the retinal tissues of the rats in the model group in the immunohistochemical assay. In contrast, SIRT3 in the Rg1-treated rats was significantly higher than that in the model group (Figure 1(f)). The VEGF-immunopositive product was indicated by brownish-yellow granular staining, and immunopositive cells were mainly distributed in the retinal ganglion cell layer, which was opposite to that observed with SIRT3 (Figure 1(g)), and in the inner nuclear layer. The results of Western blot detection also showed that compared with the control group, the expression of SIRT3 was down-regulated and VEGF was up-regulated in the model group, and Rg1 treatment reversed this phenomenon (Figure 1(h)). In summary, these findings show that Rg1 downregulates miR-2116-5p and VEGF but upregulates the lncRNA SNHG7 and SIRT3 in the retinas of diabetic rats.

3.2. Effect of Rg1 on the Proliferation, Migration, and Angiogenesis of HG-Treated HRECs. Cell viability was assessed using a CCK-8 assay to investigate the effect of Rg1 on HG-induced pathological phenomena (HREC proliferation, migration and angiogenesis). The results showed that the HG treatment significantly increased the viability of HRECs, while the Rg1 treatment significantly inhibited cell viability (Figure 2(a)). As expected, in the HG group, the qRT–PCR analysis showed that the lncRNA SNHG7 and miR-2116-5p were significantly lower and higher, respectively, and they were significantly reversed after the addition of Rg1 (Figures 2(b) and 2(c)). The number of migrating cells and angiogenesis were significantly higher in the HG group in the Transwell and angiogenesis assays, and the number of migrating cells and angiogenesis were decreased after the addition of Rg1 (Figures 2(d) and 2(e)). Similarly, the protein expression of SIRT3 was significantly lower and VEGF was elevated in the HG group as shown by the Western blot analysis. The treatment with Rg1 significantly increased the protein level of SIRT3 but significantly decreased VEGF (Figure 2(f)). Thus, these findings demonstrate that high glucose induces pathological phenomena in HRECs, but Rg1 significantly inhibits these changes.

3.3. The Targeting Relationship between the lncRNA SNHG7 and miR-2116-5p. StarBase online software was used to predict the binding sites of lncRNA SNHG7 in miR-2116-5p (Figure 3(a)). As verified by the dual luciferase assays, the luciferase activity of wild-type SNHG7 could be reduced by miR-2116-5p but had almost no effect on mutant SNHG7 (Figure 3(b)). The transfection of different siRNAs, including siRNA NC (si-NC) and siRNA-SNHG7 (si-S1/2/3), was used to knockdown SNHG7. Because the transfection of si-S2 showed the best knockdown of SNHG7, it was used in the subsequent experiments (Figure 3(c)). The knockdown or overexpression of SNHG7 was verified by a qRT-PCR analysis. The results showed that miR-2116-5p was significantly decreased after the overexpression of SNHG7, while miR-2116-5p was significantly increased after the knockdown of SNHG7 (Figure 3(d)). Thus, these findings

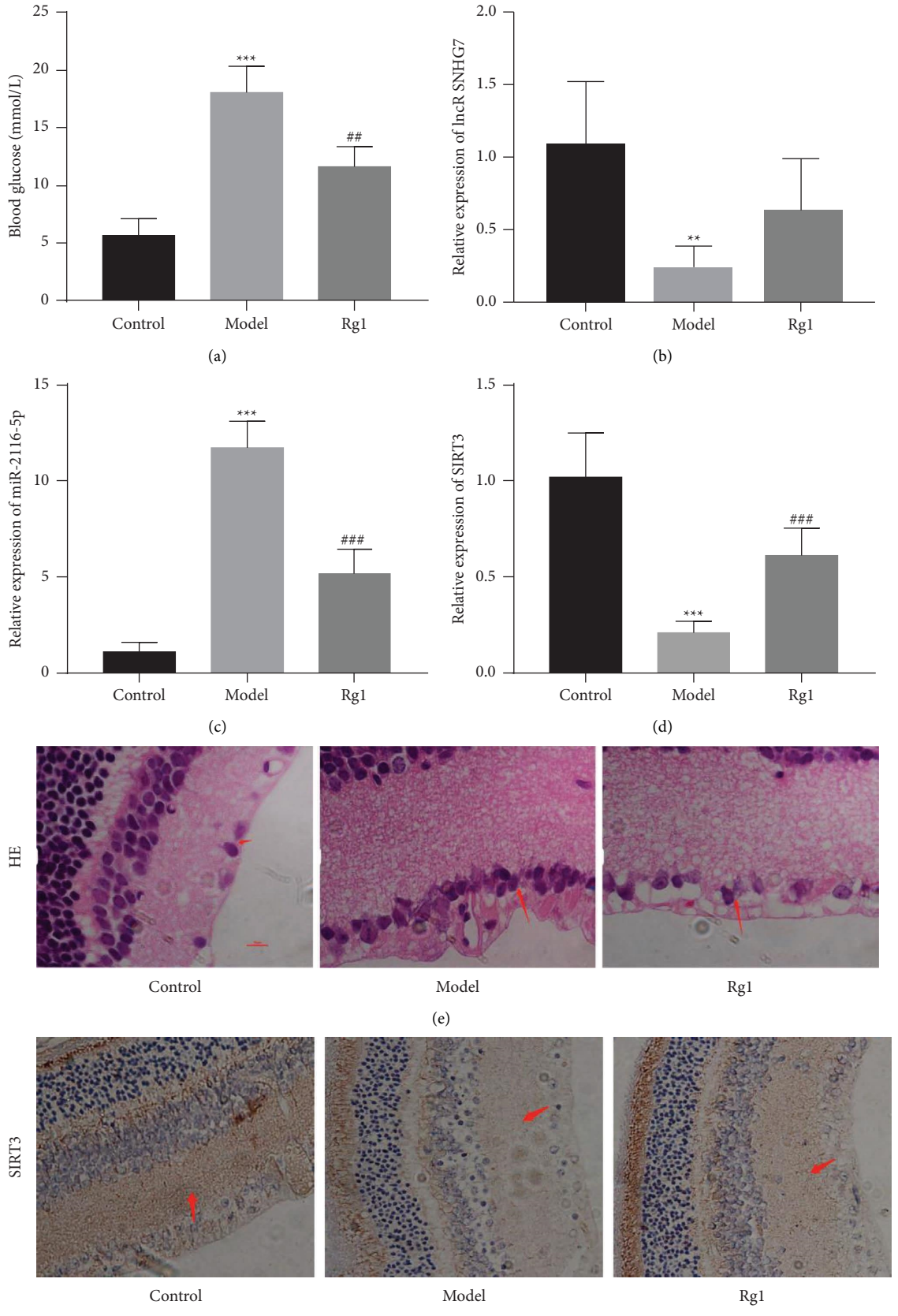

Figure 1: Continued.

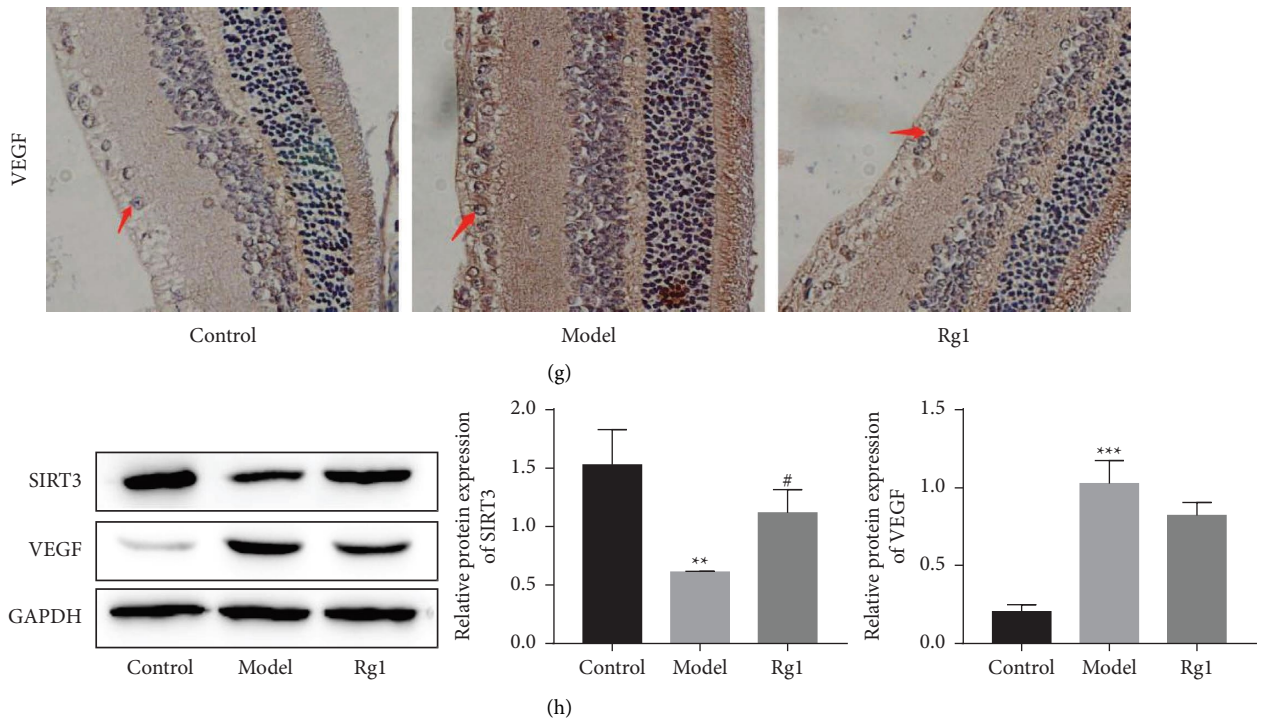

Figure 1: The effect of Rg1 on the lncRNA SNHG7, miR-2116-5p, and SIRT3 in the retinas of DR rats. (a) Blood glucose values of rats after different treatments. qRT-PCR was used to analyze the expression of the lncRNA SNHG7 (b), miR-2116-5p (c), and SIRT3 (d). (e) HE staining of rat retinal tissues. Immunohistochemical staining of SIRT3 (f) and VEGF (g). (h) SIRT3 and VEGF protein levels were detected by Western blot analysis. $^{**}P < 0.01$ and $^{***}P < 0.001$ compared to the control group; $^{\#}P < 0.05$, $^{\#\#}P < 0.01$ and $^{\#\#\#}P < 0.001$ compared to the model group.

demonstrate that the lncRNA SNHG7 negatively regulates miR-2116-5p by targeting the modulation of miR-2116-5p.

3.4. Rg1 Inhibits HG-Induced Cell Proliferation, Migration, and Angiogenesis by Upregulating the lncRNA SNHG7 in HRECs. Next, we investigated the effects of Rg1 in HG-induced HRECs via the lncRNA SNHG7. Compared with the HG group, the cell viability was reduced in the Rg1 group, however, si-SNHG7 reversed the inhibitory effect of Rg1 on cell proliferation. Furthermore, compared with the Rg1+si-SNHG7 group, the cell viability was significantly reduced in the Rg1+si-SNHG7+miR-2116-5p inhibitor group (Figure 4(a)). The results of qRT-PCR assay showed that compared with the HG group, the expression of SNHG7 was significantly increased and the expression of miR-2116-5p was significantly down-regulated in the Rg1 group, which was reversed by si-SNHG7. At the same time, compared with the Rg1+si-SNHG7 group, in the Rg1+si-SNHG7+miR-2116-5p inhibitor group, the expression of SNHG7 was up-regulated and the expression of miR-2116-5p was down-regulated (Figures 4(b) and 4(c)). Transwell and angiogenesis experiments showed that Rg1 treatment could effectively inhibit HG-induced cell proliferation and angiogenesis, while knockdown of SNHG7 could significantly attenuate the effect of Rg1. In addition, co-transfection of si-SNHG7+miR-2116-5p inhibitor could maintain the inhibitory effect of Rg1 on cell proliferation and angiogenesis to a certain extent (Figures 4(d) and 4(e)). These results suggest that Rg1 inhibits HG-induced HREC pathological phenomena through the upregulation of the lncRNA SNHG7.

3.5. Validation of the Targeting Relationship between miR-2116-5p and SIRT3. StarBase online software was used to predict the miR-2116-5p-binding sites in SIRT3, and the results are shown in Figure 5(a). As verified by the dual luciferase assays, miR-2116-5p reduced the activity of wild-type SIRT3 but had almost no effect on mutant SIRT3 (Figure 5(b)). SIRT3 was decreased after the transfection of the miR-2116-5p mimic, and the transfection of the miR-2116-5p inhibitor increased the SIRT3 expression levels (Figure 5(c)). At the expression level, SIRT3 was reduced under high glucose conditions and after the transfection of miR-2116-5p under normal glucose and HG conditions (Figure 5(d)). Thus, these data illustrate that miR-2116-5p acts by targeting the negative regulation of SIRT3.

3.6. Rg1 Affects the Proliferation, Migration and Angiogenesis of HG-Induced HRECs via miR-2116-5p/SIRT3. We further explored the effects of Rg1 via miR-2116-5p/SIRT3. The results of CCK-8 assay showed that compared with the HG group, the cell viability of the Rg1 group was reduced, but the

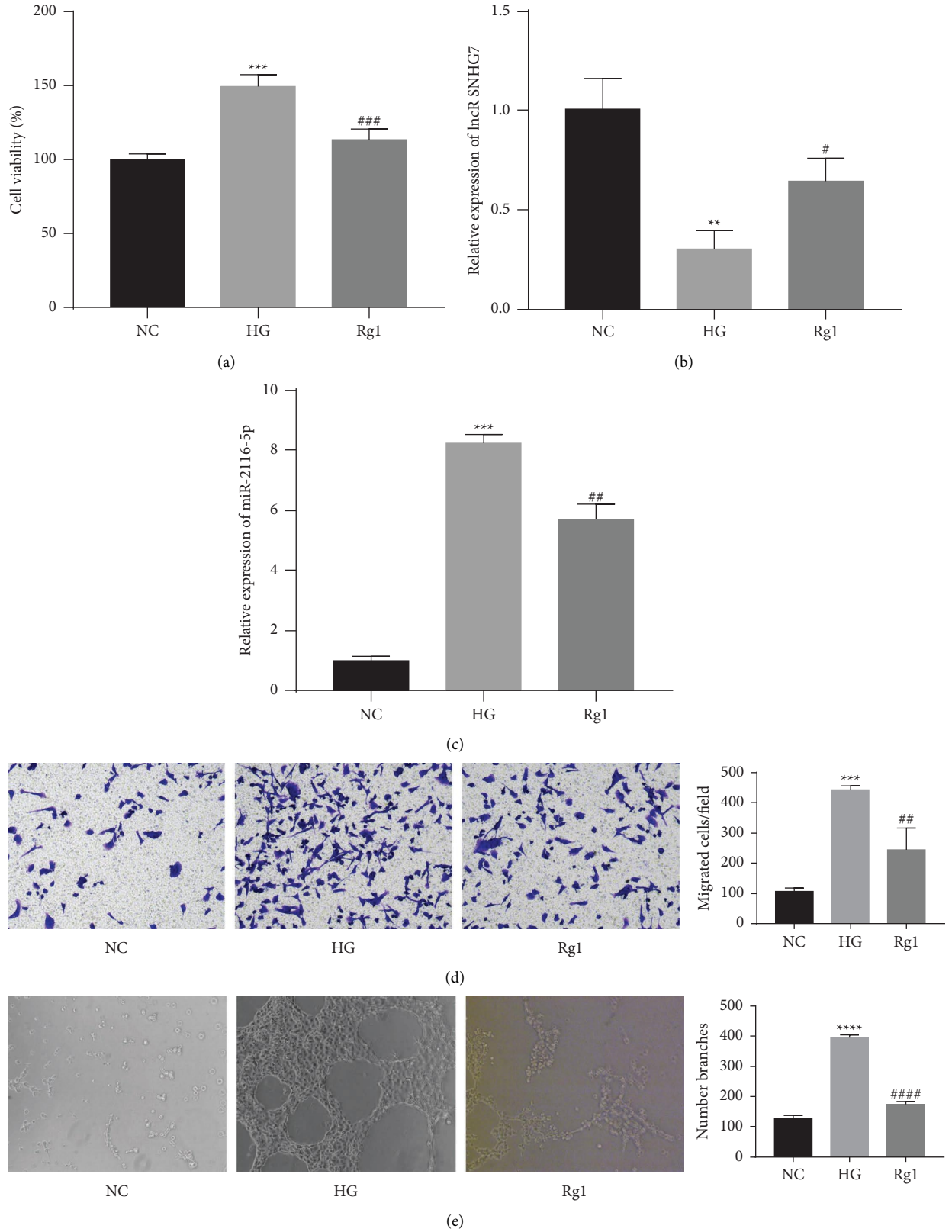

Figure 2: Continued.

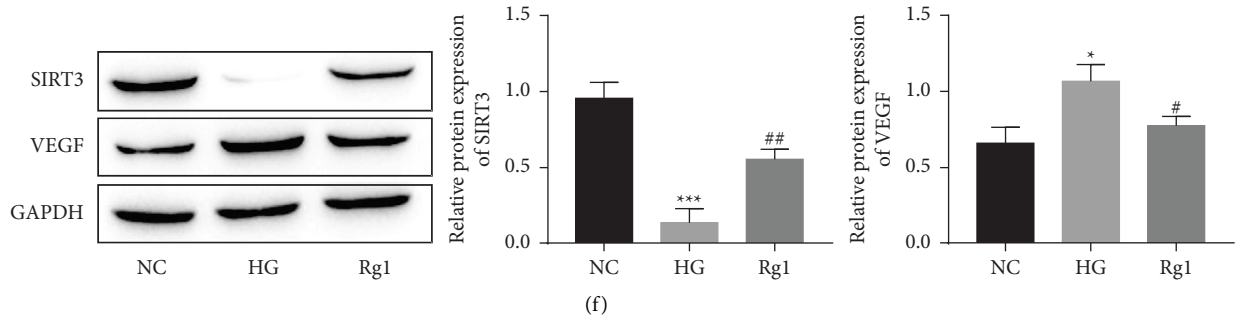

Figure 2: Effect of Rg1 on the proliferation, migration, and angiogenesis of HRECs under HG-induced conditions. (a) CCK-8 assay of cell viability. Qrt-PCR analysis of the lncRNA SNHG7 (b) and miR-2116-5p (c). (d) Transwell assay of cell migration. (e) Comparison of angiogenesis in different groups. (f) Analysis of the SIRT3 and VEGF protein levels by a Western blot analysis. $^{*}P < 0.05$, $^{**}P < 0.01$, $^{***}P < 0.001$ and $^{****}P < 0.0001$ compared to the NC group; $^{\#}P < 0.05$, $^{\#\#}P < 0.01$, $^{\#\#\#}P < 0.001$ and $^{\#\#\#\#}P < 0.0001$ compared to the HG group.

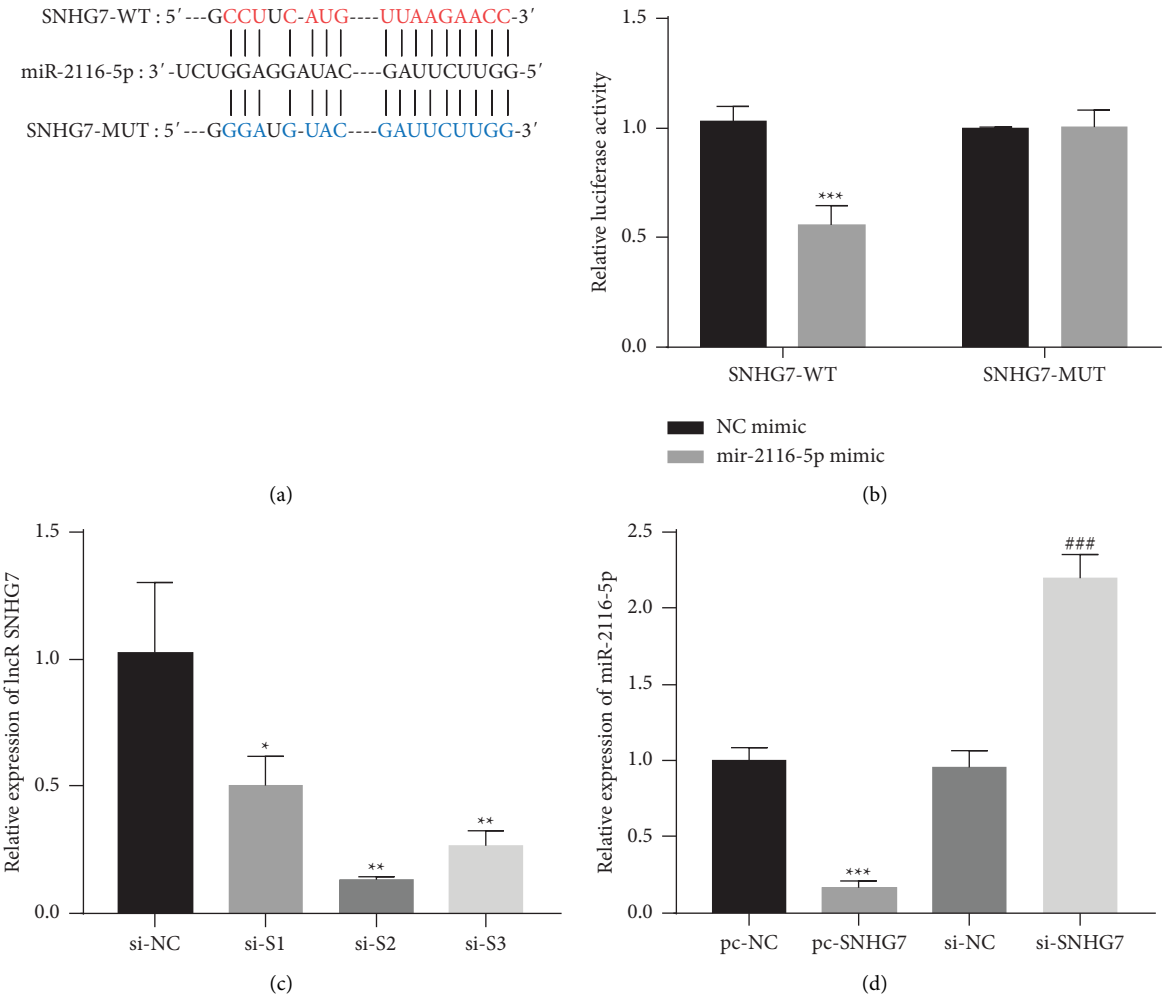

Figure 3: Validation of the relationship between the lncRNA SNHG7 and miR-2116-5p. (a) The predicted lncRNA SNHG7-binding sites in miR-2116-5p. (b) The targeting relationship between the lncRNA SNHG7 and miR-2116-5p was verified through a dual luciferase reporter assay, $^{***}P < 0.001$ compared to the NC mimic group. (c) Analysis of the lncRNA transfection efficiency of SNHG7 by qRT-PCR, $^{*}P < 0.05$ and $^{**}P < 0.01$ compared to the si-NC group. (d) The expression of miR-2116-5p was detected by qRT–PCR, $^{***}P < 0.001$ compared to the pc-NC group; $^{\#\#\#}P < 0.001$ compared to the si-NC group.

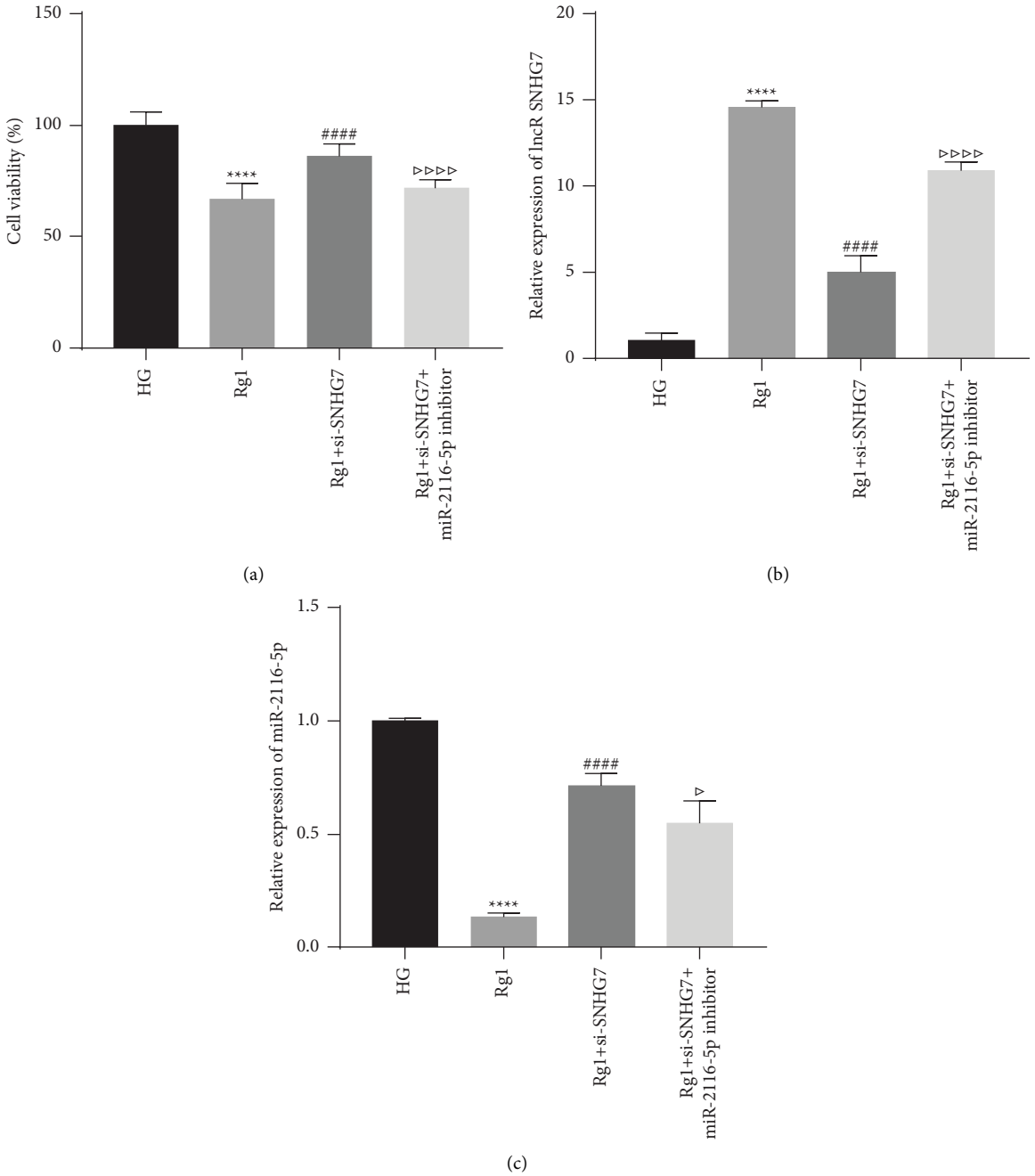

Figure 4: Continued.

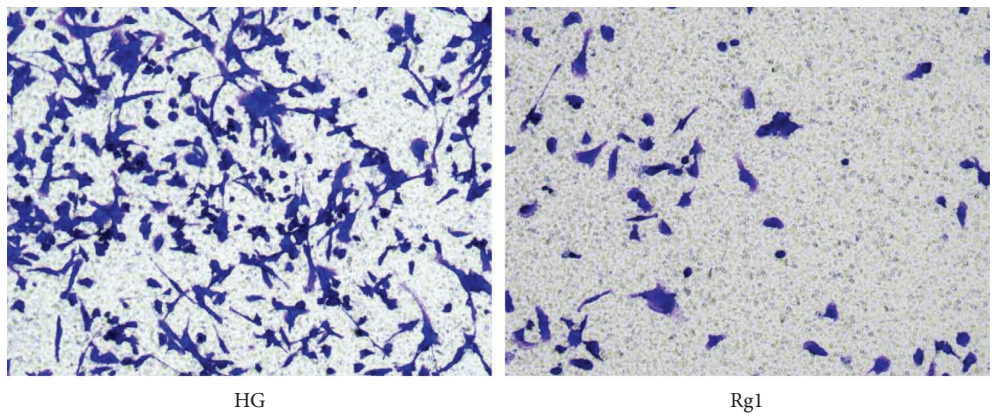

HG Rg1

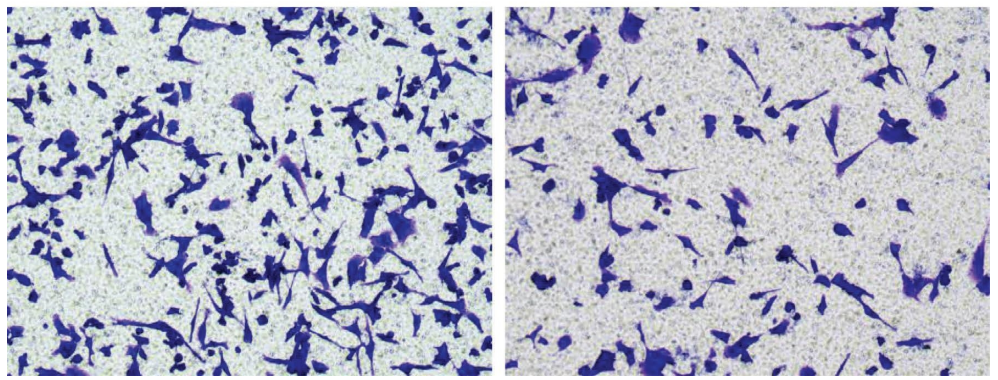

Rg1+si-SNHG7 Rg1+si-SNHG7+miR-2116-5p inhibitor

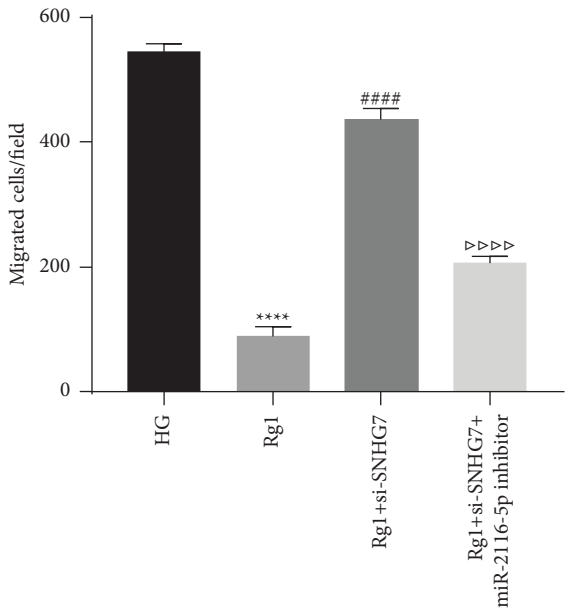

(d)

Figure 4: Continued.

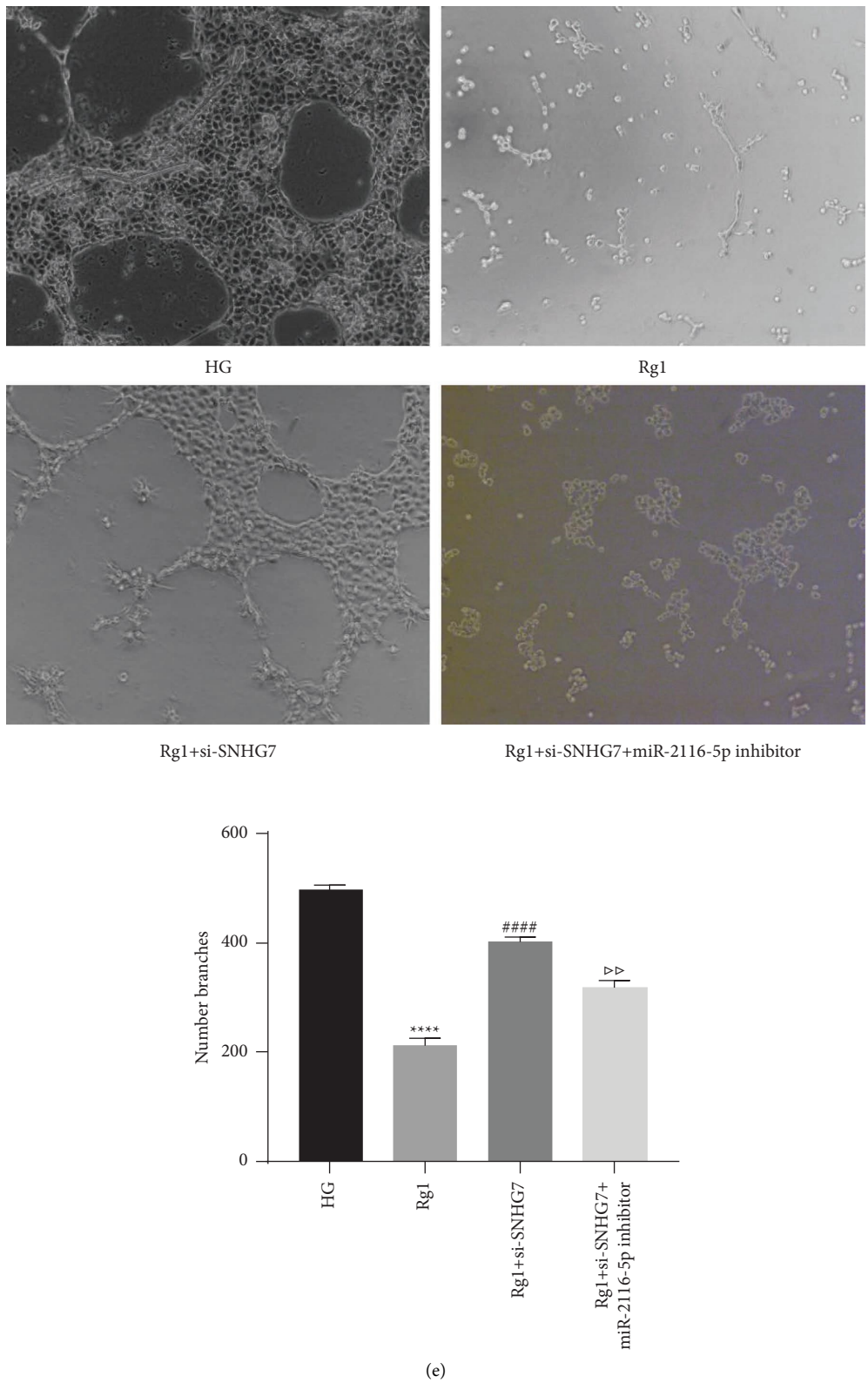

Figure 4: Rg1 inhibits HG-induced cell proliferation, migration, and angiogenesis in HRECs through the upregulation of the lncRNA SNHG7. (a) CCK-8 assay of cell viability. qRT-PCR analysis of the expression level of the lncRNA SNHG7 (b) and miR-2116-5p (c). (d) Transwell assay of cell migration. (e) Comparison of angiogenesis in different groups. $^{****}P < 0.0001$ compared to the HG group; $^{\#\#\#\#}P < 0.0001$ compared to the Rg1 group; $^{\triangle}P < 0.05$, $^{\triangle\triangle}P < 0.01$ and $^{\triangle\triangle\triangle\triangle}P < 0.0001$ compared to- the Rg1+si-SNHG7 group.

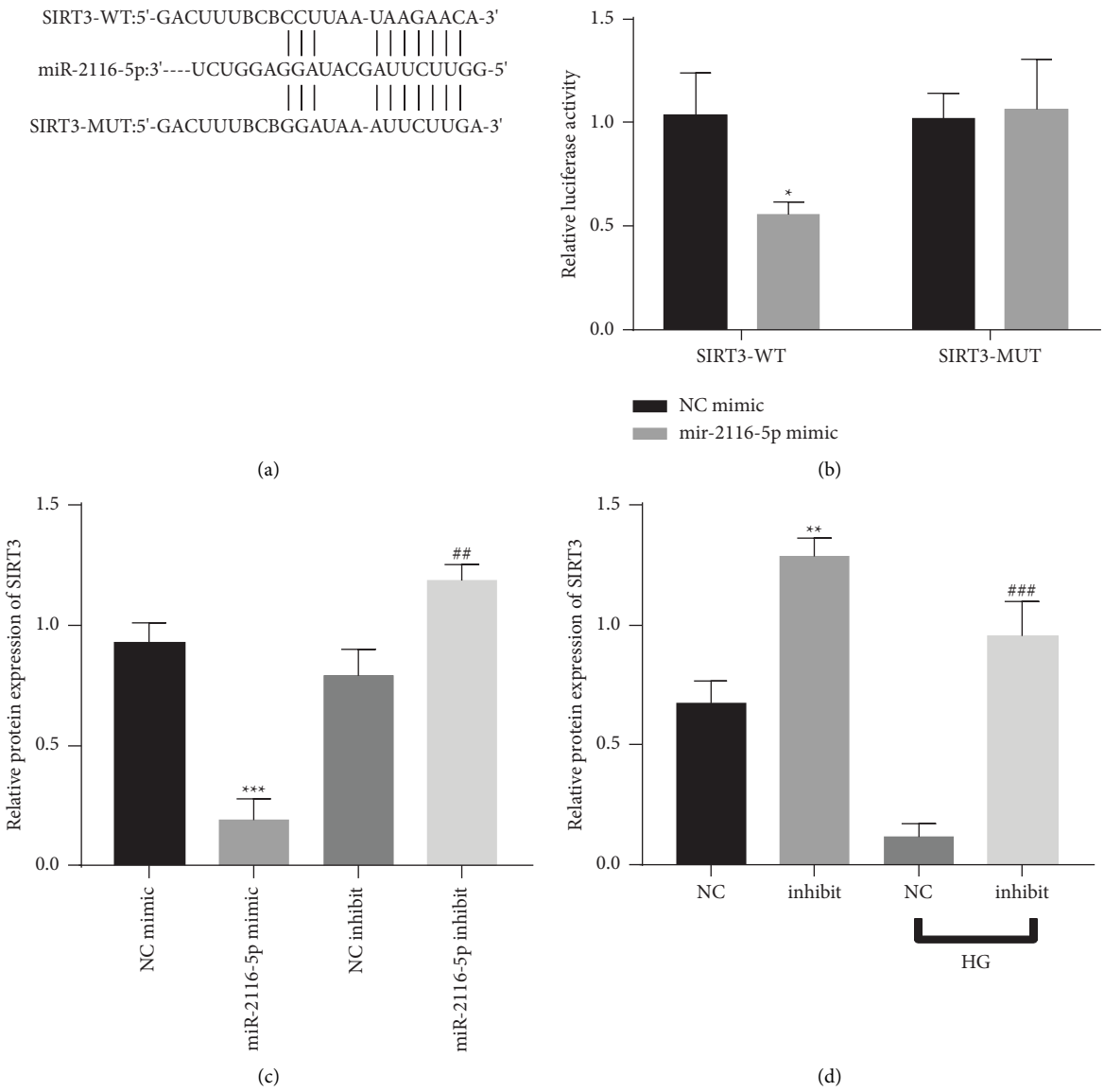

Figure 5: Validation of the relationship between miR-2116-5p and SIRT3. (a): The predicted miR-2116-5p binding sites in SIRT3. (b): Verification of the relationship between miR-2116-5p and SIRT3 by a dual luciferase reporter assay, $^{*}P < 0.05$ compared to the NC mimic group. (c) Analysis of the transfection efficiency of SIRT3 by qRT-PCR, $^{***}P < 0.001$ compared to the NC mimic group; $^{\#\#}P < 0.01$ compared to the NC inhibitor group. (d) The expression of SIRT3 was detected by qRT–PCR. $^{**}P < 0.01$ compared to the NC group; $^{\#\#\#}P < 0.001$ compared to the NC-HG group.

transfection of miR-2116-5p mimic reversed the inhibitory effect of Rg1 on cell proliferation to a certain extent. In addition, compared with the Rg1 + miR-2116-5p mimic group, the Rg1 + miR-2116-5p mimic + pc-DNA SIRT3 group had lower cell proliferation activity (Figure 6(a)). The results of qRT-PCR assay showed that compared with the HG group, Rg1 could inhibit the expression of miR-2116-5p and promote the expression of SIRT3, but this phenomenon was reversed by transfection of miR-2116-5p mimic. Meanwhile, compared with the Rg1+miR-2116-5p mimic group, the expression of miR-2116-5p was down-regulated and the expression of SIRT3 was up-regulated in the Rg1+miR-2116-5p mimic + pc-DNA SIRT3 group (Figures 6(b) and 6(c)). The results of Transwell and angiogenesis assays showed that the inhibitory effect of Rg1 on cell proliferation and angiogenesis could be reversed by transfection of miR-2116-5p mimic, but co-transfection of miR-2116-5p mimic + pc-DNA can maintain the inhibitory effect of Rg1 on cell proliferation and angiogenesis to a certain extent (Figures 6(d) and 6(e)). Similarly, Western blot detection results showed that the promoting effect of Rg1 on SIRT3 expression and the inhibitory effect of VEGF expression were reversed by the transfection of miR-2116-5p mimic, but the transfection of miR-2116-5p mimic + PC-DNA SIRT3 maintained this effect of Rg1 to a certain extent (Figure 6(f)). Thus, these findings demonstrate that Rg1 affects the proliferation, migration, and angiogenesis of HG-induced HRECs via miR-2116-5p/SIRT3.

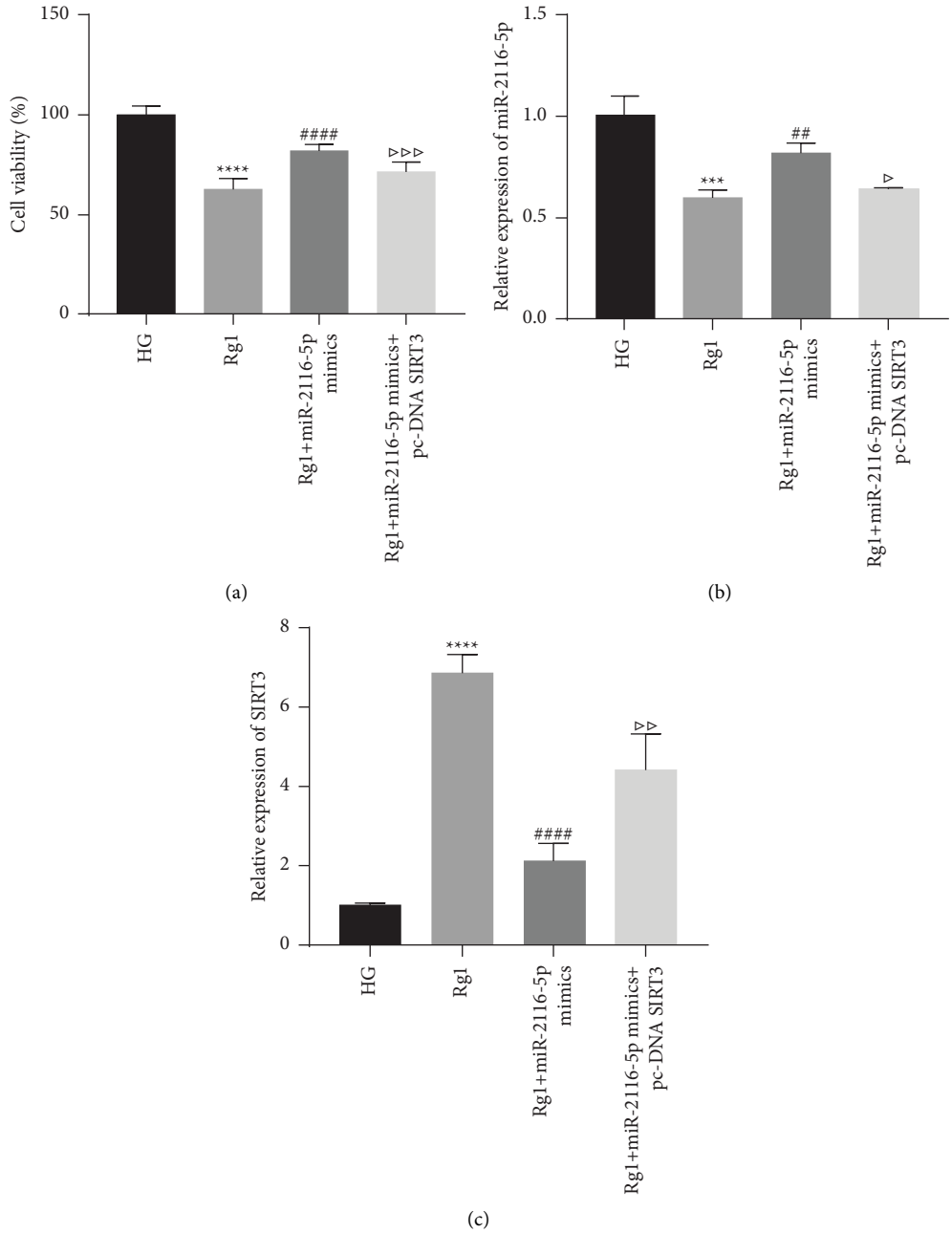

Figure 6: Continued.

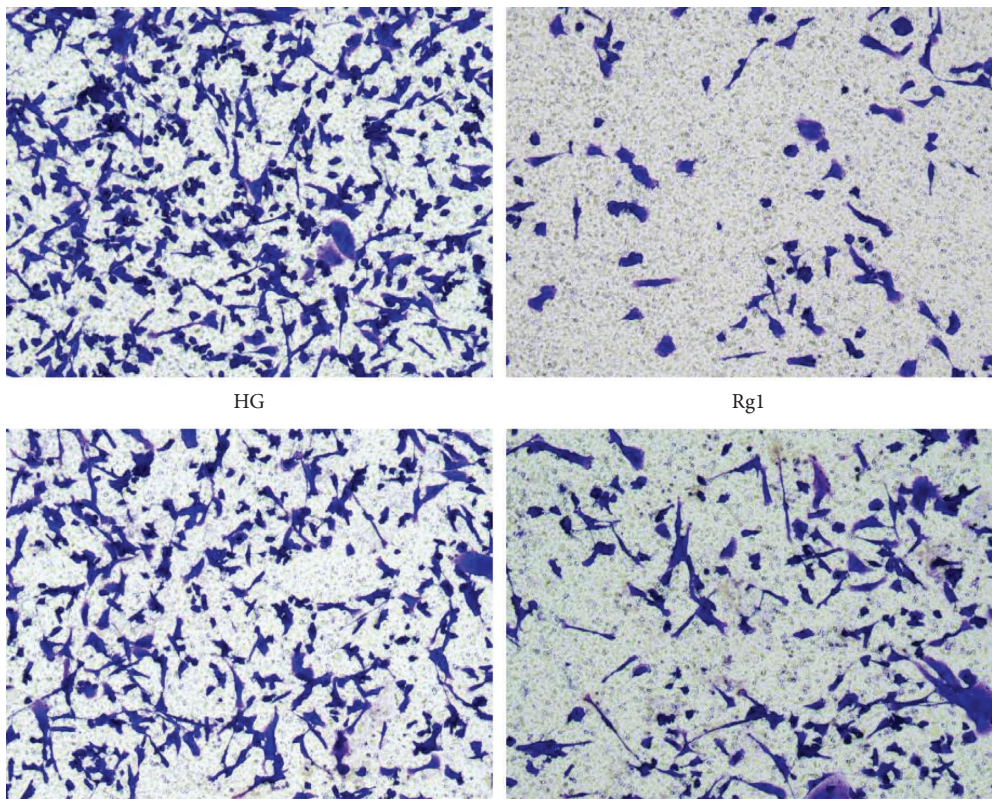

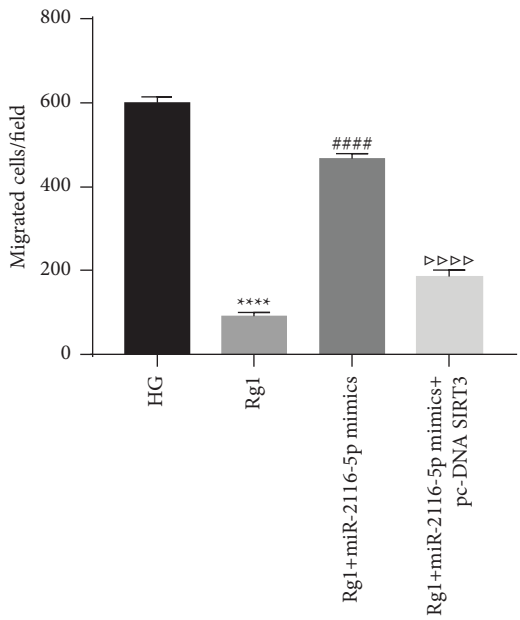

(D)

Figure 6: Continued.

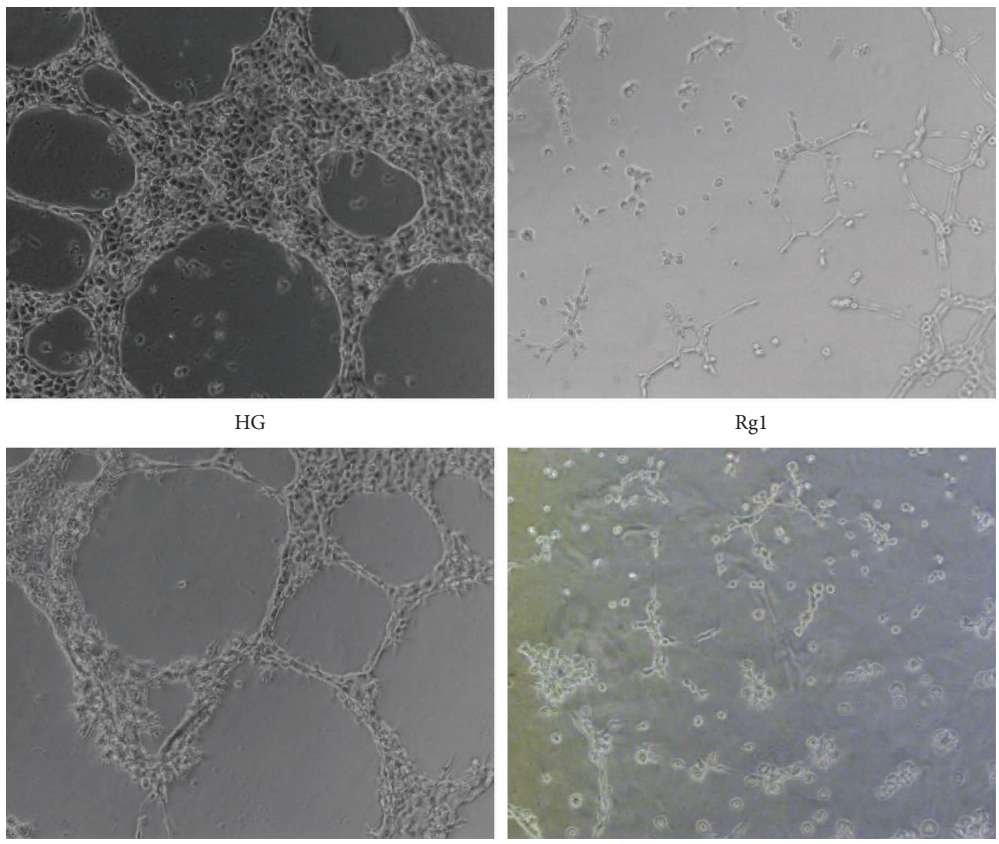

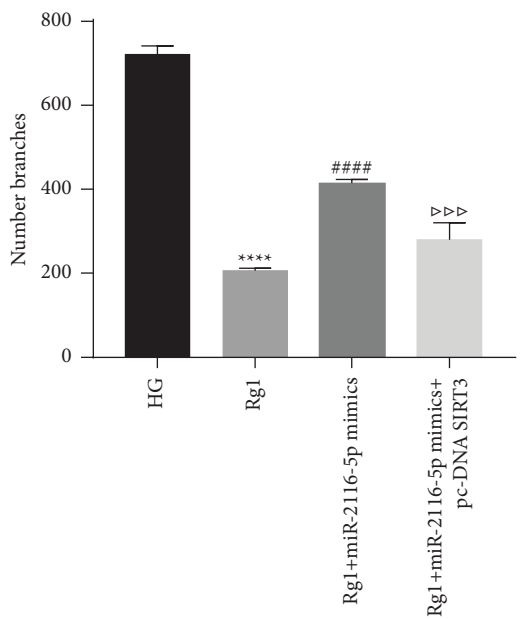

(E)

Figure 6: Continued.

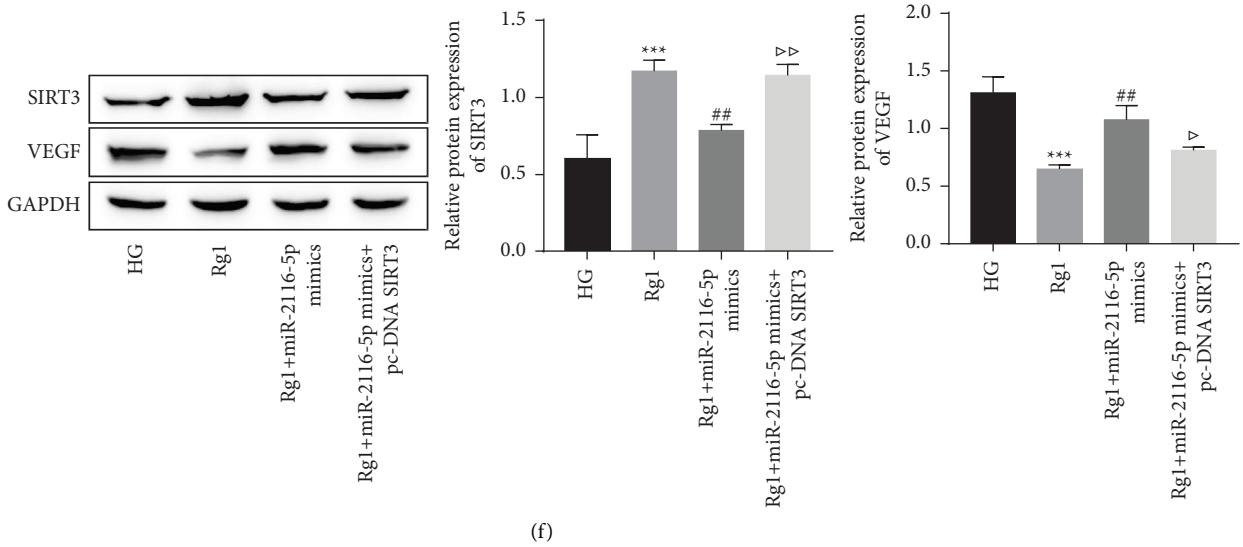

(f)

Figure 6: Rg1 affects the proliferation, migration and angiogenesis of HG-induced HRECs through miR-2116-5p/SIRT3. (a) CCK-8 assay of cell viability. qRT-PCR analysis of miR-2116-5p (b) and SIRT3 (c) expression. (D) Transwell assay of cell migration. (E) Comparison of angiogenesis in different groups. (f) Analysis of the SIRT3 and VEGF protein levels by a western blot analysis. $^{***}P < 0.001$ and $^{****}P < 0.0001$ compared to the HG group; $^{\#\#}P < 0.01$ and $^{\#\#\#\#}P < 0.0001$ compared Rg1 group; $^{\triangle}P < 0.05$, $^{\triangle\triangle}P < 0.01$ and $^{\triangle\triangle\triangle\triangle}P < 0.0001$ compared to the Rg1+miR-2116-5p mimic group.

4. Discussion

Retinopathy caused by diabetes is a serious ocular complication that mainly manifests as retinal endocrine and hematological damage [31]. Hyperglycemia and hyperlipidemia are direct factors in the development of DR [32]. Endothelial cell damage caused by HG is one of the main clinical features of DR; therefore, endothelial cell activity regulation-related molecules are considered to play a key role in the pathogenesis of DR [33]. In diabetes modeling, higher blood glucose concentrations are an important marker of success [34]. During the construction of the diabetes model in this study, we successfully constructed a diabetic rat model because the blood glucose concentration of the rats was higher than 16.7 mmol/L. One month after the onset of diabetes, peripapillary cell degeneration, retinal thickness, and retinal apoptosis were reduced in the diabetic rats [35]. In this study, the pathological features of the retinal tissue in the rats with diabetes mellitus were described, and new blood vessels were observed in the diabetic retina [36]. Moreover, there was a significant increase in cellular angiogenesis in HRECs under HG induction and a significant increase in cell viability and migration. As a key factor in diabetes, Rg1 can protect molecules from damage. In diabetic rats treated with Rg1, cardiomyocyte apoptosis is inhibited, and caspase 3 expression is downregulated [37]. In the present study, Rg1 had a protective effect on the retina of DR rats and HRECs under HG induction. Regarding the gene expression level, Rg1 increased SIRT3 but decreased VEGF in rat retinal tissue and inhibited HRECs proliferation, migration and angiogenesis. It is consistent with the finding by Gao et al. [17] that Rg1 can prevent DR by reducing apoptosis.

The lncRNA SNHG7 was reduced in HRMECs under HG stimulation, and lncRNA SNHG7 overexpression inhibited HG-induced pathological phenomena (cell migration, proliferation and angiogenesis) by regulating the miR-543/SIRT1 axis [20]. Our study also demonstrated that HG conditions downregulated SNHG7 and its inhibitory effect on HG-induced pathological phenomena. There is a targeted binding site between SNHG7 and miR-2116-5p, and the inhibition of miR-2116-5p can effectively attenuate the effect of knockdown of SNHG7 on the proliferation and angiogenesis of RG1 cells. Furthermore, we found that the target of miR-2116-5p is SIRT3. As expected, as a downstream pathway of SNHG7, miR-2116-5p/SIRT3 mediated its protective effect on HRECs, while Rg1 functioned by upregulating SNHG7 to regulate the miR-2116-5p/SIRT3 axis. As a result, these findings show that SIRT3 may play a role in regulating neovascularization [29]. The overexpression of SIRT3 has been shown to inhibit retinal neovascularization under HG and insulin-induced conditions [29]. Our study found that overexpression of SIRT3 could reverse the promoting effect of miR-2116-5p on angiogenesis, which also indicated that SIRT3 could inhibit angiogenesis. In this study, SIRT3 was significantly reduced after the development of DR. VEGF can maintain ocular vascular integrity, and its expression is low and necessary in normal healthy eyes [38]. However, in DR, the levels of VEGF are higher than normal in cells and body fluids. Elevated VEGF levels alter capillary permeability, leading to retinal neovascularization, retinal vascular hemorrhage, exudation and increased angiogenesis and visual impairment. Importantly, inhibiting the expression of VEGF can inhibit the formation of retinal neovascularization [39]. This study shows that in the DR model, VEGF expression was

increased. However, VEGF can be inhibited by SIRT3 overexpression, which may affect the formation of new blood vessels in the retina by regulating VEGF expression to protect against retinal injury.

In summary, the present study investigated the molecular mechanisms related to the alleviation of DR by Rg1. We demonstrated that Rg1 inhibits HG-induced cell proliferation, migration and angiogenesis and VEGF expression in retinal endothelial cells through the lncRNA SNHG7/miR-2116-5p/SIRT3 axis. These findings provide a theoretical basis for the clinical use of Rg1 for the treatment of DR. In addition, our study has the limitation of not verifying our molecular mechanism in vivo experiments. In the next study, we will verify that Rg1 alleviates DR through the lncRNA SNHG7/miR-2116-5p/SIRT3 axis in animal experiments.

Data Availability

The datasets used and/or analyzed during the current study are available from the corresponding author upon reasonable request.

Disclosure

Liping Xue and Min Hu are the co-first authors.

Conflicts of Interest

The authors declare that they have no competing interests.

Authors' Contributions

Liping Xue and Min Hu contributed equally to this work. Liping Xue and Min Hu conceptualized the study; Liping Xue, Min Hu, and Juanjuan Li performed the methodology; Yadi Li and Qin Zhu provided the related software platforms; Guanglong Zhou and Xiaofan Zhang performed validation; Yuan Zhou and Jieying Zhang performed formal analysis; Liping Xue, Min Hu, and Peng Ding investigated the study; Peng Ding and Liping Xue were involved in resource collection; Juanjuan Li, Yadi Li, Qin Zhu, and Guanglong Zhou collected and analyzed the data; Liping Xue, Min Hu, Xiaofan Zhang, Yuan Zhou, and Jieying Zhang drafted the manuscript; Liping Xue, Min Hu, and Peng Ding reviewed the manuscript; Yadi Li and Xiaofan Zhang were involved in visualization; Liping Xue supervised the study; Peng Ding was responsible for funding acquisition. All authors read and agreed to the published version of the manuscript.

Acknowledgments

The study was supported by the Association Foundation Program of Yunnan Provincial Science and Technology Department and Kunming Medical University (grant number 2019FE001(-169) and 202001AY070001-160); The Young and Middle-Aged Technical Academic Leaders Training Project in Yunnan Province (grant number 202005AC160021); famous doctor in Yunling; The Special Grant for High-Level Personnel of Yunnan Province (grant number L-2019020).

References

[1] I. Pearce, R. Simo, M. Lovestam-Adrian, D. T. Wong, and M. Evans, "Association between diabetic eye disease and other complications of diabetes: implications for care. A systematic review," *Diabetes, Obesity and Metabolism*, vol. 21, no. 3, pp. 467–478, 2019.

[2] X. Cao, L. D. Xue, Y. Di, T. Li, Y. J. Tian, and Y. Song, "MSC-derived exosomal lncRNA SNHG7 suppresses endothelial-mesenchymal transition and tube formation in diabetic retinopathy via miR-34a-5p/XBP1 axis," *Life Sciences*, vol. 272, no. 3, Article ID 119232, 2021.

[3] B. L. Mylari, S. J. Armento, D. A. Beebe et al., "A highly selective, non-hydantoin, non-carboxylic acid inhibitor of aldose reductase with potent oral activity in diabetic rat models: 6-(5-chloro-3-methylbenzofuran- 2-sulfonyl)-2-H-pyridazin-3-one," *Journal of Medicinal Chemistry*, vol. 46, no. 12, pp. 2283–2286, 2003.

[4] Q. Xing, G. Zhang, L. Kang et al., "The suppression of kallistatin on high-glucose-induced proliferation of retinal endothelial cells in diabetic retinopathy," *Ophthalmic Research*, vol. 57, no. 3, pp. 141–149, 2016.

[5] A. W. Stitt, T. M. Curtis, M. Chen et al., "The progress in understanding and treatment of diabetic retinopathy," *Progress in Retinal and Eye Research*, vol. 51, no. 1, pp. 156–186, 2016.

[6] W. Wang and A. Lo, "Diabetic retinopathy: pathophysiology and treatments," *International Journal of Molecular Sciences*, vol. 19, no. 6, p. 1816, 2018.

[7] S. Vasant More, I. S. Kim, and D. K. Choi, "Recent update on the role of Chinese material medica and formulations in diabetic retinopathy," *Molecules*, vol. 22, no. 1, p. 76, 2017.

[8] H. W. Zhang, H. Zhang, S. J. Grant, X. Wan, and G. Li, "Single herbal medicine for diabetic retinopathy," *Cochrane Database of Systematic Reviews*, vol. 12, no. 12, Article ID CD007939, 2018.

[9] Z. Y. Wang, J. G. Liu, H. Li, and H. M. Yang, "Pharmacological effects of active components of Chinese herbal medicine in the treatment of alzheimer's disease: a review," *The American Journal of Chinese Medicine*, vol. 44, no. 08, pp. 1525–1541, 2016.

[10] Y. Deng, T. Zhang, F. Teng et al., "Ginsenoside Rg1 and Rb1, in combination with salvianolic acid B, play different roles in myocardial infarction in rats," *Journal of the Chinese Medical Association*, vol. 78, no. 2, pp. 114–120, 2015.

[11] S. H. Kim, K. H. Choi, D. K. Lee et al., "Ginsenoside Rg1 improves In vitro-produced embryo quality by increasing glucose uptake in porcine blastocysts," *Asian-Australasian Journal of Animal Sciences*, vol. 29, no. 8, pp. 1095–1101, 2015.

[12] J. Li, D. Liu, J. Wu et al., "Ginsenoside Rg1 attenuates ultraviolet B-induced glucocortisides resistance in keratinocytes via Nrf2/HDAC2 signalling," *Scientific Reports*, vol. 6, no. 1, p. 39336, 2016.

[13] S. l. Wang, Y. b. Li, Y. Wang, J. p. Tang, and D. Chen, "Neuroprotective effects of ginsenoside Rg1-induced neural stem cell transplantation on hypoxic-ischemic encephalopathy," *Neural regeneration research*, vol. 10, no. 5, pp. 753–759, 2015.

[14] S. Bi, X. Ma, Y. Wang et al., "Protective effect of ginsenoside Rg1 on oxidative damage induced by hydrogen peroxide in

chicken splenic lymphocytes," *Oxidative Medicine and Cellular Longevity*, vol. 2019, no. 14, 13 pages, Article ID 8465030, 2019.

[15] Q. Liu, F. G. Zhang, W. S. Zhang et al., "Ginsenoside Rg1 inhibits glucagon-induced hepatic gluconeogenesis through akt-FoxO1 interaction," *Theranostics*, vol. 7, no. 16, pp. 4001–4012, 2017.

[16] H. Yu, J. Zhen, Y. Yang, J. Gu, S. Wu, and Q. Liu, "Ginsenoside Rg1 ameliorates diabetic cardiomyopathy by inhibiting endoplasmic reticulum stress-induced apoptosis in a streptozotocin-induced diabetes rat model," *Journal of Cellular and Molecular Medicine*, vol. 20, no. 4, pp. 623–631, 2016.

[17] Y. Gao, Y. Ji, Y. Luo, J. Sun, G. Sun, and X. Sun, "Ginsenoside Rg1 prevents early diabetic retinopathy via reducing retinal ganglion cell layer and inner nuclear layer cell apoptosis in db/db mice," *Annals of Translational Medicine*, vol. 8, no. 5, p. 232, 2020.

[18] X. S. Zeng, X. S. Zhou, F. C. Luo et al., "Comparative analysis of the neuroprotective effects of ginsenosides Rg1 and Rb1 extracted from Panax notoginseng against cerebral ischemia," *Canadian Journal of Physiology and Pharmacology*, vol. 92, no. 2, pp. 102–108, 2014.

[19] Q. Gong and G. Su, "Roles of miRNAs and long noncoding RNAs in the progression of diabetic retinopathy," *Bioscience Reports*, vol. 37, no. 6, Article ID BSR20171157, 2017.

[20] N. Ke, L. H. Pi, Q. Liu, and L. Chen, "Long noncoding RNA SNHG7 inhibits high glucose-induced human retinal endothelial cells angiogenesis by regulating miR-543/SIRT1 axis," *Biochemical and Biophysical Research Communications*, vol. 514, no. 2, pp. 503–509, 2019.

[21] K. Mcarthur, B. Feng, Y. Wu, S. Chen, and S. Chakrabarti, "MicroRNA-200b regulates vascular endothelial growth factor–mediated alterations in diabetic retinopathy," *Diabetes*, vol. 60, no. 4, pp. 1314–1323, 2011.

[22] Y. Cao, B. Feng, S. Chen, Y. Chu, and S. Chakrabarti, "Mechanisms of endothelial to mesenchymal transition in the retina in diabetes," *Investigative Opthalmology & Visual Science*, vol. 55, no. 11, pp. 7321–7331, 2014.

[23] H. Ji, Q. Yi, L. Chen et al., "Circulating miR-3197 and miR-2116-5p as novel biomarkers for diabetic retinopathy," *Clinica Chimica Acta*, vol. 501, no. 3, pp. 147–153, 2020.

[24] K. A. Hershberger, A. S. Martin, and M. D. Hirschey, "Role of NAD+ and mitochondrial sirtuins in cardiac and renal diseases," *Nature Reviews Nephrology*, vol. 13, no. 4, pp. 213–225, 2017.

[25] I. Salvatori, C. Valle, A. Ferri, and M. T. Carri, "SIRT3 and mitochondrial metabolism in neurodegenerative diseases," *Neurochemistry International*, vol. 109, no. 4, pp. 184–192, 2017.

[26] S. H. Dai, T. Chen, X. Li et al., "Sirt3 confers protection against neuronal ischemia by inducing autophagy: involvement of the AMPK-mTOR pathway," *Free Radical Biology and Medicine*, vol. 108, no. 8, pp. 345–353, 2017.

[27] S. You, C. Zhong, D. Zheng et al., "Monocyte to HDL cholesterol ratio is associated with discharge and 3-month outcome in patients with acute intracerebral hemorrhage," *Journal of the Neurological Sciences*, vol. 372, no. 372, pp. 157–161, 2017.

[28] J. B. Lin, J. B. Lin, H. C. Chen, T. Chen, and R. S. Apte, "Combined SIRT3 and SIRT5 deletion is associated with inner retinal dysfunction in a mouse model of type 1 diabetes," *Scientific Reports*, vol. 9, no. 1, p. 3799, 2019.

[29] X.-B. Mao, Z. P. You, C. Wu, and J. Huang, "Potential suppression of the high glucose and insulin-induced retinal neovascularization by Sirtuin 3 in the human retinal endothelial cells," *Biochemical and Biophysical Research Communications*, vol. 482, no. 2, pp. 341–345, 2017.

[30] X. B. Mao, Y. h. Cheng, K. s. Peng, and Z. p. You, "Sirtuin (sirt) 3 overexpression prevents retinopathy in streptozotocin-induced diabetic rats," *Medical Science Monitor: International Medical Journal of Experimental and Clinical Research*, vol. 26, no. 9, Article ID e920883, 2020.

[31] R. A. Kowluru, "Diabetic retinopathy, metabolic memory and epigenetic modifications," *Vision Research*, vol. 139, no. 5, pp. 30–38, 2017.

[32] D. A. Antonetti, R. Klein, and T. W. Gardner, "Diabetic retinopathy," *New England Journal of Medicine*, vol. 366, no. 13, pp. 1227–1239, 2012.

[33] J. Lechner, O. E. O'Leary, and A. W. Stitt, "The pathology associated with diabetic retinopathy," *Vision Research*, vol. 139, no. 7, pp. 7–14, 2017.

[34] H. S. Sandhu, N. Eladawi, M. Elmogy et al., "Automated diabetic retinopathy detection using optical coherence tomography angiography: a pilot study," *British Journal of Ophthalmology*, vol. 102, no. 11, pp. 1564–1569, 2018.

[35] A. Maugeri, M. G. Mazzone, F. Giuliano et al., "Curcumin modulates DNA methyltransferase functions in a cellular model of diabetic retinopathy," *Oxidative Medicine and Cellular Longevity*, vol. 2018, no. 2, 12 pages, Article ID 5407482, 2018.

[36] Z. Gurel and N. Sheibani, "O-Linked*β*-*N*-acetylglucosamine (O-GlcNAc) modification: a new pathway to decode pathogenesis of diabetic retinopathy," *Clinical Science*, vol. 132, no. 2, pp. 185–198, 2018.

[37] H. t. Yu, J. Zhen, B. Pang, J. n. Gu, and S. s. Wu, "Ginsenoside Rg1 ameliorates oxidative stress and myocardial apoptosis in streptozotocin-induced diabetic rats," *Journal of Zhejiang University - Science B*, vol. 16, no. 5, pp. 344–354, 2015.

[38] R. Roskoski and Robert, "Vascular endothelial growth factor (VEGF) and VEGF receptor inhibitors in the treatment of renal cell carcinomas," *Pharmacological Research*, vol. 120, no. 7, pp. 116–132, 2017.

[39] R. Gonzalez-Salinas, M. C. Garcia-Gutierrez, G. Garcia-Aguirre et al., "Evaluation of VEGF gene polymorphisms and proliferative diabetic retinopathy in Mexican population," *International Journal of Ophthalmology*, vol. 10, no. 1, pp. 135–139, 2017.

Hindawi
Journal of Oncology
Volume 2022, Article ID 3623570, 16 pages
https://doi.org/10.1155/2022/3623570

Research Article

ANGPTL4 Regulates Lung Adenocarcinoma Pyroptosis and Apoptosis via NLRP3\ASC\Caspase 8 Signaling Pathway to Promote Resistance to Gefitinib

Yue Fang,[1,2] Xuan Li,[1] Hao Cheng,[1] Lu Zhang,[1] and Jiqing Hao[1]

[1]*The First Affiliated Hospital of Anhui Medical University, Hefei 230022, Anhui, China*
[2]*Hefei Cancer Hospital, Chinese Academy of Sciences, Hefei 230022, Anhui, China*

Correspondence should be addressed to Jiqing Hao; haojiqing@ahmu.edu.cn

Received 11 August 2022; Revised 2 September 2022; Accepted 12 September 2022; Published 25 November 2022

Academic Editor: Recep Liman

Background. Prior research has identified ANGPTL4 as a key player in the control of the body's lipid and glucose metabolism and a contributor to the onset of numerous cardiovascular conditions. Recently, it has been shown that ANGPTL4 also plays a critical role in tumor growth and progression. Nowadays, the number of EGFR-TKI resistant patients is increasing, and it is important to investigate the role of ANGPTL4 in regulating gefitinib resistance in PC9/GR non-small-cell lung cancer (NSCLC). *Methods*. The expression of ANGPTL4 in A549, PC9, H1975, BEAS-2B and PC9/GR cells was verified by Western blot and qRT-PCR assays, and the effect of gefitinib on the proliferative ability of each cell was probed by CCK-8 assay. By using shRNA to inhibit ANGPTL4 expression in cells, the effect of ANGPTL4 on cell migratory ability was examined and the effect of ANGPTL4 on cellular gefitinib sensitivity was confirmed using the CCK-8 assay and the edu proliferation test. Mouse transplantation tumors were constructed, and the effect of ANGPTL4 on cellular gefitinib sensitivity was investigated in vivo by flow cytometry, Tunel staining assay, immunohistochemical staining, and ROS fluorescence staining assay. ANGPTL4 expression in homoRNA overexpression cells was constructed, and the changes in the expression levels of ASC\NLRP3\Caspase 8 pathway and focal and apoptotic proteins were investigated in vitro, in vivo, afterknockdown and overexpression of ANGPTL4 expression by Westen blot assay. *Results*. ANGPTL4 was highly expressed in PC9/GR cells. Interfering with ANGPTL4 expression resulted in decreased proliferation and migration ability, decreased resistance to gefitinib, and increased scorching and apoptosis in PC9/GR cells. Interfering with ANGPTL4 expression in PC9/GR cells was shown to promote sensitivity to gefitinib and to mediate the NLRP3/ASC/Caspase 8 pathway to induce cell scorching and apoptosis. *Conclusions*. ANGPTL4 promotes gefitinib resistance in PC9/GR cells by regulating the NLRP3/ASC/Caspase 8 pathway to inhibit scorch death. ANGPTL4 may be an effective new target for inhibiting EGFR-TKI resistance in lung adenocarcinoma cells.

1. Background

For many years, lung cancer has been one of the most common malignant tumours worldwide, accounting for approximately 21% of the incidence and 27% of the mortality of all cancers. Approximately 49 of every 100,000 people in China die of lung cancer [1, 2]. Non-small-cell lung cancer accounts for approximately 85% of the total lung cancer cases and is associated with a five-year survival rate of only 15% in China [3]. Non-small-cell lung cancer shows heterogeneity. Mutations in multiple genes, including epidermal growth factor receptor (*EGFR*), anaplastic lymphoma kinase (*ALK*), *ROS1*, and *KRAS*, can promote the progression of this cancer. EGFR mutation is the most common gene mutation among patients with non-small-cell lung cancer and occurs in 50%–60% of Asian patients; most patients with these mutations have a low survival rate [4]. Treatment with EGFR-tyrosine kinase inhibitors (TKIs) is associated with progression-free survival (PFS) of 10–14 months in patients with EGFR-positive mutations [5].

Adenosine triphosphate cannot bind to the tyrosine kinase region of the intracellular domain of EGFR when used in combination with the first-generation EGFR-TKI

medication gefitinib. This prevents the receptor from being phosphorylated [6]. Meta-analyses have shown that using gefitinib as a first-line treatment can improve the PFS of these patients, whereas combined chemotherapy and anti-angiogenesis therapy can improve prognosis [7–9]. However, some patients show acquired drug resistance after 9–14 months of treatment, which affects the overall survival (OS) rate of patients [10].

Angiopoietin-like 4 (ANGPTL4) is widely present in the liver and adipose tissue and can regulate the activity of lipoprotein lipase by regulating the nutritional status of the body to regulate lipid metabolism [11]. Because of its important role in lipid metabolism, ANGPTL4 was once considered a regulator of lipid metabolism, but, in recent years, studies have found that ANGPTL4 is closely related to the proliferation and metastasis of a variety of malignant tumours. For instance, Zhu et al. [12] discovered that ANGPTL4 is substantially expressed in non-small-cell lung cancer tissues and is linked to the advancement of the malignancy and a poor prognosis. Furthermore, Gong et al. [13] found that ANGPTL4 promotes the occurrence of brain metastasis of breast cancer through the TGF-β2/ANGPTL4 axis. In addition, some researchers believe ANGPTL4 is closely related to the prognosis of malignant tumours, such as thyroid, cervical, and pancreatic cancer [14, 15]. Zhou et al. found high expression of ANGPTL4 in ovarian cancer cells and a positive correlation with secondary resistance to carboplatin [16], suggesting that ANGPTL4 may be associated with secondary resistance in the treatment of tumour patients. However, to the best of our knowledge, there have been no studies on the mechanism of acquired EGFR-TKI resistance in relation to ANGPTL4 in lung adenocarcinoma cells, and it remains unknown whether ANGPTL4 is involved in EGFR-TKI resistance.

By examining the characteristics of gefitinib-resistant PC9/GR cells in nonsmall cell lung cancer cells, we investigated the function and mechanism of ANGPTL4 in the process of acquiring drug resistance in lung adenocarcinoma in the current study. The results confirm that ANGPTL4 promotes the development of resistance to EGFR-TKIs in lung adenocarcinoma cells and that ANGPTL4 may be a potential target for overcoming resistance to EGFR-TKIs.

2. Method

2.1. Cells and Culture Conditions. The PC9, A549, H1945 (lung adenocarcinoma cells, Beijing Cell Bank, Beijing, China), BEAS-2B (bronchial epithelial cells, Beijing Cell Bank), and PC9/GR (gefitinib-resistant lung adenocarcinoma cells, Cell Center of Central South University, Changsha, China) cells were cultured in Dulbecco's modified Eagle medium supplemented with 10% foetal bovine serum and 1% penicillin-streptomycin solution. The PC9/GR cell culture medium was supplemented with 1 μmol/L gefitinib to maintain cell resistance. Cells were cultured at 37°C with 5% CO_2 in cell incubators. The medium was changed every 24 h, and a passage was conducted every 48 h. Cells were cryopreserved or resuscitated as required.

2.2. Short Hairpin (sh)RNA Transfection. ANGPTL4 expression was interfered with by transfecting shRNA into cells. Three shRNAs were purchased from Jikai Gene (Shanghai, China). The shRNA sequences were as follows: ANGPTL4-shRNA1, CCACAAGCACCTAGACCAT; ANGPTL4-shRNA2, ACAGCAGGATCCAGCAACT; ANGPTL4-shRNA3, ATCTTGGA AACTTGTGGACA. The control group was transfected with an empty vector (NC-shRNA)—the sequence was TTCTCCGAACGTGTCACGT. The PC9/GR cells were evenly spread into a six-well plate, with approximately 1×10^5 cells/well, and incubated at 37°C for 16–24 h. When the cell fusion degree reached 70–80%, we configured the lip3000-shRNA liposome complex by allowing the Lipofectamine 3000 reagent to react with shRNA at 25°C for 20 min and added this to each well. The transfected cells were cultured for 12 h, and the medium was changed. After 48 h, fluorescence was observed under an inverted fluorescence microscope (Thermo Fisher Scientific, Shanghai, China). After 48–72 h of transfection, the efficiency was detected based on mRNA and protein expression using quantitative reverse transcription-polymerase chain reaction (qRT-PCR) and western blotting.

HomoRNA was used to increase the expression level of ANGPTL4. The former, the sequence of which was TCC AGGTTGGGGAGAGGCAGAGTGGACTAT, was purchased from Wanlei Biotechnology (Shenyang, China). The Lipofectamine 3000-homoRNA liposome complex was configured as described in the previous section to transfect PC9/GR cells, and the transfection efficiency was evaluated using western blotting.

2.3. qRT-PCR. Cellular mRNA or mouse tumor total RNA was extracted using the RNAeasy Animal RNA Extraction Kit (Beyotime, Shanghai, China). Then, we used the PrimeScript One-step RT-PCR Kit (Takara, Kyoto, Japan) to reverse transcribe mRNA into cDNA, which was subjected to PCR using LightCycler96 PCR (Roche, Basel, Switzerland) and the TB Green Premix Ex Taq II Kit (Takara). Using glyceraldehyde 3-phosphate dehydrogenase as an internal reference, the gene expression level was calculated according to formula $2^{-\Delta\Delta CT}$. The names and sequences of the primers used in the experiment are shown in Table 1.

2.4. Western Blot. We gently rinsed the cells in the six-well plate with phosphate-buffered saline (PBS) and added 200–300 μL of preconfigured radioimmunoprecipitation assay buffer and phenylmethylsulfonyl fluoride (99 : 1) cell lysate to each well. After completing cell lysis, the sample was centrifuged at 4°C (12,000 × g, 10 min). Then, we added 5× loading buffer ($1/5^{th}$ of the supernatant volume) and placed the tube containing this mixture in a 100°C water bath for 10 min. After 10% SDS-PAGE, the bands were transferred to a polyvinylidene fluoride membrane and incubated with specific antibodies against ANGPTL4 (1 : 1000), NOD-like receptor thermal protein domain associated protein 3 (NLRP3, 1 : 2000), B-cell lymphoma 2 (BCL-2, 1 : 2000), apoptosis-associatedspeck-like protein containing CARD (ASC, 1 : 1000), cellular FLICE-like inhibitory protein

Table 1: qRT-PCR primer names and sequences.

Primers	Primer sequences (5′-3′)
ANGPTL4	F: GTCCACCGACCTCCCGTTA R: CCTCATGGTCTAGGTGCTTGT
GAPDH	F: GGAGCGAGATCCCTCCAAAAT R: GGCTGTTGTCATACTTCTCATGG

(cFLIPL, 1 : 2000), caspase-8 (1 : 1500), cleaved caspase-8 (1 : 1500), and β-actin (1 : 2000) (Abcam, Cambridge, MA, USA). The next day, after incubation with IgG (H&L)-HRP antibody (1 : 5000), the bands were visualised on an integrated chemiluminescence imager helped by an enhanced chemiluminescence exposure solution.

2.5. Cell Viability Assay. Cells were spread evenly on a 96-well plate (3×10^4 cells/well). After culturing for 24 h, the cells were switched to a 5% serum medium containing different concentrations of gefitinib (0.01, 0.5, 1, 2, 4, 8, 16, 32, and 100 μmol/L) and 10 μL of CCK-8 solution was added to each well after 48 h. The absorbance was measured at 570 nm after incubation for 2 h. Cell survival rate was calculated as follows: cell survival rate (%) = ((administration group X − negative control group X)/(nonadministration group X − negative control group X)) × 100.

2.6. Transwell. A 12-well plate was used to construct a small chamber model; the cells were spread in the upper chamber (6×10^4 cells/well) with 200 μL/well medium, and 400 μL/well medium was added to the lower chamber. After culturing for 24 h, we gently wiped away the remaining cells from the upper chamber and placed the lower chamber in a 4% paraformaldehyde solution for 30 min; after subjecting the cells to 0.4% crystal violet staining, we used a microscope to observe the cells, as well as to count them in three randomly selected fields/well.

2.7. Apoptosis Detection by Flow Cytometry. The stabilised PC9/GR cells were plated into a six-well plate (4×10^5 cells/well), and the cells were cultured for 48 h in a medium containing different concentrations of gefitinib (0.5 and 8 μmol/L). After digestion and centrifugation (500 × g, 5 min), the cell density was adjusted to 1×10^6/mL, and the apoptosis level was measured using flow cytometry (FACScan, Shanghai, China) with an Annexin-VFITC/PI Apoptosis Kit (Univ, Shanghai, China).

2.8. EDU Cell Proliferation Assay. After adjusting the cell status, we transferred the cells in the logarithmic phase into a six-well plate (4×10^6 cells/well). When cell confluence reached 70%, we added prewarmed EdU staining solution (a final concentration of 10 μM/L) to each group of cells. After incubating for 3 h, we fixed them with 4% paraformaldehyde for 20 min at 25°C. Subsequently, we washed them twice with PBS, added 0.1 mL of 0.5% Triton X-100 (Thermo Fisher Scientific, Shanghai, China) in PBS to each well, incubated them at 25°C for 20 min, washed them twice, added Click-iT (Thermo Fisher Scientific) to the reaction solution, incubated them at 25°C for 30 min in the dark, washed the cells twice, and treated them with diluted Hoechst 33342 staining solution (1 : 2000; Thermo Fisher Scientific) for 15 min. After staining, the cells were washed twice again with PBS and photographed under a fluorescence microscope.

2.9. Nude Mouse Xenograft Model. Six-week-old BALB/c nude female mice, purchased from Beijing Vitalriver Experimental Animal Technology, were randomly divided into three groups (8 mice in each group, $n = 24$). PC-9/GR cells, Sh-NC PC-9/GR cells, and Sh-ANGPTL4 PC9/GR cells mixed with an equal number of Matrigel-9/GR cells (1×10^6) were injected subcutaneously into the left side of the mouse to construct a nude xenograft mouse model (100 μL each). All mice were fed in a specific pathogen-free animal room. When the tumor was palpable, the volume of the subcutaneously transplanted tumor was measured and recorded daily. As the tumour volume reached 50 mm^3 (calculation for volume: long diameter × short diameter × short diameter/2), the ANGPTL4-shRNA components were divided into two groups: *A* and *B*. To assess the survival rate of nude mice, the control group, NC-shRNA group, and ANGPTL4-shRNA A group were orally administered 150 mg of gefitinib/day for treatment, and the ANGPTL4-shRNA B group was orally administered an equal volume of PBS. The mice were weighed and photographed every 3 days, and the body weight curve was drawn. After 21 days of oral administration, all mice were euthanised and the tumour tissues were excised and photographed; in addition, the long diameter, short diameter, and tumor volume were calculated, and the weight of the tumour was measured. All animal experiments were conducted according to the institutional guidelines of the Animal Care and Use Committee of the First Affiliated Hospital of Anhui University.

2.10. Immunohistochemistry. Slices of the tissue embedded in wax were sequentially placed in xylene I and II; absolute ethanol I and II; 95%, 85%, and 75% ethanol; and distilled water. Subsequently, they were soaked in PBS and wiped dry. Slices were incubated in 3% H_2O_2 for 15 min at 25°C and soaked in PBS for 5 min three times. They were incubated in 1% BSA at 25°C for 15 min and a mixture of antibodies (1 : 50) overnight in a humid environment. On the next day, we washed them twice with PBS (7 min/wash). The IgG (H&L)-HRP antibody (1 : 500) was added dropwise to the tissue,

which was subsequently placed in a humid environment for 1 h. After the reaction, the cells were washed with PBS for 10 min. After washing, DAB staining solution and haematoxylin counterstaining were performed. The counterstained sections were dehydrated and sealed with neutral gum. The sections were observed under a microscope and photographed.

2.11. Detection of Apoptosis by Tunel Assay. After deparaffinisation of the tissue sections, 45 μL of 0.1% Triton X-100 was added to them dropwise. The sections were then placed at 25°C for 7 min and washed with PBS. Subsequently, they were treated with 50 μL of preconfigured terminal deoxynucleotidyl transferase-mediated reaction solution of dUTP-biotin nick end labelling (TUNEL) (enzyme solution: label solution = 1 : 9) for 1 h, washed with PBS, counterstained with 4′,6-diamidino-2-phenylindole, and incubated in the dark for 4 min. The residual reagent was washed away with PBS, and the fluorescent quencher was added dropwise to mount the slide. The sections were examined and photographed using an inverted fluorescence microscope.

2.12. ROS Fluorescence Staining. After the frozen portions had dried, the tissue was circled with a histochemical pen. 400 μl of ROS staining solution (Servicebio G1045) was added dropwise to the circles and incubated for 30 min at 37°C in the dark. The slides were washed three times for 6 min each time by shaking in PBS on a decolorizing shaker.

The slides were slightly shaken and dried; then, DAPI staining solution was added dropwise in a circle and incubated at room temperature for 10 min in the dark. The slides were then soaked in PBS and washed 3 times with shaking on a decolorizing shaker for 5 min each time. The slices were slightly shaken and then sealed with an anti-fluorescence quenching sealer. Slices were observed under a fluorescence microscope, and images were acquired (emission wavelength 515–555 nm).

2.13. Statistics. All experiments in this study were repeated three times. GraphPad Prism software (version 7.0) (GraphPad Software, Beijing, China) was used to generate graphs, and SPSS 22.0 (IBM, Armonk, New York, NY, USA) was used for the statistical analysis of the data. The experimental data are expressed as mean ± standard deviation ($\overline{x} \pm s$). We used the t-test for comparisons between groups and a one-way analysis of variance for comparison among multiple groups. The threshold of statistical significance was set at $p < 0.05$.

3. Results

3.1. ANGPTL4 Is Highly Expressed in PC9 and PC9/GR Cells. To explore ANGPTL4 expression in A549, PC9, H1975, and BEAS-2B cell lines, we performed qRT-PCR and western blotting. ANGPTL4 expression was very low in BEAS-2B cells but high in A549, PC9, and H1975 cells ($p < 0.05$); mRNA expression in PC9 cells was higher than that in A549 and H1975 cells ($p < 0.05$, Figures 1(a) and 1(b)). Therefore, the PC9 gefitinib-resistant cells and PC9 cells were cultured for subsequent experiments.

Furthermore, ANGPTL4 mRNA and protein expression in PC9 and PC9/GR cells was analysed, and it was found that ANGPTL4 expression in PC9/GR cells was significantly higher than that in PC9 cells ($p < 0.05$; Figures 1(c) and 1(d)).

3.2. ANGPTL4 Is Associated with Resistance to Gefitinib in Lung Adenocarcinoma Cells. The effect of different concentrations of gefitinib on the cell viability of A549, PC9, H1975, and BEAS-2B cells was investigated by CCK-8 assay. The IC50 of A549, PC9, H1975, and BEAS-2B cells was 2.44 ± 0.36, 2.93 ± 0.27, 2.23 ± 0.43 and 1.35 ± 0.51 μmol/l, respectively, with the IC50 of PC9 cells being significantly higher than the other three groups (Figures 2(a) and 2(b), $p < 0.05$).

Then, we transfected PC9/GR cells with shRNA and performed western blotting and qRT-PCR to verify the knockdown effect. We found that both shRNA1 and shRNA3 had a stable knockdown effect ($p < 0.01$) and that the knockdown effect of shRNA3 was more evident than that of shRNA1 (Figures 2(c) and 2(d)).

In subsequent experiments, shRNA3 was used to knock down ANGPTL4. Cell viability studies on PC9, PC9/GR, NC-shRNA, and ANGPTL4-shRNA3 cells revealed the IC_{50} values of the PC9 group (2.597 ± 0.154 μmol/L) and ANGPTL4-shRNA3 group (2.817 ± 0.245 μmol/L) were lower than those of the PC9/GR group (20.73 ± 0.25 μmol/L; both, $p < 0.001$) and NC-shRNA (20.71 ± 0.592 μmol/L; $p > 0.05$; Figures 2(e) and 2(f)).

3.3. ANGPTL4 Correlates with the Level of Invasion and Apoptosis of PC9/GR Cells. The results of the Transwell assay and scratch assay showed (Figures 3(a) and 3(b)) that increasing gefitinib concentration could inhibit PC9/GR cell invasion and migration, but the effect was lower than interfering with ANGPTL4 expression, and knocking down ANGPTL4 while increasing gefitinib drug induction could further inhibit PC9/GR cell invasion and migration ability. The results of flow cytometry and Edu proliferation assays showed that the knockdown of ANGPTL4 expression inhibited PC9/GR cell proliferation and promoted apoptosis (Figures 3(c) and 3(d)), while knockdown of ANGPTL4 expression significantly inhibited PC9/GR cell proliferation and promoted apoptosis under gefitinib induction. The above experimental results showed that ANGPTL4 positively correlated with the invasive migration and proliferation viability of PC9/GR cells, while negatively correlated with the apoptosis level.

3.4. Interference with ANGPTL4 Expression In Vivo can Inhibit Tumour Progression. To further understand the effect of ANGPTL4 on the acquired resistance of gefitinib, we used PC9/GR and ANGPTL4-shRNA cells to construct a nude xenograft mouse model (Figures 4(a) and 4(b)). Under the same treatment with gefitinib, the growth rate and weight of

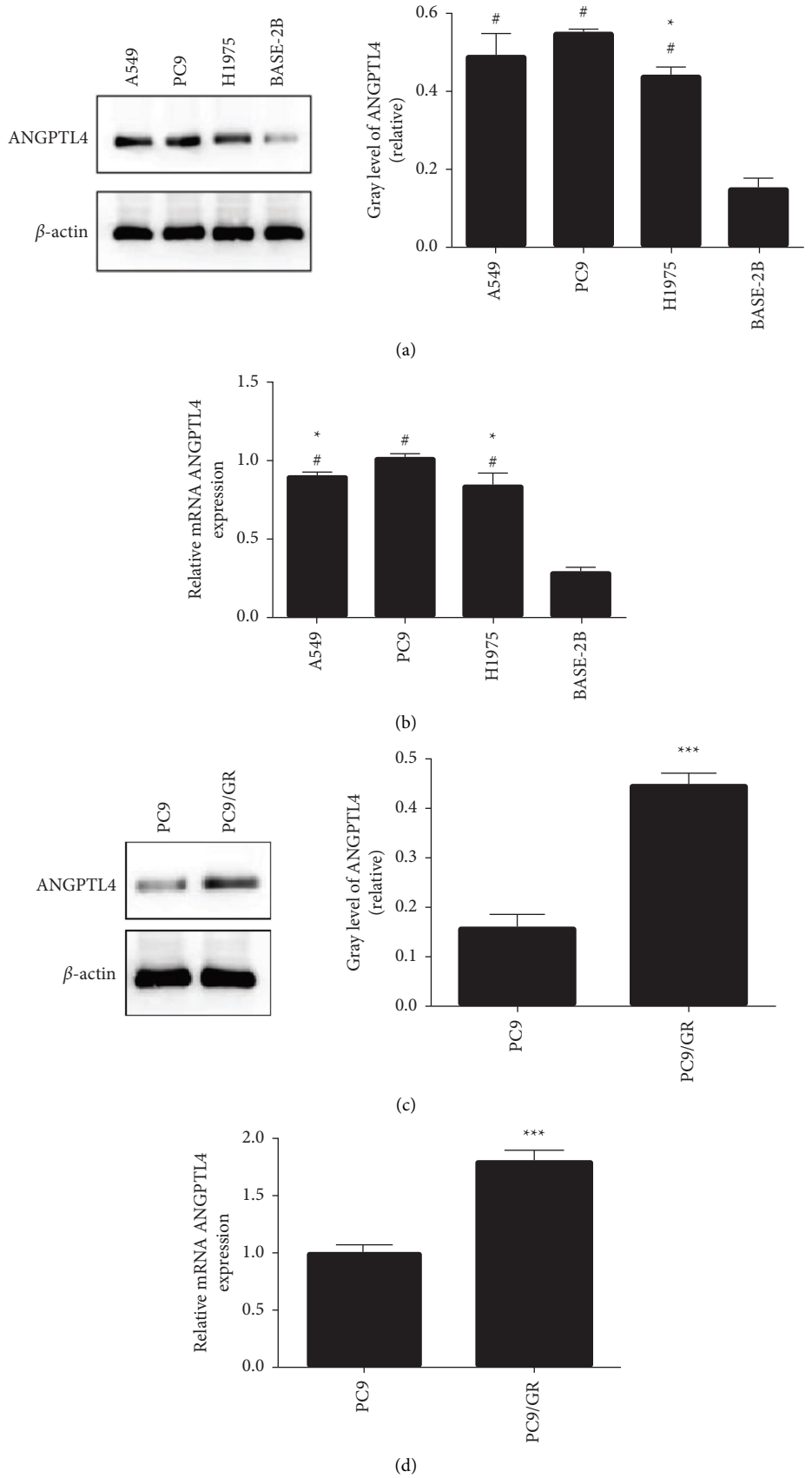

Figure 1: ANGPTL4 expression in A549, PC9, BEAS-2B, and PC9/GR cells ($\overline{x} \pm s$, $n = 3$). (a, b) ANGPTL4 protein and mRNA expression in A549, PC9, and BEAS-2B cells; (c) CCK-8 test revealed the IC_{50} in A549, PC9, and BEAS-2B cells; (c, d) ANGPTL4 protein and mRNA expression in PC9 and PC9/GR cells. $^{\#}p < 0.001$ compared to the BEAS-2B group; *, **, and $^{***}p < 0.05$, 0.01, and 0.001, respectively, compared to the PC9 cell group.

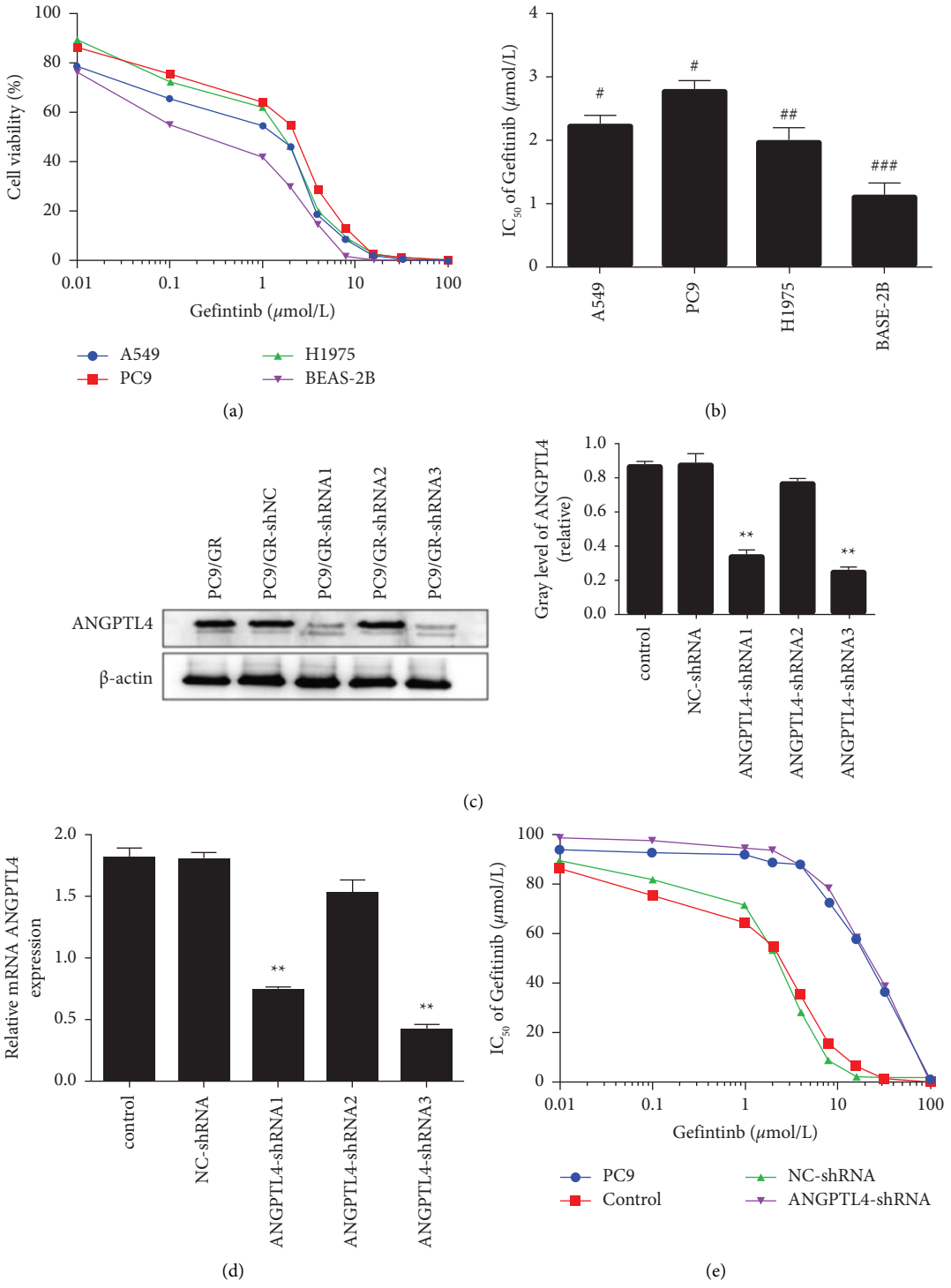

Figure 2: Continued.

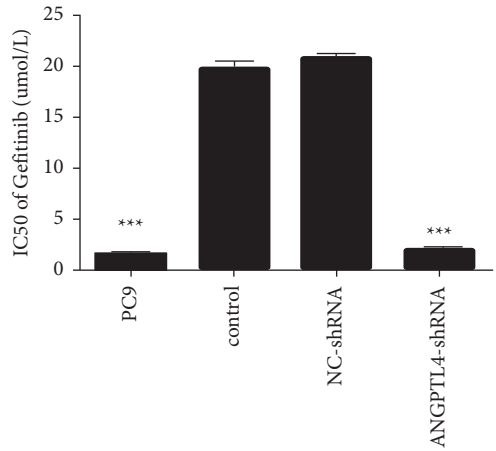

(f)

Figure 2: Knockdown with ANGPTL4 expression reduces the resistance of PC9/GR to gefitinib ($\overline{x} \pm s$, $n = 3$). (a, b) The CCK-8 test revealed the cell viability and IC_{50} of gefitinib in A549, PC9, H1975, and BEAS-2B cells. (c, d) ANGPTL4 protein and mRNA expression in PC9/GR cells after transfection with ANGPTL4-shRNA and NC-shRNA. (e, f) CCK-8 test revealed the cell viability and IC_{50} of gefitinib in PC9/GR cells after ANGPTL4 knockdown. Control: blank control group; NC-shRNA: PC9/GR cells transfected with NC-shRNA; G: PC9/GR cells + gefitinib; ANGPTL4-shRNA: PC9/GR cells transfected with ANGPTL4-shRNA; ANGPTL4-shRNA + G: PC9/GR cells transfected with ANGPTL4-shRNA + gefitinib. *, **, and ***: $p < 0.05$, 0.01, and 0.001, respectively, compared to the control group; $^{\#}$, $^{\#\#}$ and $^{\#\#\#}$: $p < 0.05$, 0.01, and 0.001, respectively, compared to the PC9 group.

the tumor in the ANGPTL4-shRNA + G group were lower than those in the control + G group ($p < 0.05$, Figures 4(d) and 4(e)). However, there was no significant difference in the body weights of the mice in each group (Figure 4(c)).

The TUNEL assay revealed that knockdown with ANGPTL4 expression increased the level of apoptosis ($p < 0.001$, Figure 5(a)). Furthermore, it showed that the apoptotic level of the ANGPTL4-shRNA group was higher than that of the control + G group ($p < 0.001$, Figure 5(d)). This suggests that ANGPTL4 is better than gefitinib for the regulation of apoptosis in vivo. Furthermore, immunohistochemical staining showed that Ki-67 levels in transplanted tumour tissue from the ANGPTL4-shRNA and ANGPTL4-shRNA + G groups were lower than those in the control + G group (both, $p < 0.001$), which suggests that ANGPTL4 promotes tumor proliferation in vivo (Figure 5(b)). Together, the inhibition of ANGPTL4 expression can inhibit tumor growth and proliferation.

The results of the ROS fluorescence staining experiment also showed that gefitinib treatment combined with reduction of ANGPTL4 increased the degree of ROS expression in PC9/GR cells.

3.5. ANGPTL4 Inhibits Pyroptosis and Apoptosis by Regulating the NLRP3\ASC\Caspase 8 Pathway. To explore the specific mechanism by which lung adenocarcinoma cells acquire gefitinib resistance, the expression levels of the pyroptosis-related proteins ACS, NLRP3, cFLIPL, and Caspase 8 in ANGPTL4 knockdown were detected by western blotting. In ANGPTL4-knockdown cells, NLRP3, ACS and cleaved-caspase 8 expression decreased and increased, respectively ($p < 0.001$, Figure 6(a)). In contrast, the expression levels of cFLIPL in ANGPTL4-knockdown cells were increased and decreased, respectively ($p < 0.001$, Figure 6(a)).

Since both in vivo and ex vivo research demonstrated that cells' levels of apoptosis rose after being knocked down with ANGPTL4, we also looked at the expression of proteins linked to apoptosis in the knockdown cells. After the knockdown of ANGPTL4, the expression of inhibitory proteins, such as Bcl-2, decreased significantly ($p < 0.05$, Figure 6(b)).

To confirm that ANGPTL4 can regulate the occurrence of pyroptosis and apoptosis through the NLRP3\ASC\-Caspase 8 pathway, we used tissue proteins from the xenograft tumor to re-verify the results. Under the conditions of drug treatment and culture, in nude mice treated with ANGPTL4-shRNA cells, ASC, NLRP3, and cleaved-caspase 8 expression was higher than that in the control group and Bcl-2 and cFLIPL expression was lower than that in the control group ($p < 0.05$, Figures 6(c) and 6(d)). Collectively, ANGPTL4 inhibits lung adenocarcinoma cell pyroptosis and apoptosis by regulating the NLRP3\ASC\Caspase 8 pathway both in vivo and in vitro.

4. Discussion

More and more specialized medications have been created as targeted lung cancer therapy research has progressed. The most frequent location of mutation among the several targets is EGFR [4]. Currently, EGFR-TKIs have been developed to the fourth generation, while the first-generation drugs, represented by gefitinib, are still widely used in Asia and other regions for their high therapeutic effectiveness and low side effects [6, 17]. However, the issue regarding the secondary resistance to EGFR-TKIs in lung adenocarcinoma patients has still not been adequately addressed. In our previous study, we found high expression of ANGPTL4 in PC9/GR cells [18], suggesting that ANGPTL4 may be one of the potential targets for gefitinib resistance in lung

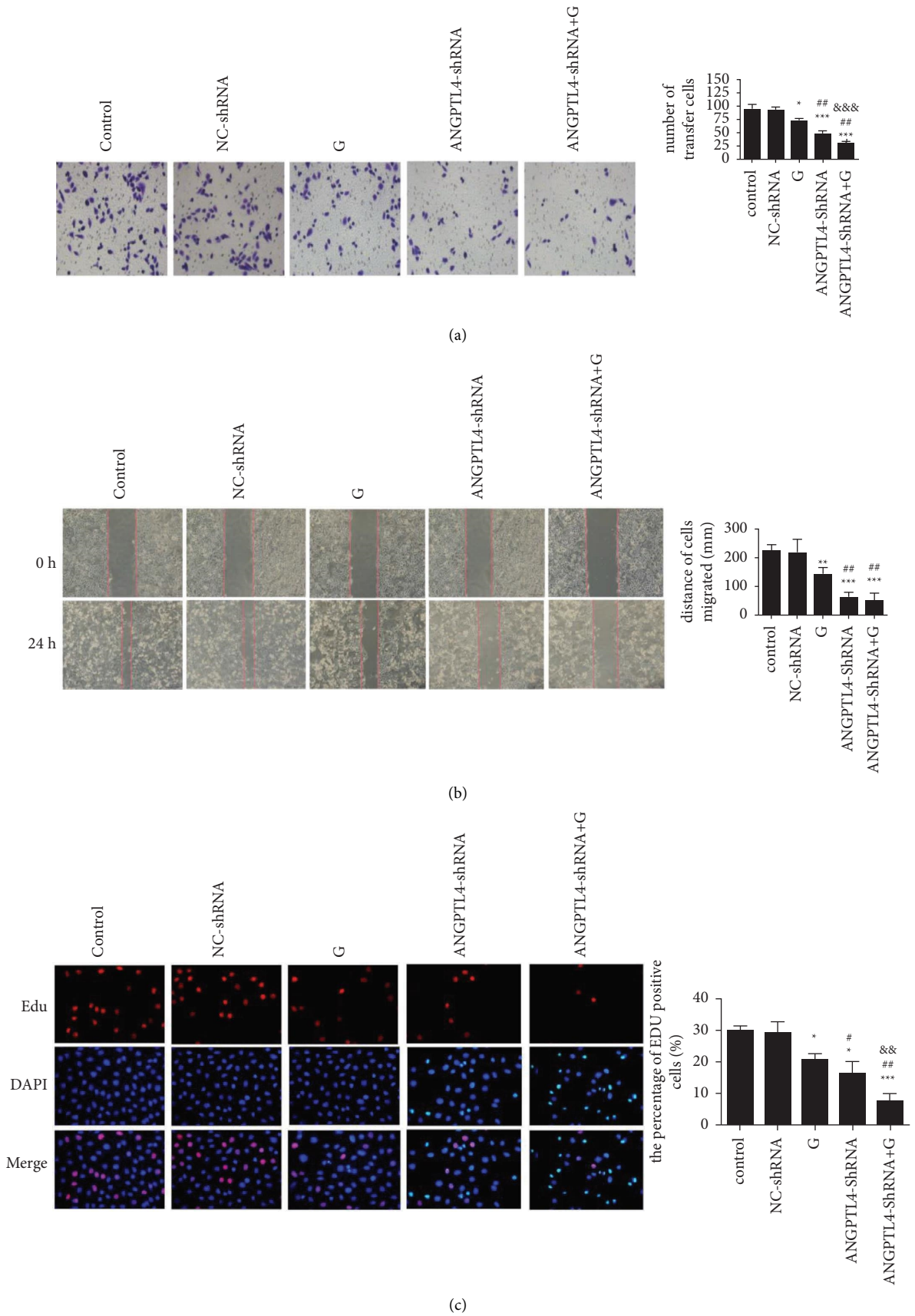

Figure 3: Continued.

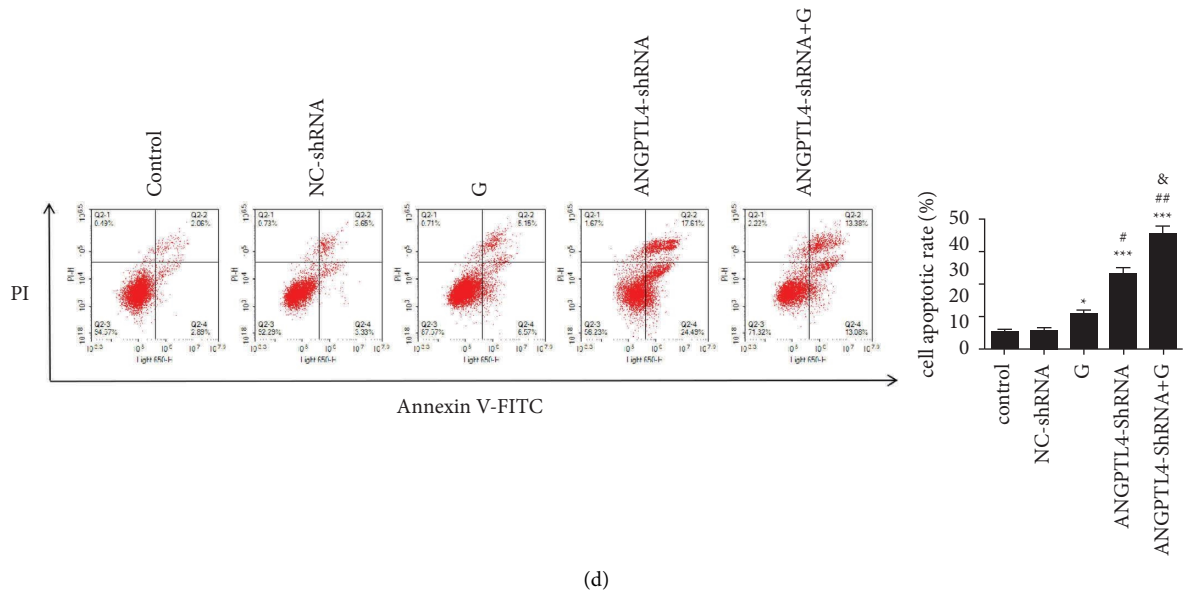

(d)

Figure 3: Knockdown with ANGPTL4 expression reduces the resistance of PC9/GR to gefitinib ($\bar{x} \pm s$, $n = 3$). (a) Transwell test revealed the correlation between ANGPTL4 knockdown and PC9/GR cell migration ability (×400). (b) Scratching experiments revealed a correlation between ANGPTL4 knockdown and the migration ability of PC9/GR cells (×200). (c) EdU proliferation test revealed the correlation between ANGPTL4 knockdown and PC9/GR cell proliferation (×400). (d) Flow cytometry showed the correlation between ANGPTL4 knockdown and PC9/GR cell apoptosis. Control: blank control group; NC-shRNA: PC9/GR cells transfected with NC-shRNA;*G*: PC9/GR cells + gefitinib; ANGPTL4-shRNA: PC9/GR cells transfected with ANGPTL4-shRNA; ANGPTL4-shRNA + G: PC9/GR cells transfected with ANGPTL4-shRNA + gefitinib. *, **, and ***: $p < 0.05$, 0.01, and 0.001, respectively, compared to the control group; $^{\#}$ and $^{\#\#}$: $p < 0.05$ and 0.01, respectively, compared to the G group; $^{\&}$, $^{\&\&}$, and $^{\&\&\&}$: $p < 0.05$, 0.01, and 0.001, respectively, compared to the ANGPTL4-shRNA group.

adenocarcinoma cells. In this study, we further confirmed that high expression of ANGPTL4 promoted secondary resistance to PC9 gefitinib in lung adenocarcinoma cells through in vivo and ex vivo experiments and explored the specific mechanism, which helps to improve the understanding of the correlation between ANGPTL4 and resistance to EGFR-TKIs.

ANGPTL4 belongs to the ANGPTL superfamily and can regulate lipid metabolism, leading to coronary heart disease and many other cardiovascular diseases [19]. Previous studies have confirmed the high expression of ANGPTL4 in a variety of malignant tumor cells and tissues, such as pancreatic cancer [20], gastric cancer [21], cholangiocarcinoma cells [22], and breast cancer [13, 19]. In our study, by comparing the expression levels of ANGPTL4 in three different lung adenocarcinoma cells and human bronchial epithelial cells BEAS-2B, we found that the expression levels of ANGPTL4 were higher in all three lung adenocarcinoma cells than in BEAS-2B cells, demonstrating that ANGPTL4 expression was upregulated in lung adenocarcinoma cells. This finding is consistent with the study by Zhu et al. [12]. A gap in the literature exists regarding the relationship between ANGPTL4 and resistance to EGFR-TKIs, despite the fact that ANGPTL4 has been identified as a tumor-promoting factor based on the series of studies mentioned above that suggest it can be upregulated and contribute to the progression of a number of malignancies.

In our study, we found that the expression of ANGPTL4 was upregulated in PC9/GR cells, which was significantly higher than that in PC9 cells. And the resistance of cells to gefitinib was significantly decreased after knockdown with ANGPTL4 expression in PC9/GR cells. In addition, knockdown with ANGPTL4 led to a decrease in the proliferation, migration, and invasion ability of PC9/GR cells and an increase in the level of apoptosis and the expression level of ROS in vivo and vitro.

Consistent with our study, ANGPTL4 was also found to be negatively correlated with apoptosis and ROS levels in ovarian cancer cells in the study by Yang et al. [23].

Pyroptosis is the same as apoptosis, and both are a type of programmed cell death [24]. The onset of pyroptosis is often accompanied by chromatin condensation and DNA breakage, cell membrane pore formation, cell swelling, and membrane rupture, which in turn leads to the release of cellular contents and pro-inflammatory mediators [24].

The current study found that intracellular focal death is activated mainly through two pathways; one of them is the classic pathway that relies on GSDMD [25]. As a central target in the classical pathway, NLRP3 has been found to be aberrantly expressed in a variety of malignancies, such as ovarian cancer [26] and breast cancer [27]. However, to date, there are still no studies on the correlation between ANGPTL4 and pyroptosis.

In the present study, we observed that after discriminating between knockdown of ANGPTL4 in PC9/GR cells, expression of pyroptosis-related proteins NLRP3, ASC, and cleaved-caspase8 were subsequently upregulated and decreased, but the expression levels of the pyroptosis inhibitor

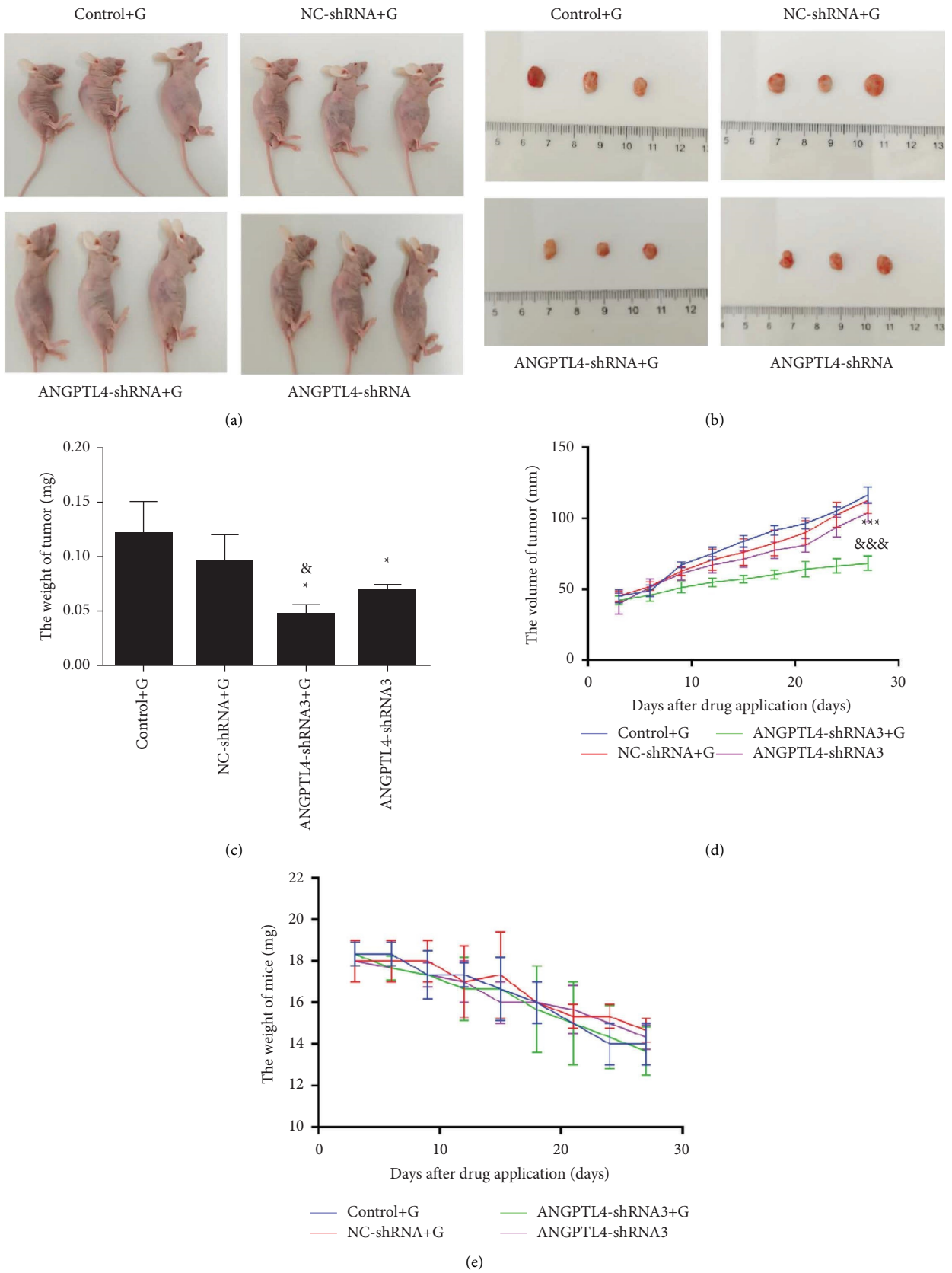

Figure 4: Knockdown with ANGPTL4 has a significant antitumour effect on the xenograft tumour model ($\bar{x} \pm s$, $n = 3$). (a) Nude mouse xenograft tumour model. (b) Xenograft tumour in each group. (c) Nude mouse weight change curve. Comparison of xenograft tumour weights between groups. (d) Volume growth curves of xenograft tumours in each group. (e) Nude mouse weight change curve. *and ***: $p < 0.05$ and 0.001, respectively, compared to the control + G group; $^{\&}$and $^{\&\&\&}$: $p < 0.05$ and 0.001, respectively, compared to the ANGPTL4-shRNA3 group.

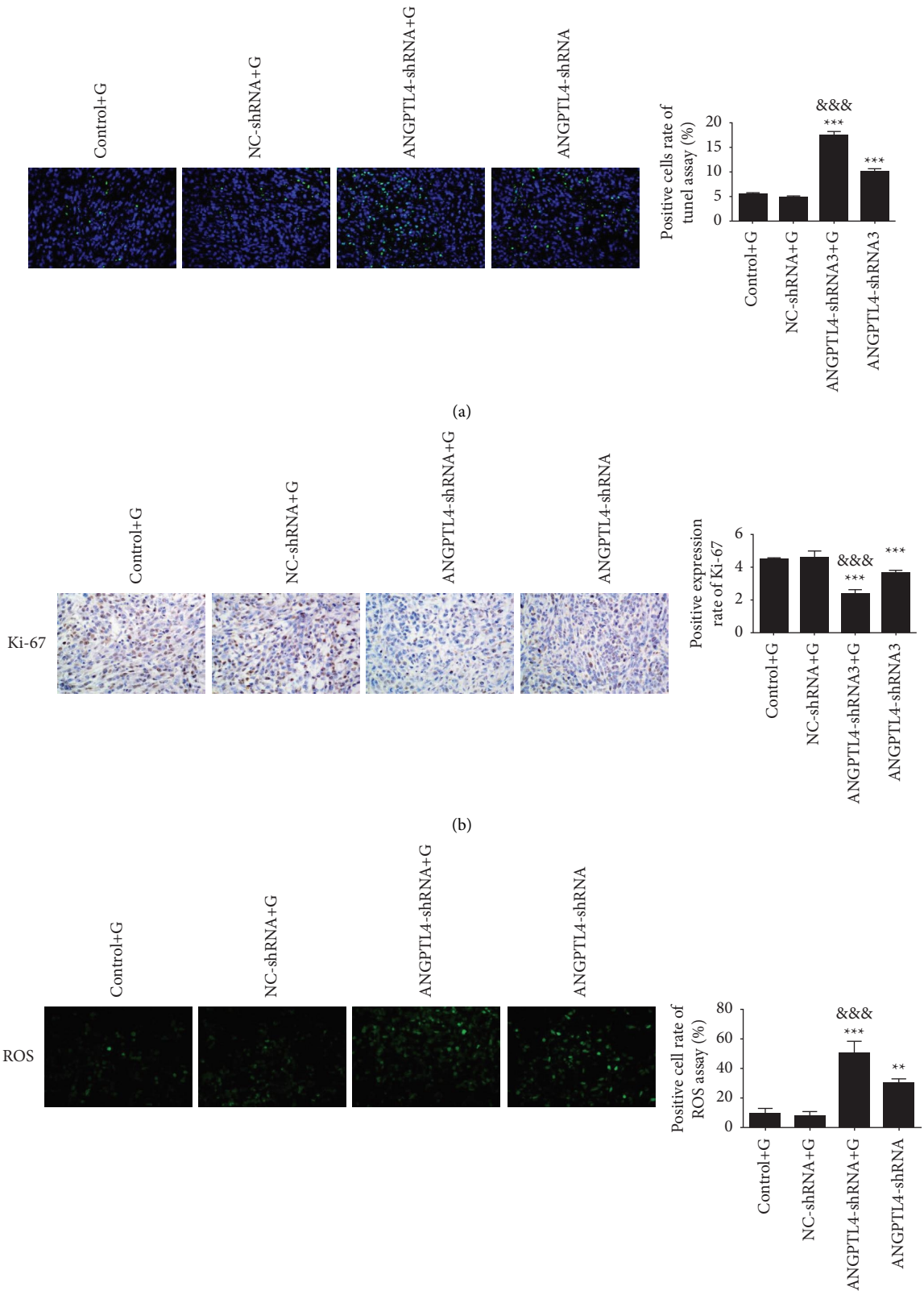

Figure 5: Continued.

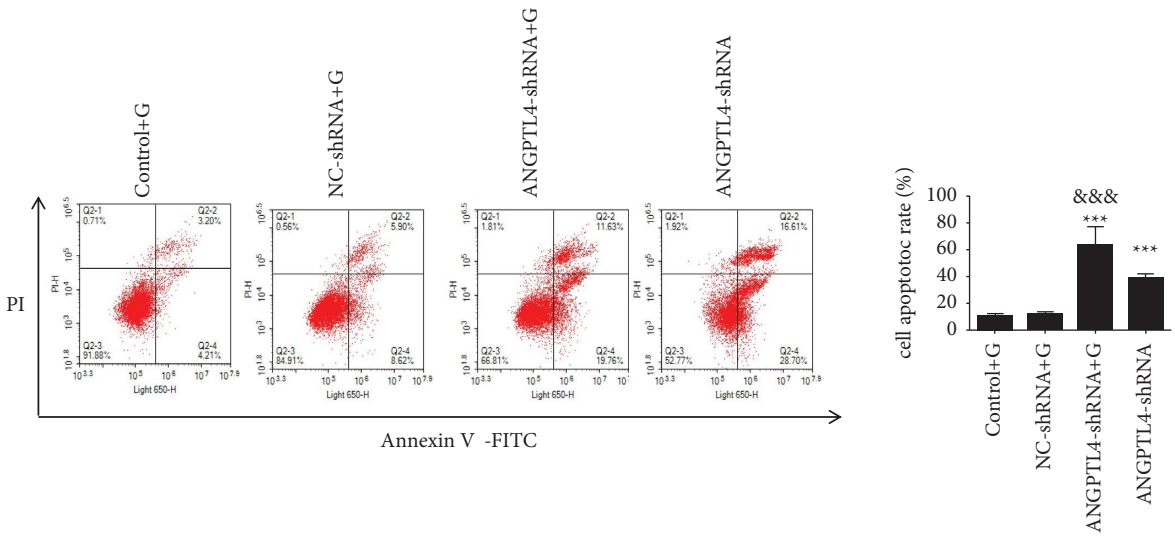

(d)

Figure 5: Effect of interfering ANGPTL4 on transplanted tumor tissue ($\overline{x} \pm s$, $n = 3$). (a) TUNEL assay was performed to detect the level of apoptosis in xenograft tissue (×400). (b) Ki-67 expression in the tumour tissue of each group. (c) ROS fluorescence staining was performed to detect the level of ROS in xenograft tissue (×400). (d) Flow cytometry showed the level of apoptosis in xenograft tissue. *and ***: $p < 0.05$ and 0.001, respectively, compared to the control + G group; $^{\&}$and $^{\&\&\&}$: $p < 0.05$ and 0.001, respectively, compared to the ANGPTL4-shRNA3 group.

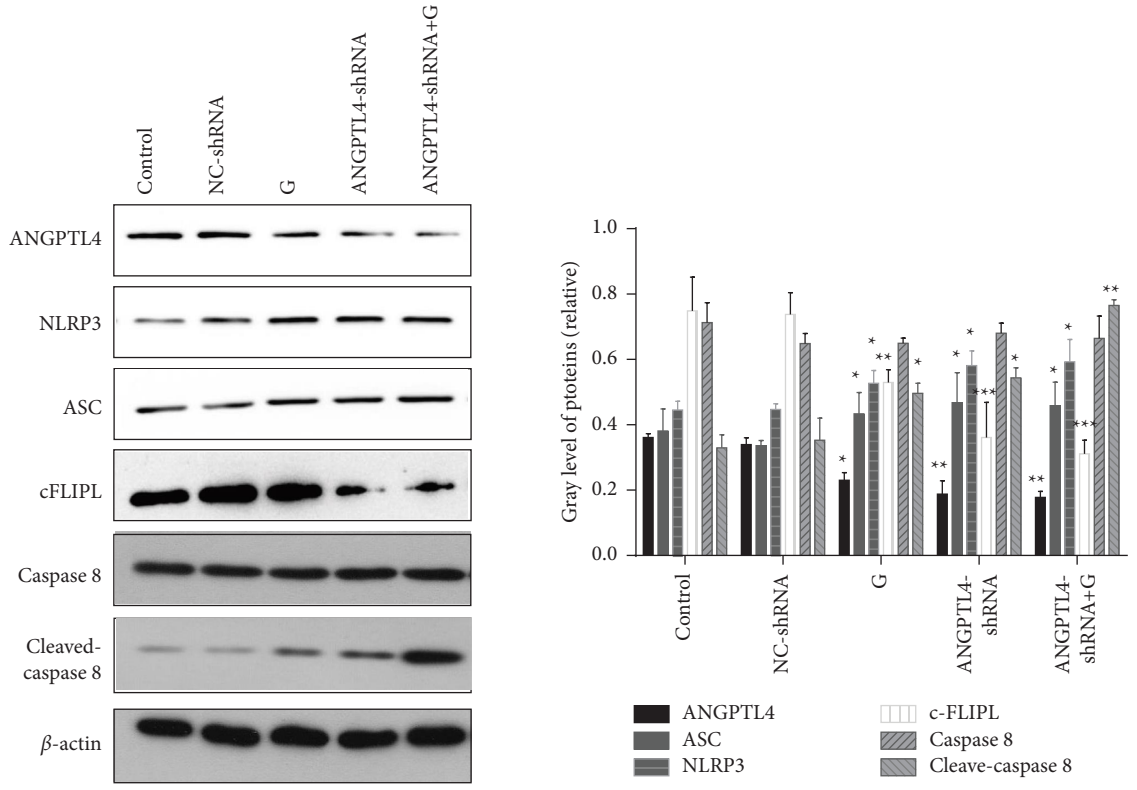

(a)

Figure 6: Continued.

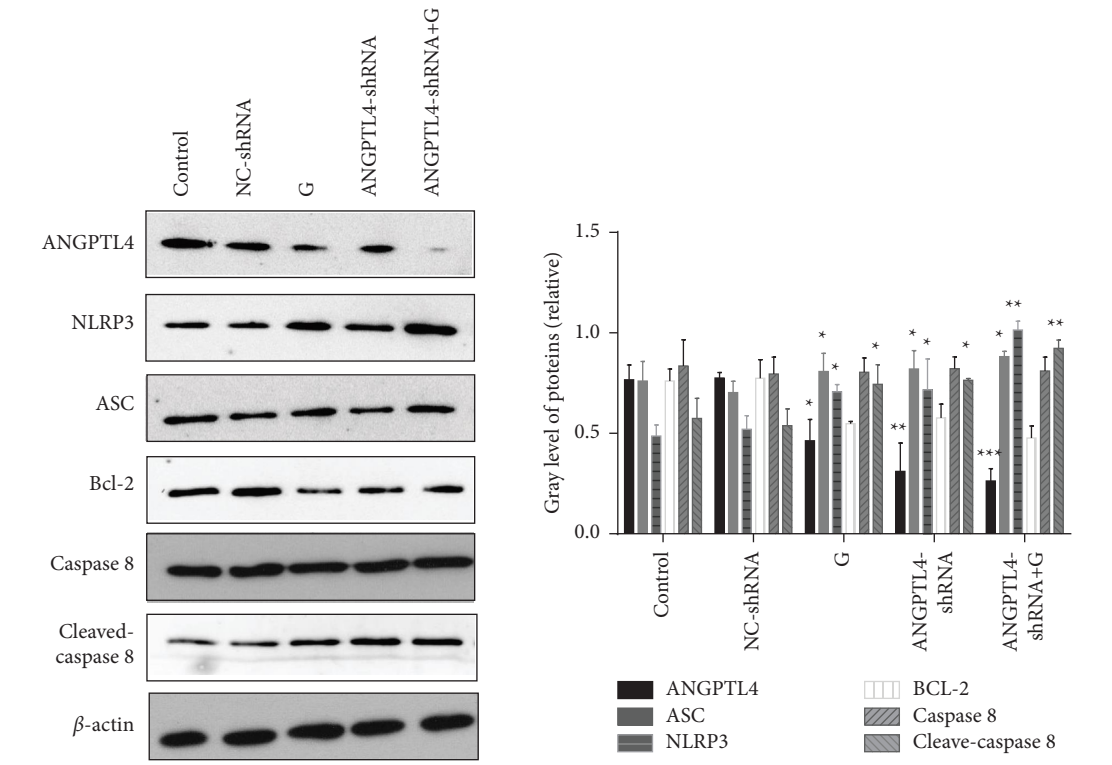

(b)

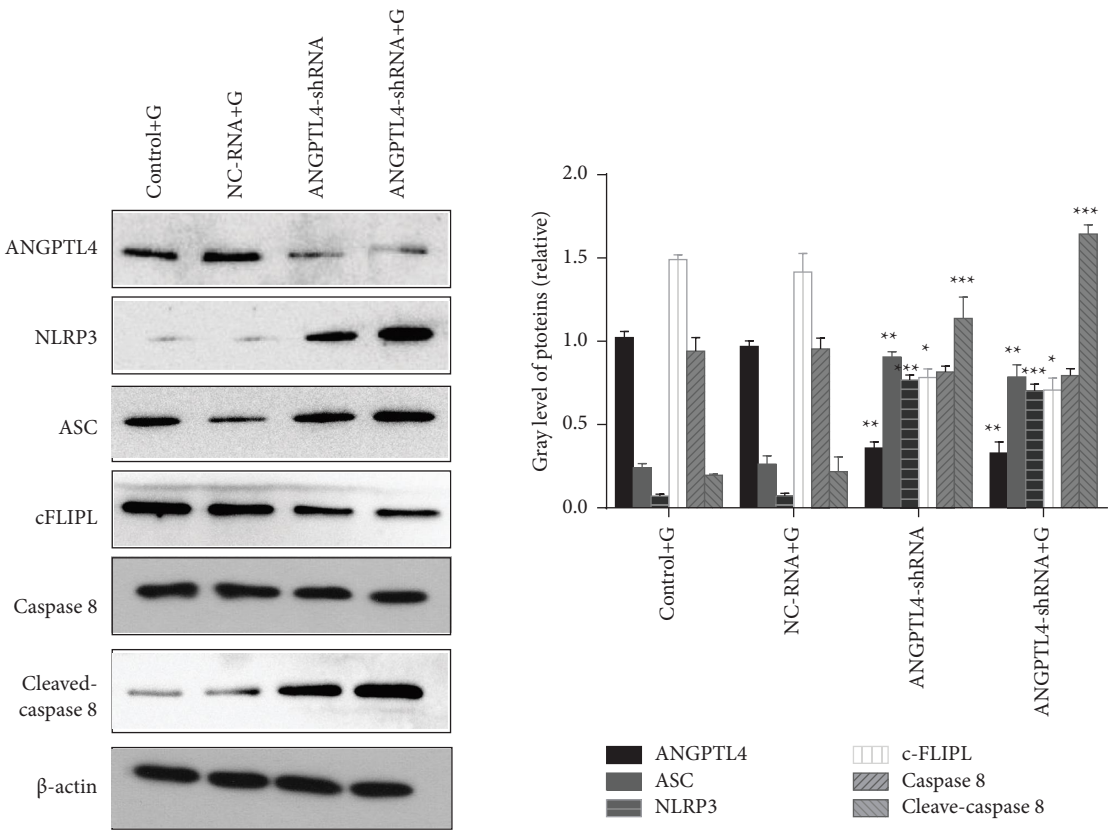

(c)

Figure 6: Continued.

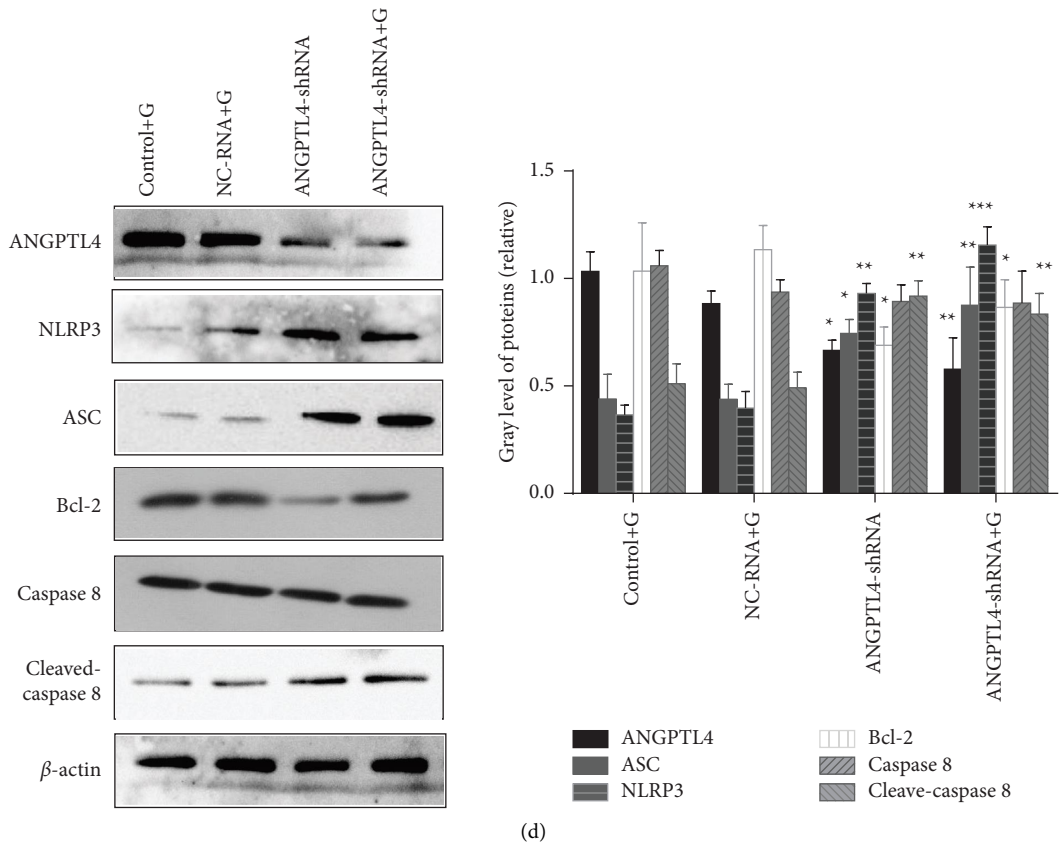

Figure 6: Changes in the expression of NLRP3\ASC\Caspase 8 pathway-related proteins after ANGPTL4 knockdown and overexpression in cells and transplanted tumour tissues ($\bar{x} \pm s$, $n = 3$). (a) NLRPS\ASC\Caspase 8 and pyroptosis-related protein expression after ANGPTL4 knockdown in PC9/GR cells. (b) Changes in the expression of NLRP3\ASC\Caspase 8 and apoptosis-related protein expression after ANGPTL4 knockdown in PC9/GR cells. (c) NLRP3\ASC\Caspase 8 and pyroptosis-related protein expression after ANGPTL4 knockdown in xenograft tumours. (d) NLRP3\ASC\Caspase 8 and apoptosis-related protein expression after ANGPTL4 knockdown in xenograft tumours. Control: PC9/GR cells; NC-shRNA: PC9/GR cells transfected with NC-shRNA;*G*: PC9/GR cells + gefitinib; ANGPTL4-shRNA: PC9/GR cells transfected with ANGPTL4-shRNA;ANGPTL4-shRNA + *G*: PC9/GR cells transfected with ANGPTL4-shRNA + gefitinib; Control + *G*: nude mice treated with gefitinib; NC-shRNA + *G*: nude mice treated with NC-shRNA cells + gefitinib; ANGPTL4-shRNA: nude mice treated with PC9/GR cells afterknockdown with ANGPTL4; ANGPTL4-shRNA + *G*: after knockdown with ANGPTL4 nude mice treated with PC9/GR cells + gefitinib. *, ** and ***: $p < 0.05$,0.01 and 0.001, respectively, compared to the control or control + *G* group.

protein cFLIPL were increasing and decreasing, respectively, in vivo and vitro. This suggests that ANGPTL4 regulates gefitinib resistance in lung adenocarcinoma cells through the NLRP3/ASC/Caspase8 pathway.

Additionally, according to certain research, pyroptotic cell death is frequently accompanied by both necrosis and apoptosis traits [28]. Moreover, our research discovered that levels of apoptosis in cells rose following ANGPTL4 knockdown. Fritsch et al. showed that caspase 8 is not only involved in the scorching of tumour cells but also plays an important role in the process of apoptosis [29]. In a study by Chi W et al., the expression levels of NLRP3, ASC, Caspase8, and apoptosis-related proteins were significantly increased in an acute diabetic mouse model [30]. Chen et al. further demonstrated that pannexin-1 promotes caspase-8 or caspase-9-dependent apoptosis by promoting the activation of NLRP3 inflammatory vesicles through the construction of GSDMD D88A knock-in mice [31]. Our study also found that the expression levels of NLRP3, ASC, and Cleaved-caspase 8 increased and decreased after knockdown and overexpression of ANGPTL4, respectively, while the expression levels of the apoptosis suppressor protein Bcl-2 were reversed suggesting that ANGPTL4 regulates apoptosis in PC9/GR cells through mediating the NLRP3/ASC/Caspase 8 pathway.

In summary, our research explored the regulatory ability and mechanism of ANGPTL4 in the resistance of PC9/GR cells to gefitinib through in vivo and in vitro experiments. ANGPTL4 inhibited pyroptosis and apoptosis by regulating the NLRP3/ASC/Caspase 8 pathway, leading to resistance to gefitinib in lung adenocarcinoma. ANGPTL4 may be an important regulator of EGFR-TKI resistance in patients with non-small-cell lung cancer. Targeting ANGPTL4 may inhibit the development of EGFR-TKI resistance, which may improve the survival rate of patients with non-small-cell lung cancer. However, our experiments had shortcomings. For example, due to the strong proliferation ability of PC9/GR cells, gefitinib treatment was added to the control group

to improve the survival rate of nude mice, which may have led to the loss of the true blank control group in animal experiments.

Data Availability

The datasets used during the current study are available from the corresponding author upon request.

Ethical Approval

All animal experiments were performed with approval of the Research Ethic Committee and conducted according to the institutional guidelines of Animal Care and Use Committee at the First Affiliated Hospital of Anhui University.

Conflicts of Interest

The authors declare that they have no conflicts of interest.

Acknowledgments

This study was supported by the Key Research and Development Plan Project of Anhui Province (grant no. 1804 h0802240).

References

[1] P. E. Goss, K. Strasser-Weippl, B. L. Lee-Bychkovsky et al., "Challenges to effective cancer control in China, India, and Russia," *The Lancet Oncology*, vol. 15, no. 5, pp. 489–538, 2014.

[2] M. Zhou, H. Wang, X. Zeng et al., "Mortality, morbidity, and risk factors in China and its provinces, 1990-2017: a systematic analysis for the Global Burden of Disease Study 2017," *Lancet*, vol. 394, no. 10204, pp. 1145–1158, 2019.

[3] J. F. Gainor and A. T. Shaw, "Emerging paradigms in the development of resistance to tyrosine kinase inhibitors in lung cancer," *Journal of Clinical Oncology*, vol. 31, no. 31, pp. 3987–3996, 2013.

[4] R. L. Siegel, K. D. Miller, and A. Jemal, "Cancer statistics," *CA: A Cancer Journal for Clinicians*, vol. 67, no. 1, pp. 7–30, 2017.

[5] Y. L. Wu, C. Zhou, C. P. Hu et al., "Afatinib versus cisplatin plus gemcitabine for first-line treatment of Asian patients with advanced non-small-cell lung cancer harbouring EGFR mutations (LUX-Lung 6): an open-label, randomised phase 3 trial," *The Lancet Oncology*, vol. 15, no. 2, pp. 213–222, 2014.

[6] J. Rawluk and C. F. Waller, "Recent results in cancer research," *Fortschritte der Krebsforschung. Progres dans les recherches sur le cancer*, vol. 211, pp. 235–246, 2018.

[7] J. Greenhalgh, K. Dwan, A. Boland et al., "First-line treatment of advanced epidermal growth factor receptor (EGFR) mutation positive non-squamousnon-small cell lung cancer," *Cochrane Database of Systematic Reviews*, no. 5, Article ID CD010383, 2016.

[8] C. K. Lee, L. Davies, Y. L. Wu et al., "Gefitinib or erlotinib vs chemotherapy for EGFR mutation-positive lung cancer: individual patient data meta-analysis of overall survival," *Journal of the National Cancer Institute (1988)*, vol. 109, no. 6, p. 109, 2017.

[9] W. Zhang, Y. Wei, D. Yu, J. Xu, and J. Peng, "Gefitinib provides similar effectiveness and improved safety than erlotinib for advanced non-small cell lung cancer: a meta-analysis," *Medicine (Baltimore)*, vol. 97, no. 16, p. e0460, 2018.

[10] C. Sun, W. Gao, J. Liu, H. Cheng, and J. Hao, "FGL1 regulates acquired resistance to Gefitinib by inhibiting apoptosis in non-small cell lung cancer," *Respiratory Research*, vol. 21, no. 1, p. 210, 2020.

[11] J. Yang, X. Li, and D. Xu, "Research progress on the involvement of ANGPTL4 and loss-of-function variants in lipid metabolism and coronary heart disease: is the "prime time" of ANGPTL4-targeted therapy for coronary heart disease approaching?" *Cardiovascular Drugs and Therapy*, vol. 35, no. 3, pp. 467–477, 2021.

[12] X. Zhu, X. Guo, S. Wu, and L. Wei, "ANGPTL4 correlates with NSCLC progression and regulates epithelial-mesenchymal Transition via ERK pathway," *Lung*, vol. 194, no. 4, pp. 637–646, 2016.

[13] X. Gong, Z. Hou, M. P. Endsley et al., "Interaction of tumor cells and astrocytes promotes breast cancer brain metastases through TGF-β2/ANGPTL4 axes," *Npj Precision Oncology*, vol. 3, no. 1, p. 24, 2019.

[14] L. Yang, Y. Wang, R. Sun et al., " ANGPTL4 promotes the proliferation of papillary thyroid cancer via AKT pathway< ," *OncoTargets and Therapy*, vol. 13, pp. 2299–2309, 2020.

[15] D. Nie, Q. Zheng, L. Liu, X. Mao, and Z. Li, "Up-regulated of angiopoietin-like protein 4 predicts poor prognosis in cervical cancer," *Journal of Cancer*, vol. 10, no. 8, pp. 1896–1901, 2019.

[16] S. Zhou, R. Wang, and H. Xiao, "Adipocytes induce the resistance of ovarian cancer to carboplatin through ANGPTL4," *Oncology Reports*, vol. 44, no. 3, pp. 927–938, 2020.

[17] A. F. M. M. Rahman, H. M. Korashy, and M. G. Kassem, *Profiles of Drug Substances, Excipients and Related Methodology*, vol. 39, pp. 239–264, 2014.

[18] F. Yue, X. Li, H. Chen, and J. Hao, "ANGPTL4 regulates the migration and invasion mechanism of human lung adenocarcinoma PC9/GR cells," *Journal of Anhui Medical University*, vol. 57, no. 06, pp. 902–907, 2022, [in Chinese].

[19] J. Zhao, J. Liu, N. Wu et al., "ANGPTL4 overexpression is associated with progression and poor prognosis in breast cancer," *Oncology Letters*, vol. 20, no. 3, pp. 2499–2505, 2020.

[20] B. Hui, H. Ji, Y. Xu et al., "RREB1-induced upregulation of the lncRNA AGAP2-AS1 regulates the proliferation and migration of pancreatic cancer partly through suppressing ANKRD1 and ANGPTL4," *Cell Death & Disease*, vol. 10, no. 3, p. 207, 2019.

[21] H. Kubo, Y. Kitajima, K. Kai et al., "Regulation and clinical significance of the hypoxia-induced expression of ANGPTL4 in gastric cancer," *Oncology Letters*, vol. 11, no. 2, pp. 1026–1034, 2016.

[22] T. T. San, P. Khaenam, V. Prachayasittikul, B. Sripa, N. Kunkeaw, and W. Chan-On, "Curcumin enhances chemotherapeutic effects and suppresses ANGPTL4 in anoikis-resistant cholangiocarcinoma cells," *Heliyon*, vol. 6, no. 1, Article ID e03255, 2020.

[23] W. H. Yang, Z. Huang, J. Wu, C. K. C. Ding, S. K. Murphy, and J. T. Chi, "A TAZ-ANGPTL4-NOX2 Axis regulates ferroptotic cell death and chemoresistance in epithelial ovarian cancer," *Molecular Cancer Research*, vol. 18, no. 1, pp. 79–90, 2020.

[24] J. Ruan, S. Wang, and J. Wang, "Mechanism and regulation of pyroptosis-mediated in cancer cell death," *Chemico-Biological Interactions*, vol. 323, Article ID 109052, 2020.

[25] D. Frank and J. E. Vince, "Pyroptosis versus necroptosis: similarities, differences, and crosstalk," *Cell Death & Differentiation*, vol. 26, no. 1, pp. 99–114, 2019.

[26] S. Yu, N. Zhao, M. He, K. Zhang, and X. Bi, "MiRNA-214 promotes the pyroptosis and inhibits the proliferation of

cervical cancer cells via regulating the expression of NLRP3," *Cellular and Molecular Biology (Paris, France, Print)*, vol. 66, no. 6, pp. 59–64, 2020.

[27] S. S. Faria, S. Costantini, V. C. C. de Lima et al., "NLRP3 inflammasome-mediated cytokine production and pyroptosis cell death in breast cancer," *Journal of Biomedical Science*, vol. 28, no. 1, p. 26, 2021.

[28] P. Broz and V. M. Dixit, "Inflammasomes: mechanism of assembly, regulation and signalling," *Nature Reviews Immunology*, vol. 16, no. 7, pp. 407–420, 2016.

[29] M. Fritsch, S. D. Günther, R. Schwarzer et al., "Caspase-8 is the molecular switch for apoptosis, necroptosis and pyroptosis," *Nature*, vol. 575, no. 7784, pp. 683–687, 2019.

[30] W. Chi, H. Chen, F. Li, Y. Zhu, W. Yin, and Y. Zhuo, "HMGB1 promotes the activation of NLRP3 and caspase-8 inflammasomes via NF-κB pathway in acute glaucoma," *Journal of Neuroinflammation*, vol. 12, no. 1, p. 137, 2015.

[31] K. W. Chen, B. Demarco, R. Heilig et al., "Extrinsic and intrinsic apoptosis activate pannexin-1 to drive NLRP3 inflammasome assembly," *The EMBO Journal*, vol. 38, no. 10, Article ID e101638, 2019.

Hindawi
Journal of Oncology
Volume 2022, Article ID 7905787, 10 pages
https://doi.org/10.1155/2022/7905787

Research Article

Identification of KIF21B as a Biomarker for Colorectal Cancer and Associated with Poor Prognosis

Shanshan Xu,[1] **Youran Li**,[2] **Hua Huang**,[3] **Xian Miao**,[4] **and Yunfei Gu**[2]

[1]*Major of Chinese Medicine Surgery, Nanjing University of Chinese Medicine, Nanjing, Jiangsu 210000, China*
[2]*Department of Colorectal Surgery, Affiliated Hospital of Nanjing University of Chinese Medicine, Nanjing, Jiangsu 210000, China*
[3]*Department of Anorectal, Changshu Hospital Affiliated to Nanjing University of Chinese Medicine, Nanjing, Jiangsu 215500, China*
[4]*Department of Oncology, Nantong Hospital of Traditional Chinese, Nantong, Jiangsu 226001, China*

Correspondence should be addressed to Yunfei Gu; yfy0052@njucm.edu.cn

Received 4 August 2022; Revised 24 August 2022; Accepted 16 September 2022; Published 21 November 2022

Academic Editor: İbrahim Hakkı Cigerci

Objective. This study is aimed at exploring the function of KIF21B in colorectal cancer. *Methods*. The expression of KIF21B was analyzed by the UALCAN database, GEPIA site, and TIMER site. The survival rate was analyzed by Kaplan-Meier curves, and the prognosis was analyzed by ROC. Relevant signaling pathways and biological processes were analyzed by GO-KEGG enrichment analysis. The correlation between KIF21B and cancer immune infiltrates was analyzed by TIMER. The functional state of KIF21B in various types of cancers was conducted by single-cell RNA-sequencing. Furthermore, the expression of KIF21B was verified by real-time qPCR and Western blotting. The cell proliferation was measured by CCK8 assay. The cell apoptosis was analyzed by flow cytometry. Cell migration and invasion were determined by the transwell assay. *Results*. Combination analysis of bioinformatics methods revealed that KIF21B is high expression in CRC, associated with poor survival. KIF21B and associated genes were significantly enriched in covalent chromatin modification. The expression of KIF21B was positively correlated with infiltrating levels of CD4+ T cells and neutrophils, cell apoptosis, and metastasis. KIF21B was upregulated expression in CRC cell lines. KIF21B deficiency reduced cell proliferation, migration, and invasion. *Conclusions*. Our study suggested that KIF21B may be a biomarker in CRC.

1. Introduction

Colorectal cancer is the third most common cancer in the world and the second leading cause of cancer-related deaths. In 2018, there were approximately 1.8 million new cases and 860,000 deaths [1]. By 2040, the annual global burden of colorectal cancer is expected to increase to more than 3 million new cases and 6 million deaths [1]. The incidence of colorectal cancer varies between countries, and studies on international immigrants have shown that diet and other lifestyle factors play a role in disease progression [2]. Therefore, people are paying more and more attention to formulating public health programs to reduce the incidence of colorectal cancer by targeting modifiable risk factors. Despite advances in treatment and early diagnosis in recent decades, the 5-year survival rate of CRC patients is still unsatisfactory [3]. At present, the prognosis model established based on clinical predictive indicators such as age, gender, and TNM staging is a commonly used clinical prognosis model for CRC. However, due to the high degree of heterogeneity of the disease, the prognosis based on conventional clinical predictors is not accurate, resulting in inaccurate prediction of the survival of CRC patients [4]. Therefore, the establishment of more comprehensive predictive indicators has important implications for more effective treatment.

Kinesin superfamily proteins belong to a class of microtubule-dependent molecular motors that utilize ATP hydrolysis yield in eukaryotes to move cargo such as proteins, macromolecules, and organelles such as chromosomes and vesicles along the cytoskeletal microtubule network. They play important roles in all aspects of intracellular trafficking and are involved in a wide variety of physiological processes, including embryonic development, axonal transport, and cell division. Many kinesins play important roles

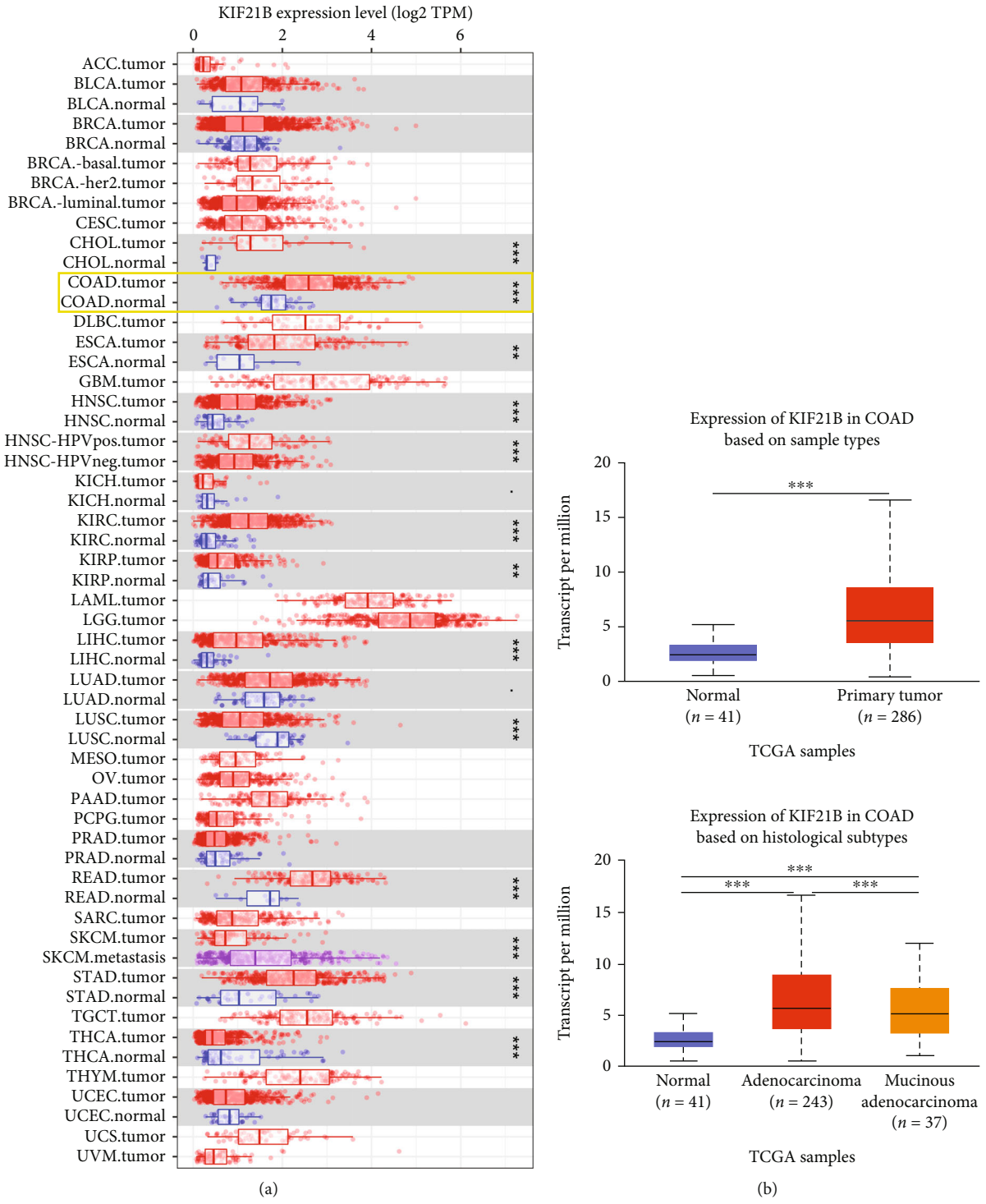

Figure 1: Continued.

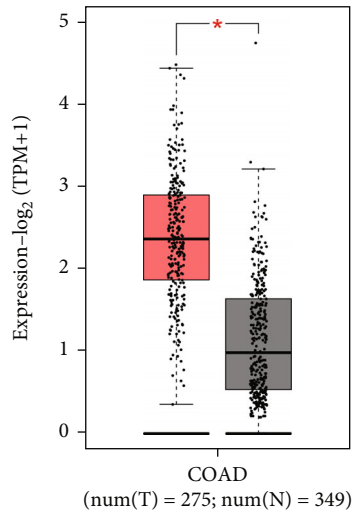

Figure 1: The expression of KIF21B was increased in colorectal cancer. (a) KIF21B expression in CRC was analyzed by TIMER database (https://cistrome.shinyapps.io/timer/). (b) KIF21B expression in CRC was analyzed by UALCAN database (http://ualcan.path.uab.edu/analysis.html). (c) KIF21B expression in CRC was analyzed by GEPIA database (http://gepia.cancer-pku.cn/).

in cell division, and kinesin overexpression is associated with cancers such as retinoblastoma [5]. Recent study reported that KIFs participate in the division of mitotic cells by participating in the movement of chromosomes and spindles, suggesting that the release of KIFs may be related to the occurrence of tumors [6]. KIF21B is a classical kinesin that inhibits the growth of microtubules through the tail domain and participates in the regulation of microtubule dynamics as a potential microtubule suspension factor [7, 8]. Both play important roles in intercellular signal transduction, malignancy, tumorigenesis, and metastasis [9]. Studies have shown that increasing expression of KIF21B is correlated with poor disease-free survival in patients with prostate cancer [10]. KIF21B is upregulated in hepatocellular carcinoma and is significantly associated with prognosis [11]. KIF21B is abnormally expressed in osteosarcoma and affects the proliferation and apoptosis of osteosarcoma cells by regulating the PI3K/AKT pathway [12]. However, the function of KIF21B in colorectal cancer has not been reported.

In this study, the TCGA data platform was used to analyze the expression of KIF21B in colorectal cancer and its impact on survival and prognosis and to provide potential molecular markers for the diagnosis and treatment of colorectal cancer.

2. Methods and Materials

2.1. Cells and shRNA. NCM460, HT29, HCT116, SW48, and HCT15 cells were purchase from Procell. All cells were cultured in DMEM with 10% FBS and penicillin-streptomycin. shRNA were purchased from Sigma. Lipofetamine 3000 reagent was used to related transfection assays as direction of manual handbook.

2.2. Gene Expression Analysis. The expression of KIF21B in COAD was analyzed by online platform, including TIMER (https://cistrome.shinyapps.io/timer/), UALCAN (http://ualcan.path.uab.edu/analysis.html), and GEPIA (http://gepia.cancer-pku.cn/).

2.3. Kaplan-Meier Analysis and ROC Analysis. Based on TCGA-COAD dataset to draw the survival prognosis curve by using the survivor package in R. Based on TCGA-GTEx-COAD and TCGA-COAD dataset to do ROC analysis by using the pROC package.

2.4. GO-KEGG Enrichment Analysis. Firstly, the genes with an expression correlation to KIF21B in COAD were selected from UALCAN dataset, then the genes with Pearson score ≥ 0.4 were screened for GO-KEGG enrichment analysis through the enrichplot package of R.

2.5. Correlation Analysis. Correlation analysis was performed as described as previously depicted [13, 14]. The correlation between KIF21B and genes associated with immune infiltration were analyzed by Spearman score. The data comes from TIMER.

2.6. Single-Cell RNA-Sequence Analysis. Single-cell RNA isolation and sequencing were performed as previously depicted [15]. The functional status of KIF21B in different kinds of cancers was analyzed by CancerSEA (http://biocc.hrbmu.edu.cn/CancerSEA/). The expression profile of KIF21B in single cells obtained from CRC tissue was analyzed by t-SNE. The correlation between KIF21B and apoptosis, metastasis, DNA damage, and hypoxia was analyzed by Pearson score.

2.7. RT-qPCR and Western Blotting Analysis. RNA isolation and protein extraction were performed as previously described [16]. Cell were harvested, washed, and treated with TRIzol reagent for the extraction of RNA, then cDNA

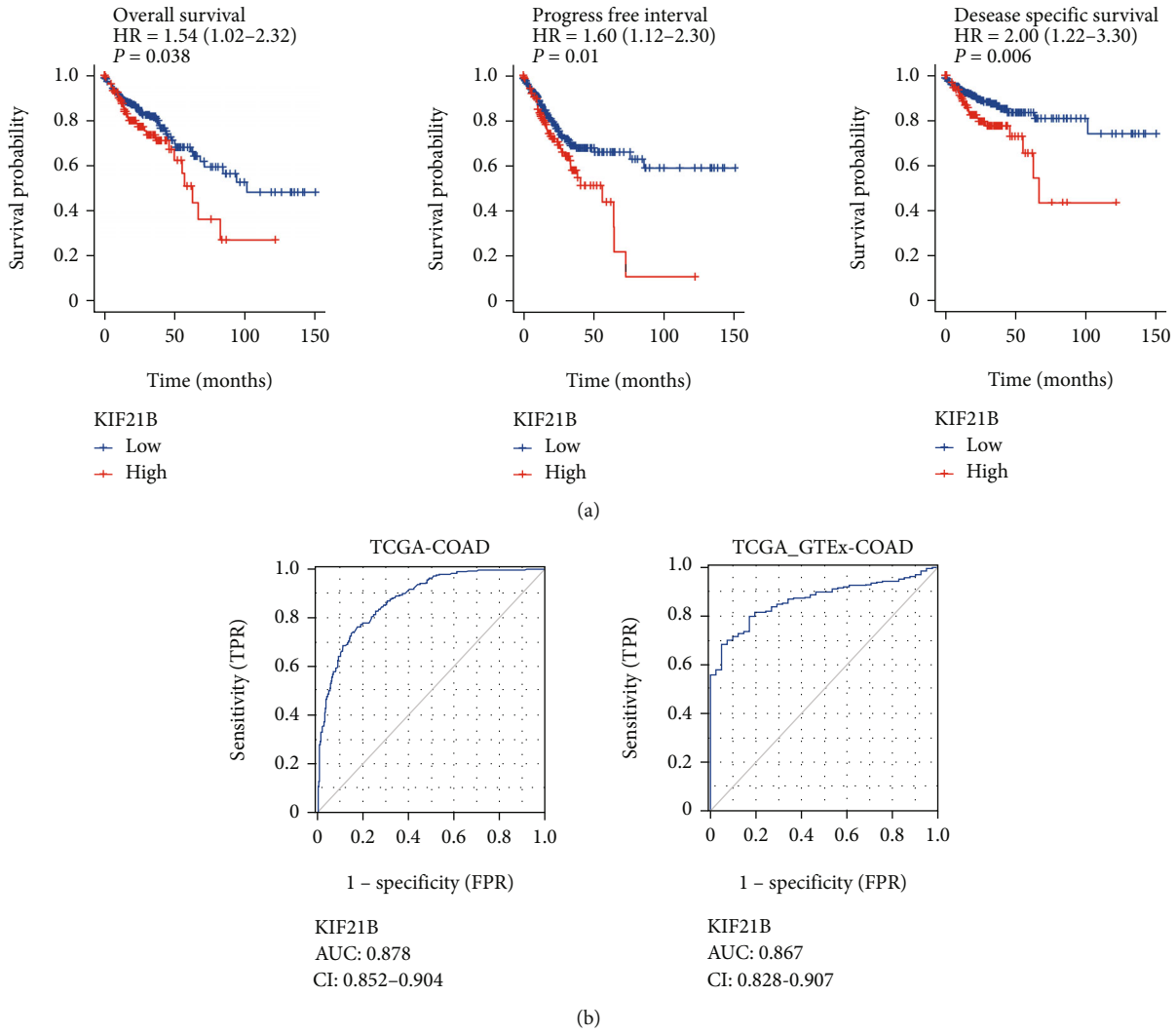

Figure 2: The high expression of KIF21B in colorectal cancer was related to poor prognosis. (a) Kaplan-Meier analysis of the correlation between KIF21B and prognosis from TCGA-COAD database. (b) ROC curve analysis of KIF21B in clinical diagnosis from GTEx-COAD, TCGA-COAD.

was produced by the reverse transcription of RNA. The primers were list as follows:

KIF21B forward: 5′-ACCTATGACTTTGTCTTCGACCT-3′;

KIF21B reverse: 5′-CAGCACCGTGGCATTATAGC-3′;

GAPDH forward: 5′-AGGTCGGTGTGAACGGATTTG-3′; and

GAPDH reverse: 5′-GGGGTCGTTGATGGCAACA-3′.

For Western blotting, protein lysate was deprived from cell lysis by RIPA buffer with protein inhibitor. And immunoblotted with the following antibodies: antimouse KIF21B (1 : 1000, Santa, sc-517174, USA) and antimouse β-actin (1 : 1000, Santa, sc-8432, USA).

2.8. Cell Viability and Apoptosis Analysis. The survival analysis of CRC cell lines was performed as described as previously depicted [17]. CCK8 assay was used to analyze cell viability. Cell lines were counted, seeded into 96-well plate, then analyzed the cell viability at 0 h, 24 h, 48 h, 72 h, and 96 h. Cell apoptosis was analyzed by flow cytometry. Cells were harvested, washed, then stained with PI or/and annexin V.

2.9. Cell Migration and Invasion. For migration assays, transwells with an 8 μm pore size filter are inserted into a 24-well plate. The cell serum was starved overnight and then added to the upper chamber (2.5×10^4 cells per insertion), and the lower chamber used a complete culture medium supplemented with 10% fetal bovine serum as a chemical attractant. After 24 hours of incubation, the remaining uninvaded cells on the upper surface of the filter were removed. The cells that passed through the filter and attached to the bottom of the membrane were fixed and stained. In each experiment, under a phase-contrast microscope, 7 areas were randomly selected from 3 repeated cells, and the number of invading cells was counted. For invasion assays, the Matrigel was spread in filter, then 4×10^4 cells were seeded

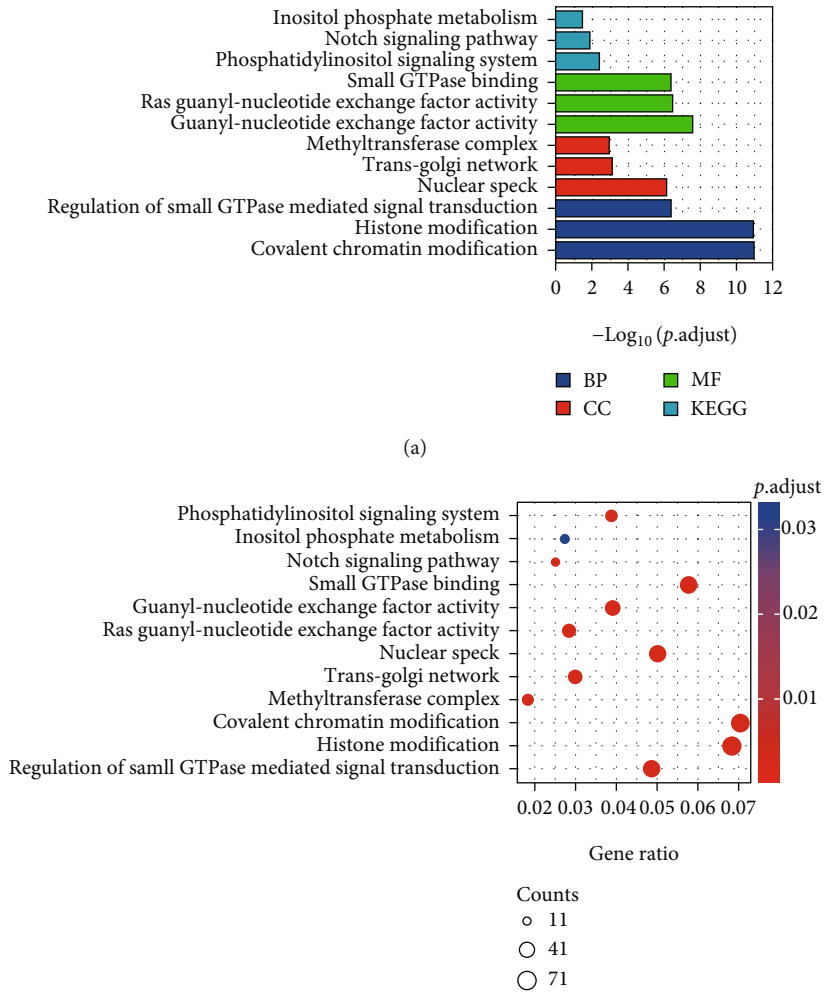

Figure 3: Enrichment analysis of KIF21B expression-related genes in colorectal cancer. (a, b) Based on UALCAN database analysis of genes associated with KIF21B expression in COAD, genes with Pearson CC ≥ 0.4 were selected for GO-KEGG enrichment analysis. Data was shown as column chart (a) and bubble chart (b).

into chamber. And the subsequent steps were same with migration assays.

2.10. Statistical Analysis. Student's *t*-test and two-way ANOVA were used in statistical analyses and performed by SPSS 22.0 software. Data were presented as mean ± SEM of three independent experiments. A *P* value of 0.05 or less were considered to be significant.

3. Results

3.1. KIF21B Was Increased Expression in Colorectal Cancer. First of all, we analyzed the expression of KIF21B in CRC from TIMER database. As shown in Figure 1(a), KIF21B was upregulated expression in tumor tissues compared to normal tissues of COAD. Moreover, KIF21B was also significant overexpression in primary tumor specimens compared with normal group based on the sample type in COAD. Based on the histological subtype of COAD, the expression of KIF21B was also increased expression in adenocarcinoma ($n = 243$)/mucinous adenocarcinoma ($n = 37$) compared to normal tissues ($n = 43$) from UALCAN database. In addition, KIF21B was elevated expression in tumor specimens ($n = 275$) compared with normal specimens ($n = 349$) from GEPIA database. Collectively, our data indicated that KIF21B is upregulated expression in CRC.

3.2. Overexpression of KIF21B in Colorectal Cancer Was Related to Poor Prognosis. Then, we analyzed the correlation between KIF21B expression and survival of patients. As shown in Figure 2(a), there was a better survival, including overall survival, disease specific survival, and progress free interval, in patients with low expression of KIF21B compared to the high expression groups from TCGA–COAD dataset. In addition, the AUC values were all greater than 0.8, and the confidence interval was between 0.8 and 0.9 by AUC analysis from GTEx-COAD and TCGA-COAD database (Figure 2(b)). Taken together, our data suggested that KIF21B has a value as a diagnostic marker in CRC.

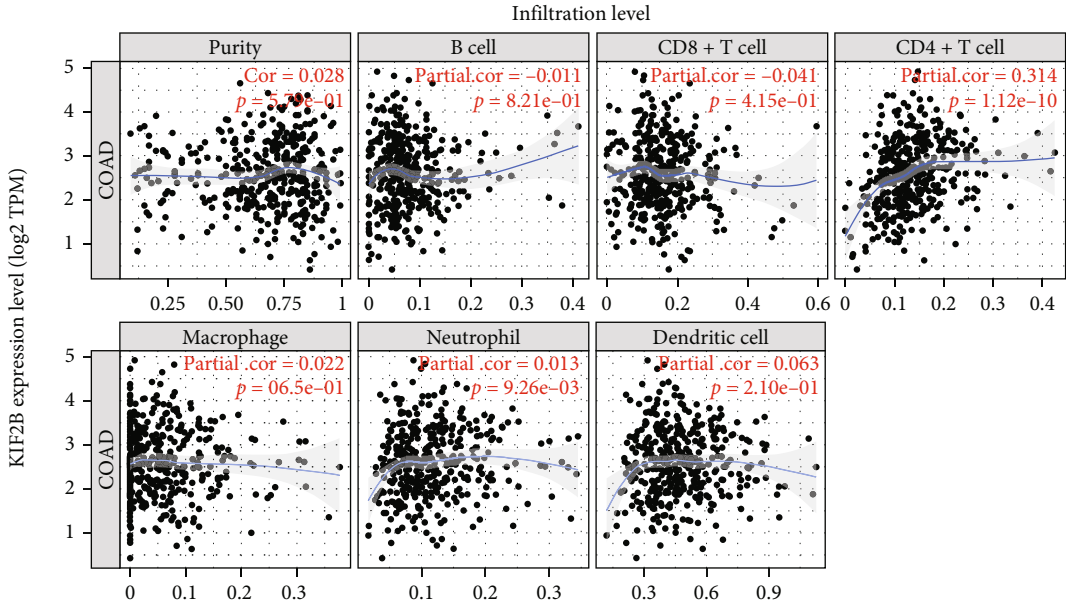

Figure 4: The correlation between KIF21B and immune infiltration. Correlation between KIF21B and immune infiltration in related cell lines.

3.3. Enrichment Analysis of KIF21B Expression-Related Genes in Colorectal Cancer. In order to clarify the underlying function of KIF21B, we used GO-KEGG signal pathway analysis to confirm the networks of KIF21B in CRC. As shown in Figures 3(a) and 3(b), KIF21B mainly exerted important role in notch signaling pathway, inositol phosphate metabolism, phosphatidylinositol signaling system, and histone modification. Moreover, KIF21B and related genes are significantly enriched in covalent chromatin modification. There was a positive correlation between KIF21B expression with CD4+ T cells (cor = 0.352, $P = 1.12e-10$) and neutrophil cells (cor = 0.352, $P = 9.26e-3$) (Figure 4). Collectively, our data indicated that KIF21B is correlated with immune infiltrates in CRC.

3.4. The Correlation between KIF21B and the Biological Function of Colorectal Cancer Cells. Next, to better understand the expression correlation and underlying mechanisms of KIF21B in cancer, we analyzed the functional status of KIF21B in diversity cancers from the CancerSEA database. KIF21B has been studied at the single-cell level in 12 kinds of cancer (Figure 5(a)), including AML, ALL, CML, GBM, Glioma, AST, ODG, LUAD, MEL, RCC, BRCA, and PC. KIF21B was positively correlated with CRC cell apoptosis (cor = 0.414, $P = 0.007$) and migration (cor = 0.352, $P = 0.024$). However, KIF21B was not significantly associated with any of the 14 functional states in CRC except for apoptosis and metastasis. We also analyzed the single-cell expression distribution of KIF21B in CRC tissues by t-SNE plot, as shown in Figure 5(b), there was a differential expression of KIF21B in single-cell level. Furthermore, KIF21B expression was significantly positive correlation with apoptosis (cor = 0.41) and metastasis (cor = 0.35) (Figure 5(c)). And there was also a positive correlation between KIF21B expression and DNA damage (cor = 0.89) and hypoxia (cor = 0.79) (Figure 5(d)). Taken together, our data suggested that KIF21B is involved in the phenotype of CRC.

3.5. KIF21B Was Upregulated Expression in CRC Cells and Promotes Cell Migration and Invasion. To better clarify the function of KIF21B in CRC, we analyzed the expression of KIF21B in cell level, as shown in Figures 6(a) and 6(b). KIF21B was upregulated expression in CRC cell lines, including HT29, HCT116, SW480, and HCT15, compared with normal intestinal epithelial cells NCM460. Then, we constructed KIF21B knockdown HCT116 and HT29 cell lines by shRNA (Figure 6(c)). And we analyzed cell proliferation in the cell lines by CCK8 assay, as shown in Figure 6(d), knockdown of KIF21B decreased cell proliferation in HT29 and HCT116 cell lines. Moreover, KIF21B deficiency induced cell apoptosis in HT29 and HCT116 cell lines (Figure 6(e)). Apart from this, cell migration and invasion were also suppressed in HT29 and HCT116 cell lines with shKIF21B treatment (Figures 6(f) and 6(g)). Collectively, our data suggested that KIF21B positively regulates cell proliferation, migration, and invasion in CRC.

4. Discussion

Colorectal cancer (CRC) as the third most common malignancy and the second mortality in diversities of cancer, which accounts for 10.2% morbidity and 9.2% mortality in all types of cancer worldwide [1]. And with the development of society, the morbidity and mortality of CRC have increased year by year in the past three decades. Therefore, it is essential to find out the key biomarker of poor survival in regulating of CRC development and progression. In this study, KIF21B was high expression in CRC cells and tissues. Overexpression of KIF21B was associated with poor survival. KIF21B was correlated with immune infiltrates in

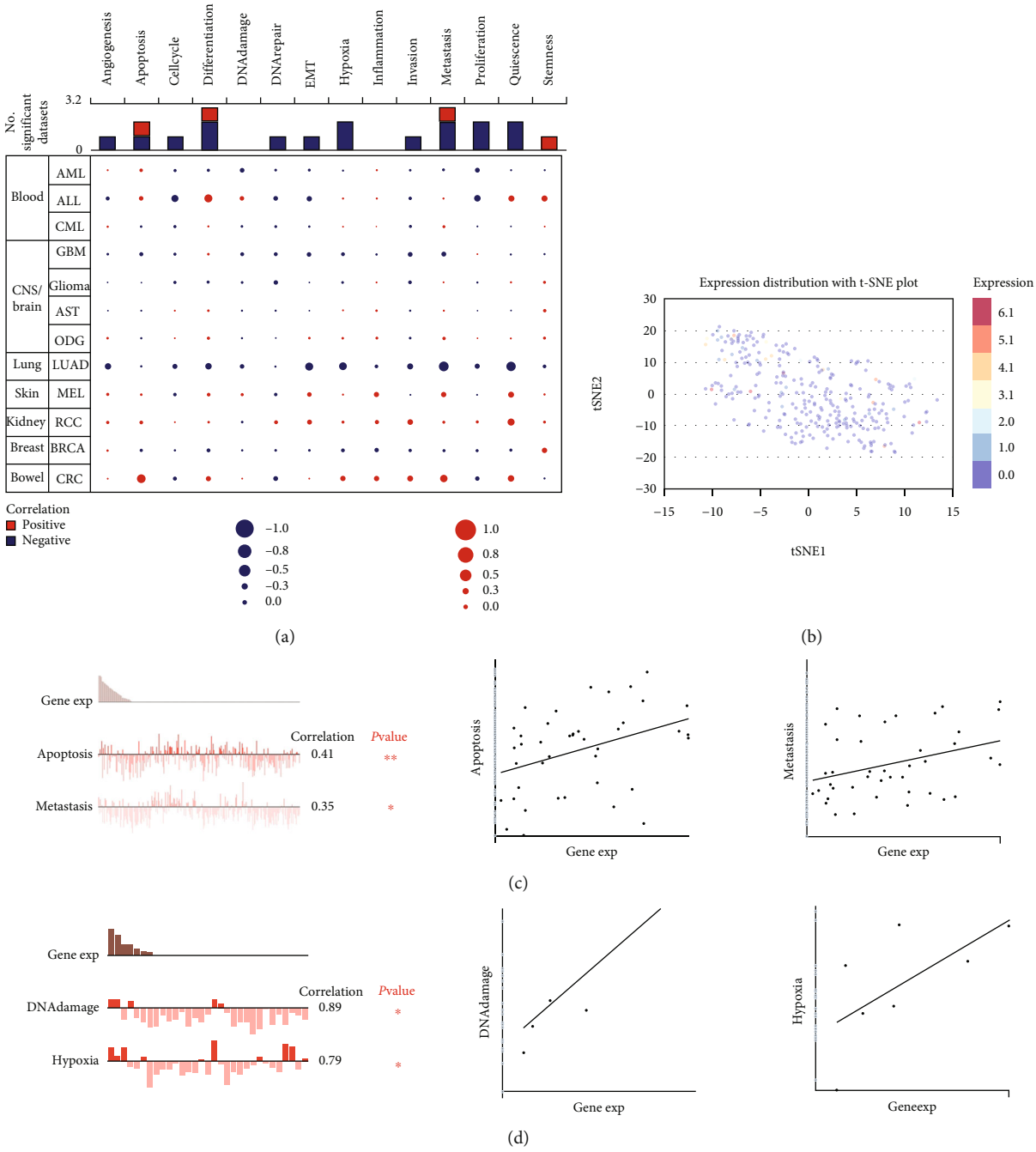

Figure 5: Single-cell-sequencing to analyze the correlation between KIF21B and the biological function of colorectal cancer cells. (a) Function analysis of KIF21B in different kinds of cancer CancerSEA (http://biocc.hrbmu.edu.cn/CancerSEA/). (b) The expression profile of KIF21B in single cell from CRC tissue was analyzed by T-SNE. (c) The correlation analysis of KIF21B with apoptosis and migration. (d) The correlation analysis of KIF21B with DNA damage and hypoxia.

CRC. Furthermore, single-cell sequencing indicated that KIF21B exerts positive correlation with cell apoptosis and metastasis. In addition, knockdown of KIF21B reduced cell viability, metastasis, and invasion, whereas increased cell apoptosis in CRC cell lines.

KIF21B belongs to a superfamily of motor proteins, exerted critical role in intracellular trafficking, cell mitosis, and cytoskeletal reorganization [8]. In the past few years, many research reported that the change of kinesins acts important role in cell growth, cell migration, cell invasion, and tumorigenesis in diversity of cancers, including prostate cancer, breast cancer, bladder cancer, pancreatic cancer, gastric cancer, hepatocellular carcinoma, colorectal cancer, and lung cancer [18]. And KIF21B, as a member of kinesins family proteins, also exerted important role in gastric cancer [19], HCC [11], and NSCLC [20]. Here, we were firstly demonstrated that KIF21B plays key role in CRC. Generally, KIF21B exerted a function of ATP-dependent microtubule motor protein, which

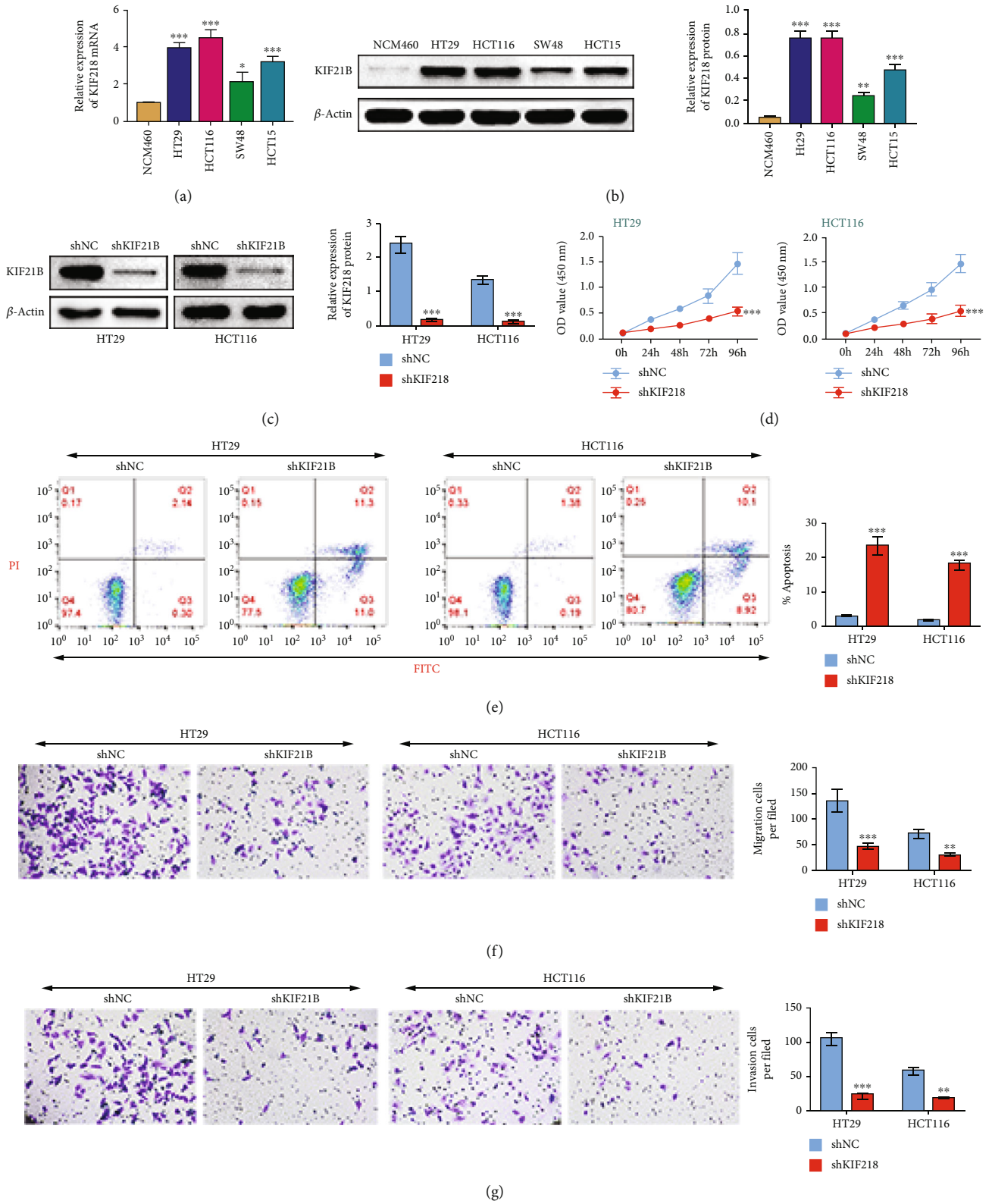

Figure 6: KIF21B was upregulated in colorectal cancer cells and promotes survival, increases migration and invasion. (a) KIF21B mRNA expression in CRC cell lines was measured by RT-qPCR. (b) Western blotting assay was used to analyze KIF21B protein expression in CRC cell lines. (c) HT29 and HCT116 cell lines were transfected with shNC and shKIF21B, respectively. The expression of KIF21B was measured by Western blotting. (d) KIF21B-knockdown HCT116 and HT29 cell lines were cultured as the indicated time (0 h, 24 h, 48 h, 72 h, and 96 h), then the cell proliferation was measured by CCK8 assay. (e) Cell apoptosis in KIF21B deficiency HCT116 and HT29 cell lines was measured by flow cytometry. (f, g) Cell migration and invasion were measured by transwell assay without or with matrigel.

participates in regulation of microtubule dynamics, including growth rate and mutation frequency [7]. Based on the important role of kinesins and microtubules in signaling transduction, transport, metastasis, malignancy, and tumorigenesis, we also clarified the key role of KIF21B in cell proliferation, apoptosis, migration, and invasion in CRC.

Previous study reported that KIF21B is overexpression in HCC cells and tissues, and KIF21B deficiency significantly suppressed cell proliferation and increased cell apoptosis, which indicated that KIF21B is a potential diagnostic and prognostic marker for HCC [11]. Moreover, Sun et al. also reported that KIF21B was overexpression in non-small-cell lung cancer tissues and associated with poor prognosis. Knockdown of KIF21B remarkably reduced cell proliferation, cell migration, cell invasion, and increased cell apoptosis in NSCLC [20]. Similarly, we confirmed the result of KIF21B in regulation of cell viability and apoptosis in CRC. Apart from this, KIF21B deficiency reduced the expression of Bcl-2 and induced the expression of Bax and active caspase 3 in NSCLC [20]. KIF21B decreasing expression facilitated cell apoptosis and impeded cell growth and tumorigenesis in nude mice through the inhibition of PI3K/AKT pathway and decreasing of Bcl-2 and increasing of Bax expression in osteosarcoma [12]. The underlying mechanism of KIF21B in regulating of cell apoptosis in CRC needs to be further investigated.

In our research, KIF21B mainly exerted important role in notch signaling pathway, inositol phosphate metabolism, and phosphatidylinositol signaling system by KEGG enrichment analysis, which was similar with the previous study of critical role of KIF21B in osteosarcoma [12]. They also demonstrated that KIF21B expression regulates cell proliferation and apoptosis through the PI3K/AKT pathway. Here, the underlying mechanism of KIF21B involved in phosphatidylinositol signaling needs further study. KIF21B was associated with DNA damage and hypoxia by single-cell sequencing. For the development and progression of cancer, hypoxia and DNA damage acted as an inducer in promoting cancer [21, 22]. Therefore, we speculated that KIF21B may induce CRC via DNA damage and hypoxia-related signal pathway by single-cell-sequencing analysis. Additionally, KIF21B was positively correlated with CD4+ T cell and neutrophil cell, which involved in regulation of immune infiltrate of cancer cells. Next, we plan to further study the underlying molecular mechanisms of KIF21B in regulation of DNA damage and immunity in CRC.

In conclusion, KIF21B was an increasing expression in Colorectal cancer cell lines and tissue specimens, which was correlated with poor survival, immune infiltrates, cell growth, and metastasis. KIF21B may be a biomarker in the diagnosis of CRC.

Data Availability

All data generated or analyzed during this study are included in this published article.

Conflicts of Interest

The authors state that there are no conflicts of interest to disclose.

Authors' Contributions

Shanshan Xu and Youran Li designed the study and supervised the data collection. Hua Huang analyzed the data and interpreted the data. Xian Miao and Yunfei Gu prepared the manuscript for publication and reviewed the draft of the manuscript. All authors have read and approved the manuscript. Shanshan Xu and Youran Li contributed equally to this work.

Acknowledgments

This work was supported by the Postgraduate Research & Practice Innovation Program of Jiangsu Province (Grant no. SJCX21_0729), the National Natural Science Foundation of China for Youth (Grant no. 81904204), the Natural Science Youth Fund of Jiangsu Province (BK20191091), and the Peak Academic Talent Project of Jiangsu Hospital of Traditional Chinese Medicine (y2021rc35).

References

[1] F. Bray, J. Ferlay, I. Soerjomataram, R. L. Siegel, L. A. Torre, and A. Jemal, "Global cancer statistics 2018: GLOBOCAN estimates of incidence and mortality worldwide for 36 cancers in 185 countries," *CA: a Cancer Journal for Clinicians*, vol. 68, no. 6, pp. 394–424, 2018.

[2] A. Bahrami, F. Amerizadeh, S. M. Hassanian et al., "Genetic variants as potential predictive biomarkers in advanced colorectal cancer patients treated with oxaliplatin-based chemotherapy," *Journal of Cellular Physiology*, vol. 233, no. 3, pp. 2193–2201, 2018.

[3] R. L. Siegel, K. D. Miller, S. A. Fedewa et al., "Colorectal cancer statistics, 2017," *CA: a Cancer Journal for Clinicians*, vol. 67, no. 3, pp. 177–193, 2017.

[4] U. Lee, C. Frankenberger, J. Yun et al., "A prognostic gene signature for metastasis-free survival of triple negative breast cancer patients," *PLoS One*, vol. 8, no. 12, p. e82125, 2013.

[5] N. Hirokawa and Y. Tanaka, "Kinesin superfamily proteins (KIFs): various functions and their relevance for important phenomena in life and diseases," *Experimental Cell Research*, vol. 334, no. 1, pp. 16–25, 2015.

[6] Y. Liu, P. Zhan, Z. Zhou et al., "The overexpression of KIFC1 was associated with the proliferation and prognosis of non-small cell lung cancer," *Journal of Thoracic Disease*, vol. 8, no. 10, pp. 2911–2923, 2016.

[7] M. Muhia, E. Thies, D. Labonté et al., "The kinesin KIF21B regulates microtubule dynamics and is essential for neuronal morphology, synapse function, and learning and memory," *Cell Reports*, vol. 15, no. 5, pp. 968–977, 2016.

[8] W. E. van Riel, A. Rai, S. Bianchi et al., "Kinesin-4 KIF21B is a potent microtubule pausing factor," *eLife*, vol. 6, 2017.

[9] M. He, R. Subramanian, F. Bangs et al., "The kinesin-4 protein Kif7 regulates mammalian hedgehog signalling by organizing the cilium tip compartment," *Nature Cell Biology*, vol. 16, no. 7, pp. 663–672, 2014.

[10] T. Arai, S. Kojima, Y. Yamada et al., "Pirin: a potential novel therapeutic target for castration-resistant prostate cancer regulated by miR-455-5p," *Molecular Oncology*, vol. 13, no. 2, pp. 322–337, 2019.

[11] H. Q. Zhao, B. L. Dong, M. Zhang et al., "Increased KIF21B expression is a potential prognostic biomarker in hepatocellular carcinoma," *World Journal of Gastrointestinal Oncology*, vol. 12, no. 3, pp. 276–288, 2020.

[12] S. Ni, J. Li, S. Qiu, Y. Xie, K. Gong, and Y. Duan, "KIF21B expression in osteosarcoma and its regulatory effect on osteosarcoma cell proliferation and apoptosis through the PI3K/AKT pathway," *Frontiers in Oncology*, vol. 10, p. 606765, 2020.

[13] L. Yu, X. Huang, W. Zhang et al., "Critical role of DEK and its regulation in tumorigenesis and metastasis of hepatocellular carcinoma," *Oncotarget*, vol. 7, no. 18, pp. 26844–26855, 2016.

[14] J. H. Pan, H. Zhou, L. Cooper et al., "LAYN is a prognostic biomarker and correlated with immune infiltrates in gastric and colon cancers," *Frontiers in Immunology*, vol. 10, p. 6, 2019.

[15] W. Dai, J. Feng, X. Hu et al., "SLC7A7 is a prognostic biomarker correlated with immune infiltrates in non-small cell lung cancer," *Cancer Cell International*, vol. 21, no. 1, p. 106, 2021.

[16] L. Dong, L. Yu, H. Li et al., "An NAD^+-Dependent Deacetylase SIRT7 Promotes HCC Development Through Deacetylation of USP39," *Iscience*, vol. 23, no. 8, p. 101351, 2020.

[17] L. Dong, L. Yu, C. Bai et al., "USP27-mediated cyclin E stabilization drives cell cycle progression and hepatocellular tumorigenesis," *Oncogene*, vol. 37, no. 20, pp. 2702–2713, 2018.

[18] O. Rath and F. Kozielski, "Kinesins and cancer," *Nature Reviews. Cancer*, vol. 12, no. 8, pp. 527–539, 2012.

[19] X. Zheng, X. Wang, L. Zheng et al., "Construction and analysis of the tumor-specific mRNA-miRNA-lncRNA network in gastric cancer," *Frontiers in Pharmacology*, vol. 11, p. 1112, 2020.

[20] Z. G. Sun, F. Pan, J. B. Shao, Q. Q. Yan, L. Lu, and N. Zhang, "Kinesin superfamily protein 21B acts as an oncogene in non-small cell lung cancer," *Cancer Cell International*, vol. 20, no. 1, p. 233, 2020.

[21] X. Jing, F. Yang, C. Shao et al., "Role of hypoxia in cancer therapy by regulating the tumor microenvironment," *Molecular Cancer*, vol. 18, no. 1, p. 157, 2019.

[22] R. X. Huang and P. K. Zhou, "DNA damage response signaling pathways and targets for radiotherapy sensitization in cancer," *Signal Transduction and Targeted Therapy*, vol. 5, no. 1, p. 60, 2020.

Hindawi
Journal of Oncology
Volume 2022, Article ID 1403454, 10 pages
https://doi.org/10.1155/2022/1403454

Research Article

Mechanism of PDZK1 in Hepatocellular Carcinoma Complicated with Hyperuricemia

Linqi Guo,[1,2] Wenda Jiang,[2] Lingli Quan,[3] Xinli Teng,[4] Jing Zhao,[1,2] and Hongbin Qiu [1,5]

[1]*School of Basic Medicine Jiamusi University, Jiamusi 154000, China*
[2]*Department of General Surgery, The First Affiliated Hospital of Jiamusi University, Jiamusi 154000, China*
[3]*Pulmonary and Critical Care Medicine 1, The Affiliated Zhuzhou Hospital Xiangya Medical College CSU, Zhuzhou 412000, China*
[4]*Medical Oncology, The Tumor Hospital of Jiamusi, Jiamusi 154000, China*
[5]*School of Public Health Jiamusi University, Jiamusi 154000, China*

Correspondence should be addressed to Hongbin Qiu; qiuhongbin99@163.com

Received 9 August 2022; Revised 27 September 2022; Accepted 11 October 2022; Published 14 November 2022

Academic Editor: Muhammad Muddassir Ali

Background. Hepatocellular carcinoma (HCC) is a kind of primary liver cancer that accounts for more than 90% of primary hepatocellular carcinomas. Hyperuricemia is closely related to the development, recurrence, metastasis, and prognosis of cancer. Previous studies have proved that the serum uric acid level can increase the incidence rate and mortality of malignant tumors. However, the specific pathogenesis remains unstudied. *Methods*. RT-qPCR analysis showed that the mRNA expression of PDZK1 and ABCG2 increased significantly after HCC cells were exposed to different concentrations of soluble uric acid (2.5, 5, 10, 20 mg/dl) for 24 hours. Then, in HCC shRNAs, PDZK1, or over expression PDZK1 were used. CCK8, wound healing, and Transwell assay showed that PDZK1 regulates cell proliferation, invasion, and migration. Flow cytometry results revealed that PDZK1 affects cell apoptosis. Western blot results show that PDZK1 affects the STAT3/C-myc pathway. Then, in vivo tumorigenesis, allopurinol maybe an effective drug to advance: the prognosis of HCC. *Results*. In our study, RT-qPCR analysis showed that the mRNA expression of PDZK1 and ABCG2 increased significantly after different concentrations of soluble uric acid in HCC. Then, PDZK1 affects the proliferation, migration, and apoptosis of HCC through the STAT3/C-myc pathway. *Conclusions*. Hyperuricemia response affects the expression of PDZK1; PDZK1 affects the proliferation, migration, and apoptosis through the STAT3/C-myc pathway in hepatocellular carcinoma. It is suggested that PDZK1 maybe closely related to the occurrence, development, and prognosis of HCC and allopurinol maybe have potential anticancer effects.

1. Introduction

Hepatocellular carcinoma (HCC) is a type of primary liver cancer that accounts for more than 90% of primary hepatocellular carcinomas. HCC is currently the fifth most common cause of cancer in the world [1]. The second-leading cause of cancer death in men is HCC. The five-year survival rate of HCC is about 18%, just after pancreatic cancer [2, 3]. Important risk factors for hepatocellular carcinoma include viral hepatitis B or viral hepatitis C, alcoholic liver disease, nonalcoholic fatty liver disease, and so on [4, 5]. Approximately 80%–90% of patients with cirrhosis develop liver cancer [6]. Therefore, it is very important to explore the occurrence, development, and potential molecular mechanism of liver cancer.

A product of purine oxidative metabolism is uric acid (UA). Some studies point out that the proportion of tumor patients with ranges hyperuricemia from high to low for vocal cord cancer, maxillary cancer, hypopharyngeal cancer, bladder cancer, liver cancer, and ovarian cancer [7–10]. Because of its proinflammatory characteristics, hyperuricemia may have an important role in the pathogenesis of cancer. Its mechanism may be related to reactive oxygen species (ROS), inflammatory corpuscle activation, and

xanthine oxidoreductase (XO) mediated production of active free radicals [11–15]. It is closely related to the incidence, mortality, and prognosis of many solid tumors.

Allopurinol is the first-line medicine to treat hyperuricemia. Combining allopurinol with other medicines had been extensively explored. Previous clinical trials have shown that allopurinol has a positive association with prostate cancers, patients treated with allopurinol could decreased the incidence of prostate cancer. And the combined use of allopurinol for one month can reduce the level of NF kappaB in patients with colonic adenoma [16–19]. It is suggested that the drug that reduces uric acid levels have potential anticancer effects and provides a new idea for tumor treatment.

PDZ domain-containing 1 (PDZK1) is located on chromosome 1 q21.1. It has a relative molecular mass of 63 KDa and contains 519 amino acids. It contains 4 protein domains; the PDK domain of PDZK1 is mainly involved in regulating the subcellular localization of various uric acid transporters, and some studies have found that its rs12129861 mutation is bound up with hyperuricemia and gout pathogenesis [20–22]. In recent years, studies have found that the abnormal expression level of PDZK1 was found in various tumors, for example breast cancer, renal cell carcinoma, and gastric cancer [23–25]. However, the molecular mechanism of PDZK1 in HCC remains unclear.

In our study, the mRNA expression of PDZK1 was significantly increased after HCC after different concentrations of soluble uric acid treatment, and PDZK1 affects the proliferation, migration, and apoptosis of HCC through the STAT3/C-myc pathway. PDZK1 maybe closely related to the occurrence, development, and prognosis of HCC and allopurinol may have potential anticancer effects.

2. Materials and Methods

2.1. Cell Culture and Construction Lentivirus Vectors. HepG2 and Hep3B cells were acquired from ATCC, Huh7, and PVTT cells were acquired from the Institute of Cell Biochemistry, Chinese Academy of Sciences. The cells were incubated in RPMI-1640 (Gibco, CA, USA) medium containing 10% FBS (Invitrogen, CA, USA) and cultured at 37°C and 5%CO_2 incubator. sh-PDZK1 (SH1, SH2) and sh-control (SC) were constructed by ribobio Biotechnology Co., Ltd (GuangZhou China). The overexpression vector of PDZK1 (pcDNA-PDZK1, PDZK1) and control lntivirus vectors (pcDNA-NC, vector) were constructed by GenePharma Biotechnolog Co., Ltd (Suzhou, China). The cells were transfected by using Lipofectamine™ 3000 (Invitrogen, CA, USA) followed by the protocols of the manufacturer.

2.2. CCK8 Analysis. HepG2, Hep3B cells (2×10^3) or Huh7, and PVTT cells (4×10^3) were incubated in a 96-hole plate after 48 hours of transfection, after 24 hours, 48 hours, and 72 hours. CCK8 reagent (10 μL) was added into each hole for 2 h, and each group repeated 3 times. The absorbance of each hole was measured by a microplate assay (EnSpire 2300, PerkinElmer, USA) at a wavelength of 450 nm.

2.3. Wound Healing. HepG2, Hep3B cells (5×10^5) or Huh7, and PVTT cells (8×10^5) were incubated into the 6-hole plate after 48 hours of transfection, after 24 hours, a vertical line was drawn evenly in the middle of the hole base using a 20 μL pipette tip, and each group was repeated 3 times. Images were taken at 0 and 24 hours under a light microscope to observe cell migration.

2.4. Transwell Assay. Cells (1×10^5) were added to the Transwell upper chamber without fetal bovine serum after 48 hours of transfection. A culture medium (600 μL) containing 15% fetal bovine serum was added into the lower chamber. After 48 hours, the noninvasive cells in the upper chamber were gently wiped away by a cotton swab. The lower chamber cells were stained with crystal violet. Then, observed and counted cells by inverted microscope. Each group was repeated 3 times.

2.5. Flow Cytometry Assay. 5×10^7 cells were collected in centrifuge tubes after 48 hours of transfection, then, PBS was washed twice. Cells were stained with 5–10 μL propidium iodides (PI) and 5–10 μL Annexin V-FITC into 100ul stain buffer, 15 mins later, cell apoptosis was detected by BD FACSCalibur (BD, USA), each group was repeated 3 times, and analyzed by Cell Quest software.

2.6. RNA Extraction and RT-PCR Analysis. Cells (5×10^6) were collected after 48 hours of transfection, and total RNA was extracted by Trizol. 1 μg RNA was used to synthesis of cDNA according to the instructions of the reverse transcription kit (Agilent, USA). The mRNA expression of PDZK1 was determined by RT-PCR on the CFX96Tm real-time System (Bio-Rad, USA), as follow: 95°C, 3 min, then, 95°C20 s and 70°C 1 min for 40 cycles. The calculation method of relative expression used the comparative Ct ($2^{-\Delta\Delta Ct}$) method [26], and each group was repeated 3 times.

2.7. Western Blot Assay. Transfected HCC cells were collected after 48 hours, the culture medium was discarded, PBS was washed twice, and then, cell lysate was added. Following the manufacturer's protocol of the BCA Kit (Thermo Scientific, USA) to quantify total protein, then, the primary antibodies (STAT3, p-STAT3, C-myc, and GAPDH) (Cell Signaling Technology, USA) were incubated for 12 hours, and the second antibody (Cell Signaling Technology, USA) were added for 2 hours. Future, chemiluminescent reagent was added and incubated in the dark for 5 min, developed for 30 s, fixed for 10 s, and each group was repeated 3 times. The gray value of electrophoresis band of the protein was analyzed by Image J software.

2.8. In Vivo Tumorigenesis. Transfected HCC cells were collected after 48 hours. Then, digestion by trypsin, centrifuged, counted. The corresponding volume of cell suspension was measured by the subcutaneous injection of

5×10^6 cells into mice with hyperuricemia. After subcutaneous transplantation of mice, allopurinol was fed every four days. After 4 weeks, the serum of the tail vein of nude mice was taken, the animals were killed, and the tumor tissue was taken. Measure the tumor size with a vernier caliper and calculate the tumor volume formula: volume = 0.5 * length * width * width.

2.9. Statistical Analysis. SPSS 20 was used to analyze the experimental data. A Mean ± standard was used to represent data between groups. A one-way ANOVA test was used for statistical analysis, and a *t*-test was used for the comparison between two groups.

3. Results

3.1. The Expression of PDZK1 and ABCG2 in Hepatocellular Cells Is Mediated by the Stimulation of Soluble Uric Acid. RT-qPCR analysis showed that the mRNA expression of PDZK1 and ABCG2 increased significantly were exposed to different concentrations of soluble uric acid (2.5, 5, 10, and 20 mg/dl) in HCC cells (Figures 1(a) and 1(b)). After the cells were treated with 10 mg/dl soluble uric acid for 4, 8, 16, 32, 48, and 64 hours, the expression of PDZK1 and ABCG2 peaked at 32 hours (Figures 1(c) and 1(d)). It indicates that hyperuricemia response affects the expression changes of PDZK1 is more obvious, and then, we choose PDZK1 in the next study.

3.2. PDZK1 Affects the Proliferation, Migration, and Apoptosis of HCC. We used shRNAs to knock down PDZK1 in HepG2 and Hep3B cells. The interfering shRNA was transfected into negative control cells. Western blot and RT-qPCR analysis showed that PDZK1 shRNAs strongly inhibited the expression of PDZK1, and the expression level decreased significantly (Figures 2(a)–2(d)). CCK8, wound healing, and transwell assay showed that sh-PDZK1 could inhibit ell proliferation, invasion and migration (Figures 2(e)–2(h)). Flow cytometry results revealed that sh-PDZK1 induced cell apoptosis (Figures 2(i) and 2(j)).

Western blot and RT-qPCR analysis showed that pcDNA3.1-PDZK1 strongly over expression of PDZK1 (Figures 3(a)–3(c)), and the expression level increased significantly. CCK8, wound healing, and Transwell assay showed that pcDNA3.1- PDZK1 promote cell proliferation, invasion and migration (Figures 3(d)–3(i)), flow cytometry results revealed that sh-PDZK1 induced cell apoptosis (Figures 3(j) and 3(k)).

3.3. PDZK1 Affects HCC Function through STAT3/C-myc Pathway. Uric acid may cause tumor immune response, so PDZK1 may also be related to tumor immune progress. The STAT3/C-myc pathway is closely related to tumor immune response. To investigated whether PDZK1 can affect liver cancer cell processes through the STAT3/C-myc pathway. Western blot results show that, compared with the control group, p-STAT3, C-myc protein expression significantly increased in the pcDNA3.1-PDZK1 groups, and the expression of these proteins were significantly decreased in the sh-PDZK1 group (Figures 4(a) and 4(b)).

3.4. Allopurinol Is an Effective Drug to Improve the Prognosis of HCC. We used high uric acid mice for tumorigenesis, $2 * 10^6$ cells into mice with hyperuricemia. After subcutaneous transplantation of mice, allopurinol was fed every four days. The tumor volume of PDZK1 overexpression group are increased, and treat with allopurinol, the tumor volume is decreased (Figure 5(a)). Ki67 result showed that after treatment with allopurinol, the proliferation of tumor was more reduced compare with PDZK1 overexpression group (Figure 5(b)). Immunofluores result showed that, the p-STAT3 and C-myc expression was increased in PDZK1 overexpression group, and p-STAT3 and C-myc was decreased after treatment with allopurinol (Figure 5(c)).

3.5. PDZK1 Is Related to the Occurrence and Development of HCC in Clinically. We used the publicly online tools TGCA database, and showed that compared with normal, the expression of PDZK1 are increased in HCC, and increased in base individual cancer stage (1, 2, 3, and 4) and tumor grade (1, 2, 3, and 4) (Figures 6(a)–6(c)). Kaplan–Meier Plotter results showed the prognosis of high expression of PDZK1 is poor in HCC (Figure 6(d)).

4. Discussion

Hyperuricemia is a metabolic disease, which can be secondary to gout and increase the risk of other diseases, especially cardiovascular diseases, metabolic diseases, and kidney diseases, such as metabolic syndrome or heart failure [27, 28]. In recent years, through various clinical observations and studies, it has been found that hyperuricemia maybe an independent risk factor for a variety of solid tumors, including prostate cancer, colon cancer, and breast cancer [29–34]. In our study, the mRNA expression of PDZK1 was significantly increased after HCC after different concentrations of soluble uric acid treatment, which is similar to Chen et al. results [35]. The tumor volume of PDZK1 overexpression group are increased and after treat with allopurinol the tumor volume is decreased. Hyperuricemia may be related to the occurrence, development, and metastasis of malignant tumors.

With the deepening of research on the relationship between hyperuricemia and tumor, it is found that different immune cell subsets, cell surface receptors, and cytokines have significant effects on the pathogenesis of gout and tumor, and the relationship between hyperuricemia and tumor shows a complex trend. On the one hand, urate crystals can activate effective immune stimulants and trigger anticancer immune responses directly by reversing immunosuppression or as adjuvants. On the other hand, the interaction between urate crystals and immune cells can enhance immunosuppression and promote angiogenesis [36], thus, affecting the biological characteristics of malignant tumors.

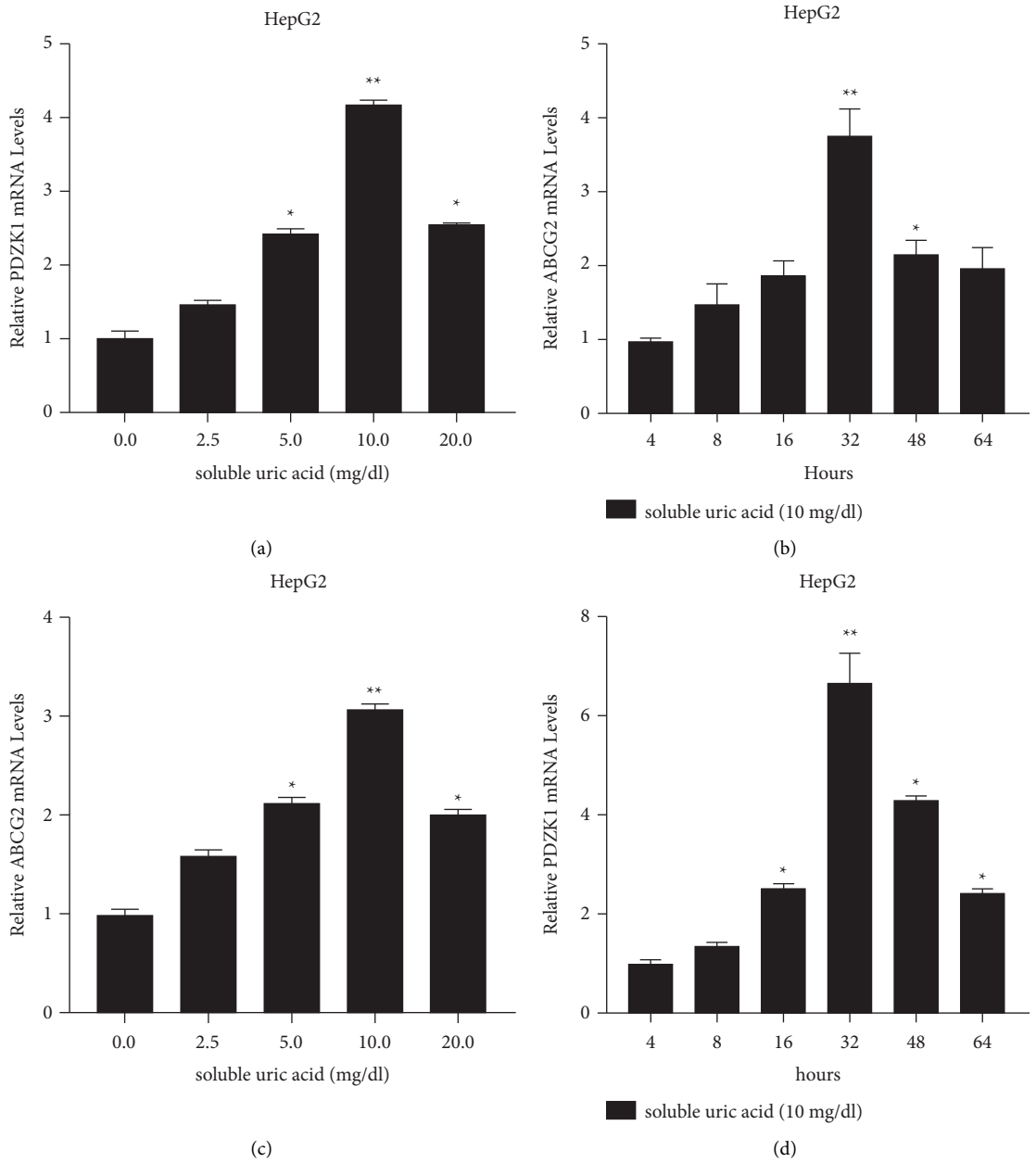

Figure 1: The expression of PDZK1 and ABCG2 in HCC is mediated by the stimulation of soluble uric acid. (a, b) The mRNA expression of PDZK1 and ABCG2 were significantly increased in hepatocellular cells were exposed to different concentrations of soluble uric acid (2.5, 5, 10, and 20 mg/dl) for 24 hours. (c, d) The mRNA expression of PDZK1 and ABCG2 after treated with 10 mg/dl soluble uric acid for 4, 8, 16, 32, 48, and 64 hours, data represent mean ± SD. $^{*}P < 0.05$ compare with negative control.

Studies have shown that almost all PDZK1 proteins can combine with SLC17A1, ABCG2, URAT1, SLC17A3, and other transporters related to uric acid transport to form a complex regulating the absorption and excretion of uric acid [37], and act on the reabsorption and excretion of uric acid together. Our study shows that PDZK1 protein is highly expressed in HCC. Regulatory PDZK1 expression can affect the proliferation, migration, and apoptosis of HCC; uric acid may cause tumor immune response. It suggests that PDZK1 may be related to tumor immunity [38–40]. We detected the expression changes of STAT3/C-myc signal pathway protein after sh-PDZK1 or over expression of PDZK1. Knockdown of PDZK1 can reduce the expression of p-STAT3 and C-myc, Similar to previous results [41]. We also found that allopurinol maybe an effective drug to improve the prognosis of liver cancer.

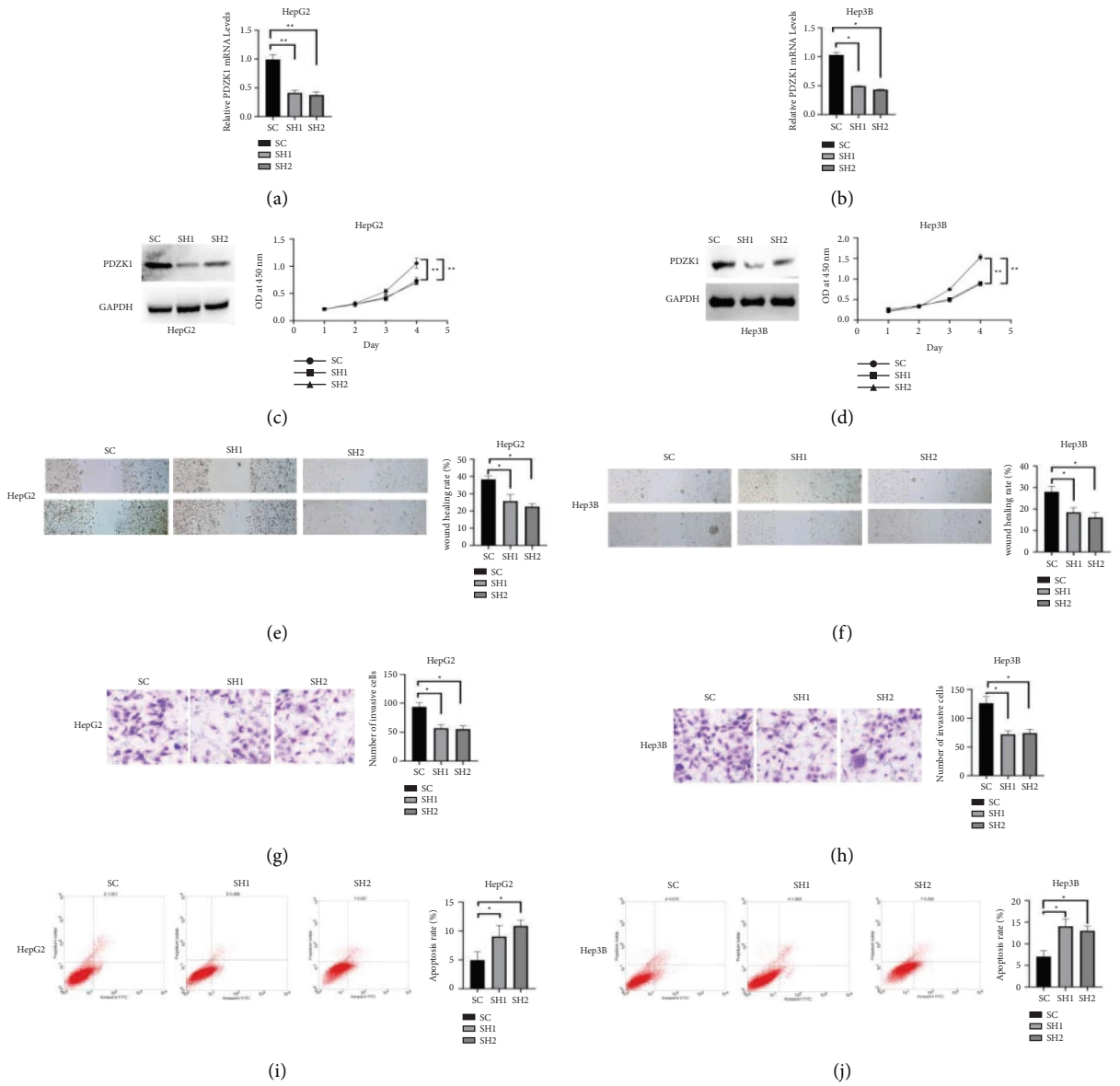

Figure 2: sh-PDZK1 inhibit the proliferation, migration, and promote apoptosis of HCC. (a, b, c, d) Western blot and RT-qPCR analysis showed that PDZK1 shRNAs strongly inhibited the expression of PDZK1, and the expression level decreased significantly. (e, f, g, h) CCK8, wound healing, and transwell assay showed that sh-PDZK1 induced the inhibition of cell proliferation, invasion, and migration. (i, j) Flow cytometry results revealed that sh-PDZK1 induced cell apoptosis. Data represent mean ± SD. $^{*}P < 0.05$ compare with negative control.

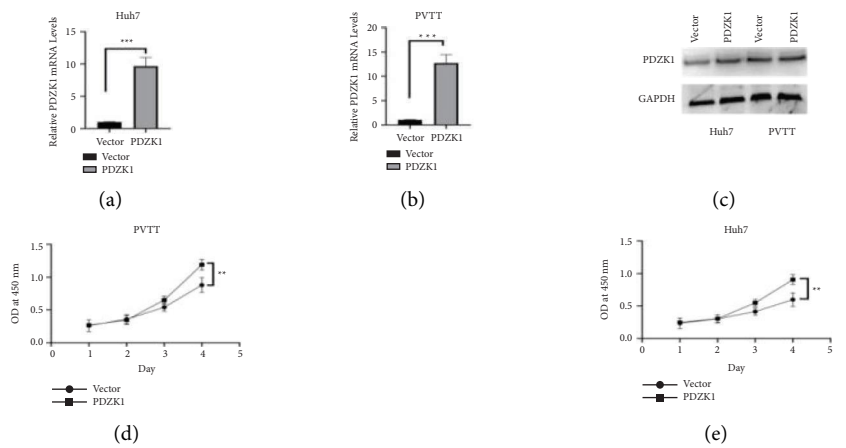

Figure 3: Continued.

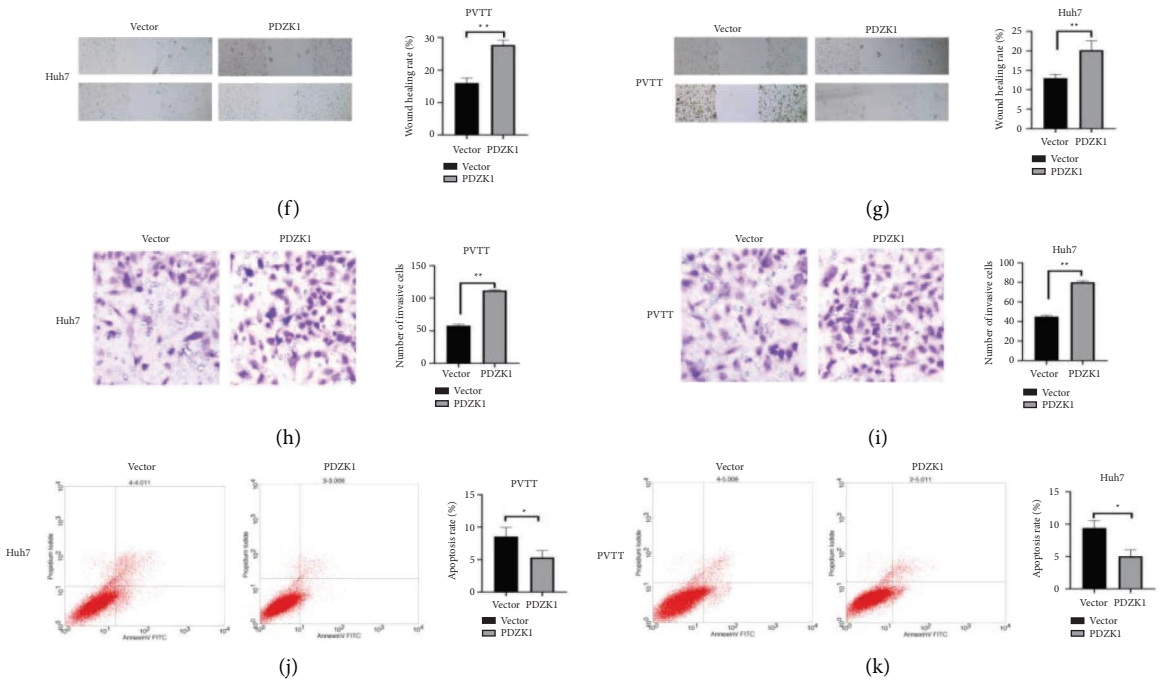

Figure 3: pcDNA3.1-PDZK1 affects the proliferation, migration, and apoptosis of HCC. (a, b, c) Western blot and RT-qPCR analysis showed that pcDNA3.1-PDZK1 strongly overexpression of PDZK1. (d, e, f, g, h, i) CCK8, wound healing, and transwell assay showed that pcDNA3.1-PDZK1 promote cell proliferation, invasion and migration. (j, k) Flow cytometry results revealed that pcDNA3.1-PDZK1 inhibit cell apoptosis. Data represent mean ± SD. $^{*}P < 0.05$ compare with negative control.

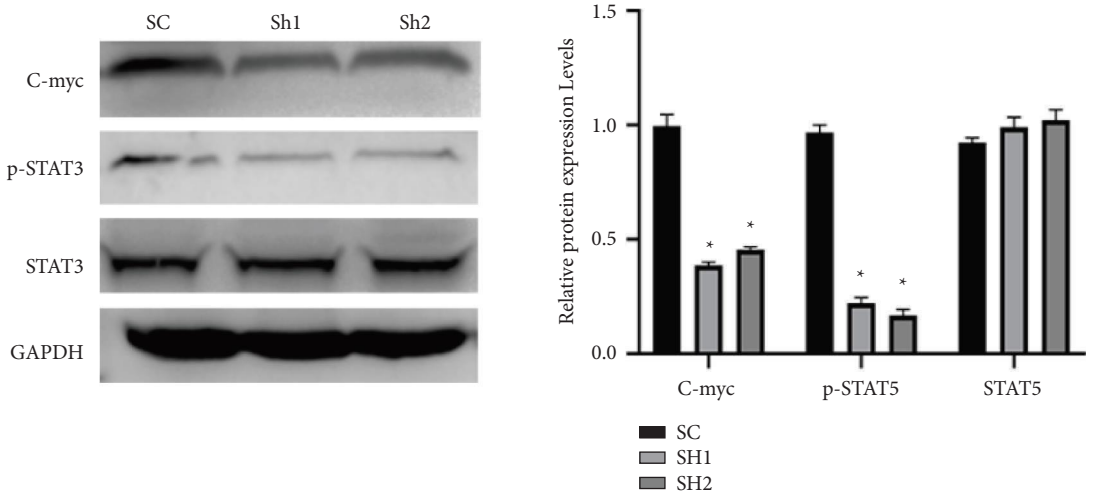

Figure 4: Continued.

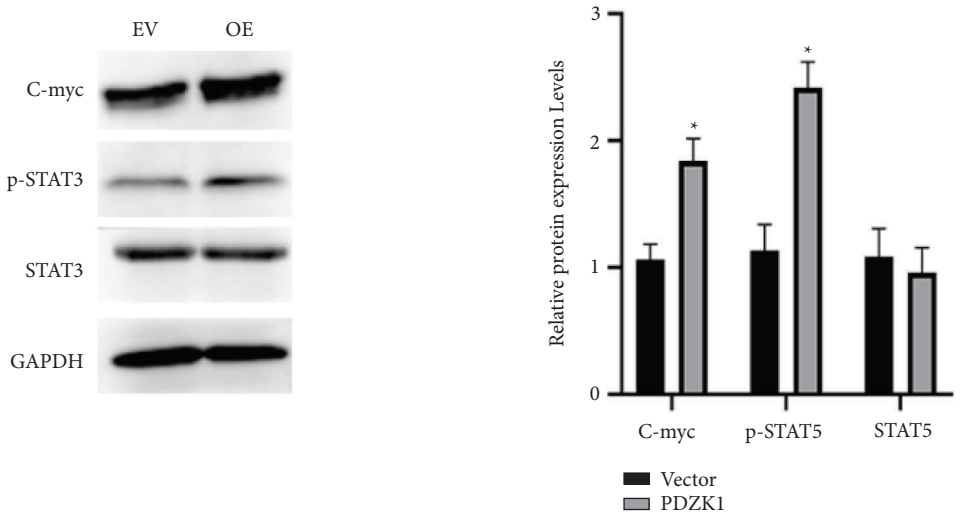

(b)

Figure 4: PDZK1 affects HCC function through STAT3/C-myc pathway. (a) Western blot results show that, compared with the control group, p-STAT3, C-myc protein expression significantly significantly decreased in the sh-PDZK1 group. (b) Western blot results show that, compared with the control group, p-STAT3, C-myc protein expression significantly increased in the pcDNA3.1-PDZK1 groups.

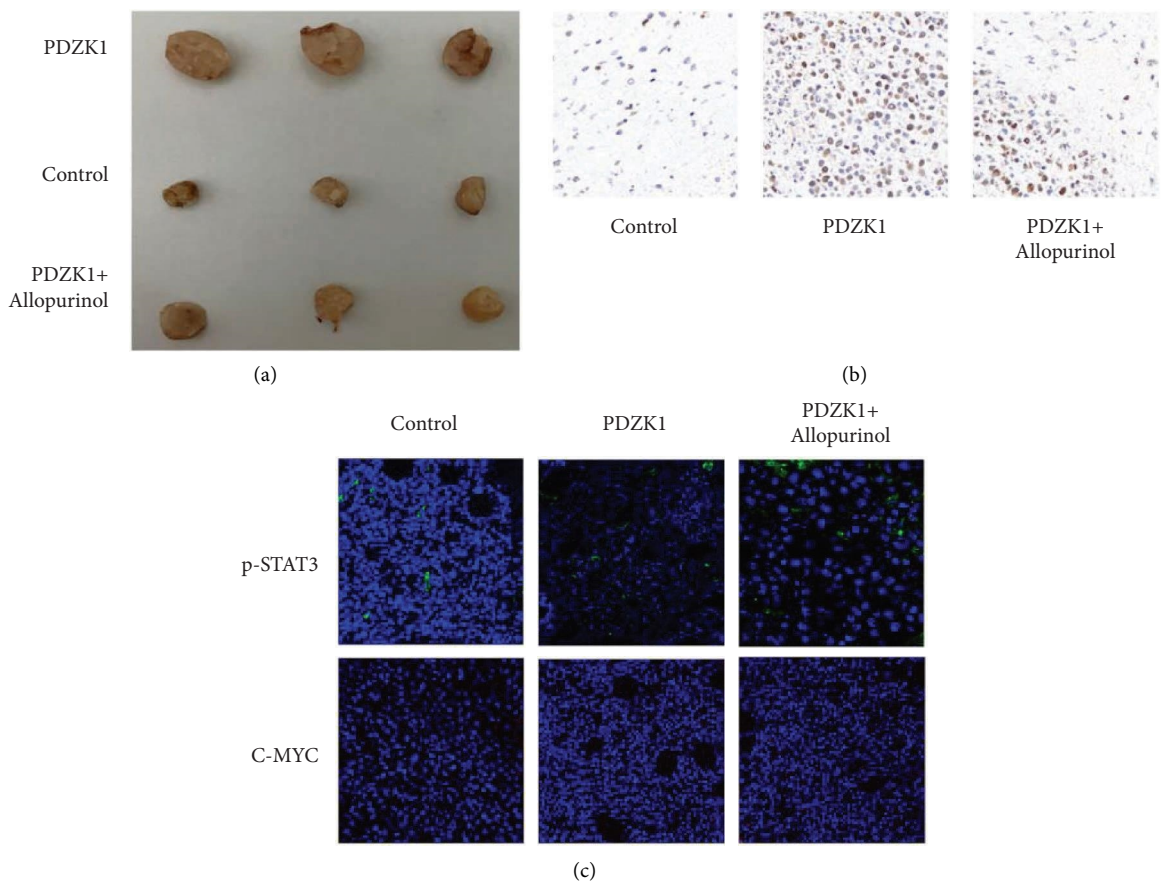

(c)

Figure 5: Allopurinol is an effective drug to improve the prognosis of HCC; (a) the tumor volume of PDZK1 overexpression group are increased, and treat with Allopurinol, the tumor volume is decreased; (b) Ki67 result showed that after treatment with Allopurinol, the proliferation of tumor was more reduced compare with PDZK1 overexpression group; (c) immunofluores result showed that,the p-STAT3 and C-myc expression was increased in PDZK1 overexpression group, and p-STAT3 and C-myc was decreased after treatment with allopurino.

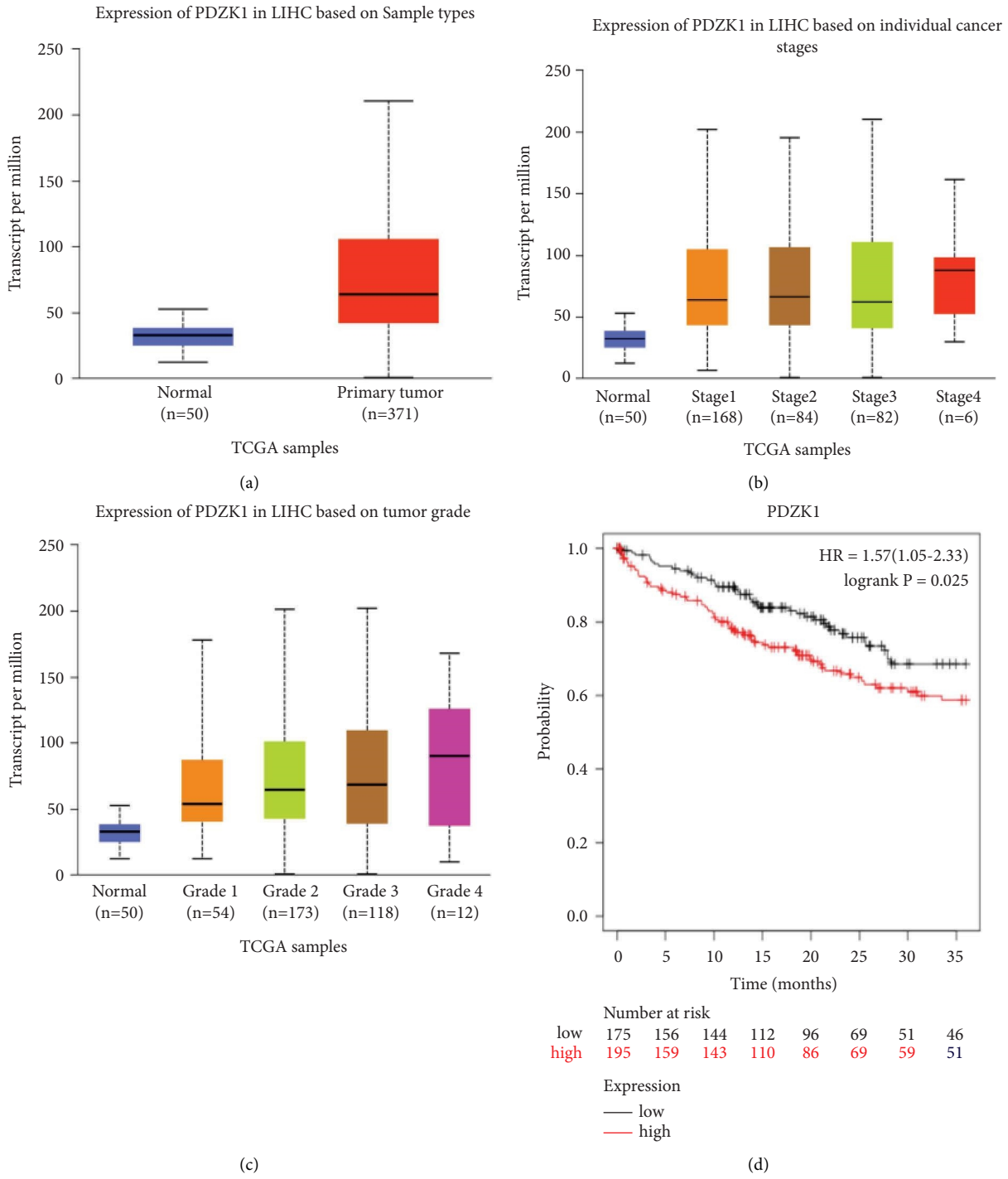

Figure 6: PDZK1 is related to the occurrence and development of HCC in clinically (a, b, c) the publicly online tools TGCA database, and showed that compared with normal, the expression of PDZK1 are increased in liver cancer, and increased in cancer stage (1, 2, 3, 4) and tumor grade (1, 2, 3, 4) (d) Kaplan–Meier Plotter results showed the prognosis of high expression of PDZK1 is poor in liver cancer.

Data Availability

The basic data supporting our research results can be found through the e-mail of the corresponding author (qiuhongbin99@163.com).

Ethical Approval

All male athymic nude mice used in this study were approved by the Ethical Committee of the School of Basic Medicine Jiamusi University.

Conflicts of Interest

The authors declare that they have no conflicts of interest.

Acknowledgments

This study was supported by the Scientific and Technological Innovation Team of Jiamusi University (cxtd202101) and Key program of Natural Science Foundation of Heilongjiang Province of China (ZD2022H006).

References

[1] H. Sung, J. Ferlay, R. L. Siegel et al., "Global cancer statistics 2020: GLOBOCAN estimates of incidence and mortality worldwide for 36 cancers in 185 countries," *CA: A Cancer Journal for Clinicians*, vol. 71, no. 3, pp. 209–249, 2021.

[2] R. Pinyol, S. Torrecilla, H. Wang et al., "Molecular characterisation of hepatocellular carcinoma in patients with non-alcoholic steatohepatitis," *Journal of Hepatology*, vol. 75, no. 4, pp. 865–878, 2021.

[3] F. Foerster, S. J. Gairing, L. Muller, and P. R. Galle, "NAFLD-driven HCC: s," *Journal of Hepatology*, vol. 76, no. 2, pp. 446–457, 2022.

[4] P. Konyn, A. Ahmed, and D. Kim, "Current epidemiology in hepatocellular carcinoma," *Expert Review of Gastroenterology & Hepatology*, vol. 15, no. 11, pp. 1295–1307, 2021.

[5] K. Patel and G. Sebastiani, "Limitations of non-invasive tests for assessment of liver fibrosis," *JHEP Reports*, vol. 2, no. 2, Article ID 100067, 2020.

[6] H. Samant, K. Kohli, K. Patel et al., "Clinical presentation of hepatocellular carcinoma in african Americans vs. Caucasians: a retrospective analysis," *Pathophysiology*, vol. 28, no. 3, pp. 387–399, 2021.

[7] K. L. Martens, P. R. Khalighi, S. Li et al., "Comparative effectiveness of rasburicase versus allopurinol for cancer patients with renal dysfunction and hyperuricemia," *Leukemia Research*, vol. 89, Article ID 106298, 2020.

[8] B. Rahmani, S. Patel, O. Seyam et al., "Current understanding of tumor lysis syndrome," *Hematological Oncology*, vol. 37, no. 5, pp. 537–547, 2019.

[9] I. Krecak, M. Lucijanic, V. Gveric-Krecak, and N. Durakovic, *Leukemia and Lymphoma*, vol. 61, no. 7, pp. 1744–1747, 2020.

[10] I. J. Nunez-Gil, O. Vedia, M. Almendro-Delia et al., "En nombre de los investigadores RETAKO," *Medical Clinics of North America*, vol. 155, no. 12, pp. 521–528, 2020.

[11] T. Tsukamoto, M. Tsujii, K. Odake et al., *Free Radical Research*, vol. 55, no. 7, pp. 810–820, 2021.

[12] H. Komori, K. Yamada, and I. Tamai, "Hyperuricemia enhances intracellular urate accumulation via down-regulation of cell-surface BCRP/ABCG2 expression in vascular endothelial cells," *Biochimica et Biophysica Acta (BBA) - Biomembranes*, vol. 1860, no. 5, pp. 973–980, 2018.

[13] D. Cui, S. Liu, M. Tang et al., "Phloretin ameliorates hyperuricemia-induced chronic renal dysfunction through inhibiting NLRP3 inflammasome and uric acid reabsorption," *Phytomedicine*, vol. 66, Article ID 153111, 2020.

[14] M. M. Chen and L. H. Meng, *The Double Faced Role of Xanthine Oxidoreductase in cancer*, Acta Pharmacol Sin, Shanghai, China, 2021.

[15] H. Li, X. Liu, M. H. Lee, and H. Li, "Vitamin C alleviates hyperuricemia nephropathy by reducing inflammation and fibrosis," *Journal of Food Science*, vol. 86, no. 7, pp. 3265–3276, 2021.

[16] S. W. Lai, Y. H. Kuo, and K. F. Liao, "Allopurinol and the risk of prostate cancer," *Postgraduate Medical Journal*, vol. 96, no. 1132, p. 102, 2020.

[17] V. Kukko, A. Kaipia, K. Talala et al., "Allopurinol and risk of benign prostatic hyperplasia in a Finnish population-based cohort," *Prostate Cancer and Prostatic Diseases*, vol. 21, no. 3, pp. 373–378, 2018.

[18] T. Yasuda, T. Yoshida, A. E. Goda et al., "Anti-gout agent allopurinol exerts cytotoxicity to human hormone-refractory prostate cancer cells in combination with tumor necrosis factor–related apoptosis-inducing ligand," *Molecular Cancer Research*, vol. 6, no. 12, pp. 1852–1860, 2008.

[19] N. Serling-Boyd, Z. Quandt, and N. Allaudeen, *Mol Clin Oncol*, vol. 6, no. 4, pp. 589–592, 2017.

[20] X. Sun, R. Zhang, F. Jiang et al., "Common variants related to serum uric acid concentrations are associated with glucose metabolism and insulin secretion in a Chinese population," *PLoS One*, vol. 10, no. 1, Article ID e0116714, 2015.

[21] M. Li, Q. Li, C. G. Li et al., *International Journal of Clinical and Experimental Medicine*, vol. 8, no. 8, pp. 13911–13918, 2015.

[22] G. Gunjaca, M. Boban, M. Pehlic et al., "Predictive value of 8 genetic loci for serum uric acid concentration," *Croatian Medical Journal*, vol. 51, no. 1, pp. 23–31, 2010.

[23] C. Zhao, T. Tao, L. Yang et al., "Loss of PDZK1 expression activates PI3K/AKT signaling via PTEN phosphorylation in gastric cancer," *Cancer Letters*, vol. 453, pp. 107–121, 2019.

[24] M. G. Ghosh, D. A. Thompson, and R. J. Weigel, *Cancer Research*, vol. 60, no. 22, pp. 6367–6375, 2000.

[25] T. Tao, X. Yang, J. Zheng et al., "PDZK1 inhibits the development and progression of renal cell carcinoma by suppression of SHP-1 phosphorylation," *Oncogene*, vol. 36, no. 44, pp. 6119–6131, 2017.

[26] K. J. Livak and T. D. Schmittgen, "Analysis of relative gene expression data using real-time quantitative PCR and the $2-\Delta\Delta CT$ method," *Methods*, vol. 25, no. 4, pp. 402–408, 2001.

[27] P. A. Heidenreich, B. Bozkurt, D. Aguilar et al., "2022 AHA/ACC/HFSA guideline for the management of heart failure: executive summary: a report of the American college of cardiology/American heart association joint committee on clinical practice guidelines," *Journal of the American College of Cardiology*, vol. 79, no. 17, pp. 1757–1780, 2022.

[28] J. S. Chavez-Iniguez, S. J. Sanchez-Villaseca, and L. A. Garcia-Macias, "Cardiorenal syndrome: classification, pathophysiology, diagnosis and management. Literature review," *Archivos de Cardiología de México*, vol. 92, no. 2, pp. 253–263, 2022.

[29] M. Macarie, S. Bataga, S. Mocan et al., "Correlation of metabolic risk factors with sessile serrated lesions," *Journal of Gastrointestinal and Liver Diseases*, vol. 29, no. 2, pp. 175–179, 2020.

[30] A. Yerlikaya, T. Dagel, C. King et al., "Dietary and commercialized fructose: sweet or sour," *International Urology and Nephrology*, vol. 49, no. 9, pp. 1611–1620, 2017.

[31] F. Jin, M. Yang, Y. Chen, L. Jiang, and L. Liu, "Ixazomib-associated tumor lysis syndrome in multiple myeloma: a case report," *Medicine (Baltimore)*, vol. 99, no. 45, Article ID e22632, 2020.

[32] S. H. Desai, G. Al-Shbool, S. Desale, J. Veis, and V. Malkovska, *Leukemia and Lymphoma*, vol. 61, no. 12, pp. 2923–2930, 2020.

[33] M. G. Battelli, M. Bortolotti, L. Polito, and A. Bolognesi, "Metabolic syndrome and cancer risk: the role of xanthine oxidoreductase," *Redox Biology*, vol. 21, Article ID 101070, 2019.

[34] A. Lonardo, F. Nascimbeni, M. Maurantonio, A. Marrazzo, L. Rinaldi, and L. E. Adinolfi, "Nonalcoholic fatty liver disease: e," *World Journal of Gastroenterology*, vol. 23, no. 36, pp. 6571–6592, 2017.

[35] M. Chen, X. Lu, C. Lu et al., "Soluble uric acid increases PDZK1 and ABCG2 expression in human intestinal cell lines via the TLR4-NLRP3 inflammasome and PI3K/Akt signaling pathway," *Arthritis Research and Therapy*, vol. 20, no. 1, p. 20, 2018.

[36] I. Andia and E. Rubio-Azpeitia, *Muscles Ligaments Tendons J*, vol. 4, no. 3, pp. 292–297, 2014.

[37] W. Zhu, Y. Deng, and X. Zhou, "Multiple membrane transporters and some immune regulatory genes are major genetic factors to gout," *The Open Rheumatology Journal*, vol. 12, no. 1, pp. 94–113, 2018.

[38] S. Vadakedath and V. Kandi, "Probable potential role of urate transporter genes in the development of metabolic disorders," *Cureus*, vol. 10, no. 3, Article ID e2382, 2018.

[39] N. S. Eyre, H. E. Drummer, and M. R. Beard, "The SR-BI p facilitates hepatitis C virus entry," *PLoS Pathogens*, vol. 6, no. 10, Article ID e1001130, 2010.

[40] D. Xiang, T. Wu, C. Y. Feng et al., "Upregulation of PDZK1 by *cbs* may play an important role in restoring biliary transport function in intrahepatic cholestasis," *Evidence-based Complementary and Alternative Medicine*, vol. 2017, Article ID 1640187, 7 pages, 2017.

[41] J. Klawitter, J. Klawitter, V. Schmitz et al., "Low-salt diet and cyclosporine nephrotoxicity: changes in kidney cell metabolism," *Journal of Proteome Research*, vol. 11, no. 11, pp. 5135–5144, 2012.

Hindawi
Journal of Oncology
Volume 2022, Article ID 9351911, 7 pages
https://doi.org/10.1155/2022/9351911

Research Article

Prediction of Cervical Lymph Nodes Metastasis in Papillary Thyroid Carcinoma (PTC) Using Nodal Staging Score (NSS)

Jianliang Zhang,[1] Guangwei Jia,[1] Yang Su,[1] Zhongji Zhang,[1] Hui Xiong,[1] Qiu Xu,[1] and Shan Meng[2]

[1]*Thyroid and Breast Surgery, Nanyang First People's Hospital, Nanyang, Henan Province 473010, China*
[2]*Department of Nuclear Medicine, Nanyang First People's Hospital, Nanyang, Henan Province 473010, China*

Correspondence should be addressed to Shan Meng; 535089372@qq.com

Received 29 July 2022; Revised 31 August 2022; Accepted 7 September 2022; Published 15 October 2022

Academic Editor: Muhammad Muddassir Ali

Background. Cervical lymph node metastasis is commonly seen in papillary thyroid carcinoma. Surgery is the preferred treatment for PTC with cervical lymph node metastasis. There is no alternate ultrasound, neck CT, and thyroglobulin (Tg) methods to assess the occult lymph node metastasis. For moderate-and high-risk PTC, the number of lymph nodes to be dissected should be increased to remove the occult lymph node metastasis. *Objective*. This study was designed to develop a nodal staging score model to predict the likelihood of lymph node metastasis in papillary thyroid carcinoma (PTC), and further guide the treatments. *Material and Methods.* Data were collected from the SEER database. Patients with PTC from 2000 to 2005 were selected. The beta-binomial model was adopted to establish a nodal staging score (NSS)-based model. The NSS-based model was built according to gender, age, extrathyroidal invasion, tumor multifocality, tumor size, and T stage of the patients. A total of 12,431 PTC patients were included in our study. Various types of lymph nodes were examined based on various categories (incidence, risk assessment) to evaluate the results. *Results.* 5,959 (47.9%) patients in the study were positive and 6,472 (52.1%) were confirmed negative for lymph node metastasis. The corrected incidence of lymph node metastasis was higher than that of direct calculation, regardless of the factors that affected lymph node metastasis. There were significant differences in the OS of PTC patients among the four groups and T stage (p is less than 0.05), indicating that cervical lymph node metastasis would have an impact on the prognosis of patients. *Conclusion*. In conclusion, an NSS-based model base on a variety of clinicopathological factors can be used to predict lymph node metastasis. It is important to evaluate the risk of occult lymph node metastasis in the treatment of PTC.. Since, this statistical model can describe the risk of occult lymph node metastasis in patients; therefore, it can be used as basis for decision-making related to the number of lymph nodes that can be dissected in operations.

1. Introduction

Papillary thyroid carcinoma (PTC) is the most common pathological type of thyroid cancer [1–15]. Cervical lymph node metastasis is commonly seen in PTC and occurs in 20–50% of patients before the initial treatment [1–3]. Surgery is the preferred treatment for PTC with cervical lymph node metastasis. At present, the American Thyroid Association (ATA) recommends that preventive central lymph node dissection should be performed in the treatment of primary tumors for patients with moderate-and high-risk PTC, and cervical or mediastinal lymph node dissection should be performed after the metastasis is confirmed through puncture pathology [4]. Currently,ultrasound is recommended as the main means of preoperative lymph node evaluation [2, 5, 6]. However, for patients with no abnormal lymph nodes clinically before surgery, 77% of them still developed persistent disease of lymph nodes after receiving thyroid cancer surgery [7], requiring reoperation. Now there is no better method to assess occult lymph node metastasis other than ultrasound, neck CT, and thyroglobulin (Tg) [8]. So, lymph node metastasis can be detected by postoperative pathology. In the case of moderate-and high-risk PTC, the number of lymph nodes that are involved in dissection should be

increased to remove the occult lymph node to the maximum extent [9]. But if this number is increased, an individual's life might be at risk. Therefore, an individualized plan for this purpose can increase the thoroughness of the procedure and additional trauma can be averted as much as possible. This study offers a quantitative and intuitive assessment method for the negative predictive value of lymph node examination. The prediction of metastasis and recurrence by the NSS model has not been carried out due to a data type limitation in the SEER database. In the SEER database, the metastatic areas have not been classified, so a further search cannot be carried out. Therefore, a perfect NSS model requires further research with a larger sample size and more comprehensive data.

2. Materials and Methods

2.1. Sample Collection. Sample data was collected from Surveillance, Epidemiology, and End Results (SEER), National Cancer Institute, USA [10]. A total of 12,431 patients with PTC (ICD-O-3 codes: 8050, 8260, 8340, 8341, 8343, and 8344) from 2000–2005 were selected for our study. The patients were divided into two groups according to their ages: (1) patients who were of age 45 or under 45 and (2) patients older than 45. Four groups according to tumor size included: (1) patients whose tumor sizes were less than 1 cm, (2) between 1 cm and 2 cm, (3) between 2 cm and 4 cm, and (4) larger than 4 cm.

The patients' gender, age, extrathyroidal invasion, multifocality, tumor size, and T stage were the inclusion criteria for the study. Indicators such as lymph node metastasis, the extent of surgical dissection, pathological subtype, and gene mutation were the exclusion criteria. The ratio of males to females was about 1 : 3, and the median age was 43 years.

2.2. The Nodal Staging Score (NSS) Statistical Model. In this study, the beta-binomial distribution was used to establish a nodal staging score (NSS) model [11, 12]. The beta-binomial distribution is a compound distribution that assumes that the parameter p in the binomial distribution is a random variable and obeys the β distribution [13]. Thus, this method was adopted.

2.3. Statistical Analysis. The NSS model was built through R 3.3.2 (R Foundation for Statistical Computing, Vienna, Austria). The parameters α and β to be estimated in the beta-binomial distribution were calculated by the maximum likelihood estimation method using the VGAM package. Other data were statistically analyzed using SPSS version 22.0 (SPSS Inc., Chicago, IL, USA). Comparisons were made using the χ^2 test for categorical variables and the t-test for continuous variables in the basic patient characteristics. It was believed that there was a statistically significant differences where p is less than 0.05.

3. Results

3.1. Basic Information of the Patients. A total of 12,431 patients with PTC in the SEER database from 2000 to 2005 met the inclusion/exclusion criteria and were included in this study. Six clinicopathological factors that may affect lymph node metastasis and the negative predictive value of lymph nodes were grouped and analyzed. In addition, 4,866 (39.1%) patients received total thyroidectomy and 2,450 (19.7%) underwent lateral cervical lymphadenectomy. Among the 12,431 patients, 5,959 (47.9%) were positive for lymph node metastasis, and 6,472 (52.1%) were confirmed negative, which shows a significant difference in the proportion of patients with all study factors between these two groups ($p > 0.05$). The basic information about the patients and the number of examined lymph nodes are shown in Table 1.

3.2. Calculation of the Probability of False-Negative Lymph Node Metastasis. A total of 5,959 patients with PTC had at least one lymph node metastasis. The beta-binomial distribution model was used to analyze the distribution of lymph node metastasis rates in patients, and the parameters to be estimated were $\alpha = 1.51$ and $\beta = 1.15$. As shown in Figure 1, when one, three, five, or eight nodes are examined, the false-negative probabilities of metastatic lymph nodes in PTC patients are 42.2%, 18.3%, 9.3%, and 5.6%, respectively. When more than eight lymph nodes are examined, the probability of false-negative lymph node metastasis is less than 5%. The calculation of the false-negative probability of lymph node metastasis is determined only by the total number of lymph nodes examined, and there is no correlation between tumor pathology and patient factors.

3.3. Evaluation of the Incidence of Lymph Node Metastasis. The incidence of lymph node metastasis should be evaluated based on the total number of examined lymph nodes and possible factors. The incidence of lymph node metastasis was assessed in all 12,431 PTC patients (Table 2). The corrected incidence of lymph node metastasis was higher than that of direct calculation, regardless of which factors affected lymph node metastasis.

3.4. Assessment of Occult Lymph Node Metastasis Risks. Based on the previous calculation of the possibility of false-negative lymph node metastasis and the adjusted incidence of lymph node metastasis, we have further assessed the risk of occult lymph node metastasis in PTC patients after receiving lymphadenectomy, i.e., the nodal staging score (NSS) model. The gender, age, extrathyroidal invasion, multifocality, tumor size, and T stage of patients were included in the derivation process, respectively, and the corresponding NSS results are shown in Figure 2. Regardless of the influencing factors of lymph node metastasis, these results suggest the number of lymph nodes to be removed to achieve a certain predictive value (Table 3) and illustrate the risk of residual occult lymph node metastasis after a certain number of lymph nodes are removed (Table 4).

To achieve a negative predictive value of more than 90%, 12 and 6 lymph nodes were examined in males and females, respectively; for PTC patients who were at age of 45 or less or more, 8 and 6 lymph nodes were examined, respectively; twenty-two and five lymph nodes were examined in individuals with and without extrathyroidal

Table 1: Basic information of the patients and the number of examined lymph nodes.

	The number of patients (%)[&]			p value	The number of examined lymph nodes	
	Total (n = 12431)	LN + (n = 5959)	LN − (n = 6472)		The median	IQR[#]
Gender				<0.05		
Male	2886(23.2)	1825(30.6)	1061(16.4)		3	1(-10)
Female	9545(76.8)	4134(69.4)	5411(83.6)		2	1(-6)
Age (years old)				<0.05		
≤45	7127(57.3)	3706(62.2)	3421(52.9)		3	1(-7)
>45	5304(42.7)	2253(38.7)	3051(47.1)		2	1(-5)
Extrathyroidal invasion				<0.05		
Negative	9496(76.4)	3752(63.0)	5744(88.8)		2	1(-5)
Positive	2935(23.6)	2207(37.0)	728(11.2)		4	2(-12)
Multifocal				<0.05		
No	8431(67.8)	4157(69.8)	4274(66.0)		3	1(-7)
Yes	4000(32.2)	1802(30.2)	2198(34.0)		2	2(-3)
Tumor size*				<0.05		
≤1 cm	3517(28.3)	1137(19.1)	2380(36.8)		2	1(-4)
1–2 cm	3803(30.6)	1817(30.5)	1986(30.7)		2	1(-6)
2–4 cm	3190(25.7)	1780(29.9)	1410(21.8)		3	1(-7)
> 4 cm	1062(8.5)	683(11.5)	379(5.9)		4	1(-12)
T stage				<0.05		
T1	6121(49.2)	2072(34.8)	4049(62.6)		2	1(-5)
T2	2237(18.0)	1060(17.8)	1177(18.2)		2	1(-6)
T3	3146(25.3)	2094(35.1)	1052(16.3)		3	1(-10)
T4	927(7.5)	733(12.3)	194(3.0)		4	2(-14)

Note: *Tumor size data were not available for 859 (6.9%) of these patients; #IQR refers to interquartile range; &: In the number of patients, LN+ indicates patients with positive lymph node metastasis, and LN- indicates patients with negative lymph node metastasis.

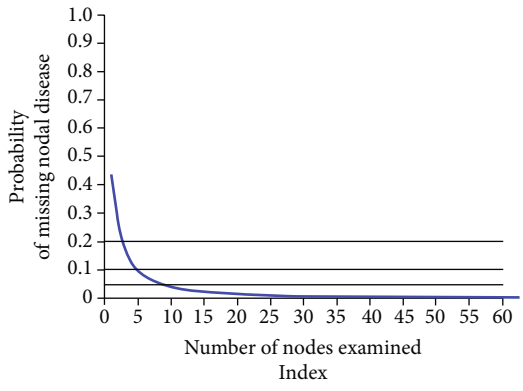

Figure 1: The relationship between the number of lymph nodes examined and the probability of false-negative lymph node metastasis.

invasion, respectively; patients with and without multifocal tumors, examination of seven and six lymph nodes was required, respectively; for patients whose tumor sizes were> 1 cm, 1-2 cm, 2-4 cm, and> 4 cm, four, seven, nine, and thirteen lymph nodes were examined, respectively; and for patients in T1, T2, and T3 stages, four, six, and [1]fifteen lymph nodes were examined, respectively.

3.5. Impact of NSS Assessment on Patient Survival. The NSS results calculated based on the affecting factors of lymph node metastasis were divided into four groups following their respective quartiles to evaluate the impact of the risk of occult lymph node metastasis on the prognosis of patients, and the overall survival (OS) among the four groups was compared by Log-rank method. The results showed that there were significant differences in the OS of PTC patients among the four groups in terms of gender, age, extrathyroidal invasion, tumor multifocality, tumor size, and T stage (p is less than 0.05), indicating that cervical lymph node metastasis would have an impact on the prognosis of patients, and the NSS model can better predict the cervical lymph node metastasis.

4. Discussion

Cervical lymph node metastasis often occurs in PTC, and cervical lymph node recurrence is a common type of postoperative recurrence in PTC [1, 3, 14]. Therefore, both proper assessments of lymph node metastasis and appropriate treatment are very important for improving the disease-free survival of patients. The inaccuracy of preoperative lymph node metastasis assessment will affect the formulation of treatment plans. Occult central lymph node metastases are easily missed due to the occlusion of the thyroid lobes

Table 2: Incidence of lymph node metastasis in patients with PTC and its adjustment results.

	Incidence of lymph node metastasis	
	Incidence of the sample (%)	The adjusted incidence (%) #
Gender		
Male	63.2	77.6
Female	43.3	53.8
Age		
≤45	52.0	63.2
>45	42.5	53.8
Extrathyroidal invasion		
Negative	39.5	49.5
Positive	75.2	90.5
Multifocal		
No	49.3	60.6
Yes	45.1	56.3
Tumor size		
≤1 cm	32.3	40.2
1-2 cm	47.8	59.1
2-4 cm	55.8	68.8
> 4 cm	64.3	76.0
T stage		
T1	33.9	42.4
T2	47.4	58.3
T3	66.6	81.5
T4	79.1	95.7

Note: #: In consideration of the possibility of false-negative lymph node metastasis, the incidence of lymph node metastasis calculated directly was revised.

during preoperative ultrasonography, and 66% of the central lymph node metastases are smaller than 5 mm [15]. Therefore, the Guideline for Diagnosis and Treatment of Thyroid Nodule and Differentiated Thyroid Cancer (2012 edition) of China recommends that at least an ipsilateral lobule and isthmus resection and ipsilateral central lymph node dissection should be operated on patients with differentiated thyroid cancer, but there is still a lack of opinions on the number of lymph nodes to be dissected [16]. Furthermore, lymph node metastasis in PTC patients is one of the indicators to be evaluated for postoperative radioactive iodine therapy. It is particularly important to correctly assess the patient's lymph node metastasis considering the possible side effects of radioactive iodine therapy [4]. However, for patients with no evidence of lymph node metastasis by preoperative ultrasound and Tg evaluation, who had received thyroid and/or lymph node dissection, and were followed up regularly with ultrasound and Tg after surgery, 77% still showed abnormalities within one year after the surgery [7], which may be related to postoperative occult lymph node metastasis. Preventive central lymph node dissection is widely adopted recently, while lateral cervical lymph node dissection is only carried out upon high suspicion/confirmation of metastasis through pathological biopsy [17]. For PTC patients, we would study how many lymph nodes will be removed for examination during lymph node dissection is enough to determine metastasis, and determine that patients with negative lymph node metastases are still at risk for occult metastases based on postoperative pathology reports. The lymph node dissection for thyroid cancer still lacks an "indicator" like "the sentinel lymph node" for breast cancer [14] due to the advanced cervical lymphatic circulation system. The thoroughness of surgery is still needed in the treatment of the occult metastatic lymph nodes. Therefore, this study is aimed at exploring the NSS model of cervical lymph node metastasis in PTC patients with the help of a large sample database and statistical analysis model. Individualized therapy is increasingly important in oncology treatment, and the NSS model can provide an individualized assessment of the risk of occult lymph node metastasis in patients with PTC.

Occult lymph node metastases are lymph node metastases that are not detected by clinical examination and procedure and are later confirmed by pathological examination, with a reported incidence of up to 50% in PTC. The current preoperative examination of lymph node metastases in patients with PTC is primarily based on ultrasonography [2, 14]. The inaccuracy of preoperative lymph node metastasis assessment will affect the formulation of the treatment plan. Because occult lymph node metastases are commonly observed in the central area, many physicians are in support of prophylactic central lymph node dissection, but there is a lack of opinions on the number of lymph nodes removed.

The NSS model is mainly used to assess the negative predictive value of lymph nodes in patients through a comprehensive analysis of the number, metastasis, and factors affecting the lymph nodes, and therefore can be used in assessments of the patient's condition and guide for relevant treatment strategies. Robinson et al. have reported the establishment of an assessment system for lymph node metastasis in patients with colon cancer using the NSS model, and Gonen et al. later preliminarily explored the application of the NSS model in PTC patients [11, 12].

Following are the main conditions for establishment of this model: (1) no false-positive metastasis in lymph nodes; (2) all lymph nodes have the same possibility of metastasis; and (3) the examinations are equally sensitive to true positives and false negatives. The adjusted incidence is higher than the incidence of lymph node metastasis calculated which evaluates the possibility of lymph nodes.

Based on the analysis of the survival data in patients with PTC, we have found that cervical lymph node metastasis can affect the prognosis of patients, and the NSS can better predict cervical lymph node metastasis. Besides, the NSS calculation was also carried out on age and extrathyroidal invasion. For any patient, however, the impact of each factor on lymph node metastasis was not completely independent. Moreover, one of the premises of this study is that each lymph node has the same probability of metastasis. But for PTC, the possibility of lymph node metastasis varies in different areas, with the most common metastasis in the central area, followed by the metastasis in the cervical area, while the incidence of mediastinal metastasis is the lowest [2].

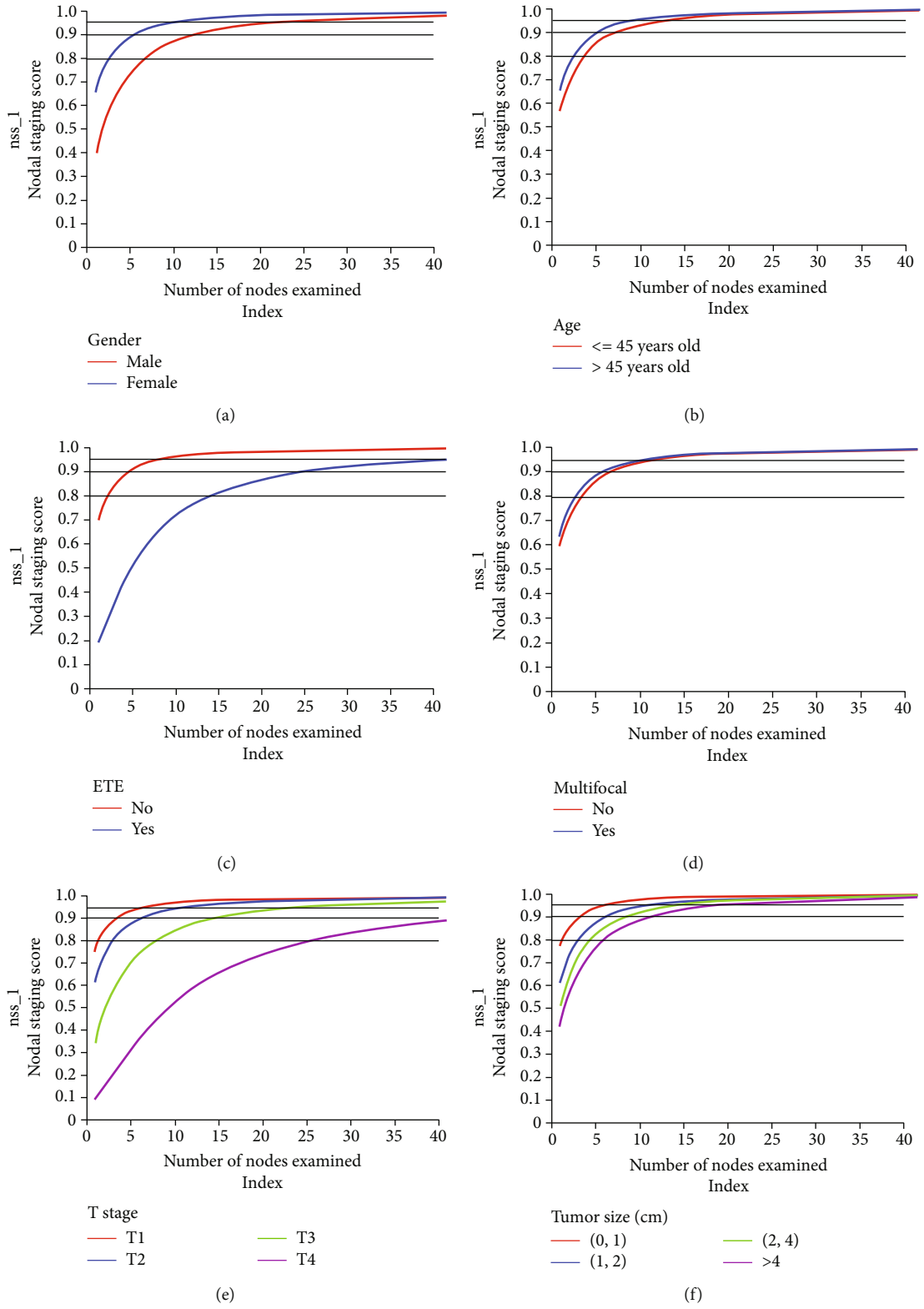

Figure 2: NSS results of lymph node metastasis corresponding to different clinicopathological factors. (a) Patient's gender; (b) patient's age (age 45 and under 45; older than 45 years old); (c) extrathyroidal invasion; (d) multifocal tumor; (e) T stages in line with the 7th edition of AJCC staging (T1, T2, T3, and T4); (f) tumor size (less than 1 cm; between 1 cm and 2 cm; between 2 cm and 4 cm; larger than 4 cm).

Table 3: NSS corresponds to the number of lymph nodes examined.

NSS	The number of lymph nodes examined			
	80%	85%	90%	95%
Gender				
Male	7	9	12	21
Female	3	4	6	10
Age				
≤45	4	5	8	13
>45	3	4	6	10
Extrathyroidal invasion				
Negative	2	3	5	9
Positive	14	18	22	40
Multifocal				
No	4	5	7	12
Yes	3	4	6	10
Tumor size				
≤1 cm	2	2	4	6
1-2 cm	3	5	7	11
2-4 cm	5	6	9	15
> 4 cm	4	8	13	20
T stage				
T1	2	3	4	7
T2	3	5	6	11
T3	3	11	15	25
T4	25	32	—	—

Table 4: Number of lymph nodes examined corresponding to NSS values.

The number of lymph nodes examined	NSS (%)					
	1	5	10	15	20	25
Gender						
Male	40.0	74.7	87.6	92.4	94.8	96.0
Female	66.5	89.8	95.5	97.3	98.2	98.7
Age						
≤45	57.4	85.6	93.4	96.1	97.4	98.1
>45	66.5	89.8	95.5	97.3	98.2	98.6
Extrathyroidal invasion						
Negative	70.2	91.3	96.1	97.7	98.5	98.9
Positive	19.4	51.7	71.9	81.6	88.3	91.8
Multifocal						
No	60.0	86.9	94.1	96.5	97.6	98.3
Yes	64.2	88.8	95.0	97.1	98.0	98.5
Tumor size						
≤1 cm	77.4	93.9	97.4	98.5	99.0	99.2
1-2 cm	61.5	87.7	94.5	96.7	97.8	98.3
2-4 cm	51.2	82.3	91.8	95.1	96.9	97.4
> 4 cm	42.1	76.4	88.6	93.1	95.0	95.9
T stage						
T1	75.9	93.3	97.1	98.3	98.9	99.2
T2	62.3	88.0	94.6	96.8	97.5	98.0
T3	34.4	69.9	84.7	90.6	93.3	95.0
T4	9.4	31.6	49.0	65.6	73.3	80.0

5. Conclusion

This paper provides an intuitive and quantitative assessment for the predictive value of a negative lymph node examination based on factors such as gender, age, extrathyroidal invasion, tumor multifocality, tumor size, and T stage, and establishes a lymph node assessment system, which is mainly used for the assessment of the risk of occult lymph node metastasis and offers guidance on patient treatment strategies.

Data Availability

The data used to support the findings of this study are included within the article.

Conflicts of Interest

The authors declare that they have no competing interests.

Authors' Contributions

Jianliang Zhang and Guangwei Jia contributed to this manuscript equally as the co-first author.

References

[1] S. A. Hundahl, I. D. Fleming, A. M. Fremgen, and H. R. Menck, "A National Cancer Data Base report on 53,856 cases of thyroid carcinoma treated in the U.S., 1985-1995," *Cancer: Interdisciplinary International Journal of the American Cancer Society*, vol. 83, no. 12, pp. 2638–2648, 1998.

[2] S. K. Grebe and I. D. Hay, "Thyroid cancer nodal metastases: biologic significance and therapeutic Considerations," *Surgical Oncology Clinics of North America*, vol. 5, no. 1, pp. 43–63, 1996.

[3] G. F. Scheumann, O. Gimm, G. Wegener, H. Hundeshagen, and H. Dralle, "Prognostic significance and surgical management of locoregional lymph node metastases in papillary thyroid cancer," *World Journal of Surgery*, vol. 18, no. 4, pp. 559–567, 1994, discussion 567-8.

[4] B. R. Haugen, E. K. Alexander, K. C. Bible et al., "2015 American Thyroid Association management guidelines for adult patients with thyroid nodules and differentiated thyroid Cancer: the American Thyroid Association guidelines task force on thyroid nodules and differentiated thyroid Cancer," *Thyroid*, vol. 26, no. 1, pp. 1–133, 2016.

[5] M. F. Berger, J. Z. Levin, K. Vijayendran et al., "Integrative analysis of the melanoma transcriptome," *Genome Research*, vol. 20, no. 4, pp. 413–427, 2010.

[6] H. S. Oh, J. H. Ahn, E. Song et al., "Individualized follow-up strategy for patients with an indeterminate response to initial therapy for papillary thyroid carcinoma," *Thyroid*, vol. 29, no. 2, pp. 209–215, 2019.

[7] M. F. Bates, M. R. Lamas, R. W. Randle et al., "Back so soon? Is early recurrence of papillary thyroid cancer really just persistent disease?," *Surgery*, vol. 163, no. 1, pp. 118–123, 2018.

[8] J. H. Jung, C. Y. Kim, S. H. Son et al., "Preoperative prediction of cervical lymph node metastasis using primary tumor SUVmax on 18F-FDG PET/CT in patients with papillary thyroid carcinoma," *PLoS One*, vol. 10, no. 12, article e0144152, 2015.

[9] D. M. Hartl, S. Leboulleux, and A. Al Ghuzlan, "Optimization of staging of the neck with prophylactic central and lateral neck dissection for papillary thyroid carcinoma," *Annals of Surgery, (2012)*, vol. 255, no. 4, pp. 777–783, 2012.

[10] "SEER Cancer Statistics Review, [National Cancer Institute]," 2019, https://seer.cancer .gov/statfacts/html/thyro.html.

[11] T. J. Robinson, S. Thomas, M. A. Dinan, S. Roman, J. A. Sosa, and T. Hyslop, "How many lymph nodes are enough? Assessing the adequacy of lymph node yield for papillary thyroid cancer," *Journal of Clinical Oncology*, vol. 34, no. 28, pp. 3434–3439, 2016.

[12] M. Gonen, D. Schrag, and M. R. Weiser, "Nodal staging score: a tool to assess adequate staging of node-negative colon cancer," *Journal of Clinical Oncology*, vol. 27, no. 36, pp. 6166–6171, 2009.

[13] G. Chen and S. Yang, "Q. β-binomial distribution and its medical application," *Chinese Journal of Health Statistics*, vol. 13, no. 2, pp. 10–13.

[14] S. I. Sherman, "Thyroid carcinoma," *The Lancet*, vol. 361, no. 9356, pp. 501–511, 2003.

[15] S. Vergez, J. Sarini, J. Percodani, E. Serrano, and P. Caron, "Lymph node management in clinically node-negative patients with papillary thyroid carcinoma," *European Journal of Surgical Oncology*, vol. 36, no. 8, pp. 777–782, 2010.

[16] M. Gao, "Guideline for diagnosis and treatment of thyroid nodular and differentiated thyroid carcinoma," *Chinese Journal of Clinical Oncology*, vol. 39, no. 17, pp. 1249–1272, 2012.

[17] A. Machens, S. Hauptmann, and H. Dralle, "Lymph node dissection in the lateral neck for completion in central node-positive papillary thyroid cancer," *Surgery*, vol. 145, no. 2, pp. 176–181, 2009.

[18] Z. G. Xu and S. Y. Liu, "Expert Consensus on Cervical Lymph Node Dissection in Differentiated Thyroid Carcinoma (2017 Edition)," *Chinese Journal of Practical Surgery*, 2017.

[19] I. Alroy and Y. Yarden, "The ErbB signaling network in embryogenesis and oncogenesis: signal diversification through combinatorial ligand-receptor interactions," *FEBS Letters*, vol. 410, no. 1, pp. 83–86, 1997.

[20] J. Ferlay, M. Colombet, I. Soerjomataram et al., "Estimating the global cancer incidence and mortality in 2018: GLOBOCAN sources and methods," *International Journal of Cancer*, vol. 144, no. 8, pp. 1941–1953, 2019.

Hindawi
Journal of Oncology
Volume 2022, Article ID 2909095, 14 pages
https://doi.org/10.1155/2022/2909095

Research Article

The Critical Gene Screening to Prevent Chromophobe Cell Renal Carcinoma Metastasis through TCGA and WGCNA

Cheng Yan,[1] Yan Yang,[1] Yunxiang Tang,[2] Xiaojing Zheng,[1] and Bin Xu[2]

[1]*Department of Oncology and Hematology, Chongqing Emergency Medical Center, Chongqing University Central Hospital, Chongqing 400014, China*
[2]*Department of Nuclear Medicine, Chongqing Emergency Medical Center, Chongqing University Central Hospital, Chongqing 400014, China*

Correspondence should be addressed to Bin Xu; doctorxubinnuclear@163.com

Received 22 August 2022; Revised 16 September 2022; Accepted 26 September 2022; Published 15 October 2022

Academic Editor: Muhammad Muddassir Ali

Common chromophobe renal cell carcinoma (chRCC) has a good prognosis when cured by surgery. However, clinical practice shows that a small number of patients with chRCC will produce metastasis, and the prognosis after metastasis is poor. In this regard, we try to find potential biological targets to prevent CRCC metastasis. In this experiment, we analyzed the clinical traits and gene expression data of chRCC samples which were provided by the TCGA database by the WGCNA method. On this basis, we selected MEtan, a module with a significant positive correlation with the M phase of chRCC, for subsequent analysis. The MEtan module genes in the biological process of chRCC were mainly related to steroid metabolic process, cholesterol metabolic process and STEM cell differentiation. KEGG analysis showed that these genes were mainly enriched in cancer-related signaling pathways, such as Neuroactive Ligand–receptor interaction, cAMP signaling pathway, and Wnt signaling pathway. Subsequently, we mapped the PPI interaction network and screened the key gene beta-arrestin 2 (ARRB2). Expression analysis showed that there was a significantly increased expression of ARRB2 in chRCC patients in comparison to the normal group. Expression survival analysis indicated that ARRB2 was inversely associated with overall survival. We firmly believe that the key genes identified in this study would be able to provide new clues and research basis for the treatment of chRCC.

1. Introduction

Over 400,000 cases of renal cell carcinoma (RCC) are diagnosed each year in the world, making it one of the most common renal malignancies [1]. Pathologically, RCC is divided into three types: clear cell renal cell carcinoma (ccRCC), papillary carcinoma (pRCC), and chromophobe carcinoma (chRCC). ChRCC is the third subtype of RCC recognized by the World Health Organization (WHO) in 2016 [2]. An estimated 5-10% of all kidney cancers are chRCC, which are equally common in men and women, with a higher incidence in those aged 50-60 [3–5]. ChRCC behaves differently than other types of renal cell carcinomas. Recent statistics indicate an increase in chRCC incidence [6, 7]. Patients with chRCC may present with hematuria or tumor compression symptoms, and a few show diffuse growth and invasion of the perirenal region [8, 9].

A large number of clinical practices have shown that chRCC is usually cured by surgery, and the prognosis of patients is good, with 5-year survival rates of 78-100% and 10-year survival rates of 80-90%; however, there are still 5-10% of patients with chRCC who will develop metastases [10, 11]. Approximately 14 percent of patients with metastatic RCC will survive five years, similar to those with definite metastatic chRCC [12]. Therefore, an in-depth study of the genes related to the pathogenesis of chRCC will comprehensively explain the pathogenesis and disease progression of chRCC, which is of great significance for its treatment and prevention.

There is currently no more comprehensive tumor gene expression profile database than the Cancer Genome Atlas (TCGA), which is distinguished by its large sample size and rich clinical information [13]. An analysis of gene-phenotype relationships called Weighted Gene Coexpression Network Analysis (WGCNA) has gained popularity for its

ability to investigate complex relationships between genes and phenotypes. With the WGCNA method, researchers are able to transform gene expression data into coexpression modules and provide insights into signaling networks that may be responsible for the phenotypic characteristics of the object of interest [14].

Data from gene chips related to chRCC disease were integrated and analyzed using bioinformatics technology: GO and KEGG pathway enrichment analyses were performed first to filter out the differential genes; then, we commenced WGCNA to analyze the clinical characteristics and gene expression data of chRCC samples provided by TCGA database, and made PPI interaction network to find the key genes in the pathogenesis and development of renal chromophobe cell carcinoma; the final step of our study was to investigate the survival of the genes mined to reconstruct the mechanism of renal chromophobe cell carcinoma.

2. Materials and Methods

2.1. Data Capturing. The TCGA Datasets (https://www.cancer.gov/about-nci/organization/ccg/research/structural-genomics/tcga) in the database were accessed with the keyword of chromophobe takes cell carcinoma to search, and the genome data of renal color cell cancer was downloaded. The data included 65 chromophobe cell carcinoma tumor samples and 25 normal tissue samples.

2.2. DEG Capturing. Standardizing and analyzing renal chromophobe cell carcinoma datasets were done by using the DESeq2 algorithm in R software. A difference factor (log2) absolute value higher than 1 was used to screen upregulated genes. Ggplot2 software package was used for data visualization.

2.3. WGCNA Analysis. WGCNA provides R functions that help analyze gene expression data using weighted correlation networks.

The source code and other materials for this R package are available for free at http://genetics.ucla.edu/labs/horvath/CoexpressionNetwork/Rpackages/WGCNA. Our coexpression network was built using the WCCNA R package. In the first step, clustering the samples was performed to identify any outliers. Next, the coexpression network was constructed using the automatic network construction function. Coexpression similarity is proposed to reckon the adjacency with the R function pickSoftThreshold.

2.4. Module-Trait Relationship Analysis. The corresponding gene modules were sorted according to the WGCNA modules; then, the ME for each module was calculated and correlated with clinical parameters, with statistical significance defined as $P < 0.05$.

2.5. Differentially Expressed Genes Enriched in GO and KEGG. DAVID database (DAVID; https://david.ncifcrf.gov) was used to analyze GO enrichment and KEGG pathway enrichment of significant different genes screened. The R software and clusterProfiler package were used for annotation and visualization, and a P value less than 0.05 was considered statistically significant.

2.6. Screening for Hub Genes in the PPI Network and Construction of a Protein-Protein Interaction Network. Interactions between proteins were identified and predicted using the STRING database (https://string-db.org/). Protein-protein interaction (PPI) networks were constructed using STRING for analysis of differentially expressed genes, and screening for hub genes in the STRING PPI network was performed using the Cytohubba plug-in in Cytoscape software.

2.7. Key Gene Survival Analysis. R software was used to analyze the survival of the selected key genes, and an analysis to Kaplan-Meier survival curves was carried out to determine the relationship between the key genes and renal chromophobe cell carcinoma recurrence. An evaluation of the survival difference between key genes was conducted via a log-rank test and the overall survival rate for renal chromophobe cell carcinoma patients was $P < 0.05$, deemed significant.

3. Results

3.1. Differentially Expressed Genes Analysis. An analysis of the transcriptome data from TCGA database was conducted on 65 chromophobe cell carcinoma tumor samples and 25 normal tissue samples. The DESeq2 tool identified 13472 DEGs, of which 6066 were upregulated and 7406 were downregulated (Figures 1(a) and 1(b)). We ran KEGG enrichment analyses on the top 30 DEGs with a $P < 0.05$ standard, and results showed that they mainly concentrated on pathways of cAMP, Cytokine–cytokine receptor interaction, Calcium, and Neuroactive Ligand–receptor interaction, etc. (Figures 2(a) and 2(b)). A GO enrichment analysis identified three biological processes associated with DEGs: ion transmembrane transport, membrane potential regulation, and organic anion transport; cell composition included an apical area, extracellular matrix containing collagen, and synaptic membrane; there were several molecular functions that were examined, such as passive transmembrane transporter activity, channel activity, receptor ligand activity, and signaling receptor activator activity (Figures 2(c) and 2(d)).

3.2. A Weighted Coexpression Network Analysis. Our first step in constructing the WGCNA network was to calculate the soft threshold power β. It was determined that the soft threshold power was 3-; the scale independence was 0.9, and the average connectivity was relatively high (Figure 3(a)). Our gene network construction and module identification was done via the WGCNA R package's one-step network construction function. Figure 3(b) displayed the color-coded coexpressed gene modules identified via WGCNA method, where the grey by default was those genes that could not be classified into any module. It was found that these modules could be classified into two categories and 23 subclasses, and that there was correlation amid these modules (Figures 3(c) and 3(d)). A second purpose of WGCNA is to analyze the correlation between modules and clinical parameters (R value). Analysis to the correlation amid the module genes and chRCC showed that the modules

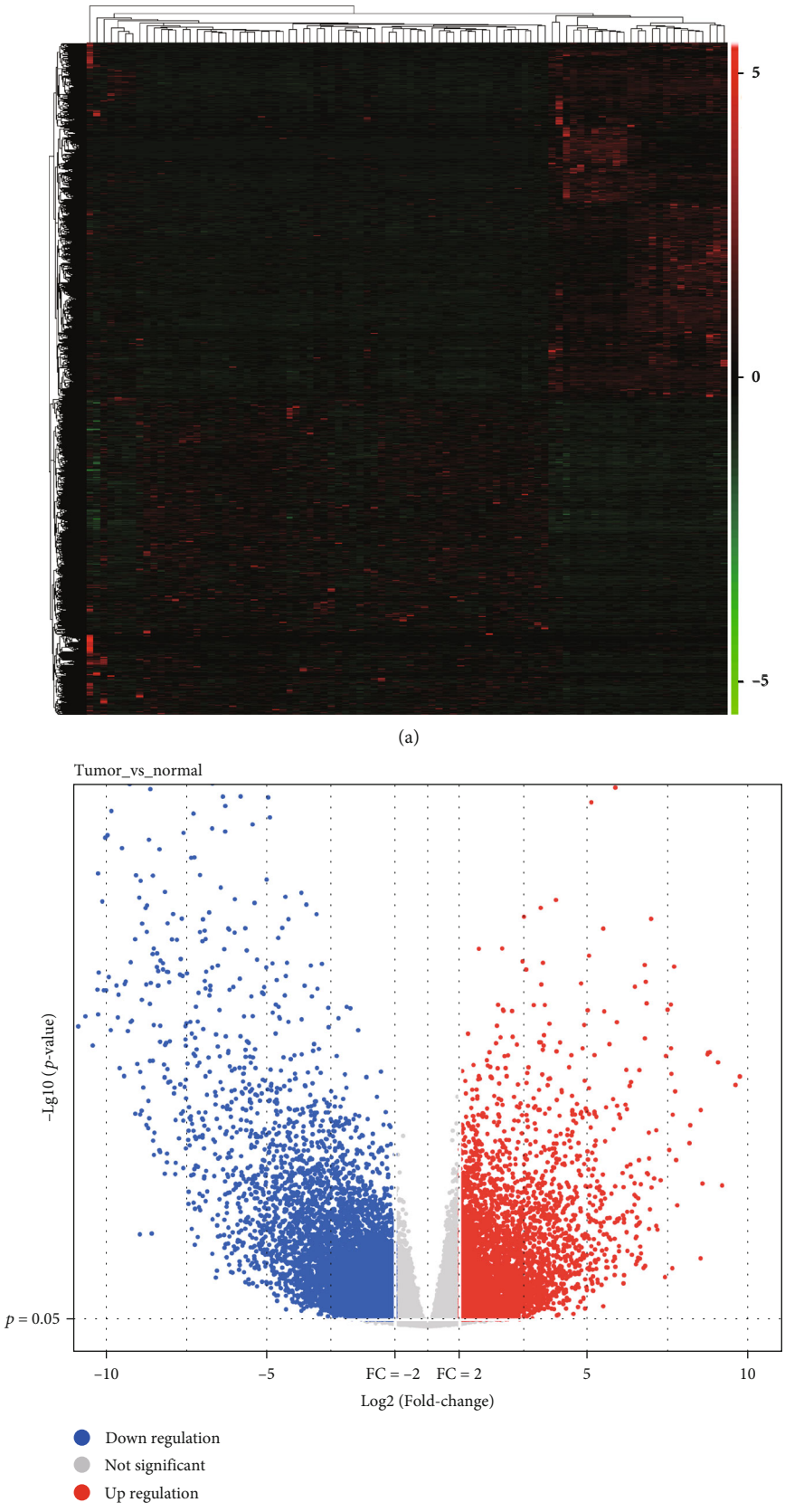

Figure 1: DEG analysis. (a) heat maps; (b) volcanic map.

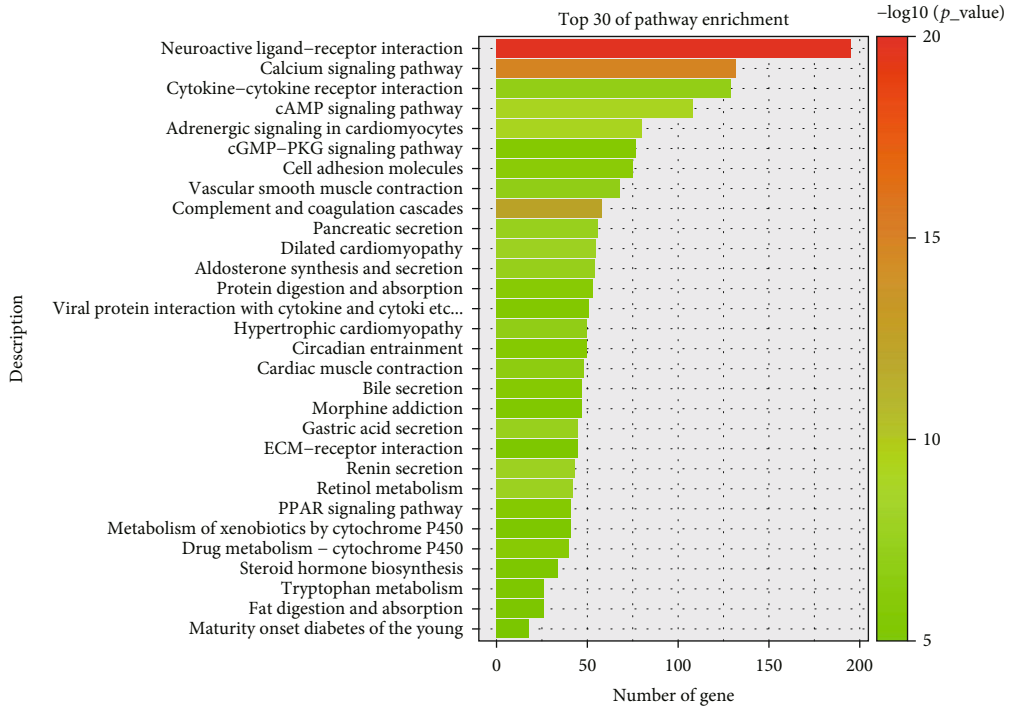

(a)

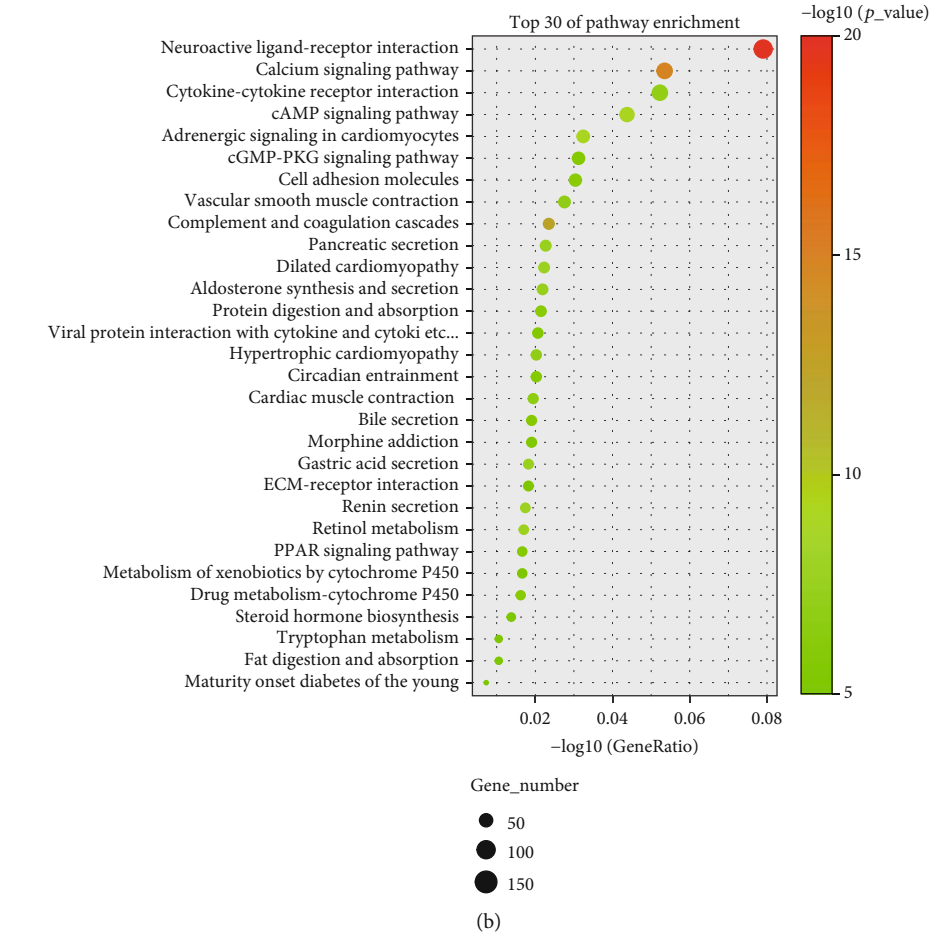

(b)

Figure 2: Continued.

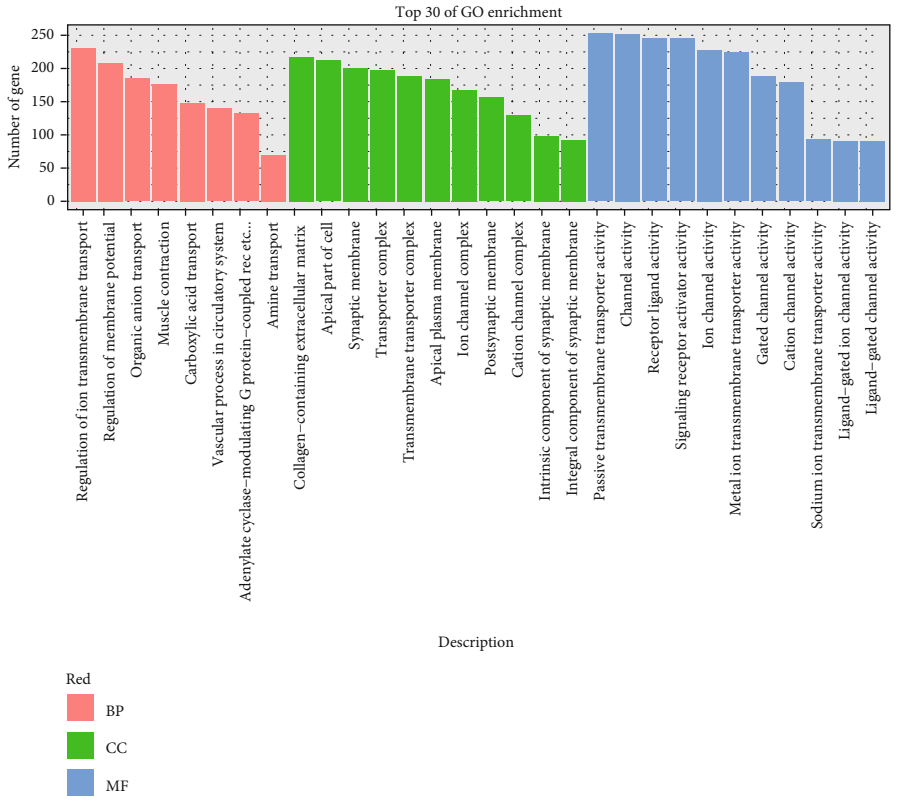

(c)

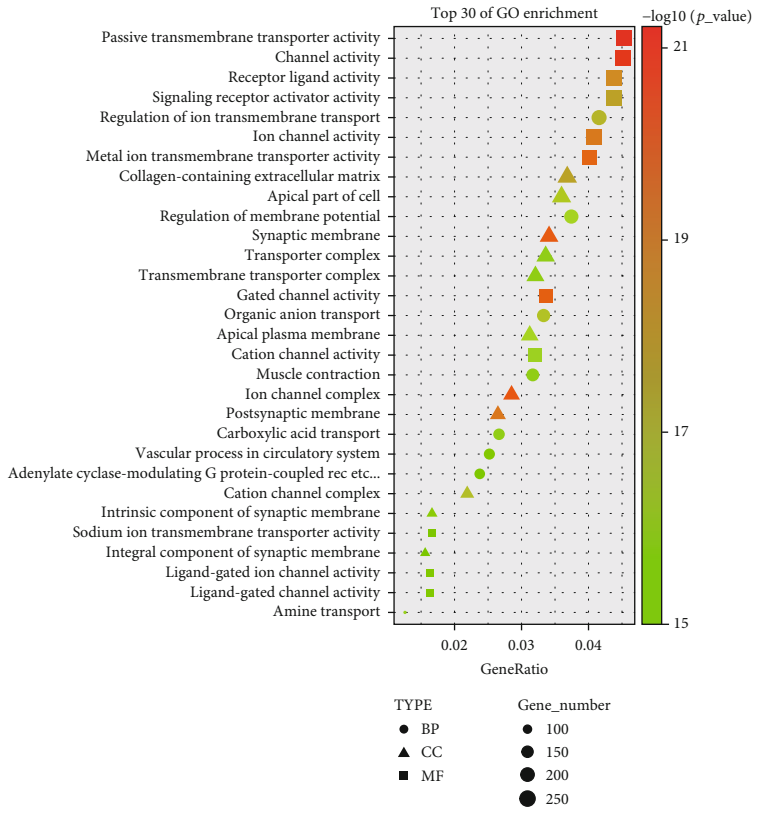

(d)

Figure 2: DEG pathway enrichment analysis. (a and b) KEGG enrichment analysis; (c and d) GO enrichment analysis.

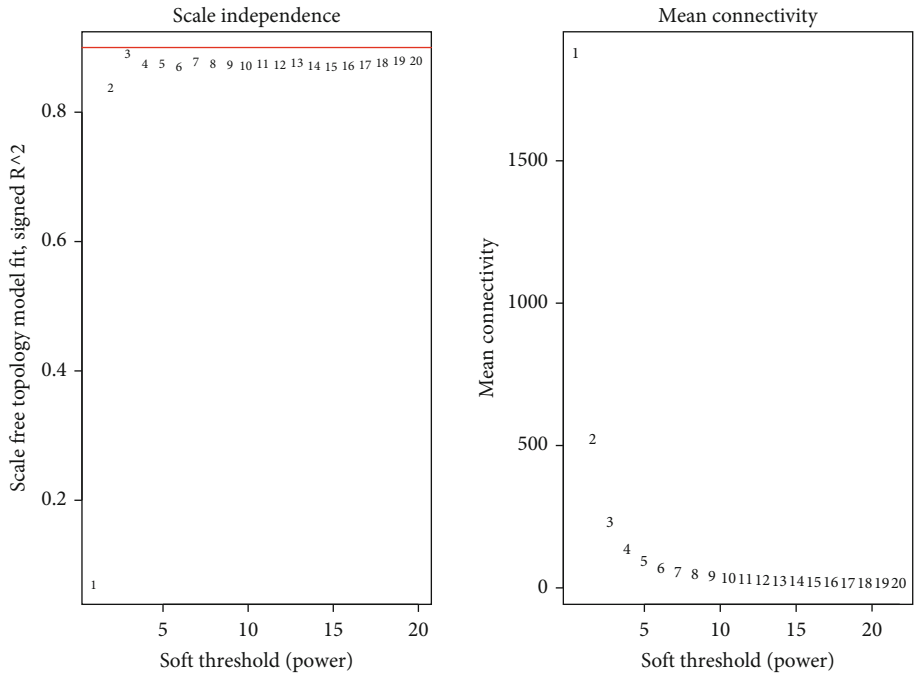

(a)

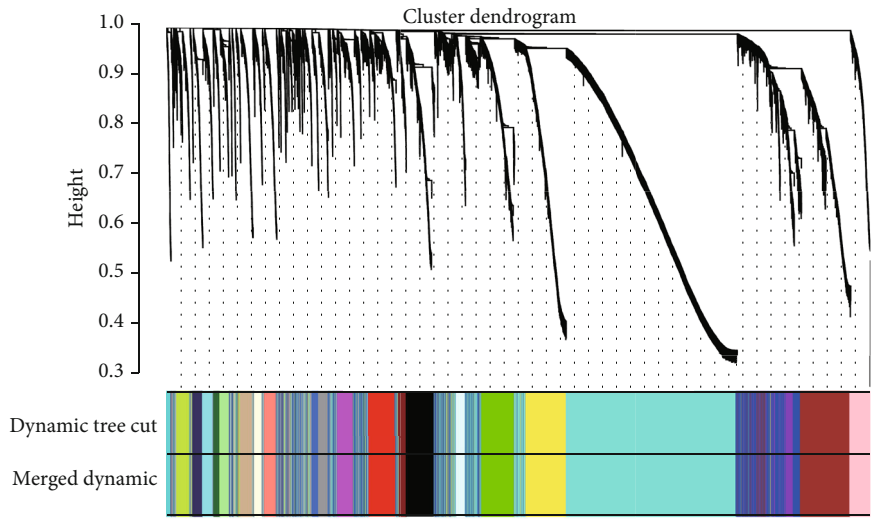

(b)

Figure 3: Continued.

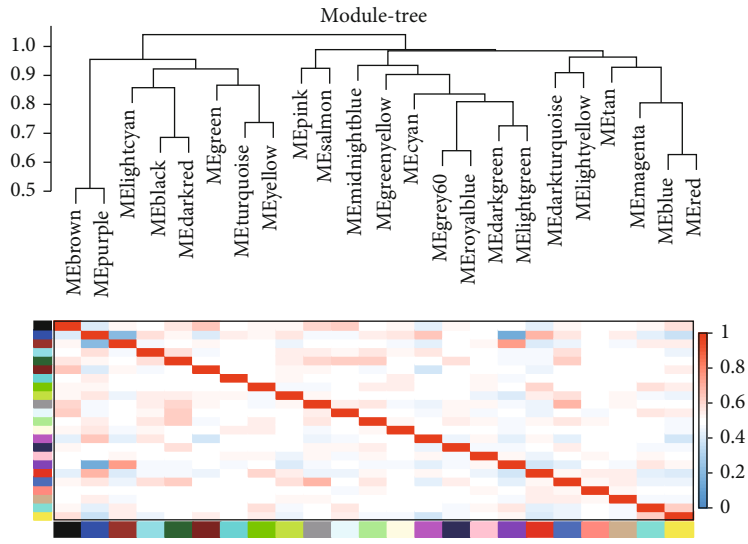

(c)

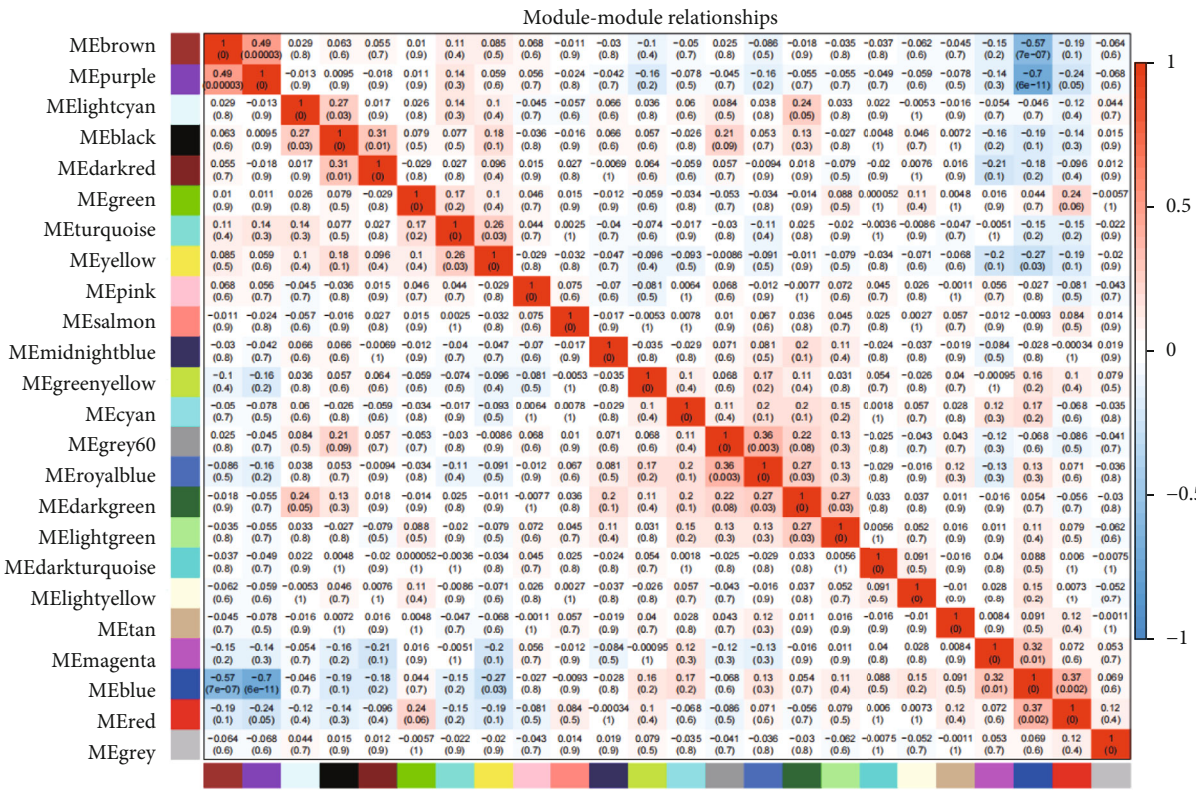

(d)

Figure 3: Continued.

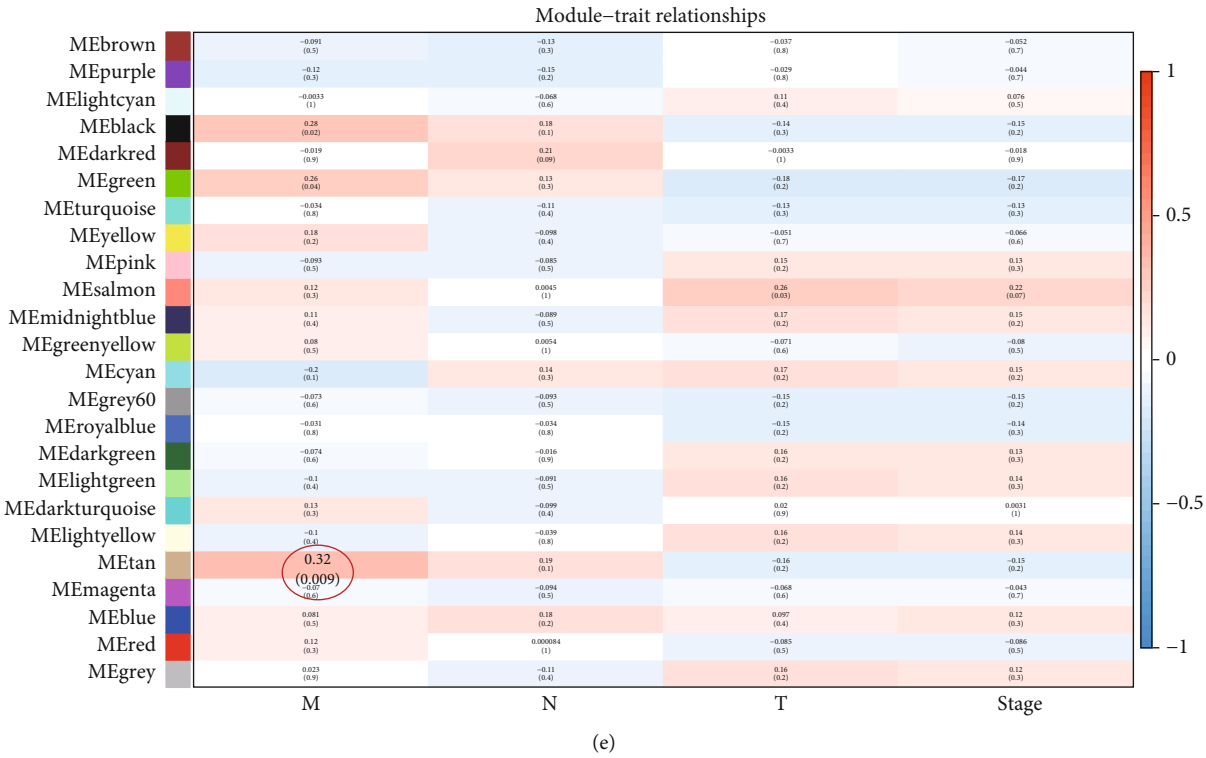

(e)

Figure 3: DEG analysis was carried out by weighted gene coexpression network analysis (WGCNA) method and gene cluster tree analysis of modular feature genes. (a) Scale-free exponential analysis to various soft threshold powers (β). (b) The color of the module represented by each dendrogram of the cluster module of the DEG (top) and the color band (bottom). (c) Clustering dendrograms of different genes based on topological overlap, and the colors assigned to the corresponding modules. (d) Correlation analysis onto different modules. (e) Correlation analysis onto modules and traits. ME: module characteristic gene.

MEblack, MEgreen, and MEtan were significantly positively correlated with the M phase of chRCC, and the correlation coefficients r were 0.28, 0.26, and 0.32, respectively ($P < 0.05$, Figure 3(e)). According to Figure 3(e), MEdarkred was positively correlated with T phase, and the correlation coefficient r was 0.21 ($P < 0.05$). Figure 3(e) illustrated a positive correlation between MEdarkred and T phase ($r = 0.21$; $P < 0.05$).

3.3. Module MEtan Gene Functional Enrichment Analysis. The above analysis led us to select MEtan for further analysis, because it has a significant positive correlation with the M phase of chRCC. GO analysis revealed that steroid metabolism, cholesterol metabolism, and stem cell differentiation were the top chRCC biological processes of MEtan module genes (Figures 4(a) and 4(b)). Genes enriched in cancer-related pathways, such as Neuroactive–Ligand receptor interaction, cAMP signaling pathway, and Wnt signaling pathway, were identified in KEGG analysis. (Figures 4(c) and 4(d)).

3.4. Screening to Hub Genes. With the help of the STRING online database and Cytoscape software, DEGs from MEtan modules were analyzed, and PPI networks were constructed in order to identify key genes. Cytoscape's CytoHubba plugin was used to screen the PPI network for key genes. MAG, CHRM1, and ARRB2 were in the center of the 36 nodes in the PPI network for module MEtan (Figure 5(a)). Finally, ARRB2 and MAG were the main genes we screened out (Figure 5(b)).

3.5. Survival Analysis. In contrast to the normal group, chRCC patients expressed significantly more ARRB2 than do normal individuals (Figure 6(a), $P < 0.05$). Kaplan-Meier survival curves were constructed to analyze chRCC 's overall survival rate. All chRCC samples were divided into high expression group and low expression group of key genes, and compared with the median value of key genes; according to expression survival analysis, ARRB2 was negatively correlated with overall survival (Figure 6(b), $P > 0.05$).

4. Discussion

ChRCC develops from dark cells in the collecting duct epithelium of the kidney [15]. There was 89.3% recurrence-free survival (RFS) and 93% cancer-specific survival (CSS) rates for chRCC after 5 years [16]. Metastatic disease accounts for only 6% of chRCC patients [17]. However, patients with metastatic chRCC illness have a poor prognosis, who more frequently show nodular characteristics and have a low incidence of treatment response [18, 19]. On postoperative follow up, Geramizadeh et al. found that only 20 (16%) of 123 CRCC patients progressed (local recurrence, metastasis, or death) [20]. Therefore, an in-depth study to related genes coexpressed in various stages and links of

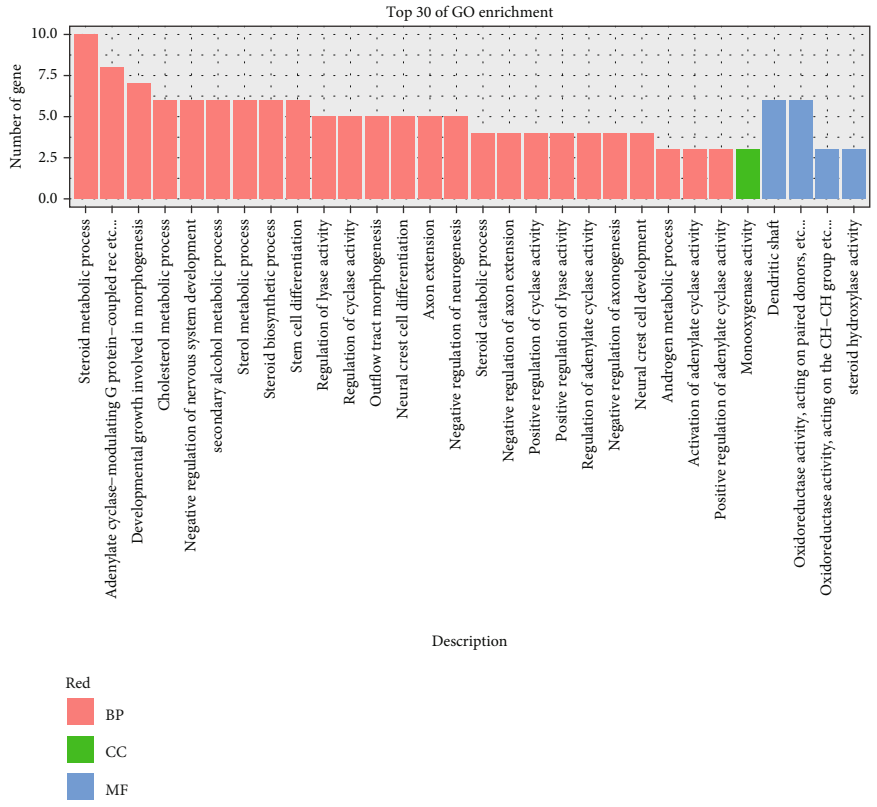

(a)

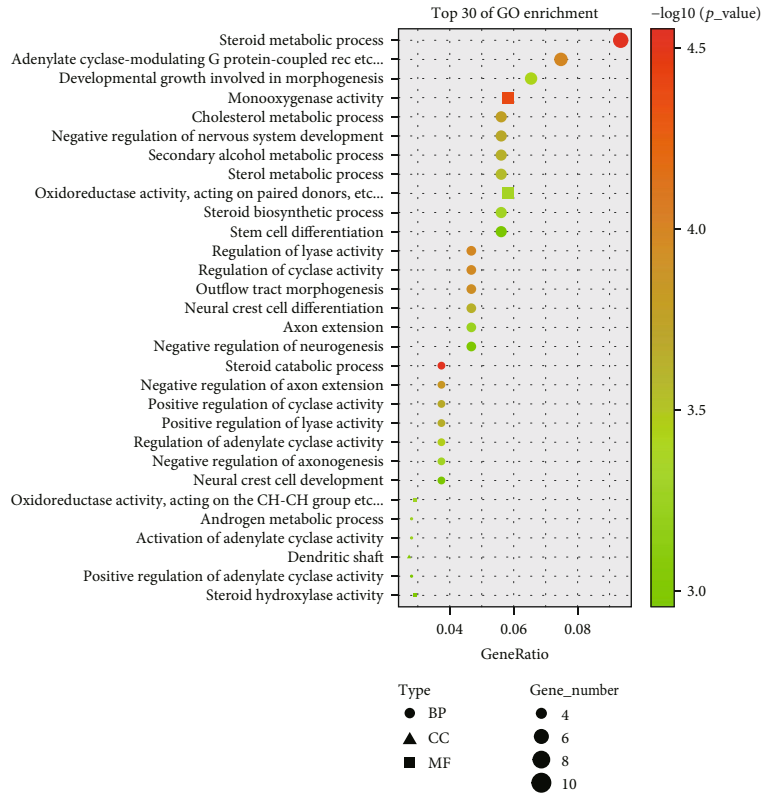

(b)

Figure 4: Continued.

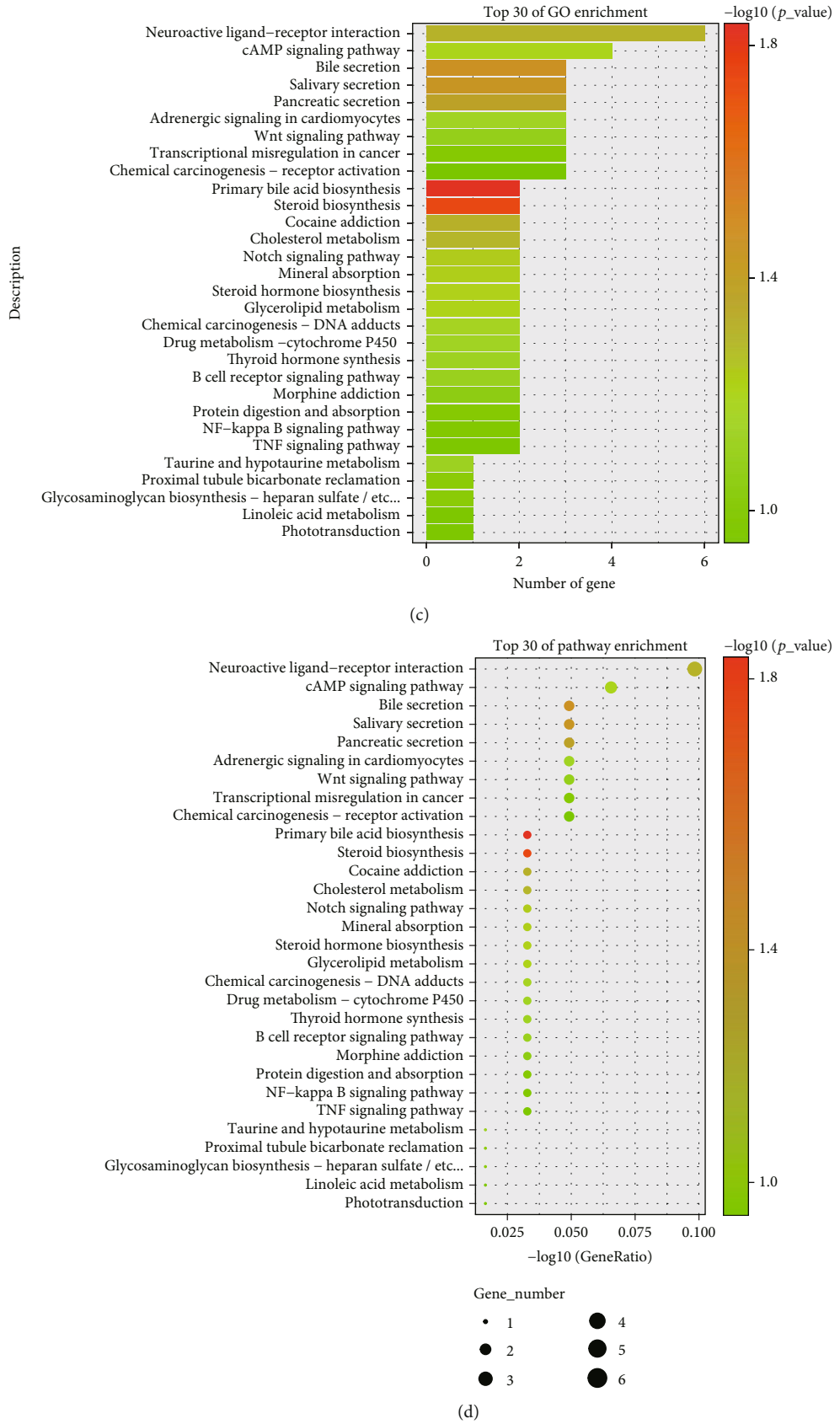

Figure 4: GO and KEGG analysis for module genes. (a and b) GO-term analysis and (c and d) KEGG enrichment analysis of MEtan module.

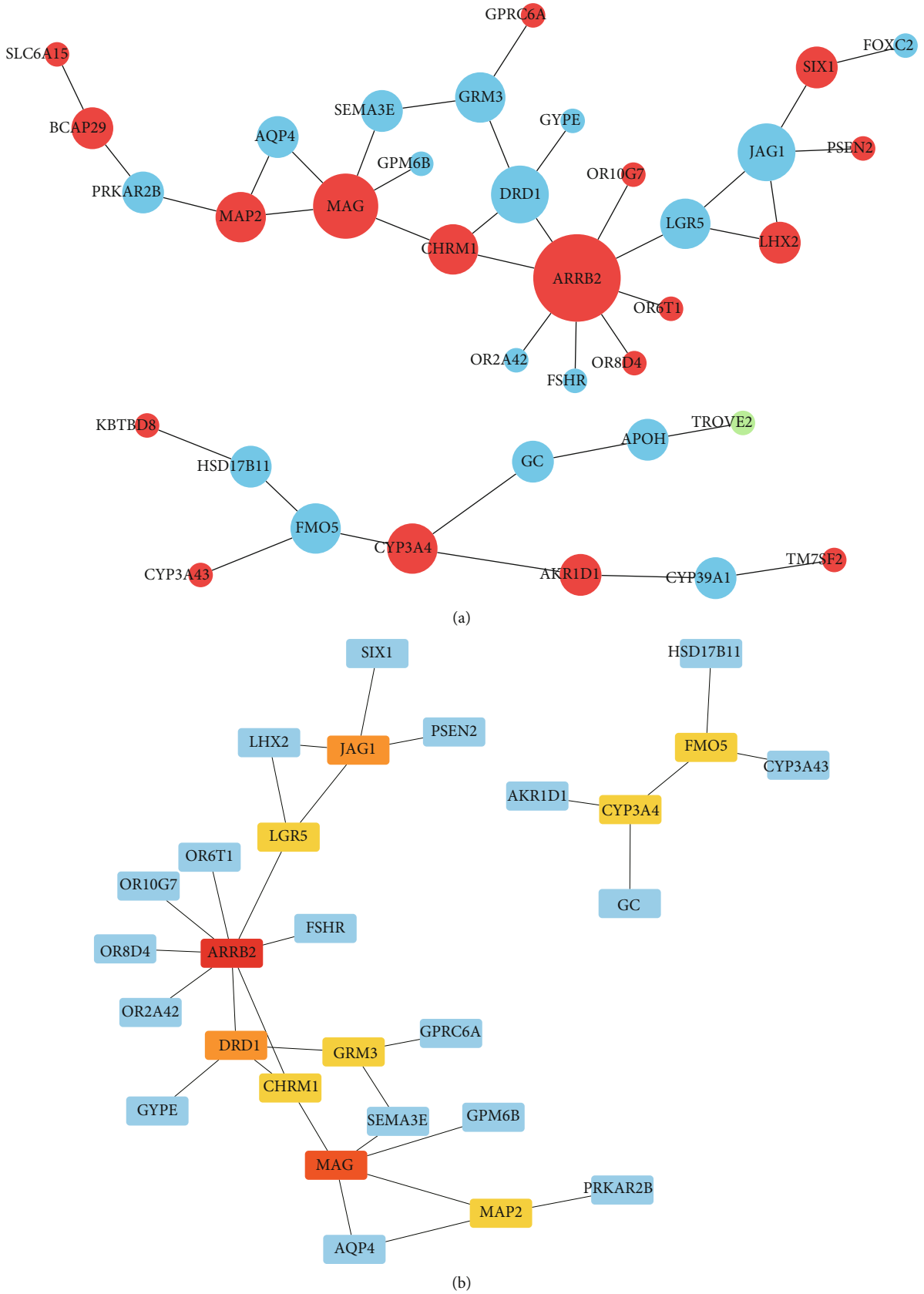

Figure 5: Construction of PPI network and screening to the key genes. (a) Protein-protein interaction network construction of differentially expressed genes in the MEtan module and (b) Cytoscape analysis. Note: The darker the color, the stronger the correlation.

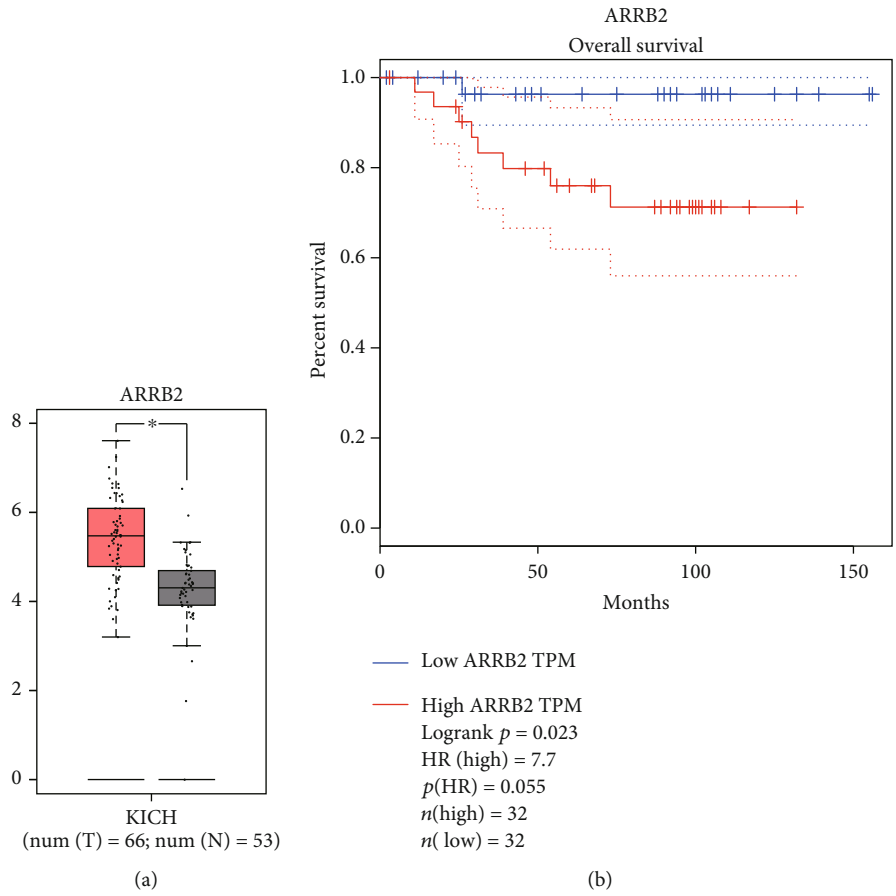

Figure 6: Overall survival analysis. (a) expression analysis to ARRB2 the key gene in MEtan module; (b) correlation analysis to ARRB2 expression and chRCC patients' overall survival; KICH: kidney chromophobe.

chRCC and discovery of genes that play a crucial regulatory role in its occurrence; furthermore, the development of the disease is indispensable for understanding its mechanism and improving treatment measures.

An in-depth analysis of the key genes involved in renal chromophobe cell carcinoma development and progression was undertaken in this study. A total of 13466 differentially expressed genes of renal chromophobe cell carcinoma were screened and mined by searching TCGA database, among which 6066 genes were upregulated and 7406 genes were downregulated. Several of these DEGs converged on the signaling pathways involving cAMP, cytokine-cytokine receptor interaction, calcium signaling pathway, and Neuroactive Ligand–receptor interaction.

An advantage of the WGCNA method is that it explores the association between clinical traits and coexpression modules, with higher reliability and biological significance [21]. TCGA database samples were analyzed through the WGCNA method to analyze clinical traits and gene expression data. According to the results, the modules MEblack, MEgreen, and MEtan were positively correlated with the M phase of chRCC; the module MEdarkred was positively correlated with the T phase of chRCC; moreover, MEsalmon is also positively correlated with the stage of chRCC. MEtan, which has a significant positive correlation with the M phase of chRCC, was selected for further analysis. Main chRCC biological processes of MEtan module genes include steroid metabolic process, cholesterol metabolic process, and STEM cell differentiation; besides, KEGG analysis revealed that these genes were primarily enriched in cancer-related signaling pathways such as Neuroactive Ligand–receptor interaction, cAMP signaling pathway, and Wnt signaling pathway.

Studies have shown that cyclic adenosine monophosphate (cAMP) plays an important role in controlling cell proliferation [22]. A total of 19 secreted glycoproteins make up the Wnt family, which regulates cell proliferation, differentiation, survival, migration, and stem cell self-renewal [23, 24]. There is an association between high Wnt1 expression in ccRCCs, increased tumor diameter, and more advanced stages [25]. A significant increase in WNT10A expression was also observed in RCC cells and tissues, and it plays an oncogenic role [26].

With the help of the STRING online database and Cytoscape software, DEGs from MEtan modules were analyzed, and PPI networks were constructed in order to identify key genes, and the key gene was ARRB2. In comparison with the normal group, ARRB2 expression was significantly higher in chRCC patients. ARRB2 expression was negatively correlated with overall survival, according to an expression survival analysis. There is a widespread expression of Arrb2, a multifunctional protein that regulates the desensitization and intracellular transport of G protein-

coupled receptors (GPCRs) [27, 28]. Furthermore, Arrb2 is involved in a variety of signaling pathways, including those that involve extracellular signal-regulated kinases (ERK) and protein kinase B (Akt) [29, 30].ARRB2 has been shown to be involved in the metastasis of a variety of cancer cells. Defective SUMOylation of ARRB2 inhibits the migration of breast cancer cells and has been shown to be involved in ARRB2-dependent metabolic regulation of breast cancer cells [31]. ARRB2 plays a negative regulatory role in glioma growth, invasion, and metastasis by reducing HIF-1α expression and inhibiting angiogenesis [32]. It was found that inhibition of ARRB2 expression reduced local and metastatic RCC tumor growth [33]. In summary, ARRB2 may consider as a target for therapeutic intervention against tumour development and metastasis in the studies of future. This study provides a reference for the clinical application of ARRB2 as a prognostic biomarker and potential therapeutic target, and we will enrich its mechanism of action in chRCC through more experiments in the future.

5. Conclusion

This study screened TCGA databases for genes associated with chRCC occurrence and development and discussed key genes related to chRCC. A possible therapeutic target and prognostic marker for renal chromophobe cell carcinoma may be ARRB2. However, since there have been no studies on the gene level related to chRCC, there is an urgent need for more research into the biological role of chRCC in renal chromophobe cell carcinoma pathogenesis, so that new clues and directions will be offered for the treatment of renal chromophobe cell carcinoma.

Data Availability

The data that support this study are in the article.

Conflicts of Interest

The authors declare that they have no conflicts of interest.

Authors' Contributions

Yan Cheng and Yang Yan contributed equally to this work.

Acknowledgments

This study was supported by Chongqing Science and Health Joint Medical Research Project "FMRI's early monitoring of the efficacy of EGFR-TKI in the treatment of brain metastasis in non-small cell lung cancer" (Project no. 2019MSXM011).

References

[1] F. Bray, J. Ferlay, I. Soerjomataram, R. L. Siegel, L. A. Torre, and A. Jemal, "Global cancer statistics 2018: GLOBOCAN estimates of incidence and mortality worldwide for 36 cancers in 185 countries," *CA: a Cancer Journal For Clinicians*, vol. 68, no. 6, pp. 394–424, 2018.

[2] P. A. Humphrey, H. Moch, A. L. Cubilla, T. M. Ulbright, and V. E. Reuter, "The 2016 WHO classification of tumours of the urinary system and male genital organs–part B: prostate and bladder tumours," *European Urology*, vol. 70, no. 1, pp. 106–119, 2016.

[3] J. Casuscelli, M. F. Becerra, K. Seier et al., "Chromophobe renal cell carcinoma: results from a large single-institution series," *Clinical Genitourinary Cancer*, vol. 17, no. 5, pp. 373–379.e4, 2019.

[4] M. B. Amin, G. P. Paner, I. Alvarado-Cabrero et al., "Chromophobe renal cell carcinoma: histomorphologic characteristics and evaluation of conventional pathologic prognostic parameters in 145 cases," *The American Journal of Surgical Pathology*, vol. 32, no. 12, pp. 1822–1834, 2008.

[5] A. M. Badowska-Kozakiewicz, M. P. Budzik, P. Koczkodaj, and J. Przybylski, "Selected tumor markers in the routine diagnosis of chromophobe renal cell carcinoma," *Archives of Medical Science: AMS*, vol. 12, no. 4, pp. 856–863, 2016.

[6] W. M. Linehan and C. J. Ricketts, "The cancer genome atlas of renal cell carcinoma: findings and clinical implications," *Nature Reviews Urology*, vol. 16, no. 9, pp. 539–552, 2019.

[7] L. Li, X. Chen, L. Hao, Q. Chen, H. Liu, and Q. Zhou, "Exploration of immune-related genes in high and low tumor mutation burden groups of chromophobe renal cell carcinoma," *Bioscience Reports*, vol. 40, no. 7, 2020.

[8] G. Martignoni, M. Pea, M. Chilosi et al., "Parvalbumin is constantly expressed in chromophobe renal carcinoma," *Modern Pathology*, vol. 14, no. 8, pp. 760–767, 2001.

[9] L. Zini, X. Leroy, L. Lemaitre et al., "Tumour necrosis in chromophobe renal cell carcinoma: clinical data to distinguish aggressive variants," *European Journal of Surgical Oncology: the Journal of the European Society of Surgical Oncology and the British Association of Surgical Oncology.*, vol. 34, no. 6, pp. 687–691, 2008.

[10] J. Zhou, X. Yang, L. Zhou, P. Zhang, and C. Wang, "Combined immunohistochemistry for the "three 7" markers (CK7, CD117, and Claudin-7) is useful in the diagnosis of chromophobe renal cell carcinoma and for the exclusion of mimics: diagnostic experience from a single institution," *Disease Markers*, vol. 2019, Article ID 4708154, 9 pages, 2019.

[11] J. C. Cheville, C. M. Lohse, H. Zincke, A. L. Weaver, and M. L. Blute, "Comparisons of outcome and prognostic features among histologic subtypes of renal cell carcinoma," *The American Journal of Surgical Pathology*, vol. 27, no. 5, pp. 612–624, 2003.

[12] J. Bellmunt, J. Puente, J. Garcia de Muro et al., "SEOM clinical guidelines for the treatment of renal cell carcinoma," *Clinical & Translational Oncology*, vol. 16, no. 12, pp. 1043–1050, 2014.

[13] J.-G. Zhou, J. Yang, S.-H. Jin et al., "Development and validation of a gene signature for prediction of relapse in stage I testicular germ cell tumors," *Frontiers in Oncology*, vol. 10, p. 1147, 2020.

[14] J. Zhong, S. Shi, W. Peng et al., "Weighted gene co-expression network analysis (WGCNA) reveals the functions of syndecan-1 to regulate immune infiltration by influenced T cells in glioma," *Frontiers in Genetics*, vol. 13, article 792443, 2022.

[15] Z. B. Sari, M. F. Açikalin, D. Arik, A. Özen, C. Can, and E. Çolak, "The role of CK7, S100A1, and CD82 (KAI1) expression in the differential diagnosis of chromophobe renal cell carcinoma and renal oncocytoma," *Applied Immunohistochemistry*

& Molecular Morphology: AIMM, vol. 29, no. 7, pp. 534–540, 2021.

[16] Y. Ayari, S. Ben Rhouma, H. Boussaffa et al., "Metachronous isolated locally advanced pancreatic metastasis from chromophobe renal cell carcinoma," *International Journal of Surgery Case Reports*, vol. 60, pp. 196–199, 2019.

[17] Y. Ged, Y.-B. Chen, A. Knezevic et al., "Metastatic chromophobe renal cell carcinoma: presence or absence of sarcomatoid differentiation determines clinical course and treatment outcomes," *Clinical Genitourinary Cancer*, vol. 17, no. 3, pp. e678–e688, 2019.

[18] V. Michalaki and C. Gennatas, "Chromophobe renal cell carcinoma with prolonged response to targeted therapy: a case report," *Journal of Medical Case Reports*, vol. 6, no. 1, p. 115, 2012.

[19] S. R. Granter and A. A. Renshaw, "Fine-needle aspiration of chromophobe renal cell carcinoma. Analysis of six cases," *Cancer*, vol. 81, no. 2, pp. 122–128, 1997.

[20] B. Geramizadeh, M. Ravanshad, and M. Rahsaz, "Useful markers for differential diagnosis of oncocytoma, chromophobe renal cell carcinoma and conventional renal cell carcinoma," *Indian Journal of Pathology & Microbiology*, vol. 51, no. 2, pp. 167–171, 2008.

[21] W.-C. Chou, A.-L. Cheng, M. Brotto, and C.-Y. Chuang, "Visual gene-network analysis reveals the cancer gene co-expression in human endometrial cancer," *BMC Genomics*, vol. 15, no. 1, p. 300, 2014.

[22] M. Massimi, F. Ragusa, S. Cardarelli, and M. Giorgi, "Targeting cyclic AMP signalling in hepatocellular carcinoma," *Cells*, vol. 8, no. 12, 2019.

[23] J. N. Anastas and R. T. Moon, "WNT signalling pathways as therapeutic targets in cancer," *Nature Reviews Cancer*, vol. 13, no. 1, pp. 11–26, 2013.

[24] K. Willert and K. A. Jones, "Wnt signaling: is the party in the nucleus?," *Genes & Development*, vol. 20, no. 11, pp. 1394–1404, 2006.

[25] S. Kruck, C. Eyrich, M. Scharpf et al., "Impact of an altered Wnt1/β-catenin expression on clinicopathology and prognosis in clear cell renal cell carcinoma," *International Journal of Molecular Sciences*, vol. 14, no. 6, pp. 10944–10957, 2013.

[26] R.-J. Hsu, J.-Y. Ho, T.-L. Cha et al., "WNT10A plays an oncogenic role in renal cell carcinoma by activating WNT/β-catenin pathway," *PLoS One*, vol. 7, no. 10, article e47649, 2012.

[27] F. K. Kuhr, Y. Zhang, V. Brovkovych, and R. A. Skidgel, "ß-arrestin 2 is required for B1 receptor-dependent post-translational activation of inducible nitric oxide synthase," *FASEB Journal: Official Publication of the Federation of American Societies For Experimental Biology*, vol. 24, no. 7, pp. 2475–2483, 2010.

[28] L. Wang, Y. Zhu, L. Wang et al., "Effects of chronic alcohol exposure on ischemia-reperfusion-induced acute kidney injury in mice: the role of β-arrestin 2 and glycogen synthase kinase 3," *Experimental & Molecular Medicine*, vol. 49, no. 6, article e347, 2017.

[29] J. Kim, L. Zhang, K. Peppel et al., "Beta-arrestins regulate atherosclerosis and neointimal hyperplasia by controlling smooth muscle cell proliferation and migration," *Circulation Research*, vol. 103, no. 1, pp. 70–79, 2008.

[30] K. Taguchi, T. Matsumoto, K. Kamata, and T. Kobayashi, "G protein-coupled receptor kinase 2, with β-arrestin 2, impairs insulin-induced Akt/endothelial nitric oxide synthase signaling in Ob/Ob mouse aorta," *Diabetes*, vol. 61, no. 8, pp. 1978–1985, 2012.

[31] C. Dong, Y. Li, Q. Niu et al., "Sumoylation involves in β-arrestin-2-dependent metabolic regulation in breast cancer cell," *Biochemical and Biophysical Research Communications*, vol. 529, no. 4, pp. 950–956, 2020.

[32] W.-Y. Bae, J.-S. Choi, S. Nam, and J.-W. Jeong, "β-arrestin 2 stimulates degradation of HIF-1α and modulates tumor progression of glioblastoma," *Cell Death and Differentiation*, vol. 28, no. 11, pp. 3092–3104, 2021.

[33] J. Masannat, H. T. Purayil, Y. Zhang et al., "βarrestin2 mediates renal cell carcinoma tumor growth," *Scientific Reports*, vol. 8, no. 1, p. 4879, 2018.

Hindawi
Journal of Oncology
Volume 2022, Article ID 2495361, 16 pages
https://doi.org/10.1155/2022/2495361

Research Article

Cancer Progression Mediated by CAFs Relating to HCC and Identification of Genetic Characteristics Influencing Prognosis

Li Song[1], **Qiankun Li**[2], **Yao Lu**[2], **Xianqi Feng**[1], **Rungong Yang**[2], **and Shouguo Wang**[1]

[1]*Academy of Advanced Interdisciplinary Studies, Qilu University of Technology (Shandong Academy of Sciences), Jinan, Shandong Province 250353, China*
[2]*Department of Tissue Repair and Regeneration, The First Medical Center of Chinese PLA General Hospital, Beijing, Beijing 250353, China*

Correspondence should be addressed to Xianqi Feng; qlu-xianqifeng@qlu.edu.cn, Rungong Yang; 13911598119@139.com, and Shouguo Wang; wangshouguo@aoe.ac.cn

Received 8 August 2022; Accepted 9 September 2022; Published 15 October 2022

Academic Editor: Muhammad Muddassir Ali

Background. Hepatocellular carcinoma (HCC) is one of the most common malignancies, and although there are several treatment options, the overall results are not satisfactory. Cancer-associated fibroblasts (CAFs) can promote cancer progression through various mechanisms. *Methods*. HCC-associated mRNA data were sourced from The Cancer Genome Atlas database (TCGA) and International Cancer Genome Consortium (ICGC) database. First, the differentially expressed CAF-related genes (CAF-DEGs) were acquired by difference analysis and weighted gene coexpression network analysis (WGCNA). Moreover, a CAF-related risk model was built by Cox analysis. Kaplan-Meier (K-M) curves and receiver operating characteristic (ROC) curves were utilized to evaluate the validity of this risk model. Furthermore, enrichment analysis of differentially expressed genes (DEGs) between the high- and low-risk groups was executed to explore the functions relevant to the risk model. Furthermore, this study compared the differences in immune infiltration, immunotherapy, and drug sensitivity between the high- and low-risk groups. Finally, we verified the mRNA expression levels of selected prognostic genes by quantitative real-time polymerase chain reaction (qRT-PCR). *Results*. 107 CAF-DEGs were identified in the HCC samples, and five prognosis-related genes (*ACTA2*, *IGJ*, *CTHRC1*, *CXCL12*, and *LAMB1*) were obtained by Cox analysis and utilized to build a CAF-related risk model. K-M analysis illustrated a low survival in the high-risk group, and ROC curves revealed that the risk model could accurately predict the 1-, 3-, and 5-year overall survival (OS) of HCC patients. In addition, Cox analysis demonstrated that the risk score was an independent prognostic factor. Enrichment analysis illustrated that DEGs between the high- and low-risk groups were related to immune response, amino acid metabolism, and fatty acid metabolism. Furthermore, risk scores were correlated with the tumor microenvironment, CAF scores, and TIDE scores, and CAF-related marker genes were positively correlated with all five model genes. Notably, the risk model was relevant to the sensitivity of chemotherapy drugs. Finally, the results of qRT-PCR demonstrated that the expression levels of 5 model genes were in accordance with the analysis. *Conclusion*. A CAF-related risk model based on *ACTA2*, *IGJ*, *CTHRC1*, *CXCL12*, and *LAMB1* was built and could be utilized to predict the prognosis and treatment of HCC.

1. Introduction

Liver cancer is one of the commonest malignancies. In accordance with the Global Cancer Statistics 2020, liver cancer is the 6th for incidence and 3rd in mortality among malignancy-related deaths [1–3]. Secondary, liver cancer includes hepatocellular carcinoma (HCC) and intrahepatic cholangiocarcinoma (ICC), of which HCC accounts for about 75-85%. Although various options such as chemotherapy with sorafenib, surgical resection, and liver transplantation are

applied in treating HCC, but there is still a poor overall prognosis, with an overall survival (OS) of 3-5% [4–6]. Therefore, it is essential to find available targets for HCC treatment [7].

Cancer-associated fibroblasts (CAFs) can secrete growth factors, cytokines, and inflammatory ligands, which stimulate epithelial-mesenchymal transformation (EMT), promote tumor proliferation and migration, and induce therapy resistance and immune exclusion [8–10]. Studies showed that CAFs engaged in bidirectional signaling with liver progenitor cells and can act as cancer stem cells, suggesting a close link between cirrhosis and liver cancer development [11]. In addition, CAFs support tumor growth in the liver. For example, CAFs can influence tumorigenesis by altering ECM stiffness. For example, CAFs can influence tumorigenesis by altering ECM stiffness; moreover, the cytokines and other factors secreted by CAFs may promote tumor growth, tumor angiogenesis, and epithelial to mesenchymal transition (EMT) [12].

In this study, samples in the TCGA dataset were grouped into high CAF/low CAF score groups with CAF scores, and then, 107 differentially expressed CAF-associated genes (CAF-DEGs) were utilized for risk regression analysis. Furthermore, 5 prognostic genes were gotten and utilized to establish a risk model, which provided a reference for applying CAF-associated genes (CAFGs) in the clinical prognosis and treatment outcome of HCC.

2. Materials and Methods

2.1. Data Source. The mRNA expression data of 50 normal and 371 HCC samples, of which 360 HCC samples have available survival data, were sourced from The Cancer Genome Atlas database (TCGA). The mRNA expression data of 243 HCC samples were acquired from the International Cancer Genome Consortium (ICGC) database as a validation set.

2.2. Evaluation of the CAF Status in HCC. xCell can calculate the abundance of various cells based on the single-sample gene set enrichment analysis (ssGSEA), which includes cancer-associated fibroblasts [13]. This study counted the mass of 21 immune cells in 421 samples of TCGA-HCC dataset by xCell. The samples were grouped into high and low CAF with the median number of CAF cells. Kaplan-Meier (K-M) survival analysis was performed based on the high and low CAF groups and the survival information of the HCC samples. Then, we collated the clinical traits of the samples, STAGE subgroups, and GRADE subgroups and compared the differences in the proportion of CAF cells between the STAGE subgroups and GRADE subgroups using chi-square tests.

2.3. Identification of CAFGs by Weighted Gene Co-expression Network Analysis (WGCNA). The genes with similar expression patterns can be gathered, and the module that was highly correlated with traits can be filtered by WGCNA, thus finding the target genes relevant to the study [14]. To further identify CAFGs, we performed a WGCNA analysis. First, we clustered the 371 HCC samples to see the overall correlation of all samples in the dataset. The soft threshold was determined to ensure that the interaction between genes maximally conformed to the scale-free distribution, and then, the coefficient of dissimilarity between genes was introduced based on the adjacency between genes, and the systematic clustering tree between genes was obtained accordingly. Similar modules analyzed by the dynamic tree cutting algorithm were merged (MEDissThres = 0.2). Finally, the correlations between the modules and CAF were calculated, and the key modules were selected with the criteria of $|\text{cor}| > 0.4$, $p < 0.05$. Moreover, the genes in the key modules were the CAFGs.

2.4. Identification of CAF-DEGs. We performed a differential analysis in the TCGA dataset for high CAF samples and low CAF samples to obtain differentially expressed genes (DEGs) between high and low CAF samples and differential analysis for normal and HCC samples. The screening condition for the differential analysis was p adjust. < 0.05 and $|\log 2\text{FC}| > 0.5$. To identify CAF-DEGs, we crossed CAFGs, DEGs between high and low CAF, and DEGs between normal and HCC samples.

2.5. Construction and Validation of the Risk Model. In this study, 360 samples containing survival information in the TCGA dataset were grouped into a training set and a test set with 7 : 3 (252 : 108), and the data in the training set were utilized to establish the risk model; firstly, the genes were verified as risk factors by univariate Cox regression analysis. Then, the genes with $p < 0.05$ were used to construct the multivariate Cox regression model, using the stepwise regression function step, with the parameter direction set to both, to adjust the multivariate regression model, and the obtained genes were used as prognostic factors to build the model.

The risk value of each patient was counted by the expression of the genes, and the patients were grouped into high and low risk with the median risk value. Then, the risk profile was plotted and survival analysis for the high- and low-risk groups was conducted. In addition, we plotted the receiver operating characteristic (ROC) curve, and the area under curve (AUC) was used to indicate the prediction accuracy. Finally, the correlations between the risk model and clinical traits (age, gender, M, N, T, and other clinical data) were assessed using the chi-square test.

Next, we validated the risk model using the TCGA test set and the ICGC validation set. In these two datasets, cases were spanided into high and low risks, respectively, and risk profiles, survival curves, and ROC plots were plotted, and correlations between risk factors and clinical traits were analyzed.

2.6. Correlation of Risk Model and Clinical Traits. The clinical traits in the training set of TCGA-HCC data were collated, including age, sex, disease stage, T, N, and M. The samples were grouped according to the different clinical traits, and the risk values were compared between the different groups to see if there were significant differences and visualized by box plots.

Table 1: Primer sequences of genes used in qRT-PCR validation.

Gene	Forward	Reverse
GAPDH	CCCATCACCATCTTCCAGG	CATCACGCCACAGTTTCCC
ACTA2	CACAGAGCAAAAGAGGAATC	TCAGCAGTAGTAACGAAGGA
IGJ	CTCAAGAAGGTGAAAGGATT	TTTTTACAGAGGTCAGACAA
CTHRC1	AAGGAAGCCCTGAAATGAAT	CCACAGAAGAAGTGCGATGA
CXCL12	CACTCCAAACTGTGCCCTTC	CTTGTCTGTTGTTGTTCTTC
AMB1	GTTGTAAATCTTGTGCTTGC	CTCCGCTTCATAGAGGTAGT

2.6.1. Independent Prognostic Analysis. The clinicopathological factors in the training set samples were added to the Cox analysis to investigate the independent prognosis of the risk model and clinicopathological factors. On this basis, a nomogram graph of the survival rate of the risk model and clinical factors was constructed. The factors that obtained significant results from the above multivariate Cox analysis were plotted, and the OS was predicted according to the total score. The correction curve was utilized to evaluate the prediction results of the model.

2.6.2. Enrichment Analysis. We divided the TCGA dataset into the high- and low-risk groups. The samples in the high- and low-risk groups were analyzed for differences using the "limma" R package, and the log2|FC| were then sorted from highest to lowest. Gene Set Enrichment Analysis (GSEA) was conducted using the "clusterProfiler" R package to find the common functions and related pathways of a large number of genes in the differentially expressed gene set [15]. The thresholds set were $|NES| > 1$, NOM $p < 0.05$, and $q < 0.25$, and the databases used for GSEA were Kyoto Encyclopedia of Genes and Genomes (KEGG) and Gene Ontology (GO).

2.7. Correlation of Risk Score with Other Scores. To further validate the accuracy of the risk model in predicting CAF, we executed Spearman correlation analysis on the risk score, stroma score, immune score, ESTIMATE score, tumor score, the proportion of CAF predicted by xCell, and the proportion of CAF predicted by EPIC, MCP-counter, and Tumor Immune Dysfunction and Exclusion (TIDE). Firstly, the "ESTIMATE" R package was utilized for ESTIMATE analysis to obtain the immune score, stromal score, ESTIMATE score, and tumor score for each sample. The EPIC algorithm analyzed the percentage of infiltration of eight-cell types, including CAFs, based on expression data [16]. We used the MCP-counter to attribute the content of CAFs in the samples. The xCell algorithm can also predict the proportion of CAFs. Finally, the CAF content was obtained using TIDE. The correlations between risk scores and each index were calculated using the Spearman correlation analysis. $p < 0.05$ represents significant correlation.

2.8. Correlation between CAF Marker Genes and Prognostic Genes. There were 23 CAF-associated marker genes, including *ACTA2*, *ASPN*, *CAV1*, *COL11A1*, *COL1A1*, *COL1A2*, *COL3A1*, *EMILIN1*, *FAP*, *FN1*, *FOXF1*, *MFAP5*, *MMP11*, *MMP2*, *OGN*, *PDGFRA*, *PDGFRB*, *PDPN*, *S100A4*, *SLC16A4*, *SPARC*, *TNC*, and *ZEB1* [17, 18]. Then, we calculated the correlations between prognostic genes and risk scores with CAF marker genes.

2.9. Inferring Immune Cell Abundance in High- and Low-Risk Groups Using the ssGSEA Algorithm. ssGSEA is a single-sample GSEA method by which we can obtain the immune cell, of each sample [19]. Using 28 immune-related gene sets, we can get the immune activity. Then, the differences in 28 immune activities between the high- and low-risk groups were compared, and the differential immune activities were related to the risk scores.

2.10. Chemotherapy Drug Sensitivity Prediction. We know that the Genomics of Drug Sensitivity in Cancer (GDSC) database has many drug sensitivity and genomic datasets that are important for the discovery of potential oncology therapeutic targets. IC50 refers to the half amount of a drug that inhibits specific biological processes. The "pRRophetic-Predict" R package (version 0.5) was utilized to calculate 138 drugs included in the database and compare differences in drug IC50 between the high- and low-risk groups.

2.11. Quantitative Real-Time Polymerase Chain Reaction (qRT-PCR) Validation. First, RNA was extracted from control cells WRL68 and HCC cells Huh7, Hepg2, and sk-sep-1, followed by a reverse transcription reaction, and finally, the target gene was amplified by PCR reaction. The RNA extraction kit was TRIzol Reagent (ref.: 15596018) kit provided by Ambion. The reverse transcription kit was the SweScript RT I First-strand cDNA Synthesis All-in-One™ First-Strand cDNA Synthesis Kit (cat.: G33330-50) from Servicebio. PCR reactions were performed with the 2x Universal Blue SYBR Green qPCR Master Mix (cat.:G3326-05) kit from Servicebio. Primer sequences are shown in Table 1. The PCR reaction process was 95°C predenaturation for 1 min and then 40 cycles. Each cycle included 95°C denaturation for 20 s, 55°C annealing for 20 s, and 72°C extension for 30 s. The internal reference for gene detection is GAPDH. The expression of *ACTA2*, *IGJ*, *CTHRC1*, *CXCL12*, and *LAMB1* in normal cell WRL68 and HCC cells Huh7, Hepg2, and sk-sep-1 were compared by analysis of variance (ANOVA), and $p < 0.05$ was a difference.

3. Results

3.1. Evaluation of the CAF Status in HCC. We calculated the immune cell content of 421 samples in the TCGA dataset (Figure 1(a)). After screening out the normal samples, there

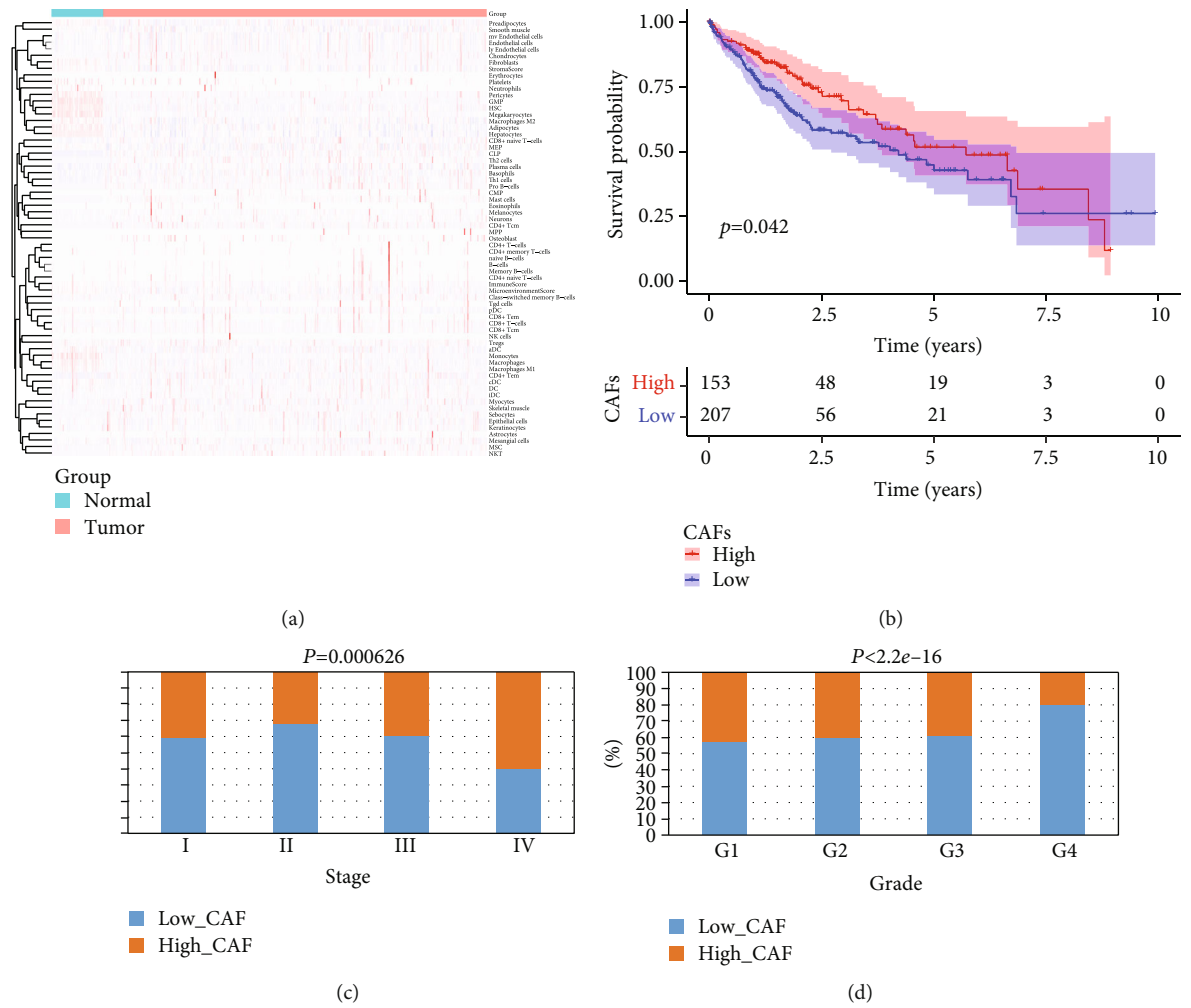

Figure 1: The changing trend of CAF in the TCGA-LIHC queue analyzed by the XCELL algorithm. (a) Heat map of different cell concentrations calculated by xCell. (b) K-M curve of high and low CAF group. (c) Correlation of CAF cells in different STAGE groups. (d) Correlation of CAF cells in different GRADE groups.

were 158 high CAF samples and 213 low CAF samples. The results of K-M analysis of the high and low CAF groups were shown (Figure 1(b)), and it can be seen that there was a significant survival difference between the high and low CAF groups. The results of clinical trait correlation between high and low CAF groups showed that CAF cells were different between different STAGE groups and between different GRADE groups (Figures 1(c) and 1(d)).

3.2. Identification of CAFGs by WGCNA Analysis. The clustering of the samples in the TCGA dataset was shown in Figure 2(a), and the samples were not deleted. The power threshold was chosen as 13, so that the interactions between genes conformed to the scale-free network (Figure 2(b)). From the module clustering tree, we can see that 12 modules were clustered, and after merging, 6 modules were obtained (Figure 2(c)). Finally, the key modules were filtered according to their correlation with CAF, and we got the green module (Figure 2(d)). Therefore, 898 genes in the green module were used as CAFGs.

3.3. Identification of CAF-DEGs. There were 676 DEGs between the high and low CAF groups (Figure 3(a)). 6265 DEGs were found between normal and HCC samples (Figure 3(b)). CAFGs and DEGs between high and low CAF and DEGs between normal and HCC samples were crossed to obtain 107 CAF-DEGs, and the Venn diagram is shown (Figure 3(c), Table S1).

3.4. A Risk Model Based on 5 Genes Was Built. In the TCGA training set, univariate Cox analysis yielded 7 genes (Figure 4(a), Table 2). After multivariate Cox analysis, 5 genes appeared in multivariate Cox analysis (Figure 4(b), Table 3): *ACTA2*, *IGJ*, *CTHRC1*, *CXCL12*, and *LAMB1*. The risk value of each patient was counted from the expression of these five genes, and the cases were classified into high and low risks (median value = 0.988) (Figure 4(c)). The survival analysis of the high- and low-risk groups illustrated there was a significant survival difference between the high- and low-risk groups (Figure 4(d)). The AUC at 1, 3, and 5 years in the ROC curve were 0.661, 0.686, and 0.608,

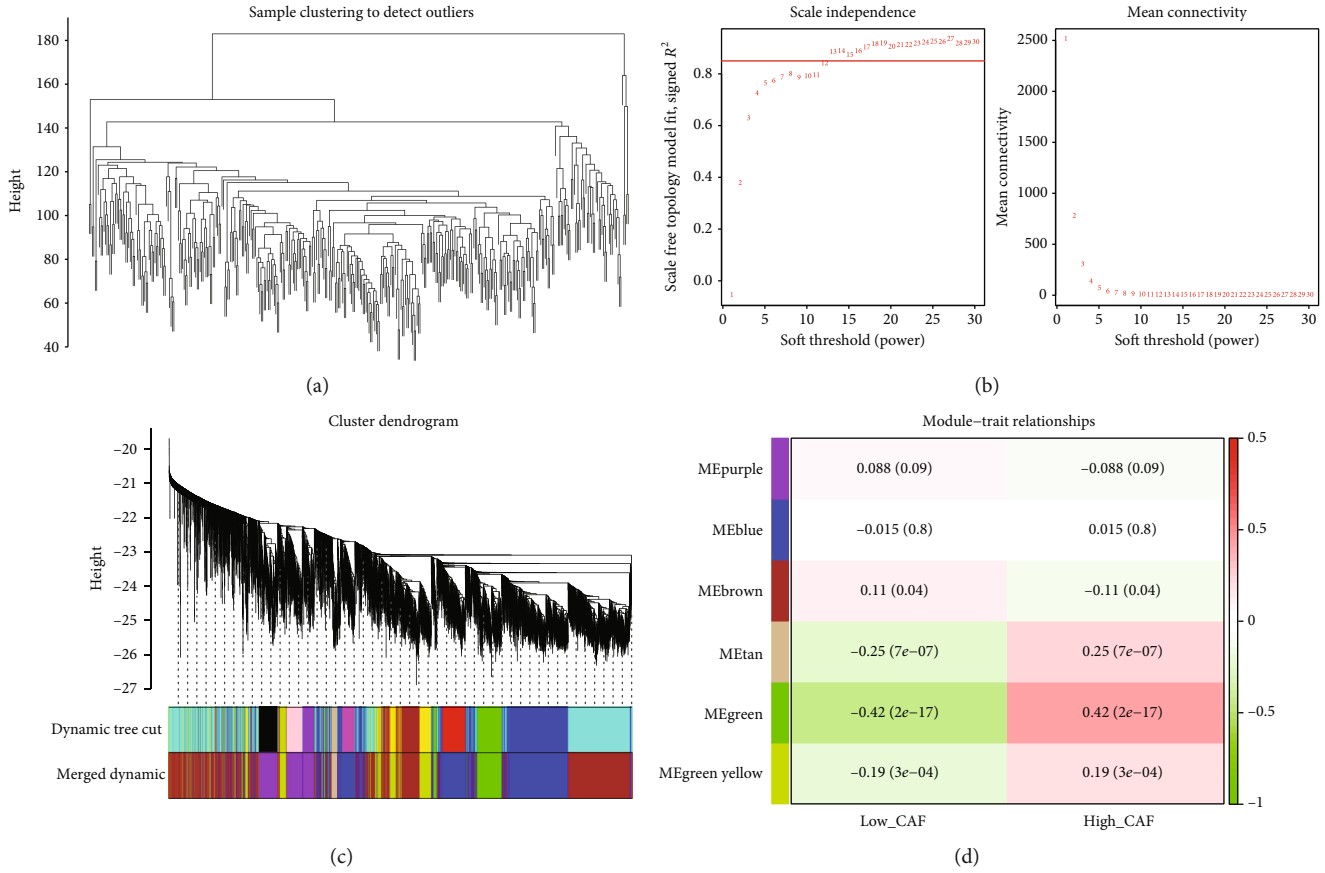

Figure 2: Identification of CAFGs by WGCNA analysis. (a) Sample clustering of TCGA dataset. (b) Scale-free soft threshold distribution. (c) Cluster tree of modules. (d) Heat map of correlation between modules and clinical traits. Each row corresponds to a module eigengene and each column to a trait. Each cell contains the corresponding correlation and p value. The table is color-coded by correlation according to the color legend.

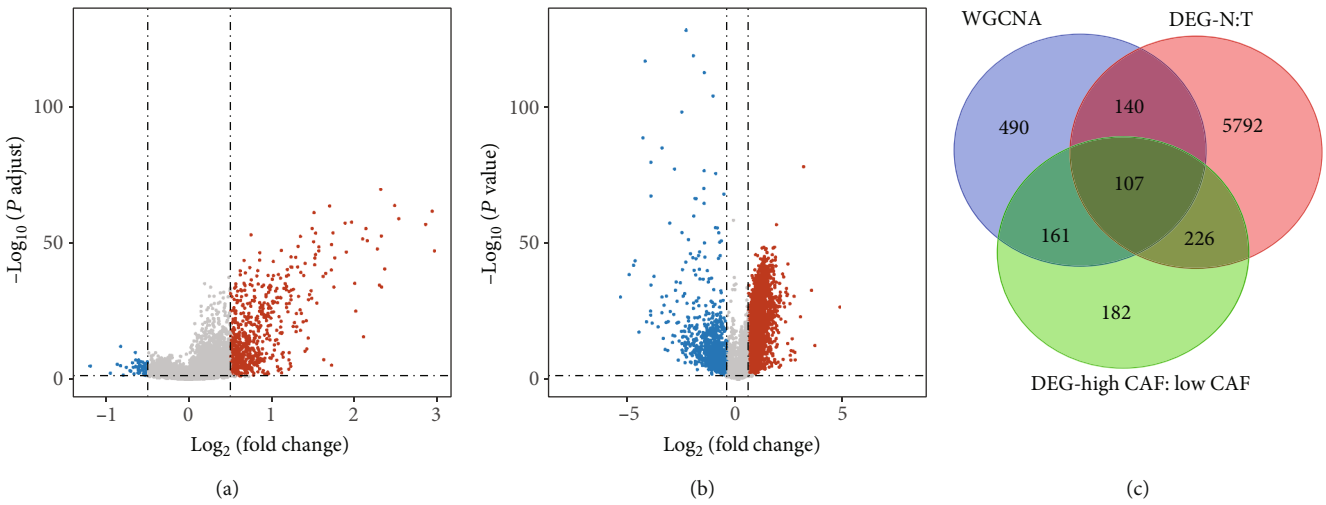

Figure 3: Identification of CAF-DEGs. (a) Volcano map of the gene from high CAF vs. low CAF samples. (b) Volcano map of the gene from HCC vs. the normal sample; (c) Venn diagram of CAFGs, DEGs between high and low CAF, and DEGs between normal and HCC samples. Red dots represent upregulation, and blue dots indicate downregulation.

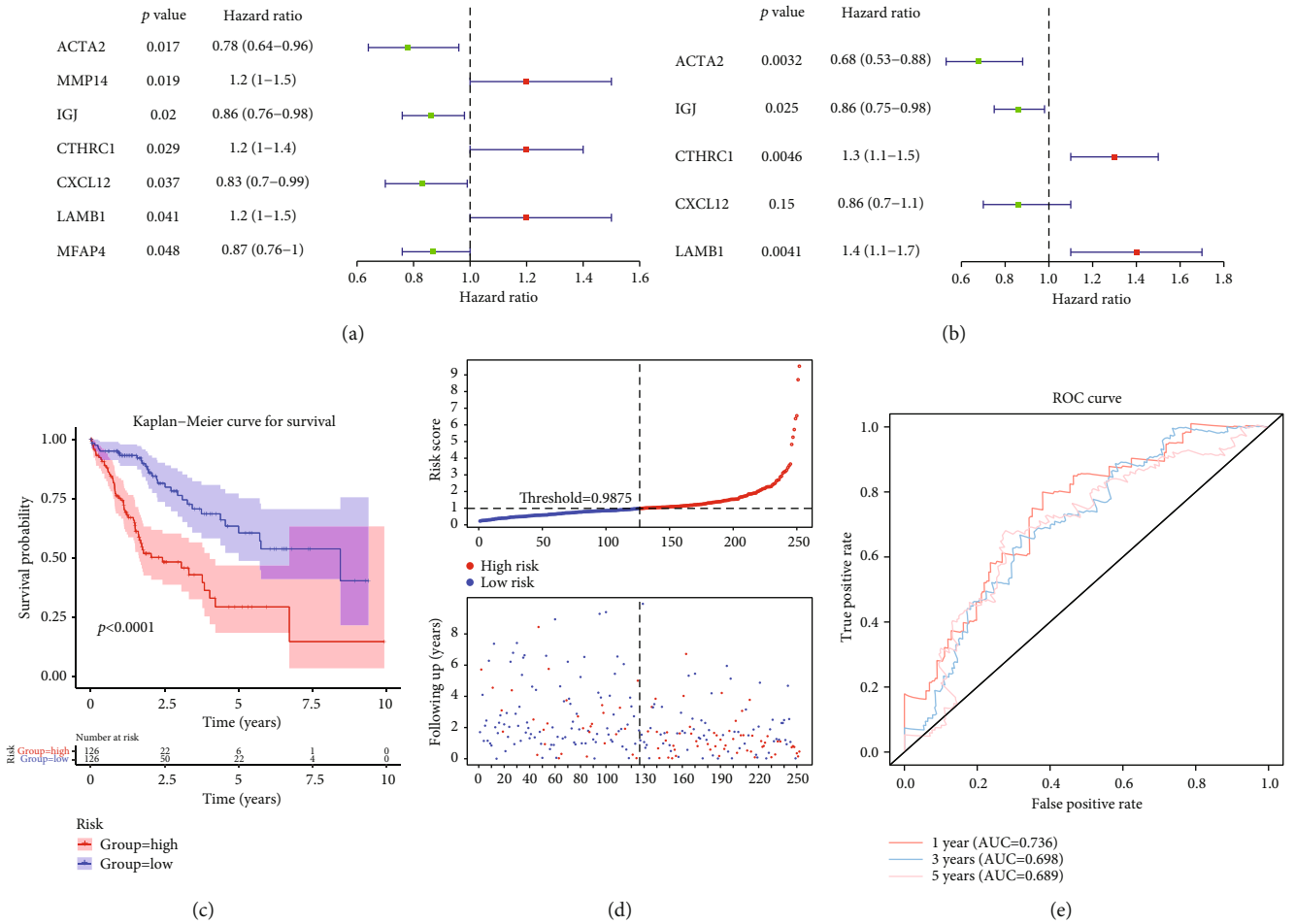

Figure 4: Identification of prognostic genes and evaluation of risk regression models. (a) Forest map of univariate Cox results. (b) Forest map with multivariate Cox results. (c) K-M survival curve of risk score. (d) Risk curves for the high- and low-risk groups. (e) The ROC curve evaluating the validity of the risk model.

Table 2: Univariate Cox regression analysis results.

Id	z	HR	HR.95L	HR.95H	p value
ACTA2	-2.382667536	0.7794916	0.635062344	0.956767726	0.017187709
MMP14	2.354059963	1.237687278	1.036344401	1.478147415	0.018569615
IGJ	-2.321172984	0.861330023	0.759325083	0.977037931	0.02027751
CTHRC1	2.184086222	1.176830023	1.016848758	1.361981212	0.028955913
CXCL12	-2.086278679	0.833517888	0.702454325	0.989035222	0.036953387
LAMB1	2.044172937	1.224712344	1.008385361	1.487447541	0.040936466
MFAP4	-1.973675604	0.871707401	0.760598958	0.999046587	0.048418641

Table 3: Multivariate cox regression analysis results.

Id	Coef	HR	HR.95L	HR.95H	p value
ACTA2	-0.379760522	0.684025199	0.531595384	0.880162783	0.003153906
IGJ	-0.152683995	0.858400938	0.751217636	0.980877092	0.024851869
CTHRC1	0.236265717	1.266510799	1.075666699	1.491214339	0.004578553
CXCL12	-0.153407609	0.857780012	0.69754989	1.054815661	0.145913422
LAMB1	0.313651044	1.368412138	1.104754211	1.694994017	0.004075463

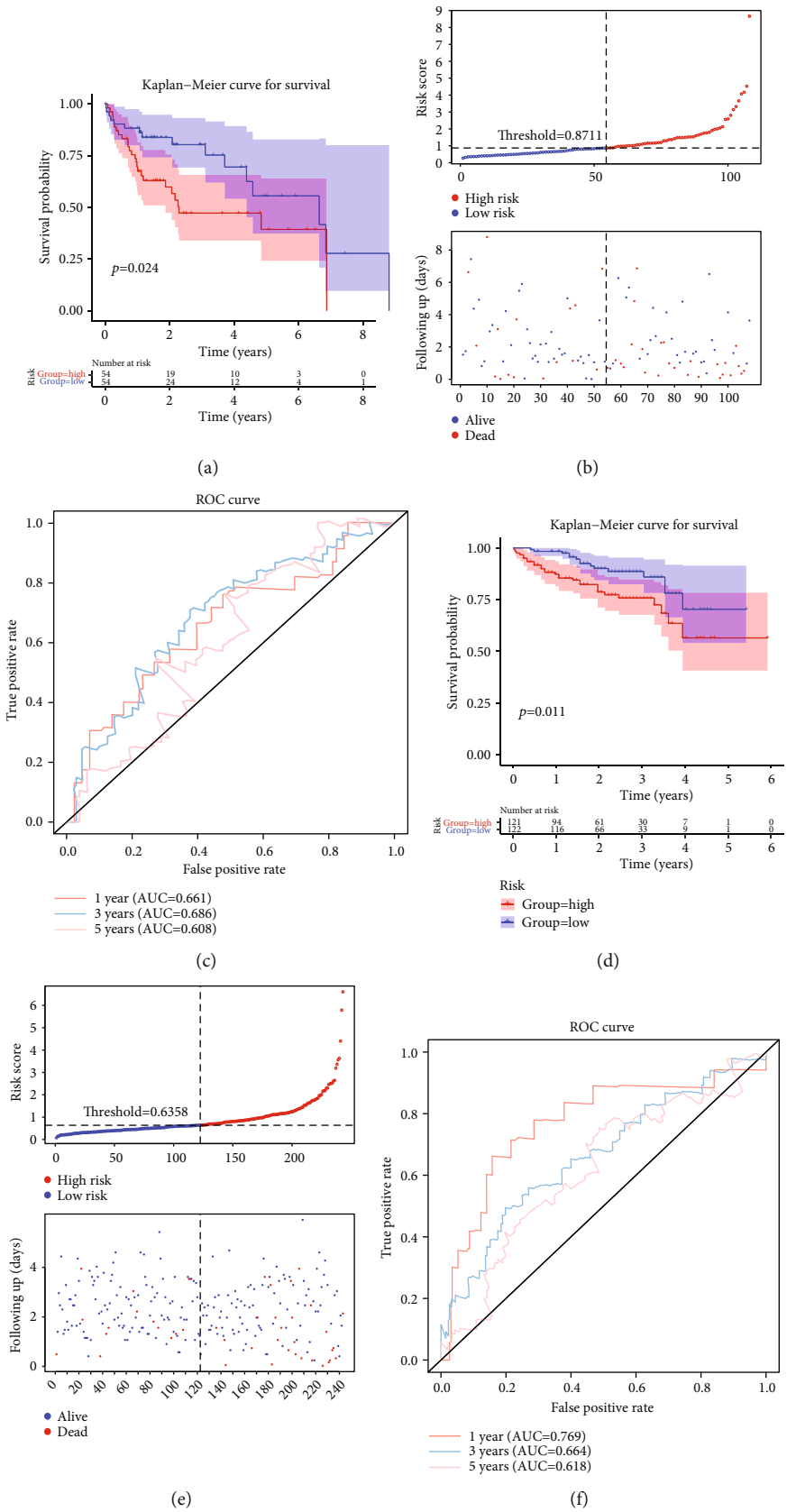

Figure 5: Continued.

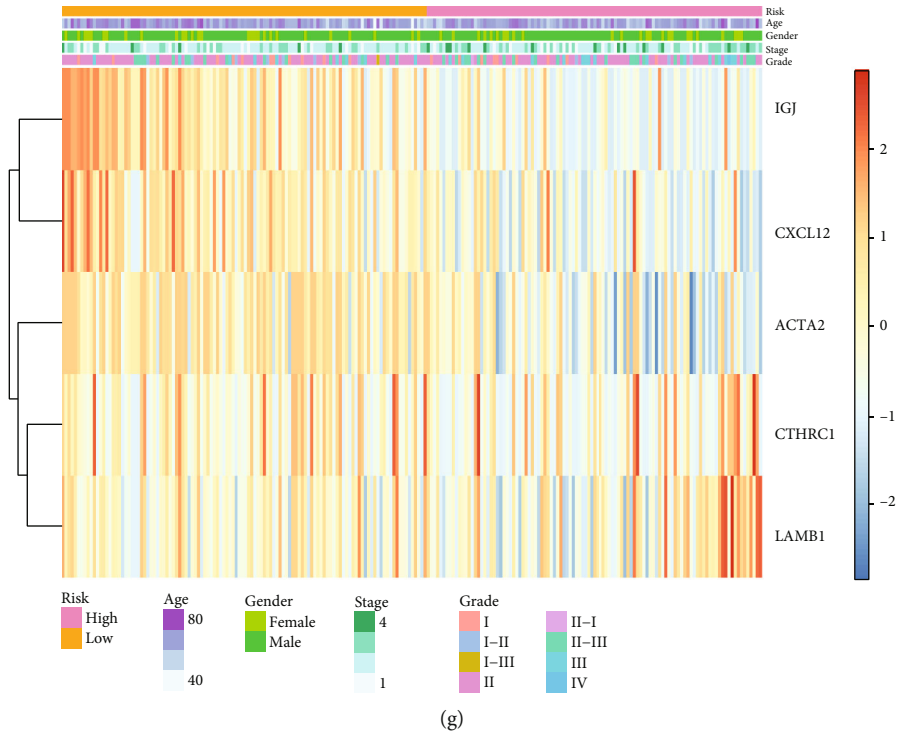

Figure 5: Testing and validation of the risk model. (a) K-M survival curve of risk score in the test set. (b) Risk curves for the high- and low-risk groups in the test set. (c) ROC curve in the test set evaluating the validity of the risk model. (d) K-M survival curve of risk score in the validation set. (e) Risk curves for the high- and low-risk groups in the validation set. (f) ROC curve in the validation set evaluating the validity of the risk model. (g) Overview of the correlation between risk score and clinical features in validation.

respectively (Figure 4(e)). In addition, in both the TCGA test set and ICGC validation set, the survival of the high-risk group was lower, and the AUC at 1, 3, and 5 years was more significant than 0.65 (Figures 5(a)–5(g)). In addition, in the ICGC validation set, grade was different between the high- and low-risk groups. It indicated that the risk model could be effectively used as a prognostic model.

3.5. Correlation of Risk Model and Clinical Traits. The correlation between the risk model and clinical traits showed that the risk values differed significantly between stages I-II and stages III-IV. And the risk values were quite different between $T1-2$ and $T3-4$ stages. The results were shown (Figures 6(a)–6(f)).

3.6. Risk Score and Stage Were Independent Prognostic Factors. The factors with $p < 0.05$ in the univariate Cox regression analysis were T, risk score, and stage (Figure 7(a), Table 4). The three significant factors were added to the multivariate Cox analysis (Figure 7(b), Table 5), and the results showed that risk score and stage were significant. The survival nomogram graph was shown (Figure 7(c)). In the corrected curve, the *c*-index was 0.703, and the corrected *c*-index was 0.696, and the slopes were calculated to be 0.697, 0.406, and 0.300 at 1, 3, and 5 years, which demonstrated the best prediction at one year (Figure 7(d)).

3.7. Enrichment Analysis of High- and Low-Risk Groups. A total of 73 KEGG paths and 1968 GO paths were enriched by GSEA, and we selected the top 10 KEGG paths and GO paths to visualize them. As can be seen (Figure 8(a)), the top 10 KEGG pathways obtained have activation of the immune response, alcohol metabolic process, alpha-amino acid metabolic process, and B cell-mediated immunity. The top 10 GO functions were autoimmune thyroid disease, cell cycle, graft versus host disease, peroxisome, PPAR signaling pathway, and retinol metabolism (Figure 8(b)).

3.8. Correlation of Risk Scores with Other Scores and Correlation of CAF Marker Genes with Prognostic Genes. The correlation results of the risk score with other scores suggested that the risk score was negatively relevant to the immune score, ESTIMATE score, stromal score, xCell-predicted CAF ratio, and TIDE-predicted CAF ratio, and positively relevant with the tumor score (Figure 9(a)). The correlations between prognostic genes and risk scores with CAF marker genes were calculated, and the results were as follows. The correlation results illustrated that risk scores were negatively related to*ACTA2*, *ASPN*, *COL1A1*, *COL1A2*, *COL3A1*, *EMILIN1*, *FAP*, *FOXF1*, *MFAP5*, *MMP2*, *OGN*, *PDGFRA*, *PDPN*, *S100A4*, *SLC16A4*, *SPARC*, and *TNC* genes. FN1 with LAMB1, CTHRC1, and SLC16A4 was positively associated with *ACTA2*, *IGJ*, *CXCL12*, and *LAMB1*. In addition, the remaining 21 CAF-related marker genes were positively associated with five prognostic genes (Figure 9(b)).

3.9. Inferring Immune Cell Abundance Using the ssGSEA Algorithm. As can be seen (Figure 10(b)), among the 28 cells,

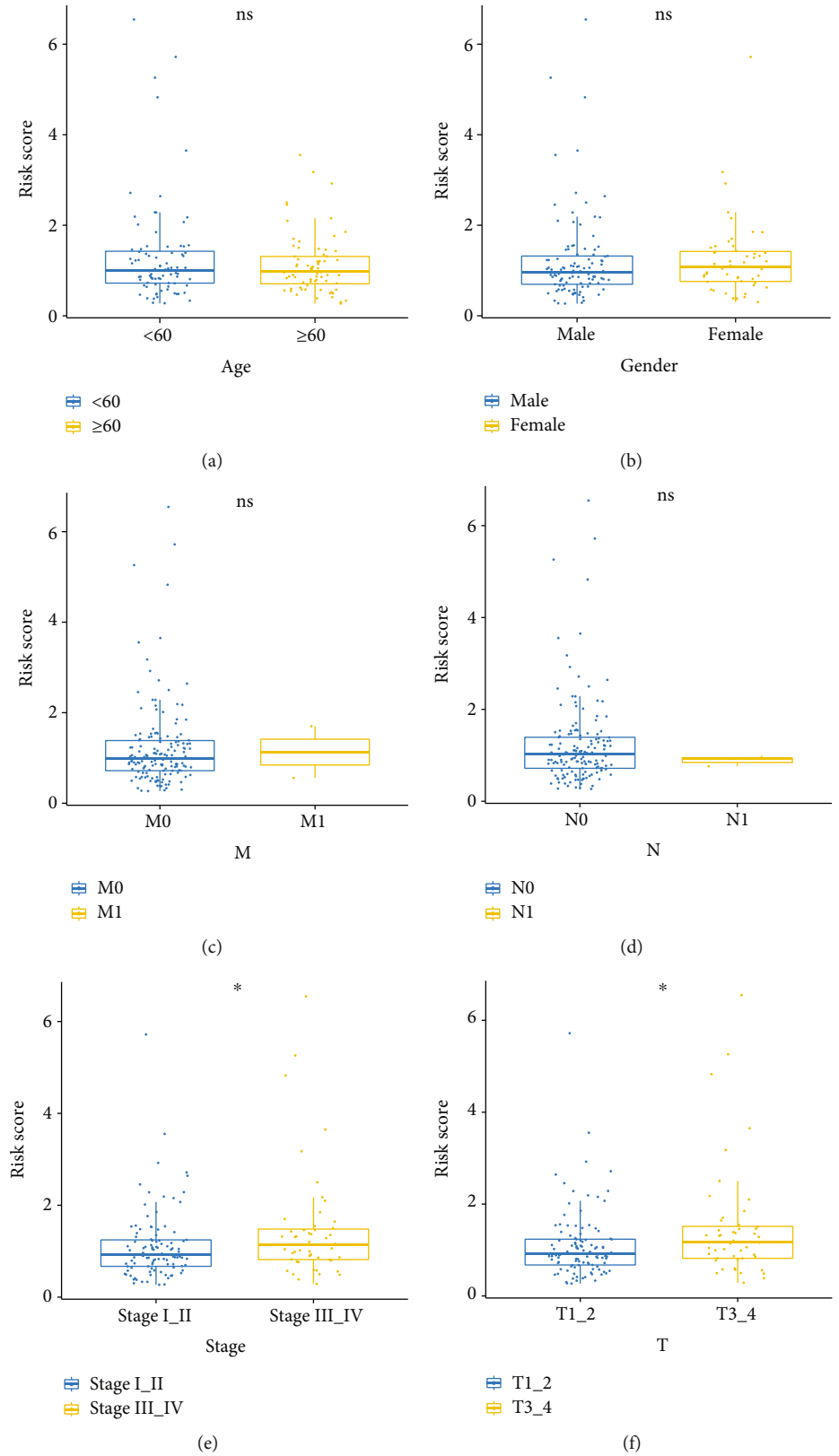

FIGURE 6: Correlation of risk model and clinical traits. (a) Correlation between risk models and age traits. (b) Correlation of risk models with gender. (c) Correlation between risk model and M traits. (d) Correlation between risk model and N traits. (e) Correlation between risk model and stage traits. (f) Correlation between risk model and T traits.

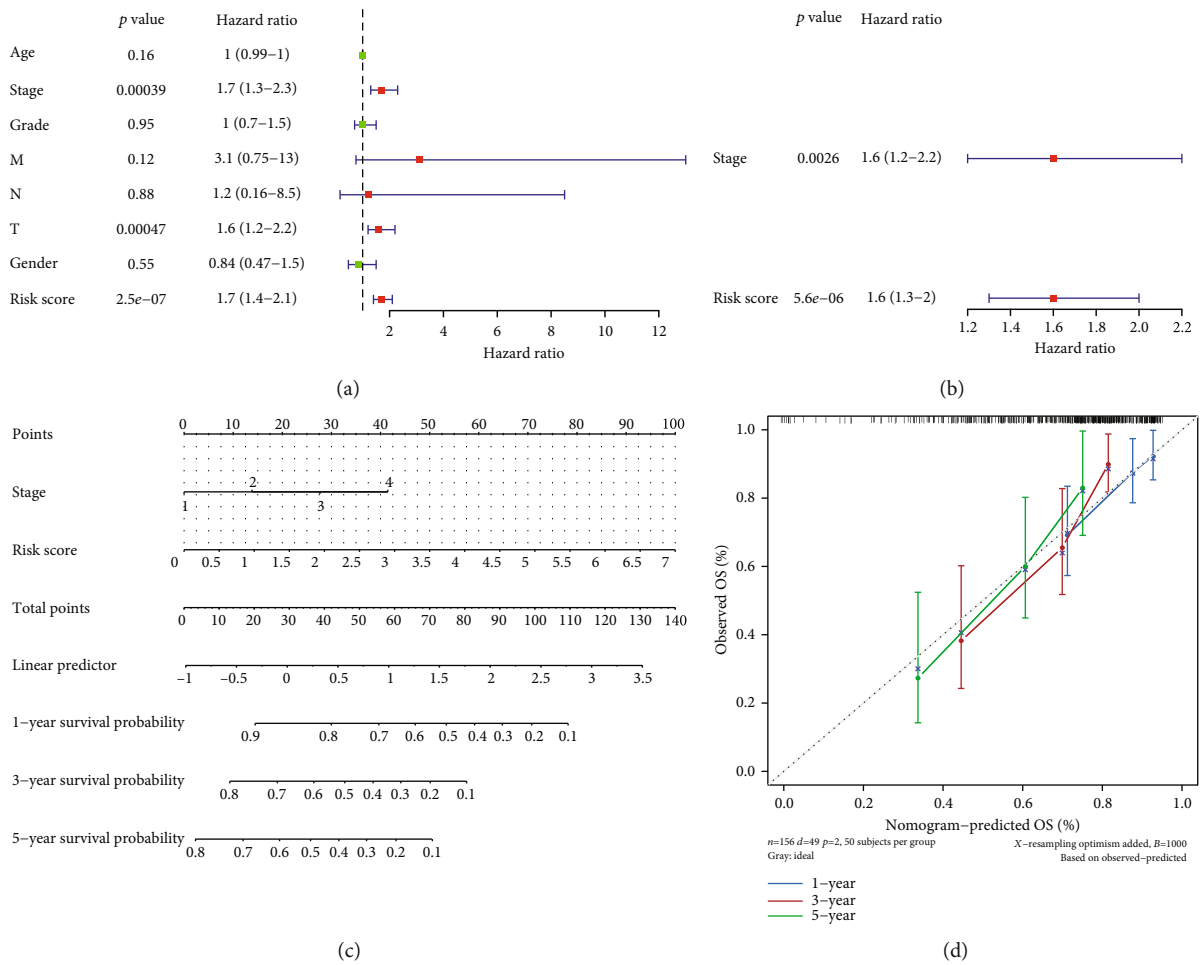

Figure 7: Risk model-independent prognosis in the training set. (a) Forest map of univariate Cox results. (b) Forest map with multivariate Cox results. (c) Survival nomogram graph. (d) Correction curve for line graph.

Table 4: Independent prognostic univariate cox analysis results.

Variable	Coef	HR	HR.95 L	HR.95H	*p* value
riskScore	0.554622883	1.741284194	1.41049963	2.149642991	2.47E-07
STAGE	0.543228104	1.721555261	1.274933191	2.324633586	0.000392502
T	0.499131316	1.647289675	1.245504476	2.178686088	0.000467059
M	1.131809556	3.101263336	0.748842494	12.8436011	0.118512375
Age	0.016505353	1.016642319	0.993511015	1.040312175	0.15985152
Gender	-0.17646729	0.838226197	0.472510705	1.486999448	0.546261178
N	0.15060375	1.162535912	0.159530784	8.471654902	0.88185331
Grade	0.011591034	1.01165847	0.696375217	1.469685933	0.951493367

Table 5: Independent prognostic multivariate cox analysis results.

Id	Coef	HR	HR.95L	HR.95H	*p* value
STAGE	0.47806429	1.612949176	1.181104647	2.202688011	0.002639371
riskScore	0.493909346	1.638709999	1.323983571	2.028250591	5.65*E* − 06

20 cells were different between the high- and low-risk groups, including activated B cell, CD56bright natural killer (NK) cell, CD56dim NK cell, central memory CD4 T cell, central memory CD8 T cell, and Type 1 T helper cell, and the 20 significant cells were plotted separately from the risk score in a lollipop plot as follows (Figure 10(a)).

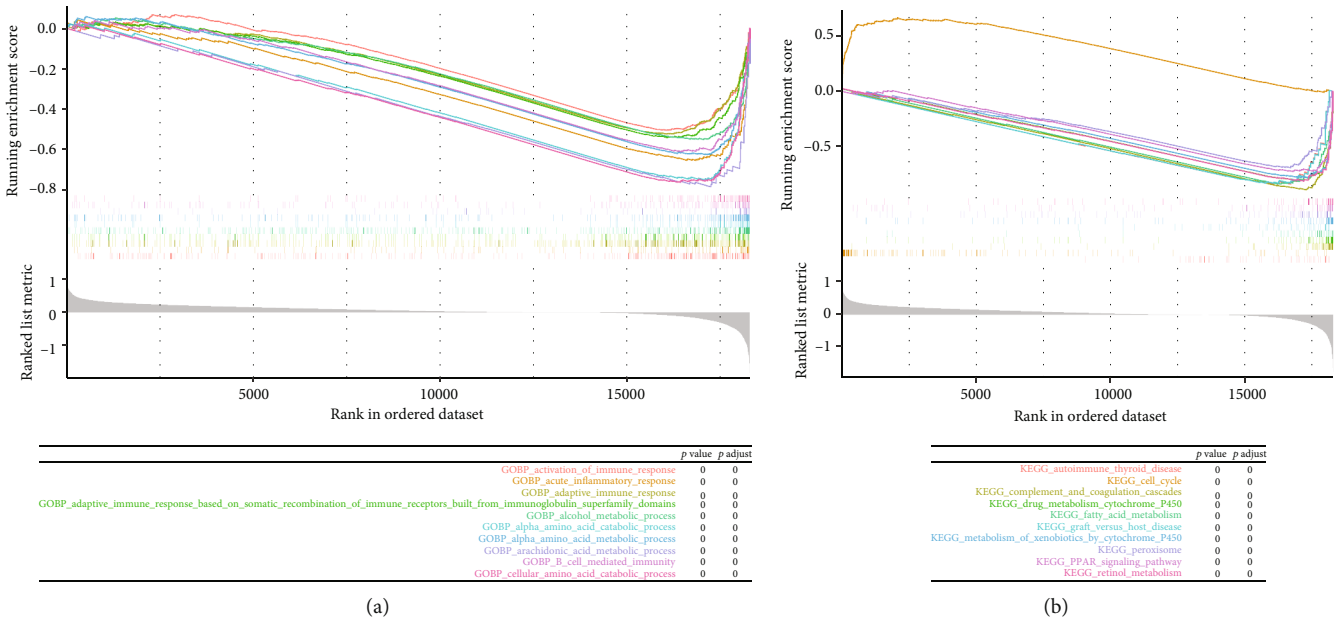

Figure 8: Enrichment analysis of the high- and low-risk groups. (a) The top10 KEGG pathways. (b) The top10 GO pathways.

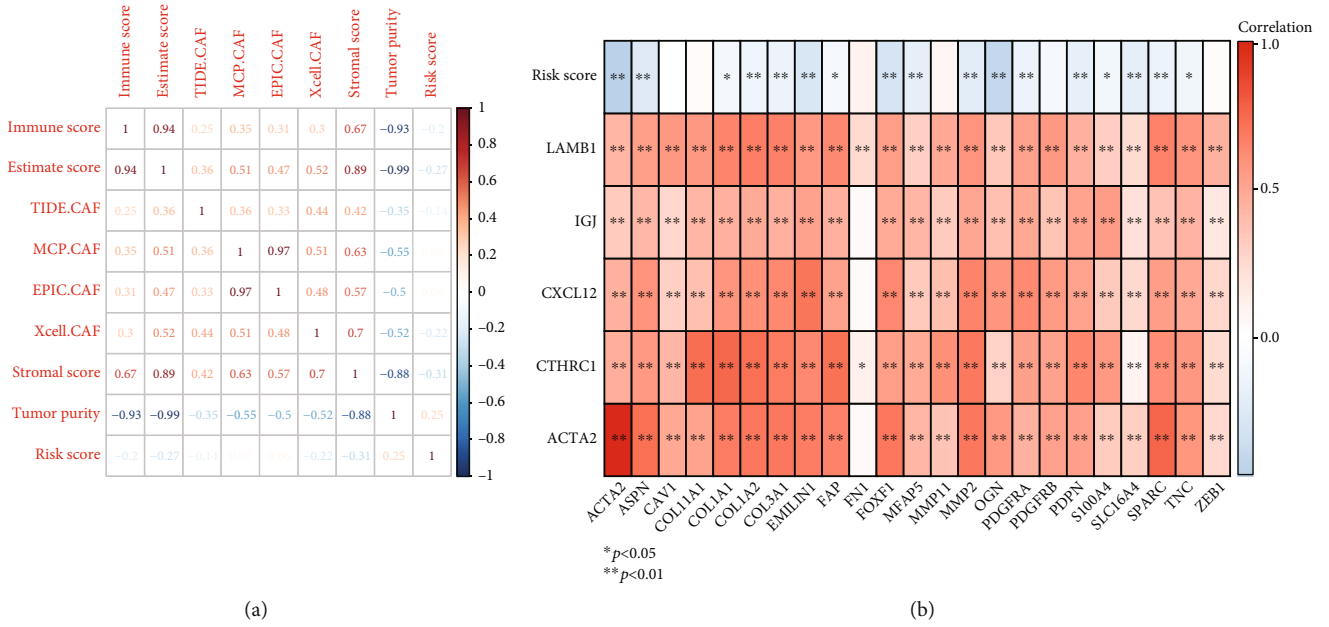

Figure 9: Correlation of risk scores with other scores and correlation of CAF marker genes with prognostic genes. (a) Heat map of correlations between risk score and other scores. (b) Heat map of correlations between CAF marker genes and prognostic genes.

3.10. Chemotherapy Drug Sensitivity Prediction. According to the calculation results, 65 drugs showed differences in the high- and low-risk groups, which were temsirolimus, CI.1040, NU.7441, AZD8055, AICAR, AMG.706, DMOG, KU.55933, Metformin, EHT.1864, Dasatinib, NVP.BEZ235, PD.0325901, AZD.0530, NVP.TAE684, AKT.inhibitor.VIII, Vorinostat, GDC0941, PD.173074, Erlotinib, Docetaxel, WO2009093972, Rapamycin, AZD6244, JNJ.26854165, BI.D1870, MG.132, BX.795, A.770041, PD.0332991, Z.LLNle.CHO, AP.24534, Parthenolide, GW.441756, Nilotinib, OSI.906, X17.AAG, GDC.0449, AZD6482, WH.4.023, PF.4708671, Axitinib, TW.37, SB590885, Thapsigargin, NSC.87877, Cyclopamine, CMK, RDEA119, Gefitinib, Sorafenib, CEP.701, Imatinib, Methotrexate, ABT.263, Vinblastine, AZD7762, Lapatinib, AZ628, GNF.2, Bryostatin.1, Camptothecin, Nutlin.3a, FH535, and ZM.447439 (Table S2); they were visualized as a box plot as shown in the figure below. Figure 11 showed box plots for just the six drugs in the high- and low-risk groups.

3.11. qPCR Validation. The results of qPCR demonstrated that expression levels of *ACTA2*, *IGJ*, *CTHRC1*, *CXCL12*,

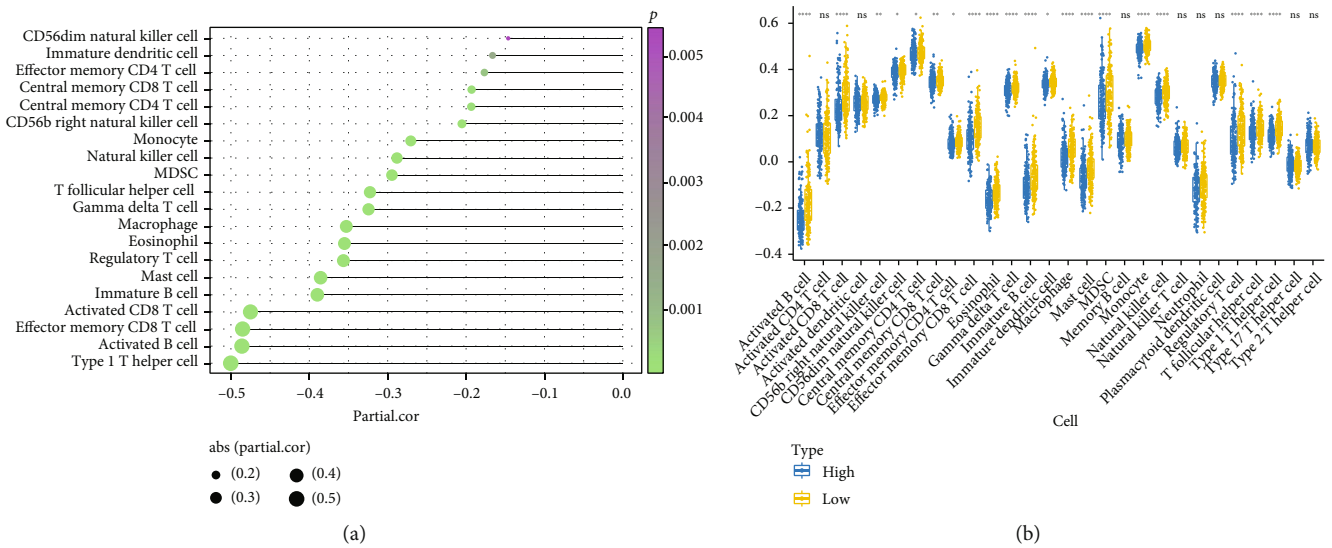

Figure 10: Inferring immune cell abundance in the high- and low-risk groups by the ssGSEA algorithm. (a) Correlation between cell contents and risk values. (b) Box plots of cell contents between the high- and low-risk groups.

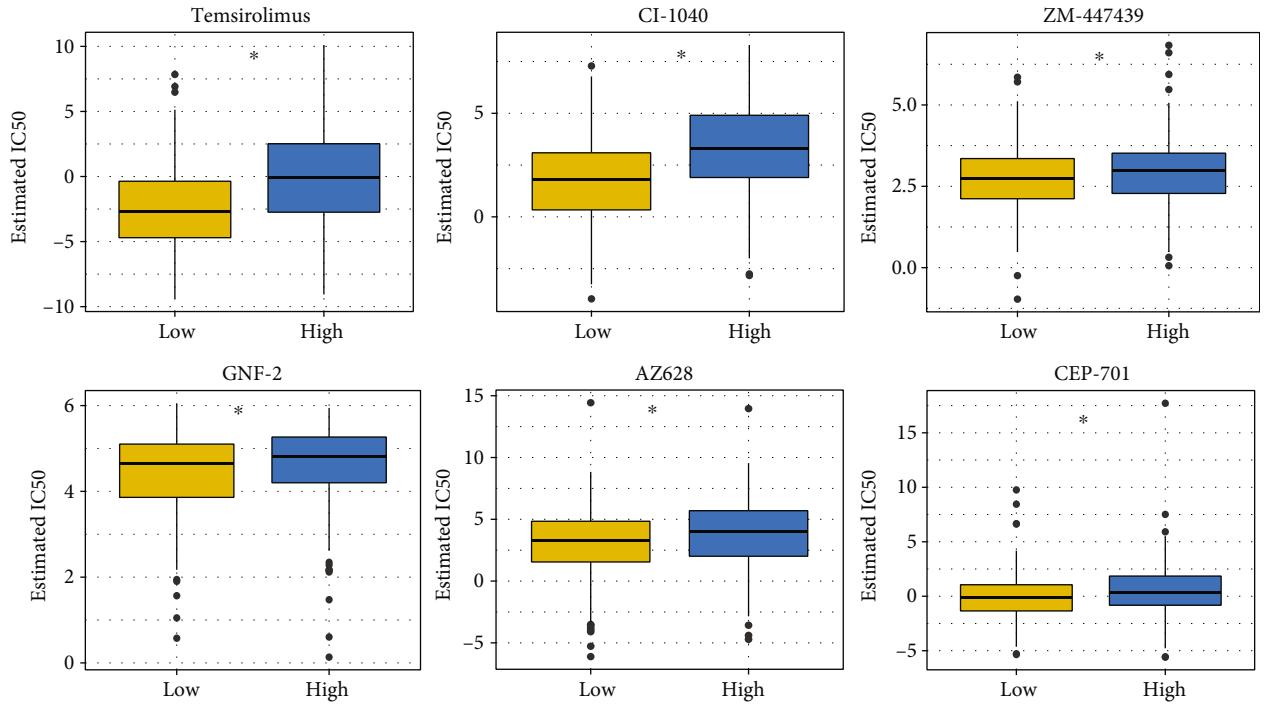

Figure 11: Significant differences of 6 drugs between the high- and low-risk groups.

and *LAMB1* genes were different in normal cells WRL68 and HCC cells Huh7, Hepg2, and sk-sep-1. Specifically, *ACTA2*, *CTHRC1*, and *LAMB1* genes were significantly upregulated in HCC cells Huh7, Hepg2, sk-sep-1, and *IGJ*, *CXCL12* were downregulated in HCC cells (Figure 12).

4. Discussion

While there have been advances in diagnostic techniques and treatment of HCC, [20, 21] the survival prognosis remains poor because of its high recurrence and metastasis rates [22]. CAFs are the main cellular component that can affect the formation of liver fibrosis, which in turn results in the development of HCC [10, 12]. Many prognostic models for HCC have been presented by far. Zhang et al. built a prognostic model which was able to reasonably predict the prognosis of HCC patients and provided a new idea to study HCC of different histological grades [21]. Long et al. developed a four-gene prognostic model to probe the differences in mRNA expression between HCC and neighboring liver to obtain potential genetic biomarkers [2]. Wang et al. screened immune-related differentially expressed genes

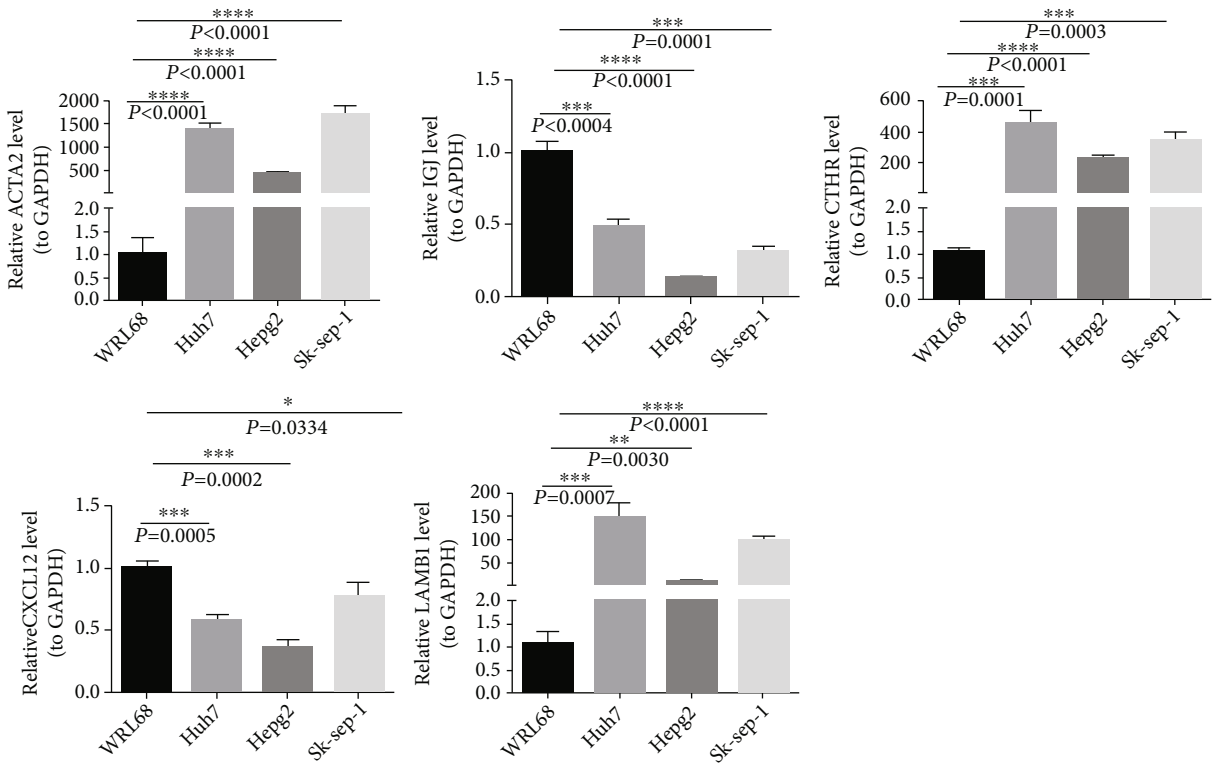

Figure 12: Validating the expression levels of the five genes in normal and HCC cells by RT-qPCR.

closely related to HCC and further detected genes associated with prognosis [23]. However, because of the limitations of the public database data, further validation of the proposed prediction models is necessary or regression modeling methods need to be applied to determine if the prediction accuracy can be further improved. More than that, the validity of the prediction model should be confirmed in a large sample of HCC. In this study, we sought five biomarkers basing CAFGs for a prognostic model for HCC by bioinformatics method, conducted an independent prognostic analysis and functional enrichment analysis, and calculated the differences between immunoassay (immune infiltration, immunotherapy) and drug sensitivity at all levels. At last, qRT-PCR verified the expression levels of *ACTA2*, *IGJ*, *CTHRC1*, *CXCL12*, and *LAMB1* genes in normal and HCC cells, which is a relatively complete work for the prognostic building.

In the present study, five genes have been obtained for the HCC prognostic model. *ACTA2*, actin alpha 2, which contributed to cell-generated mechanical tension and maintenance of cell shape and movement, was highly expressed in carcinomas [24]. Meanwhile, a previous study showed that CAFs enhanced the tumor-initiating and tumorigenic properties of HCC cells, and *ACTA2* was exactly a biomarker of CAFs. The upregulation of *ACTA2* level indicated poor survival HCC patients [25]. It was demonstrated that a linking chain of multisomal IgA and IgM is also present in *IGJ* [26]. It is possible that their upregulation may enhance the anticancer immune response to sorafenib treatment and facilitate the survival of HCC [27, 28]. In addition, overexpression of *CTHRC1* contributes to tumorigenesis and progression through positive regulation of tumor spread, invasion, migration, adhesion, and metastasis [29–31]. Immunohistochemical analysis demonstrated that CTHRC1 expression levels were elevated in HCC tissues [32]. Stromal-derived-factor-1 (*SDF-1*) was expressed in more than 23 different types and participated in tumor metastasis [33]. Interestingly, *SDF-1* protein for the HCC cells was expressed in the cytoplasm and nucleus [34]. Notably, the level of SDF-1 was lower in HCC. Patients with relatively high *SDF-1* showed longer OS [35]. *LAMB1* consists of laminins [36]. LamB1 mediated β1 integrin signaling and can regulate cell migration, proliferation, and survival by activating specific p67kDa laminin receptors (LamR) [37–39]. HCC patients have shown elevated levels of LamB1 in cirrhotic tissues, with further increased expression in HCC [40]. In HCC, the expression of the b1 integrin receptor and LamR were upregulated, which was relevant with enhanced tumor aggressiveness and poor patient survival [41, 42].

Based on the enrichment analysis of the high- and low-risk groups by GSEA, function ways of fatty acid metabolism, amino acid metabolism, and immune response were related to the progress of HCC seriously. Firstly, a specific reprogramming xiang of fatty acid metabolism has been found in the nonalcoholic steatohepatitis (NASH) stage of nonalcoholic fatty liver disease (NAFLD). The liver is involved in the context of MetS and simple steatosis can progress to liver fibrosis or even cirrhosis, and eventually to HCC [43]. Metabolic reprogramming can support hepatocyte proliferation by participating in fatty acid synthesis

and oxidation [44]. Second, the synthesis of nonessential amino acids is vital for the maintenance of liver function [45, 46]. In HCC, abnormalities in amino acid and protein metabolism occur [47].

Tumor immune cells can be participated in the immune response to cancer and also predict treatment efficacy and survival [48]. In the current study, there were 20 immune cells that differed between the high- and low-risk groups, including B cells, T cells, and NK cells. Regulatory B (Breg) cells accumulate in the tumor environment, and it can produce high levels of IL-10. Breg can suppress the host immune responses to promote tumorigenesis in HCC [49]. Regulatory T cells (Tregs), expressing CD25 and forkhead boxP3 (FoxP3), were negative during immune surveillance, resulting in tumor tolerance [50]. There are fewer NK cells in HCC tissue and NK cells can inhibit cytokine production and cytotoxic activity [51]. Zhu et al. constructed the prognostic model and the recurrence risk model and found that patients with high risk scores responded strongly to immune checkpoint inhibitor therapy and that low-risk patients may derive more significant clinical benefit from chemotherapy [52].

65 drugs showed differences in the high- and low-risk groups. Temsirolimus is a prodrug of sirolimus. Studies have shown that temsirolimus has an inhibitory effect on HCC cells, and in phase I/II clinical trial, it was well-tolerated in HCC patients [53]. Moreover, temsirolimus is an mTOR inhibitor that can block cell cycle transition and affects cell proliferation by inhibiting mTOR and growth factors [54]. CI-1040, another drug predicted by our prognostic model, is an oral inhibitor of extracellular signal-regulated kinase (MEK) [55], It is a new candidate for targeted treatment of HCC because of its potential antitumor efficacy [56]. ZM447439 (ZM) induces apoptosis in HCC cells by interfering with spindle integrity and chromosome segregation [57]. These three drugs are representatives of anti-HCC drugs. However, among the 65 drugs, there are also some news, of which the effects on HCC are not definite. For example, GNF-2 inhibits the enzymatic and cellular kinase activities of ABL1, ABL2, and recombinant ABL and can inhibit the proliferation of fibroblasts. Still, its effect on anti-HCC have not been elucidated [58]. Then, AZ628, another new drug for HCC, can be involved in fibrosarcoma formation, and AstraZeneca can effectively inhibit cancer cell proliferation by inhibiting the activity of Raf [59]. CEP-701 can effectively inhibit trk receptors, leading to cell death in prostate cancer (PC), and it can also limit tissue penetration by binding serum proteins [60].

5. Conclusion

This study concentrated on the prognostic value of CAFs for HCC and identified CAF-related genes. A prognostic model of 5 CAFGs for HCC was developed in this research, and the expression of the five genes were verified by the qRT-PCR method. It provides new directions for the treatment of HCC. Nonetheless, one shortcoming of this study should be addressed, there are no clinical trials.

Data Availability

The TCGA dataset can freely be acquired from the TCGA database (https://portal.gdc.cancer.gov/), and the ICGC-HCC datasets can freely be downloaded from the ICGC database (http://dcc.icgc.org).

Ethical Approval

For all obtained data, they were used in accordance with GEO and TCGA data access policies. Both mRNA profile data and clinical information were made publicly available and open access. This study does not involve animal studies.

Conflicts of Interest

All authors claimed no conflicts of interest in this work.

Authors' Contributions

Li Song, Xianqi Feng, and Shouguo Wang designed the study. Rungong Yang, Qiankun Li, and Yao Lu managed the study materials and samples. Li Song performed sequencing experiments. Li Song collected and aggregated the data. Li Song, Qiankun Li, and Yao Lu analyzed the data. Li Song drafted the manuscript. Moreover, all the authors approved the submitted version.

Acknowledgments

This study was funded by the National Natural Science Foundation of China (No. 81901971).

Supplementary Materials

Supplementary 1. Table S1: 107 CAF-DEGs.

Supplementary 2. Table S2: 65 drugs that were different between the high-risk and low-risk groups.

References

[1] J. X. Zhang, G. Chen, J. Y. Zhang, P. Zhang, and Y. Ye, "Construction of a prognostic model based on nine immune-related genes and identification of small molecule drugs for hepatocellular carcinoma (HCC)," *American Journal of Translational Research*, vol. 12, no. 9, pp. 5108–5130, 2020.

[2] J. Y. Long, L. Zhang, X. S. Wan et al., "A four-gene-based prognostic model predicts overall survival in patients with hepatocellular carcinoma," *Journal of Cellular and Molecular Medicine*, vol. 22, no. 12, pp. 5928–5938, 2018.

[3] A. Forner, J. M. Llovet, and J. Bruix, "Hepatocellular carcinoma," *The Lancet*, vol. 379, no. 9822, pp. 1245–1255, 2012.

[4] S. J. Yu, "A concise review of updated guidelines regarding the management of hepatocellular carcinoma around the world: 2010-2016," *Clinical and Molecular Hepatology*, vol. 22, no. 1, pp. 7–17, 2016.

[5] J. Y. Long, A. Q. Wang, Y. Bai et al., "Development and validation of a TP53-associated immune prognostic model for hepatocellular carcinoma," *eBioMedicine*, vol. 42, pp. 363–374, 2019.

[6] J. K. Heimbach, L. M. Kulik, R. S. Finn et al., "AASLD guidelines for the treatment of hepatocellular carcinoma," *Hepatology*, vol. 67, no. 1, pp. 358–380, 2018.

[7] J. Y. Long, J. Z. Lin, A. Q. Wang et al., "PD-1/PD-L blockade in gastrointestinal cancers: lessons learned and the road toward precision immunotherapy," *Journal of Hematology & Oncology*, vol. 10, no. 1, p. 146, 2017.

[8] G. Biffi and D. A. Tuveson, "Diversity and biology of cancer-associated fibroblasts," *Physiological Reviews*, vol. 101, no. 1, pp. 147–176, 2021.

[9] M. E. Fiori, S. di Franco, L. Villanova, P. Bianca, G. Stassi, and R. de Maria, "Cancer-associated fibroblasts as abettors of tumor progression at the crossroads of EMT and therapy resistance," *Molecular Cancer*, vol. 18, no. 1, p. 70, 2019.

[10] K. F. Li, H. Kang, Y. J. Wang, T. Hai, G. Rong, and H. Sun, "Letrozole-induced functional changes in carcinoma-associated fibroblasts and their influence on breast cancer cell biology," *Medical Oncology*, vol. 33, no. 7, p. 64, 2016.

[11] L. Kaps and D. Schuppan, "Targeting cancer associated fibroblasts in liver fibrosis and liver cancer using nanocarriers," *Cell*, vol. 9, no. 9, p. 2027, 2020.

[12] J. Baglieri, D. A. Brenner, and T. Kisseleva, "The role of fibrosis and liver-associated fibroblasts in the pathogenesis of hepatocellular carcinoma," *International Journal of Molecular Medicine*, vol. 20, no. 7, p. 1723, 2019.

[13] D. Aran, Z. C. Zicheng Hu, and A. J. Butte, "xCell: digitally portraying the tissue cellular heterogeneity landscape," *Genome Biology*, vol. 18, no. 1, p. 220, 2017.

[14] P. Langfelder and S. Horvath, "WGCNA: an R package for weighted correlation network analysis," *BMC Bioinformatics*, vol. 9, no. 1, p. 559, 2008.

[15] G. H. Yu, L. G. Wang, Y. Y. Han, and Q. Y. He, "clusterProfiler: an R package for comparing biological themes among gene clusters," *OMICS*, vol. 16, no. 5, pp. 284–287, 2012.

[16] Z. Yang, X. Y. Wei, Y. T. Pan et al., "A new risk factor indicator for papillary thyroid cancer based on immune infiltration," *Cell Death & Disease*, vol. 12, no. 1, p. 51, 2021.

[17] C. C. Han, T. Y. Liu, and R. Yin, "Biomarkers for cancer-associated fibroblasts," *Biomarker Research*, vol. 8, no. 1, p. 64, 2020.

[18] H. Zheng, H. S. Liu, H. Y. Li, W. Dou, and X. Wang, "Weighted gene co-expression network analysis identifies a cancer-associated fibroblast signature for predicting prognosis and therapeutic responses in gastric cancer," *Frontiers in Molecular Biosciences*, vol. 8, p. 744677, 2021.

[19] B. Xiao, L. Y. Liu, A. Y. Li et al., "Identification and verification of immune-related gene prognostic signature based on ssGSEA for osteosarcoma," *Frontiers in Oncology*, vol. 10, p. 607622, 2020.

[20] F. Kanwal and A. G. Singal, "Surveillance for hepatocellular carcinoma: current best practice and future direction," *Gastroenterology*, vol. 157, no. 1, pp. 54–64, 2019.

[21] H. Zhang, R. Z. Liu, L. Sun, and X. Hu, "A reliable prognostic model for HCC using histological grades and the expression levels of related genes," *Journal of Oncology*, vol. 2021, Article ID 9512774, 9 pages, 2021.

[22] R. J. Liu, G. F. Wang, C. Zhang, and D. Bai, "A prognostic model for hepatocellular carcinoma based on apoptosis-related genes," *World Journal of Surgical Oncology*, vol. 19, no. 1, p. 70, 2021.

[23] Z. Wang, J. Zhu, Y. J. Liu et al., "Development and validation of a novel immune-related prognostic model in hepatocellular carcinoma," *Journal of Translational Medicine*, vol. 18, no. 1, p. 67, 2020.

[24] S. J. Mehdi, A. M. Herzog, and H. K. Wong, "Normal and cancer fibroblasts differentially regulate TWIST1, TOX and cytokine gene expression in cutaneous T-cell lymphoma," *BMC Cancer*, vol. 21, no. 1, p. 492, 2021.

[25] Q. Luo, C. Q. Wang, L. Y. Yang et al., "FOXQ1/NDRG1 axis exacerbates hepatocellular carcinoma initiation via enhancing crosstalk between fibroblasts and tumor cells," *Cancer Letters*, vol. 417, pp. 21–34, 2018.

[26] G. Shanying, W. Q. O'Neill, T. N. Teknos, and Q. Pan, "Plasma cell marker, immunoglobulin J polypeptide, predicts early disease-specific mortality in HPV+ HNSCC," *Journal for Immunotherapy of Cancer*, vol. 9, no. 3, article e001259, 2021.

[27] T. Lin, Z. M. Lin, P. P. Mai, E. Zhang, and L. Peng, "Identification of prognostic biomarkers associated with the occurrence of portal vein tumor thrombus in hepatocellular carcinoma," *Aging*, vol. 13, no. 8, pp. 11786–11807, 2021.

[28] H. S. Kim, S. J. Yu, I. J. Yeo et al., "Prediction of response to sorafenib in hepatocellular carcinoma: a putative marker panel by multiple reaction monitoring-mass spectrometry (MRM-MS)," *Molecular & Cellular Proteomics*, vol. 16, no. 7, pp. 1312–1323, 2017.

[29] H. F. Zhou, L. B. Su, C. Liu et al., "CTHRC1 may serve as a prognostic biomarker for hepatocellular carcinoma," *Oncotargets and Therapy*, vol. 12, pp. 7823–7831, 2019.

[30] P. Pyagay, M. Heroult, Q. Z. Wang et al., "Collagen triple helix repeat containing1, a novel secreted protein in injured and diseased arteries, inhibits collagen expression and promotes cell migration," *Circulation Research*, vol. 96, no. 2, pp. 261–268, 2005.

[31] D. Mei, Y. Zhu, L. L. Zhang, and W. Wei, "The role of CTHRC1 in regulation of multiple signaling and tumor progression and metastasis," *Mediators of Inflammation*, vol. 2020, Article ID 9578701, 13 pages, 2020.

[32] N. Li, L. C. Chen, C. Y. Liu, Y. Jiang, and J. Rong, "Elevated CTHRC1 expression is an indicator for poor prognosis and lymph node metastasis in cervical squamous cell carcinoma," *Human Pathology*, vol. 85, pp. 235–241, 2019.

[33] W. Q. Zhou, S. C. Guo, M. L. Liu, M. E. Burow, and G. Wang, "Targeting CXCL12/CXCR4 Axis in tumor immunotherapy," *Current Medicinal Chemistry*, vol. 26, no. 17, pp. 3026–3041, 2019.

[34] B. Nikkhoo, A. Jalili, S. Fakhari et al., "Nuclear pattern of CXCR4 expression is associated with a better overall survival in patients with gastric cancer," *Journal of Oncology*, vol. 2014, Article ID 808012, 7 pages, 2014.

[35] A. Semaan, D. Dietrich, D. Bergheim et al., "CXCL12 expression and PD-L1 expression serve as prognostic biomarkers in HCC and are induced by hypoxia," *Virchows Archiv*, vol. 470, no. 2, pp. 185–196, 2017.

[36] M. Aumailley, "The laminin family," *Cell Adhesion & Migration*, vol. 7, no. 1, pp. 48–55, 2013.

[37] V. G. Horwitz, B. Davidson, and R. Reich, "Laminin-induced signaling in tumor cells," *Cancer Research*, vol. 64, no. 10, pp. 3572–3579, 2004.

[38] M. Patarroyo, K. Karl Tryggvason, and I. Virtanen, "Laminin isoforms in tumor invasion, angiogenesis and metastasis," *Cancer Biology*, vol. 12, no. 3, pp. 197–207, 2002.

[39] M. Määttä, I. Virtanen, R. Burgeson, and H. Autio–Harmainen, "Comparative analysis of the distribution of laminin chains in the basement membranes in some malignant epithelial tumors: the α1 chain of laminin shows a selected expression pattern in human carcinomas," *The Journal of Histochemistry and Cytochemistry*, vol. 49, no. 6, pp. 711–725, 2001.

[40] S. O. Lim, S. J. Park, W. Kim et al., "Proteome analysis of hepatocellular carcinoma," *Biochemical and Biophysical Research Communications*, vol. 291, no. 4, pp. 1031–1037, 2002.

[41] L. X. Liu, H. C. Jiang, Z. H. Liu et al., "Intergrin gene expression profiles of human hepatocellular carcinoma," *World Journal of Gastroenterology*, vol. 8, no. 4, pp. 631–637, 2002.

[42] I. Ozaki, K. Yamamoto, T. Mizuta et al., "Differential expression of laminin receptors in human hepatocellular carcinoma," *Gut*, vol. 43, no. 6, pp. 837–842, 1998.

[43] R. Dhanasekaran and D. W. Felsher, "A tale of two complications of obesity: NASH and hepatocellular carcinoma," *Hepatology*, vol. 70, no. 3, pp. 1056–1058, 2019.

[44] H. R. Yang, Q. M. Deng, T. Ni et al., "Targeted inhibition of LPL/FABP4/CPT1 fatty acid metabolic axis can effectively prevent the progression of nonalcoholic steatohepatitis to liver cancer," *International Journal of Biological Sciences*, vol. 17, no. 15, pp. 4207–4222, 2021.

[45] R. Gao, J. H. Cheng, C. L. Fan et al., "Serum metabolomics to identify the liver disease-specific biomarkers for the progression of hepatitis to hepatocellular carcinoma," *Scientific Reports*, vol. 5, 2015.

[46] L. Tang, J. Zeng, P. Y. Geng et al., "Global metabolic profiling identifies a pivotal role of proline and hydroxyproline metabolism in supporting hypoxic response in hepatocellular carcinoma," *Clinical Cancer Research*, vol. 24, no. 2, pp. 474–485, 2018.

[47] Z. Y. Li and H. F. Zhang, "Reprogramming of glucose, fatty acid and amino acid metabolism for cancer progression," *Cellular and Molecular Life Sciences*, vol. 73, no. 2, pp. 377–392, 2016.

[48] R. M. Zou, R. H. Gu, X. Yu et al., "Characteristics of infiltrating immune cells and a predictive immune model for cervical cancer," *Journal of Cancer*, vol. 12, no. 12, pp. 3501–3514, 2021.

[49] Q. J. Han, H. J. Zhao, Y. Jiang, C. Yin, and J. Zhang, "HCC-derived exosomes: critical player and target for cancer immune escape," *Cell*, vol. 8, no. 6, p. 558, 2019.

[50] Y. A. Gao, M. J. You, J. L. Fu et al., "Intratumoral stem-like CCR4+ regulatory T cells orchestrate the immunosuppressive microenvironment in HCC associated with hepatitis B," *Journal of Hepatology*, vol. 76, no. 1, pp. 148–159, 2022.

[51] S. Y. Tan, Y. Xu, Z. H. Wang et al., "Tim-3 hampers tumor surveillance of liver-resident and conventional NK cells by disrupting PI3K signaling," *Cancer Research*, vol. 80, no. 5, pp. 1130–1142, 2020.

[52] J. Y. Zhu, B. F. Tang, Y. Gao et al., "Predictive models for HCC prognosis, recurrence risk, and immune infiltration based on two exosomal genes: MYL6B and THOC2," *Journal of Inflammation Research*, vol. 14, pp. 4089–4109, 2021.

[53] H. G. Kang, B. Z. Wang, J. Zhang, M. R. Liu, and Y. X. Li, "Combination of temsirolimus and Adriamycin exhibits an enhanced antitumor effect in hepatocellular carcinoma," *Clinics and Research in Hepatology and Gastroenterology*, vol. 41, no. 2, pp. 197–203, 2017.

[54] V. E. Kwitkowski, T. M. Prowell, A. Ibrahim et al., "FDA approval summary: temsirolimus as treatment for advanced renal cell carcinoma," *The Oncologist*, vol. 15, no. 4, pp. 428–435, 2010.

[55] J. Rinehart, A. A. Adjei, P. M. LoRusso et al., "Multicenter phase II study of the oral MEK inhibitor, CI-1040, in patients with advanced non-small-cell lung, breast, colon, and pancreatic cancer," *Journal of Clinical Oncology*, vol. 22, no. 22, pp. 4456–4462, 2004.

[56] D. L. Ou, Y. C. Shen, J. D. Liang et al., "Induction of bim expression contributes to the antitumor synergy between sorafenib and mitogen-activated protein kinase/extracellular signal-regulated kinase kinase inhibitor CI-1040 in hepatocellular carcinoma," *Clinical Cancer Research*, vol. 15, no. 18, pp. 5820–5828, 2009.

[57] Z. J. Long, J. Xu, M. Yan et al., "ZM 447439 inhibition of aurora kinase induces Hep2 cancer cell apoptosis in three-dimensional culture," *Cell Cycle*, vol. 7, no. 10, pp. 1473–1479, 2008.

[58] J. K. Jones and E. M. Thompson, "Allosteric inhibition of ABL kinases: therapeutic potential in cancer," *Molecular Cancer Therapeutics*, vol. 19, no. 9, p. 1763, 2020.

[59] S. M. Hossain, J. Shetty, K. K. Tha, and E. H. Chowdhury, "α-Ketoglutaric acid-modified carbonate apatite enhances cellular uptake and cytotoxicity of a Raf- Kinase inhibitor in breast cancer cells through inhibition of MAPK and PI-3 kinase pathways," *Biomedicine*, vol. 7, no. 1, p. 4, 2019.

[60] C. Collins, M. A. Carducci, M. A. Eisenberger et al., "Preclinical and clinical studies with the multikinase inhibitor CEP-701 as treatment for prostate cancer demonstrate the inadequacy of PSA response as a primary endpoint," *Cancer Biology & Therapy*, vol. 6, no. 9, pp. 1360–1367, 2007.

Hindawi
Journal of Oncology
Volume 2022, Article ID 8998493, 13 pages
https://doi.org/10.1155/2022/8998493

Research Article

Identification and Validation of a Novel Multiomics Signature for Prognosis and Immunotherapy Response of Endometrial Carcinoma

Zhicheng Wu,[1] **Qiu Wang**,[1] **Xiuqing Liu**,[2] **Jiantong Zheng**,[3] **Ling Ji**,[1] **and Xiaofeng Li**[1]

[1]*Department of Laboratory Medicine, Peking University Shenzhen Hospital, Shenzhen, China*
[2]*Department of Laboratory Medicine, Shenzhen Second People's Hospital, Shenzhen, China*
[3]*Shenzhen Dymind Biotechnology Company Limited, Shenzhen, China*

Correspondence should be addressed to Xiaofeng Li; 13530597138@163.com

Received 6 July 2022; Revised 31 July 2022; Accepted 6 August 2022; Published 15 October 2022

Academic Editor: Recep Liman

Purpose. Cancer development and immune escape involve DNA methylation, copy number variation, and other molecular events. However, there are remarkably few studies integrating multiomics genetic profiles into endometrial cancer (EC). This study aimed to develop a multiomics signature for the prognosis and immunotherapy response of endometrial carcinoma. *Methods*. The gene expression, somatic mutation, copy number alteration, and DNA methylation data of EC were analyzed from the UCSC Xena database. Then, a multiomics signature was constructed by a machine learning model, with the ROC curve comparing its prognostic power with traditional clinical features. Two computational strategies were utilized to estimate the signature's performance in predicting immunotherapy response in EC. Further validation focused on the most frequently mutant molecule, ARID1A, in the signature. The association of ARID1A with survival, MSI (Microsatellite-instability), immune checkpoints, TIL (tumor-infiltrating lymphocyte), and downstream immune pathways was explored. *Results*. The signature consisted of 22 multiomics molecules, showing excellent prognostic performance in predicting the overall survival of patients with EC (AUC = 0.788). After stratifying patients into a high and low-risk group according to the signature's median value, low-risk patients displayed a greater possibility of respond to immunotherapy. Further validation on ARID1A suggested it could induce immune checkpoints upregulation, promote interferon response pathway, and interact with Treg (regulatory T cell) to facilitate immune activation in EC. *Conclusion.* A novel multiomics prognostic signature of EC was identified and validated in this study, which could guide clinical management of EC and benefit personalized immunotherapy.

1. Introduction

As the most prevalent gynecologic malignancy, endometrial carcinoma (EC) is one of the leading causes of female mortality worldwide [1]. Endometrial cancer develops in about 142,000 women worldwide every year, and an estimated 42,000 women die from this cancer. The introduction of ICB (Immune Checkpoint Blockade) has achieved favorable clinical effects in patients with end-stage EC where the chemotherapy regimen has little progression [2, 3]. However, more than 80% of patients are nonresponders, or NDB (no durable clinical benefit), to immunotherapy, and the underlying factors resulting in heterogeneous prognoses are poorly understood. In fact, cancer development and immune response are determined by multiple factors, including genomic mutation [4], DNA methylation [5], and copy number variance [6], et al. Therefore, analysis incorporating multiomics data is urgently needed for EC management.

We utilized meta-dimensional strategies to seek genetically susceptible molecules from gene expression, somatic mutation, copy number alteration, and DNA methylation data of EC, aiming to develop a multiomics signature for prognosis and immunotherapy response of EC. The signature was built by machine learning model, and its efficiency

was compared with traditional clinical features. Two computational approaches were also deployed to estimate the signature's performance in predicting immunotherapy response. Further validation focused on the most frequently mutant molecule in the signature: ARID1A. The association of ARID1A with survival, MSI (Microsatellite-instability), immune checkpoints, TIL (tumor-infiltrating lymphocyte), and downstream immune pathways were explored and potential mechanisms was given.

The present study constructed a novel multiomics prognostic signature for prognosis and immunotherapy response of EC, which could guide clinical management of EC and benefit from personalized immunotherapy.

2. Methods and Materials

2.1. Data Acquisition. Multiomics data of EC (endometrial carcinoma) were acquired from databases, such as the TCGA-UCEC cohort (The Cancer Genome Atlas Endometrial Cancer, 543 tumors, and 35 normal samples) at the UCSC Xena website [7] (https://xenabrowser.net/datapages/).These data included datasets of Copy Number Variation (CNV), DNA methylation (450k), RNA-seq of raw counts, somatic mutation (MuTect2 method), and survival data. In parallel, gene sets of 482 mutated genes with alteration frequency >5% and 380 copy number varied genes with alteration frequency >1% in EC were retrieved from Cbioportal [8] (https://www.cbioportal.org) and OncoKB [9] database (https://oncokb.org).

2.2. Differential Expression and Function Enrichment Analysis. To reveal the molecules of real value for EC in these multiomics datasets, a series of *R* packages were used for screening, for example, the limma package [10] to seek out differentially expressed genes between 543 tumor and 35 normal samples with $|\log2 \text{ Fold Change (FC)}| > 1.5$ and P value < 0.05 as the threshold, as well as the ChAMP package [11] to identify differential methylation loci with $|\log2 \text{ Fold Change (FC)}| > 0.5$ and P value $< 10^{-15}$.

A heatmap and volcano plot were used to display the 457 differentially expressed genes (DEG) and 746 CpG sites between tumor and normal samples, with GO (https://wego.genomics.org.cn) and KEGG (https://wego.genomics.org.cn) enrichment analysis to dissect their biological function and related signaling pathways. Meanwhile, oncoprintplot was employed to present the top 30 mutated and copy number varied genes in EC.

2.3. Construction of the Multiomics Prognostic Signature for EC. Subsequent filtration of the 457 significant DEGs, 746 differential methylation loci, 482 mutated, and 380 copy number varied genes was completed by LASSO penalized Cox regression with overall survival as the dependent variable. Finally, 22 molecules were adopted for modeling. Next, Kaplan–Meier curves were depicted to show the prognostic power of the 22-gene-signature where the risk score of each patient was calculated with the following formula: $\sum_i^n \text{Coef}_i * X_i$ (Coef_i: cox regression coefficient, X_i: expression value of corresponding molecule, $n = 22$). Following that, patients were stratified into a high- and low-risk group according to the median risk score. A ROC (receiver operator characteristic) curve and multivariate Cox regression were also used to evaluate its prognostic performance and independent prognostic efficiency.

2.4. Relationship of the Prognostic Signature with Immunotherapy Response in EC. To assess the relationship of the signature with immunotherapy, algorithms of TIDE [12] (tumor immune dysfunction and exclusion) and Immune Cell AI [13] were applied to predict patients' responses to ICB (immune checkpoint blockade) treatment. A hundred-percent bar-chart and a heatmap were used to display the response difference to ICB between the high and low-risk groups.

2.5. Validation on ARID1A for Its Prognostic Ability and Association with Immunotherapy. Further validation focused on the most frequently mutant molecule in the signature: ARID1A. The association of ARID1A mutation with patients' survival, MSI (microsatellite-instability), immune checkpoints or T cell exhaustion markers (LAG3, SIGLEC15, CTLA4, HAVCR2 (TIM3), PDCD1LG2 (PD-L2), CD274 (PD-L1), PDCD1 (PD1), and TIGIT) and downstream immune pathways were explored. In addition, the impact of the ARID1A mutation on the abundances of 22 tumor-infiltrating immune cells was assessed by the CIBERSORT algorithm.

2.6. Underlying Mechanism from ARID1A Mutation to Cancer Immune Activation. To identify the underlying mechanism from ARID1A mutation to cancer immune activation, a ternary interaction network was constructed. First, differential expression analysis was carried out between 235 ARID1A-mut samples and 291 ARID1A-wild tumor samples of the UCEC cohort, with 25 upregulated and 46 downregulated DEGs being obtained. By performing correlation analyses between the71 DEGs, abundances of 22 immune cells computed by the CIBERSORT, and enrichment scores of 29 cancer specialized immune pathways [14] quantified by GSVA [15], the interaction pairs of DEG-Immune Cell and DEG-Immune Pathway with a correlation coefficient >0.3 were screened out. A further regulating network of 71 DEG, 22 immune cells, and 29 immune pathways was completed by Cytoscape software (https://cytoscape.org/).

2.7. Statistical Analysis. Data processing and all analyses were accomplished by *R* 4.0.4. (Package: limma, ggplot2, survminer, ChAMP, ggcorrplot, GSVA, CIBERSORT, and so on). A chi-square test was used for counting data. Wilcoxon or Kruskal–Wallis tests were applied for comparisons between groups, while the Pearson and Spearman's rank correlation were adopted to estimate the statistical correlation of parametric or nonparametric variables. Two-sided $P < 0.05$ was considered a significant threshold for all statistical tests.

3. Results

3.1. Differential Expression Analysis between Tumor and Normal Samples. The study protocol was illustrated in Figure 1 and Table 1 summarized the demographic features of the TCGA-UCEC cohort. 457 differentially expressed genes (DEG) and 746 differential CpG sites are shown in the heatmap and volcano-plot (Figure 2(a)-2(b)). Those DEGs were mainly enriched in thermogenesis and neutrophil activation involved in immune response pathways (Figures 2(c) and 2(d)). The top 30 mutant and copy number varied genes are displayed in the oncoprint-plot (Figures 2(e) and 2(f)).

3.2. Construction of the Multiomics Prognostic Signature. 22 molecules stood out in LASSO-Cox analysis after shrinking most factors' coefficient towards zero (Figure 3(a)-3(b)), including 9 genes with somatic mutation, 4 with copy number variance, 3 with differential CpG sites, and 6 DEGs, their regression coefficients are shown in Table 2. The risk score of each patient was illustrated which well-stratified patients into two groups, according to the median value, with a huge discrepancy in survival probability (Figures 3(c)–3(d)). Patients were illustrated from a database. ROC curve showed a better prognostic performance of the signature than traditional clinical features, such as pathological stage and tumor grade (Figure 3(e)). Subsequent univariate and multivariate Cox analyses proved the signature can be an independent factor for the prognosis of EC (Figures 3(f)–3(g)).

3.3. Relationship of the Prognostic Signature with Immunotherapy Response. In light of immunotherapy, no matter TIDE or Immune Cell AI algorithm, more patients were seen to be responders to ICB treatment (anti-PD-1 or anti-CTLA4) in the low-risk group than people in the high-risk group (71 vs 46 and 130 vs 74, respectively, $P < 0.001$) with statistically significant difference (Figure 4(a) and 4(b)).

3.4. Validation on ARID1A for Its Prognostic Ability and Association with Immunotherapy. As the most frequently mutant gene in EC (Figures 4(c)–4(d), ARID1A can well stratify patients into two groups with noticeable survival differences in the UCEC cohort (4E-4 F), but did not affect their mRNA transcription. ARID1A mutation was also associated with MSI-H status, higher level of immune checkpoints expression, and TIL (tumor-infiltrating lymphocyte) (Figure 5(a)–5(c)).

3.5. ARID1A May Interact with Treg and Promote Type-I–IFN–Response Pathway to Facilitate Tumor Immune Activation in EC. Of the 71 DEGs, 25 were upregulated and 46 were downregulated between ARID1A mut and ARID1A-wild tumor samples (Figure 6(a)). They were mainly enriched into the p53 signaling, mTOR, DNA damage, and stem cell development signaling pathways (Figure 6(b)). These DEGs also exhibited extensive association with 22 immune cells and 29 immune pathways in the correlation heatmap (Figures 6(c) and 6)(d). Within the final interaction network, the type-I–IFN–Response pathway and T cell regulatory showed a major connection with DEGs, indicating that ARID1A may interact with Treg and promote Type-I–IFN–Response pathway to facilitate tumor immune response in EC (Figure 6)(e).

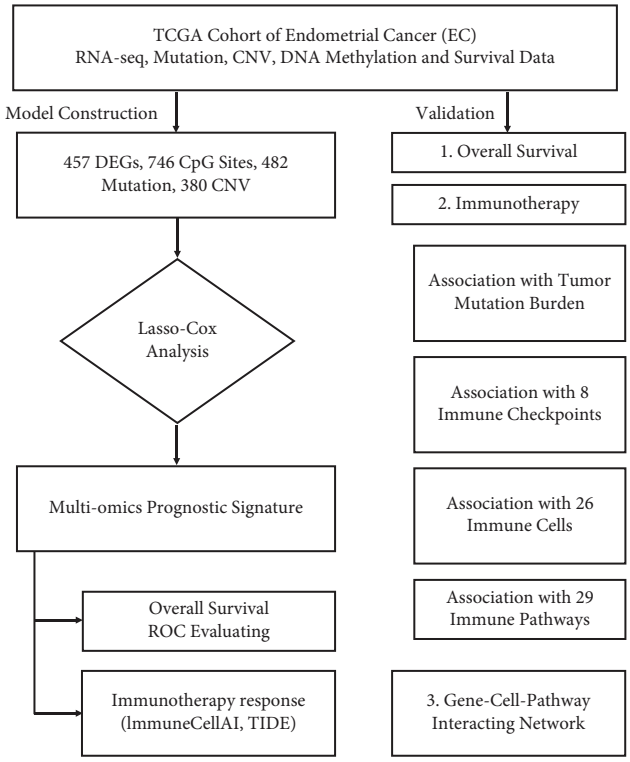

Figure 1: Study protocol.

Table 1: Clinical feature of TCGA-UCEC cohort.

	ARID1A-mut	ARID1A-wild	*P*value
SAMPLE	233	288	
AGE	61.49 ± 10.66	65.89 ± 11.02	<0.001
BMI	34.11 ± 15.06	33.54 ± 9.28	0.608
STAGE			0.009
Stage I	164 (70.39%)	159 (55.21%)	
Stage II	21 (9.02%)	29 (10.07%)	
Stage III	44 (18.87%)	77 (26.73%)	
Stage IV	4 (1.72%)	23 (7.99%)	
DIABETES			0.76
NO	120 (74.07%)	138 (72.63%)	
YES	42 (25.93%)	52 (27.37%)	
HYPERTENSION			0.992
NO	75 (42.37%)	84 (42.42%)	
YES	102 (57.63%)	114 (57.58%)	
GRADE			0.025
G1	52 (22.32%)	44 (15.28%)	
G2	58 (24.89%)	57 (19.79%)	
G3	121 (51.93%)	180 (62.50%)	
High grade	2 (0.86%)	7 (2.43%)	
STATUS			<0.001
Alive	213 (91.42%)	223 (77.43%)	
Dead	20 (8.58%)	65 (22.57%)	

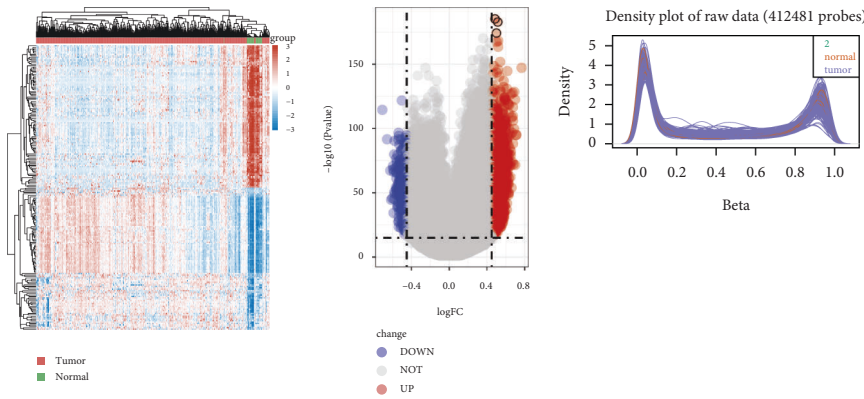

(a) (b) (c)

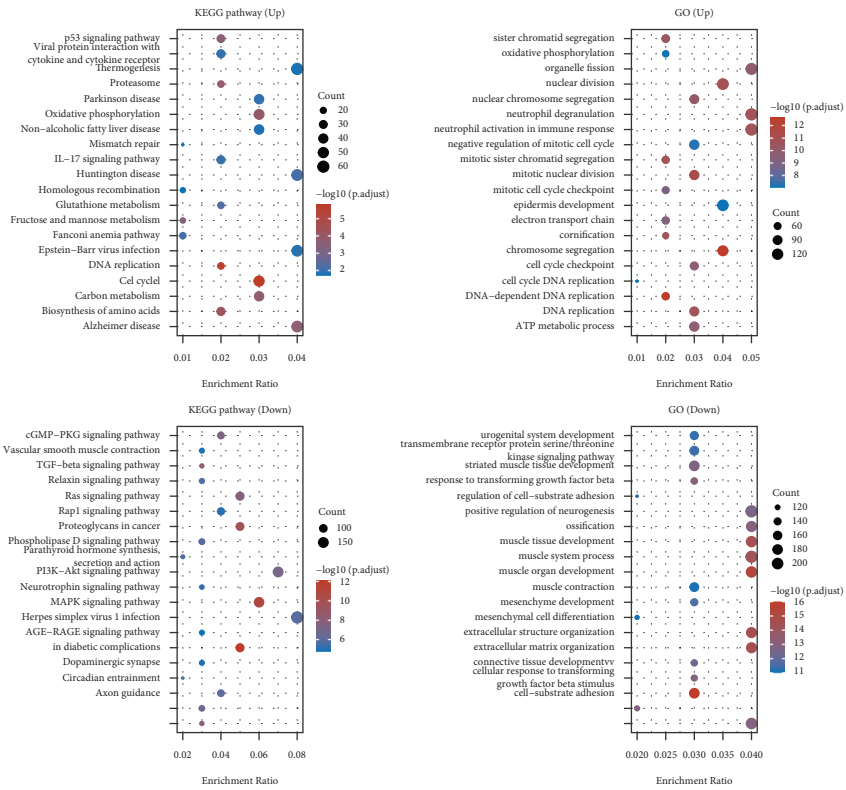

(d)

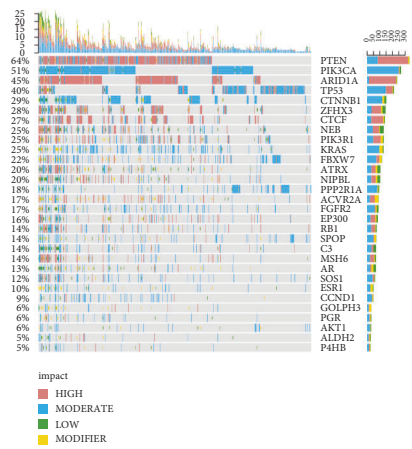

(e)

Figure 2: Continued.

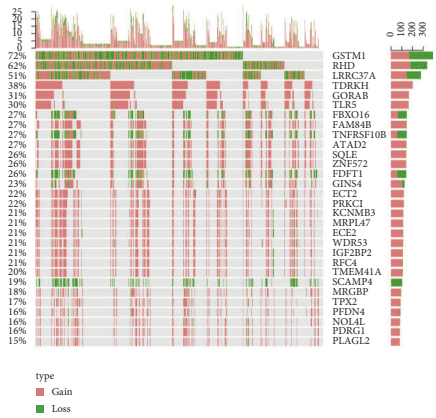

(f)

Figure 2: Differential expression and function enrichment analysis. (a) Heatmap of 457 DEGs (differentially expressed genes) between tumor and normal samples. (b) Volcano-plot of 746 differential CpG sites, 3 most upregulated sites marked. (c) Bimodal distribution of Beta value for methylation among tumor and normal samples. (d) KEGG and GO enrichment analysis. (e) Top 30 mutant genes in EC. (f) TOP 30 genes with copy number variance. (UP: upregulated DEGs; DOWN: downregulated DEGs, KEGG : Kyoto Encyclopedia of Genes and Genomes; GO : Gene Ontology).

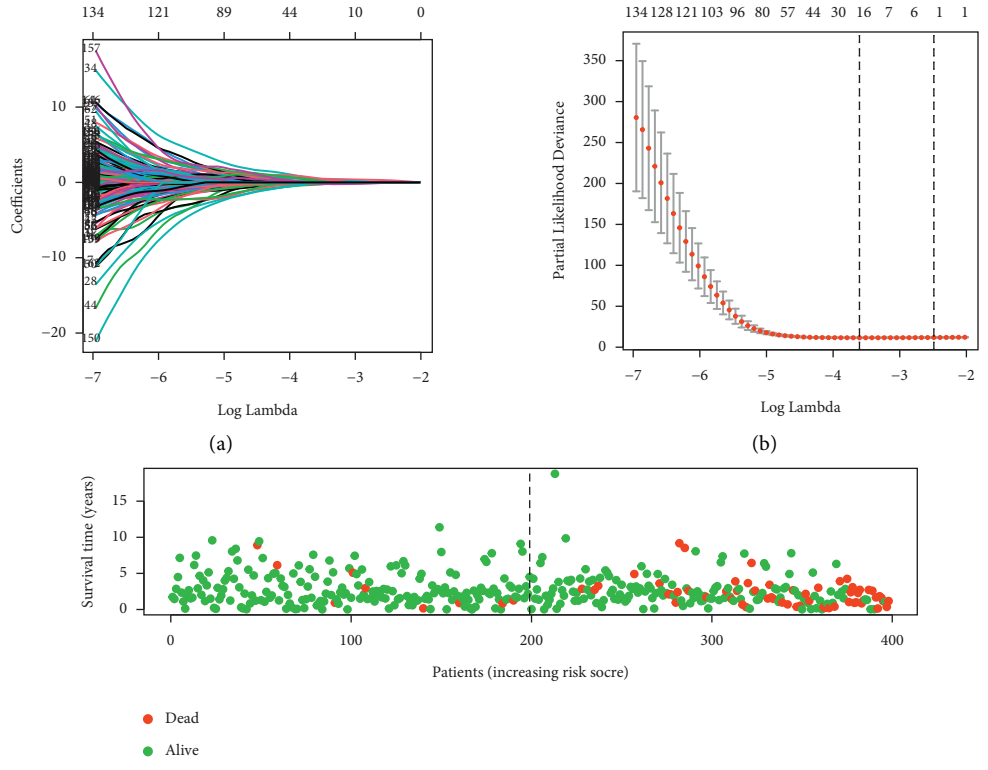

Figure 3: Continued.

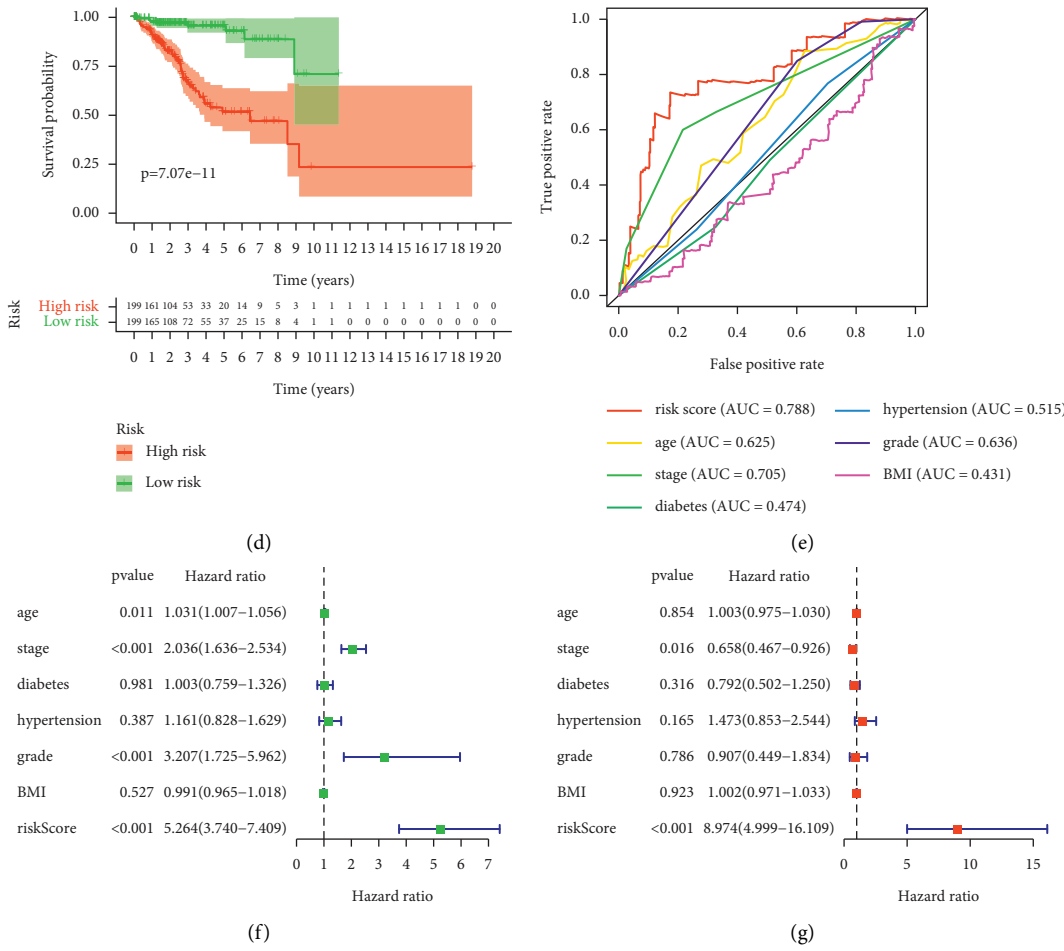

Figure 3: Construction and evaluation of the prognostic signature. (a) Most factors' coefficients were penalized toward zero by LASSO regression. (b) 22 variables were screened out with a minimal partial likelihood deviance. (c) Patients' survival status, ranking by their risk score. (d) Survival analysis between high-risk and low-risk group. (e) Risk score out-weights common clinical features in predicting patients' survival with higher AUC of 0.788. (f) (g) Univariate and multivariate Cox regression demonstrated the prognostic signature can be an independent prognostic factor. (AUC : Area under the curve; BMI : Body mass index).

4. Discussion

The present study constructed a novel multiomics prognostic signature for prognosis and immunotherapy response of EC, which could guide clinical management of EC and benefit personalized immunotherapy. Following validation, it indicated the ARID1A mutation may interact with Treg and promote Type-I–IFN–Response pathway to facilitate tumor immune response and better survival outcomes for EC patients.

ARID1A (BAF250a), though connected with a superior outcome of ICB treatment in several cancer types, has rarely been reported for its prognostic and predictive ability in the immunotherapy cohort of EC [16–18]. As a subunit of the SWI/SNF chromatin-remodeling complex, it harbors an N-terminal DNA binding ARID (~110 residues) and a C-terminal folded region (~250 residues) [19], which are essential to increasing chromatin accessibility, binding to the promoter regions and facilitating transcription of multiple genes [20]. Inconsistently, the majority of DEGs were found to be downregulated in the ARID1A-mut group in our study (46 vs 25), partly accounting for the tumor suppression effect of ARID1A deficiency in a wide range of cancer types [21–23]. These results were in line with the advantageous role of ARID1A mutation for patients' survival outcomes in the TCGA-UCEC in this study.

In fact, association between ARID1A mutation and favorable ICB treatment outcome in other cancer types is not scarce. Shen *J* et al. have reported a greater proportion of ICB responses in the ARID1A-deficient group than in the ARID1A-wild group in ovarian cancer mouse models [24]. A similar result was also observed in two melanoma cohorts [25–27] (42.86% responders versus 25.81% nonresponders and 100% responders versus 51.43% nonresponders, respectively). In addition, favorable survival outcomes in ARID1A mutant patients when receiving ICB treatment were also revealed in a pan-cancer study [16], but merely 10 EC samples with the ARID1A mutation were included, not sufficient to demonstrate the survival difference.

Elsewhere, ARID1A mutation was seen to be involved in Type-I–IFN–Response pathway and regulatory T cell to interact with EC development, partly accounting for its

Table 2: 22 key molecules identified by LASSO-Cox regression.

Molecules	Annotation	Coefficient
ACVR1 (Activin A Receptor Type 1)	Mutation	−0.31351085
ARID1A (AT-Rich Interaction Domain 1A)	Mutation	−0.230538257
ATM (Ataxia Telangiectasia Mutated)	Mutation	−0.095420173
BIRC6 (Baculoviral IAP Repeat Containing 6)	Mutation	−0.13931703
ERBB3 (Erb-B2 Receptor Tyrosine Kinase 3)	Mutation	−0.167684278
HOXA11 (Homeobox A11)	Mutation	0.340669897
POLE (DNA Polymerase Epsilon)	Mutation	−0.18491545
POLQ (DNA Polymerase Theta)	Mutation	−0.035077258
SPOP (Speckle Type BTB/POZ Protein)	Mutation	−0.094758819
GINS4 (SLD5,GINS Complex Subunit 4)	CNV	0.058592508
GORAB (Golgin, RAB6 Interacting)	CNV	0.074299734
GSTM1 (Glutathione S-Transferase Mu 1)	CNV	0.172758754
KCNMB3 (Potassium Calcium-Activated Channel Subfamily M Regulatory Beta Subunit 3)	CNV	−0.111711137
PTPN22 (Protein Tyrosine Phosphatase Non-Receptor Type 22)	DEG	−0.074886487
CDH18 (Cadherin 18)	DEG	0.197447688
KCNK3 (Potassium Two Pore Domain Channel Subfamily K Member 3)	DEG	0.047114247
PCSK1 (Proprotein Convertase Subtilisin/Kexin Type 1)	DEG	0.114882922
KCNJ12 (Potassium Inwardly Rectifying Channel Subfamily J Member 12)	DEG	0.131411471
NCMAP (Non-Compact Myelin Associated Protein)	DEG	−0.024703756
cg07792478	CpG of IR124-2	0.327359364
cg13703871	CpG of NF177	0.583394392
cg14398860	CpG of INPP5A	0.133967149

(CNV, copy number variance; DEG, differentially expressed genes)

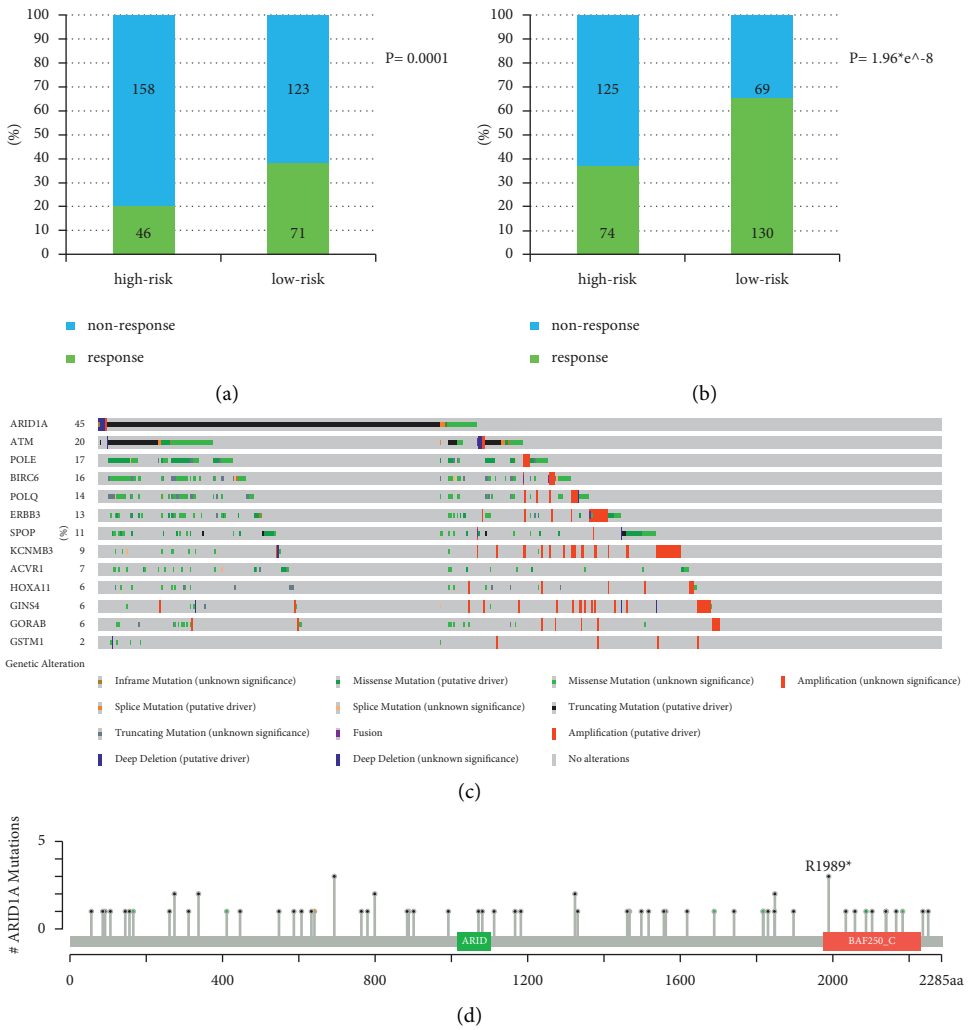

Figure 4: Continued.

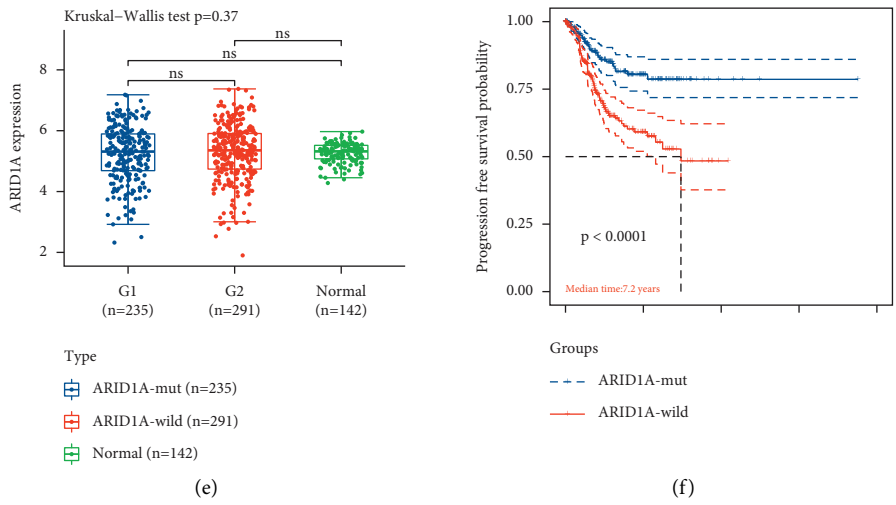

Figure 4: Validation on ARID1A's ability to predict patients' survival outcome. A, b: Difference of immunotherapy response rate between high-risk and low-risk group, predicted by TIDE and Immune cell AI algorithms, respectively. c: Alteration spectrum of 9 mutant and 4 copy number varied genes screened above. d: Mutation sites of ARID1A in EC. e: There were no difference of ARID1A mRNA expression between ARID1A mutant and wild groups. f: ARID1A mutant group showed a better survival outcome in UCEC (Uterine Corpus Endometrial Carcinoma) cohort. (ns: not significant; response and nonresponse: patient response to immunotherapy or vice versa; ARID1A-mut and ARID1A-wild: group with ARID1A mutation or vice versa).

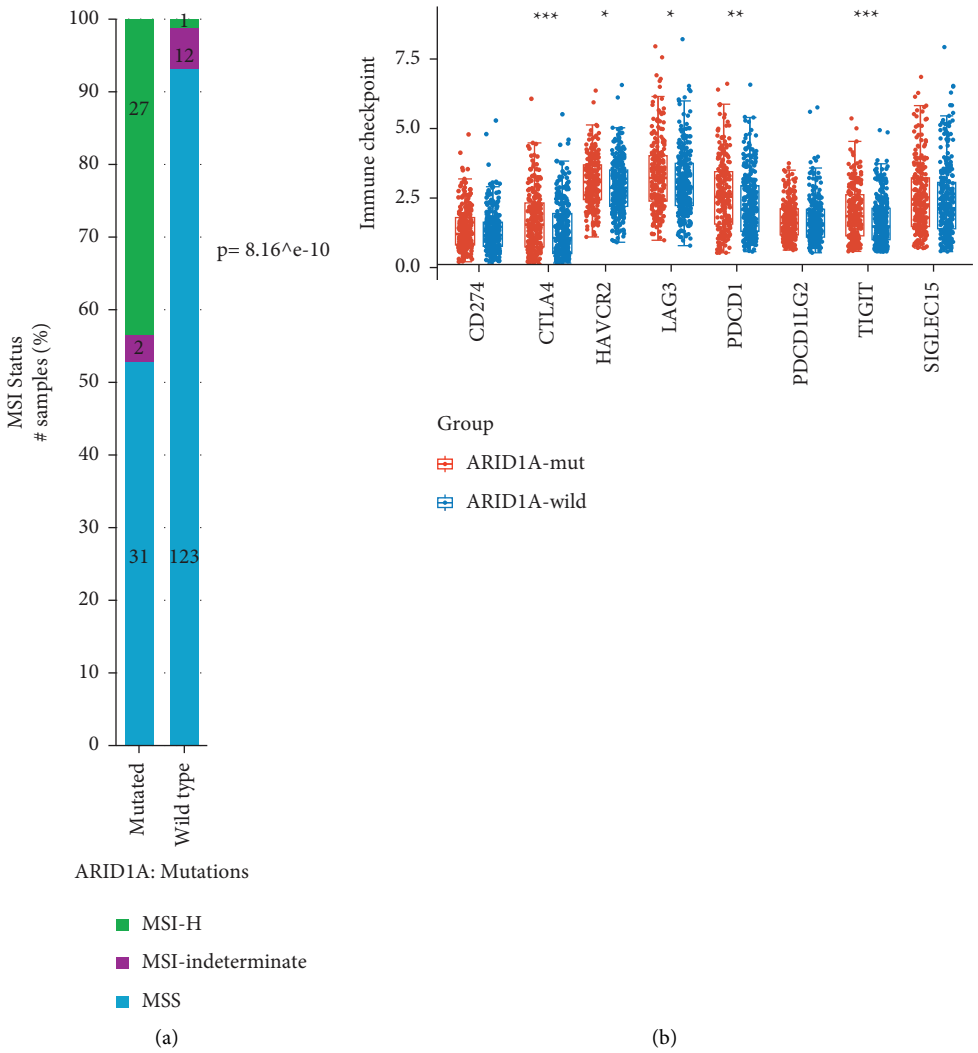

Figure 5: Continued.

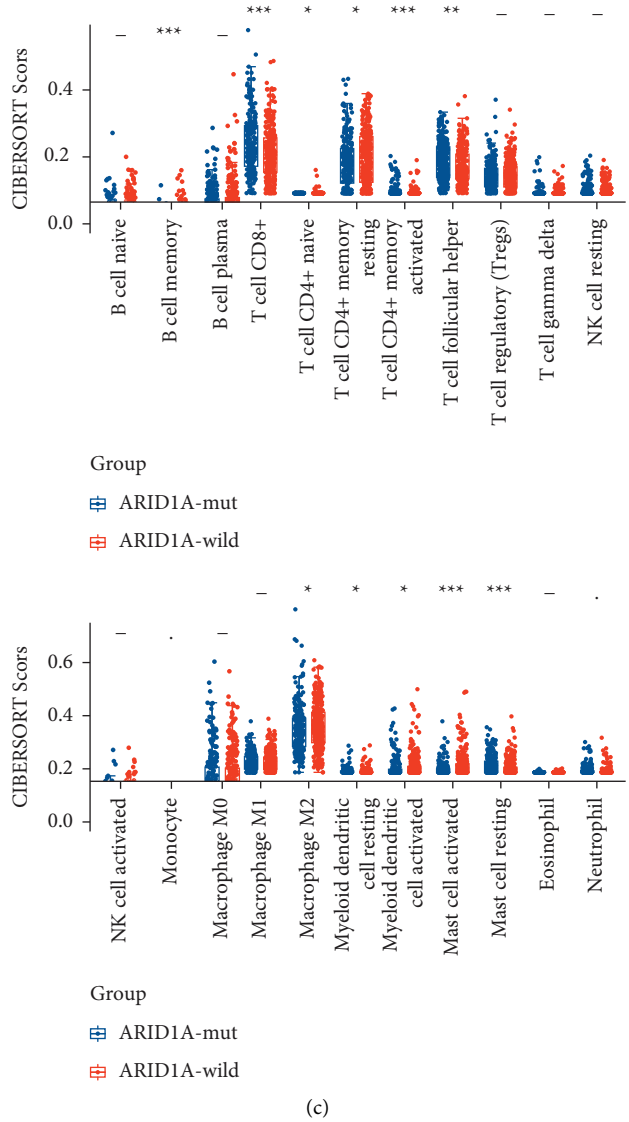

(c)

Figure 5: Effect of ARID1A mutation on MSI (microsatellite instability), 8 immune checkpoints and 26 immune cells in EC (endometrial carcinoma). (a) ARID1A mutant group showed higher proportion of MSI-H than wild group in EC. (b) ARID1A mutant group displayed higher level of PDCD1, LAG3, and TIGIT than wild group in EC. (c) ARID1A mutant group exhibited higher infiltration of CD8+ T cell than wild group in EC. (MSI-H : Microsatellite-instability-high; MSS : Microsatellite stability; *: $P < 0.05$; **: $P < 0.01$; ***: $P < 0.001$).

advantageous role in many kinds of cancer. The previous study has already linked IFN I [28] and IFN II [29] pathway to ICB therapy outcome in multiple cancers and there was data also connecting the ARID1A mutation with IFN I and II Response pathway activity [17]. Apart from IFN pathways, in agreement with our findings, ARID1A mutation could also result in a higher level of PD-1, MSI, and T cell infiltration [30–32] to promote cancer immunity and potentiating favorable ICB treatment response.

Given the inherent fault of bioinformatics analysis-lacking of convincing data from reality. The conclusion of this study may be constrained. Furthermore, multicentric clinical studies and experiments at the cell and animal levels are warranted to validate the results under different circumstances. Following validation, it indicated that ARID1A mutation may interact with Treg and promote Type-I–IFN–Response pathway to facilitate tumor immune response and better survival outcomes for EC patients.

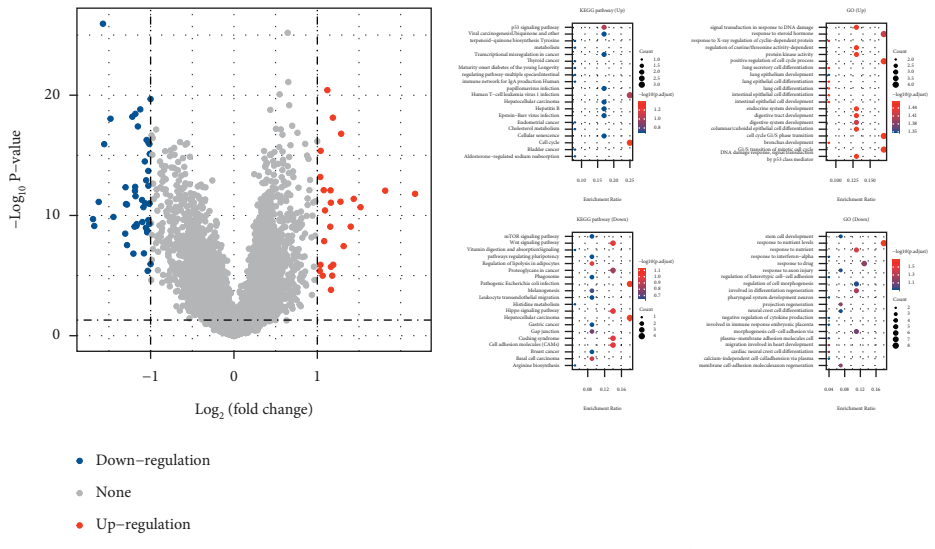

(a) (b)

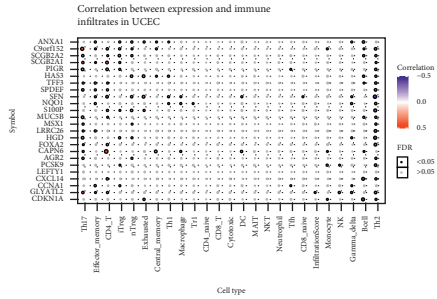

(c)

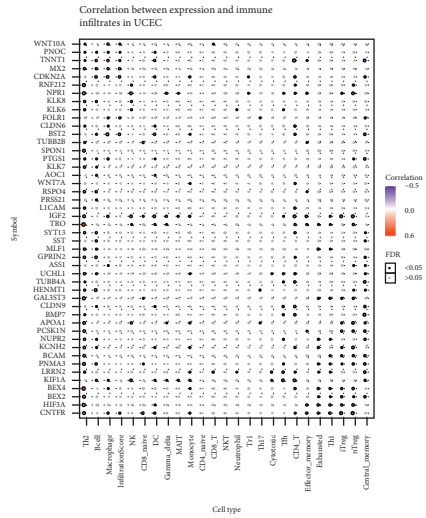

(d)

Figure 6: Continued.

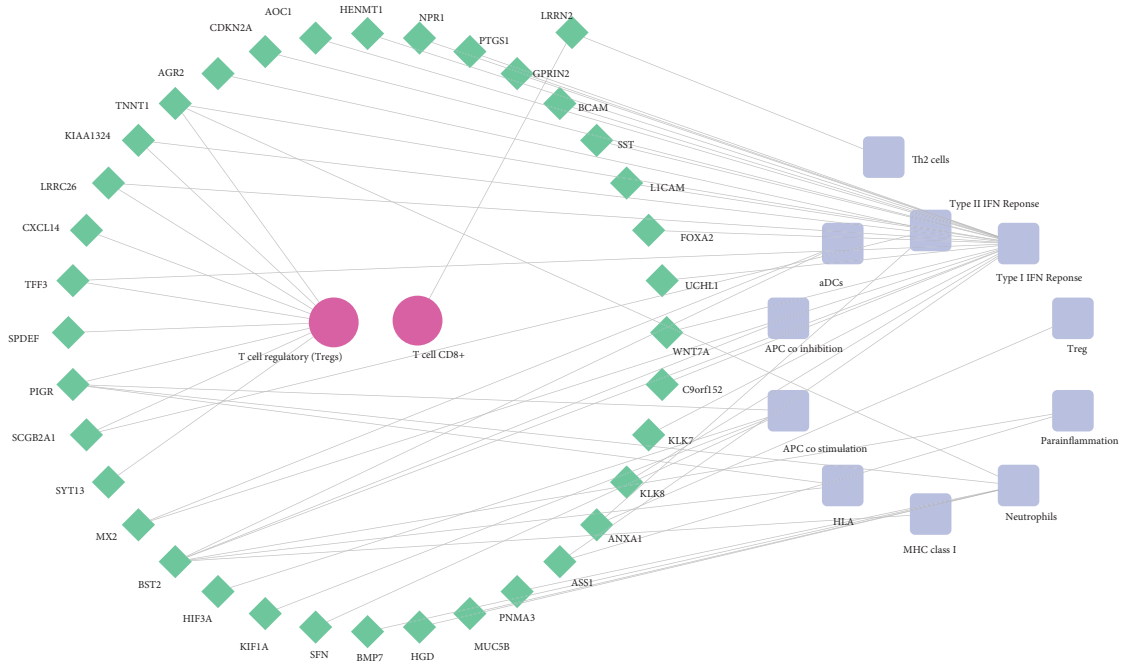

(e)

Figure 6: ARID1A mutation may interact with Treg and promote Type-I–IFN–Response pathway to facilitate tumor immune response in EC (endometrial cancer). (a) 71 DEGs (differentially expressed genes), 25 upregulated and 46 downregulated, between ARID1A mutant and wild group in UCEC (uterine corpus endometrial carcinoma) cohort. (b) KEGG and GO enrichment analysis of the 71 DEGs. (c-d) correlation between 25 upregulated genes/46 downregulated genes and abundances of 26 immune cells, respectively. (e) Regulating network between immune pathways (purple), tumor infiltrating cells (red), and DEGs (green). (UCEC : The Cancer Genome Atlas-Uterine Corpus Endometrial Carcinoma cohort; FDR : False Discovery Rate; KEGG : Kyoto Encyclopedia of Genes and Genomes; GO : Gene Ontology).

5. Conclusion

The present study constructed a novel multiomics prognostic signature for prognosis and immunotherapy response of EC, which could guide clinical management of EC and benefit from personalized immunotherapy.

Abbreviation

EC: Endometrial carcinoma
TCGA-UCEC: The Cancer Genome Atlas-Uterine Corpus Endometrial Carcinoma cohort
ICB: Immune checkpoint blockade
CNV: Copy number variation
MSI: Microsatellite instability
MSI: Microsatellite-instability
TIL: Tumor infiltrating lymphocyte
DEG: Differentially expressed genes
OS: Overall survival
PFS: Progression-Free survival.

Data Availability

This study was based on secondary databases which are publicly available in the TCGA (https://xenabrowser.net/datapages/)[7], Cbioportal (https://www.cbioportal.org)[8], and OncoKB database (https://oncokb.org)[9], without identification of individual data.

Ethical Approval

As all datasets involved in this study were from public databases, ethics approval is not required.

Consent

All authors approved the submission and the International Committee of Medical Journal Editors (ICMJE) criteria for authorship were met.

Conflicts of Interest

Author Jiantong Zheng was employed by the company *Shenzhen Dymind Biotechnology Company Limited*. The remaining authors declare that the research conducted have no conflicts of interest.

Authors' Contributions

XFL and LJ conceived of the idea and wrote the manuscript. ZCW, QW, XQL, and JTZ prepared the data and analyzed

the results. XFL and LJ supervised this work. Zhicheng Wu, Qiu Wang and Xiuqing Liu contributed equally to this study.

Acknowledgments

The authors acknowledge and thank all participants contributing to this study, especially Prof. Ling Ji, for her kind advice and support. The authors also acknowledge the TCGA and Cbioportal for their efforts on these public datasets. The study was supported in part by the Shenzhen Project of Science and Technology (Grant no. JCYJ20190809094407602) to L.X.F, the Scientific Research Foundation of Peking University Shenzhen Hospital (No. KYQD2021104) to L.X.F, and the fund of the "San-ming" Project of Medicine in Shenzhen (No.SZSM201812088) and Wu Jieping Medical Foundation (Grant no. 320.6750.2022-06-21) to W.Z.C.

References

[1] A. S. Felix, D. Scott McMeekin, D. Mutch et al., "Associations between etiologic factors and mortality after endometrial cancer diagnosis: the NRG Oncology/Gynecologic Oncology Group 210 trial," *Gynecologic Oncology*, vol. 139, no. 1, pp. 70–76, 2015.

[2] V. Makker, D. Rasco, N. J. Vogelzang et al., "Lenvatinib plus pembrolizumab in patients with advanced endometrial cancer: an interim analysis of a multicentre, open-label, single-arm, phase 2 trial," *The Lancet Oncology*, vol. 20, no. 5, pp. 711–718, 2019.

[3] M. M. Rubinstein, I. Caird, Q. Zhou et al., "A phase II trial of durvalumab with or without tremelimumab in patients with persistent or recurrent endometrial carcinoma and endometrial carcinosarcoma," *Journal of Clinical Oncology*, vol. 37, p. 5582, 2019.

[4] Y. Chen, Y. Li, Y. Guan et al., "Prevalence of PRKDC mutations and association with response to immune checkpoint inhibitors in solid tumors," *Molecular Oncology*, vol. 14, no. 9, pp. 2096–2110, 2020.

[5] H. E. Ghoneim, Y. Fan, A. Moustaki et al., "De novo epigenetic programs inhibit PD-1 blockade-mediated T cell rejuvenation," *Cell*, vol. 170, no. 1, 2017.

[6] P. Response, "Resistance to immunotherapy," *%J Cancer discovery*, vol. 7, p. OF2, 2017.

[7] M. Goldman, *The UCSC Xena Platform for Public and Private Cancer Genomics Data Visualization and Interpretation*, 2019, https://www.biorxiv.org/content/10.1101/326470v5.

[8] E. Cerami, J. Gao, U. Dogrusoz et al., "The cBio cancer genomics portal: an open platform for exploring multidimensional cancer genomics data," *Cancer Discovery*, vol. 2, no. 5, pp. 401–404, 2012.

[9] D. Chakravarty, J. Gao, S. M. Phillips et al., "OncoKB: a precision oncology knowledge base," *JCO precision oncology*, vol. 2017, no. 1, pp. 1–16, 2017.

[10] M. D. Robinson, D. J. McCarthy, and G. K. Smyth, "edgeR: a Bioconductor package for differential expression analysis of digital gene expression data," *Bioinformatics*, vol. 26, no. 1, pp. 139-140, 2010.

[11] Y. Tian, T. J. Morris, A. P. Webster et al., "ChAMP: updated methylation analysis pipeline for Illumina BeadChips," *Bioinformatics*, vol. 33, no. 24, pp. 3982–3984, 2017.

[12] P. Jiang, S. Gu, D. Pan et al., "Signatures of T cell dysfunction and exclusion predict cancer immunotherapy response," *Nature Medicine*, vol. 24, no. 10, pp. 1550–1558, 2018.

[13] Y. Miao, Q. Zhang, Q. Lei et al., "ImmuCellAI: a unique method for comprehensive T-cell subsets abundance prediction and its application in cancer immunotherapy," *Advanced Science*, vol. 7, Article ID 1902880, 2020.

[14] Y. He, Z. Jiang, C. Chen, and X. Wang, "Classification of triple-negative breast cancers based on Immunogenomic profiling," *Journal of Experimental & Clinical Cancer Research*, vol. 37, no. 1, p. 327, 2018.

[15] S. Hänzelmann, R. Castelo, and J. G. S. V. A. Guinney, "GSVA: gene set variation analysis for microarray and RNA-Seq data," *BMC Bioinformatics*, vol. 14, no. 1, p. 7, 2013.

[16] R. Okamura, S. Kato, S. Lee, R. E. Jimenez, J. K. Sicklick, and R. Kurzrock, "ARID1A alterations function as a biomarker for longer progression-free survival after anti-PD-1/PD-L1 immunotherapy," *J Immunother Cancer*, vol. 8, no. 1, p. e000438, 2020.

[17] J. Li, W. Wang, Y. Zhang et al., "Epigenetic driver mutations in ARID1A shape cancer immune phenotype and immunotherapy," *Journal of Clinical Investigation*, vol. 130, no. 5, pp. 2712–2726, 2020.

[18] T. Jiang, X. Chen, C. Su, S. Ren, and C. Zhou, "Pan-cancer analysis of ARID1A alterations as biomarkers for immunotherapy outcomes," *Journal of Cancer*, vol. 11, no. 4, pp. 776–780, 2020.

[19] R. D. Finn, P. Coggill, R. Y. Eberhardt et al., "The Pfam protein families database: towards a more sustainable future," *Nucleic Acids Research*, vol. 44, no. D1, pp. D279–D285, 2016.

[20] M. R. Wilson, J. J. Reske, J. Holladay et al., "ARID1A and PI3-kinase pathway mutations in the endometrium drive epithelial transdifferentiation and collective invasion," *Nature Communications*, vol. 10, no. 1, p. 3554, 2019.

[21] U. S. Jung, K. W. Min, D. H. Kim, M. J. Kwon, H. Park, and H. S. Jang, "Suppression of ARID1A associated with decreased CD8 T cells improves cell survival of ovarian clear cell carcinoma," *Journal of Gynecologic Oncology*, vol. 32, no. 1, p. e3, 2021.

[22] P. Bala, A. K. Singh, P. Kavadipula, V. Kotapalli, R. Sabarinathan, and M. D. Bashyam, "Exome sequencing identifies ARID2 as a novel tumor suppressor in early-onset sporadic rectal cancer," *Oncogene*, vol. 40, no. 4, pp. 863–874, 2021.

[23] R. C. Wu, T. L. Wang, and I. M. Shih, "The emerging roles of ARID1A in tumor suppression," *Cancer Biology & Therapy*, vol. 15, no. 6, pp. 655–664, 2014.

[24] J. Shen, Z. Ju, W. Zhao et al., "ARID1A deficiency promotes mutability and potentiates therapeutic antitumor immunity unleashed by immune checkpoint blockade," *Nature Medicine*, vol. 24, no. 5, pp. 556–562, 2018.

[25] W. Hugo, J. M. Zaretsky, L. Sun et al., "Genomic and transcriptomic features of response to anti-PD-1 therapy in metastatic melanoma," *Cell*, vol. 165, no. 1, pp. 35–44, 2016.

[26] E. M. Van Allen, D. Miao, B. Schilling et al., "Genomic correlates of response to CTLA-4 blockade in metastatic melanoma," *Science (New York, N.Y.)*, vol. 350, no. 6257, pp. 207–211, 2015.

[27] L. Li, M. Li, Z. Jiang, and X. Wang, "ARID1A mutations are associated with increased immune activity in gastrointestinal cancer," *Cells*, vol. 8, 2019.

[28] S. Dorta-Estremera, "Targeting interferon signaling and CTLA-4 enhance the therapeutic efficacy of anti-PD-1

immunotherapy in preclinical model of HPV oral cancer," *Journal for immunotherapy of cancer*, vol. 7, p. 252, 2019.

[29] S. J. Patel, N. E. Sanjana, R. J. Kishton et al., "Identification of essential genes for cancer immunotherapy," *Nature*, vol. 548, no. 7669, pp. 537–542, 2017.

[30] R. Tokunaga, J. Xiu, R. M. Goldberg et al., "The impact of ARID1A mutation on molecular characteristics in colorectal cancer," *European Journal of Cancer*, vol. 140, pp. 119–129, 2020.

[31] Y. Kim, J. M. Ahn, W. J. Bae, C. O. Sung, and D. J. I. Lee, "Functional loss of ARID1A is tightly associated with high PD-L1 expression in gastric cancer," *International Journal of Cancer*, vol. 145, no. 4, pp. 916–926, 2019.

[32] G. Hu, W. Tu, L. Yang, G. Peng, and L. Yang, "ARID1A deficiency and immune checkpoint blockade therapy: from mechanisms to clinical application," *Cancer Letters*, vol. 473, pp. 148–155, 2020.

Hindawi
Journal of Oncology
Volume 2022, Article ID 9494910, 10 pages
https://doi.org/10.1155/2022/9494910

Research Article

Exosome-Mediated Transfer of miR-3613-5p Enhances Doxorubicin Resistance by Suppression of PTEN Expression in Breast Cancer Cells

Lin Luo,[1] Xin Zhang,[2] Yiliyaer Rousuli,[1] and Alibiyati Aini[1]

[1]*Department of Head and Neck Surgery, Affiliated Cancer Hospital of Xinjiang Medical University, Urumqi, Xinjiang Uygur Autonomous Region 830011, China*
[2]*Department of Medical Administration, Affiliated Cancer Hospital of Xinjiang Medical University, Urumqi, Xinjiang Uygur Autonomous Region 830011, China*

Correspondence should be addressed to Alibiyati Aini; alibiyati1120@163.com

Received 8 August 2022; Revised 16 September 2022; Accepted 22 September 2022; Published 14 October 2022

Academic Editor: Recep Liman

Breast cancer is the most common malignancy among women worldwide, and patients easily develop resistance to the first-line drug doxorubicin. To elucidate the molecular mechanism of drug resistance in breast cancer is imperative. Exosomes mediate the crosstalk between neighboring cells and intercellular communication. Incorporation of miRNAs into exosomes prevents the degradation and facilitates the intercellular communication, which has been indicated in regulation of drug resistance. qRT-PCR revealed that miR-3613-5p is upregulated in drug-resistant breast cancer, and miR-3613-5p exists in exosomes. It is predicted that miR-3613-5p can bind to the tumor suppressor gene PTEN. In this study, our results showed that miR-3613-5p was upregulated in drug-resistant tissue and in exosomes of breast cancer cells resistant to doxorubicin. CCK8, crystal violet staining, and flow cytometry analysis demonstrated that exosome mediated miR-3613-5p transfer and enhanced the resistance to doxorubicin of breast cancer cells. Western blotting showed that miR-3613-5p could target PTEN and regulate the expression of PTEN. Exosome-mediated transfer of miR-3613-5p enhanced the resistance to doxorubicin by inhibition of PTEN in breast cancer cells.

1. Introduction

Breast cancer is the most common malignancy in women worldwide, and the incidence continues to rise [1]. Despite substantial progress and improvements have been achieved over past few decades, it is still a major cause of mortality [1]. Metastasis remains a leading cause of mortality in breast cancer patients, accounting for more than 90% of mortality [1, 2]. Doxorubicin is the most extensively used first-line drug for breast cancer treatment. However, the rapid development of drug resistance has fundamentally weakened its anticancer efficacy [3]. Therefore, it is imperative to explore the potential molecular mechanisms of doxorubicin resistance and find new therapeutic targets for breast cancer.

Emerging studies have demonstrated that exosomes secreted by cells can alleviate drug resistance and improve prognosis of malignancies [4–6]. Exosomes are nanoscale membrane vesicles with a diameter of 30-150 nm, and they participate in intercellular communication by transporting of lipids and nucleic acids to recipient cells [7]. Cell-secreted exosomes mediate the crosstalk between neighboring cells and transport to distal tissues, where signals and messages were sent to specific recipient cells [7].

MicroRNAs (miRNAs) are small noncoding RNAs with a length of about 22 nucleotides, which can posttranscriptionally regulate gene expression [8, 9]. Dysregulated miRNAs have been implicated in many different pathophysiological processes [10]. Multiple evidence indicate that miRNAs are involved in the regulation of drug resistance. miRNAs are protected by bilateral membrane structures upon its incorporation into exosomes, thereby reducing miRNA degradation and promoting intercellular

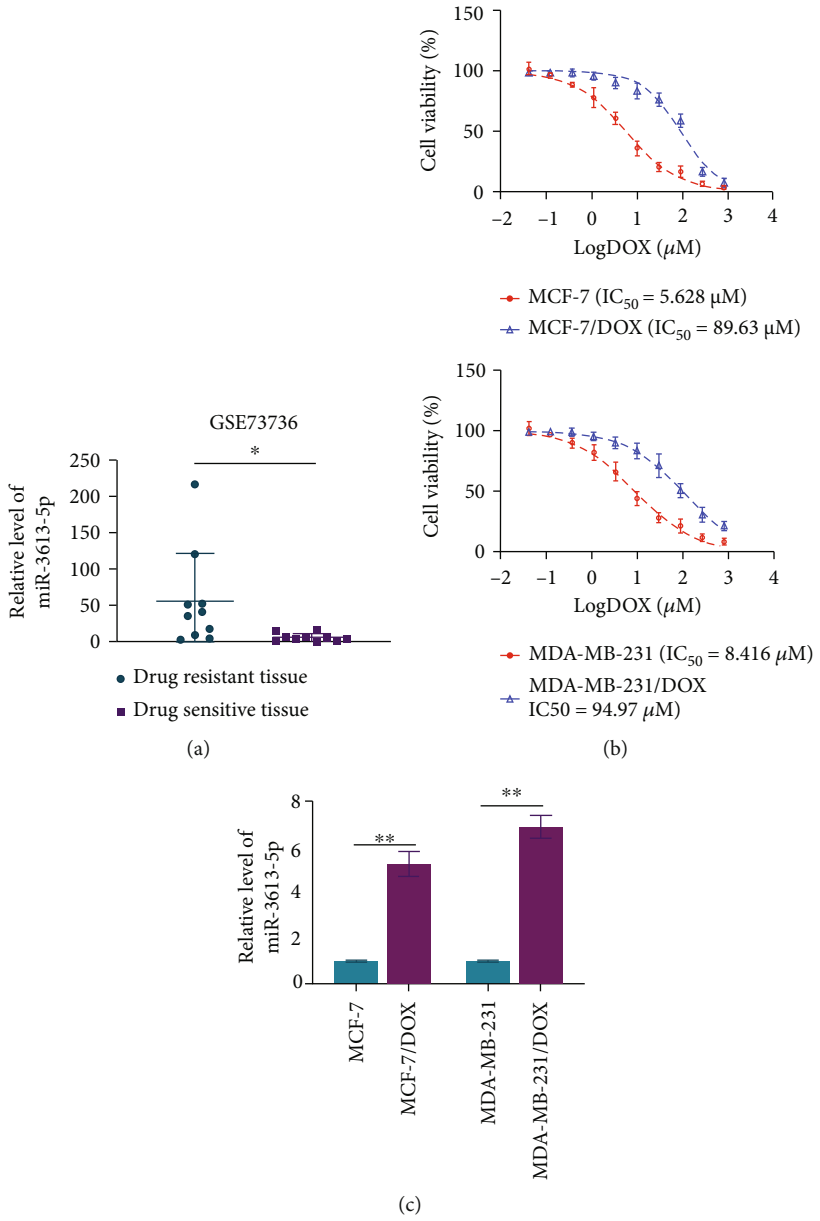

Figure 1: miR-3613-5p is upregulated in drug-resistant tissue and breast cancer cells. (a) The expression level of miR-3613-5p in GEO chip (GSE73736) of drug-sensitive tissue and drug-resistant tissue. $^{*}p < 0.05$, $n = 10$. (b) Cell viability of doxorubicin nonresistant and resistant breast cancer cell lines (MCF-7 and MDA-MB-231, MCF-7/DOX, and MDA-MB-231/DOX, respectively) after different doses of doxorubicin treatments was assessed with CCK8. (c) qRT-PCR was performed to assess the relative levels of miR-3613-5p in MCF-7, MCF-7/DOX, MDA-MB-231, and MDA-MB-231/DOX. $^{**}p < 0.01$. Data are mean ± S.D. of 3 independent experiments.

communication [11]. Overexpressed miR-567 can be packaged into exosomes and incorporated into recipient cells, which then inhibits autophagy and reverses chemoresistance by targeting ATG5 [12]. miR-155 is induced in exosomes isolated from cancer stem cells and resistant breast cancer cells, and exosome-mediated transfer of miR-155 into breast cancer cells enhances resistance to chemotherapeutic drugs [13].

Based on the GEO database, miR-3613-5p is found to be upregulated in chemoresistant breast cancer, indicating that miR-3613-5p may be involved in the drug resistance of breast cancer. However, exosome-mediated miR-3613-5p transfer in drug resistance of breast cancer has not been studied yet. This present work demonstrated that exosome-mediated transfer of miR-3613-5p enhanced the resistance of breast cancer cells to doxorubicin by inhibition of PTEN.

2. Materials and Methods

2.1. Human Cell Lines and Reagents. MDA-MB-231 and MCF-7 cells were purchased from ATCC and maintained in rich DMEM. Fetal bovine serum was purchased from Thermo Fisher Scientific. CCK8 kit (96992) was purchase from Sigma-Aldrich.

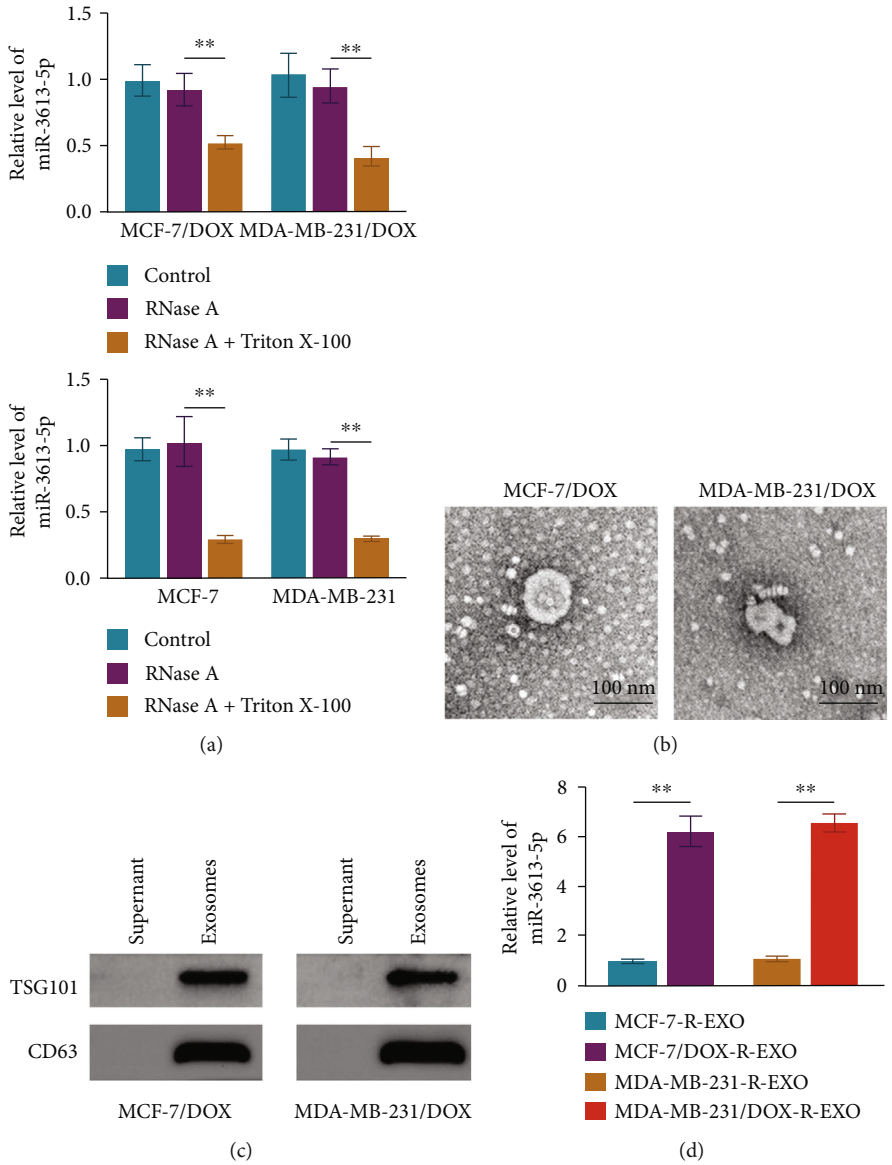

Figure 2: The expression of miR-3613-5p is upregulated in exosomes of doxorubicin-resistant breast cancer cells. (a) qRT-PCR was performed to assess the relative level of miR-3613-5p in MCF-7/DOX, MDA-MB-231/DOX, MCF-7, and MDA-MB-231 after the treatments of RNase A and Triton X-100. $^{**}p < 0.01$. Data are mean ± S.D. of 3 independent experiments. (b) Exosomes were isolated, and the structure was observed by TEM. (c) Western blotting was used to detect the protein expression of TSG101 and CD63 in supernatant and exosomes of MCF-7/DOX and MDA-MB-231/DOX cells. (d) qRT-PCR was performed to assess the relative level of miR-3613-5p in the exosomes of MCF-7, MCF-7/DOX, MDA-MB-231, and MDA-MB-231/DOX. $^{**}p < 0.01$. Data are mean ± S.D. of 3 independent experiments.

2.2. RNase A Treatment. The culture medium was supplemented with 10 mg/ml RNase A and incubated at 37°C for 1 h to remove RNA contamination.

2.3. GEO Data Analysis. Gene Expression Omnibus (GEO) series dataset (GSE73736) was downloaded from GEO. Differential expression analysis in drug-resistant and sensitive tissue of breast cancer was conducted. Estimation of the relative subsets of RNA transcript was performed.

2.4. Transmission Electron Microscopy (TEM). Exosomes solution was dropped onto the formvar grid. Filter paper was used to remove excess water. The exosomes were fixed with 2% phosphotungstic acid for 10 min and then rinsed with deionized water. Then, exosomes were stained with 1% uranyl acetate for 15 min. Philips EM208S TEM (Netherlands) at 100 kV was used to photograph the exosome's morphology.

2.5. Real-Time Quantitative PCR (qRT-PCR). TRIzol (Invitrogen) was used for total RNA extraction. The reaction mixture was prepared according to the instruction of SYBR Green (Takara, Japan). The reaction was initiated and detected with ABI Prism 7500 RT PCR instrument. The

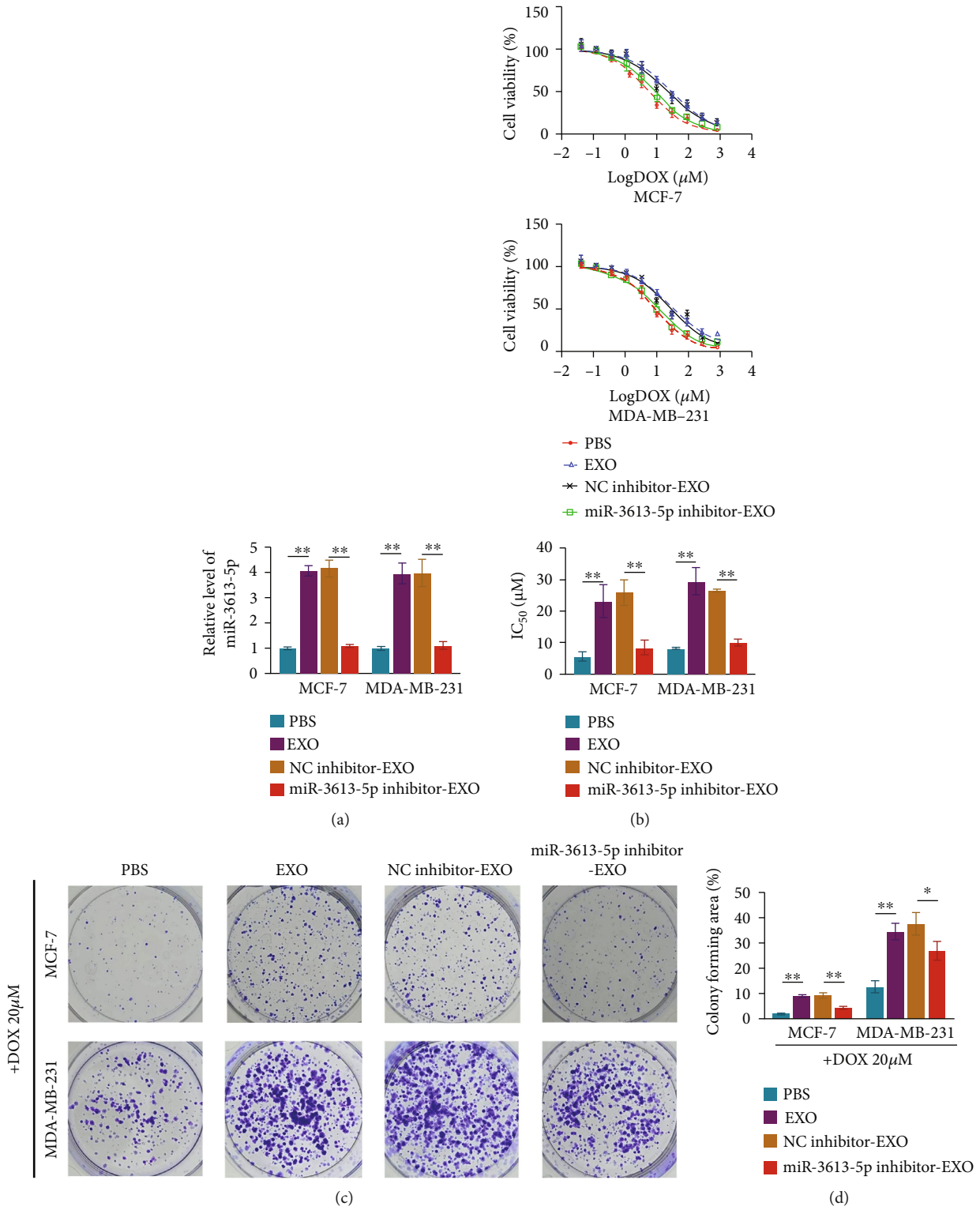

Figure 3: Continued.

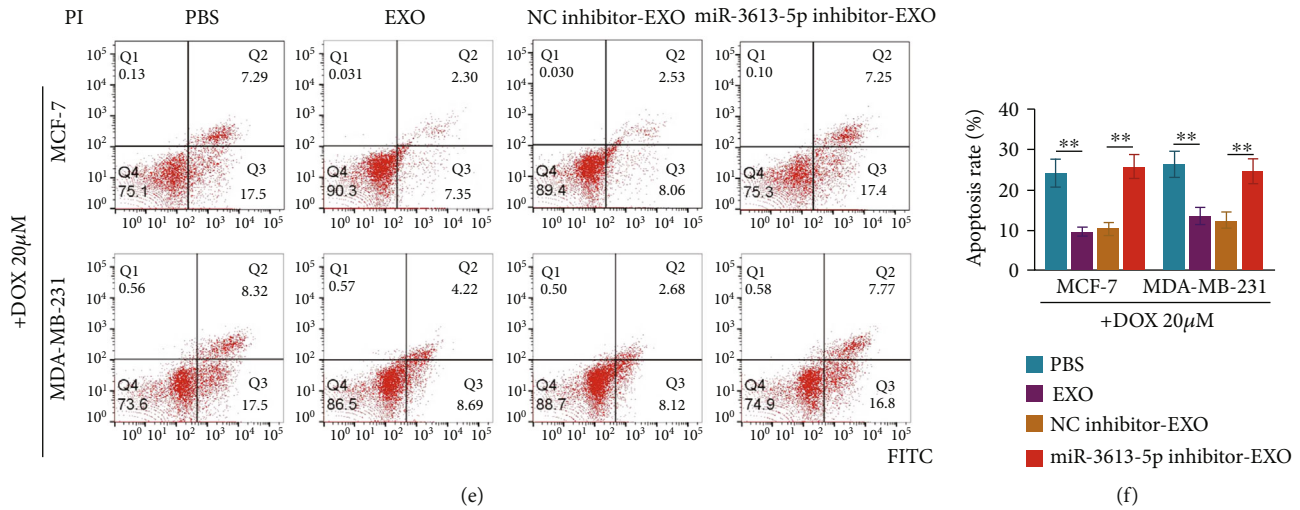

Figure 3: Exosome-mediated miR-3613-5p transfer enhances the resistance of breast cancer cells to doxorubicin. (a) qRT-PCR was used to assess the relative level of miR-3613-5p in MCF-7 and MDA-MB-231 cells after incubation with exosomes isolated from doxorubicin-resistant cells (EXO) and with the treatments of NC inhibitor (NC inhibitor-EXO) or miR-3613-5p inhibitor (miR-3613-5p inhibitor-EXO). $^{**}p < 0.01$. Data are mean ± S.D. of 3 independent experiments. (b) CCK8 was used to assess cell viability of MCF-7 and MDA-MB-231 cells after the treatments of PBS, EXO, NC inhibitor-EXO, or miR-3613-5p inhibitor-EXO. (Upper and middle) Curve of cell viability after indicated treatments in MCF-7 and MDA-MB-231 cells. (Lower) Half maximal inhibitory concentration (IC_{50}) values of doxorubicin (DOX) in MCF-7 and MDA-MB-231 cells. $^{**}p < 0.01$. Data are mean ± S.D. of 3 independent experiments. (c) Crystal violet staining to detect colony formation of MCF-7 and MDA-MB-231 cells after the cells treated with 20 μM DOX combined with treatments of PBS, EXO, NC inhibitor-EXO, or miR-3613-5p inhibitor-EXO. (d) Colony forming area (%) detected by crystal violet staining in (c). $^{*}p < 0.05$, $^{**}p < 0.01$. Data are mean ± S.D. of 3 independent experiments. (e, f) Flow cytometry was used to detect the cell apoptosis rate of MCF-7 and MDA-MB-231 cells after the cells treated with 20 μM DOX combined with treatment of PBS, EXO, NC inhibitor-EXO, or miR-3613-5p inhibitor-EXO. $^{**}p < 0.01$. Data are mean ± S.D. of 3 independent experiments.

relative level of mRNA was quantified with the $2^{-\triangle\triangle Ct}$ method. The primers were as follows: U6-forward: 5′-GCTTCGGCAGCACATATACTAAAAT-3′ and U6-reverse: 5′-CGCTTCACGAATTTGCGTGTCAT-3′; miR-3613-5p-forward: 5′-CTTGTTTTTTTTTTCATGTTGT-3′ and miR-3613-5p-reverse: 5′-AGTCTCAGGGTCCGAG GTATTC-3′; PTEN-forward: 5′-TGGATTCGACTTAGAC TTGACCT-3′ and PTEN-reverse: 5′-GGTGGGTTATG GTCTTCAAAAGG-3′; and GAPDH-forward: 5′-GTCTCC TCTGACTTCAACAGCG-3′ and GAPDH-reverse: ACCA CCCTGTTGCTGTAGCCAA.

For generation of PTEN knockdown cell line, the primers used to generate into pLKO.1-puro vector were as follows: sh-NC-sense strand: 5′-ACTGCCCTGATGCTAG CTAGCACCGGT-3′ and sh-NC-antisense strand: 5′-GCUCGATCCTGCTAGATCUUCGCUAC-3′; sh-PTEN-sense strand: 5′-GACAAAGCCAACCGATACTTT-3′; and sh-PTEN-antisense strand: 5′-AAAGTATCGGTTGGCT TTGTC-3′.

2.6. Exosome Isolation. Exosomes were isolated and purified with an ExoQuick precipitation kit (System Biosciences, LLC, Palo Alto, CA). Briefly, cell culture medium was collected and centrifuged at 3000 × g for 15 min. Supernatant was collected and mixed with ExoQuick precipitation solution. The mixture was incubated at 4°C for 30 min and centrifuged at 1500 × g for 30 min. The supernatant was carefully removed and resuspended in 100 μl PBS.

2.7. Flow Cytometry. Cells were collected and washed with prechilled PBS. Cells were incubated with Annexin V-PE/7-AAD and propidium iodide (PI) for 10 min at room temperature in accordance with the manufacturer's instruction. Cell apoptosis was detected with a flow cytometer.

2.8. Soft Agar Colony Formation Assay. The base layer was prepared with 5 ml rich medium supplemented with 0.75% agar. The top layer was prepared with 3 ml rich medium supplemented with 0.36% agar at a concentration of 3×10^4 cells/ml, incubated at 37°C for 3 weeks, and stained with 0.04% crystal violet in PBS and photographed with a scanner.

2.9. Dual-Luciferase Activity Assay. Cells were harvested and washed with PBS by centrifugation at 600 × g for 5 min. Cells were resuspended in reporter lysis buffer and kept on ice for 20 min. After a centrifugation at maximum speed for 10 min, the supernatant was collected. 20 μL supernatant and 100 μL luciferase assay reagent were mixed together. A luminometer was used to detect the fluorescence.

2.10. Cell Transfection. NC mimic, miR-3613-5p-mimic, and miR-3613-5p inhibitor were synthesized by GenePharma. Cells were transfected with a polyethylenimine- (PEI-) mediated method. Briefly, DNA was mixed with PEI at a

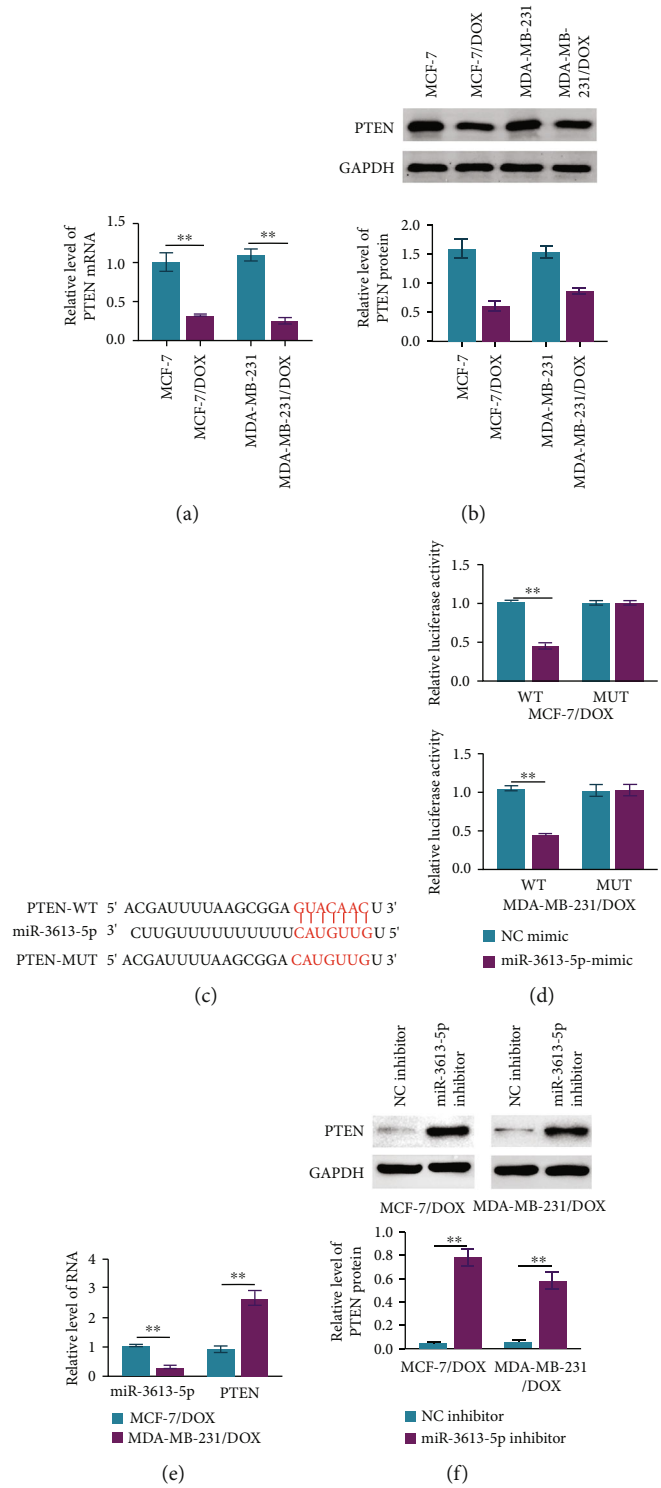

Figure 4: miR-3613-5p targets PTEN. (a) qRT-PCR was used to assess the relative level of PTEN in MCF-7, MCF-7/DOX, MDA-MB-231, and MDA-MB-231/DOX cells. $^{**}p < 0.01$. Data are mean ± S.D. of 3 independent experiments. (b) Western blotting was used to detect the protein expression of PTEN in MCF-7, MCF-7/DOX, MDA-MB-231, and MDA-MB-231/DOX cells. $^{**}p < 0.01$. Data are mean ± S.D. of 3 independent experiments. (c) Website TargetScan predicted the binding site of PTEN to miR-3613-5p. (d) Dual luciferase reporter assay was performed to detect the luciferase activity in wild-type (WT) and mutant (MUT) of MCF-7/DOX and MDA-MB-231/DOX cells after transfection with NC mimics and miR-3613-5p mimics. $^{**}p < 0.01$. Data are mean ± S.D. of 3 independent experiments. (e) qRT-PCR was used to assess the relative levels of miR-3613-5p and PTEN in MCF-7/DOX and MDA-MB-231/DOX cells. $^{**}p < 0.01$. Data are mean ± S.D. of 3 independent experiments. (f) Western blotting was used to detect the protein expression of PTEN in MCF-7/DOX and MDA-MB-231/DOX cells after the treatments of NC inhibitor and miR-3613-5p inhibitor. $^{**}p < 0.01$. Data are mean ± S.D. of 3 independent experiments.

ratio of 1 : 3 and diluted with free DMEM medium, followed by incubation at room temperature for 15 min. The mixture was added to the cell culture rich medium.

2.11. Western Blotting. Cells were harvested and washed with PBS for three times by centrifugation at 600 × g for 5 min. Cells were lysed in RIPA lysis buffer supplemented with protease and phosphatase inhibitors. Proteins were subjected to SDS-PAGE electrophoresis and transferred to PVDF membranes. The membranes were blocked with 5% (w/v) dry milk and then incubated with corresponding primary antibodies at 4°C overnight. The membranes were washed with 1× TBST for three times and then incubated with an HRP conjugated secondary antibody at room temperature for 1 h. After the membranes were washed with 1× TBST for three times, an enhanced chemiluminescence was used to visualize the blots. The primary antibodies were supplied by Abcam (Cambridge, UK). The information of antibodies was as follows: TSG101 (ab30871), CD63 (ab134045), PTEN (ab32199), and GAPDH (ab8245). All the antibodies were diluted in TBST at 1 : 1000.

2.12. Statistical Analysis. Data shown are as mean ± SD. Statistical significance was evaluated by GraphPad Prism software. Student's *t*-test or two-way ANOVA was used for statistical analysis. $p < 0.05$ was considered as statistically significant.

3. Results

3.1. miR-3613-5p Is Upregulated in Drug-Resistant Tissue and Breast Cancer Cells. In drug-resistant tissue, the expression of miR-3613-5p was upregulated compared with drug-sensitive tissue (Figure 1(a)). Exosome-mediated transfer of long noncoding RNA H19 was used to generate resistant breast cancer cells to doxorubicin [14, 15]. Breast cancer cells became significantly resistant to the cytotoxicity of doxorubicin (Figure 1(b)). In breast cancer cells resistant to doxorubicin, the expression of miR-3613-5p was significantly increased (Figure 1(c)). These data demonstrated miR-3613-5p was upregulated in drug-resistant tissue and in breast cancer cells resistant to doxorubicin.

3.2. Expression of miR-3613-5p Is Upregulated in Exosomes of Doxorubicin-Resistant Breast Cancer Cells. The addition of RNase A to the culture medium had no effect on the miR-3613-5p level, but the combined addition of Triton X-100 led to dramatical decrease in miR-3613-5p level (Figure 2(a)). This observation indicated that miR-3613-5p was surrounded by membranes but not directly released into the medium. Exosomes were isolated, the structure was observed by TEM, and the images showed that the particles were typical goblet-shaped vesicles with a double-membrane structure, approximately 100 nm in diameter (Figure 2(b)). Immunoblotting analysis of exosome markers TSG101 and CD63 confirmed the presence of exosome (Figure 2(c)). In the exosomes from doxorubicin-resistant breast cancer cells, the relative level of miR-3613-5p was significantly enhanced (Figure 2(d)). These observations demonstrated that miR-3613-5p level was upregulated in exosomes from doxorubicin-resistant breast cancer cells.

3.3. Exosome-Mediated miR-3613-5p Transfer Enhances the Resistance of Breast Cancer Cells to Doxorubicin. Incubation with exosomes from doxorubicin-resistant breast cancer cells promoted the relative level of miR-3613-5p, and miR-3613-5p inhibitor led to a significantly decrease in miR-3613-5p level in exosomes from breast cancer cells (Figure 3(a)). Cell viability (Figure 3(b)), colony formation (Figures 3(c) and 3(d)), and flow cytometry (Figures 3(e) and 3(f)) analysis revealed that incubation with exosomes from doxorubicin-resistant breast cancer cells increased the cell resistance to doxorubicin, and miR-3613-5p inhibitor treatment sensitized cell death to doxorubicin (Figures 3(b)–3(f)). These results indicated that exosome mediated miR-3613-5p transfer and enhanced doxorubicin resistance in breast cancer cells.

3.4. miR-3613-5p Targets PTEN. The molecular mechanism through which miR-3613-5p enhanced the resistance of breast cancer cells to doxorubicin was further explored. The relative mRNA and protein levels of PTEN were dramatically declined in doxorubicin-resistant breast cancer cells (Figures 4(a) and 4(b)). The website TargetScan predicted that miR-3613-5p could bind to PTEN (Figure 4(c)). The overexpression of miR-3613-5p induced the suppression of luciferase activity in wild-type, which was abolished in PTEN mutant, indicating that miR-3613-5p could interact with PTEN (Figure 4(d)). In MDA-MB-231 cells resistant to doxorubicin, the relative level of miR-3613-5p was much lower, while the relative level of PTEN was much higher than that in doxorubicin-resistant MCF-7 cells (Figure 4(e)). miR-3613-5p inhibitor strikingly enhanced the expression level of PTEN in doxorubicin-resistant breast cancer cells (Figure 4(f)). These data suggested that miR-3613-5p could target PTEN and regulate the expression of PTEN, which was involved in doxorubicin resistance of breast cancer cells.

3.5. Exosome-Mediated Transfer of miR-3613-5p Enhances the Resistance of Breast Cancer Cells to Doxorubicin by Targeting PTEN. Incubation with exosomes from doxorubicin-resistant breast cancer cells or knockdown of PTEN led to the significant decrease in the PTEN expression, which was rescued by the treatment of miR-3613-5p inhibitor (Figures 5(a) and 5(b)). Incubation with exosomes from doxorubicin-resistant breast cancer cells or knockdown of PTEN enhanced the resistance to doxorubicin, which was prevented by the treatment of miR-3613-5p inhibitor (Figures 5(c)–5(e)). These data indicated that exosome-mediated transfer of miR-3613-5p enhanced the resistance of breast cancer cells to doxorubicin by inhibition of PTEN.

4. Discussion

Breast cancer is one of the most common malignancies with increasing incidence in women worldwide [1]. Doxorubicin is a well-accepted compound for breast cancer therapy, but patients easily develop doxorubicin resistance [3]. Therefore,

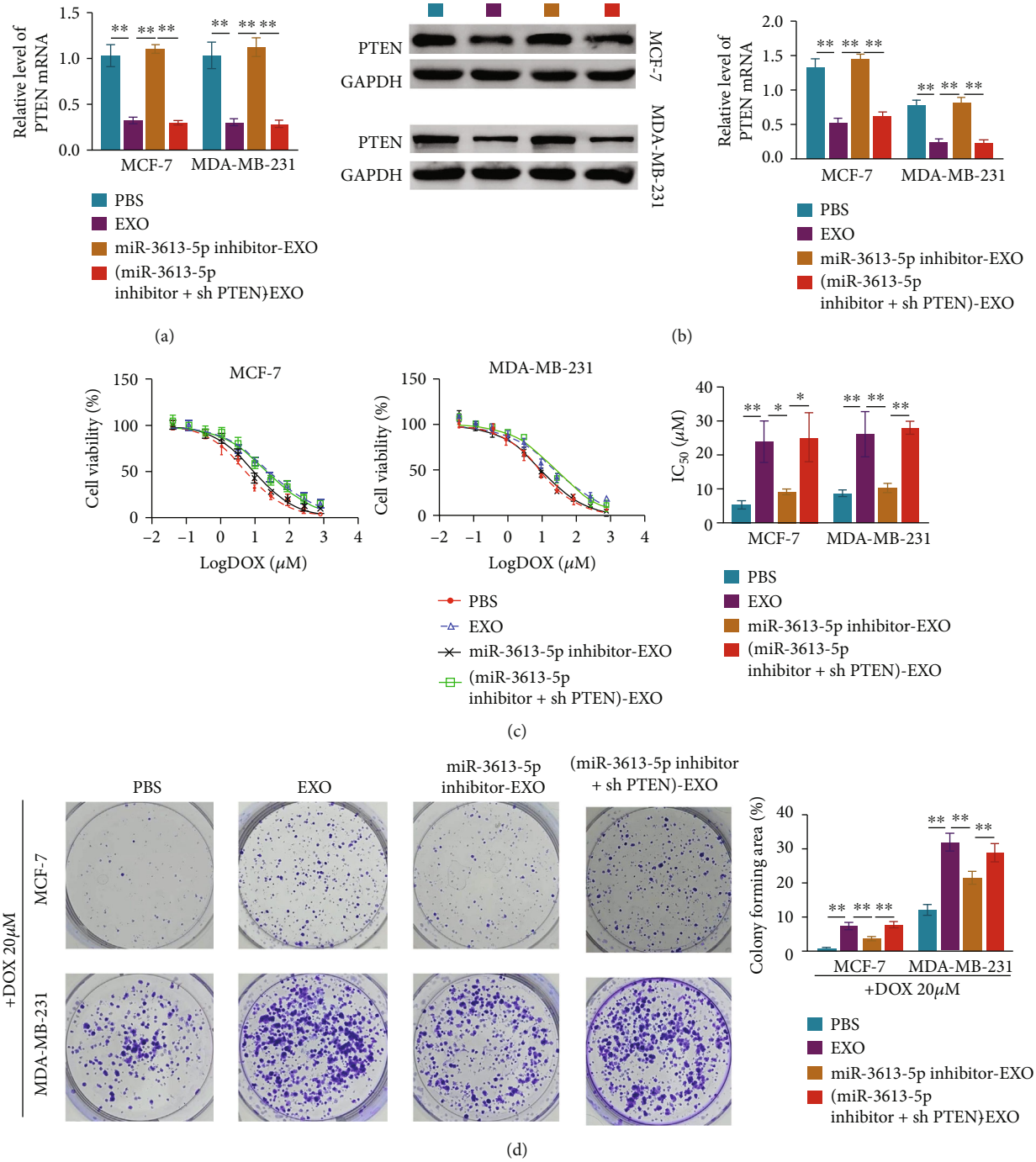

Figure 5: Continued.

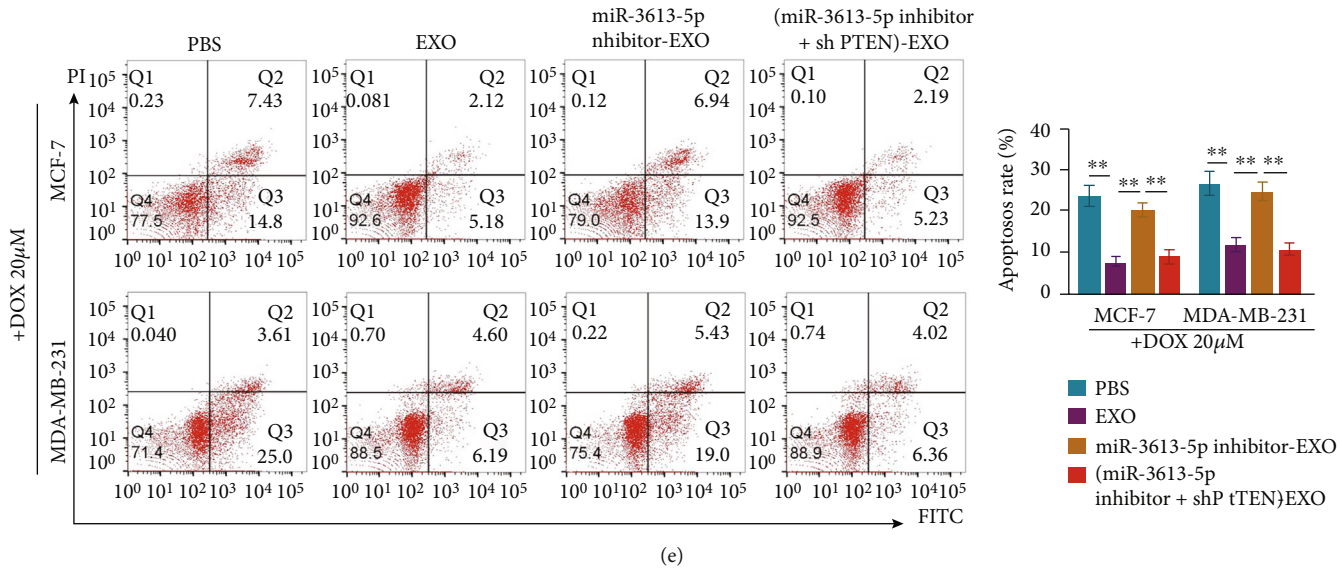

(e)

Figure 5: Exosome-mediated transfer of miR-3613-5p enhances the resistance of breast cancer cells to doxorubicin by targeting PTEN. (a) qRT-PCR was used to assess the relative level of PTEN in MCF-7 and MDA-MB-231 cells after incubation with PBS or exosomes isolated from doxorubicin resistant cells (EXO) and with the treatment of miR-3613-5p inhibitor (miR-3613-5p inhibitor-EXO) and knockdown of PTEN ((miR-3613-5p inhibitor+shPTEN)-EXO). $^{**}p < 0.01$. Data are mean ± S.D. of 3 independent experiments. (b) Western blotting was used to detect the protein expression of PTEN in MCF-7 and MDA-MB-231 cells after treatments of PBS or EXO or miR-3613-5p inhibitor-EXO or (miR-3613-5p inhibitor+shPTEN)-EXO. $^{**}p < 0.01$. Data are mean ± S.D. of 3 independent experiments. (c) CCK8 was used to assess cell viability of MCF-7 and MDA-MB-231 cells after the cells treated with PBS or EXO or miR-3613-5p inhibitor-EXO or (miR-3613-5p inhibitor+shPTEN)-EXO. (Left and middle) Curve of cell viability after indicated treatments in MCF-7 and MDA-MB-231 cells. (Right) IC_{50} values of doxorubicin (DOX) after indicated treatments in MCF-7 and MDA-MB-231 cells. $^{*}p < 0.05$, $^{**}p < 0.01$. Data are mean ± S.D. of 3 independent experiments. (d) Crystal violet staining to detect colony formation of MCF-7 and MDA-MB-231 cells after the cells treated with 20 μM doxorubicin (DOX) combined with treatments of PBS or EXO or miR-3613-5p inhibitor-EXO or (miR-3613-5p inhibitor+shPTEN)-EXO. $^{**}p < 0.01$. Data are mean ± S.D. of 3 independent experiments. (e) Flow cytometry was used to detect the cell apoptosis rate of MCF-7 and MDA-MB-231 cells after the cells treated with PBS or EXO or miR-3613-5p inhibitor-EXO or (miR-3613-5p inhibitor+shPTEN)-EXO. $^{**}p < 0.01$. Data are mean ± S.D. of 3 independent experiments.

it is urgent to further explore the molecular mechanisms of drug resistance and novel therapeutic strategy for breast cancer.

Exosomes participate in intercellular communication and mediate crosstalk between neighboring cells [7]. miRNAs are involved in many diseases and have been shown in the regulation of drug resistance [10, 11]. miRNAs are protected by bilateral membrane structures after incorporation into exosomes, which prevents the degradation of miRNAs and facilitates the intercellular communication [11]. miR-3613-5p is abnormally expressed and carcinogenic in a variety of tumors, including pancreatic cancer [16] and non-small-cell lung cancer [17]. miR-3613-5p can be present in exosomes [18]. However, whether exosome-mediated miR-3613-5p transfer can regulate the drug resistance and the molecular mechanism remains to be investigated.

According to GEO database analysis, miR-3613-5p is upregulated in drug-resistant breast cancer. It is predicted that miR-3613-5p can bind to PTEN, which is a well-known tumor suppressor gene that participates in tumor cell proliferation, cell apoptosis, invasion, migration, drug resistance, and many signaling pathways [19, 20]. It has been shown that inhibition of PTEN promotes cell proliferation of doxorubicin-resistant breast cancer cells and inhibits apoptosis, thus promoting drug resistance of breast cancer [21].

In this study, exosome-mediated transfer of long noncoding RNA H19 was used to generate doxorubicin-resistant breast cancer cells, and the expression of miR-3613-5p was significantly increased in these cells. It has been validated that miRNAs including miR-3613-5p was expressed in exosomes [18, 22], but the expression levels of miRNAs were significant differential [22]. In the exosomes from doxorubicin-resistant breast cancer cells, the relative level of miR-3613-5p was significantly enhanced. Incubation with exosomes from doxorubicin-resistant breast cancer cells promoted the relative level of miR-3613-5p and increased the resistance of breast cancer cells to doxorubicin. These results indicated that exosome mediated miR-3613-5p transfer and enhanced the resistance of breast cancer cells to doxorubicin. The molecular mechanism through which miR-3613-5p promoted drug resistance was then investigated. PTEN was known to be a key regulator of doxorubicin resistance in breast cancer [23]. miR-3613-5p could target PTEN and regulate the expression of PTEN, which was involved in doxorubicin resistance of breast cancer cells. Incubation with exosomes from doxorubicin-resistant breast cancer cells or knockdown of PTEN enhanced the resistance of breast cancer cells to doxorubicin, which was prevented by the treatment of miR-3613-5p inhibitor. These observations suggested that exosome-mediated transfer of miR-

3613-5p enhanced the resistance of breast cancer cells to doxorubicin by inhibition of PTEN. This finding will provide a therapeutic target and strategy for breast cancer treatment.

Data Availability

All data generated or analyzed during this study are included in this published article.

Conflicts of Interest

The authors state that there are no conflicts of interest to disclose.

Authors' Contributions

Lin Luo and Xin Zhang designed the study and supervised the data collection. Yiliyaer·Rousuli analyzed the data and interpreted the data. Alibiyati·Aini prepared the manuscript for publication and reviewed the draft of the manuscript. All authors have read and approved the manuscript.

Acknowledgments

This work was supported by the Natural Science Foundation of Xinjiang Uygur Autonomous Region (Grant No. 2018D01C275).

References

[1] M. A. Thorat and R. Balasubramanian, "Breast cancer prevention in high-risk women," *Best Practice & Research. Clinical Obstetrics & Gynaecology*, vol. 65, pp. 18–31, 2020.

[2] M. Solanki and D. Visscher, "Pathology of breast cancer in the last half century," *Human Pathology*, vol. 95, pp. 137–148, 2020.

[3] M. Khasraw, R. Bell, and C. Dang, "Epirubicin: is it like doxorubicin in breast cancer? A clinical review," *Breast*, vol. 21, no. 2, pp. 142–149, 2012.

[4] M. C. Boelens, T. J. Wu, B. Y. Nabet et al., "Exosome transfer from stromal to breast cancer cells regulates therapy resistance pathways," *Cell*, vol. 159, no. 3, pp. 499–513, 2014.

[5] L. Stone, "Exosome transmission of sunitinib resistance," *Nature Reviews Urology*, vol. 13, no. 6, p. 297, 2016.

[6] G. H. Palliyage, R. Ghosh, and Y. Rojanasakul, "Cancer chemoresistance and therapeutic strategies targeting tumor microenvironment," *ScienceAsia*, vol. 46, no. 6, p. 639, 2020.

[7] L. M. Doyle and M. Z. Wang, "Overview of extracellular vesicles, their origin, composition, purpose, and methods for exosome isolation and analysis," *Cells*, vol. 8, no. 7, p. 727, 2019.

[8] J. Wang, J. Ruan, M. Zhu et al., "Predictive value of long noncoding RNA ZFAS1 in patients with ischemic stroke," *Clinical and Experimental Hypertension*, vol. 41, no. 7, pp. 615–621, 2019.

[9] S. Hombach and M. Kretz, "Non-coding RNAs: classification, biology and functioning," *Advances in Experimental Medicine and Biology*, vol. 937, pp. 3–17, 2016.

[10] P. Lau, C. S. Frigerio, and B. De Strooper, "Variance in the identification of microRNAs deregulated in Alzheimer's disease and possible role of lincRNAs in the pathology: the need of larger datasets," *Ageing Research Reviews*, vol. 17, pp. 43–53, 2014.

[11] J. Li, Y. Chen, X. Guo et al., "GPC1 exosome and its regulatory miRNAs are specific markers for the detection and target therapy of colorectal cancer," *Journal of Cellular and Molecular Medicine*, vol. 21, no. 5, pp. 838–847, 2017.

[12] M. Han, J. Hu, P. Lu et al., "Exosome-transmitted miR-567 reverses trastuzumab resistance by inhibiting ATG5 in breast cancer," *Cell Death & Disease*, vol. 11, no. 1, p. 43, 2020.

[13] J. C. Santos, N. D. S. Lima, L. O. Sarian, A. Matheu, M. L. Ribeiro, and S. F. M. Derchain, "Exosome-mediated breast cancer chemoresistance via miR-155 transfer," *Scientific Reports*, vol. 8, no. 1, article 829, 2018.

[14] X. Wang, X. Pei, G. Guo et al., "Exosome-mediated transfer of long noncoding RNA H19 induces doxorubicin resistance in breast cancer," *Journal of Cellular Physiology*, vol. 235, no. 10, pp. 6896–6904, 2020.

[15] X. Dong, X. Bai, J. Ni et al., "Exosomes and breast cancer drug resistance," *Cell Death & Disease*, vol. 11, no. 11, p. 987, 2020.

[16] R. Cao, K. Wang, M. Long et al., "miR-3613-5p enhances the metastasis of pancreatic cancer by targeting CDK6," *Cell Cycle*, vol. 19, no. 22, pp. 3086–3095, 2020.

[17] T. He, H. Shen, S. Wang et al., "MicroRNA-3613-5p promotes lung adenocarcinoma cell proliferation through a RELA and AKT/MAPK positive feedback loop," *Molecular Therapy-Nucleic Acids*, vol. 22, pp. 572–583, 2020.

[18] D. C. Penoni, S. R. Torres, M. L. Farias, T. M. Fernandes, R. R. Luiz, and A. T. Leão, "Association of osteoporosis and bone medication with the periodontal condition in elderly women," *Osteoporosis International*, vol. 27, no. 5, pp. 1887–1896, 2016.

[19] Y. Chen, Y. Sun, L. Chen et al., "miRNA-200c increases the sensitivity of breast cancer cells to doxorubicin through the suppression of E-cadherin-mediated PTEN/Akt signaling," *Molecular Medicine Reports*, vol. 7, no. 5, pp. 1579–1584, 2013.

[20] Q. Tang, S. Wan, X. Qiao, F. Wang, and Y. Wang, "miR-29 promotes ovarian carcinoma cell proliferation through the PTEN pathway," *European Journal of Gynaecological Oncology*, vol. 41, no. 5, pp. 774–778, 2020.

[21] T. Liu, J. Guo, and X. Zhang, "MiR-202-5p/PTENmediates doxorubicin-resistance of breast cancer cells via PI3K/Akt signaling pathway," *Cancer Biology & Therapy*, vol. 20, no. 7, pp. 989–998, 2019.

[22] S. Yan, H. Zhang, W. Xie et al., "Altered microRNA profiles in plasma exosomes from mesial temporal lobe epilepsy with hippocampal sclerosis," *Oncotarget*, vol. 8, no. 3, pp. 4136–4146, 2017.

[23] S. Chu, G. Liu, P. Xia et al., "miR-93 and PTEN: key regulators of doxorubicin-resistance and EMT in breast cancer," *Oncology Reports*, vol. 38, no. 4, pp. 2401–2407, 2017.

Hindawi
Journal of Oncology
Volume 2023, Article ID 9835164, 1 page
https://doi.org/10.1155/2023/9835164

Retraction

Retracted: Red Blood Cell Membrane-Camouflaged Gold Nanoparticles for Treatment of Melanoma

Journal of Oncology

Received 11 July 2023; Accepted 11 July 2023; Published 12 July 2023

This article has been retracted by Hindawi following an investigation undertaken by the publisher [1]. This investigation has uncovered evidence of one or more of the following indicators of systematic manipulation of the publication process:

(1) Discrepancies in scope
(2) Discrepancies in the description of the research reported
(3) Discrepancies between the availability of data and the research described
(4) Inappropriate citations
(5) Incoherent, meaningless and/or irrelevant content included in the article
(6) Peer-review manipulation

The presence of these indicators undermines our confidence in the integrity of the article's content and we cannot, therefore, vouch for its reliability. Please note that this notice is intended solely to alert readers that the content of this article is unreliable. We have not investigated whether authors were aware of or involved in the systematic manipulation of the publication process.

Wiley and Hindawi regrets that the usual quality checks did not identify these issues before publication and have since put additional measures in place to safeguard research integrity.

We wish to credit our own Research Integrity and Research Publishing teams and anonymous and named external researchers and research integrity experts for contributing to this investigation.

The corresponding author, as the representative of all authors, has been given the opportunity to register their agreement or disagreement to this retraction. We have kept a record of any response received.

References

[1] L. Zhao, H. Xie, and J. Li, "Red Blood Cell Membrane-Camouflaged Gold Nanoparticles for Treatment of Melanoma," *Journal of Oncology*, vol. 2022, Article ID 3514984, 11 pages, 2022.

Hindawi
Journal of Oncology
Volume 2022, Article ID 3514984, 11 pages
https://doi.org/10.1155/2022/3514984

Research Article

Red Blood Cell Membrane-Camouflaged Gold Nanoparticles for Treatment of Melanoma

Lei Zhao,[1,2,3] Hongfu Xie ,[1,2,3] and Ji Li[1,2,3]

[1]*Department of Dermatology, Xiangya Hospital, Central South University, Changsha, Hunan 410008, China*
[2]*Hunan Key Laboratory of Aging Biology, Xiangya Hospital, Central South University, Changsha, Hunan 410008, China*
[3]*National Clinical Research Center for Geriatric Disorders, Xiangya Hospital, Central South University, Changsha, Hunan 410008, China*

Correspondence should be addressed to Hongfu Xie; xiehongfucsu@163.com

Received 26 July 2022; Revised 14 September 2022; Accepted 21 September 2022; Published 14 October 2022

Academic Editor: Muhammad Muddassir Ali

Background. Patients with melanoma have poor response and low long-term survival to conventional cisplatin (CP). Recently, biomimetic nanoparticles have played a significant role in tumor therapy. The purpose of this study was to mechanistically evaluate the effect of red blood cell membrane camouflaged gold nanoparticles loaded with CP (RBCm@AuNPs-CP) on enhancing chemotherapy in melanoma. *Methods*. Treated B16-F10 cells with RBCm@AuNPs-CP, the antimelanoma effect *in vitro* was explored by detecting cell viability, apoptosis rate, level of reactive oxygen species (ROS), and singlet oxygen. RBCm@AuNPs-CP was injected into the melanoma-bearing mice via tail vein, and the target-ability, therapeutic effect, and toxicity were detected in melanoma tumor-bearing mice. *Results*. RBCm@AuNPs-CP had an antiproliferation and apoptosis-inducing effect on B16-F10 cells, which might be mediated by oxidative stress of ROS, and its effect was significantly enhanced compared with the CP treatment group. *In vivo* experiments suggested the same outcome, with better target-ability of RBCm@AuNPs-CP. *Conclusion*. The erythrocyte camouflage nanosystem RBCm@AuNPs-CP exhibited well passive tumor target-ability and promoted apoptosis of melanocytes by inducing ROS. RBCm@AuNPs-CP as a novel safe and effective targeted drug delivery system may provide a promising choice for the treatment of melanoma.

1. Introduction

Melanoma is a type of skin cancer caused by melanocytes. The pigment-producing cells are found in tissues such as epidermis, hair follicles, and iris. Melanomas most commonly occur in sun-exposed areas of the skin (such as the chest, neck, and legs), and these can also be found in the eyes and areas of the body that are not exposed to the sunshine. In most countries, the incidence of melanoma has been increasing over the past few decades [1]. Melanoma accounts for only about 1% of skin cancer, far less than other types of skin cancer [2]. Despite rarity, it is the major cause of skin cancer-related death [3]. The poor prognosis of melanoma is mainly due to the high metastatic capacity of melanoma cells [4].

Cisplatin (CP) is a kind of common chemotherapeutic medication for melanoma. It is used to postoperative adjuvant chemotherapy to reduce metastasis of lymph node and improve the survival rate of patients [5]. However, due to the resistance of patients to CP, conventional therapy has a disappointing effect [6]. Besides, CP also has systemic toxicity, including central nervous system damage and nephrotoxicity [7]. All of these factors limit its application in the treatment of melanoma.

Nanoparticles are a type of particles with size between 10 and 100 nm, which make themselves easy to penetrate and retain into the tumor microenvironment (TME) for coming into force. With small volume, high specific surface area, and low toxicity [8, 9], nanoparticles are ideal drug delivery platforms for tumor therapy. Gold nanoparticles (AuNPs) are recognized as safe and effective nanodrug delivery systems, but they are easily cleared by the mononuclear macrophage system in vivo, which might exist low bioavailability or potential hazards [10, 11].

Erythrocyte membrane is a kind of biomimetic membrane that is easy to obtain with excellent biocompatibility. In our study, AuNPs were encapsulated by erythrocyte membrane, with CP efficiently loaded, to construct a nanodrug loading system RBCm@AuNPs-CP. RBCm@AuNPs-CP passively targeted melanoma through permeability and retention (EPR) effect and controlled release of CP. We evaluate the effect and mechanism in treatment of melanoma (Figure 1).

2. Method

2.1. Synthesis of RBCm@AuNPs-CP. AuNPs were synthesized according to the method described [9], combining nanoparticles, 1-ethyl-3-(3-dimethylaminopropyl)-carbodiimide (EDC), and N-hydroxysuccinimide (NHS) with CP by mixing in borate buffer (50 mM pH 8.8) for 1 hour. CP was then added to the mixture to give a final concentration of 1 μM for Au, 50 μM for CP, 5 mM for EDC, and 10 mM for NHS. Conjugation was performed in the dark at 20°C for 24 h, then filtered through a 2 K MWCO membrane, and washed 3 times with ddH_2O.

Whole blood from heparin-anticoagulated mice (Balb/c-nu, female) was taken, centrifuged at 2500 rpm, and washed 3 times to obtain red blood cells. Add hypotonic solution (PBS : ddH20 = 1 : 1) and shake for 2 hours to break red blood cells. After sonication (42 kHz, 100 W) for 2 min, RBCm vesicles with a size of about 200 nm were obtained.

Equal volume of RBCm vesicle suspension and AuNPs-CP was dispersed and fused by sonication (5 min, 42 kHz, 100 W) and then squeezed back and forth through 200 nm needle filter for 20 times. The surplus RBCm was centrifuged (2500 rpm for 10 min, 4°C), and the supernatant was discarded, while the RBCm@AuNPs-CP was prepared.

2.2. Characterization of RBCm@AuNPs. The morphology and size of RBCm@AuNPs and AuNPs were observed by transmission electron microscope (TEM) to confirm whether RBCm was encapsulated on the nanoparticles. The size and surface charge of RBCm@AuNPs and AuNPs were detected by Zetasizer Nano ZS (Malvern Nano series, Malvern, UK). Polyacrylamide gel electrophoresis (SDS-PAGE) was used to detect the proteins on RBCm@AuNPs, RBCm, and AuNPs to verify whether RBCm@AuNPs completely retained the whole surface proteins of RBCm.

2.3. CP Loading and Releasing of RBCm@AuNPs. 1 mL of RBCm@AuNPs-CP (CP 50 μM) was placed in the dialysis membrane, placed in 20 mL of PBS with pH 7.4 and pH 5.4, respectively, and dialyzed at 37°C for 1, 2, 3, 4, 6, 8, 12, 24, and 48 h; the dialysate was collected; and the concentration of CP in the dialysate was detected to calculate the cumulative release rate of RBCm@AuNPs-CP at different pH. The concentration of CP was detected by microplate reader EnSpire 2300 Multilabel Plate Reader (Waltham, MA) at 300 nm and calculated by the standard curve. The encapsulation efficiency (EE) and loading efficiency (LE) of the calculated drug of RBCm@AuNPs-CP were calculated by the following formulas.

$$\mathrm{EE} = \left(\frac{R_L}{R_i}\right) \times 100\%. \quad (1)$$

R_L is the amount of rosmarinic acid entrapped in liposomes, and R_i is the initial amount of rosmarinic acid added to the liposomes.

The LE was calculated using the following equation:

$$\mathrm{LE} = \left(\frac{R_t}{L_t}\right) \times 100\%. \quad (2)$$

R_t is the amount of rosmarinic acid entrapped in liposomal formulation, and L_t is the amount of phospholipid and cholesterol added to the liposomal formulation.

2.4. Antiphagocytic Ability of RBCm@AuNPs. The in vitro immune evasion ability of RBCm@AuNPs was detected. First, AuNPs and Rhodamine B (RhoB) were mixed and stirred overnight, washed 3 times with PBS, and then resuspended. RAW264.7 was plated in a 6-well plate, about 3×10^5 cells per well, and RBCm@AuNPs-RhoB was added. After coincubating RAW 264.7 cells for 4 h, Hoechst 33342 was used to stain the nuclei, confocal microscopy (CLSM) (LSM 800, Carl Zeiss, Oberkochen, Germany) was used to observe the phagocytosis of RBCm@AuNPs-RhoB, and flow cytometry (FCM) (FACSCantoTM II, BD, USA) was used to calculate the fluorescence intensity.

2.5. Biocompatibility of RBCm@AuNPs. The hemolysis rate of RBCm@AuNPs was detected to reflect their compatibility in blood. Different concentrations of RBCm@AuNPs (3.125 to 100 μg/ml) were mixed with 5% mouse erythrocyte suspension and incubated at 37°C for 2 h. Centrifuge at 3500 rpm for 5 min, took the supernatant to measure its absorbance at 545 nm with microplate reader, and added ultrapure water and PBS as positive and negative controls.

The hemolytic rate was calculated as follows:

$$\text{Hemolytic rate} = \frac{(\text{experimental sample A} - \text{negative control A})}{(\text{positive control A} - \text{negative control A})} \times 100\%. \quad (3)$$

2.6. In Vitro Target-Ability of RBCm@AuNPs. To explore the *in vitro* targeting ability of RBCm@AuNPs, the B16-F10 Cells uptake experiment was executed. B16-F10 cells were plated in a 6-well plate, about 3×10^5 cells per well, and AuNPs-RhoB and RBCm@AuNPs-RhoB were added. After coincubating B16-F10 cells for 24 h, confocal microscopy (CLSM) (LSM 800, Carl Zeiss, Oberkochen, Germany) was used to observe the fluorescence of RBCm@AuNPs-RhoB in cells, and flow cytometry (FCM) (FACSCantoTM II, BD, USA) was used to calculate the fluorescence intensity.

2.7. Evaluation of In Vitro Antimelanoma Effects of RBCm@AuNPs. The cytotoxicity of RBCm@AuNPs-CP on B16-F10 cells was detected by CCK-8, treated with PBS, AuNPs, CP, AuNPs-CP, and RBCm@AuNPs-CP for 24 h, respectively. The concentration of CP in each group

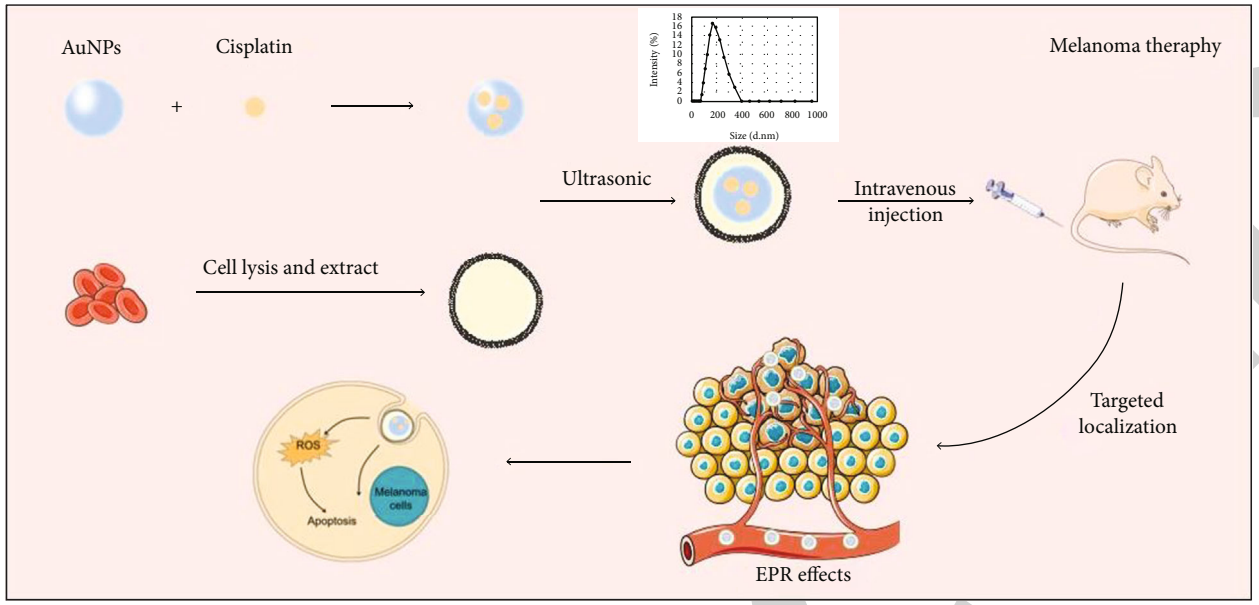

Figure 1: Schematic illustration of RBCm@AuNPs-CP fabrication and application for tumor-targeted chemotherapy therapy in mice.

was 0.3 μM, and the cell viability in each treatment group was calculated.

In order to further prove the in vitro anti-tumor effect of RBCm@AuNPs-CP, Annexin V-FITC/PI apoptosis detection kit was used to detect the apoptosis of B16-F10 cells in each group after 24 h treatment. The cells were plated in small culture flasks (1×10^6/flask), and the above treatments were added, respectively. After 24 hours of digestion with EDTA-free trypsin, the cell suspension was taken and centrifuged at 1000 g for 5 min, the supernatant was discarded, and 195 μL Annexin was added. The cells were gently resuspended in V-FITC binding solution, 5 μL Annexin V-FITC staining solution was added, 10 μL PI was added and mixed, and the apoptosis of cells was analyzed by FCM.

2.8. ROS and Singlet Oxygen Levels Detected. B16-F10 cells were seeded in 6-well plates, and the cells were collected 24 hours after adding each treatment group. After washing 3 times with PBS, adding DCFH-DA, incubating at 37°C for 20 minutes, and washing three times, the level of ROS was detected by FCM.

The singlet oxygen detection kit was used in above treated cells, and the expression level of singlet oxygen was observed under the CLSM.

2.9. Construction of Melanoma-Bearing Mice. 6-8-week-old BALb/c-nu mice were adaptively fed for 1 week at an SPF animal breeding center. The B16-F10 cells cultured *in vitro* were digested, washed, and resuspended to obtain a cell suspension. Cell suspensions were injected into the subcutaneous tissue of the legs of nude mice at an injection volume of 1×10^6/cell. The tumor was observed, and the tumor size was measured every other day. All animal procedures were approved by the Animal Welfare and Research Ethics Committee of Xiangya Hospital.

2.10. In Vivo Target-Ability of RBCm@AuNPs. The AuNPs and RBC@AuNPs were mixed with Cy-5 and stirred for 24 h, and the unbound Cy-5 was removed using a 2KD dialysis bag. On the 10th day, tumor-bearing Cy-5-labeled AuNPs and RBC@AuNPs were injected into B16-F10 tumor-bearing mice through the tail vein. Tumor-bearing mice were anesthetized with isoflurane after 6 h and 24 h, respectively, and the distribution of AuNPs and RBC@AuNPs in mice was detected on Xenogen IVIS lumina XR imaging system (Caliper Life Science, USA). After 48 hours, the tumor-bearing mice were euthanized. The tumor, heart, liver, spleen, lung, and kidney were removed, and the fluorescence intensity of AuNPs and RBC@AuNPs in the tumor site of each tissue was detected by the XR imaging system, respectively.

2.11. In Vivo Antimelanoma Ability of RBCm@AuNPs. When the tumor volume was about 100 mm^3, it was recorded as day 0 (D0), and they were randomly divided into 5 groups ($n = 3$ per group) by tail vein injection of PBS, AuNPs, CP, AuNPs-CP, and RBCm@AuNPs-CP, in which the dose of CP was 10 μmol/kg/d, once a day for 3 consecutive days. Tumor size and mouse body weight were recorded every other day, and all animals were anesthetized and euthanasia on day 14 (D14). Anticoagulated whole blood, tumors, and major organs (heart, liver, spleen, lung, and kidney) were collected. The major organs and tumors were fixed with 4% paraformaldehyde, then paraffin-embedded and then stained with H&E.

3. Results

3.1. Construction and Characterization of RBCm@AuNPs-CP. As shown in Figures 2(a) and 2(b), AuNPs were spherical nanoparticles with the size of 45.3 ± 12.34 nm and zeta potential of −42.1 ± 6.3 mV, which showed well dispersion and uniformity. Red blood cell membrane vesicles (RBCm)

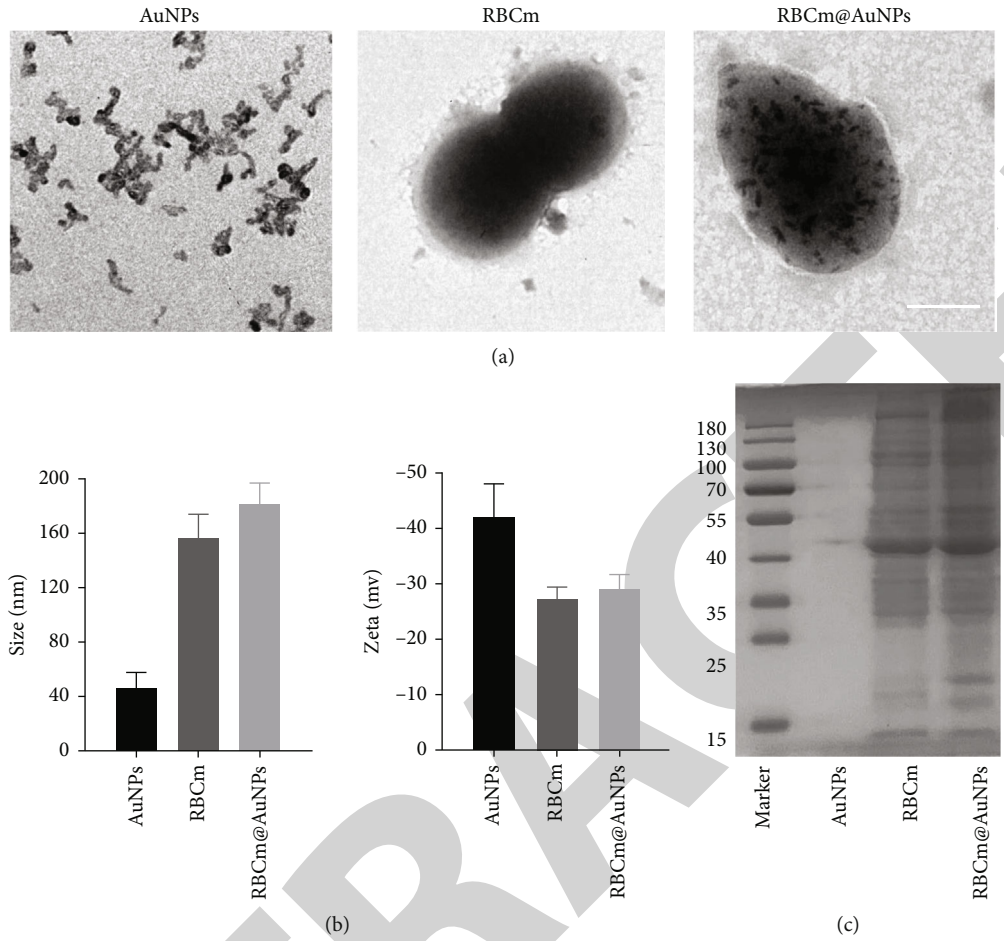

Figure 2: A characterization of the RBCm@AuNPs. (a) The TEM micrographs of nanovehicles. Scale bar: 50 nm. (b) The particle size and zeta potential of AuNPs after coating with RBCm. (c) SDS-PAGE protein analysis.

were 156.1 ± 18.3 nm with zeta potential of −27.3 ± 2.0 mV. The size of the erythrocyte membrane-coated gold nanoparticles (RBCm@AuNPs) synthesized was 181.4 ± 16.1 nm, while zeta potential was −29.1 ± 2.6 mV. The increase in size and potential indicated that the erythrocyte membrane was successfully encapsulated. The same results could also be observed in the TEM image, where multiple AuNPs were encapsulated in the RBCm.

From the SDS-PAGE test (Figure 2(c)), it could be found that RBCm@AuNPs and RBCm had the same protein bands, indicating that the synthesized RBCm@AuNPs retain the integrated protein on RBCm, which provided the possibility of good biocompatibility.

3.2. Drug Loading and Release of RBCm@AuNPs. As shown in Figure 3(a), the EE of RBCm@AuNPs loaded with CP was 88.2 ± 4.6%, and LE was 158.3 ± 21.4%, indicating a high loading efficiency. Figure 3(b) showed the drug release curves of the nanoplatforms at different time points. After AuNPs-CP was incubated in the buffer at pH 7.4 and pH 5.4 for 48 h, the release rates of CP were 17.6 ± 2.1% and 79.8 ± 5.4%, respectively; the release rates of RBCm@AuNPs-CP in the pH 7.4 and pH 5.4 buffers at 48 h were 18.2 ± 1.9% and 77.3 ± 10.0%, respectively. The AuNPs-CP after erythrocyte membrane camouflaged (RBC@AuNPs-CP group) was no significant different from AuNPs-CP on the release of CP. RBCm@AuNPs-CP released a little drug in the normal physiological status (pH 7.4), while released mounts of CP in the acidic microenvironment as melanoma (pH 5.4), which was significantly increased. The RBCm@AuNPs-CP constructed in this study could efficiently transport CP to melanoma and achieve the goals of controlled release.

3.3. Antiphagocytosis of RBCm@AuNPs-CP. After being coincubated RhoB-labeled RBCm@AuNPs with macrophages for 4 h, it was suggested by CLSM and FSM analysis that the red fluorescence was strong in macrophages in the AuNPs group, with an average fluorescence intensity of 3075.9 ± 256.3. While the same concentration of RBCm@AuNPs was incubated for the same time, the fluorescence in macrophages was decreased significantly, with a mean fluorescence intensity of 247.7 ± 62.4 (Figures 4(a) and 4(b)). The nanoplatform RBCm@AuNPs camouflaged by the red blood cell membrane could significantly reduce the recognition and clearance of nanoparticles by the monocyte-macrophage system and improve bioavailability.

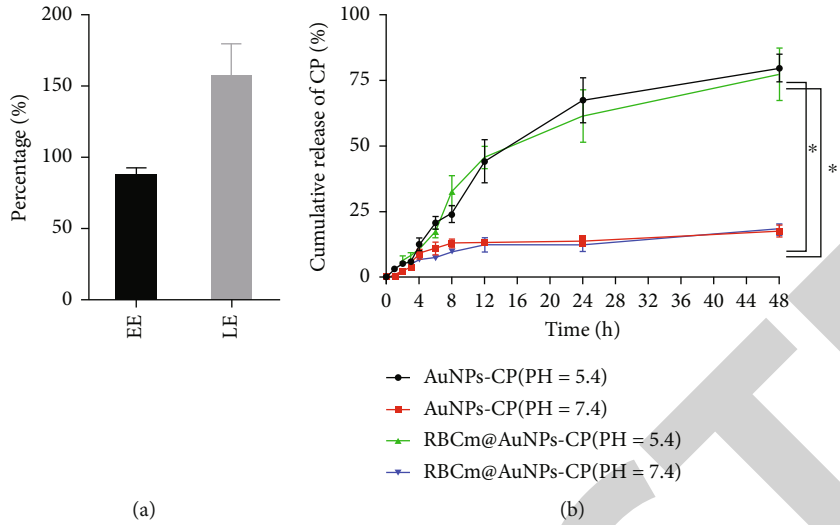

(a) (b)

Figure 3: Drug loading and release of RBCm@AuNPs-CP. (a) EE and LE of RBCm@AuNPs-CP with CP. (b) The release of CP from AuNPs-CP and RBCm@AuNPs-CP at different pH (5.4 and 7.4). Data are mean ± SD ($n = 3$). $^{*}P < 0.05$. EE: encapsulation efficiency; LE: loading efficiency.

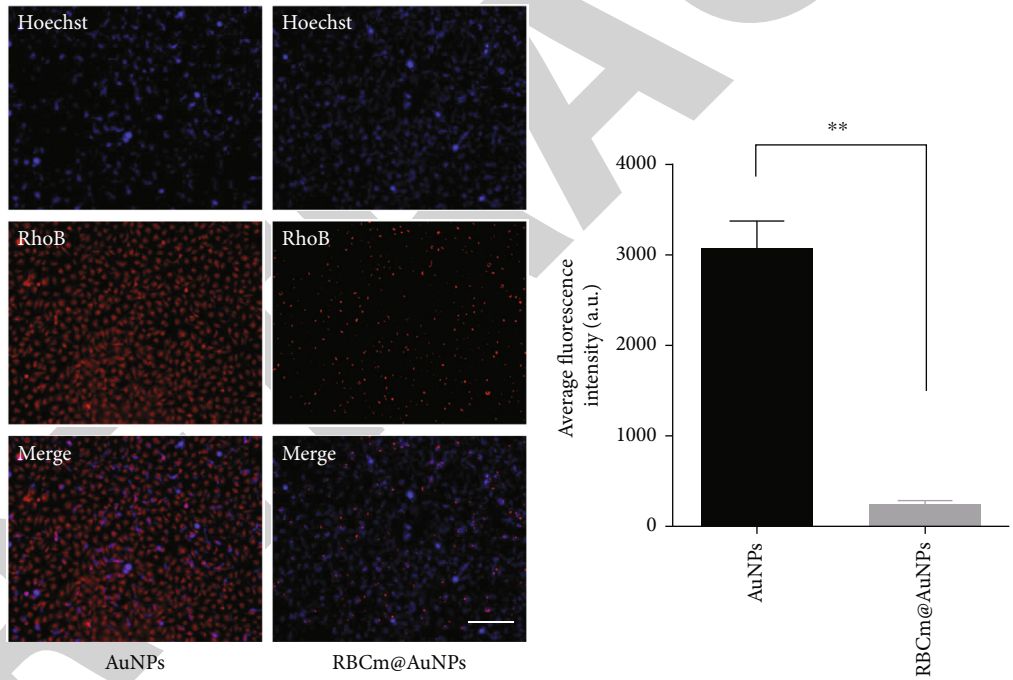

(a) (b)

Figure 4: The biocompatibility of RBCm@AuNPs. (a) CLSM micrographs of macrophages after cultured with AuNPs-CP and RBCm@AuNPs for 4 h. The scale bar: 50 μm. (b) Fluorescence intensities of collected cells after treatment with AuNPs and RBCm@AuNPs, as quantified by FCM. $^{**}P < 0.01$.

3.4. Biocompatibility of Nanoplatforms. As shown in Figures 5(a) and 5(b), there was no distinct hemolysis (the hemolysis rate was less than 1%) after coincubated erythrocytes with AuNPs or for 2 h, furthermore, the hemolysis rate of RBCm@AuNPs was lower than that of unmodified AuNPs. It was proved that the RBCm@AuNPs nanoplatform was well compatible in circulation and, therefore, was safe for intravenous administration into the blood.

3.5. In Vitro Antitumor Therapy of RBCm@AuNPs-CP. In vitro antitumor effect of RBCm@AuNPs-CP was detected by CCK-8 assay. As shown in Figure 6(a), the viability rates of B16-F10 cells treated with PBS, AuNPs, CP, AuNPs-CP, and RBCm@AuNPs-CP for 24 h were 100.1 ± 3.9%, 95.2 ± 11.6 %, 72.6 ± 18.3%, 35.4 ± 13.4%, and 30.2 ± 17.0%, respectively. Among them, the inhibition rate of melanoma cells by the traditional chemotherapeutic CP was only 17.4%, but the

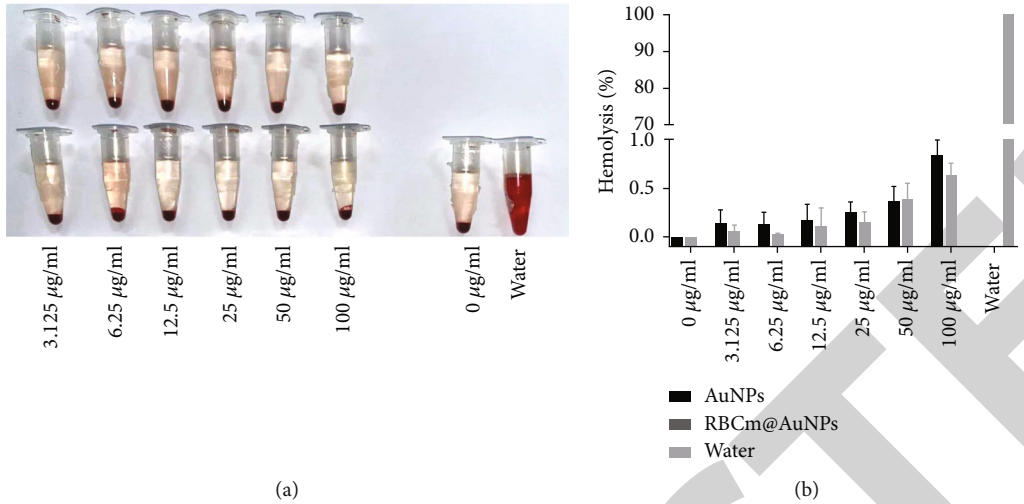

Figure 5: Imaging (a) and hemolysis rate (b) of RBCs at various concentrations of AuNPs and RBCm@AuNPs at 37°C after 2 h. Different concentrations of RBCm@AuNPs and AuNPs (3.125 to 100 μg/mL) were mixed with 5% mouse erythrocyte suspension. Data are mean ± SD ($n = 3$).

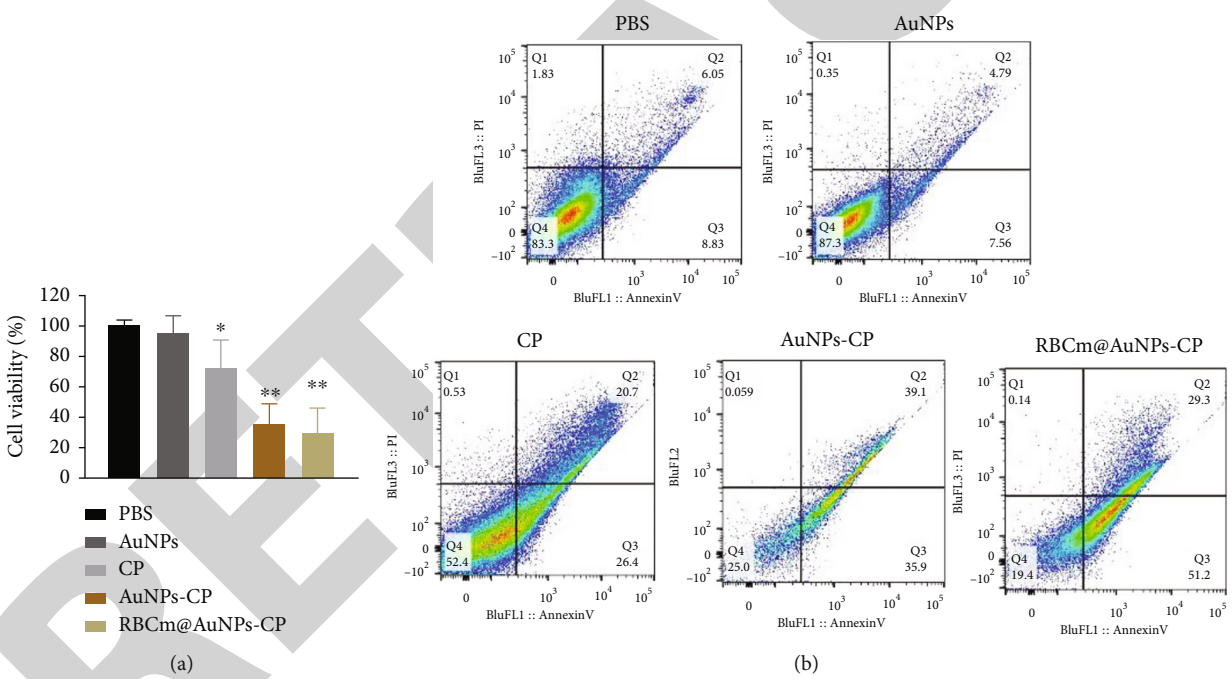

Figure 6: *In vitro* antitumor efficiency of RBCm@AuNPs-CP. (a) Cell viability and (b) analysis of apoptosis rate by FCM of B16-F10 cells treated with PBS, AuNPs, CP, AuNPs-CP, and RBCm@AuNPs-CP for 24 h. Data are mean ± SD ($n = 3$). $^{*}P < 0.05$ and $^{**}P < 0.01$ vs. PBS.

constructed nanocomposite system RBCm@AuNPs-CP could inhibit 70.8% growth of the melanoma cells.

The results of the apoptosis analysis were also consistent with those of FCM. As shown in Figure 6(b), after RBCm@AuNPs-CP treated for 24 h, the early and late apoptosis rates of B16-F10 cells were 51.2% and 29.3%, respectively. This was significantly higher than 35.9% and 39.1% for AuNPs-CP, 26.4% and 20.7% for CP, and 7.6% and 4.8% for AuNPs. This showed that the biomimetic nanocarrier constructed in this study had a more prominent antitumor effect than the traditional CP and could induce apoptosis in a large number of melanoma cells.

3.6. RBCm@AuNPs-CP Induced ROS. In order to further explore the mechanism of RBCm@AuNPs-CP induced death in melanoma cells, the level of ROS in B16-F10 cells after differently treated was detected by FCM. As shown in Figure 7(a), it was found that RBCm@AuNPs-CP could increase the expression of ROS in cells (the positive rate was 85.5%), which was much higher than that treated by

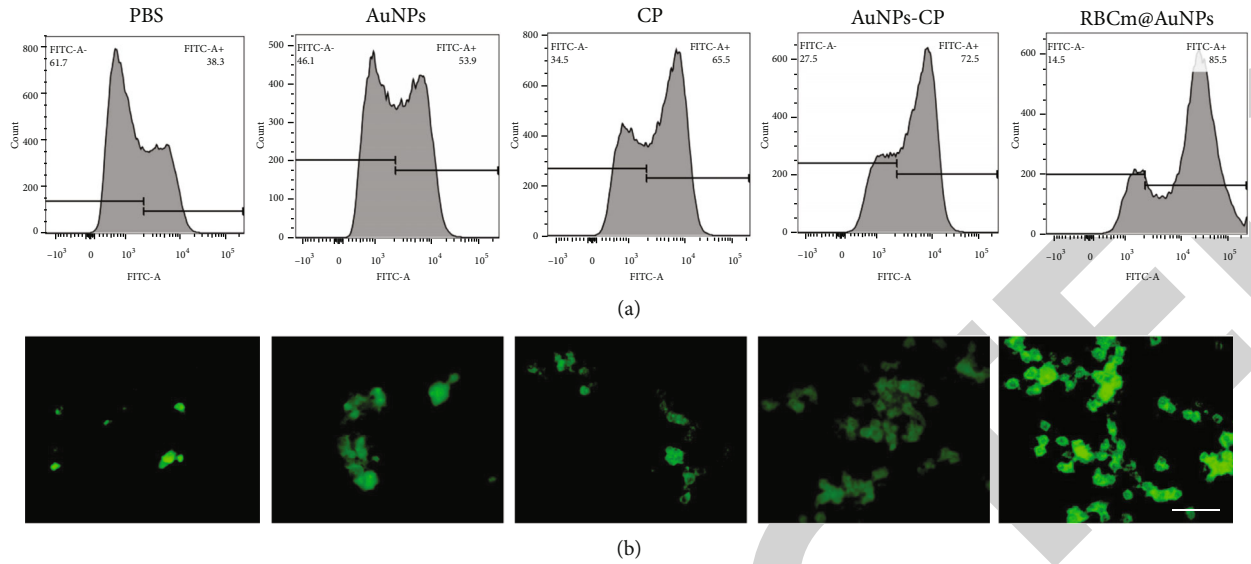

Figure 7: RBCm@AuNPs-CP induces oxidative stress damage. (a) ROS levels of B16-F10 cells after treatment with PBS, AuNPs, CP, AuNPs-CP, and RBCm@AuNPs-CP for 24 h were detected by FCM. (b) Singlet oxygen in B16-F10 cells detected by singlet oxygen detection kit. The scale bar: 20 μm.

CP alone (65.6%). As shown in Figure 7(b), RBCm@AuNPs-CP induced an increase in the expression of singlet oxygen with stronger green fluorescence in B16-F10 cells. These suggested that RBCm@AuNPs-CP might induce melanoma cells apoptosis through ROS oxidative stress damage.

3.7. Target-Ability of RBCm@AuNPs. To probe the target-ability of RBCm@AuNPs *in vitro*, the cellular uptake experiments of RBCm@AuNPs in B16-F10 were carried out. After coincubated RhoB-labeled RBCm@AuNPs and AuNPs with B16-F10 for 24 h, the red fluorescence was stronger in cells treated with RBCm@AuNPs than which in AuNP9s groups, with an average fluorescence intensity of 4873.1 ± 2973.2 and 538.7 ± 62.1, respectively (Figures 8(a) and 8(b)).

To further evaluate the tumor targeting ability of RBCm@AuNPs camouflaged by erythrocyte membrane *in vivo*, Cy5-labeled AuNPs-CP and RBCm@AuNPs were injected into B16-F10 tumor-bearing mice via the tail vein. At different time periods, the distribution of nanocomplexes in mice was analyzed by *in vivo* imaging. As shown in Figure 8(c), both AuNPs and RBCm@AuNPs were distributed evenly throughout the body at 6 h. However, due to the immune evasion effect and the EPR effect of RBCm@AuNPs after red blood cell camouflage, the fluorescence intensity of RBCm@AuNPs was significantly higher than that of AuNPs at 24 h in tumor site.

After 24 hours, the major organs and tumors were taken out for additional imaging analysis of their fluorescence intensity, as shown in Figures 8(d) and 8(e). It was found that AuNPs mainly accumulated in the liver, lung, spleen, kidney, and tumor. In contrast, the fluorescence intensity of RBCm@AuNPs at the tumor site was 5.1 times higher than that of AuNPs ($P < 0.01$), and the accumulation of RBCm@AuNPs in other organs was also reduced.

The erythrocyte membrane camouflage nanocarriers RBCm@AuNPs had the ability to passively target tumors *in vivo*. This provided the possibility of effectively transport pharmaceuticals to tumor sites for antitumor effects.

3.8. In Vivo Antimelanoma Effects of RBCm@AuNPs-CP. To evaluate the antitumor effect of RBCm@AuNPs-CP, the tumor size of B16-F10 tumor-bearing mice treated with PBS, AuNPs, CP, AuNPs-CP, and RBCm@AuNPs-CP groups was dynamically observed and recorded. The tumor tissue was sectioned and stained with H&E. As shown in Figure 9(a), the tumor growth curves of the nanoparticle AuNPs group were similar to those of the control group, with tumor size 8.4 and 9.5 times lager after 14 days of treatment than before the initial treatment. On the 14th day of treatment with CP and AuNPs-CP alone, the tumor size was 4.2 times and 1.6 times than that before initial treatment, respectively, which inhibited the growth of tumors. It suggested that the RBCm@AuNPs-CP nanocomposites constructed significantly inhibited the growth of tumors, furthermore, the tumors showed a decreasing trend, which was 0.5 times than initial tumor size on the 14th day of treatment ($P < 0.01$). The body weight of the mice did not differ significantly between the groups, although it changed compared to the control group (Figure 9(b)). After the mice were sacrificed on D14, ex vivo representative tumor tissue was taken a picture (Figure 9(c)), which showed the same result that the tumor size of the RBCm@AuNPs-CP group was smaller than that of the control group. This indicated that the constructed AuNPs-CP nanoplatform exerts an excellent antimelanoma effect, and that RBCm@AuNPs-CP, camouflaged by the erythrocyte membrane, could further enhance antitumor effect as high pharmaceuticals concentration at the tumor site by evading from mononuclear macrophage system and EPR effect.

As shown in Figure 9(d), it could be found from the H&E staining of ex vivo tumor tissues that after RBCm@AuNPs-CP treatment, extensive and distinct cell damage, necrosis, and

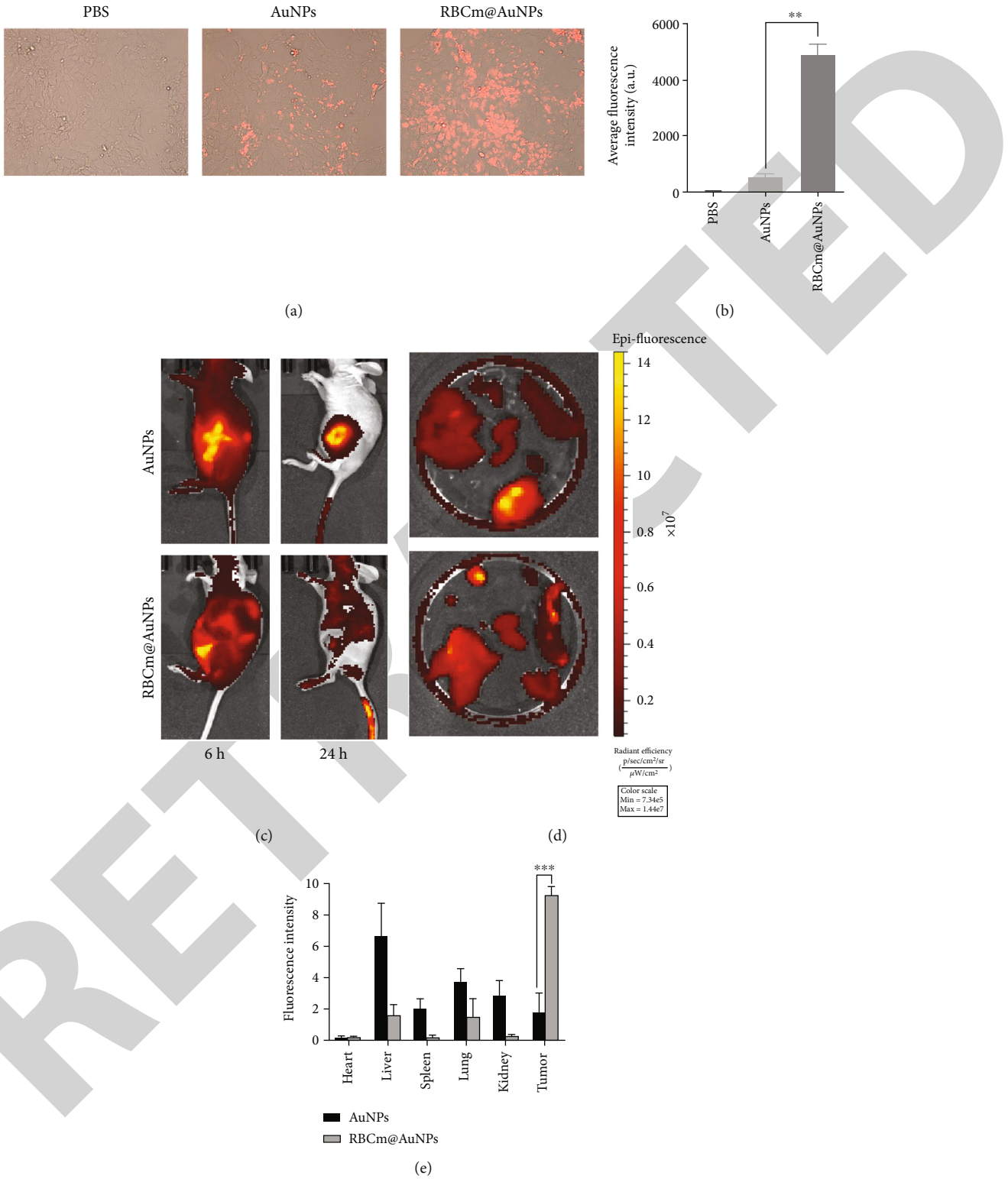

Figure 8: Targeting ability of RBCm@AuNPs. (a) The cellular uptake ability of Rho B-labeled AuNPs and Rho B-labeled RBCm@AuNPs in B16-F10. (b) Fluorescence intensities of collected B16-F10 after treatment with AuNPs and RBCm@AuNPs, as quantified by FCM. (c) *In vivo* fluorescence images of B16-F10 xenograft model at 6 h, 24 h after intravenous injection of cy5-labeled RBCm@AuNPs and AuNPs. (d) Ex vivo bioluminescent images of the main organs and tumor at 24 h post injection. (e) Semiquantitative analysis of fluorescence intensity from tumor and other tissues. Data are mean ± SD ($n = 3$). $^{**}P < 0.01$, and $^{***}P < 0.001$.

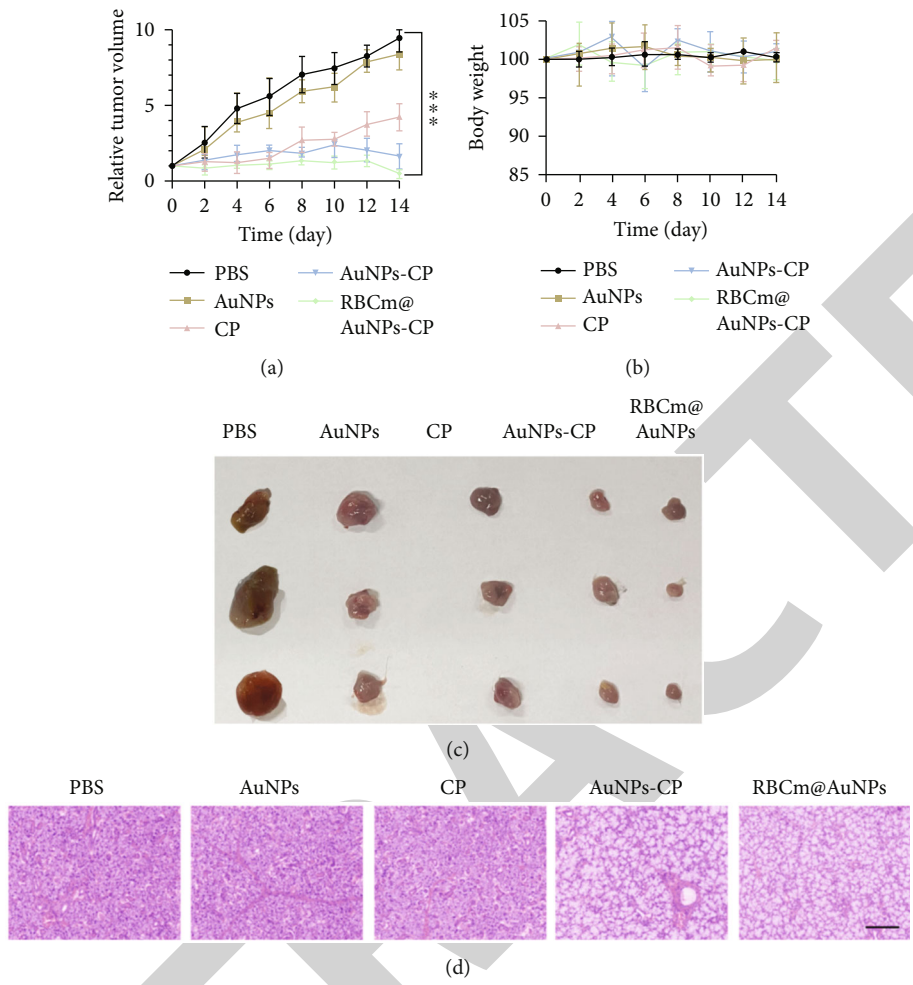

Figure 9: *In vivo* antitumor effect of RBCm@AuNPs-CP. (a) Tumor growth patterns after various treatments for 14 days. Tumor volumes were normalized to the baseline values. (b) The body weight changes of B16-F10 xenograft model during treatments were normalized to baseline values. (c) Representative images of tumors after intravenous injection of different formulations at day 14. (d) The histological observation of the tumor tissues after the treatment with different group stained with hematoxylin and eosin (H&E). Scale bar: 200 μm. Data are mean ± SD ($n = 3$). $^{***}P < 0.001$.

even lysis occurred at the tumor site. Different degrees of cell necrosis morphological characteristics appeared in tumor sites of the CP or AuNPs-CP treatment groups, while the PBS and AuNPs groups maintained the original morphological characteristics of the tumor tissue.

3.9. Biosafety of RBCm@AuNPs-CP. Since the constructed RBCm@AuNPs-CP nanocomposite is a heterologous substance, verifying its safety is crucial for its clinical application. This study verified the safety of RBCm@AuNPs-CP in terms of body weight and H&E staining of major tissues. As shown in Figure 9(b), no significant changes in animal body weight were found throughout the treatment period, provided that RBCm@AuNPs-CP had less systemic toxicity.

According to the H&E staining of major organ in melanoma mice after treatment (Figure 10), there was no distinct abnormality observed from micrographs in all treatment groups. RBCm@AuNPs-CPs showed good biocompatibility *in vivo*, which provided the possibility of further clinical applications.

4. Discussion

One of the important factors that make traditional nanodrug delivery systems difficult to apply in the clinic are heterogeneity, immunogenicity, and toxicity. Nanoparticles are easily recognized and eliminated by the mononuclear macrophage system and immune system *in vivo*; meanwhile, their particle size is too small to long-term retention in circulation as it is metabolized by the liver and/or kidney [12]. In our study, the red blood cell membrane camouflaged nanoparticles RBCm@AuNPs-CP constructed in a simple and economical way to reduce the clearance rate of the nanodrug delivery system by the mononuclear macrophage system and improve the therapeutic efficiency of the nanodrug.

CP is a commonly used chemotherapeutic pharmaceuticals for the treatment of melanoma. It exerts excellent antitumor effects by entering into cells to damage DNA and induce apoptosis in oxidatively damaged cells [13, 14]. However, the accompanying side effects limit its clinical application. Studies have found that in tumor sites, cisplatin seems

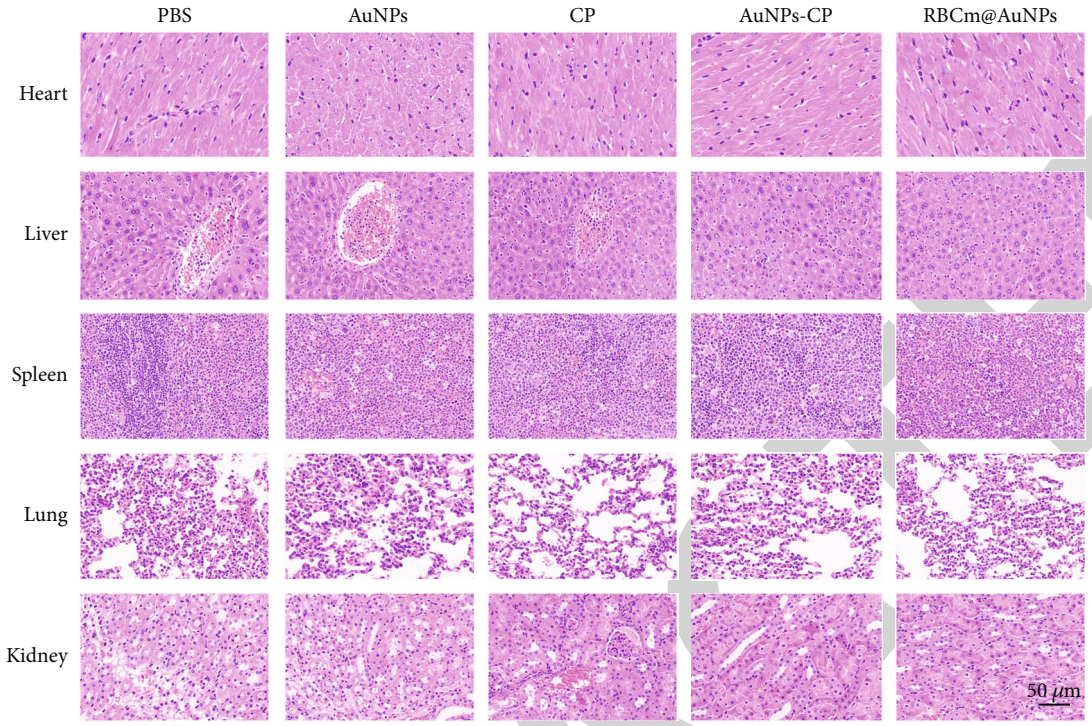

Figure 10: Histological observation of major organs collected from the B16-F10 tumor-bearing mice after the treatment. The major organ sections were stained with hematoxylin and eosin (H&E). Scale bar: 50 μm.

to be more likely to accumulate in the following specific sites, such as kidney, liver, neurons, and inner ear [15–17], resulting in nephrotoxicity [18], hepatotoxicity [19], neurotoxicity [20], and ototoxicity [21]. The biomimetic nanoparticles loaded with CP constructed in this study could target tumor site specifically through the EPR effect of the nanoparticles at tumor site, which greatly reduces its aggregation in the liver, kidney, and other sites. It provides the possibility of reducing the toxicity of CP. Subsequent experiments could also show that there was no distinct damage to vital organs after RBCm@AuNPs-CP treatment.

At present, the engineered nanodrugs that have been widely used in clinical antitumor therapy are mainly chemotherapeutic drugs in the form of liposomes, like cytarabine liposome injection (Dypocyt) [22] and doxorubicin (Doxil) [23]. Many of these drugs have been approved by the FDA and are widely used in clinical practice. Liposomal drug delivery represents a highly adaptable therapeutic platform, which could reduce the toxicity of chemotherapy drugs; however, it does not own tumor-targeting properties, resulting in low bioavailability [24]. Although new multifunctional nanoscale antitumor drugs are emerging in an endless stream, it is embarrassing to achieve clinical translation. The huge obstacle is their safety and immunogenicity. The RBCm-wrapped gold nanoparticle biomimetic drug delivery system constructed in this study completely retains the surface proteins of the RBCm. These characteristic proteins achieve its targeted and safe role, which provides the possibility of its later clinical transformation.

In this study, RBCm@AuNPs-CP treatment of melanoma cells was found to promote the expression of singlet oxygen, increase the level of ROS, and induce apoptosis in B16-F10 cells. ROS could cause DNA damage through lipid peroxidation, depletion of sulfhydryl groups, and induction of signal transduction pathways, resulting in apoptosis [6]. Mitochondria are one of the most important targets of oxidative stress, and ROS might affect mitochondrial respiratory function and lead to cellular dysfunction [25]. ROS cause mtDNA damage and lead to a decrease in mitochondrial permeability transition [26], thereby promoting mitochondrial rupture [27]. Mitochondrial rupture releases cytochrome C and procaspase-9 [28]. Activated caspase-9 then interacts with other caspases to activate caspase-3, caspase-6 and caspase-7, thereby inducing apoptosis [29].

5. Conclusion

The erythrocyte camouflage nanosystem RBCm@AuNPs-CP possessed excellent monodispersity and high drug loading rate. The red blood cell membrane wrapped on its surface could effectively escape the immune system with well EPR effect at the tumor site, so that it could be retained at the tumor site and reduce its concentration in the heart, liver, spleen, lung, kidney, and other tissues, which was passive tumor target-ability. Meanwhile, RBCm@AuNPs-CP promoted early apoptosis and necrosis of melanocytes by inducing oxidative stress damage. This makes RBCm@AuNPs-CP a potentially novel, safe, and effective targeted drug delivery system for the treatment of melanoma.

Hindawi
Journal of Oncology
Volume 2022, Article ID 5813522, 20 pages
https://doi.org/10.1155/2022/5813522

Research Article

Prognostic Model and Immune Infiltration of Ferroptosis Subcluster-Related Modular Genes in Gastric Cancer

Huachu Deng,[1] Yongjian Lin,[1] Fu Gan,[2] Baibei Li,[3] Zhenshan Mou,[3] Xingan Qin,[1] Xiaoyu He,[4] and Yunchao Meng[5]

[1]*Department of Gastrointestinal and Gland Surgery, The First Affiliated Hospital of Guangxi Medical University, Nanning 530021, China*
[2]*Department of Urology Surgery, The Affiliated Hospital of Youjiang Medical University for Nationalities, Baise 533000, China*
[3]*Department of Hepatobiliary, The First Affiliated Hospital of Guangxi Medical University, Nanning 530021, China*
[4]*Department of Thoracic Surgery, The Shenzhen Bao'an District Songgang People's Hospital, Shenzhen 518105, China*
[5]*Department of Gastroenterology, Nanxishan Hospital of Guangxi Zhuang Autonomous Region, Guilin 541002, China*

Correspondence should be addressed to Xingan Qin; drqinxingan@126.com, Xiaoyu He; drhexiaoyu@126.com, and Yunchao Meng; yunchaomeng@163.com

Received 9 July 2022; Revised 28 August 2022; Accepted 5 September 2022; Published 13 October 2022

Academic Editor: İbrahim Hakkı Cigerci

Background. Gastric cancer (GC) is one of the gastrointestinal tumors with the highest mortality rate. The number of GC patients is still high. As a way of iron-dependent programmed cell death, ferroptosis activates lipid peroxidation and accumulates large reactive oxygen species. The role of ferroptosis in GC prognosis was underrepresented. The objective was to investigate the role of ferroptosis-related genes (FRGs) in the prognosis and development of GC. *Methods*. Datasets of GC patients were obtained from the Gene Expression Omnibus (GEO) and The Cancer Genome Atlas (TCGA) database that include clinical information and RNA seq data. Through nonnegative matrix factorization (NMF) clustering, we identified and unsupervised cluster analysis of the expression matrix of FRGs. And we constructed the co-expression network between genes and clinical characteristics by consensus weighted gene co-expression network analysis (WGCNA). The prognostic model was constructed by univariate and multivariate regression analysis. The potential mechanisms of development and prognosis in GC were explored by Kyoto Encyclopedia of Genes and Genomes (KEGG) analysis, gene ontology (GO), tumor immune microenvironment (TIME), and tumor mutation burden (TMB). *Results*. Two molecular subclusters with different expression patterns of FRGs were identified, which have significantly different survival states. Ferroptosis subcluster-related modular genes were identified by WGCNA. Based on 8 ferroptosis subcluster-related modular genes (collagen triple helix repeat containing 1 (CTHRC1), podoplanin (PDPN), procollagen-lysine,2-oxoglutarate 5-dioxygenase 2 (PLOD2), glutamine-fructose-6-phosphate transaminase 2 (GFPT2), ATP-binding cassette subfamily A member 1 (ABCA1), G protein-coupled receptor 176 (GPR176), serpin family E member 1 (SERPINE1), dual specificity phosphatase 1 (DUSP1)) and clinicopathological features, a nomogram was constructed and validated for their predictive efficiency on GC prognosis. Through receiver operating characteristic (ROC) analysis, the results showed that the area under the curve (AUC) of 1-, 3-, and 5-year survival were 0.721, 0.747, and 0.803, respectively, indicating that the risk-scoring model we constructed had good prognosis efficacy in GC. The degree of immune infiltration in high-risk group was largely higher than low-risk group. It indicated that the immune cells have a good response in high-risk group of GC. The TMB of high-risk group was higher, which could generate more mutations and was more conducive to the body's resistance to the development of cancer. *Conclusion*. The risk-scoring model based on 8 ferroptosis subcluster-related modular genes has shown outstanding advantages in predicting patient prognosis. The interaction of ferroptosis in GC development may provide new insights into exploring molecular mechanisms and targeted therapies for GC patients.

1. Introduction

GC is one of the gastrointestinal tumors with the highest mortality rate [1]. The number of GC patients is still high. By 2022, about 26,380, new cases are expected with a mortality rate of 42% [2]. Although the current predominant treatment for GC takes the standard surgical strategy combined limited lymph node dissection strategy [3], there are still patients with heterogeneous prognosis, such as distant metastases, significant drug resistance, and toxic effects [4]. Meanwhile, early GC commonly lacked dysphagia, weight loss, and typical gastrointestinal symptoms. So most people are diagnosed with advanced GC. The survival for advanced GC is always low [5]. Therefore, identifying high-tech diagnostic and prognostic biomarkers is crucial for the management of GC. Relevant advances in the field of tumor mutational burden and gene mutation might be immediately applicable to guide immunotherapeutic effect of GC [6, 7].

Programmed cell death (PCD) includes cell apoptosis, necroptosis, autophagy, pyroptosis, cuproptosis, and ferroptosis. They have different morphologies and biochemical characteristics. For example, apoptosis is usually associated with cell contraction, while necrotizing apoptosis involves cell swelling and leakage of cell contents [8]. Necroptosis is a form of regulated cell death that critically depends on receptor-interacting serine-threonine kinase 3 (RIPK3) and mixed lineage kinase domain-like (MLKL) and generally manifests with morphological features of necrosis [9]. Autophagy is a process by which cellular material is degraded by lysosomes or vacuoles and recycled [10]. Cuproptosis is a new type of cell death and is characterized by the dependence on mitochondrial respiration and protein lipoylation [11]. As a way of iron-dependent programmed cell death, ferroptosis activates lipid peroxidation and accumulates large reactive oxygen species [12]. The main mechanism of ferroptosis is to catalyze the production of lipid peroxidation of highly expressed unsaturated fatty acids on cell membranes under the action of divalent ferroxygenase or ester oxygenase, thereby inducing cell death. In addition, it also showed a decrease of GPX4, the core enzyme regulating the antioxidant system (glutathione system) [13]. The main characteristics of ferroptosis were as follows: (1) In terms of cell morphology, ferroptosis could lead to smaller mitochondria, increase membrane density, and reduce crest. There was no obvious morphological change in the nucleus. (2) In terms of cell components, iron death showed increased lipid peroxidation and ROS. This process is present in tumor development and therapeutic response, including genetic mutations, stress response pathways, and epithelial-to-mesenchymal transition [14]. Ferroptosis was closely associated with antitumor, drug resistance and metastasis. Ni et al. have illustrated miR-375/SLC7A11 regulatory axes triggering gastric cancer stem cell iron sagging, attenuated metastasis, and drug resistance [15]. Other studies have shown that poor prognosis in patients with GC was largely associated with cancer cell antiferroptosis, and its underlying mechanisms may involve alterations in cancer stem cells and regulation of cell cycle-related proteins [16]. In addition, inducing ferroptosis was one of the main mechanisms mediating antitumor activity. Liu et al. found that Jiyuan oridonin A (JDA) was a natural compound isolated from Jiyuan Rabdosia rubescens with antitumor activity, which could inhibit the growth of GC cells by inducing ferroptosis [17]. However, the role of ferroptosis in GC prognosis was underrepresented, especially with the presence of mutant types of GC. Therefore, in this study, a novel GC prognosis model was constructed through ferroptosis subgroup-related module genes.

In this study, we aimed to identify FRG co-expression modules in GC through WGCNA, develop a risk-scoring model to quantify the level of ferroptosis in individual patients, and explore its prognostic role in GC patients. In addition, functional studies were conducted on tumor immune microenvironment and mutation burden to initially elucidate the mechanisms that affect prognosis, providing a basis for clinical diagnosis, personalized immune targeted therapy, and antitumor drug resistance.

2. Methods

2.1. Sources of Data. The mRNA sequencing and somatic mutation data of GC patients were obtained from the Cancer Genome Atlas (TCGA) (https://tcga-data.nci.nih.gov/tcga/), which contains 375 GC samples. And these samples were used as a training set for this study, while the validation set was selected from the GSE84437 dataset in the Gene Expression Omnibus (GEO) database (https://www.ncbi.nlm.nih.gov/geo/). The dataset contains gene expression data from 433 patients with GC. 383 FRGs were derived from ferroptosis database (http://www.zhounan.org/ferrdb/) [18–20]. The "limma" package was used for integration and difference analysis between datasets [21].

2.2. Identification of Subclusters of FRGs in GC. The NMF algorithm has a great advantage in the distance [22]. The "NMF" package in R was used to identify and unsupervised cluster analysis of the expression matrix of FRGs obtained from the TCGA dataset. Each parameter was selected in the following way, using the "brunet" package in R, with the number of iterations (nrun) set to 10 and ranks set from 2 to 10. Then the new subcluster classification was obtained.

2.3. Identification of Ferroptosis Subcluster-Related Modular Genes in GC. The differential expression genes with different ferroptosis genotyping between cluster 1 (C1) and cluster 2 (C2) group were identified with the "limma" R package according to the cut-off value FDR<0.05, log2|fold change (FC)| ≥2. The co-expression network between genes and clinical characteristics was constructed using the "WGCNA" R package [23], and the samples with an expression less than 0.5 were removed. Subsequently, we computed the topological matrix of the scale-free distribution. We used the "PickSoftThreshold" function to select the optimal soft threshold β and then calculated the Pearson correlation coefficient for each gene. We construct a neighbor-joining matrix using weighted correlation coefficients. Then, a topological overlap

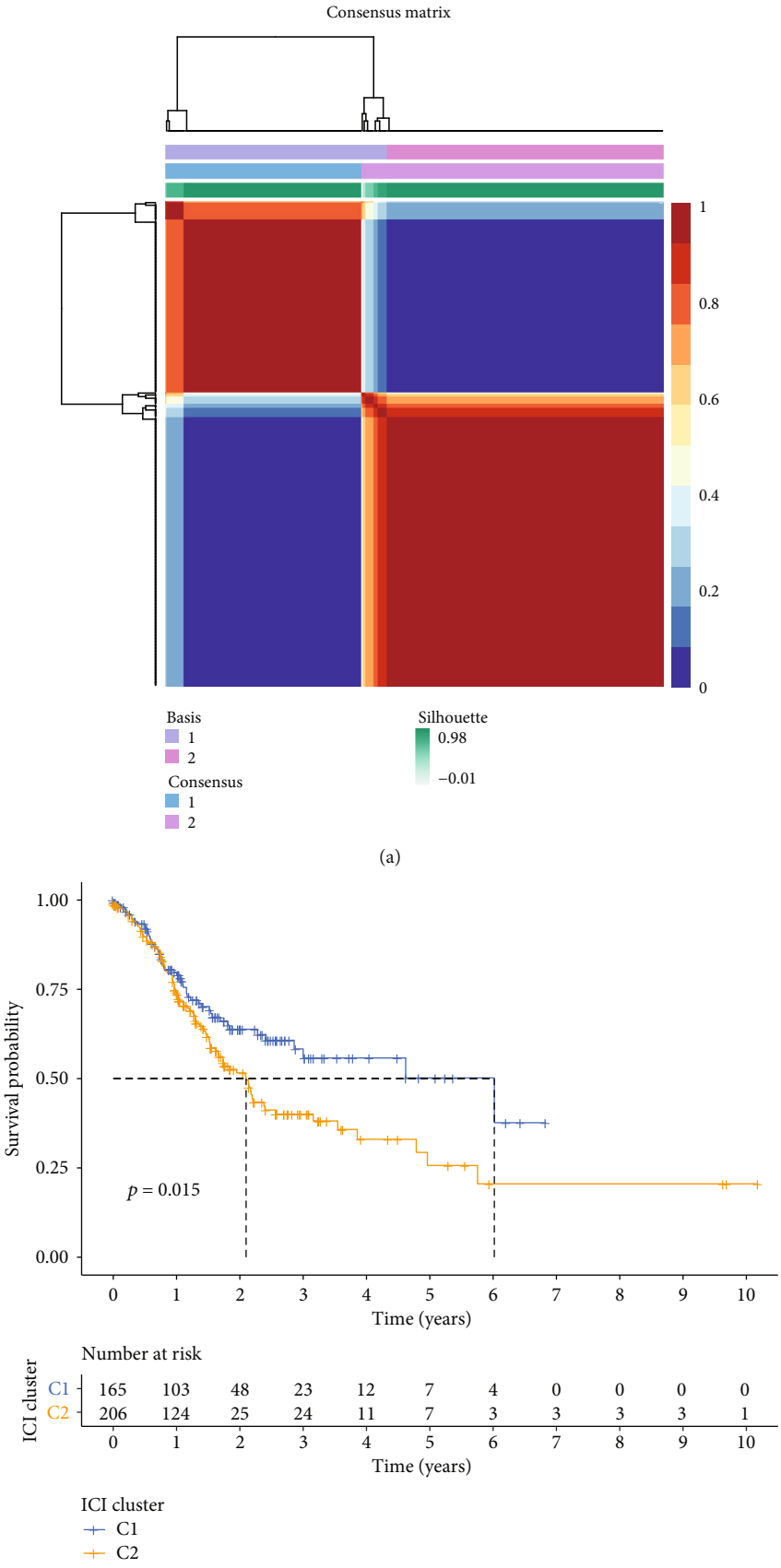

Figure 1: Continued.

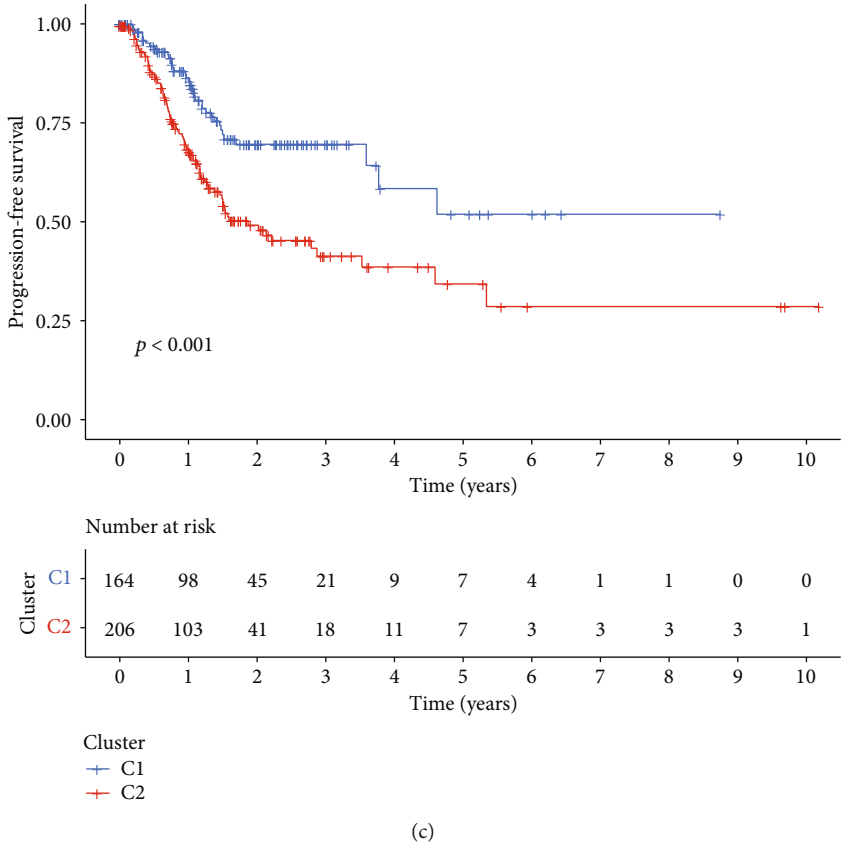

(c)

Figure 1: Identification of ferroptosis-associated subclusters. (a) Through NMF consensus clustering using FRGs, the optimal k value was determined to be 2. Patients were divided into C1 and C2. (b) K-M survival curves of OS in C1 and C2. (c) K-M survival curves of PFS in C1 and C2. C1: cluster 1; C2: cluster 2; OS: overall survival; PFS: progression-free survival; GC: gastric cancer; NMF: nonnegative matrix factorization; K-M: Kaplan-Meir; FRG: ferroptosis-related genes.

matrix was constructed based on the neighbor-joining matrix to construct a clustering tree. The number of genes in the module greater than 150 was retained, and the modules with similarities greater than 0.25 were merged. Finally, the significant models were identified, and the genes of the significant modules were extracted.

The "VennDiagram" package was applied to calculate the intersection genes of difference genes between C1 and C2 and the FRGs of the significant modules. That is the ferroptosis subcluster-related modular genes.

2.4. Construction and Validation of a Prognostic Model. The TCGA dataset was used as the training set, and the genes associated with patients' prognosis were screened out through COX regression analysis. Using the least absolute shrinkage and selection operator (LASSO) regression method, these genes were analyzed by the "glmnet" software package in R. And the λ min with the lowest error was chosen after 10-fold cross-validation [24] to construct a stable prognostic model. Followed by multivariable cox regression analysis to construct the best risk-scoring model and calculate regression coefficient for each gene regression coefficient. The risk score in the model was calculated by the following formula: $\text{riskScore} = \sum_{x=1}^{n}(\text{coef mRNA} \times \text{Expr mRNA})$. The risk score for each sample was calculated using this formula, and the low- and high-risk groups were divided by the median [25]. Through "survival" and "timeROC" package in R, the Kaplan-Meir (K-M) survival curve and ROC curve were, respectively, plotted to determine the efficacy of the model. In addition, for more intuitive prediction, we incorporated clinical characteristics (including age, gender, tumor location, and metastasis) into the model, constructed a nomogram using the "Regplot" package in R, and validated the stability with calibration and ROC curves.

To demonstrate accuracy of the model, we used the GSE84437 dataset for external validation of the risk model construction, including survival curves and ROC curves.

2.5. Functional Analysis of Prognostic FRGs. Functional enrichment analysis of GO and KEGG pathways were performed to describe functions of prognostic FRGs. Through the "clusterProfiler" package in R, functional enrichment analysis of prognostic FRGs was performed. Items with adjusted $P < 0.05$ were selected from the enrichment results for display.

2.6. Analysis between Immune Infiltration and Risk Score of GC. Through the single-sample GSEA (ssGSEA) algorithm, the "GSVA" package of R was applied to calculate the

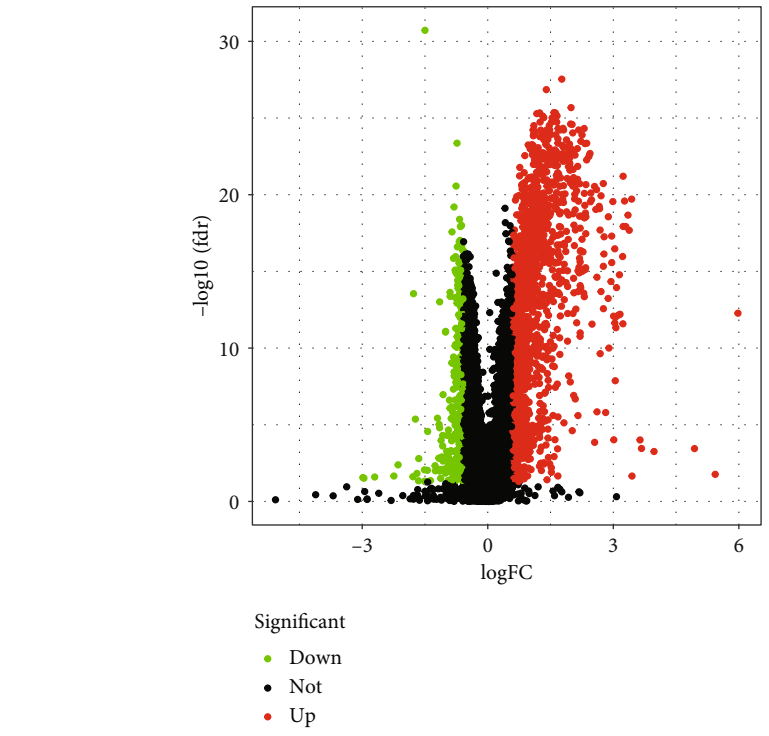

(a)

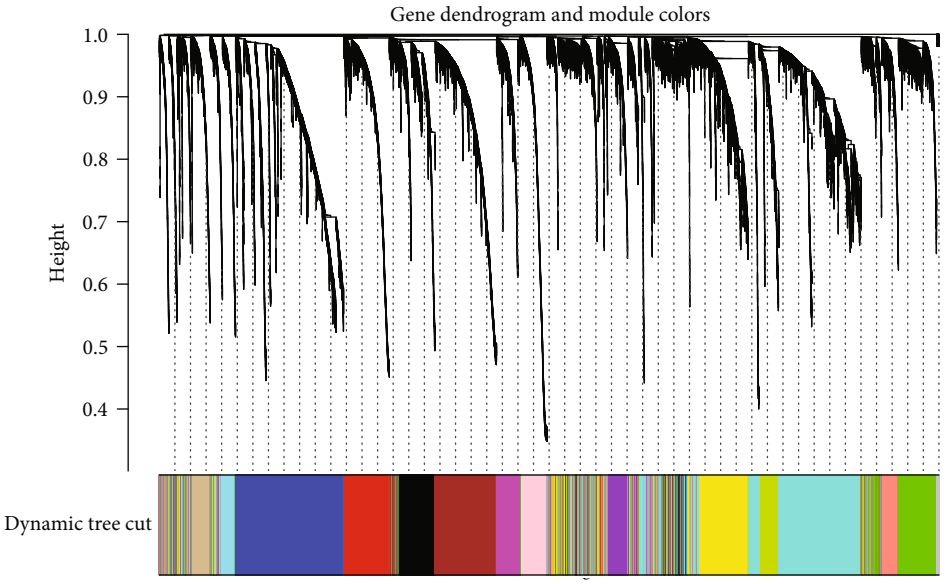

(b)

Figure 2: Continued.

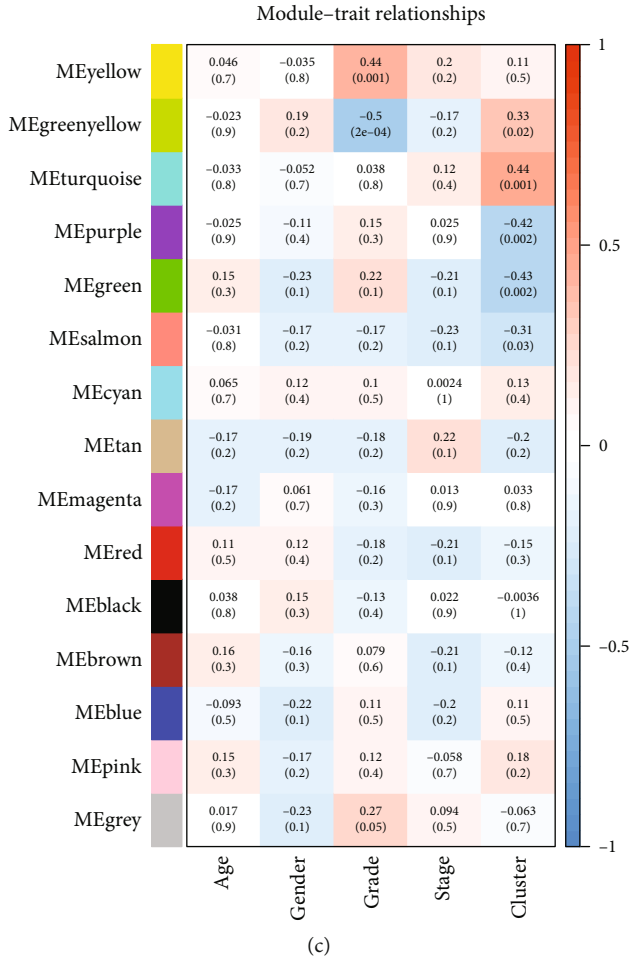

(c)

Figure 2: Identification of differential molecular subcluster genes associated with ferroptosis. (a) Volcano plots of mRNA-seq differential analysis for C1 and C2. (b) Based on the hierarchical clustering analysis of the TCGA dataset, genes with similar characteristics are assigned to modules of the same color. (c) Heat map of correlations between eigenvalues and individual modules. C1: cluster 1; C2: cluster 2; TCGA: the Cancer Genome Atlas.

relative content of different kinds of immune cells in the TCGA cohorts and explore the differences in immune infiltration. And we applied the "estimate" package to perform ESTIMATE algorithm to analyze the data of TCGA cohorts and evaluate the TIME from three aspects: tumor purity, immunity score, and matrix score.

2.7. Tumor Mutational Burden (TMB) Analysis of GC. Based on the corresponding mutation data, we calculated their nonsynonymous mutations to determine the TMB of GC patients with different ferroptosis subclusters. We extracted GC patient driver gene data from the R "maftool" package and compared the somatic changes in driver genes of different ferroptosis subtypes. Finally, the overall mutation level was represented by the top 20 driver genes by mutation frequency.

2.8. Statistical Analysis. All data were statistically analyzed using R (Version 3.6.2). K-M method, Log-rank test, and Cox regression were used to analyze the prognosis of each characteristic value, the survival curve, and the independent prognostic factors, respectively. ROC curve analysis was used to predict overall survival with R package "pROC". Continuous variables (e.g., age, gender, stage, and tumor grade) were transformed into dichotomous variables. Student's *t*-test and chi-square test were adopted to compare differences in pathology and molecular characteristics between different patient groups. And Welch's t test was used when appropriate. When $P < 0.05$, analysis was considered statistically significant.

3. Results

3.1. Construction of Subclusters of FRGs in GC. Through NMF clustering analysis of FRGs, 375 GC samples from TCGA were divided into two subclusters: C1 and C2 (Figure 1(a)). Survival analysis showed that there were significant differences between the C1 and C2 in the overall survival (OS) and progression-free survival (PFS). The survival rate of the C1 is superior to the C2, and K-M curve is shown in Figures 1(b) and 1(c).

3.2. Difference Analysis of Subclusters in GC and Construction of Ferroptosis-Related Modules by WGCNA.

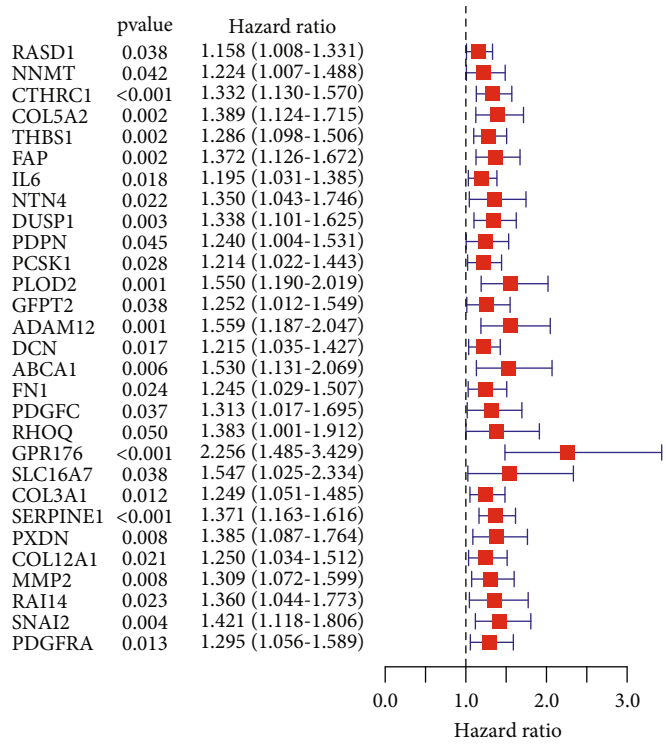

(a)

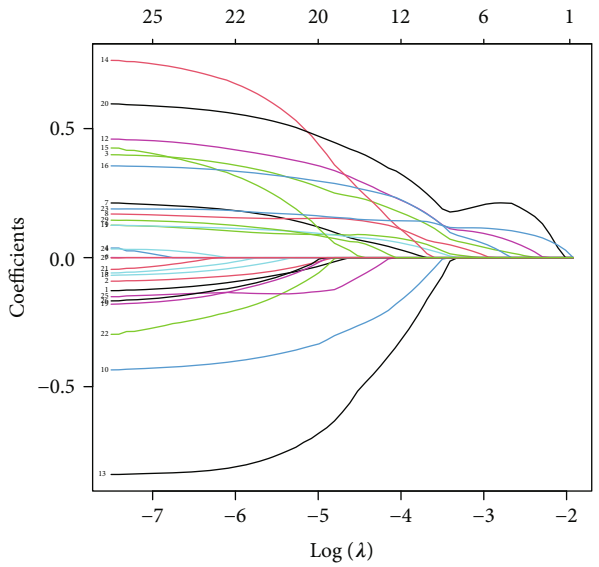

(b)

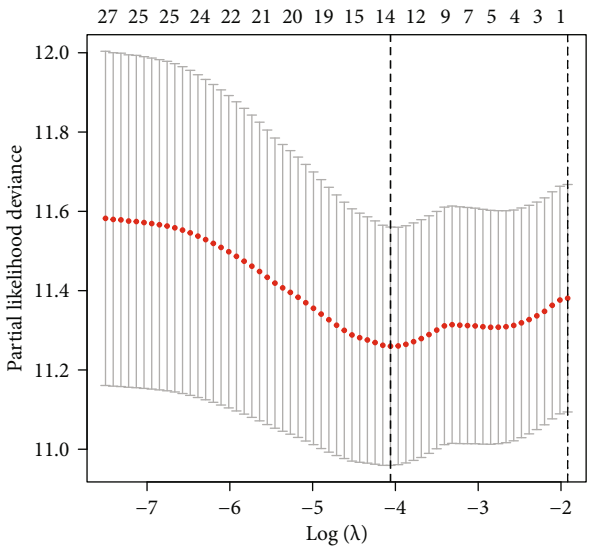

(c)

Figure 3: Continued.

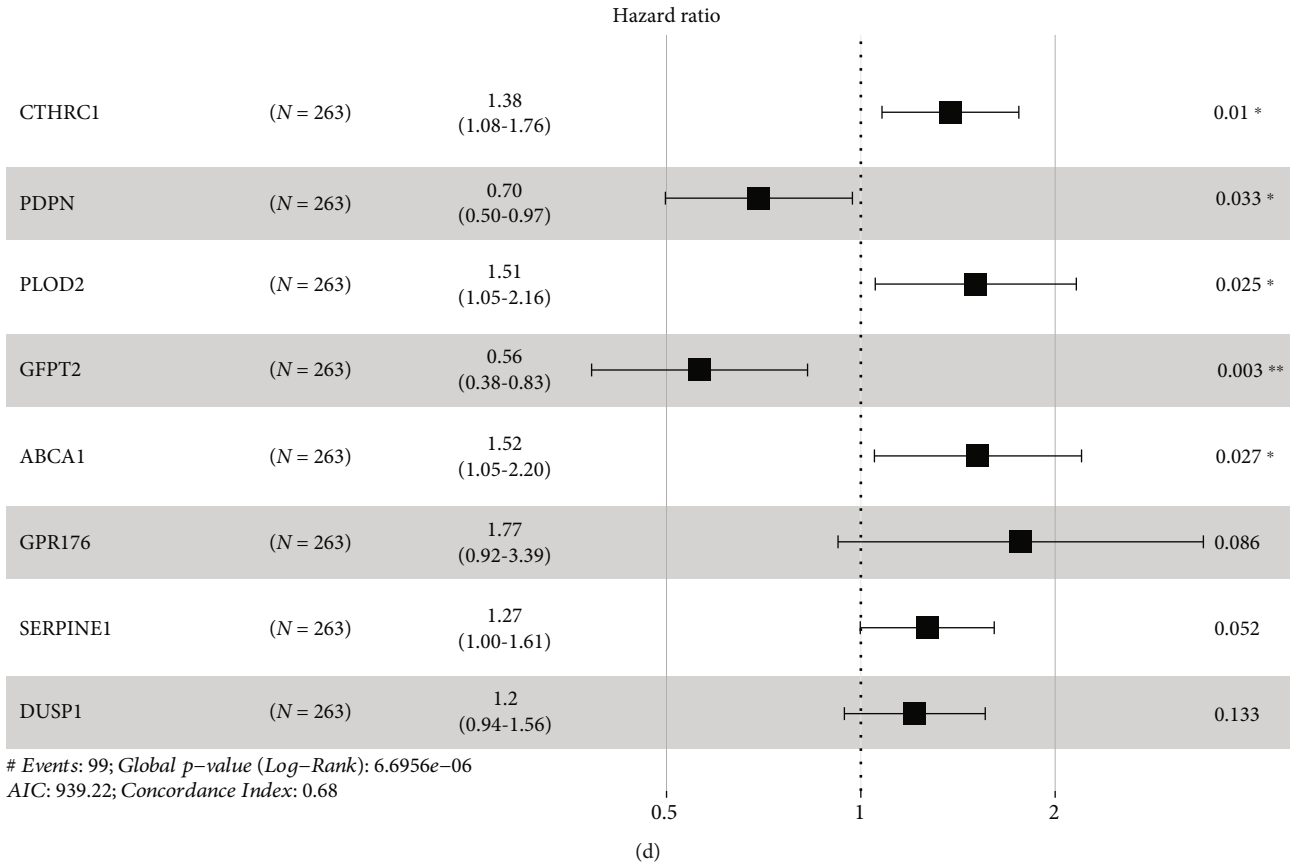

Figure 3: Screening of prognostic FRGs. (a) Univariate Cox regression analysis screened out 29 prognostic FRGs. (b) Trajectory changes of 8 genes. (c) Confidence interval for each λ value. (d) Multivariate Cox regression analysis screened out 8 prognostic FRGs. C1: cluster 1; C2: cluster 2; FRGs: ferroptosis-related genes.

Difference analysis of C1 and C2 was performed through the "limma" package, and a total of 1846 differential genes met the requirements, and the differential genes were displayed in a volcanic map (Figure 2(a)). During the analysis of WGCNA, we calculated the soft threshold $\beta = 5$ using R, and then obtained a hierarchical cluster tree by dynamic cutting method (Figure 2(b)), and combined similar modules to obtain a total of 15 modules. From the Pearson correlation analysis matrix of the module features, the green yellow and yellow modules were related to the ferroptosis-related phenotype in GC. The green yellow module showed the highest correlation ($R = -0.5$, $P < 0.001$) (Figure 2(c)). To construct a risk-scoring model associated with ferroptosis, 555 genes in the green yellow module were taken to intersect with 1846 DEGs for C1 and C2, and finally, 80 key genes were obtained.

3.3. Construction and Validation of Risk-Scoring Model. Through univariate Cox regression analysis, with $P < 0.01$ as a filter, 29 genes associated with GC prognosis were obtained in the training set (Figure 3(a)). To prevent the model from overfitting, we took Lasso regression analysis to test these 29 genes and determined that there was no over-fitting of the model for these 29 genes (Figures 3(b) and 3(c)). Finally, we identified 8 prognostic-related genes using multivariate Cox regression analysis (Figure 3(d)) and plotted K-M curves for 8 genes (Figure 4). Based on these 8 genes, we constructed a risk-scoring model for GC. Risk Score = 0.320*CTHRC1 + (−0.364)*PDPN + 0.410*PLOD2 + (−0.575)*GFPT2 + 0.418*ABCA1 + 0.570*GPR176 + 0.237*SERPINE1 + 0.192*DUSP1. According to the median risk score value, the GC samples were divided into high- and low-risk group. And we have drawn the K-M curve through "survival" package of R (Figure 5(a)). It was demonstrated that there was a significant survival difference between the low- and high-risk groups. In addition, the ROC analysis showed that the AUC of 1-, 3-, and 5-year survival were 0.721, 0.747, and 0.803, respectively. (Figure 5(b)) It meant that the model we constructed had great diagnostic efficacy in GC.

To ensure the accuracy of the risk-scoring model, we verified the model on an external validation set (GEO database) and found that the survival of low- and high-risk groups of the GEO dataset was significantly different in the K-M survival curve (Figure 5(c)). The ROC analysis showed that the AUC of 1, 3, and 5 years were 0.605, 0.615, and 0.594, respectively (Figure 5(d)). It demonstrated that the prognostic model of FRGs had good accuracy in the validation set.

3.4. Nomogram Construction through Risk Score and Clinicopathological Features. In the risk-scoring model

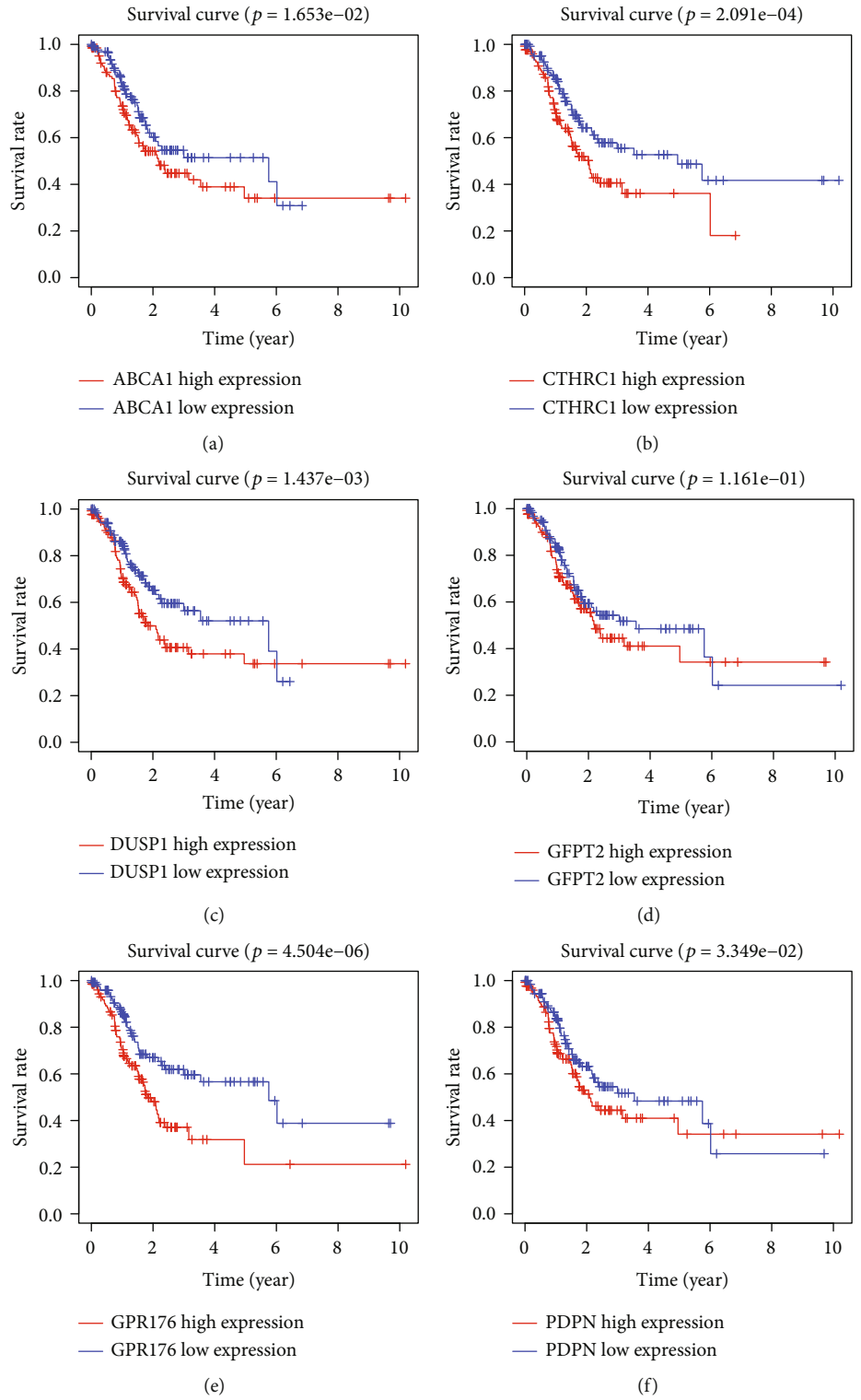

Figure 4: Continued.

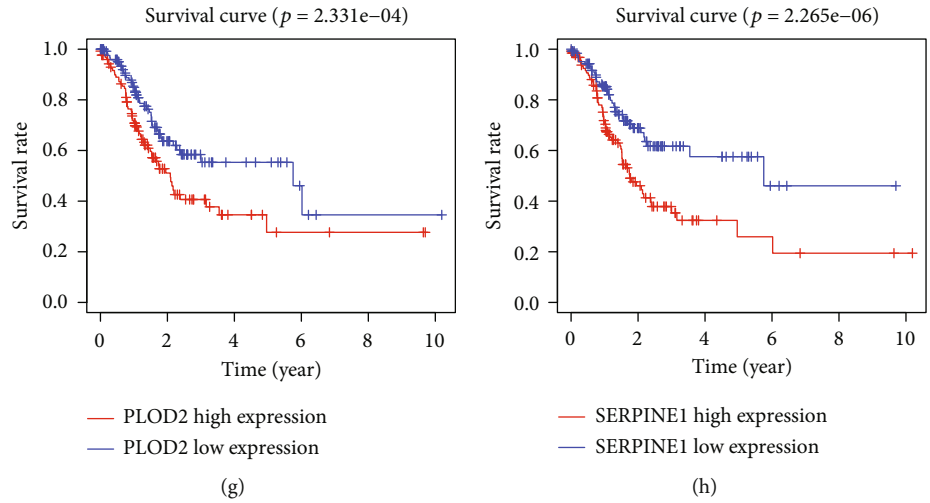

Figure 4: K-M survival curves of 8 genes with independent prognostic potency. K-M: Kaplan-Meir.

constructed based on 8 ferroptosis subcluster-related modular genes, we incorporated clinicopathological features in GC. Then, the analysis of eigenvalues was followed by Cox regression analysis. Prognosis of GC was correlated with age and risk score. And both of them were independent prognostic factors (Figure 6). At the same time, the analysis of K-M survival curves showed significant differences in survival at different age, gender, tumor grade, and stage (Figure 7). Based on clinicopathological features and risk score, we established a nomogram that could predict the prognosis of GC (Figure 8(a)). The 1-, 3-, and 5-year survival of GC could be predicted by scoring each characteristic value. Besides, we used ROC curves to determine their accuracy (Figure 8(b)). Through results of decision curve analysis (DCA), we believe that the nomogram has high clinical application value (Figure 8(c)). In conclusion, the model could accurately predict the survival of GC patients.

3.5. Functional Enrichment Analysis. We preformed GO and KEGG enrichment analysis to annotate the biological characteristics of 8 genes by "clusterProfiler" package in R (Figures 9(a) and 9(b)). GO enrichment analysis indicated that these genes were mainly enriched in extracellular matrix, organization extracellular structure, organization external encapsulating, wound healing, and other biological processes (BP). Besides, they were enriched in collagen-containing extracellular matrix, endoplasmic reticulum lumen, collagen trimer, and other cellular constituents (CC). Molecular functions (MF) were enriched in growth factor binding, extracellular matrix structural constituent, and cytokine binding extracellular matrix. KEGG analysis indicated that they were related to PI3K−Akt, TGF, JAK −STAT, and other metabolic signaling pathway.

3.6. Analysis of Immune Cell Infiltration. Through ssGSEA algorithm, we obtained 16 kinds of immune cells and 13 kinds of immune-related mechanisms in GC. It demonstrated that the degree of immune infiltration in low-risk group was lower than that in high-risk group (Figures 10(a) and 10(b)). Macrophages, mast cells, neutrophils, Treg, and T helper cells showed significantly different distribution, and T cells were the most abundant immune cells in GC tissue infiltration. The result suggested that the immune cells have a good response in high-risk group of GC. According to the ESTIMATE algorithm of "estimate" R package, the heat map showed that compared with the low-risk group, the high-risk group had lower tumor purity and higher stromal score, immune score, and estimate score. The tumor purity of TME decreased, and the infiltration of stromal and immune cells increased significantly ($P < 0.05$) (Figure 10(c)).

3.7. Analysis of TMB for GC. The TMB was a way for somatic cells to increase the types of antigens by mutation and thus resist cancer [26]. The TMB was calculated and compared between two groups by "maftools" package (Figures 11(a) and 11(b)). Higher TMB could generate more mutations and was more conducive to the body's resistance to the development of cancer. In this study, the waterfall diagrams showed that TTN and TP53 genes in the two groups had the highest mutation rates. TTN gene was 44% of mutations in both groups, while TP53 was 43% of the mutations in high-risk group and 33% of the mutations in low-risk group.

4. Discussion

GC is a common tumor worldwide, with a large number of cases, especially in East Asian countries. The prognosis of GC varies widely between countries. Early detection and intervention could improve the prognosis [1]. In this study, we developed a unique prognostic model for FRG in GC using TCGA and GSE84437 cohort data. Then, we constructed a quantitative scoring system and further evaluated the effect of FRG on immune infiltration. Ferroptosis, a novel form of cell death, is characterized by unique morphology, gene expression, and molecular pathways. Previous studies identified that GSH, GPX4 activity inhibition, and

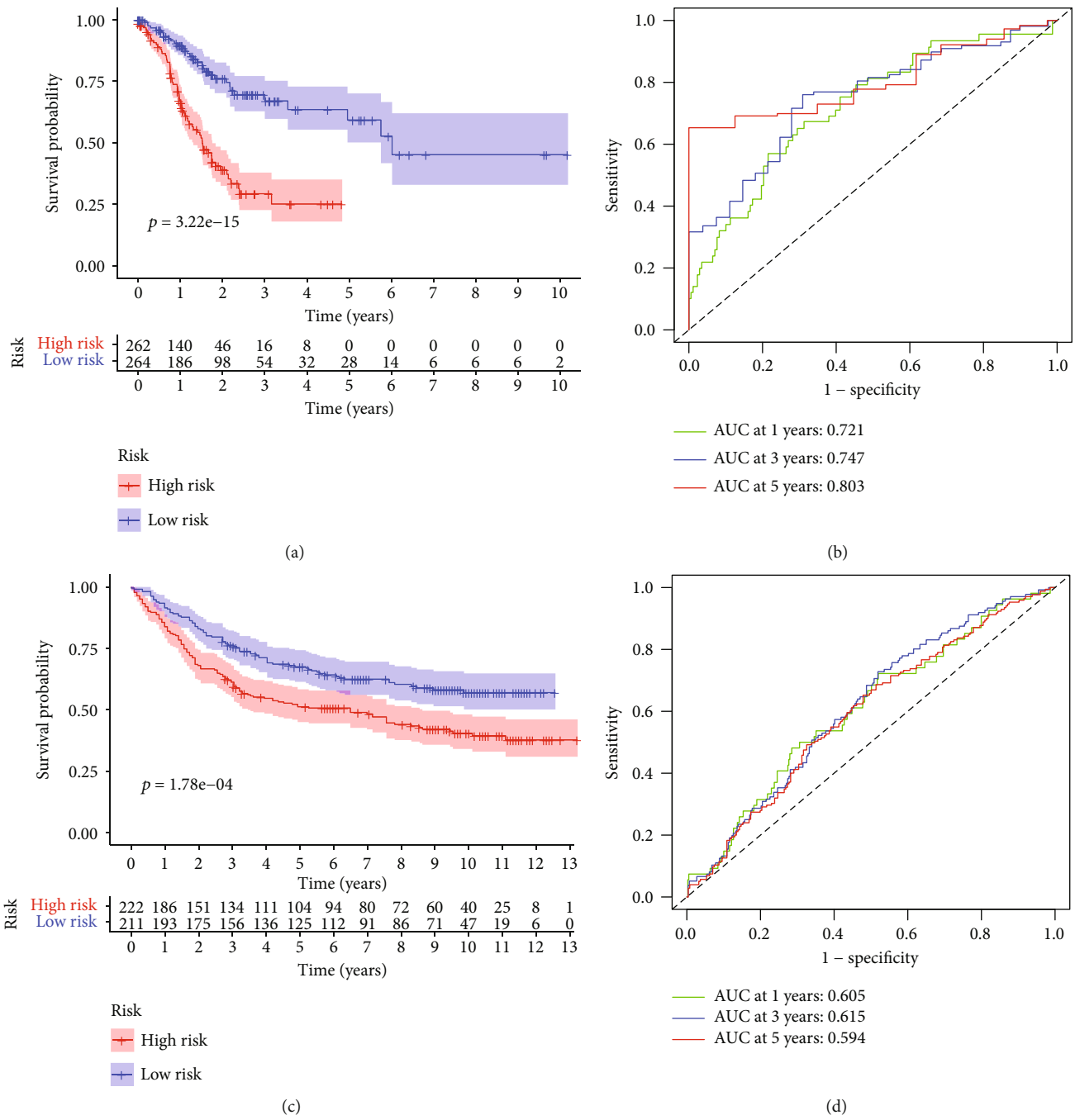

Figure 5: Identification and validation of FRGs signatures. (a) K-M survival curves of low- and high-risk groups in TCGA total cohort. (b) ROC curves of 1-, 3-, and 5-year survival for TCGA total cohort. (c) K-M survival curves of low- and high-risk groups in GEO cohort. (d) ROC curves of 1-, 3-, and 5-year survival for GEO cohort. FRGs: ferroptosis-related genes; K-M: Kaplan-Meir; TCGA: the Cancer Genome Atlas; GEO: Gene Expression Omnibus; ROC: receiver operating characteristic.

iron-dependent ROS burst were the critical factors inducing ferroptosis [27]. FRGs are associated with TIME and TMB, which is helpful to predict the prognosis of GC. Mutations in DNA damage-responsive genes are the main cause of elevated TMB and can be used to predict immune checkpoint inhibitor responses. Many mutations in the exon region of somatic cells lead to an increase in the production of neoantigens recognized by T cells, thereby enhancing the antitumor immune response. As a result, patients with high TMB may develop a stronger immune response and be more sensitive to immune checkpoint inhibitor therapy [28]. For example, activation of the Keap1/Nrf2/HO-1 pathway and ferritin phage-mediated ferroptosis contributed to EMT inhibition of GC cell proliferations and altered the cellular redox environment [29]. Besides, ferroptosis-related lncRNA regulated the invasiveness of GC. lncRNA-BDNF-

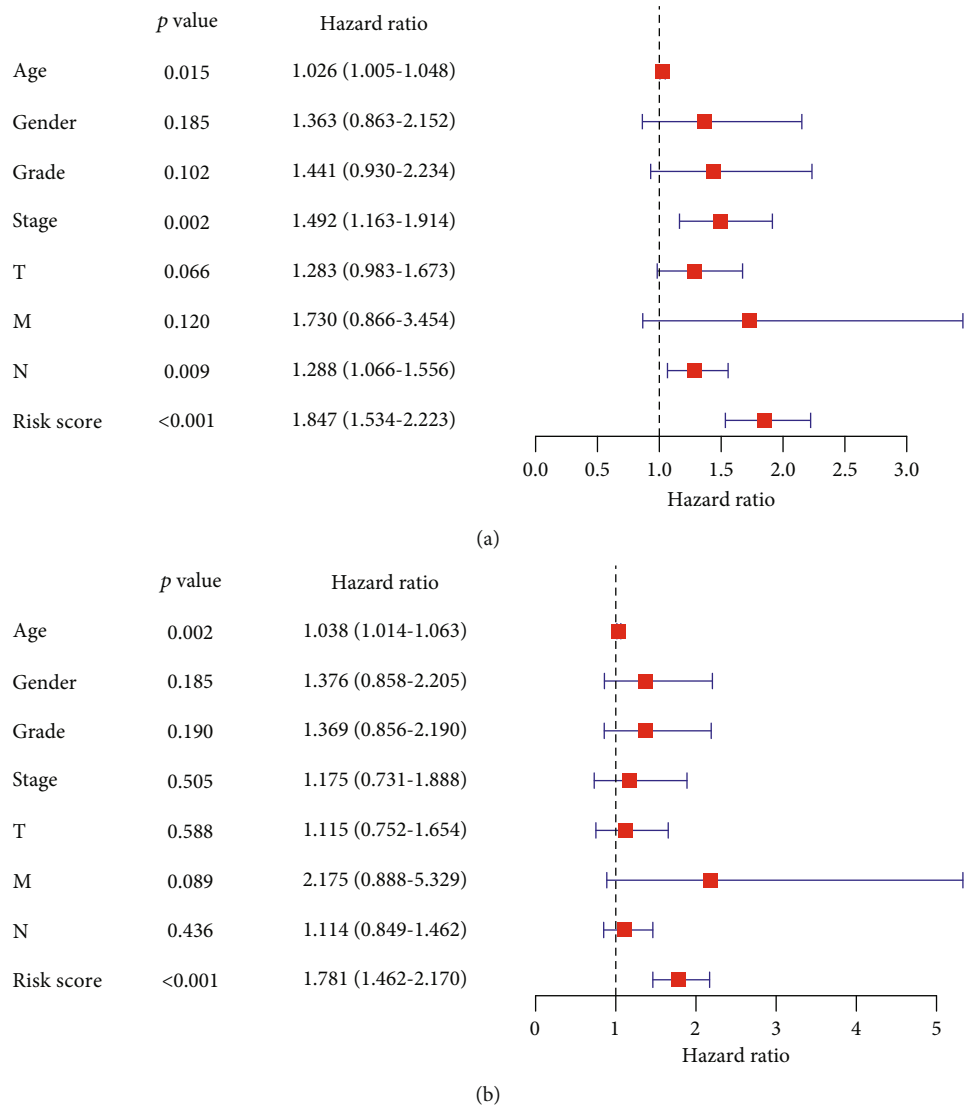

Figure 6: (a) Univariate and (b) multivariate Cox regression analysis of clinicopathological features.

AS/WDR5/FBXW7 axis regulated VDAC3 ubiquitination and then mediates ferroptosis in GC peritoneal metastasis [30]. Ferroptosis can also inhibit drug resistance in GC. Ferroptosis induced by ATF3 overexpression can reduce cisplatin resistance in GC [31]. Other studies have shown that change in lipid metabolism around cancer cells under stress determines the ferroptosis sensitivity of GC [32]. Interestingly, TMB was significant in high-risk group. Therefore, we can reasonably speculate that FRGs were key genes for the prognosis of GC.

In this study, through TCGA dataset, we identified two FRGs subclusters (C1 and C2) through NMF cluster analysis. There were significant differences in the survival status of the two clusters. WGCNA was applied to identify ferroptosis subcluster-related modular genes. Through Cox regression analysis, we selected the prognostic genes related to ferroptosis and established the prognostic risk-scoring model. We also used GSE84437 dataset to externally verify the prognostic risk-scoring model. At the same time, we integrated clinicopathological features and risk-scoring model to construct a nomogram for clinical application. The function of TIME and TMB was studied to preliminarily clarify the mechanism of its influence on prognosis, so as to provide basis for clinical diagnosis, individualized immune-targeted therapy, and antitumor drug resistance.

Based on the above intersection genes, a novel prognostic model integrating 8 FRGs (CTHRC1, PDPN, PLOD2, GFPT2, ABCA1, GPR176, SERPINE1, and DUSP1) was firstly constructed. For example, CTHRC1 was used as a marker of colorectal cancer (CRC) intratumoral metastasis, and Zhang et al. confirmed that CTHRC1 promoted liver metastasis of CRC and earlier predicted targets by TGF-β remodeling infiltrating macrophage signaling [33]. PDPN (+) CAF, the representative of immunosuppressive microenvironment of lung adenocarcinoma, can induce macrophage M2 polarization and inhibit immune-related lymphocytes, serving as a bridge between fiber microenvironment and immunosuppression [34]. In patients with large tumor or

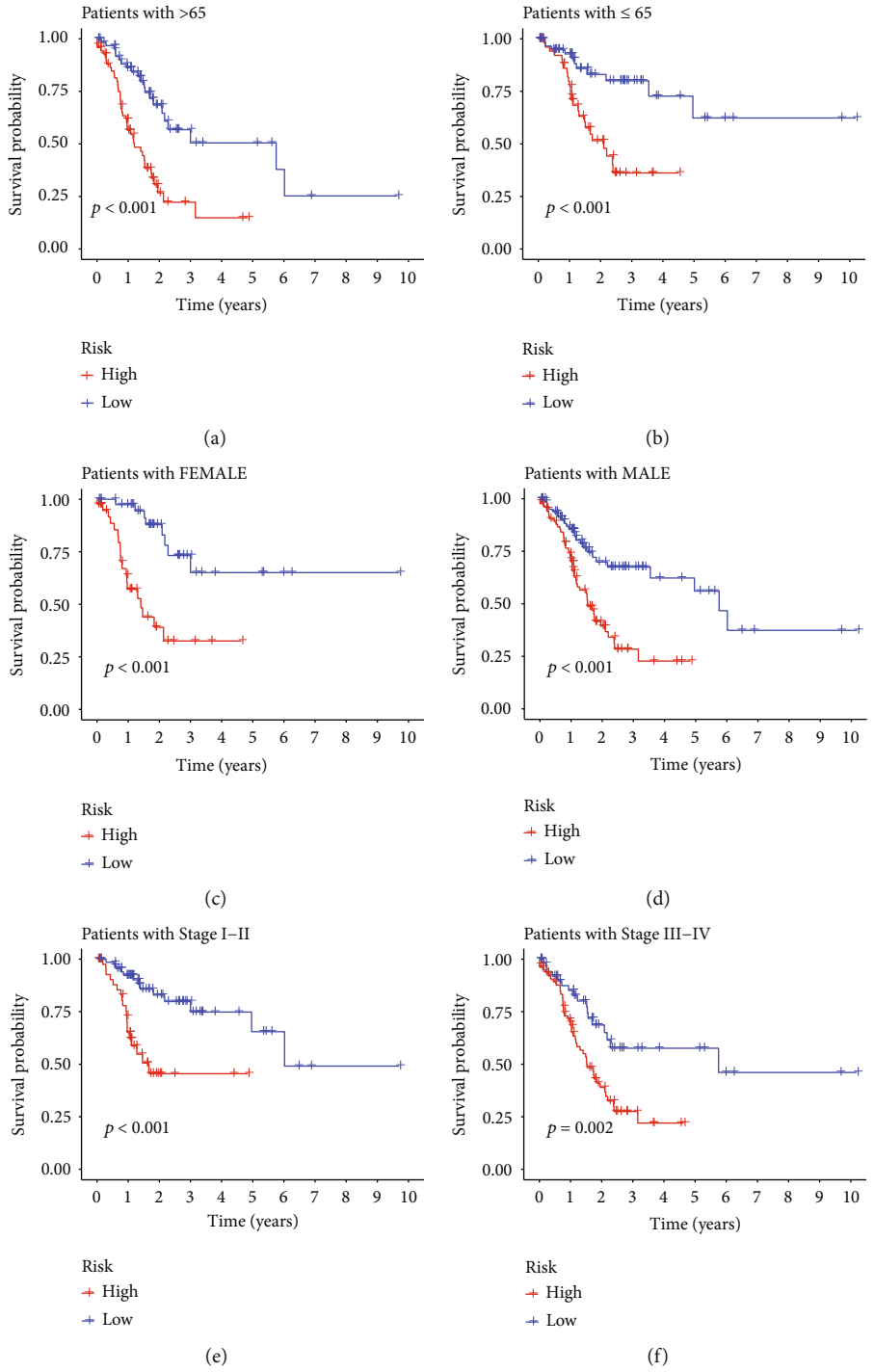

Figure 7: Continued.

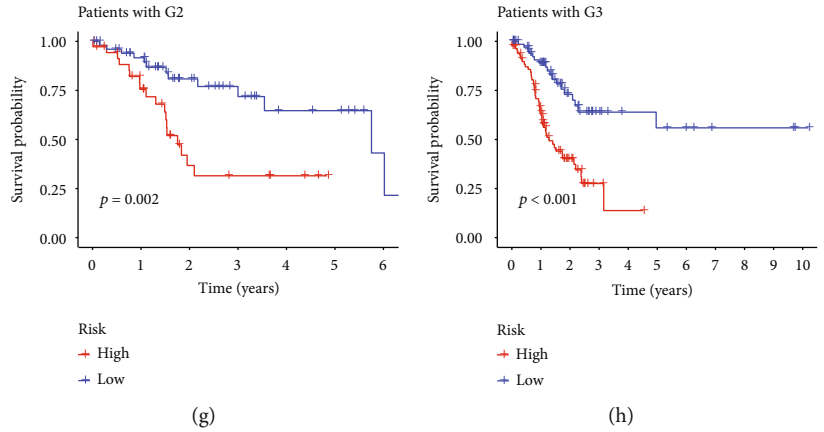

FIGURE 7: Survival analysis of clinicopathological features. (a–h) K-M survival curves of low- and high-risk groups at age (≤65, >65), gender (female, male), stage (stage I-II, stage III-IV), and grade (G2, G3).

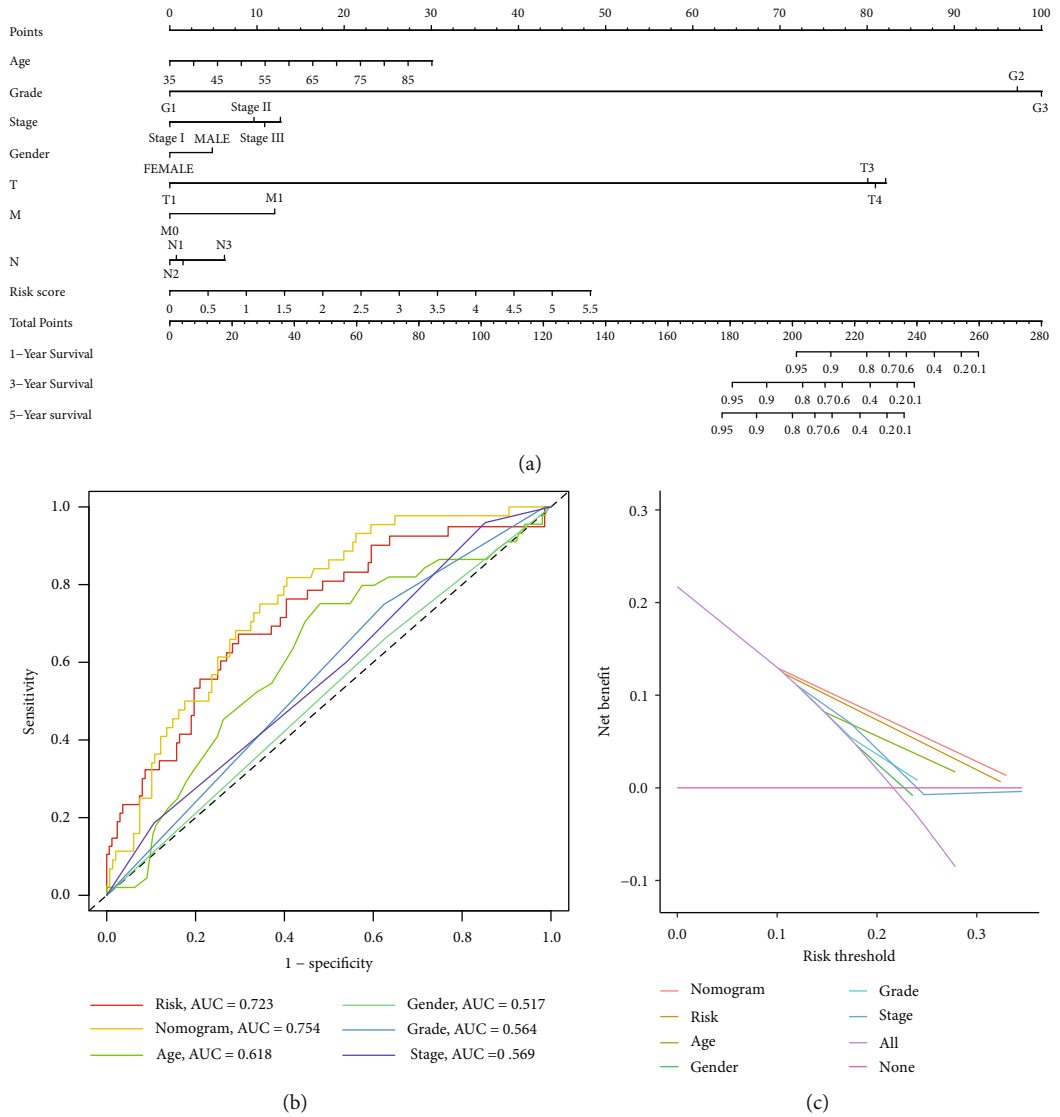

FIGURE 8: Construction and validation of a prognostic model for GC patients. (a) Nomogram for predicting GC patients for 1-, 3-, and 5-year survival based on the TCGA total cohort. (b) ROC curve containing age, gender, grade, stage, risk score, and nomogram. (c) DCA of the nomogram. The net benefit was plotted versus the threshold probability. GC: gastric cancer; TCGA: the Cancer Genome Atlas; ROC: receiver operating characteristic; DCA: decision curve analysis.

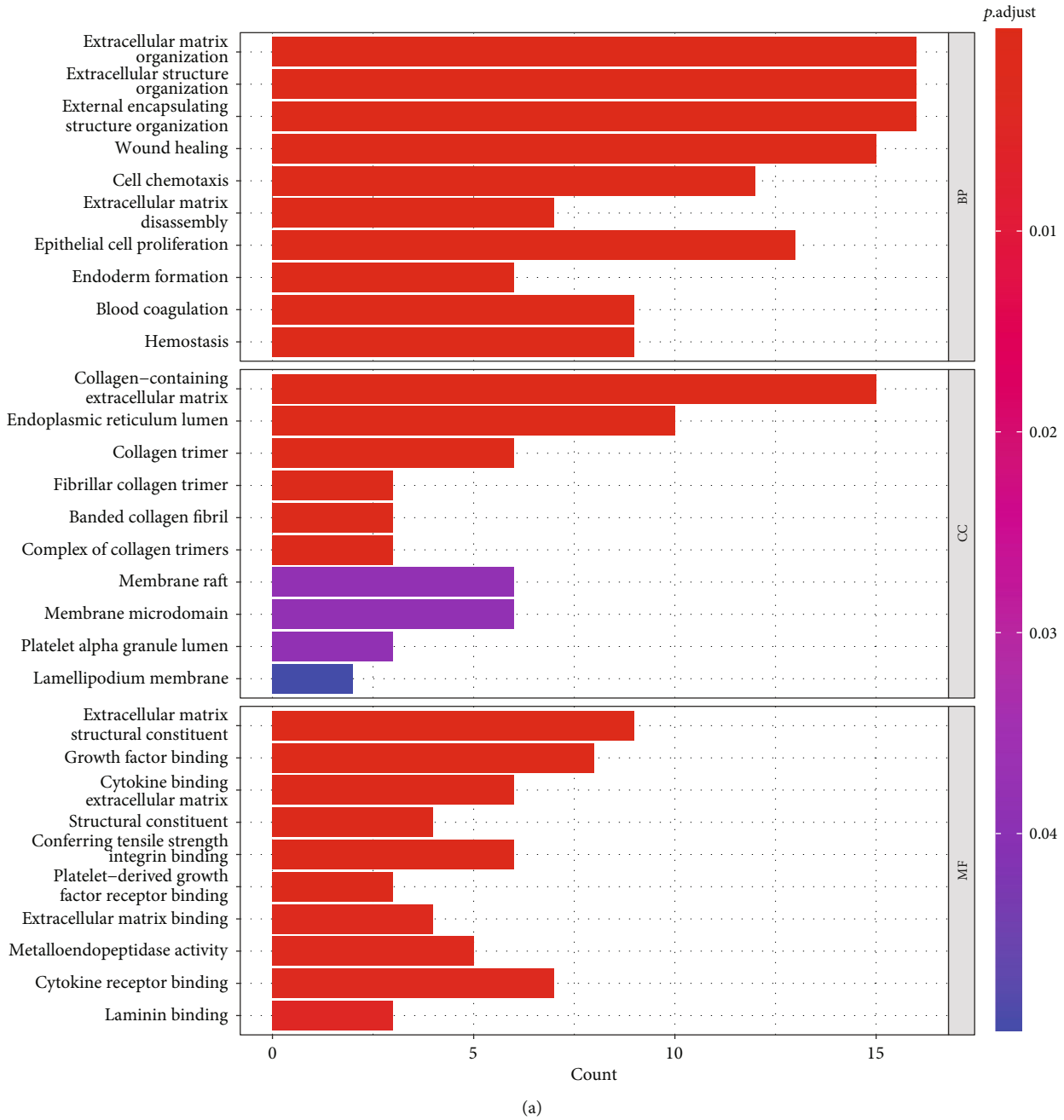

(a)

Figure 9: Continued.

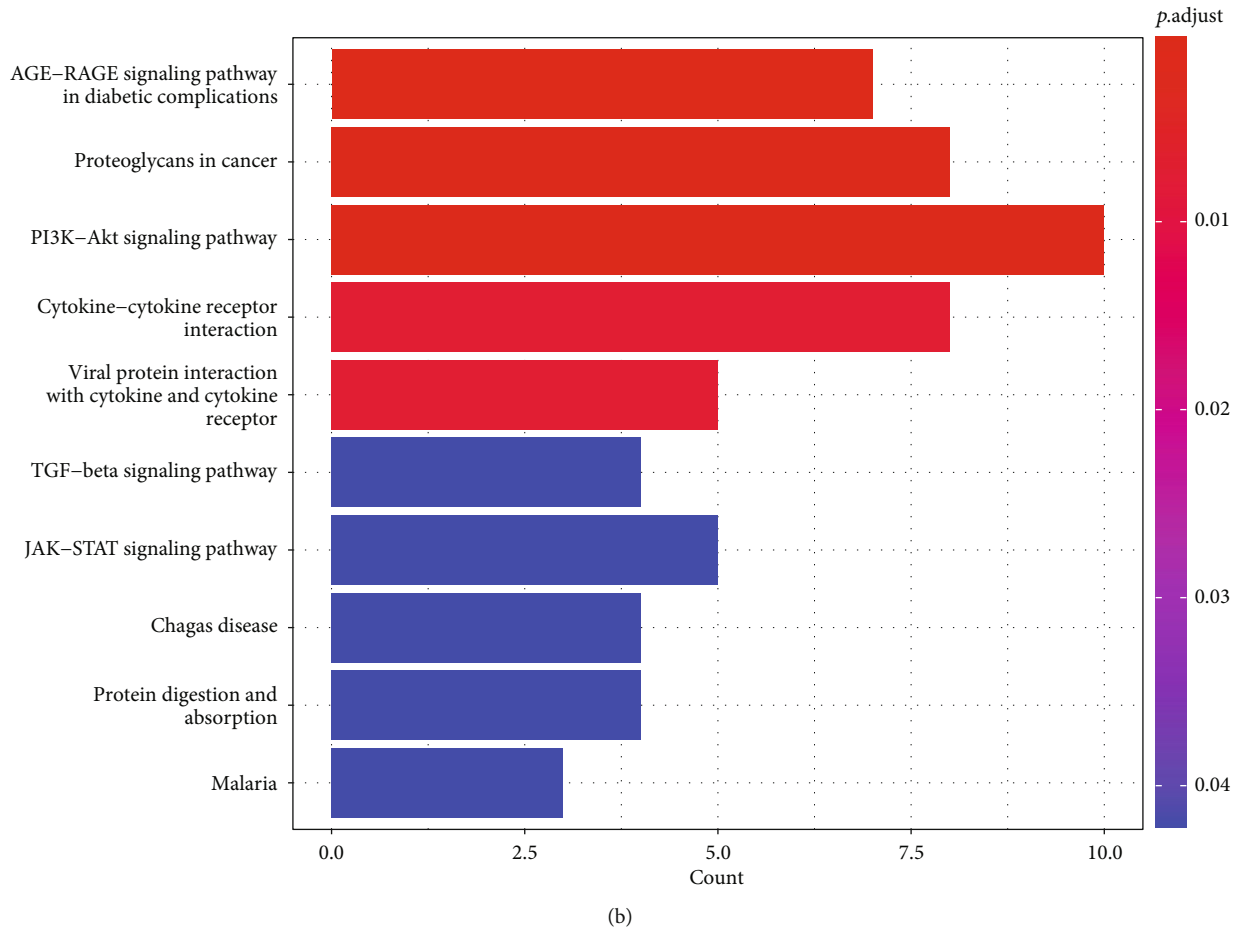

Figure 9: GO and KEGG analysis of prognostic FRGs. (a) Histogram of GO enrichment analysis for prognostic FRGs. (b) Histogram of KEGG enrichment analysis for prognostic FRGs. GO: gene ontology; KEGG, Kyoto Encyclopedia of Genes and Genomes; FRGs: ferroptosis-related genes.

solid tumor metastases, PDPN expression induced poor prognosis in cancer-associated fibrous tissue [35]. And PLOD family genes can affect the progression and prognosis of human digestive tract tumors. As a member of them, PLOD2 was not only related to the histological grading of pancreatic cancer, but also overexpressed in TP53 and KRAS types [36]. GFPT2 in the study was also closely related to the prognosis, microenvironment, immunity, and drug sensitivity of other digestive system tumors, and the specific internal mechanism remained to be further studied [37]. Besides, GFPT2 expression was inhibited by the oxidative stress regulator GSK3-β. GFPT2 was a marker of poor prognosis in the D492 EMT model of breast cancer, which controlled growth and invasion [38]. Compared with other FRGs, ABCA1 may be a tumor suppressor that was methylated after dysregulation of transforming growth factor-β signaling in ovarian cancer, presenting a poor prognosis. In contrast, SERPINE1-upregulated GC patients showed poor OS and PFS. It was considered that it may regulate VEFF and JAK-STAT3 inflammatory signaling pathways to affect GC cell proliferation and migration [39]. DUSP1 was also observed to be an oncogene associated with drug resistance during cancer intervention. At present, the role of GPR176 in GC prognosis is unclear. Upregulation of GPR176 stimulates the function of Sirtuin6. Sirtuin6 overexpression inhibited breast cancer stem cell biogenesis in cells with a PI3K mutation and murine PyMT mammary tumor progression in vivo [40]. And there are few reports on the use of ferroptosis to correlate TIME and TMB in GC prognostic models.

FRGs plays a crucial role in TME, as shown in Figure 10(a). By comparing the immune infiltration between risk score groups, we found that T cells were the most extensively infiltrated immune cells in GC samples, and macrophages, mast, and T helper cells showed significantly different distribution [41, 42]. Some studies have reported the immune potential of tertiary lymphocyte structures around primary GC, in which DC was a set that affected the reactivity, cytotoxicity, and monitoring escape status of anticancer cells [43]. Clinical validation of GC suggested that TAM M1 macrophages were associated with antitumor activity. M2 promoted pro-angiogenic and immunosuppressive signals in tumors, such as diffuse GC subtypes [44]. In the high-risk group, T cell infiltration levels were elevated. It meant that high-risk group with FRGs had a better chance of taking advantage of

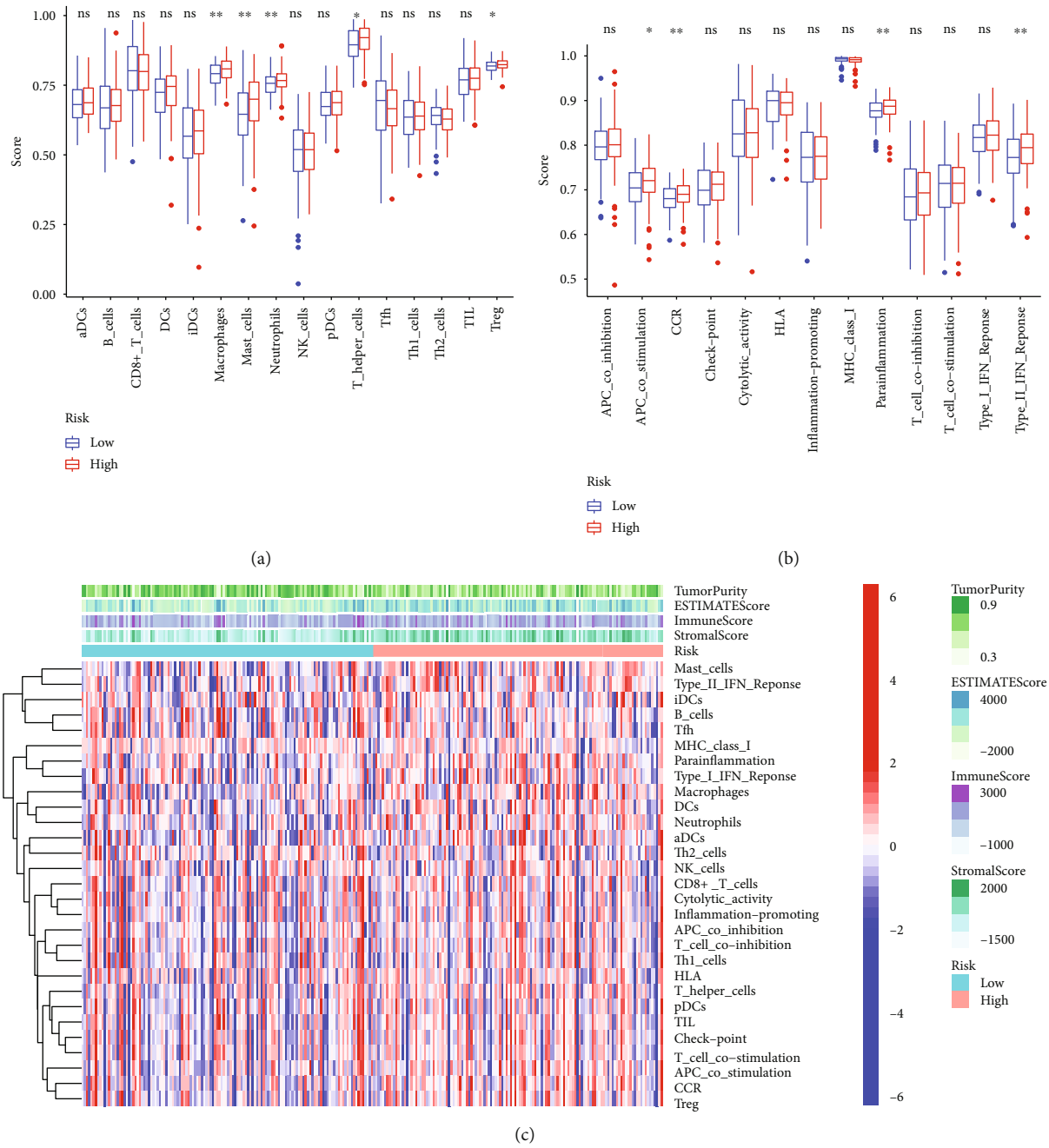

Figure 10: Analysis of immune infiltration. (a) Analyze the immune differences between low- and high-risk groups from 16 immune cells. (b) Analyze the immune differences between low- and high-risk groups from 13 immune-related functions. (c) Heat map of stromal score, immune score, and estimate score in low- and high-risk groups.

cellular immune-personalized therapy regiments. We also enriched biological signaling pathways, for instance, PI3K −Akt, TGF-β, and JAK-STAT. Recent studies have indicated that MAPK pathway participated in resistance to GC ferroptosis. And inhibition of MAPK signaling can protect GC cells from ferroptosis [45]. In addition, activated TGF-β was identified to promote ferroptosis [46]. In our study, the tumor purity of TME decreased, and the infiltration of stromal and immune cells increased significantly. Low purity of GC in high-risk group was associated with poor prognosis. Therefore, these results detailed the conditions and ways in which FRGs regulate GC development, which may be conducive to further study of immune escape surveillance. In addition, ferroptosis-related reactive oxygen species and iron uptake could lead to somatic nonsynonymous mutations and microsatellite instability, resulting in increasing immunogenicity and immune infiltrates [47, 48], which was consistent with our findings.

There are still a few limitations. First, all data sources came from public databases. There is a lack of real world samples and prospective clinical data validation. Secondly,

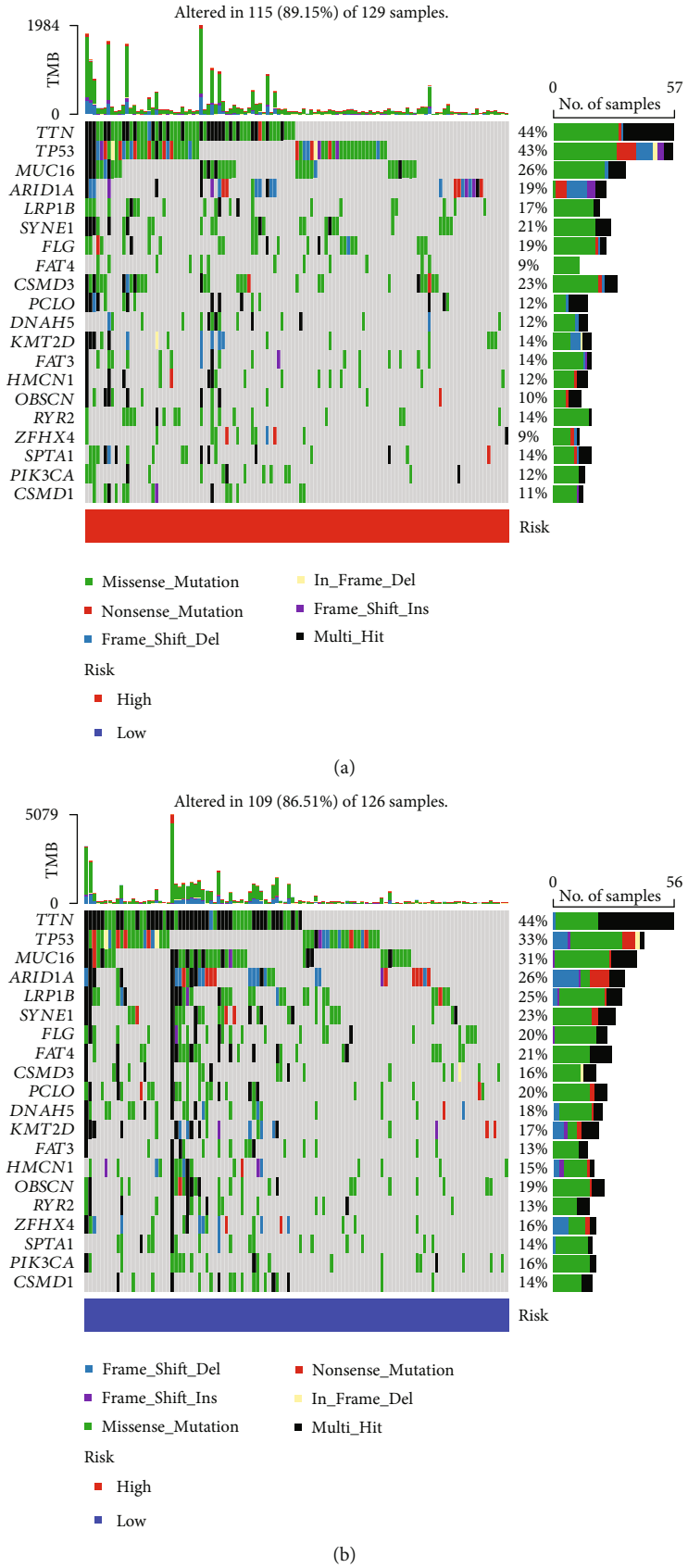

Figure 11: The waterfall diagram demonstrates the top 20 driver genes with the highest mutation frequency in high-risk group (a) and low-risk group (b).

ferroptosis is not a unique mechanism in GC, and whether ferroptosis is involved in the mechanism of TIME is still uncertain. Besides, FRGs obtained from previous studies may be incomplete, which requires further improvement of the FRGs database from future studies. Finally, whether prognosis FRGs directly regulates the ferroptosis process in GC requires further experimental verification.

5. Conclusion

In conclusion, the risk-scoring model based on 8 ferroptosis subcluster-related modular genes has shown outstanding advantages in predicting patient prognosis. The interaction of ferroptosis in GC development may provide new insights into exploring molecular mechanisms and targeted therapies for GC patients.

Data Availability

Data available on request from the authors.

Conflicts of Interest

The authors declare that there are no conflicts of interest regarding the publication of this paper.

Authors' Contributions

The author contributions are as follows: H.D, F.G, and Y.L designed the study; H.D and Y.L developed the inclusion and exclusion criteria; B.L and Z.M conducted the statistical analysis; H.D wrote the article; X.Q, X.H, and Y.M reviewed the article. Huachu Deng, Yongjian Lin, and Fu Gan contributed equally to this work.

Acknowledgments

We thank the First Affiliated Hospital of Guangxi Medical University for their help in the statistical analysis. This study is supported by the Guangxi Medical and Health Appropriate Technology Development and Promotion Application Project (S201657).

References

[1] E. C. Smyth, M. Nilsson, H. I. Grabsch, N. C. T. van Grieken, and F. Lordick, "Gastric cancer," *Lancet*, vol. 396, no. 10251, pp. 635–648, 2020.

[2] R. L. Siegel, K. D. Miller, H. E. Fuchs, and A. Jemal, "Cancer statistics, 2022," *CA: a Cancer Journal for Clinicians*, vol. 72, no. 1, pp. 7–33, 2022.

[3] T. Yokota, S. Ishiyama, T. Saito, S. Teshima, M. Shimotsuma, and H. Yamauchi, "Treatment strategy of limited surgery in the treatment guidelines for gastric cancer in Japan," *Lancet Oncology*, vol. 4, no. 7, pp. 423–428, 2003.

[4] W. Feng, Y. Wang, S. Chen, and X. Zhu, "Intra-tumoral heterogeneity and immune responses predicts prognosis of gastric cancer," *Aging-Us*, vol. 12, no. 23, pp. 24333–24344, 2020.

[5] G. Maconi, G. Manes, and G. B. Porro, "Role of symptoms in diagnosis and outcome of gastric cancer," *World Journal of Gastroenterology*, vol. 14, no. 8, pp. 1149–1155, 2008.

[6] S. S. Joshi and B. D. Badgwell, "Current treatment and recent progress in gastric cancer," *CA: a Cancer Journal for Clinicians*, vol. 71, no. 3, pp. 264–279, 2021.

[7] X. Li, B. Pasche, W. Zhang, and K. Chen, "Association of muc16 mutation with tumor mutation load and outcomes in patients with gastric cancer," *JAMA Oncology*, vol. 4, no. 12, pp. 1691–1698, 2018.

[8] D. Moujalled, A. Strasser, and J. R. Liddell, "Molecular mechanisms of cell death in neurological diseases," *Cell Death and Differentiation*, vol. 28, no. 7, pp. 2029–2044, 2021.

[9] L. Galluzzi, O. Kepp, F. K. Chan, and G. Kroemer, "Necroptosis: mechanisms and relevance to disease," *Annual Review of Pathology*, vol. 12, no. 1, pp. 103–130, 2017.

[10] N. Mizushima, "Autophagy: process and function," *Genes & Development*, vol. 21, no. 22, pp. 2861–2873, 2007.

[11] D. Tang, X. Chen, and G. Kroemer, "Cuproptosis: a copper-triggered modality of mitochondrial cell death," *Cell Research*, vol. 32, no. 5, pp. 417-418, 2022.

[12] X. Jiang, B. R. Stockwell, and M. Conrad, "Ferroptosis: mechanisms, biology and role in disease," *Nature Reviews Molecular Cell Biology*, vol. 22, no. 4, pp. 266–282, 2021.

[13] Y. Mou, J. Wang, J. Wu et al., "Ferroptosis, a new form of cell death: opportunities and challenges in cancer," *Journal of Hematology & Oncology*, vol. 12, no. 1, p. 34, 2019.

[14] X. Chen, R. Kang, G. Kroemer, and D. Tang, "Broadening horizons: the role of ferroptosis in cancer," *Nature Reviews. Clinical Oncology*, vol. 18, no. 5, pp. 280–296, 2021.

[15] H. Ni, H. Qin, C. Sun et al., "Mir-375 reduces the stemness of gastric cancer cells through triggering ferroptosis," *Stem Cell Research & Therapy*, vol. 12, no. 1, p. 325, 2021.

[16] C. Wang, M. Shi, J. Ji et al., "Stearoyl-coa desaturase 1 (scd1) facilitates the growth and anti-ferroptosis of gastric cancer cells and predicts poor prognosis of gastric cancer," *Aging-Us*, vol. 12, no. 15, pp. 15374–15391, 2020.

[17] Y. Liu, Z. Song, Y. Liu et al., "Identification of ferroptosis as a novel mechanism for antitumor activity of natural product derivative a2 in gastric cancer," *Acta Pharmaceutica Sinica B*, vol. 11, no. 6, pp. 1513–1525, 2021.

[18] T. Liu, H. Luo, J. Zhang, X. Hu, and J. Zhang, "Molecular identification of an immunity- and ferroptosis-related gene signature in non-small cell lung cancer," *BMC Cancer*, vol. 21, no. 1, p. 783, 2021.

[19] J. Jin, C. Liu, S. Yu et al., "A novel ferroptosis-related gene signature for prognostic prediction of patients with lung adenocarcinoma," *Aging (Albany NY)*, vol. 13, no. 12, pp. 16144–16164, 2021.

[20] Y. Hong, M. Lin, D. Ou, Z. Huang, and P. Shen, "A novel ferroptosis-related 12-gene signature predicts clinical prognosis and reveals immune relevancy in clear cell renal cell carcinoma," *BMC Cancer*, vol. 21, no. 1, p. 831, 2021.

[21] M. E. Ritchie, B. Phipson, D. Wu et al., "Limma powers differential expression analyses for rna-sequencing and microarray studies," *Nucleic Acids Research*, vol. 43, no. 7, p. e47, 2015.

[22] J. Xia, Y. Zhang, J. Song, Y. Chen, Y. Wang, and S. Liu, "Revisiting dimensionality reduction techniques for visual cluster analysis: an empirical study," *IEEE Transactions on Visualization and Computer Graphics*, vol. 28, no. 1, pp. 529–539, 2022.

[23] P. Langfelder and S. Horvath, "Wgcna: an r package for weighted correlation network analysis," *BMC Bioinformatics*, vol. 9, no. 1, p. 559, 2008.

[24] N. Simon, J. Friedman, T. Hastie, and R. Tibshirani, "Regularization paths for cox's proportional hazards model via coordinate descent," *Journal of Statistical Software*, vol. 39, no. 5, pp. 1–13, 2011.

[25] Y. Cao, H. Zhu, J. Tan et al., "Development of an immune-related lncrna prognostic signature for glioma," *Frontiers in Genetics*, vol. 12, p. 678436, 2021.

[26] A. Addeo, A. Friedlaender, G. L. Banna, and G. J. Weiss, "Tmb or not tmb as a biomarker: that is the question," *Critical Reviews in Oncology/Hematology*, vol. 163, p. 103374, 2021.

[27] W. S. Yang and B. R. Stockwell, "Ferroptosis: death by lipid peroxidation," *Trends in Cell Biology*, vol. 26, no. 3, pp. 165–176, 2016.

[28] H. C. Zhang, S. H. Deng, Y. N. Pi et al., "Identification and validation in a novel quantification system of ferroptosis patterns for the prediction of prognosis and immunotherapy response in left- and right-sided colon cancer," *Frontiers in Immunology*, vol. 13, p. 855849, 2022.

[29] D. Guan, W. Zhou, H. Wei et al., "Ferritinophagy-mediated ferroptosis and activation of keap1/nrf2/ho-1 pathway were conducive to emt inhibition of gastric cancer cells in action of 2,2'-di-pyridineketone hydrazone dithiocarbamate butyric acid ester," *Oxidative Medicine and Cellular Longevity*, vol. 2022, Article ID 3920664, 2022.

[30] G. Huang, Z. Xiang, H. Wu et al., "The lncrna bdnf-as/wdr5/fbxw7 axis mediates ferroptosis in gastric cancer peritoneal metastasis by regulating vdac3 ubiquitination," *International Journal of Biological Sciences*, vol. 18, no. 4, pp. 1415–1433, 2022.

[31] D. Fu, C. Wang, L. Yu, and R. Yu, "Induction of ferroptosis by atf3 elevation alleviates cisplatin resistance in gastric cancer by restraining nrf2/keap1/xct signaling," *Cellular & Molecular Biology Letters*, vol. 26, no. 1, p. 26, 2021.

[32] J.-Y. Lee, M. Nam, H. Y. Son et al., "Polyunsaturated fatty acid biosynthesis pathway determines ferroptosis sensitivity in gastric cancer," *Proceedings of the National Academy of Sciences of the United States of America*, vol. 117, no. 51, pp. 32433–32442, 2020.

[33] X.-L. Zhang, L.-P. Hu, Q. Yang et al., "CTHRC1 promotes liver metastasis by reshaping infiltrated macrophages through physical interactions with TGF-β receptors in colorectal cancer," *Oncogene*, vol. 40, no. 23, pp. 3959–3973, 2021.

[34] T. Sakai, K. Aokage, S. Neri et al., "Link between tumor-promoting fibrous microenvironment and an immunosuppressive microenvironment in stage i lung adenocarcinoma," *Lung Cancer*, vol. 126, pp. 64–71, 2018.

[35] K. Hirayama, H. Kono, Y. Nakata et al., "Expression of podoplanin in stromal fibroblasts plays a pivotal role in the prognosis of patients with pancreatic cancer," *Surgery Today*, vol. 48, no. 1, pp. 110–118, 2018.

[36] J. Zhang, Y. Tian, S. Mo, and X. Fu, "Overexpressing plod family genes predict poor prognosis in pancreatic cancer," *International journal of general medicine*, vol. Volume 15, pp. 3077–3096, 2022.

[37] X. Ding, H. Liu, Y. Yuan, Q. Zhong, and X. Zhong, "Roles of gfpt2 expression levels on the prognosis and tumor microenvironment of colon cancer," *Frontiers in Oncology*, vol. 12, pp. 811559–811559, 2022.

[38] Q. Wang, S. T. Karvelsson, A. Kotronoulas, T. Gudjonsson, S. Halldorsson, and O. Rolfsson, "Glutamine-fructose-6-phosphate transaminase 2 (gfpt2) is upregulated in breast epithelial-mesenchymal transition and responds to oxidative stress," *Molecular & Cellular Proteomics*, vol. 21, no. 2, p. 100185, 2022.

[39] S. Chen, Y. Li, Y. Zhu et al., "Serpine1 overexpression promotes malignant progression and poor prognosis of gastric cancer," *Journal of Oncology, vol.*, vol. 2022, pp. 1–17, 2022.

[40] D. J. Schultz, A. Krishna, S. L. Vittitow et al., "Transcriptomic response of breast cancer cells to anacardic acid," *Scientific Reports*, vol. 8, no. 1, p. 8063, 2018.

[41] H. Zhang, R. Yue, P. Zhao et al., "Proinflammatory follicular helper t cells promote immunoglobulin g secretion, suppress regulatory b cell development, and correlate with worse clinical outcomes in gastric cancer," *Tumor Biology*, vol. 39, no. 6, p. 101042831770574, 2017.

[42] Y. Yamada, H. Saito, and M. Ikeguchi, "Prevalence and clinical relevance of th17 cells in patients with gastric cancer," *Journal of Surgical Research*, vol. 178, no. 2, pp. 685–691, 2012.

[43] Y. Yamakoshi, H. Tanaka, C. Sakimura et al., "Immunological potential of tertiary lymphoid structures surrounding the primary tumor in gastric cancer," *International Journal of Oncology*, vol. 57, no. 1, pp. 171–182, 2020.

[44] V. Gambardella, J. Castillo, N. Tarazona et al., "The role of tumor-associated macrophages in gastric cancer development and their potential as a therapeutic target," *Cancer Treatment Reviews*, vol. 86, p. 102015, 2020.

[45] L. Magnelli, N. Schiavone, F. Staderini, A. Biagioni, and L. Papucci, "Map kinases pathways in gastric cancer," *International Journal of Molecular Sciences*, vol. 21, no. 8, p. 2893, 2020.

[46] D. H. Kim, W. D. Kim, S. K. Kim, D. H. Moon, and S. J. Lee, "Tgf-β1-mediated repression of slc7a11 drives vulnerability to gpx4 inhibition in hepatocellular carcinoma cells," *Cell Death & Disease*, vol. 11, no. 5, p. 406, 2020.

[47] J. Ma, X. Hu, Y. Yao et al., "Characterization of two ferroptosis subtypes with distinct immune infiltration and gender difference in gastric cancer," *Frontiers in Nutrition*, vol. 8, 2021.

[48] Y.-C. Yan, G.-X. Meng, Z.-N. Ding et al., "Somatic mutation and expression of bap1 in hepatocellular carcinoma: an indicator for ferroptosis and immune checkpoint inhibitor therapies," *Journal of Cancer*, vol. 13, no. 1, pp. 88–101, 2022.

Hindawi
Journal of Oncology
Volume 2022, Article ID 4811260, 13 pages
https://doi.org/10.1155/2022/4811260

Research Article

LIMS2 is Downregulated in Osteosarcoma and Inhibits Cell Growth and Migration

Chenying Su,[1] Xiaona Cai,[2] Taotao Xu,[3] Yungang Wu,[1] Licong Wang,[1] Pinjie Chen,[1] and Chenxian Su[4]

[1]*Department of Traditional Chinese Medicine Orthopedics, The First Affiliated Hospital of Wenzhou Medical University, Wenzhou, Zhejiang 325000, China*
[2]*Department of Ultrasonography, The First Affiliated Hospital of Wenzhou Medical University, Wenzhou, Zhejiang 325000, China*
[3]*Department of Orthopedics, The First Affiliated Hospital of Zhejiang Chinese Medical University, Hangzhou, Zhejiang 310006, China*
[4]*Department of Orthopedics, The First Affiliated Hospital of Wenzhou Medical University, Wenzhou, Zhejiang 325000, China*

Correspondence should be addressed to Chenxian Su; cxsu8002@163.com

Received 9 August 2022; Accepted 27 September 2022; Published 13 October 2022

Academic Editor: İbrahim Hakkı Cigerci

Background/objective. LIM and LIM zinc finger domain containing 2 (*LIMS2*) is one of the two members of LIMS family, which plays crucial roles in regulating cell-extracellular matrix adhesion and cell motility. Here, we explored the expression and methylation levels of *LIMS2* in osteosarcoma (OS) and the role of *LIMS2* in OS progression. *Methods*. GEO, GEPIA, and UALCAN databases were used to assess *LIMS2* expression in OS. UALCAN and CCLE databases were applied to assess the methylation levels of *LIMS2* in OS tissues and cells, which was verified in OS cells using the methylation specific PCR. The effects of *LIMS2* on regulating OS cell growth, migration and invasion were determined by CCK-8, Edu staining, and transwell chambers, respectively. The role of *LIMS2* in the activation of MAPK signaling was assessed using western blotting assay in OS cells. *Results*. *LIMS2* expression was declined in OS tissues and cells, while its methylation level was increased. The low expression of *LIMS2* was associated with shorter overall survival and disease-free survival. Overexpression of *LIMS2* inhibited cell growth, migration, and invasion and decreased the levels of p-ERK/ERK, p-P38/P38, and p-JNK/JNK. *Conclusion*. *LIMS2* expression was decreased in OS, which was associated with hypermethylation level and poor prognosis. *LIMS2* overexpression inhibited OS cell growth and migration, which may be caused by the suppression of MAPK signaling.

1. Introduction

Osteosarcoma (OS), which mostly affects adolescents, is the most frequently detected primary bone malignant tumor [1, 2]. The 5-year survival rate of low-grade OS is >70%, but drops significantly to below 20% in patients with high-grade OS, which is characterized by early metastasis and high recurrence rate [3, 4]. Unfortunately, about 20% of OS are diagnosed with metastasis at first diagnosis, resulting in poor response rate and prognosis [1]. Thus, it is of great significance to further reveal the mechanisms underlying the progression of OS.

LIMS family consisting of two members, *LIMS1* (also known as *PINCH-1*) and *LIMS2* (also known as *PINCH-2*), plays crucial roles in regulation cell-extracellular matrix adhesion and movement [5–7]. *LIMS1* and *LIMS2* share 92% sequence homology and compete for binding to the ankyrin repeat domain of ILK with similar affinities [8]. Like *LIMS1*, studies have shown that *LIMS2* takes part in cancer migration and invasion [9–11]. The expression of *LIMS2* was decreased in gastric cancer, which was significantly associated with the increased CpG island methylation. In addition, silencing of *LIMS2* promoted the proliferation and migration of gastric cancer cells [12]. Moreover, *LIMS2* expression was declined in colon cancer, and *LIMS2* overexpression could inhibit the migration of colon cancer cells [11]. However, the role of *LIMS2* in the progression of other types of cancers, such as OS remains unknown.

Table 1: Primer sequences.

Gene	Sense (5′-3′)	Antisense (5′-3′)
LIMS2	GAGCGGCTCTTGGCCTTTTT	GTACAGCTCCCCATTGCTGT
β-Actin	TGGAACGGTGAAGGTGACAG	CGCATCTCATATTTGGAATGACT

In this study, we analyzed *LIMS2* expressions in OS using GEO and TCGA databases, and the results revealed that *LIMS2* expression was decreased in OS biopsy samples. In addition, UALCAN and CCLE databases revealed that the methylation level of *LIMS2* promoter in OS tissues and cells were increased. All these findings suggested that *LIMS2* may play a role in the progression of OS. To this end, we conducted this study to explore *LIMS2* expression in OS and to reveal its role in the progression of OS and its potential mechanisms.

2. Materials and Methods

2.1. GEO Datasets and Identification of DEGs. The raw RNA transcriptome dataset (GSE42352) containing the expression data of 84 high-grade OS biopsy samples and 13 normal tissue samples was obtained from the Gene Expression Omnibus (GEO, http://www.ncbi.nlm.nih.gov/geo/) database. The mRNA expression profiling was assessed from the chip-based platform GPL10295 Illumina human-6 v2.0 expression beadchip with nuIDs as an identifier. The DEGs (differently expressed genes) between OS tissues and normal tissues were screened using the R software version 4.1.3 (http://www.R project. Org/) [13, 14]. Background correction, standardization, and the calculation of expression values were carried out using package Affy, Impute, and Limma of R software. The limma package was applied to normalize the median value of all samples. After that, a robust multichip average (RMA) was created, and the raw data were log-transformed. Once the p adjust value <0.05 and $|\log 2 \text{ fold change (FC)}| > 1$, the genes were identified as DEGs. Pheatmap and ggplot2 in R software were applied to build the heat map and Volcano plot, respectively [15].

2.2. GEPIA, UALCAN, and CCLE Databases. GEPIA (http://gepia.cancer-pku.cn/index.html) was used to assess *LIMS2* expression and its association with the overall survival in OS; UALCAN database (http://ualcan.path.uab.edu/) was used to evaluate the expression methylation levels of *LIMS2* in OS, as well as predict the genes correlated to *LIMS2*; CCLE database (https://portals.broadinstitute.org/ccle/) was also applied to analyze the methylation level of *LIMS2*.

2.3. Functional Enrichment. R software was applied to assess the enriched pathways of *LMIS2* and its associated genes identified from the UALCAN database with a Pearson − CC ≥ 0.4, including Gene Ontology (GO) and Kyoto Encyclopedia of Genes and Genomes (KEGG) pathways. Three modules, biological processes (BP), cellular component (CC), and molecular function (MF), were included in the GO analysis. p adjust value < 0.05 was thought as statistically significant.

2.4. Cell Culture. U-2OS, MG-63, Saos-2 and MNNG/HOS, 4 human OS cell lines, and one human normal osteoblast cell line hFOB 1.19 were obtained from American Type Culture Collection (Manassas, VA, USA). Another lung cancer cell line PC-9 was obtained from BeNa Culture Collection (Beijing, China). U-2OS and Saos-2 cells were cultured in McCoy's 5a Medium, while MG-63 and MNNG/HOS cells were grown in Eagle's Minimum Essential Medium, all with the supplementation of 10% FBS (Fetal Bovine Serum) and 1% (v/v) penicillin/streptomycin. hFOB 1.19 cells were maintained in a 1 : 1 mixture of Ham's F12 Medium and Dulbecco's Modified Eagle's Medium, supplemented with 2.5 mM L-glutamine, 0.3 mg/ml G418, and 10% FBS. All cell lines were placed at 37 °C with 5% CO_2. Cell culture mediums were purchased from Thermo Fisher Scientific (MA, USA).

2.5. Upregulation of LIMS2 Expression. Cells were transfected with the overexpressed plasmid to overexpress *LIMS2* and the negative control vector (NC) (cat no. RC229173, Beijing, China) with the help of lipofectamine 2000 (Thermo) according to the manufacture's descriptions.

2.6. Methylation-Specific PCR (MS-PCR). Genomic DNA (gDNA) was extracted with a QIAamp DNA Mini Kit (Qiagen, Germany) and submitted to sodium bisulfite modification with DNA Methylation Detection Kit (BioChain, USA) in the light of the manufacturer's descriptions. Then, PCR was carried out using the modified DNA in reaction system of 25 μL with the following conditions: 35 cycles of 95 °C for 30 s, 58 °C for 30 s, and 72 °C for 30 s. PCR products were separated in 3% agarose gel supplemented with ethidium bromide and the DNA blots were visualized under UV illumination. Unmethylation-specific primers: forward-5′-GGTTGGATT TTTAGATTGTAGATGA-3′, reverse-5′-AACAATAAAAA TAAACAAAAACAAA-3′;

methylation-specific primers: forward-5′-TGGGTTGGA TTTTTAGATTGTAGAC-3′, reverse-5′-AACGATAAAAA TAAACGAAAACGAA-3′.

2.7. Quantitative Reverse Transcription-PCR (qRT-PCR). Total RNA samples were extracted using TRIzol reagent (Invitrogen, USA). The RNAs were then reverse transcribed into cDNA using PrimeScript RT Master Mix kit (RR036A; Takara) in accordance with the descriptions. Next, the PCRs detection was performed using 2 × SYBR Green PCR Mastermix (Solarbio, Beijing, China) in a 7500 Real-Time PCR System (Applied Biosystems, USA). Primers applied are shown in Table 1.

2.8. Western Blotting. Total protein was isolated with the RIPA lysis buffer (Solarbio, Beijing, China) and added with 1% protease inhibitor (Solarbio) from cells. Subsequently, same amount

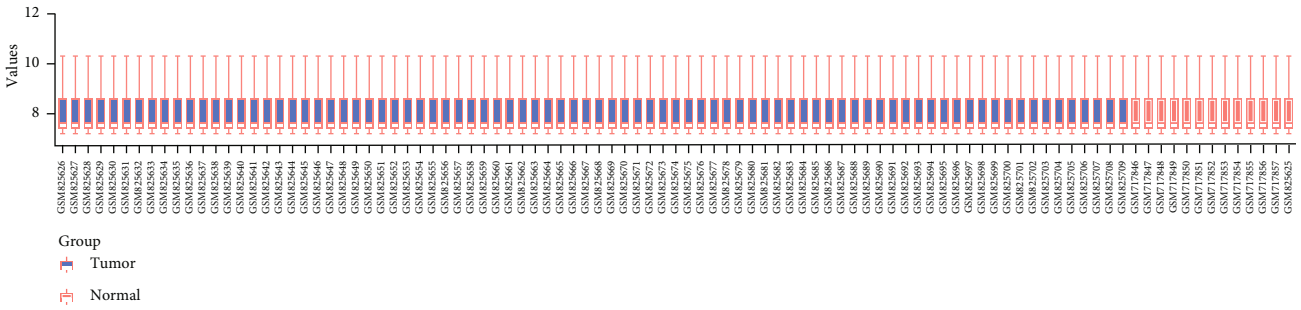

(a)

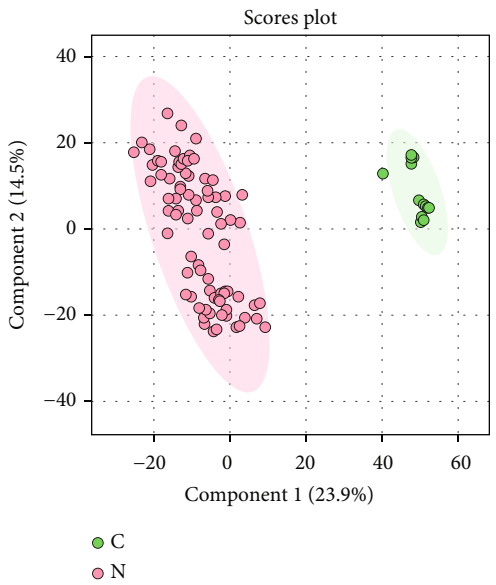

(b)

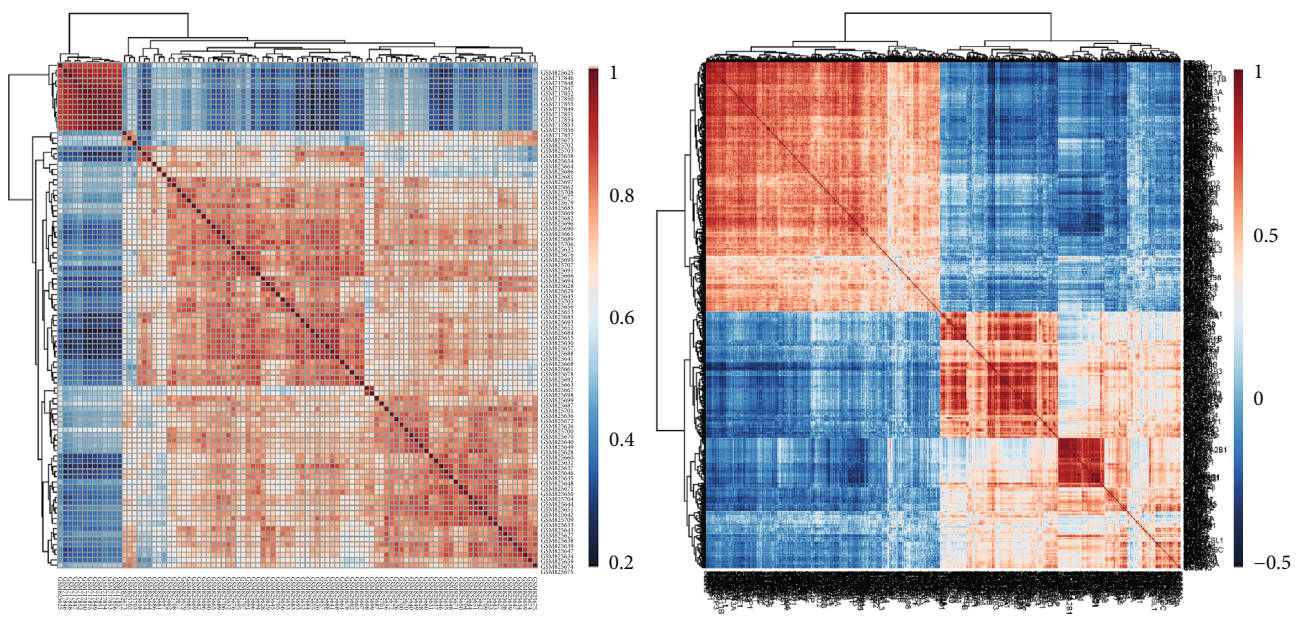

(c)

Figure 1: Continued.

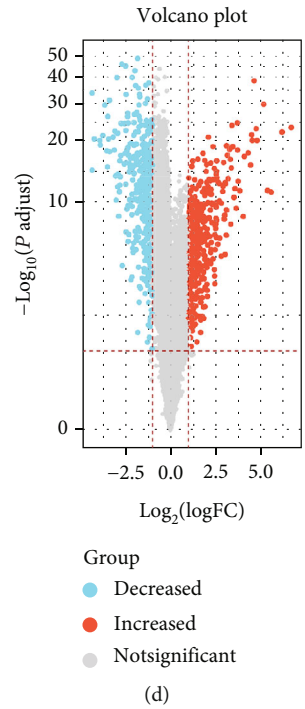

Figure 1: Identification of the DEGs in OS using the GEO database. (a) The correction histogram of removing batch of tumor and normal groups. (b) PCA of the tumor group and normal group. (c) Correlation heat maps of different groups and genes. (d) DEGs were shown in the volcano plot (blue dots represented the significantly downregulated genes, and red dots represented the significantly upregulated genes).

of proteins (about 20 μg) from each group were separated by 10% SDS-polyacrylamide gelsis and transferred onto the polyvinylidene difluoride membranes (PVDF; Millipore, Billerica, MA, USA). After that, the membranes were blocked with 5% non-fat milk at room temperature for 60 min to prevent the nonspecific bindings, followed by primary antibody incubation at 4 °C for overnight, including anti-β-actin antibody (cat no. ab8226, Abcam, MA, USA; 1 : 5000 dilution), anti-LIMS2 antibody (cat no. ab272666, Abcam; 1: 2000 dilution), anti-p-ERK (cat no. 4370, CST; 1: 2000 dilution), anti-ERK (cat no. 4695, CST; 1: 2000 dilution), anti-p-P38 (cat no. 4511, CST; 1: 1000 dilution), anti-P38 (cat no. 8690, CST; 1: 1000 dilution), anti-p-JNK (cat no. 9251, CST; 1: 1000 dilution), and anti-JNK (cat no. 9252, CST; 1: 1000 dilution) antibodies. After that, the membranes were probed with HRP-conjugated secondary antibodies at room temperature for 1 hour. ProfiBlot-48 (Tecan, Switzerland) was applied to evaluate protein signaling following immersing in ECL reagent (Millipore, USA). ImageJ software was used for protein quantification.

2.9. CCK-8 (Cell Counting Kit-8) Assay. Cells were placed in 96-well plates with 4,000 cells in each well. For cell growth assessment, cells were cultured with 10% (v/v) CCK-8 solution (Beyotime, Beijing, China) for 4 hours at 37 °C. Then, the OD values (450 nm) were detected with a Spectrophotometer (Fisherbrand™ accuSkan™ GO UV/Vis, Thermo).

2.10. Edu (5-Ethynyl-2′-Deoxyuridine) Staining. EdU staining was performed to assess cell proliferation using the EdU Assay/EdU Staining Proliferation Kit (cat no. ab222421, Abcam). Each well of the 24-well plate 6×10^4 cells were plated into each well of the 24-well plate and then transfected with indicated plasmids. After 48 hours, the cells were cultured with 50 μM EdU reagent for 2 hours and fixed with 4% formaldehyde for 0.5 hour, followed by incubation with glycine (2 mg/mL) for 0.25 hour and 0.5% Triton X-100 for 0.33 hour to permeabilize. Next, the cells were incubated with Hoechst 33342 for nuclear staining. The percentage of EdU positive cells was assessed under a fluorescence microscopy (Olympus IX73, Japan).

2.11. Transwell Chamber Assay. Transwell chambers (pore size, 8 μm; BD Biosciences) were applied to detect the effect of *LIMS2* on cell migration and invasion capacities. To detect cell migration, 5×10^4 cells were seeded into the upper chamber, while 0.60 ml of cell culture medium containing 15% FBS were added into the lower chamber. Following incubation at 37 °C for 24 hours, the cells on the upper side of the filters were removed with cotton swabs, while cells below the filters were first fixed with methanol for 15 min and then stained with 0.1% crystal violet. To detect cell invasion, the transwell chambers precoated with Matrigel were used and proceed as described as the migration assay. The number of migrated and invaded cells was counted under the microscope.

2.12. Statistical Analysis. Each experiment was repeated for three independent times in the current study. SPSS21.0 software (IBM, Armonk, NY, USA) was applied for the statistical analysis with student's t-test or one-way ANOVA with Tukey's tests. The p value less than 0.05 was considered a statistical significance.

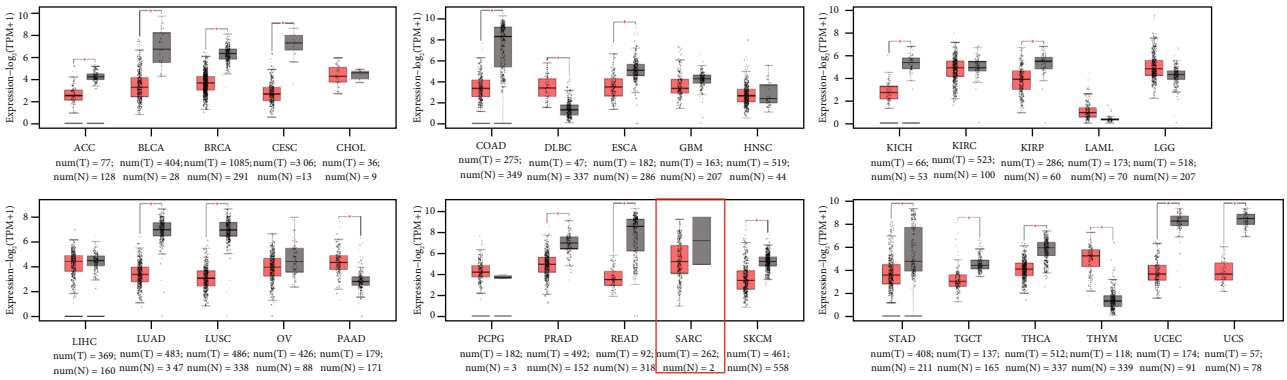

(a)

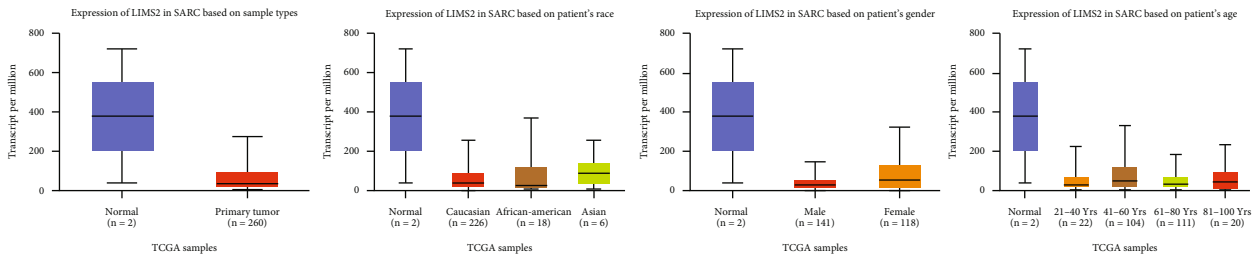

(b)

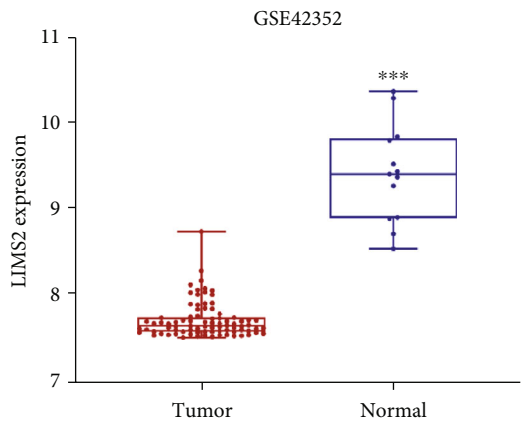

(c)

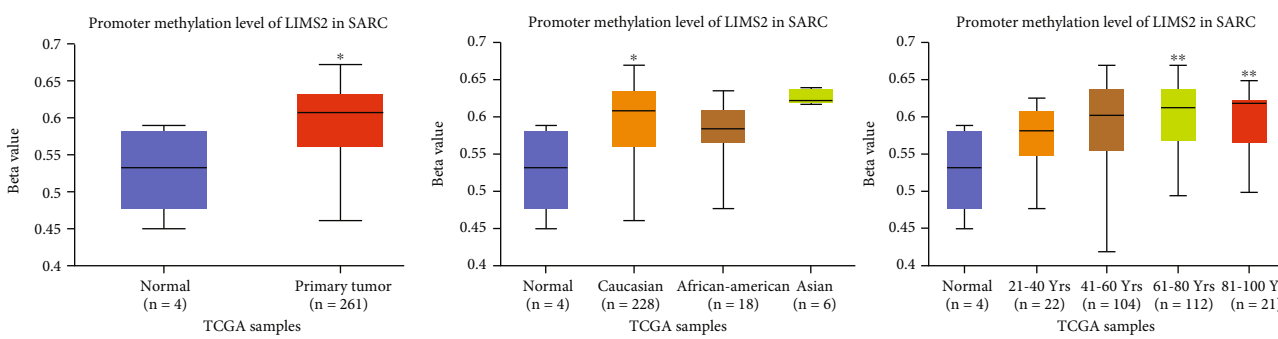

(d)

Figure 2: Continued.

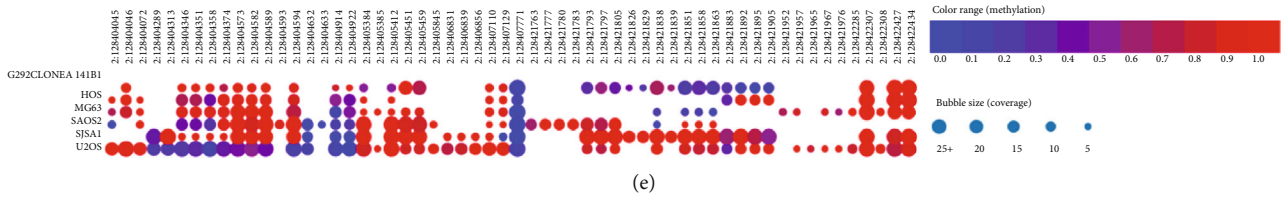

(e)

Figure 2: Bioinformatics analysis of the expression and methylation levels of *LIMS2* in OS. (a) *LIMS2* expressions in different kinds of cancers were assessed using the GEPIA database. (b) *LIMS2* expression in sarcoma was assessed by UALCAN database. (c) *LIMS2* expression in normal and tumor tissues was evaluated from the GEO (GSE42352). (d) The methylation levels of *LIMS2* in sarcoma tissues and normal tissues were analyzed using the ualcan database. (e) CCLE database was applied to assess the methylation levels of *LIMS2* in OS cells.

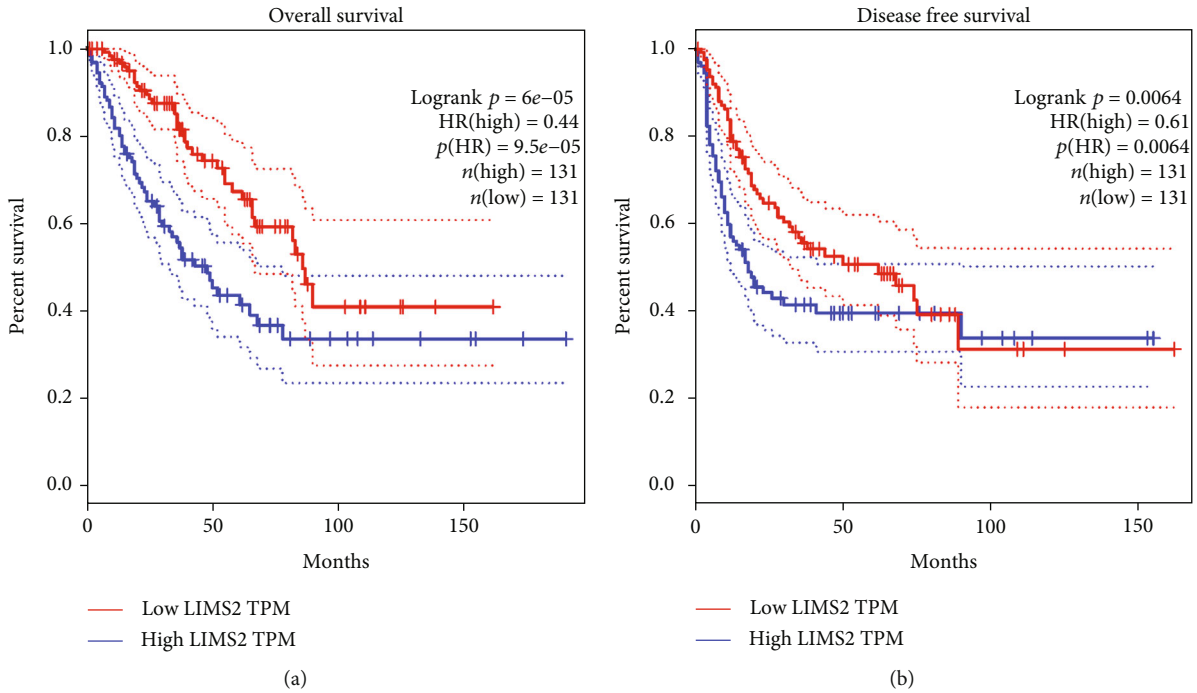

Figure 3: Low expression of *LIMS2* was linked to poor prognosis in OS. The relationships between *LIMS2* expression levels and (a) the overall survival and (b) the disease-free survival rates of patients with OS were evaluated using the GEPIA database.

3. Results

3.1. Bioinformatics Analysis Showed that LIMS2 Expression Was Downregulated While Its Methylation Level Was Increased in OS. To reveal the mechanisms underlying the progression of OS, first, the transcription data of 84 OS tissues and 13 normal tissues were downloaded from the GEO database to identify the DEGs. Figure 1(a) was the correction diagram of removing batch. The PCA (principal component analysis) showed that the tumor group and normal group could be well districted (Figure 1(b)). Moreover, we observed a good correlation between groups and genetic characteristics (Figure 1(c)). A total of 429 upregulated genes and 418 downregulated genes (including *LIMS2*) were found between tumor and normal groups, as shown by the volcano plot (Figure 1(d)). These results indicated that *LIMS2* was downregulated in OS.

To further explore the expression of *LIMS2* in OS, we recruited the GEPIA and UALCAN database. We observed that the expression of *LIMS2* was decreased in many kinds of cancers, including sarcoma (SARC) (Figures 2(a)–2(c)) regardless of race, gender, and age (Figure 2(b)). In addition, the promoter methylation level of *LIMS2* was significantly increased in sarcoma compared to normal group, as shown in the UALCAN database (Figure 2(d)). Consistently, the CpG island methylation level of *LIMS2* showed a high level in OS cell lines (Figure 2(e)). Moreover, the low expression level of *LIMS2* was linked to lower overall survival rate and lower disease-free survival rate in OS (Figures 3(a) and 3(b)). These results further revealed a lower expression pattern of *LIMS2* in OS, which was accompanied by high methylation level and related to poor prognosis.

3.2. LIMS2-Related Genes Were Enriched in MAPK Signaling Pathway. Then, we assessed the enriched pathways involved *LIMS2* and its related genes identified by the UALCAN database. The GO analysis showed that the genes were enriched in muscle system process, cell-substrate junction, cell

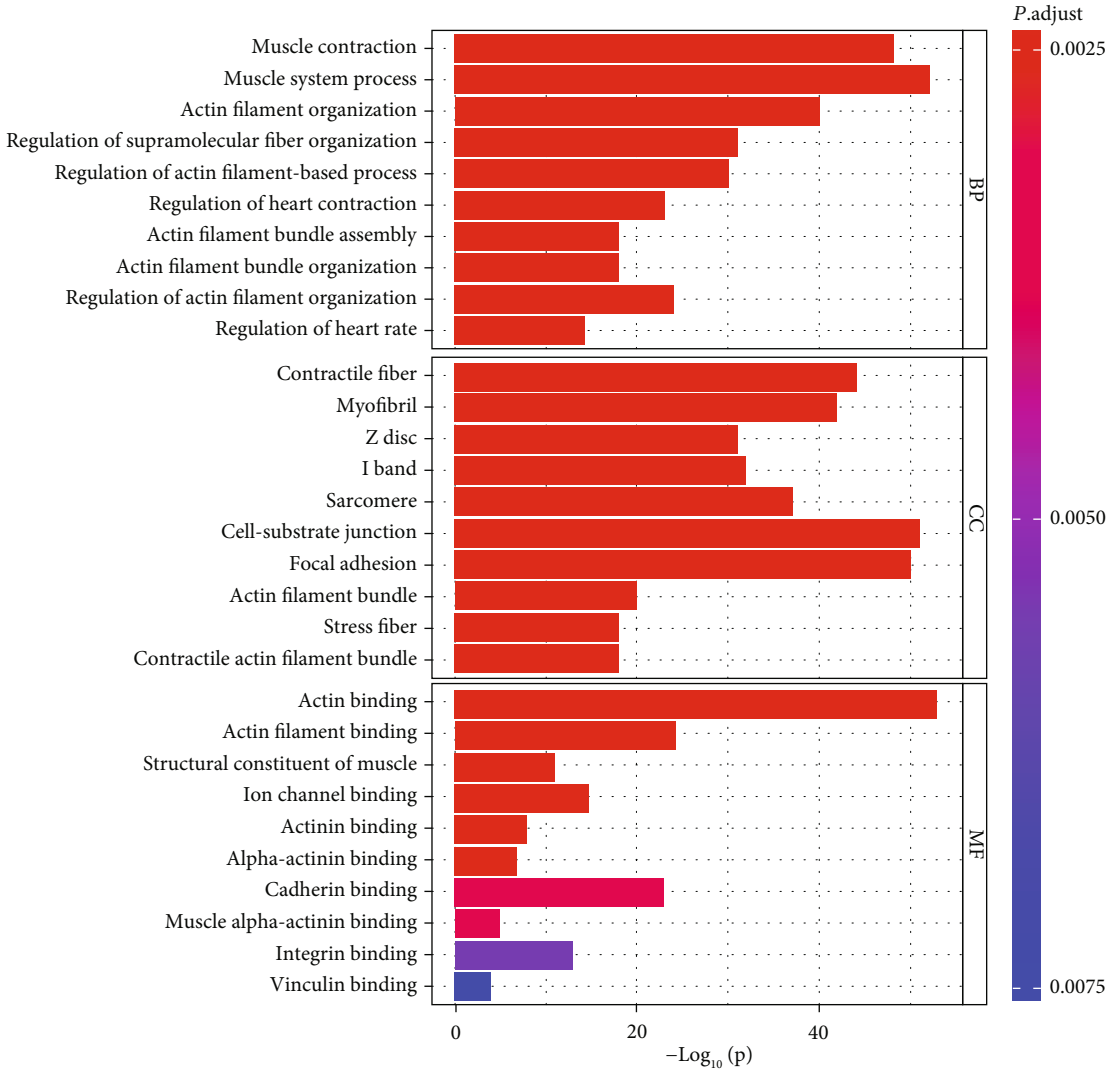

(a)

Figure 4: Continued.

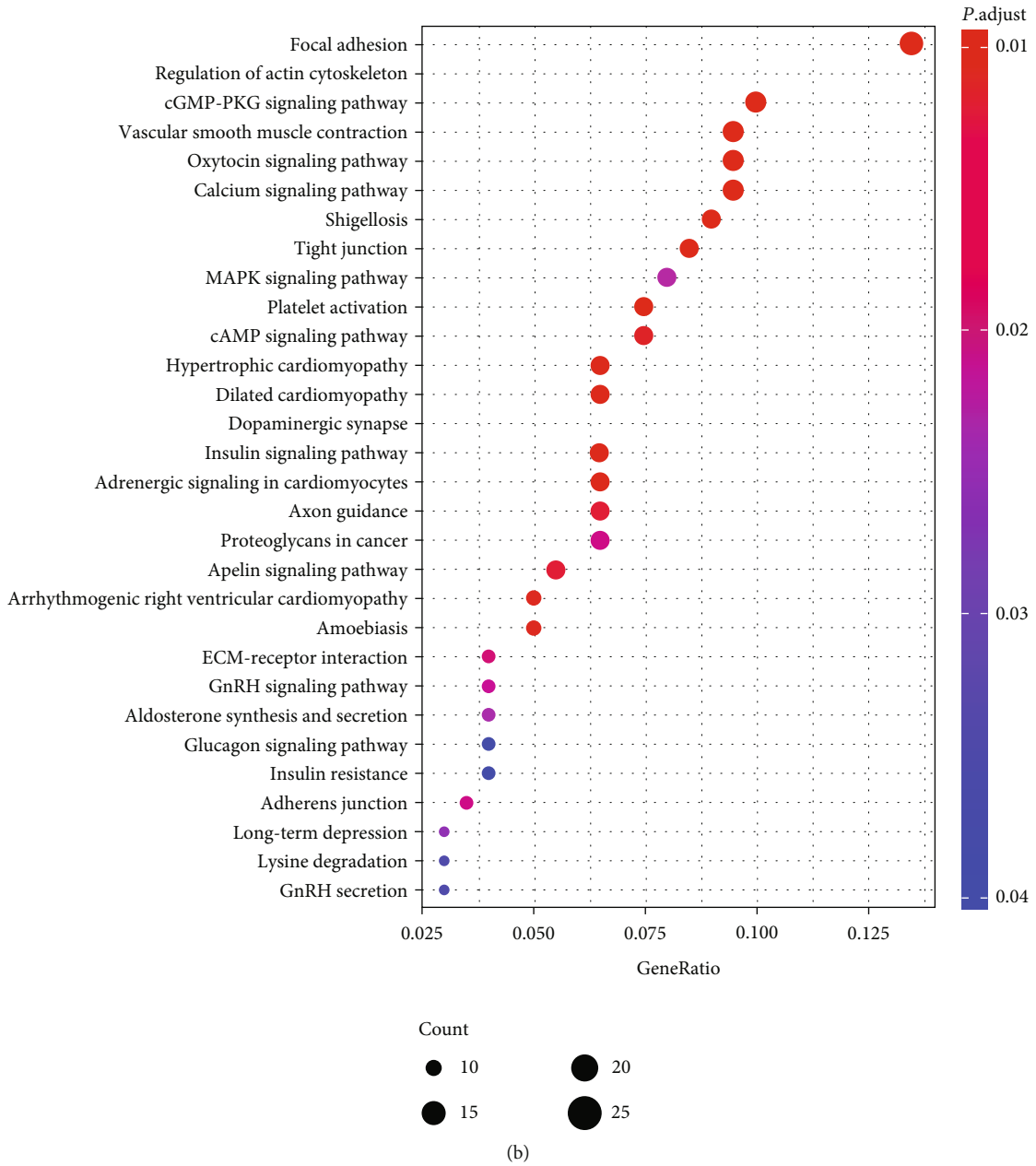

Figure 4: Enrichment analysis of *LIMS2* and its correlated genes. (a) GO and (b) KEGG analysis of the *LIMS2* and its correlated genes.

adhesion, actin binding, and cadherin binding pathways (Figure 4(a)). KEGG analysis showed that the genes were mainly enriched in focal adhesion, tight junction, MAPK signaling pathway, and adherens junction (Figure 4(b)). These results indicated that LIMS2-related genes may play a role in regulating cell motility.

3.3. LIMS2 Expression Was Downregulated in OS Cells. Next, we assessed *LIMS2* expression and methylation levels in OS tissues. Compared with the expression level of *LIMS2* in normal osteoblast cell line hFOB 1.19, both the mRNA (Figure 5(a)) and protein (Figures 5(b) and 5(c)) levels of LIMS2 were decreased in OS cell lines (U-2OS, MG-63, Saos-2, and MNNG/HOS). In contrast, *LIMS2* methylation level was increased in OS cell lines compared with hFOB 1.19 cells (Figure 5(d)). These results verified *LIMS2* level was declined in OS.

3.4. LIMS2 Inhibited OS Cell Growth and Migration. Additionally, we assessed the role of *LIMS2* in OS progression *in vitro*. *LIMS2* expression was remarkable increased in U-2OS and Saos-2 cells following the cell transfection with *LIMS2* plasmid (Figure 6(a)). In comparison with the control group, cell growth was significantly suppressed when *LIMS2* expression was upregulated, as determined by the CCK-8 assay (Figure 6(b)) and Edu staining (Figure 6(c)). In addition, *LIMS2* overexpression caused significant inhibition in cell migration (Figure 6(d)) and invasion

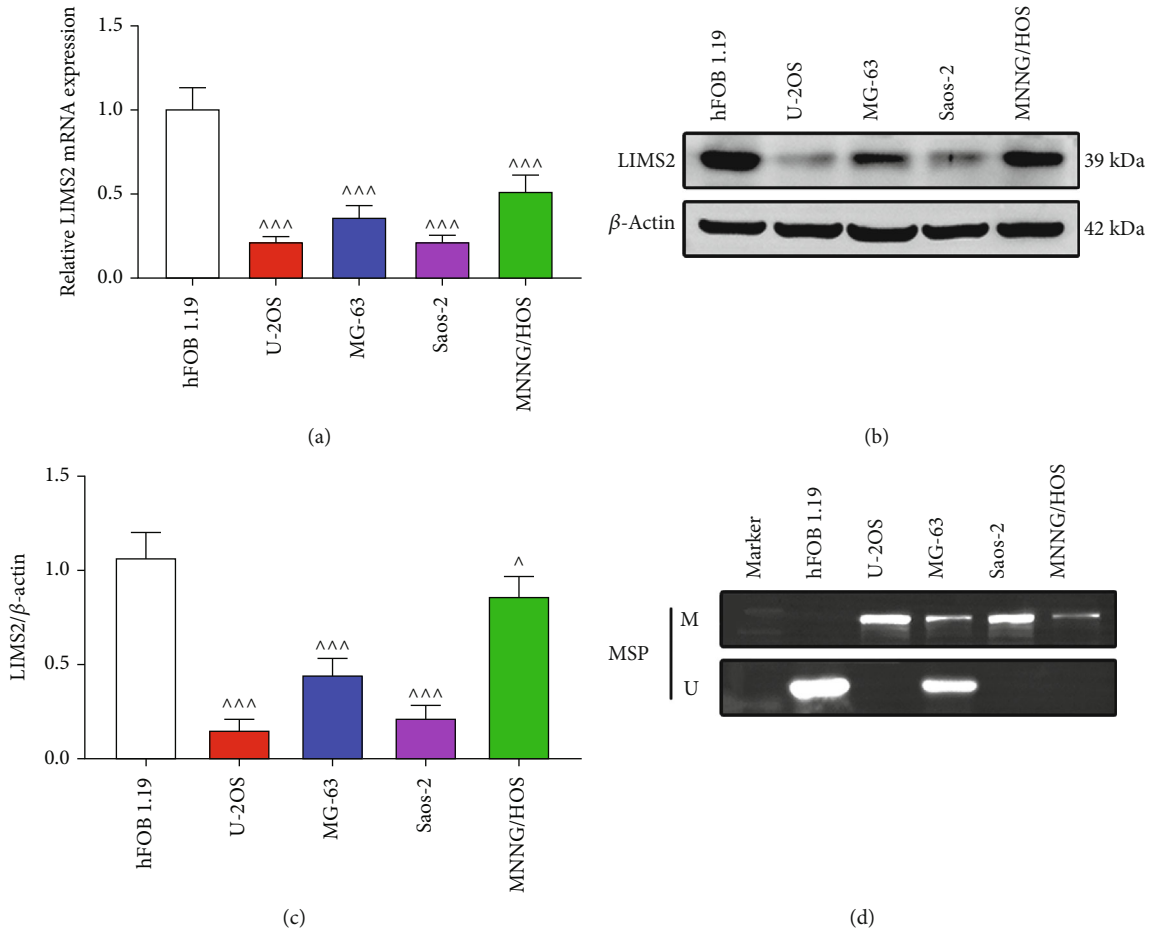

Figure 5: *LIMS2* expression was declined in OS cells. (a) qRT-PCR and (b,cC) western blotting assays were applied to assess the mRNA and protein levels of LIMS2 in normal hFOB 1.19 cells and OS cell lines (U-2OS, MG-63, Saos-2, and MNNG/HOS). (d) MS-PCR was applied to detect the methylation levels of *LIMS2* in hFOB 1.19 cells and OS cell lines (U-2OS, MG-63, Saos-2, and MNNG/HOS) ($n = 3$, $^{}p < 0.05$, and $^{^^^}p < 0.001$).

(Figure 6(e)). These results demonstrated that *LIMS2* overexpression could suppress cell growth and migration in OS.

3.5. LIMS2 Overexpression Inhibited the Activation of MAPK Signaling in OS Cells. Since the *LIMS2* and its associated genes were enriched in the MAPK signaling pathway, we assessed the effects of *LIMS2* on the activation of MAPK signaling *in vitro*. The results demonstrated that *LIMS2* overexpression significantly decreased the levels of p-ERK/ERK, p-P38/P38, and p-JNK/JNK in U-2OS and Saos-2 cell lines (Figure 7). These results confirmed that *LIMS2* overexpression could repress the activation of MAPK signaling in OS.

4. Discussion

Bioinformatics databases have shown that *LIMS2* expression was decreased in OS tissues, indicating that *LIMS2* may be involved in OS progression. In the current study, we first explored *LIMS2* role in the motility of OS. The results verified a downregulated expression of *LIMS2* in OS, while its methylation level was increased, and overexpression of *LIMS2* caused significant suppressions of cell growth and migration abilities in OS.

Currently, evidence has demonstrated that *LIMS2* is implicated in the carcinogenesis of several kinds of cancers. For example, Kim et al. [12] reported that hypermethylation induced silencing of *LIMS2* was observed in majority of the gastric cancer cell lines and about half of primary gastric tumors and silencing of *LIMS2* promoted the viability and migration of gastric cancer cells. *LIMS2* expression was declined in colon cancer, and overexpression of *LIMS2* significantly inhibited the migration of colon cancer cells [11]. In addition, *LIMS2* was highly expressed in melanoma cells with heparinase gene silencing (HPSE), leading to cell apoptosis [16]. Consistently, it has been shown by the online database that *LIMS2* expression was decreased in OS, which was then verified in OS cells using the western blotting assay. Moreover, the low expression of *LIMS2* was related to lower overall survival and disease-free survival rates of patients with OS. Interestingly, we found that the methylation level at the promoter of *LIMS2* gene was increased in OS cells compared with the normal osteoblast, which was consistent with the finding in gastric cancer [12]. However, *LIMS2* mRNA level was increased in malignant mesothelioma compared with carcinomas involving serosal cavities [17], with its function in the progression of malignant mesothelioma

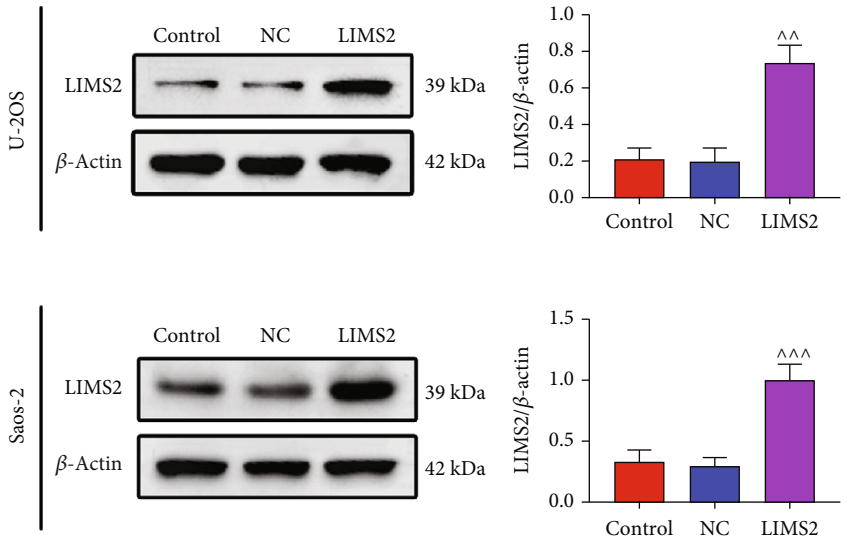

(a)

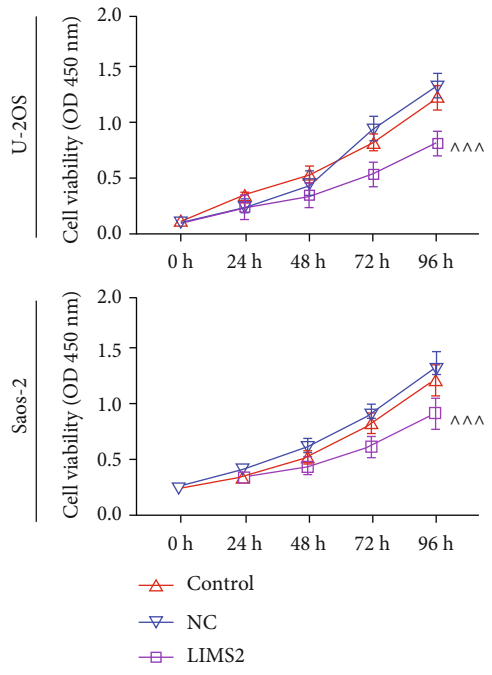

(b)

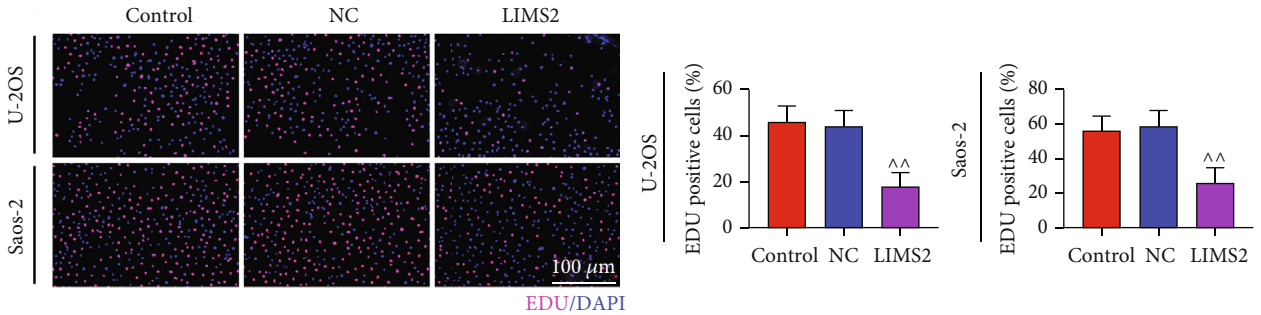

(c)

Figure 6: Continued.

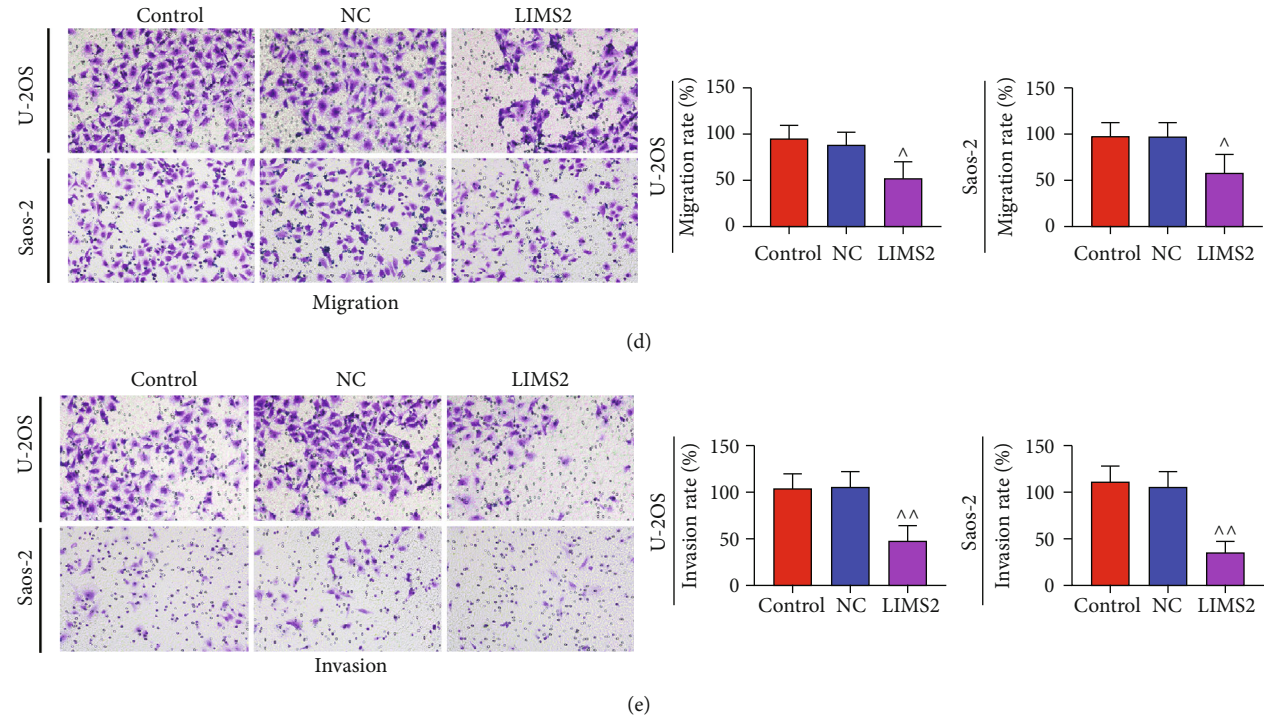

Figure 6: *LIMS2* inhibited OS cell growth and migration. U-2OS and Saos-2 cells divided into control, NC and LIMS2 groups were collected for the following assays. (a) LIMS2 protein levels in different groups were determined using western blotting assay. (b) CCK-8 assay and (d) Edu staining were applied for cell growth detection. (d, e) Cell migration and invasion capacities were tested with the transwell chambers ($n = 3$, $^{\wedge}p < 0.05$, $^{\wedge\wedge}p < 0.01$, $^{\wedge\wedge\wedge}p < 0.001$, and LIMS2 group vs. NC group).

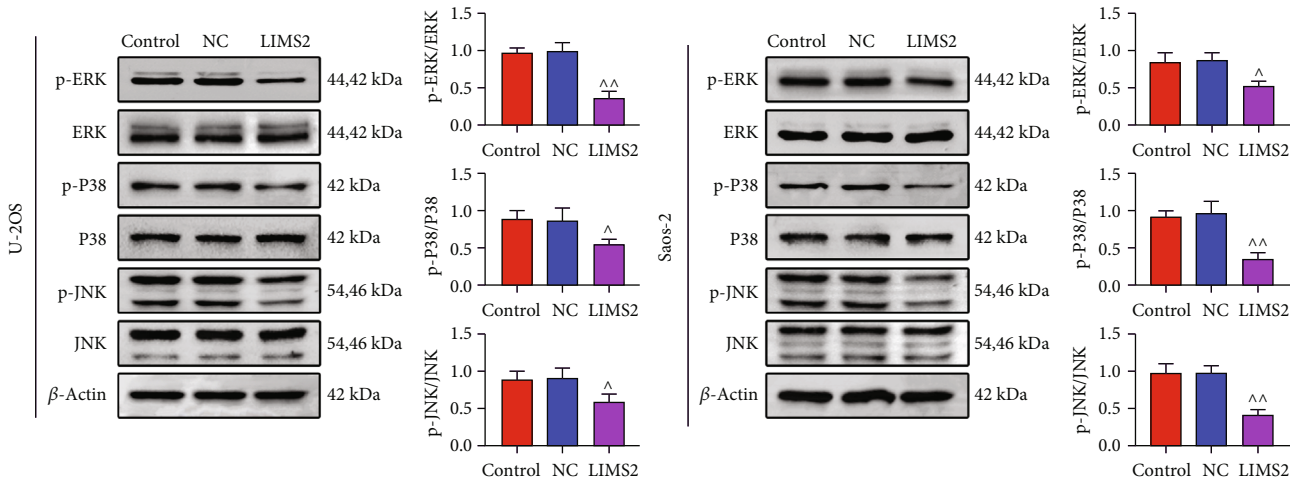

Figure 7: *LIMS2* overexpression inhibited the activation of MAPK signaling in OS cells. The protein levels of ERK, p-ERK, P38, p-P38, JNK, and p-JNK in different groups of U-2OS and Saos-2 cells were detected by western blotting assay ($n = 3$, $^{\wedge}p < 0.05$, $^{\wedge\wedge}p < 0.01$, LIMS2 group vs. NC group).

remaining unknown. Different cancer types may cause this expression difference. Moreover, the *in vitro* assay showed that *LIMS2* overexpression inhibited the growth, migration, and invasion of OS cells, suggesting that *LIMS2* functioned as a tumor suppressor in OS, which was similar as reported in gastric cancer [12] and colon cancer [11].

The MAPK signaling exerts an important role in the regulation of the progression of OS [18–20]. Here, the pathway enrichment analysis showed that *LIMS2* and its correlated genes were mainly enriched in the MAPK signaling. Western blotting assay results showed that *LIMS2* overexpression led to significant inhibitions in the levels of p-ERK, p-P38, and p-JNK, further suggesting that the MAPK signaling may be a downstream pathway through which *LIMS2* inhibited the progression of OS. Chen et al. [21] reported that *LIMS1* regulated the ERK-Bim pathway and triggered

apoptosis resistance in cancer cells, indicating a link between PINCH family and MAPK signaling. Montanez et al. [22] demonstrated that deletion of *LIMS1* led to a sustained activity of JNK in primitive endoderm (PrE) cells. Here, we first explored *LIMS2* effect on the activation of MAPK signaling in cancer cells, and our results demonstrated that overexpression of *LIMS2* could significantly inhibit the activation of MAPK signaling. However, whether MAPK signaling is involved in *LIMS2*-mediated inhibitions of cell growth and migration in OS remains to be further studied.

There are still limitations for the current study. The expression of *LIMS2* should be detected in human OS tissues, and its association with patients' prognosis should also be explored. As mentioned earlier, another limitation is that we did not explore the underlying mechanisms by which *LIMS2* inhibits cell growth and migration in OS, such as the MAPK signaling. We intend to explore these in future studies.

In summary, this study demonstrated that *LIMS2* expression was decreased in OS, which was associated with hypermethylation level and poor prognosis. *LIMS2* overexpression inhibited OS cell proliferation and migration, which may be mediated by the suppression of MAPK signaling. Regents used to upregulate *LIMS2* expression, such as the methylation inhibitor, might be a potential treatment method to repress cell migration in OS.

Data Availability

All data generated or analyzed during this study are included in this published article.

Conflicts of Interest

The authors state that there are no conflicts of interest to disclose.

Authors' Contributions

Chenying Su and Xiaona Cai designed the study, completed the experiment, and supervised the data collection, Taotao Xu and Yungang Wu analyzed the data and interpreted the data. Licong Wang, Pinjie Chen, and Chenxian Su prepared the manuscript for publication and reviewed the draft of the manuscript. All authors have read and approved the manuscript.

References

[1] S. Wagle, S. H. Park, K. M. Kim et al., "DBC1/CCAR2 is involved in the stabilization of androgen receptor and the progression of osteosarcoma," *Scientific Reports*, vol. 5, no. 1, p. 13144, 2015.

[2] X. Zhao, Q. Wu, X. Gong, J. Liu, and Y. Ma, "Osteosarcoma: a review of current and future therapeutic approaches," *BioMedical Engineering Online*, vol. 20, no. 1, p. 24, 2021.

[3] M. S. Isakoff, S. S. Bielack, P. Meltzer, and R. Gorlick, "Osteosarcoma: current treatment and a collaborative pathway to success," *Journal of Clinical Oncology*, vol. 33, no. 27, pp. 3029–3035, 2015.

[4] L. Kager, G. Tamamyan, and S. Bielack, "Novel insights and therapeutic interventions for pediatric osteosarcoma," *Future Oncology*, vol. 13, no. 4, pp. 357–368, 2017.

[5] T. Fukuda, K. Chen, X. Shi, and C. Wu, "PINCH-1 is an obligate partner of integrin-linked kinase (ILK) functioning in cell shape modulation, motility, and survival," *The Journal of Biological Chemistry*, vol. 278, no. 51, pp. 51324–51333, 2003.

[6] Y. Zhang, K. Chen, L. Guo, and C. Wu, "Characterization of PINCH-2, a new focal adhesion protein that regulates the PINCH-1-ILK interaction, cell spreading, and migration," *The Journal of Biological Chemistry*, vol. 277, no. 41, pp. 38328–38338, 2002.

[7] C. Wu, "PINCH, N (i) ck and the ILK: network wiring at cell-matrix adhesions," *Trends in Cell Biology*, vol. 15, no. 9, pp. 460–466, 2005.

[8] A. Braun, R. Bordoy, F. Stanchi et al., "PINCH2 is a new five LIM domain protein, homologous to PINCHand localized to focal adhesions," *Experimental Cell Research*, vol. 284, no. 2, pp. 239–250, 2003.

[9] J. Wang-Rodriguez, A. D. Dreilinger, G. M. Alsharabi, and A. Rearden, "The signaling adapter protein PINCH is up-regulated in the stroma of common cancers, notably at invasive edges," *Cancer*, vol. 95, no. 6, pp. 1387–1395, 2002.

[10] J. T. Zhang, Q. X. Li, D. Wang et al., "Up-regulation of PINCH in the stroma of oral squamous cell carcinoma predicts nodal metastasis," *Oncology Reports*, vol. 14, no. 6, pp. 1519–1522, 2005.

[11] C. H. Park, S. Y. Rha, J. B. Ahn et al., "PINCH-2 presents functional copy number variation and suppresses migration of colon cancer cells by paracrine activity," *International Journal of Cancer*, vol. 136, no. 10, pp. 2273–2283, 2015.

[12] S. K. Kim, H. R. Jang, J. H. Kim et al., "The epigenetic silencing of LIMS2 in gastric cancer and its inhibitory effect on cell migration," *Biochemical and Biophysical Research Communications*, vol. 349, no. 3, pp. 1032–1040, 2006.

[13] M. E. Ritchie, B. Phipson, D. Wu et al., "Limma powers differential expression analyses for RNA-sequencing and microarray studies," *Nucleic Acids Research*, vol. 43, no. 7, article e47, 2015.

[14] B. M. Bolstad, R. A. Irizarry, M. Astrand, and T. P. Speed, "A comparison of normalization methods for high density oligonucleotide array data based on variance and bias," *Bioinformatics*, vol. 19, no. 2, pp. 185–193, 2003.

[15] C. B. Dean and J. D. Nielsen, "Generalized linear mixed models: a review and some extensions," *Lifetime Data Analysis*, vol. 13, no. 4, pp. 497–512, 2007.

[16] T. Song and D. Spillmann, "Transcriptomic analysis reveals cell apoptotic signature modified by heparanase in melanoma cells," *Journal of Cellular and Molecular Medicine*, vol. 23, no. 7, pp. 4559–4568, 2019.

[17] Y. Yuan, H. P. Dong, D. A. Nymoen, J. M. Nesland, C. Wu, and B. Davidson, "PINCH-2 expression in cancers involving serosal effusions using quantitative PCR," *Cytopathology*, vol. 22, no. 1, pp. 22–29, 2011.

[18] M. Mikulcic, N. G. Tabrizi-Wizsy, E. M. Bernhart et al., "15d-PGJ2 Promotes ROS-Dependent Activation of MAPK-Induced Early Apoptosis in Osteosarcoma Cell In Vitro and in an Ex Ovo CAM Assay," *International Journal of Molecular Sciences*, vol. 22, no. 21, article 11760, 2021.

[19] D. Zhu, X. Xu, M. Zhang, and T. Wang, "Enhanced expression of KIF4A in osteosarcoma predicts a poor prognosis and

facilitates tumor growth by activation of the MAPK pathway," *Experimental and Therapeutic Medicine*, vol. 22, no. 5, p. 1339, 2021.

[20] M. K. Fan, G. C. Zhang, W. Chen et al., "Siglec-15 promotes tumor progression in osteosarcoma via DUSP1/MAPK pathway," *Frontiers in Oncology*, vol. 11, article 710689, 2021.

[21] K. Chen, Y. Tu, Y. Zhang, H. C. Blair, L. Zhang, and C. Wu, "PINCH-1 regulates the ERK-Bim pathway and contributes to apoptosis resistance in cancer cells," *The Journal of Biological Chemistry*, vol. 283, no. 5, pp. 2508–2517, 2008.

[22] E. Montanez, E. Karakose, D. Tischner, A. Villunger, and R. Fassler, "PINCH-1 promotes Bcl-2-dependent survival signalling and inhibits JNK-mediated apoptosis in the primitive endoderm," *Journal of Cell Science*, vol. 125, pp. 5233–5240, 2012.

Hindawi
Journal of Oncology
Volume 2022, Article ID 5040458, 27 pages
https://doi.org/10.1155/2022/5040458

Research Article

Identification and Development of an Age-Related Classification and Signature to Predict Prognosis and Immune Landscape in Osteosarcoma

Jinjiong Hong,[1] **Xiaofeng Wang**,[1] **Liang Yu**,[2] **Jie Li**,[3] **Haoliang Hu**,[1] **and Weisheng Mao**[1]

[1]*Department of Hand Surgery, Department of Plastic Reconstructive Surgery, Ningbo No. 6 Hospital, Ningbo 315040, China*
[2]*Department of Spine Surgery, Ningbo No. 6 Hospital, Ningbo 315040, China*
[3]*Department of Orthopedics, Ningbo Medical Center Lihuili Hospital, Ningbo 315040, China*

Correspondence should be addressed to Weisheng Mao; nblymws@163.com

Received 11 August 2022; Accepted 17 September 2022; Published 12 October 2022

Academic Editor: İbrahim Hakkı Cigerci

Background. In childhood and adolescence, the prevailing bone tumor is osteosarcoma associated with frequent recurrence and lung metastasis. This research focused on predicting the survival and immune landscape of osteosarcoma by developing a prognostic signature and establishing aging-related genes (ARGs) subtypes. *Methods*. The training group comprised of the transcriptomic and associated clinical data of 84 patients with osteosarcoma accessed at the TARGET database and the validation group consisted of 53 patients from GSE21257. The aging-related subtypes were identified using unsupervised consensus clustering analysis. The ARG signature was developed utilizing multivariate Cox analysis and LASSO regression. The prognostic value was assessed using the univariate and multivariate Cox analyses, Kaplan-Meier plotter, time-dependent ROC curve, and nomogram. The functional enrichment analyses were performed by GSEA, GO, and KEGG analysis, while the ssGSEA, ESTIMATE, and CIBERSORT analyses were conducted to reveal the immune landscape in osteosarcoma. *Results*. The two clusters of osteosarcoma patients formed based on 543 ARGs, depicted a considerable difference in the tumor microenvironment, and the overall survival and immune cell infiltration rate varied as well. Among these, the selected 23 ARGs were utilized for the construction of an efficient predictive prognostic signature for the overall survival prediction. The testing in the validation group of osteosarcoma patients confirmed the status of the high-risk score as an independent indicator for poor prognosis, which was already identified as such using the univariate and multivariate Cox analyses. Furthermore, the ARG signature could distinguish different immune-related functions, infiltration status of immune cells, and tumor microenvironment, as well as predict the immunotherapy response of osteosarcoma patients. *Conclusion*. The aging-related subtypes were identified and a prognostic signature was developed in this research, which determined different prognoses and allowed for treatment of osteosarcoma patients to be tailored. Additionally, the immunotherapeutic response of individuals with osteosarcoma could also be predicted by the ARG signature.

1. Introduction

Osteosarcoma (OS) is the major prevailing bone tumor in childhood and adolescence worldwide that originates from the bone marrow mesenchymal stem cells or osteoclasts [1, 2]. Osteosarcoma occurs mostly in the metaphysis of long bones near an active bone growing region and is generally more prevalent in the femur (42%), the tibia (19%), and the humerus (10%) [3]. The incidence rate of osteosarcoma is relatively low with only 3-4 people being affected per million annually, but the high probability of recurrence and distant metastasis and the absence of identifying symptoms at an early stage together with its highly malignant nature leads to poor prognosis of osteosarcoma patients [4]. Currently, therapeutic management for patients with osteosarcoma mainly depends on surgical resection, chemotherapy, radiation therapy, immunotherapy, and targeted therapy which has caused the 5-year survival rate to increase to 60%-70% in osteosarcoma patients without metastasis, whereas patients with recurrence or metastasis still have a 5-year

survival rate less than 30% [5, 6]. The identification of the process behind the occurrence and progression of osteosarcoma is extremely necessary to create effective treatments. The examination of biomarkers to identify effective prognostic markers for osteosarcoma that can enhance the active interventions for the disease and the development of novel therapies may help in increasing the survival rate.

Aging presents the characteristics of gradual deterioration in internal physiological function and is linked to the onset and progression of multiple chronic conditions, including cancers [7]. Cytologically, aging has been linked to the cumulative damage caused by abnormalities such as genomic instability, mitochondrial dysfunction, cellular senescence, which has been related to the development of aging-linked malignancies [8]. Cellular senescence occurs in response to many different triggers, including DNA damage, telomere dysfunction, oncogene activation, and organelle stress, and has been linked to the aging processes [9]. Senescence cells have a highly complex effect on the growth of cancers. The consequent activation of the SASP system results in the secretion of a variety of signaling molecules such as cytokines or chemokines, as well as growth factors, and extracellular matrix proteases which affect tumor growth by either arresting the cell cycle or regulating the immune clearance [10]. The onset of aging-associated malignancies can be delayed by targeting the aging mechanism, which makes the identification of these aging-related markers extremely necessary [11, 12]. The reports from multiple recent studies have demonstrated the involvement of specific genes in modulating cellular senescence, such as *APOE* [13] and *FOXO3* [14]. Peters et al. [15] also performed a population-based large-scale transcriptomic analysis to determine aging-related genes (ARGs). Although osteosarcoma is an age-dependent disease, nevertheless, there is a lack of systemic research on the association between ARGs and the prognosis of osteosarcoma.

In this research, the expression profile of ARGs was utilized to identify two aging-related molecular subtypes in the TARGET database, and the underlying differences between subtypes were systematically revealed. Afterward, the ARGs associated with independent prognosis were filtered out, and an ARGs prognostic signature was constructed to provide a new method for assessing clinical outcomes in patients with osteosarcoma, which was further verified utilizing the Gene Expression Omnibus (GEO) dataset, GSE21257. Moreover, a predictive nomogram utilized for the prediction of accurate survival rates among patients with osteosarcoma was established comprising the ARG signature and clinical features. Finally, the link between the risk model and the immune infiltration landscape was studied to search for new targeted therapies for osteosarcoma.

2. Materials and Methods

2.1. Data Source. The RNA-seq expression profiles and corresponding clinical and pathological information of 88 osteosarcoma patients were accessed at TARGET datasets (https://ocg.cancer.gov/programs/target, updated January 16, 2022). Afterward, three patients without prognostic information and one patient without clinicopathological information were excluded, and 84 individuals with osteosarcoma were left in the training set. For the validation set, 53 osteosarcoma patients in the GSE21257 were obtained from the Gene Expression Omnibus database (https://www.ncbi.nlm.nih.gov/geo/query/acc.cgi?acc=GSE21257).
Table 1 demonstrates the relevant clinical data of patients with osteosarcoma studied in this research.

2.2. Consensus Clustering. A total of 543 aging-related genes were accessed at the Human Aging Genome Resource dataset [16] (HAGR, https://www.genomics.senescence.info/) and the CellAge dataset (https://genomics.senescence.info/cells/) after the elimination of duplicate genes. The different aging-related molecular subtypes were identified according to the aging-related genes by employing the ConsensusClusterPlus package of R. The increase from 2 to 9 in the clustering variable (k) was carried out to select the optimum number of subtypes, and the stability of the results was enhanced by replicating the process 1,000 times.

2.3. Functional Enrichment Analyses between Aging-Related Subtypes. The differentially expressed genes (DEGs) were identified utilizing the "limma" R package by applying the criteria $|\log2FC| \geq 0.5$ and FDR $P < 0.05$ to study the biological function and pathways between aging-related subtypes. These DEGs were analyzed using the Kyoto Encyclopedia of Genes and Genomes (KEGG) pathway analysis and Gene Ontology (GO) enrichment analyses. The annotation and visualization were carried out by the "clusterProfiler," "http://org.Hs.eg.db," "ggplot2," and "enrichment plot" R packages. The different pathways between aging-related subtypes were assessed as described previously utilizing the Gene Set Enrichment Analysis (GSEA) [17].

2.4. Evaluation of Immune Characteristics between Aging-Related Subtypes. The tumor microenvironment (TME) scores such as stromal content (StromalScore), tumor purity, and the degree of infiltration of immune cells (ImmuneScore) were measured utilizing the program ESTIMATE [18]. The immune cells infiltration score and the activity level of pathways associated with the immune system were measured using the single-sample Gene Set Enrichment Analysis (ssGSEA) by applying the "gsva" package.

2.5. Construction of an Aging-Related Risk Signature for Osteosarcoma. A prognostic predictive risk model was constructed, and the coefficients were identified using the multivariate Cox regression, which was utilized for predicting the risk scores of individuals with osteosarcoma. For the construction of this model, the relevant genes were identified by univariate Cox regression in the TARGET cohort, and the Least Absolute Shrinkage and Selection Operator (LASSO) regression was applied to define the optimum range of aging-related genes utilized in the model. The prognostic aging-relevant genes were identified using the "survival" package and were optimized in the signature by utilizing the "glmnet" package in the aforementioned analyses. The formula mentioned below was utilized to derive the

Table 1: Clinical characteristics of the individuals with osteosarcoma in this research.

Covariates	Type	Target		GSE21257	
		Number	Percent	Number	Percent
Age	≤14	39	46.43%	15	28.30%
	>14	45	53.57%	38	71.70%
Gender	Female	37	44.05%	19	35.85%
	Male	47	55.95%	34	64.15%
Race	White	51	60.71%	—	—
	Asian	6	7.14%	—	—
	Black or African American	7	8.33%	—	—
Primary tumor site	Leg	76	90.48%	44	83.02%
	Arm	6	7.14%	8	15.09%
	Pelvis	2	2.38%	—	—
Metastatic status	Yes	21	25.00%	14	26.42%
	No	63	75.00%	39	73.58%
Survival status	Dead	27	32.14%	23	43.40%
	Alive	57	67.86%	30	56.60%

risk score of each individual in the validation and TARGET cohorts:

$$\text{Risk score} = \sum_{i=1}^{n} \text{coefficient} \times \text{aging-related gene expression}. \quad (1)$$

The individuals with osteosarcoma were divided based on the median into two groups: the high- and low-risk groups. The prognostic value of the risk model for individuals with osteosarcoma was analyzed using the principal component analysis (PCA), Kaplan-Meier curves, time-dependent receiver operating characteristics (ROC) curves, C-index, decision curve analysis (DCA) [19], univariate and multivariate Cox regression analysis, and survival subgroup analyses. The risk model performance was verified using the validation cohort, which consisted of 53 osteosarcoma patients from the GSE21257. To determine whether our ARG signature had a superior predictive ability [20–23], four previous signatures were selected with which the values of the following parameters were compared such as time-dependent ROC, C-index, and restricted mean survival time (RMST).

2.6. Development of Nomograms to Predict the Outcome of Patients with Osteosarcoma. The nomogram was generated for the prediction of the 1-, 3-, and 5-year rates of survival of individuals with osteosarcoma, and its performance was analyzed using various software. The risk score and clinicopathological parameters such as age, gender, and metastasis were utilized for the prediction of the overall survival (OS) rate by using the "rms" package, while the time-dependent ROC and calibration curves were utilized to analyze the nomogram's performance in prognosis prediction.

2.7. Evaluation of Immune Characteristics between High-Risk and Low-Risk Group. The variation in the ESTMATEScore, StromalScore, and ImmuneScore content in the TME and the score of pathways associated with the immune system were analyzed between the two risk groups. The ssGSEA was utilized for the comparison of the pathway scores, whereas the CIBERSORT algorithm [24] examined 22 immune cells to determine their infiltration degree. The treatment response of immune checkpoint inhibitors was predicted by examining the level of expression of several important genes associated with immune checkpoints between the two groups.

2.8. Statistical Analysis. The R software 4.1.0 was utilized for statistical analysis and visualization of the data involved in this research. The differences between groups were determined by utilizing Wilcoxon signed-rank and chi-square tests. The Pearson correlation analysis analyzed the link between groups. The significant level was selected as P values <0.05.

3. Results

3.1. Consensus Clustering Analysis Based on ARGs. The workflow was drawn (Figure 1(a)), and 543 ARGs were identified in total from the CellAge and HAGR database (Figure 2(a)). The ARGs clusters of individuals with osteosarcoma were determined by employing the consensus clustering method based on the aforementioned genes. The value of (clustering variable) $k = 2$ results in similarity in values in the same group, while group-to-group variation in the values exists (Figures 2(b) and 2(c)). Therefore, individuals with osteosarcoma in the TARGET cohort were categorized into Cluster 1 (57 samples) and Cluster 2 (27 samples) with distinct ARG expression patterns.

3.2. Functional Enrichment Analysis. The Kaplan-Meier survival curves (Figure 3(a)) indicated that the OS status of the Cluster 1 subtype was considerably poorer as compared to the Cluster 2 subtype ($P = 0.023$). The Gene Set Enrichment

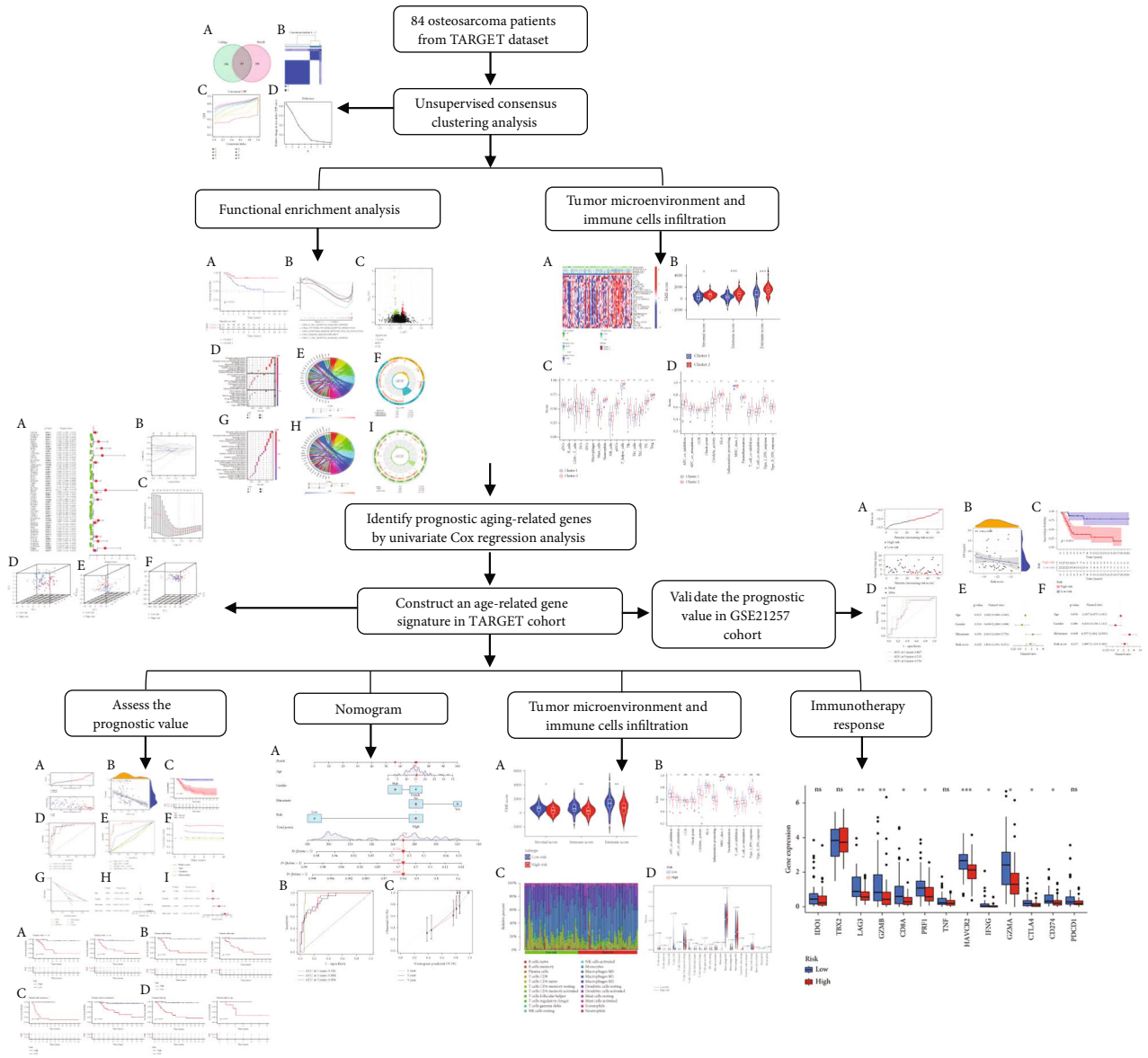

Figure 1: Study flow chart.

Analysis (GSEA) analyzed the enrichment of signaling pathways associated with the immune system in the Cluster 2 group, including IgA production using the intestinal immune pathway, cytokine-cytokine receptor interaction, and primary immunodeficiency, as well as B cell and T cell receptor signaling pathways (Figure 3(b)). The molecular mechanism between two clusters was examined using 278 DEGs which included 119 upregulated and 159 downregulated genes utilizing the Limma R package (Figure 3(c)). The GO analysis (Figures 3(d)–3(f)) and KEGG analysis (Figures 3(g)–3(i)) depicted the enrichment of DEGs in functions linked to immunity, including neutrophil-mediated immunity, neutrophil activation involved in immune response, T cell activation, B cell differentiation, and immune receptor activity. This analysis demonstrated that the Cluster 2 subtype was closely linked to the increased immune activity in the microenvironment.

3.3. Immune Landscape Analysis between Cluster 1 and Cluster 2 Subtype. The above findings were taken into consideration, and the composition of the TME and immune-related function between the two subtypes was analyzed (Figure 4(a)). The ImmuneScore and StromalScore were higher in Cluster 2 compared to the Cluster 1 subtype (Figure 4(b)), indicating that Cluster 2 harbored more immune cells and stromal components. The variation in the TME of both the subtypes was analyzed by conducting a ssGSEA in each sample, which resulted in an increased enrichment of immune-related cells (including CD8+ T cells, macrophage, and helper T cells; Figure 4(c)) and immune-related functions (Figure 4(d)) in Cluster 2 subtype.

3.4. Construction and Validation of an ARG Signature for Osteosarcoma. The univariate Cox analysis resulted in the

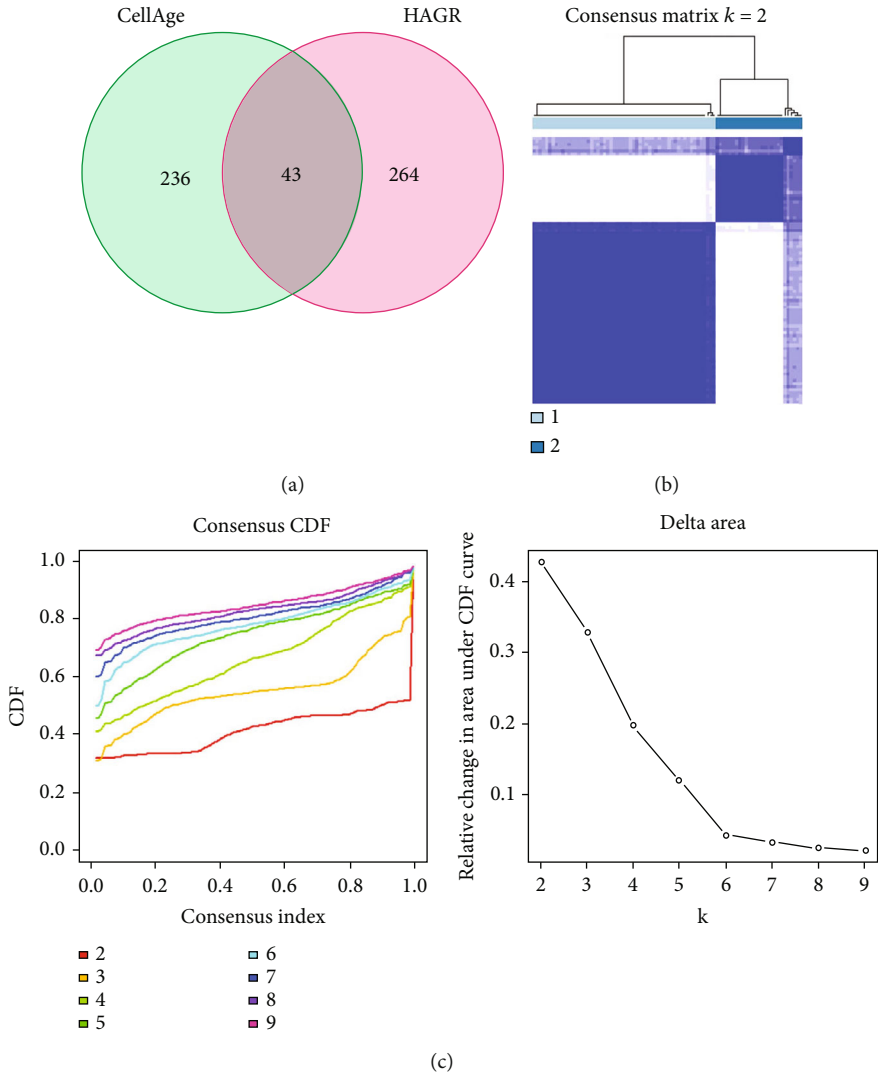

Figure 2: Identification of subtypes linked to aging in osteosarcoma. (a) 543 aging-related genes from CellAge and Human Ageing Genomic Resources (HAGR) database. (b) Consensus clustering solution map ($k = 2$). (c) The corresponding change in the area under the cumulative distribution function (CDF) curve for $k = 2$ to 9 is indicated by the consensus clustering-based Delta area curve.

identification of 52 ARGs that showed a considerable link to OS for individuals with osteosarcoma (Figure 5(a)). Afterward, a total of 23 ARGs were identified as hub genes to establish the ARG signature for osteosarcoma utilizing the LASSO analysis and the multivariate Cox regression (Figures 5(b) and 5(c)). Each sample was scored using the formula, and the coefficients were shown in Table 1S. Afterward, the patients were then classified based on the median value into the two risk groups. The PCA analysis demonstrated that ARGs in the signature (Figure 5(d)) could discriminate and differentiate the two risk groups to a higher degree as compared to all ARGs (Figure 5(e)) and the whole genome (Figure 5(f)). The OS time demonstrated a negative link to the risk score ($r = -0.58$) (Figures 6(a) and 6(b)), which can be depicted using the Kaplan-Meier analysis that illustrated a link between the high-risk group and a shorter OS time compared to the low-risk group (Figure 6(c)). The risk model was further evaluated for its prediction accuracy by deriving the area under the curve (AUC). The AUCs of the 1-, 3-, and 5-years OS yielded the following respective values of 0.901, 0.927, and 0.950 (Figure 6(d)), which outperformed the AUCs obtained with clinicopathological variables (Figure 6(e)), including age, stage, and metastasis with respective values of 0.469, 0.437, and 0.694. C-index (Figure 6(f)) and DCA analysis (Figure 6(g)) also confirmed that the prediction capacity of the risk score outperformed that of age, stage, and metastasis. The risk score could also function as an independent predictor of the poor OS of patients with osteosarcoma, as demonstrated by the univariate (Figure 6(h)) and multivariate (Figure 6(i)) Cox analyses. The survival probability and the risk score relationship in age (Figure 7(a)), gender (Figure 7(b)), metastasis (Figure 7(c)), and tumor site (Figure 7(d)) subgroup were also investigated. The analysis indicated that the OS duration of the patients with the higher risk score was shorter in each subgroup, except in the no leg group, possibly due to too

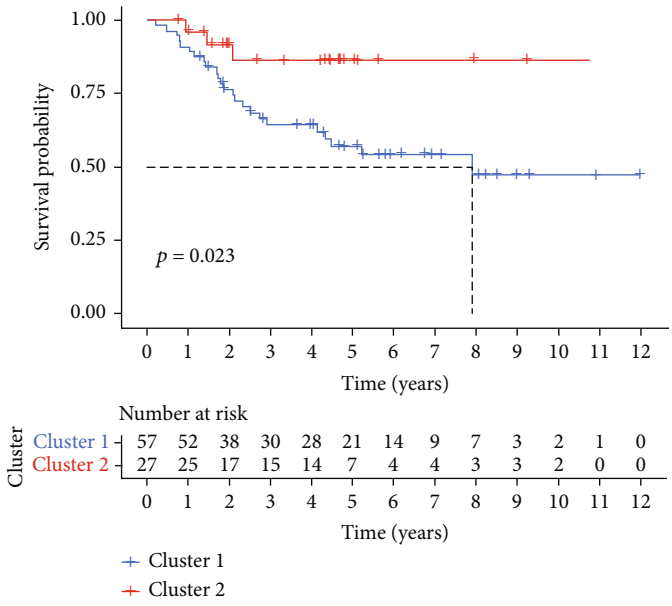

(a)

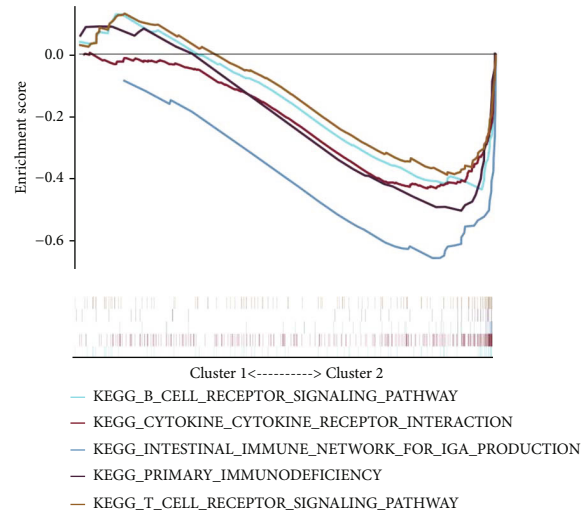

(b)

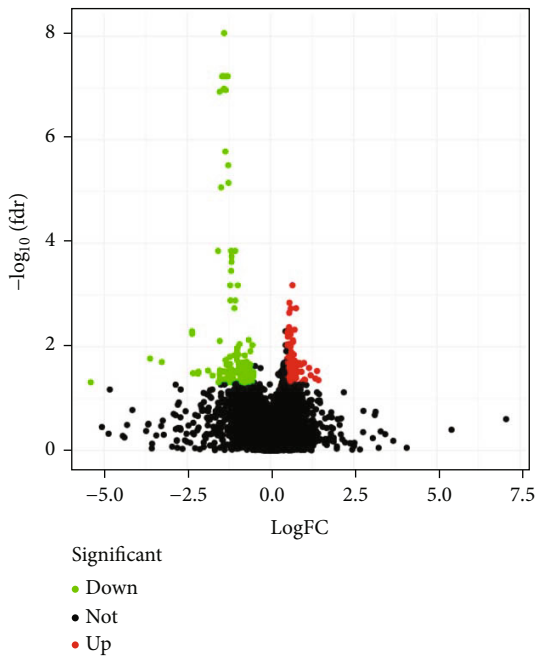

(c)

Figure 3: Continued.

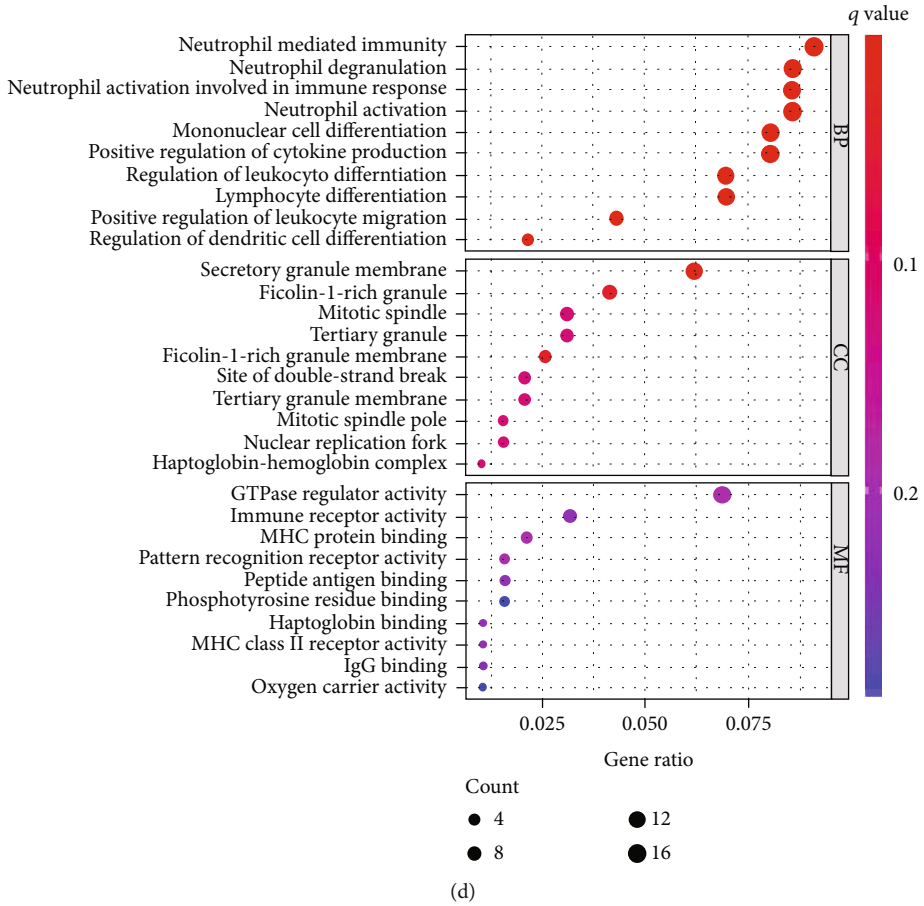

(d)

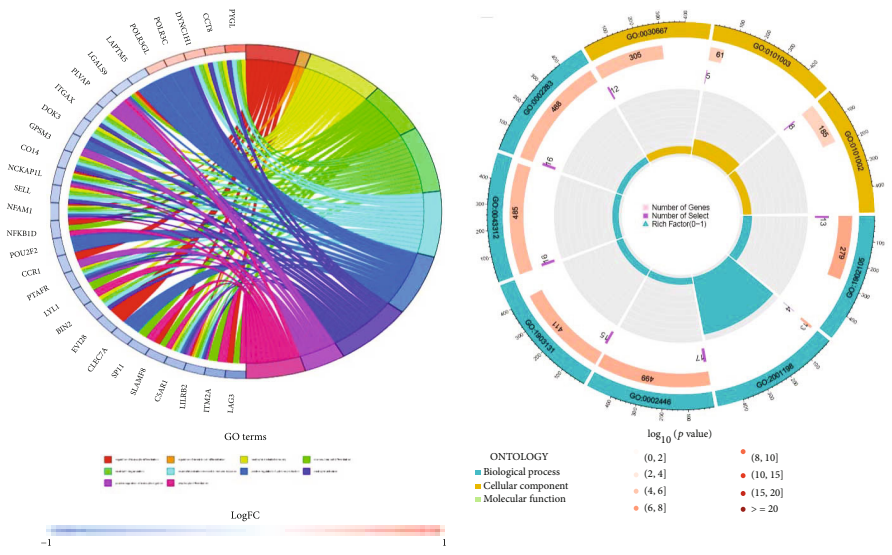

(e) (f)

Figure 3: Continued.

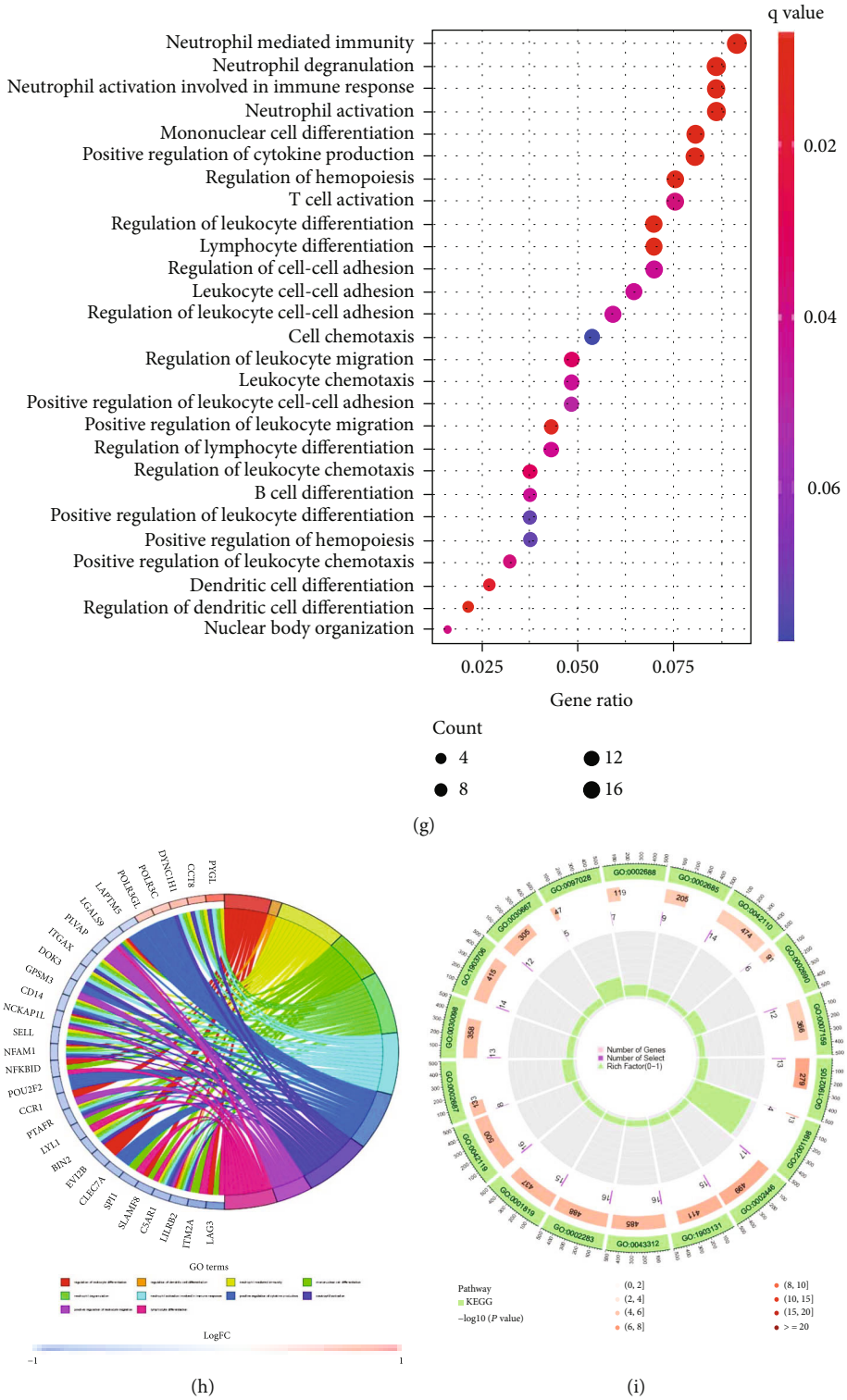

Figure 3: Functional enrichment analysis. (a) Kaplan-Meier curves of OS in Cluster 1 and Cluster 2 subtypes. (b) Gene Set Enrichment Analysis (GSEA) for determination of the underlying signaling pathway in Clusters 1 and 2 subtypes. (c) Volcano plot presents DEGs between Cluster 1 and Cluster 2 subtypes with threshold of |log2 FC| >0.5 and $P < 0.05$. Bubble diagram (d), chord plot (e), and circle plot (f) of Gene Ontology (GO) enrichment analysis by 278 DEGs. Bubble diagram (g), chord plot (h), and circle plot (i): Kyoto Encyclopedia of Genes and Genomes (KEGG) enrichment analysis by 278 DEGs.

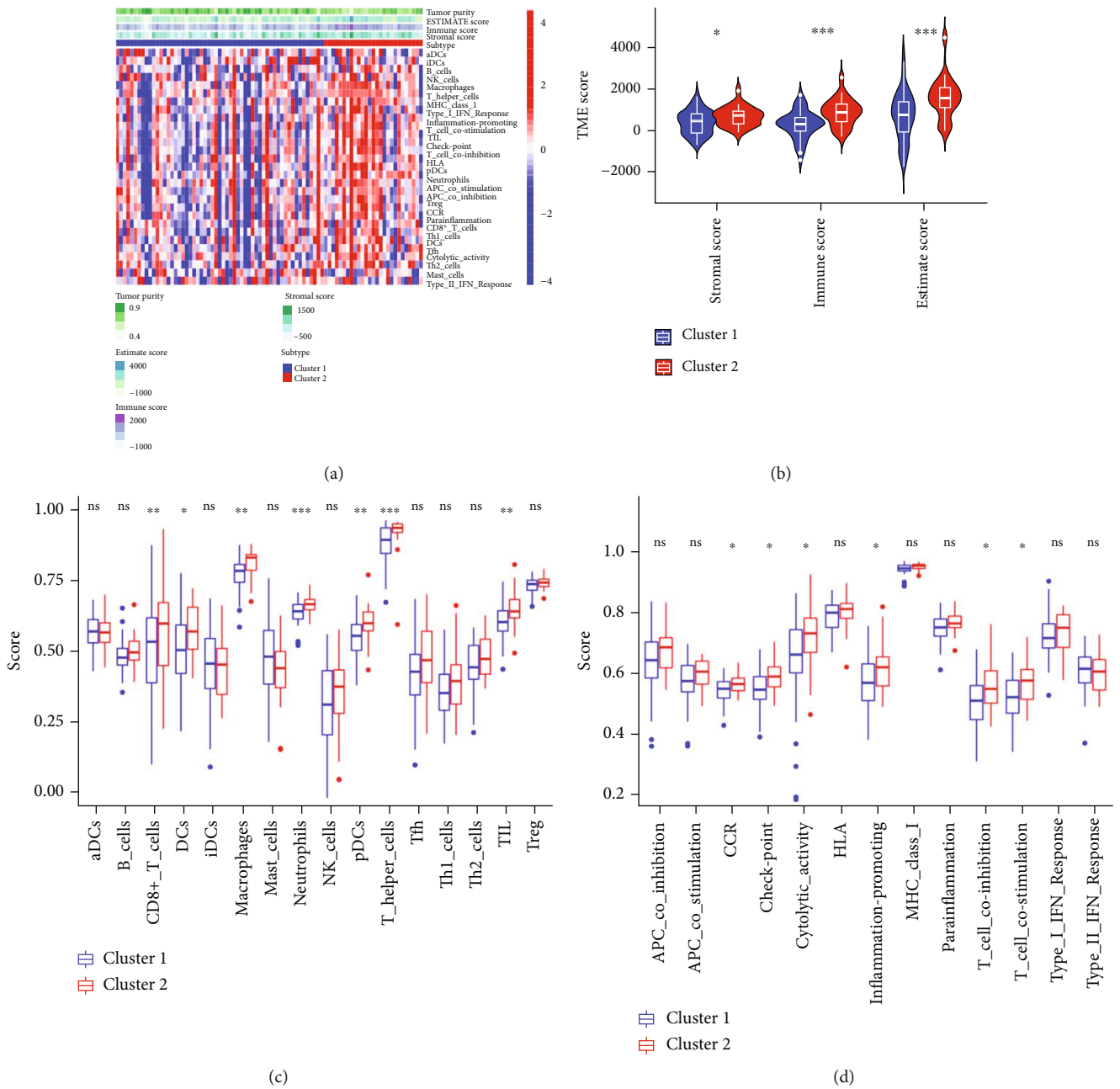

Figure 4: Immune landscape between Cluster 1 and Cluster 2 subtypes. (a) The heatmap shows the tumor microenvironment score, infiltration level of immune cells, and pathways related to the immune system in Clusters 1 and 2 subtypes. (b) Violin plots show the StromalScore, ImmuneScore, and ESTIMATEScore in Clusters 1 and 2 subtypes. (c) Box plots present the infiltration levels of different immune cells in Clusters 1 and 2 subtypes. (d) Box plots present the different immune-related pathways in Clusters 1 and 2 subtypes.

small sample size. Subsequently, the validation cohort was set as 53 osteosarcoma patients in the GSE21257 where the risk score was negatively linked to OS time ($r = -0.29$, Figures 8(a) and 8(b)). In this cohort, the link between the higher risk score of patients and the poor survival rate was established using the Kaplan-Meier analysis (Figure 8(c)). The respective AUCs of the 1-, 3-, and 5-years OS were 0.827, 0.713, and 0.827 (Figure 8(d)). These results were further verified by the univariate Cox analysis that linked the risk score values with the OS rates (Figure 8(e); HR = 1.816, $P = 0.022$). Furthermore, multivariate Cox analysis indicated a poor prognosis for individuals with osteosarcoma who demonstrated higher risk scores (Figure 8(f); HR = 1.887, $P = 0.017$).

3.5. The ARG Signature Performed Better than Others in Prognostic Prediction for Osteosarcoma. The ARG prognosis model was compared with four other previously published gene signatures to examine their relative performance in prognosis prediction such as autophagy-related [20], ferroptosis-related [21], immune-related [22], and metabolism-related genes signatures [23]. Although these

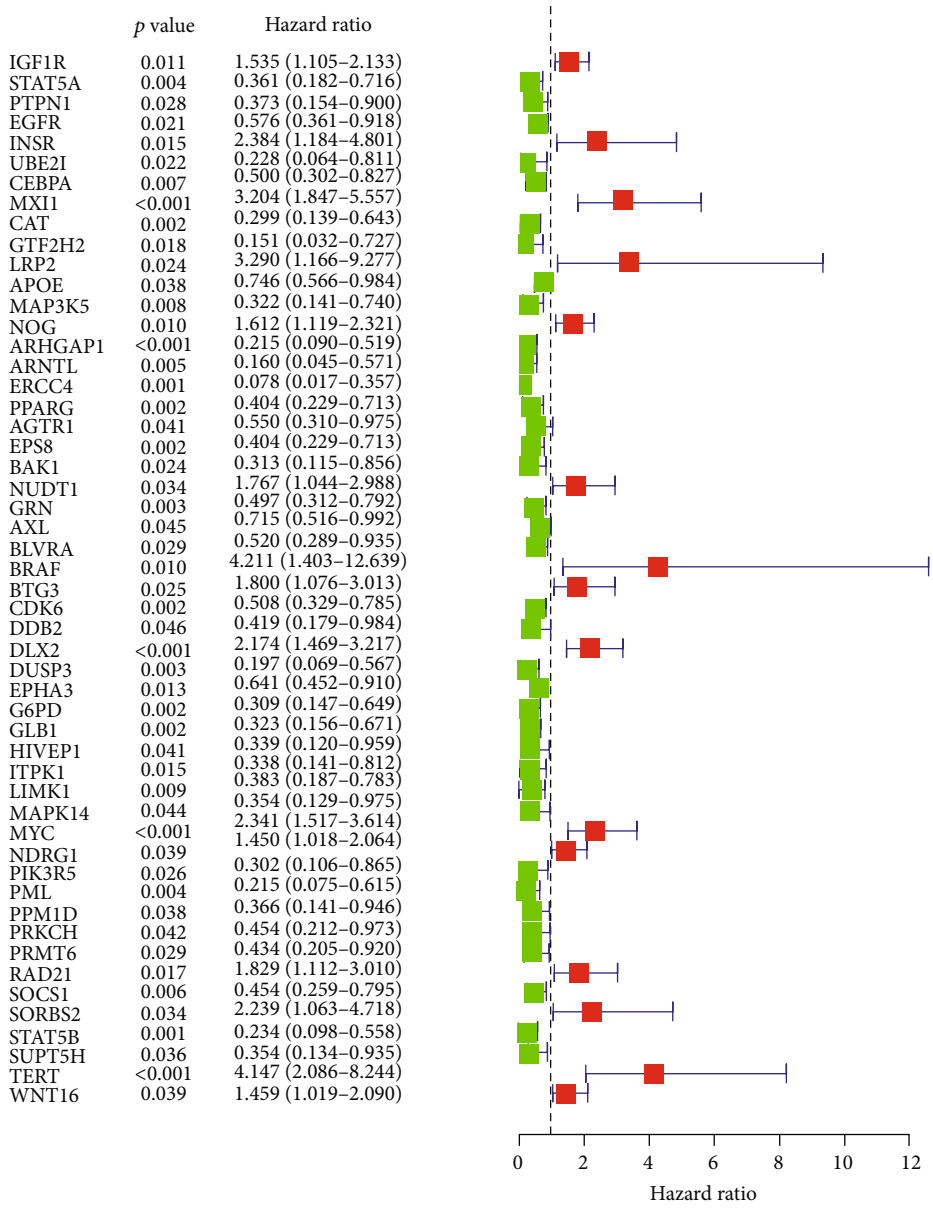

(a)

Figure 5: Continued.

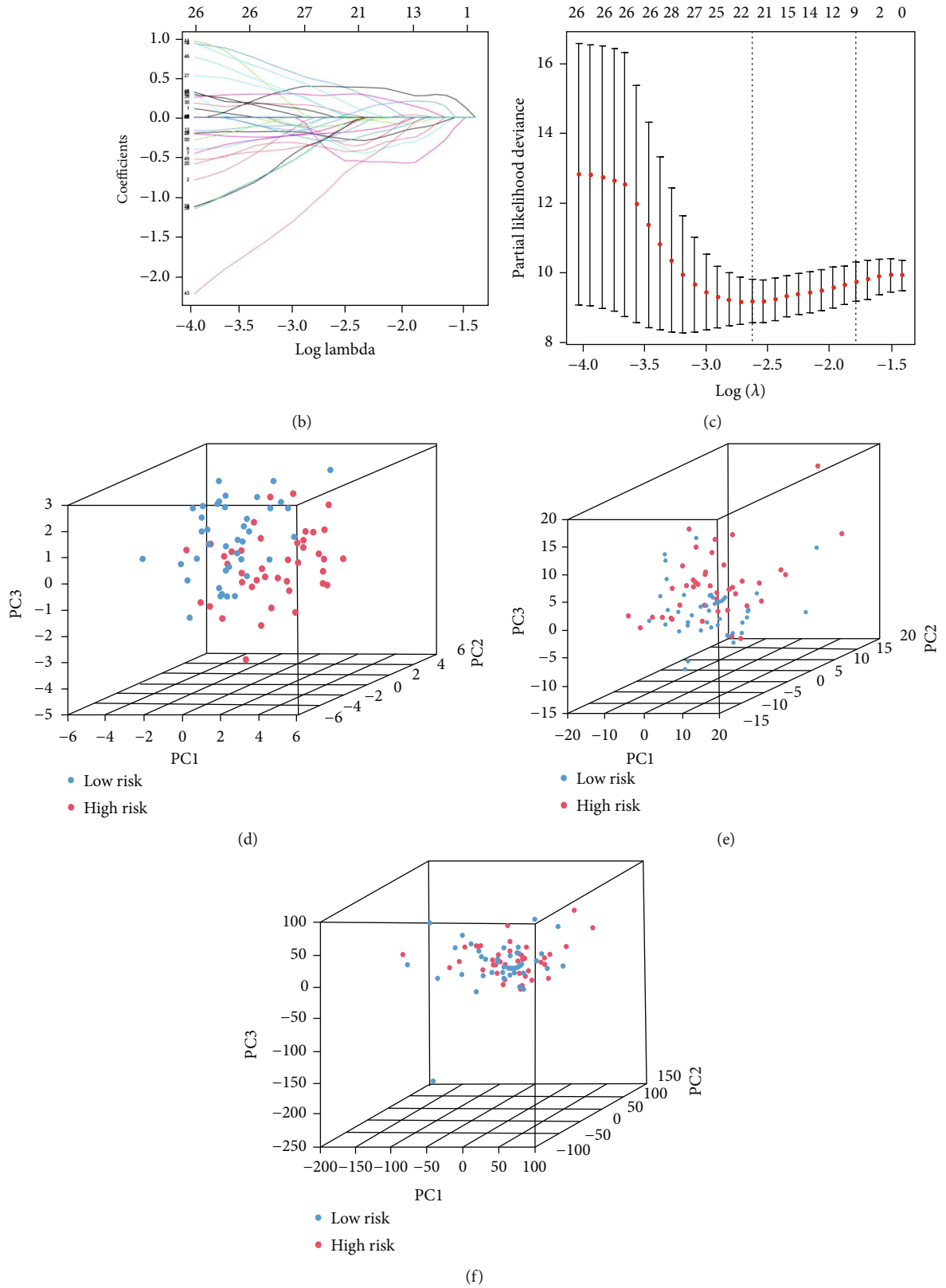

Figure 5: Construction of an aging-related risk model with prognostic value in osteosarcoma. (a) Forest plot utilizing the univariate Cox analysis to depict the prognosis-related aging-associated genes linked to OS. (b and c) The Least Absolute Shrinkage and Selection Operator (LASSO) regression analysis; the super parameter value was validated by means of 10-fold cross-validation. Principal component analysis (PCA) of genes in the signature (d), all aging-related genes (e), and the whole genome (f).

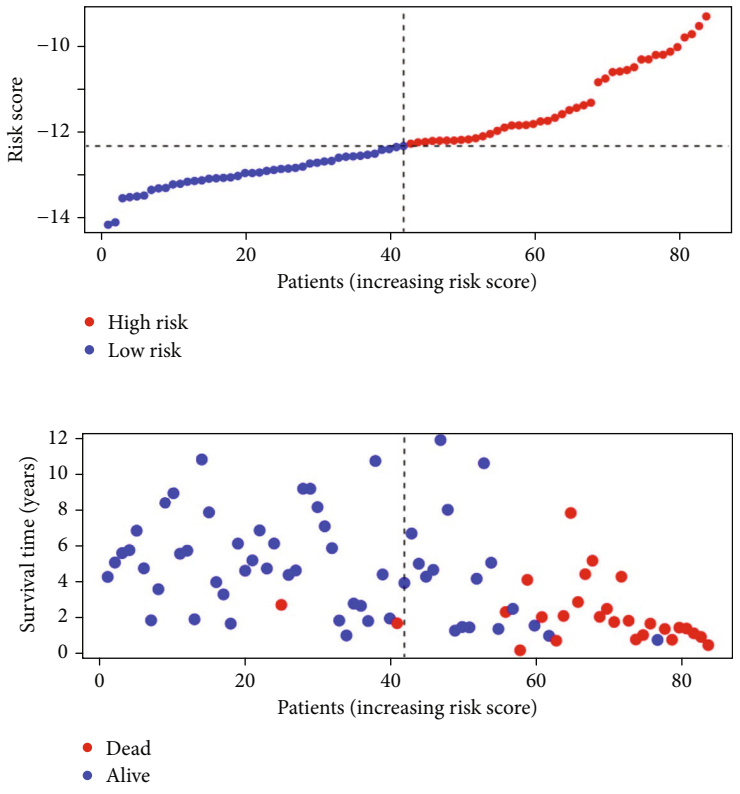

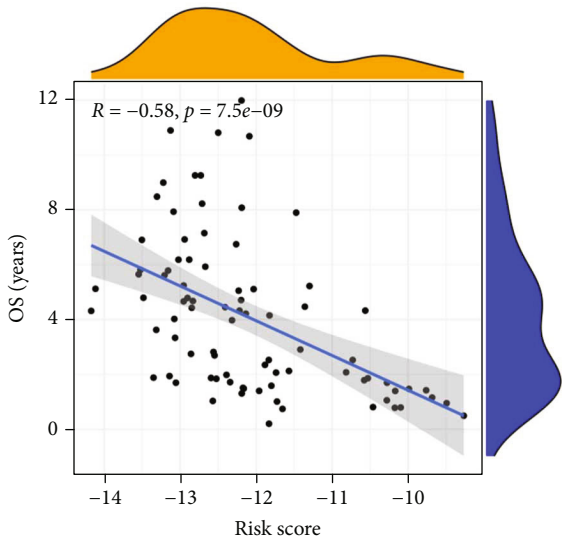

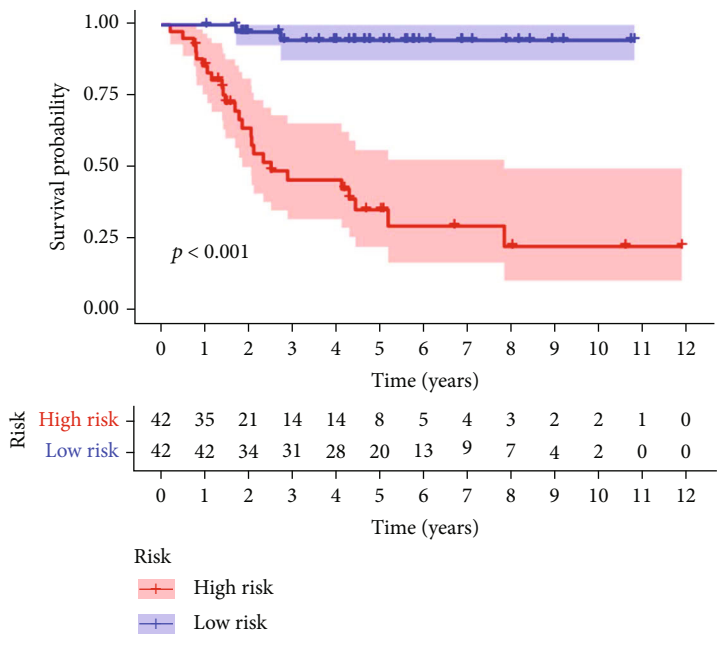

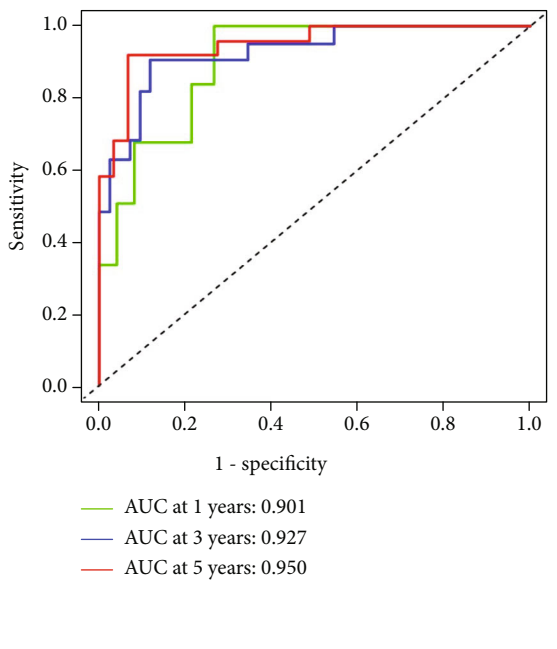

Figure 6: Continued.

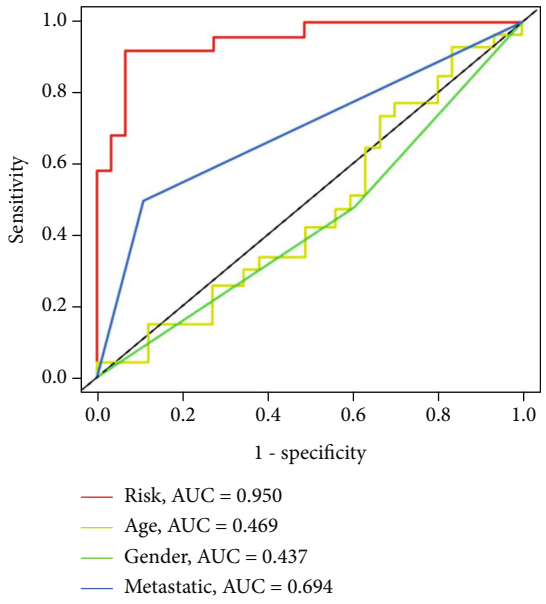

(e)

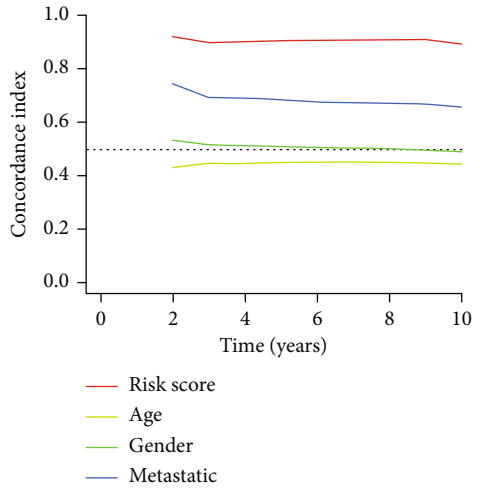

(f)

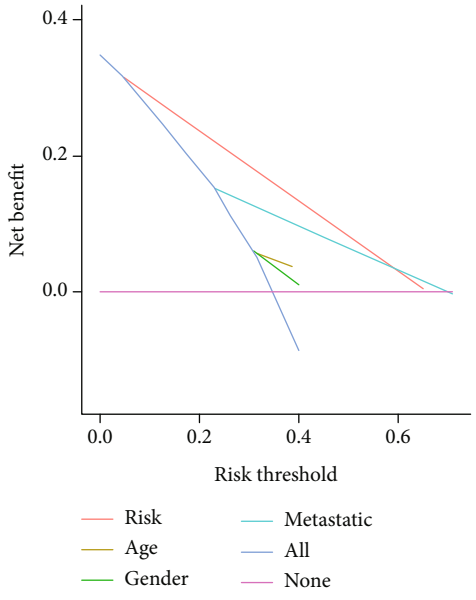

(g)

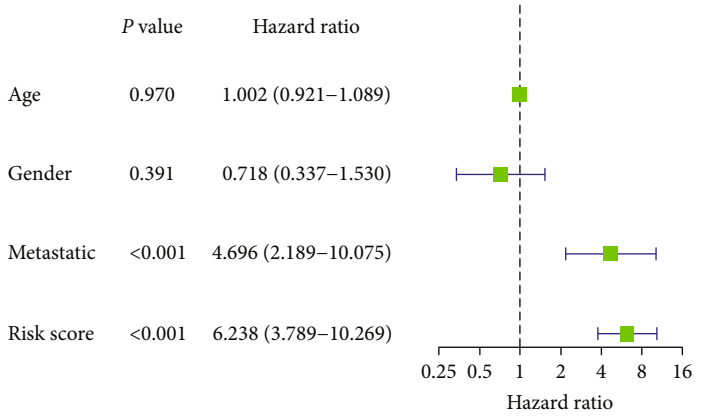

(h)

Figure 6: Continued.

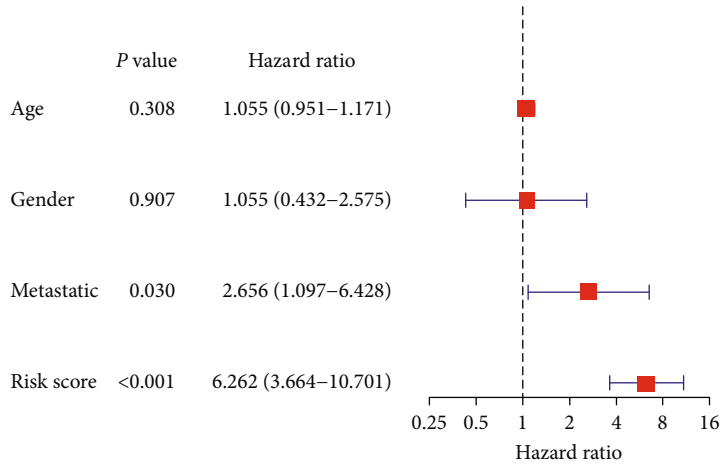

(i)

Figure 6: Validation of the gene signature linked to aging in the TARGET cohort. (a) Risk score, survival time, and survival status of individuals with osteosarcoma in the TARGET cohort. (b) The correlation between the risk score and survival time in the TARGET cohort. (c) Kaplan-Meier survival curve generated on the basis of an aging-related gene signature in the TARGET cohorts. (d) Risk model's ROC curve for 1-, 3-, and 5-year OS in the TARGET cohort. (e) ROC curve of the risk score, age, gender, and metastasis. (f) C-index for the risk score, age, gender, and metastasis. (g) Decision curve analysis (DCA) for the risk score, age, gender, and metastasis. Univariate (h) and multivariate (i) Cox analyses assess the risk model's independent prognostic value for individuals with osteosarcoma in the TARGET cohort using Cox analyses.

gene signatures were effective in creating two subgroups with considerably varied prognostic outcomes for the patients (Figures 9(a), 9(c), 9(e), and 9(g)), however, the ROC curve analysis and restricted mean survival time (RMST) values indicated the superiority of the model developed in this research. The aforementioned models depicted lower values of AUC as calculated by the former analysis for 1-, 3-, and 5-year survival compared to this model (Figures 9(b), 9(d), 9(f), and 9(h)), while this model had the highest C-index at 0.905 as calculated by RMST and obtained after comparison with the other models (Figures 9(i) and 9(j)).

3.6. Construction and Validation of the Nomogram Based on the Risk Model. To enable the nomogram to give a very accurate prediction, the clinical factors such as sex and age of the individual as well as tumor metastasis and tumor site were integrated into the prognostic signature (Figure 10(a)). The respective AUC of the 1-, 3-, and 5-year nomograms were 0.941, 0.884, and 0.896 (Figure 10(b)). The performance of nomograms was visualized utilizing the calibration curves for 1-, 3-, and 5-year OS, where the 45° line stands for the most accurate prediction ability. The closer the calibration curves for 1-, 3-, and 5-year were to the ideal curve, the better the nomogram performed (Figure 10(c)).

3.7. Correlation between Risk Model and Clinicopathological Parameters, as well as Infiltrating Immunocyte Fractions. The heatmap (Figure 11(a)) showed the clinicopathological parameters of patients in the two risk groups. The chi-squared test (Figure 11(b)) and Wilcoxon signed-rank test (Figure 11(c)) confirmed that the risk scores in individuals experiencing metastasis were increased as compared to those with no metastasis. The increased TME scores (including the StromalScore, ImmuneScore, and ESTIMATEScore) of the group with low-risk scores were further analyzed by TME analysis (Figure 12(a)), indicating that of the two risk groups, the one with the lower risk scores had an increased infiltration level of immune cells as compared to the group with higher risk scores. The analysis of the immune-related function through ssGSEA in the two risk groups demonstrated a higher level of enrichment of these functions in the group with low-risk scores. The level of infiltration of immune cells was analyzed through CIBERSORT where the immune cells were plotted using a bar graph to estimate their percentage in each risk group (Figure 12(c)). The abundance of activated memory CD4+ T cells and CD8+ T cells was significantly increased in the low-risk group (Figure 12(d)).

3.8. Immunotherapy Response Prediction. The correlation between the risk model and the expression of genes related to the immune checkpoints was studied, which indicated an enhanced immune activity in the TME that led to arresting the tumor growth in the low-risk group. The enhanced immunological activity was seen due to an increase in the expression levels of genes associated with the immunological checkpoints such as *PD-L1* (*CD274*), *CTLA4*, *LAG3*, *GZMB*, *CD8A*, *PRF1*, *HAVCR2*, *IFNG*, and *GZMA* (Figure 13). These results demonstrate the increased effectiveness of immunotherapy in targeting the immune checkpoints in the group with low risk scores.

4. Discussion

Osteosarcoma is a common malignant tumor originating from bone tissue in children and adolescents. Osteosarcoma has a high degree of invasion and potential for distant

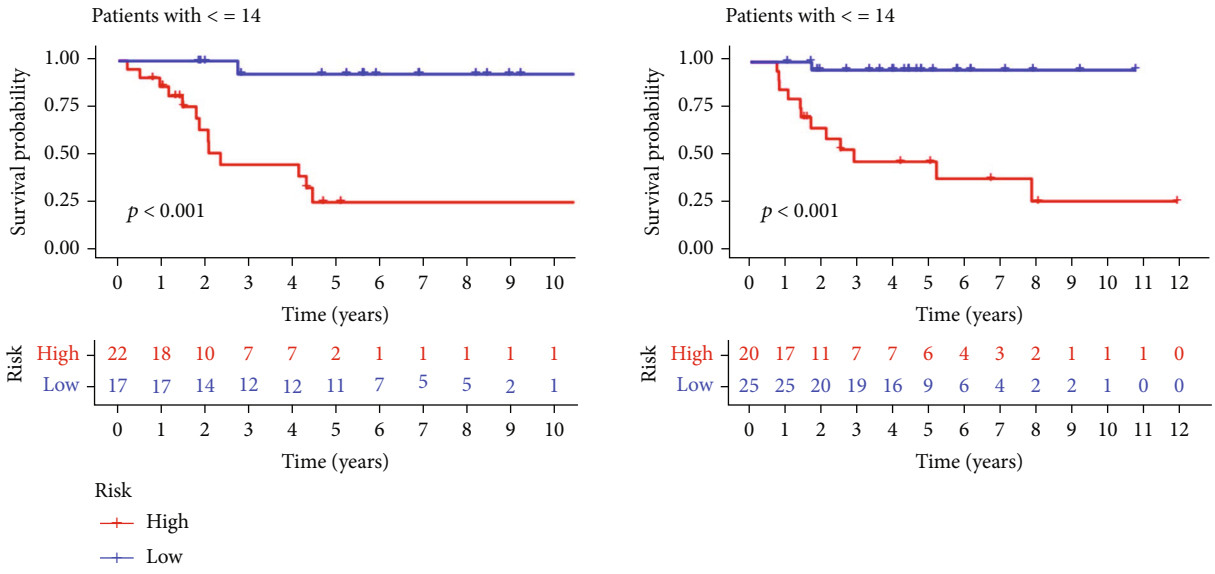

(a)

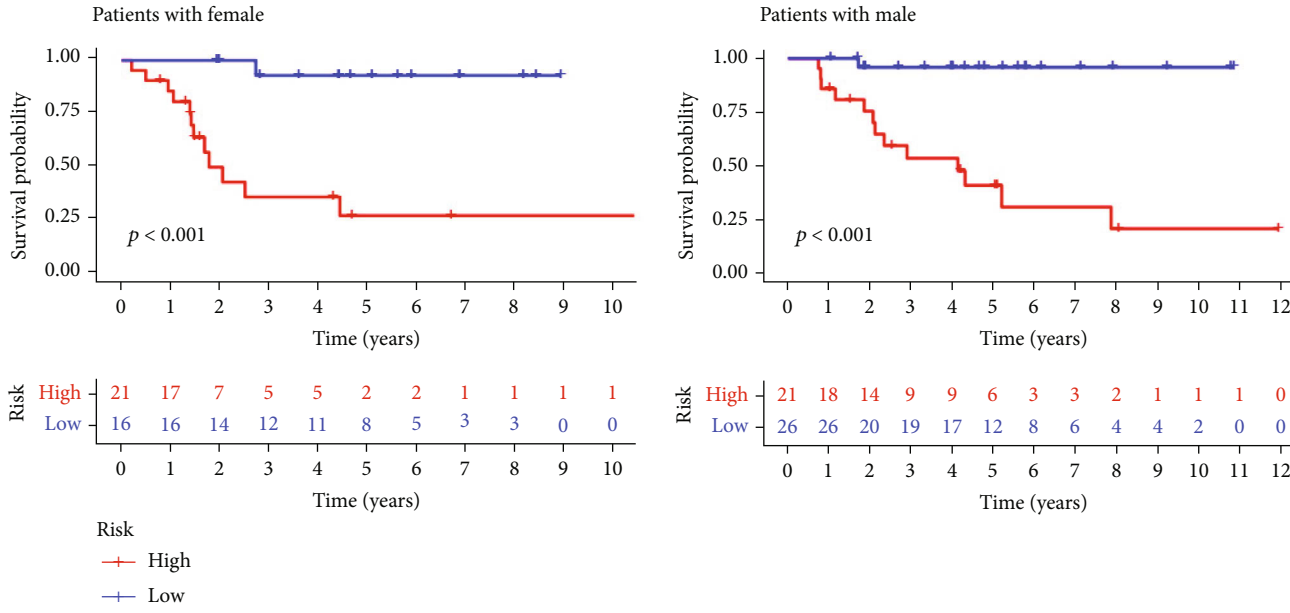

(b)

Figure 7: Continued.

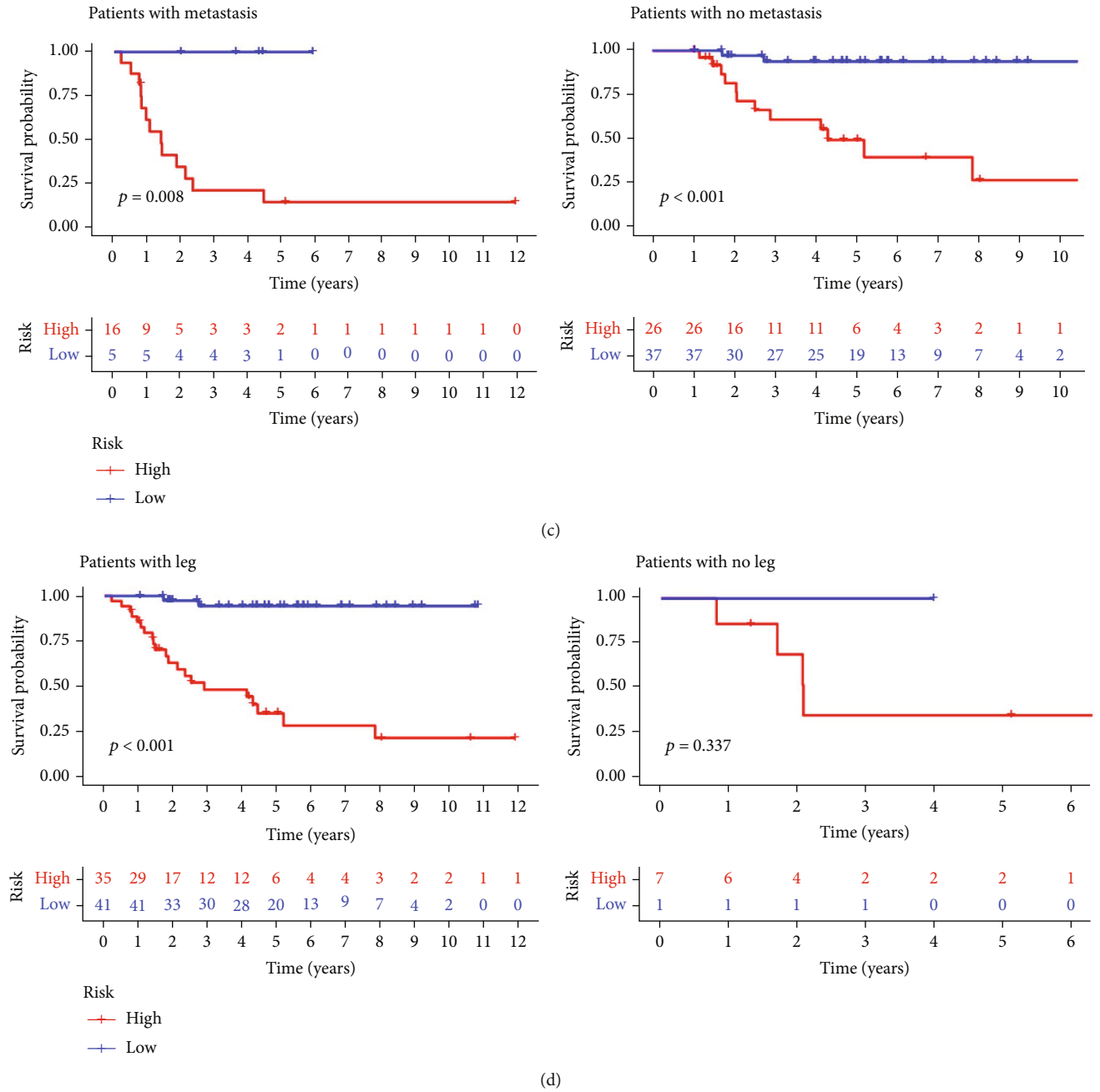

Figure 7: Kaplan-Meier survival curves in subgroup analyses on the basis of various clinical variables. (a) Subgroup survival analysis of risk model per age. (b) Subgroup survival analysis of risk model per gender. (c) Subgroup survival analysis of risk model as per metastatic status. (d) Subgroup survival analysis of risk model as per primary tumor site.

metastases and is prone to hematogenous metastases at the early stage and after surgery, especially in the case of lung metastases [25, 26]. In recent years, despite great progress in surgery and adjuvant chemotherapy, such patients still exhibit a poor prognosis, with a high recurrence rate [27]. Therefore, identifying effective prognostic markers for risk stratification of osteosarcoma patients to adopt more aggressive interventions is expected to improve OS and might serve as potential therapeutic targets.

Aging is characterized by the accumulation of damage to macromolecules and cell architecture resulting in a progressive decrease in the function of tissue and organ due to nutrition, genetic and environmental factors, and lifestyle [28]. The accumulation of these damaged arrested cells was observed with the increase in age [29], and these senescent cells were noted to contribute to diseases that are related to aging, such as renal damage [30], alcoholic fatty liver disease [31], cerebrovascular disorders [32], diabetes [12], and Alzheimer's disease [33]. Cellular senescence is an inherent process that inhibits tumor progression, contributing to arresting the cells autonomously in the cell cycle and preventing further divisions. This process also causes the

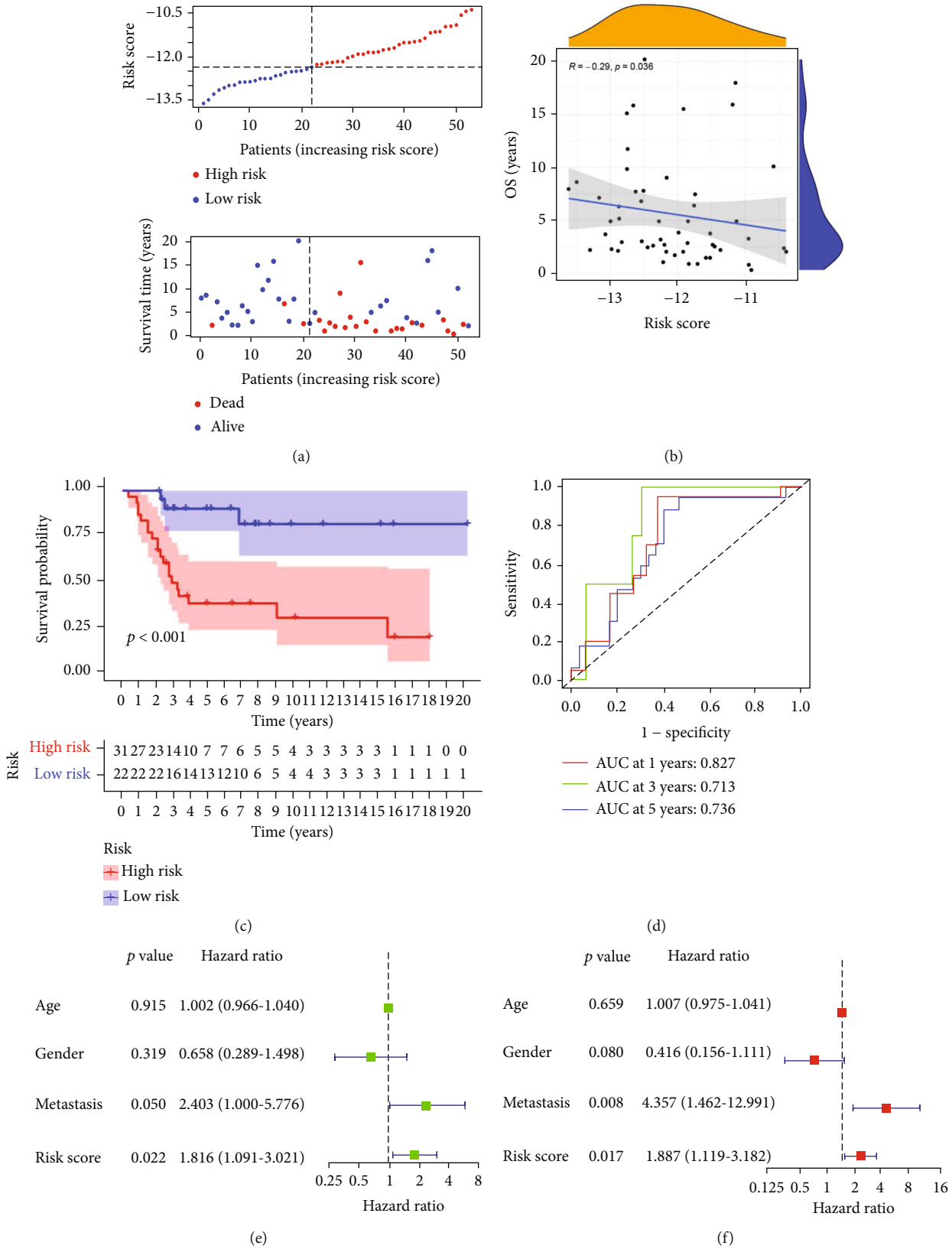

Figure 8: Verification of the aging-related gene signature in the GSE21257 cohort. (a) Risk score, survival time, and survival status of individuals with osteosarcoma in the GSE21257 cohort. (b) Correlation analysis between the risk score and survival time in the GSE21257 cohort. (c) Kaplan-Meier survival curve on the basis of an aging-related gene signature in the GSE21257 cohorts. (d) ROC curve of the risk model for 1-, 3-, and 5-year OS in the GSE21257 cohort. Evaluation of the independent prognostic value of the risk model using univariate (e) and multivariate (f) Cox analyses for osteosarcoma patients in the GSE21257 cohort.

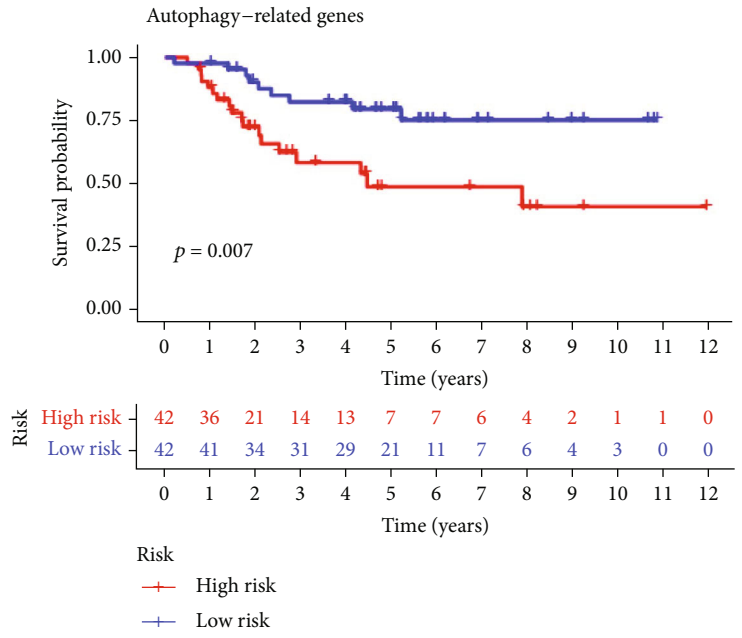

(a)

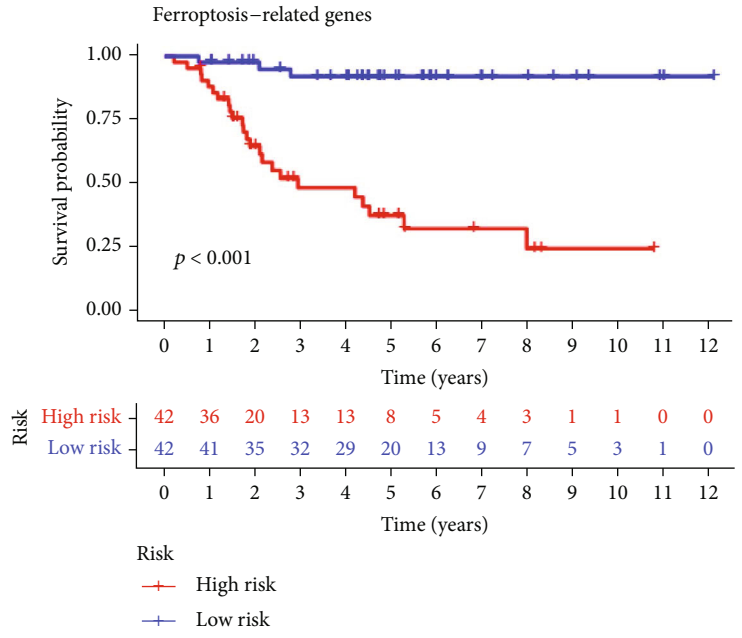

(b)

Figure 9: Continued.

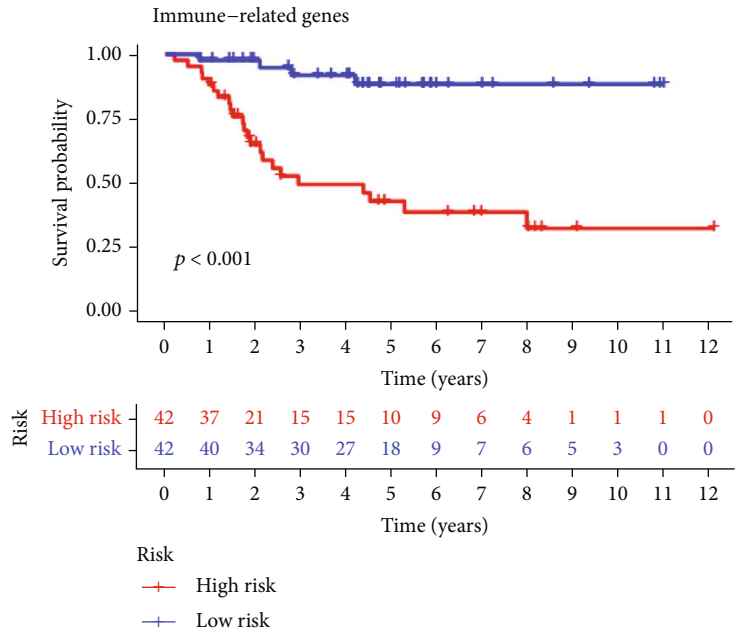

(c)

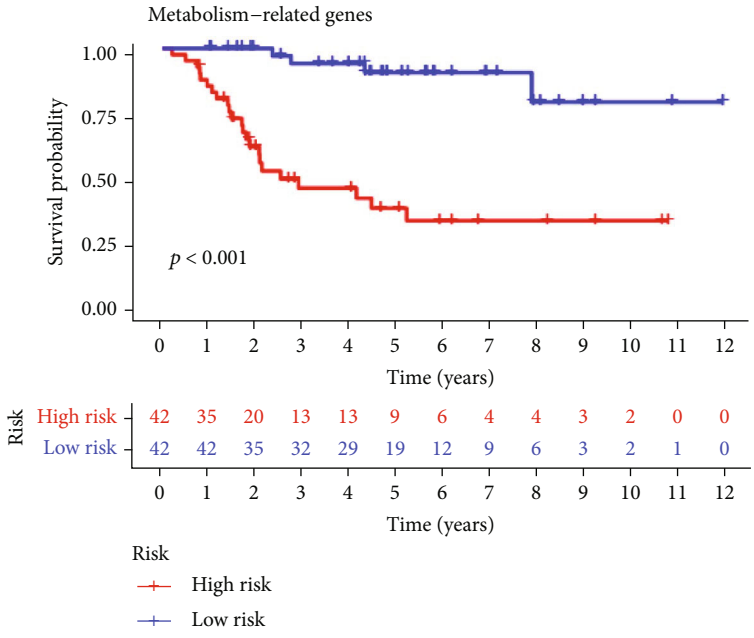

(d)

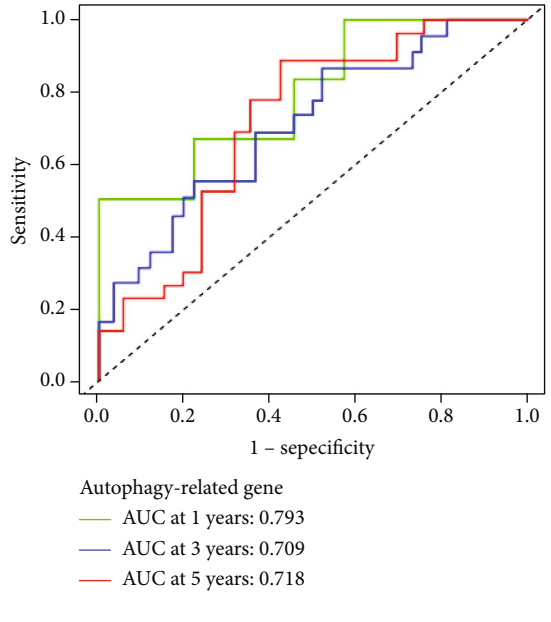

(e)

Figure 9: Continued.

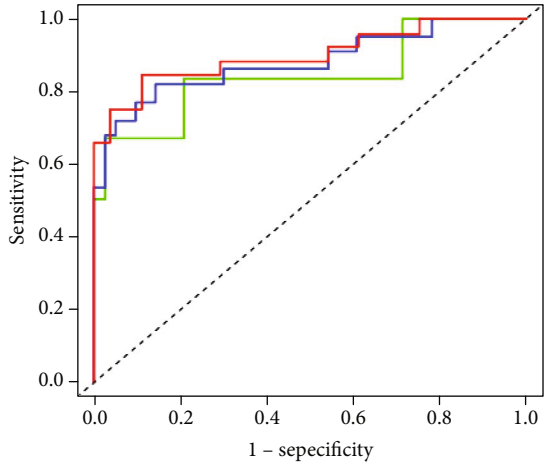

(f)

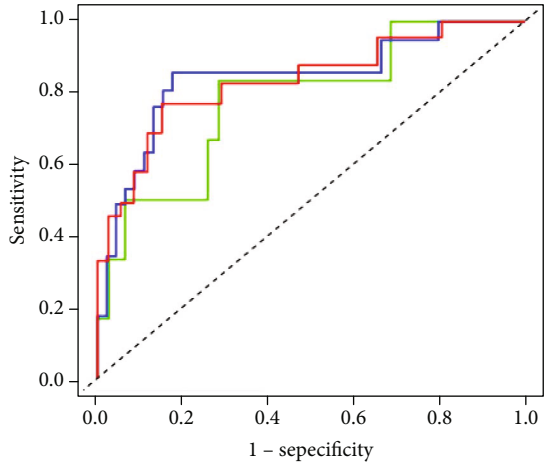

(g)

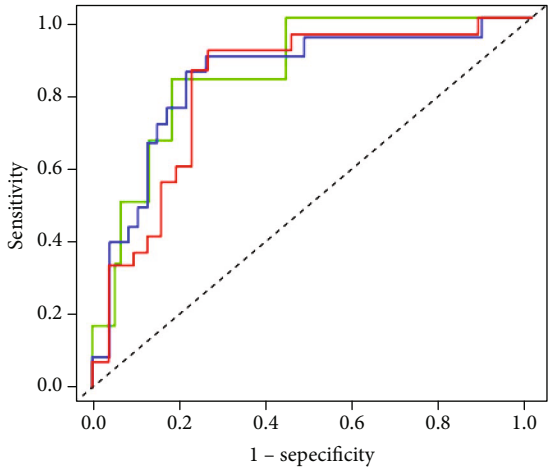

(h)

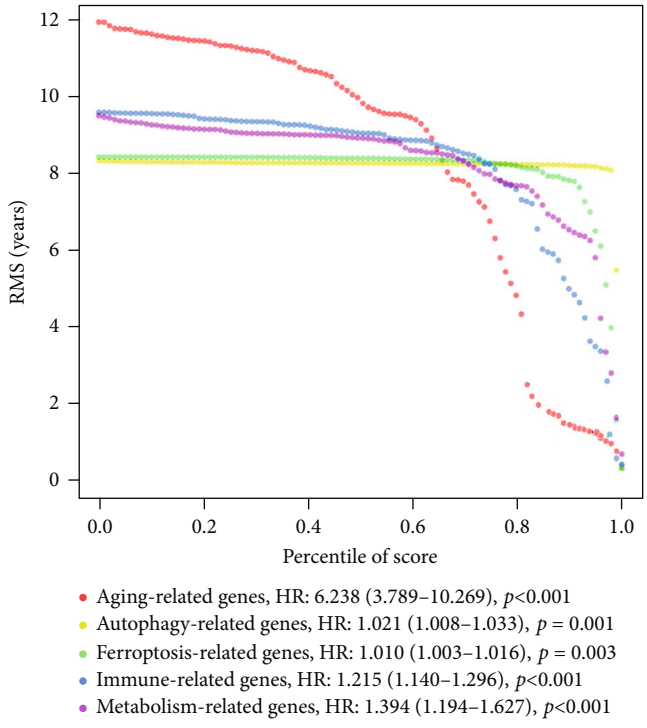

(i)

Figure 9: Continued.

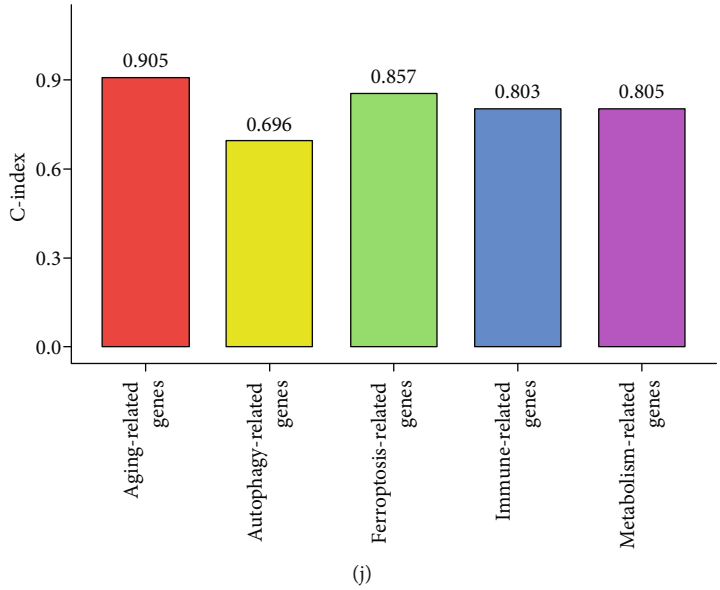

Figure 9: Comparison of the performance of the constructed seven-gene signature to previous signatures in the TARGET cohort. Kaplan-Meier survival analysis of autophagy-related genes signature (a), ferroptosis-related genes signature (b), immune-related genes signature (c), and metabolism-related genes signature (d). Time-dependent ROC curves of autophagy-related genes signature (e), ferroptosis-related genes signature (f), immune-related genes signature (g), and metabolism-related genes signature (h). (i) Restricted mean survival time (RMST) curve for all signatures. (j) C-index for all signatures.

removal of these damaged cells by activating the immune system through the SASP, but if the cells evade this fate, it may lead to tumorigenesis [34]. Emerging evidence showed that several ARGs may be the cause of onset and advancement of cancers due to regulation of the process of aging and cellular senescence by these ARGs and could be used as a target for cancer therapy [35, 36]. Consequently, to analyze the exact role that aging plays in osteosarcoma, the transcriptome of the ARGs needs to be investigated thoroughly.

In the current study, using the unsupervised consensus clustering analysis, two subtypes in the TARGET cohort were determined that were related to aging, and both groups exhibited considerably varied outcomes regarding the prognosis. Furthermore, various analyses gave results that were favorable for Cluster 2 that indicated an enrichment of the signaling pathways associated with the immune response and an enhanced infiltration rate of immune cells in the TME. The GSEA was carried out for the former to determine the extent of the response by the immune system as those values could be used for observation of the progression of cancer [37]. In addition, the active immune response led to a good prognosis of the Cluster 2 subtype. The TME is an intricate network of immune cells, tumor cells, and stromal cells that contribute to tumor biology and therapeutic response. An increased infiltration level due to increased enrichment of immune effector cells was detected in Cluster 2 during the analysis of the TME, such as CD8+ T cells, macrophages, and helper T cells which can act as a protective factor against multiple cancers, such as epithelial ovarian cancer [38], head and neck squamous cell carcinoma [17, 39], and non-small-cell lung cancer [40]. These partly explain that patients belonging to the Cluster 2 subtype had a higher antitumor immune response and good prognosis.

The construction of an accurate and efficient model for cancer monitoring has become a research hotspot due to advances in RNA-sequencing and bioinformatics tools. Research has shown a considerable correlation of several ARG signatures with the prognosis of cancers such as Zhang et al. [41], Wang *et al.* [42], and others who developed gene signatures. In both cases, gene signatures that were aging-related were designed to evaluate the potential prognosis prediction efficiency of a biomarker for malignancy and study the effect of chemo- and immunotherapies. The former studied lung adenocarcinoma, while the latter studied rectal cancer. In other studies, results similar to these were detected such as in malignant melanoma [43] and lung squamous carcinoma [44]. Nevertheless, there are fewer studies about the function of ARGs as a prognosis-determining factor in osteosarcoma. In this research, an ARG signature was demonstrated to better predict the prognosis of osteosarcoma than conventional clinicopathological characteristics utilizing LASSO regression and multivariate Cox regression analysis. The risk scores and metastasis could predict the patients' prognosis independently as depicted by the univariate and multivariate Cox regression analyses, which was consistent with the finding in the validation cohort. Moreover, compared to previously reported signatures for osteosarcoma prognosis [20–23], the time-dependent ROC curve analysis and C-index revealed a better ability of this ARG model to predict the prognosis of patients with osteosarcoma. Subsequently, using risk scores and clinical characteristics, a nomogram was developed that depicted more convenient usage in clinical settings. The

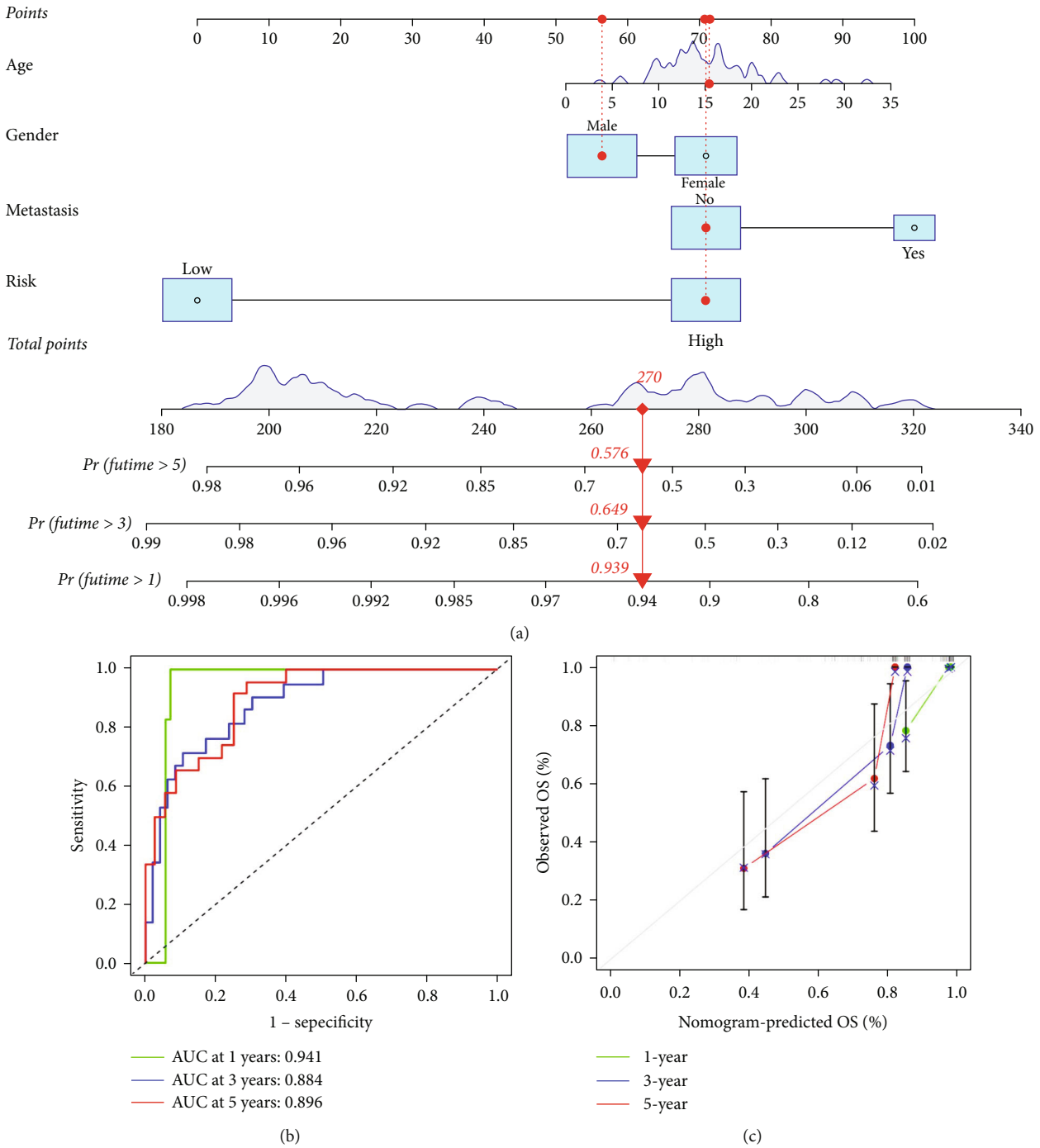

Figure 10: Predicting the outcome of patients with osteosarcoma using nomograms. (a) Nomogram established by the risk score, age, gender, and metastasis. (b) Nomogram's ROC curves for prediction of OS over 1, 3, and 5 years. (c) Calibration curves of the nomogram for prediction of 1-year, 3-year, and 5-year OS.

nomogram exhibited better performance than the single ARG risk model in predicting short-term OS. Based on the above finding, the ARG risk model was a promising novel prognostic marker and could improve individualized treatment strategy.

Emerging immunotherapy, including anti-CTLA4 [45], anti-LAG3 [46], anti-PD-1, and anti-PD-L1 antibodies [47], has been proven to be efficacious and increased the survival rate of patients with several advanced cancers, including metastatic osteosarcoma patients [48]. However, considering the heterogeneity and complexity of osteosarcoma, only a few patients had a favorable response to immunotherapy [49]. The components and activity of TME are critical determinants of the response to immunotherapy [50]. As compared with other cancers, osteosarcoma has low immune infiltration in TME, which may be one reason

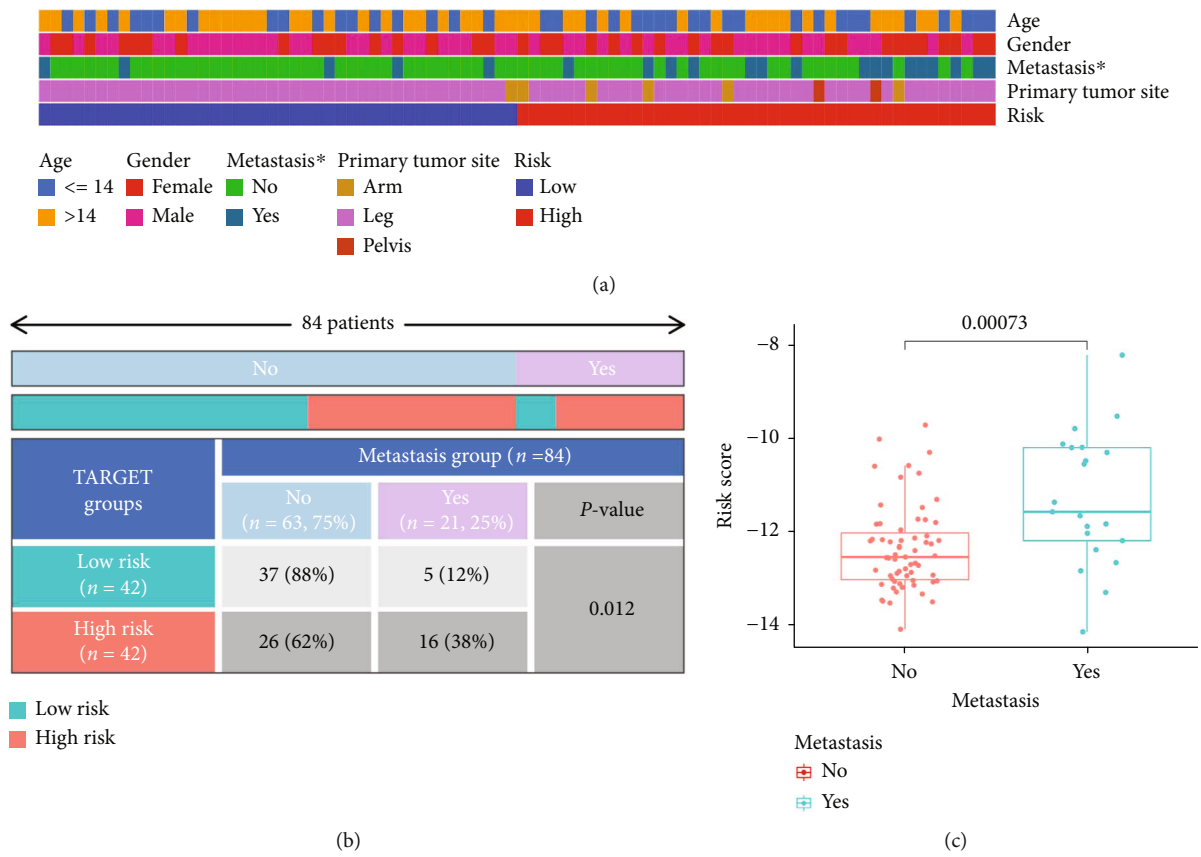

Figure 11: The correlation of the risk score with the clinical characteristics of osteosarcoma. (a) The heatmap of clinicopathological parameters in the high- and low-risk groups in the TARGET cohort. (b) The association between risk score and metastatic status by the chi-squared test. (c) Box plot presents the higher risk score in the metastasis patients than no metastasis patients by the Wilcoxon signed-rank test.

for unsatisfactory immunotherapy results [49, 51]. In this research, the group with the lower risk scores had increased StromalScore, ImmuneScore, and immune functions, indicating that the risk group with low scores demonstrated increased immune infiltration level and immunogenicity in comparison with the high-risk group, which probably contributed to the better survival outcomes. The CIBERSORT analysis showed that CD8+ T cells and activated memory CD4+ T cells were more infiltrated in the low-scoring risk group. CD8+ T cells are essential in the antitumor activity and are a favorite prognosis marker for osteosarcoma patients [52]. The CD8+ T cells can be differentiated into cytotoxic T lymphocytes (CTLs) by CD4+ T cells through multiple mechanisms, as well as maintaining and enhancing the antitumor response of CTLs [53]. Intriguingly, CD4+ T cells have been identified as having direct antitumor cytolytic function [54]. The efficiency of blockade therapy based on immune checkpoints is primarily dependent on the expression of genes associated with immune checkpoints and T cell-dependent immune response [55]. Unsurprisingly, in the low-risk group, the immune checkpoint genes were expressed more, particularly PD-L1, CTLA4, and LAG3, showing that the low-risk patients could be more benefited from the immune checkpoint blockade therapy. Therefore, this study indicates that the ARG signature may be useful in filtering patients who can benefit from immunotherapy.

This study had some limitations. Both the TARGET-OS cohort and the GSE21257 cohort have relatively small sample sizes, and the finding based on bioinformatics analysis was insufficient for clinical practice. Therefore, the results need to be verified by utilizing large study samples and *in vitro* or *in vivo* experimental verification. Furthermore, the specific functions of ARGs in the signature in osteosarcoma remain ambiguous and need more study.

5. Conclusion

In conclusion, this study identified two aging-related subtypes and an ARG prognostic signature that depicted robust performance in the prognosis prediction of osteosarcoma patients, which might help in guiding clinical management. Furthermore, ARG prognostic signature showed the different immune landscapes for osteosarcoma patients, which guide the personalized application of immunotherapy. However, before applying aging-related subtypes and prognostic signatures, these findings need to be verified by more clinical samples.

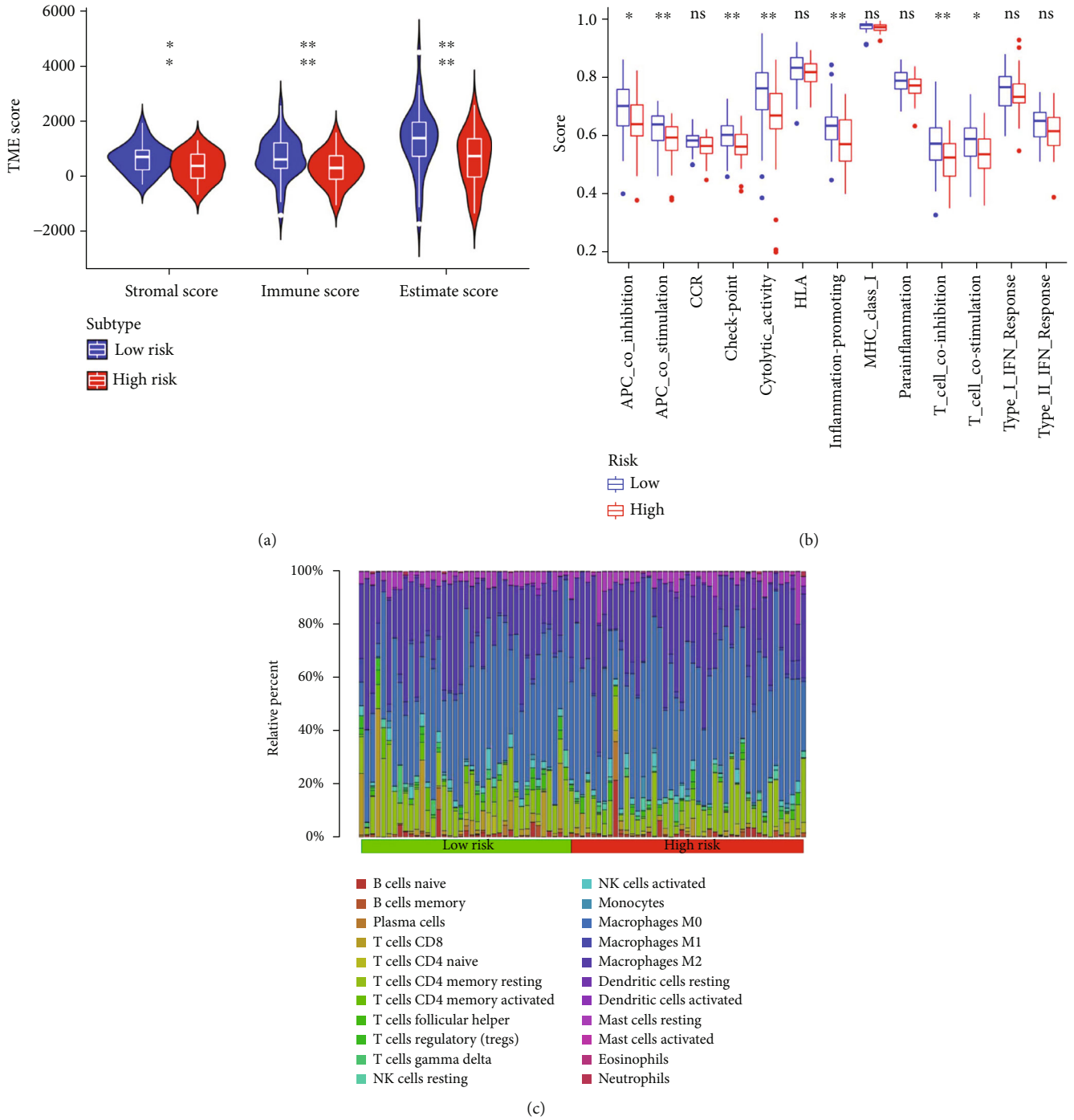

Figure 12: Continued.

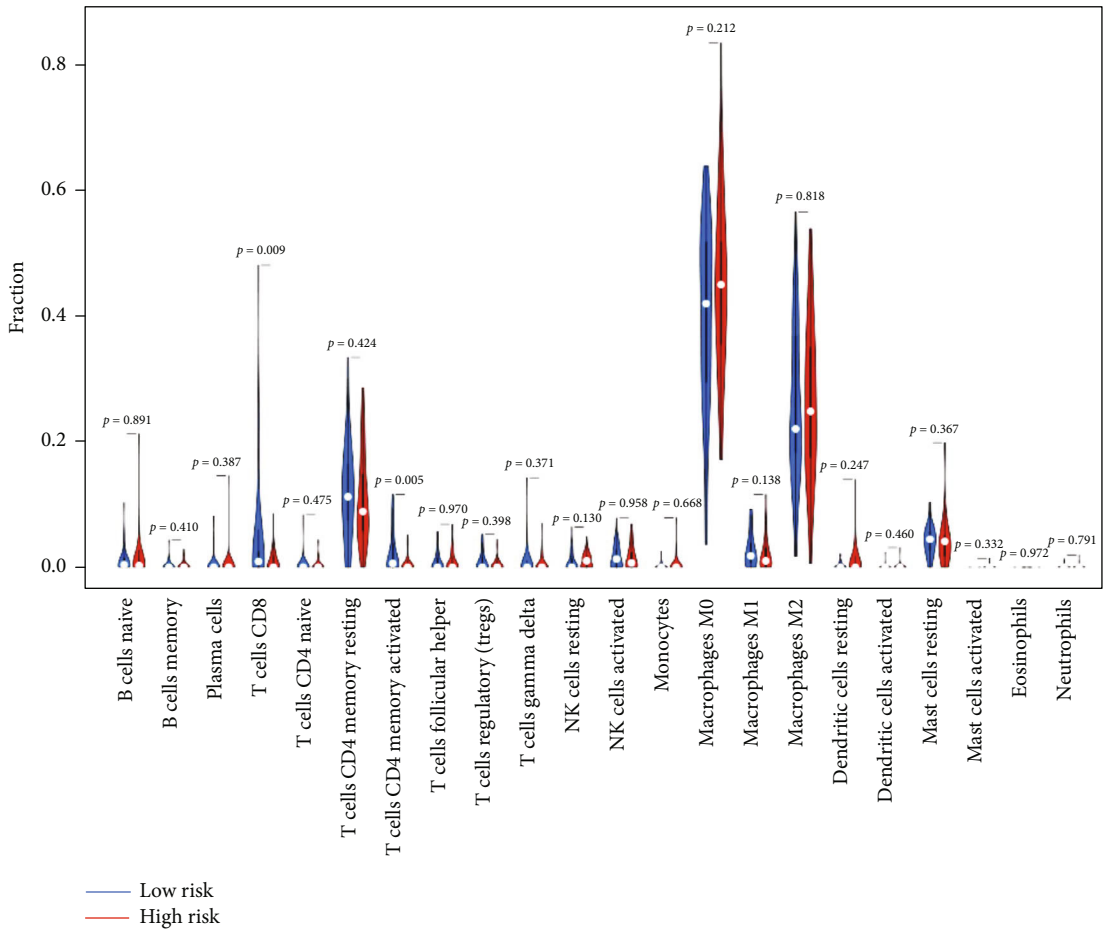

(d)

Figure 12: Immune landscape between the high-risk and low-risk groups. (a) Violin plots show the StromalScore, ImmuneScore, and ESTIMATEScore between the high-risk and low-risk groups. (b) Box plots present the difference in immune-related pathways between the high-risk and low-risk groups. (c) Relative proportion of infiltration levels of immune cells in the high-risk and low-risk groups. (d) Violin plot illustrates the considerable variation in immune cells between both risk groups.

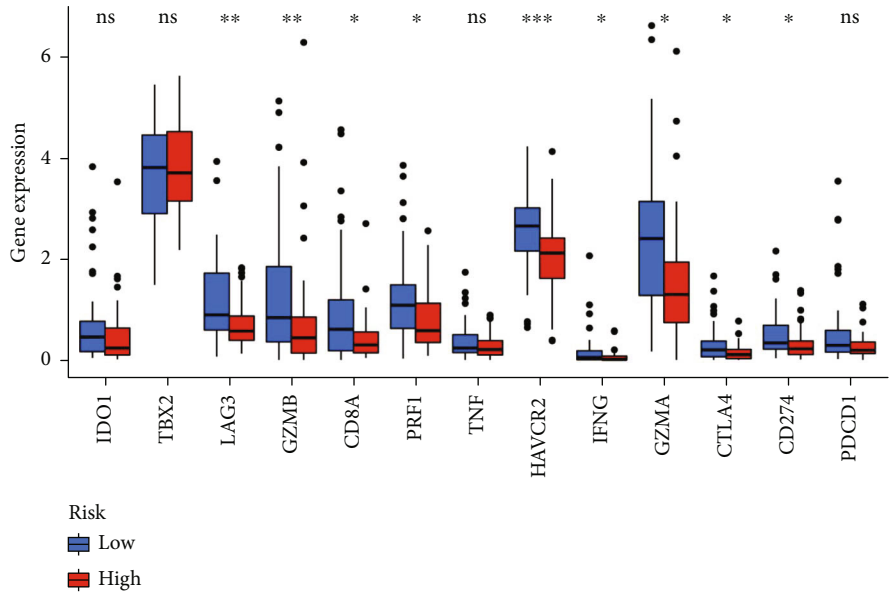

Figure 13: Differential expression of multiple immune checkpoint genes between the high- and low-risk groups.

Data Availability

The TARGET datasets and Gene Expression Omnibus database provided the supporting data for the conclusions drawn in this study and can be accessed at their websites: (https://ocg.cancer.gov/programs/target) and (https://www.ncbi.nlm.nih.gov/geo), respectively.

Conflicts of Interest

The authors declared no financial or any other conflicts of interest associated with this study.

Authors' Contributions

The present research was designed by JH and WM. JH acquired the information and wrote the manuscript. The data was analyzed by XW, LY, JL, and HH. The manuscript was reviewed by all the authors.

Acknowledgments

The study was funded by the Natural Science Foundation of Ningbo (202003 N4298) and the Medical Health Science and Technology Project of Zhejiang (2022KY341).

Supplementary Materials

Table 1S: the coefficients of aging-related genes in the signature. *(Supplementary Materials)*

References

[1] I. J. Lewis, M. A. Nooij, J. Whelan et al., "Improvement in histologic response but not survival in osteosarcoma patients treated with intensified chemotherapy: a randomized phase III trial of the European Osteosarcoma Intergroup," *Journal of the National Cancer Institute*, vol. 99, no. 2, pp. 112–128, 2007.

[2] B. A. Lindsey, J. E. Markel, and E. S. Kleinerman, "Osteosarcoma overview," *Rheumatology and Therapy*, vol. 4, no. 1, pp. 25–43, 2017.

[3] G. Ottaviani and N. Jaffe, "The epidemiology of osteosarcoma," *Cancer Treatment and Research*, vol. 152, pp. 3–13, 2009.

[4] S. Cole, D. M. Gianferante, B. Zhu, and L. Mirabello, "Osteosarcoma: a surveillance, epidemiology, and end results program-based analysis from 1975 to 2017," *Cancer*, vol. 128, no. 11, pp. 2107–2118, 2022.

[5] C. Adamopoulos, A. N. Gargalionis, E. K. Basdra, and A. G. Papavassiliou, "Deciphering signaling networks in osteosarcoma pathobiology," *Experimental Biology and Medicine*, vol. 241, no. 12, pp. 1296–1305, 2016.

[6] K. Song, J. Song, K. Lin et al., "Survival analysis of patients with metastatic osteosarcoma: a surveillance, epidemiology, and end results population-based study," *International Orthopaedics*, vol. 43, no. 8, pp. 1983–1991, 2019.

[7] A. P. Gomes, D. Ilter, V. Low et al., "Age-induced accumulation of methylmalonic acid promotes tumour progression," *Nature*, vol. 585, no. 7824, pp. 283–287, 2020.

[8] C. Lopez-Otin, M. A. Blasco, L. Partridge, M. Serrano, and G. Kroemer, "The hallmarks of aging," *Cell*, vol. 153, no. 6, pp. 1194–1217, 2013.

[9] R. Di Micco, V. Krizhanovsky, D. Baker, and F. d'Adda di Fagagna, "Cellular senescence in ageing: from mechanisms to therapeutic opportunities," *Nature Reviews Molecular Cell Biology*, vol. 22, no. 2, pp. 75–95, 2021.

[10] S. G. Rao and J. G. Jackson, "SASP: tumor suppressor or promoter? Yes!," *Yes! Trends Cancer*, vol. 2, no. 11, pp. 676–687, 2016.

[11] D. McHugh and J. Gil, "Senescence and aging: causes, consequences, and therapeutic avenues," *The Journal of Cell Biology*, vol. 217, no. 1, pp. 65–77, 2018.

[12] A. S. Meijnikman, C. C. van Olden, O. Aydin et al., "Hyperinsulinemia is highly associated with markers of hepatocytic senescence in two independent cohorts," *Diabetes*, vol. 71, no. 9, pp. 1929–1936, 2022.

[13] L. Broer, A. S. Buchman, J. Deelen et al., "GWAS of longevity in CHARGE consortium confirms APOE and FOXO3 candidacy," *The Journals of Gerontology Series A, Biological Sciences and Medical Sciences*, vol. 70, no. 1, pp. 110–118, 2015.

[14] C. V. Anselmi, A. Malovini, R. Roncarati et al., "Association of the FOXO3A locus with extreme longevity in a southern Italian centenarian study," *Rejuvenation Research*, vol. 12, no. 2, pp. 95–104, 2009.

[15] M. J. Peters, R. Joehanes, L. C. Pilling et al., "The transcriptional landscape of age in human peripheral blood," *Nature Communications*, vol. 6, no. 1, p. 8570, 2015.

[16] R. Tacutu, D. Thornton, E. Johnson et al., "Human ageing genomic resources: new and updated databases," *Nucleic Acids Research*, vol. 46, no. D1, pp. D1083–D1090, 2018.

[17] C. Zhou, Y. Shen, Y. Jin et al., "A novel pyroptosis-related long non-coding RNA signature for predicting the prognosis and immune landscape of head and neck squamous cell carcinoma," *Cancer Medicine*, 2022.

[18] K. Yoshihara, M. Shahmoradgoli, E. Martinez et al., "Inferring tumour purity and stromal and immune cell admixture from expression data," *Nature Communications*, vol. 4, no. 1, p. 2612, 2013.

[19] K. F. Kerr, M. D. Brown, K. Zhu, and H. Janes, "Assessing the clinical impact of risk prediction models with decision curves: guidance for correct interpretation and appropriate use," *Journal of Clinical Oncology*, vol. 34, no. 21, pp. 2534–2540, 2016.

[20] J. Li, X. Tang, Y. Du et al., "Establishment of an autophagy-related clinical prognosis model for predicting the overall survival of osteosarcoma," *BioMed Research International*, vol. 2021, Article ID 5428425, 17 pages, 2021.

[21] T. Lei, H. Qian, P. Lei, and Y. Hu, "Ferroptosis-related gene signature associates with immunity and predicts prognosis accurately in patients with osteosarcoma," *Cancer Science*, vol. 112, no. 11, pp. 4785–4798, 2021.

[22] M. Cao, J. Zhang, H. Xu et al., "Identification and development of a novel 4-gene immune-related signature to predict osteosarcoma prognosis," *Frontiers in Molecular Biosciences*, vol. 7, article 608368, 2020.

[23] W. B. Zhang, F. M. Han, L. M. Liu, H. B. Jin, X. Y. Yuan, and H. S. Shang, "Characterizing the critical role of metabolism in osteosarcoma based on establishing novel molecular subtypes," *European Review for Medical and Pharmacological Sciences*, vol. 26, no. 8, pp. 2926–2943, 2022.

[24] A. M. Newman, C. L. Liu, M. R. Green et al., "Robust enumeration of cell subsets from tissue expression profiles," *Nature Methods*, vol. 12, no. 5, pp. 453–457, 2015.

[25] R. Maeda, N. Isowa, H. Onuma, H. Miura, H. Touge, and Y. Kawasaki, "Appearance of lung metastasis from osteosarcoma 21 years after initial treatment," *General Thoracic and Cardiovascular Surgery*, vol. 56, no. 12, pp. 613–615, 2008.

[26] I. Munajat, W. Zulmi, M. Z. Norazman, and W. I. Wan Faisham, "Tumour volume and lung metastasis in patients with osteosarcoma," *Journal of Orthopaedic Surgery*, vol. 16, no. 2, pp. 182–185, 2008.

[27] A. Luetke, P. A. Meyers, I. Lewis, and H. Juergens, "Osteosarcoma treatment - where do we stand? A state of the art review," *Cancer Treatment Reviews*, vol. 40, no. 4, pp. 523–532, 2014.

[28] G. Martemucci, P. Portincasa, A. Di Ciaula, M. Mariano, V. Centonze, and A. G. D'Alessandro, "Oxidative stress, aging, antioxidant supplementation and their impact on human health: an overview," *Mechanisms of Ageing and Development*, vol. 206, article 111707, 2022.

[29] A. Mylonas and A. O'Loghlen, "Cellular senescence and ageing: mechanisms and interventions," *Frontiers in Aging*, vol. 3, article 866718, 2022.

[30] S. Shen, C. Ji, and K. Wei, "Cellular senescence and regulated cell death of tubular epithelial cells in diabetic kidney disease," *Frontiers in Endocrinology*, vol. 13, article 924299, 2022.

[31] X. Qi, S. Zheng, M. Ma et al., "Curcumol suppresses CCF-mediated hepatocyte senescence through blocking LC3B-Lamin B1 interaction in alcoholic fatty liver disease," *Frontiers in Pharmacology*, vol. 13, article 912825, 2022.

[32] Y. Zha, W. Zhuang, Y. Yang, Y. Zhou, H. Li, and J. Liang, "Senescence in vascular smooth muscle cells and atherosclerosis," *Frontiers in Cardiovascular Medicine*, vol. 9, article 910580, 2022.

[33] Q. Behfar, A. Ramirez Zuniga, and P. V. Martino-Adami, "Aging, senescence, and dementia," *The Journal of Prevention of Alzheimer's Disease*, vol. 9, no. 3, pp. 523–531, 2022.

[34] K. Yin, D. Patten, S. Gough et al., "Senescence-induced endothelial phenotypes underpin immune-mediated senescence surveillance," *Genes & Development*, vol. 36, no. 9-10, pp. 533–549, 2022.

[35] M. Extermann, C. G. Hernandez-Favela, S. Perez, E. de Celis, and R. Kanesvaran, "Global aging and cancer: advancing care through innovation," *American Society of Clinical Oncology Educational Book*, vol. 42, pp. 1–8, 2022.

[36] M. Wu, C. Deng, T. H. Lo, K. Y. Chan, X. Li, and C. M. Wong, "Peroxiredoxin, senescence, *and cancer*," *Cells*, vol. 11, no. 11, p. 1772, 2022.

[37] F. Guo, J. K. Das, K. S. Kobayashi et al., "Live attenuated bacterium limits cancer resistance to CAR-T therapy by remodeling the tumor microenvironment," *Journal for Immunotherapy of Cancer*, vol. 10, no. 1, article e003760, 2022.

[38] L. Zhang, J. R. Conejo-Garcia, D. Katsaros et al., "Intratumoral T cells, recurrence, and survival in epithelial ovarian cancer," *The New England Journal of Medicine*, vol. 348, no. 3, pp. 203–213, 2003.

[39] N. Nguyen, E. Bellile, D. Thomas et al., "Tumor infiltrating lymphocytes and survival in patients with head and neck squamous cell carcinoma," *Head & Neck*, vol. 38, no. 7, pp. 1074–1084, 2016.

[40] G. Kayser, L. Schulte-Uentrop, W. Sienel et al., "Stromal CD4/CD25 positive T-cells are a strong and independent prognostic factor in non-small cell lung cancer patients, especially with adenocarcinomas," *Lung Cancer*, vol. 76, no. 3, pp. 445–451, 2012.

[41] W. Zhang, Y. Li, J. Lyu et al., "An aging-related signature predicts favorable outcome and immunogenicity in lung adenocarcinoma," *Cancer Science*, vol. 113, no. 3, pp. 891–903, 2022.

[42] Y. Wang, Y. Liu, C. Zhu, X. Zhang, and G. Li, "Development of an aging-related gene signature for predicting prognosis, immunotherapy, and chemotherapy benefits in rectal cancer," *Frontiers in Molecular Biosciences*, vol. 8, article 775700, 2022.

[43] N. Zeng, C. Guo, Y. Wang et al., "Characterization of aging-related genes to predict prognosis and evaluate the tumor immune microenvironment in malignant melanoma," *Journal of Oncology*, vol. 2022, Article ID 1271378, 17 pages, 2022.

[44] W. Y. Zhai, F. F. Duan, S. Chen et al., "An aging-related gene signature-based model for risk stratification and prognosis prediction in lung squamous carcinoma," *Frontiers in Cell and Development Biology*, vol. 10, article 770550, 2022.

[45] L. Lisi, P. M. Lacal, M. Martire, P. Navarra, and G. Graziani, "Clinical experience with CTLA-4 blockade for cancer immunotherapy: from the monospecific monoclonal antibody ipilimumab to probodies and bispecific molecules targeting the tumor microenvironment," *Pharmacological Research*, vol. 175, article 105997, 2022.

[46] L. Chocarro, E. Blanco, H. Arasanz et al., "Clinical landscape of LAG-3-targeted therapy," *Immuno-Oncology and Technology*, vol. 14, article 100079, 2022.

[47] P. Pandey, F. Khan, H. A. Qari, T. K. Upadhyay, A. F. Alkhateeb, and M. Oves, "Revolutionization in cancer therapeutics via targeting major immune checkpoints PD-1, PD-L1 and CTLA-4," *Pharmaceuticals*, vol. 15, no. 3, p. 335, 2022.

[48] S. Miwa, T. Shirai, N. Yamamoto et al., "Current and emerging targets in immunotherapy for osteosarcoma," *Journal of Oncology*, vol. 2019, Article ID 7035045, 8 pages, 2019.

[49] H. A. Tawbi, M. Burgess, V. Bolejack et al., "Pembrolizumab in advanced soft-tissue sarcoma and bone sarcoma (SARC028): a multicentre, two-cohort, single-arm, open-label, phase 2 trial," *The Lancet Oncology*, vol. 18, no. 11, pp. 1493–1501, 2017.

[50] P. Sharma, S. Hu-Lieskovan, J. A. Wargo, and A. Ribas, "Primary, adaptive, and acquired resistance to cancer immunotherapy," *Cell*, vol. 168, no. 4, pp. 707–723, 2017.

[51] C. C. Wu, H. C. Beird, J. Andrew Livingston et al., "Immunogenomic landscape of osteosarcoma," *Nature Communications*, vol. 11, no. 1, p. 1008, 2020.

[52] M. X. Liu, Q. Y. Liu, Y. Liu et al., "Interleukin-35 suppresses antitumor activity of circulating $CD8^+$ T cells in osteosarcoma patients," *Connective Tissue Research*, vol. 60, no. 4, pp. 367–375, 2019.

[53] M. Binnewies, A. M. Mujal, J. L. Pollack et al., "Unleashing type-2 dendritic cells to drive protective antitumor $CD4^+$ T cell immunity," *Cell*, vol. 177, no. 3, pp. 556–571.e16, 2019.

[54] M. A. Curran, T. L. Geiger, W. Montalvo et al., "Systemic 4-1BB activation induces a novel T cell phenotype driven by high expression of eomesodermin," *The Journal of Experimental Medicine*, vol. 210, no. 4, pp. 743–755, 2013.

[55] M. Larroquette, C. Domblides, F. Lefort et al., "Combining immune checkpoint inhibitors with chemotherapy in advanced solid tumours: a review," *European Journal of Cancer*, vol. 158, pp. 47–62, 2021.

Hindawi
Journal of Oncology
Volume 2022, Article ID 9766954, 22 pages
https://doi.org/10.1155/2022/9766954

Research Article

A Novel Oxidative Stress-Related lncRNA Signature That Predicts the Prognosis and Tumor Immune Microenvironment of Breast Cancer

Jinlai Zhao,[1,2,3,4,5] **Haiyan Ma**,[1,2,3,4] **Ruigang Feng**,[1,2,3,4,6] **Dan Li**,[1,2,3,4] **Bowen Liu**,[1,2,3,4] **YueYu**,[1,2,3,4] **Xuchen Cao**,[1,2,3,4] **and Xin Wang**[1,2,3,4]

[1]*The First Department of Breast Cancer, Tianjin Medical University Cancer Institute & Hospital, National Clinical Research Center for Cancer, Tianjin 300060, China*
[2]*Tianjin's Clinical Research Center for Cancer, Tianjin 300060, China*
[3]*Key Laboratory of Breast Cancer Prevention and Therapy, Tianjin Medical University, Ministry of Education, Tianjin 300060, China*
[4]*Key Laboratory of Cancer Prevention and Therapy, Tianjin 300060, China*
[5]*Department of Gastrointestinal Surgery, Central Hospital of Tangshan, Tangshan, Hebei 063000, China*
[6]*Department of General Surgery, Second Central Hospital of Baoding, Baoding, Hebei 071000, China*

Correspondence should be addressed to Xin Wang; wangxin@tjmuch.com

Received 19 August 2022; Revised 9 September 2022; Accepted 15 September 2022; Published 12 October 2022

Academic Editor: İbrahim Hakkı Cigerci

Background. The association between oxidative stress and lncRNAs within the cancer-related researching field has been a controversial subject. At present, the exact function of oxidative stress as well as lncRNAs exert in breast cancer (BC) are still unclear. Therefore, the present study examined the lncRNAs oxidative stress-related in BC. *Methods*. Transcriptome data of BC obtained from TCGA (The Cancer Genome Atlas) database were used to generate synthetic matrices. Patients with breast cancer were randomly assigned to training, testing, or combined groups. The prognostic signature of oxidative stress was created using the selection operator Cox regression method, and the difference in prognosis between groups was examined using Kaplan-Meier curves, the accuracy of which was calculated using a receiver-operating characteristic-area through the curve (ROC-AUC) analysis with internal validation. Also, the Gene Set Enrichment Analyses (GSEA) was applied for the analysis of the risk groups. To conclude, the half-maximal inhibitory concentration (IC50) of these groups were investigated by immunoassay assay. *Results*. A model based on 7 lncRNAs related to oxidative stress was proposed, and the calibration plots and projected prognosis matched well. For prognosis at 5, 3, and 1 year, the area under the ROC curve (AUC) values were 0.777, 0.777, and 0.759. The functions of target genes identified by GSEA appear to be mainly expressed in metabolism, signal transduction, tumorigenesis, and also the progression. The remarkable differences in IC50 and gene expression between risk groups in this study provide a deep insight for further systemic treatment. Higher macrophage scores were acquired in the high-risk group, of which patients showed more response to conventional chemotherapy drugs, such as AKT inhibitor VIII and Lapatinib, as well as immunotherapy strategies including anti-CD80, TNF SF4, CD276, and NRP1. *Conclusion*. The prognosis of breast cancer can be independently predicted by the markers, which sheds light on further research of the specific role of lncRNAs which are oxidative stress-related and clinical treatment of breast cancer.

1. Introduction

Breast cancer is the most commonly diagnosed feminine malignant tumor with an increasing incidence. Studies have shown that in 2018 there were approximately 2.08 million new diagnosed cases and 630,000 deaths globally [1]. With the improvement of surgery, radiotherapy, and chemotherapy, the overall survival condition of breast cancer patients

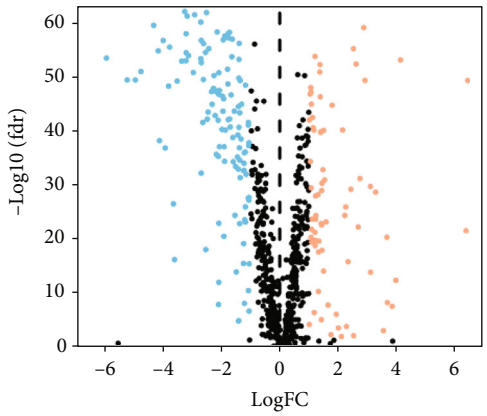

(a)

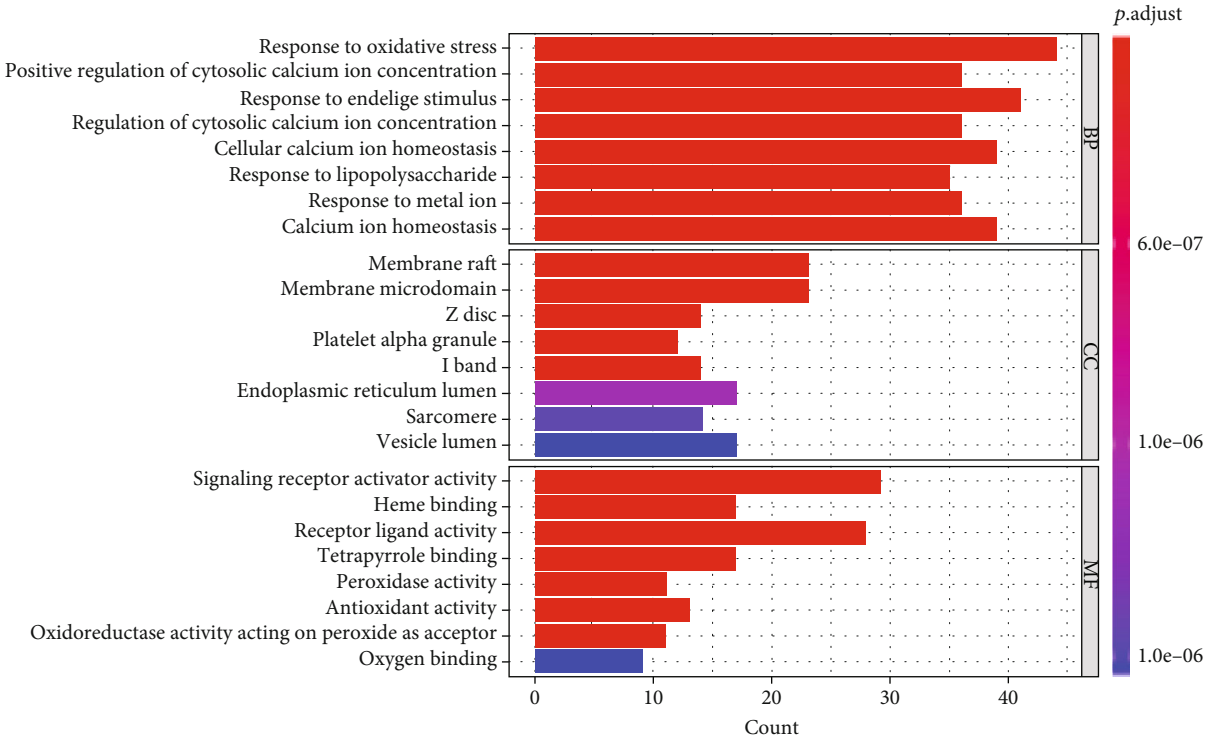

(b)

Figure 1: Continued.

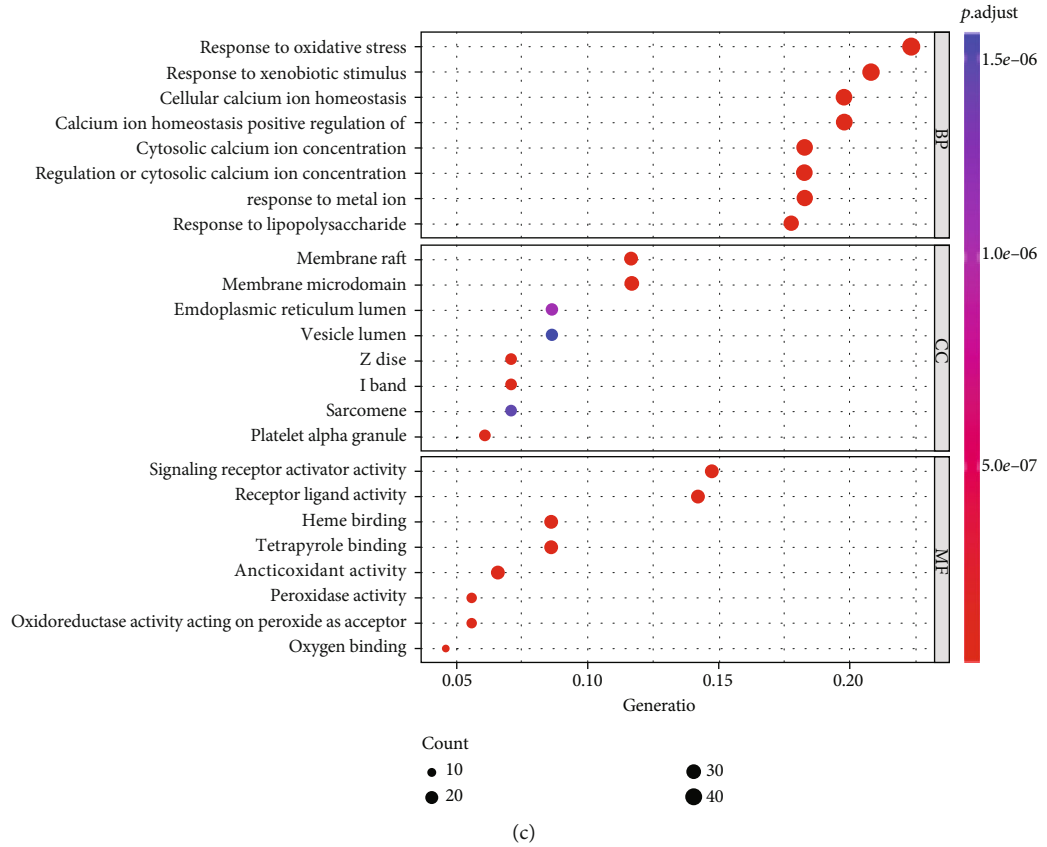

(c)

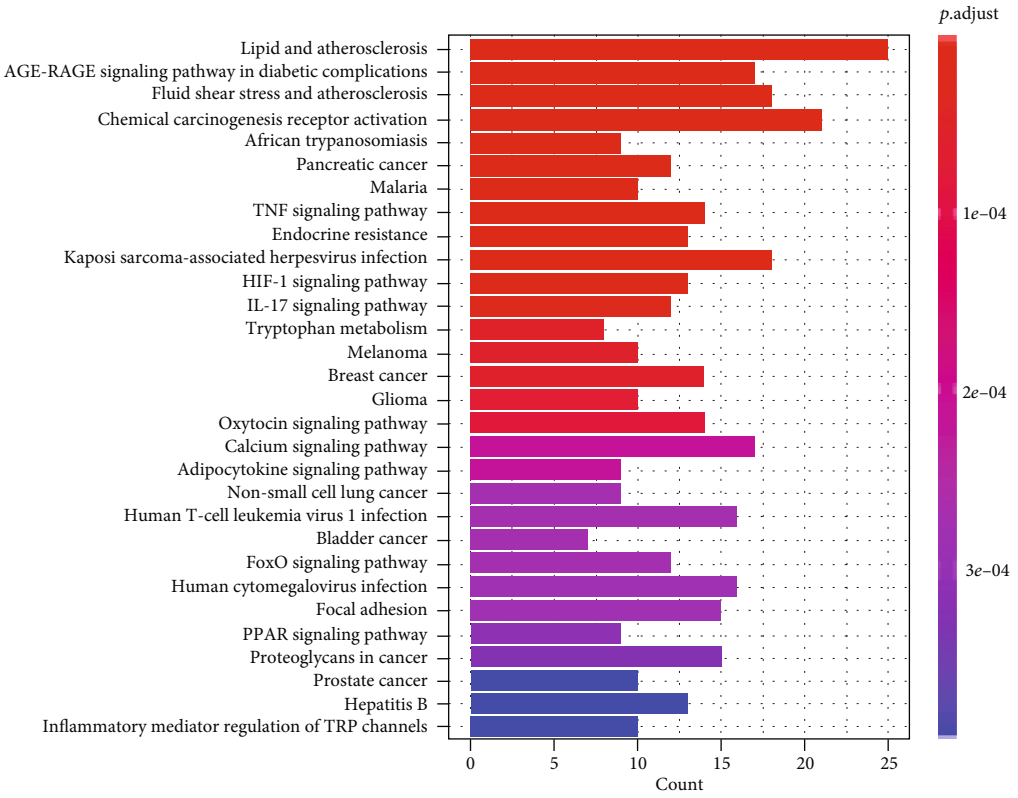

(d)

Figure 1: Continued.

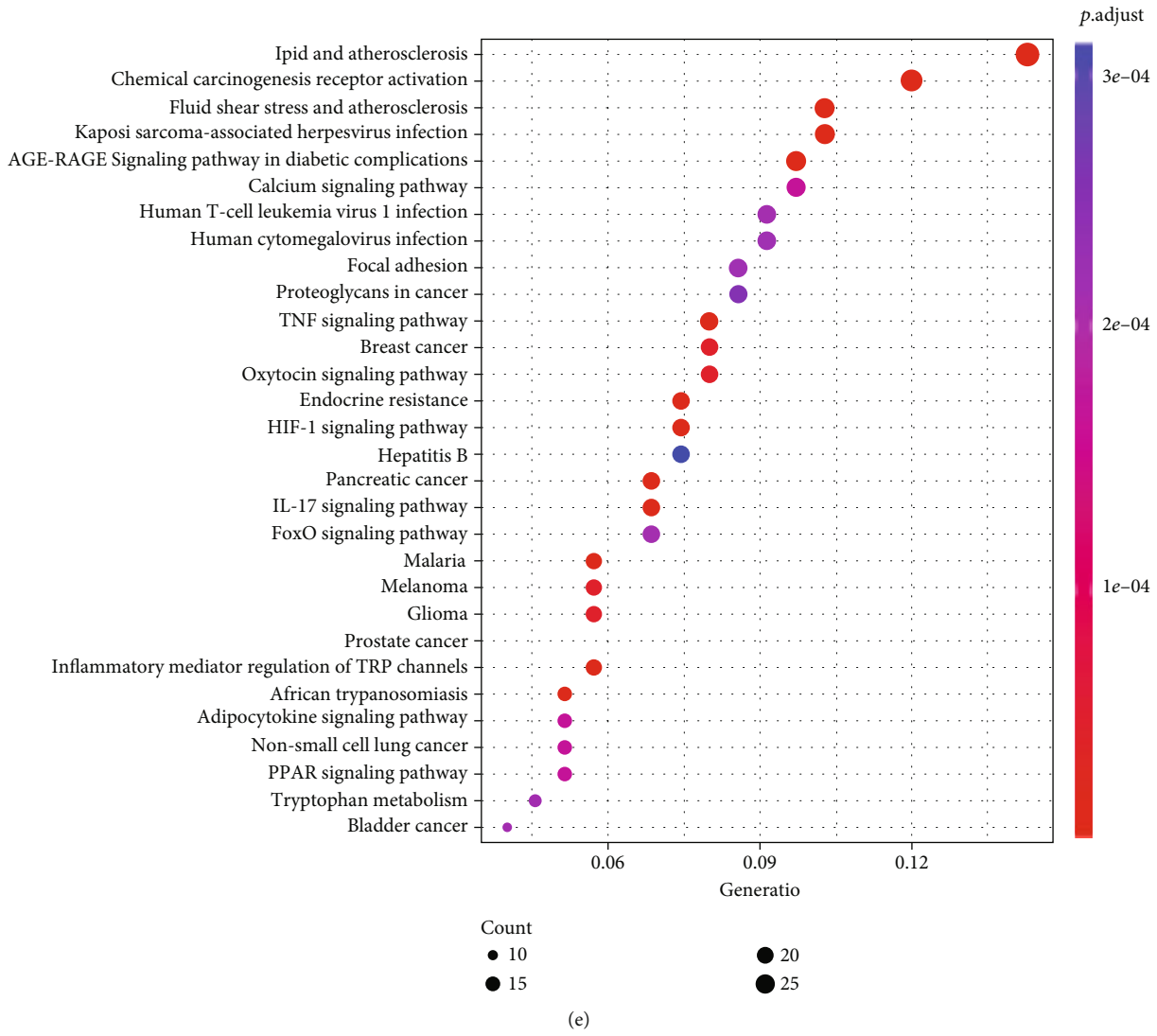

Figure 1: GO and KEGG analyzing of DEGs related to oxidative stress in cancer and normal tissues. (a) Volcano plot of 794 genes related to oxidative stress in BC. Light salmon dots represent for upregulated genes and blue dots for downregulated ones. (b, c) GO analysis of DEGs related to oxidative stress. (d, e) KEGG analysis of DEGs related to oxidative stress. GO: Gene Ontology; DEGs: differentially expressed genes; KEGG: Kyoto Encyclopedia of Genes and Genomes; fdr: false discovery rate; FC: fold change; CC: cellular components; BP: biological process; MF: molecular function.

has improved significantly. However, breast cancer is insidious in its onset and highly malignant. By the time a patient presents with typical symptoms of BC, the tumor has often progressed to an intermediate to advanced stage. At this time, common interventions are less likely to yield desired results, and this significantly affects the prognosis of patients [2, 3]. Therefore, it is very important to dig into the molecular biological mechanism of breast cancer and to find molecular biological markers for early identification and development of breast cancer.

Oxidative stress refers to the overproduction of highly reactive molecules including reactive oxygen species (ROS) and reactive nitrogen species (RNS), by the body in response to various damaging stimuli. Physiological and pathological reactions in cells and tissues are caused by the imbalance of oxidation-antioxidation *in vivo*. Many factors, such as radiation, age, infectious diseases, and heat stress, may lead to increased intracellular ROS concentrations, which stimulate intracellular oxidative stress response and protect or destroy cells [4]. In recent years, scholars have gradually clarified the participation of oxidative stress in the occurrence and prognosis of tumors. Oxidative stress causes DNA mutations in tumor cells, mediates the action of proto-oncogenes, and causes aberrant cell amplification and tumor formation [5]. Moreover, oxidative stress can also promote the metabolism of tumor by altering the key enzymes of metabolism, inducing changes in the metabolic genome and activating signaling pathways, thus promoting the further development of tumors [6].

Long noncoding RNA (lncRNA) is considered as one of the important members among the noncoding RNA family, whose length was more than 200 nucleotides and are a

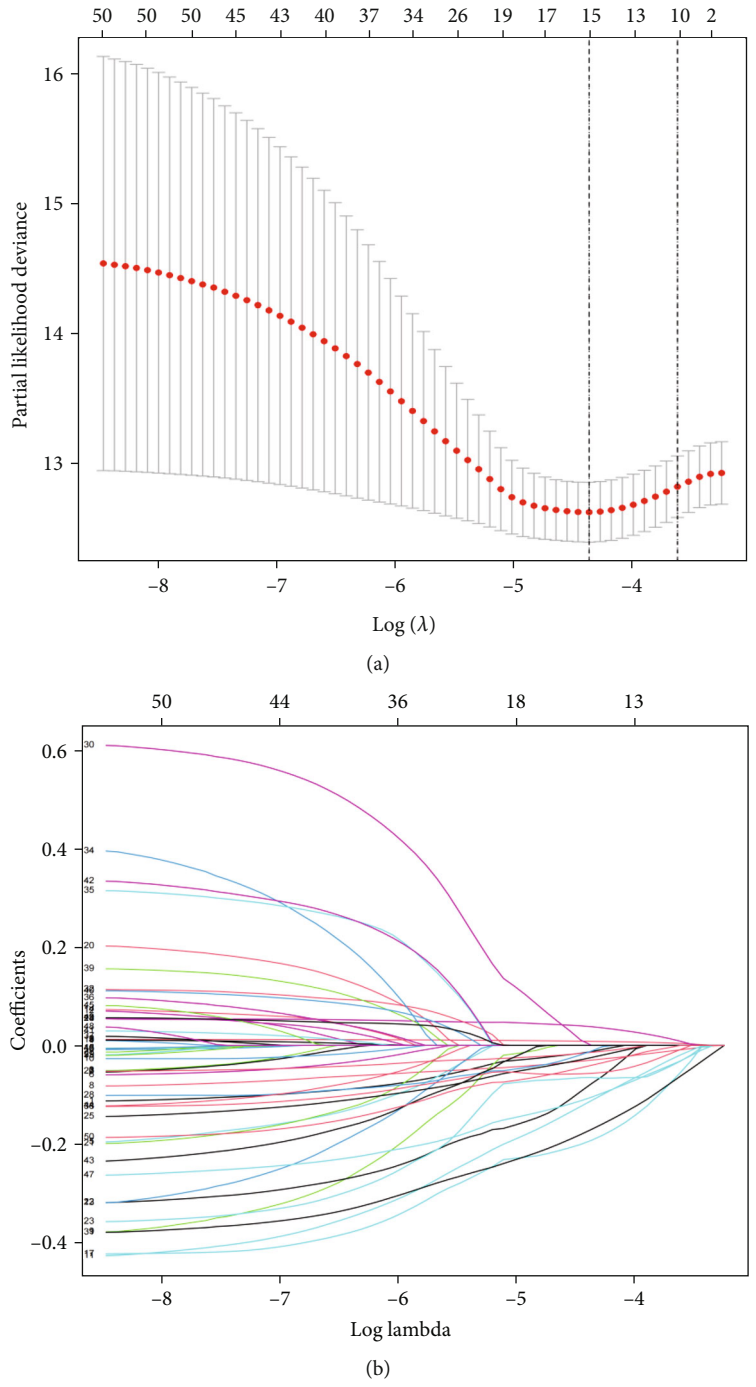

Figure 2: Oxidative stress-associated lncRNA selection through the screening of Lasso model. (a) Lasso coefficients of the 15 lncRNAs which are oxidative stress-related in BC, where the optimal log (lambda) value is marked by vertical dashed lines. (b) Lasso coefficient profiles.

subtype of RNA transcripts [7]. In recent years, researches have proved that multiple lncRNAs participate in various biological processes as a vital part, especially in the incidence and progression of invasive tumors. Many lncRNAs have been illustrated to be closely linked to the breast cancer development and can be broadly classified into two types: cancer-promoting and cancer-inhibiting [7]. Their mechanisms of action are to affect the amplification, invasion, distant metastasis, apoptosis, and drug resistance of breast cancer cells. lncRNAs which are oxidative stress-related have not been studied in breast cancer.

In this research, we aimed to identify lncRNAs associated with oxidative stress regarding breast cancer and to elucidate the participation of lncRNAs in tumor microenvironment (TME) and breast cancer prognosis. To identify the underlying mechanisms, a gene enrichment analysis was performed.

2. Materials and Methods

2.1. Data Identification and Acquisition of Oxidative Stress-Associated lncRNAs. In order to obtain comprehensive data matrices about BC with normal tissue, the RNA transcriptome datasets (HTSeq-FPKM) and the germane clinical information were acquired online from The Cancer Genome Atlas (TCGA) database (https://http://portal.gdc.cancer.gov/). 1109 BC tissue samples and 113 normal breast tissue samples were acquired as control samples. Furthermore, extensive clinical information on patients was obtained from the TCGA. Samples with a follow-up period of less than a month were excluded from further screening using clinical information. As all the data enrolled were obtained from The Cancer Genome Atlas Database and strictly followed guidelines of TCGA publication (http://cancergenome.nih.gov/abouttcga/policies/publicationguidelines), ethics committee approval was not required.

2.2. Screening Analysis of Oxidative Stress-Related Genes and lncRNAs. The lncRNA profiles were acquired firstly from the dataset of RNA seq. Total RNA expressing panel was normalized before the analyzation through log2 transformation. A list of genes related to oxidative stress was downloaded from an online website (https://www.genecards.org/) to screen for gene sets associated with oxidative stress with a correlation score greater than 7.

2.3. Functional Enrichment Analyzation of Differentially Expressed Genes Linked to Oxidative Stress. A false discovery rate (FDR) < 0.05 and $|\log 2 - \text{fold change (FC)} > 1|$ were applied in this experiment as screening criteria to acquire the panel of oxidative stress-related different expressing genes (DEGs). Gene Ontology (GO) were conducted for the research aim, as well as Genes Kyoto Encyclopedia and Genomes (KEGG) analyzation in the "ggplot2" package (Figure 1).

2.4. Identification of Prognostic lncRNAs Related to Oxidative Stress. We utilized the "limma" package for the calculation of the correlation between genes related to oxidative stress as well as lncRNAs. The square of correlation coefficient $|R^2| > 0.3$ in combination of $p < 0.001$ was identified as lncRNAs which are oxidative stress-related. We performed univariate Cox regression analysis for lncRNAs which are oxidative stress-related associated to the cancer prognosis in breast cancer patients, followed by Lasso Cox regression and multivariate Cox regression analyzation of lncRNAs which are oxidative stress-related for constructing the predictive signature of lncRNAs which are oxidative stress-related. The computational equation adapted is descried as follows:

$$\text{risk score} = \sum_{i=1}^{n} * (\text{Coef}_i * x_i). \quad (1)$$

Coef stands for the coefficient value, and x for selected lncRNAs expressing value. This formula was utilized to assess the risk score for each individual diagnosed with breast cancer. The patients were divided into two separate groups on the basis of the median risk score: low-risk along with high-risk groups [8, 9]. Differences of survival condition between groups were compared through the log-rank test.

Table 1: Multivariate Cox analyzation towards the lncRNAs on the basis of TCGA COAD data.

lncRNA	Coefficient	HR	95% CI of HR
DLG5-AS1	-0.651	0.521	0.307-0.887
LINC01235	0.400	1.492	1.184-1.881
SEMA3B-AS1	-0.245	0.783	0.563-1.088
LINC00987	-0.684	0.504	0.303-0.841
ST7-AS1	-1.181	0.307	0.139-0.675
MAPT-AS1	-0.782	0.458	0.281-0.744
LINC01871	-0.714	0.490	0.332-0.721

2.5. The Prognostic Model Development. A model for independent prognostic was developed using Cox regression. Nomogram was applied for the prediction of the patient survival. The calibration curves, receiver-operating characteristic (ROC), and concordance index (C-index) curves were developed for exploring this model's accuracy. Demographic variables were included in the multivariate Cox regression analysis to see if the risk score could independently predict the development of breast cancer. The stability of the prediction model conducted in this experiment was also examined within the testing and training groups.

2.6. Functional Analysis. The online CBioPortal (http://www.cbioportal.org/) was taken to describe the mutation profiles of each key gene. Gene set enrichment analysis was applied for interpreting the functional enrichment of gene expressing panel [10]. The enrichment of lncRNAs related to oxidative stress with a classified prognosis value was explored and 10 GO and KEGG pathways related to oxidative stress were visualized.

2.7. The Investigation of the Immunocheckpoints, TME, and the Model in the Clinical Treatment. Limma, GSVA, ggpubr R, and ggplot2 packages as well as GSEABase were utilized to determine the expression differences of 29 immunocells and 47 immune checkpoint genes within the studied groups and to guide the immunotherapy of breast cancer [9]. "pRRophetic," "ggpubr," "ggplot2," etc. R packages were applied to classify the differential expression of IC50 in the two groups of breast cancer and to perform clinical chemotherapy against breast cancer [11].

2.8. Statistical Analysis. All statistical analyzation involved were completed using R software (Version 4.1.2). The Wilcoxon test was used to compare the expression levels of DEGs in cancer and normal tissue samples. Univariate Cox regression analyzation was performed for determination of the relationship of lncRNAs which are oxidative stress-related with overall survival, and lncRNAs which are oxidative stress-related were screened using multivariate Cox analysis for the construction of predicting signature discussed in this research. The Kaplan-Meier method

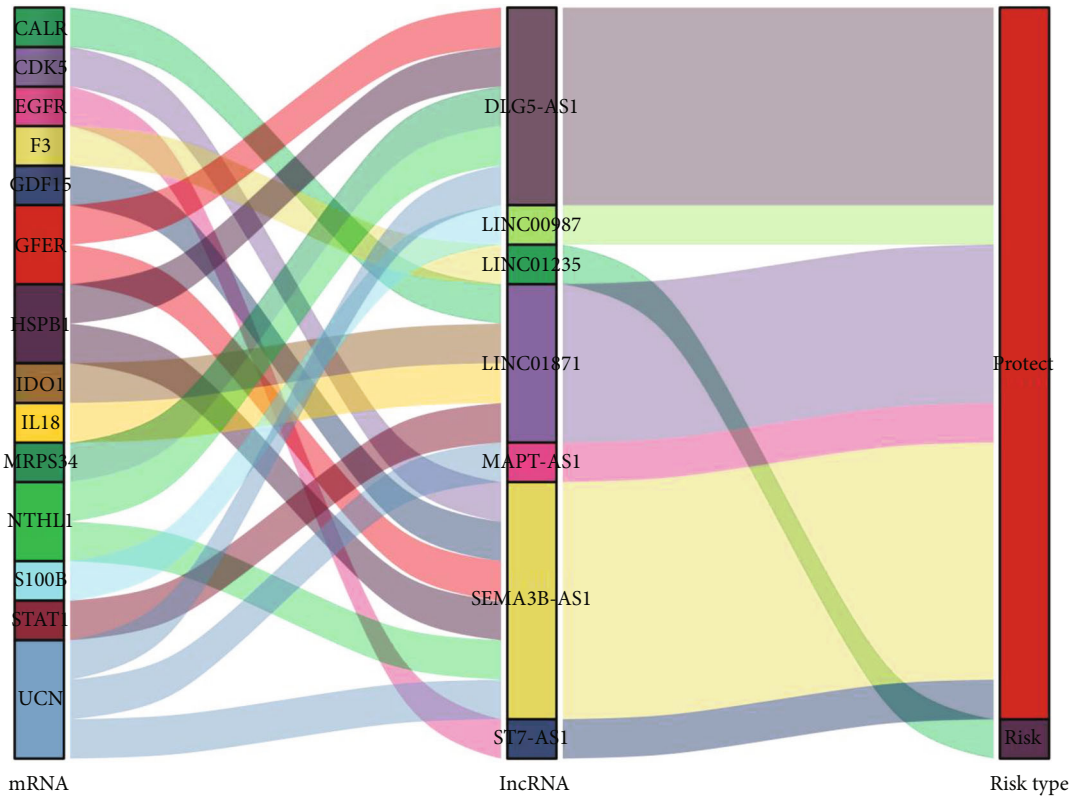

Figure 3: The Sankey diagram of prognostic.

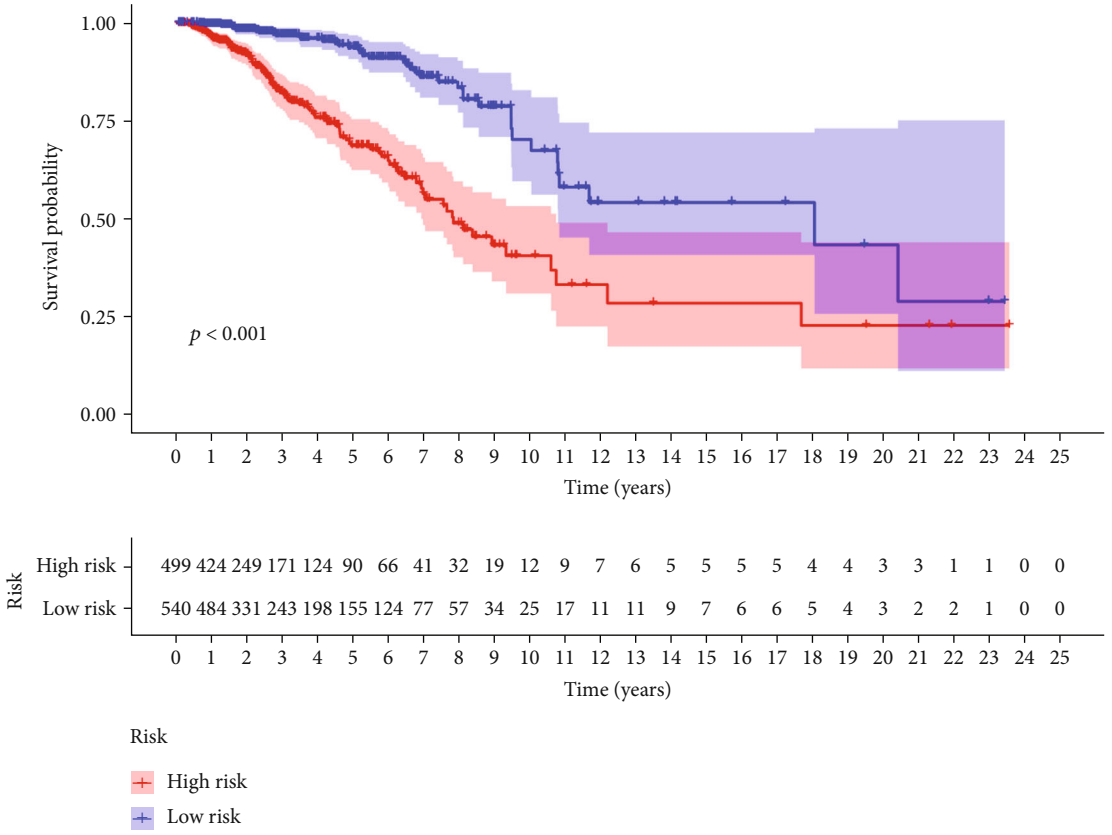

Figure 4: The KM survival curve of risking score on the basis of 7 lncRNAs which are oxidative stress-related.

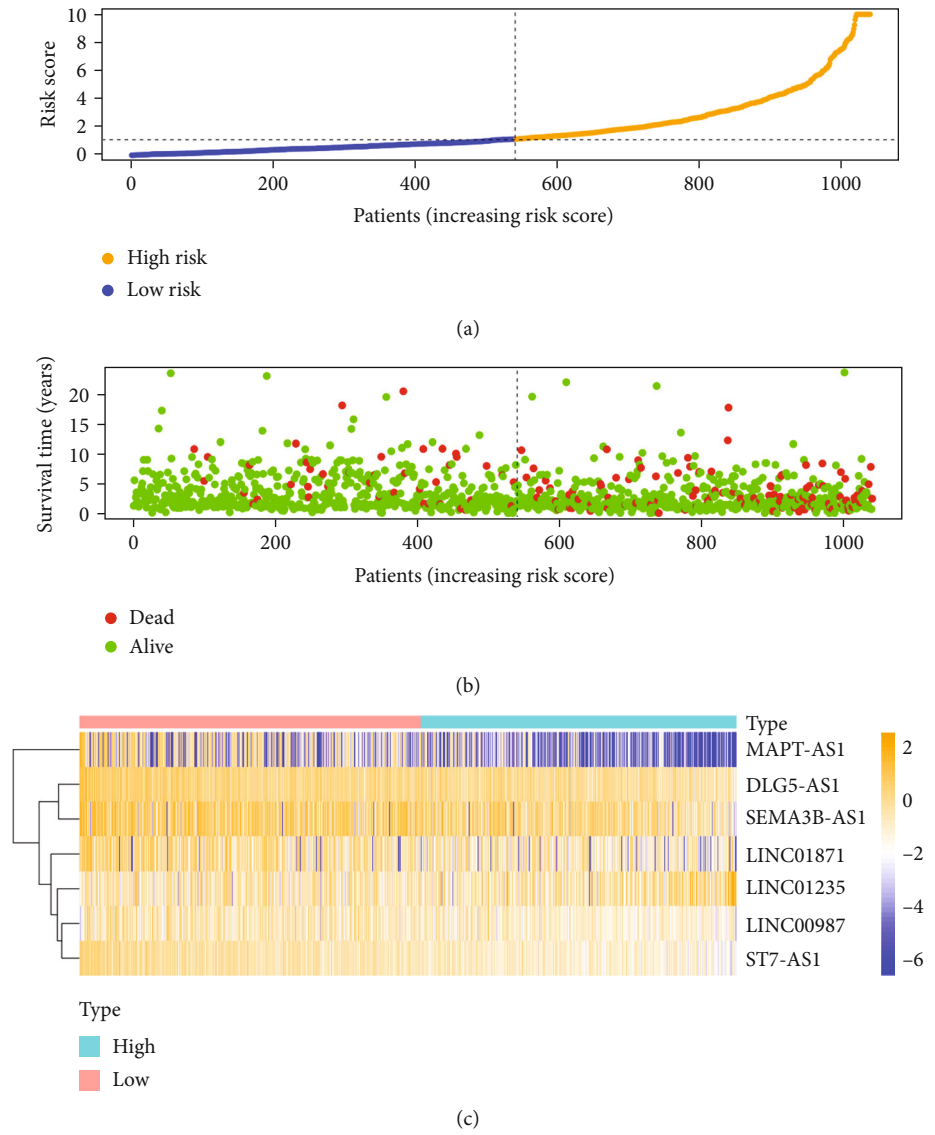

Figure 5: The analysis of signature regarding lncRNA which are oxidative stress-related for BC patients. (a) The risk scores of the investigated groups. (b) The patients' survival time. (c) Heat map of the ten lncRNA expression. As the color shifts yellow, the expression level becomes higher.

combined with log-rank test were applied for analyzation of the OS of patients in the two groups. The "survival ROC" package was applied for drawing the ROC curves and for determination of the area below the curve (AUC) values. Principal component analysis (PCA) method was utilized to discover the distribution of patients ranked at differed risk scores. Statistical tests turned out to be bilateral, with $p < 0.05$ being significant.

3. Results

3.1. Identification of Prognostic lncRNAs Which Were Oxidative Stress-Related. 14,142 counted lncRNAs were gained from TCGA-COAD, among which 1086 lncRNAs linked to oxidative stress were identified. Univariate Cox regression analyzation uncovered that 50 of them were linked to the development of BC. Lasso Cox regression analyzation displayed in Figure 2 showed that 15 lncRNAs which are oxidative stress-related had a connection with the BC development. Finally, multivariate Cox regression analysis uncovered that 7 lnccRNAs which are oxidative stress-related were linked to the development of BC. DLG5-AS1, LINC01235, SEMA3B-AS1, LINC00987, ST7-AS1, MAPT-AS1, and LINC01871 were identified as construct predictive signatures (Table 1). The risk scores were calculated as: risk score = − 0.65107016 × DLG 5− AS 1 expressing level + 0.40027496 × LINC 01235 expressing level + − 0.244710708 × SEMA 3 B − AS 1 expressing level + − 0.684301493 × LINC 0 0987 expressing level + − 1.181200718 × ST 7 − AS 1 expressing level + − 0.781949407 × MAPT − AS 1 expressing level + − 0. 713957256 × LINC 01871 level. The lncRNAs were further visualized with the ggalluvial, ggplot R software package. From the Sankey diagram, one lncRNA (LINC01235) was a detrimental prognostic factor, and the others

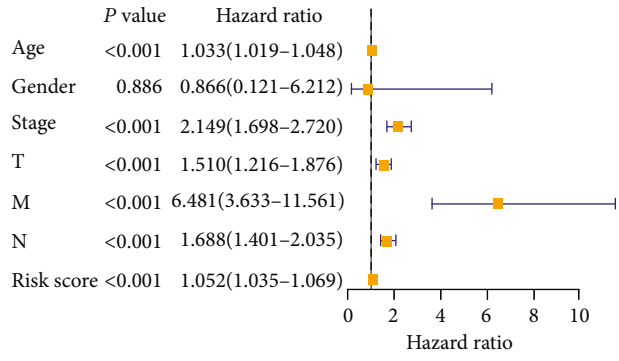

(a)

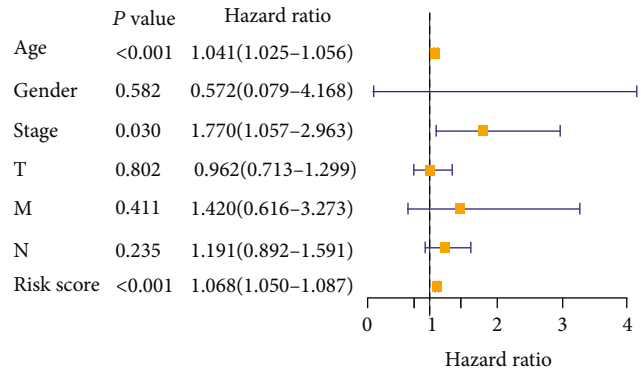

(b)

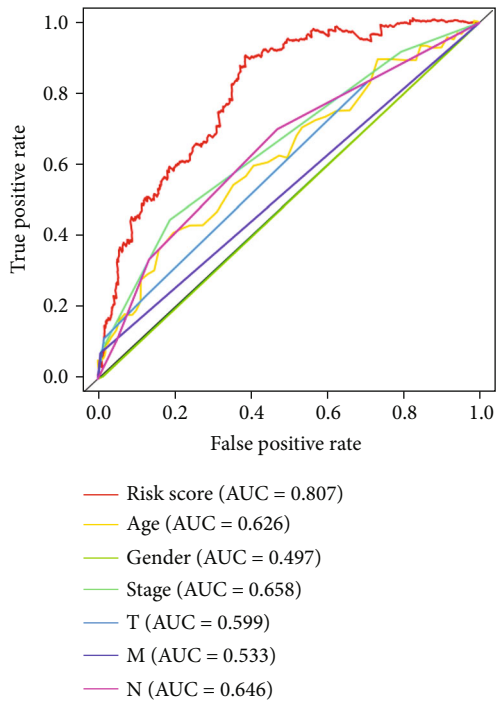

(c)

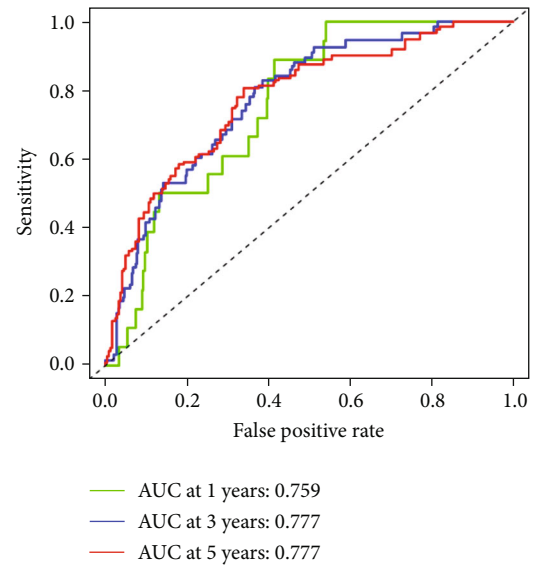

(d)

Figure 6: Continued.

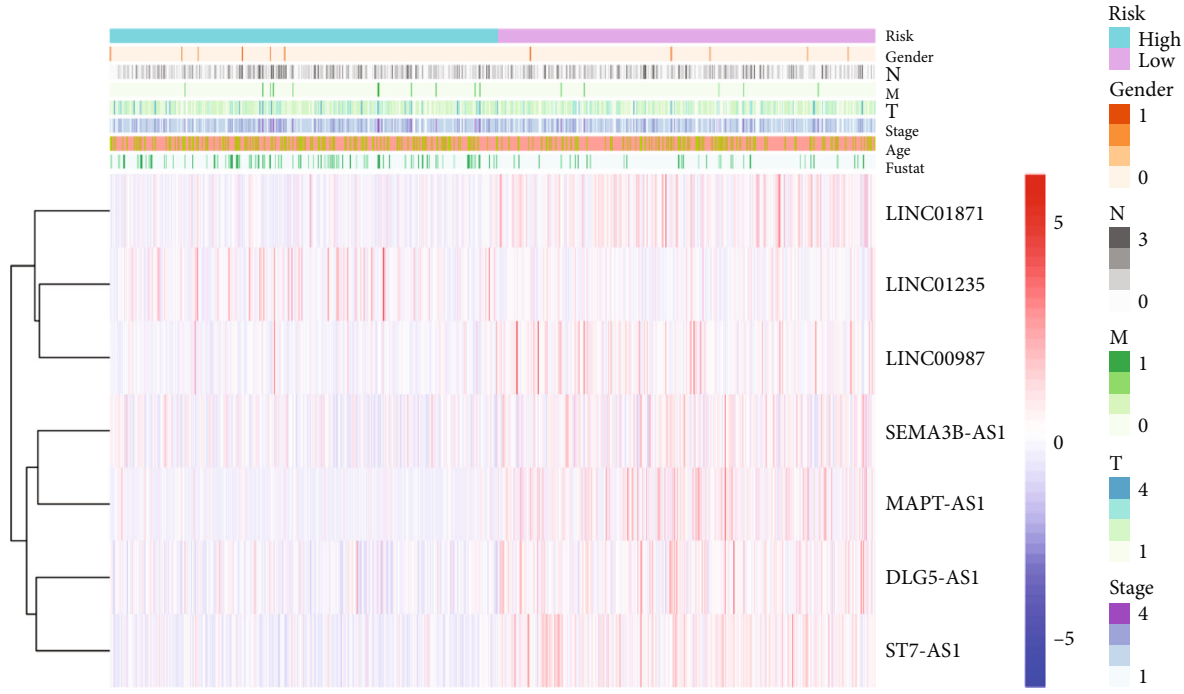

(e)

Figure 6: The correlation of the predictive signature with the development of BC. (a) The forest plot regarding univariate Cox regression analyzation. (b) The forest plot regarding multivariate Cox regression analyzation. (c) The ROC curve illustrating the clinicopathological variables and the risk scores. (d) ROC curves along with corresponding AUCs at 1-, 3-, and 5-year survival with the predictive signature. (e) The heat map of distribution for the clinicopathological variables and seven prognostic lncRNAs in the two risk groups.

(DLG5-AS1, SEMA3B-AS1, LINC00987, ST7-AS1, MAPT-AS1, and LINC01871) were positive prognostic factors (Figure 3).

3.2. The Prognostic Impact of the Signature Established. Risk score was linked to the survival condition of BC patients significantly. There was a shorter OS in the group with high-risk ($p < 0.001$, log-rank test) (Figure 4). Cox regression suggested significant developing impact on the risk score for the BC patients (Figure 5).

3.3. Clinical Value of the Signature regarding lncRNA Oxidative Stress-Related. The results of univariate cox regression analysis suggested that general information including age, T stage, N stage, M stage, stage, and risking score was related to the survival condition in BC patients (Figure 6(a)). As suggested by multivariate Cox regression analyzation, age and risk score appear to be separate predictors of OS in BC patients (Figure 6(b) and Table 2). The AUC of the risk score was 0.807, which outperformed clinicopathological variables in predicting the development of BC (Figure 6(c)). The AUCs of 5-, 3-, and 1-year survival ratios were accordingly recorded as 0.777, 0.777, and 0.759, which indicated positive predictive capability (Figure 6(d)). The clinicopathological variable differences between the groups were analyzed, while N stage ($p < 0.05$) along with stage ($p < 0.05$) were uncovered to be different between the two groups discussed (Figure 6(e) and Table 3).

Table 2: Risk scores as well as clinical characteristics regarding BC through analysis of multivariate Cox regression.

Variable	HR	HR95L	HR95H	*p* value
Age	1.041	1.025	1.056	1.55*E*-07
Gender	0.572	0.079	4.168	0.582
Stage	1.770	1.057	2.963	0.030
T	0.962	0.712	1.299	0.802
M	1.420	0.616	3.273	0.411
N	1.191	0.892	1.591	0.235
Risk score	1.068	1.050	1.087	3.91*E*-14

To predict the development of breast cancer further, a nomogram including clinicopathological variable as well as the risk score was constructed, which could predict the 1-, 3-, and 5-year prognosis (Figure 7(a)). Curves of calibration implied a positive consistency of the actual OS conditions along with the predicted survival conditions at separate period (Figures 7(b)–7(d)).

3.4. Internal Validation of the Predictive Characteristics. For the verification of the applicability of the predictive characteristics for OS on the basis of the TCGA dataset, 856 patients with BC were randomly separated into two grouping cohorts (training cohort $n = 427$, test cohort $n = 429$). The demographic information of patients enrolled are illustrated in Table 4. Complying with the results observed, OS

Table 3: Clinical impacts of the risk score characteristics (as identified by the TCGA-COAD data).

Clinical	*n*	Mean	SD	*t*	*p*
Risk score					
Age					
>65	222	2.064	2.442	1.378	0.169
≤65	634	1.805	2.304		
Gender					
Female	845	1.878	2.354	1.322	0.212
Male	11	1.465	1.001		
Stage					
I-II	655	1.708	2.169	-3.282	0.001
III-IV	201	2.408	2.773		
T					
T1-2	734	1.794	2.21	-1.938	0.055
T3-4	122	2.342	2.987		
M					
M0	840	1.851	2.323	-1.504	0.153
M1	16	3.014	3.076		
N					
N0	420	1.661	2.087	-2.605	0.009
N1-3	436	2.076	2.55		

rates of patients in the group with high-risk tended to be lower ($p = 9.65e - 10$). (Figure 8(a)) In the testing cohort, the prognosis of the group with high-risk turns to be worse ($p = 1.15e - 05$) (Figure 8(c)) The ROC curves of two cohorts appears to be a positive predictive capability. In the training cohort, the AUCs of 5-, 3-, and 1-year prognosis conditions were, respectively, 0.797, 0.807, and 0.85 (Figure 8(b)), while within the test cohort, the AUCs of 5-, 3-, and 1-year survival conditions were, respectively, 0.747, 0.761, and 0.689. (Figure 8(d)).

3.5. Function Analyzation. 5484 GO analysis and 178 KEGG analysis were conducted. In GO analysis, the lncRNAs oxidative stress-related were enriched in biological processes like regulation of cell cycle and of mitosis (Figure 9(a)). KEGG analysis uncovered that these lncRNAs were mainly enriched into metabolism, malignant tumor formation, signal transduction, etc. (Figure 9(b)). Furthermore, it was proposed that the gene clusters were associated to critical biological processes, genesis functional pathways, and cancer prognosis, for example, JAK-STAT as well as VEGF signaling pathway ($p < 0.05$) was solidly linked to the cancer invasion and metastasis.

3.6. Immune Cell Infiltration. With PCA maps, it was feasible to visualize the patients' distribution based on oxidative stress-related gene sets, the entire genome, oxidative stress-related lncRNAs, and important genes. The results implied that the key gene appears to be the best for patients. Patients with differential risking score were distributed in differed quadrants (Figure 10).

To discover the correlation between risking score and immune cells further, the GSEA enrichment scores for different immune cell clusters were assessed. The results showed DCs, aDCs, B_cells, plasmacytoid dendritic cells (pDCs), CD8+_T_cells, mast cells, immature dendritic cells (iDCs), neutrophils, macrophages, NK cells, T follicular helper (Tfh) cells, tumor infiltrating lymphocyte (TIL), T helper cells, T helper type 1 (Th1) cells, and T helper type 2 (Th2) cells were significantly varied between the groups discussed (Figure 11). Only macrophages in the group with high risk exhibited a high score, suggesting that the function of macrophages was more active.

3.7. Linage Between the Predictive Signature and BC Therapy. The expression of CD80, TNFSF4, CD276, and NRP1 was higher significantly in the group with high risk, suggesting a potential response to anti-CD80, TNFSF4, CD276, and NRP1 immunotherapy in high-risk patients (Figure 12(a)). This provides a new therapeutic target for immunotherapy of BC. Combined with immunotherapy, we also surveyed the linkage between the predicting feature and the general chemotherapy efficacy, then revealed that the AKT inhibitor VIII, AZD6482, bicalutamide, BMS.708163, imatinib, lapatinib, pazopanib, and thapsigargin in the high-risk group exhibited a lower IC50 compared with the other group (Figures 12(b)–12(i)), and the methotrexate exhibited a higher IC50 in the group with high-risk (Figure 12(j)), which could help explore personalized treatment schemes appropriate for both high- and low-risk group individualized patients.

3.8. Mutation Landscape of Key Genes. The OncoPrint view of key genes in the CBioPortal database were applied to visualize mutations within the seven key genes on the basis of data acquired from 1084 BC patients. Nearly 1/4 of these patients (23.7%) had mutations in all seven key genes. The highest rate of mutations was found in DLG5-AS1 (7%) and ST7-AS1 (7%) (Figure 13).

4. Discussion

Breast cancer looks to be a large malignant tumor that endangers both women's physical and mental well-being. The incidence of BC appears to be growing year by year in recent years, with a definite trend toward younger age. It is therefore essential to establish an accurate tool for the prediction of the development of BC to guide clinical diagnosis and treating strategy.

Tumor generation is a complex multistep process requiring three stages: onset, promotion, and development. A large number of studies have illustrated that reactive oxygen species (ROS), products of oxidative stress, are involved in all stages of tumor formation [12]. Tumorigenesis is closely correlated with ROS-induced oxidative damage to nuclear chromosome, and ROS can also promote the activation and transformation of tumoral cells. What has been reported is that the ROS level in tumors correlates with the degree of malignancy [13]. As ROS levels rise in hypoxia, malignant tumor cells become more aggressive and more likely to

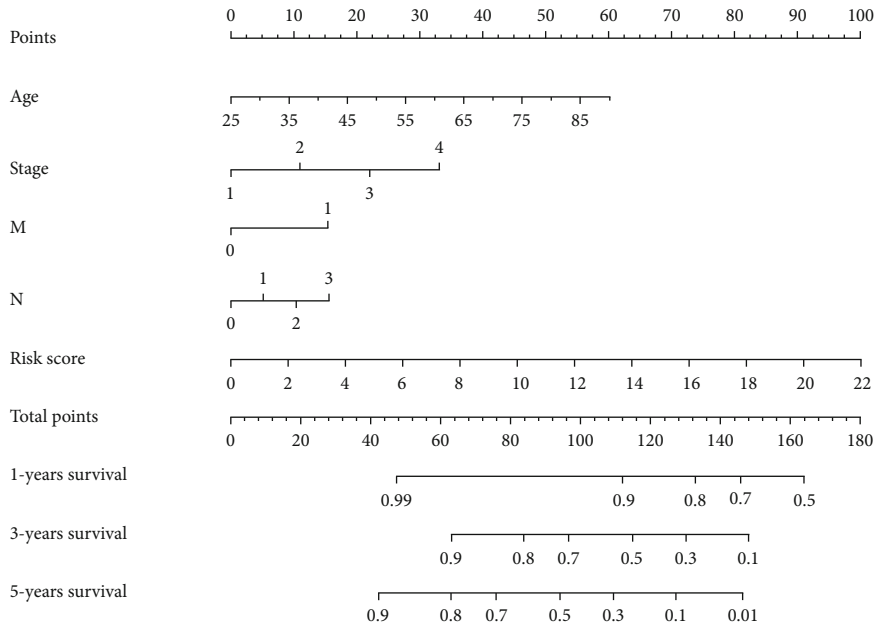

(a)

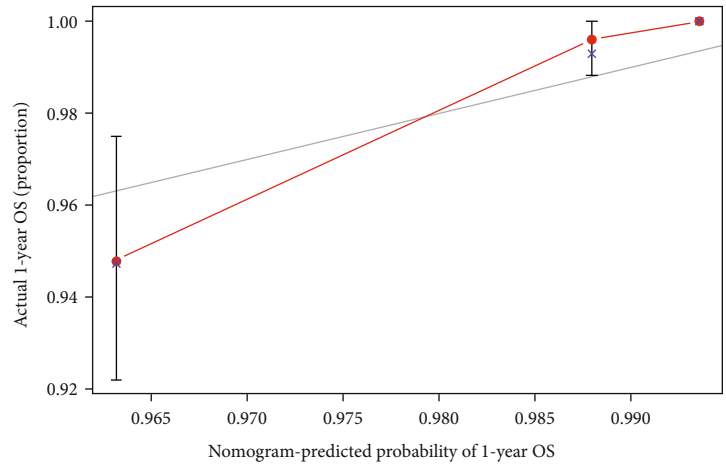

(b)

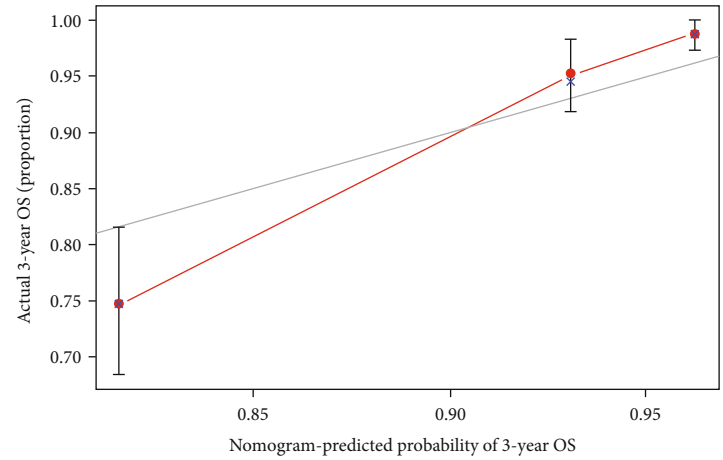

(c)

Figure 7: Continued.

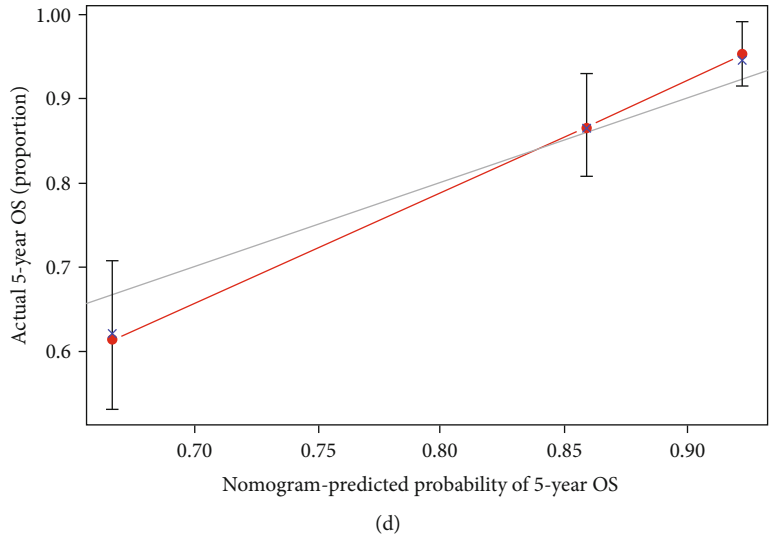

Figure 7: The nomogram construction and verification. (a) A nomogram in combination of risk scores and clinicopathological variables. (b–d) Calibration curves across the actual and predicted OS rates at 1, 3, and 5 years.

Table 4: The different clinical features of patients across separate cohorts.

Variables	Entire TCGA dataset ($n = 856$)	Validation cohort	
		Training cohort ($n = 427$)	Testing cohort ($n = 429$)
Age (%)			
≤65	634 (74.1)	321 (75.2)	313 (73.0)
>65	222 (26.9)	106 (24.8)	116 (27.0)
Gender (%)			
Female	845 (98.7)	419 (98.1)	426 (99.3)
Male	11 (1.3)	8 (1.9)	3 (0.7)
Stage (%)			
I + II	655 (76.5)	324 (75.9)	331 (77.2)
III + IV	201 (23.5)	103 (24.1)	98 (22.8)
T (%)			
T1+T2	734 (85.7)	369 (86.4)	365 (85.1)
T3+T4	122 (14.3)	58 (13.6)	64 (14.9)
M (%)			
M0	840 (98.1)	420 (98.4)	420 (97.9)
M1	16 (1.9)	7 (1.6)	9 (2.1)
N (%)			
N0	420 (49.1)	210 (49.2)	2109 (49.0)
N1+N2+N3	436 (50.9)	217 (50.8)	219 (51.0)

M: metastasis; N: lymph node; T: tumor.

spread. Chronic and ongoing oxidative stress induces epithelial-mesenchymal transition (EMT) and migration [14]. It is evident that oxidative stress participates as a vital part in tumorigenesis and progression. At present, there is no report on predicting the development of breast cancer patients by building oxidative stress-related lncRNA prediction signals.

With this study, lncRNAs which are oxidative stress-related were screened by generating a lncRNA coexpression network and genes which are oxidative stress-related. Furthermore, using Lasso as well as Cox regression, the following seven lncRNAs which are oxidative stress-related with good prognosis were obtained: DLG5-AS1, LINC01235, SEMA3B-AS1, LINC00987, ST7-AS1, MAPT-AS1, and LINC01871. These seven lncRNAs which are oxidative stress-related may be targeting markers of potential clinical therapy and development for the BC patients. We also found mRNAs (MRPS34, HSPB1, GFER, NTHL1, UCN, F3, CDK5, GDF15, S100B, EGFR, STAT1, CALR, IL18, and IDO1) coexpressed significantly with the lncRNAs mentioned.

Five lncRNAs associated with oxidative stress (LINC01235, SEMA3B-AS1, LINC00987, ST7-AS1, and

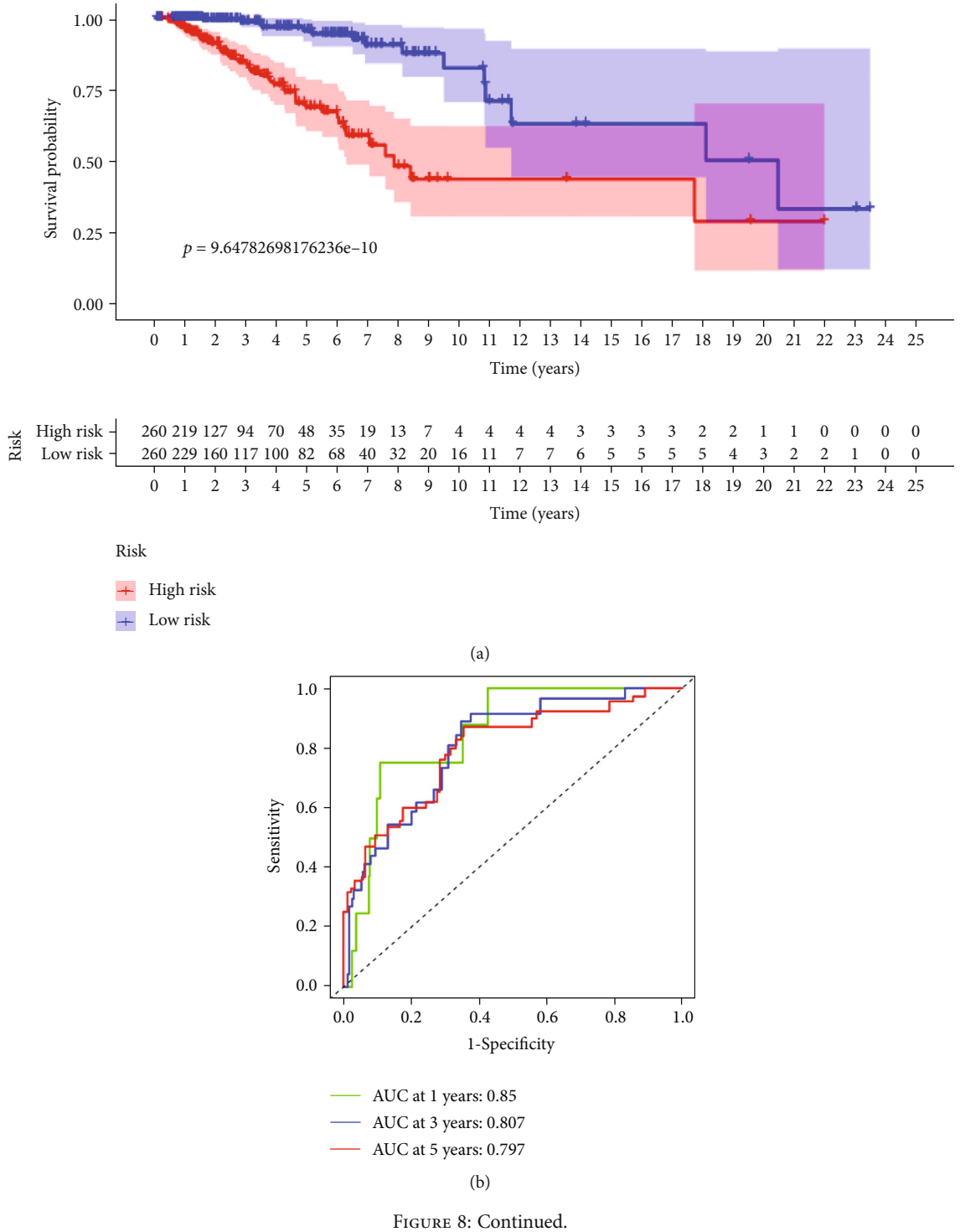

(a)

(b)

Figure 8: Continued.

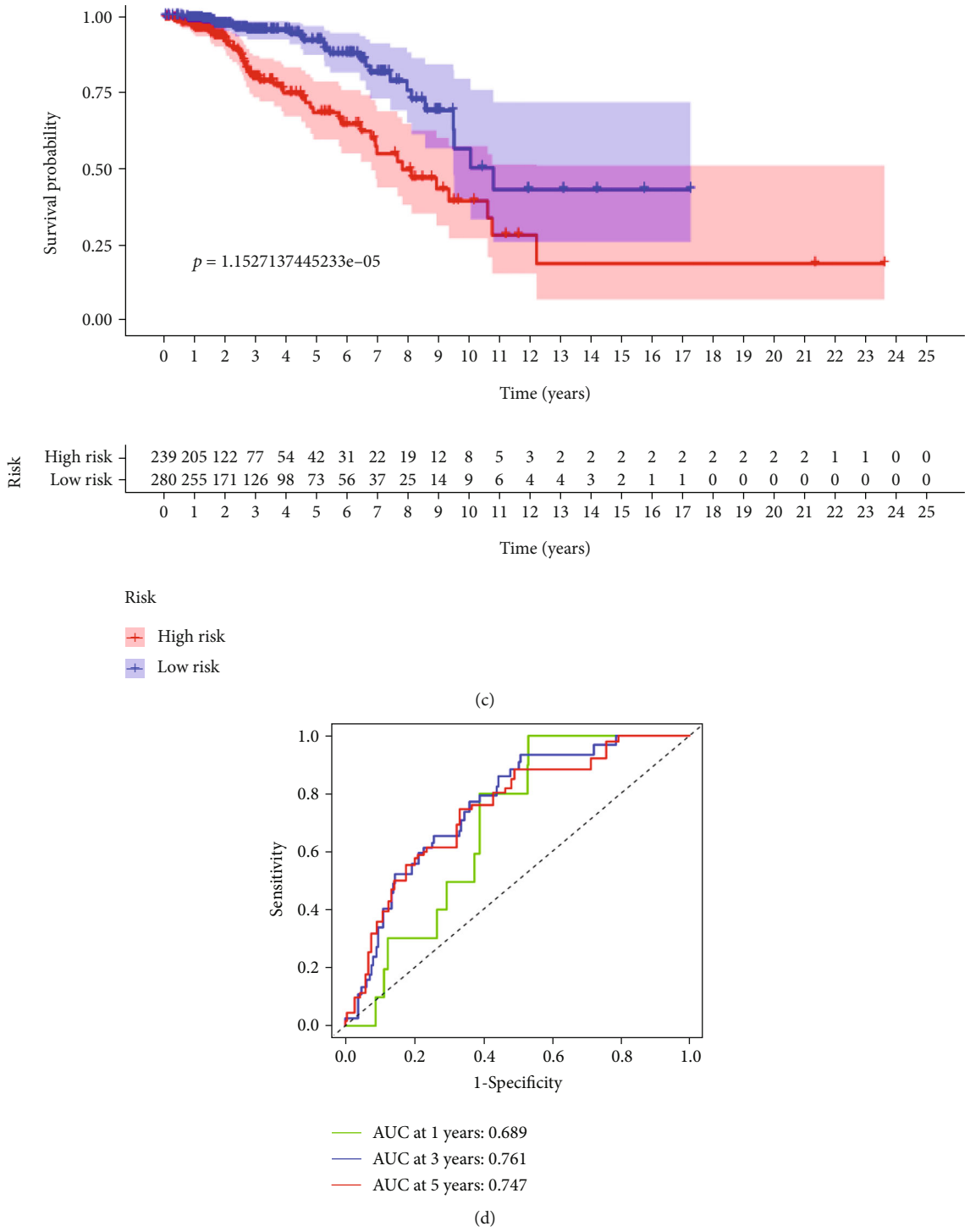

Figure 8: Internal confirmation of the predictive feature for over survival condition on the basis of the TCGA dataset. (a) Kaplan-Meier survival curving plot in the internal training cohort. (b) ROC curving plot and AUCs at 1-year, 3-year, and 5-year survival condition in the training internal cohort. (c) Kaplan-Meier survival curving plot in the internal testing cohort. (d) ROC curving plot and AUCs at 1-, 3-year, and 5-year survival in the internal testing cohort. AUC: area under the curve; ROC: receiver-operating characteristic; TCGA: The Cancer Genome Atlas; OS: overall survival.

MAPT-AS1) have been reported to be linked to cancer. (1) Functional loss experiments suggest that upregulated LINC01235 promotes gastric cancer cell metastasis through EMT and may be a valuable prognostic biomarker and treating target for metastatic gastric cancer [15]. (2) Overexpression of SEMA3B-AS1 inhibits gastric cancer cell proliferation and invasion in vitro. Sema3b-as1 can be used as a tumor suppressor and as a clinical therapy target for antitumor therapy [16]. (3) Silencing LINC00987 inhibits proliferation and invasion of osteosarcoma cells by

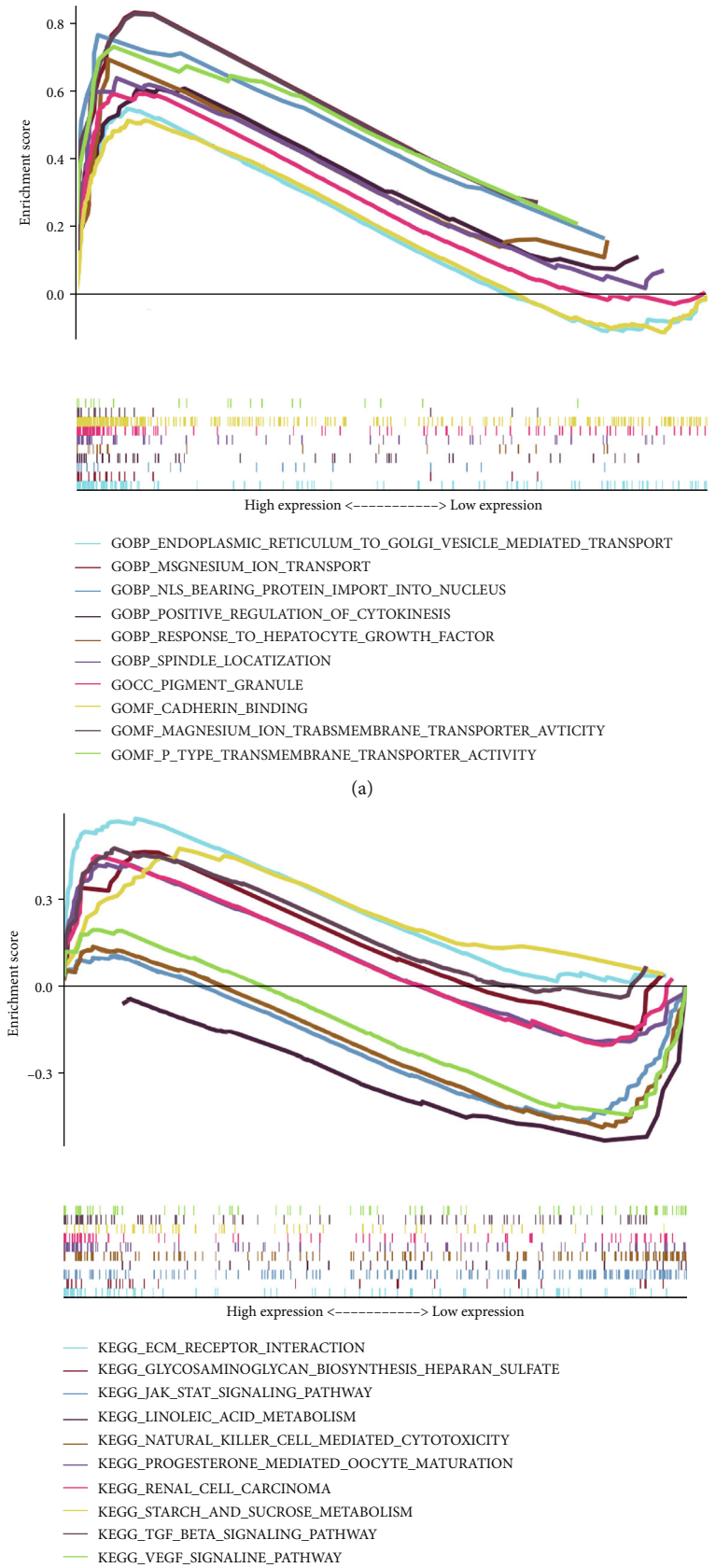

Figure 9: The functional analysis based on lncRNAs which are oxidative stress-related. (a) GO; (b) KEGG.

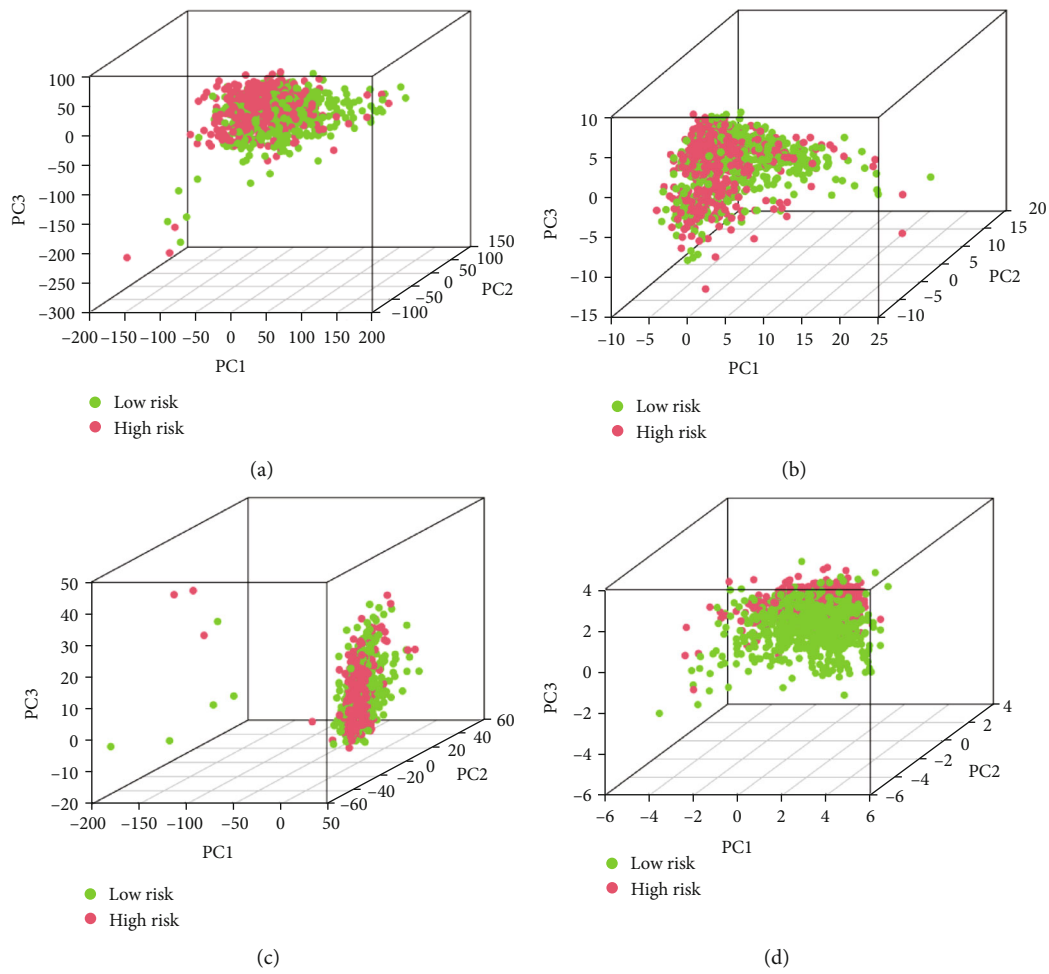

Figure 10: Patients with different risk scores have different oxidative stress statuses. PCA maps show the distribution of patients on the basis of the (a) complete genome; (b) oxidative stress-related gene clusters; (c) lncRNAs related to oxidative stress; and (d) lncRNA feature. The segmentation across the red and green dots becomes stronger when tested using only signature lncRNA.

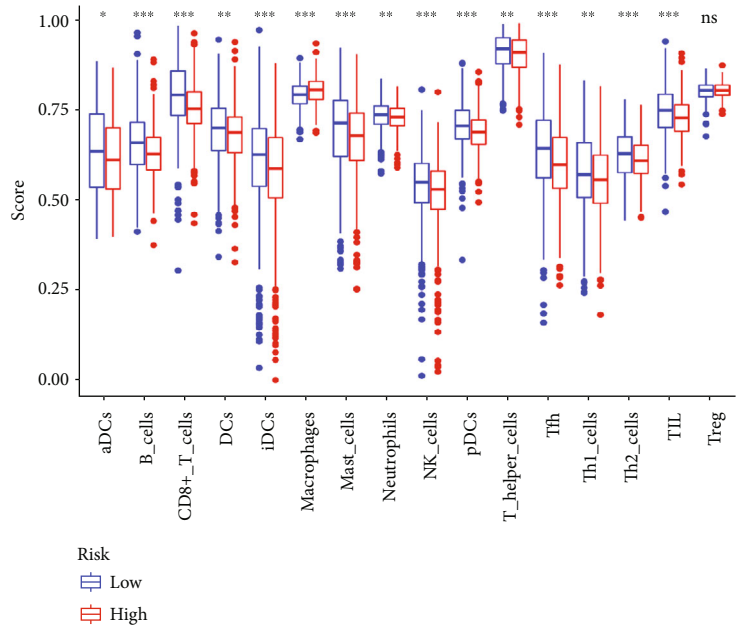

Figure 11: The immune infiltrating cell scores in high-risk as well as low-risk groups.

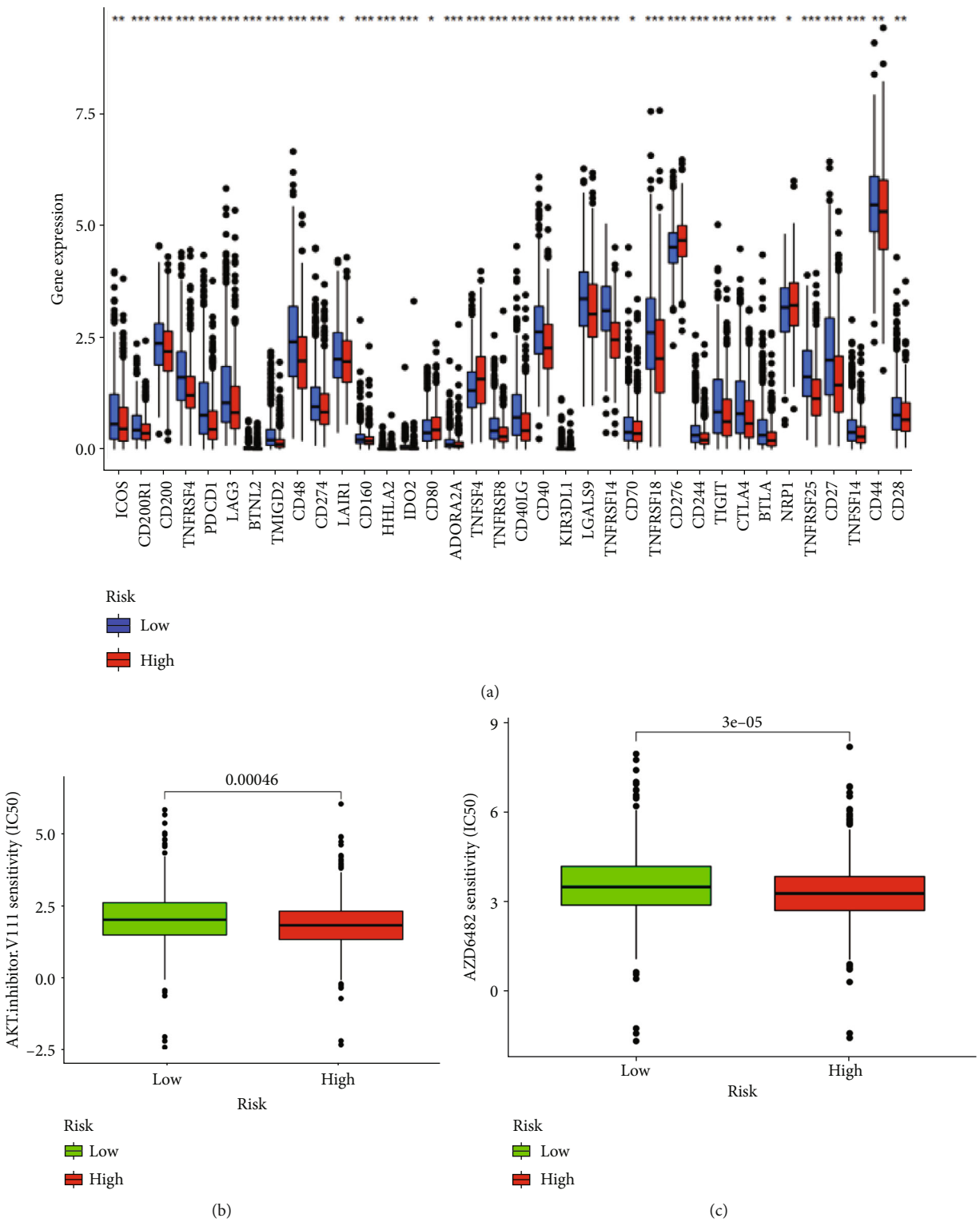

Figure 12: Continued.

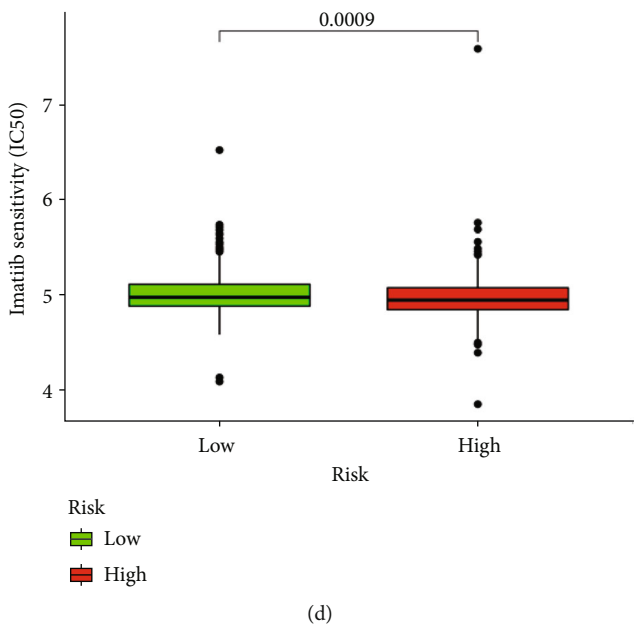

(d)

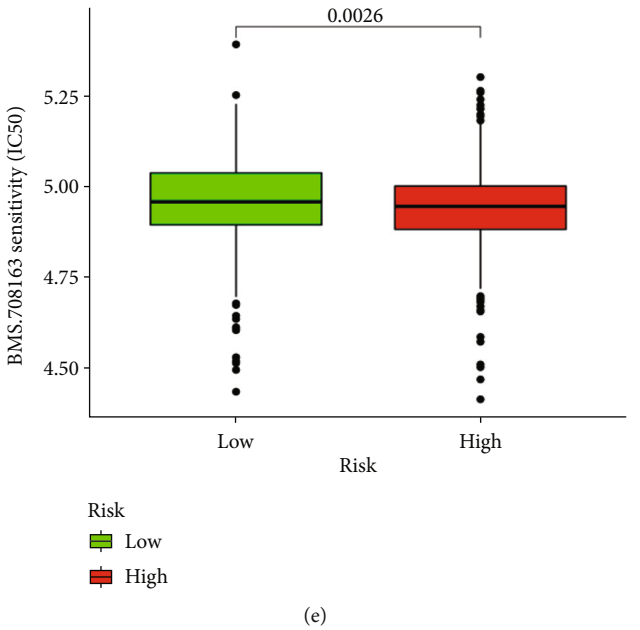

(e)

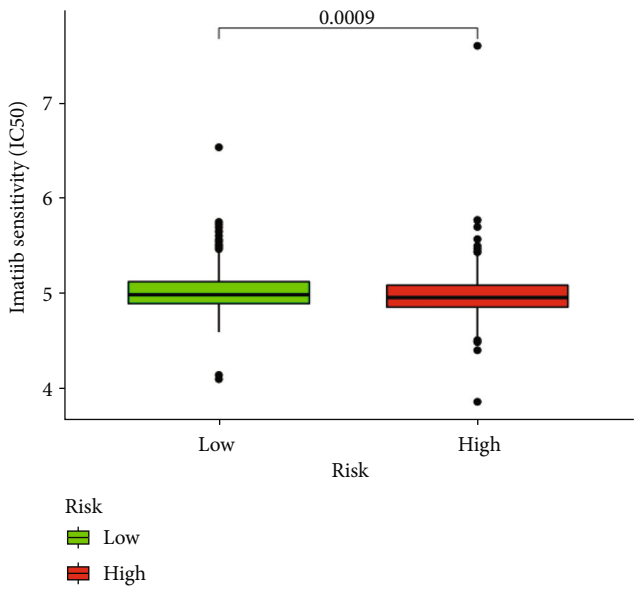

(f)

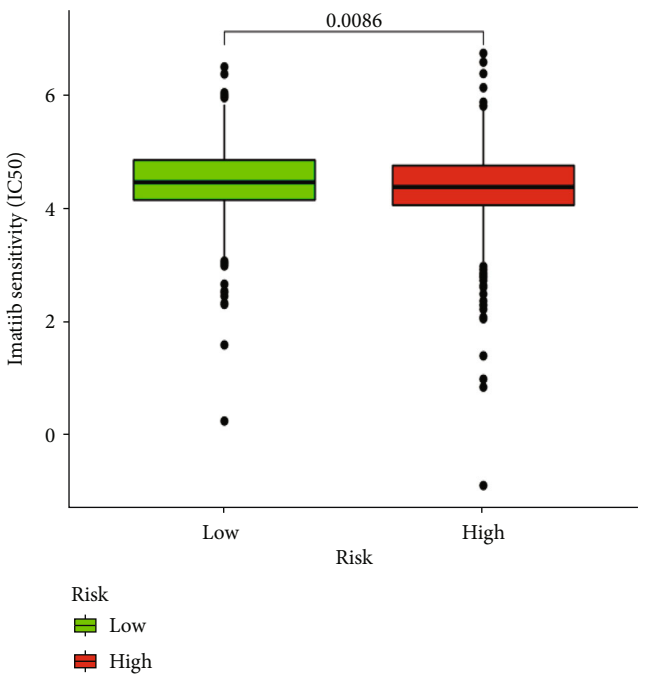

(g)

Figure 12: Continued.

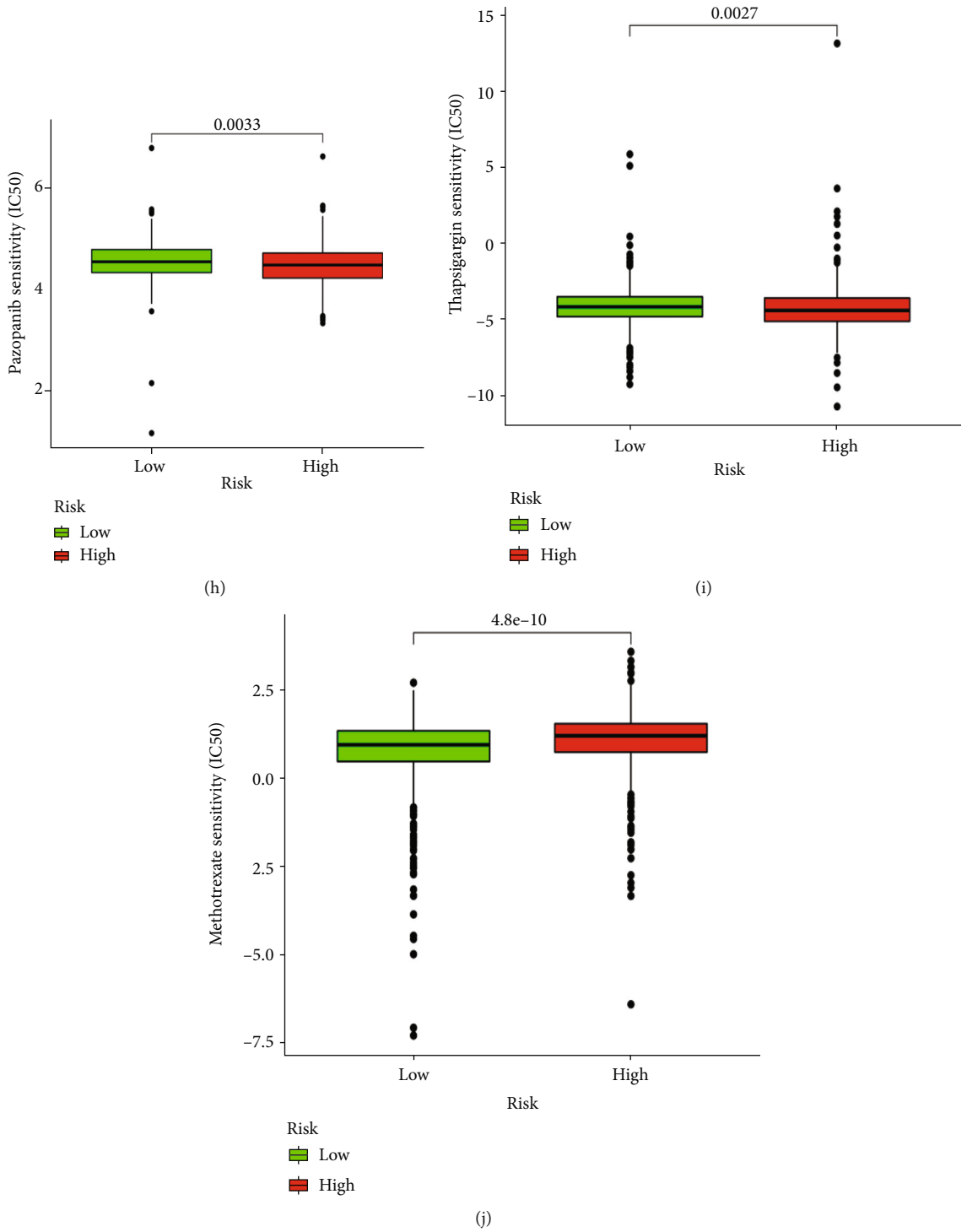

Figure 12: Comparison of sensitivity to treating drugs across high- and low-risk groups. (a) CD80, TNFSF4, CD276, and NRP1 expressions between groups. (b) IC50 of AKT inhibitor VIII between groups. (c) IC50 of AZD6482 between groups. (d) IC50 of bicalutamide between groups. (e) IC50 of BMS.708163 in the two risk groups. (f) IC50 of imatinib in the two risk groups. (g) IC50 of lapatinib in the two risk groups. (h) IC50 of pazopanib between groups, (i) IC50 of thapsigargin in the two risk groups, and (j) IC50 of methotrexate between groups.

regulating FNBP1 expression through cavernous Mir-376A-5p [17]. (4) ST7-AS1 promotes the lung adenocarcinoma cells malignancy by regulating Mir-181B-5p/KPNA4 axis. Therefore, aiming at ST7-AS1 and KPNA4 or upregulation of Mir-181B-5p may be beneficial for the treating lung adenocarcinoma [18]. (5) MAPT-AS1 has been identified as a solid prognostic marker of renal clear cell carcinoma (ccRCC), inhibiting the invasion and proliferation of ccRCC [19]. And its upregulation were associated with positive survival in breast cancer patients [20].

One of the lncRNAs associated with oxidative stress, LINC01871, may serve as a marker of BC prognosis, but

Figure 13: Mutations in the seven key genes, based on BC data in TCGA. Bar plots showing mutations in the seven key genes.

has not been studied in depth for the pathogenesis of BC [21]. Another lncRNA, DLG5-AS1, has not been studied for its prognostic significance in cancer. As a result, more research is needed to determine how this lncRNA affects the development of patients with BC via oxidative stress.

The development of BC was significantly predicted based on the characteristics of seven lncRNAs associated with oxidative stress. Consistent with previous studies, the OS of the low-risk group was higher. These results suggest that risk score features have some potential in prediction of survival condition. Univariate and multivariate Cox analysis results indicated that this trait might be used as an independent prognostic predictor. The model demonstrated superior distinction and accuracy based on the *c*-index, calibration curve, ROC curve, and internal validation data, indicating that it can be used as a possible predictive tool.

Subsequent GSEA results showed that macrophages scored higher in the group with high-risk. The results indicate that tumor-associated macrophages (TAMs) are key cells promoting tumor in tumoral microenvironment. Preclinical TAM stimulates progression of breast tumor, including tumor cell growth and metastasis. In BC models, TAMs also causes resistance to a number of therapies. The previous work found that oxidative stress signalling has a role in BC cell proliferation and migration. Initially, important components of oxidative stress signalling were discovered to substantially correlate with clinical and pathological characteristics of BC. These connections were not independent of TNM staging or clinical subtype, implying that oxidative stress activation is a common feature associated with BC development. Internal identification proved that the predicting signature has positive predictive performance. PCA suggested that seven lncRNAs associated with oxidative stress could be differentiated according to the oxidative stress condition of the patients.

The results of GSEA implied that macrophages scored higher in the high-risk group. It was revealed that tumor-associated macrophages (TAMs) are key cells promoting tumor in tumoral microenvironment. Preclinical TAMs stimulate progression of breast tumor, including tumor cell growth and metastasis. TAMs also attributed to resistance to a series of treatment in BC models [22].

Our study also showed that patients high ranked may be sensitive to and resistant to demethotrexate against TNF, CD80, CD276, SF4, and NRP1 immunotherapy and conventional chemotherapy drugs including AZD6482, bicaluamide, AKT inhibitor VIII, BMS.708163, imatinib, lapatinib, pazolparib, and toxic carotene. This suggests that the group of patients with high risk may alleviate the disease from the combination of immunotherapy and chemotherapy, providing the basis for precise, individualized treatment of BC patients.

However, there are some limitations to our study. First, external validation of data from other databases is required to test the suitability of the predictive signatures. Secondly, the mechanism of lncRNA oxidative stress in BC needs further experimental verification.

5. Conclusions

In conclusion, lncRNAs with oxidative stress features can independently predict BC prognosis, providing support for the underlying mechanism of oxidative stress of lncRNAs and their response to clinical treatment therapy within BC; however, more research is needed.

Data Availability

The dataset used in this paper are available from the corresponding author upon request.

Disclosure

A preprint has been published [23].

Conflicts of Interest

The authors declared that they have no conflicts of interest regarding this work.

Authors' Contributions

WX designed the study, revised it critically for important intellectual content, and approved the final manuscript; ZJL performed the statistical analysis, drafted the paper, collected the data, and approved the final manuscript; MHY, FRG, LD, LBW, and CXC performed some data analyses, provided research materials, revised some of the contents, and approved the final manuscript.

Acknowledgments

This study was supported by the grants from the National Natural Science Foundation of China (no. 8217103088), and we also thank all the staff involved in setting up the TCGA database.

References

[1] F. Bray, J. Ferlay, I. Soerjomataram, R. L. Siegel, L. A. Torre, and A. Jemal, "Global cancer statistics 2018: GLOBOCAN estimates of incidence and mortality worldwide for 36 cancers in 185 countries," *CA: a Cancer Journal for Clinicians*, vol. 68, no. 6, pp. 394–424, 2018.

[2] L. Fan, K. Strasser-Weippl, J. J. Li et al., "Breast cancer in China," *The Lancet Oncology*, vol. 15, no. 7, pp. e279–e289, 2014.

[3] T. G. Yoo, I. Cranshaw, R. Broom, S. Pandanaboyana, and A. Bartlett, "Systematic review of early and long-term outcome of liver resection for metastatic breast cancer: is there a survival benefit?," *Breast*, vol. 32, no. 4, pp. 162–172, 2017.

[4] F. Guéraud, M. Atalay, N. Bresgen et al., "Chemistry and biochemistry of lipid peroxidation products," *Free Radical Research*, vol. 44, no. 10, pp. 1098–1124, 2010.

[5] P. L. de Sá Jr., D. A. D. Câmara, A. S. Porcacchia et al., "The roles of ROS in cancer heterogeneity and therapy," *Oxidative Medicine and Cellular Longevity*, vol. 2017, Article ID 2467940, 12 pages, 2017.

[6] L. B. Sullivan and N. S. Chandel, "Mitochondrial reactive oxygen species and cancer," *Cancer & Metabolism*, vol. 2, no. 1, p. 17, 2014.

[7] K. Struhl, "Transcriptional noise and the fidelity of initiation by RNA polymerase II," *Nature Structural & Molecular Biology*, vol. 14, no. 2, pp. 103–105, 2007.

[8] T. Meng, R. Huang, Z. Zeng et al., "Identification of prognostic and metastatic alternative splicing signatures in kidney renal clear cell carcinoma," *Frontiers in Bioengineering and Biotechnology*, vol. 7, p. 270, 2019.

[9] W. Hong, L. Liang, Y. Gu et al., "Immune-related lncRNA to construct novel signature and predict the immune landscape of human hepatocellular carcinoma," *Molecular Therapy-Nucleic Acids*, vol. 22, pp. 937–947, 2020.

[10] A. Subramanian, P. Tamayo, V. K. Mootha et al., "Gene set enrichment analysis: a knowledge-based approach for interpreting genome-wide expression profiles," *Proceedings of the National Academy of Sciences of the United States of America*, vol. 102, no. 43, pp. 15545–15550, 2005.

[11] P. Geeleher, N. J. Cox, and R. Huang, "Clinical drug response can be predicted using baseline gene expression levels and in vitro drug sensitivity in cell lines," *Genome Biology*, vol. 15, no. 3, article R47, 2014.

[12] M. Panayiotidis, "Reactive oxygen species (ROS) in multistage carcinogenesis," *Cancer Letters*, vol. 266, no. 1, pp. 3–5, 2008.

[13] J. Yi, J. Yang, R. He et al., "Emodin enhances arsenic trioxide-induced apoptosis via generation of reactive oxygen species and inhibition of survival signaling," *Cancer Research*, vol. 64, no. 1, pp. 108–116, 2004.

[14] T. Li, F. Deng, S. Qin, Y. Wu, Y. Shan, and Q. Li, "Advances in Nrf2-ARE-mediated flavonoids against oxidative stress," *Food and Machinery*, vol. 32, no. 6, pp. 201–207, 2016.

[15] C. Zhang, Y. Liang, C. D. Zhang et al., "The novel role and function of LINC01235 in metastasis of gastric cancer cells by inducing epithelial-mesenchymal transition," *Genomics*, vol. 113, no. 3, pp. 1504–1513, 2021.

[16] W. Guo, X. Liang, L. Liu et al., "MiR-6872 host gene SEMA3B and its antisense lncRNA SEMA3B-AS1 function synergistically to suppress gastric cardia adenocarcinoma progression," *Gastric Cancer*, vol. 22, no. 4, pp. 705–722, 2019.

[17] R. Cao, J. Shao, W. Zhang, Y. Lin, Z. Huang, and Z. Li, "Silencing long intergenic non-protein coding RNA 00987 inhibits proliferation, migration, and invasion of osteosarcoma cells by sponging miR-376a-5p to regulate FNBP1 expression," *Discov Onc*, vol. 12, no. 1, p. 18, 2021.

[18] R. H. Hu, Z. T. Zhang, H. X. Wei et al., "lncRNA ST7-AS1, by regulating miR-181b-5p/KPNA4 axis, promotes the malignancy of lung adenocarcinoma," *Cancer Cell International*, vol. 20, no. 1, p. 568, 2020.

[19] X. Han, Y. Sekino, T. Babasaki et al., "Microtubule-associated protein tau (MAPT) is a promising independent prognostic marker and tumor suppressive protein in clear cell renal cell carcinoma," *Urologic Oncology*, vol. 38, no. 6, pp. 605.e9–605.e17, 2020.

[20] D. Wang, J. Li, F. Cai et al., "Overexpression of MAPT-AS1 is associated with better patient survival in breast cancer," *Biochemistry and Cell Biology*, vol. 97, no. 2, pp. 158–164, 2019.

[21] X. Li, F. Jin, and Y. Li, "A novel autophagy-related lncRNA prognostic risk model for breast cancer," *Journal of Cellular and Molecular Medicine*, vol. 25, no. 1, pp. 4–14, 2021.

[22] S. Q. Qiu, S. J. H. Waaijer, M. C. Zwager, E. G. E. de Vries, B. van der Vegt, and C. P. Schröder, "Tumor-associated macrophages in breast cancer: innocent bystander or important player?," *Cancer Treatment Reviews*, vol. 70, pp. 178–189, 2018.

[23] J. Zhao, H. Ma, R. Feng et al., *A new necroptosis-related lncRNA signature predicts the prognosis and tumor immune microenvironment of breast cancer patients*, 2022.

Hindawi
Journal of Oncology
Volume 2022, Article ID 6233904, 10 pages
https://doi.org/10.1155/2022/6233904

Research Article

Evaluating the Diagnostic Potentials of Circulating Tumor DNA against Melanoma: A Systematic Review and Meta-Analysis

Jianchao Zhang,[1,2] Da Qian,[1] Xiaochen Xu,[1] Ming Xu,[1] Ke Wang,[1] Hui Lu,[1] and Guoliang Shen[2]

[1]*Department of Burn and Plastic Surgery-Hand Surgery, First People's Hospital of Changshu City, Changshu Hospital Affiliated to Soochow University, No. 1 Shuyuan Street, Changshu, Soochow 215500, China*
[2]*Department of Burn and Plastic Surgery, First Affiliated Hospital of Soochow University, No. 188 Shizi Street, Soochow 215000, China*

Correspondence should be addressed to Da Qian; drqianda@hotmail.com and Guoliang Shen; sdfyysgl@163.com

Received 3 August 2022; Revised 30 August 2022; Accepted 15 September 2022; Published 12 October 2022

Academic Editor: Muhammad Muddassir Ali

Background. The accurate detection of circulating tumor (ct) DNA is affected by multiple factors, and several controversies still persists regarding clinical applications. In order to assess the consistency of ctDNA gene mutation detection findings in matched melanoma tissue samples and peripheral blood, a meta-analysis was performed and provided evidence-based analysis for its clinical applications. *Method*. As of May 20, 2019, the database has been searched using the Embase, PubMed, and Cochrane Library search engines. The ctDNA investigations mentioned in this review may be used to directly or indirectly get the true positive (TP), true negative (TN), false positive (FP), and false negative (FN) values of melanoma patients. To be excluded from the study are duplicate publications, research that do not offer a full text, inadequate material or an inability to extract data, and animal trials. *Results*. Overall, the pooled specificity, sensitivity, NLR, PLR, and DOR were 0.94 (95% CI: 0.91-0.96), 0.73 (95% CI: 0.70-0.75), 0.32 (95% CI: 0.22-0.45), 8.21 (95% CI: 4.67-14.43), and 32.72 (95% CI: 14.81-72.30), respectively. Additionally, we calculated AUC by drawing the SROC curve, and the value of AUC is 0.9287, which indicates that the accuracy of ctDNA in diagnosing melanoma is 92.87% of the gold standard. Furthermore, we conducted a subgroup analysis for different countries, sample sources, and ctDNA detection methods. The pooled results showed that different countries, sample sources, and ctDNA detection methods showed significantly large differences in terms of sensitivity of ctDNA in diagnosing melanoma, while the specificity basically remained the same. *Conclusion*. We discovered that the diagnostic outcomes between matched tumor samples and ctDNA remained more reliable in melanoma patients. ctDNA has the advantages of low trauma, convenient dynamic monitoring, and simple operation. ctDNA is expected to become an auxiliary method for the diagnosis of melanoma gene mutations.

1. Introduction

Melanoma is a very aggressive skin tumor caused by the excessive proliferation of melanocytes. It mostly occurs in the skin, mucous membrane, and extremities. Although its incidence is only 10% of skin tumors, it is related to 80% of skin tumor deaths [1]. The 2018 Global Cancer Report indicated that there were 287,723 new cases of melanoma and 60,712 deaths [2]. In the early stage of melanoma, surgical resection is the first choice, while for advanced patients, traditional radiotherapy and chemotherapy showed very little effects for melanoma patients who cannot be surgically removed or who have metastasized and have BRAF V600E mutations. The treatment of melanoma has entered the age of targeted therapy after the U.S. Food and Drug Administration (U.S. Food and Drug Administration, FDA) authorized vemurafenib as a targeted drug in 2011 [3].

Traditionally, archival formalin-fixed, paraffin-embedded (FFPE) tumor tissues obtained after diagnosis and/or additional biopsies or surgery are used to identify somatic

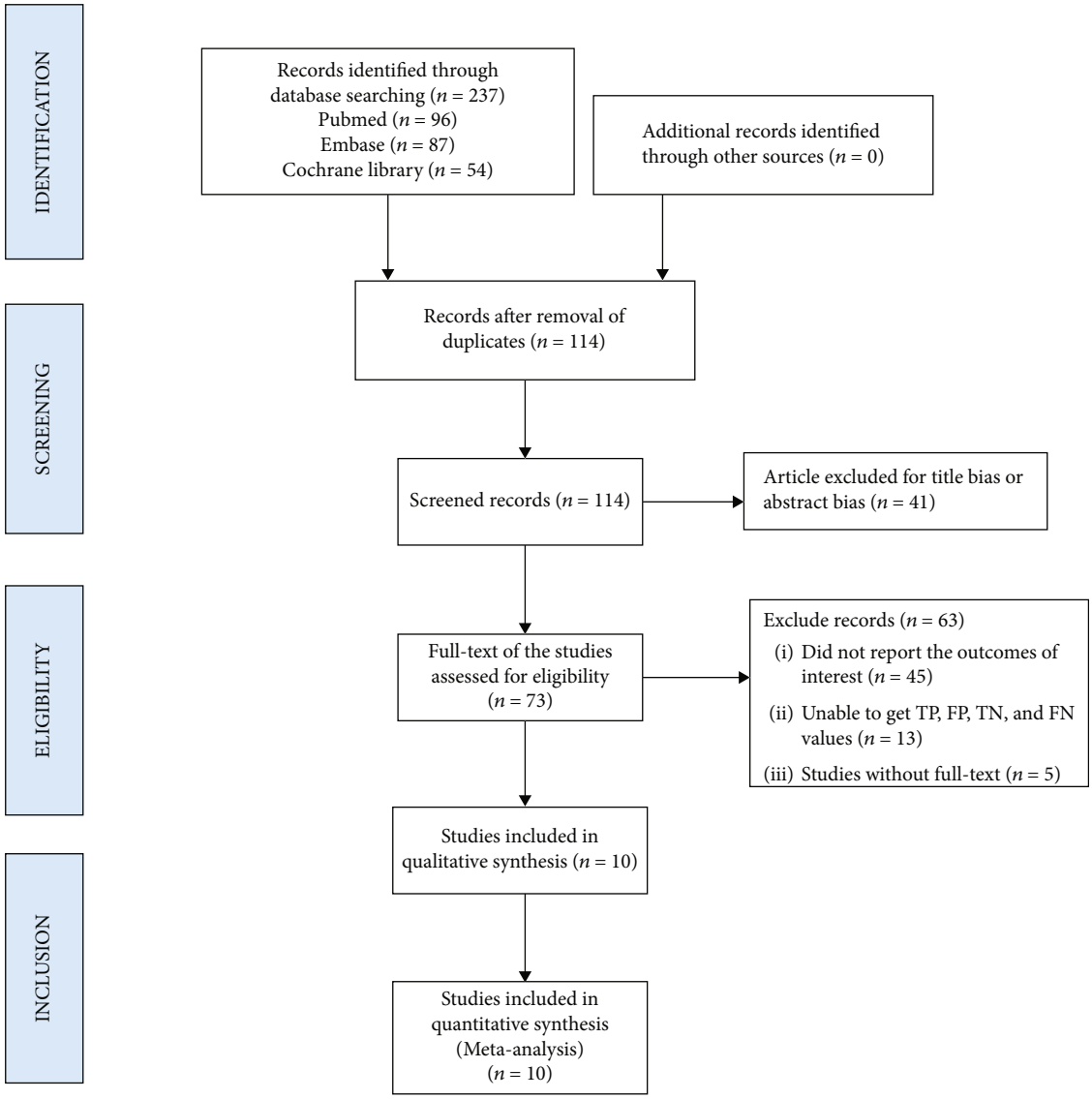

Figure 1: Showing the flowchart for selected studies.

mutations. The high risk of puncture, the inability to find the tumor in an anatomical position, the high expense, and the intricacy of the tumor tissue are just a few of the problems with mutation testing on archival tumor material, though [4, 5]. Circulating tumor DNA (ctDNA) detection is an emerging method that has been used to detect genetic mutations in humans in recent years. ctDNA is a DNA fragment that enters the blood circulatory system after the DNA of tumor cells falls off or undergoes apoptosis, which can be used as a special tumor marker. It is possible that ctDNA analysis might provide a more comprehensive view of the tumor's subclones [6]. A larger amount of tumor-specific somatic mutations may be discovered in circulating free DNA (ctDNA) in individuals with advanced cancer than in healthy persons [7, 8]. Pinzani et al. [9] pointed out that in patients with melanoma, the sensitivity of ctDNA detection was 72%, the specificity was 89%, and the consistency with tumor pathology detection results was 80% compared with the results of tumor tissue detection. A report by Tang et al. [10]. Demonstrated that the test results between tumor tissue and ctDNA were 70% consistent in 58 melanoma patients. There is still debate over the relevance of ctDNA detection in clinical settings because its accuracy depends on a number of variables, including the detection tool, sample source, and area.

In this study, quantitative Meta-analysis was used to evaluate the consistency of ctDNA gene mutation detection results in matched melanoma tissue samples and peripheral blood and provide evidence-based basis for clinical application.

2. Methods

2.1. Inclusion/Exclusion Criteria for Literature. The following were the inclusion criteria: (1) true positive (TP), true negative (TN), false positive (FP), and false negative (FN) values of patients with melanoma may be directly retrieved from the original article or indirectly based on the information supplied in the literature. (2) ctDNA were used for the diagnosis of melanoma in patients with the following

Table 1: Baseline characteristics of the included studies.

Author	Year	Country	Sample size	TNM staging	Sample source	ctDNA detection method	Mutation alleles	TP	FP	FN	TN	Sensitivity	Specificity
Yancovitz [12]	2007	USA	17	IV	Plasma	Mutant-specific PCR	BRAF	7	2	5	3	58%	60%
Board [13]	2009	USA	94	IV	Serum	Allele-specific PCR	BRAF	25	3	20	46	56%	94%
Pinzani [9]	2010	Italy	46	II-IV	Plasma	Allele-specific PCR	BRAF	45	3	1	15	97%	83%
Aung [14]	2014	UK	108	IV	Serum	Allele-specific PCR	BRAF	31	2	43	32	42%	94%
					Plasma	Allele-specific PCR	BRAF	38	2	36	32	51%	94%
Santiago-Walker [15]	2015	USA	746	III-IV	Plasma	BEAMing	BRAF	504	2	157	83	72%	89%
Janku [16]	2016	USA	36	IV	Plasma	Allele-specific PCR	BRAF	17	2	9	8	65%	80%
Mosko [17]	2016	UK	122	III-IV	Plasma	UltraSEEK	BRAF	53	2	19	48	74%	96%
Rowe [18]	2018	USA	55	IV	Plasma	BEAMing	BRAF	33	0	5	17	87%	100%
Long-Mira [19]	2018	France	19	IV	Plasma	Allele-specific PCR	BRAF	8	1	2	8	80%	89%
Haselmann [20]	2018	USA	187	III-IV	Plasma	BEAMing	BRAF	56	8	9	114	86%	93%

exclusionary conditions: (1) FeNO patients' true positive (TP), false positive (FP), true negative (TN), and false negative (FN) diagnostic values are not included in the study data and cannot be estimated; (2) studies lacking full text, inadequate information, or the incapacity to extract data; (3) case reports, reviews, and systematic reviews. (4) Repeated publishing.

2.2. Search Strategy. We searched Pubmed, Embase, and the Cochrane Library from the time the databases were first launched until May 2021 for the purposes of this meta-analysis. The following are the mesh glossary terms: "Circulating Tumor DNA," "Cell-Free Tumor DNA," and "Melanoma".

2.3. Literature Screening and Data Extraction. The literature review, screening, and data extraction are carried out independently by two researchers. Disagreements are settled through discussion or by asking a third party for their opinion. An author's name and year, as well as a sample's size and origin, as well as the technique used to identify ctDNA and TP, FP, TN, and FN may all be found in the data that is extracted and used to diagnose patients with melanoma.

2.4. Literature Quality Assessment. Two researchers used the QUADAS-2 tool [11] to assess the quality of each piece of included literature, which consists of 11 different components (for details, see the labelling of the bias risk graph and the bias risk summary graph in the results section). After cross-checking the findings, if there are still differences of opinion, a decision will be reached via discussion or consultation with a third party based on the assessment results being classified as "high" or "low" risk. Review manager 5.3 software is used to build bias risk maps and bias risk summary maps once all items have been evaluated.

2.5. Data Synthesis and Statistical Analysis. Using Meta-Disc1.4 software, which also did heterogeneity testing, the sensitivity, specificity, and 95 percent confidence interval of each independent research were calculated. First, the Spearman correlation coefficient P value is determined. This is done if the correlation coefficient P value falls below 0.05, which indicates a threshold effect. The area under the SROC curve (AUC) is determined. The opposite is true, which suggests that there is no threshold effect. In this case, we may combine the sensitivity, specificity, positive likelihood ratio (PLR), negative likelihood ratio (NLR), and diagnostic odds ratio (DOR) as well as other indications and construct a complete SROC curve. The heterogeneity test caused by nonthreshold effects is calculated by calculating the $\chi 2$ or Q value and the I2 value. Random effects models are utilized if I^2 is more than 50%; otherwise, the fixed effects models are used. Heterogeneity may be tracked down via sensitivity analysis or subgroup analysis. If the heterogeneity still exists, a random effects model is used; otherwise, a descriptive analysis is used instead. Deeks' funnel plot asymmetry test may be performed using STATA15.1 software to determine publication bias.

3. Results

3.1. The Results of Literature Search. A total of 237 studies were selected from the database for this research. 114 studies remained after removing duplicates. After going through the titles and abstracts, 73 papers were found. It was eventually

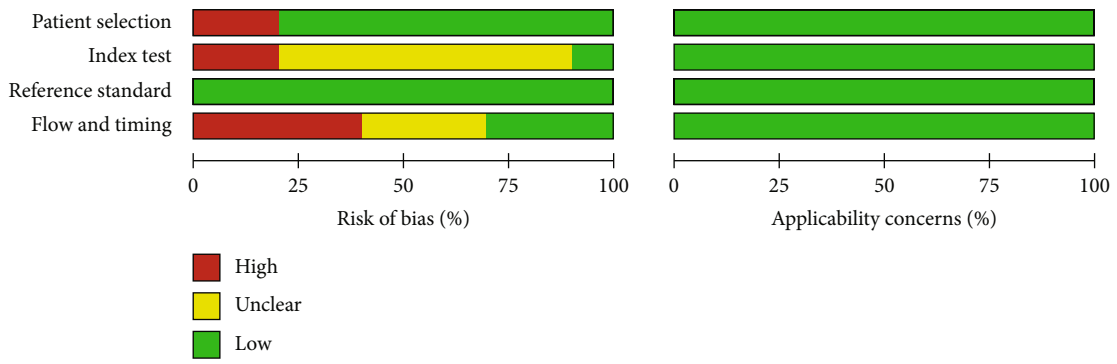

Figure 2: A graph of methodological quality.

completed by going through the full-texts of the 10 studies (Figure 1).

3.2. Baseline Characteristics and Study Quality

3.2.1. Baseline Characteristics. Additionally, Table 1 displays the baseline characteristics and quality rating of the included studies. 10 publications with 1430 patients were included in this meta-analysis. There are 4 articles from Europe and 6 articles from North America. Most of the literature has been published in the past 5 years; the research objects are mainly patients with stage III to IV; ctDNA detection methods were mainly allele-specific polymerase chain reaction (Allele-specific polymerase chain reaction, allele-specific PCR), BEAMing, UltraSEEK, etc.

3.2.2. Quality Assessment of the Included Studies. We assessed the methodological quality of each study in accordance with the QUADAS-2 criteria from four angles. Six of the trials to be reviewed did not mention the use of testing blinding, and the other three studies were carried out knowing the outcomes of the tissue test (Figure 2), so there may be unknown or significant risk variations. Since not all patients were included, or there was an inappropriate time interval between the study to be evaluated and the gold standard, the risk of deviation of the case flow and progress of 8 studies was unknown or high. In all studies, the applicability is very high (Figure 3).

3.3. Results of Meta-Analysis. The Spearman correlation value is -0.564 ($P = 0.090 > 0.05$), suggesting the absence of a threshold effect. The combined sensitivity of $\chi 2 = 91.34$ ($P \leq 0.001$) and $I^2 = 89.1$ percent indicates that there is heterogeneity produced by nonthreshold effects, hence the random effects model is employed to combine sensitivity. The combined specificity of $\chi 2 = 15.09$ ($P = 0.1289$), $I^2 = 33.7$ percent, indicates that there is no heterogeneity produced by nonthreshold effects, hence the fixed effects model is employed to combine the specificity. There is heterogeneity due to nonthreshold effects in the combined PLR of Cochran-$Q = 21.86$ ($P = 0.0158$), $I^2 = 54.3$ percent, hence the random effects model is employed to combine the PLR. The random effects model is utilized to combine the NLR because the combined NLR of Cochran-$Q = 96.48$

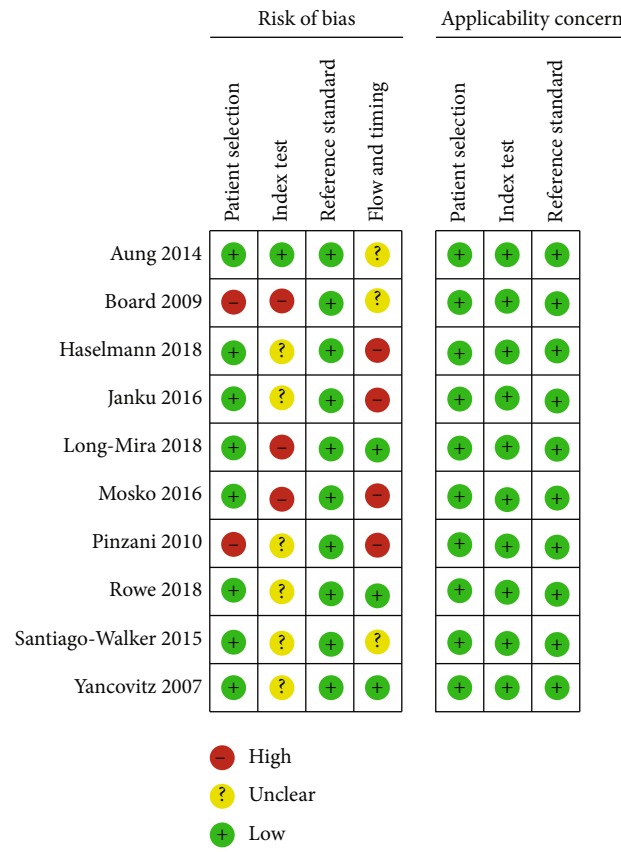

Figure 3: An overview of the methodological quality.

($P \leq 0.001$), $I^2 = 89.6$ percent, demonstrating heterogeneity driven by nonthreshold effects. Random effects model is used to combine Cochran-combined Q's DOR of 24.88 ($P = 0.0056$) and I^2 of 59.8 percent, which indicates that there is heterogeneity due by nonthreshold effects. The pooled sensitivity, specificity, PLR, NLR, and DOR are 0.73 (95% CI: 0.70-0.75), 0.94 (95% CI: 0.91-0.96), 8.21 (95% CI: 4.67-14.43), 0.32 (95% CI: 0.22-0.45), and 32.72 (95% CI: 14.81-72.30), respectively. Additionally, we calculate AUC by drawing the SROC curve, and the value of AUC is 0.9287, which indicates that the accuracy of ctDNA in diagnosing melanoma is 92.87% of the gold standard (Figures 4–9).

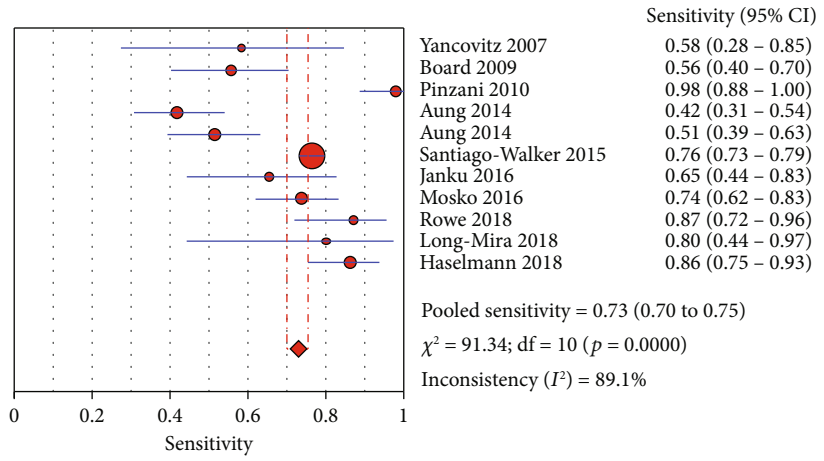

Figure 4: The sensitivity of ctDNA in diagnosing melanoma.

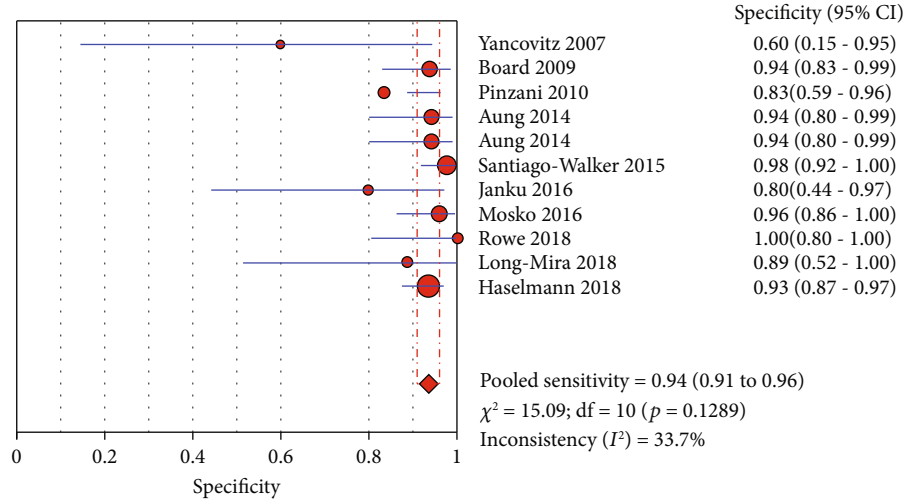

Figure 5: The specificity of ctDNA in diagnosing melanoma.

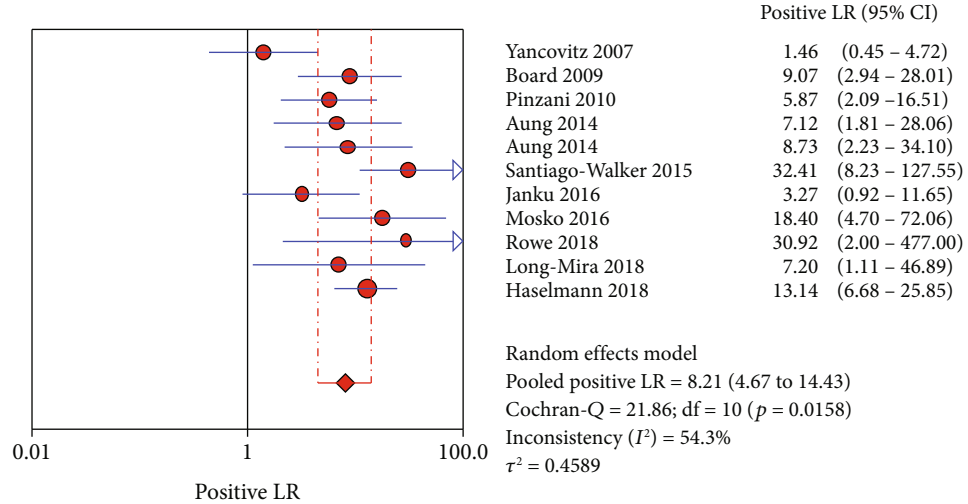

Figure 6: The PLR of ctDNA in diagnosing melanoma.

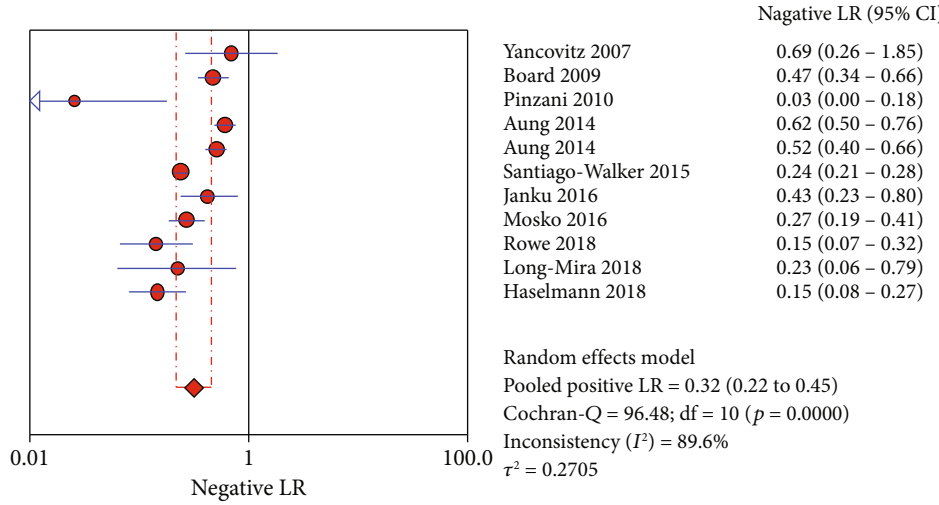

Figure 7: The NLR of ctDNA in diagnosing melanoma.

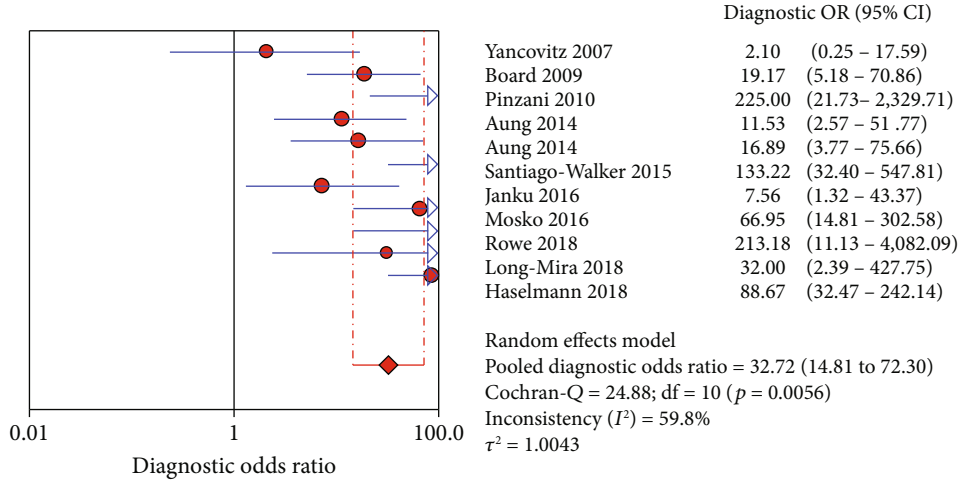

Figure 8: The DOR of ctDNA in diagnosing melanoma.

3.4. Subgroup Analysis. The research is somewhat heterogeneous, which may be due to various nations, sample sources, and ctDNA detection techniques. For the three aforementioned potential causes, we thus performed a subgroup study. The pooled sensitivity of North America is 0.76 (0.73-0.79), while the pooled sensitivity of Europe is 0.63 (0.57-0.69). The pooled specificity of North America is 0.94 (0.91-0.97), and the pooled specificity of Europe is 0.93 (0.88-0.97). The AUC of ctDNA in European melanoma patients is higher than that in North American patients (0.9576 vs. 0.8018).

In terms of sample source, the pooled sensitivity of plasma is 0.76 (0.73-0.78), while the pooled sensitivity of serum is 0.47 (0.38-0.56). The pooled specificity of plasma is 0.94 (0.91-0.96), and the pooled specificity of serum is 0.94 (0.86-0.98).

In addition, the results of the detection method showed that the sensitivity of Allele-specific PCR detection was 0.60 (0.54-0.65), while the sensitivity of BEAMing detection was 0.78 (0.74-0.81). The pooled specificity of Allele-specific PCR detection was 0.92 (0.86-0.95), and the sensitivity of BEAMing detection was 0.96 (0.92-0.98) (Table 2).

3.5. Publication Bias. The following is an example of the study's funnel plot. In this research, the *P* value of Deek's funnel plot asymmetry test is 0,12, which indicates that there is no apparent publication bias (Figure 10).

3.6. Sensitivity Analysis. Analyzing each included study one at a time to see if single included research has an undue influence on meta-analysis findings is known as a sensitivity analysis. Findings from the meta-analysis indicated no studies had a significant influence on its findings; this suggests the remaining studies' findings are consistent and credible.

4. Discussion

The new ctDNA can be utilized as a supplement to tissue biopsy for clinical diagnosis and disease monitoring due to its advantages of noninvasiveness, ease of access, continuous

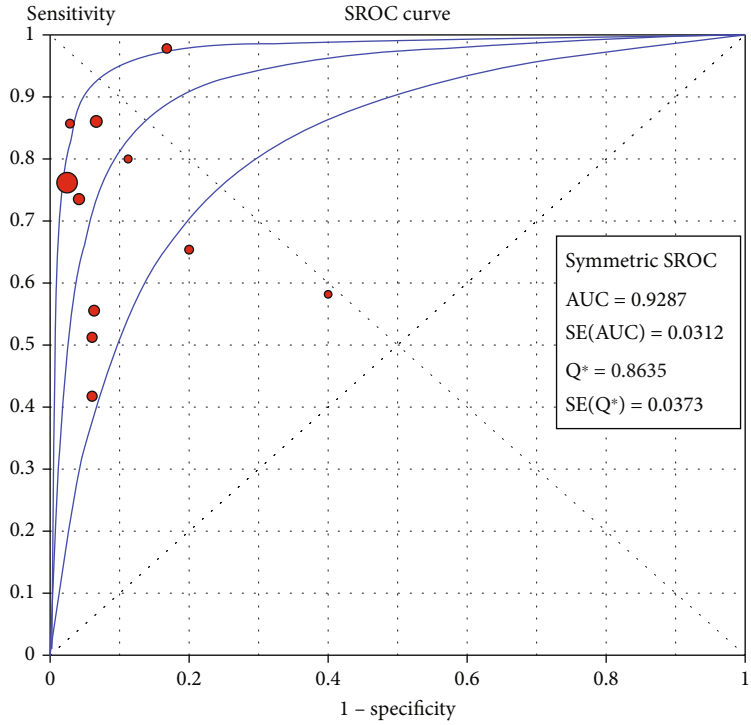

Figure 9: The SROC curve of ctDNA in diagnosing melanoma.

sampling, and overcoming tumor heterogeneity [21]. Traditional tissue biopsy has numerous inherent drawbacks. However, due to the existence of many influencing factors, the diagnostic value of ctDNA in melanoma is still controversial. In this study, 10 articles that met the inclusion criteria were meta-analyzed, and the subjects involved a total of 1430 melanoma patients.

The combined sensitivity of ctDNA for melanoma detection was 0.73 (95% CI: 0.70-0.75), combined specificity was 0.94 (95% CI: 0.91-0.96), and combined AUC was 0.9287. It should be noted that AUC is a comprehensive index, and the closer its value is to 1, the higher the diagnostic value. Our pooled results show that the diagnostic accuracy of ctDNA is 92.87% of the gold standard, indicating that it has a higher diagnostic value in melanoma.

The pooled PLR is 8.21 (95% CI: 4.67-14.43), which indicates that the probability of ctDNA detection in melanoma patients is about 8.21 times that of false positives. The combined NLR is 0.32 (95% CI: 0.22-0.45), indicating that 32% of false negatives may be present in the negative results of ctDNA. DOR is the ratio of the positive results in the experimental group to the positive results in the control group, which can better reflect the "differentiation" ability of the diagnostic test, and the DOR value is positively correlated with its discrimination ability. The pooled DOR is 32.72 (95% CI: 14.81-72.30), indicating that ctDNA detection has a higher comprehensive diagnostic efficiency.

The accuracy of ctDNA detection was examined in this study along with its influencing factors. [13] Board et al. pointed noted that there is a strong correlation between ctDNA level and tumor stage, that ctDNA mutations rely on tumor stage, and that early detection is typically inaccurate. Compared with stage I patients, stage IV patients have higher levels of ctDNA [22], and ctDNA levels are related to tumor metastasis [23]. In addition, the heterogeneity of the tumor may result in inconsistent gene mutation detection results between ctDNA and the corresponding tumor tissue. Tumor heterogeneity comes from three aspects: intratumor, intertumor, and temporal heterogeneity. Tissue only represents the mutation information of the tumor tissue site, while ctDNA represents the mutation information of all tumor tissues [6, 24]. The preprocessing and testing methods of blood samples will also affect the test results. Our pooled results found that there is a big difference in sensitivity between plasma and serum-derived ctDNA [0.76 (0.73-0.78) vs 0.47 (0.38-0.56)] but are basically the same in specificity [0.94 (0.91-0.96) vs 0.94 (0.86-0.98)]. At present, the ctDNA extraction efficiency of different extraction kits vary greatly, and there is no uniform quality judgment standard between different extraction methods [25, 26]. In the investigation of detection methods, we found that BEAMing (0.78, 95% CI: 0.74-0.81) has a higher sensitivity than Allele-specific PCR (0.60, 95% CI: 0.54-0.65). In addition, we also found that ctDNA has a higher sensitivity in the diagnosis of melanoma patients in North America [0.76 (0.73-0.79) vs. 0.63 (0.57-0.69)], while the specificity difference is small [0.94 (0.91-0.97) vs. 0.93 (0.88-0.97)]. The above results indicate that different regions, different sample sources, and different detection methods will have an impact on the diagnostic performance.

There are still the following issues with this study: first, there aren't many research on the reliability of melanoma

Table 2: Subgroup analysis of ctDNA in diagnosing melanoma.

Variables		Number of studies	Sensitivity			Specificity			Pooled PLR	Pooled NLR	Pooled DOR	Pooled AUC
			I^2 (%)	P value	Pooled sensitivity	I^2 (%)	P value	Pooled specificity				
Country	North America	6	74	0.0018	0.76 (0.73-0.79)	57.9	0.0366	0.94 (0.91-0.97)	8.15 (2.95-22.51)	0.30 (0.19-0.45)	30.39 (8.63-10.7.01)	0.8018
	Europe	5	92.9	≤0.001	0.63 (0.57-0.69)	0.0	0.5482	0.93 (0.88-0.97)	9.07 (5.01-16.43)	0.35 (0.20-0.61)	28.66 (13.33-61.63)	0.9576
Sample source	Plasma	9	83.8	≤0.001	0.76 (0.73-0.78)	46.9	0.0576	0.94 (0.91-0.96)	8.30 (4.08-16.88)	0.27 (0.18-0.40)	40.36 (15.75-103.43)	0.9282
	Serum	2	52.4	0.1474	.0.47 (0.38-0.56)	0.0	0.9639	0.94 (0.86-0.98)	8.12 (3.39-19.47)	0.56 (0.42-0.73)	14.93 (5.57-40.02)	/
ctDNA detection method	Allele-specific PCR	6	90.5	≤0.001	0.60 (0.54-0.65)	0.0	0.6026	0.92 (0.86-0.95)	6.73 (4.00-11.35)	0.45 (0.32-0.64)	18.29 (9.44-35.46)	0.9271
	BEAMing	3	65.8	0.0538	0.78 (0.74-0.81)	46.2	0.1556	0.96 (0.92-0.98)	21.36 (10.40-43.84)	0.18 (0.10-0.33)	117.66 (50.17-275.94)	0.9539

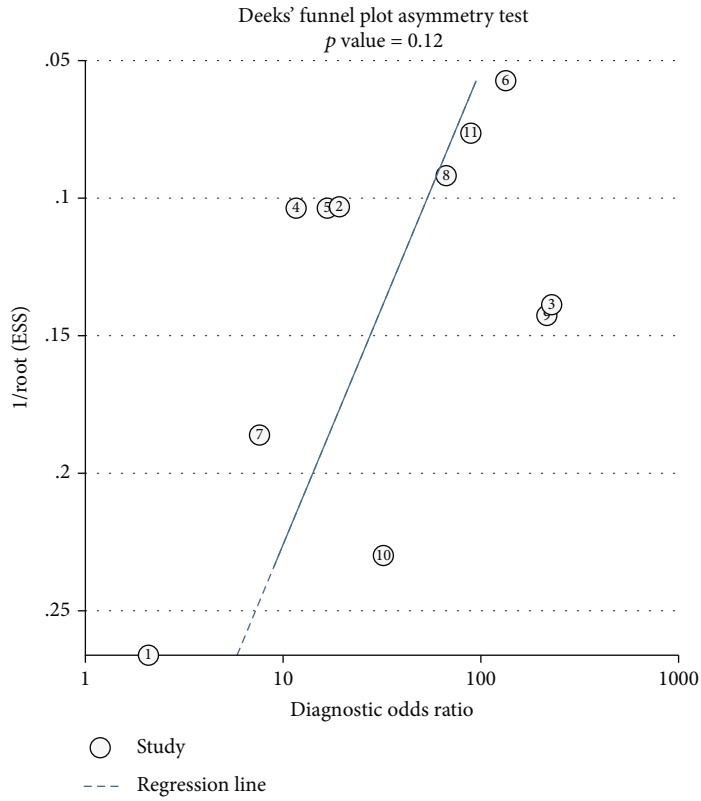

Figure 10: Deek's funnel plot asymmetry test of ctDNA in diagnosing melanoma.

diagnosis by ctDNA; as a result, the group's literature is smaller and of varying quality. In the future, more studies of higher quality need to be included, and further studies on possible heterogeneity factors will be made. Second, the included literature uses the assessment of the consistency of ctDNA and tissue biopsy results as evaluation indicators, and there is a possibility that the authors prefer to publish positive results. Third, the number of cases included in the enrollment literature is small, which will affect the accuracy of the statistical results.

5. Conclusion

In patients with melanoma, the diagnostic outcomes between ctDNA and matched tumor tissues were more reliable, according to our pooled results. ctDNA has the advantages of low trauma, convenient dynamic monitoring, simple operation, etc., and it is expected to become an auxiliary method for the diagnosis of melanoma gene mutations.

Data Availability

Data are present in the manuscript.

Conflicts of Interest

The authors declare no conflict of interest.

Authors' Contributions

Jianchao Zhang, Da Qian, and Xiaochen Xu had equal contribution.

Acknowledgments

This study was supported by Science and Technology Project of Changshu Health Commission (csws2020005).

References

[1] J. J. Luke, K. T. Flaherty, A. Ribas, and G. V. Long, "Targeted agents and immunotherapies: optimizing outcomes in melanoma," *Nature Reviews Clinical Oncology*, vol. 14, no. 8, pp. 463–482, 2017.

[2] F. Bray, J. Ferlay, I. Soerjomataram, R. L. Siegel, L. A. Torre, and A. Jemal, "Global cancer statistics 2018: GLOBOCAN estimates of incidence and mortality worldwide for 36 cancers in 185 countries," *CA: a Cancer Journal for Clinicians*, vol. 68, no. 6, pp. 394–424, 2018.

[3] I. Ingram, "FDA approves vemurafenib for treatment of metastatic melanoma," *Oncology (Williston Park)*, vol. 25, no. 906, 2011.

[4] L. V. Sequist, J. A. Engelman, and T. J. Lynch, "Toward noninvasive genomic screening of lung cancer patients," *Journal of Clinical Oncology*, vol. 27, no. 16, pp. 2589–2591, 2009.

[5] T. P. Plesec and J. L. Hunt, "KRAS mutation testing in colorectal cancer," *Advances in Anatomic Pathology*, vol. 16, no. 4, pp. 196–203, 2009.

[6] M. Fleischhacker and B. Schmidt, "Cell-free DNA resuscitated for tumor testing," *Nature Medicine*, vol. 14, no. 9, pp. 914-915, 2008.

[7] M. Fleischhacker and B. Schmidt, "Circulating nucleic acids (CNAs) and cancer–a survey," *Biochimica et Biophysica Acta*, vol. 1775, no. 1, pp. 181–232, 2007.

[8] H. Schwarzenbach, D. S. Hoon, and K. Pantel, "Cell-free nucleic acids as biomarkers in cancer patients," *Nature Reviews Cancer*, vol. 11, no. 6, pp. 426–437, 2011.

[9] P. Pinzani, F. Salvianti, R. Cascella et al., "Allele specific Taqman-based real-time PCR assay to quantify circulating $BRAF^{V600E}$ mutated DNA in plasma of melanoma patients," *Clinica Chimica Acta*, vol. 411, no. 17-18, pp. 1319–1324, 2010.

[10] H. Tang, Y. Kong, L. Si et al., "Clinical significance of $BRAF^{V600E}$ mutation in circulating tumor DNA in Chinese patients with melanoma," *Oncology Letters*, vol. 15, no. 2, pp. 1839–1844, 2018.

[11] S. Schueler, G. M. Schuetz, and M. Dewey, "The revised QUADAS-2 tool," *Annals of Internal Medicine*, vol. 156, no. 4, p. 323, 2012, author reply 323-324.

[12] M. Yancovitz, J. Yoon, M. Mikhail et al., "Detection of mutant *BRAF* alleles in the plasma of patients with metastatic melanoma," *The Journal of Molecular Diagnostics*, vol. 9, no. 2, pp. 178–183, 2007.

[13] R. E. Board, G. Ellison, M. C. Orr et al., "Detection of *BRAF* mutations in the tumour and serum of patients enrolled in the AZD6244 (ARRY-142886) advanced melanoma phase II study," *British Journal of Cancer*, vol. 101, no. 10, pp. 1724–1730, 2009.

[14] K. L. Aung, E. Donald, G. Ellison et al., "Analytical validation of *BRAF* mutation testing from circulating free DNA using the amplification refractory mutation testing system," *The Journal of Molecular Diagnostics*, vol. 16, no. 3, pp. 343–349, 2014.

[15] A. Santiago-Walker, R. Gagnon, J. Mazumdar et al., "Correlation of BRAF mutation status in circulating-free DNA and tumor and association with clinical outcome across four BRAFi and MEKi clinical trials," *Clinical Cancer Research*, vol. 22, no. 3, pp. 567–574, 2016.

[16] F. Janku, H. J. Huang, B. Claes et al., "*BRAF* mutation testing in cell-free DNA from the plasma of patients with advanced cancers using a rapid, automated molecular diagnostics system," *Molecular Cancer Therapeutics*, vol. 15, no. 6, pp. 1397–1404, 2016.

[17] M. J. Mosko, A. A. Nakorchevsky, E. Flores et al., "Ultrasensitive detection of multiplexed somatic mutations using MALDI-TOF mass spectrometry," *The Journal of Molecular Diagnostics*, vol. 18, no. 1, pp. 23–31, 2016.

[18] S. P. Rowe, B. Luber, M. Makell et al., "From validity to clinical utility: the influence of circulating tumor DNA on melanoma patient management in a real-world setting," *Molecular Oncology*, vol. 12, no. 10, pp. 1661–1672, 2018.

[19] E. Long-Mira, M. Ilie, E. Chamorey et al., "Monitoring BRAF and NRAS mutations with cell-free circulating tumor DNA from metastatic melanoma patients," *Oncotarget*, vol. 9, no. 90, pp. 36238–36249, 2018.

[20] V. Haselmann, C. Gebhardt, I. Brechtel et al., "Liquid profiling of circulating tumor DNA in plasma of melanoma patients for companion diagnostics and monitoring of BRAF inhibitor therapy," *Clinical Chemistry*, vol. 64, no. 5, pp. 830–842, 2018.

[21] F. Diehl, K. Schmidt, M. A. Choti et al., "Circulating mutant DNA to assess tumor dynamics," *Nature Medicine*, vol. 14, no. 9, pp. 985–990, 2008.

[22] Y. C. Yang, D. Wang, L. Jin et al., "Circulating tumor DNA detectable in early- and late-stage colorectal cancer patients," *Bioscience Reports*, vol. 38, no. 4, 2018.

[23] S. H. Lim, T. M. Becker, W. Chua et al., "Circulating tumour cells and circulating free nucleic acid as prognostic and predictive biomarkers in colorectal cancer," *Cancer Letters*, vol. 346, no. 1, pp. 24–33, 2014.

[24] M. Gerlinger, A. J. Rowan, S. Horswell et al., "Intratumor heterogeneity and branched evolution revealed by multiregion sequencing," *The New England Journal of Medicine*, vol. 366, no. 10, pp. 883–892, 2012.

[25] J. C. M. Wan, C. Massie, J. Garcia-Corbacho et al., "Liquid biopsies come of age: towards implementation of circulating tumour DNA," *Nature Reviews Cancer*, vol. 17, no. 4, pp. 223–238, 2017.

[26] G. Siravegna, S. Marsoni, S. Siena, and A. Bardelli, "Integrating liquid biopsies into the management of cancer," *Nature Reviews Clinical Oncology*, vol. 14, no. 9, pp. 531–548, 2017.

Hindawi
Journal of Oncology
Volume 2023, Article ID 9850715, 1 page
https://doi.org/10.1155/2023/9850715

Retraction

Retracted: Deep Learning-Based Health Management Model Application in Extreme Myopia Eye Vision Monitoring and Risk Prediction

Journal of Oncology

Received 11 July 2023; Accepted 11 July 2023; Published 12 July 2023

This article has been retracted by Hindawi following an investigation undertaken by the publisher [1]. This investigation has uncovered evidence of one or more of the following indicators of systematic manipulation of the publication process:

(1) Discrepancies in scope
(2) Discrepancies in the description of the research reported
(3) Discrepancies between the availability of data and the research described
(4) Inappropriate citations
(5) Incoherent, meaningless and/or irrelevant content included in the article
(6) Peer-review manipulation

The presence of these indicators undermines our confidence in the integrity of the article's content and we cannot, therefore, vouch for its reliability. Please note that this notice is intended solely to alert readers that the content of this article is unreliable. We have not investigated whether authors were aware of or involved in the systematic manipulation of the publication process.

Wiley and Hindawi regrets that the usual quality checks did not identify these issues before publication and have since put additional measures in place to safeguard research integrity.

We wish to credit our own Research Integrity and Research Publishing teams and anonymous and named external researchers and research integrity experts for contributing to this investigation.

The corresponding author, as the representative of all authors, has been given the opportunity to register their agreement or disagreement to this retraction. We have kept a record of any response received.

References

[1] Z. Huang, X. Xu, and W. Cheng, "Deep Learning-Based Health Management Model Application in Extreme Myopia Eye Vision Monitoring and Risk Prediction," *Journal of Oncology*, vol. 2022, Article ID 4537021, 8 pages, 2022.

Hindawi
Journal of Oncology
Volume 2022, Article ID 4537021, 8 pages
https://doi.org/10.1155/2022/4537021

Research Article

Deep Learning-Based Health Management Model Application in Extreme Myopia Eye Vision Monitoring and Risk Prediction

Zhaoxia Huang, Xue Xu, and Wenhui Cheng

Affiliated Hospital of Southwest Medical University, Luzhou, 646000 Sichuan, China

Correspondence should be addressed to Wenhui Cheng; 2019212369@mail.chzu.edu.cn

Received 2 August 2022; Revised 31 August 2022; Accepted 17 September 2022; Published 12 October 2022

Academic Editor: İbrahim Hakkı Cigerci

According to statistics released by the WHO, China has the highest prevalence of myopia in the world, with a frequency that is 1.5 times higher than the global average. Asians have the highest prevalence of myopia worldwide. The Ministry of Education and the State General Administration of Sports "2010 National Student Physical Fitness and Health Research Results" show that the incidence of poor vision among primary and secondary school students in China is 67.3%, and elementary school students' vision has decreased by 40.9%. Low vision among youth has become a major cause of affecting the quality of the population and improving national physical fitness; therefore, how to improve and enhance the vision level of youth has become a major issue for the government, sports, and educators face as a major issue. In order to address this issue, this research suggests a deep learning-based vision monitoring and risk prediction model for high myopia eyes and develops a deep artificial neural network that unsupervised learns essential characteristics of physiological time-series data.

1. Introduction

When the eye is in a relaxed state, when parallel light passes through the refractive system of the eye and forms a focal point in front of the retina, it is called myopia. There are two types of myopia: simple myopia and pathological myopia. The normal range for simple myopia is -6.00 D. This type of myopia is free of pathological changes. Pathological myopia usually exceeds -6.00 D. In addition to poor distance vision, it is associated with flying mosquitoes, night vision loss, floaters, and flashing lights [1]. In addition to the accompanying clinical manifestations, the eye axis of highly myopic patients will gradually elongate and the posterior polar region will overstretch, forming posterior scleral chylomalacia, causing a series of fundus changes: myopic arc (optic disc temporal choroidal atrophy arc). In the macular area, choroidal and pigment epithelial cells all show varying degrees of atrophy. In the macula, there is a vitreous membrane-like rupture with hemorrhagic patches, yellow-white streaks (lacquer-like fractures), black circular microraised spots, and choroidal neovascularization. Because of retinal and choroid atrophy, those with high myopia are more likely to suffer from severe retinal detachment. Myopic patients are prone to exotropia or strabismus due to the inability to utilize visual accommodation mechanisms when viewing at close range [2], resulting in a relatively reduced ability to gather. Myopia is the result of a combination of genetics, lifestyle habits, and multiple environmental factors, and one study showed that patients with myopic parents had 7.15 times the myopia rate of the general population.

Infants are generally farsighted. There is a gradual transition to orthophoria until development reaches school age. Adolescence is the period of high prevalence of myopia, especially from 10-16 years old. Living and learning habits, unscientific parental education management, and poor learning environment may cause the onset, development, and deterioration of myopia. In recent years, with the increasing pressure of study [3], work, and life, the incidence of myopia has increased significantly for both elementary school students, middle school students, high school students, and adults.

With the rapid development of electronic devices such as large screen cell phones, computers, and tablets, people's lives have become more convenient and colorful. Nowadays, adults, students, and children use electronic products for work, study, and entertainment. As for whether watching

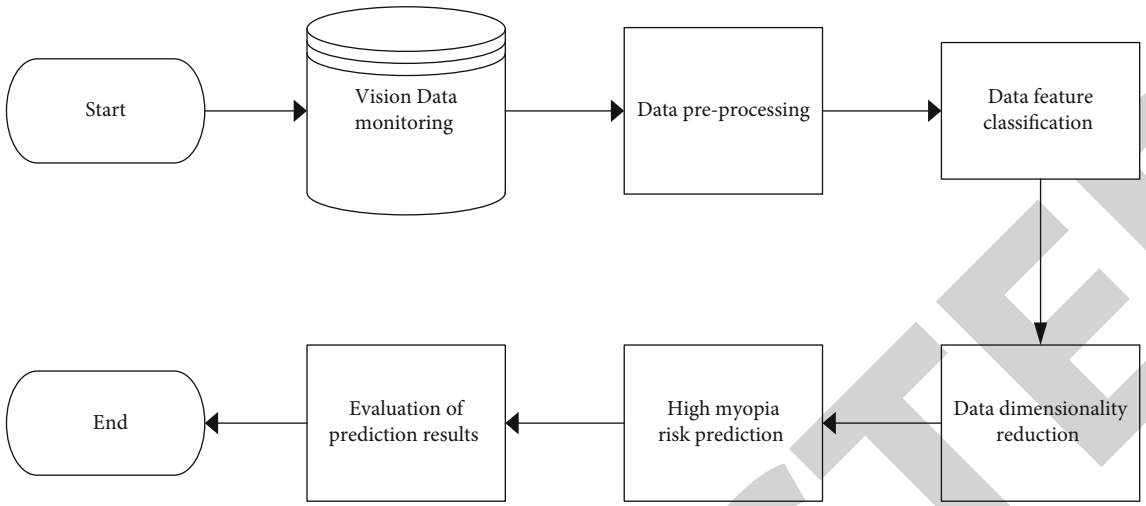

Figure 1: Flow chart of multilevel prediction model.

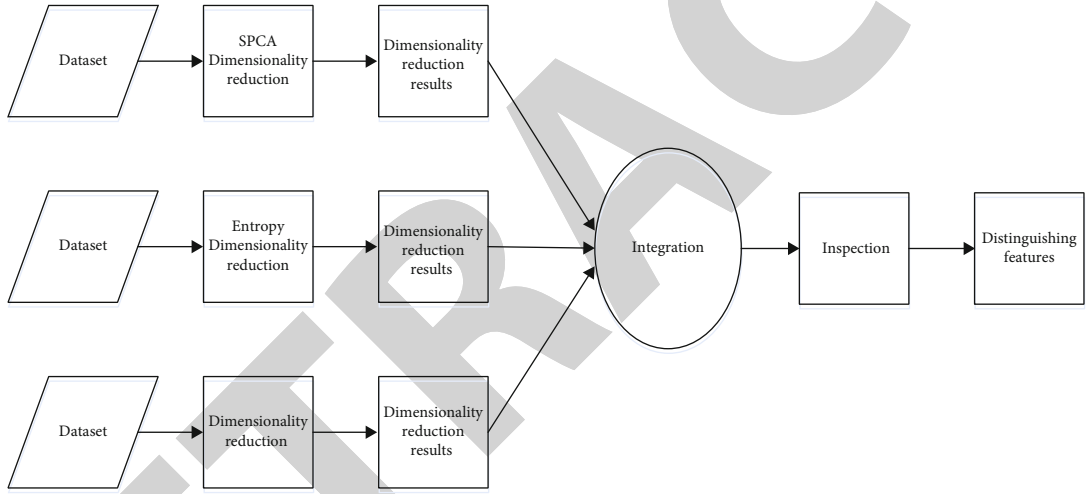

Figure 2: Flow chart of feature fusion with dimensionality reduction.

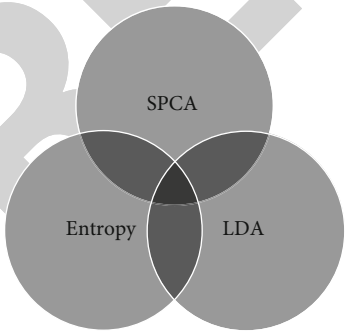

Figure 3: Venn diagram.

TV for a long time will affect vision, there is no clear conclusion yet. Many studies have reported that women are more likely to suffer from myopia than men, probably because they prefer to do some indoor sports at home and have fewer opportunities to look far away [4].

In the United States, more than $3.9 billion is spent annually on screening and treatment of refractive errors, including glasses, contact lenses, or refractive orthoptic surgery. Myopia is already a global health problem. Not only does it have adverse physical and psychological effects during school [5] but also, it can easily lead to injuries when wearing glasses for activities outside and certain related professions such as further education and employment, which can also pose hidden risks to the quality of life in the future and increase the financial burden on families [6–8]. The pathogenesis of myopia is still unclear, and there is no cure for it [9]. Therefore, this paper proposes a deep learning-based health management model for visual acuity monitoring and risk assessment of patients with high myopia, combining relevant research on myopia at home and abroad in recent years.

The paper's organization paragraph is as follows: the introduction to related work is presented in Section 2. Section 3 analyzes application method design. Section 4 discusses the applications of practical experiments. Finally, in Section 5, the research work is concluded.

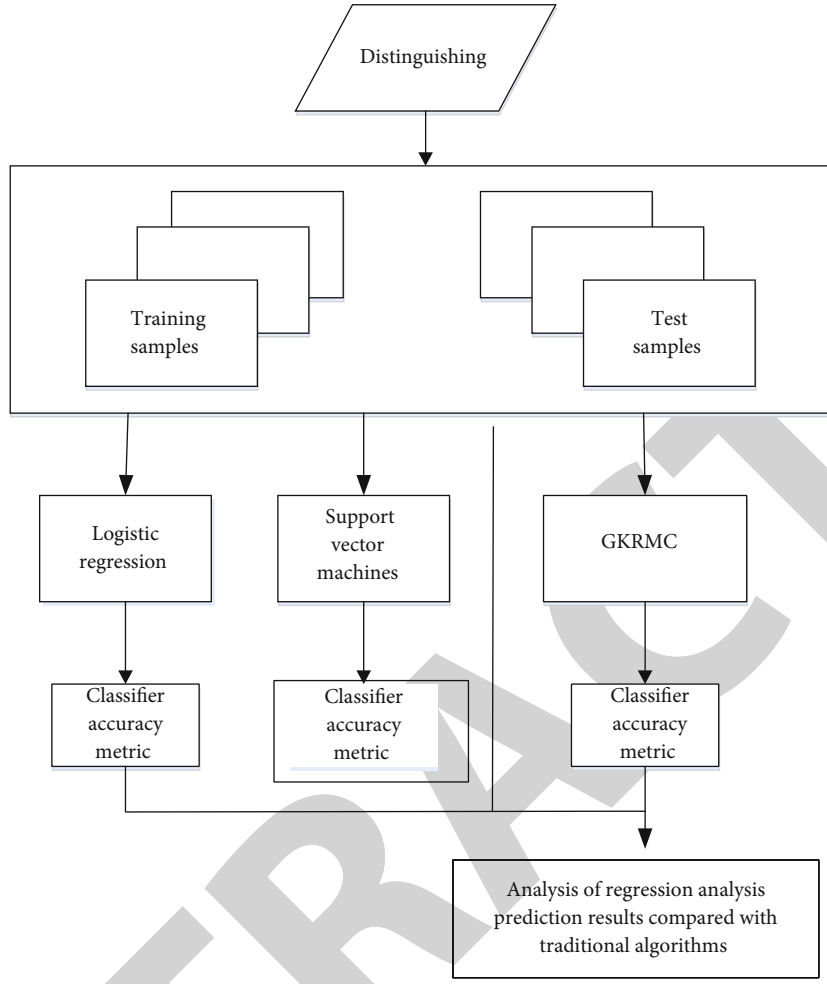

Figure 4: Flow chart of regression analysis prediction experiment.

Table 1: Information about the dataset.

Dataset	Class	Sample distribution	Attributes
CRC	2	369 : 929	85

2. Introduction to Related Theories

2.1. Deep Learning Theory. Deep learning is an emerging discipline based on machine learning, which is the latest theoretical achievement of ANN in recent years. There have been significant advances in temporal data prediction, speech recognition, image recognition, and computer vision research. Deep ANN was originally designed to build a model that emulates the neurons of the human brain to mimic the work of the human brain [10]. The method uses multiple higher-order function levels for data characteristics based on data characteristics, such as temporal data, images, speech ,and text, and thus obtains an efficient representation for recognizing the characteristics of the task.

An algorithm having more levels than its hidden layers—-shallow learning—is the "depth of deep learning." When the network algorithm is finally utilized for learning, the resulting feature representation is shallow since many shallow learning techniques entail manually generalizing the data's features before training the algorithm. However, in the unsupervised case, deep learning maps the sample data from a feature representation in one space to a new feature space; resulting in a feature with hierarchical features that are more useful for classification and regression prediction.

Another feature of deep learning is that if a model can be represented by a network structure with k layers, then its parameters increase exponentially, thus overfitting the network and thus losing generality; thus, the number of network layers is a very critical parameter in deep neural networks.

2.2. Medical Data Mining and Medical Examination Data. Because of the tremendous advancements in science and technology, the medical system has benefited greatly from information technology. The current medical system has a large amount of medical data and pathological data, which allows medical personnel to classify patients according to their conditions and risk factors and make corresponding predictions so that appropriate treatment plans can be developed [11].

The physical database is a medical database, the same as a general database, but with its own unique features. The physical examination database contains data on physical examinations performed on patients who have no symptoms

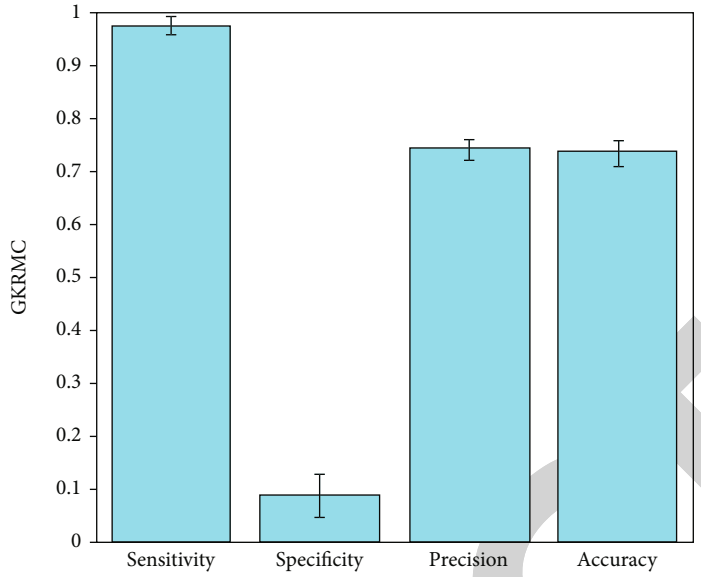

Figure 5: Regression prediction results of GKRMC algorithm.

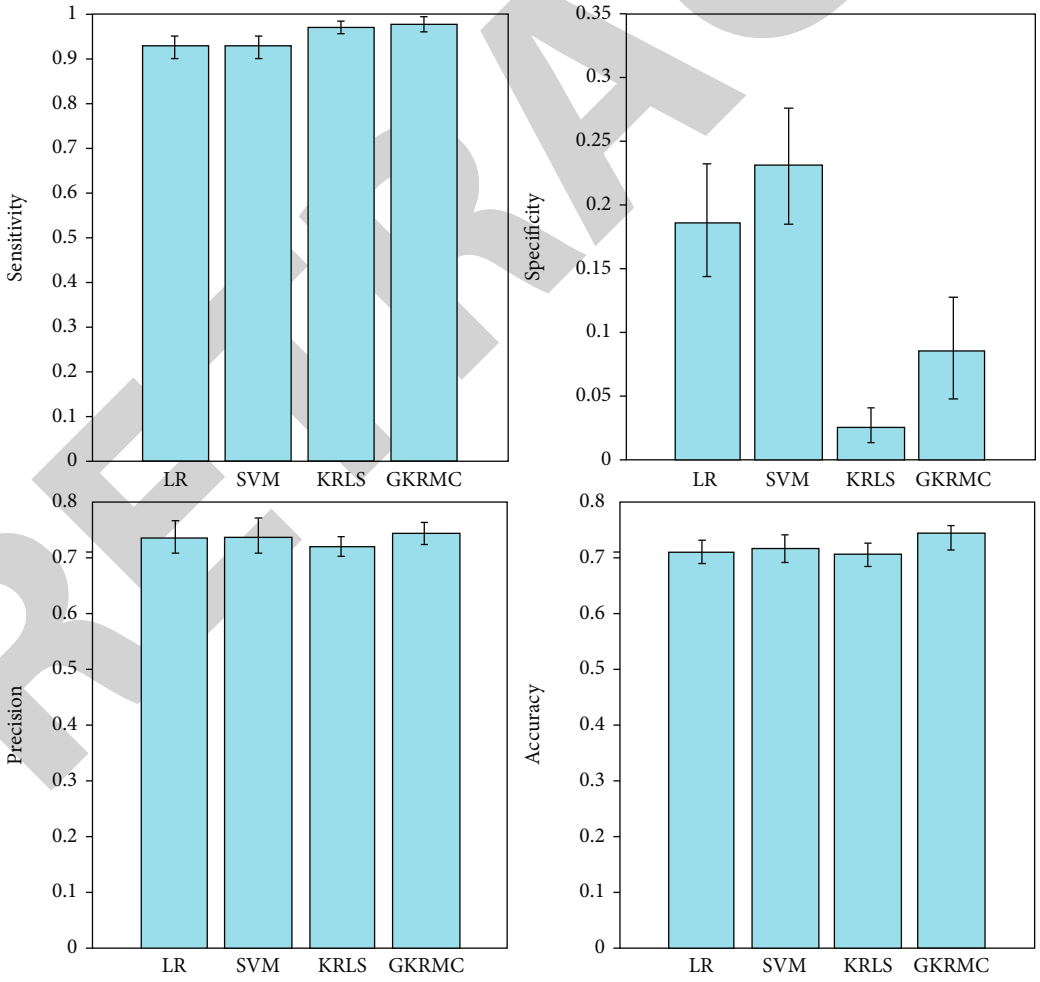

Figure 6: Comparison of predicted effects.

Table 2: p values of GKRMC and conventional methods.

Measures	GKRMC and LR	GKRMC and SVM	GKRMC and KRLS
Sensitivity	1.5085e-04	1.8243e-04	6.1475e-04
Specificity	1.2106e-04	3.4075e-04	5.7708e-04
Precision	2.3059e-04	3.1205e-04	3.3256e-04
Accuracy	1.1208e-04	1.6654 e-04	6.2045e-04

Table 3: Comparison of visual acuity of myopic children aged 7-8 years in the experimental and control groups before training (M ± SD).

	Experimental group	Control group
Visual acuity in the right eye	4.63 ± 0.16	4.65 ± 0.11
Visual acuity test left eye vision	4.67 ± 0.08	4.66 ± 0.10

or are long-term patients. Certain chronic diseases can be tracked if a physical examiner performs a yearly physical examination and collects a series of physical examination data [12]. The health screening database is important for the prevention and diagnosis of chronic diseases. This thesis explores a risk prediction model for patients with high myopia based on data mining techniques, using health checkup information as the basis.

3. Application Method Design

3.1. Construction of Health Management Model. The health management model of this research project is partly modeled by using three key steps: classification of myopia physical examination data, data downscaling and high myopia risk prediction analysis, so as to monitor high myopia risk as well as prediction feedback. The flow chart of the health management model is shown in Figure 1.

Figure 1 illustrates the detailed flow of the high myopia prediction model proposed in this thesis [13]. The whole prediction model is divided into four parts.

3.2. Data Preprocessing. We analyzed information on high myopia, which included incompleteness (missing attribute values), noise (including errors or deviations from expected values), and inconsistency [14]. The quality of the data can be significantly increased by the use of data preparation techniques, which also aid in the precision and efficiency of subsequent data mining.

First, we found that certain properties of much of the original highly myopic information were not recorded. We used a common way of handling missing data values in data mining.

Moreover, our data often have some random errors or are very different due to different data. Therefore, when performing data analysis, it is often necessary to normalize the data to remove the scale relationship between the features to ensure the comparability of the data. Commonly used data normalization methods include automatic, random, and standard scan. In this paper, the standard scan method is used. Standard scan, also known as z-scan [15], is to divide the difference between the current data and the attribute in which the current data is located by the standard deviation. It is calculated by the formula $z = (-u)/\sigma$ where x is a specific score, u is the mean, and σ is the standard deviation.

3.3. Data Dimensionality Reduction. In light of this, we are interested in the crucial role that data dimensionality reduction approaches play when working with large-scale, complexly structured datasets. Before regression forecasting, we also need to further streamline the data by data dimensionality reduction techniques to reduce the impact on regression forecasting, reduce the impact on regression forecasting, and make it more generalized [16].

For a large amount of data, the partial features obtained by one dimensionality reduction method can reflect most of the information of the original variable more accurately, while the local features obtained by one dimensionality reduction method can only represent a part of the original high myopia data, and the regional features obtained by different dimensionality reduction methods have different focuses, which leads to the height described by the regional features obtained by a single dimensionality reduction method. Myopia information is more one-sided, thus limiting the accuracy of regression prediction. In order to obtain traits with significant effects, we will use three methods in dimensionality reduction, namely, principal component analysis, information entropy, and linear discriminant analysis to deal with four aspects of genetic information, namely, demographic characteristics [17], lifestyle, and food; then, we will use Venn diagram to fuse the dimensionality reduction results of the above datasets; finally, we will use U test to select traits with significant differences, and the experimental process is shown in Figure 2.

In these steps, the process of fusion is described in detail. Assuming that a dataset contains N features, the data obtained by sparse principal component analysis is dimensioned down to the set SPCA, the dimensionality reduction obtained by information entropy is the set Entropy, and the dimensionality reduction obtained by linear discriminant is the set LDA. In the Venn diagram, we select the intersection of three dimensionality reduction data such as SPCA, Entropy, and LDA and dimension them down as shown in Figure 3 in the the overlapping region that is shown.

3.4. High Myopia Risk Prediction. After the data were downscaled, we discovered a number of factors that significantly impacted high myopia. We must gather pertinent information from numerous trials and observations in order to better understand the association between these traits and high myopia. We next utilize regression analysis to discover the relationship between the data. One of the commonly used methods is regression analysis. The prediction of regression analysis is well understood, it is equal to $y = f(x)$, which shows the relationship between the independent variable x due to the variable y. The most common problem is to look, smell, ask, and cut as a way to determine if a person is sick or what kind of disease they have. To look and smell is to

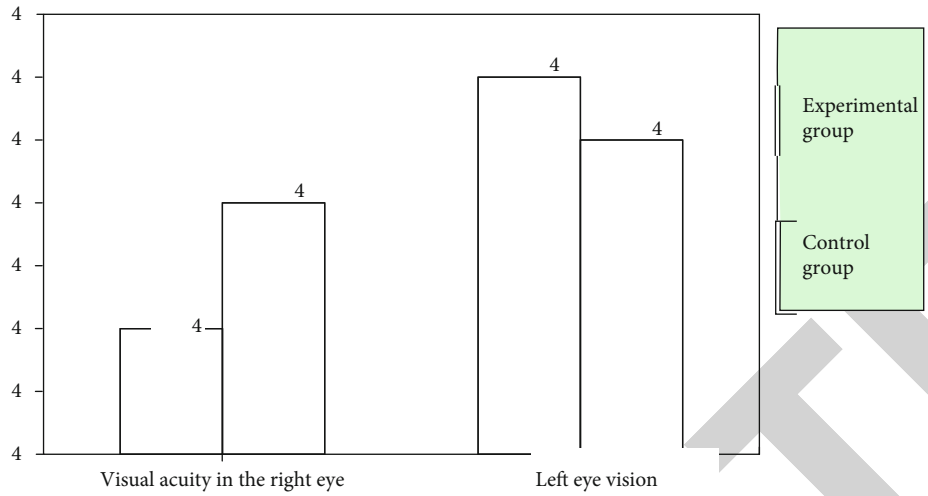

Figure 7: Comparison of the results of the left and right eye visual acuity tests between the two groups before prediction.

Table 4: Comparison of visual acuity of myopic children aged 7-8 years in the experimental and control groups after training (M ± SD).

	Experimental group	Control group
Visual acuity of the right eye	$4.89 \pm 0.08^{**}$	4.61 ± 0.11
Visual acuity test left eye visual acuity	$4.85 \pm 0.07^{**}$	4.62 ± 0.10

Note: **indicates that the visual acuity test results of the experimental group after training were very significantly different from the visual acuity condition of the control group, $p < 0.01$.

obtain an independent variable x, which is an eigenvalue, to determine if a person is sick [18].

In the previous data downscaling, we have classified the characteristics of people with high myopia, which is equivalent to the large amount of data we have used to identify the environment and genes associated with the risk of high myopia [19, 20]. Therefore, in this part, we will use regression analysis to predict the risk of high myopia patients using the above factors. The experimental procedure is shown in Figure 4.

4. Application of Practical Experiments

4.1. Experimental Data Preparation. The data used in this paper were mined from hospital ophthalmology patients using data mining techniques. The clinical data of 369 patients with high myopia are reported in this paper. The control group was made up of 929 individuals with low to moderate myopia, whose age, gender, and lifestyle choices were very similar to those of the case group. All of the controls came from the same hospital's case group of patients who underwent ophthalmology. The initial collection of raw high myopia data was preprocessed with data to obtain 1298 data, a typical dichotomy, including 369 patients with high myopia and 929 in the nonhigh myopia group with 85 characteristics. Table 1 gives the information about the high myopia dataset.

4.2. Results of Data Downscaling. In the data downscaling phase, we found 10 items that may have a significant effect on high myopia, including 4 behaviors, 5 genes, and 1 lifestyle habit. In fact, a large number of epidemiological surveys provided the basis for our data on risk/protective factors for high myopia. In conclusion, the biomarkers we selected, after extensive studies, showed that they were significantly associated with the risk of high myopia, so these 10 biomarkers could be used as a classification for the prediction phase of the high myopia risk prediction analysis.

4.3. Model Prediction Performance Analysis Experiments. This part focuses on the application of the GKRMC algorithm in the regression analysis. The results showed that the data of highly myopic patients were preprocessed to obtain 1298 samples, including 369 cases of highly myopic patients and 929 cases of those who did not develop high myopia. We used a random sampling method to randomly select 973 samples, and the remaining 325 were trial data. Simultaneously, to avoid the randomness created by a single trial and to ensure the algorithm's stability and the rigour of scientific research; this study used the maintenance method for ten trials before averaging the overall value by ten trials. In each trial, we randomly selected a sample from three-fourths of the sampled data, and one-fourth of the sample was used as the test sample for categorical prediction, and feedback was provided on the prediction results of the indicators. Finally, the prediction results of the regression analysis were evaluated using risk indicators.

The results are shown in Figure 5, which shows the mean and variance of the four indicators of sensitivity, specificity, precision, and accuracy, respectively, after 10 predictions of regression analysis using the GKRMC algorithm.

Figure 5 demonstrates that the GKRMC algorithm continues to produce positive outcomes in terms of sensitivity, precision, and accuracy. We decide to contrast it with the conventional regression techniques of logistic regression and support vector machine in order to ascertain whether the

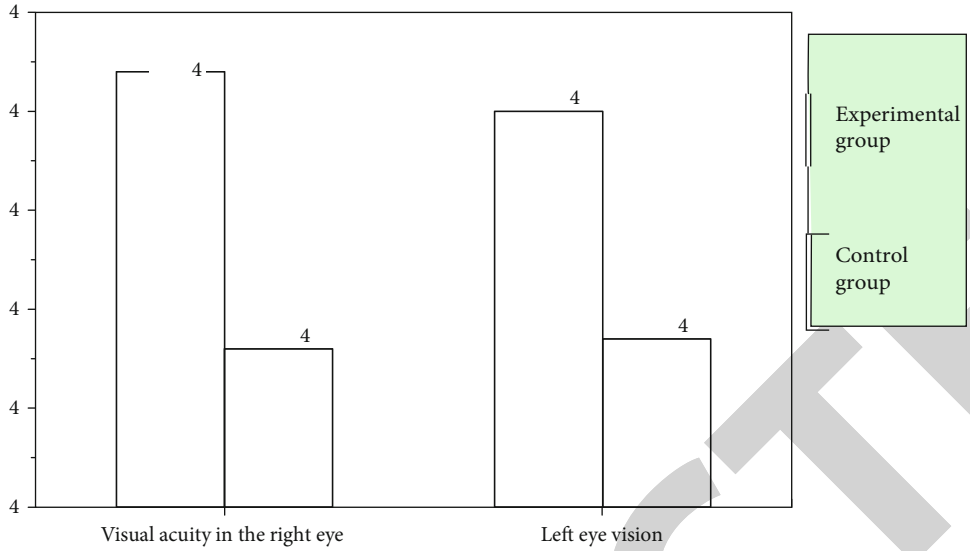

Figure 8: Comparison of visual acuity prediction results between the two groups.

regression prediction outcomes of the GKRMC algorithm are accurate and reliable. The results are shown in Figure 6.

As shown in Figure 6, the GKRMC algorithm was compared with the other three regression methods, and the results showed that the stability of the GKRMC algorithm was better than the other three methods after 10 trials. In conclusion, from the results, the GKRMC algorithm proposed in this paper can perform regression analysis and forecasting better.

The p values were used to assess if the test results of the GKRMC and the conventional test were statistically significant after the 10 test data measured by the GKRMC were tested against 10 test data from four angles using the statistical test method. The p values for the statistical analysis are shown in Table 2.

As can be seen from Table 2, the p values of GKRMC and the conventional method show that the experimental results calculated by the GKRMC method are very different from the conventional ones, which illustrates the superiority of the GKRMC method in terms of prediction accuracy and precision.

4.4. High Myopia Monitoring and Risk Prediction Experiment

(1) Experimental preparation

Before the experiment, the visual acuity of the two groups of students was tested, not only to verify the rationality of the experimental group but also to provide a basis for future comparative studies. The experimental group used the risk prediction model for prevention, while the control group did not use the risk prediction model for prevention.

The children in the experimental group and the control group's visual acuity before the experiment was conducted were tested, and the results are displayed in Table 3.

The results showed that the right eye visual acuity and left eye visual acuity of the experimental group were 4.63 and 4.67, respectively; and those of the control group were 4.65 and 4.66, respectively. Compared with the control group, the right eye visual acuity of the experimental group was slightly inferior to that of the control group, but the left eye visual acuity was slightly better, and the statistical analysis showed that there was no significant difference between the experimental and control groups in terms of left eye visual acuity ($p > 0.05$), which indicated that the grouping status of the study met the experimental requirements.

In order to understand and predict the visual acuity of the first two groups more clearly, we sorted out the visual acuity test results of the experimental group and the control group before the experiment as shown in Figure 7.

(2) Predicted visual acuity of myopic children in the two groups

As can be seen from Table 4 and Figure 8, the mean visual acuity of the right and left eyes in the experimental group was 4.89 and 4.85, respectively, after the test, and their mean visual acuity was 4.61 and 4.62 in the right and left eyes, respectively, in the control group. The results showed that there was a significant difference between the visual acuity of the left and right eyes in both the experimental and control groups ($p < 0.01$), indicating that the risk of high myopia prediction application was very effective in improving the visual acuity of myopic children.

5. Conclusion

This paper proposes a deep learning-based health management model for high myopia eye vision monitoring and risk prediction, for which the relevant background and related theories are first introduced, followed by an explanation of the model construction method, and finally the model's performance analysis experiments and specific application experiments. After the experiments, it can be known that the formation of high myopia is a combination of multiple

Hindawi
Journal of Oncology
Volume 2022, Article ID 3798741, 15 pages
https://doi.org/10.1155/2022/3798741

Research Article

Identification of a 5-Hydroxymethylation Signature in Circulating Cell-Free DNA for the Noninvasive Detection of Colorectal Cancer

Hongwei Liu,[1] Tao Tang,[2] Huixian Zhang,[1] Weiren Ting,[1] Peng Zhou,[1] Ying Luo,[1] Huaxing Qi,[1] Yanmei Liu,[1] Yongxin Liu,[1] Meifang Zhou,[1] Weiguo Yin,[1] and Jinduan Lin[1]

[1]*Department of Laboratory Medicine, The Sixth Affiliated Hospital of Guangzhou Medical University, Qingyuan People's Hospital, Guangdong Qingyuan, China*
[2]*Department of Molecular Diagnostics, Sun Yat-sen University Cancer Center, Guangdong Guangzhou, China*

Correspondence should be addressed to Jinduan Lin; 2020620649@gzhmu.edu.cn

Received 6 July 2022; Revised 1 August 2022; Accepted 13 August 2022; Published 12 October 2022

Academic Editor: İbrahim Hakkı Cigerci

Background. As a crucial epigenetic modification, DNA 5-hydroxymethylcytosine (5-hmC) plays a key role during colorectal cancer (CRC) carcinogenesis. Nevertheless, the levels of 5-hmC-related genes in the circulating DNA of CRC remain largely unknown. *Methods and Results*. The GSE81314 dataset from the Gene Expression Omnibus (GEO), which was generated by chemical marking-based low-input shotgun sequencing to detect 5-hmC in circulating cell-free DNA (cfDNA) was used in the present study. The GSE81314 dataset includes data for 8 plasma samples from healthy individuals and 4 plasma samples from CRC patients. The difference in the 5-hmC levels in cfDNA between the CRC group and healthy individuals was analyzed by the differentially expressed genes (DEG) package. Weighted gene coexpression network analysis (WGCNA) was conducted to analyze gene coexpression modules associated with sample characteristics. DEG analysis identified 19 upregulated and 9 downregulated 5-hmC-related genes. WGCNA showed that the pink, purple, and brown modules, which contain 531 genes in total, were significantly correlated with CRC (0.66, 0.61, and -0.59, respectively). We used gene set enrichment analysis (GSEA) software to compare 5-hmC-related genes and pathways between CRC patients and healthy controls. We further performed a protein–protein interaction (PPI) analysis and identified 4 nodes (LCN2, LRG1, S100P, and TACSTD2) that played key roles in the network, and we analyzed the expression of these nodes S100P in the GEPIA database. Consistent with the 5-hmC levels in CRC patient plasma, our external validation results from the GEPIA and UALCAN databases showed that LCN2, LRG1, S100P, and TACSTD2 were highly expressed in CRC tissue compared with controls. The DNA promoter methylation levels of LCN2, LRG1, and S100P were lower in CRC tissue than in normal control tissue. *Conclusion*. The present findings suggest that abnormality in cell-free DNA hydroxylation in plasma may be associated with CRC. In addition, the 5-hmC levels of LCN2, LRG1, S100P, and TACSTD2 in circulating cfDNA may be used as potential noninvasive markers for CRC.

1. Introduction

Colorectal cancer (CRC), which involves neoplastic transformation in normal intestinal epithelial cells due to the accumulation of anomalous genetic and epigenetic alterations, is one of the most frequent malignant gastrointestinal neoplasms worldwide. The diagnosis of CRC is showing an upward trend in China [1–5]. Colonoscopy, as the gold standard method for detecting colorectal cancer, is widely used for screening and has an obvious effect on the early diagnosis, prevention, and treatment of CRC. However, endoscopic screening requires a specific time for preparation, bowel preparation, and laxatives to ensure visibility of the intestinal tract, and it is invasive and uncomfortable, thereby dissuading participation. Therefore, the compliance rate of colonoscopy is still low. Recently, the use of easily accessible sample types, such as stool and blood, for CRC noninvasive screening has gradually

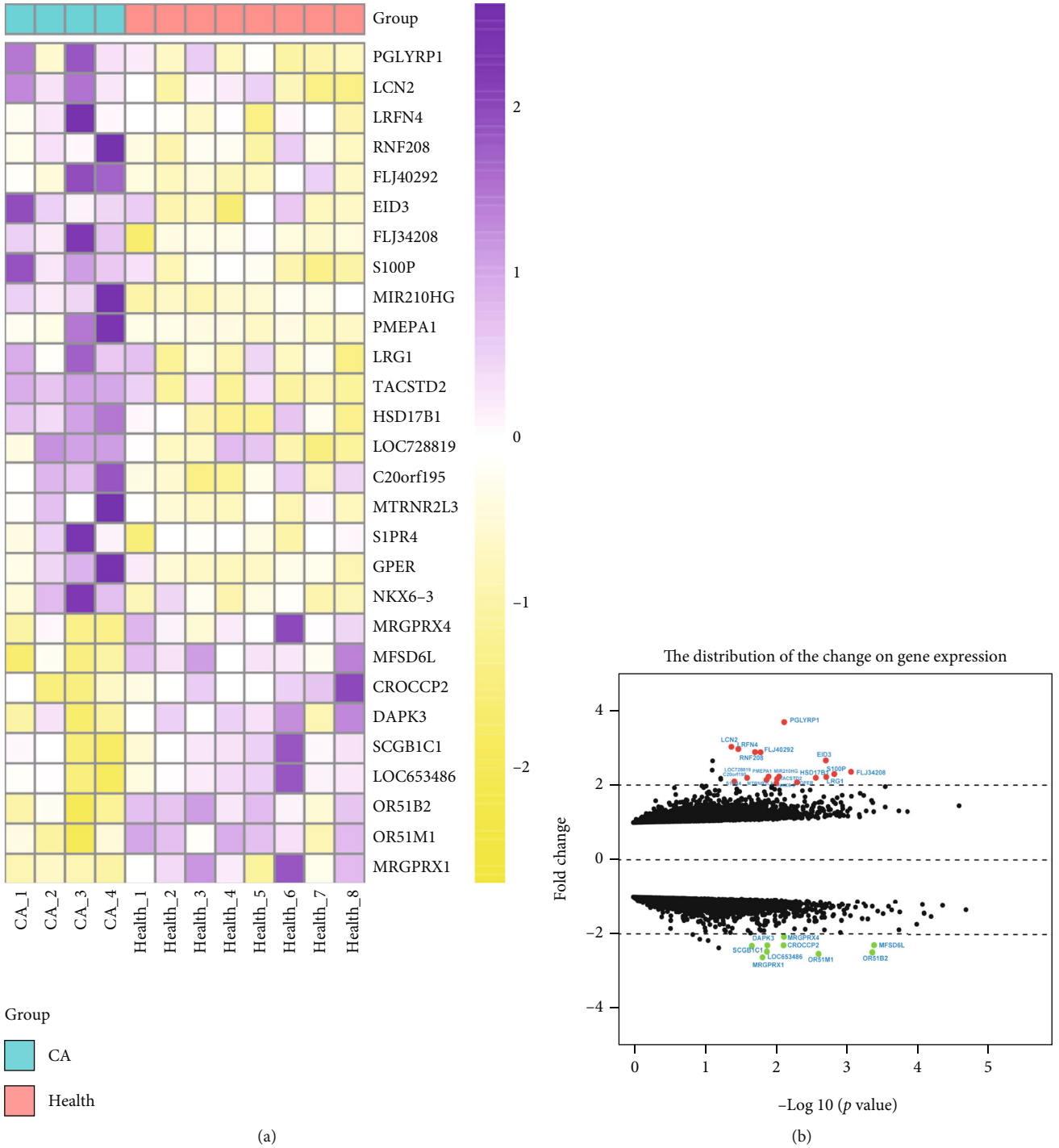

Figure 1: Heatmap clustering and volcano plot of 5-hmC-related DEG in the plasma of CRC patients and healthy individuals. (a) Heatmap clustering of the DEG. The red bars represent the CRC group, and the green bars represent the healthy group. (b) Volcano plot of the DEG. The red nodes represent upregulated DEG, and the green nodes represent downregulated DEG.

been applied in the clinic due to their advantages compared to colonoscopy. Blood-based liquid biopsy has been utilized in the clinic for CRC noninvasive screening because it is noninvasive and rapid, and it is more acceptable than stool-based assays [6]. In recent studies, circulating cell-free DNA (cfDNA) has become the predominant tool for liquid biopsies to understand the mutational landscape of cancer. Cancer cells shed naked DNA molecules into the circulation, and these molecules are called circulating tumor DNA (ctDNA). ctDNA has been used for clinical diagnosis and prognosis prediction. Few but promising data are available about the use of liquid biopsy for the early diagnosis of CRC, and the main limitation is sensitivity due to low concentrations of ctDNA in this setting. In terms of the prediction of the response to chemoradiation, only inconclusive data are available about the utility

of a pretreatment liquid biopsy, whereas some studies report a positive correlation with dynamic (pre/posttreatment) monitoring. The presence of minimal residual disease by ctDNA is consistently associated with a poor prognosis across studies [7]. Laboratory tests of DNA-related epigenetic changes in cfDNA can be performed from plasma or serum fractions, which are primarily derived from tumor cells. Epigenetic changes are important causes of CRC, and abnormal DNA methylation and 5-hmC modification impair cancer development and progression [8–11]. 5-hmC is generated from 5-mC by the Tet protein family. 5-hmC modifications are ubiquitous in the DNA of embryonic stem cells and many other issues, and they are implicated in many human diseases, including CRCs [10–12]. Li et al. found robust cancer-associated 5-hmC signatures in cfDNA that were characteristic of specific cancer types. 5-hmC-based biomarkers of circulating cfDNA are highly predictive of colorectal and gastric cancer prognosis and are superior to conventional biomarkers and comparable to 5-hmC biomarkers from tissue biopsies [13]. Nonetheless, no previous studies have investigated the potential for CRC detection based on the presence of colorectal-related 5-hmC genes in circulating cfDNA, a concept that may help to develop noninvasive screening tools in CRC detection.

In the present study, microarray data (GSE81314) were used to compare the 5-hmC levels of hub genes between healthy controls and CRC patients. First, we downloaded the data (GSE81314) from the GEO database and analyzed the differences in the 5-hmC level of cfDNA in plasma between the healthy and CRC groups by the DEG package. We then performed weighted gene coexpression network analysis (WGCNA) to identify hub genes at the 5-hmC level that are closely related to CRC. In addition, protein–protein interaction (PPI) studies were conducted to determine the interaction network of genes that showed critical expression. Finally, we verified the expression level, stage characteristics, and survival time of the 5-hmC-related genes between the CRC and healthy control groups in the Gene Expression Profiling Interactive Analysis (GEPIA) database. The present study aimed to identify 5-hmC-related genes and pathways that are highly associated with CRC in plasma and to elucidate the potential mechanisms.

2. Materials and Methods

2.1. Data. The GSE81314 dataset was downloaded from the Gene Expression Omnibus (GEO) database (https://www.ncbi.nlm.nih.gov/geo/query/acc.cgi?acc=GSE81314). This dataset contains sequenced cfDNA with 5-hmC data from 49 patients with seven different cancer types, including 8 plasma samples from healthy individuals and 4 plasma samples from CRC patients, and it also contains distinct features that can be used for monitoring disease status and progression. The dataset was based on the GPL18573 Illumina NextSeq 500 (Homo sapiens) platform.

2.2. DEG Analysis. We analyzed the DEG to evaluate the different 5-hmC levels of cfDNA in plasma between healthy individuals and CRC patients by the limma package [14]. The parameter settings were set according to a previous study [15].

Table 1: Different 5-hmC levels of hub genes with logFC>1.

	logFC	*t*	*P* value
PGLYRP1	2.55	2.77	0.012
LCN2	1.88	3.20	0.008
LRFN4	1.60	2.28	0.041
RNF208	1.57	2.40	0.033
FLJ40292	1.53	2.70	0.019
EID3	1.53	2.79	0.016
FLJ34208	1.41	3.94	0.002
S100P	1.24	4.40	0.001
MIR210HG	1.20	4.09	0.001
PMEPA1	1.16	3.11	0.009
LRG1	1.16	2.93	0.013
TACSTD2	1.15	3.94	0.002
HSD17B1	1.13	3.76	0.003
LOC728819	1.13	2.56	0.025
C20orf195	1.11	3.08	0.009
MTRNR2L3	1.10	2.89	0.013
S1PR4	1.07	2.33	0.038
GPER	1.06	3.42	0.005
NKX6-3	1.03	3.07	0.009
MRGPRX4	-1.06	-3.20	0.008
MFSD6L	-1.20	-4.83	0.0004
CROCCP2	-1.20	-3.19	0.008
DAPK3	-1.20	-2.91	0.0132
SCGB1C1	-1.21	-2.64	0.022
LOC653486	-1.30	-2.90	0.013
OR51B2	-1.31	-4.79	0.0004
OR51M1	-1.34	-3.81	0.002
MRGPRX1	-1.39	-2.83	0.015

2.3. WGCNA. We used the WGCNA package [16] to determine the coexpression modules and the interconnectedness between each module, and the coexpressed genes in the control and CRC patients according to a previously published method [15].

2.4. GSEA. We downloaded the hallmark gene set and gene symbols from the GSEA website to obtain 5-hmC-associated genes in CRC.

2.5. GO and KEGG Pathway Enrichment Analyses. We used Gene Ontology (GO) [17] to annotate the GO function of 5-hmC-related genes in cfDNA, and we performed Kyoto Encyclopedia of Genes and Genomes (KEGG) [18] pathway analysis to determine the 5-hmC-related signaling pathways. GO and KEGG pathway analyses were performed to identify the related functions of 5-hmC-related genes, and they were based on the DEG and WGCNA results, which provided 5-hmC-related genes significantly associated with CRC. The threshold for statistical significance was set at $p < 0.05$. The detailed operation procedure was performed as previously reported [15].

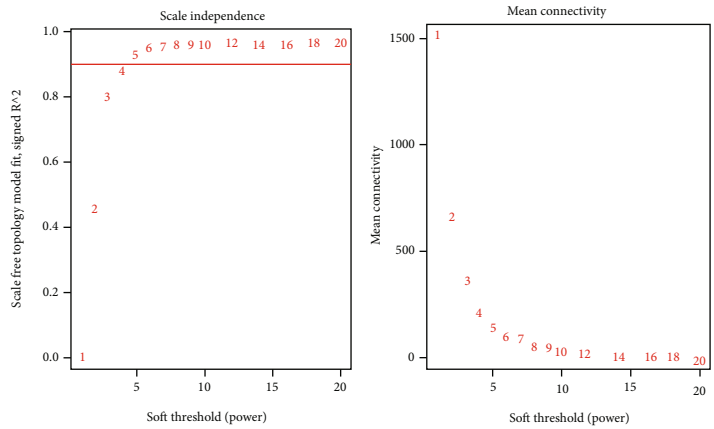

(a)

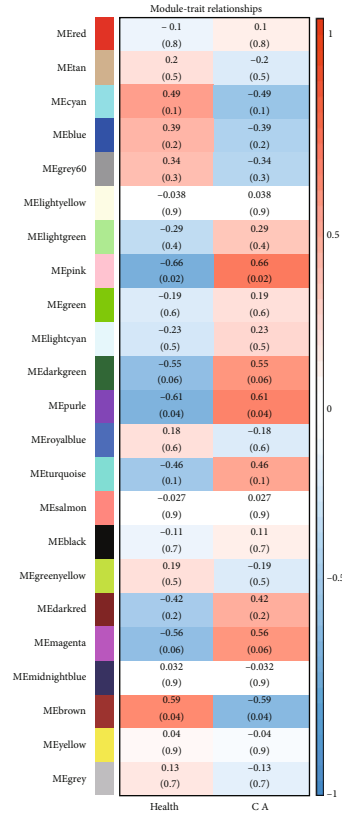

(b)

Figure 2: Continued.

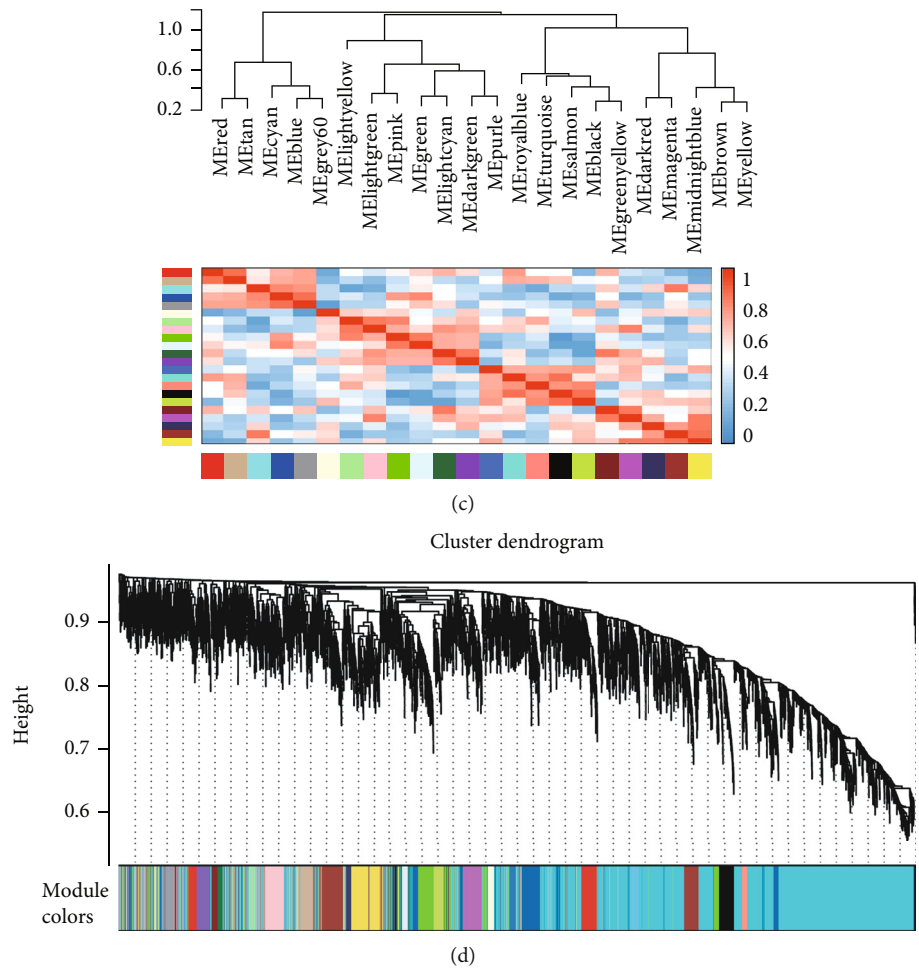

Figure 2: Identification of key modules associated with CRC. (a) Network topology of different soft-thresholding powers of the CRC coexpression network. (b–c) Heatmap of the correlation between module eigengenes and the two groups of plasma. (d) 5-hmC gene clustering module of the CRC coexpression network.

2.6. PPI Network Analysis. GeneMANIA software [19] was used to assess gene interactions and to predict gene function. The 5-hmC-related genes in the cfDNA of CRC patients were identified using the GeneMANIA plugin in Cytoscape 3.8.0. Network analysis was performed according to methods described in a previous study [15]. Genes with degree values of three or greater were considered hub genes and used for further analysis.

2.7. Analysis of the RNA Expression Level and DNA Promoter Methylation of 5-hmC-Related Hub Genes in CRC Tissue in Public Databases. We analyzed the mRNA levels analyzing the DNA promoter methylation levels of the 5-hmC-related target genes linked to CRC via the GEPIA database [20] (including 275 CRC tissues and 349 normal samples from the TCGA and the GTEx projects), and the UALCAN database [21] (including 41 normal tissues and 286 primary CRC tissues for mRNA expression analysis, 37 normal tissues and 313 primary CRC tissues for prompter methylation level analysis, and 279 CRC cases for survival analysis).

2.8. Analysis of the Correlations of 5-hmC-Related Hub Genes with Clinical Characteristics in Public CRC Datasets. We analyzed the relationship between CRC stage, overall survival, and the mRNA expression levels of the 5-hmC-related target genes linked to CRC in the GEPIA database and the UALCAN database.

3. Results

3.1. DEG Analysis. The 5-hmC levels of the hub genes in plasma between healthy controls and CRC patients were analyzed by the DEG package. Figure 1 shows that 28 genes, including 19 upregulated genes and 9 downregulated genes, were differentially expressed. The average logFC values of the upregulated and downregulated genes were 1.35 and -1.25, respectively. The genes with logFC >1 or logFC <-1 are shown in Table 1.

3.2. WGCNA. With a soft threshold of 4, all genes were grouped into 23 modules by cluster analysis, and the correlations of the 5-hmC level genes with phenotype were analyzed. As shown in Figure 2, the pink, purple, and brown

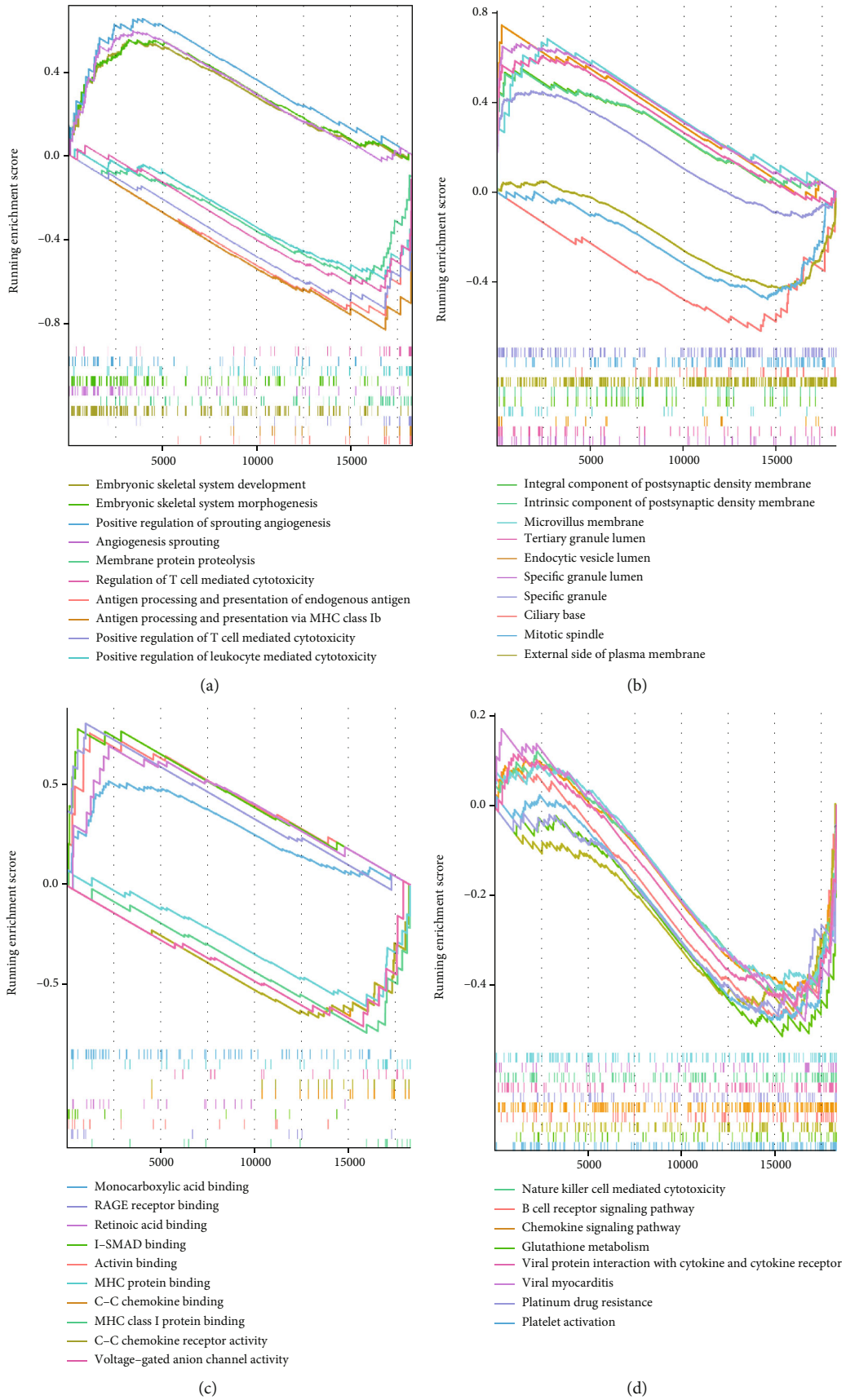

Figure 3: Continued.

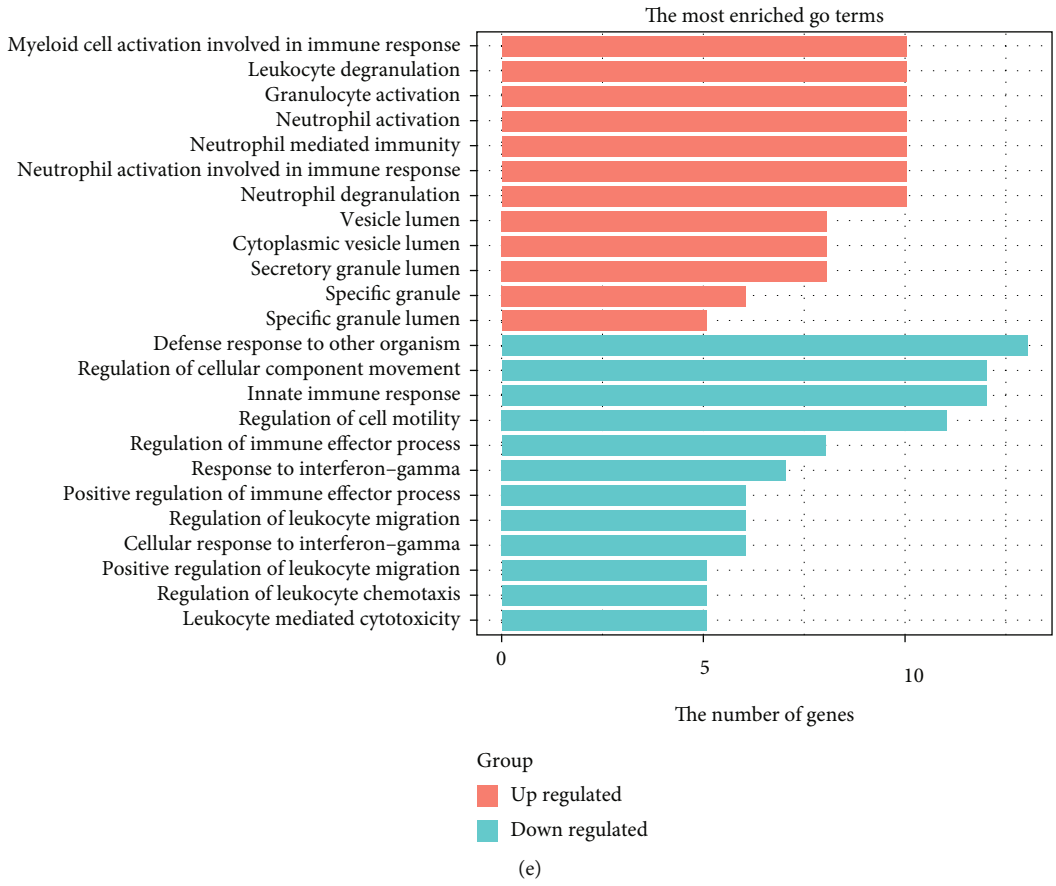

Figure 3: Potential functions of the 5-hmC-related genes in plasma according to GSEA. Plasma 5-hmC-related genes of CRC were significantly enriched in the listed BPs (a), CCs (b), MFs (c), and KEGG pathways (d).

modules were significantly correlated with CRC with values of 0.66, 0.61, and -0.59, respectively. These three modules contained 531 genes in total (pink, 147; purple, 84; and brown, 300). The detailed results are shown in Supplement table 1.

3.3. GSEA, GO, and KEGG Analyses. We performed GSEA software to extract the 5-hmC-associated genes and pathways between CRC patient and healthy control plasma. GSEA and GO results of the microarray data (GSE81314) showed that the upregulated 5-hmC-related genes were highly enriched in angiogenesis sprouting, specific granule lumen, antigen processing, embryonic skeletal system development, and positive regulation of T-cell-mediated cytotoxicity. The 5-hmC-associated genes upregulated in CRC patients compared to healthy controls were enriched in pathways related to immune functions, platelet activation, and platinum drug resistance (Figures 3(a)–3(d)). The other related pathways are shown in Table 2.

3.4. GO and KEGG Pathway Enrichment Analyses. GO, Reactome, and KEGG pathway analyses were utilized to determine the upregulated 5-hmC genes, downregulated 5-hmC genes, and 5-hmC genes significantly correlated with CRC (pink, purple, and brown modules). The GO results indicated that the upregulated 5-hmC-related genes were highly enriched in leukocyte activation involved in the immune response and secretory activity process. The downregulated DEG was mainly associated with the cellular chemotaxis process (Table 2).

In CRC, the genes in the 5-hmC-related modules were enriched in platelet activation, the B-cell receptor signaling pathway, the chemokine signaling pathway, cytokine–cytokine receptor interaction, and the cell metabolism-related pathway. The KEGG and Reactome pathway results indicated the involvement of the upregulated molecules in the B-cell signaling pathway and in diseases of the immune system (Figure 3(e) and Table 3).

3.5. PPI Network Analysis. PPI network analysis was performed to investigate the 28 genes that were both DEG and in the highly correlated modules. Based on previously reported criteria [15], we obtained a total of four genes, all of which were upregulated. As shown in Figure 4(a), the four molecules with the highest degree value in the network were LCN2 (logFC = 1.88), S100P (logFC = 1.24), TACSTD2 (logFC = 1.16), and TACSTD2 (logFC = 1.15), and these genes significantly impacted the network.

3.6. Exploration of the Expression and DNA Promoter Methylation Levels of Critical Genes. The four genes that had a significant influence on the PPI network were used

Table 2: GO analysis of the DEG and genes in the highly correlated modules.

GO ID	Description	*P* value	No. genes
Upregulated genes			
GO:0035580	Specific granule lumen	2.83E-06	5
GO:0043312	Neutrophil degranulation	8.04E-06	10
GO:0002283	Neutrophil activation involved in immune response	8.44E-06	10
GO:0002446	Neutrophil-mediated immunity	1.00E-05	10
GO:0042119	Neutrophil activation	1.00E-05	10
GO:0036230	Granulocyte activation	1.12E-05	10
GO:0043299	Leukocyte degranulation	1.81E-05	10
GO:0042581	Specific granule	1.97E-05	6
GO:0034774	Secretory granule lumen	2.00E-05	8
GO:0060205	Cytoplasmic vesicle lumen	2.16E-05	8
GO:0002275	Myeloid cell activation involved in immune response	2.18E-05	10
GO:0031983	Vesicle lumen	2.25E-05	8
GO:0002444	Myeloid leukocyte-mediated immunity	2.41E-05	10
GO:0002274	Myeloid leukocyte activation	9.22E-05	10
GO:0030141	Secretory granule	1.58E-04	11
GO:0002366	Leukocyte activation involved in immune response	1.76E-04	10
GO:0002263	Cell activation involved in immune response	1.85E-04	10
GO:0031960	Response to corticosteroid	3.83E-04	5
GO:0045055	Regulated exocytosis	4.58E-04	10
GO:0099503	Secretory vesicle	6.86E-04	11
GO:0002443	Leukocyte-mediated immunity	1.13E-03	10
Downregulated genes			
GO:0034341	Response to interferon-gamma	2.54E-06	7
GO:0071346	Cellular response to interferon-gamma	1.92E-05	6
GO:0001909	Leukocyte-mediated cytotoxicity	2.04E-05	5
GO:0045087	Innate immune response	2.57E-05	12
GO:0098542	Defense response to other organisms	3.88E-05	13
GO:0002688	Regulation of leukocyte chemotaxis	4.38E-05	5
GO:0051270	Regulation of cellular component movement	4.70E-05	12
GO:0002685	Regulation of leukocyte migration	4.86E-05	6
GO:0002687	Positive regulation of leukocyte migration	7.21E-05	5
GO:0002699	Positive regulation of immune effector process	7.40E-05	6
GO:0002697	Regulation of immune effector process	9.47E-05	8
GO:2000145	Regulation of cell motility	1.01E-04	11
GO:0040012	Regulation of locomotion	1.46E-04	11
GO:0002703	Regulation of leukocyte-mediated immunity	4.34E-04	5
GO:0050920	Regulation of chemotaxis	6.42E-04	5
GO:0030595	Leukocyte chemotaxis	7.56E-04	5
GO:0004930	G protein-coupled receptor activity	9.04E-04	9
GO:0032103	Positive regulation of response to external stimulus	9.04E-04	7
GO:0030335	Positive regulation of cell migration	1.03E-03	7
GO:2000147	Positive regulation of cell motility	1.31E-03	7
GO:0040017	Positive regulation of locomotion	1.53E-03	7

Notes. GO, Gene Ontology; DEG, differentially expressed genes.

for further analysis. We used the GEPIA database to analyze the expression difference between CRC and normal tissues. Consistent with our results, the four genes were all upregulated in CRC tissues (Figure 4(b)). 5-Methylcytosine (5mC) in DNA can be iteratively oxidized by Tet proteins to generate 5-hmC, which can be further processed by thymine-

Table 3: KEGG and Reactome pathway enrichment analyses of the DEG and genes in the highly correlated modules.

ID	Description	*P* value	NES_abs
hsa04611	Platelet activation	1.96E-03	1.82
hsa00480	Glutathione metabolism	2.02E-03	1.72
hsa05414	Dilated cardiomyopathy	2.01E-03	1.70
hsa04662	B-cell receptor signaling pathway	2.00E-03	1.69
hsa04062	Chemokine signaling pathway	2.10E-03	1.65
hsa01524	Platinum drug resistance	5.93E-03	1.65
hsa04650	Natural killer cell-mediated cytotoxicity	2.00E-03	1.63
hsa00410	Beta-alanine metabolism	3.75E-02	1.57
hsa00670	One carbon pool by folate	2.94E-02	1.51
hsa04060	Cytokine–cytokine receptor interaction	3.96E-03	1.51
hsa04550	Signaling pathways regulating pluripotency of stem cells	8.08E-03	1.49
hsa00515	Mannose type O-glycan biosynthesis	4.70E-02	1.48
hsa02010	ABC transporters	3.43E-02	1.47

Abbreviations. KEGG, Kyoto Encyclopedia of Genes and Genomes; DEG, differentially expressed genes.

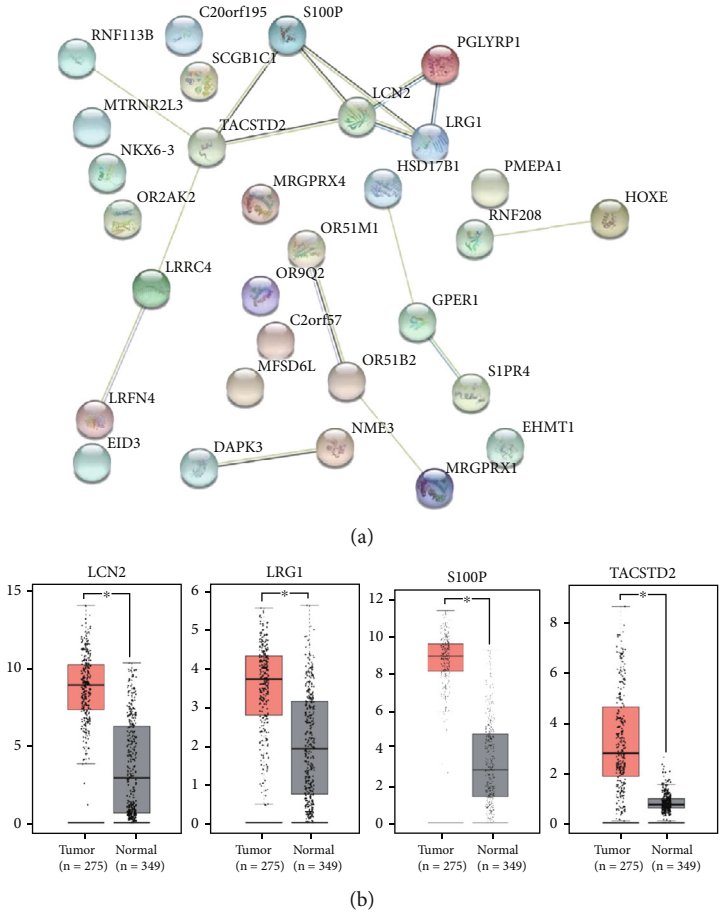

Figure 4: PPI network analysis and expression of plasma 5-hmC hub genes in tissue. (a) PPI network analysis of the DEG. (b) Expression levels in tissue of the plasma 5-hmC hub genes between CRC and healthy controls in the GEPIA database.

DNA glycosylase (TDG) followed by base excision repair or by replication-dependent dilution leading to DNA demethylation. In summary, Tet proteins suppress gene methylation by increasing the 5-hmC level. We performed external validation of this mechanism by exploring the DNA promoter demethylation level of the hub genes in the public database UALCAN. As expected, the DNA promoter demethylation levels of LCN2, LRG1, and S100P were significantly lower

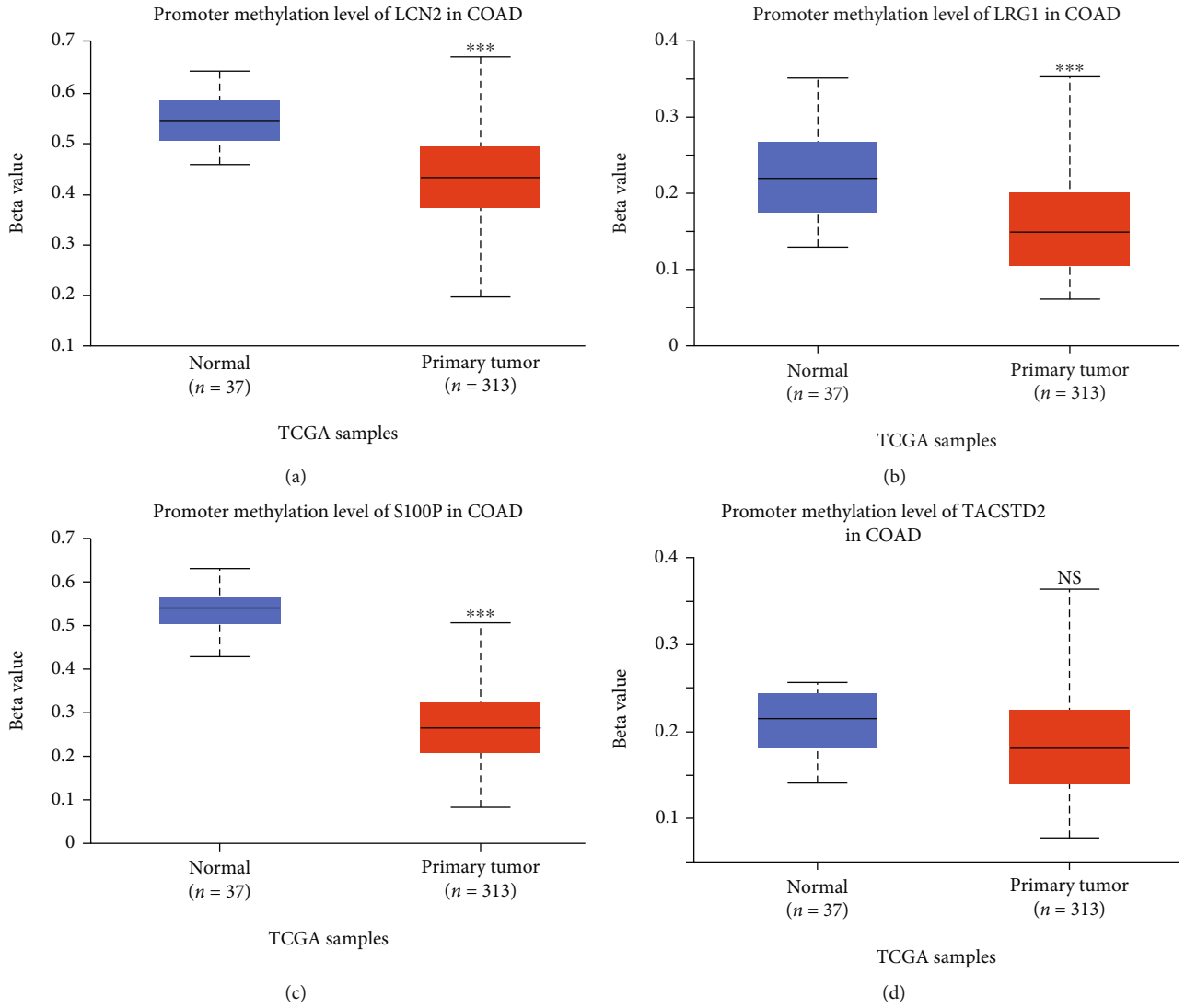

Figure 5: External validation of DNA promoter methylation of the four 5-hmC hub genes in CRC tissue in UALCAN database. DNA promoter methylation levels in tissue of LCN2 (a), LRG1 (b), S100P (c), and TACSTD2 (d) between CRC and healthy controls in the UALCAN database.

in CRC tissue than in the normal tissues (Figure 5). Because the DNA promoter demethylation level can often affect the RNA level, lower DNA promoter methylation level can often lead to a higher RNA expression level, which is consistent with the results shown in Figure 4(b).

3.7. Analysis of the Correlations of 5-hmC-Related Hub Genes with Clinical Characteristics in Public CRC Datasets. The four genes that had a significant influence on the PPI network were used for clinical correlation analysis. We used the GEPIA database to analyze the mRNA expression levels of the 5-hmC related hub genes at different CRC stages. We also explored the relationship between the overall survival time and the mRNA levels of the four genes in the UALCAN database. We found that TACSTD2 was associated with the stage of CRC (Figure 6), and S100P was associated with the overall survival of CRC patients. A high expression level of S100P was a predictor of a poor prognosis in CRC patients (Figure 7).

4. Discussion

Recent studies have reported that 5-hmC may be associated with human cancer [22, 23]. In the present study, the 5-hmC level of the hub genes in CRC patients was different from that in healthy patients. Our study found 19 upregulated genes and 9 downregulated 5-hmC-related hub genes in plasma between healthy controls and CRC patients. Next, we set the criteria of degree more than or equal to three to screen hub genes as biomarkers of circulating cfDNA in cancer by PPI analysis The present findings suggested that the 5-hmC levels of LCN2, LRG1, S100P, and TACSTD2 in circulating cfDNA may be used as potential noninvasive marker genes for CRC, resulting in several notable

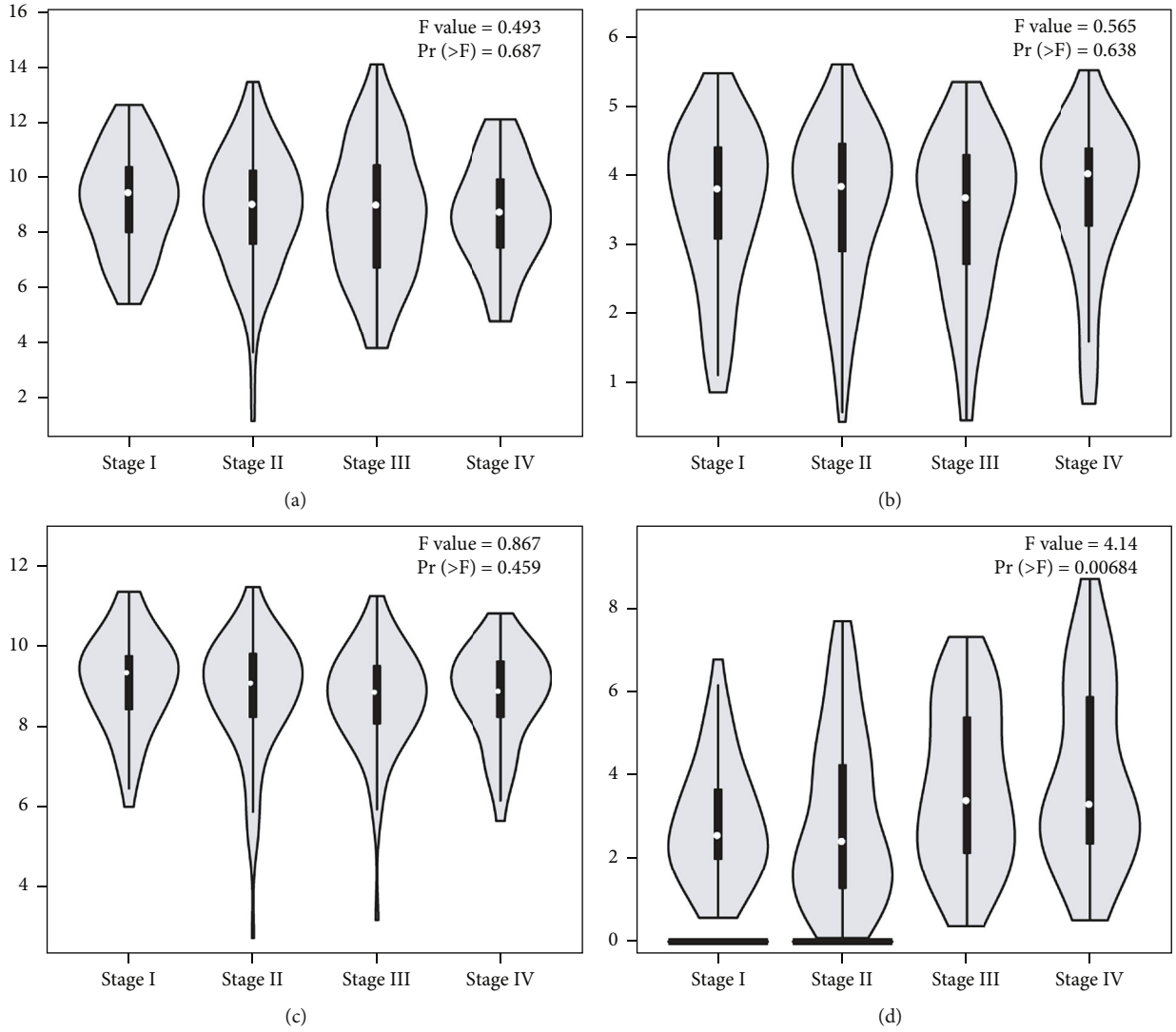

Figure 6: Analysis of the correlation between the 5-hmC-related hub genes and CRC stage in GEPIA database. The correlations between LCN2 (a), LRG1 (b), S100P (c), and TACSTD2 (d) and CRC stage in the GEPIA database.

advantages. First, in contrast to previous genome-wide analyses of hydroxylation, we used sequencing and bioinformatics to analyze the differential level of hydroxylation-related genes between CRC patients and healthy controls. Second, we analyzed genes with different levels of hydroxylation modification of cfDNA in plasma to offer a new strategic method for noninvasive screening of CRC.

In humans, DNA methylation is an important epigenetic modification that is closely related to tumor development and progression. DNA methylation includes various patterns, such as 5-mC and 5-hmC. 5-mC is converted by oxidative demethylation by the ten-eleven translocation enzyme family (TET1, TET2, and TET3) or by passive demethylation of copies [24]. It is reported that 5-methylcytosine (5mC) in DNA can be iteratively oxidized by a family of proteins known as Tet proteins to generate 5-hydroxymethylcytosine (5hmC), which can be further processed by thymine-DNA glycosylase (TDG) followed by base excision repair or replication-dependent dilution leading to DNA demethylation. In summary, Tet proteins downregulated gene methylation by upregulating the 5-hmc level [21]. In addition, 5-hmC levels are low in many cancers, including CRC [25, 26]. Li etal found that the correlation of 5-hmC changes in cancer between the discovery and validation datasets was higher in plasma cfDNA (cancer patients vs. healthy individuals) than in tissue gDNA (tumors vs. adjacent tissues), especially for 5-hmC in gene bodies. The predicted cancer probability based on the 5-hmC classifier from plasma cfDNA showed a significant trend associated with clinical stage. After surgery, patients had predicted scores undistinguishable from those of healthy individuals. However, the hub 5-hmC-related genes for CRC remain largely unknown, and whether 5-hmC-related genes can be used as CRC diagnostic biomarkers needs to be verified in future studies [13]. In the present study, we identified aberrant changes in the 5-hmC levels of 28 genes in the plasma of CRC individuals. WGCNA, GSEA, and GO

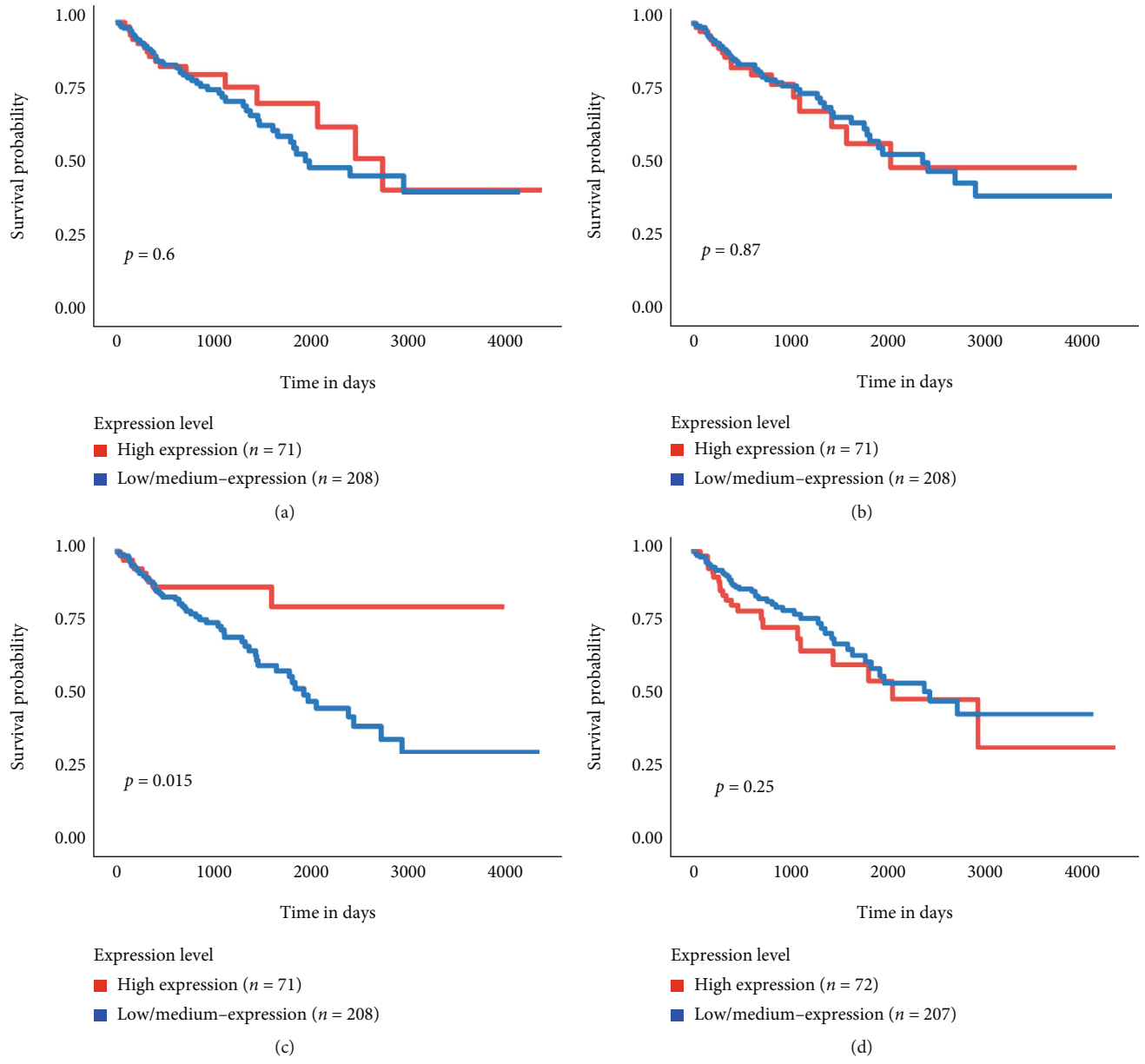

Figure 7: Analysis of the correlation between the 5-hmC-related hub genes and CRC patients' overall survival time in the UALCAN database The correlation between LCN2 (a), LRG1 (b), S100P (c), and TACSTD2 (d) and CRC patients' overall survival time in the UALCAN database.

analysis demonstrated that the 5-hmC levels of some hub genes in the plasma of CRC patients were significantly different than those in the plasma of healthy controls, and these hubs were mainly enriched in the immune response, angiogenesis, drug resistance, and other related signaling pathways. Cell motility is a complex, multistep, and multicomponent process intrinsic to progression and metastasis. Motility is dependent on the activities of integrin receptors and Rho family GTPases, resulting in the remodeling of the actin cytoskeleton and the formation of various motile actin-based protrusions [27]. In our study, GO and KEGG pathway enrichment analyses showed that the 5-hmC level of motility pathway-related genes was downregulated in CRC patients. The lower 5-hmC level of motility pathway-related genes was related to increase mRNA expression of motility pathway-related genes. This may play an important role in CRC progression and metastasis. GO and KEGG pathway enrichment analyses showed that the B-cell receptor signaling pathway related gens was in a higher 5-hmC level in CRC patients' plasma but T-cell immunity was not. This phenomenon may be related to the type of sample we studied. In this study, we used plasma to detect 5-hmC in circulating cfDNA. B-cell immunity is humoral immunity, which mainly depends on antibodies and receptors. Its receptors and antibodies can exist in plasma. T-cell immunity is a type of cellular immunity and mainly plays a role in tissues. T-cells in the blood mainly exist in the monolayer. Because we used plasma samples, no

differences were detected in the T-cell immunity pathway. Our study found elevated levels of 5-hmC in the B-cell receptor pathway in CRC patients, suggesting that the B-cell receptor pathway is inhibited in CRC patients.

The PPI network analysis and further analyses in the GEPIA and UALCAN databases suggested that LCN2, LRG1, S100P, and TACSTD2 are both expressed and methylated in the plasma of CRC patients. 5-hmC is used as a marker of DNA demethylation. Examples of aberrant methylation levels in the genome include hypermethylation of tumor suppressor genes and hypermethylation of oncogenes. Although PGLYRP1 is the highest difference expression gene in the DEGs analysis list, it shows that PGLYRP1 is only two related genes in PPI analysis. So, we did not verified PGLYRP1 in the GEPIA database or ULCAN database.

LCN2, also known as neutrophil gelatinase-associated lipocalin (NGAL), was first discovered as a protein related to neutrophil gelatinase. Recent studies have shown that LCN2 is mainly involved in cellular immunity. LCN2 expression starts in the fetal stages but is fairly low in healthy adult humans. LCN2 has been reported to play a key role in the development and progression of several tumors, such as breast cancer [28], thyroid cancer, CRC, non-small-cell lung cancer, hepatocellular carcinoma, and leukemia [27, 29]. In most cancers, LCN2 is upregulated, but the underlying mechanism remains largely unknown. The present study demonstrated that LCN2 was upregulated in CRC tissue and that the 5-hmC level of LCN2 in CRC patient plasma was also upregulated. We speculated that in CRC patients, the 5-hmC level of LCN2 is increased, leading to upregulated LCN2 demethylation, thereby promoting its expression. LRG1 is a highly conserved member of the leucine-rich repetitive sequence family, which was first identified in human serum in 1977 [30]. LRG1 is a secreted glycoprotein that mediates the interaction between proteins and has been studied as a tumor-promoting factor that participates in signal transduction, cell proliferation, migration, invasion, adhesion, survival, and apoptosis [31–33]. Previous studies have identified LRG1 as a new proangiogenic gene that enhances cancer growth and diabetic retinopathy. Zhang found that overexpression of LRG1 significantly enhances the migration and tube formation capabilities of HUVECs [34]. Similar to LCN2, the present study showed that the 5-hmC and mRNA levels of LRG1 were upregulated in CRC patients compared to healthy individuals. LRG1 was enriched in the angiogenesis-related pathway. Abnormal levels of TACSTD2 are associated with the progression of many tumors. The present study demonstrated that TACSTD2 was upregulated in CRC tissue and CRC patient plasma compared to plasma from healthy individuals, and the mRNA level of TACSTD2 is positive associated with CRC stage. Similar to our study, Katzendorn et al. reported that the DNA methylation of TACSTD2 loci is related to clinically aggressive renal cell cancers [35]. S100P is S100 calcium binding protein P, and the protein encoded by this gene is a member of the S100 family of proteins containing 2 EF-hand calcium-binding motifs. S100 proteins are localized in the cytoplasm and/or nucleus of a wide range of cells and are involved in the regulation of a number of cellular processes such as cell cycle progression and differentiation. Recent studies have reported that S100P is a new target gene of MACC1 that drives colorectal cancer metastasis and serves as a prognostic biomarker [36]. Consistent with this, we found that the 5-hmC level of S100P in CRC patients' plasm was significant higher than that in the plasma of healthy individuals. The mRNA expression level was upregulated in CRC tissue, which was associated with a poor prognosis in CRC patients. It is reported that DNA hydroxymethylation increases the susceptibility to reactivation of methylated P16 alleles in cancer cells, and 5-hmc may play an important role in gene transcription [37]. This may partly explain our research that LCN2, LRG1, S100P, and TACSTD2 DNA hydroxymethylation levels were positively correlated with their mRNA levels. In addition, the 5-hmC levels ofLCN2, LRG1, S100P, and TACSTD2 in circulating cfDNA may be used as potential noninvasive markers for CRC. Although we found that abnormalities in cell-free DNA hydroxylation in plasma may be associated with an abnormal immune response to CRC. However, this study only used 4 CRC samples from the GEO, so the number of samples is limited, and more samples are needed for validation. On the other hand, due to the level of 5-hmC in the blood is very low, quantitative and high-resolution analysis of active DNA demethylation activity remains challenging. We have not verified the 5-hmC level of the hub genes in clinical samples; we are looking forward to advances in the new technology. In addition, the underline mechanism on how the LCN2, LRG1, S100P, and TACSTD2 function in CRC occurrence, development, and outcome needs to be explored in the further researches.

5. Conclusion

The abnormal expression of some 5-hmC-related genes in the plasma of patients with CRC may influence the 5-hmC expression level through the methylation level of related genes in CRC. The 5-hmC level of some genes in plasma may act as biomarker for CRC.

Abbreviations

5-hmC: 5-hydroxymethylcytosine
CRC: Colorectal cancer
GEO: Gene expression omnibus
DEG: Differentially expressed genes
WGCNA: Weighted gene coexpression network analysis
GO: Gene ontology
PPI: Protein–protein interaction
cfDNA: Circulating cell-free DNA.

Data Availability

All data generated or analyzed during this study are included in this published article.

Consent

All authors have read the manuscript and approved its submission to this journal.

Conflicts of Interest

The authors declare that there are no competing interests.

Authors' Contributions

Hongwei Liu and Tao Tang performed the statistical analyses and drafted the manuscript. Xiujin Hu, Weiren Ding, Meifang Zhou, Peng Zhou, Ying Luo, Chen Chen, Weiguo Yin, and Yanmei Liu participated in the statistical analyses. Jinduan Lin conceived the study and participated in its design and coordination. All authors read and approved the final manuscript. Hongwei Liu and Tao Tang contributed equally to this study.

Acknowledgments

This work was partly supported by a grant from the Guangdong Medical Research Foundation (No. B2018133), the Qingyuan Science and Technology Projects (No. 2018A001), the Qingyuan People's Hospital Fund (No. 20190213), and the Sixth Affiliated Hospital of Guangzhou Medical University, Qingyuan People's Hospital (No. 2011-305).

Supplementary Materials

The correlations between the 5-hmC level with phenotype by WGCNA. *(Supplementary Materials)*

References

[1] J. Yin, Z. Bai, J. Zhang et al., "Burden of colorectal cancer in China, 1990-2017: findings from the global burden of disease study 2017," *Chinese Journal of Cancer Research*, vol. 31, no. 3, pp. 489–498, 2019.

[2] R. M. Feng, Y. N. Zong, S. M. Cao, and R. H. Xu, "Current cancer situation in China: good or bad news from the 2018 global cancer statistics?," *Cancer Communications*, vol. 39, no. 1, p. 22, 2019.

[3] F. Bray, J. Ferlay, I. Soerjomataram, R. L. Siegel, L. A. Torre, and A. Jemal, "Global cancer statistics 2018: GLOBOCAN estimates of incidence and mortality worldwide for 36 cancers in 185 countries," *CA: a Cancer Journal for Clinicians*, vol. 68, no. 6, pp. 394–424, 2018.

[4] W. Cao, H. D. Chen, Y. W. Yu, N. Li, and W. Q. Chen, "Changing profiles of cancer burden worldwide and in China: a secondary analysis of the global cancer statistics 2020," *Chinese Medical Journal*, vol. 134, no. 7, pp. 783–791, 2021.

[5] H. Sung, J. Ferlay, R. L. Siegel et al., "Global cancer statistics 2020: GLOBOCAN estimates of incidence and mortality worldwide for 36 cancers in 185 countries," *CA: a Cancer Journal for Clinicians*, vol. 71, no. 3, pp. 209–249, 2021.

[6] A. Ferrari, I. Neefs, S. Hoeck, M. Peeters, and G. Van Hal, "Towards novel non-invasive colorectal cancer screening methods: A Comprehensive Review," *Cancers*, vol. 13, no. 8, p. 1820, 2021.

[7] D. Massihnia, E. G. Pizzutilo, A. Amatu et al., "Liquid biopsy for rectal cancer: a systematic review," *Cancer Treatment Reviews*, vol. 79, p. 101893, 2019.

[8] A. Kasprzak and A. Adamek, "Insulin-like growth factor 2 (IGF2) signaling in colorectal cancer-from basic research to potential clinical applications," *International Journal of Molecular Sciences*, vol. 20, no. 19, p. 4915, 2019.

[9] J. Petit, G. Carroll, T. Gould, P. Pockney, M. Dun, and R. J. Scott, "Cell-free DNA as a diagnostic blood-based biomarker for colorectal cancer: a systematic review," *The Journal of Surgical Research*, vol. 236, pp. 184–197, 2019.

[10] B. Fu, P. Yan, S. Zhang et al., "Cell-free circulating methylated SEPT9 for noninvasive diagnosis and monitoring of colorectal cancer," *Disease Markers*, vol. 2018, Article ID 6437104, 11 pages, 2018.

[11] J. Sun, F. Fei, M. Zhang et al., "The role of mSEPT9 in screening, diagnosis, and recurrence monitoring of colorectal cancer," *BMC Cancer*, vol. 19, no. 1, p. 450, 2019.

[12] D. H. Kang, D. J. Jeong, T. S. Ahn et al., "Expression of AMP-activated protein kinase/ten-eleven translocation 2 and their clinical relevance in colorectal cancer," *Oncology Letters*, vol. 21, no. 2, p. 164, 2021.

[13] W. Li, X. Zhang, X. Lu et al., "5-Hydroxymethylcytosine signatures in circulating cell-free DNA as diagnostic biomarkers for human cancers," *Cell Research*, vol. 27, no. 10, pp. 1243–1257, 2017.

[14] M. E. Ritchie, B. Phipson, D. Wu et al., "Limma powers differential expression analyses for RNA-sequencing and microarray studies," *Nucleic Acids Research*, vol. 43, no. 7, article e47, 2015.

[15] K. Jia, Y. Wu, J. Ju et al., "The identification of gene signature and critical pathway associated with childhood-onset type 2 diabetes," *PeerJ*, vol. 7, article e6343, 2019.

[16] P. Langfelder and S. Horvath, "WGCNA: an R package for weighted correlation network analysis," *BMC Bioinformatics*, vol. 9, no. 1, p. 559, 2008.

[17] M. Ashburner, C. A. Ball, J. A. Blake et al., "Gene ontology: tool for the unification of biology. The gene ontology consortium," *Nature Genetics*, vol. 25, no. 1, pp. 25–29, 2000.

[18] M. Kanehisa and S. Goto, "KEGG: Kyoto encyclopedia of genes and genomes," *Nucleic Acids Research*, vol. 28, no. 1, pp. 27–30, 2000.

[19] J. Montojo, K. Zuberi, H. Rodriguez et al., "GeneMANIA Cytoscape plugin: fast gene function predictions on the desktop," *Bioinformatics*, vol. 26, no. 22, pp. 2927-2928, 2010.

[20] Z. Tang, C. Li, B. Kang, G. Gao, C. Li, and Z. Zhang, "GEPIA: a web server for cancer and normal gene expression profiling and interactive analyses," *Nucleic Acids Research*, vol. 45, no. W1, pp. W98–W102, 2017.

[21] D. S. Chandrashekar, B. Bashel, S. Balasubramanya et al., "UALCAN: a portal for facilitating tumor subgroup gene expression and survival analyses," *Neoplasia*, vol. 19, no. 8, pp. 649–658, 2017.

[22] J. Shekhawat, K. Gauba, S. Gupta et al., "Ten-eleven translocase: key regulator of the methylation landscape in cancer," *Journal of Cancer Research and Clinical Oncology*, vol. 147, no. 7, pp. 1869–1879, 2021.

[23] S. Yamada, K. Misawa, M. Mima et al., "Telomere shortening in head and neck cancer: association between DNA demethylation and survival," *Journal of Cancer*, vol. 12, no. 8, pp. 2165–2172, 2021.

[24] M. Tahiliani, K. P. Koh, Y. Shen et al., "Conversion of 5-methylcytosine to 5-hydroxymethylcytosine in mammalian DNA by MLL partner TET1," *Science*, vol. 324, no. 5929, pp. 930–935, 2009.

[25] G. P. Pfeifer, S. Kadam, and S. G. Jin, "5-hydroxymethylcytosine and its potential roles in development and cancer," *Epigenetics & Chromatin*, vol. 6, no. 1, p. 10, 2013.

[26] M. C. Haffner, A. Chaux, A. K. Meeker et al., "Global 5-hydroxymethylcytosine content is significantly reduced in tissue stem/progenitor cell compartments and in human cancers," *Oncotarget*, vol. 2, no. 8, pp. 627–637, 2011.

[27] I. H. Chung, C. Y. Chen, Y. H. Lin et al., "Thyroid hormone-mediated regulation of lipocalin 2 through the met/FAK pathway in liver cancer," *Oncotarget*, vol. 6, no. 17, pp. 15050–15064, 2015.

[28] A. Tyagi, S. Sharma, K. Wu et al., "Nicotine promotes breast cancer metastasis by stimulating N2 neutrophils and generating pre-metastatic niche in lung," *Nature Communications*, vol. 12, no. 1, p. 474, 2021.

[29] G. S. Santiago-Sanchez, V. Pita-Grisanti, B. Quinones-Diaz, K. Gumpper, Z. Cruz-Monserrate, and P. E. Vivas-Mejia, "Biological functions and therapeutic potential of lipocalin 2 in cancer," *International Journal of Molecular Sciences*, vol. 21, no. 12, p. 4365, 2020.

[30] H. Haupt and S. Baudner, "Isolierung und Charakterisierung eines bisher unbekannten leucinreichen 3.1S-α2-Glykoproteins aus Humanserum," *Hoppe-Seyler's Zeitschrift für Physiologische Chemie*, vol. 358, no. 1, pp. 639–646, 1977.

[31] A. Zhang, H. Fang, J. Chen, L. He, and Y. Chen, "Role of VEGF-A and LRG1 in abnormal angiogenesis associated with diabetic nephropathy," *Frontiers in Physiology*, vol. 11, p. 1064, 2020.

[32] C. H. Wang, M. Li, L. L. Liu et al., "LRG1 expression indicates unfavorable clinical outcome in hepatocellular carcinoma," *Oncotarget*, vol. 6, no. 39, pp. 42118–42129, 2015.

[33] T. Furuta, Y. Sugita, S. Komaki et al., "The multipotential of leucine-rich α-2 glycoprotein 1 as a clinicopathological biomarker of glioblastoma," *Journal of Neuropathology and Experimental Neurology*, vol. 79, no. 8, pp. 873–879, 2020.

[34] J. Zhang, L. Zhu, J. Fang, Z. Ge, and X. Li, "LRG1 modulates epithelial-mesenchymal transition and angiogenesis in colorectal cancer via HIF-1α activation," *Journal of Experimental & Clinical Cancer Research*, vol. 35, no. 1, p. 29, 2016.

[35] O. Katzendorn, I. Peters, N. Dubrowinskaja et al., "DNA methylation of tumor associated calcium signal transducer 2 (TACSTD2) loci shows association with clinically aggressive renal cell cancers," *BMC Cancer*, vol. 21, no. 1, p. 444, 2021.

[36] J. S. Yordy, R. Li, V. I. Sementchenko, H. Pei, R. C. Muise-Helmericks, and D. K. Watson, "SP100 expression modulates ETS1 transcriptional activity and inhibits cell invasion," *Oncogene*, vol. 23, no. 39, pp. 6654–6665, 2004.

[37] P. Li, Y. Gan, S. Qin et al., "DNA hydroxymethylation increases the susceptibility of reactivation of methylatedP16alleles in cancer cells," *Epigenetics-Us*, vol. 15, no. 6-7, pp. 618–631, 2020.

Hindawi
Journal of Oncology
Volume 2022, Article ID 8767333, 10 pages
https://doi.org/10.1155/2022/8767333

Research Article

Overexpression of FAM83A Is Associated with Poor Prognosis of Lung Adenocarcinoma

Xin Liu,[1] **Meng Fu**,[2,3,4] **Daqing Xia**,[2] **Zimei Ji**,[2] **Nana Hu**,[2] **Zaijun Leng**,[2] **Wang Xie**,[2] **Yuan Fang**,[2] **and Junqiang Zhang**[1,2]

[1]*Bengbu Medical College, Bengbu, 233030 Anhui, China*
[2]*Department of Respiratory and Critical Care Medicine, The First Affiliated Hospital of USTC, Division of Life Science and Medicine, University of Science and Technology of China, Hefei, Anhui 230001, China*
[3]*Anhui Province Key Laboratory of Medical Physics and Technology, Institute of Health and Medical Technology, Hefei Institutes of Physical Science, Chinese Academy of Sciences, Hefei 230031, China*
[4]*University of Science and Technology of China, Hefei 230026, China*

Correspondence should be addressed to Junqiang Zhang; yany1980@126.com

Received 26 July 2022; Revised 23 August 2022; Accepted 15 September 2022; Published 5 October 2022

Academic Editor: Muhammad Muddassir Ali

Family with sequence similarity 83, member A (FAM83A) plays an essential and fundamental role in the proliferation, progression, and apoptosis of many malignant tumors, including lung cancer. This study aimed to determine the expression pattern of FAM83A in lung adenocarcinoma (LUAD) and its correlation with the prognosis of cancer and the survival of the patients. Bioinformatics analysis, immunohistochemistry, and Western blotting were used to explore and detect the expression of FAM83A in LUAD cells. The mechanism of FAM83A in proliferation and migration was examined. The correlation between FAM83A expression and survival rate was assessed by the Kaplan-Meier and Cox regression. FAM83A expression was elevated in LUAD tissues and was related to shorter overall survival ($P < 0.05$). A significant increase in FAM83A protein was observed in the LUAD tissue ($P < 0.05$). Compared with patients with early-stage tumors (stage I-II), those with advanced stage tumors (stage III-IV) had significantly higher FAM83A expression levels ($P < 0.05$). Downregulation of FAM83A led to a reduction in cell proliferation, a decrease in migration ability, and diminished epithelial-mesenchymal transition (EMT) in the lung cancer cell lines. Overexpression of FAM83A was associated with early lymph node metastasis and poor overall survival among LUAD patients. The findings indicated that FAM83A may play a critical role in promoting the LUAD progression and thus might serve as a novel prognostic marker in LUAD.

1. Introduction

Lung cancer is one of the most common forms of cancer worldwide and also the leading cause of cancer mortalities worldwide [1]. In the recent years, the rate of incidence and mortality has significantly increased with significant gender and geographic differences. This is due to diversity in lifestyles and socioeconomic development [2]. GLOBOCAN reported approximately 2.21 million new lung cancer cases (11.4% of the total new cancer cases) and 1.80 million deaths (18.0% of the total cancer deaths) worldwide in 2020 [3]. Despite many therapies for cancer, no satisfactory clinical results have been observed because of early metastasis of tumor. Therefore, the main concern is on targeted therapies in order to increase the rate of recovery of the disease [4]. Traditional chemotherapies as the cornerstone of therapy in the first line setting in an advanced stage of lung cancer. In the past decade, significant improvements in survival rate have been observed. These improvements are due to the development of targeted therapies, i.e., epidermal growth factor receptor tyrosine kinase inhibitors (EGFR-TKIs), for lung adenocarcinoma through specific driver genes. Previous studies have demonstrated better therapeutic outcomes and fewer toxic effects via EGFR-TKIs compared with the traditional chemotherapies in patients with non-small cell lung cancer (NSCLC) and EGFR mutations [5–8]. However,

resistance to EGFR-TKIs seems inevitable and limits its application in clinical practice. Despite the initial response, patients who were treated with third-generation EGFR-TKI Osimertinib would develop acquired resistance and disease progression occurred 9 to 18 months after treatment [9–11]. The patients' disease usually deteriorates rapidly following drug resistance.

FAM83A consists of 8 genes, FAM83A-H, and is a member of the FAM83 protein family which is located on chromosome 8q24 [12]. The FAM83 family of proteins contains a highly conserved DUF1699 domain at the N-terminal, which is thought to be closely related to the biological characteristics of the tumor [13]. Previous studies indicated the overexpression of FAM83A in a variety of tumors, such as lung and breast cancers, and suggested it as a potential biomarker for cancer prognosis and a therapeutic target [14]. FAM83A could be used to predict LUAD prognosis, while FAM83B could predict the prognosis of lung squamous cell carcinoma [15]. In addition to that, FAM83A (serine and protein rich) is correlated with the poor prognosis, in the case of lung adenocarcinoma. In EMT of lung cancer, FAM83A is also involved in the Wnt/β-catenin signaling pathway [16, 17]. The public databases of bioinformatics analysis demonstrated the possible role of FAM83A overexpressed in lung cancer. Several experimental studies have reported high expression levels of FAM83A mRNA in lung cancer tissue and circulating tumor cells [18, 19]. It is also evaluated by a bioinformatics analysis that there is correlation between the expression of FAM83A and programmed death-ligand-1(PD-L1) [20]. Shi et al. proposed that long non-coding antisense RNA FAM83A-AS1 could increase FAM83A expression and promote lung cancer cell growth [21]. However, most of the conducted studies mainly focused on detecting FAM83A expression at mRNA or antisense RNA levels, rather than on protein levels. Clear that increased mRNA expression does not always indicate high protein expression, while protein is the basic and ultimate biological functional unit of genes. Consequently, to clarify the biological significance of FAM83A in lung cancer, studies on protein levels rather than mRNA levels are required. In this regard, FAM83A expression at the protein level, the role of FAM83A in LUAD biological characteristics, and its effects on the clinical and pathological characteristics of LUAD patients were investigated in the present study.

2. Materials and Methods

2.1. Collection of LUAD Tissue Samples and Clinical Information. The tissue chip contained 84 paraffin-embedded LUAD and para-cancer tissue samples of lung cancer specimens surgically removed from patients. The surgical procedures were performed in The First Affiliated Hospital of the University of Science and Technology of China (USTC) from October 2004 to August 2008. The correlation of clinical and pathological features with FAM83A expression is shown in Table 1. All experimental protocols were approved by the Institutional Research Ethics Committee of The First Affiliated Hospital of USTC (No. 2019-P-017).

Table 1: Correlations between FAM83A expression and clinical/pathological characteristics in LUAD.

Characteristics	FAM83A		*P*-value
	Low	High	
Age (y)			0.547
≥60	13	20	
<60	23	28	
Gender			0.784
Male	19	27	
Female	17	21	
T classification			0.634
T1	8	8	
T2	21	26	
T3	6	10	
T4	1	4	
N classification			0.007
N0	22	13	
N1	8	17	
N2	4	15	
N3	2	3	
M classification			0.235
M0	35	44	
M1	1	4	
Clinical stage			0.008
I	17	8	
II	10	12	
III	8	24	
IV	1	4	

2.2. Immunohistochemistry. The expression of FAM83A protein in the lung tissue was assessed by immunohistochemistry. The tissue sections were deparaffinized and rehydrated by a LEICA Autostainer (Leica ST5010, Autostainer XL, Germany) at room temperature. Antigen retrieval (AR) was performed with the citric acid solution. The tissue pieces were washed and covered with rabbit anti-FAM83A antibody (1 : 400; No: orb183622, Biorbyt, Cambridge, UK) and incubated overnight at 4°C. Then, the slides were washed with phosphate buffer saline (PBS) and incubated with secondary antibody (Envision+/HRP, Rabbit, Dako, Sweden) and diaminobenzidene (DAB) solution for 30 and 5 min at room temperature, respectively, and counterstained with hematoxylin. The stained slides were examined and quantitatively analyzed using Image J, and average optical density (AOD) was evaluated. The AOD median value (MAOD) of the detected LUAD samples was calculated. The specimen with AOD ≥ MAOD and AOD < MAOD were defined as high and low expression, respectively [17].

2.3. Cell Culture. A549, H1395, H1795, and Calu-3 cells were purchased from the American Tissue Tradition Collection (ATCC) (Manassas, VA, USA). The cells were cultured in Roswell Park Memorial Institute (RPMI) 1640 medium (HyClone, Logan, UT, Aldrich, St. Louis, MO) at 37°C in a humidified incubator with a 5% CO_2 atmosphere. The cells

in the logarithmic growth phase (full to 70%-90%) were selected, shaken, and cleaned with 2 mL PBS, and then digested with trypsin at 37°C for about 1 min. The digestion was stopped by adding a complete medium, and the cell precipitation was used in subsequent experiments.

2.4. Western Blotting Assay. Western blotting was used to detect FAM83A and EMT-related protein expression in the cells. Standard procedures were performed according to the manufacturer's instructions. Briefly, proteins in cell lysates were separated by sodium dodecyl sulfate-polyacrylamide gel electrophoresis (SDS-PAGE) and subsequently transferred onto polyvinylidene difluoride (PVDF) membranes (Millipore, Massachusetts, USA) and incubated with the following primary antibodies against FAM83A (1 : 1000; Sigma, Saint Louis, MO, USA), β-Actin (1 : 10000; Abcam, Cambridge, MA, USA), vimentin (1 : 1000; Cell Signaling Technology, Danvers, MA, USA), E-cadherin (1 : 1000; Cell Signaling Technology, Danvers, MA, USA), and Snail (1 : 1000 Cell Signaling Technology, Danvers, MA, USA). The β-actin was used as a loading control [17].

2.5. Lentivirus Transduction and Generation of Stable Cell Lines. An HIV-1-based, lentiviral expression vector designed to express a small hairpin RNA (pLVX-shRNA1) was used for cell transduction. The small hairpin RNA (shRNA) oligonucleotide sequences targeting human FAM83A gene mRNA was designed and synthesized by Huada Gene Scientific and Technological Co., Ltd. (Shenzhen, China). The target sequence of FAM83A was 5′-CCGGAGGAAATTCGCT GGCCAAATCTTCAAGAGAGATTTGGCCAGCGAATT TCCTTTTTTT-3′. The lentivirus with shFAM83A-gene was produced by co-transfection of 293T cells and transfected into A549 and H1795 cells. Control cells were transfected with an empty vector. Stable cells were selected with puromycin (Beyotime, Nanjing, China) after infection. Positive clones were selected for further analysis [17].

2.6. Real-Time PCR (RT-PCR). Total RNA was extracted from cultured cells using the E.Z.N.A Total RNA Kit (R6834-02, Omega, US). Reverse transcription was carried out using Prime Script RT Reagent Kit (Takara, Japan) according to the manufacturer's protocol. Reverse transcription polymerase chain reaction (RT-PCR) was then performed using SYBR Premix Ex Taq TM II Perfect Real-Time (DRR081A, TaKaRa, Japan) in Eppendorf Realplex 2S (Eppendorf, Germany). All primers were synthesized by Suzhou Jinweizhi Biotechnology Co., Ltd. (Suzhou, China). The primer sequences are as follows: FAM83A-F: 5′-CCAGACCGTCAAGCACAACA-3′, FAM83A-R: 5′-GGAGCACACAAACGAACACC-3′ [17].

2.7. Cell Proliferation Assay. Cell viability was assessed by a cell proliferation assay using cell counting kit-8 (CCK-8, Dojindo, Kumomoto, Japan). Briefly, the cell suspension was cultured in 96-well plates at a density of 1×104 cells per well. They were detected at 0, 12, 24, 48, and 72 h following the protocol. Cell growth rates were determined by measuring absorbance at 450 nm [17].

2.8. Wound-Healing Assay. Cells were cultured in a 6-well plate at a density of 1×10^6 cells per well overnight. A wound was created using a 10 μL pipette tip across the center of the well. After scratching, the wells were washed three times with PBS and incubated in a CO_2 incubator at 37°C. Images were obtained immediately and 12 h after wounding. The healing of the wound surface areas was calculated and analyzed using the Image J tool (The healing areas = 0-h areas – 24-h areas) [17].

2.9. Transwell Cell Assay. The cell invasion assays were performed using a Matrigel invasion chamber (pore size: 8 mm, BD Biosciences, USA) at a density of 1×10^6/ml. Cells in serum-free medium were plated in the upper chamber. The chemoattractant in the lower chamber was 10% fetal bovine serum. After a 24-h incubation, the invaded cells were fixed with paraformaldehyde (PFA) and then stained with crystal violet. Finally, invaded cells were observed under an inverted microscope (Leica DMI 4000 B, Leica, Wetzlar, Germany) and manually quantified.

2.10. Bioinformatics Analysis. The study data and clinical information were provided from The Cancer Genome Atlas (TCGA) database. The University of Alabama at Birmingham cancer (UALCAN) data analysis portal (http://ualcan.path.uab.edu/analysis.html) was used to analyze the data. The Kaplan-Meier analysis was used to determine the relationship between FAM83A expression and the prognosis of the disease.

2.11. Statistical Analysis. Data was analyzed by SPSS 13.0 (Chicago, IL, USA). Correlation analysis was performed using Pearson's chi-square test. Prognostic factor analyses were performed using univariate and multivariate Cox regression analysis. $P < 0.05$ value was considered statistically significant.

3. Results

3.1. Upregulation of FAM83A in LUAD by Bioinformatics/UALCAN Analysis. UALCAN analysis of TCGA (http://ualcan.path.uab.edu/analysis.html) showed that overexpression of FAM83A occurred in NSCLC, especially LUAD (Figure 1(a)). The cluster analysis of the LUAD gene showed a significant increase in transcriptional expression of FAM83A between LUAD and the normal lung tissues (Figures 1(b) and 1(c)). Furthermore, the Kaplan-Meier analysis reported that patients with high FAM83A expression had shorter overall survival ($P < 0.0001$), as shown in Figure 1(d). In conclusion, the obtained results of the TCGA database demonstrated that FAM83A overexpressed in LUAD and closely correlated with a worse prognosis.

3.2. High Expression of FAM83A in LUAD is Related to Advanced Clinical and Pathological Characteristics. Immunohistochemical staining was used to detect FAM83A protein in the LUAD tissue chip. The obtained results indicated that the FAM83A protein was dyed brown and located mostly in the cytoplasm, with a few in the nucleus (Figure 2(a)). Moreover, high expression of FAM83A in

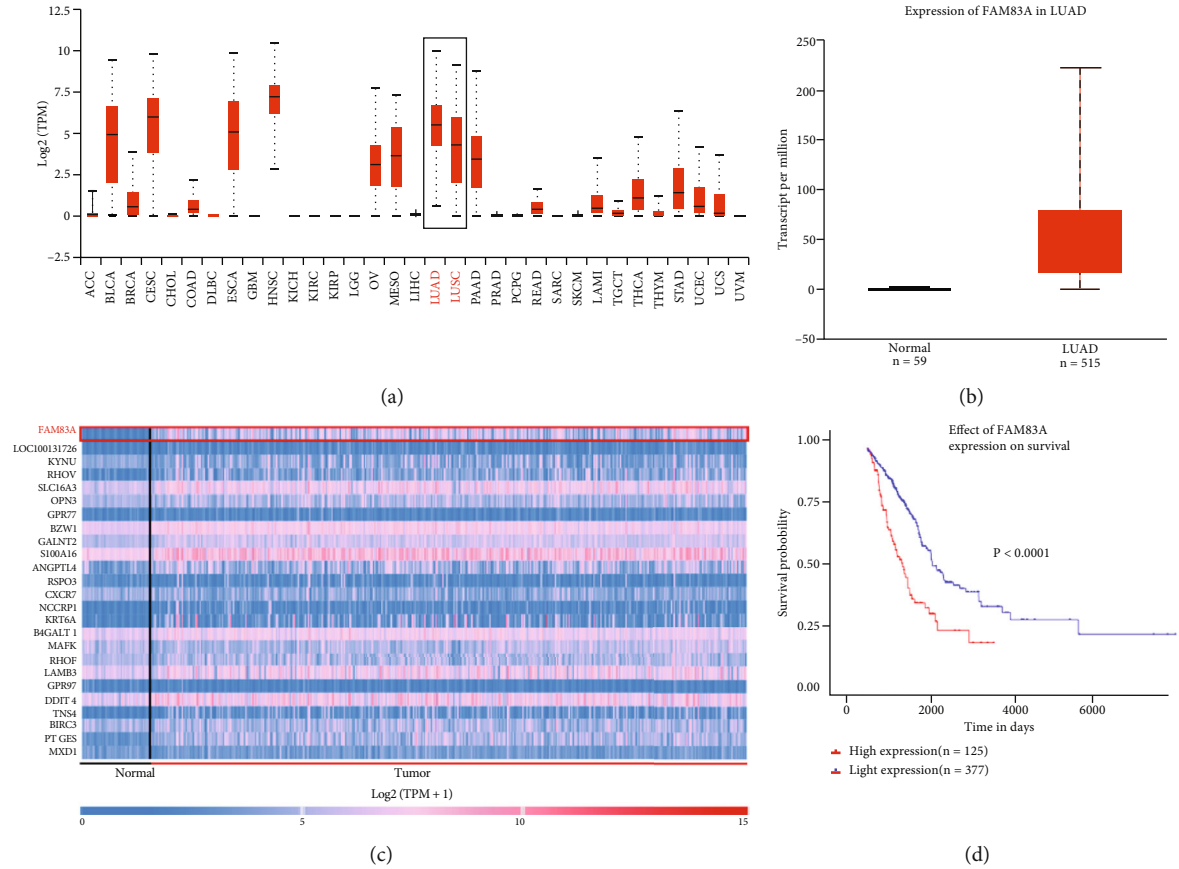

Figure 1: UALCAN analysis of TCGA showed FAM83A is overexpressed in LUAD. (a) UALCAN analysis showed FAM83A is overexpressed in lung adenocarcinoma (LUAD) and lung squamous carcinoma (LUSC), especially the former. (b, c) Cluster analysis showed a significant over expression of FAM83A in LUAD (tumor) than in normal lung tissue (normal). (d) Kaplan-Meier analysis showed that patients with high FAM83A expression had shorter overall survival, $P < 0.0001$.

LUAD and low expression in the adjacent normal tissue were found ($P < 0.01$, Figure 2(b)). Subgroup analysis showed that stage III-IV patients had higher FAM83A expression than stage I-II patients ($P < 0.05$, Figure 2(c)). Subsequent correlation analysis suggested that FAM83A expression was correlated with clinical stages ($P = 0.008$) and lymph node classifications ($P = 0.007$), but not with T classification ($P = 0.634$) or metastasis classification ($P = 0.235$). Univariate and multivariate Cox regression analyses indicated that FAM83A expression was an independent prognostic factor for survival in patients with LUAD (hazard ratio: 1.745, 1.879, 95% confidential interval: 1.167–2.945, 1.075–3.321, P =0.023, 0.020, respectively) (Table 2). Furthermore, the Kaplan-Meier analysis revealed that patients with high FAM83A expression had shorter overall survival ($P < 0.01$, Figure 2(d)). Consequently, the results indicated a high FAM83A expression in LUAD, which was related to advanced clinical and pathological features and poor prognosis.

3.3. FAM83A Modulated Proliferation of LUAD Cells. To investigate FAM83A expression in cancer cells, its expression in several adenocarcinoma cell lines including A549, H1395, H1795, and Calu-3 cells was detected by Western blotting assay. The results showed that FAM83A expression was higher in A549 and H1795 cells and lower in H1395 and Calu-3 cells (Figures 3(a) and 3(b)). In RT-PCR, A549 and H1795 cells were treated for stable FAM83A-knockdown by shRNA (shFAM83A) and a decrease in FAM83A mRNA levels was observed (Figure 3(c)). A CCK8 cell proliferation assay revealed that FAM83A knockdown could suppress cell proliferation activity in H1795 cells. The proliferation rate of H1795-shFAM83A decreased significantly compared with the control H1795-shRNA-NC cells at each time point (0, 12, 24, 48, and 72 h) (Figure 3(e), $P < 0.001$). In contrast, the suppression was not observed in A549 cells and it was indicated that FAM83A knockdown had no obvious effects on A549 cell proliferation (Figure 3(d), $P > 0.05$).

3.4. FAM83A Promoted LUAD Cell Migration Ability. To investigate the roles of FAM83A in cell migration, wound-healing and transwell cell assays were performed in A549 and H1795 cells. The wound-healing assay showed a significant decrease in the healing area in FAM83A knocked down cells (A549, H1795) (Figures 4(a) and 4(b)), indicating that FAM83A knockdown significantly inhibited the migration ability of A549 and H1795 cells. In addition, FAM83A knockdown in A549 and H1795 cells significantly impaired cell migration ability, as shown in the transwell cell migration assay (Figures 4(c) and 4(d)). More cells passed through

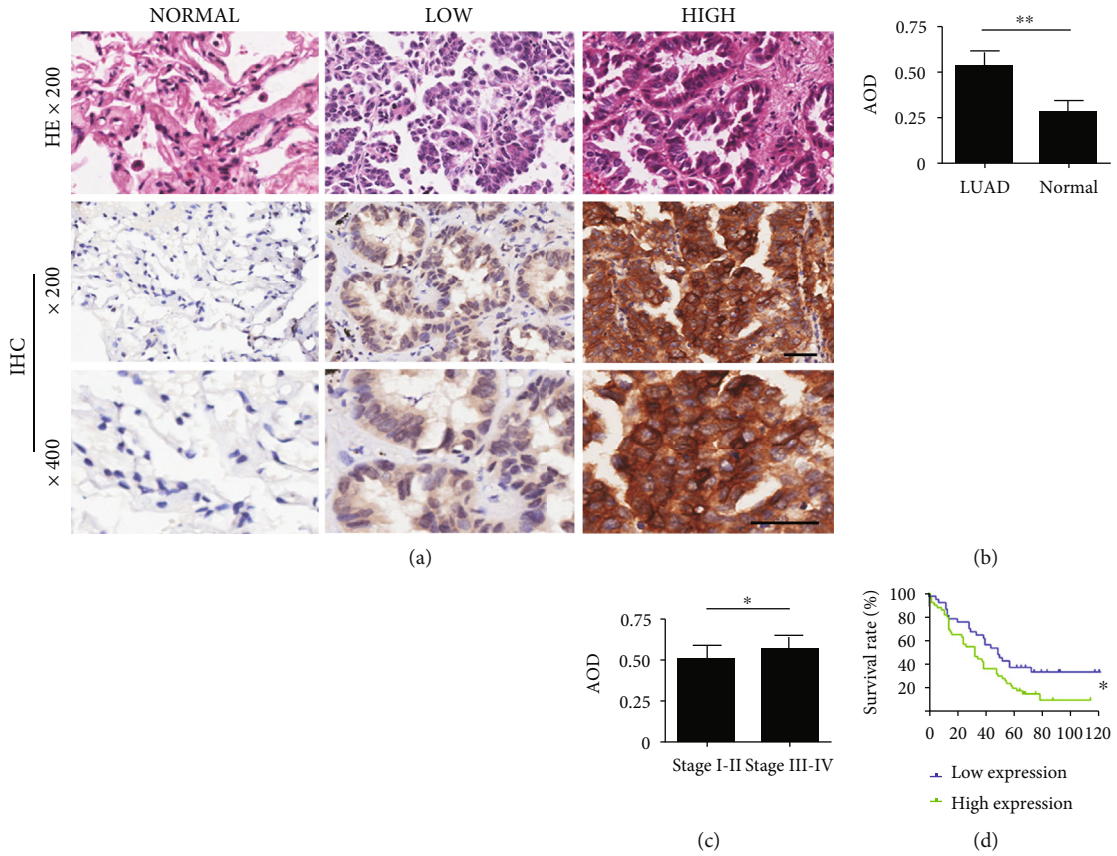

Figure 2: FAM83A protein was overexpressed in LUAD and higher FAM83A expressions related to poor overall patient survival. (a) Representative hematein-eosin (HE) and immunohistochemistry (IHC) images of FAM83A expressions in adjacent normal tissues (NORMAL) and LUAD with low (LOW) and high (HIGH) FAM83A expressions. The short bar is equal to 50 microns; the long bar is equal to 100 microns. (b) The average optical density (AOD) of FAM83A in LUAD tissues and adjacent normal lung tissues. (c) AOD of FAM83A in LUAD tissues in stage I-II and stage III-IV. (d) Kaplan-Meier survival analysis showed a significant difference in 84 LUAD patients grouped by low and high FAM83A expression. $^{*}P < 0.05$, $^{**}P < 0.01$.

Table 2: Univariate and multivariate analyses for over survival in patients with LUAD.

Characteristics	Univariate analysis			Multivariate analysis		
	HR	95% CI	*P*-value	HR	95% CI	*P*-value
FAM83A	1.745	1.167-2.945	0.023	1.879	1.075-3.321	0.020

HR: hazard ratio; CI: confidence interval.

the basement membrane of the transwell in FAM83A knocked-down cells, compared with in the controls. The results indicated the promotion of invasion and migration of FAM83A in the lung cancer cell.

3.5. FAM83A Induced EMT in LUAD Cells. EMT can promote tumor invasion and is a vital step during the early stage of metastasis. In this study, the expression of EMT-related markers was observed in A549 and H1795 cells. FAM83A depletion resulted in upregulation of epithelial marker E-cadherin expression and downregulation of vimentin expression as a mesenchyme marker. Furthermore, the EMT-related transcription factor Snail was downregulated when FAM83A was depleted (Figures 5(a)–5(d)). The results indicated that FAM83A depletion impaired the EMT ability of LUAD cells.

4. Discussion

In the present study, high expression of FAM83A was observed in LUAD tissues and it was noticed that FAM83A could affect tumor biological characteristics including cell proliferation, invasion, and metastasis. FAM83A overexpression was associated with advanced clinical and pathological features in LUAD patients. These findings recommended FAM83A as a LUAD oncogene and a potential biomarker for the diagnosis and prognosis of LUAD.

Similar to the results of TCGA database bioinformatics analysis, the previous studies showed an increase in

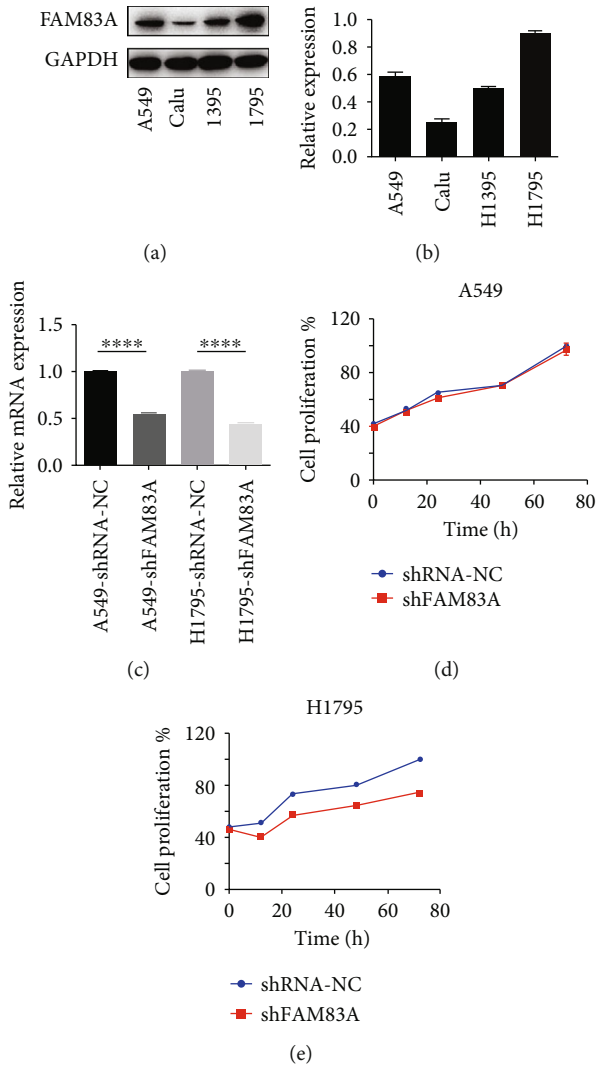

Figure 3: FAM83Apromoted proliferation of LUAD cells. (a, b) Western blotting analysis showed that FAM83A levels were higher in A549 and H1795 cells. (c) The reverse transcription-polymerase chain reaction (RT-PCR) assay demonstrated that A549 and H1795 cells transfected with FAM83A lentivirus (A549/H1795-shFAM83A), showed less FAM83A RNA expressions. (d) The cell proliferation assay showed no differences between A549-shFAM83A and A549-shRNA-NC cells at each time point. (e) The cell proliferation assay showed significant differences between H1795-shFAM83A and H1795-shRNA-NC cells. $^{***}P < 0.001$, $^{****}P < 0.0001$.

FAM83A expression in LUAD patients [18, 19]. Immunohistochemical staining confirmed that FAM83A expression was increased in LUAD tissue at the protein level. The results allayed the suspicion of whether FAM83A expression was increased at the mRNA and protein levels, as mRNA expression is not always coincident with protein expression [22].

It is well known that FAM83A plays an important role in regulating cell proliferation, differentiation, and invasion. Its role in some tumors has also been well investigated. Lee et al. reported that overexpression of FAM83A in breast cancer promoted cell proliferation and invasion [23]. Chen et al. found that overexpression of FAM83A markedly increased, whereas inhibition of FAM83A decreased cell proliferation in an in-vivo mouse model of pancreatic cancer [24]. The phosphorylation of FAM83A, downstream of EGFR, and upstream of ERK might activate the PI3K/AKT and MAPK signaling pathways, promoting the proliferation, differentiation, apoptosis, and invasion of cells [25, 26]. In the present study, depletion of FAM83A expression inhibited the proliferation, migration, and invasion of lung adenocarcinoma cells. Interestingly, the proliferation capacity of A549 cells exhibited a significant decreasing trend after FAM83A depletion. A possible reason might be a rather limited FAM83A overexpression in A549 cells compared to the H1795 cells. Consequently, the effectiveness of FAM83A knockdown by shRNA remained obscure. A recent study that detected FAM83A expression in nine adenocarcinoma cell lines including A549 cells was detected by the study of Zhou et al. High expression of FAM83A in some cell lines and relatively low expression in A549 cells were observed [27].

EMT is an essential process that promotes adherent epithelial cell movement. EMT can enhance cell mobility and promote tumor progression, and affect cancer features, especially invasion and metastasis [28–31]. In the current study,

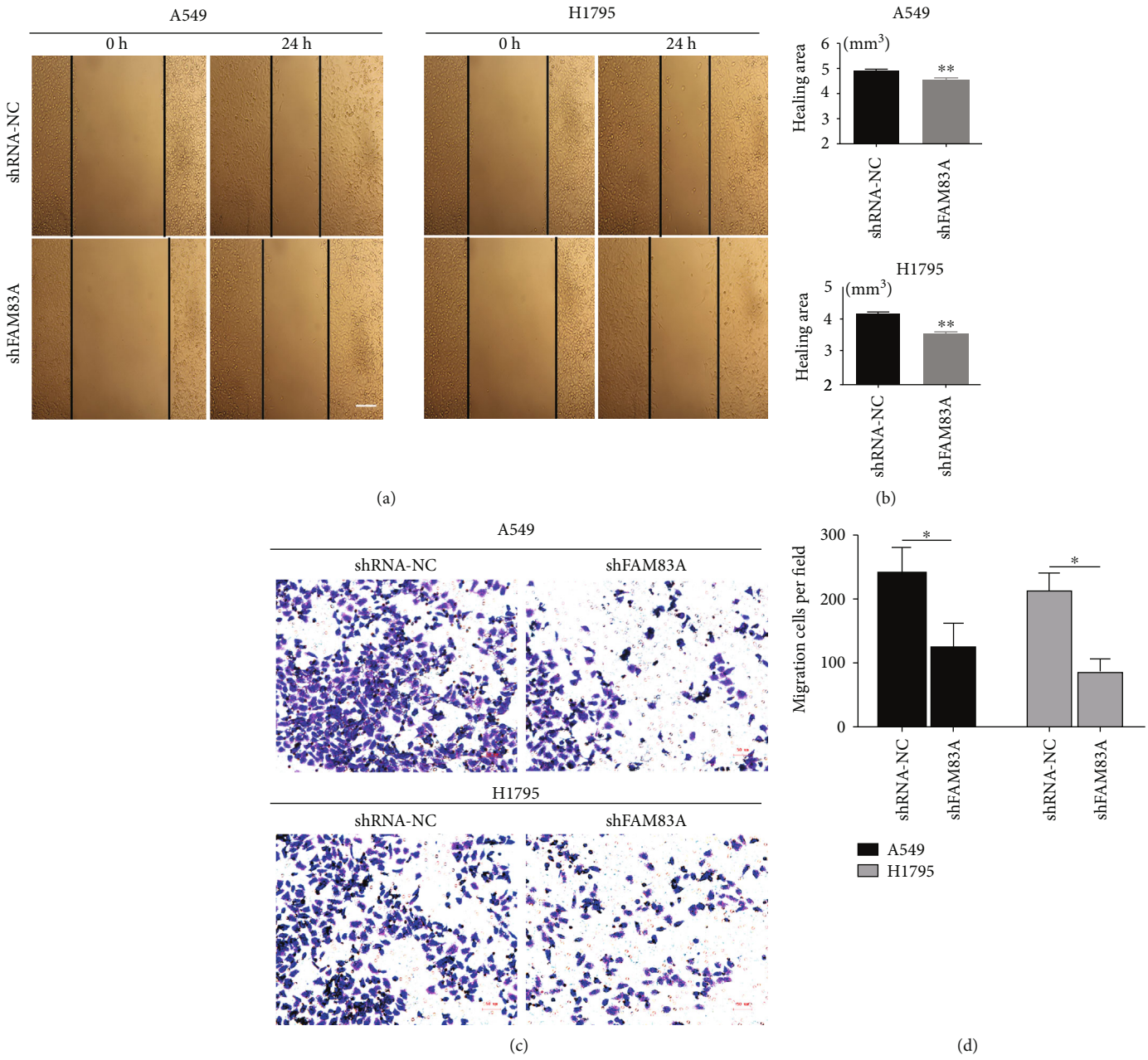

Figure 4: FAM83A promoted LUAD cell migration ability. (a, b) The wound-healing assay showed significantly larger healing area in A549-shFAM83A and H1795-shFAM83A cells. (c, d) The transwell cell migration assay showed that in A549-shFAM83A and H1795-shFAM83A, more cells passed through the basement membrane. $^{**}P < 0.01$, $^{***}P < 0.001$.

it was found that FAM83A depletion resulted in the absence of mesenchymal markers, indicating that FAM83A was involved in LUAD EMT processes. In addition, it was observed that under-expression of FAM83A reduced Snail expression, suggesting that FAM83A might regulate the EMT phenotype by inhibiting Snail expressions. Previous studies have shown that constitutive activation of the PI3K/AKT signaling cascade was closely correlated with Snail upregulation and diverse tumor cell metastasis [32–37]. Therefore, investigating whether FAM83A activates Snail and regulates EMT through the PI3K/AKT pathway is worth further studies.

The clinical significance of FAM83A in some cancer types such as breast cancer has been well studied [23]. There is convincing evidence that FAM83A is also related to the prognosis of lung cancer [15]. In the present study, the bioinformatics analysis demonstrated that overexpression of FAM83A was correlated with poor patient survival. Furthermore, immunohistochemical experiments revealed an increase in staining of FAM83A expression in stage III and IV patients, where FAM83A overexpression was positively associated with disease stage and lymph node classification. The results indicated that high FAM83A expression was related to advanced clinical and pathological LUAD

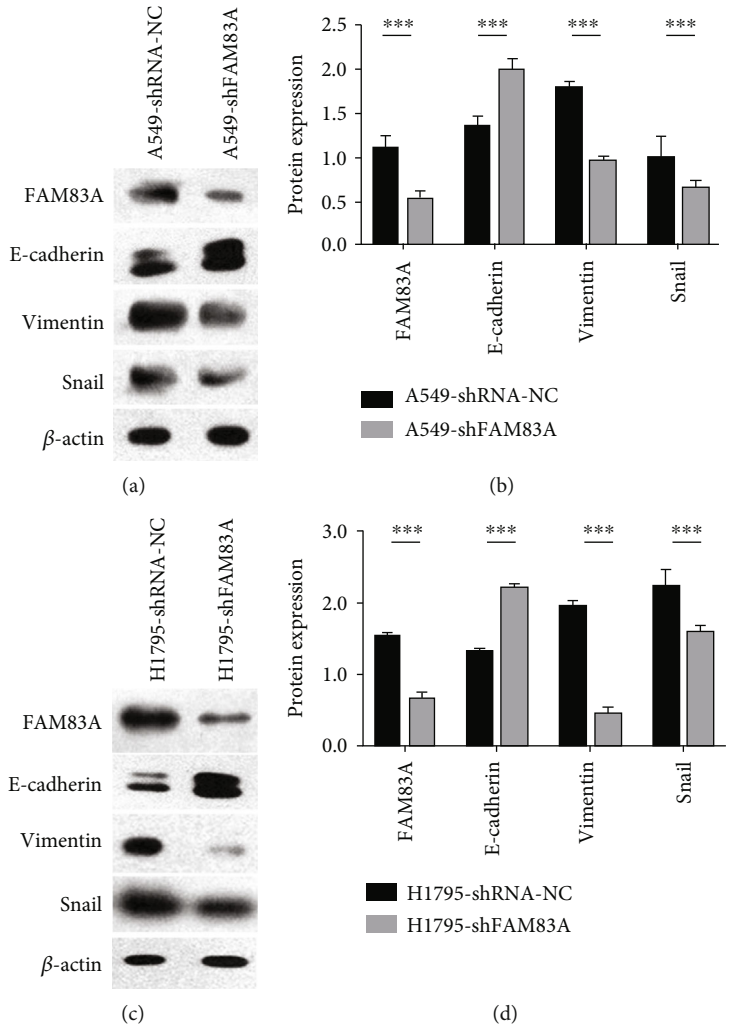

Figure 5: FAM83A induced EMT in LUAD cells. (a, b) Western blotting showed that FAM83A and E-cadherin expression increased, while Vimentin and Snail decreased when FAM83A was knocked down in A549 cells. (c, d) The same results were seen in H1795 cells. β-Actin was used as the loading control. $^{***}P < 0.001$.

characteristics. In breast cancer, FAM83A regulates the proliferation and invasion of cancer cells through the PI3K/AKT pathway. Inhibition of related kinases on this pathway can block the regulator effects of FAM83A on breast cancer [23, 37].

In the present study, the molecular mechanism of FAM83A in the regulation of proliferation, invasion, and EMT was evaluated. It is not clear whether the PI3K/AKT pathways are similarly involved in the regulatory mechanism of FAM83A in LUAD. As well as further studies are required to identify novel drug targets which may provide new therapeutic targets for LUAD. Therefore, it is suggested that these factors must be investigated and should be considered in future studies.

5. Conclusion

According to the results, at advanced stages of cancer, transcriptional expression as well as the protein level of FAM83A is increased in lung adenocarcinoma. Due to depletion of FAM83A, there is an increased expression of various types of markers, i.e., epithelial and mesenchyme. This overexpression shown the poor prognosis of FAM83A in lung cancer. In the future, FAM83A might be a potential new target for molecular targeted therapy of patients to its strong association with prognosis and expression of the disease.

Data Availability

The datasets used and/or analyzed during the current study available from the corresponding author on reasonable request.

Ethical Approval

All experimental protocols were approved by the Institutional Research Ethics Committee of The First Affiliated Hospital of USTC (No. 2019-P-017).

Conflicts of Interest

The authors declare that they have no competing interests.

Authors' Contributions

JZ and XL contributed to the conceptualization; JZ and MF contributed to the methodology; XL and MF were responsible for the software; DX, ZJ, and YF contributed to the validation; XL and WX contributed to the formal analysis; XL contributed to the investigation; XL and JZ were responsible for the resources; XL and MF contributed to the data curation; ZJ and XL contributed to the writing—original draft preparation; MF and ZJ contributed to the writing—review and editing; ZL, ZJ, and XL contributed to the visualization; ZJ contributed to the supervision; ZJ and NH contributed to the project administration. All authors have read and agreed to the published version of the manuscript. Xin Liu and Meng Fu are co-first authors and contributed equally to this work.

Acknowledgments

This work was supported by the National Natural Science Foundation of China (82000082), the Provincial Natural Science Foundation of Anhui (2008085QH353), and the Fundamental Research Funds for the Central University (WK9110000124).

References

[1] H. Brody, "Lung cancer," *Nature*, vol. 587, no. 7834, p. S7, 2020.

[2] S. Gao, N. Li, S. Wang et al., "Lung cancer in people's Republic of China," *Journal of Thoracic Oncology*, vol. 15, no. 10, pp. 1567–1576, 2020.

[3] H. Sung, J. Ferlay, R. L. Siegel et al., "Global cancer statistics 2020: GLOBOCAN estimates of incidence and mortality worldwide for 36 cancers in 185 countries," *CA: a Cancer Journal for Clinicians*, vol. 71, no. 3, pp. 209–249, 2021.

[4] H. Hu, F. Wang, M. Wang et al., "FAM83A is amplified and promotes tumorigenicity in non-small cell lung cancer via ERK and PI3K/Akt/mTOR pathways," *International Journal of Medical Sciences*, vol. 17, no. 6, pp. 807–814, 2020.

[5] T. Mitsudomi, S. Morita, Y. Yatabe et al., "Gefitinib versus cisplatin plus docetaxel in patients with non-small-cell lung cancer harbouring mutations of the epidermal growth factor receptor (WJTOG3405): an open label, randomised phase 3 trial," *The Lancet Oncology*, vol. 11, no. 2, pp. 121–128, 2010.

[6] M. Maemondo, A. Inoue, K. Kobayashi et al., "Gefitinib or chemotherapy for non-small-cell lung cancer with mutated EGFR," *The New England Journal of Medicine*, vol. 362, no. 25, pp. 2380–2388, 2010.

[7] Y. L. Wu, C. Zhou, C. K. Liam et al., "First-line erlotinib versus gemcitabine/cisplatin in patients with advanced *EGFR* mutation-positive non-small-cell lung cancer: analyses from the phase III, randomized, open-label, ENSURE study†," *Annals of Oncology*, vol. 26, no. 9, pp. 1883–1889, 2015.

[8] J. Y. Han, K. Park, S. W. Kim et al., "First-SIGNAL: first-line single-agent iressa versus gemcitabine and cisplatin trial in never-smokers with adenocarcinoma of the lung," *Journal of Clinical Oncology*, vol. 30, no. 10, pp. 1122–1128, 2012.

[9] G. R. Oxnard, M. E. Arcila, C. S. Sima et al., "Acquired resistance to EGFR tyrosine kinase inhibitors in EGFR-mutant lung cancer: distinct natural history of patients with tumors harboring the T790M mutation," *Clinical Cancer Research*, vol. 17, no. 6, pp. 1616–1622, 2011.

[10] C. Zhou, Y. L. Wu, G. Chen et al., "Erlotinib versus chemotherapy as first-line treatment for patients with advanced *EGFR* mutation-positive non-small-cell lung cancer (OPTIMAL, CTONG-0802): a multicentre, open-label, randomised, phase 3 study," *The Lancet Oncology*, vol. 12, no. 8, pp. 735–742, 2011.

[11] K. S. Thress, C. P. Paweletz, E. Felip et al., "Acquired *EGFR* C797S mutation mediates resistance to AZD9291 in non -small cell lung cancer harboring *EGFR* T790M," *Nature Medicine*, vol. 21, no. 6, pp. 560–562, 2015.

[12] C. A. Bartel, N. Parameswaran, R. Cipriano, and M. W. Jackson, "FAM83 proteins: fostering new interactions to drive oncogenic signaling and therapeutic resistance," *Oncotarget*, vol. 7, no. 32, pp. 52597–52612, 2016.

[13] L. J. Fulcher, P. Bozatzi, T. Tachie-Menson et al., "The DUF1669 domain of FAM83 family proteins anchor casein kinase 1 isoforms," *Science Signaling*, vol. 11, no. 531, 2018.

[14] A. M. Snijders, S. Y. Lee, B. Hang, W. Hao, M. J. Bissell, and J. H. Mao, "FAM83 family oncogenes are broadly involved in human cancers: an integrative multi-omics approach," *Molecular Oncology*, vol. 11, no. 2, pp. 167–179, 2017.

[15] S. Richtmann, D. Wilkens, A. Warth et al., "FAM83A and FAM83B as prognostic biomarkers and potential new therapeutic targets in NSCLC," *Cancers*, vol. 11, no. 5, 2019.

[16] Y. W. Zheng, Z. H. Li, L. Lei et al., "FAM83A promotes lung cancer progression by regulating the Wnt and Hippo signaling pathways and indicates poor prognosis," *Frontiers in Oncology*, vol. 5, no. 10, p. 180, 2020.

[17] H. Ji, H. Song, Z. Wang et al., "FAM83A promotes proliferation and metastasis via Wnt/β-catenin signaling in head neck squamous cell carcinoma," *Journal of Translational Medicine*, vol. 19, no. 1, pp. 1–3, 2021.

[18] L. Liu, G. Liao, P. He et al., "Detection of circulating cancer cells in lung cancer patients with a panel of marker genes," *Biochemical and Biophysical Research Communications*, vol. 372, no. 4, pp. 756–760, 2008.

[19] Y. Li, X. Dong, Y. Yin et al., "BJ-TSA-9, a novel human tumor-specific gene, has potential as a biomarker of lung cancer," *Neoplasia*, vol. 7, no. 12, pp. 1073–1080, 2005.

[20] Z. Fengrui, W. Xin, L. Fang, M. Qingwei, and Y. Yan, "PD-L1 expression via ERK signaling and FAM83A/PD-L1 co-expression correlates with poor prognosis in lung adenocarcinoma," *International Journal of Clinical Oncology*, vol. 25, pp. 1612–1623, 2020.

[21] R. Shi, Z. Jiao, A. Yu, and T. Wang, "Long noncoding antisense RNA FAM83A-AS1 promotes lung cancer cell progression by increasing FAM83A," *Journal of Cellular Biochemistry*, vol. 120, no. 6, pp. 10505–10512, 2019.

[22] J. Li, W. Zhao, R. Akbani et al., "Characterization of human cancer cell lines by reverse-phase protein arrays," *Cancer Cell*, vol. 31, no. 2, pp. 225–239, 2017.

[23] S. Y. Lee, R. Meier, S. Furuta et al., "FAM83A confers EGFR-TKI resistance in breast cancer cells and in mice," *The Journal of Clinical Investigation*, vol. 122, no. 9, pp. 3211–3220, 2012.

[24] S. Chen, J. Huang, Z. Liu, Q. Liang, N. Zhang, and Y. Jin, "FAM83A is amplified and promotes cancer stem cell-like traits and chemoresistance in pancreatic cancer," *Oncogenesis*, vol. 6, no. 3, p. 300, 2017.

[25] P. J. Liu, Y. H. Chen, K. W. Tsai et al., "Involvement of micro RNA-1-FAM83A axis dysfunction in the growth and motility of lung cancer cells," *International Journal of Molecular Sciences*, vol. 21, no. 22, pp. 1–17, 2020.

[26] C. A. Bartel, M. W. Jackson, and M. W. Jackson, "HER2-positive breast cancer cells expressing elevated FAM83A are sensitive to FAM83A loss," *PLoS One*, vol. 12, no. 5, 2017.

[27] F. Zhou, J. Geng, S. Xu et al., "FAM83A signaling induces epithelial-mesenchymal transition by the PI3K/AKT/Snail pathway in NSCLC," *Aging (Albany NY)*, vol. 11, no. 16, pp. 6069–6088, 2019.

[28] D. Hanahan and R. A. Weinberg, "Hallmarks of cancer: the next generation," *Cell*, vol. 144, pp. 646–674, 2011.

[29] F. Bunz, "EMT and back again: visualizing the dynamic phenotypes of metastasis," *Cancer Research*, vol. 80, no. 2, pp. 153–155, 2020.

[30] I. Pastushenko and C. Blanpain, "EMT transition states during tumor progression and metastasis," *Trends in Cell Biology*, vol. 29, no. 3, pp. 212–226, 2019.

[31] N. M. Aiello and Y. Kang, "Context-dependent EMT programs in cancer metastasis," *The Journal of Experimental Medicine*, vol. 216, no. 5, pp. 1016–1026, 2019.

[32] X. H. F. Zhang, X. Jin, S. Malladi et al., "Selection of bone metastasis seeds by mesenchymal signals in the primary tumor stroma," *Cell*, vol. 154, no. 5, pp. 1060–1073, 2013.

[33] M. J. Barberà, I. Puig, D. Domínguez et al., "Regulation of Snail transcription during epithelial to mesenchymal transition of tumor cells," *Oncogene*, vol. 23, no. 44, pp. 7345–7354, 2004.

[34] W. Wen, J. Ding, W. Sun et al., "Cyclin G1-mediated epithelial-mesenchymal transition via phosphoinositide 3-kinase/Akt signaling facilitates liver cancer progression," *Hepatology*, vol. 55, no. 6, pp. 1787–1798, 2012.

[35] A. W. Ke, G. M. Shi, J. Zhou et al., "CD151 amplifies signaling by integrin $\alpha 6\beta 1$ to PI3K and induces the epithelial–mesenchymal transition in HCC cells," *Gastroenterology*, vol. 140, no. 5, pp. 1629–1641.e15, 2011.

[36] H. Hamidi and J. Ivaska, "Every step of the way: integrins in cancer progression and metastasis," *Nature Reviews. Cancer*, vol. 18, no. 9, pp. 533–548, 2018.

[37] S. Grant, "FAM83A and FAM83B: candidate oncogenes and TKI resistance mediators," *The Journal of Clinical Investigation*, vol. 122, pp. 3048–3051, 2012.

Hindawi
Journal of Oncology
Volume 2022, Article ID 3283343, 35 pages
https://doi.org/10.1155/2022/3283343

Research Article

Qualification of Necroptosis-Related lncRNA to Forecast the Treatment Outcome, Immune Response, and Therapeutic Effect of Kidney Renal Clear Cell Carcinoma

Yisheng Yin,[1,2] Yiqun Tian,[1,2] Xiang Ren,[1,2] Jing Wang,[1,2] Xing Li,[1,2] and Xiaoyong Zeng[1,2]

[1]*Department of Urology, Tongji Hospital, Tongji Medical College, Huazhong University of Science and Technology, Wuhan, Hubei Province 430030, China*
[2]*China Institute of Urology of Hubei Province, Wuhan, Hubei Province 430030, China*

Correspondence should be addressed to Xiaoyong Zeng; miwai@163.com

Received 3 August 2022; Revised 16 August 2022; Accepted 24 August 2022; Published 3 October 2022

Academic Editor: Muhammad Muddassir Ali

Background. Kidney renal clear cell carcinoma (KIRC) is considered as a highly immune infiltrative tumor. Necroptosis is an inflammatory programmed cell death associated with a wide range of diseases. Long noncoding RNAs (lncRNAs) play important roles in gene regulation and immune function. lncRNA associated with necroptosis could systematically explore the prognostic value, regulate tumor microenvironment (TME), etc. *Method*. The patients' data was collected from TCGA datasets. We used the univariate Cox regression (UCR) to select prediction lncRNAs that are related to necroptosis. Meanwhile, risk models were constructed using LASSO Cox regression (LCR). Kaplan–Meier (KM) analysis, accompanied with receiver operating characteristic (ROC) curves, was performed to assess the independent risk factors of different clinical characteristics. The evaluated factors are age, gender, disease staging, grade, and their related risk score. Databases such as Gene Ontology (GO), Kyoto encyclopedia of genes and genomes (KEGG), and Gene set enrichment analysis (GSEA) were used to search the probable biological characteristics that could influence the risk groups, containing signaling pathway and immue-related pathways. The single-sample gene set enrichment analysis (ssGSEA) was chosen to perform gene set variation analysis (GSVA), and the GSEABase package was selected to detect the immune and inflammatory infiltration profiles. The TIDE and I C_{50} evaluation were used to estimate the effectiveness of clinical treatment on KIRC. *Results*. Based on the above analysis, we have got a conclusion that patients who show high risk had higher immune infiltration, immune checkpoint expression, and poorer prognosis. We identified 19 novel prognostic necroptosis-related lncRNAs, which could offer opinions for a deeper study of KIRC. *Conclusion*. The risk model we constructed makes it possible to predict the prognosis of KIRC patients and offers directions for further research on the prognostication and treatment strategies for KIRC.

1. Introduction

Renal cell carcinoma (RCC) is a branch of urologic tumors that extensively occurred in the world. Studies have reported that RCC is the third occurred tumor among the urinary system, the incidence of RCC is next to prostate cancer and bladder cancer [1], and almost 30% of the patients were present with distant metastases when they were diagnosed [2]. The five-year survival rate of metastatic RCC (mRCC) is only 10%, worser than nonmetastatic RCC [3]. KIRC is the most frequent pathological subtype in adults and is responsible for 80%–90% of the RCC cases [1]. In most patients with KIRC, proper surgical method remains the preferred treatment. However, the tumor that is not sensitive to chemotherapy and radiotherapy is more likely to metastasis or recur compared with other pathological RCCs [4]. Fortunately, recent studies have demonstrated that KIRC is sensitive to immunotherapy and some big data on clinical

trials have proven its worth in KIRC [5]. KIRC has been reported to be linked to significant infiltration of immune cells, and the clinical outcomes differ based on the type of cell involved [6]. Thus, identifying the cells related to immune factors would prove helpful.

lncRNAs is one type of the transcribed noncoding RNAs (ncRNAs). The length of it was longer than 200 nucleotides and they are distributed widely in cells [7]. However, lncRNAs exhibited vital roles in multifarious functions of gene expression, such as transcription, chromatin organisation, and translation [8]. Recently, some studies reported that tumor-related lncRNAs could regulate the progression of cancer by affecting the tumor microenvironment (TME) [9], cell differentiation [10], and apoptosis [11]. In addition, lncRNAs could significantly influence the immune system, including immune cell infiltration and immune activation [12]. Some studies reported that the lncRNA LINK-A could downregulate antigen presentation by inactivating the PKA pathway [13]. Moreover, the clinical progression and prognosis of some tumors, including lung cancer, prostate cancer, and BC, are associated with dysfunction of lncRNAs [7]. For instance, the lncRNA HOXD-AS1 was found to have high expression in castration-resistant prostate cancer (CRPC) cells. The multiplication could be inhibited by knockdown of HOXD-AS1 and it could be sensitive to chemotherapy after knockdown. Therefore, HOXD-AS1 showed important role in cancer development [14].

With the development of bioinformatics, several studies have been published recently regarding signature construction based on lncRNAs to handle the therapeutic effect on patients with KIRC. For instance, Sun et al. constructed a 5-immune-related-lncRNA signature to distinguish whether KIRC patients prognosis is good or not. In addition, the study analyzed the relationship between lncRNA and mRNA to find out the behavior and relationship of these RNAs [15]. Cui et al. reported that seventeen autophagy-associated lncRNAs were successfully identified and a risk profile associated with KIRC prognosis was constructed. This feature is a valid prognostic indicator and not dependent on other features for patients with KIRC [16]. However, the prediction of lncRNAs associated with necroptosis in KIRC and their relationship with immune status has not been clearly described.

In recent years, there are many ways of cell death that have been discovered and via a number of different pathways, including apoptosis, necrosis, programmed necrosis, pyroptosis, iron death, and autophagy. Apoptosis, which is the well-known programmed cell death, had characteristic morphological change with a number of specific biochemical processes. Necrosis is the uncontrolled cellular death, which is often followed by spillage of the cellular contents into surrounding tissues. For the other forms of cell death, for example, pyroptosis is also a kind of programmed cell death with collateral damage (nuclear integrity is maintained) and autophagy, which is a mechanism for both killing stressed cells and to recycle cellular components. Necroptosis is a freshly detected mechanism of cell programmed death mediated by RIP1, MLKL, and RIP3 [17, 18]. More and more studies are available suggesting that necroptosis is caught up in various diseases, such as cardiovascular disease, cancers, and neuroinflammation [18–20]. Additionally, a recent study showed that necroptosis may boost the cancer metastasis and T cells death in tumors [21]. Necroptosis serves as one of the programmed cell death in the cell, it contains the features of necrosis combined with apoptosis, suggesting it might cause and enhance antitumor immunity of tumors [17]. Park et al. have found that the key regulatory genes in necroptosis could influence the therapeutic effect in non-small-cell lung cancer [22]. In alcoholic cirrhosis, RIPK3-mediated necroptosis was always associated with poor prognosis [23]. Nonetheless, how necroptosis affect the prognosis and inflammation mechanism in KIRC is not yet clear.

Here we established risk signatures to explore the connection between necroptosis-related lncRNAs (NRLs) and the prognosis of KIRC. In addition, we studied how NRLs influenced the tumor microenvironment (TME) and their drug sensitivity in KIRC. We have provided novel prognostic predictors and data for a clearer understanding of the immune infiltrates of necroptosis in patients with KIRC.

2. Materials and Methods

2.1. Data Availability. The patients' material and their related RNA sequencing data were downloaded from The Cancer Genome Atlas (TCGA) (https://cancergenome.nih.gov/) database. Transcribed RNA data were obtained from the fragments per kilobase million (FPKM) for our study. The lncRNAs genes were analyzed using the GENCODE project (https://www.gencodegenes.org/) [24]. Patients with unavailable survival information and incomplete data were excluded.

2.2. Identification of Genes Associated with Necroptosis. 67 mRNAs related to necroptosis were extracted for identification [25]. We performed the Pearson correlation coefficient analysis in R software (version 4.0.4) to determine the lncRNAs that has a relationship with the pyroptosis-related genes. A correlation coefficient ($|R|$) value larger than 0.5 defined that a strong correlation exist, and p value less than 0.01 was regarded as the difference was different. The protein–protein interaction (PPI) network of the necroptosis-related genes was analyzed using the Search Tool for the Retrieval of Interacting Genes (STRING) (https://string-db.org/). Thereafter, PPI network was observed by the Cytoscape software (version 3.7.1).

2.3. Qualification of the Necroptosis-Associated lncRNA Prognostic Signature. The association between NRLs expression and survival data was assessed by using UCR analysis to identify necrosis-associated lncRNAs. NRLs which has been found to have a significant relationship ($p < 0.05$) were chosen as the necroptosis-related lncRNAs for KIRC. Subsequently, LCR analysis with the 'glmnet' package was applied to establish a prediction model of possible genes. The following formula could be utilized to calculate risk score:

$$\begin{aligned}\text{Expression}_{\text{gene1}} &\times \text{Coefficient}_{\text{gene1}} + \text{Expression}_{\text{gene2}} \\ &\times \text{Coefficient}_{\text{gene2}} + \cdots + \text{Expression}_{\text{gene } n} \\ &\times \text{Coefficient}_{\text{gene } n}\end{aligned} \tag{1}$$

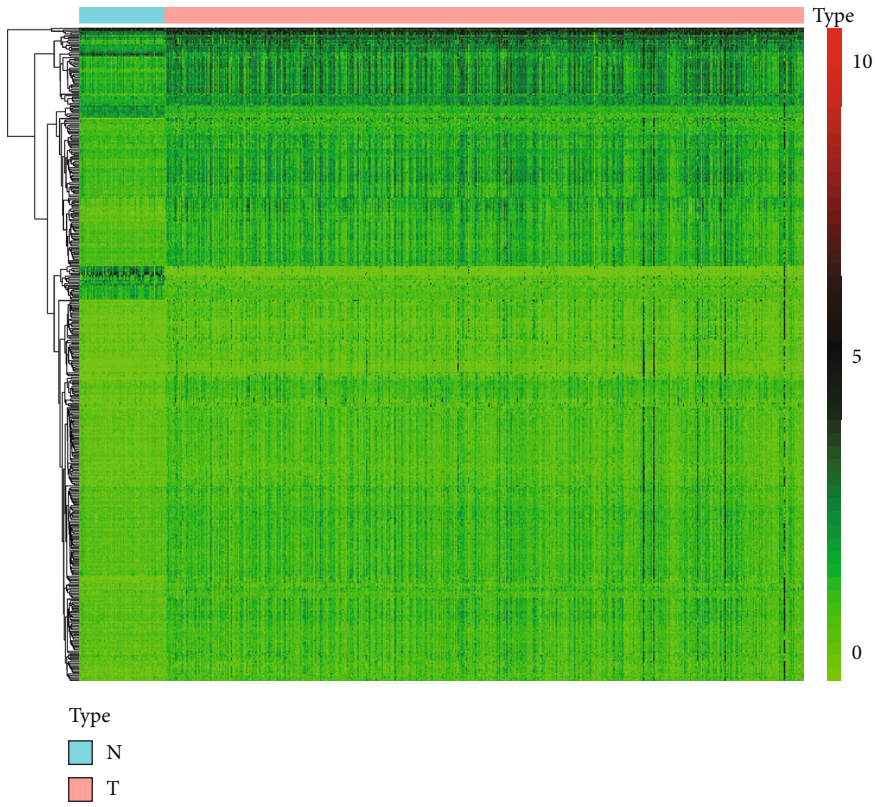

(a)

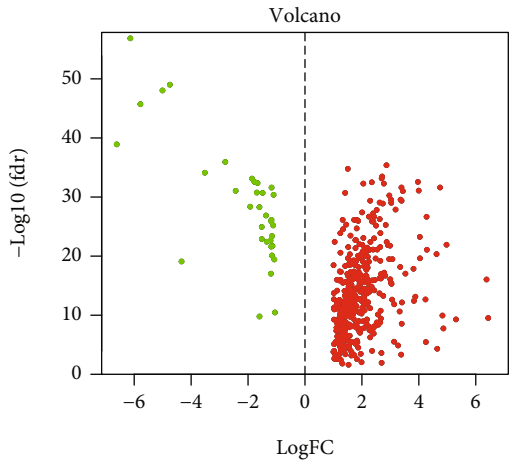

(b)

Figure 1: Continued.

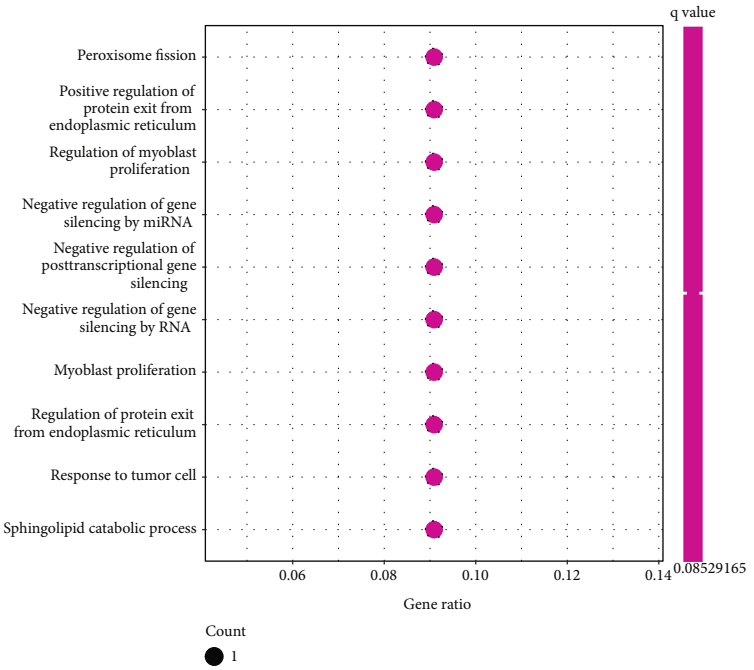

(c)

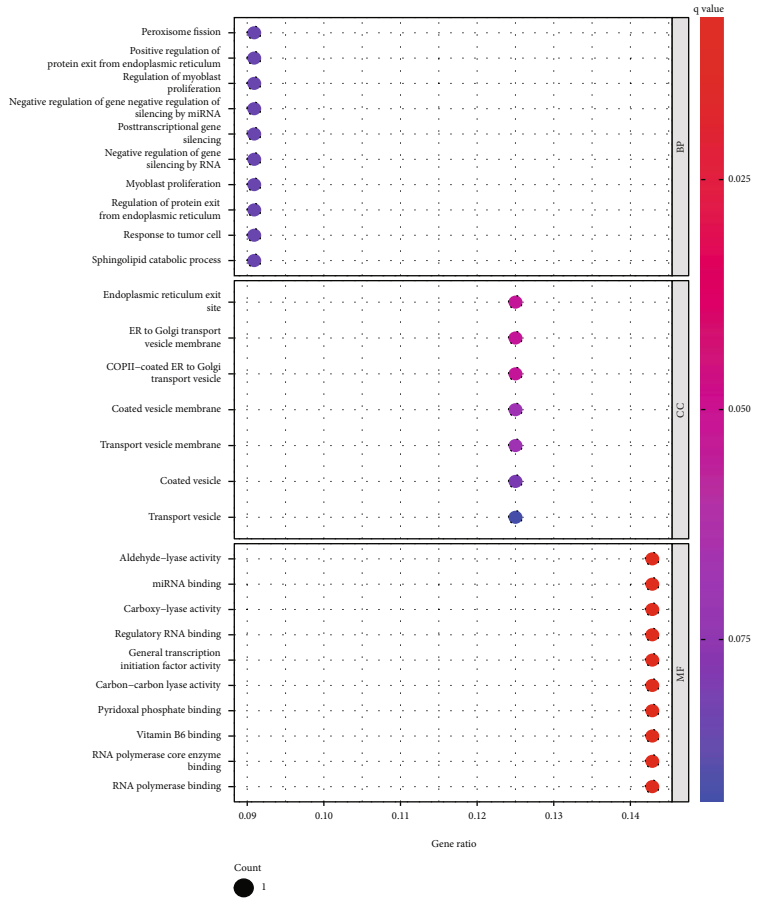

(d)

Figure 1: Identification of the necroptosis lncRNAs and analysition of its function. The distribution of necroptosis lncRNAs in lesions or regular tissues with heatmap in KIRC (a). Necroptosis lncRNAs expression level in Volcano (b). The pathway of necroptosis lncRNAs in KEGG (c). The biological function of necroptosis lncRNAs in GO (d).

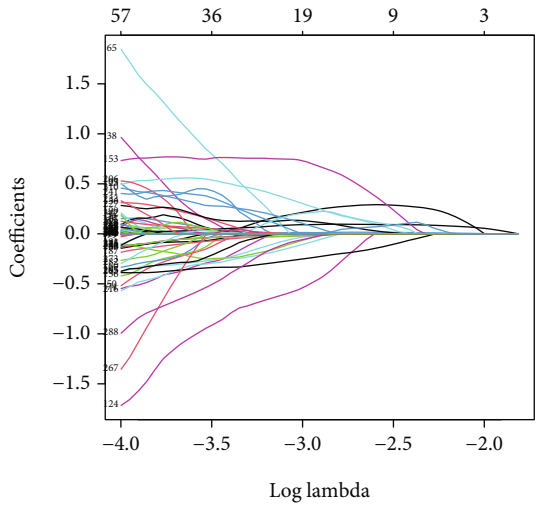

(a)

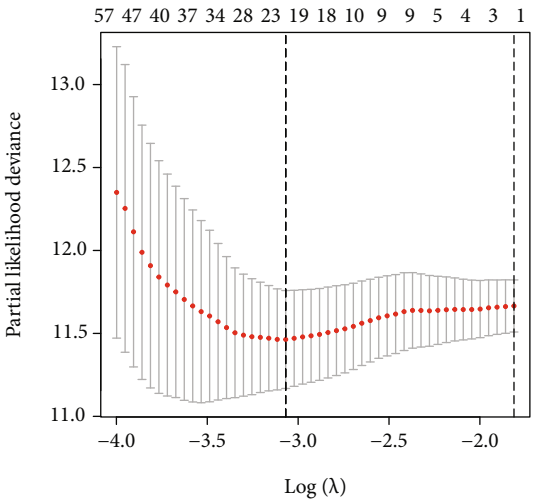

(b)

	p value	Hazard ratio
IGFL2–AS1	0.021	1.008 (1.001 – 1.014)
LINC01943	< 0.001	1.635 (1.391 – 1.923)
U62317.1	< 0.001	1.062 (1.042 – 1.082)
LASTR	< 0.001	1.189 (1.124 – 1.258)
LINC01126	0.001	1.522 (1.176 – 1.970)
AC007376.2	0.005	0.256 (0.100 – 0.658)
AC026401.3	< 0.001	1.229 (1.170 – 1.290)
MYOSLID	< 0.001	1.162 (1.091 – 1.238)
AC008050.1	< 0.001	0.265 (0.126 – 0.556)
AC025580.3	0.003	0.660 (0.499 – 0.872)
AL158212.3	0.038	0.735 (0.550 – 0.982)
ENTPD3–AS1	0.049	0.708 (0.501 – 0.999)
AC026992.1	0.019	0.623 (0.419 – 0.926)
UBE2Q1–AS1	< 0.001	2.436 (1.703 – 3.486)
APCDD1L–DT	< 0.001	1.174 (1.089 – 1.267)
AC007743.1	< 0.001	0.554 (0.422 – 0.727)
MIRLET7A1HG	0.022	0.305 (0.110 – 0.843)
AL162586.1	< 0.001	1.273 (1.155 – 1.403)
NARF–IT1	< 0.001	2.157 (1.571 – 2.963)

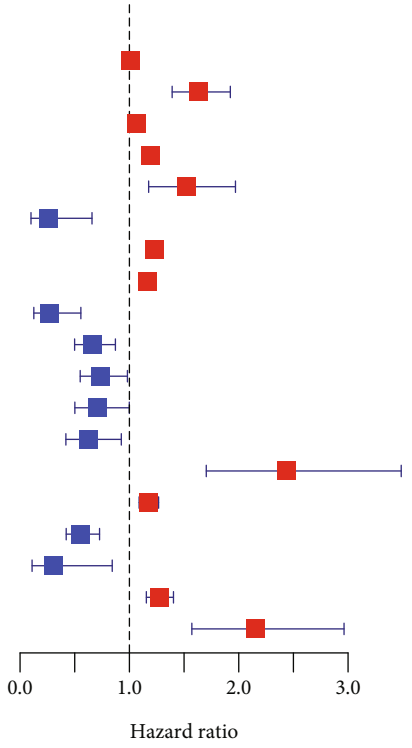

(c)

Figure 2: Continued.

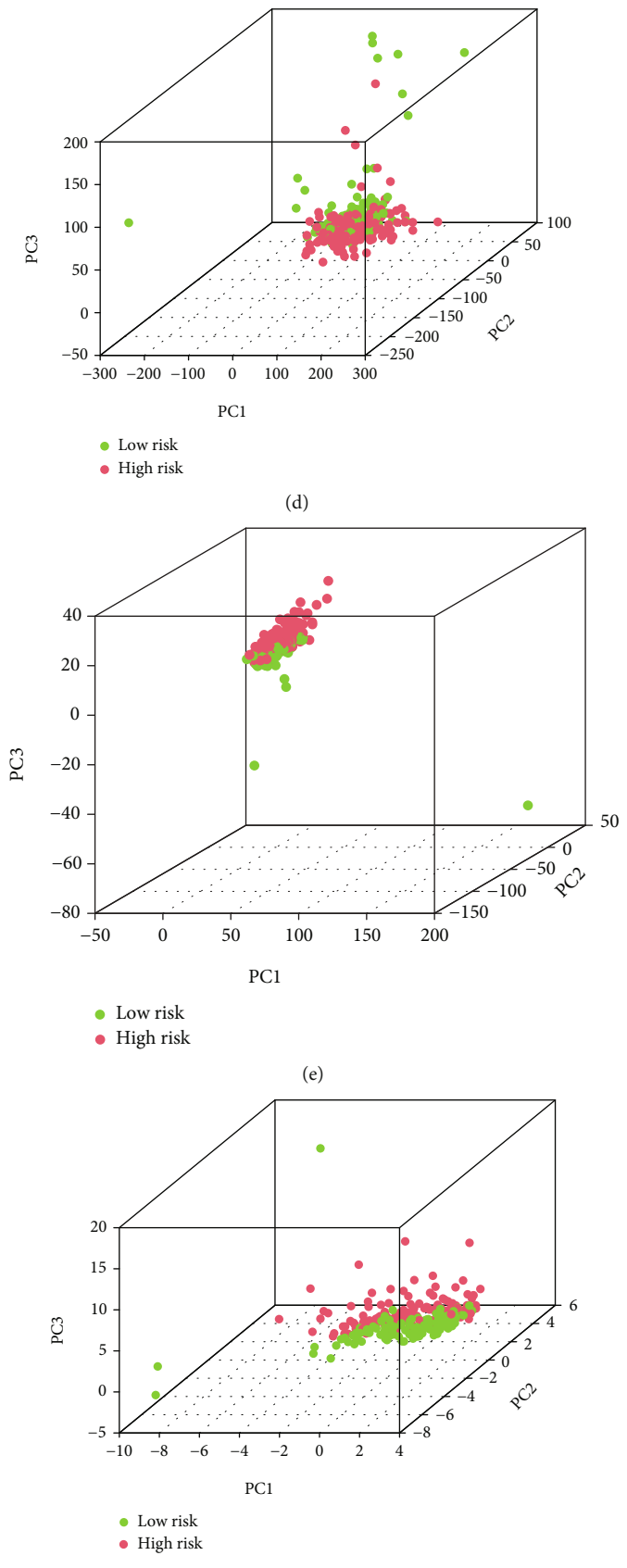

Figure 2: Construct the risk model of necroptosis related lncRNAs. The risk model built using LASSO analysis (a–c). The PCA analyses were performed to the complete gene set (d), necroptosis genes (e), and NRLs (f).

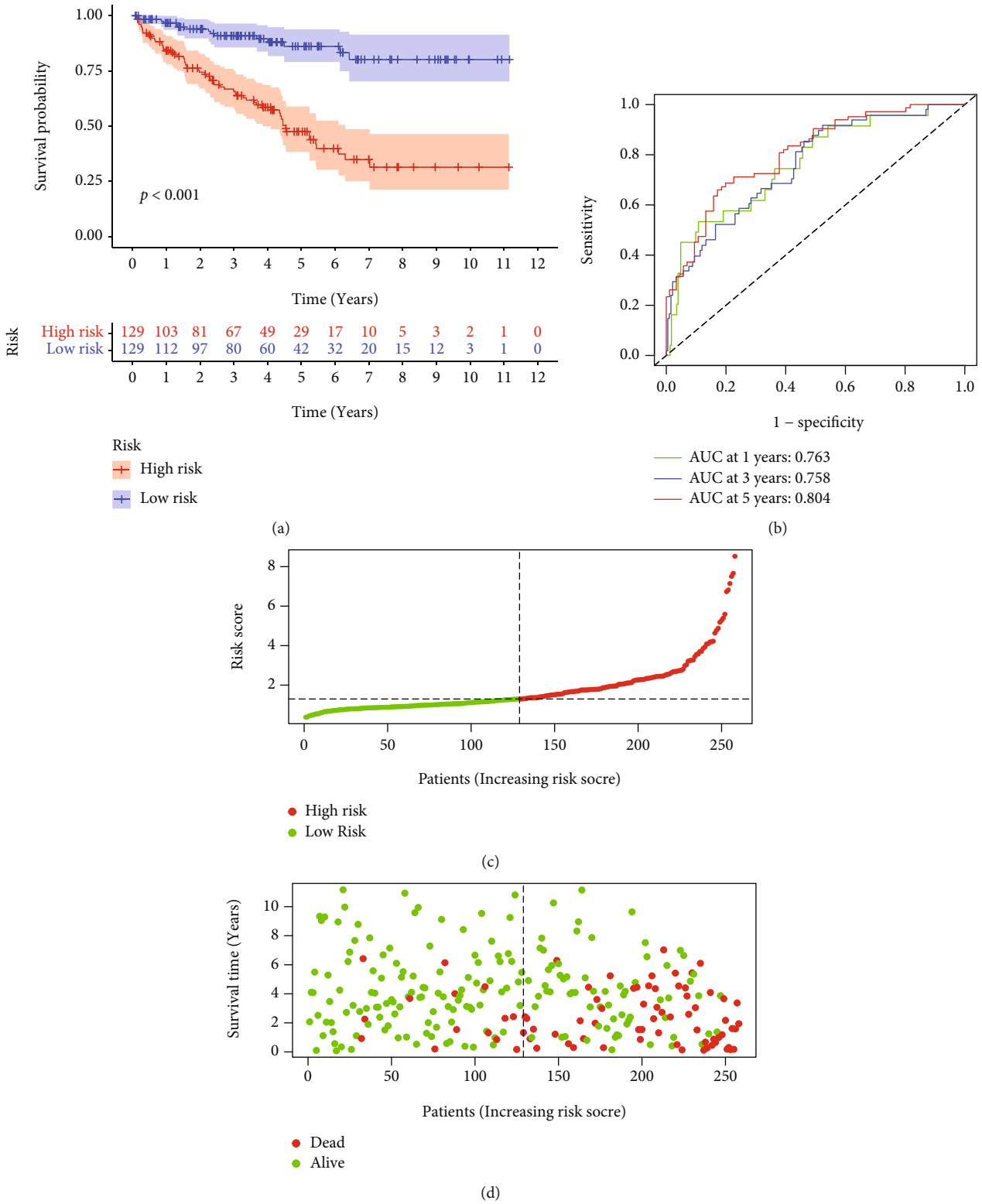

Figure 3: Continued.

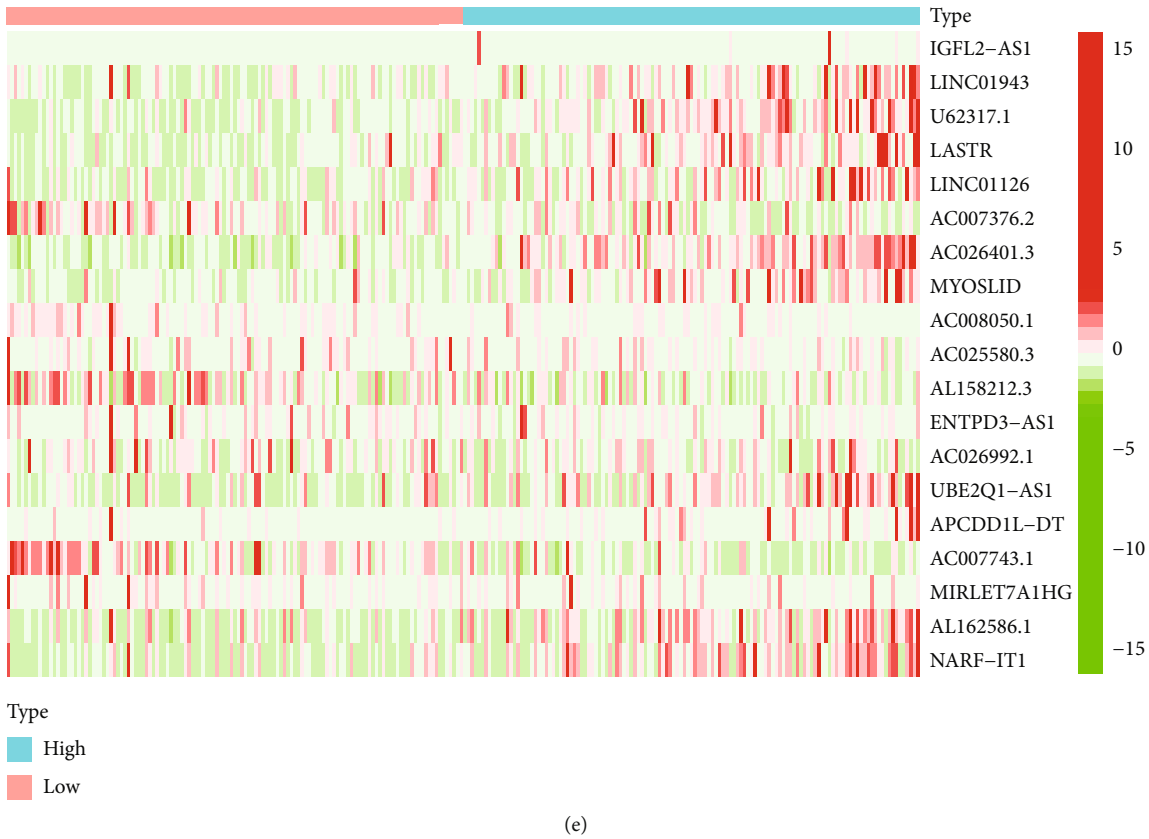

(e)

Figure 3: The risk predictive model of NRLs in KIRC. The differences of OS in the two groups (a). Time-dependent ROC curves (b). The risk score distribution of various groups (c). The survival status of patients in the two groups (d). The expression levels of 19 NRLs in risk models (e).

An individual risk score was assigned to each patient. Next, KIRC patients were separated as different risk groups using the median cut-off of risk score according to the risk model. Protective and risk prognostic factors were determined using the hazard ratios (HR) by the UCR and the multivariate Cox regression (MCR). The factor was considered risky when HR was >1 and protective when HR was <1.

2.4. Survival and ROC Analysis. We analyzed survival with the R packages survival and survminer, and the differences were distinguished via the KM analysis. We calculated whether our model for different overall survival (OS) is sensitive and specific using the package timeROC of R (version 4.0.4). In addition, we used timeROC to evaluate the independent risk factors of different clinical factors, including age, gender, stage, grade, and risk score.

2.5. Construction of Alignment Diagram and PCA of the Risk Genes. An alignment diagram was created on the basis of the NRLs with 'rms' package to evaluate the various years OS of KIRC patients. Plotting calibration curves was performed to estimate the accuracy of alignment charts. PCA was utilized to categorize the patients into groups according to the NRLs.

2.6. GO, KEGG, GSEA, and ssGSEA Analysis. For bioinformatics analysis, GO and KEGG were used to search possible biological characteristics that may influence the risk groups, including the changed signaling pathway. GSEA was used to explore the immune-related pathways. The ssGSEA was accompanied with the GSEABase package to explore the immune and inflammatory infiltration profiles.

2.7. Effectiveness of the Necroptosis-Related lncRNA Trademark in Clinical Trial. The effectiveness of immunotherapy on KIRC was estimated using TCIA. Relationship between the risk score and immunotherapy sensitive genes including PDL1, PD1, CTLA4, and TIGIT was also checked. The IC_{50} value of chemotherapeutic agents was selected to explore the response of KIRC to first-line targeted therapy based on the R package 'pRRophetic'.

3. Results

3.1. Identification of Genes Related to Necroptosis. We downloaded a total of 15,142 lncRNA expression profiles using the R package. We screened 67 necroptosis-related mRNAs analyzed using the Pearson correlation coefficient based on $|R|$ larger than 0.5 and p value smaller than 0.01 to identify NRLs. At last, 2,180 NRLs were exported. Following this, we performed "limma" R package to get 428 DE necroptosis-related lncRNAs difference from the tumor tissues and normal tissue samples (Figures 1(a) and 1(b)). Then we used GO and KEGG to search the potential

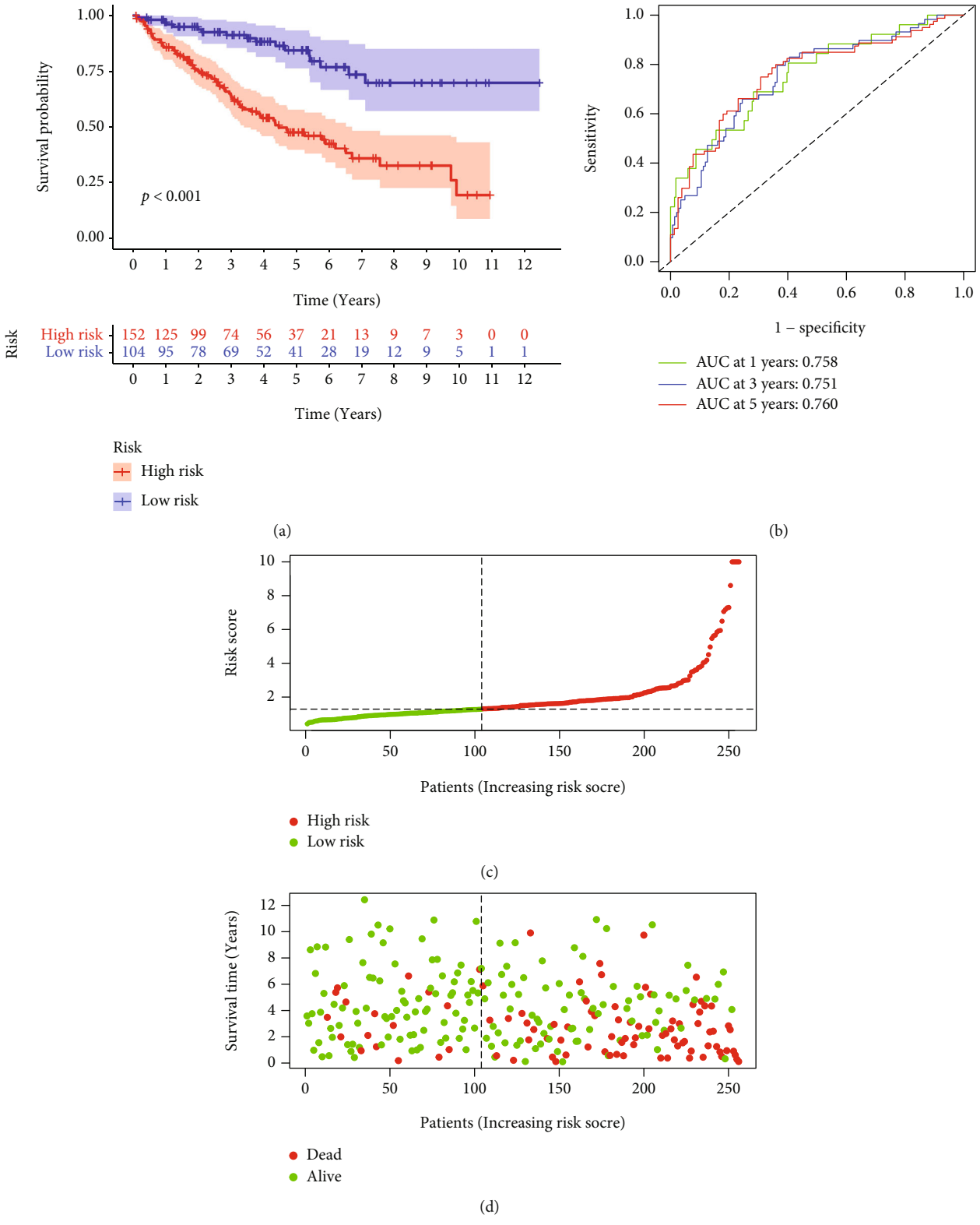

Figure 4: Continued.

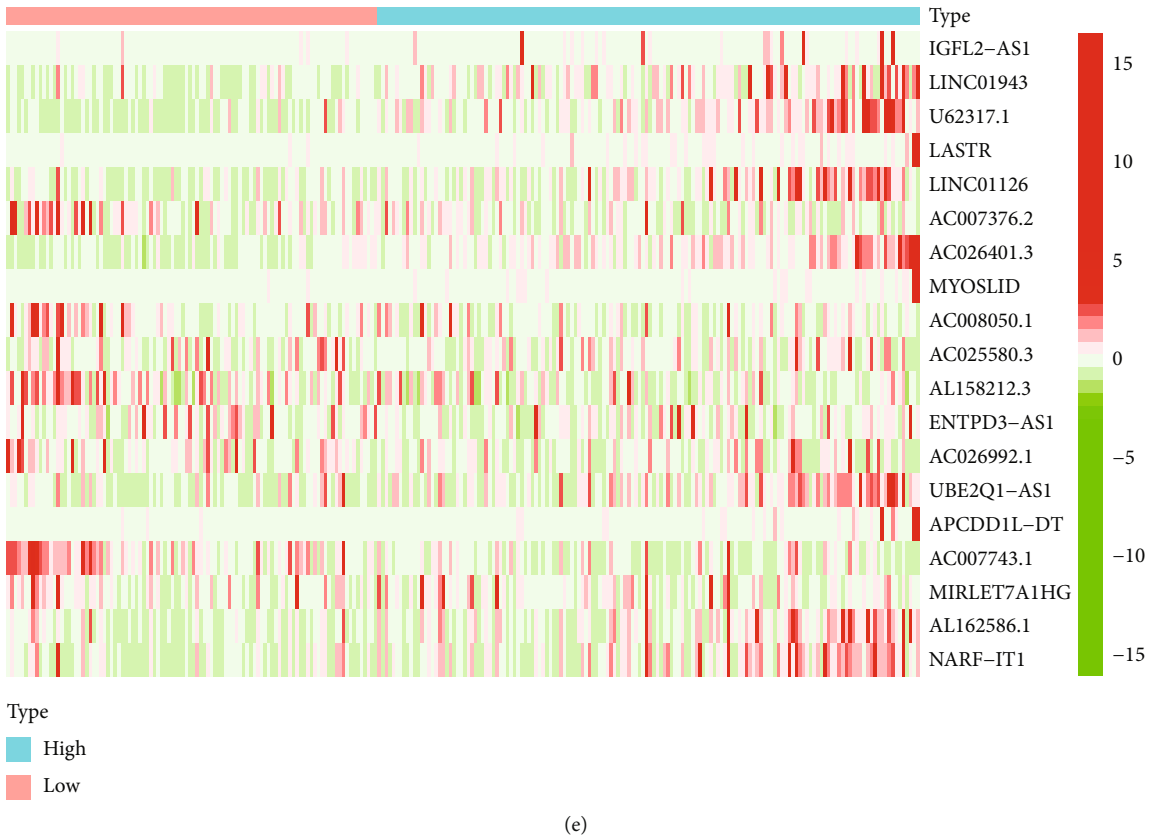

(e)

Figure 4: Affirmation of the risk model in test groups. The differences of OS in the two groups (a). Time-dependent ROC curves (b). The risk score distribution of various groups (c). The survival status of patients in the two groups (d). The expression levels of 19 NRLs in risk models (e).

biological characteristics and related pathways of the DE NRLs (Figures 1(c) and 1(d)).

3.2. Construction of the Prognostic Signature. Following this, UCR analysis was utilized to separate the lncRNAs that have prognosis functions from the DE NRLs, and 348 lncRNAs have significant association with OS in KIRC patients (Supplementary Table S1). From a total of 348 lncRNAs, we identified 19 lncRNAs by LCR to build up the prediction model (Figures 2(a) and 2(b)), the forest plot exhibited the corresponding HRs and 95% CIs of the 19 lncRNAs (IGFL2-AS, LINC01943, LINC01126, U62317.1, LASTR, MYOSLID, ENTPD3-AS1, UBE2Q1-AS1, NARF-IT1, APCDD1L-DT, MIRLET7A1HG, AC007376.2, AC0026401.3, AC008050.1, AC025580.3, AC026992.1, AC007743.1, AL162186.1, and AL158212.3). The results in Figure 2 indicate UBE2Q1-AS1 could be a risk factor of prediction in KIRC (Figure 2(c)). We separated 258 patients equally in the high and low-risk group according to the median. We performed the PCA to know the risk patterns in KIRC to estimate the effectiveness of the risk model (Figures 2(d)–2(f)). We can see that a risk model containing 19 lncRNAs had great efficiency to separate patients into different risk groups.

3.3. Survival Analysis and Proof of the NRLs Trademark. We took the KM survival analysis to figure out the OS of the risk signature. We found that the high-risk group was more likely to die than the other group ($p < 0.001$, Figure 3(a)). We also approved the accuracy of the risk model with the ROC curve. The AUC value of one-year OS was 0.763, while the value for three- and five-year OS was 0.758 and 0.804, respectively. These results indicated that the prediction risk model can precisely forecast the OS (Figure 3(b)). We also found that with an increase in the risk score, the high-risk group has more possibilities to die (Figures 3(c)–3(d)). The NRLs expression in the risk signature was also visualized (Figure 3(e)).

3.4. Affirmation of the NRLs Trademark. To confirm the truthfulness of our risk trademark in predicting the prognosis in KIRC, the KM survival analysis was further executed. Better OS was found in the low-risk groups (Figure 4(a)). The AUC values of ROC curve suggested the well predictivity of the risk trademark (Figure 4(b)). As the risk scores were increasing, the more patients were dead (Figures 4(c)–4(d)). NRLs expression was observed in the testing set (Figure 4(e)), we found different set expressed more in various groups.

3.5. Autonomous Prognostic Factors and Significance of the Prediction Model. Risk score was found to act as the autonomous factor according to UCR and MCR (HR = 1.614, 95% CI: 1.454–1.793 and HR = 1.341, 95% CI: 1.173 −1.534, respectively) Figures 5(a) and 5(b). In addition, the clinical characteristics, including age (AUC = 0.692), grade

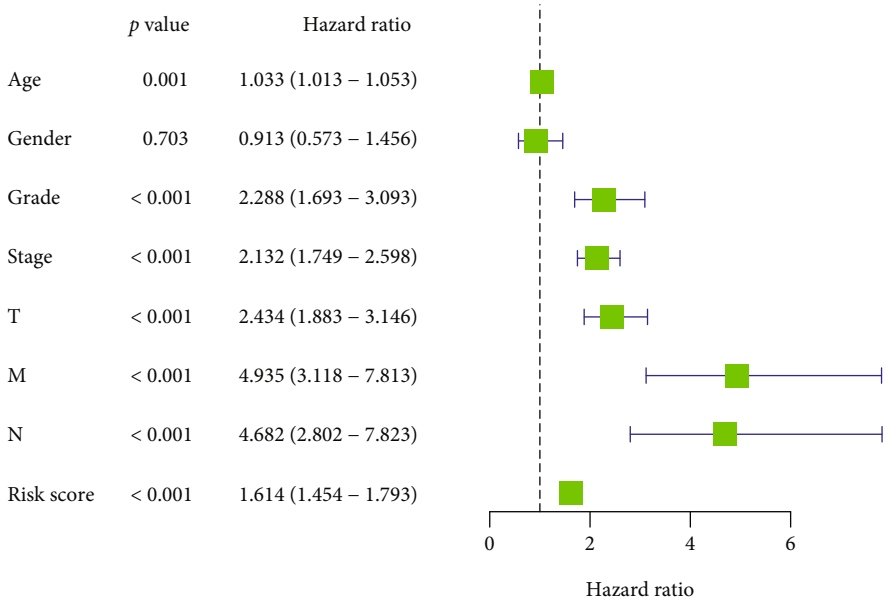

(a)

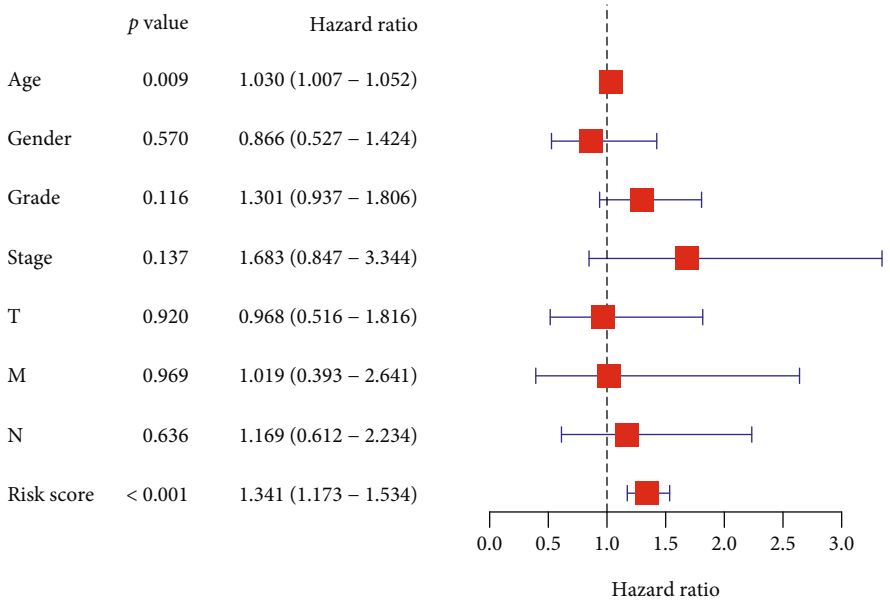

(b)

Figure 5: Continued.

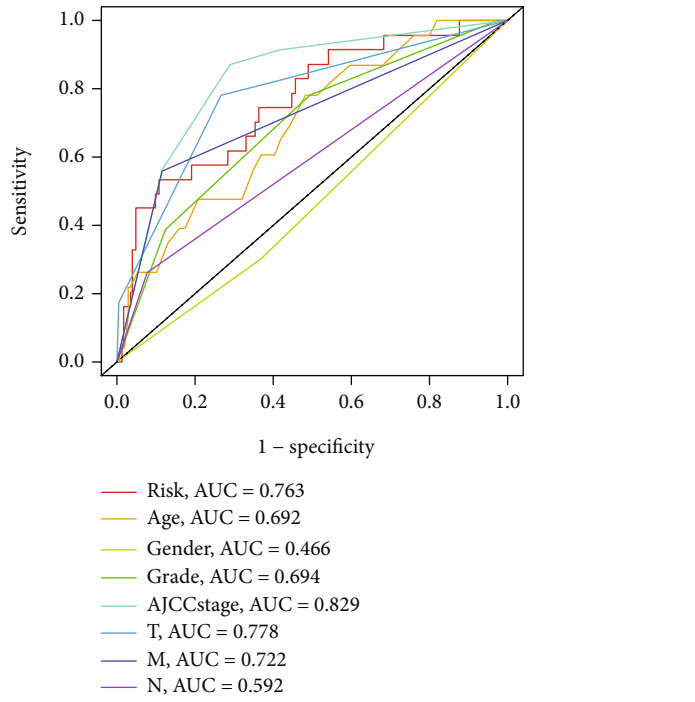

(c)

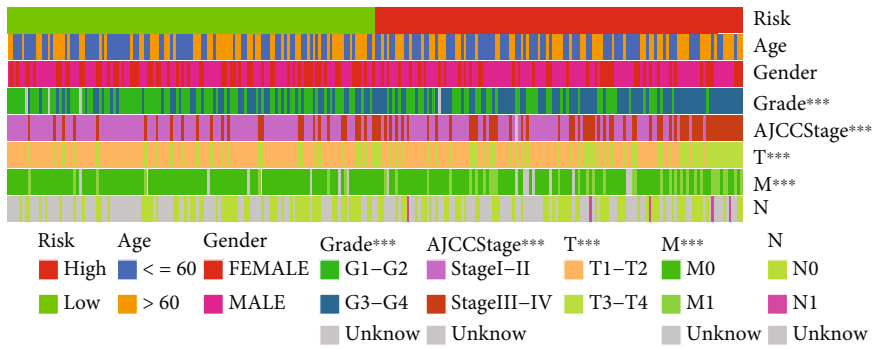

(d)

Figure 5: Continued.

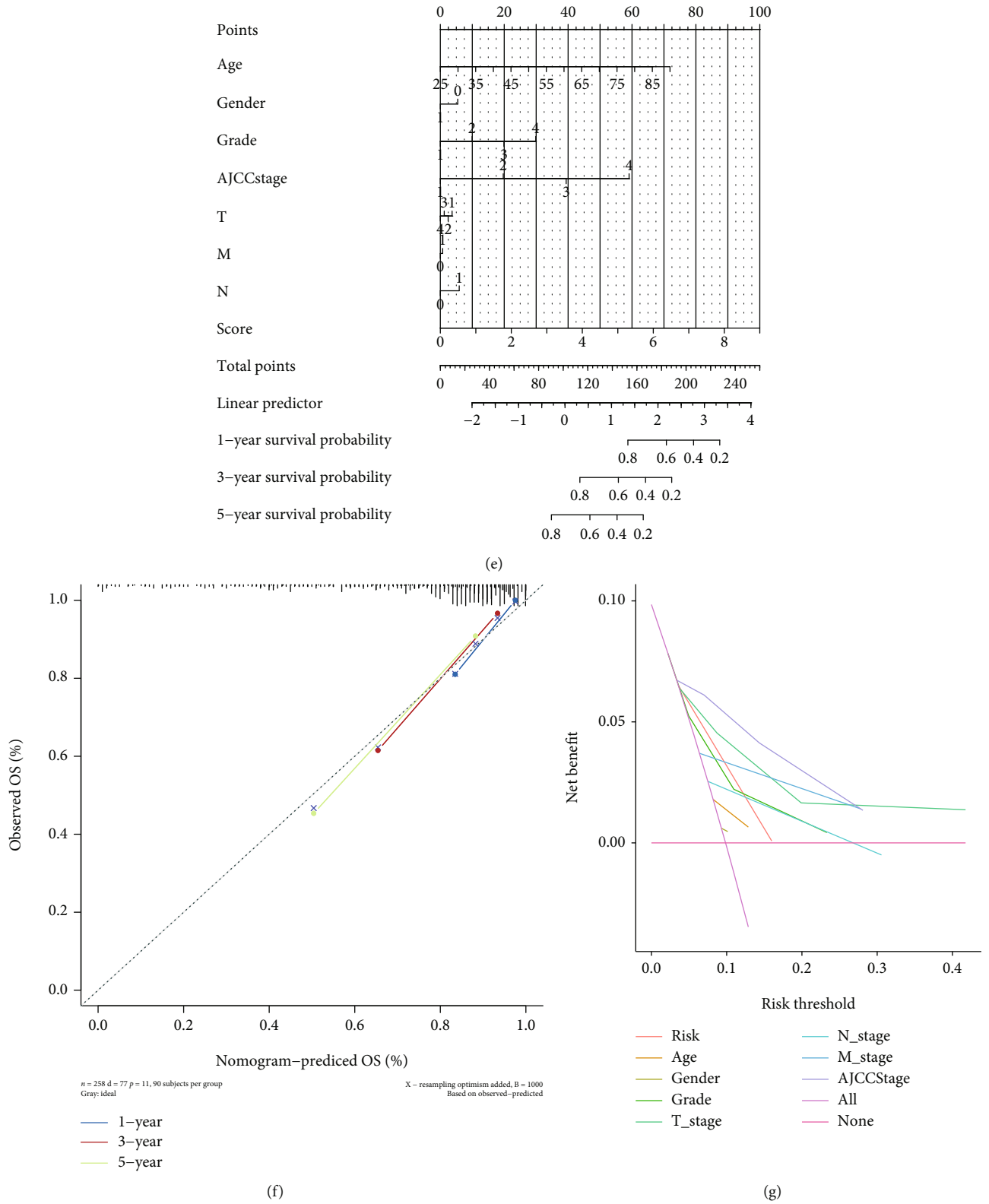

Figure 5: The clinical values of the necroptosis-related lncRNAs risk model. The connection of clinical elements and risk score by UCR and MCR (a, b). ROC curves of risk score, age, AJCC stage, gender, sex, and T, N, and M stages (c). The clinical features in two groups (d). The nomogram of clinical features to predict OS KIRC patients (e). The Calibration plots of the nomograms of OS in KIRC patients (f). The DCA analysis of clinical features (g).

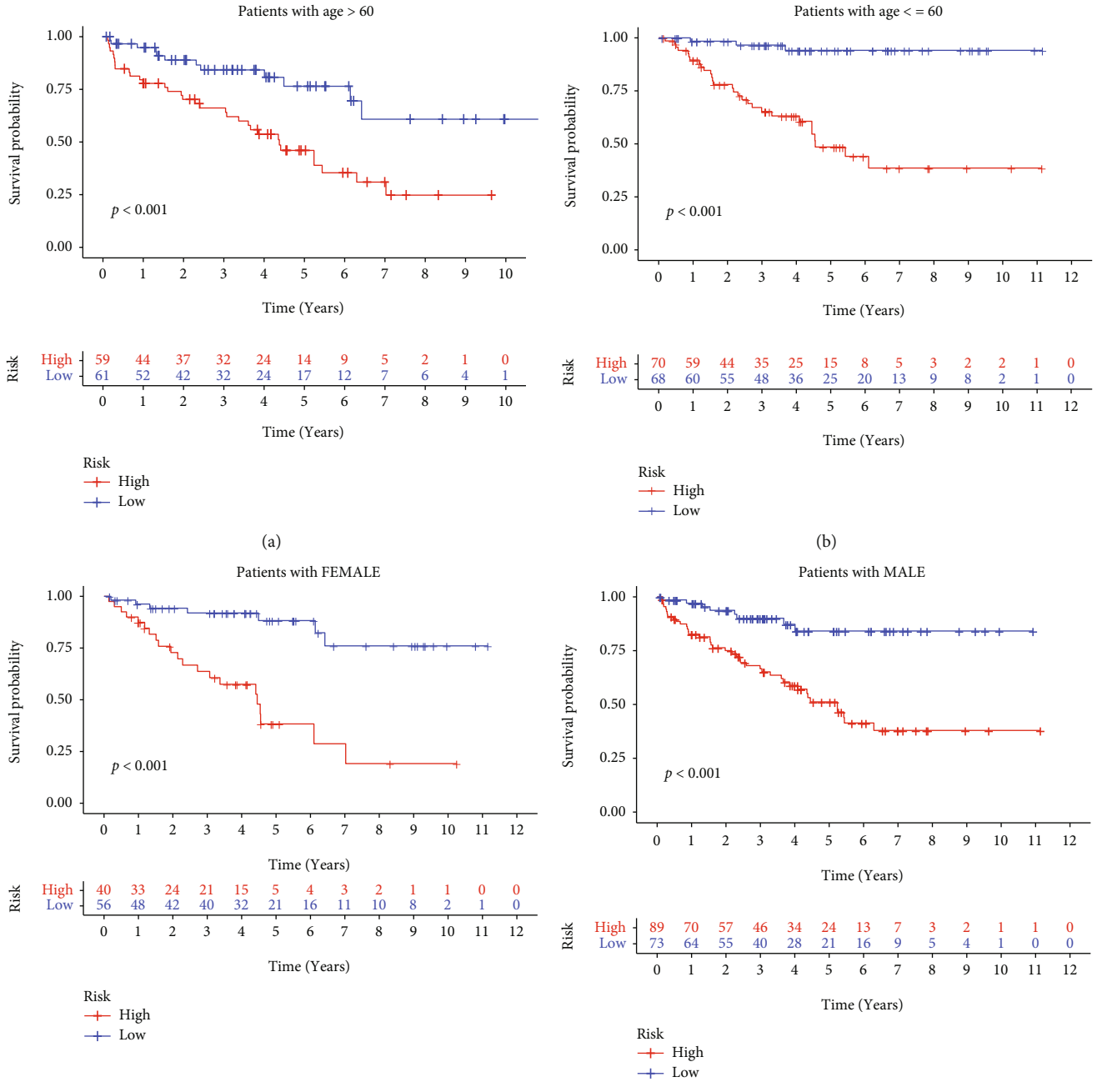

Figure 6: Continued.

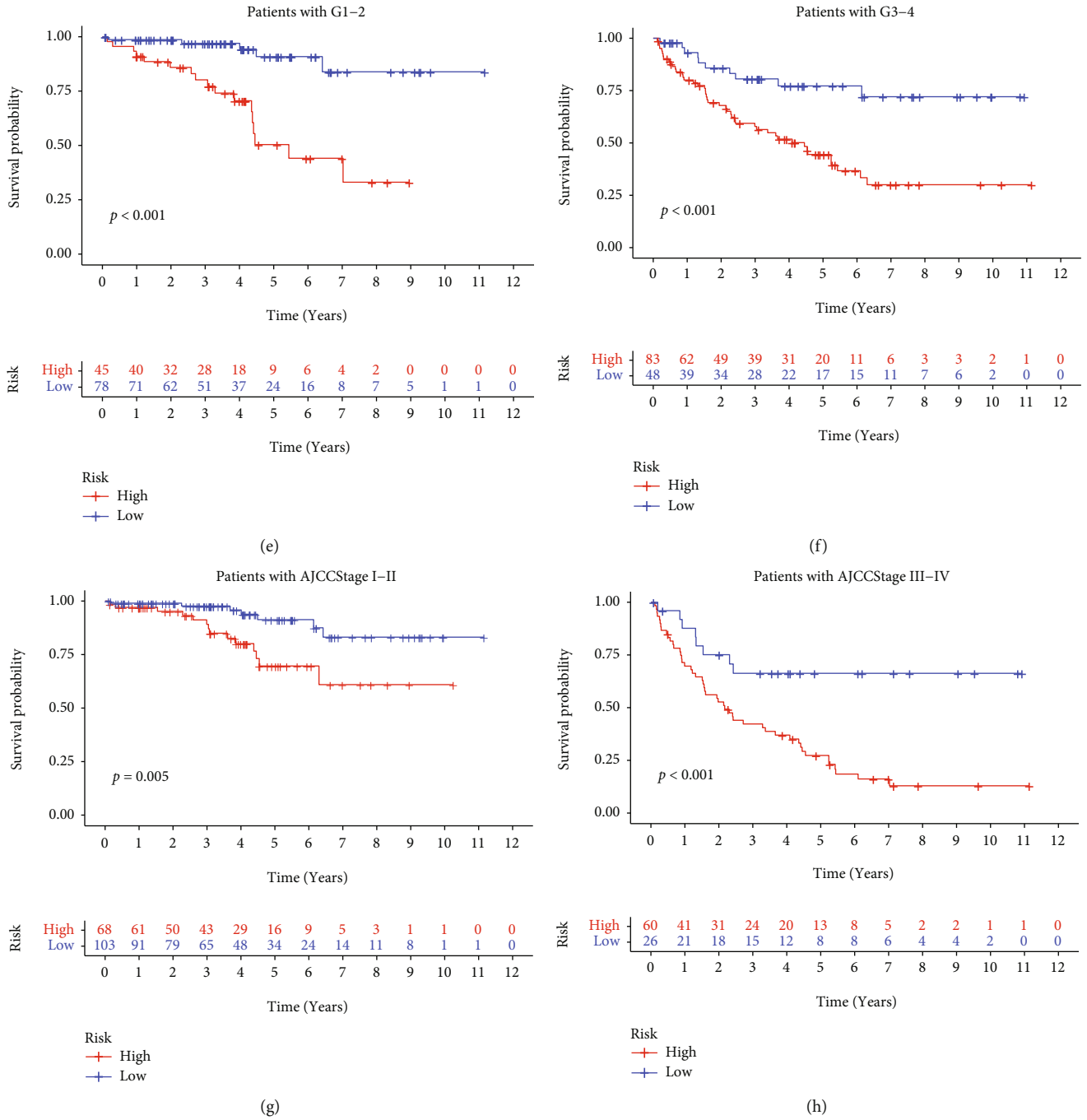

Figure 6: Continued.

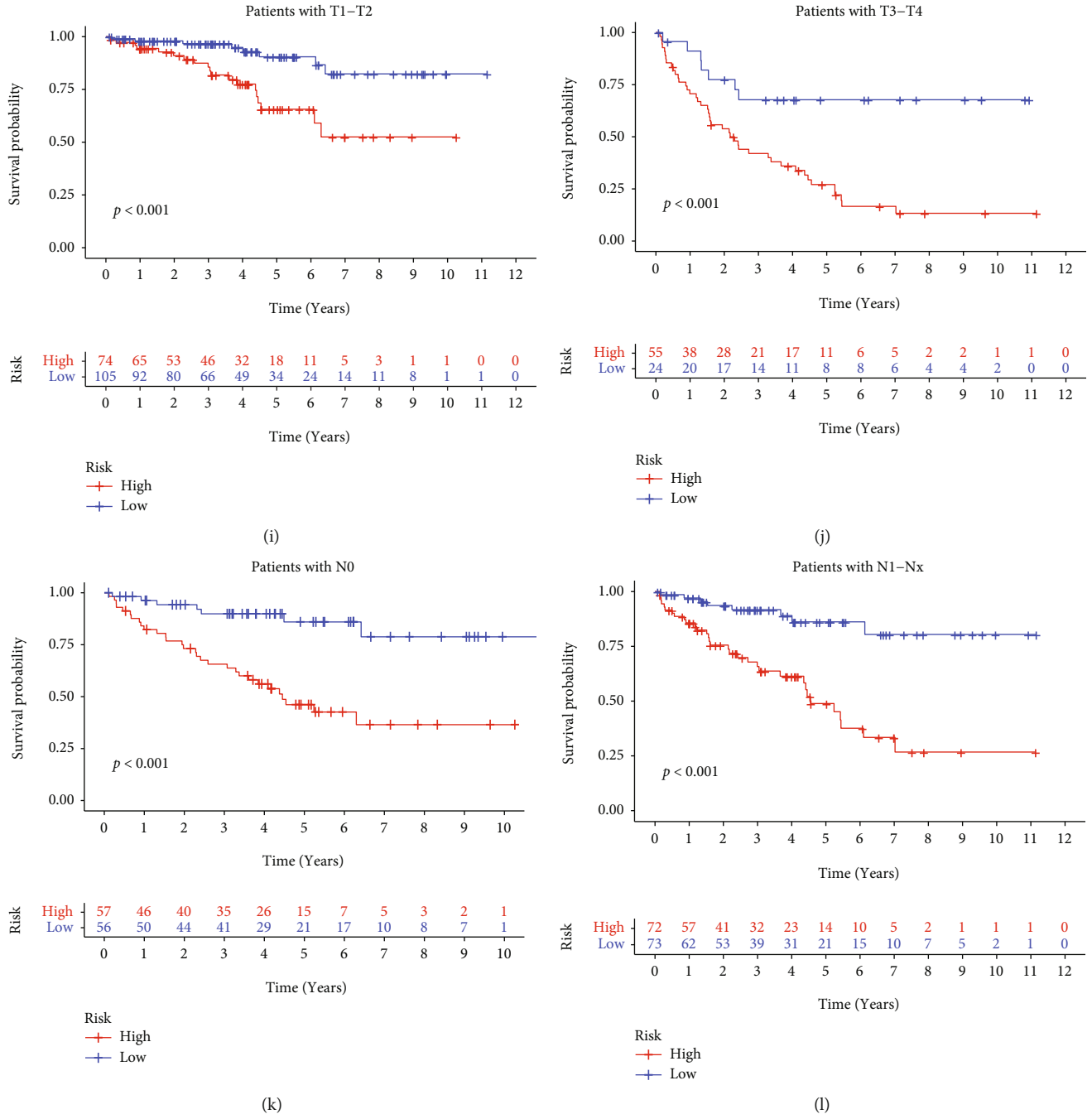

Figure 6: Continued.

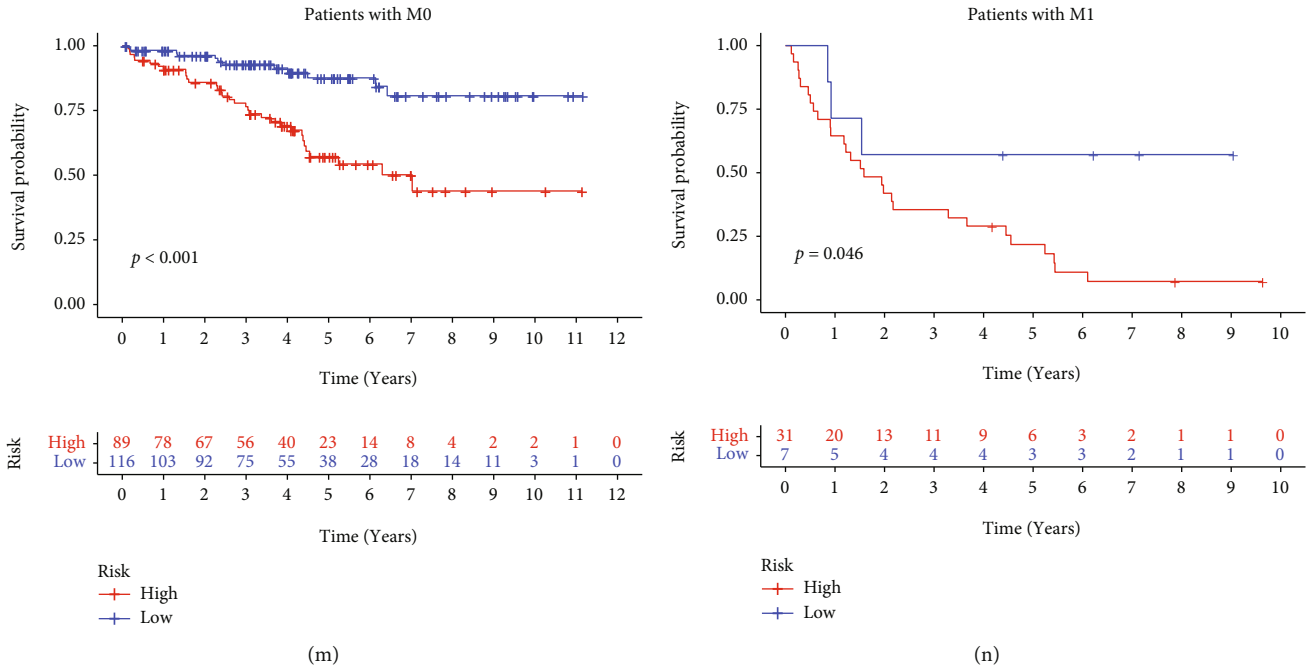

Figure 6: The different prognosis of clinical features in the risk model (a–n).

(AUC = 0.694), AJCC stage (AUC = 0.829), T stage (AUC = 0.778), and M stage (AUC = 0.722), are all vital for KIRC prediction (Figure 5(c)). The Chi-squared analysis suggested that higher risk seems to have higher levels of grade, AJCC stage, T stage, and M stage (Figure 5(d)). We built a nomogram model using risk scores to predict OS in KIRC patients (Figure 5(e)). The predictions of OS were effective as presented in the calibration plot (Figure 5(f)). The results suggested that both the risk and nomogram models were accurate. The prognostic value of various clinical features was demonstrated in the DCA plot (Figure 5(g)). To detect the prognosis in diverse clinical elements, we evaluated the survival differences of KIRC patients in various risk groups. Except for N stage, patients in the low-risk groups have longer OS than the other group. (Figures 6(a)–6(n)).

3.6. Functional Assessment of the Risk Feature. We performed GSEA to assess the action of the risk model. Processes significantly influenced the development of cancer, including MYC targets V2, DNA repair, IL-6/JAK/STAT3 signaling, and immune response. These processes existed more in the high-risk group, whereas metabolic processes were embellished in the low-risk group (Figures 7(a)–7(t)). The high-risk group can upregulate several pathways and processes linked with tumor progression and immune response, suggesting that necroptosis might influence the treatment outcomes of immunotherapy according to analysis using GSEA.

3.7. The Immune Infiltration Landscapes in Various Groups. Immune checkpoint expression can influence the therapeutic effects of chemotherapy and immunotherapy. We assessed the levels of MSH6, BTLA, LOXL2, MSH2, POLE2, BTNL2, PDCD1, TIGIT, and CTLA4 of patients from the two risk groups. More immune checkpoints were found among patients in the high-risk group (Figure 8(a)). Moreover, the interrelationship among risk scores and the immune checkpoints, indicating that higher levels of PDCD1, CTLA4, POLE2, TIGIT, BTLA, and BTNL2 were related to higher risk scores, but the levels of MSH6 and MSH2 were negative with the risk scores (Figure 8(b)).

ssGSEA were executed to catch the immune landscape in the risk groups and verified the different infiltration and components of the TME. Notably, we found that the majority of the immune cells were not the same in the two risk groups ($p < 0.05$). There were more immune cells, including APC_co_stimulation ($p < 0.001$), CCR ($p < 0.001$), CD8 + _T cells ($p < 0.001$), cytolytic activity ($p < 0.001$, HLA ($p < 0.001$), inflammation-promoting ($p < 0.001$), macrophages ($p < 0.001$), parainflammation ($p < 0.001$), pDCs ($p < 0.005$), T cell coinhibition ($p < 0.001$), T cell costimulation ($p < 0.001$), T helper cells ($p < 0.001$), Tfh ($p < 0.001$), Th1 cells and Th2 cells ($p < 0.001$) in the high-risk group (Figure 8(c)). In addition, we identified 11 immune infiltration cells that has a connection with risk score (Figure 8(d)).

Then "CIBERSORT" was applied to determine how immune cell is expressed, indicating immune cells such as plasma cells ($p < 0.001$), T cells CD8 ($p = 0.02$), T cells follicular helper ($p = 0.004$), T cells regulatory (Tregs) ($p < 0.001$), NK cells resting ($p = 0.044$), and macrophages M0 ($p = 0.04$) expressed more in the high-risk groups, which further confirmed our conclusions (Figure 8(e)). Additionally, as the risk scores were increasing, there were higher levels of the aforementioned cells (Figure 8(f)).

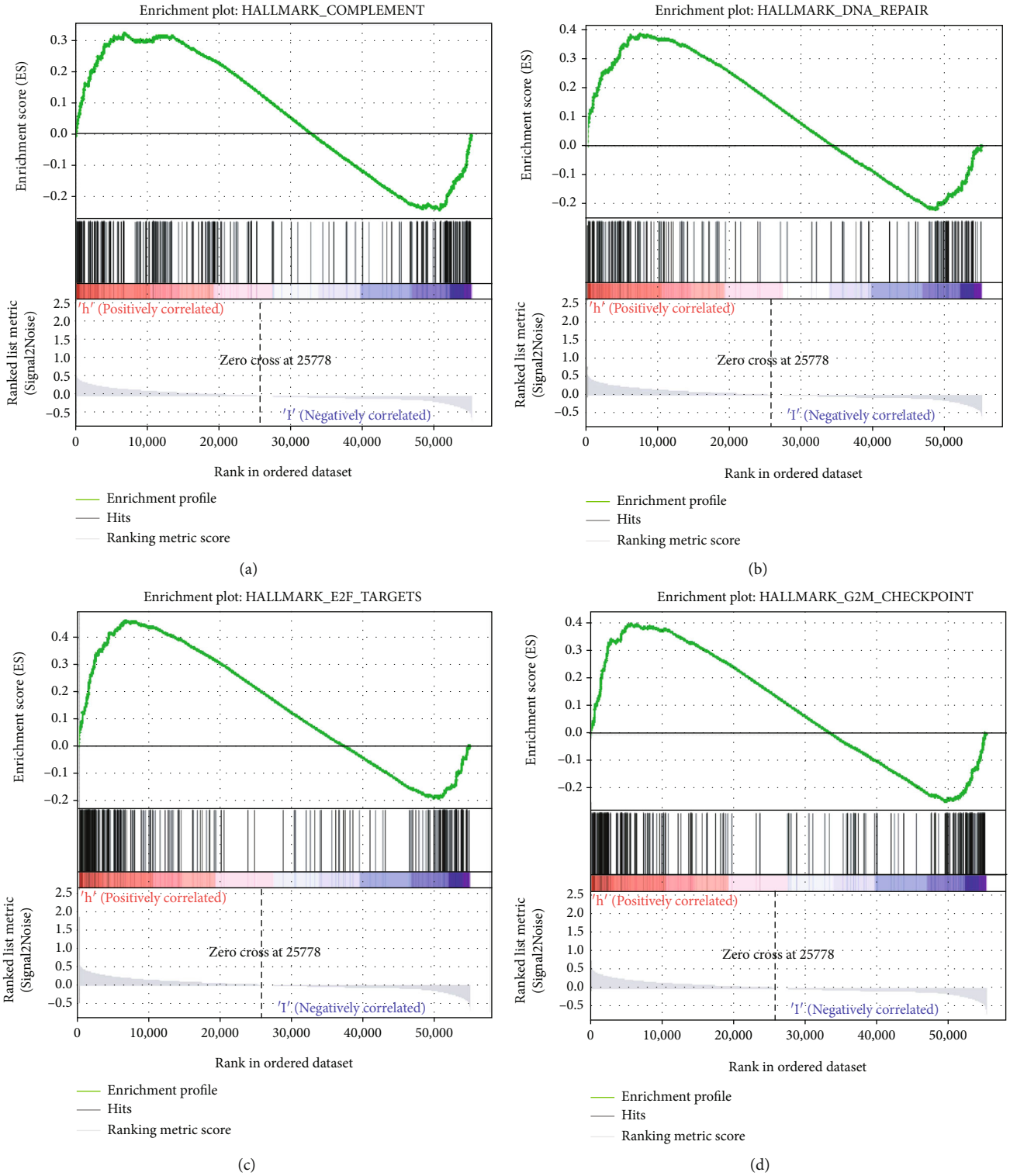

Figure 7: Continued.

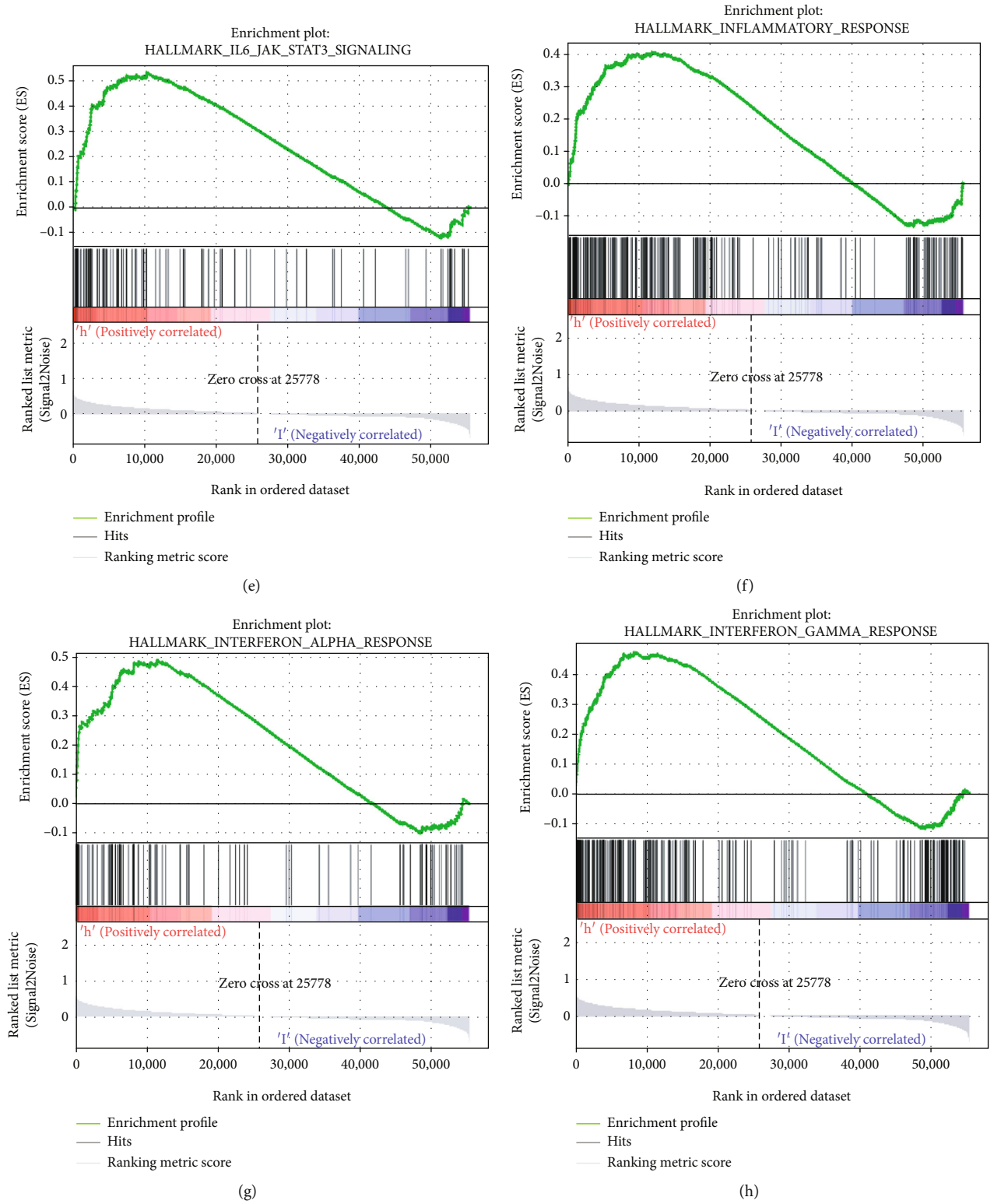

Figure 7: Continued.

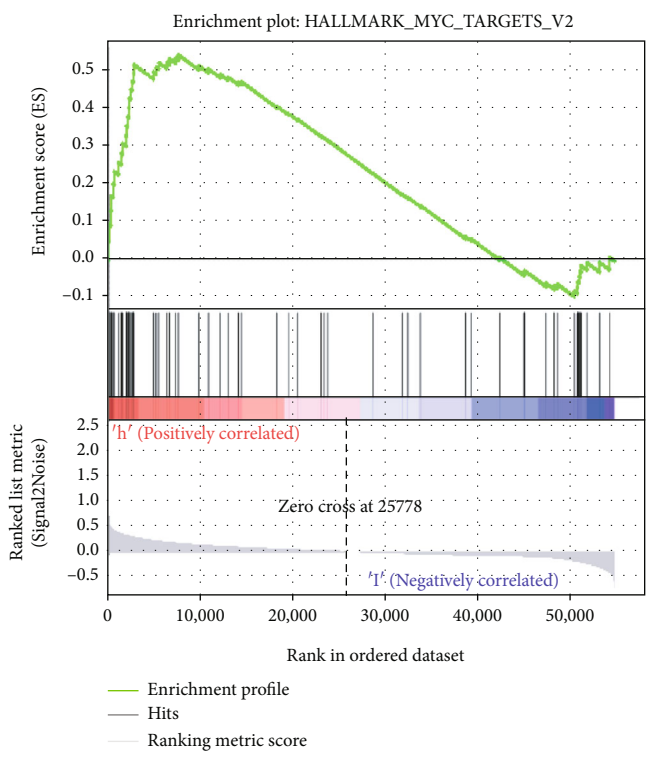

(i)

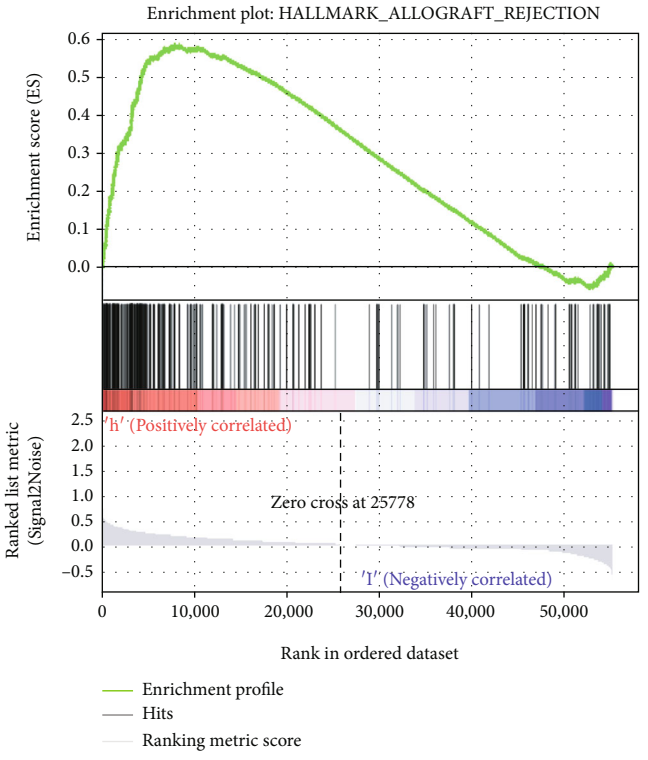

(j)

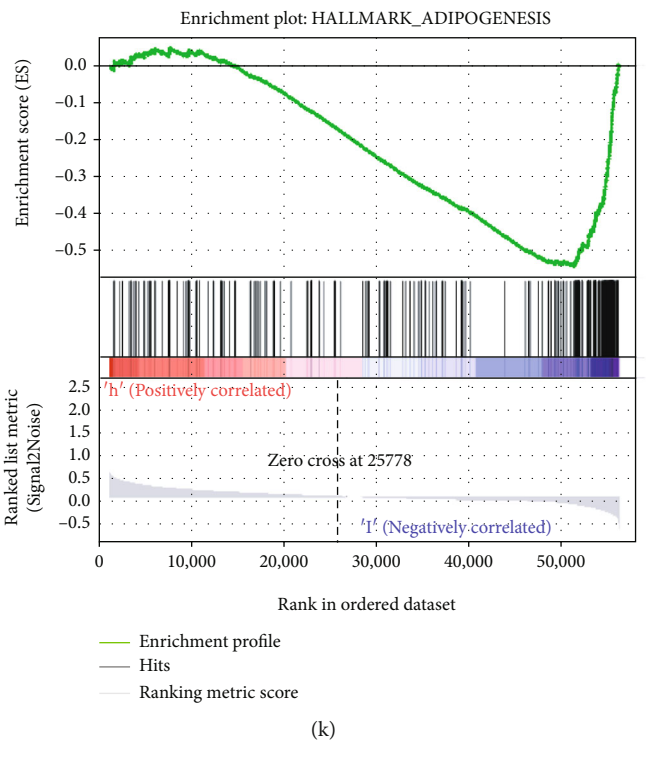

(k)

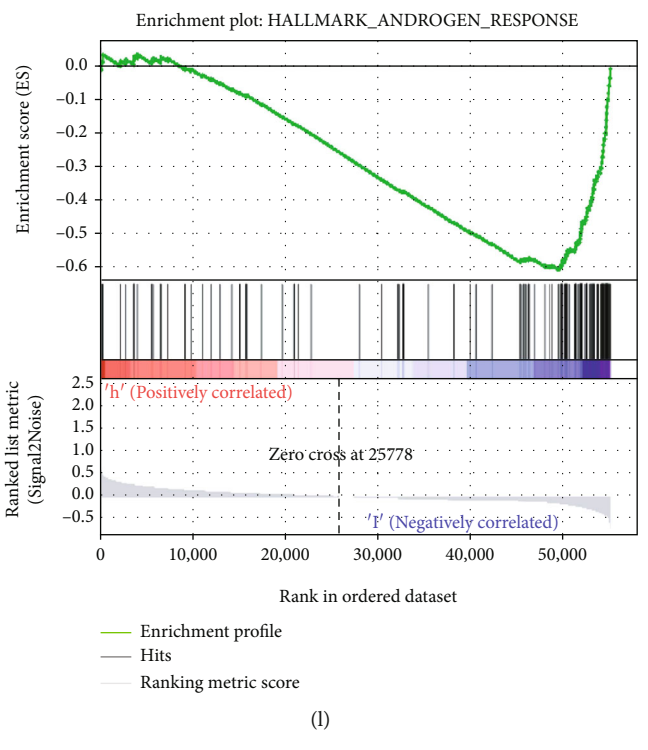

(l)

Figure 7: Continued.

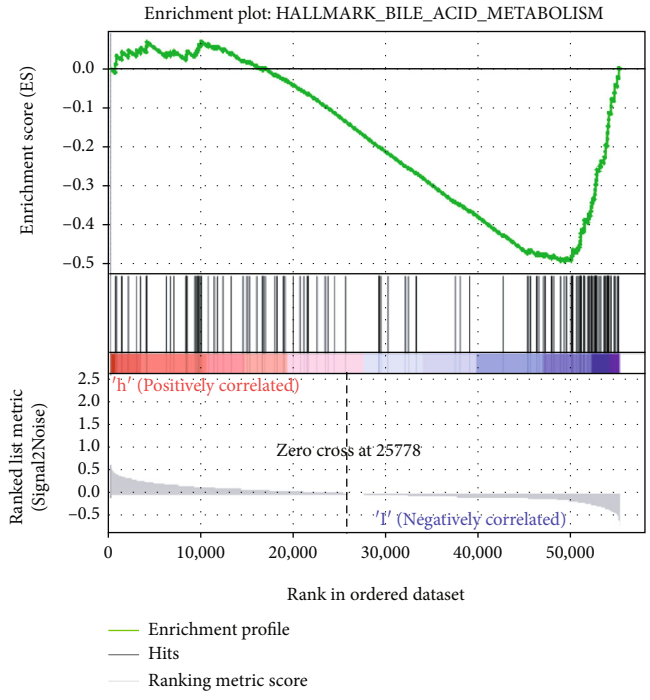

(m)

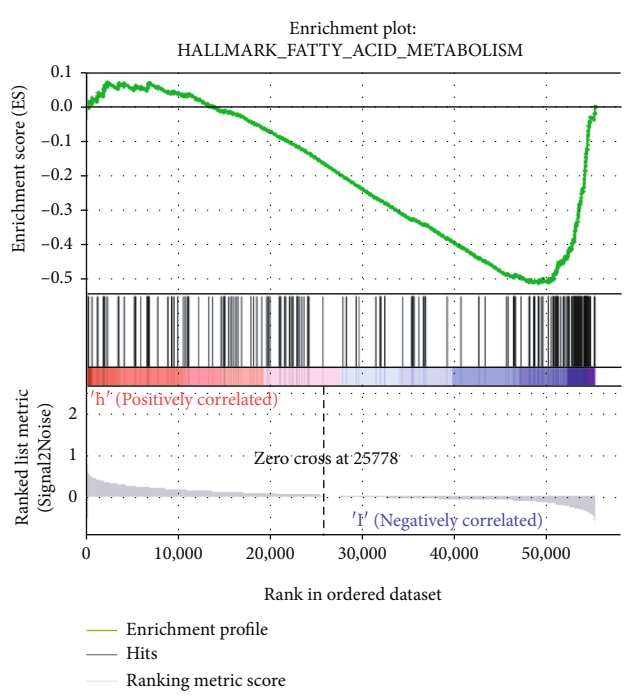

(n)

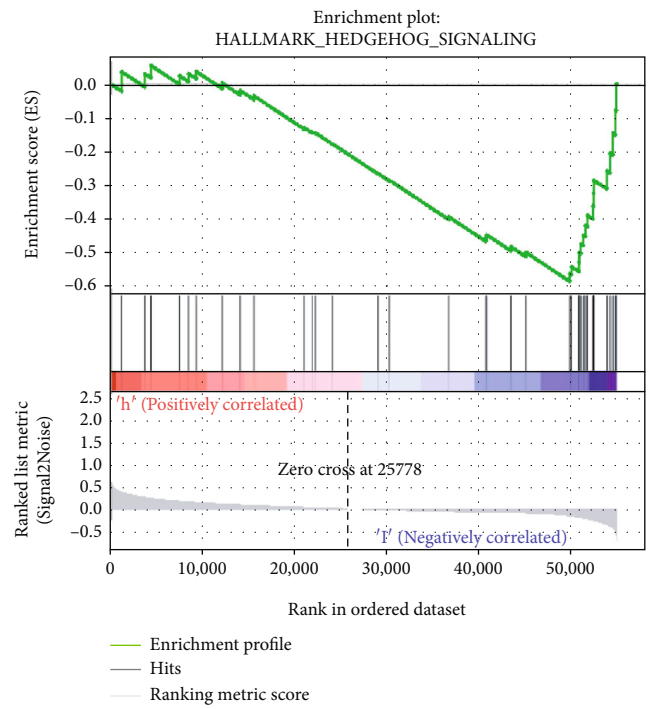

(o)

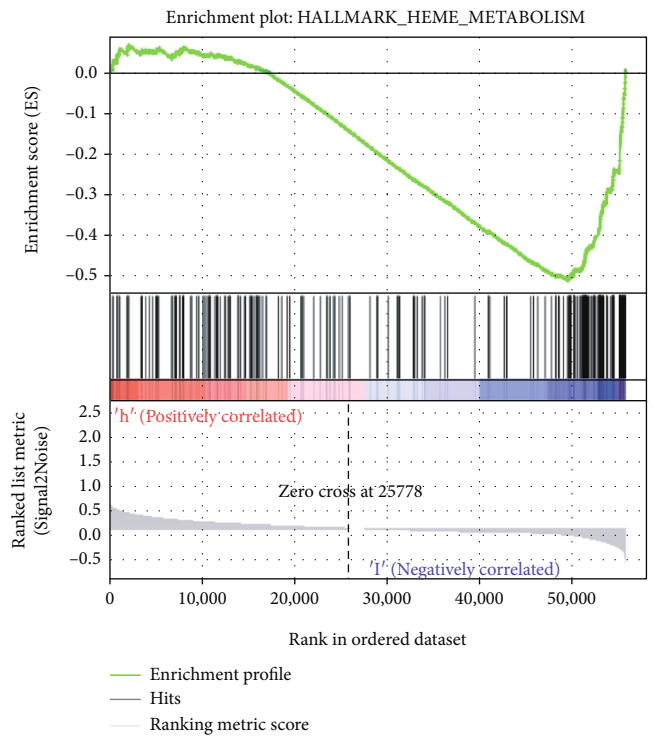

(p)

Figure 7: Continued.

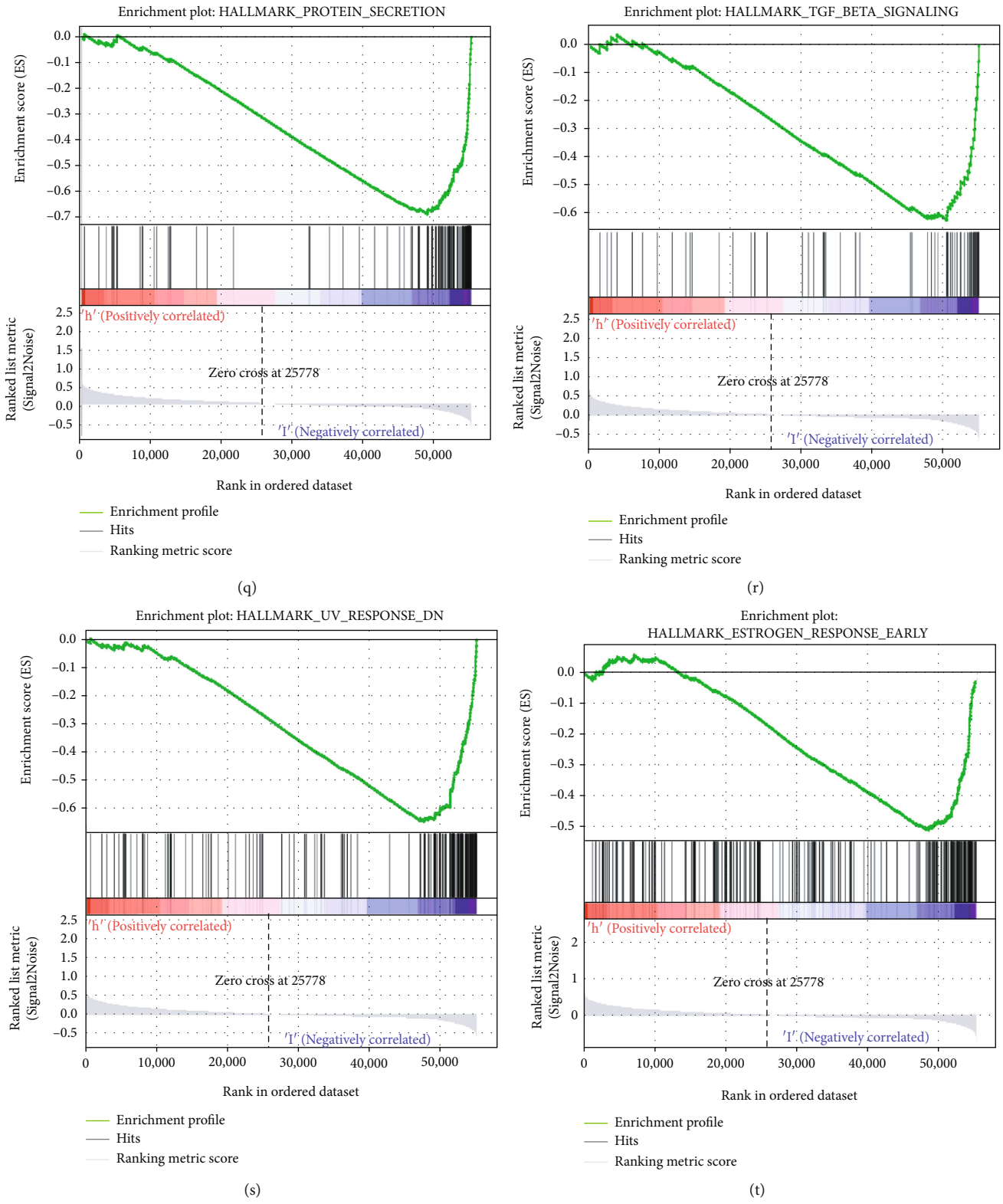

Figure 7: The GSEA analysis of the risk model (a–t).

3.8. Sensitivity in the Clinical Response. Immunotherapy scores data was collected from TCIA database to differentiate the immune responses of the two groups. We found that patients without CTLA4 and PD-1 expressed had no differences in immunotherapy scores (Figure 9(a)). But either one or two of them positive would lead to greater immunotherapy scores (Figures 9(b)–9(d)). Subsequently, we examined whether there exist a relationship in the risk groups and

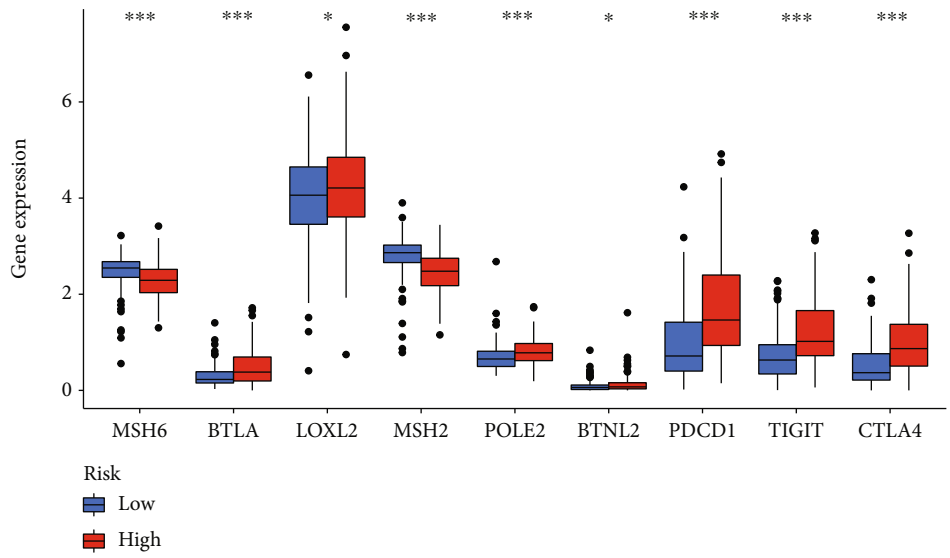

(a)

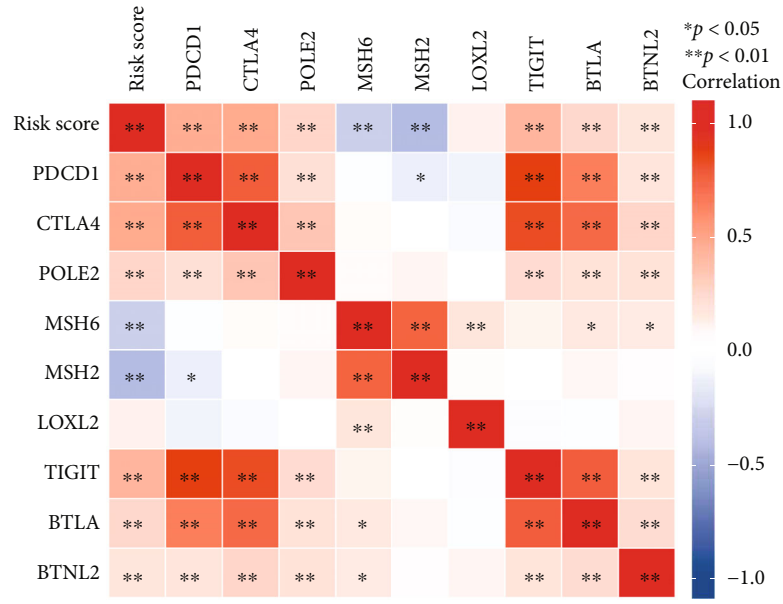

(b)

Figure 8: Continued.

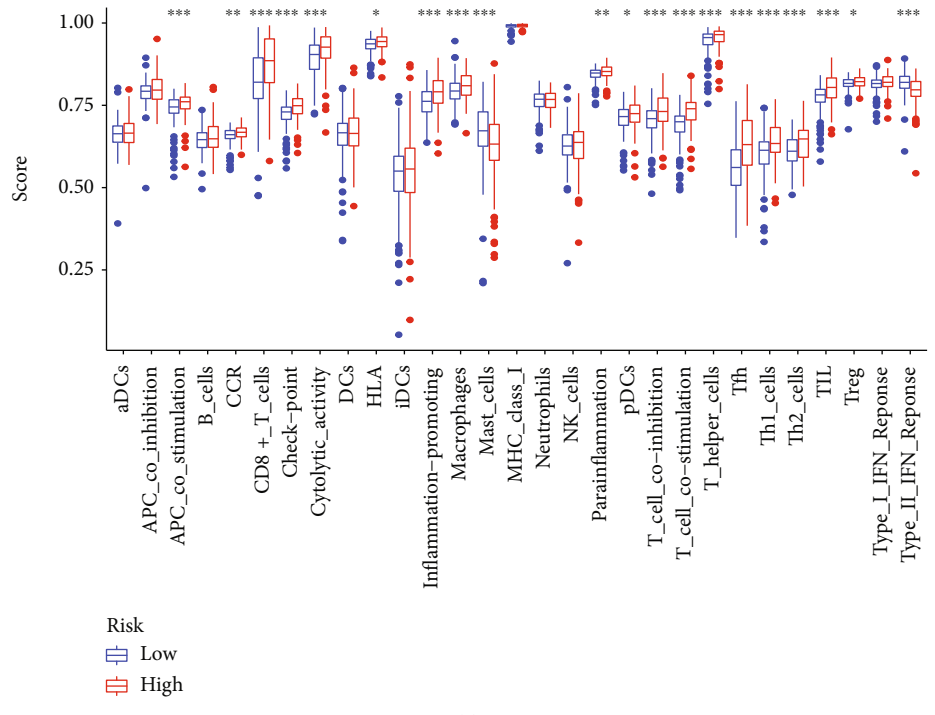

(c)

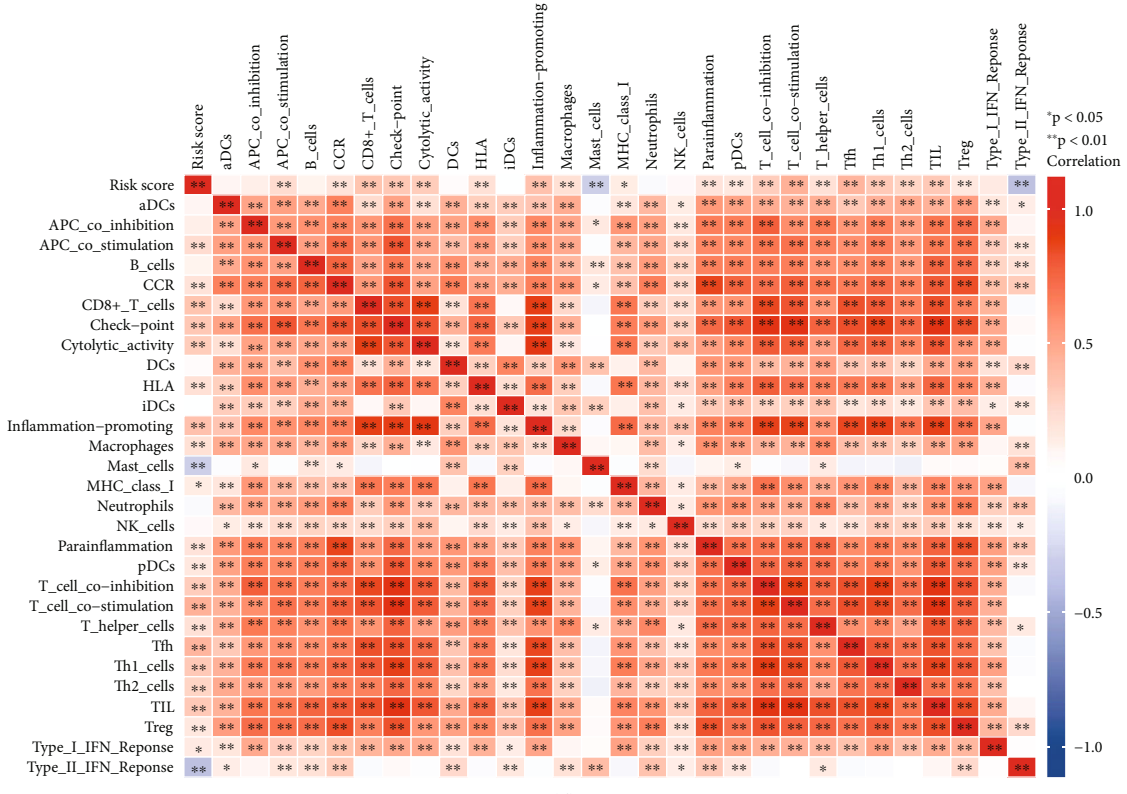

(d)

Figure 8: Continued.

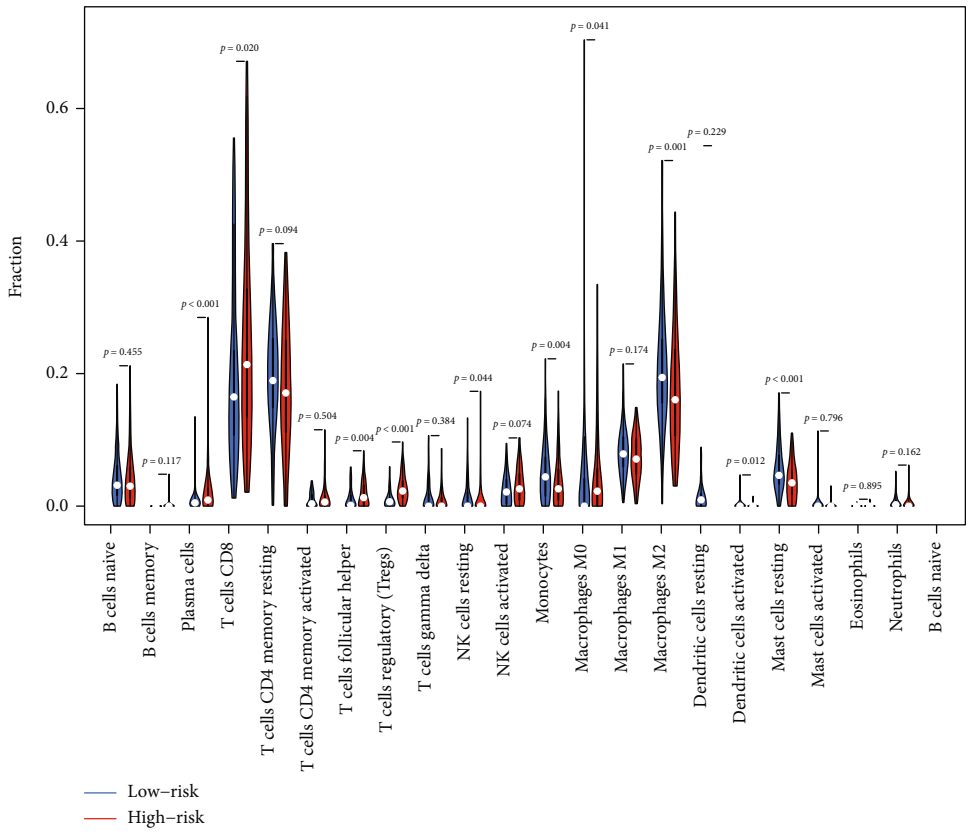

(e)

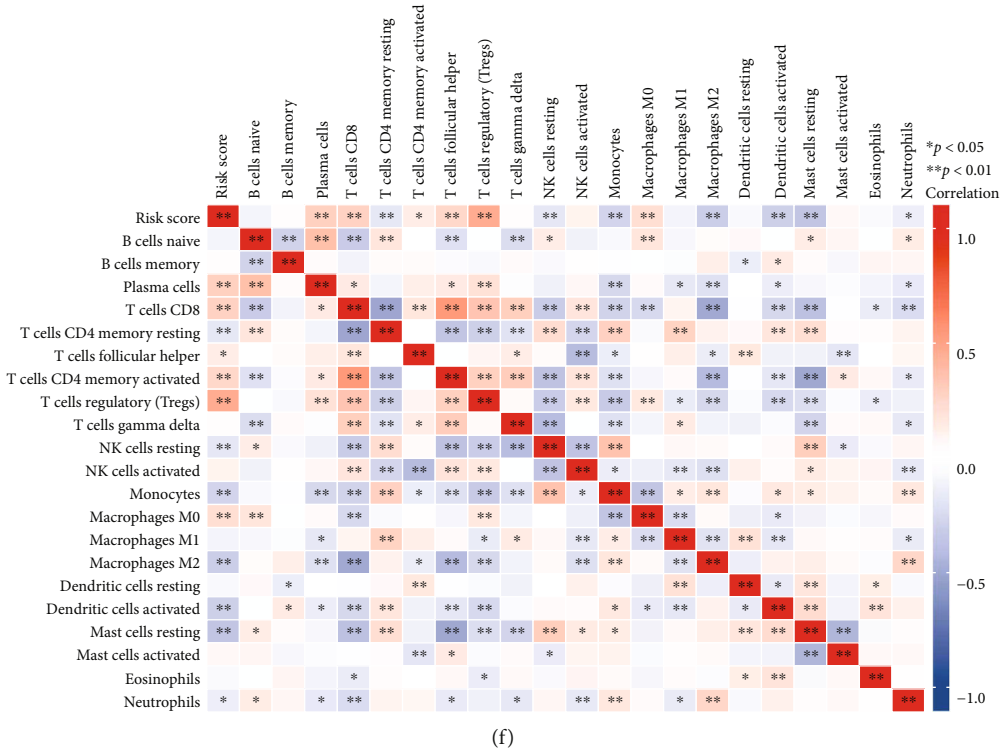

(f)

Figure 8: The immune infiltration in two groups. The immune check points expression and differences in two groups (a). The connection among immune check points and the risk score (b). The immune infiltration with ssGSEA (c). The interaction in the immune cells and the risk score (d). The immune infiltration with CIBERSORT in the two groups (e). The connection of immune cells changing along with risk score (f).

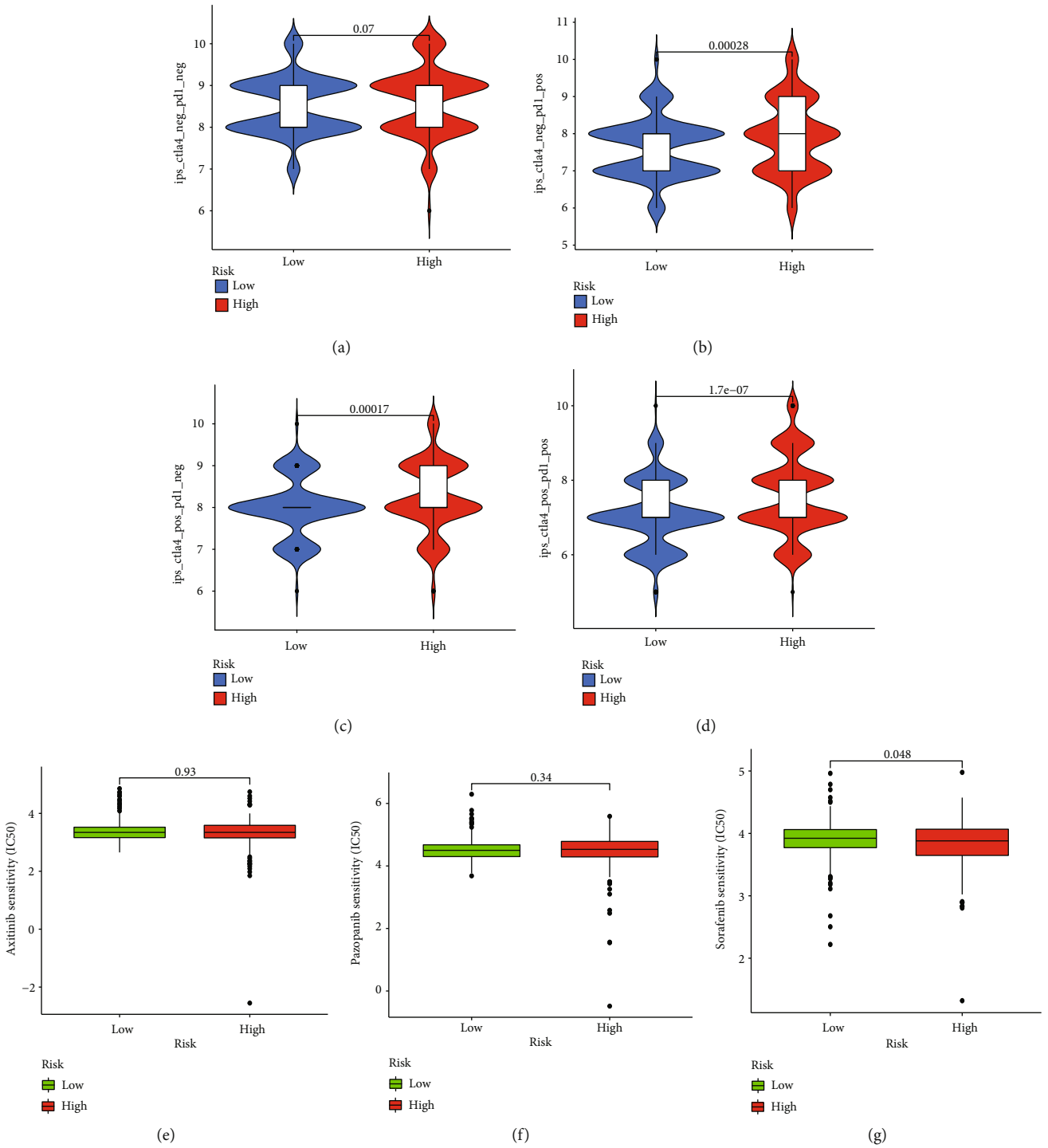

FIGURE 9: The effectiveness of clinical treatment in two groups. The therapeutic effect of immunotherapy (a–d). IC_{50} values in two groups (e–i).

chemotherapy sensitivity based on the IC_{50} values. The results seem the same in axitinib or pazopanib (Figures 9(e) and 9(f)). But more low-risk patients are sensitive to sorafenib ($p = 0.048$), sunitinib ($p < 0.001$), and temsirolimus ($p < 0.001$) (Figures 9(g)–9(i)). In conclusion, our prognostic model can be a potential indicator of the effectiveness of clinical treatment.

3.9. The Correlation between our Risk NRLs and the Related Genes. We analyzed how our prognostic NRLs could influence each other, and what interested us was that the levels of the prognostic NRLs including IGFL2-AS1, LINC01943, U62317.1, LASTR, LINC01126, AC026401.3, MYOSLID, APCDD1L-DT, AL162586.1, and NARF-IT1 were positive in increasing risk scores (Figure 10(a)). Both lncRNA-

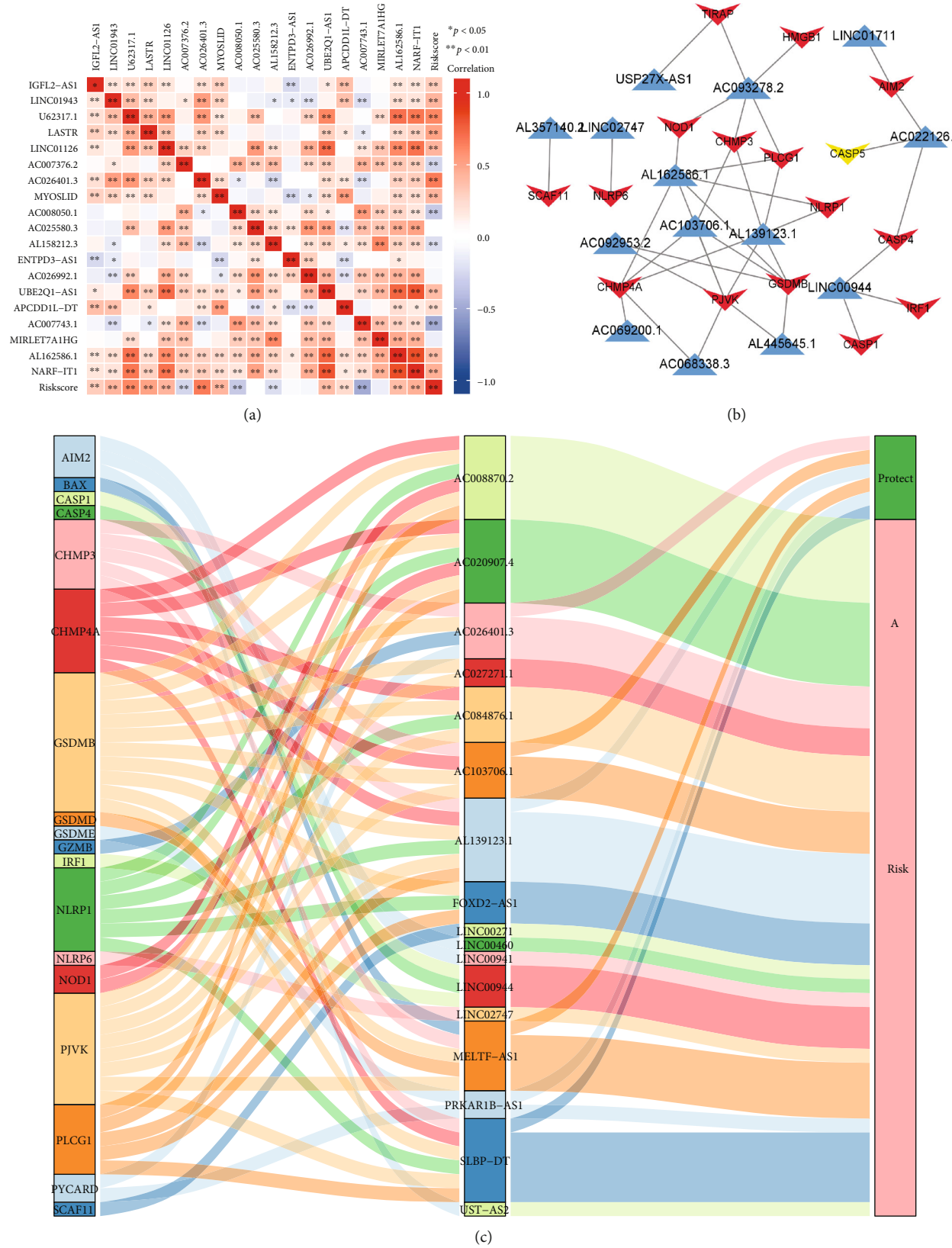

Figure 10: Continued.

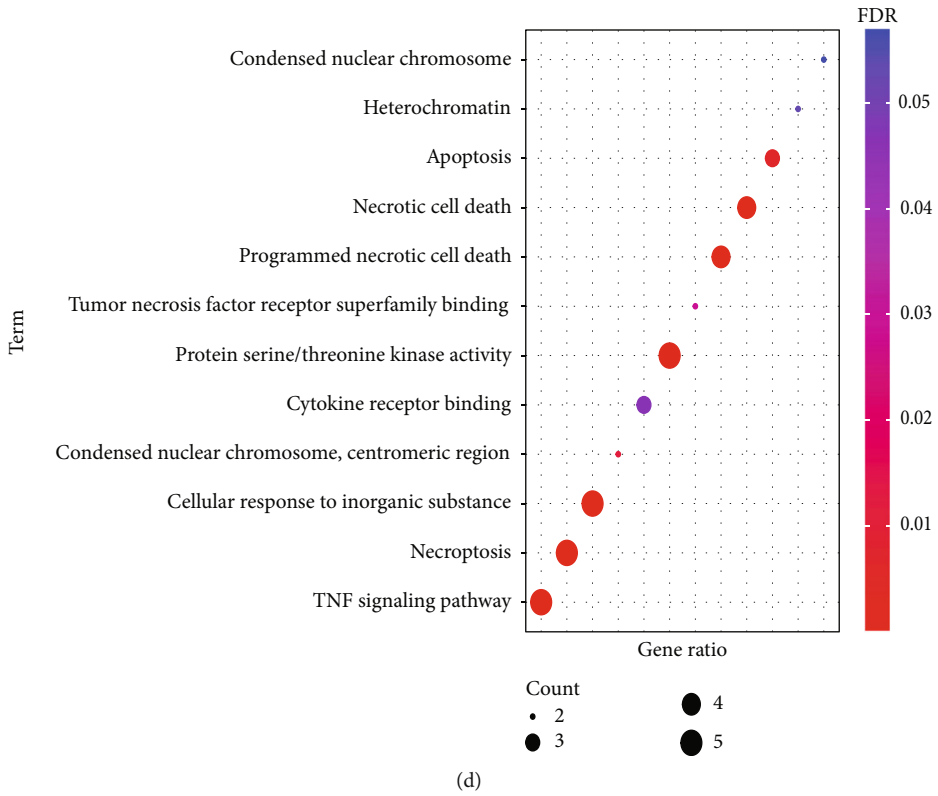

Figure 10: Coexpression between mRNAs and lncRNAs in our risk models and biological pathways of related mRNAs coexpressed with 14 lncRNAs. Interrelationship between the NRLs and the risk score (a). The network of our 19 lncRNAs related with coexpressed mRNAs (b). Sankey diagram was presented to show the connection between mRNAs, lncRNAs, and the proposed factors (c). The biological function of the coexpression mRNA (d).

mRNA expressed network was built up according to our risk signature to find the related necroptosis genes (Figure 10(b)). The Sankey diagram demonstrated the protective and risk factors of NRLs and the related mRNAs (Figure 10(c)). Finally, we explored the biological function of the related mRNAs, which were significantly associated with the procession of the cell death and progression of the cancer (Figure 10(d)).

3.10. Affirmation of 19 lncRNAs Expression in Tissues. We explored 19 NRLs expression in normal ($n = 72$) and tumor tissues ($n = 539$) of KIRC using datasets from TCGA (Figure 11(a)). We found that, with the exception of the levels of AC026992.1 ($p < 0.01$), AL158212.3, and ENTPD3-AS1 ($p < 0.01$), higher in normal tissues, other lncRNAs were all higher in tumor tissues (Figures 11(b)–11(t)).

4. Discussion

lncRNAs have been identified as crucial regulators of various kinds of cellular processes since they could function as tumor suppressors. The upregulation of lncRNA will promote the proliferation and invasion of tumor, while knockdown of its expression suppresses this process. It has been reported in many studies that the lncRNAs are altered in many types of cancers, and therefore the aberrant lncRNAs expression levels can be applied as effective diagnostic markers, and deregulated lncRNAs can be used as targets in cancer treatment. In our study, a 19-NRL risk model was built up by us to estimate the prognosis of KIRC patients. The model presented unique advantages. We used the UCR to select prognostic lncRNAs that are related to necroptosis. In the meantime, risk models were constructed using LCR. Finally, 258 patients were equally separated in the high- or low-risk group to know the 19 lncRNAs. The KM and ROC curve analyses were performed to know the treatment effect of KIRC patients, which revealed that the model was a powerful prediction tool. In addition, this model could assess the different clinical characteristics; the evaluated factors are age, gender, disease staging, grade, and their related risk score. The estimated risk score was independent with excellent sensitivity and specificity. Furthermore, via GSEA, the high-risk group was found to enhance tumor development and progression, which confirmed the differences in prognostic property based on classification by risk.

Some previous studies have contributed to the construction of the lncRNA-related model to predict the immune infiltration landscape in KIRC. Chen et al. identified four lncRNA predictive risk scoring models and found that higher risk scores were associated with higher levels of immune infiltration in the KIRC microenvironment. Higher risk score will increase activation of six immune cells, the cell types were mentioned before. [26]. Based on the extensive

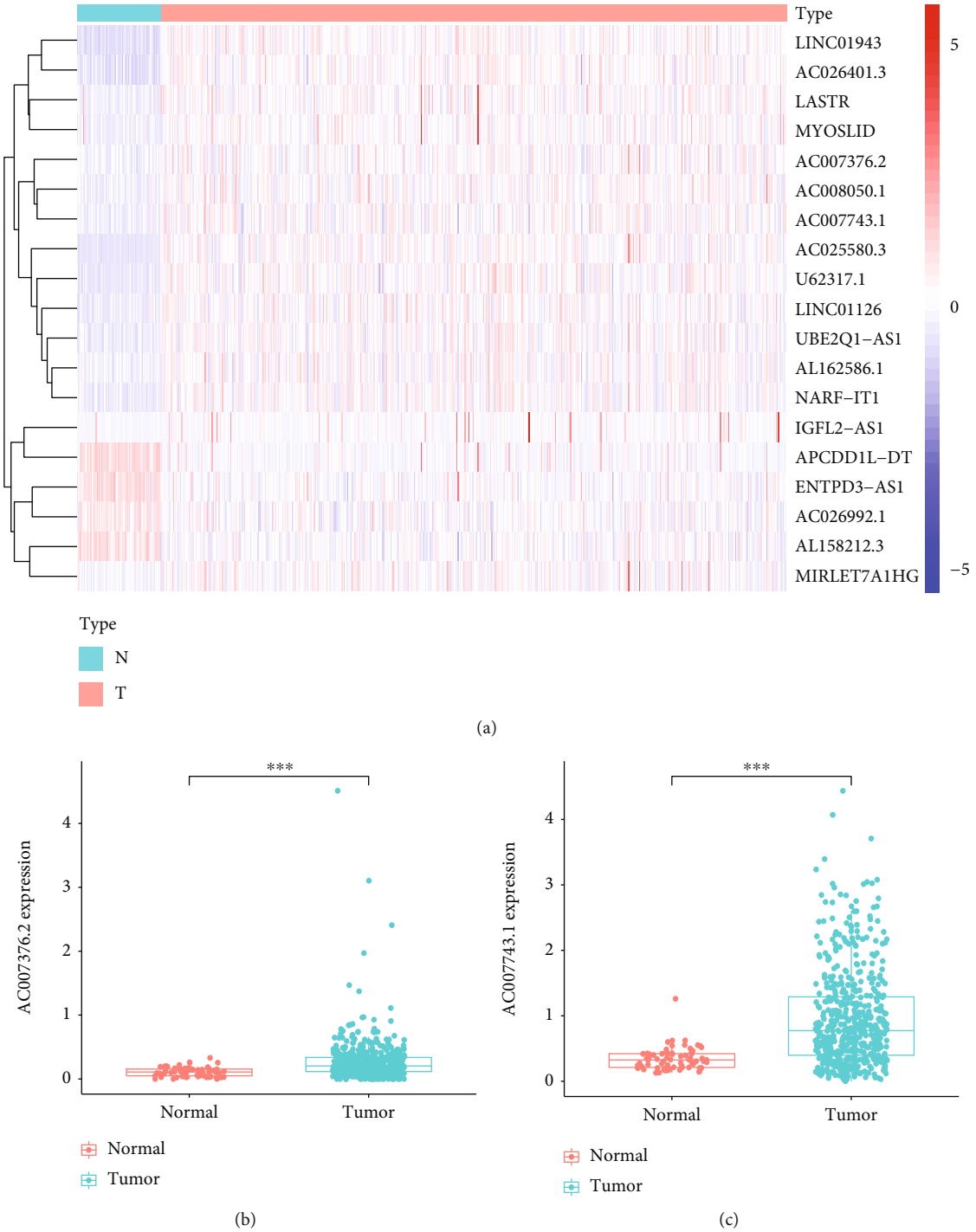

Figure 11: Continued.

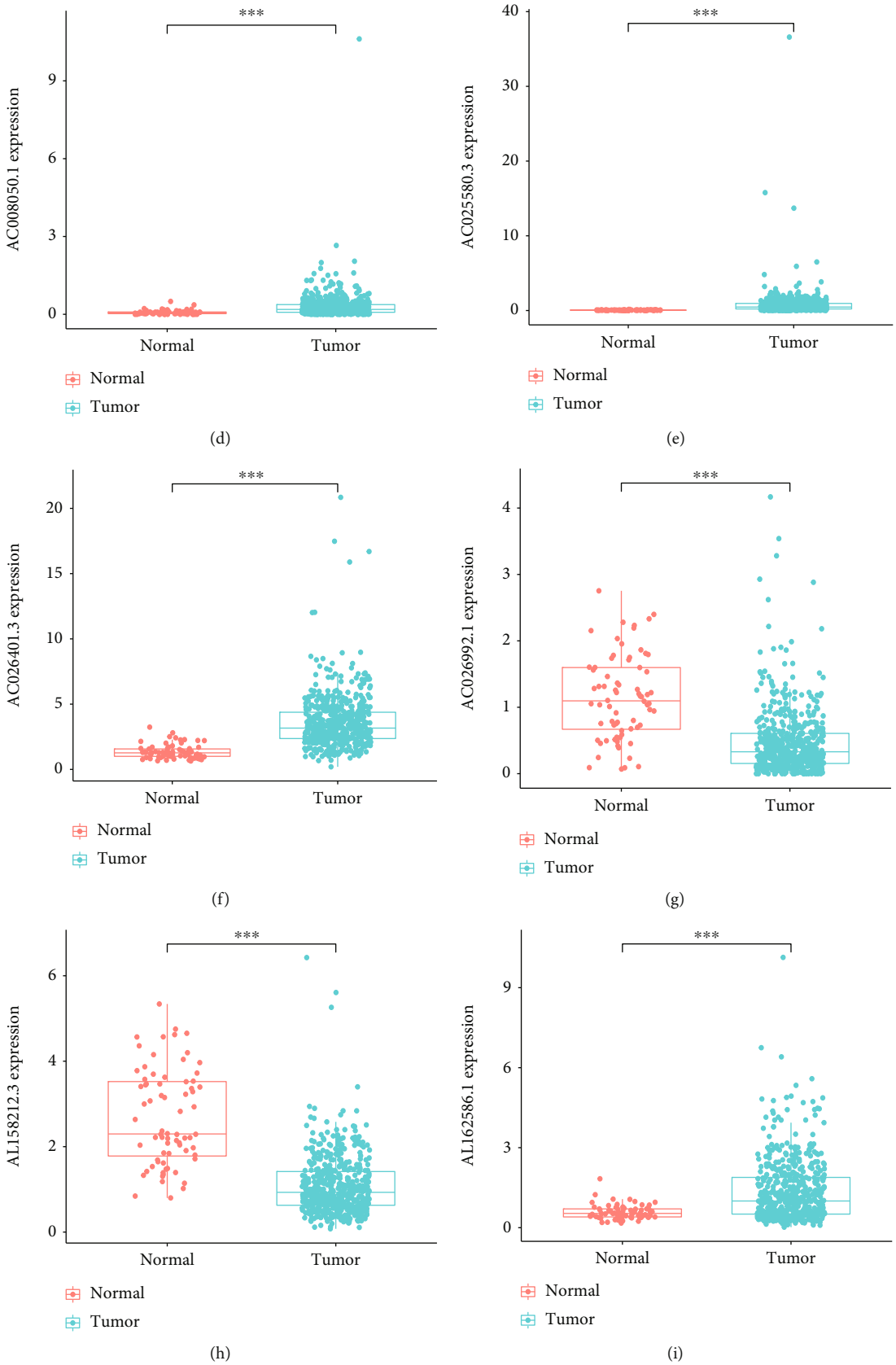

Figure 11: Continued.

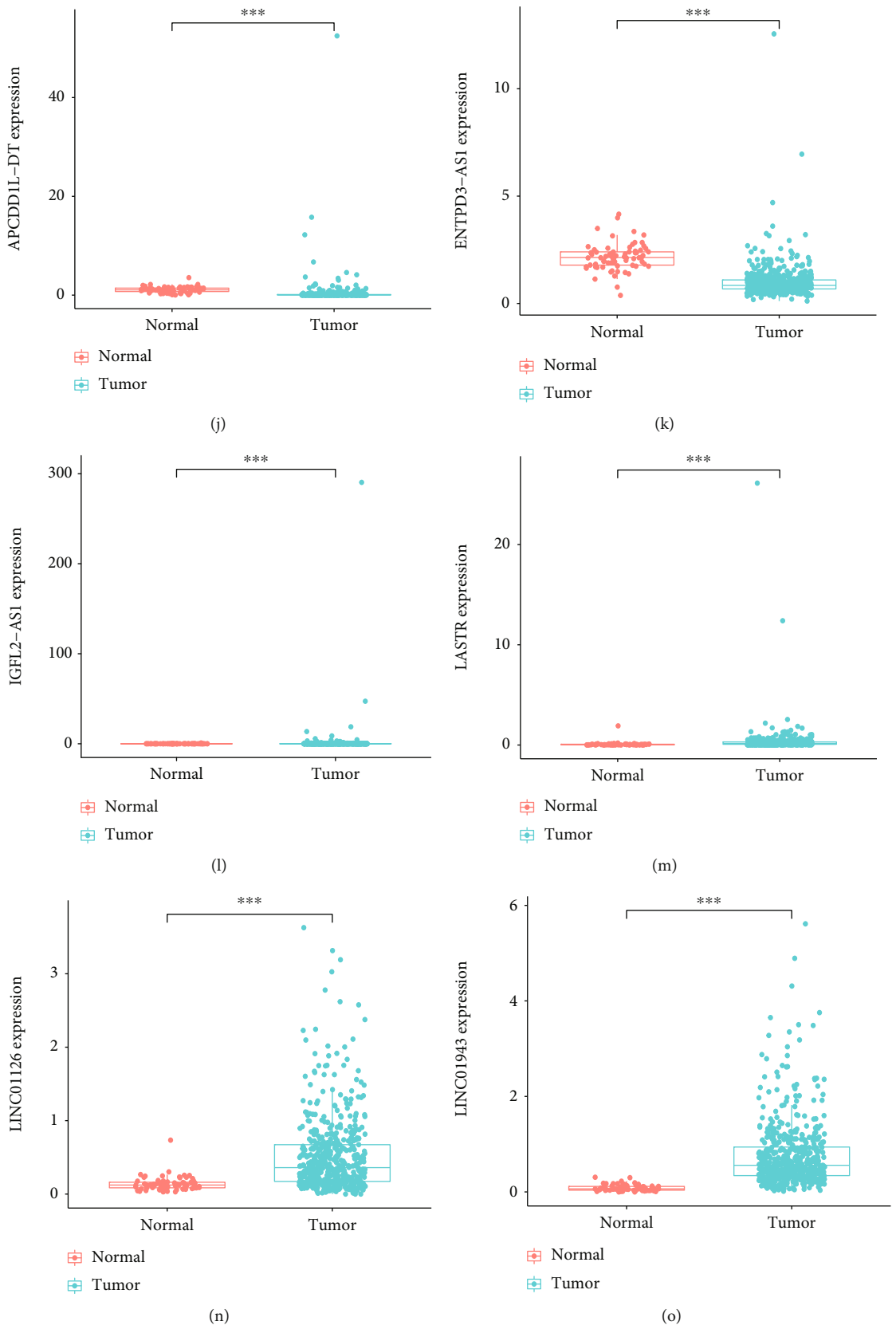

Figure 11: Continued.

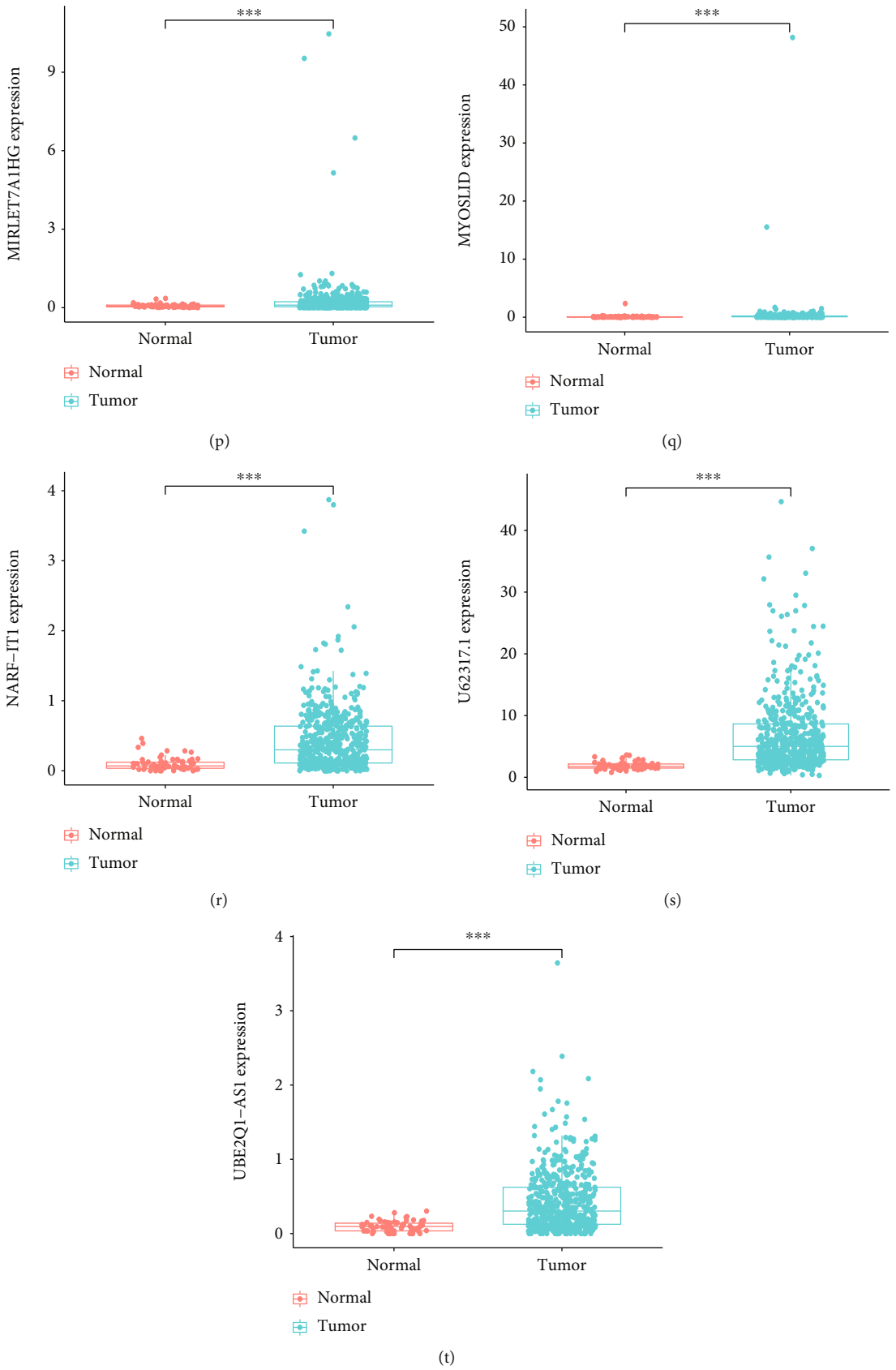

Figure 11: 19 lncRNAs expression in normal and tumor tissues in TCGA. (a) Heatmap showed the distribution of our 19 risk lncRNAs in different tissues. (b) lncRNAs expression we found in normal tissues.

participation of lncRNAs in biological processes, predicting tumor immune infiltration and the prognosis by studying the mechanism of action of lncRNAs would prove to be helpful [27]. KIRC is considered an immunogenic tumor, and infiltration of immunosuppressive cells would lead to the development of a TME [28]. However, there are limited studies on how necroptosis-related genes influence the TME in KIRC. High-risk patients may have a higher immune score and a poor prognosis, the same was reported by Xin et al. They demonstrated that better OS was related to lower immune scores. In addition, the high-risk group was infiltrated with seven immune cells, followed by worse prognosis [29]. Furthermore, we found that low-risk patients were more susceptible to sunitinib, sorafenib, and temsirolimus immunotherapy. High-risk groups expressed more immune checkpoint genes, suggesting that TME could influence the therapeutic effects in patients with KIRC. In conclusion, necroptosis probably influenced the TME and immune cell infiltration. Our risk model may provide a new perspective to explore TMR in the future and could be applied to predict immune cell infiltration.

Among the lncRNAs included in our model, IGFL2-AS1 was reported as a facilitation factor in metastatic tongue squamous cancer [30]. LINC01943 was upregulated in triple negative breast cancer (TNBC) tissues, which could regulate TGF-β expression to promote tumorigenesis, leading to worse OS [31]. U62317.1 acts as a risk factor in oral cancer and tends to be associated with the lipid metabolic process [32]. LASTR has been proved to promote the stomach adenocarcinoma growth and lung cancer [33, 34]. LINC01126 could repress proliferation, increase apoptosis, and cause inflammatory of hPDLCs in anaerobic environment via sponging miR-518a-5p to promote periodontitis pathogenesis in humans [35]. AC026401.3 and IGFL2-AS1 were involved in glycolysis and as a prognostic signature in KIRC [36]. MYOSLID was involved in the growth of osteosarcoma and amplifies the vascular smooth muscle differentiation program [37, 38]. ENTPD3-AS1 could suppress renal cancer via miR-155/HIF-1 signaling, which confirmed our results [39]. Overall, referred to former researches, we observed that the necroptosis-related risk lncRNAs identified in our study are strongly associated with immune functions. Through the identification of immune system gene set and NRL biomarkers, AC007376.2, AC007743.1, AC008050.1, AC026401.3, AC026992.1, and L158212.3, and the analysis of how immune checkpoint genes express, this work got a conclusion for the association with the risk score and the predictive genes of immunotherapeutic sensitivity such as PDL1, PD1, CTLA4, and TIGIT.

The findings in this study can provide novel mechanisms for KIRC. Novel biomarkers were identified, which may be of significance in future studies. The effectiveness of clinical treatment and differences in two groups were studied, to predict tumor microenvironment and immunotherapy response. We found that patients without CTLA4 and PD-1 expressed had no differences in immunotherapy score. However, either one or two of them positive would lead to greater immunotherapy scores. Studying the certain connection with the risk groups and chemotherapy sensitivity according to the IC_{50} values, there were no differences in axitinib or pazopanib. To the contrary, patients in the low-risk group were more sensitive to sorafenib, sunitinib, and temsirolimus, allowing for clustering KIRK affected individuals for a positive or negative response to immunotherapy.

Recently, several publications on NRLs have been produced, associated with different types of cancer, showing the importance of necroptosis genes and their regulation by lncRNAs. For instance, Luo et al. studied the association of lncRNAs with stomach adenocarcinoma, focusing on a twelve NRL signature which included LASTR, one of the lncRNAs identified in this work as NRL for KIRC [40]. Liu et al. studied lncRNAs in colon cancer and identified MYOSLID as associated to pyroptosis, linking this lncRNA to regulation of SKP1 expression via MIR-589-5p and to the miR-29c-3p-mcl-1 axis [41]. The function of lncRNAs in sequestering and inactivating one or more miRNA species was studied also in the necroptosis response in HCC [42]. In breast cancer, Xu et al., Chen et al., Xie et al., and Zhang et al. studied the link between tumor microenvironment and NLR signatures [43–46], as well as miRNA signatures [47]. An axis linking an lncRNA with a microRNA and the target gene was shown in bladder cancer progression and metastasis [48, 49]. A similar approach has been used to study laryngeal squamous cell carcinoma [50].

However, there are several mechanisms of action performed by lncRNAs, one of which is structural, interacting with protein complexes and epigenetic regulators, such as histone modifiers, polycomb complexes, and chromatin complexes. Although several publications have indicated the occurrence of necroptosis regulators in KIRC, very few data are available on the involvement of lncRNAs in controlling or decreasing the neurotrophic signaling in kidney cancer, in particular based on OTUD6B-AS1, AL162377.1, AC108449.2, AF111167.2, and hsa-miR-21-5p targeting KLF9 [51–53]. To improve the therapeutic potential of kidney cancer treatment, this paper provides an improved and extended NRL signature model for KIRC that is able to distinguish low and high overall survival rates and response to immunotherapies.

Still, this study has several limitations. Firstly, the validation of the test model is required. Secondly, larger multicentre trials are required to endorse the accuracy of the model. Moreover, more molecular experiments should be performed on the selected lncRNAs to explore how they influence the progression of tumorigenesis and immune infiltration in KIRC.

5. Conclusion

In conclusion, we established risk signatures to explore the connection between necroptosis-related lncRNAs (NRLs) and the prognosis of KIRC. Meanwhile, the relationship between NRLs and the TME, immune infiltration, prognosis prediction ability, and therapeutic effects in KIRC was investigated. The NRL risk model was constructed with the LCR to categorize patients with various risks. The risk model suggested that higher immune score might lead to worse prognosis, and low-risk patient could be cured using

chemotherapy and immunotherapy. Our research could offer new opinions regarding the importance of necroptosis in the TME and KIRC development.

Data Availability

The data used to support the findings of this study are included within the article.

Conflicts of Interest

The authors declared no potential conflicts of interest with respect to the research, authorship, and/or publication of this article.

Authors' Contributions

YS.Y got all the data we used, XY. Z and YS. Y analyzed and integrated all the data. YQ. T and YS. Y designed the study. XY. Z, X. L, and X. R did the analyzation and interpretation. YS. Y, YQ.T, and J. W wrote the manuscript. XY. Z acted as a guarantor. All authors critically revised the draft. All authors got approval of the final version.

Supplementary Materials

Supplementary Table S1: UCR analysis gene data. *(Supplementary Materials)*

References

[1] B. Ljungberg, K. Bensalah, S. Canfield et al., "EAU guidelines on renal cell carcinoma: 2014 update," *European Urology*, vol. 67, no. 5, pp. 913–924, 2015.

[2] T. K. Choueiri and R. J. Motzer, "Systemic therapy for metastatic renal-cell carcinoma," *The New England Journal of Medicine*, vol. 376, no. 4, pp. 354–366, 2017.

[3] B. C. Leibovich, C. M. Lohse, P. L. Crispen et al., "Histological subtype is an independent predictor of outcome for patients with renal cell carcinoma," *The Journal of Urology*, vol. 183, no. 4, pp. 1309–1316, 2010.

[4] J. Lu, L. Zhu, L. P. Zheng et al., "Overexpression of ULK1 represents a potential diagnostic marker for clear cell renal carcinoma and the antitumor effects of SBI-0206965," *eBioMedicine*, vol. 34, pp. 85–93, 2018.

[5] B. A. Inman, M. R. Harrison, and D. J. George, "Novel immunotherapeutic strategies in development for renal cell carcinoma," *European Urology*, vol. 63, no. 5, pp. 881–889, 2013.

[6] A. M. Newman, C. L. Liu, M. R. Green et al., "Robust enumeration of cell subsets from tissue expression profiles," *Nature Methods*, vol. 12, no. 5, pp. 453–457, 2015.

[7] C. Lin and L. Yang, "Long noncoding RNA in cancer: wiring signaling circuitry," *Trends in Cell Biology*, vol. 28, no. 4, pp. 287–301, 2018.

[8] T. R. Mercer, M. E. Dinger, and J. S. Mattick, "Long noncoding RNAs: insights into functions," *Nature Reviews. Genetics*, vol. 10, no. 3, pp. 155–159, 2009.

[9] Y. H. Lin, M. H. Wu, C. T. Yeh, and K. H. Lin, "Long noncoding RNAs as mediators of tumor microenvironment and liver cancer cell communication," *International Journal of Molecular Sciences*, vol. 19, no. 12, p. 3742, 2018.

[10] A. Fatica and I. Bozzoni, "Long non-coding RNAs: new players in cell differentiation and development," *Nature Reviews. Genetics*, vol. 15, no. 1, pp. 7–21, 2014.

[11] C. L. Han, M. Ge, Y. P. Liu et al., "Long non-coding RNA H19 contributes to apoptosis of hippocampal neurons by inhibiting let-7b in a rat model of temporal lobe epilepsy," *Cell Death & Disease*, vol. 9, no. 6, p. 617, 2018.

[12] M. K. Atianand and K. A. Fitzgerald, "Long non-coding RNAs and control of gene expression in the immune system," *Trends in Molecular Medicine*, vol. 20, no. 11, pp. 623–631, 2014.

[13] Q. Hu, Y. Ye, L. C. Chan et al., "Oncogenic lncRNA downregulates cancer cell antigen presentation and intrinsic tumor suppression," *Nature Immunology*, vol. 20, no. 7, pp. 835–851, 2019.

[14] P. Gu, X. Chen, R. Xie et al., "lncRNA HOXD-AS1 regulates proliferation and chemo-resistance of castration- resistant prostate cancer via recruiting WDR5," *Molecular Therapy*, vol. 25, no. 8, pp. 1959–1973, 2017.

[15] Z. Sun, C. Jing, C. Xiao, and T. Li, "Long non-coding RNA profile study identifies an immune-related lncRNA prognostic signature for kidney renal clear cell carcinoma," *Frontiers in Oncology*, vol. 10, p. 1430, 2020.

[16] Y. Cui, S. Zhang, C. Miao et al., "Identification of autophagy-related long non-coding RNA prognostic and immune signature for clear cell renal cell carcinoma," *Translational Andrology and Urology*, vol. 10, no. 8, pp. 3317–3331, 2021.

[17] Y. Gong, Z. Fan, G. Luo et al., "The role of necroptosis in cancer biology and therapy," *Molecular Cancer*, vol. 18, no. 1, p. 100, 2019.

[18] S. Zhe-Wei, G. Li-Sha, and L. Yue-Chun, "The role of necroptosis in cardiovascular disease," *Frontiers in Pharmacology*, vol. 9, p. 721, 2018.

[19] M. Wu, Y. Xia, Y. Wang et al., "Development and validation of an immune-related gene prognostic model for stomach adenocarcinoma," *Bioscience Reports*, vol. 40, no. 10, p. BSR20201012, 2020.

[20] J. Yuan, P. Amin, and D. Ofengeim, "Necroptosis and RIPK1-mediated neuroinflammation in CNS diseases," *Nature Reviews. Neuroscience*, vol. 20, no. 1, pp. 19–33, 2019.

[21] A. Najafov, H. Chen, and J. Yuan, "Necroptosis and cancer," *Trends Cancer*, vol. 3, no. 4, pp. 294–301, 2017.

[22] J. E. Park, J. H. Lee, S. Y. Lee et al., "Expression of key regulatory genes in necroptosis and its effect on the prognosis in non-small cell lung cancer," *Journal of Cancer*, vol. 11, no. 18, pp. 5503–5510, 2020.

[23] Z. Zhang, G. Xie, L. Liang et al., "RIPK3-mediated necroptosis and neutrophil infiltration are associated with poor prognosis in patients with alcoholic cirrhosis," *Journal of Immunology Research*, vol. 2018, Article ID 1509851, 2018.

[24] T. Derrien, R. Johnson, G. Bussotti et al., "The GENCODE V7 catalog of human long noncoding RNAs: analysis of their gene structure, evolution, and expression," *Genome Research*, vol. 22, no. 9, pp. 1775–1789, 2012.

[25] Z. Zhao, H. Liu, X. Zhou et al., "Necroptosis-related lncRNAs: predicting prognosis and the distinction between the cold and hot tumors in gastric cancer," *Journal of Oncology*, vol. 2021, Article ID 6718443, 2021.

[26] H. Chen, Y. Pan, X. Jin, and G. Chen, "Identification of a four hypoxia-associated long non-coding RNA signature and establishment of a nomogram predicting prognosis of clear cell

renal cell carcinoma," *Frontiers in Oncology*, vol. 11, article 713346, 2021.

[27] L. Statello, C. J. Guo, L. L. Chen, and M. Huarte, "Author correction: gene regulation by long non-coding RNAs and its biological functions," *Nature Reviews. Molecular Cell Biology*, vol. 22, no. 2, p. 159, 2021.

[28] C. M. Dıaz-Montero, B. I. Rini, and J. H. Finke, "The immunology of renal cell carcinoma," *Nature Reviews. Nephrology*, vol. 16, no. 12, pp. 721–735, 2020.

[29] S. Xin, J. Mao, C. Duan et al., "Identification and quantification of necroptosis landscape on therapy and prognosis in kidney renal clear cell carcinoma," *Frontiers in Genetics*, vol. 13, article 832046, 2022.

[30] R. Zhao, S. Wang, L. Tan, H. Li, J. Liu, and S. Zhang, "IGFL2-AS1 facilitates tongue squamous cell carcinoma progression via Wnt/*B*-catenin signaling pathway," *Oral Diseases*, 2021.

[31] R. Vishnubalaji and N. M. Alajez, "Epigenetic regulation of triple negative breast cancer (TNBC) by Tgf-β signaling," *Scientific Reports*, vol. 11, no. 1, p. 15410, 2021.

[32] Y. Li, X. Cao, and H. Li, "Identification and validation of novel long non-coding RNA biomarkers for early diagnosis of oral squamous cell carcinoma," *Frontiers in Bioengineering and Biotechnology*, vol. 8, p. 256, 2020.

[33] G. Wang, L. Sun, S. Wang et al., "Ferroptosis-related long non-coding RNAs and the roles of LASTR in stomach adenocarcinoma," *Molecular Medicine Reports*, vol. 25, no. 4, p. 118, 2022.

[34] M. Xia, W. Zhu, C. Tao, Y. Lu, and F. Gao, "LncRNA LASTR promote lung cancer progression through the Mir-137/Tgfa/Pi3k/Akt Axis through integration analysis," *Journal of Cancer*, vol. 13, no. 4, pp. 1086–1096, 2022.

[35] M. Zhou, H. Hu, Y. Han et al., "Long non-coding RNA 01126 promotes periodontitis pathogenesis of human periodontal ligament cells via miR-518a-5p/HIF-1α/MAPK pathway," *Cell Proliferation*, vol. 54, no. 1, article e12957, 2021.

[36] W. Ma, M. Zhong, and X. Liu, "Identification of a glycolysis-related lncRNA prognostic signature for clear cell renal cell carcinoma," *Bioscience Reports*, vol. 41, no. 8, p. BSR20211451, 2021.

[37] S. Yang, M. Chen, and C. Lin, "A novel lncRNA MYOSLID/miR-1286/RAB13 axis plays a critical role in osteosarcoma progression," *Cancer Management and Research*, vol. Volume 11, pp. 10345–10351, 2019.

[38] J. Zhao, W. Zhang, M. Lin et al., "MYOSLID is a novel serum response factor-dependent long noncoding RNA that amplifies the vascular smooth muscle differentiation program," *Arteriosclerosis, Thrombosis, and Vascular Biology*, vol. 36, no. 10, pp. 2088–2099, 2016.

[39] J. Wang, Y. Zou, B. Du et al., "SNP-mediated lncRNA-ENTPD3-AS1 upregulation suppresses renal cell carcinoma via miR-155/HIF-1α signaling," *Cell Death & Disease*, vol. 12, no. 7, p. 672, 2021.

[40] L. Luo, L. Li, L. Liu et al., "A necroptosis-related lncRNA-based signature to predict prognosis and probe molecular characteristics of stomach adenocarcinoma," *Frontiers in Genetics*, vol. 13, article 833928, 2022.

[41] L. Liu, W. Chen, Y. Li et al., "Comprehensive analysis of pyroptosis-related long noncoding RNA immune infiltration and prediction of prognosis in patients with colon cancer," *Journal of Oncology*, vol. 2022, Article ID 2035808, 2022.

[42] Y. Liu, R. Li, X. Wang, Z. Xue, X. Yang, and B. Tang, "Comprehensive analyses of MELK-associated ceRNA networks reveal a potential biomarker for predicting poor prognosis and immunotherapy efficacy in hepatocellular carcinoma," *Frontiers in Cell and Development Biology*, vol. 10, article 824938, 2022.

[43] Y. Xu, Q. Zheng, T. Zhou, B. Ye, Q. Xu, and X. Meng, "Necroptosis-related LncRNAs signature and subtypes for predicting prognosis and revealing the immune microenvironment in breast cancer," *Frontiers in Oncology*, vol. 12, article 887318, 2022.

[44] F. Chen, J. Yang, M. Fang, Y. Wu, D. Su, and Y. Sheng, "Necroptosis-related lncRNA to establish novel prognostic signature and predict the immunotherapy response in breast cancer," *Journal of Clinical Laboratory Analysis*, vol. 36, no. 4, article e24302, 2022.

[45] J. Xie, W. Tian, Y. Tang et al., "Establishment of a cell necroptosis index to predict prognosis and drug sensitivity for patients with triple-negative breast cancer," *Frontiers in Molecular Biosciences*, vol. 9, article 834593, 2022.

[46] X. Zhang, X. Zhang, G. Li et al., "A novel necroptosis-associated lncRNA signature can impact the immune status and predict the outcome of breast cancer," *Journal of Immunology Research*, vol. 2022, Article ID 3143511, 2022.

[47] T. Meng, Q. Wang, Y. Yang, Y. Ren, and Y. Shi, "Construction of a necroptosis-related miRNA signature for predicting the prognosis of patients with hepatocellular carcinoma," *Frontiers in Genetics*, vol. 13, article 825261, 2022.

[48] J.-B. Yuan, L. Gu, L. Chen, Y. Yin, and B.-Y. Fan, "Annexin A8 regulated by lncRNA-TUG1/miR-140-3p axis promotes bladder cancer progression and metastasis," *Molecular Therapy – Oncolytics*, vol. 22, pp. 36–51, 2021.

[49] J. Hou, Z. Lu, R. Dong et al., "A necroptosis-related lncRNA to develop a signature to predict the outcome, immune landscape, and chemotherapeutic responses in bladder urothelial carcinoma," *Frontiers in Oncology*, vol. 12, 2022.

[50] L. Qian, T. Ni, B. Fei, H. Sun, and H. Ni, "An immune-related lncRNA pairs signature to identify the prognosis and predict the immune landscape of laryngeal squamous cell carcinoma," *BMC Cancer*, vol. 22, no. 1, p. 545, 2022.

[51] Y. Su, T. Zhang, J. Tang et al., "Construction of competitive endogenous RNA network and verification of 3-key LncRNA signature associated with distant metastasis and poor prognosis in patients with clear cell renal cell carcinoma," *Frontiers in Oncology*, vol. 11, article 640150, 2021.

[52] J. Gu, Z. He, Y. Huang et al., "Clinicopathological and prognostic value of necroptosis-associated lncRNA model in patients with kidney renal clear cell carcinoma," *Disease Markers*, vol. 2022, Article ID 5204831, 2022.

[53] Y. Luo and G. Zhang, "Identification of a necroptosis-related prognostic index and associated regulatory axis in kidney renal clear cell carcinoma," *International Journal of General Medicine*, vol. Volume 15, pp. 5407–5423, 2022.

Hindawi
Journal of Oncology
Volume 2022, Article ID 1123839, 25 pages
https://doi.org/10.1155/2022/1123839

Research Article

FAM201A Promotes Cervical Cancer Progression and Metastasis through miR-1271-5p/Flotillin-1 Axis Targeting-Induced Wnt/β-Catenin Pathway

Yuehong Wang, Zhilian Wang, Keyan Cheng, and Qirong Hao

Department of Obstetrics and Gynecology, Second Hospital of Shanxi Medical University, China

Correspondence should be addressed to Yuehong Wang; wyh-0518@126.com

Received 3 August 2022; Revised 26 August 2022; Accepted 5 September 2022; Published 3 October 2022

Academic Editor: Muhammad Muddassir Ali

This study investigated the role of the family with sequence similarity 201-member A (FAM201A), as previously reported oncogenic, in cervical cancer (CC). FAM201A expression in CC was analyzed through bioinformatics analyses, and its distribution in CC tissues/cells was determined by *in situ* hybridization. CC cells were transfected/cotransfected with FAM201A/flotillin-1 (FLOT1) overexpression plasmids and miR-1271-5p mimics, followed by functional analysis on viability, migration and invasion. Pearson's correlation tests were performed to analyze the correlation between FAM201A and miR-1271-5p in CC tissues. The targeting relationship between miR-1271-5p and FLOT1 was confirmed by dual-luciferase reporter assay. The expressions of FAM201A, miR-1271-5p, FLOT1, matrix metalloproteinases (MMP)-9, MMP-2, E-cadherin, N-cadherin, and the Wnt/β-catenin pathway-related molecules (Wnt1, β-catenin and p-β-catenin) in CC cells or tissues were assessed by quantitative reverse transcription polymerase chain reaction (qRT-PCR) and/or western blot. The results showed that FAM201A was abundantly expressed and miR-1271-5p expression was downregulated in CC. FAM201A was enriched in CC cell cytoplasm and negatively correlated with miR-1271-5p in CC tissues. FAM201A overexpression enhanced the cell viability, migration, invasion, and tumorigenesis of CC *in vivo* and increased FLOT1 expression. These trends were all reversed by upregulating miR-1271-5p, which induced opposite effects to FAM201A overexpression. MiR-1271-5p upregulation depleted the levels of MMP-9, MMP-2, N-cadherin, and the Wnt/β-catenin pathway-related molecules and upregulated E-cadherin expression. FLOT1 was a direct target of miR-1271-5p. FLOT1 overexpression induced effects contrary to the upregulation of miR-1271-5p and abolished miR-1271-5p upregulation-induced effects in CC cells. Overall, this study showed that FAM201A promoted cervical cancer progression and metastasis by targeting the miR-1271-5p/FLOT1 axis-induced Wnt/β-catenin pathway.

1. Introduction

Cervical cancer (CC) is one of the most common malignant tumors affecting women worldwide, second to breast cancer [1], and is the leading cause of cancer-related mortality in some developing countries [2]. The progression of CC is featured as a multistage and multistep process involving the activation of proto-oncogenes and (or) inhibiting tumor-suppressive genes [3]. Currently, the antitumor treatment for CC remains less effective owing to its late-appearing symptom, leading to unsuccessful disease diagnoses and advanced-stage disease by the time of diagnosis [4]. It is reported that the five-year survival rate for metastatic CC patients is 16.5%, compared to 91.5% for localized CC patients [5]. Therefore, metastasis is accountable for most unfavorable prognoses, recurrence and high morbidity of CC [6].

Long noncoding RNAs (lncRNAs), a type of transcripts constituted by over 200 nucleotides with no translation ability, have emerged as pivotal regulators for the carcinogenesis and progression of cancers, including CC [6]. Epithelial-mesenchymal transition (EMT), a highly conserved trans-differentiation program considered the major driver of cancer progression, is reported to facilitate metastasis of cancer cells by promoting migration and invasion and conferring

Table 1: Primers used in quantitative reverse transcription polymerase chain reaction for target genes.

Genes	Species	Forward	Reverse
FAM201A	Human	5′-TCTCTGATGGGAGCCTCTTTA-3′	5′-CAAGCCACAGA CGGAGAAA-3′
miR-1271-5p	Human	5′-CTTGGCACCTAGCAAGCACTCA-3′	5′-GCGAGCACAGA ATTAATACGAC-3′
Flotillin-1	Human	5′-CCATCTCGTCACTGGCATT-3′	5′-CGCCAACATCT CCTTGTTC-3′
MMP-2	Human	5′-TACAGGATCATTGGCTACACACC-3′	5′- GGTCACATCGC TCCAGACT-3′
MMP-9	Human	5′-TGTACCGCTATGGTTACACTCG -3′	5′- GGCAGGGACAG TTGCTTCT-3′
E-cadherin	Human	5′-ATTCTGATTCTGCTGCTCTTG-3′	5′-AGTCCTGGTCC TCTTCTCC-3′
N-cadherin	Human	5′- AACCTAGCCTACTGGCCAAA -3′	5′- AACATCGAGGT CGTAAACCC-3′
Wnt1	Human	5′- CGATGGTGGGGTATTGTGAAC-3′-	5′- CCGGATTTTGG CGTATCAGAC-3′
β-Cadherin	Human	5′- GAGCTGCCATGTTCCCTGAG -3′	5′- CAGTTGTCAAT TTGATTAAC-3′
GAPDH	Human	5′-GAGAAGGCTGGGGCTCATTT-3′	5′-AGTGATGGCAT GGACTGTGG-3′
U6	Human	5′-CTCGCTCGGCAGAACA-3′	5′-AACGCTTCACG AATTTGCGT-3′

an apoptosis-resistant property [7]. By directly or indirectly reversing EMT, lncRNAs can repress tumorigenesis, cancer progression, and metastasis, demonstrating their therapeutic potential [8]. The family with sequence similarity 201-member A (FAM201A) is a long nonprotein coding RNA derived from an open reading frame (ORF)-lacking RNA transcripts transcribed from a 2.9 Kbp-long gene that is located in genomic 9p13.1 [9]. Several studies exploring anticancer strategies have revealed the involvement of FAM201A in inducing carcinogenesis and promoting the progression of triple-negative breast cancer (TNBC) [10], lung squamous cell cancer (LSCC) [11], and lung adenocarcinoma (LUAD) [12]. Additionally, highly expressed FAM201A was reported to provoke short-term radio-resistance, leading to inferior survival in patients with esophageal squamous cell cancer [13] and nonsmall-cell lung cancer [14]. However, little is known about the biological roles and clinical significance of FAM201A in CC.

Interactive analyses have identified FAM201A as a key regulator in cancer progression in a lncRNA-miRNA-mRNA competing endogenous RNA (ceRNA) network, via which FAM201A was found to indirectly regulate the expression of messenger RNA (mRNA) by sponging its targeted microRNAs (miRNAs) [10, 14, 15]. Without lncRNA-directed sponging effects, miRNAs, a class of small noncoding RNAs with 18-24 nucleotides in length that are endogenous and evolutionarily conserved, can destabilize mRNAs or inhibit translation, thereby repressing mRNA expression by complementarily binding to the 3'-untranslated regions of the mRNAs [16, 17].

A large number of miRNAs have been implicated in CC-associated ceRNA networks. For instance, MiR-1271-5p expression was previously reported to be aberrantly downregulated in acute myeloid leukemia [18], colon cancer [19], multiple myeloma [20], and LUAD [21], indicating that it played a tumor-suppressive role in the progression of these cancers through related ceRNA networks. Meanwhile, upregulated miR-1271-5p expression was shown to induce oncogenic effects and associated with unfavorable prognoses in hepatocellular carcinoma (HCC) [22]. However, whether FAM201A regulates miR-1271-5p through the ceRNA network and thus participates in CC progression remains unconfirmed.

In this study, we investigated the effects of FAM201A in CC progression using bioinformatics tools and determined the potential miR-1271-5p-targeted mRNA for identifying a FAM201A-miR-1271-5p-mRNA ceRNA regulatory network in CC, with the hope to propose an original molecular therapy for CC.

2. Materials and Methods

2.1. Ethics Statement. Written informed consent was obtained from all human participants. All animal experiments were performed following the guidelines of the China Council on Animal Care and Use [23]. The human and animal studies

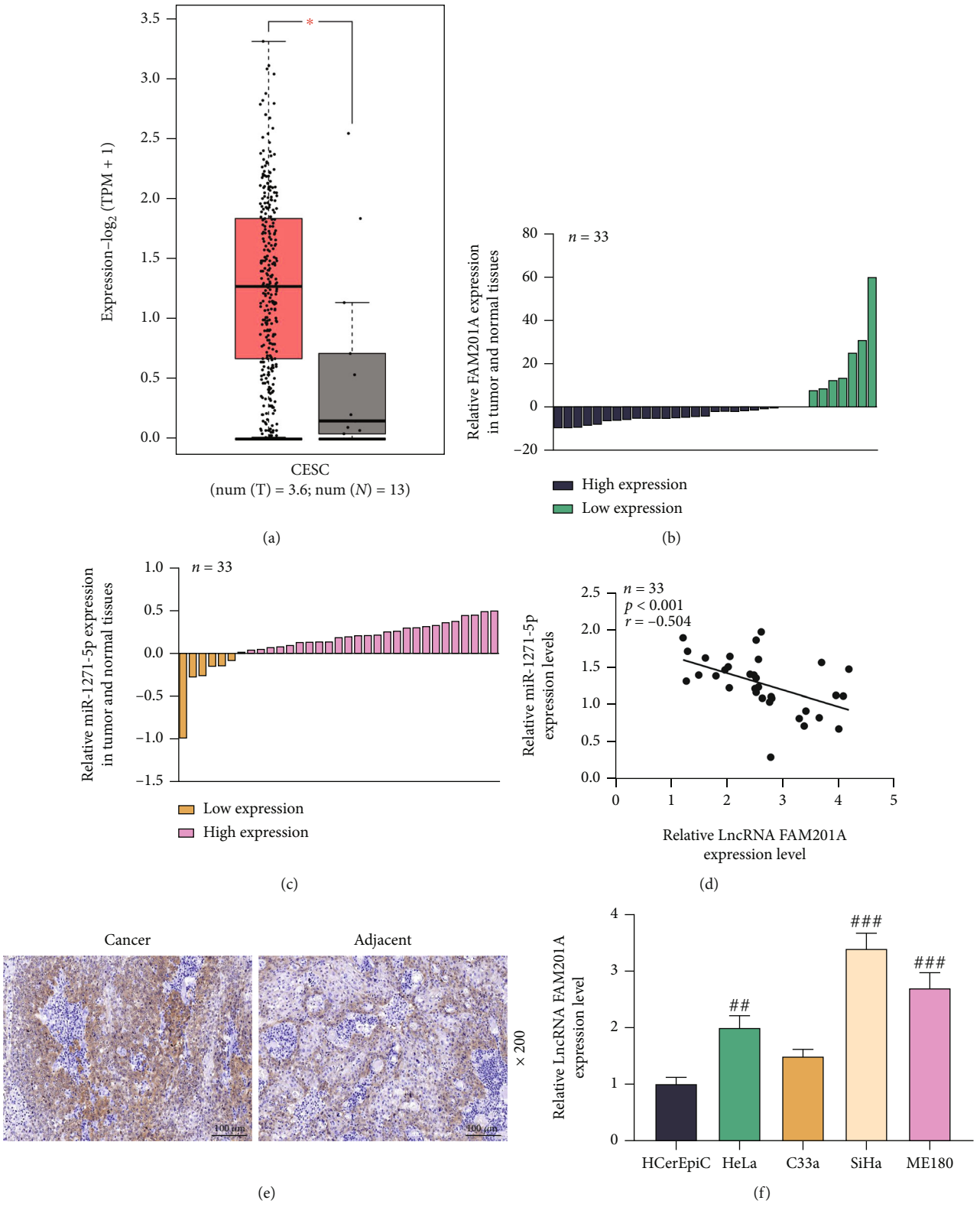

Figure 1: Continued.

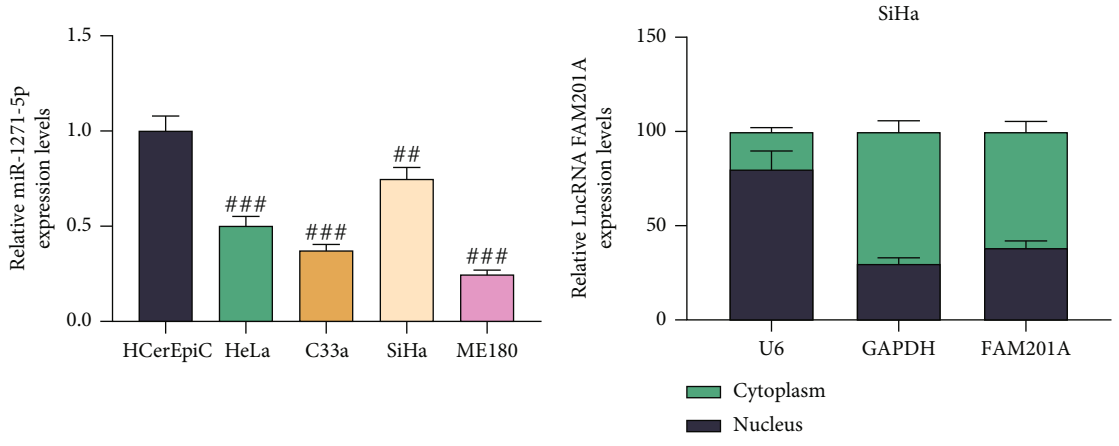

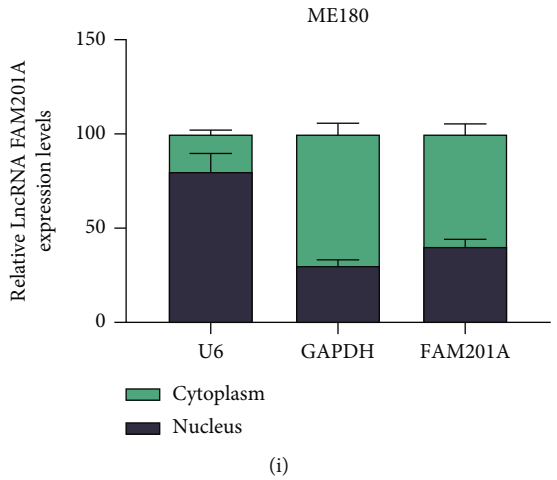

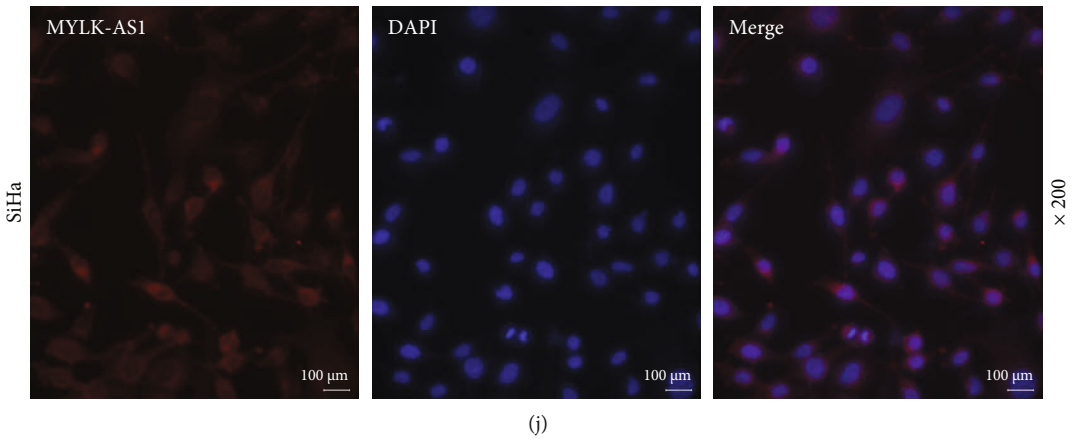

Figure 1: Continued.

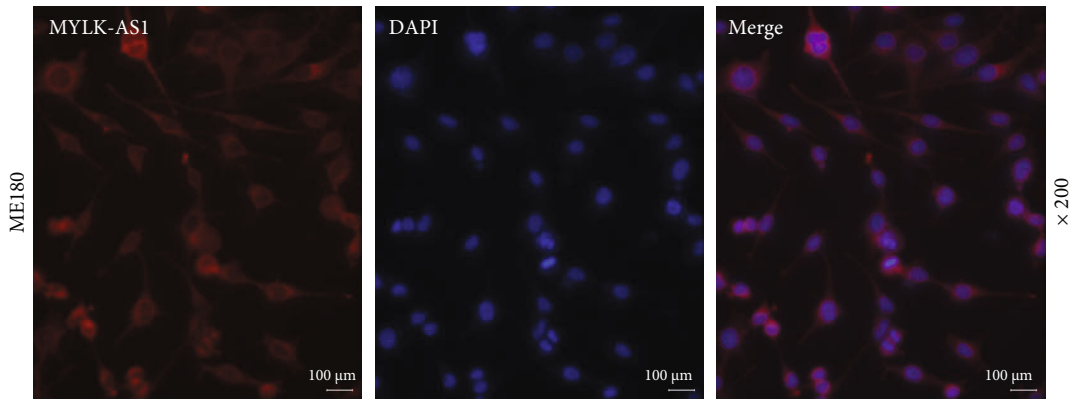

(k)

Figure 1: FAM201A was highly expressed in CC and enriched in CC cell cytoplasm, and its expression was negatively correlated with miR-1271-5p. (a) The expression of FAM201A was analyzed in the TCGA-CESC database, including CC samples ($n = 306$) and normal samples ($n = 13$) by GEPIA. (b, c, f, g) The expressions of FAM201A (b, f) and miR-1271-5p (c, g) in CC tissues and the adjacent normal tissues (b, c) as well as in HeLa, C33a, SiHa, ME180 and human endocervical epithelial HCerEpiC cells (f, g) were analyzed by qRT-PCR. (d) The correlation between FAM201A and miR-1271-5p in CC tissues was analyzed by Pearson's correlation tests. (e) The expression of FAM201A in CC tissues and the adjacent normal tissues was assessed by fluorescence *in situ* hybridization (magnification: ×200; scale: 100 μm). (h, i) The subcellular localization of FAM201A was determined by qRT-PCR. (j, k) The expression of FAM201A in SiHa cells and ME180 cells was evaluated by fluorescent *in situ* hybridization (magnification: ×200; scale: 100 μm). $^{\#\#}P < 0.01$; $^{\#\#\#}P < 0.001$; $^{\#}$ vs. HCerEpiC. CC: cervical cancer; qRT-PCR: quantitative reverse transcription polymerase chain reaction; NC: negative control; FAM201A: the family with sequence similarity 201-member A; M: miR-1271-5p mimic; MC: mimic control; GEPIA: Gene Expression Profiling Interactive Analysis; TCGA-CESC: Cancer Genome Atlas Cervical Squamous Cell Carcinoma and Endocervical Adenocarcinoma; qRT-PCR: quantitative reverse transcription polymerase chain reaction.

were approved by the Ethics Committee and the Committee of Experimental Animals of Nanfang Hospital (approval number: GD202004020/GD202007027), respectively.

2.2. Clinical Sample. CC tissues ($n = 33$) and adjacent normal tissues ($n = 33$) were collected during surgical operation at the Second Hospital of Shanxi Medical University in 2020 from CC patients without preoperative chemotherapy, radiotherapy, or immunotherapy. Fresh samples were immediately frozen in liquid nitrogen and stored at -80°C.

2.3. Cell Culture. Human cervical endometrial epithelial cells (HCerEpiC; CP-H058, Procell Life Science&Technology Co., Ltd, Wuhan, China) were cultured in EpiLife Media (MEPI500CA, ThermoFisher, Waltham, MA, USA) to reach a confluence around 75% within 10–14 days. CC cell lines, including HeLa (CCL-2), C33a (HTB-31), SiHa (HTB-35), and ME180 (HTB-33) purchased from American Type Culture Collection (ATCC, Manassas, VA, USA), were cultivated in high-glucose Dulbecco's Modified Eagle Medium complete media (DMEM; 11965092, ThermoFisher, USA) supplemented with 2 mM L-glutamine (25030081, ThermoFisher, USA), 10% Fetal Bovine Serum (FBS; 16140071, ThermoFisher, USA), and 1% penicillin-streptomycin (V900929, Sigma-Aldrich, St. Louis, MO, USA) at 37°C with 5% CO_2.

2.4. General/Fluorescent in Situ Hybridization. The expression and subcellular location of FAM201A were determined by General/Fluorescent *in situ* hybridization using Digoxigenin-labeled Probe Detection kits (Boster Biological Technology, Wuhan, China). As per the manufacturer's instructions, CC tissues and adjacent normal tissues were fixed in 4% paraformaldehyde (16005, Sigma-Aldrich, USA), dehydrated by ethanol, and transparentized by xylene (95682, Sigma-Aldrich, USA). Then, the tissues were embedded in paraffin (1496904, Sigma-Aldrich, USA) and cut into 4 μm-thick sections, following which the sections underwent dewaxation with xylene and rehydration by ethanol. SiHa and ME180 cells were cultured to reach a concentration of 1×10^5 cells/mL and fixed in 4% paraformaldehyde for 4 hours (h). Afterward, the sections and cells were treated with a standard prehybridization buffer at 68°C for 20 h. Digoxigenin-labeled DNA probes complementary to FAM201A were denaturalized via boiling water bath for 10 minutes (min) and added into the standard prehybridization buffer to formulate prehybridization buffer. The prehybridization buffer was then incubated with the tissues and cells at 68°C for another 20 h. After washing using Wash Solution I, a biotin-labeled anti-Digoxigenin antibody was added to the tissues, followed by the 3,3'-Diaminobenzidine (DAB) treatment for the color-development of the tissues. The cells were supplemented with anti-Digoxigenin antibody (ab420, Abcam, Cambridge, MA, USA) and incubated with Goat anti-mouse IgG H&L (ab150115, Abcam, USA). The nuclei of the cells were dyed using 4',6-diamidino-2-phenylindole (DAPI; D21490, ThermoFisher, USA). Color and fluorescent color signals were observed by a confocal microscope (Raman DXR™3, ThermoFisher, USA) at the magnification of ×200.

2.5. Cell Transfection. The pcDNA™3.1/Hygro(+) mammalian expression vectors were used to construct overexpression plasmids of FAM201A and FLOT1, and the empty vector was

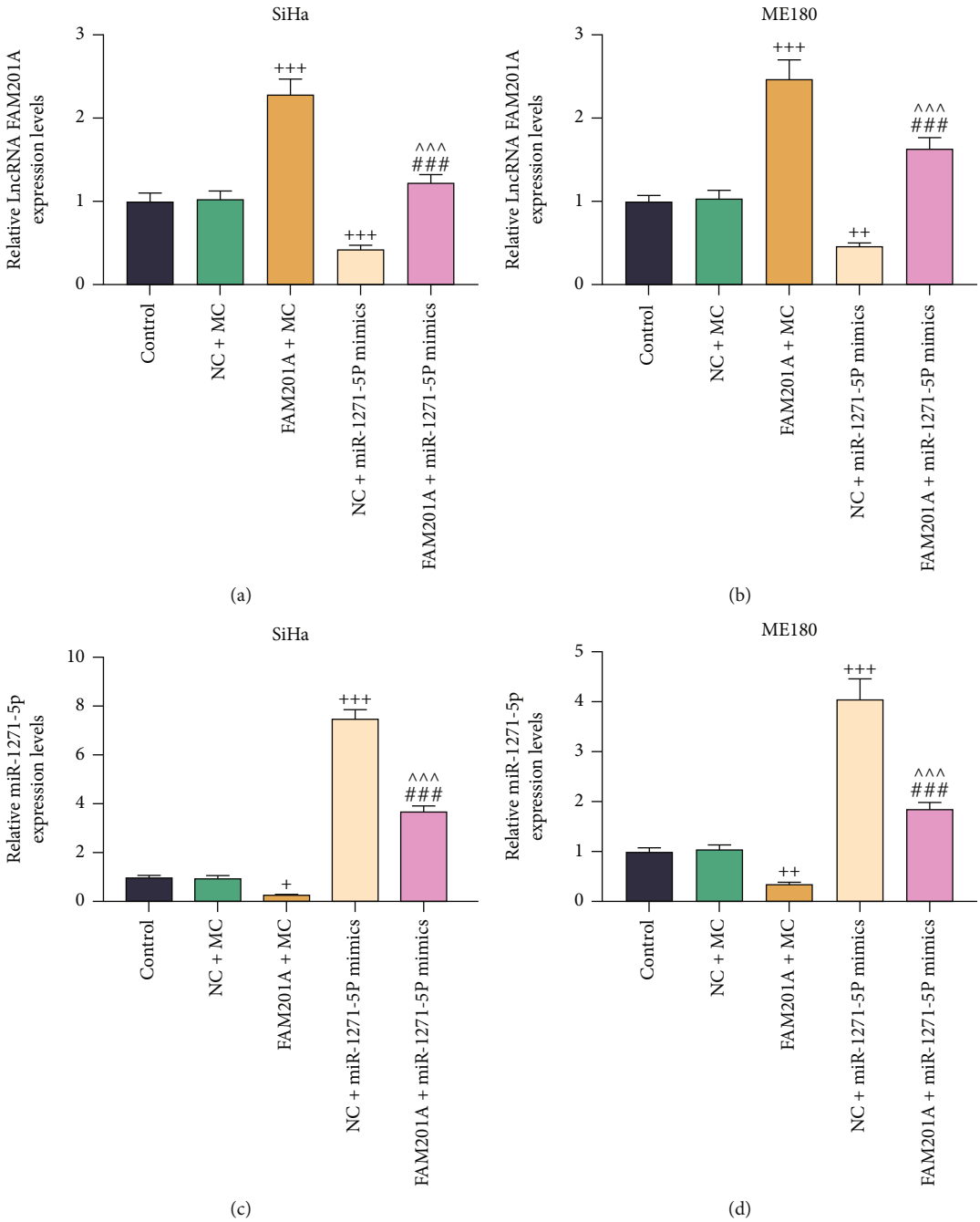

Figure 2: Continued.

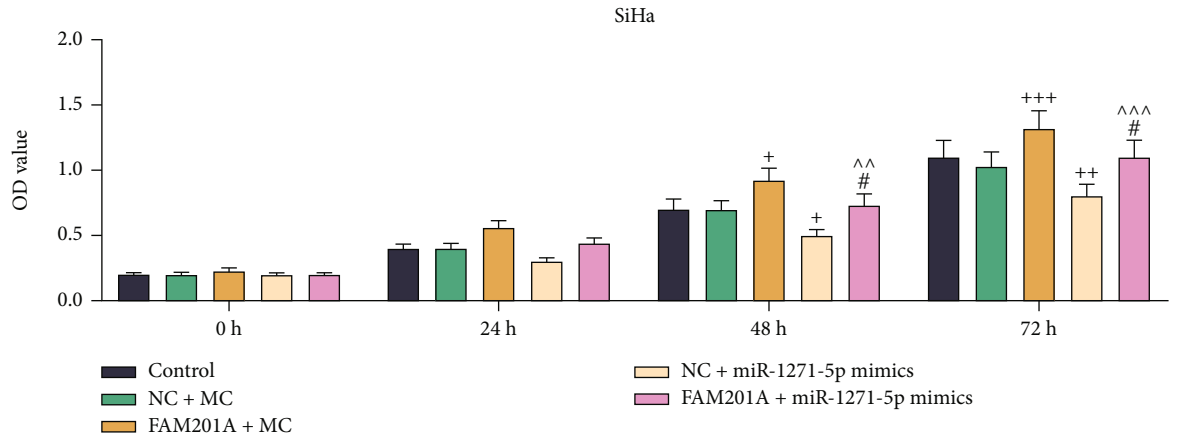

(e)

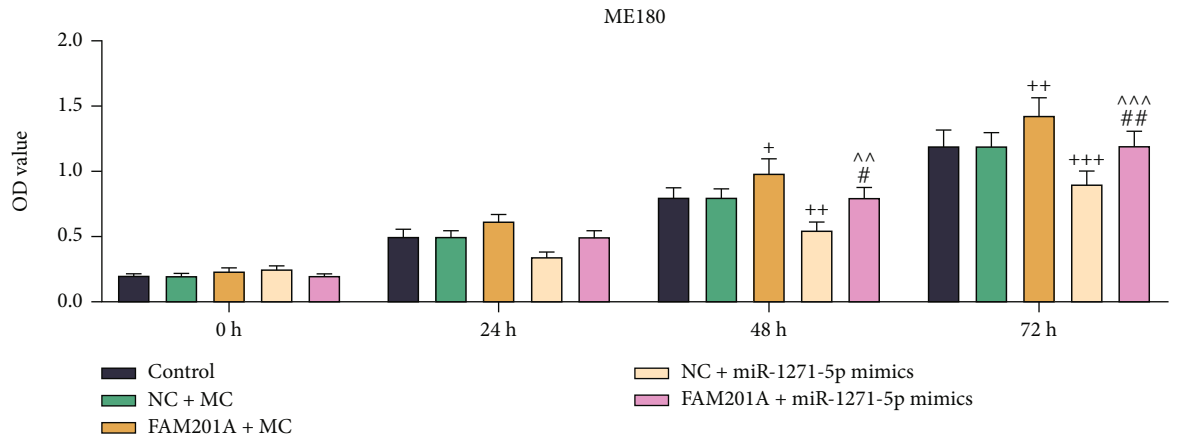

(f)

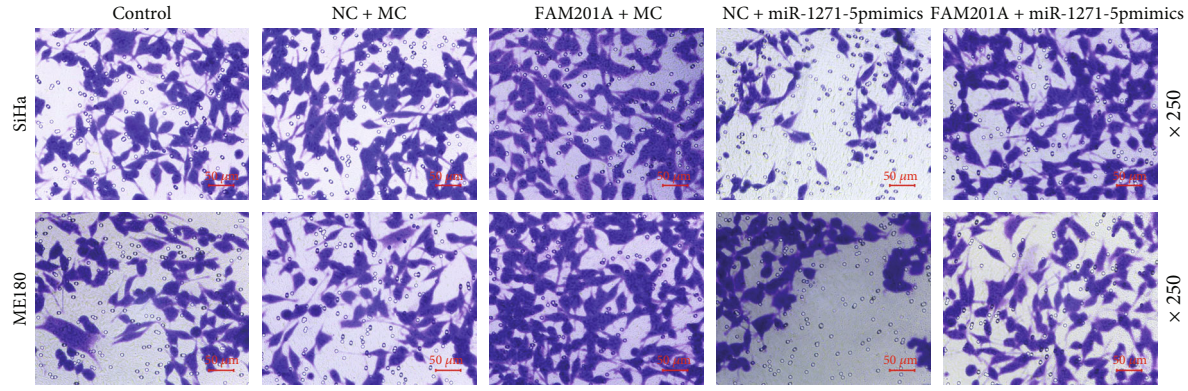

(g)

Figure 2: Continued.

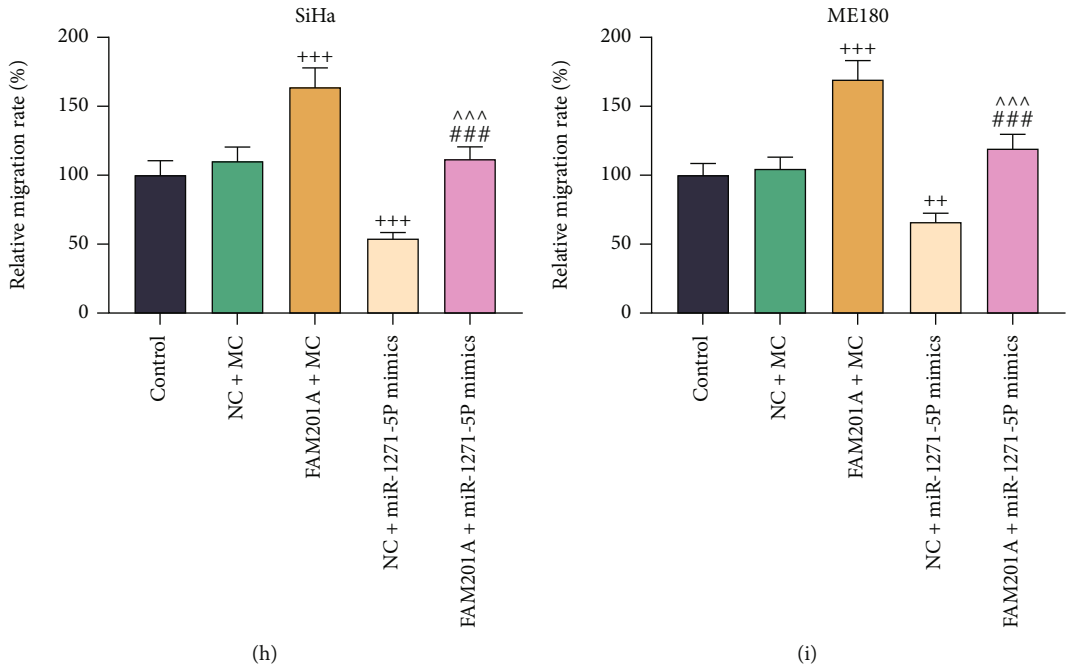

Figure 2: FAM201A overexpression increased CC cell viability and promoted migration by downregulating miR-1271-5p expression. (a-d) The expressions of FAM201A (a, b) and miR-1271-5p (C/D) in CC (SiHa and ME180) cells transfected with FAM201A overexpression plasmids or miR-1271-5p mimic alone or in combination were analyzed by qRT-PCR. (e, f) The viability of CC (SiHa and ME180) cells after transfection with FAM201A overexpression plasmids or miR-1271-5p mimic alone or in combination was measured by CCK-8 assay at 24-, 48-, and 72-h post-transfection. (g-i) The migration of CC (SiHa and ME180) cells after transfection with FAM201A overexpression plasmids or miR-1271-5p mimic alone or in combination was evaluated by the Transwell assay (magnification: ×250; scale: 50 μm). ^{+}P or $^{\#}P < 0.05$; ^{++}P or $^{\wedge\wedge}P$ or $^{\#\#}P < 0.01$; ^{+++}P or $^{\wedge\wedge\wedge}P$ or $^{\#\#\#}P < 0.001$; $^{+}$ vs. NC+MC; $^{\wedge}$*vs*. FAM201A+MC; $^{\#}$ vs. NC+miR-1271-5p M. CC: cervical cancer; qRT-PCR: quantitative reverse transcription polymerase chain reaction; CCK-8: cell counting kit-8; NC: negative control; FAM201A: the family with sequence similarity 201-member A; M: miR-1271-5p mimic; MC: mimic control.

set as negative control (NC). MiR-1271-5p mimic/mimic control (MC) (miR10005796-1-5/miR1N0000001-1-5) was purchased from RIBOBIO (Guangzhou, China). C33a or ME180 cells (4×10^4) were seeded in 96 well plates until 80% confluence was reached. Transfection working solutions (0.15 μL) were prepared by mixing Lipofectamine 3000 transfection reagents (L3000015, ThermoFisher, USA) and Opti-MEM media (31985062, ThermoFisher, USA). Subsequently, the above plasmids were (2 μg) added into Opti-MEM media (10 μL) together with a P3000 reagent (0.4 μL). Next, the processed plasmids were mixed with the transfection working solution at a ratio of 1 : 1 to obtain an RNA-lipid complex, of which 10 μL of the complex mixture was incubated with the cells at 37°C for 24 h or 48 h.

2.6. Cell Counting Kit- (CCK-) 8 Assay. The viability of SiHa or ME180 cells was evaluated using a CCK-8 kit (96992, Sigma-Aldrich, USA). After transfection with FAM201A/FLOT1 overexpression plasmids or miR-1271-5p mimic alone or in combination, SiHa or ME180 cells were seeded into 96-well plates at a density of 1×10^4 cells/well supplemented with complete media and cultured. The cells in each well were treated with the CCK-8 reagent (10 μL) and incubated for 4 h, at 24-, 48- and 72-h post-transfection. The optical density at a wavelength of 450 nm was determined by a microplate reader (ELx808, BioTek, Winooski, VT, USA).

2.7. Bioinformatics Analysis. The targeting relation between FLOT1 and miR-1271-5p was predicted by Targetscan (http://www.targetscan.org/vert_71/).

2.8. Dual-Luciferases Reporter Assay. Dual-Luciferase Reporter Assay System (E1910, Promega, Madison, WI, USA) was used to verify the targeting relationships between FAM201A and miR-1271-5p and between miR-1271-5p and FLOT1. SiHa or ME180 cells (4×10^4) were then cultured to attain 70% confluence. Sequences of wild type FLOT1 (WT) (5′-CCCCTCATCUCTCCTTGCCAAAT-3′) and mutant FLOT1 (MUT) (5′-CCCCTCATCUCTCCTGGACAAAT-3′) were cloned onto pMirGLO luciferase vectors (50 ng, E1330, Promega, USA). The cells were cotransfected with the pMirGLO cloned with FLOT1-WT or FLOT1-MUT (2 μg) and miR-1271-5p mimic (2 μg) using Lipofectamine 3000 transfection reagent for 48 h. After cotransfection, the cells were lysed by diluted Lysis Buffer (50 μL, 16189, ThermoFisher, USA) and added with Luciferase Assay Reagent II (100 μL). The activity of firefly luciferase, which was normalized to that of *Renilla* luciferase, was measured using a luminometer (GloMax®20/20, Promega, USA).

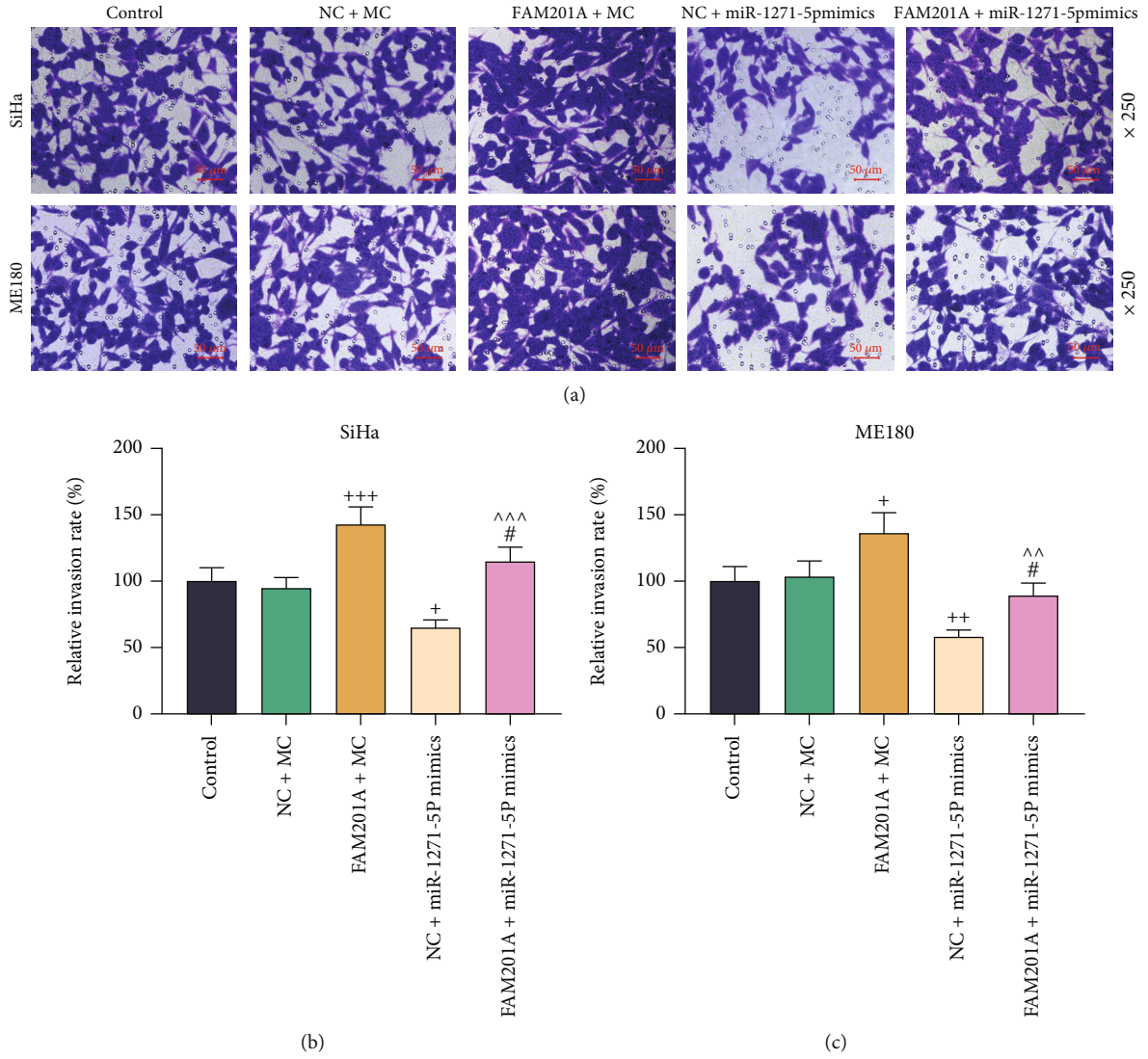

Figure 3: Continued.

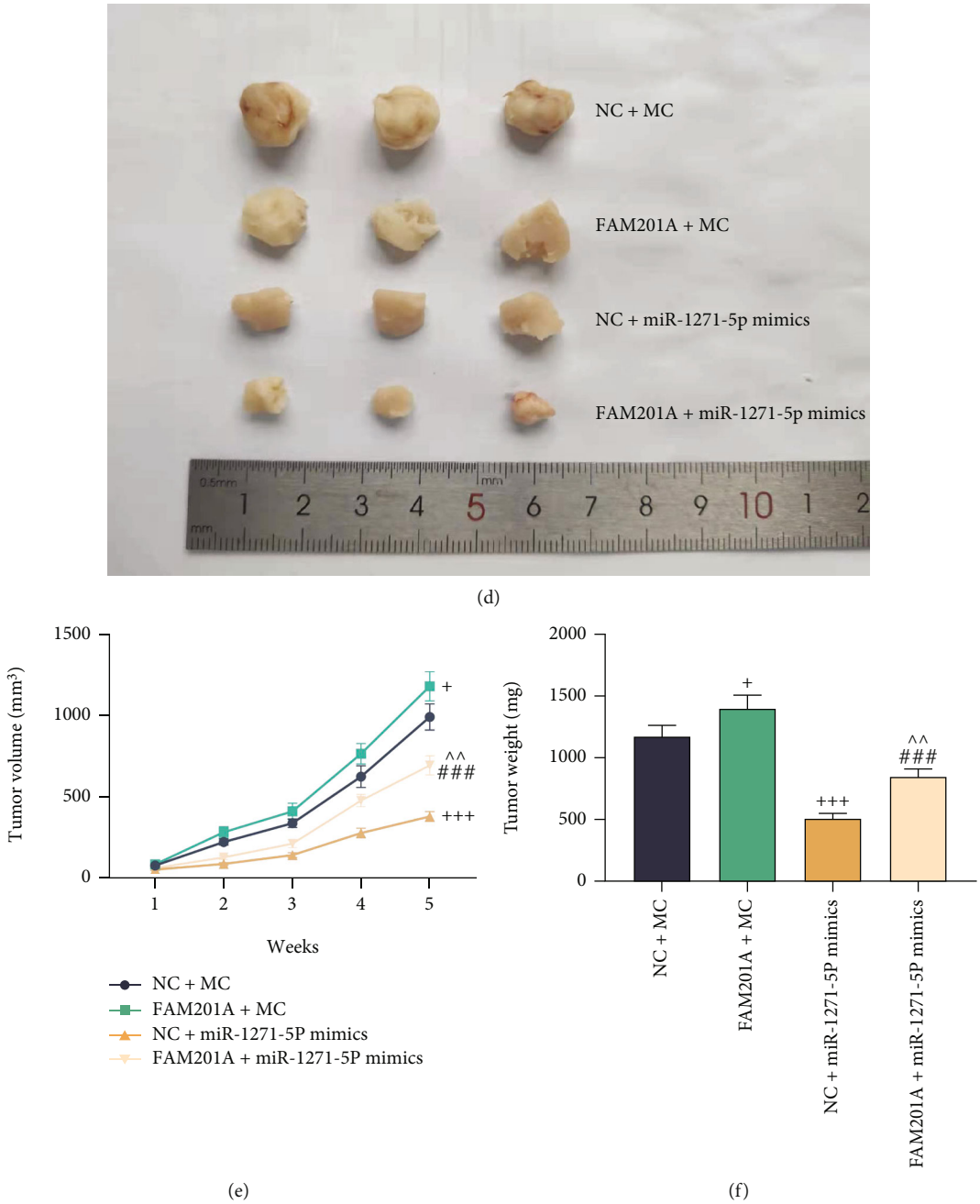

Figure 3: FAM201A overexpression promoted CC cell invasion and CC tumorigenesis *in vivo* by downregulating miR-1271-5p expression. (a-c) The invasion of CC (SiHa and ME180) cells transfected with FAM201A overexpression plasmids or miR-1271-5p mimic alone or in combination was evaluated by the Transwell assay (magnification: ×250; scale: 50 μm). (d) Pictures of subcutaneous xenografts formed by SiHa cells with stable overexpressed FAM201A, miR-1271-5p or both (e, f). The volume (e) and weight (f) of subcutaneous xenografts formed by SiHa cells with stable overexpressed FAM201A, miR-1271-5p or both were measured weekly (e) or at the fifth week after resection (f). ^{+}P or $^{\#}P < 0.05$; ^{++}P or $^{\wedge\wedge}P < 0.01$; ^{+++}P or $^{\wedge\wedge\wedge}P$ or $^{\#\#\#}P$;$^{+}$ vs. NC+MC; $^{\wedge}$ vs. FAM201A+MC; $^{\#}$ vs. NC+miR-1271-5p M. CC: cervical cancer; qRT-PCR: quantitative reverse transcription polymerase chain reaction; NC: negative control; FAM201A: the family with sequence similarity 201-member A; M: miR-1271-5p mimic; MC: mimic control.

2.9. Transwell Assay. Transwell chambers (3428, Corning, Corning, NY, USA) were used to assess the migratory and invasive abilities of SiHa cells and ME180 cells after transfection with FAM201A/FLOT1 overexpression plasmids or miR-1271-5p M alone or in combination. The upper chamber was precoated by Matrigel (dilution: 1 : 3; 356234, Corning, USA) for cell invasion assay, while that without Matrigel was used for cell migration assay. The cells were cultured to prepare a cell suspension at a concentration of 5×10^5 cells/ml. Then, 100 μL of the cell suspension was poured into the upper chamber, and 600 μL of DMEM containing 10% FBS was added to the lower chamber. The whole Transwell set

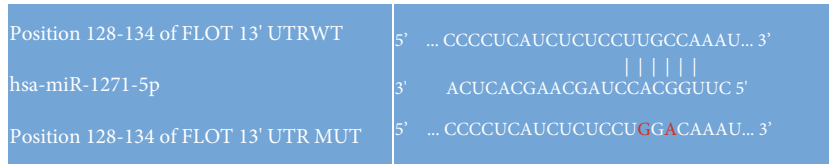

(a)

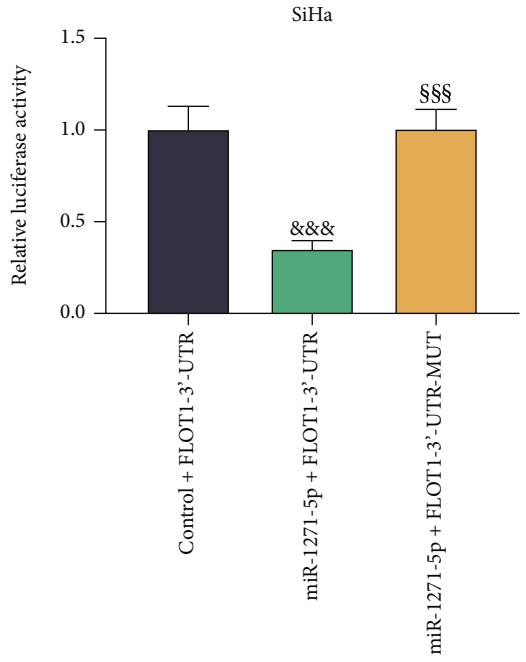

(b)

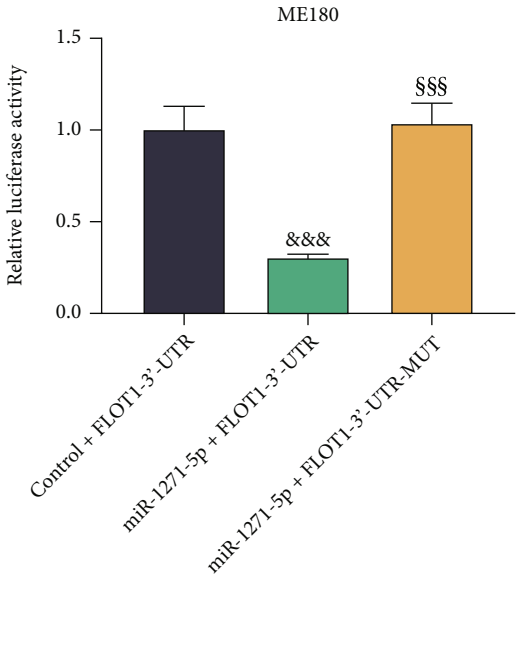

(c)

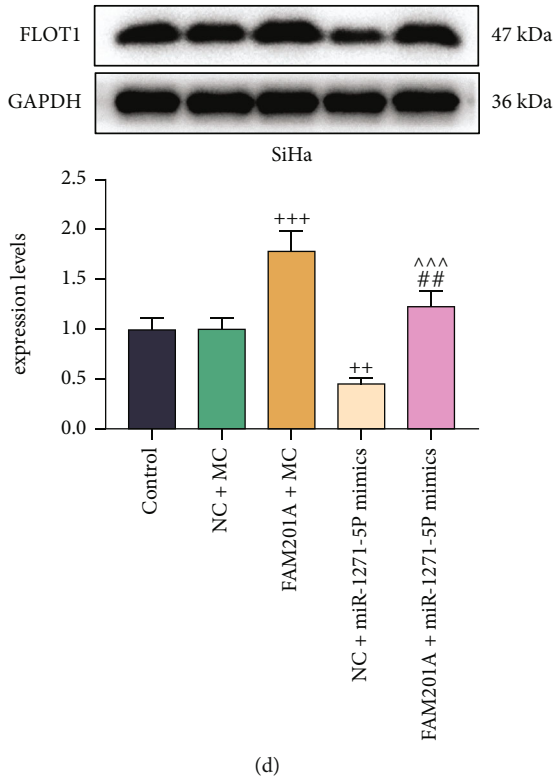

(d)

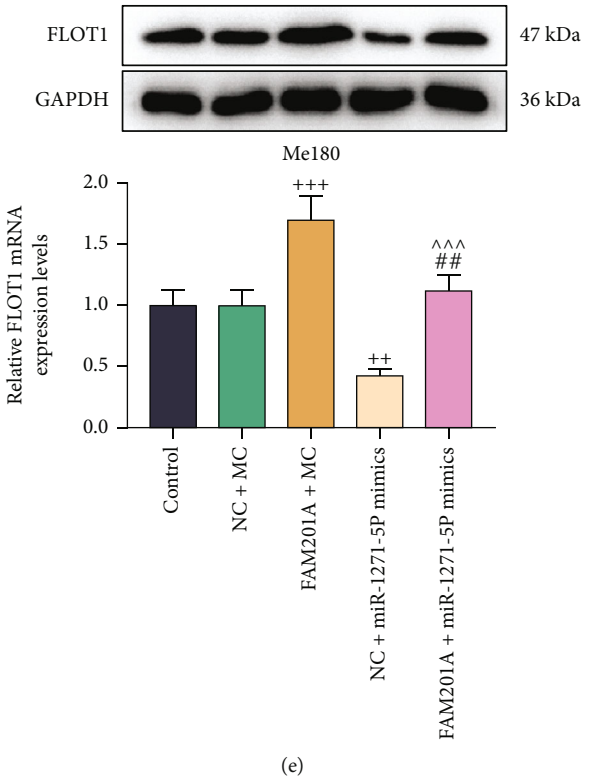

(e)

Figure 4: Continued.

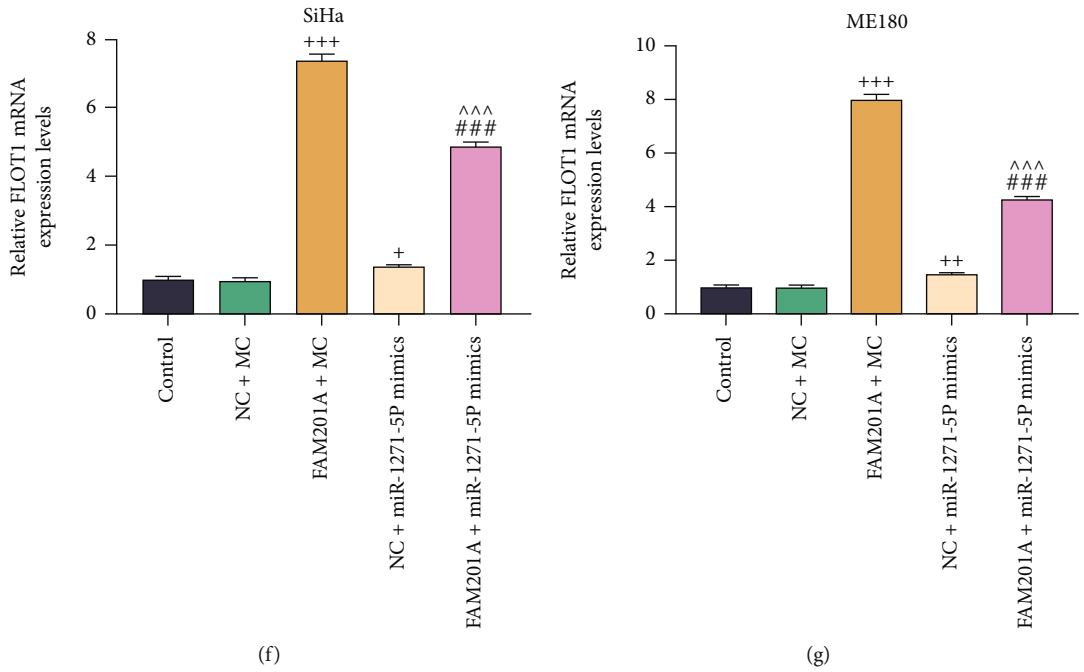

Figure 4: FAM201A sponged miR-1271-5p to increase the expression of FLOT1, a direct target of miR-1271-5p, in CC cells. (a) The targeting relationship between miR-1271-5p and LINC01106 was identified by Targetscan. (b, c) FLOT1 was confirmed as the target of LINC01106 by dual-luciferase reporter assay. (d-g) The expression of FLOT1 in CC (SiHa and ME180) cells after transfection with FAM201A overexpression plasmids or miR-1271-5p mimic alone or in combination was analyzed by qRT-PCR (f, g) and western blot (d, e), with GAPDH as the reference gene. $^{+}P < 0.05$; ^{++}P or $^{\#\#}P < 0.01$; ^{+++}P or $^{\wedge\wedge\wedge}P$ or $^{\#\#\#}P < 0.001$; $^{+}$ vs. NC+MC; $^{\wedge}$ vs. FAM201A +MC; $^{\#}$ vs. NC+miR-1271-5p M; $^{\&}$ vs. control+ FLOT1-3'-UTR; $^{\$}$vs. miR-1271-5p+FLOT1-3'-UTR. CC: cervical cancer; qRT-PCR: quantitative reverse transcription polymerase chain reaction; NC: negative control; M: miR-1271-5p mimic; MC: mimic control; FLOT1: flotillin 1; 3'-UTR: 3'-untranslated regions.

was incubated at 37°C for 24 h. Later, the lower chamber was washed twice with phosphate-buffered saline (P5493, Sigma-Aldrich, USA), fixed with 4% paraformaldehyde (P6148 Sigma-Aldrich, USA) and stained with 800 μL Giemsa (10092013, ThermoFisher, USA). After removing nonmigratory or noninvading cells, the remaining cells were observed under ×200 magnification using an inverted microscope (IX71; Olympus, Tokyo, Japan). Cells in five randomly selected fields were counted using ImageJ software and cell migration and invasion rates were calculated.

2.10. Murine Xenograft Assay. BALB/c nude mice (Male, 5–6-week-old) were purchased from the Vital River Laboratories (Beijing, China). The mice were maintained under a specific condition (22~24°C, 50% humidity, a 12 h:12 h circadian cycle), with free access to a standard mice chow and water. Then, the mice were randomized into four groups ($n = 6$ per group): NC+MC group, FAM201A+MC group, NC+miR-1271-5p M group, and FAM201A+miR-1271-5p M group. After transfection, SiHa cells (5×10^6) with stable expressions of FAM201A, miR-1271-5p or both were subcutaneously injected into the posterior flank of the mice. The size of subcutaneous xenografts (length and width) was measured by a caliper every 7 days, with 5 times in total, and the volume of the xenografts was calculated according to the formula: $0.5 \times \text{length} \times \text{width}^2$. Five weeks after the injection, the mice were sacrificed via spinal dislocation under anesthetization using pentobarbital sodium (P010, Sigma-Aldrich, USA), following which the subcutaneous xenografts were resected and weighed.

2.11. Quantitative Reverse Transcription Polymerase Chain Reaction (qRT-PCR). Total mRNAs and miRNAs from CC cell lines and HCerEpiC, as well as CC tissues and the adjacent normal tissues, were extracted by TRIzol lysis buffer (15596018, ThermoFisher) and Small RNA kits (9753Q, TaKaRa, Liaoning, China), respectively. Chloroform (48520-U, Sigma-Aldrich, USA) was used to extract the lysate of mRNA and miRNA. The extracted lysate was centrifuged (12000 × g) at 4°C for 15 min. Then, isopropanol (W292907, Sigma-Aldrich, USA) was applied to precipitate the lysate from water layers via centrifugation (12000 × g) at 4°C for 10 min, which was then washed with 75% ethanol (32205, Sigma-Aldrich, USA) and then isolated from the supernatant. Next, it was resuspended and centrifugated (7500 × g) at 4°C for 10 min and dissolved in 20 μL diethyl pyrocarbonate (DEPC; 40718, Sigma-Aldrich, USA). First-strand cDNAs of the isolated mRNA and miRNA were synthesized using a Synthesis Kit (K1621, ThermoFisher, USA). qPCR was performed on an Applied Biosystems 7500 FAST real-time PCR machine (Applied Biosystems, Foster City, CA, USA) with TB Green® Premix Ex Taq II (Tli RNaseH Plus, RR820Q, TAKARA, China). The primers used are shown in Table 1. The thermocycling conditions were set

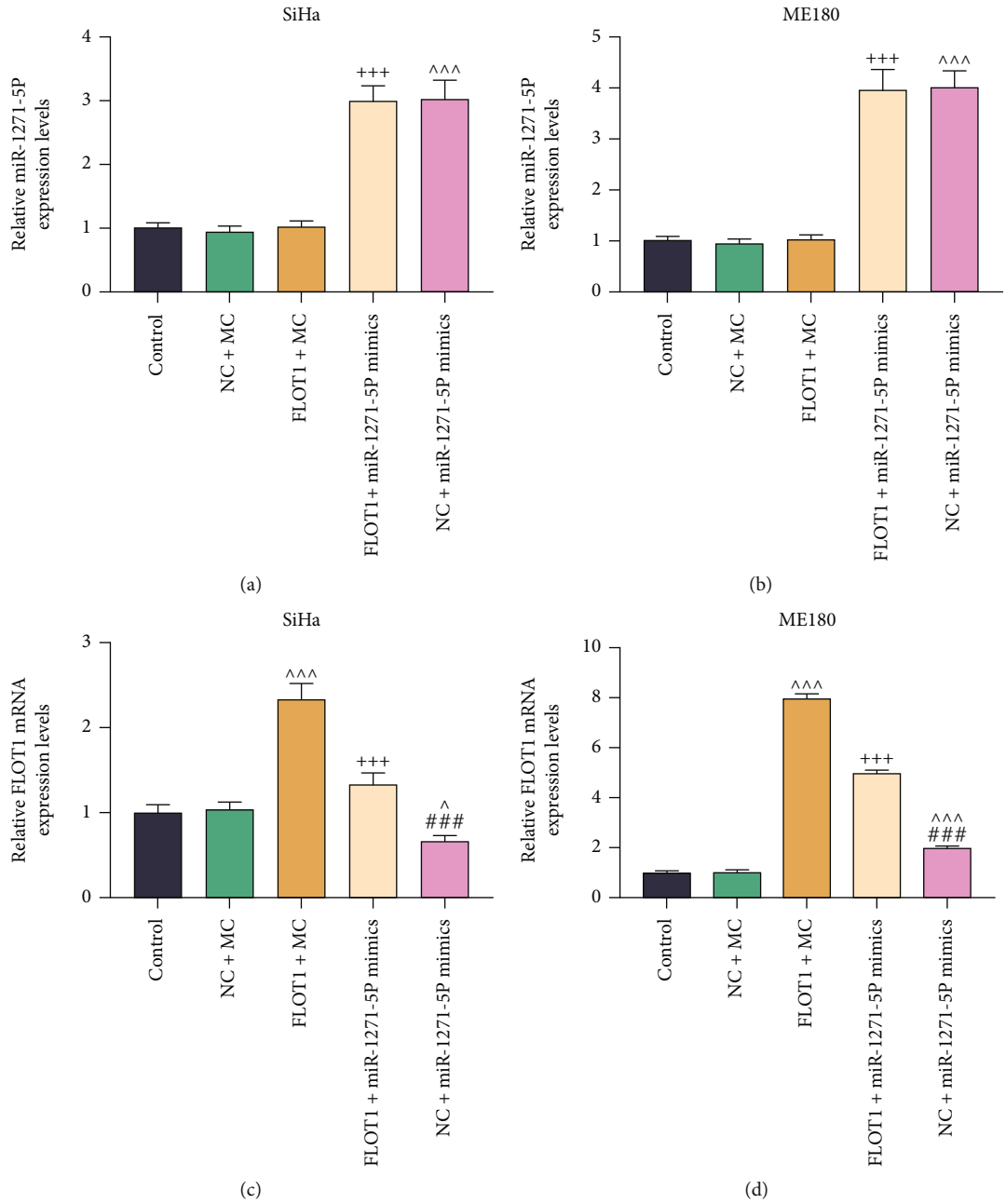

Figure 5: Continued.

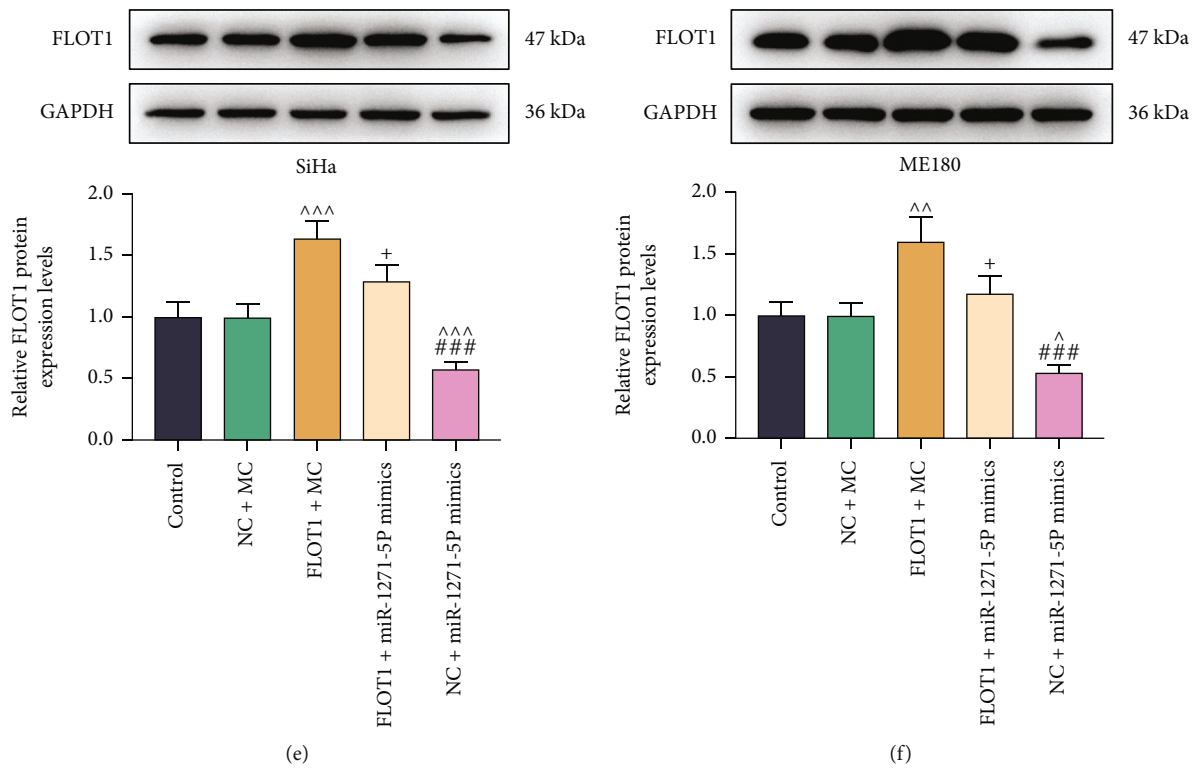

Figure 5: FLOT1 expression was repressed by miR-1271-5p upregulation in CC cells. (a, b, c, d) The expressions of miR-1271-5p (a, b) and FLOT1 (c, d) in CC (SiHa and ME180) cells following transfection with FLOT1 overexpression plasmids or miR-1271-5p mimic alone or in combination were analyzed by qRT-PCR. (e, f) The expression of FLOT1 in CC (SiHa and ME180) cells after transfection with FLOT1 overexpression plasmids or miR-1271-5p mimic alone or in combination was analyzed by western blot, with GAPDH as the reference gene. ^{+}P or $^{\wedge}P < 0.05$; $^{\wedge\wedge}P < 0.01$; ^{+++}P or $^{\wedge\wedge\wedge}P$ or $^{\#\#\#}P < 0.001$; $^{+}$ vs. FLOT1+MC; $^{\wedge}$ vs. NC+MC; $^{\#}$ vs. FLOT1+miR-1271-5p M. CC: cervical cancer; qRT-PCR: quantitative reverse transcription polymerase chain reaction; NC: negative control; M: miR-1271-5p mimic; MC: mimic control; WT: wild type; MUT: mutant type; FLOT1: flotillin 1.

as follows: 95°C for 10 min, followed by 40 cycles of 95°C for 15 s, and 60°C for 1 min. The expressions of relative genes normalized to U6 or GAPDH were calculated using the $2^{-\Delta\Delta CT}$ method [24].

2.12. Western Blot Analysis. RIPA Lysis and Extraction Buffer (89901, ThermoFisher, USA) was used to harvest total protein from SiHa cells and ME180 cells. The protein concentration was quantitated by the bicinchoninic acid (BCA) Protein Assay Kits (23227, ThermoFisher, USA). The protein (40 μg) and marker (4 μL) (PR1910, Solarbio, Beijing, China) were separated by 10%-12% sodium dodecyl sulfate-polyacrylamide gel electrophoresis (SDS-PAGE) gels (P0670, P0672, Beyotime, Shanghai, China) and laid onto polyvinylidene fluoride (PVDF) membranes (FFP28, Beyotime, China). Afterward, the membranes were blocked with 5% skim milk in Tris Buffered Saline and Tween 20 (TA-999-TT, ThermoFisher, USA) at room temperature for 1 h. Primary antibodies against FLOT1 (ab133497, 47 kDa, 1 : 10000, Abcam, USA), matrix metalloproteinase (MMP)-9 (ab73734, 78 kDa, 1 : 1000, Abcam, USA), MMP-2 (ab37150, 72 kDa, 1 : 1000, Abcam, USA), E-cadherin (ab40772, 97 kDa, 1 : 10000, Abcam, USA), N-cadherin (ab18203, 130 kDa, 1 μg/ml, Abcam, USA), Wnt1 (ab15251, 41 kDa, 1 : 1000, Abcam, USA), β-catenin (ab16051, 95 kDa, 1 : 1000, Abcam, USA), p-β-catenin (ab27798, 92 kDa, 1 : 500, Abcam, USA), and GAPDH (ab8245, 36 kDa, 1 : 1000, Abcam, USA) were incubated with the membranes at 4°C overnight. Then, secondary antibodies, including Goat Anti-Rabbit IgG (ab205718, 1 : 2000, Abcam, USA) and Goat Anti-Mouse IgG (ab6789, 1 : 2000, Abcam, USA), were incubated with the membranes. The obtained protein was photo-developed using Enhanced Chemiluminescent (ECL) Substrate Reagent Kit (WP20005, ThermoFisher, USA) on an imaging system (iBright CL1500, ThermoFisher, USA). Analysis of the gray value of protein bands was conducted using the ImageJ software (version. 1.52 s, National Institutes of Health, Bethesda, MA, USA).

2.13. Statistical Analysis. Measurement data with normal distribution were expressed as mean ± standard deviation (SD). All the experiments were conducted in triplicate. SPSS software (version 21.0, SPSS Inc., Chicago, IL, USA) was used for statistical analysis. The differences between CC tissues and the adjacent normal tissues were analyzed by paired t-test. Comparison between the other two groups was performed by independent t-test, and those between multiple

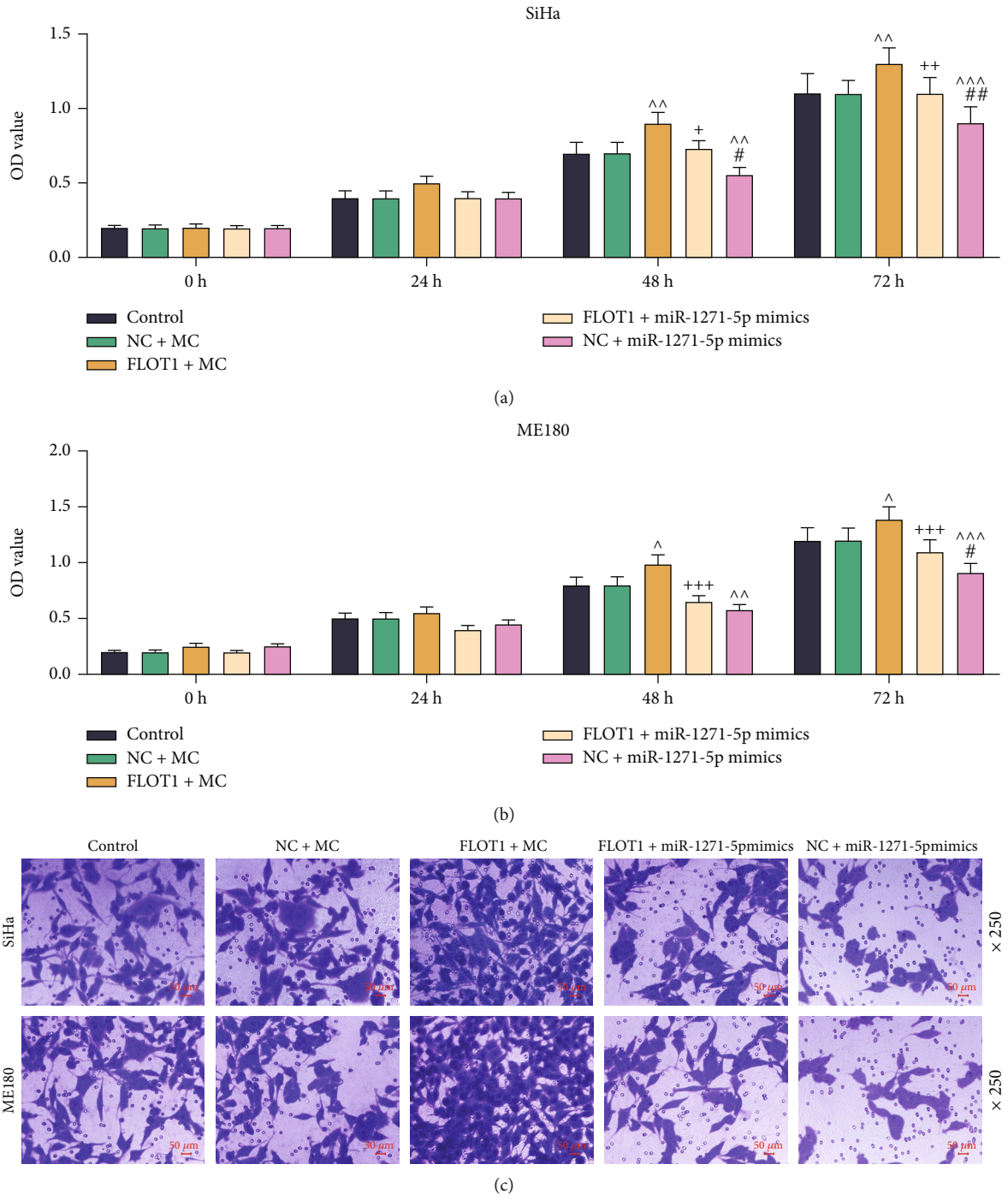

Figure 6: Continued.

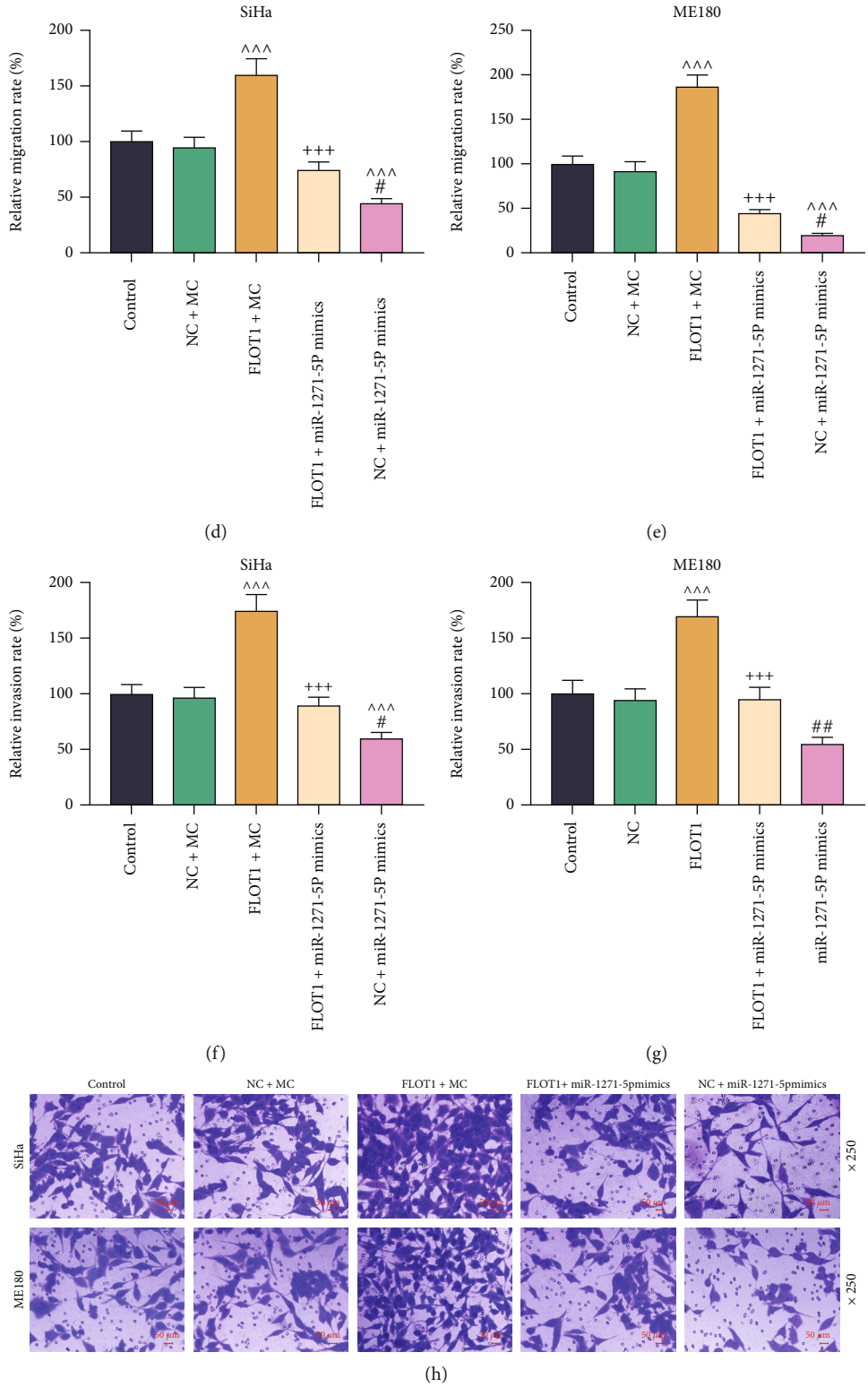

Figure 6: FLOT1 overexpression resisted miR-1271-5p upregulation-induced viability and inhibition in migration and invasion of CC cells. (a, b) The viability of CC (SiHa and ME180) cells transfected with FLOT1 overexpression plasmids or miR-1271-5p mimic alone or in combination was measured by CCK-8 assay at 24-, 48-, and 72-h posttransfection. (c-h). The migration (c-e) and invasion (f-h) of CC (SiHa and ME180) cells after transfection with FLOT1 overexpression plasmids or miR-1271-5p mimic alone or in combination were evaluated by the Transwell assay (magnification: ×250; scale: 50 μm). ^{+}P or $^{\wedge}P$ or $^{\#}P < 0.05$; ^{++}P or $^{\wedge\wedge}P$ or $^{\#\#}P < 0.01$; ^{+++}P or $^{\wedge\wedge\wedge}P$ or $^{\#\#\#}P < 0.001$; $^{+}$ vs. FLOT1+MC; $^{\wedge}$ vs. NC+MC; $^{\#}$ vs. FLOT1+miR-1271-5p M. CC: cervical cancer; qRT-PCR: quantitative reverse transcription polymerase chain reaction; CCK-8: cell counting kit-8; NC: negative control; M: miR-1271-5p mimic; MC: mimic control; FLOT1: flotillin 1.

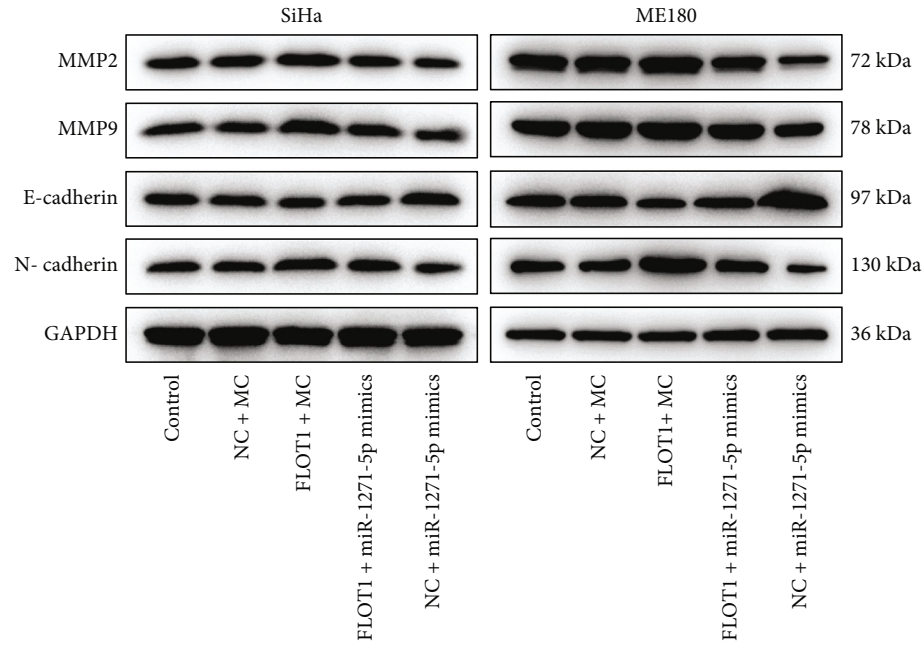

(a)

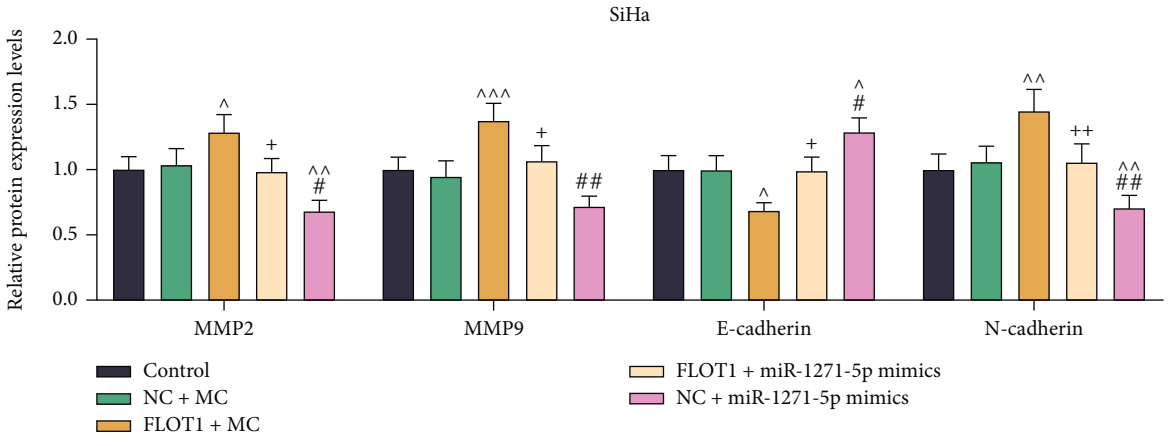

(b)

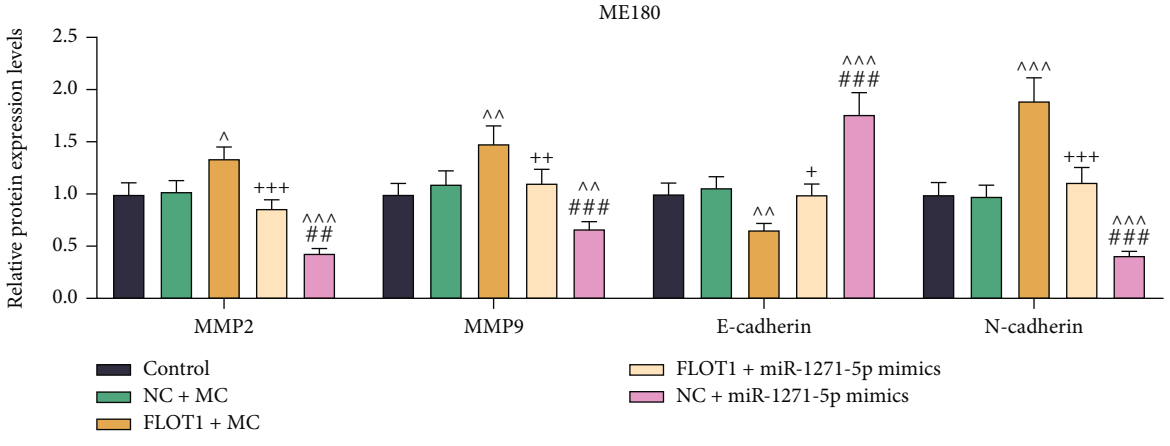

(c)

Figure 7: Continued.

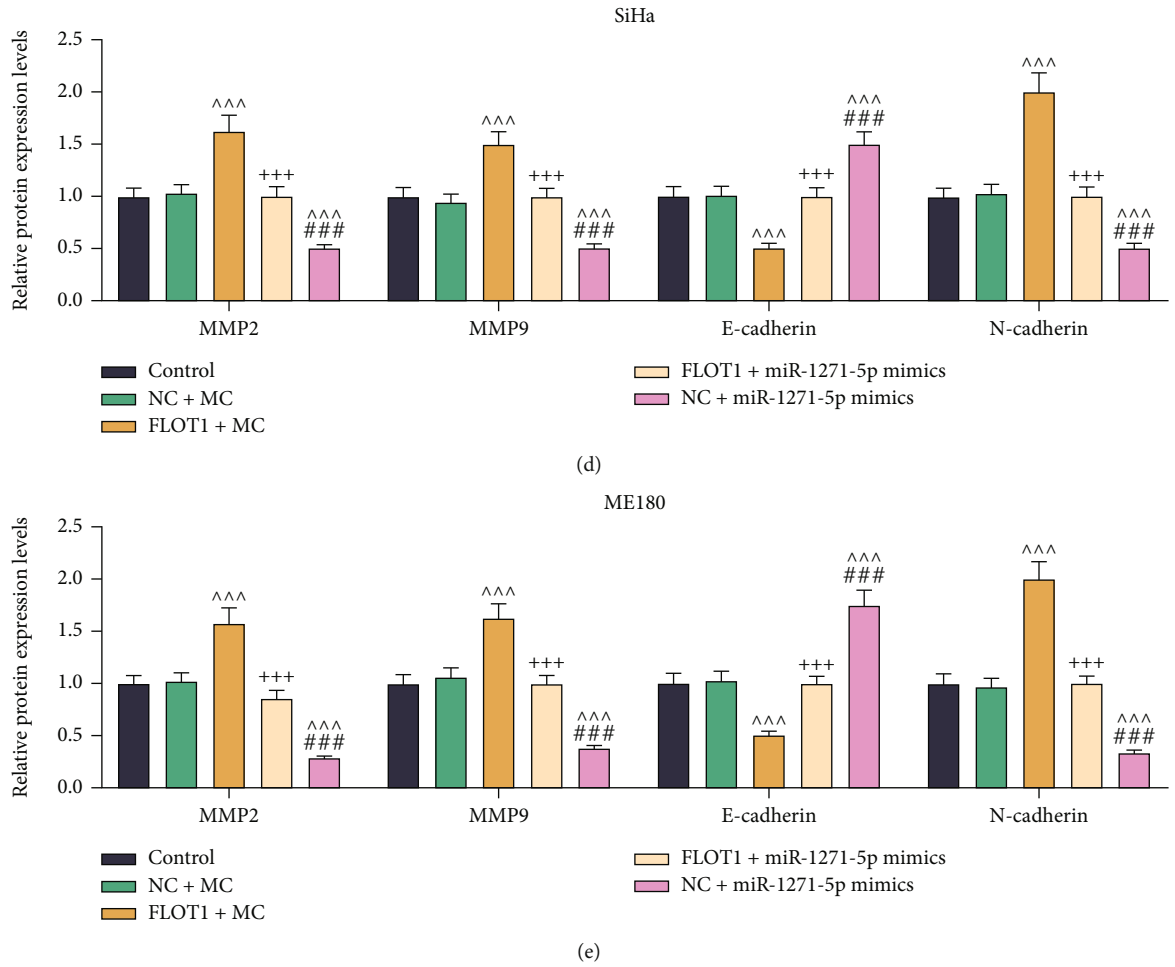

Figure 7: FLOT1 overexpression resisted miR-1271-5p upregulation-induced inhibition of EMT in CC cells. (a-e) The expressions of MMP2, MMP9, E-cadherin and N-cadherin in CC (SiHa and ME180) cells after transfection with FLOT1 overexpression plasmids or miR-1271-5p mimic alone or in combination were analyzed by qRT-PCR (a-c) and western blot (d, e), with GAPDH as the reference gene. ^{+}P or $^{\wedge}P$ or $^{\#}P < 0.05$; ^{++}P or $^{\wedge\wedge}P$ or $^{\#\#}P < 0.01$; ^{+++}P or $^{\wedge\wedge\wedge}P$ or $^{\#\#\#}P < 0.001$; $^{+}$ vs. FLOT1+MC; $^{\wedge}$ vs. NC+MC; $^{\#}$ vs. FLOT1+miR-1271-5p M. CC: cervical cancer; qRT-PCR: quantitative reverse transcription polymerase chain reaction; NC: negative control; M: miR-1271-5p mimic; MC: mimic control; FLOT1: flotillin 1; MMP2: matrix metalloproteinase-2; MMP9: matrix metalloproteinase-9.

groups were conducted by one-way analysis of variance (ANOVA) followed by Dunnett's or Turkey's post-hoc test. Pearson's correlation tests were used to analyze the correlation between FAM201A and miR-1271-5p in CC tissues. Statistics with $P < 0.05$ were considered statistically significant.

3. Results

3.1. FAM201A Was Highly Expressed in CC, Enriched in CC Cell Cytoplasm, and Its Expression Was Negatively Correlated with miR-1271-5p. According to Gene Expression Profiling Interactive Analysis (GEPIA) based on Cancer Genome Atlas Cervical Squamous Cell Carcinoma and Endocervical Adenocarcinoma (TCGA-CESC) database, FAM201A expression level was higher in CC tissues than that in normal tissues ($P < 0.05$; Figure 1(a)). Then, we harvested 33 pairs of clinical samples including CC tissues and the adjacent normal tissues for the examination of FAM201A expression. The results showed that FAM201A was highly expressed in CC tissues compared with adjacent normal tissues (Figure 1(b)). Considering that miR-1271-5p has been widely reported as a regulator of tumor growth, in this present study, miR-1271-5p expression was downregulated CC clinical samples and compared with adjacent normal tissues (Figure 1(c)), which showed a negative correlation between miR-1271-5p and lncRNA FAM201A via Pearson's correlation analysis (Figure 1(d)). Meanwhile, fluorescence *in situ* hybridization assay confirmed that FAM201A was highly expressed in CC tissues compared with adjacent normal tissues (Figure 1(e)). Moreover, in comparison with HCerEpiC, FAM201A expression level was also highly expressed in CC (HeLa, C33a, SiHa, and ME180) cells, while miR-1271-5p expression was decreased ($P < 0.01$; Figures 1(f) and 1(g)). A relatively higher expression level of FAM201A was seen in SiHa cells and ME180 cells than in other cells above. Therefore, to investigate the role of FAM201A during the progression of CC, SiHa cells

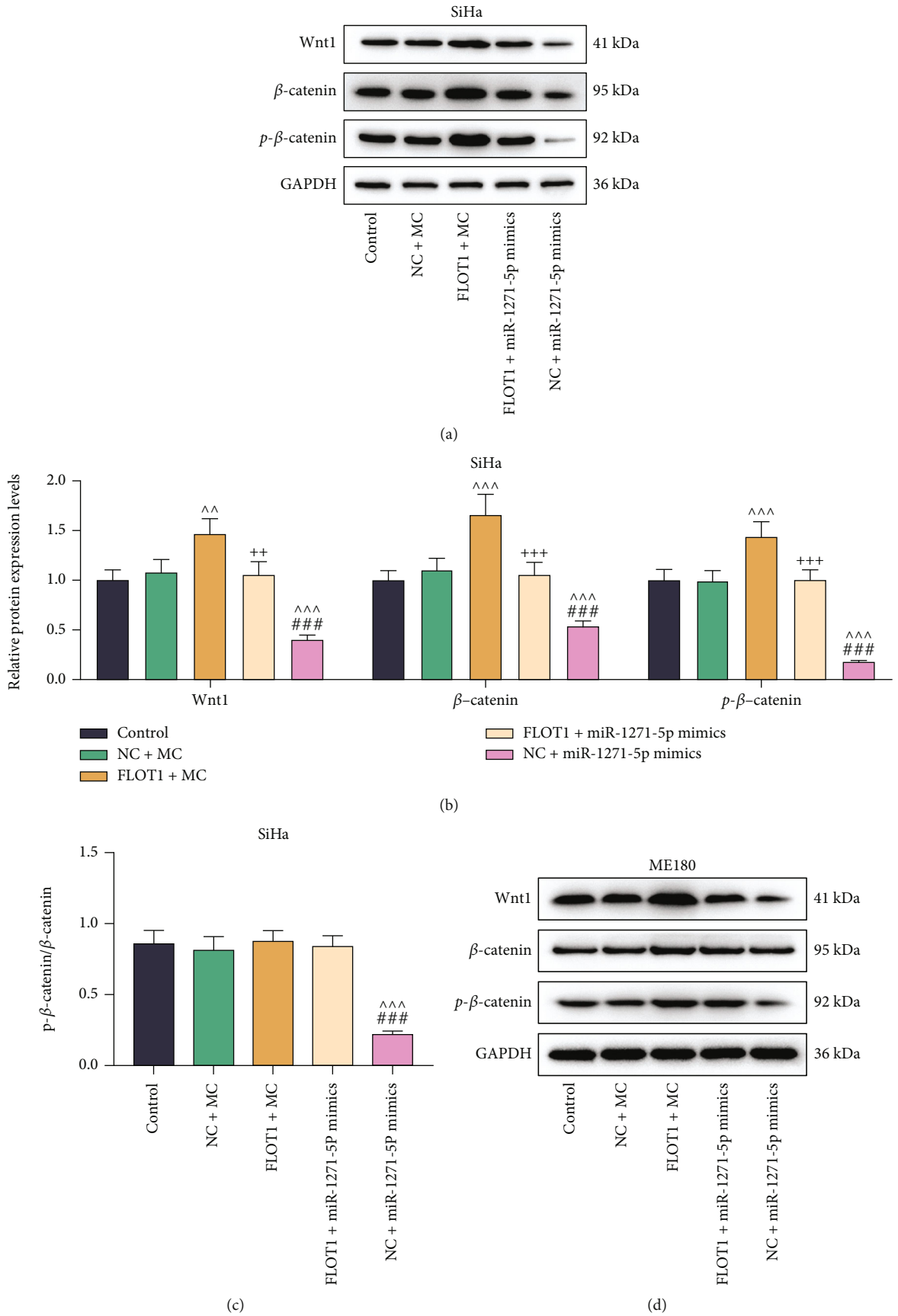

Figure 8: Continued.

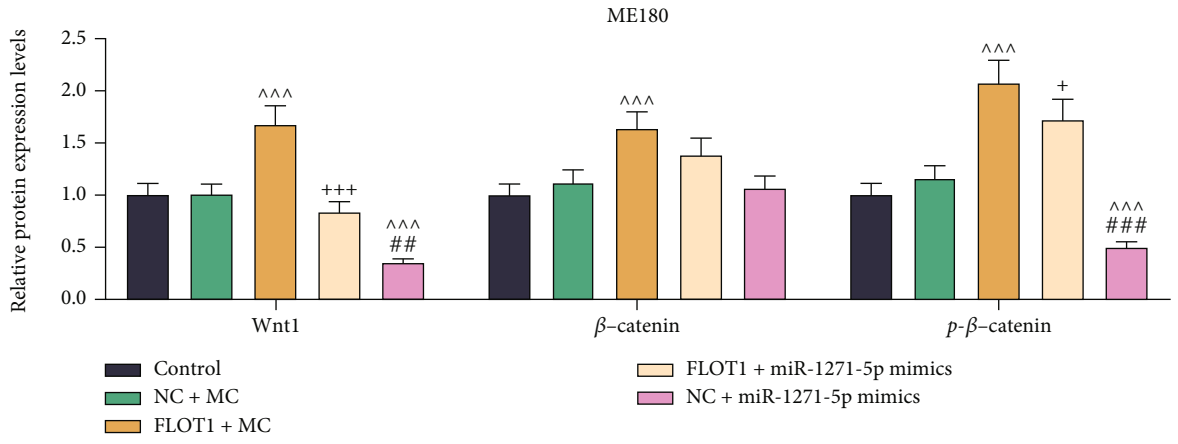

(e)

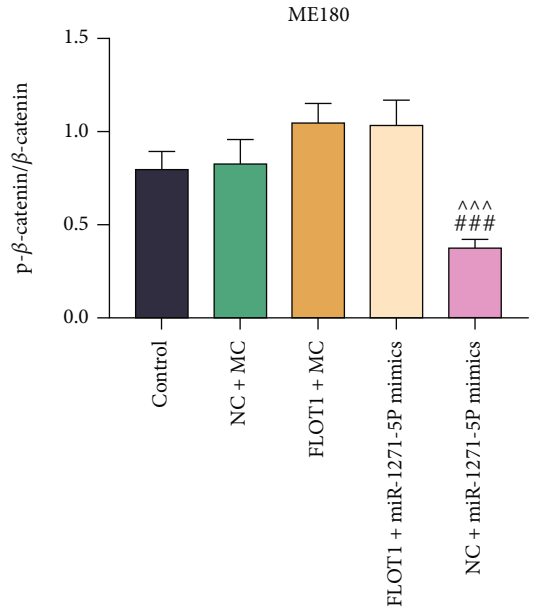

(f)

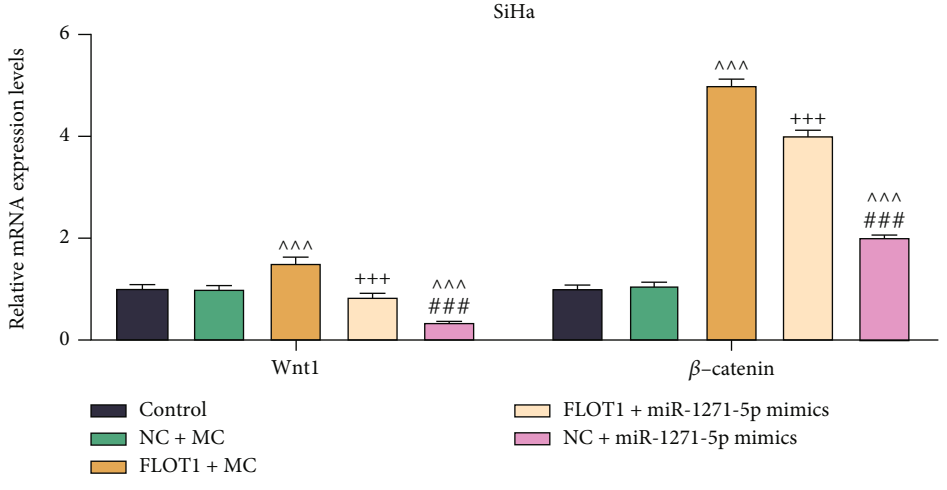

(g)

Figure 8: Continued.

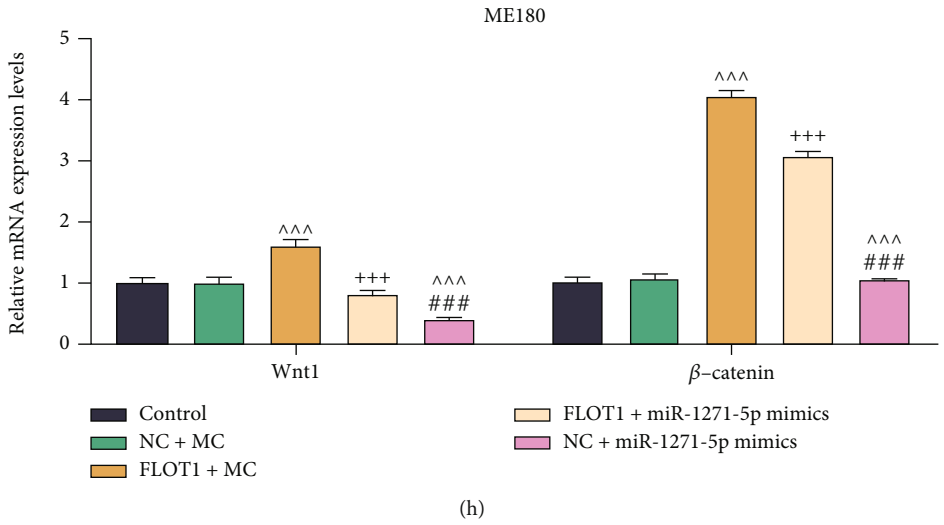

Figure 8: FLOT1 overexpression resisted miR-1271-5p upregulation-induced suppression on the Wnt/β-catenin signaling pathway in CC cells. (a-h). The expressions of Wnt1, β-catenin, p-β-catenin and p-β-catenin/β-catenin in CC (SiHa and ME180) cells transfected with FLOT1 overexpression plasmids or miR-1271-5p mimic alone or in combination were determined by qRT-PCR (G/H) and western blot (a-f), with GAPDH as the reference gene. $^{+}P < 0.05$; ^{++}P or $^{\wedge\wedge}P$ or $^{\#\#}P < 0.01$; ^{+++}P or $^{\wedge\wedge\wedge}P$ or $^{\#\#\#}P < 0.001$; $^{+}$ vs. FLOT1+MC; $^{\wedge}$ vs. NC +MC; $^{\#}$ vs. FLOT1+miR-1271-5p M. CC: cervical cancer; qRT-PCR: quantitative reverse transcription polymerase chain reaction; NC: negative control; M: miR-1271-5p mimic; MC: mimic control; FLOT1: flotillin 1.

and ME180 cells were chosen as cell models in the following related experiments to achieve obvious overexpression of FAM201A. Subsequently, qRT-PCR and fluorescent *in situ* hybridization were performed to determine the subcellular localization of FAM201A. As shown in Figures 1(h) and 1(i) (qRT-PCR) and Figures 1(j) and 1(k) (fluorescent *in situ* hybridization), FAM201A was abundantly expressed in the cytoplasm rather than in the nucleus, suggesting a role of FAM201A in post-transcriptional regulation.

3.2. FAM201A Overexpression Increased the Cell Viability, Migration, Invasion and Tumorigenesis of CC In Vivo by Downregulating miR-1271-5p Expression. Here, functional experiments, including CCK-8, qRT-PCR, Transwell, and murine xenograft assays, were performed. Prior to these assays, the transfection efficiency of FAM201A overexpression plasmids and miR-1271-5p mimic was validated by qRT-PCR, through which we observed that the transfection of both FAM201A overexpression plasmid and miR-1271-5p mimic induced the upregulation of FAM201A and miR-1271-5p expression, respectively ($P < 0.001$; Figures 2(a) and 2(c)). Moreover, upregulation of miR-1271-5p via miR-1271-5p mimic decreased the level of FAM201A, and likewise, FAM201A overexpression caused a lower level of miR-1271-5p ($P < 0.05$; Figures 2(a)–2(d)). Meanwhile, FAM201A overexpression plasmid and miR-1271-5p mimic counteracted the effect of each other on the expressions of FAM201A and miR-1271-5p ($P < 0.001$; Figures 2(a)–2(d)). Then, assays for FAM201A functional examination were performed. CCK-8 assay revealed that FAM201A overexpression enhanced the viability of CC cells at 24, 48, and 72 h, while miR-1271-5p upregulation decreased the viability of CC cells at 24, 48, and 72 h ($P < 0.05$) (Figures 2(e) and 2(f)). Transwell assay demonstrated that CC cells transfected with FAM201A overexpression plasmid migrated and invaded to a greater extent, while the transfection with miR-1271-5p mimic led to repressed migration and invasion ($P < 0.01$; Figures 2(g)–2(i) and 3(a)–3(c)). In murine xenograft assay, the increased trends of tumor volumes and weight gain were found under the promotion of FAM201A overexpression but inhibited by miR-1271-5p upregulation ($P < 0.05$; Figures 3(e)–3(f)). FAM201A overexpression and miR-1271-5p upregulation mutually reversed the effects of each other (Figures 2(e)–2(i) and 3(a)–3(f)).

Taken together, the above results suggested that FAM201A-directed sponging of miR-1271-5p was associated with CC progression.

3.3. FAM201A Sponged miR-1271-5p to Increase the Expression of FLOT1, a Direct Target of miR-1271-5p, in CC Cells. Prediction using StarBase displayed the complementary binding sites of miR-1271-5p and FLOT1 (Figure 4(a)). Dual-luciferase reporter assay showed that transfection of miR-1271-5p mimic suppressed the luciferase activity of CC cells transfected with vectors inserted with FLOT1-WT ($P < 0.001$), but exerted no obvious effects on the luciferase activity of CC cells transfected with vectors inserted with FLOT1-MUT (Figures 4(b) and 4(c)). Furthermore, FLOT1 expression was found to be upregulated by FAM201A overexpression, but the mRNA and protein levels were knocked down by miR-1271-5p upregulation compared with those in the NC+MC group ($P < 0.05$; Figures 4(d)–4(g)). Also, FAM201A overexpression reversed the miR-1271-5p upregulation-induced FLOT1 knockdown ($P < 0.01$). This trend was further offset by miR-1271-5p upregulation ($P < 0.001$; Figures 4(d)–4(g)).

We observed that no obvious change on miR-1271-5p expression in CC cells after transfection with FLOT1 overexpression plasmid (Figures 5(a) and 5(b)), but CC cells transfected with miR-1271-5p mimic still increased miR-1271-5p expression in cells transfected with the plasmid overexpressing FLOT1 ($P < 0.001$; Figures 5(a) and 5(b)). In addition, compared with miR-1271-5p mimic control, miR-1271-5p upregulation decreased FLOT1 mRNA and protein expressions in negative control-transfected and FLOT1 overexpression plasmid-transfected CC cells, while FLOT1 overexpression plasmid demonstrated the opposite results ($P < 0.05$). Moreover, the effects of miR-1271-5p upregulation and FLOT1 overexpression plasmid were mutually counteractive ($P < 0.05$; Figures 5(c)–5(f)).

3.4. FLOT1 Overexpression Resisted miR-1271-5p Upregulation-Induced Decrease in Viability and Inhibition in Migration, Invasion and EMT in CC Cells. The miRNA-mRNA networks are widely known to regulate CC progression [25]. Here, as FLOT1 was identified as a target mRNA of miR-1271-5p, we investigated FLOT1-miR-1271-5p network-delivered regulation on CC cell phenotypes. The results showed that CC cells transfected with plasmid overexpressing FLOT1 exhibited increased viability at 48 h and 72 h ($P < 0.05$; Figures 6(a) and 6(b)) and more aggressive migration and invasion ($P < 0.001$; Figures 6(c)–6(h)). Additionally, FLOT1 overexpression could counteract miR-1271-5p upregulation-induced effects on the viability of CC cells at 48 h and 72 h ($P < 0.05$), together with their migration and invasion ($P < 0.05$); in turn, miR-1271-5p upregulation also reversed the effects of FLOT1 overexpression on the viability at 48 h and 72 h, migration and invasion of CC cells ($P < 0.05$; Figures 6(a)–6(h)).

EMT, a biological process, displays distinctive cellular phenotypes and plays vital roles in both cell growth and cancer progression [26]. Thus, the protein and mRNA levels of EMT-related markers were assessed by western blot and qRT-PCR. Both the protein and mRNA levels of MMP-9, MMP-2, and N-cadherin were upregulated by FLOT1 overexpression in CC cells compared with those in the NC+MC group ($P < 0.05$), while compared with those in the NC+MC group, miR-1271-5p upregulation depleted the expressions of these markers ($P < 0.01$) and abolished the FLOT1 overexpression-induced effects on the expressions of these markers ($P < 0.05$) (Figures 7(a)–7(e)). Additionally, the effects of miR-1271-5p upregulation on these EMT-related markers were counteracted by FLOT1 overexpression ($P < 0.05$) (Figures 1(f) and 7(a)). Conversely, E-cadherin, an EMT-related marker, and its protein and mRNA levels were downregulated by FLOT1 overexpression but elevated by miR-1271-5p upregulation ($P < 0.05$), compared with those in the NC + MC group (Figures 8(a)–8(f)). Furthermore, FLOT1 overexpression counteracted the effects of miR-1271-5p upregulation on E-cadherin expression, and miR-1271-5p upregulation also reversed the effects of FLOT1 overexpression ($P < 0.05$) (Figures 8(a)–8(f)).

Collectively, these results indicated that FAM201A sponged miR-1271-5p to induce FLOT1 expression, thereby promoting CC progression.

3.5. FLOT1 Overexpression Resisted miR-1271-5p Upregulation-Induced Suppression on the Wnt/β-Catenin Signaling Pathway in CC Cells. The Wnt/β-catenin signaling pathway, a developmental pathway, is crucial in normal stem cell function and is frequently aberrantly activated in various types of cancer [27–29]. In this research study, the protein and mRNA levels of Wnt1, β-catenin and p-β-catenin were determined by western blot and qRT-PCR assays. The result showed they were uniformly upregulated by FLOT1 overexpression but downregulated by miR-1271-5p upregulation ($P < 0.001$), compared with those in the NC+MC group (Figures 8(a)–8(e) and 8(g)–8(h)). Moreover, when compared with the NC+MC group, the p-β-catenin/β-catenin ratio was also depleted by miR-1271-5p upregulation in CC cells but not significantly changed by FLOT1 overexpression ($P < 0.01$) (Figures 8(g) and 8(h)).

Besides, FLOT1 overexpression resisted the miR-1271-5p upregulation-induced inhibitory effect in the protein and mRNA expressions of Wnt1 and β-catenin ($P < 0.01$). It also increased the p-β-catenin/β-catenin ratio in CC cells transfected with miR-1271-5p mimic and the increase in these markers expression levels by FLOT1 overexpression were reversed by miR-1271-5p upregulation ($P < 0.01$) (Figures 8(a)–8(e) and 8(g)–8(h)).

Overall, these results indicated that FAM201A overexpression-mediated miR-1271-5p/FLOT1 axis promoted CC progression by activating the Wnt/β-catenin signaling pathway.

4. Discussion

In 2003, the World Health Organization considered CC preventable in women [20]. However, due to metastasis, the median survival time of CC patients remains mediocre [30]. Metastasis is a distinctive malignant sign that can be subdivided into two types, hematogenous metastasis and lymphatic metastasis [6, 31], of which lymph metastasis is the leading factor for CC-associated poor prognosis and death [32]. Metastasis in most human cancers implicates both cellular and molecular alterations [33], identifying that the molecular mechanism in CC is very important for hindering the development of metastasis and other malignant phenotypes.

LncRNA-mediated mechanisms have been widely unveiled in the carcinogenesis, progression, and therapy resistance of CC [34]. Numerous lncRNAs, including FAM201A, have been confirmed to function as an oncogene in multiple types of human cancers by suppressing malignant phenotypes such as cancer cell proliferation, migration, invasion, and *in vivo* tumorigenesis [10–12]. In line with these studies, our study newly identified FAM201A as a key player in promoting CC carcinogenesis and progression. Analysis of the TCGA-CESC database showed that FAM201A was highly expressed in CC. To increase the credibility of this study's results, CC tissues and cell lines (HeLa, C33a, SiHa, and ME180) were used to assess FAM201A expression. We detected a unanimous increase in FAM201A expression in all CC *in vitro* and *in vivo* samples, which was consistent with the FAM201A expression patterns in TNBC

and lung cancer, where FAM201A played oncogenic roles [10–12]. The specific tumor-promoting role of FAM201A was illustrated in previous studies, which reported that knocking down FAM201A led to significantly suppressed proliferation, migration, and invasion of TNBC or LSCC cells [10–12]. In line with the role of FAM201A in TNBC and LSCC, our study discovered a positive association between FAM201A overexpression and the biological behaviors of CC, including cell viability, migration, invasion, and *in vivo* tumorigenesis, which suggested that this oncogenic role of FAM201A also existed in CC.

Functional analyses of FAM201A-miRNA-mRNA ceRNA networks indicated that FAM201A could sponge miRNAs and unleash mRNAs from the binding of FAM201A, with miRNAs critical for the promotion of cancer progression [10]. Our study found that miR-1271-5p was negatively correlated with FAM201A in CC tissues, implying that FAM201A sponged miR-1271-5p in CC. Previous studies reported that miR-1271-5p expression was significantly downregulated and miR-1271-5p exerted a tumor-suppressive effect in several cancers [18, 35]. Preventing oncogene-directed sponging of miR-1271-5p led to the inhibition of cancer progression, as evidenced by Zhang et al. [35], who found that miR-1271-5p upregulation from the knockdown of lncRNA-ZFAS1 constrained *in vitro* development of glioma. In light of Zhang et al.'s evidence, our findings demonstrated that miR-1271-5p upregulation reversed the promotive effect of FAM201A overexpression on the progression of CC, suggesting that FAM201A facilitated the progression of CC by sponging miR-1271-5p.

Furthermore, it was reported that miRNA-mRNA interaction emerged following the interaction between lncRNA and miRNA in ceRNA networks associated with the pathological conditions in cancer [36]. Wang et al. showed that the upregulation of miR-1271-5p by MALAT1 knockdown inhibited the growth and migration of ovarian cancer cells and simultaneously silenced its target mRNA E2F5 [37]. In our study, bioinformatics prediction theoretically identified FLOT1 as the target of miR-1271-5p, which was subsequently validated by our dual-luciferase reporter assay results. Similarly, our findings showed that FAM201A overexpression downregulated miR-1271-5p expression to elevate FLOT1 expression and concomitantly promoted *in vitro* CC progression, indicating that the overexpressed FAM201A-directed ceRNA network with the miR-1271-5p/FLOT1 axis promoted CC progression.

FLOT1, a pivotal marker of lipid rafts that modulates membrane receptor signaling, has been reported to participate in membrane trafficking and affect cell adhesion and invasion, thereby displaying a role in tumorigenesis [38, 39]. The overexpression of FLOT1 has been previously discovered to promote migration and invasion and induce recurrence of bladder transitional cell carcinoma [38], activate oncogenic ALK signaling to drive malignant phenotypes of neuroblastoma [40], and sustain inflammatory signaling to facilitate the growth and invasion of esophageal squamous cell carcinoma cells [40, 41]. For CC, FLOT1 was shown to serve as the downstream target of miR-1294 to form a miR-1294/FLOT1 axis, and its expression can be repressed by the upregulation of miR-1294, thereby inhibiting the progression of CC malignant phenotypes [42, 43]. Likewise, in our *in vitro* experiments, miR-1271-5p upregulation decreased FLOT1 expression and offset FLOT1 overexpression-induced promotion. Meanwhile, FLOT1 overexpression could also counteract the inhibitory effects of miR-1271-5p upregulation on cell viability, migration and invasion. According to these findings, we concluded that targeting the miR-1271-5p/FLOT1 axis could be the underlying mechanism via which FAM201A induced CC progression.

Accumulating evidence indicated that EMT, a hallmark of carcinogenesis, functionally contributed to tumor invasion, migration and metastatic dissemination [44]. The phenotype of EMT mainly involves the transformation of epithelial cells to mesenchymal-like cells, allowing them to invade surrounding tissues [45, 46]. Induction of EMT is accompanied by the loss of epithelial adhesion molecule E-cadherin [47] and an increase in mesenchymal marker N-cadherin [48]. Moreover, during EMT, MMPs, a family of zinc-dependent endoproteases, degrade the extracellular matrix to facilitate EMT [49]. Secretion of MMP-2 and MMP-9 was shown to break down the basement membrane and promote lymph node invasion and cancer metastasis, thus leading to poor prognoses [50, 51]. In this study, we found that E-cadherin levels in CC cells were decreased by FLOT1 overexpression but increased by miR-1271-5p upregulation, and an opposite trend was seen on the levels of N-cadherin, MMP-2, and MMP-9 when FLOT1 was overexpressed or miR-1271-5p expression was upregulated. Besides, we discovered that FLOT1 overexpression counteracted miR-1271-5p upregulation-induced effects on the expressions of these EMT-related markers and vice versa. Collectively, these findings indicated that FAM201A facilitated EMT and promoted CC progression by targeting the miR-1271-5p/FLOT1 axis.

The Wnt/β-catenin pathway, which plays an essential role in embryogenesis, homeostasis, and stem cell regeneration and pluripotency, is activated in CC as a promoter of cancer progression [52, 53]. Likewise, our results demonstrated that the levels of Wnt1, β-catenin and p-β-catenin in CC cells were positively correlated with FLOT1 overexpression, while the levels of these markers were negatively correlated with miR-1271-5p upregulation. Besides, our study revealed that FLOT1 overexpression could also restore the expressions of Wnt1, β-catenin, and p-β-catenin in CC cells after the upregulation of miR-1271-5p, which indicated that FLOT1 overexpression counteracted the inhibitory effects induced by miR-1271-5p upregulation on the Wnt/β-catenin pathway, thus promoting the progression of CC.

Considering that FAM201A was overexpressed in CC cells and acted through the FAM201A-miR-1271-5p-FLOT1 ceRNA network, they might be targeted and used to develop novel potential molecular target to improve CC treatment outcomes, with FAM201A as a potential diagnostic biomarker for CC and possible indicator of FAM201A-targeted treatment for individualized treatment of patients

expressing high levels of FAM201A. However, considering limitations such as lack of survival analysis, no assessment to determine the association of FAM201A with pharmacological treatment, and others, these findings should be further verified in translational and clinical studies.

5. Conclusion

In conclusion, the current study revealed that FAM201A, which was highly expressed in CC, promoted CC progression via sponging miR-1271-5p to upregulate FLOT1 expression. Moreover, CC progression was also promoted via regulating the miR-1271-5p/FLOT1 axis by activating the Wnt/β-catenin pathway. Thus, this study proposed the FAM201A-miR-1271-5p-FLOT1 ceRNA network as an original molecular target for prevention against CC.

Data Availability

The analyzed data sets generated during the study are available from the corresponding author on reasonable request.

Conflicts of Interest

The authors declare that there is no conflict of interest regarding the publication of this paper.

References

[1] E. L. Franco, N. F. Schlecht, and D. Saslow, "The epidemiology of cervical cancer," *The Cancer Journal*, vol. 9, no. 5, pp. 348–359, 2003.

[2] World Health Organization, *Strategic framework for the comprehensive control of cancer cervix in South-East Asia Region*, WHO, 2015.

[3] T. T. Ma, L. Q. Zhou, J. H. Xia, Y. Shen, Y. Yan, and R. H. Zhu, "LncRNA PCAT-1 regulates the proliferation, metastasis and invasion of cervical cancer cells," *European Review for Medical and Pharmacological Sciences*, vol. 22, no. 7, pp. 1907–1913, 2018.

[4] M. S. G. Naz, N. Kariman, A. Ebadi, G. Ozgoli, V. Ghasemi, and F. R. Fakari, "Educational interventions for cervical cancer screening behavior of women: a systematic review," *Asian Pacific Journal of Cancer Prevention*, vol. 19, no. 4, pp. 875–884, 2018.

[5] J. Ferlay, E. Steliarova-Foucher, J. Lortet-Tieulent et al., "Cancer incidence and mortality patterns in Europe: estimates for 40 countries in 2012," *European Journal of Cancer*, vol. 49, no. 6, pp. 1374–1403, 2013.

[6] L. Peng, X. Yuan, B. Jiang, Z. Tang, and G. C. Li, "LncRNAs: key players and novel insights into cervical cancer," *Tumor Biology*, vol. 37, no. 3, pp. 2779–2788, 2016.

[7] V. Mittal, "Epithelial mesenchymal transition in tumor metastasis," *Annual Review of Pathology*, vol. 13, pp. 395–412, 2018.

[8] R. Heery, S. P. Finn, S. Cuffe, and S. G. Gray, "Long noncoding RNAs: key regulators of epithelial-mesenchymal transition, tumour drug resistance and cancer stem cells," *Cancers*, vol. 9, no. 4, p. 38, 2017.

[9] S. J. Humphray, K. Oliver, A. R. Hunt et al., "DNA sequence and analysis of human chromosome 9," *Nature*, vol. 429, no. 6990, pp. 369–374, 2004.

[10] H. Jia, D. Wu, Z. Zhang, and S. Li, "TCF3-activated FAM201A enhances cell proliferation and invasion via miR-186-5p/TNKS1BP1 axis in triple-negative breast cancer," *Bioorganic Chemistry*, vol. 104, article 104301, 2020.

[11] W. He, Z. X. Qiao, and B. Ma, "Long noncoding RNA FAM201A mediates the metastasis of lung squamous cell cancer via regulating ABCE1 expression," *European Review for Medical and Pharmacological Sciences*, vol. 23, no. 23, pp. 10343–10353, 2019.

[12] J. Huang, Q. Yu, Y. Zhou, Y. Chu, F. Jiang, and Q. Wang, "FAM201A knockdown inhibits proliferation and invasion of lung adenocarcinoma cells by regulating miR-7515/GLO1 axis," *Journal of Cellular Physiology*, vol. 236, no. 8, pp. 5620–5632, 2021.

[13] M. Chen, P. Liu, Y. Chen et al., "Long noncoding RNA FAM201A mediates the radiosensitivity of esophageal squamous cell cancer by regulating ATM and mTOR cxpression via miR-101," *Frontiers in Genetics*, vol. 9, p. 611, 2018.

[14] A. M. Liu, Y. Zhu, Z. W. Huang, L. Lei, S. Z. Fu, and Y. Chen, "Long noncoding RNA FAM201A involves in radioresistance of non-small-cell lung cancer by enhancing EGFR expression via miR-370," *European Review for Medical and Pharmacological Sciences*, vol. 23, no. 13, pp. 5802–5814, 2019.

[15] F. Sun, W. Liang, K. Tang, M. Hong, and J. Qian, "Profiling the lncRNA-miRNA-mRNA ceRNA network to reveal potential crosstalk between inflammatory bowel disease and colorectal cancer," *PeerJ*, vol. 7, article e7451, 2019.

[16] D. P. Bartel, "MicroRNAs: target recognition and regulatory functions," *Cell*, vol. 136, no. 2, pp. 215–233, 2009.

[17] K. Breving and A. Esquela-Kerscher, "The complexities of microRNA regulation: mirandering around the rules," *The International Journal of Biochemistry & Cell Biology*, vol. 42, no. 8, pp. 1316–1329, 2010.

[18] X. Chen, S. Yang, J. Zeng, and M. Chen, "miR-1271-5p inhibits cell proliferation and induces apoptosis in acute myeloid leukemia by targeting ZIC2," *Molecular Medicine Reports*, vol. 19, no. 1, pp. 508–514, 2019.

[19] X. W. Zhang, S. L. Li, D. Zhang, X. L. Sun, and H. J. Zhai, "RP11-619L19.2 promotes colon cancer development by regulating the miR-1271-5p/CD164 axis," *Oncology Reports*, vol. 44, no. 6, pp. 2419–2428, 2020.

[20] N. Liu, S. Feng, H. Li, X. Chen, S. Bai, and Y. Liu, "Long noncoding RNA MALAT1 facilitates the tumorigenesis, invasion and glycolysis of multiple myeloma via miR-1271-5p/SOX13 axis," *Journal of Cancer Research and Clinical Oncology*, vol. 146, no. 2, pp. 367–379, 2020.

[21] G. Fan, J. Jiao, F. Shen, and F. Chu, "Upregulation of lncRNA ZFAS1 promotes lung adenocarcinoma progression by sponging miR-1271-5p and upregulating FRS2," *Thoracic Cancer*, vol. 11, no. 8, pp. 2178–2187, 2020.

[22] M. F. Lin, Y. F. Yang, Z. P. Peng et al., "FOXK2, regulted by miR-1271-5p, promotes cell growth and indicates unfavorable prognosis in hepatocellular carcinoma," *The International Journal of Biochemistry & Cell Biology*, vol. 88, pp. 155–161, 2017.

[23] H. C. Rowsell, "The Canadian Council on Animal Care–its guidelines and policy directives: the veterinarian's

responsibility," *Canadian Journal of Veterinary Research*, vol. 55, no. 3, p. 205, 1991.

[24] M. W. Pfaffl, "A new mathematical model for relative quantification in real-time RT-PCR," *Nucleic Acids Research*, vol. 29, no. 9, 2001.

[25] X. Yang, H. Ye, M. He et al., "LncRNA PDIA3P interacts with c-Myc to regulate cell proliferation via induction of pentose phosphate pathway in multiple myeloma," *Biochemical and Biophysical Research Communications*, vol. 498, no. 1, pp. 207–213, 2018.

[26] Y. Zhang and R. A. Weinberg, "Epithelial-to-mesenchymal transition in cancer: complexity and opportunities," *Frontiers of Medicine*, vol. 12, no. 4, pp. 361–373, 2018.

[27] R. Gedaly, R. Galuppo, M. F. Daily et al., "Targeting the Wnt/beta-catenin signaling pathway in liver cancer stem cells and hepatocellular carcinoma cell lines with FH535," *PLoS One*, vol. 9, no. 6, article e99272, 2014.

[28] C. Jin, L. Samuelson, C. B. Cui, Y. Sun, and D. A. Gerber, "MAPK/ERK and Wnt/beta-Catenin pathways are synergistically involved in proliferation of Sca-1 positive hepatic progenitor cells," *Biochemical and Biophysical Research Communications*, vol. 409, no. 4, pp. 803–807, 2011.

[29] A. Lachenmayer, C. Alsinet, R. Savic et al., "Wnt-pathway activation in two molecular classes of hepatocellular carcinoma and experimental modulation by sorafenib," *Clinical Cancer Research*, vol. 18, no. 18, pp. 4997–5007, 2012.

[30] D. Dong, D. Zhao, S. Li et al., "Nomogram to predict overall survival for patients with non-metastatic cervical esophageal cancer: a SEER-based population study," *Annals of Translational Medicine*, vol. 8, no. 23, p. 1588, 2020.

[31] D. K. Dhar, H. Naora, H. Kubota et al., "Downregulation of KiSS-1 expression is responsible for tumor invasion and worse prognosis in gastric carcinoma," *International Journal of Cancer*, vol. 111, no. 6, pp. 868–872, 2004.

[32] S. Gouy, P. Morice, F. Narducci et al., "Prospective multicenter study evaluating the survival of patients with locally advanced cervical cancer undergoing laparoscopic para-aortic lymphadenectomy before chemoradiotherapy in the era of positron emission tomography imaging," *Journal of Clinical Oncology*, vol. 31, no. 24, pp. 3026–3033, 2013.

[33] S. Valastyan and R. A. Weinberg, "Tumor metastasis: molecular insights and evolving paradigms," *Cell*, vol. 147, no. 2, pp. 275–292, 2011.

[34] H. Aalijahan and S. Ghorbian, "Long non-coding RNAs and cervical cancer," *Experimental and Molecular Pathology*, vol. 106, pp. 7–16, 2019.

[35] B. Zhang, J. Chen, M. Cui, and Y. Jiang, "LncRNA ZFAS1/miR-1271-5p/HK2 promotes glioma development through regulating proliferation, migration, invasion and apoptosis," *Neurochemical Research*, vol. 45, no. 12, pp. 2828–2839, 2020.

[36] J. J. Chan and Y. Tay, "Noncoding RNA:RNA regulatory networks in cancer," *International Journal of Molecular Sciences*, vol. 19, no. 5, 2018.

[37] Y. Wang, X. Wang, L. Han, and D. Hu, "LncRNA MALAT1 regulates the progression and cisplatin resistance of ovarian cancer cells via modulating miR-1271-5p/E2F5 Axis," *Cancer Management and Research*, vol. 12, pp. 9999–10010, 2020.

[38] Y. Guan, H. Song, G. Zhang, and X. Ai, "Overexpression of flotillin-1 is involved in proliferation and recurrence of bladder transitional cell carcinoma," *Oncology Reports*, vol. 32, no. 2, pp. 748–754, 2014.

[39] A. Banning, A. Tomasovic, and R. Tikkanen, "Functional aspects of membrane association of reggie/flotillin proteins," *Current Protein and Peptide Science*, vol. 12, no. 8, pp. 725–735, 2011.

[40] A. Tomiyama, T. Uekita, R. Kamata et al., "Flotillin-1 regulates oncogenic signaling in neuroblastoma cells by regulating ALK membrane association," *Cancer Research*, vol. 74, no. 14, pp. 3790–3801, 2014.

[41] L. Song, H. Gong, C. Lin et al., "Flotillin-1 promotes tumor necrosis factor-α receptor signaling and activation of NF-κB in esophageal squamous cell carcinoma cells," *Gastroenterology*, vol. 143, no. 4, pp. 995–1005, 2012.

[42] X. Q. Kan, Y. B. Li, B. He, S. Cheng, Y. Wei, and J. Sun, "MiR-1294 acts as a tumor inhibitor in cervical cancer by regulating FLOT1 expression," *Journal of Biological Regulators and Homeostatic Agents*, vol. 34, no. 2, 2020.

[43] C. Liu, Z. Shang, Y. Ma, J. Ma, and J. Song, "HOTAIR/miR-214-3p/FLOT1 axis plays an essential role in the proliferation, migration, and invasion of hepatocellular carcinoma," *International Journal of Clinical and Experimental Pathology*, vol. 12, no. 1, pp. 50–63, 2019.

[44] C. Dominguez, J. M. David, and C. Palena, "Epithelial-mesenchymal transition and inflammation at the site of the primary tumor," *Seminars in Cancer Biology*, vol. 47, pp. 177–184, 2017.

[45] J. P. Thiery, H. Acloque, R. Y. Huang, and M. A. Nieto, "Epithelial-mesenchymal transitions in development and disease," *Cell*, vol. 139, no. 5, pp. 871–890, 2009.

[46] R. Kalluri, "EMT: when epithelial cells decide to become mesenchymal-like cells," *The Journal of Clinical Investigation*, vol. 119, no. 6, pp. 1417–1419, 2009.

[47] J. P. Coppe, C. K. Patil, F. Rodier et al., "Senescence-associated secretory phenotypes reveal cell-nonautonomous functions of oncogenic RAS and the p53 tumor suppressor," *PLoS Biology*, vol. 6, no. 12, pp. 2853–2868, 2008.

[48] S. J. Serrano-Gomez, M. Maziveyi, and S. K. Alahari, "Regulation of epithelial-mesenchymal transition through epigenetic and post-translational modifications," *Molecular Cancer*, vol. 15, no. 1, 2016.

[49] B. N. Smith and N. A. Bhowmick, "Role of EMT in metastasis and therapy resistance," *Journal of Clinical Medicine*, vol. 5, no. 2, 2016.

[50] S. J. Sun, N. Wang, Z. W. Sun, J. Chen, and H. W. Cui, "MiR-5692a promotes the invasion and metastasis of hepatocellular carcinoma via MMP9," *European Review for Medical and Pharmacological Sciences*, vol. 22, no. 15, pp. 4869–4878, 2018.

[51] B. Wang, Y. M. Ding, P. Fan, B. Wang, J. H. Xu, and W. X. Wang, "Expression and significance of MMP2 and HIF-1α in hepatocellular carcinoma," *Oncology Letters*, vol. 8, no. 2, pp. 539–546, 2014.

[52] Y. Wu, A. Wang, B. Zhu et al., "KIF18B promotes tumor progression through activating the Wnt/beta-catenin pathway in cervical cancer," *OncoTargets and Therapy*, vol. 11, pp. 1707–1720, 2018.

[53] M. Chen, L. Li, and P. S. Zheng, "SALL4 promotes the tumorigenicity of cervical cancer cells through activation of the Wnt/β-catenin pathway via CTNNB1," *Cancer Science*, vol. 110, no. 9, pp. 2794–2805, 2019.

Hindawi
Journal of Oncology
Volume 2022, Article ID 7742035, 8 pages
https://doi.org/10.1155/2022/7742035

Research Article

Construction of Nomogram-Based Prediction Model for Clinical Prognosis of Patients with Stage II and III Colon Cancer Who Underwent Xelox Chemotherapy after Laparoscopic Radical Resection

Qiang Sun, Kai Xu, Shifeng Teng, Wenqiang Wang, Wei Zhang, Xinxing Li, and Zhiqian Hu

Department of General Surgery, Tongji Hospital, School of Medicine, Tongji University, Shanghai 200092, China

Correspondence should be addressed to Xinxing Li; 41807020@xs.ustb.edu.cn and Zhiqian Hu; huzhiq163@163.com

Received 9 August 2022; Revised 23 August 2022; Accepted 30 August 2022; Published 30 September 2022

Academic Editor: Recep Liman

Objective. To construct a nomogram-based prediction model for the clinical prognosis of patients with stage II and III colon cancer who underwent Xelox chemotherapy after laparoscopic radical resection based on large data sets. *Methods*. A total of 7,832 patients with colorectal cancer who received postoperative Xelox-based chemotherapy were screened from the Surveillance, Epidemiology, and End Results database (USA) as the training data set. In addition, 348 domestic patients were screened as the validation data set. Multivariate Cox regression analysis was performed to identify variables for inclusion in the nomogram-based prediction model. The predictive accuracy of the model was assessed using C-index and calibration curve. *Results*. Age, cell differentiation, nerve invasion, T and N stages of tumours, number of dissected lymph nodes, and carcinoembryonic antigen (CEA) level were found to influence the efficacy of postoperative chemotherapy. The nomogram-based prediction model was successfully constructed. The C-index of both the training set and validation set were higher than those of the 7th edition of TNM staging system published by the American Joint Commission on Cancer (C – index of training data set = 0.728, C – index of validation data set = 0.734). The prediction results of the model in the calibration curve showed a good fit with the actual situation. *Conclusion*. We successfully constructed a nomogram-based model to predict the clinical prognosis of patients with colorectal cancer receiving postoperative Xelox-based chemotherapy after laparoscopic radical resection, which showed good clinical application value for predicting the efficacy of postoperative Xelox-based chemotherapy in patients with colorectal cancer.

1. Introduction

Colorectal cancer is a common malignant tumour in China and is associated with a high mortality rate. Currently, surgical resection supplemented with chemotherapy is the main treatment modality for colorectal cancer. Most patients undergoing surgery have advanced stage disease and are at a high risk of postoperative recurrence and/or metastasis. Therefore, chemotherapy is typically used to achieve disease control in clinical settings [1]. The National Comprehensive Cancer Network guidelines recommend Xelox-based chemotherapy (Oxaliplatin: 130 mg/m^2, intravenically given, 2 h, d1; Capecitabine: 1800 mg/(m^2·d), two oral cycles, d1-14, every 21 days) as the first-line regimen after surgery for colorectal cancer. It is a widely used chemotherapy regimen in clinical settings owing to the ease of administration and high efficacy [2]. Despite the advances in surgery and chemotherapy regimens, a large proportion of patients with colorectal cancer develop postoperative recurrence and metastasis, leading to poor prognosis. Thus,

identification of prognostically relevant clinical factors and their use to predict the treatment outcomes may help individualise the treatment plan and improve the prognosis of patients [3]. Nomograms assign scores for various influencing factors calculated by the statistical model; the obtained total score of individual risk can help predict the risk of morbidity. Therefore, in this study, a nomogram-based model was constructed to predict the prognosis of patients with colorectal cancer receiving postoperative Xelox-based chemotherapy by analysing the relevant data.

2. Subjects and Methods

2.1. Subjects. Data pertaining to patients with colorectal cancer recorded in the Surveillance, Epidemiology, and End Results (SEER) database (USA) from 2011 to 2016 was used as the training data set. The inclusion criteria were as follows: age ≥ 18 years; primary tumour, located at the colorectum (code: C18.0, C18.2–C18.7, C19.0, C20.0, C20.X01); pathological diagnosis: adenocarcinoma (code: M81400); patients who underwent surgery (code: 20~80) and received postoperative Xelox-based chemotherapy. The exclusion criteria were as follows: patients with incomplete clinically relevant data, including age, gender, tumour stage and grade, laboratory examination results, and follow-up data. According to the inclusion and exclusion criteria, 7,832 patients were finally screened as the training data set. Simultaneously, a validation data set was established. From 2014 to 2016, a total of 348 patients who underwent colorectal resection and Xelox-based chemotherapy were identified from the electronic medical record system at our hospital. Complete clinical information was available for all patients. Identical inclusion and exclusion criteria were adopted for both the training and validation data sets.

2.2. Methods

2.2.1. Data Collection. Detailed clinical data were retrieved for patients in both the training and validation data sets, including gender, age, tumour location, tumour stage, cell differentiation, depth of cancer invasion, lymph node metastasis, and carcinoembryonic antigen (CEA) level.

2.2.2. Follow-Up. Complete follow-up data was available for all patients in the training data set. All patients in the validation set were followed up for 3 years; the patients were followed up once a month in the first year, every three months in the second year, and at six-month intervals in the third year. Follow-up data of patients were obtained mainly through face-to-face interview in the doctors' office or through telephonic contact. If the patient could not be contacted, the relevant information was obtained from the patient's family or community doctors. A follow-up record was established for every patient to document the detailed prognosis of patients after discharge. According to the follow-up results, the overall survival (OS) and progression-free survival (PFS) were calculated and a detailed list was made, which were used as the end points of the study. OS was defined as the time from diagnosis to death or the end of follow-up; PFS was defined as the time from diagnosis to the first tumour progression, death, or the end of follow-up.

2.2.3. Statistical Analysis. Data were sorted and analysed using SPSS Statistics 26 (IBM) and R language 3.6.2 (Bell Laboratories). The categorical variables were expressed as percentage (%) and between-group differences assessed using the chi-squared test. For the analysis of prognostic factors, univariate analysis was performed with the log-rank χ^2 test. Variables that showed a significant association with prognosis on univariate analysis ($P < 0.05$) were included in multivariate Cox regression analysis to identify the factors influencing OS and PFS. Finally, the nomogram-based prediction model was constructed using variables screened by the multivariate analysis. The accuracy of the model was verified by Harrell's C-statistic and calibration curve. Two-tailed $P < 0.05$ were considered indicative of statistical significance. Calibration, which refers to how closely the predicted probabilities by the nomogram agree with the observed survival probabilities, was visually assessed by plotting actual survival probabilities against predicted survival probabilities for each group. The horizontal and vertical axes of the calibration plot showing the predicted versus the observed probability of the 5-year overall survival and progression-free survival. The gray line represents the optimal line in case of complete concordance between predicted and observed progression-free survival. Decision curve analysis (DCA) was used to evaluate the clinical benefits and utility of the nomogram compared with an American Joint Council on Cancer (AJCC) staging system alone.

3. Results

3.1. Baseline Data of Patients. The 7,832 patients in the training data set included 3,822 males and 4,010 females (mean age: 54.7 ± 8.9 years); the OS was 30.4 (10.3–36) months and PFS was 18.3 (6.2–31.8) months. The 348 patients included in the validation data set included 172 males and 176 females (mean age: 53.2 ± 8.5 years; the OS was 29.8 (10.1–36) months and PFS was 18.4 (5.9–32.7) months). The baseline data in the two data sets are compared in Table 1.

3.2. Factors Influencing the Efficacy of Postoperative Chemotherapy. On univariate analysis, age, cell differentiation, nerve invasion, T and N stages of tumours, number of dissected lymph nodes, and CEA level were found to have a significant influence on OS and PFS ($P < 0.05$). Multivariate Cox regression analysis showed that the above variables were independent predictors of OS and PFS ($P < 0.05$) (Table 2).

3.3. Construction and Validation of Nomogram-Based Prediction Model. Cox regression analysis identified seven variables that influenced the prognosis of patients with colorectal cancer receiving Xelox-based chemotherapy. The nomogram-based prediction model was constructed; on the basis of the model, individualised risk scoring was

Table 1: Comparison of baseline data of patients.

Variable	Training data set ($n = 7832$) n (%)	Validation data set ($n = 348$) n (%)	χ^2	P
Gender			0.052	0.819
Male	3822 (48.8)	172 (49.4)		
Female	4010 (51.2)	176 (50.6)		
Age			0.167	0.682
≤60	3305 (42.2)	143 (41.1)		
>60	4527 (57.8)	205 (58.9)		
Tumour location			0.146	0.703
Rectum	5325 (68.0)	240 (69.0)		
Colon	2507 (32.0)	108 (31.0)		
Cell differentiation			0.496	0.920
High	407 (5.2)	16 (4.6)		
Middle	5864 (74.9)	266 (76.4)		
Low	1253 (16.0)	53 (15.2)		
Undifferentiated	308 (3.9)	13 (3.7)		
Nerve invasion			0.001	0.976
Invasive	6657 (85.0)	296 (85.1)		
Noninvasive	1175 (15.0)	52 (14.9)		
T staging			0.407	0.939
T1	289 (3.7)	12 (3.4)		
T2	971 (12.4)	46 (13.2)		
T3	4825 (61.6)	216 (62.1)		
T4	1747 (22.3)	74 (21.3)		
Number of lymphadenectomy			0.250	0.883
None	110 (1.4)	6 (1.7)		
1~3	71 (0.9)	3 (0.9)		
≥4	7651 (97.7)	339 (97.4)		
N staging			5.009	0.082
N0	4104 (52.4)	163 (46.8)		
N1	2318 (29.6)	109 (31.3)		
N2	1410 (18.0)	76 (21.8)		
CEA level			0.618	0.432
Rise	3344 (42.7)	156 (44.8)		
Normal	4488 (57.3)	192 (55.2)		

performed, and the 3-year and 5-year survival rates (OS and PFS) were predicted (Figures 1 and 2).

For OS, the C-index of the training data set and validation data set was 0.792 and 0.753, respectively. For PFS, the C-index was 0.783 and 0.761, respectively. All these values were higher than those of the 7th edition of TNM staging system published by the American Joint Commission on Cancer (AJCC) (C – index of training data set = 0.728, C – index of validation data set = 0.734). The results suggested a slightly more accurate prediction ability of the model compared with the traditional staging method. In addition, the calibration curve was drawn using the survival rate predicted by the model as the horizontal ordinate and the actual survival as the longitudinal ordinate. For the end-point indicators OS and PFS, the results of the prediction model showed a good fit with the actual situation; this suggested high discriminative ability and accuracy of the prediction model constructed in this study (Figure 3). The 5-year DCA curves also revealed that the nomogram had better clinical performance than the AJCC staging system among all study subjects (Figure 4).

4. Discussion

4.1. Application of Xelox Regimen in Patients with Colorectal Cancer after Surgery. Currently, colorectal cancer is one of the common malignant tumours of the digestive tract and is associated with high mortality and poor prognosis.

Table 2: Analysis of influencing factors of OS and PFS in colorectal cancer patients during training data set.

Variable	OS				PFS			
	Single-factor analysis		Multifactor analysis		Single-factor analysis		Multifactor analysis	
	OR (95% CI)	*P*	OR (95% CI)	*P*	OR (95% CI)	*P*	OR (95% CI)	*P*
Gender	—	0.137	—	—	—	0.231	—	—
Age								
≤60	1.00	—	—	—	1.00	—	—	—
>60	2.17 (1.97~2.64)	0.002	2.56 (1.98~2.79)	<0.001	2.31 (1.86~2.53)	0.003	2.43 (1.91~2.68)	<0.001
Tumour location	—	0.261	—	—	—	0.164	—	—
Differentiation								
High	1.00	—	—	—	1.00	—	—	—
Middle	1.34 (1.13~1.56)	0.005	1.11 (1.03~1.23)	<0.001	1.23 (1.13~1.54)	<0.001	1.14 (1.03~1.21)	<0.001
Low	1.53 (1.38~1.87)	<0.001	1.25 (1.12~1.37)	0.004	1.47 (1.31~1.81)	<0.001	1.28 (1.18~1.33)	0.001
Undifferentiated	2.16 (1.76~2.68)	<0.001	1.36 (1.26~1.48)	<0.001	2.23 (1.85~2.45)	0.017	1.34 (1.21~1.48)	0.021
Nerve invasion								
Invasive	1.00	—	—	—	1.00	—	—	—
Noninvasive	2.11 (1.82~2.41)	0.014	1.37 (1.21~1.51)	<0.001	2.25 (1.91~2.42)	0.001	1.41 (1.24~1.67)	<0.001
T staging								
T1	1.00	—	—	—	1.00	—	—	—
T2	1.23 (1.14~1.42)	<0.001	1.13 (1.04~1.25)	<0.001	1.22 (1.11~1.55)	<0.001	1.15 (1.04~1.26)	<0.001
T3	1.42 (1.31~1.63)	0.002	1.31 (1.21~1.54)	<0.001	1.67 (1.42~1.89)	<0.001	1.41 (1.28~1.61)	<0.001
T4	2.43 (2.01~2.83)	<0.001	1.54 (1.36~1.78)	0.006	2.43 (1.93~2.75)	0.004	1.57 (1.35~1.81)	0.017
Number of lymphadenectomy								
None	1.23 (0.92~2.12)	0.164	1.42 (0.97~2.18)	0.761	1.23 (0.93~2.01)	0.182	1.51 (0.94~2.12)	0.687
1~3	1.51 (1.02~2.24)	0.031	1.83 (1.15~2.63)	0.003	1.41 (1.12~2.31)	0.042	1.91 (1.32~2.28)	0.003
≥4	1.00	—	—	—	1.00	—	—	—
N staging								
N0	1.00	—	—	—	1.00	—	—	—
N1	1.91 (1.62~2.15)	<0.001	1.61 (1.37~1.83)	0.006	1.82 (1.59~2.03)	<0.001	1.72 (1.47~1.93)	0.002
N2								
CEA level								
Normal	1.00	—	—	—	1.00	—	—	—
Rise	2.57 (2.28~2.87)	<0.001	1.98 (1.69~2.18)	0.021	2.47 (2.18~2.73)	0.029	2.01 (1.83~2.34)	0.017

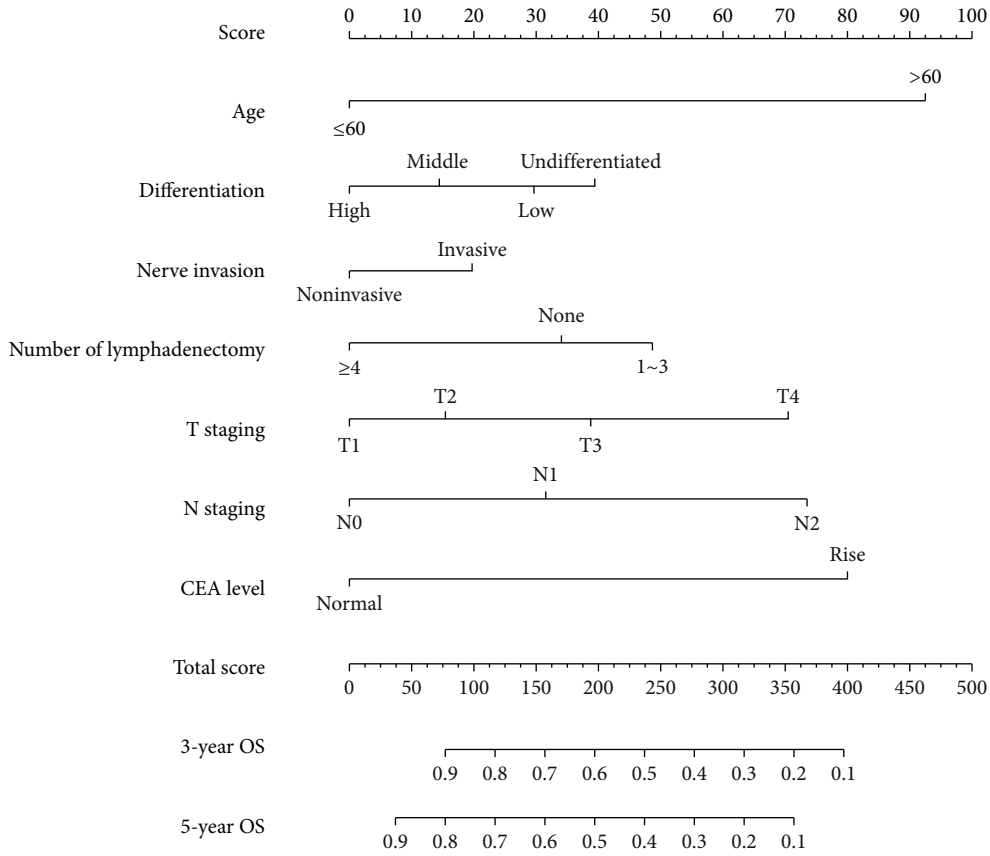

Figure 1: OS nomogram of 3-year and 5-year prognoses for colorectal cancer patients.

Surgery is the only potential curative treatment recognised in clinical practice [1]. However, owing to the lack of obvious symptoms in the early stage of the disease, patients with colorectal cancer are typically diagnosed in the middle and late stages; most of these patients are past the optimal time to achieve radical cure. Moreover, there is a high risk of postsurgical recurrence and metastasis [4]. Therefore, postoperative chemotherapy is typically administered to patients with colorectal cancer who undergo surgery. However, patients with colorectal cancer often have digestive dysfunction, physical weakness, and multiple comorbid conditions. All these factors contribute to chemotherapy intolerance; therefore, selection of the appropriate chemotherapy regimen is a key imperative for these patients.

Xelox-based chemotherapy (also known as the CapeOX regimen) consists of oxaliplatin injection administered in combination with oral Xeloda. Owing to its efficacy and ease of administration, it is used as the main postoperative adjuvant chemotherapy regimen for patients with colorectal cancer in clinical settings [5]. However, approximately 50% of patients who received postoperative Xelox-based chemotherapy were found to develop recurrence and metastasis at different time points after surgery; in addition, the prognosis of these patients is still not very ideal [6]. Therefore, construction of statistical models based on appropriate clinical indicators to predict the prognosis of patients can facilitate individualised treatment decision-making and help improve the prognosis of patients.

4.2. Factors Influencing the Efficacy of Postoperative Chemotherapy in Patients with Colorectal Cancer. In this study, age, cell differentiation, nerve invasion, T and N stages of tumours, number of dissected lymph nodes, and CEA level were found to influence OS and PFS. Our results are consistent with those of previous studies, but not exactly the same.

In our study, age was the most important determinant of prognosis. The older the patient, the worse was the prognosis. Therefore, the benefit of surgical treatment for older patients should be carefully considered based on individualised analysis and assessment of the general condition of the patient [7]. For elderly patients with poor tolerance, the risk of surgery may outweigh the benefits. Additionally, dissection of 1–3 lymph nodes was found to be more dangerous than no dissection; therefore, clinicians should consider increasing the number of dissected lymph nodes in patients scheduled to undergo lymph node dissection [7, 8]. The prognostic value of cell differentiation, nerve invasion, and tumour stage was in line with that found in previous studies [9–11]. In this study, levels of CEA were included in the model as factors influencing the prognosis. The final results showed that all three

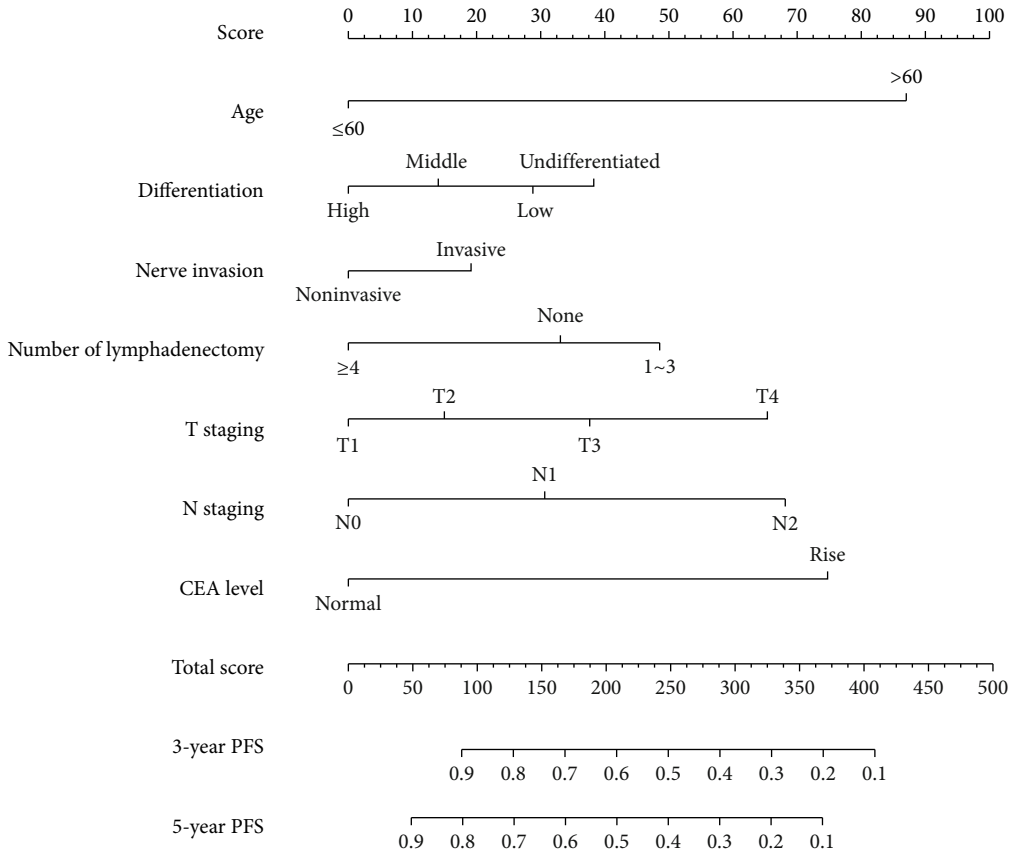

Figure 2: PFS nomogram of 3-year and 5-year prognoses for colorectal cancer patients.

factors were independent predictors of prognosis. As a proteoglycan compound of the digestive system, CEA is a commonly used tumour marker; the correlation of the CEA level with the prognosis of patients with colorectal cancer is well documented [12–15].

4.3. Advantages of the Prediction Model Constructed in This Study. Nomogram-based prediction models provide visual representation of individual risk assessment. It employs multiple clinical indicators, scores the value of each indicator, and finally predicts the corresponding situation of patients according to the total score of individuals. Use of nomograms to predict the incidence and prognosis is a current research hot spot. It can intuitively and accurately display complex mathematical formulas in the form of images and has high clinical application value [16]. However, the prediction model for the efficacy of postoperative chemotherapy in patients with colorectal cancer has rarely been reported.

In this study, we constructed a nomogram-based prediction model using variables identified on multivariate analysis; the prediction model was found to accurately predict individual prognosis. The model showed high discriminative ability and accuracy in the validation cohort. In addition, we compared our nomogram-based model with the 7th edition of the TNM staging system published by the AJCC; our model showed higher prediction ability in both the training and validation data sets. Visual analysis of the calibration curve showed a good fit of the prediction of the training data set with the actual situation; however, the fit of the verification data set showed a certain deviation. This deviation may be attributable to bias caused by insufficient sample size, ethnic differences, and variable selection of the verification data set. The DCA results also demonstrated that our nomogram provided greater clinical value than the AJCC grading system.

4.4. Limitations and Reflection. The prediction model constructed in this study effectively predicted the efficacy of postoperative chemotherapy in patients with colorectal cancer; however, some limitations of the study should be considered while interpreting the results. Firstly, due to the limitations of SEER data, the grouping criteria for some indicators were different from those used in actual clinical practice. For example, for the grouping of the number of dissected lymph nodes, a cut-off value of 12 lymph nodes is used in clinical settings; however, four lymph nodes were used as the cut-off value in the database [17]. Secondly, there were inevitable limitations during data acquisition owing to the retrospective nature of the study. Moreover, there may be a certain bias in the selection of variables. Further studies are required to confirm our results and to further improve the prediction model.

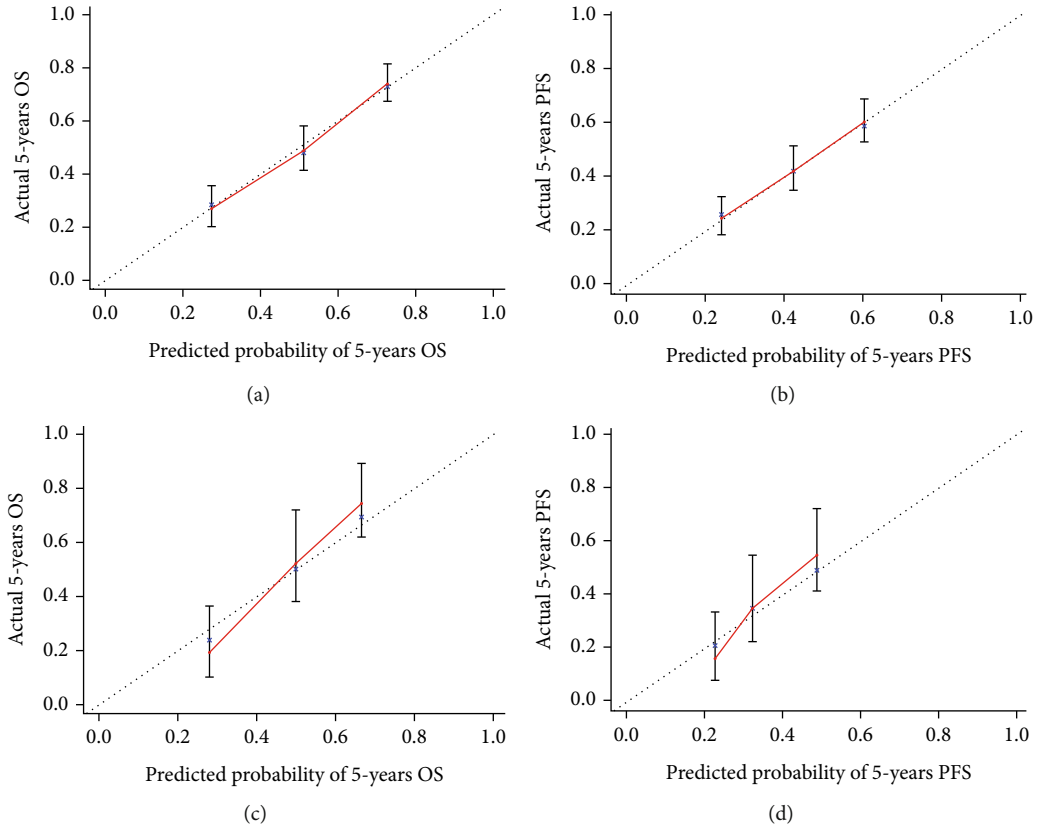

Figure 3: Fitting curve (OS and PFS) between prediction model and actual survival of patients: (a, b) training data set; (c, d) validation data set.

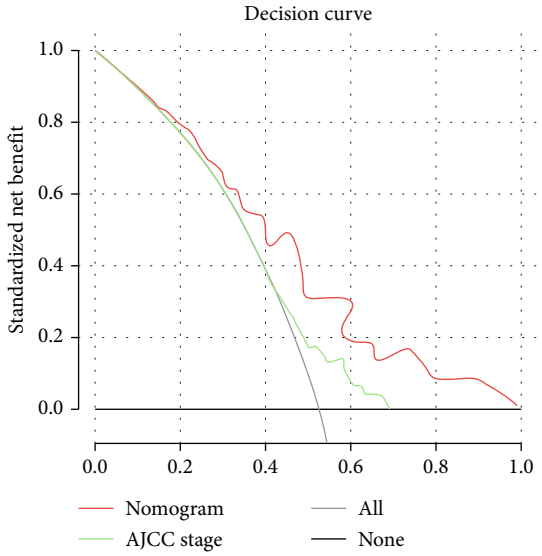

Figure 4: Decision curve analysis for the nomogram and the AJCC stage.

5. Conclusion

Based on the SEER database and our institutional medical record database, we successfully constructed a prediction model for OS and PFS. The model showed good clinical application value for predicting the efficacy of postoperative Xelox-based chemotherapy in patients with colorectal cancer. Both the training and validation data sets showed higher predictive ability when compared with the 7th edition of the TNM staging system published by the AJCC.

Data Availability

The experimental data used to support the findings of this study are available from the corresponding authors upon request.

Conflicts of Interest

The authors declared that they have no conflicts of interest regarding this work.

Authors' Contributions

Qiang Sun, Kai Xu, and Shifeng Teng are common first authors.

References

[1] E. Dekker, P. J. Tanis, J. Vleugels, P. M. Kasi, and M. B. Wallace, "Colorectal cancer," *The Lancet*, vol. 394, no. 10207, pp. 1467–1480, 2019.

[2] Y. Guo, B. H. Xiong, T. Zhang, Y. Cheng, and L. Ma, "XELOX vs. FOLFOX in metastatic colorectal cancer: an updated meta-analysis," *Cancer Investigation*, vol. 34, no. 2, pp. 94–104, 2016.

[3] K. Heinimann, "Erblicher darmkrebs: klinik, diagnostik und management," *Therapeutische Umschau*, vol. 75, no. 10, pp. 601–606, 2018.

[4] L. O. The, "Colorectal cancer: a disease of the young?," *The Lancet Oncology*, vol. 18, no. 4, p. 413, 2017.

[5] Y. Wang, X. Cheng, Y. H. Cui et al., "Efficacy after preoperative capecitabine and oxaliplatin (Xelox) versus docetaxel, oxaliplatin and S1 (DOS) in patients with locally advanced gastric adenocarcinoma: a propensity score matching analysis," *BMC Cancer*, vol. 18, no. 1, p. 702, 2018.

[6] T. Mizushima, M. Ikeda, T. Kato et al., "Postoperative Xelox therapy for patients with curatively resected high-risk stage II and stage III rectal cancer without preoperative chemoradiation: a prospective, multicenter, open-label, single-arm phase II study," *BMC Cancer*, vol. 19, no. 1, p. 929, 2019.

[7] L. C. Connell, J. M. Mota, M. I. Braghiroli, and P. M. Hoff, "The rising incidence of younger patients with colorectal cancer: questions about screening, biology, and treatment," *Current Treatment Options in Oncology*, vol. 18, no. 4, p. 23, 2017.

[8] E. Porcellini, N. Laprovitera, M. Riefolo, M. Ravaioli, I. Garajova, and M. Ferracin, "Epigenetic and epitranscriptomic changes in colorectal cancer: diagnostic, prognostic, and treatment implications," *Cancer Letters*, vol. 419, pp. 84–95, 2018.

[9] B. Bogner, "Predictive markers of immunotherapy of colorectal cancer," *Magyar Onkologia*, vol. 63, no. 3, pp. 192–195, 2019.

[10] M. Khalfallah, W. Dougaz, H. Jerraya, R. Nouira, I. Bouasker, and C. Dziri, "Prognostic factors in rectal cancer: where is the evidence?," *La Tunisie Médicale*, vol. 95, no. 2, pp. 79–86, 2017.

[11] L. Deantonio, A. Caroli, E. Puta et al., "Does baseline [18F] FDG-PET/CT correlate with tumor staging, response after neoadjuvant chemoradiotherapy, and prognosis in patients with rectal cancer?," *Radiation Oncology*, vol. 13, no. 1, p. 211, 2018.

[12] M. Campos-da-Paz, J. G. Dórea, A. S. Galdino, Z. G. Lacava, and M. F. M. A. Santos, "Carcinoembryonic antigen (CEA) and hepatic metastasis in colorectal cancer: update on biomarker for clinical and biotechnological approaches," *Recent Patents on Biotechnology*, vol. 12, no. 4, pp. 269–279, 2018.

[13] C. Lertudomphonwanit, R. Mourya, L. Fei et al., "Large-scale proteomics identifies MMP-7 as a sentinel of epithelial injury and of biliary atresia," *Science Translational Medicine*, vol. 9, no. 417, pp. 22–29, 2017.

[14] M. Vočka, D. Langer, V. Fryba et al., "Serum levels of TIMP-1 and MMP-7 as potential biomarkers in patients with metastatic colorectal cancer," *The International Journal of Biological Markers*, vol. 34, no. 3, pp. 292–301, 2019.

[15] C. S. Melincovici, A. B. Boşca, S. Şuşman et al., "Vascular endothelial growth factor (VEGF) - key factor in normal and pathological angiogenesis," *Romanian Journal of Morphology and Embryology*, vol. 59, no. 2, pp. 455–467, 2018.

[16] M. Zare, J. Jafari-Nedooshan, K. Aghili et al., "Association of MMP-7 -181A>G polymorphism with colorectal cancer and gastric cancer susceptibility: a systematic review and meta-analysis," *Arquivos Brasileiros de Cirurgia Digestiva*, vol. 32, no. 3, p. 1449, 2019.

[17] N. Brouwer, R. Stijns, V. Lemmens et al., "Clinical lymph node staging in colorectal cancer; a flip of the coin?," *European Journal of Surgical Oncology*, vol. 44, no. 8, pp. 1241–1246, 2018.

Hindawi
Journal of Oncology
Volume 2022, Article ID 1752827, 14 pages
https://doi.org/10.1155/2022/1752827

Research Article

Low Complement Factor H-Related 3 (CFHR3) Expression Indicates Poor Prognosis and Immune Regulation in Cholangiocarcinoma

Haoran Wang, Meng He, Zheng Zhang, Wenze Yin, Bixuan Ren, and Yujia Lin

Department of Hepatobiliary Surgery, Second Affiliated Hospital of Harbin Medical University, Harbin, Heilongjiang, China

Correspondence should be addressed to Yujia Lin; linyujia@hrbmu.edu.cn

Received 8 August 2022; Revised 6 September 2022; Accepted 12 September 2022; Published 30 September 2022

Academic Editor: Muhammad Muddassir Ali

Background. Cholangiocarcinoma (CCA) is a cancerous tumor that leads to a high rate of morbidity and death. Complement factor H-related 3 (CFHR3) is a gene belonging to the CFHR gene family. In this study, we investigated the usefulness of CFHR3 in the diagnostic stage and CCA prognosis prediction. In the interim, we looked at its coexpressed genes and their roles. The correlation between CFHR3 and immunological infiltration was also investigated. *Methods*. The expression of the genes data and the clinical information were obtained from the databases of The Cancer Genome Atlas (TCGA) together with the Gene Expression Omnibus (GEO). The crucial gene was found to be the overlapping gene in the two databases. The area under the curve (AUC) and the Kaplan-Meier survival curve were used to describe the usefulness of the predictive prognosis of CCA patients. Univariate regression analysis and multivariate survival analysis were performed to find the independent prognosis factors. The PPI network was constructed based on the STRING database, and the coexpression approach was utilized in predicting the coexpression genes. Gene Ontology (GO) and Kyoto Encyclopedia of Genes and Genomes (KEGG) enrichment analyses were also performed to identify the related functions. Additionally, the probable mechanism of the important gene was examined using gene set enrichment analysis (GSEA). The correlation between CFHR3 and immune infiltration was discovered using TIMER. The LncACTdb 3.0 database was used to analyze the location of CFHR3 in the cell. The cBioPortal database was used to find the mutation in CFHR3. *Results*. TCGA datasets and GEO datasets revealed an elevated expression level of CFHR3 in normal tissues as well as a lower expression level in cholangiocarcinoma tissues in the present research. The low expression level of CFHR3 was related to an unfavorable prognosis. Using CFHR3 expression in diagnosis and predicting the patient prognosis (AUC = 1.000) is valuable. Using the CFHR3 gene and a time-lapse prediction, we could estimate survival rates over 1, 2, and 3 years. The AUC values were more than 0.6(AUC = 0.808 ; 0.760 ; 0.711). Functional enrichment analysis revealed a substantial correlation between this signature and complement and coagulation cascades. The same outcomes from GSEA were achieved. We found the key gene widely exists in the nucleus, exosomes, and cytoplasm of normal cells using the LncACTdb 3.0 database. In immune regulation analysis, we identified that the expression level of CFHR3 had a positive correlation with infiltrating levels of B cells, neutrophils, and macrophages, but correlated negatively with cholangiocarcinoma cells, CD8+ T cells, and monocytes.

1. Introduction

Cholangiocarcinoma (CCA) is the second most common tumor found in the liver. CAA is characterized as such by originating from the biliary system [1]. The incidence and mortality rates of cholangiocarcinoma are increasing year by year all over the world [2]. The primary method for treating tumors is surgical resection, however, patients frequently miss the best window for surgery and pass away because the tumor is discovered at an advanced stage [3]. Therefore, it is important to screen certain valuable genes for a more efficient prognosis prediction and to provide optimal customized treatment.

Recent studies have shown that some genes, such as LIMA1, HDAC1, ITGA3, ACTR3, GSK3B, ITGA2, THOC2, PTGES3, HEATR1, and ILF2, are associated with the

prognosis of patients with cholangiocarcinoma [4]. However, there is still an urgent need to identify more genes to obtain more accurate predictions. CFHR3 belongs to a gene family that also consists of CFHR1, CFHR2, CFHR4, and CFHR5. A collection of complement proteins with these genes are closely related [5]. According to reports, CFHR3 may be a potential biomarker for the disease hepatocellular carcinoma (HCC) [6]; however, as the second highest type of cancer in the liver, the correlation between CFHR3 expression and its clinical significance of CCA remains unclear.

Here, we identified CFHR3 as a key gene and hypothesized that CFHR3 has a correlation with prognosis and immune regulation of cholangiocarcinoma. Bioinformatics was used to assess this theory. To better understand CFHR3 function, we also looked into the coexpression genes and the protein-protein interaction (PPI) network. Immune infiltration was also explored to confirm that the expression of CFHR3 correlates with immune regulation. Finally, we performed a further investigation of the molecular mechanism of CFHR3. CFHR3 might be employed as a marker in predicting immune and prognosis-related status in patients with CCA.

The paper's organization paragraph is as follows: the materials and methods is presented in Section 2. Section 3 discusses the experiments and results. Section 4 analyzes the discussion of the proposed work. Finally, in Section 5, the research work is concluded.

2. Materials and Methods

2.1. Data Obtaining. The TCGA database (https://portal.gdc.cancer.gov/) was utilized in evaluating the CFHR3 expression. Other datasets, including GSE40367, GSE31370, and GSE32879 [7–9], were collected from the GEO database (https://www.ncbi.nlm.nih.gov/geo/) and utilized to examine CFHR3 expression and further validate our findings.

2.2. Differential Analysis of the Key Gene. In the four datasets, differentially expressed genes were evaluated with the aid of the online tools UCSC Xena (https://xena.ucsc.edu/) [10] together with GEO2R (https://www.ncbi.nlm.nih.gov/geo/geo2r/) with the condition used being adjusted p value < 0.05 coupled with $|\log 2 \text{ fold change (FC)}| > 1$.

Using univariate regression analysis, the survival-related genes in the TCGA database were initially identified. In order to give further clinical details, the Genotype-Tissue Expression Project (GTEx) database was also utilized. The overlapping gene was selected and illustrated using the "Venn" package [11]. The volcano maps and box plots were completed using ggplot2 package R software and GEO2R online tools to illustrate the differential appearance.

2.3. Survival Analysis. The TCGA database provided the data necessary for the survival analysis. The Kaplan–Meier curves were constructed with the aid of GEPIA (http://gepia.cancer-pku.cn/index.html) [12].

The Kaplan-Meier curves were used to compare the differences reported in the OS and DFS. We were thorough in our evaluation and got rid of some information that did not match the requirements. Patients were classified into two groups according to their CFHR3 expression levels, namely, the high- and low-CFHR3 expression groups. This data was used to build the baseline data table and to perform both the univariate and multivariate regression analyses. To confirm the key gene's accuracy as a prognostic molecule, ROC curves of patient diagnosis were generated using R packages pROC and ggplot2.

Table 1: The genes related with prognosis in TCGA-CHOL database.

Gene	KM	HR	HR.95 L	HR.95H	p value
GCNT4	0.002408	0.618419	0.453554	0.843211	0.002382
APBA2	0.006801	0.727395	0.547252	0.966837	0.028361
TTC29	0.041737	5.246029	1.065476	25.82960	0.041556
KLRB1	0.012578	0.575461	0.371508	0.891383	0.013325
NPY2R	0.000147	15.56928	1.694302	143.0692	0.015271
EIF5AL1	0.005824	5.862329	1.983363	17.32759	0.001382
TRIM31	0.037284	1.454294	1.103465	1.916662	0.007838
FAM183A	0.010867	1.629543	1.091789	2.432163	0.016860
AVPR1B	0.041278	0.445101	0.201530	0.983055	0.045259
SPDYE2	0.002466	0.306656	0.110388	0.851887	0.023362
MYBPC1	0.002620	1.759721	1.206972	2.565610	0.003305
COL4A4	0.001696	0.641426	0.454693	0.904844	0.011420
CFHR3	0.009203	1.216593	1.007963	1.468405	0.041092
GOLGA7B	0.046302	0.624614	0.411890	0.947201	0.026740
PPP1R2P1	0.024259	0.321206	0.121624	0.848299	0.021906
GRK1	0.035320	10.98407	1.455779	82.87638	0.020116
GH1	0.002271	0.005099	5.94E-05	0.437617	0.020138
C5orf46	0.015935	1.356822	1.021947	1.801428	0.034851
SERPINB13	0.007693	5.151513	1.167473	22.73123	0.030433
SLC6A14	0.035360	1.209221	1.000416	1.461608	0.049500
CRLF1	0.034175	1.656919	1.047114	2.621856	0.031038
ACR	0.024025	0.309656	0.124652	0.769232	0.011567
CST1	0.047236	1.220925	1.014977	1.468661	0.034202
PRSS35	0.001770	0.534249	0.296876	0.961419	0.036509
KRT40	0.005217	0.228907	0.053879	0.972522	0.045748
CHRM5	0.015362	0.363946	0.143565	0.922629	0.033202

2.4. Enrichment Analysis and Construction of PPI Network. CFHR3-related genes were screened with the use of STRING (http://string.embl.de/) [13].

The medium confidence rate > 0.4 was regarded as significant. The enrichment analysis was conducted with the aid of DAVID (https://david.ncifcrf.gov/) [14]. Gene ontology (GO) analysis and Kyoto Encyclopedia of Genes and Genomes (KEGGs) pathway analyses are the two types of enrichment analysis for the key gene. The criterion was fixed at $p < 0.05$. ggplot2 package and R software were used to complete visualization. GSEA software (http://software.broadinstitute.org/gsea/index.jsp) was utilized in performing the gene set enrichment analysis [15].

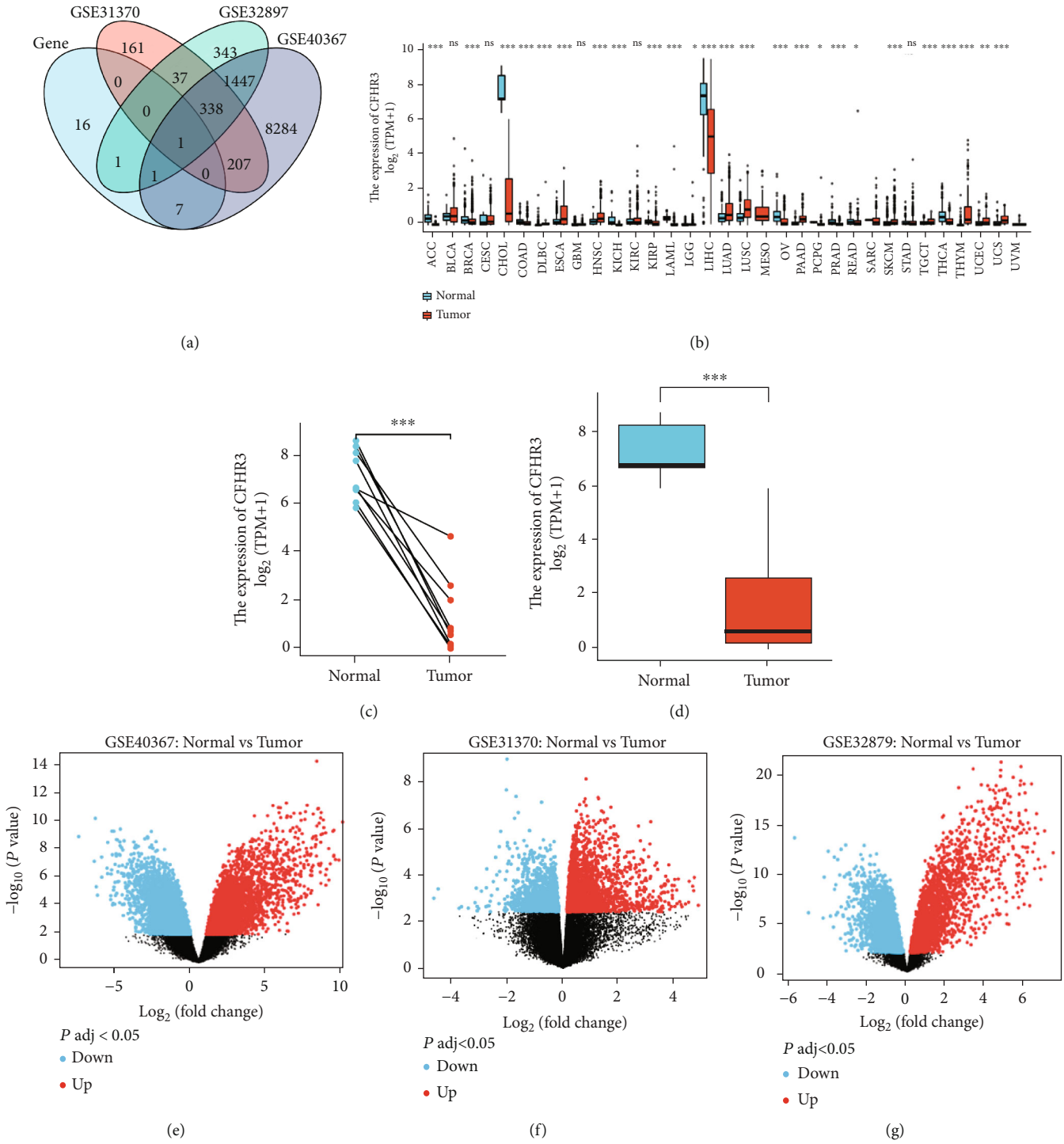

Figure 1: The difference expression of CFHR3 in CCA. (a) A Venn diagram of intersection of genes related with prognosis from the TCGA and GSE40367, GSE31370, and GSE32879. (b) The expressions of CFHR3 in common tumors. (c) A line diagram of the difference expression of CFHR3 in CCA. (d) A box plot of the difference expression of CFHR3 in CCA. (e–g) The volcano maps of CFHR3 in GSE40367, GSE31370, and GSE32879.

2.5. Coexpression Gene Screening and Functional Annotation. To determine the coexpression relationship, Pearson's correlation coefficients were computed between the main gene and other genes. We selected genes having a |Pearson's correlation coefficient| > 0.5 as well as p value < 0.05. We selected the top15 lncRNA, mRNA, and all miRNAs to create a heat map using R software. Alluvial plotting was performed to show the associations between these genes. The functional annotation of the genes was completed with the aid of Metascape (http://metascape.org/gp/index.html#/main/step1) [16].

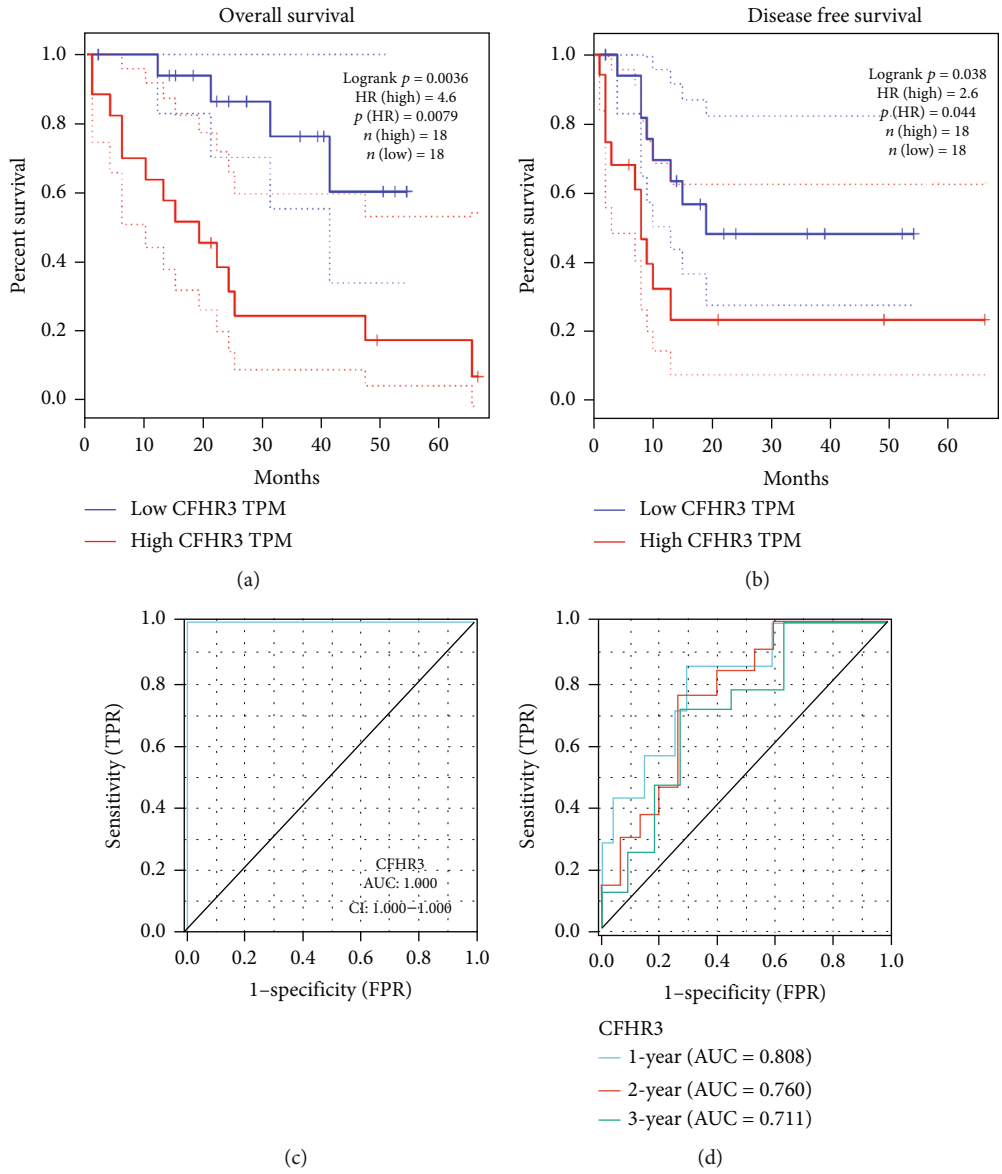

Figure 2: The value of CFHR3 in predicting the prognosis. (a) The OS survival curves comparing patients with high (red) and low (blue) CFHR3 expression in CCA ($p < 0.05$) (b) The DFS survival curves comparing patients with high (red) and low (blue) CFHR3 expression in CCA ($p < 0.05$). (c) The ROC curve to confirm accurate value of CFHR3 expression in diagnosis and predicting prognosis ($AUC = 1.000$) (d) Time-dependent survival ROC curve of CFHR3 to predict 1-, 2-, and 3-year survival rates. All AUC values were above 0.6(AUC = 0.808 ; 0.760 ; 0.711).

2.6. Immune Cell Infiltration Analysis. To examine the expression profiles of several immune cells, we utilized the Human Protein Atlas (HPA, https://www.proteinatlas.org/). TIMER (https://cistrome.shinyapps.io/timer/) was utilized to investigate the relationship between the expression of CFHR3 and immune cell infiltration and immune cell biomarkers in cholangiocarcinoma [17, 18].

2.7. CFHR3 Genetic Location and Alteration Analysis. The position of CFHR3 in the cell was analyzed using LncACTdb 3.0 database (http://www.bio-bigdata.net/LncACTdb/) [19]. The cBioPortal database (http://www.cbioportal.org/) was used to show the key gene alteration [20, 21].

2.8. Statistical Analysis. R software and its resource packages were used for statistical analysis and to create related visualization graphics. A Wilcoxon rank-sum test or Student's t -test was used to calculate the difference in expression between normal and cholangiocarcinoma tissues. The relationship between other genes and CFHR3 was determined using Pearson's correlation.

To determine the significance of the difference among the survival curves, Kaplan-Meier plots were plotted and log-rank tests were conducted. Statistically significant differences were defined as those with a value of $p < 0.05$. For all statistical tests in this passage, $p < 0.05$ was set as the criterion of the statistical significance.

Table 2: The baseline table of clinical information in CCA.

Characteristic	Low expression of CFHR3	High expression of CFHR3	p value
n	18	18	
Age, n (%)			1.000
≤65	9 (25%)	8 (22.2%)	
>65	9 (25%)	10 (27.8%)	
Gender, n (%)			0.315
Female	12 (33.3%)	8 (22.2%)	
Male	6 (16.7%)	10 (27.8%)	
T stage, n (%)			0.651
T1	8 (22.2%)	11 (30.6%)	
T2	7 (19.4%)	5 (13.9%)	
T3	3 (8.3%)	2 (5.6%)	
T4	0 (0%)	0 (0%)	
N stage, n (%)			1.000
N0	14 (45.2%)	12 (38.7%)	
N1	3 (9.7%)	2 (6.5%)	
M stage, n (%)			0.656
M0	15 (45.5%)	13 (39.4%)	
M1	2 (6.1%)	3 (9.1%)	
Pathologic stage, n (%)			0.543
Stage I	8 (22.2%)	11 (30.6%)	
Stage II	6 (16.7%)	3 (8.3%)	
Stage III	1 (2.8%)	0 (0%)	
Stage IV	3 (8.3%)	4 (11.1%)	
Histological type, n (%)			0.346
Distal	2 (5.6%)	0 (0%)	
Hilar/perihilar	1 (2.8%)	3 (8.3%)	
Intrahepatic	15 (41.7%)	15 (41.7%)	
CA19-9 level, n (%)			0.299
Abnormal	9 (30%)	7 (23.3%)	
Normal	5 (16.7%)	9 (30%)	
Vascular invasion, n (%)			0.648
No	16 (47.1%)	13 (38.2%)	
Yes	2 (5.9%)	3 (8.8%)	
Perineural invasion, n (%)			1.000
No	14 (42.4%)	12 (36.4%)	
Yes	4 (12.1%)	3 (9.1%)	
Age, mean ± SD	60.56 ± 15.45	65.5 ± 9.39	0.254

3. Results

3.1. Key Gene Identified and Differential Expression Analysis. Data was collected from TCGA and GEO datasets. We completed the differential analysis and preliminary univariate regression analysis. Twenty-six (26) genes were selected as target genes (Table 1). Upon examination, we found three datasets, the GSE40367, GSE31370, and GSE32879, which contained the cholangiocarcinoma information and normal information. Differential analysis was performed to find the target genes. Finally, the overlapping gene was screened by the Venn diagram as our key gene (Figure 1(a)).

We did a series of differential expression analyses after identifying the crucial gene, CFHR3. We first discovered a difference in expression between cholangiocarcinoma and other malignancies. The expression of CFHR3 varies widely across 21 cancer types (Figure 1(b)). A higher expression of CFHR3 in normal tissues and a lower expression in cholangiocarcinoma tissues was observed in TCGA datasets (Figures 1(c) and 1(d)). Low expression of CFHR3 in CCA was observed in GSE40367, GSE31370, and GSE32879 based on the GEO database data (Figures 1(e)–1(g)). This data demonstrates that CFHR3 expression differs between normal tissues and cholangiocarcinoma tissues.

3.2. Correlation between Clinical Features and CFHR3 Expression of Cholangiocarcinoma. We used GEPIA to create Kaplan-Meier survival curves to evaluate the relationship between clinical prognosis and the main gene. As the curves shown, cholangiocarcinoma patients with lower CFHR3 expression showed a lower OS (log-rank $p = 0.0036$) and a poorer DFS (log-rank $p = 0.038$). The low expression level of CFHR3 is related to an unfavorable prognosis. (Figures 2(a) and 2(b)).

The ROC curve was used to confirm accurate values of CFHR3 expression in diagnosis and prognosis prediction (AUC = 1.000) (Figure 2(c)). To predict the survival rates over 1, 2, and 3 years, the time-dependent survival ROC curve of CFHR3 was generated. AUC values were all more than 0.6(AUC = 0.808 ; 0.760 ; 0.711) (Figure 2(d)). All of these results suggest that our key gene has an effective prognostic value.

The clinical data was gathered from the TCGA database and utilized to screen for the independent prognostic factor. Variables including age, gender, TNM stages, pathology stage, histological type, CA199 level, vascular invasion, and perineural invasion were included.

These results are shown in the baseline information table (Table 2). Next, we completed both univariate cox analysis and multivariate cox analysis (Table 3). Consequently, the perineural invasion was identified as an independent prognostic factor ($p < 0.05$).

3.3. PPI Network Construction and Underlying Function Analysis of CFHR3. Ten (10) genes were screened for CFHR3-related genes with remarkable interaction, including CFHR1, CFH, CF8, CFI, C3, NIPA2, MNS1, NIPA1, TUBGCP5, and CYFIP1. With the aid of the STRING database, we carried out the PPI network analysis of CFHR3 and CFHR3-related genes (Figure 3(a)).

The key gene and its corresponding genes were strongly enriched in the BP category, which included regulation of humoral immune response, regulation of complement activation, and regulation of protein activation cascade, according to the GO analysis.

In the CC category, there was an enrichment of genes in blood microparticles, mRNA cap-binding complex, as well as dendrite terminus.

Table 3: The univariate and multivariate regression analysis of cholangiocarcinoma.

Characteristics	Total (*n*)	Univariate analysis		Multivariate analysis	
		Hazard ratio (95% CI)	*p* value	Hazard ratio (95% CI)	P value
CFHR3	36	1.265 (0.987-1.621)	0.063	1.252 (0.937-1.672)	0.128
Age	36				
≤65	17	Reference			
>65	19	1.268 (0.499-3.221)	0.617		
Gender	36				
Female	20	Reference			
Male	16	1.387 (0.544-3.534)	0.494		
T stage	36				
T1	19	Reference			
T2	12	2.612 (0.939-7.263)	0.066		
T3	5	0.986 (0.204-4.767)	0.986		
N stage	31				
N0	26	Reference			
N1	5	2.289 (0.602-8.700)	0.224		
M stage	33				
M0	28	Reference			
M1	5	1.650 (0.462-5.891)	0.440		
Pathologic stage	36				
Stage I	19	Reference			
Stage II	9	2.046 (0.646-6.476)	0.223		
Stage III	1	0.000 (0.000-Inf)	0.998		
Stage IV	7	2.279 (0.719-7.224)	0.162		
Histological type	36				
Distal	2	Reference			
Hilar/perihilar	4	130157029.581 (0.000-Inf)	0.998		
Intrahepatic	30	69806426.989 (0.000-Inf)	0.998		
CA19-9 level	30				
Abnormal	16	Reference			
Normal	14	1.003 (0.349-2.883)	0.995		
Vascular invasion	34				
No	29	Reference			
Yes	5	1.764 (0.488-6.372)	0.387		
Perineural invasion	33				
No	26	Reference			
Yes	7	4.264 (1.184-15.352)	0.026	4.871 (1.308-18.139)	0.018

Magnesium ion transmembrane transporter activity, serine-type endopeptidase activity, and serine-type peptidase activity were all enriched in the MF category.

Results recorded from the KEGG pathway analysis indicated that the enrichment of genes was primarily in two pathways, namely, complement and coagulation cascades, and staphylococcus aureus infection. (Figure 3(b)).

We also analyzed the GSEA results of the TCGA database. As the maps show, the CFHR3 expression group was enriched in the drug metabolism cytochrome P450, complement and coagulation cascades, steroid hormone biosynthesis, and primary bile acid biosynthesis (Figures 3(c)–3(g)).

Finally, we observed CFHR1 in the PPI network, which is a member of the CFHR gene family; therefore, we performed the differential analysis of the CFHR gene family in cholangiocarcinoma. It was surprising that the data showed that all of the genes in this gene family had low expression in tumor tissue and high expression in normal tissues (Figures 3(h)–3(k)).

3.4. Coexpression Molecular Analysis of CFHR3 and Functional Annotation. The coexpression method was used to predict the correlations among DElncRNAs, DEmiRNAs, and DEmRNAs with CFHR3 expression in patients with cholangiocarcinoma. The differential expression found in lncRNAs, miRNAs, and mRNAs is shown in the volcano maps and heat maps (Figures 4(a)–4(f)). The interrelationships between these genes are also illustrated in Figure 4(g).

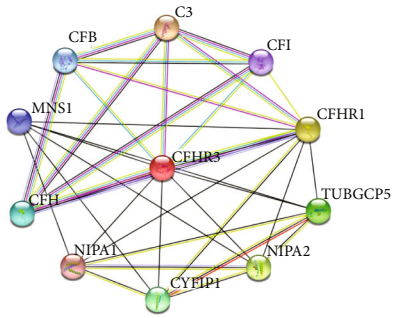

(a)

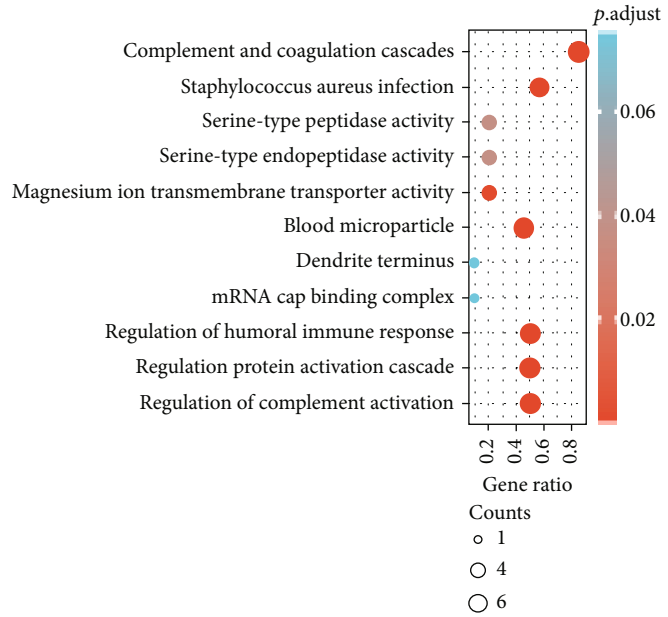

(b)

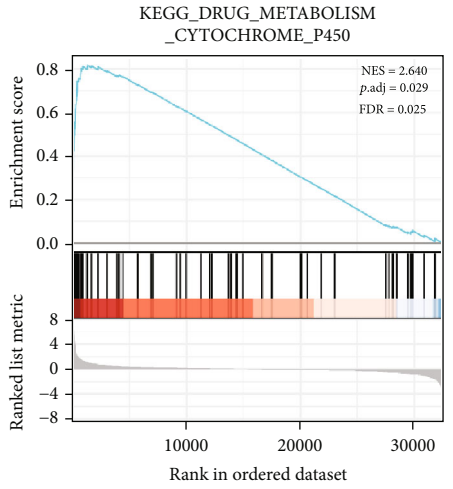

(c)

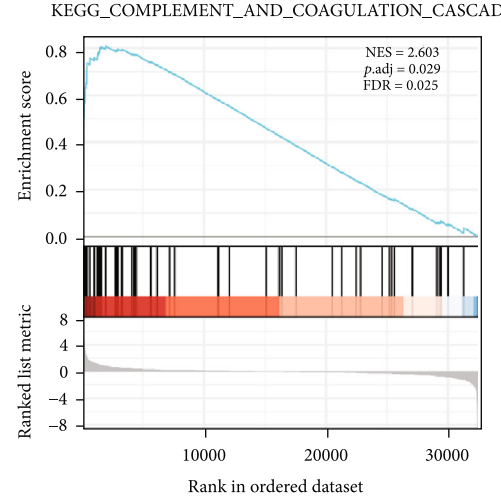

(d)

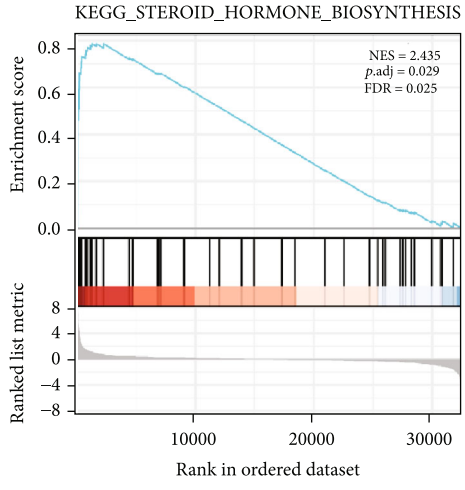

(e)

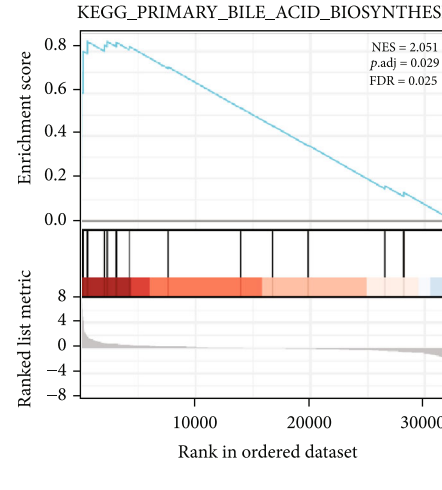

(f)

Figure 3: Continued.

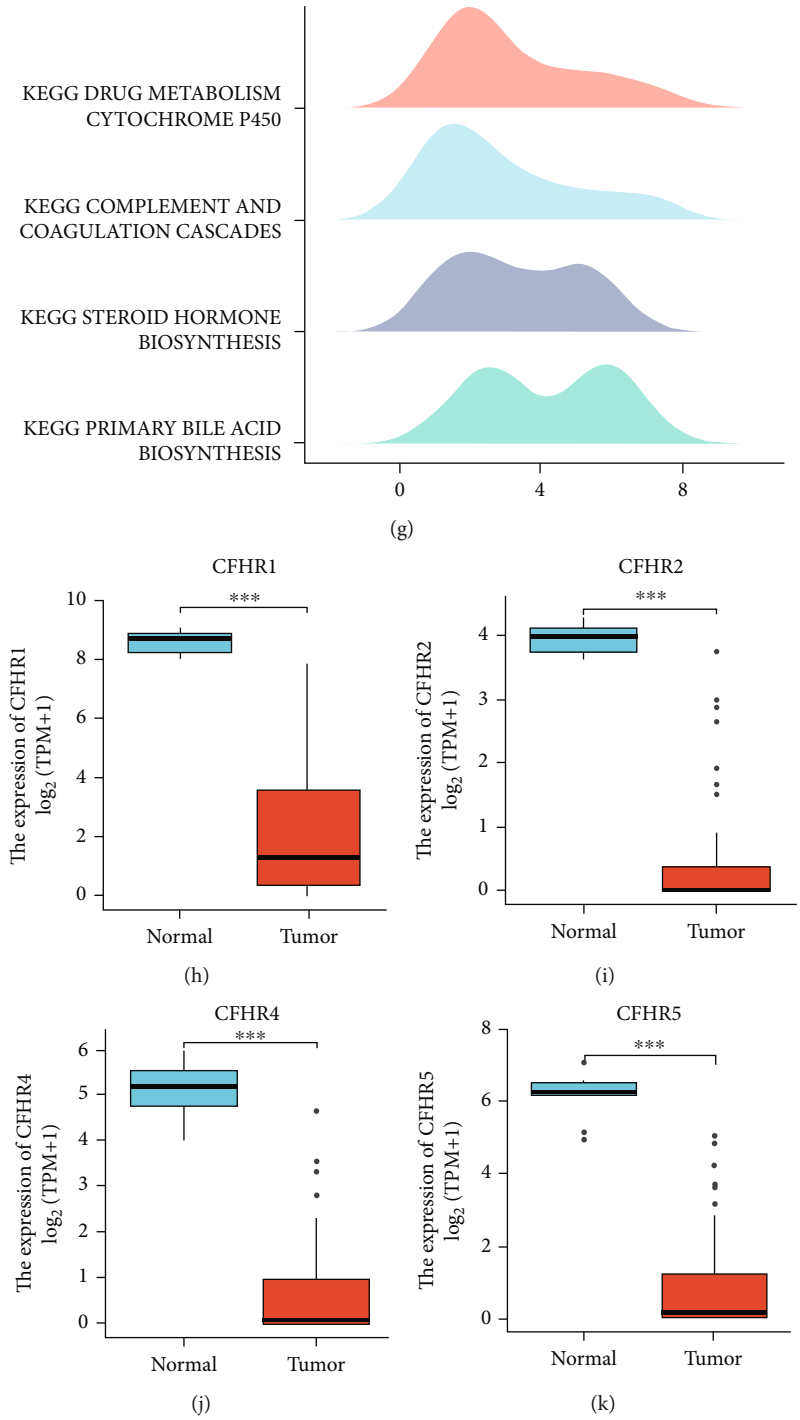

Figure 3: The PPI network and GO, KEGG analysis. (a) PPI network of CFHR3 in STRING. (b) GO and KEGG enrichment of interacted genes of CFHR3. (c–g) GSEA enrichment analysis of CFHR3. (h-k) The expression of CFHR1, CFHR2, CFHR4, and CFHR5.

Both GO and KEGG analyses showed that the functions of these genes were highly enriched in lipid catabolic process, monocarboxylic acid metabolic process, regulation of complement cascade, and gene silencing by miRNA (Figure 4(h)).

3.5. CFHR3 Is Associated with Immune Infiltration. The Human Protein Atlas (HPA) and TIMER database were utilized for additional investigation on the correlation between tumor immune microenvironment and genes.

The HPA database was used to determine the expression of eight (8) different types of immune cells: granulocytes, monocytes, T cells, B cells, dendritic cells, NK cells, progenitors, and total peripheral blood mononuclear cells (PBMCs). To investigate the relationship between immune cells and CFHR3, TIMER was utilized (Figure 5(a)). The results were as follows; the expression level of CFHR3 had a positive relationship with the infiltrating levels of B cells ($r = 0.354$, $p = 3.67e - 02$), neutrophils ($r = 0.364$, $p = 3.15e$

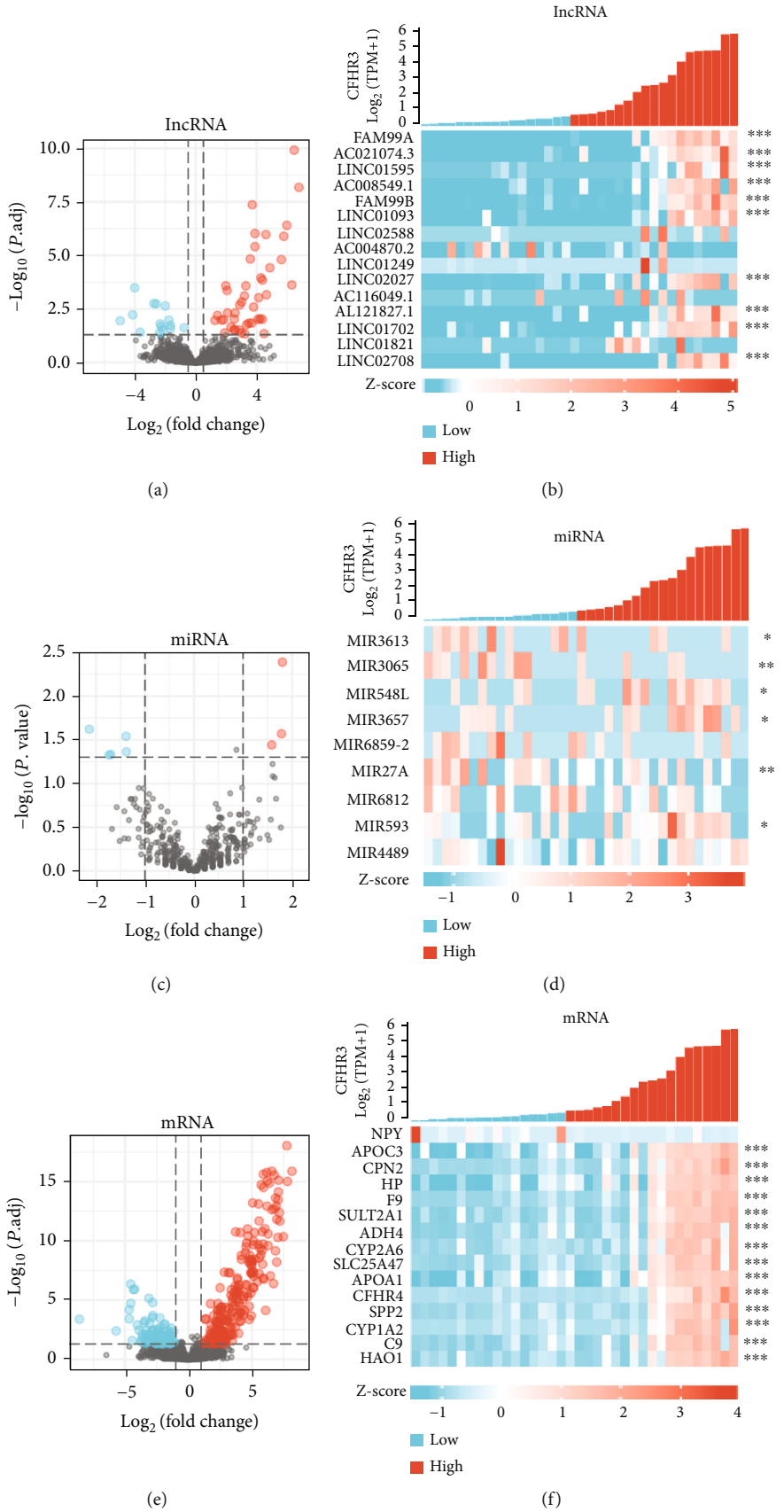

Figure 4: Continued.

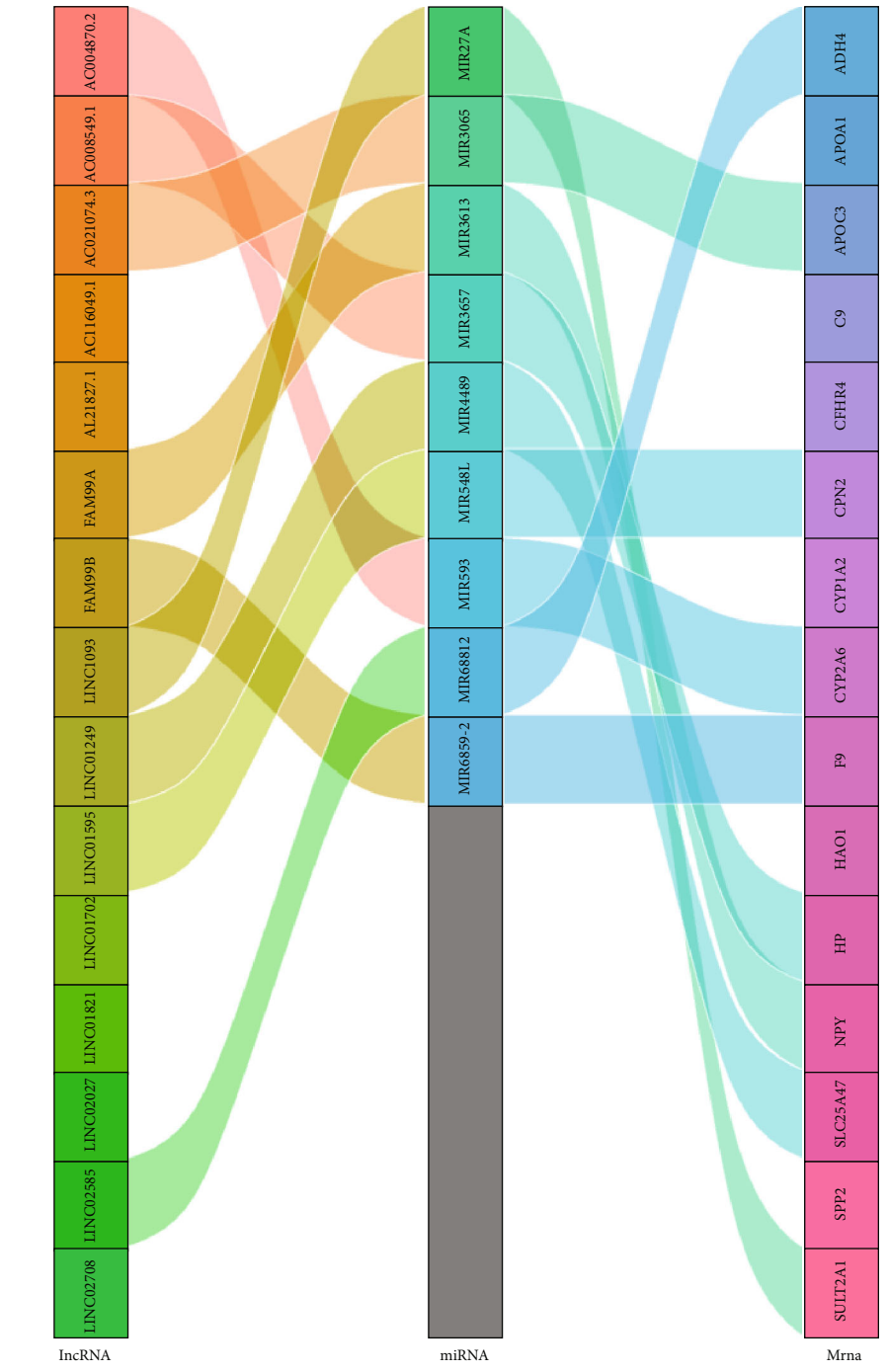

Figure 4: The coexpression genes analysis. The volcano map (a) and the heat map (b) of DElncRNAs. The volcano map (c) and the heat map (d) of DEmiRNAs. The volcano map (e) and the heat map (f) of DEmRNAs. (g) A Sankey diagram to show the relationship of the DElncRNAS, DEmiRNAs, and DEmRNAS. (h) The functional annotation of these genes in Metascape.

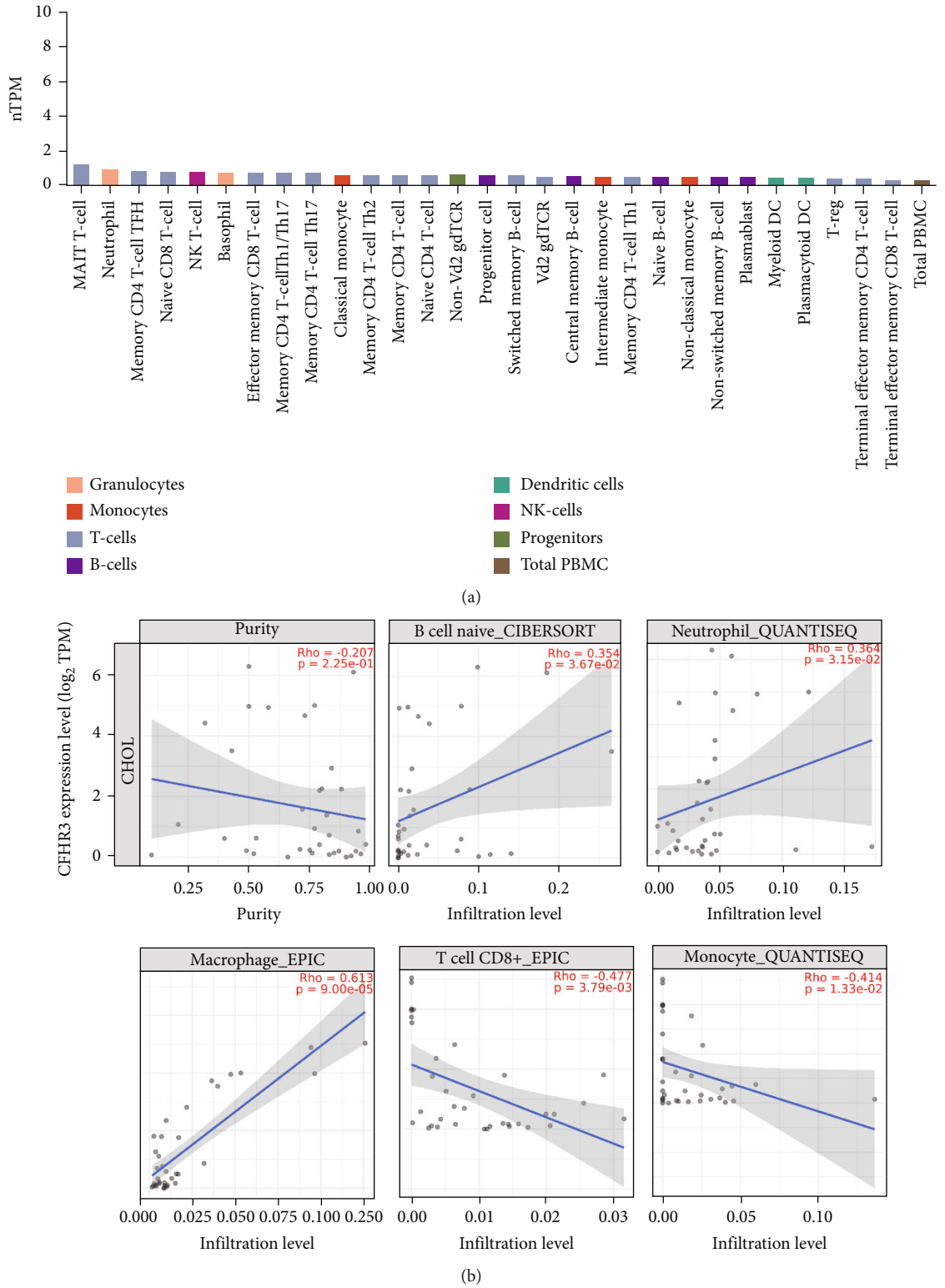

Figure 5: The immune infiltration analysis results. (a) The expression of immune cells in HPA. (b) The relationship between immune cells and CFHR3.

-02), macrophages ($r = 0.613$, $p = 9.00e-05$), but negatively correlated with tumor purity ($r = -0.207$, $p = 2.25e-01$), CD8+ T cell ($r = -0.477$, $p = 3.79e-03$), and monocytes ($r = -0.414$, $p = 1.33e-02$) (Figure 5(b)).

3.6. CFHR3 Genetic Location and Alteration Analysis in Patients with Cholangiocarcinoma. To further understand the molecular mechanism, we undertook location and alteration analysis. The LncACTdb 3.0 database was retrieved in

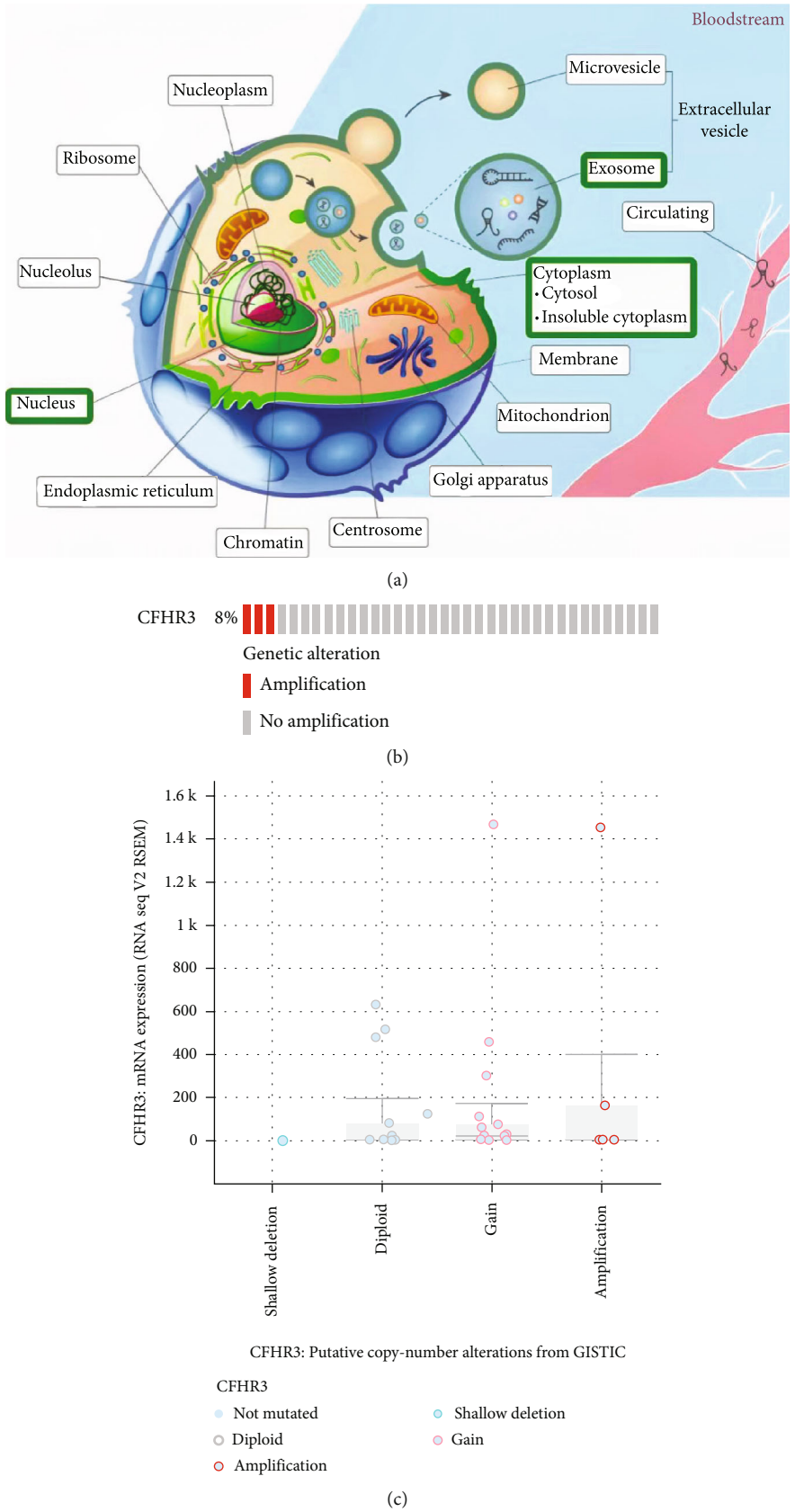

Figure 6: The location and mutation analysis of key gene. (a) The location of CFHR3 in the cell. (b) The mutation situation of CFHR3 in CCA. (c) An OncoPrint plot of CFHR3 in CCA.

analyzing the CFHR3 location in the cells. As demonstrated in Figure 6(a), the key gene widely exists in the nucleus, exosome, and cytoplasm (Figure 6(a)).

cBioPortal was used to show the key gene alteration. As the OncoPrint plot shows, there was an 8% genetic alteration in the key gene in the TCGA CHOL dataset (Figure 6(b)). One diagram shows an alteration of the CFHR3 (Figure 6(c)).

4. Discussion

Cholangiocarcinoma is a slow-growing malignancy of the bile duct [22]. In recent years, the incidence of cholangiocarcinoma has been increasing worldwide, which makes cholangiocarcinoma a health problem of increasing concern. Current treatment options for cholangiocarcinoma are limited because early detection and surgical treatment are difficult [2]. There is an urgent need to understand the genes associated with prognosis in cholangiocarcinoma. As medical technology advances, immune checkpoint blockade (ICB) has become a new method of cancer treatment. Cholangiocarcinoma (CCA) has an abundant tumor immune microenvironment [23]. According to these findings, immune research performs a crucial role in cholangiocarcinoma treatment.

In this work, we discovered a crucial gene for predicting prognosis in CCA patients. First, we found that decreased CFHR3 expression was associated with a poor prognosis in cholangiocarcinoma patients, including overall survival and recurrence-free survival. Second, we used Cox regression analysis to show that our prognostic signature had good predictive accuracy. After 1, 2, and 3 years, low-expression CFHR3 was still a risk factor for CCA. Additionally, in the univariate and multivariate regression analysis, we found that perineural invasion could be an independent prognosis factor. A recent report has shown that an important feature of cholangiocarcinoma is peripheral nerve invasion. This may be connected with the aggressive behaviour of CCA and its poor response to treatment [24]. Therefore, CFHR3 could be a biomarker for prognosis in cholangiocarcinoma. So, the role of CFHR3 should be further investigated.

According to functional annotation, we discovered the function and pathways of CFHR3 and other coexpression genes. We analyzed the results from the GSEA analysis of the TCGA database. The drug metabolism cytochrome P450, complement and coagulation cascades, steroid hormone biosynthesis, and primary bile acid biosynthesis were all enhanced in the CFHR3 expression group. Some epidemiologic research have found that bile production and excretion may play a role in the aetiology of cholangiocarcinoma. Therefore, we identified and screened the potential coexpression genes, and the lncRNA-miRNA and lncRNA-mRNA regulation network was completed. Next, we conducted the GO and KEGG analyses for the purpose of demonstrating that these genes might participate in the complement and coagulation cascades, monocarboxylic acid metabolic process, and lipid catabolic process.

By performing the TIMER analysis, we established that there was a positive relationship between CFHR3 and the infiltration of B cells, neutrophils, and macrophages but negatively correlated with tumor purity, CD8+ T cells, and monocytes. Tumor occurrence, development, and evolution can be coordinated by immune mechanisms. B cells have been identified as a type of tumor infiltration with the adaptive immune system's ability to identify and target emerging tumor cells [25]. Recent studies indicate that the inflammatory response plays a crucial role in the microenvironment alterations of normal tissue. Neutrophils and macrophages are the important cells involved in this process [26]. Therefore, these immune cells have a close relationship with cholangiocarcinoma, which is of great significance in the treatment of CCA.

Our research has some limitations. First, our data came from the GEO and TCGA datasets, and the amount of clinical data we had was modest. Hence, larger-sample studies are needed to estimate the clinical relevance of CFHR3. Besides, in this passage, we found the difference expression of CFHR family in cholangiocarcinoma and the specific molecular mechanism should be further studied.

5. Conclusions

In conclusion, our findings show that reduced CFHR3 expression is associated with a poor prognosis and immune regulation in CCA patients. Further studies should be performed to study the molecular effects of CFHR3 in CCA.

Data Availability

The publicly available datasets analyzed in this study can be found in the TCGA databases (https://portal.gdc.cancer.gov/) and GEO databases (https://www.ncbi.nlm.nih.gov/geo/).

Ethical Approval

The authors are accountable for all aspects of the work in ensuring that questions related to the accuracy or integrity of any part of the work are appropriately investigated and resolved.

Conflicts of Interest

The authors declare that there is no conflict of interest.

Authors' Contributions

Meng He and Zheng Zhang contributed equally to this work.

Acknowledgments

We are grateful for the fundings provided by the National Natural Science Foundation of China (NO.81901576) and the Health Commission of Heilongjiang Province (NO.2018348) in this study.

References

[1] G. Lendvai, T. Szekerczés, I. Illyés et al., "Cholangiocarcinoma: classification, histopathology and molecular carcinogenesis," *Pathology Oncology Research*, vol. 26, no. 1, pp. 3–15, 2020.

[2] S. Rizvi, S. A. Khan, C. L. Hallemeier, R. K. Kelley, and G. J. Gores, "Cholangiocarcinoma — evolving concepts and therapeutic strategies," *Nature Reviews Clinical Oncology*, vol. 15, no. 2, pp. 95–111, 2018.

[3] S. C. Olthof, A. Othman, S. Clasen, C. Schraml, K. Nikolaou, and M. Bongers, "Imaging of cholangiocarcinoma," *Visceral Medicine*, vol. 32, no. 6, pp. 402–410, 2016.

[4] J. Liu, W. Liu, H. Li et al., "Identification of key genes and pathways associated with cholangiocarcinoma development based on weighted gene correlation network analysis," *Peer J*, vol. 7, article e7968, 2019.

[5] N. Medjeral-Thomas and M. C. Pickering, "The complement factor H-related proteins," *Immunological Reviews*, vol. 274, no. 1, pp. 191–201, 2016.

[6] J. Liu, W. Li, and H. Zhao, "CFHR3 is a potential novel biomarker for hepatocellular carcinoma," *Journal of Cellular Biochemistry*, vol. 121, no. 4, pp. 2970–2980, 2020.

[7] S. Roessler, G. Lin, M. Forgues et al., "Integrative genomic and transcriptomic characterization of matched primary and metastatic liver and colorectal carcinoma," *International Journal of Biological Sciences*, vol. 11, no. 1, pp. 88–98, 2015.

[8] J. Y. Seok, D. C. Na, H. G. Woo et al., "A fibrous stromal component in hepatocellular carcinoma reveals a cholangiocarcinoma-like gene expression trait and epithelial-mesenchymal transition," *Hepatology*, vol. 55, no. 6, pp. 1776–1786, 2012.

[9] N. Oishi, M. R. Kumar, S. Roessler et al., "Transcriptomic profiling reveals hepatic stem-like gene signatures and interplay of miR-200c and epithelial-mesenchymal transition in intrahepatic cholangiocarcinoma," *Hepatology*, vol. 56, no. 5, pp. 1792–1803, 2012.

[10] M. J. Goldman, B. Craft, M. Hastie et al., "Visualizing and interpreting cancer genomics data via the Xena platform," *Nature Biotechnology*, vol. 38, no. 6, pp. 675–678, 2020.

[11] H. Chen and P. C. Boutros, "VennDiagram: a package for the generation of highly-customizable Venn and Euler diagrams in R," *BMC Bioinformatics*, vol. 12, no. 1, p. 35, 2011.

[12] Z. Tang, C. Li, B. Kang, G. Gao, C. Li, and Z. Zhang, "GEPIA: a web server for cancer and normal gene expression profiling and interactive analyses," *Nucleic Acids Research*, vol. 45, no. W1, pp. W98–W102, 2017.

[13] D. Szklarczyk, A. L. Gable, D. Lyon et al., "STRING v11: protein-protein association networks with increased coverage, supporting functional discovery in genome-wide experimental datasets," *Nucleic Acids Research*, vol. 47, no. D1, pp. D607–D613, 2019.

[14] D. W. Huang, B. T. Sherman, and R. A. Lempicki, "Systematic and integrative analysis of large gene lists using DAVID bioinformatics resources," *Nature Protocols*, vol. 4, no. 1, pp. 44–57, 2009.

[15] A. Subramanian, P. Tamayo, V. K. Mootha et al., "Gene set enrichment analysis: a knowledge-based approach for interpreting genome-wide expression profiles," *Proceedings of the National Academy of Sciences of the United States of America*, vol. 102, no. 43, pp. 15545–15550, 2005.

[16] Y. Zhou, B. Zhou, L. Pache et al., "Metascape provides a biologist-oriented resource for the analysis of systems-level datasets," *Nature Communications*, vol. 10, no. 1, p. 1523, 2019.

[17] T. Li, J. Fan, B. Wang et al., "TIMER: A web server for comprehensive analysis of tumor-infiltrating immune cells," *Cancer Research*, vol. 77, no. 21, pp. e108–e110, 2017.

[18] B. Li, E. Severson, J. C. Pignon et al., "Comprehensive analyses of tumor immunity: implications for cancer immunotherapy," *Genome Biology*, vol. 17, no. 1, p. 174, 2016.

[19] P. Wang, X. Li, Y. Gao et al., "LncACTdb 2.0: an updated database of experimentally supported ceRNA interactions curated from low- and high-throughput experiments," *Nucleic Acids Research*, vol. 47, no. D1, pp. D121–D127, 2019.

[20] J. Gao, B. A. Aksoy, U. Dogrusoz et al., "Integrative Analysis of Complex Cancer Genomics and Clinical Profiles Using the cBioPortal," *Science Signaling*, vol. 6, no. 269, p. pl1, 2013.

[21] E. Cerami, J. Gao, U. Dogrusoz et al., "The cBio cancer genomics portal: an open platform for exploring multidimensional cancer genomics data," *Cancer Discovery*, vol. 2, no. 5, pp. 401–404, 2012.

[22] N. Razumilava and G. J. Gores, "Cholangiocarcinoma," *The Lancet*, vol. 383, no. 9935, pp. 2168–2179, 2014.

[23] E. Loeuillard, J. Yang, E. Buckarma et al., "Targeting tumor-associated macrophages and granulocytic myeloid-derived suppressor cells augments PD-1 blockade in cholangiocarcinoma," *The Journal of Clinical Investigation*, vol. 130, no. 10, pp. 5380–5396, 2020.

[24] X. Tan, S. Sivakumar, J. Bednarsch et al., "Nerve fibers in the tumor microenvironment in neurotropic cancer–pancreatic cancer and cholangiocarcinoma," *Oncogene*, vol. 40, no. 5, pp. 899–908, 2021.

[25] L. Fabris, M. J. Perugorria, J. Mertens et al., "The tumour microenvironment and immune milieu of cholangiocarcinoma," *Liver International*, vol. 39, pp. 63–78, 2019.

[26] A. V. G. Fruchtenicht, A. K. Poziomyck, A. M. D. Reis, C. R. Galia, G. B. Kabke, and L. F. Moreira, "Inflammatory and nutritional statuses of patients submitted to resection of gastrointestinal tumors," *Revista do Colégio Brasileiro de Cirurgiões*, vol. 45, no. 2, p. e1614, 2018.

Hindawi
Journal of Oncology
Volume 2022, Article ID 2735251, 16 pages
https://doi.org/10.1155/2022/2735251

Research Article

Identification of Six N7-Methylguanosine-Related miRNA Signatures to Predict the Overall Survival and Immune Landscape of Triple-Negative Breast Cancer through In Silico Analysis

Jing Xu, Xiaoxia Cen, Yu Yao, Suo Zhao, Wei Li, Wei Zhang, and Ming Qiu

Department of General Surgery, Changzheng Hospital, Naval Medical University, Shanghai 200003, China

Correspondence should be addressed to Wei Zhang; zhangwei412@aliyun.com and Ming Qiu; qium127@smmu.edu.cn

Jing Xu, Xiaoxia Cen, and Yu Yao contributed equally to this work.

Received 15 July 2022; Accepted 5 September 2022; Published 26 September 2022

Academic Editor: Muhammad Muddassir Ali

Triple-negative breast cancer (TNBC) is a widely prevalent breast cancer, with a mortality rate of up to 25%. TNBC has a lower survival rate, and the significance of N7-methylguanosine (m7G) modification in TNBC remains unclear. Thus, this study is aimed at investigating m7G-related miRNAs in TNBC patients through in silico analysis. In our research, RNA sequencing and clinical data were obtained from The Cancer Genome Atlas (TCGA) database. The miRNAs targeting typical m7G modification regulators Methyltransferase-like 1 (METTL1) and WD repeat domain 4 (WDR4) were predicted on the TargetScan website. A miRNA risk model was built, and its prognostic value was evaluated by R soft packages. Single-sample gene set enrichment analysis was used to assess immune infiltration, and further expression of immune checkpoints was investigated. As a result, miR-421, miR-5001-3p, miR-4326, miR-1915-3p, miR-3177-5p, and miR-4505 were identified to create the risk model. A nomogram consisting of the stage N and risk model predicted overall survival effectively among TNBC patients. Treg and TIL were shown to be strongly linked to the risk model, and the high-risk group had higher levels of four immune checkpoints expression (CD28, CTLA-4, ICOS, and TNFRSF9). A risk model consisting of m7G-related miRNAs was constructed. The findings of the current study could be used as a prognostic biomarker and can provide a novel immunotherapy insight for TNBC patients.

1. Introduction

Breast cancer has become the first killer threatening women's health recently. Triple-negative breast cancer (TNBC) is considered an independent clinicopathological type, accounting for 15% to 20% of all breast cancers, with a mortality rate of up to 25% [1]. It has the clinical characteristics of early-onset age, large primary tumor size, high pathological grade, strong invasiveness, early recurrence, and metastasis [2–4]. In addition, regardless of tumor stage, TNBC patients have the poorest prognosis of any kind of breast cancer [5]. Therefore, appropriate prognostic strategies for TNBC are considered of vital importance in disease management [6]. A thorough analysis of publicly available genetic data to discover novel and distinctive gene prediction signals might assist patients with prognostic categorization and precise treatment.

N7-methylguanosine (m7G) modification is a type of posttranscriptional regulation base modification, which exists on tRNA, rRNA, and eukaryotic mRNA 5′caps [7–9], and is essential for the biological functions of RNA [10]. Unlike m6A regulators, the studies of m7G modification regulators

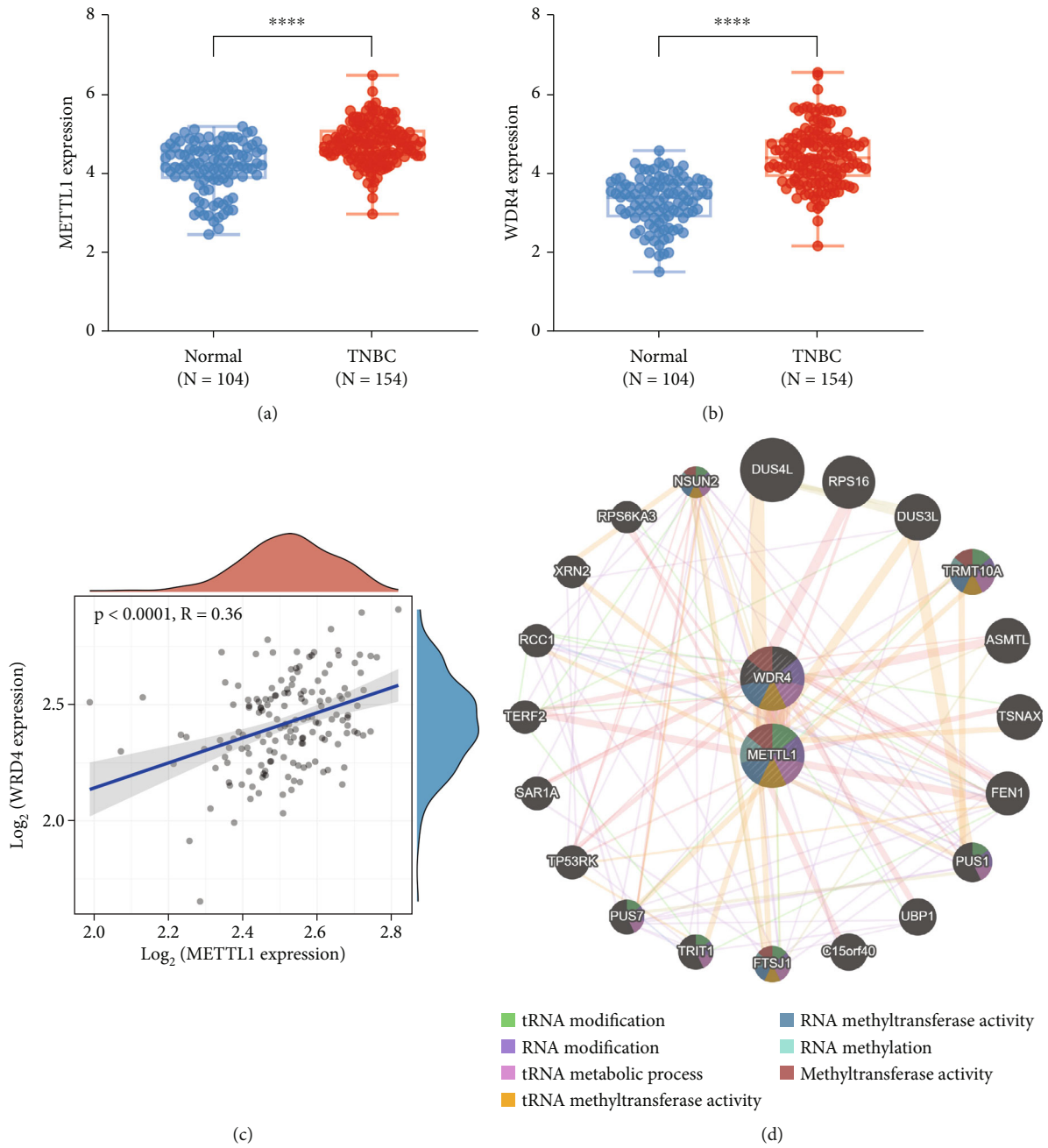

Figure 1: The expression of METTL1 and WDR4 in TNBC patients from TCGA database. (a, b) METTL1 and WDR4 upregulated in TNBC. (c) Correlation between METTL1 and WDR4. (d) Putative METTL1 and WDR4 PPI network.

influencing cancer are limited. Methyltransferase-like 1 (METTL1) and WD repeat domain 4 (WDR4) are the most typical regulators, and they form the methyltransferase complex, where the former is the m7G catalytic enzyme, while the latter stabilizes that complex [11]. Several studies showed that m7G modification was associated with lung cancer, squamous cell carcinoma of the head and neck, acute myeloid leukemia, and esophageal squamous cell carcinoma in tumor proliferation and progression [12–15], which indicated the key impact of METTL1 and WDR4 on m7G modification in tumors. Williams-Beuren syndrome chromosome region 22 (WBSCR22) is also a type of methyltransferases and mediates m7G modification in rRNA [16]. Several studies indicated that WBSCR22 overexpressed in glioma and colon cancer [17, 18], while downregulated in pancreatic cancer [19], similarly affected tumor occurrence and invasion. To our knowledge, only one research has involved regulators of m7G modification in breast cancer. In their study, they discovered that METTL1 was overexpressed in the MCF7 cell line [20]; however, further researches about the influence on tumor biological functions have not been performed.

MicroRNA (miRNA) is a form of RNA molecule found in eukaryotes that is 21 to 23 nucleotides in length. The miRNAs are noncoding RNAs that cannot be translated further

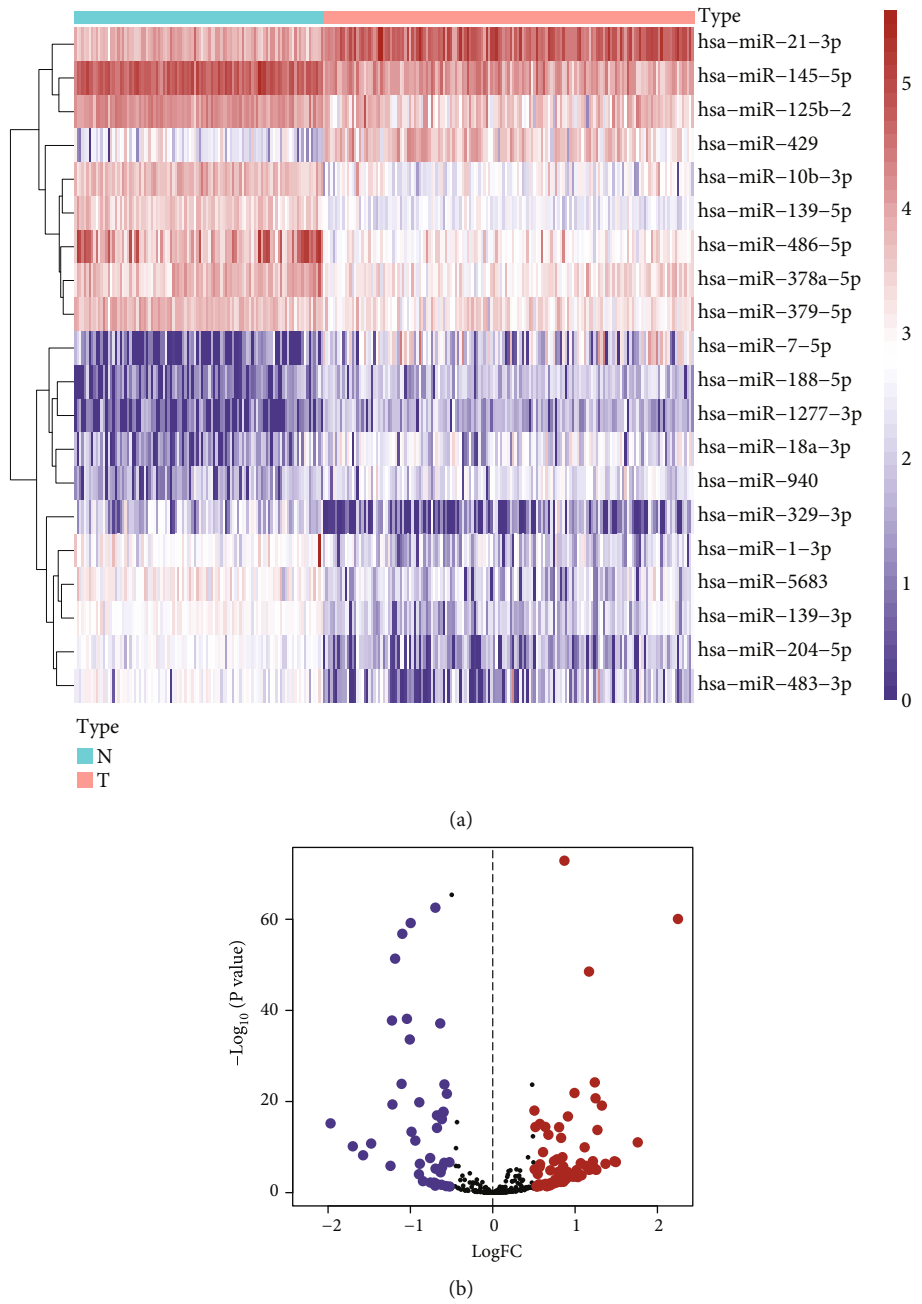

Figure 2: DEmiRNAs targeting METTL1 or WDR4. (a) Heatmap of top 20 DEmiRNAs between normal breast (N) tissues and TNBC (T) tissues. (b) The volcano plot of 126 DEmiRNAs.

Table 1: Six m7G-related miRNAs identified from univariate Cox regression analysis.

miRNA	HR (95% CI)	*p*
miR-421	1.2387 (1.0312, 1.4878)	0.0221
miR-5001-3p	1.3397 (1.0363, 1.7318)	0.0256
miR-4326	1.3298 (1.0145, 1.7432)	0.0390
miR-1915-3p	2.1104 (1.1069, 4.0237)	0.0233
miR-3177-5p	2.2276 (1.0612, 4.6758)	0.0343
miR-4505	5.4048 (1.9407, 15.0528)	0.0012

HR: hazard ratio; CI: confidence interval.

into proteins. They are involved in gene expression, cell proliferation and apoptosis, and fat metabolism [21, 22]. Many miRNAs could promote or inhibit TNBC occurrence and metastasis [23]. Previous studies have revealed that RNA modification, especially N6-methyladenosine (m6A), exists on miRNAs [24]. In addition, the study by Pandolfini et al. demonstrated that METTL1 mediated m7G modification of miRNA and participated in the progression of lung cancer [25]. However, the possible involvement of METTL1/WDR4-related miRNAs in TNBC progression needs further investigation. So, the current study was designed to explore this mechanism.

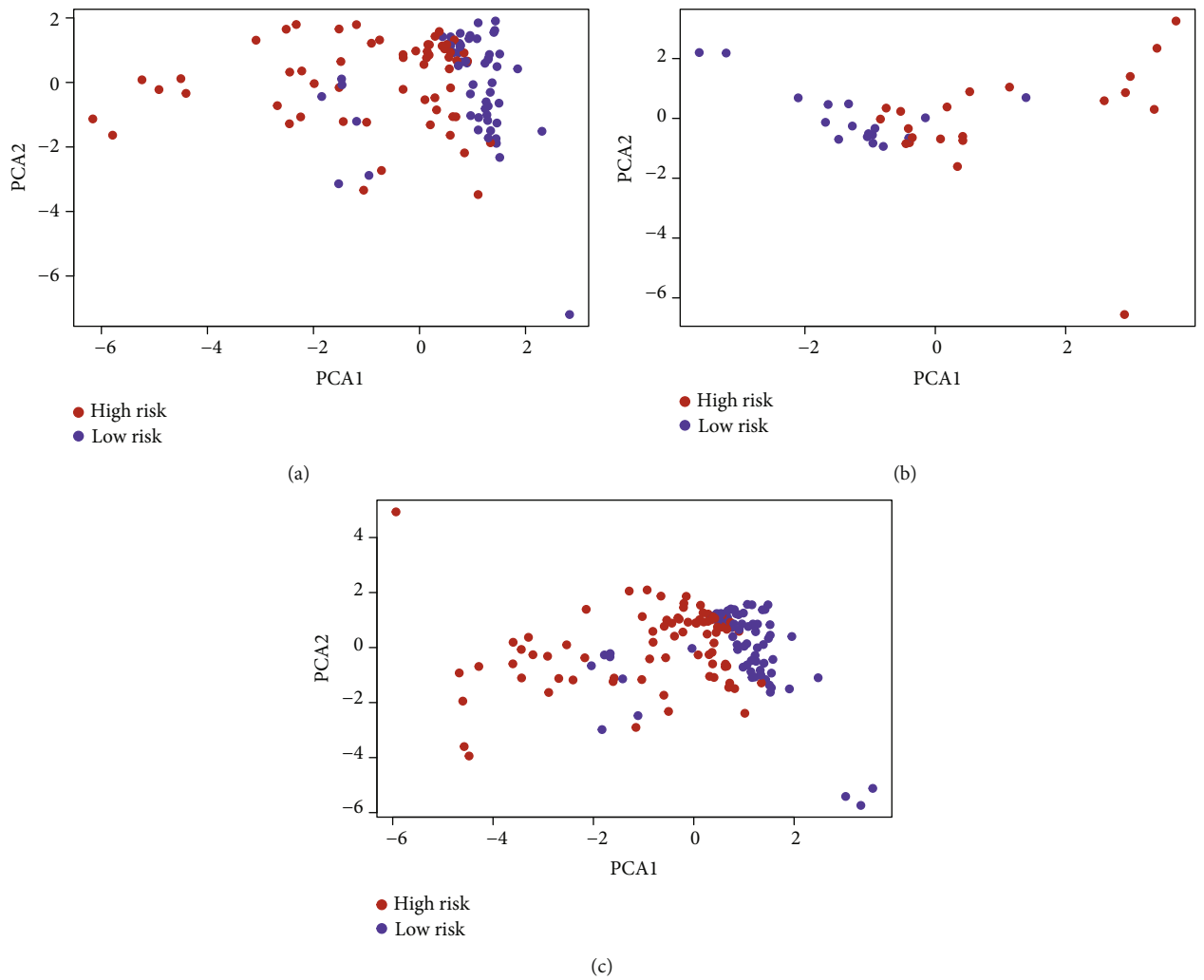

Figure 3: The PCA plots of two groups in the (a) training, (b) testing, and (c) total sets.

2. Materials and Methods

2.1. Data Source. The miRNA and mRNA sequencing data of TNBC were acquired from The Cancer Genome Atlas (TCGA) database (https://portal.gdc.cancer.gov/). The related clinical data were obtained from TCGA and UCSC Xena website (https://xena.ucsc.edu/). TNBC patients with unknown OS information were excluded. Out of those, 104 normal breast tissues and 154 TNBC tumor tissues were included. In addition, based on previous researches, METTL1/WDR4-mediated m7G RNA methylation was demonstrated; thus, the miRNAs targeting METTL1 or WDR4 were predicted from the TargetScan database (http://www.targetscan.org/).

2.2. METTL1/WDR4 Expression and Protein-Protein Interaction Network. To make the gene expression analysis more reliable, the expression data of METTL1 and WDR4 were normalized from counts to TPM. Moreover, the association between METTL1 and WDR4 in TNBC patients was investigated. An assumed protein-protein interaction (PPI) network for METTL1 and WDR4 was created by the online analysis tool GeneMANIA (http://genemania.org/).

2.3. Construction and Validation of m7G-Related miRNA Prognostic Signature. TNBC patients were further divided into training set ($n = 116$) and testing set ($n = 38$) randomly, using the 3 : 1 ratio. The differentially expressed miRNAs (DEmiRNAs) targeting METTL1 or WDR4 were identified between TNBC and normal tissues by the R software package "limma" ($|\log_2 FC| > 0.5$, $p < 0.05$). Firstly, prognostic DEmiRNAs were assessed by univariate Cox regression analysis. miRNAs with $p < 0.05$ were then selected to build a risk model for TNBC patients. The risk score was calculated with the "predict" function in the R software package:

$$\text{Risk score} = h_0(t)e^{\sum_{i=1}^{n} \text{Coef}i \times xi}. \quad (1)$$

To determine the predictive capability of the risk score model, the areas under the receiver operating characteristic (ROC) curve (AUC) were computed by the "timeROC" package. TNBC patients were grouped depending on the risk score median, and then, risk-related survival curves were plotted.

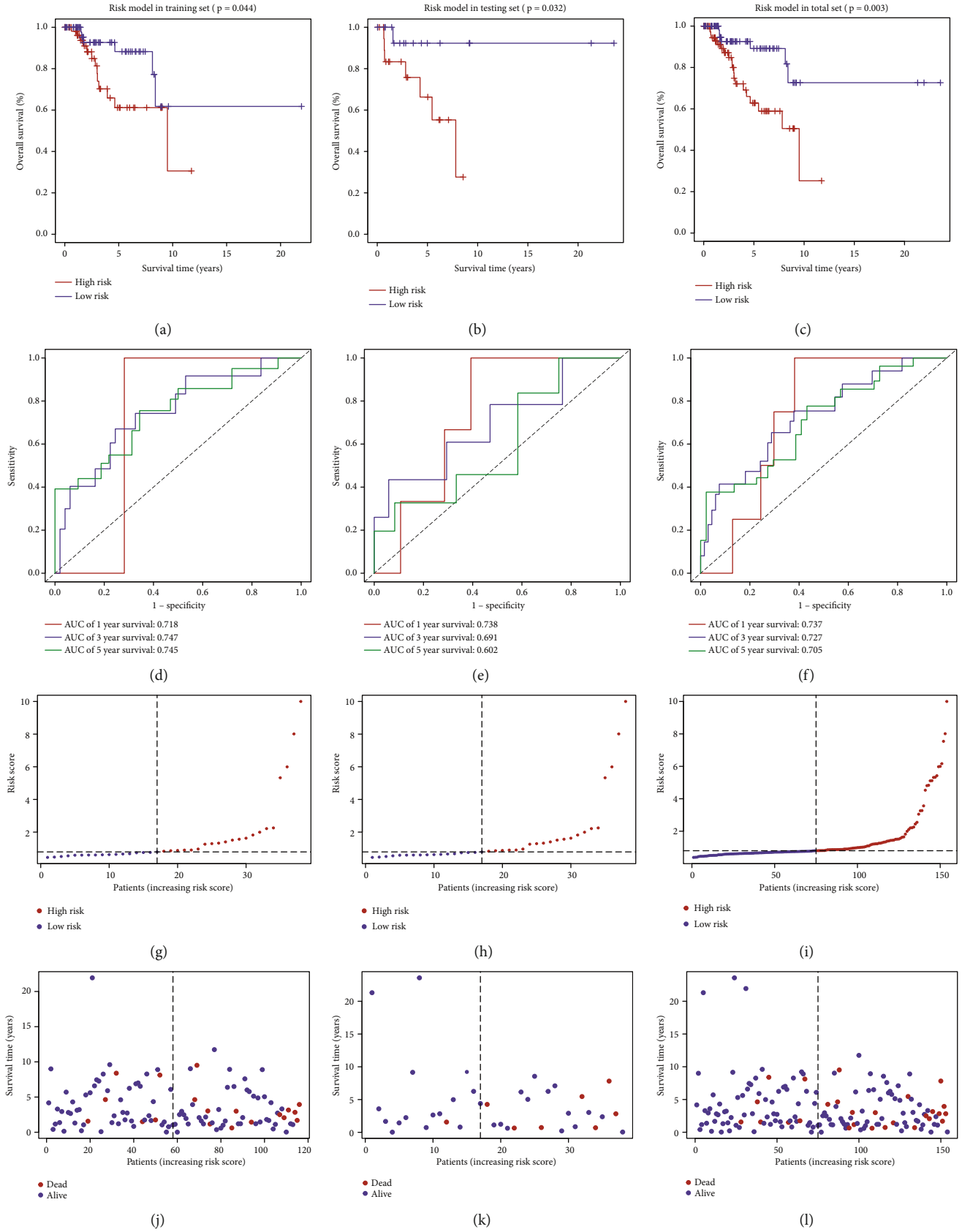

Figure 4: Prognostic value of the risk model in the training, testing, and total sets. (a–c) OS analyses of the risk model. (d–f) ROC curves for TNBC survival rates at 1, 3, and 5 years. (g–i) The distribution of patients' risk scores. (j–l) Survival time and status of patients.

Table 2: Characteristics of TNBC patients.

Clinical characteristic	*N* (154)
Age (years)	54.29 ± 11.71
Stage	
I	28
II	93
III	29
IV	2
Unknown	2
T stage	
T1	39
T2	94
T3	15
T4	5
TX	1
N stage	
N0	96
N1	36
N2	14
N3	8
M stage	
M0	133
M1	2
MX	19

Furthermore, principal component analysis (PCA) was used to estimate the accuracy of grouping. Subsequently, uni- and multivariate Cox regression analyses including clinicopathological factors and the risk score were performed. The final model predicting the OS of TNBC was shown by a visualized nomogram. The concordance index (*C*-index) assessed the final model's discriminant capacity, followed by calibration plots.

2.4. Enrichment Analyses. Gene Ontology (GO) enrichment analysis was carried out to reveal the association of the GO terms and differentially expressed mRNAs (DEmRNAs), which were identified between two groups, with $|\log_2 FC| > 1$ and $p < 0.05$. Kyoto Encyclopedia of Genes and Genomes (KEGG) pathway analysis was performed to reveal the associated signaling pathways. The analyses were performed by "org.Hs.eg.db," "clusterProfiler," and "enrichplot" packages of R.

2.5. Immunological Analysis. Single-sample gene set enrichment analysis (ssGSEA) was used to quantify the immune activity or enrichment levels of 29 immune signatures, including 13 types of immune-associated functions and 16 types of immune cells in each patient. The internal correlation of various immune signatures was investigated using the Pearson coefficient test, and then, the Wilcoxon test was applied to analyze the differences between two groups in immune cells and functions. We then performed correlation analyses between immune cells and METTL1 and WDR4 by the Spearman coefficient test. Finally, immune checkpoint-related genes acquired from prior research were examined for differences in expression between the two groups, in order to anticipate the effect of immune checkpoint blocking treatment.

2.6. Statistical Analysis. R software was used to conduct all analyses and plots (version 4.1.3). To compare the two groups' differences, the Wilcoxon test was used. The statistical significance level was set at $p < 0.05$.

3. Results

3.1. METTL1 and WDR4 Upregulated and Interplayed in TNBC. Both METTL1 and WDR4 were overexpressed in TNBC patients (Figures 1(a) and 1(b)), and their expression correlation was positive ($r = 0.36$, $p < 0.001$) (Figure 1(c)). Furthermore, we imported METTL1 and WDR4 into the GeneMANIA tool for establishing a PPI network. As Figure 1(d) showed, a total of 22 genes and 128 links were contained in the PPI network. These 22 genes were mostly involved in RNA methylation modification and methyltransferase activity.

3.2. Construction and Validation of m7G-Related miRNA Risk Model. A total of 760 miRNAs targeting METTL1 or WDR4 were predicted from the TargetScan website. Among them, 126 DEmiRNAs were identified between 154 TNBC and 104 normal samples, with 84 upregulated and 42 downregulated (Figures 2(a) and 2(b)). Furthermore, six miRNAs related to OS were identified from the DEmiRNAs (miR-421, miR-5001-3p, miR-4326, miR-1915-3p, miR-3177-5p, and miR-4505) using the univariate Cox regression analysis (Table 1). Subsequently, we performed a multivariate Cox analysis including six miRNAs and conducted the risk model in the training set: Risk score = exp (0.06813 × miR-421 + 0.29448 × miR-5001-3p + 0.08756 × miR-4326 + 0.38769 × miR-1915-3p − 0.02726 × miR-3177-5p + 1.65602 × miR-4505 − 0.9681). TNBC patients were categorized into two groups by the risk score median. The risk scores of the testing set and the total sample set were also calculated based on the above formula. The cutoff point of grouping was the same as the training set. PCA results revealed the accuracy in grouping of the risk model (Figures 3(a)–3(c)). The survival curves indicated longer OS among low-risk patients in the three data sets (Figures 4(a)–4(c)). The risk model performed well in predicting OS, as evidenced by ROC curves. The AUCs of 1-, 3-, and 5-year OS in the training, testing, and total sets were 0.718, 0.747, and 0.745, 0.738, 0.691, and 0.602 and 0.737, 0.727, and 0.705, respectively (Figures 4(d)–4(f)). Figures 4(g)–4(l) depicted the patients' risk score distribution and their survival status in three data sets.

3.3. Independent Prognostic Factors of Final Model. The clinical characteristics of 154 TNBC patients were illustrated in Table 2. The risk model was combined with age and clinicopathological factors for uni- and multivariate Cox regression analyses. The univariate analysis showed that pathologic stage ($p < 0.0001$), stage T ($p = 0.001$), stage N ($p < 0.0001$), stage M ($p = 0.0025$), and risk score ($p < 0.0001$) were related to the OS of TNBC patients (Figure 5(a)). However, only stage N ($p < 0.001$) and the risk score ($p = 0.0184$) were

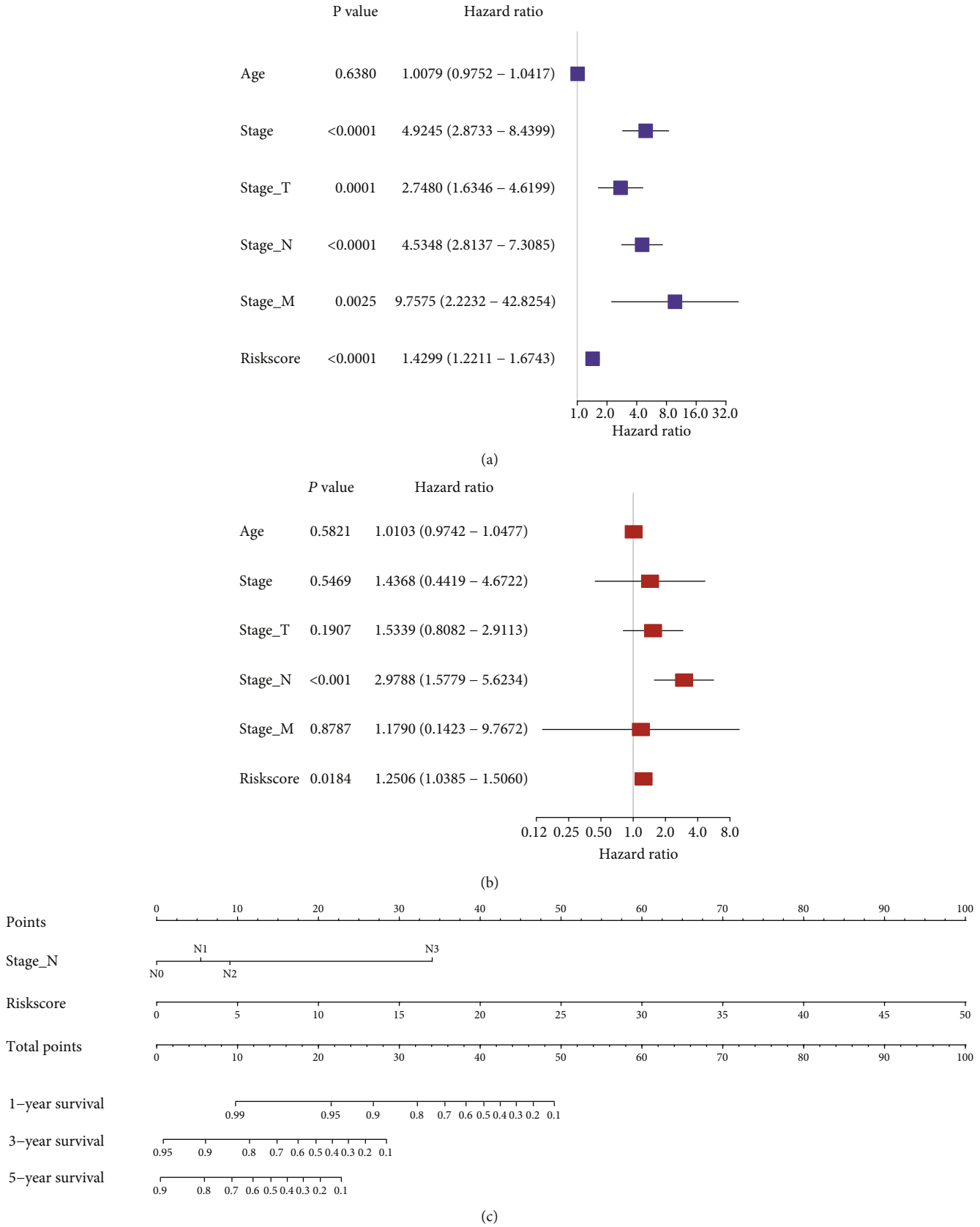

Figure 5: Nomogram construction of the prognostic model. (a, b) Cox regression analysis with the risk score and clinicopathological covariates. (c) The nomogram of prediction model.

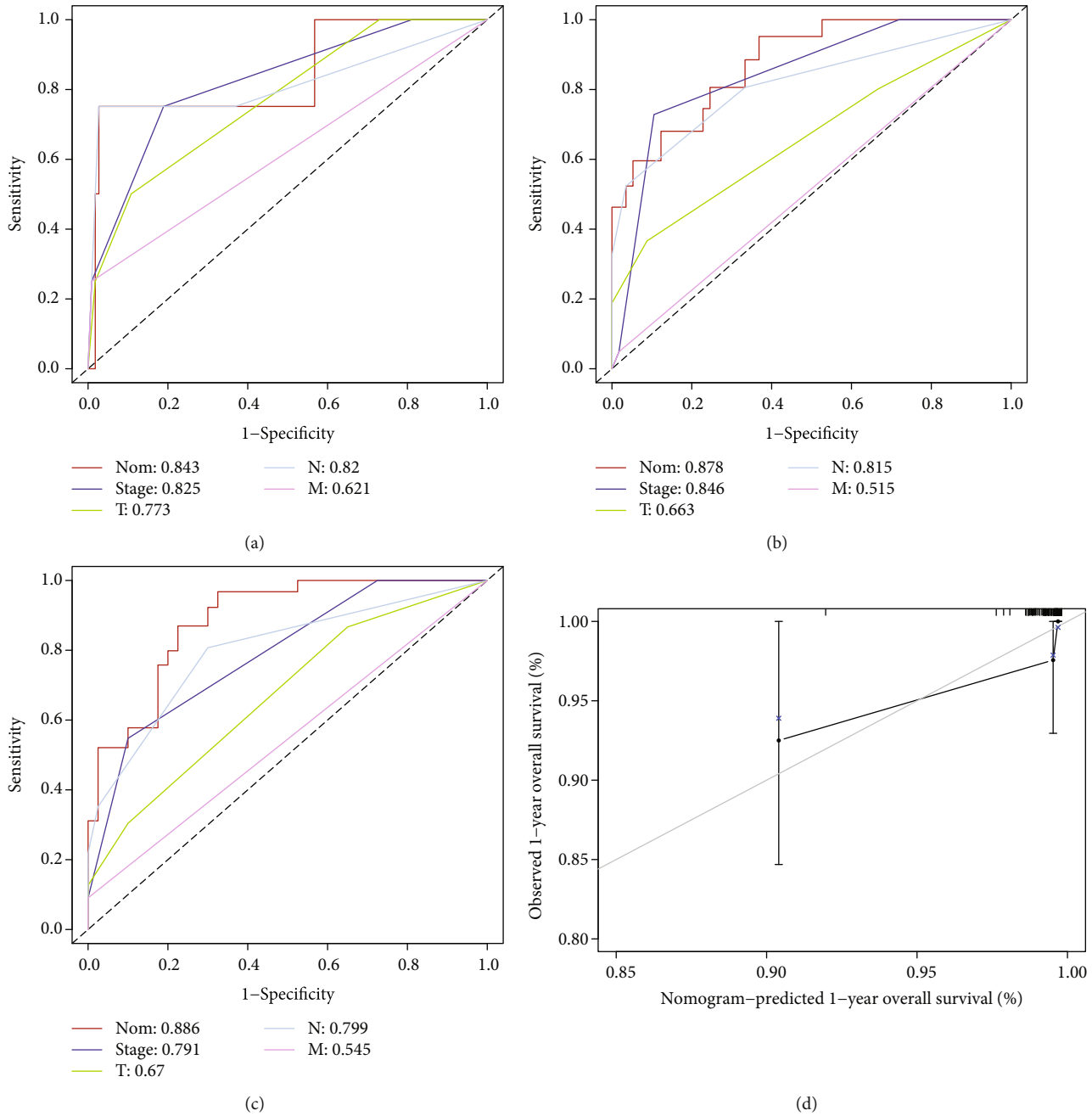

Figure 6: Continued.

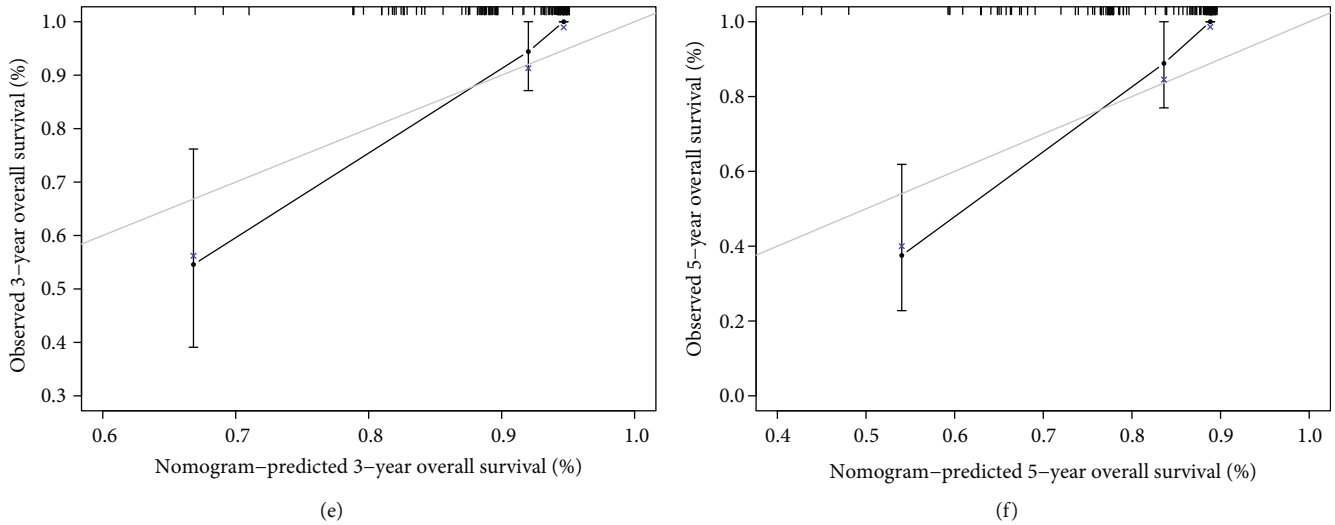

Figure 6: Assessment of the prognostic model. (a–c) ROC curves for 1-, 3-, and 5-year OS rate of nomogram and clinicopathological factors. (d–f) Nomogram calibration curves for 1-, 3-, and 5-year OS prediction.

retained as independent factors for OS after the multivariate Cox analysis (Figure 5(b)).

3.4. Prognostic Model Construction and Detection. A nomogram was created for predicting visually, including the stage N and risk score, and the overall scores could predict the likelihood of overall survival for TNBC patients (Figure 5(c)). The nomogram model's *C*-index was found to be 0.868, which indicated the excellent discriminant performance of the final model. Moreover, 1-, 3-, and 5-year AUCs were 0.843, 0.878, and 0.886, respectively, which were all better than clinicopathological characteristics in predictive ability (Figures 6(a)–6(c)). The calibration curve demonstrated good discrimination of the nomogram model (Figures 6(d)–6(f)). In general, the nomogram model accurately predicted the OS of TNBC patients.

3.5. Enrichment Analyses. Analyses of 658 DEmRNAs using GO and KEGG were carried out (Figure 7). GO analysis identified 97 biological processes (BP), 42 molecular functions (MF), and 24 cellular components (CC). Under BP, significant enrichments were observed in keratinization, epidermis development, and skin development. For CC, DEmRNAs were enriched in synaptic membrane, postsynaptic membrane, and cornified envelope. The MF involved in receptor ligand activity, channel activity, and signaling receptor activator activity. In addition, KEGG analysis revealed 8 related pathways and the results showed that the DEmRNAs were mostly enriched in drug metabolism-cytochrome P450 and neuroactive ligand-receptor interaction.

3.6. Relationship between the Risk Model and Immune Signatures. Since the treatment of TNBC patients is limited and could only benefit from chemotherapy, immunotherapy may provide new treatment strategies for TNBC patients. Thus, we performed immunological analyses related to our risk model. We used ssGSEA to calculate the enrichment scores for the immune activity or enrichment level in each sample (Figure 8(a)). The correlation analysis of immune cells revealed that pDCs were positively and strongly correlated with TIL ($r = 0.91$), while the correlations of immune-related functions were all positive, where the T cell coinhibition and checkpoint were found to have the strongest correlation ($r = 0.98$) (Figures 8(b) and 8(c)). The box plot revealed the differences in the immune cells, of which Treg, TIL, Th1 cells, and T helper cells were upregulated in high-risk patients. Similarly, the immune functions, of which T cell costimulation/inhibition, MHC class I, checkpoint, and APC costimulation, were also upregulated (Figures 8(d) and 8(e)). Thus, the m7G-related miRNAs risk model is envisaged to have a potential role in predicting the immune response. Furthermore, the connection between immune cells and METTL1 and WDR4 was investigated using the Spearman coefficient test. It was discovered that Treg, TIL, T helper cells, neutrophils, mast cells, macrophages, and B cells were negatively correlated with METTL1 and WDR4 (Figure 8(f)). The intersection of different immune cells and m7G-related immune cells was taken to obtain the significant m7G-related immune cells (Treg and TIL). In addition, the high-risk group had higher levels of CD28, CTLA-4, ICOS, and TNFRSF9 ($p < 0.01$), indicating that these four immune checkpoints may be potential targets of immune therapy for TNBC patients at high risk (Figure 9).

4. Discussion

Unlike ER, PR, or Her-2 positive breast cancer, the treatment strategies for TNBC patients are limited [26]. Thus, identifying novel biomarkers could provide novel methods for TNBC patients. In total, 154 TNBC patients were obtained in this study to assess the prognostic role of m7G-related miRNAs. The patients were grouped depending on the risk score median, where high-risk patients were found to have a shorter OS. A multivariate Cox regression analysis was performed combining

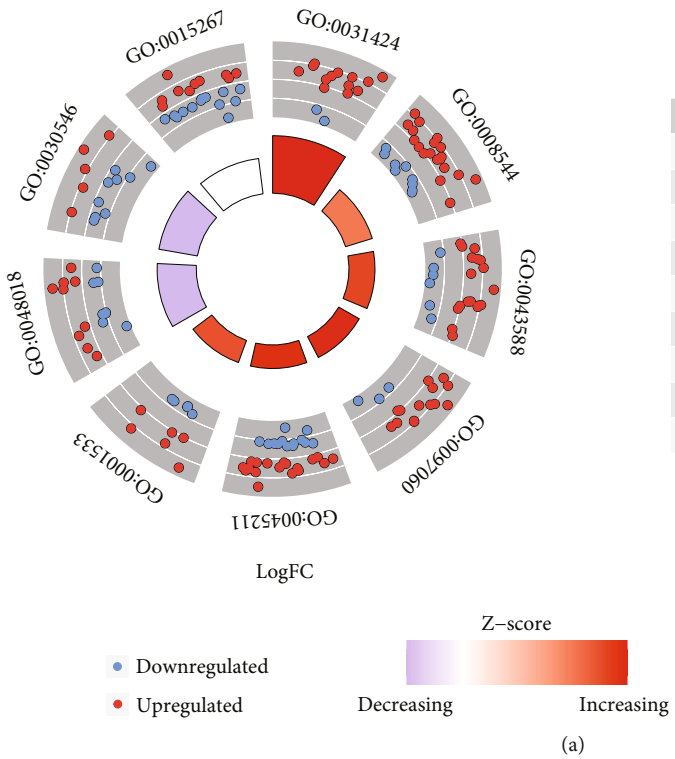

ID	Description
GO:0031424	Keratinization
GO:0008544	Epidermis development
GO:0043588	Skin development
GO:0097060	Synaptic membrane
GO:0045211	Postsynaptic membrane
GO:0001533	Cornified envelope
GO:0048018	Receptor ligand activity
GO:0030546	Signaling receptor activator activity
GO:0015267	Channel activity

(a)

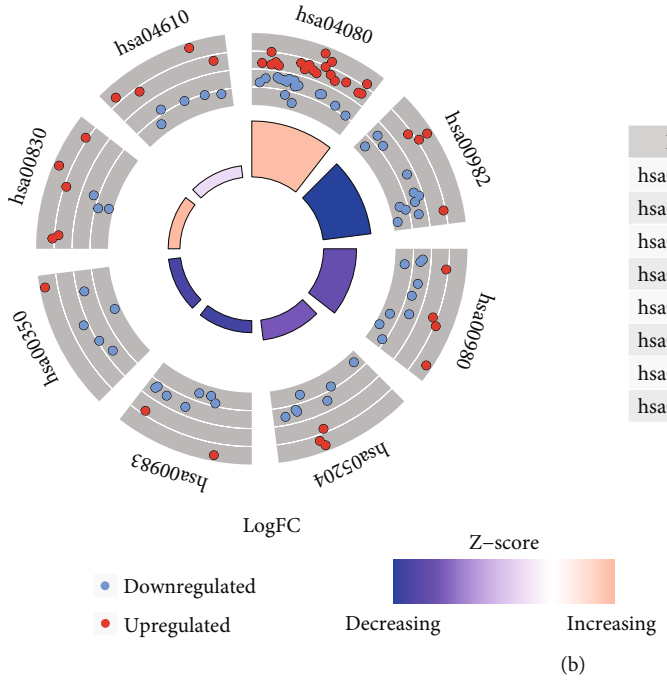

ID	Description
hsa04080	Neuroactive ligand–receptor interaction
hsa00982	Drug metabolism – cytochrome P450
hsa00980	Metabolism of xenobiotics by cytochrome P450
hsa05204	Chemical carcinogenesis – DNA adducts
hsa00983	Drug metabolism – other enzymes
hsa00350	Tyrosine metabolism
hsa00830	Retinol metabolism
hsa04610	Complement and coagulation cascades

(b)

Figure 7: Functional enrichment for DEmRNAs between two groups. (a) GO analysis. (b) KEGG pathway analysis.

clinicopathological parameters and the risk score, revealing the independent prognostic effect of the risk model on OS.

Several researches have suggested that m7G modification may have an essential role in carcinogenesis, but how it functions in regulating miRNAs during TNBC remains unknown. Only one research by Pandolfini et al. has successfully detected internal m7G mediated by METTL1 in miRNAs, demonstrating that m7G not only exists on tRNAs, rRNAs, and mRNAs but also on miRNAs. Their study found that m7G modifications showed features different from the m6A and 5′-methyl phosphate features. The m7G affected the pri-miRNAs' secondary structure to promote miRNAs processing and suppress cell migration [25]. miRNA m7G modification mediated by METTL1 promotes lung cancer occurrence and inhibits cancer metastasis; however, the researchers did not rule out the effect of METTL1 on mRNA.

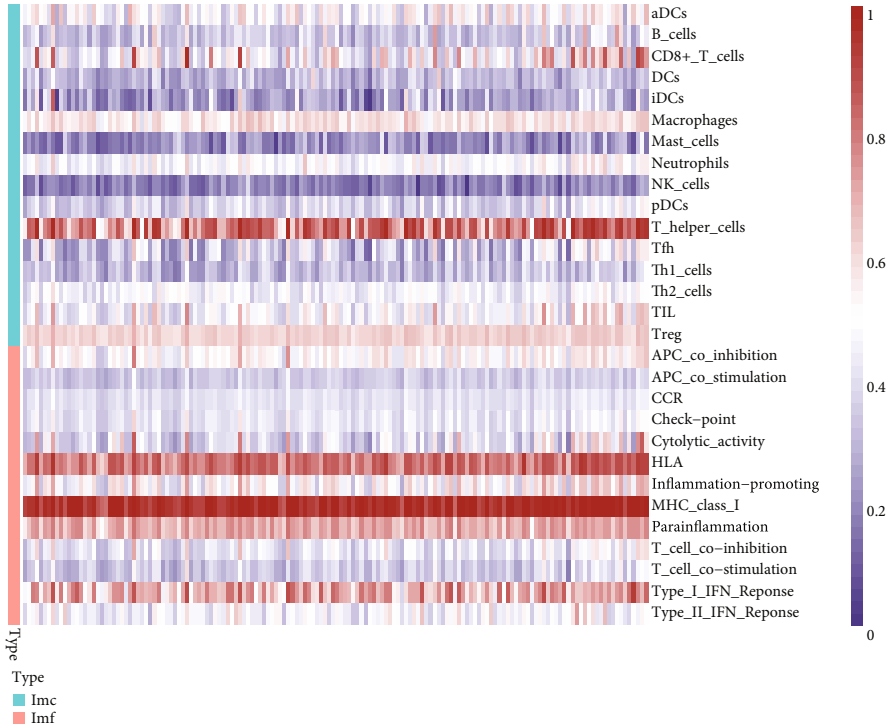

(a)

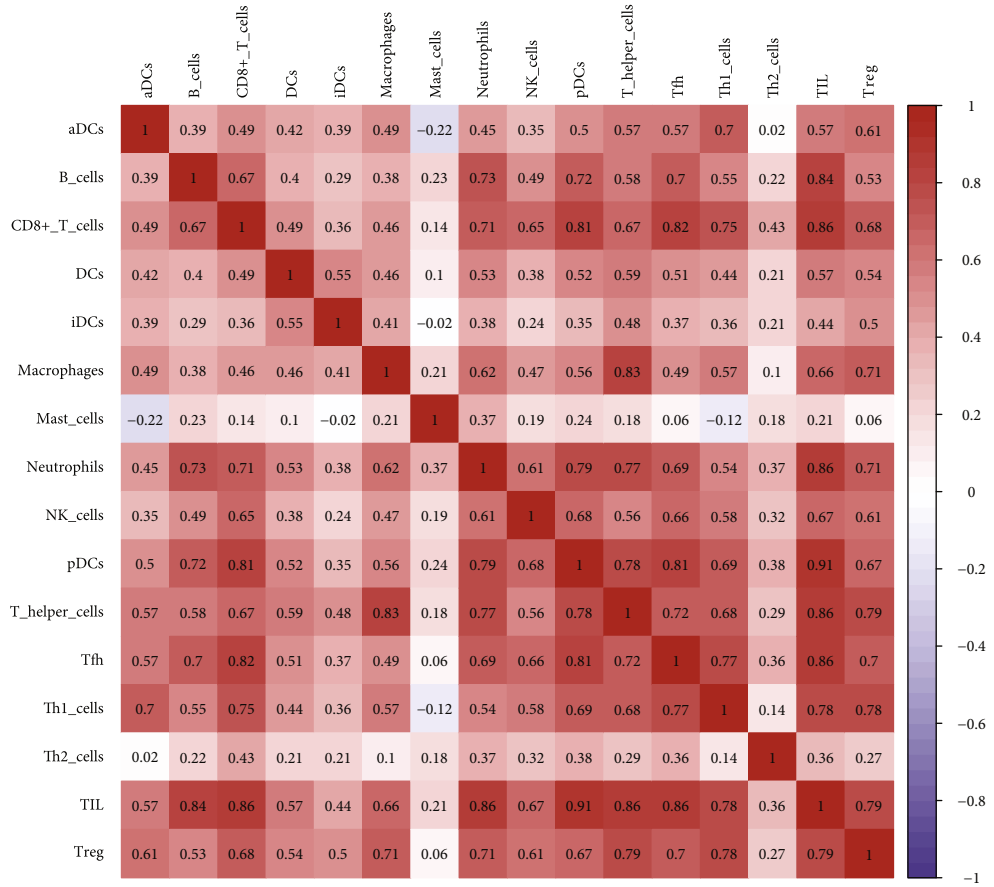

(b)

Figure 8: Continued.

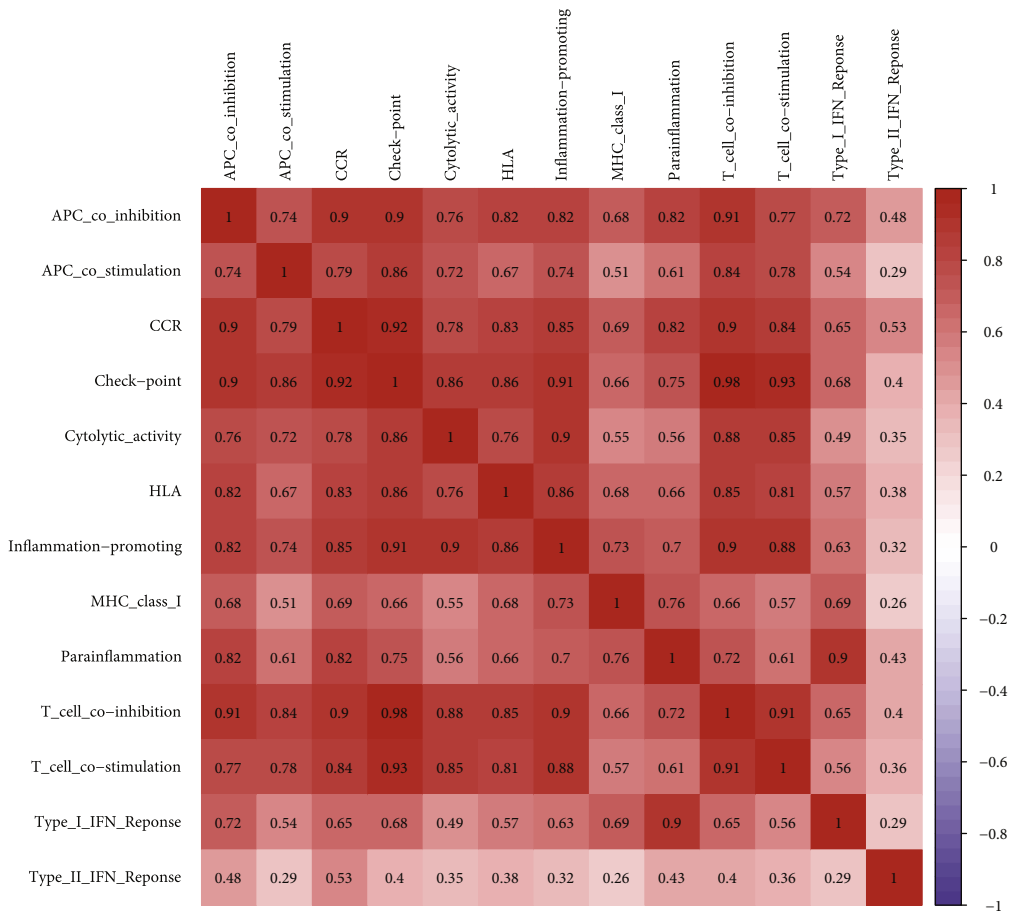

(c)

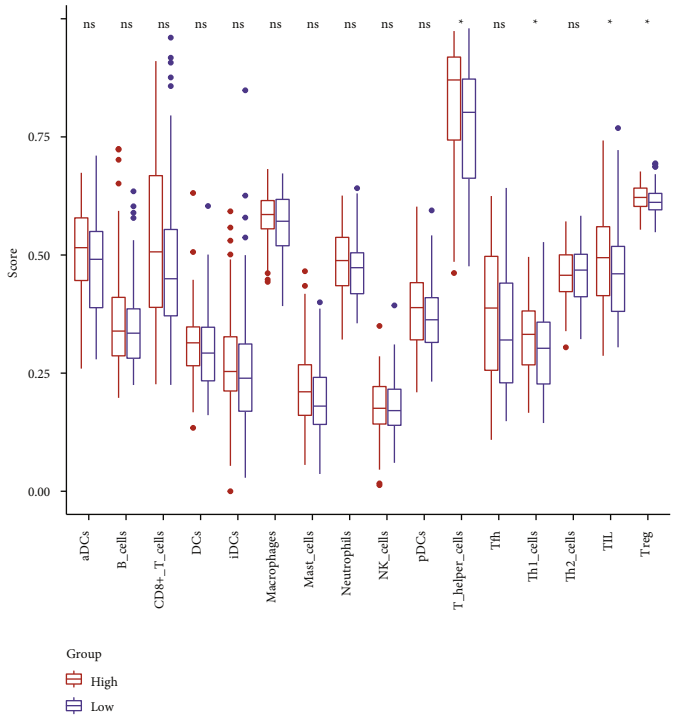

(d)

Figure 8: Continued.

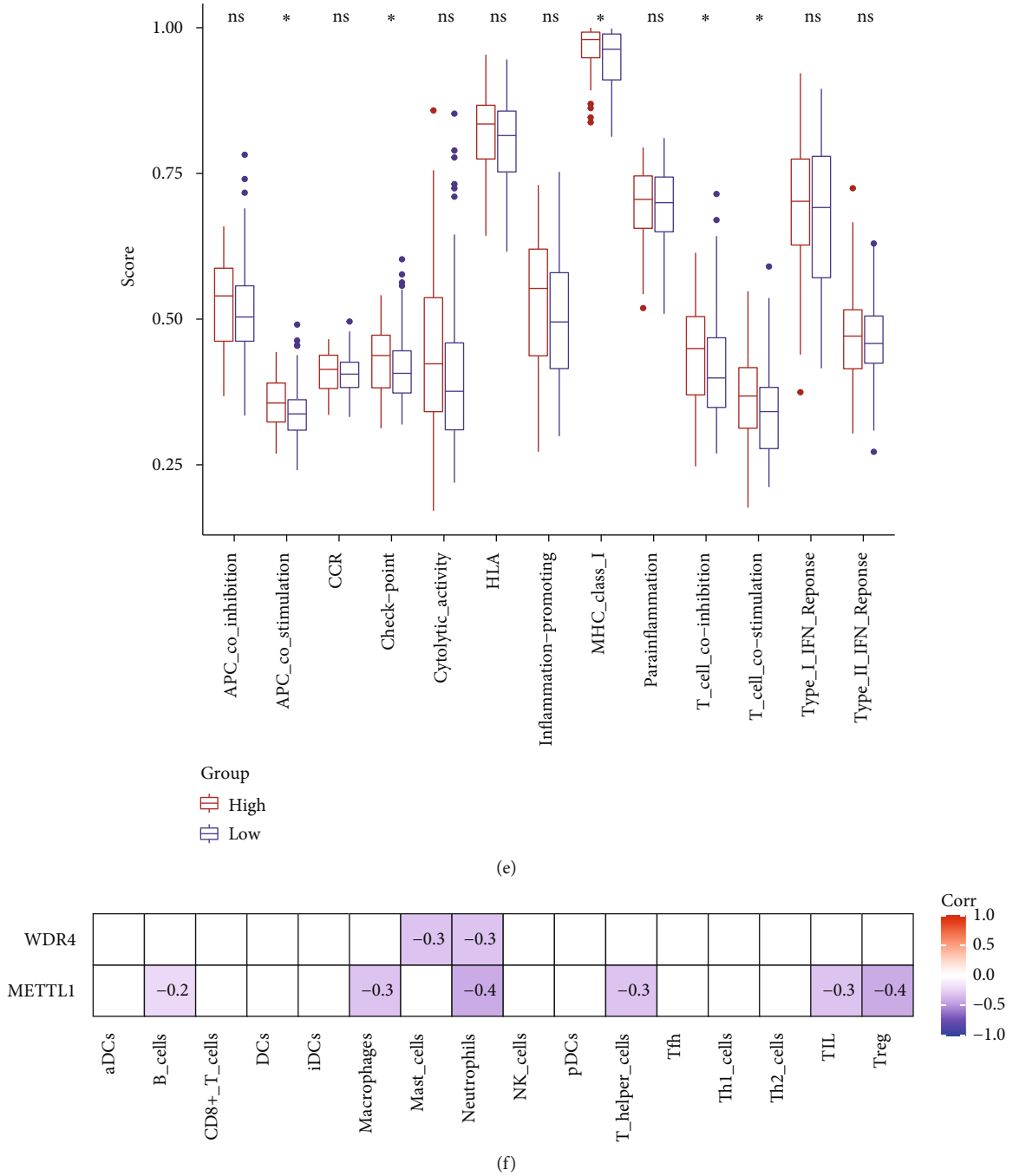

Figure 8: Immunological analyses. (a) Enrichment scores of 29 immune signatures in each patient calculated by ssGSEA. (b, c) Correlation between immune signatures. (d, e) Comparison between two groups in immune signatures. (f) Correlation between immune cells and METTL1 and WDR4.

Internal m7G in miRNAs have been detected by another study and they revealed that m7G in miRNAs remained to be shown [27]. In the current study, it was assumed that miRNAs may participate in m7G modification by regulating their target genes (m7G modification regulators METTL1 and WDR4). Thus, the interaction of m7G modification and miRNAs needs further research. The m7G modification might be a new function regulator of miRNA and could help find new therapeutic strategies in cancer.

Additionally, six m7G-related prognostic miRNAs from 154 TNBC patients were identified. miR-421 upregulates in cancer [28, 29], and it can promote disease progression and shorten OS [30–32]. miR-4326 has a proliferative effect in lung cancer and activates the Wnt pathway [33]. miR-1915-3p has been demonstrated as a feasible biomarker for liver cancer, immune diseases, and gastric and thyroid cancer [34–37]. A few miRNAs have been associated with tumor progression. However, few reports have been published

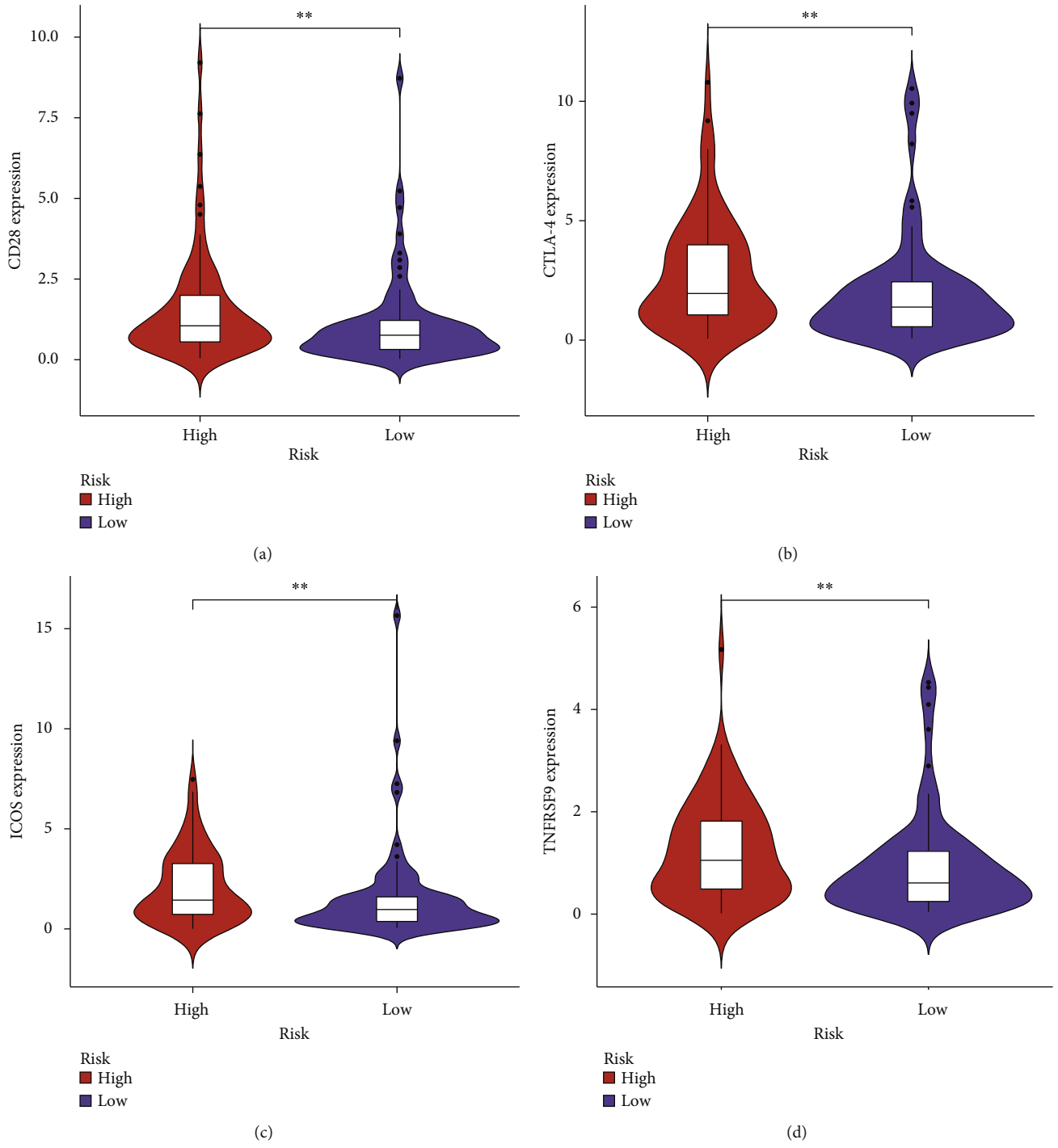

Figure 9: Immune checkpoints expression between the high- and low-risk groups ($p < 0.01$).

regarding TNBC, and reports on the correlation between miRNAs and m7G-related genes have been even rarer. Thus, this study may help identify the prognostic miRNAs that target m7G modifications to contribute ideas of potential value in TNBC occurrence and progress.

In the last part of our study, we found two immune cells, TIL and Treg, were closely associated with the m7G-related miRNAs risk model. TIL and Treg were upregulated in high-risk patients, while they were negatively correlated with m7G regulators METTL1 and WDR4. Treg cells can inhibit anticancer immunity and block the effective antitumor immune response of tumor hosts; thus, they accelerate the occurrence and development of tumors [38]. And immune checkpoint inhibitors (ICIs) mainly affect Treg cells, for example, ICIs targeting programmed cell death 1 could strengthen the ability of Treg cells for immunosuppression, which is the reason for the unsatisfactory efficacy of ICIs on TNBC patients. However, Treg cells could be depleted

by CTLA-4 inhibitors [39]. In this study, high-risk patients had a higher level of Treg cell infiltration and CTLA-4 expression, so CTLA-4 inhibitors may treat high-risk TNBC patients effectively. Among early TNBC patients receiving adjuvant chemotherapy, the increase of TIL level meant a prognosis improvement [40]. Another research about neoadjuvant therapy of TNBC revealed that patients with high TIL level meant high pathological complete response so that the patients could obtain a better prognosis [41]. The high-risk patients had a higher level of TIL in our study, which meant our risk model may not only predict the OS but also predict the response of adjuvant therapy for TNBC patients. For high-risk patients, their poor prognosis could be improved after regular therapies. In recent years, TIL therapy has been increasingly used in the treatment of cancers. Like CAR-T therapy, TIL therapy is also a form of adoptive immunotherapy. TILs are derived from tumor tissues and could naturally target patients' tumor-specific antigens, while other cellular immunotherapies are mostly derived from blood, which reduces the ability to recognize tumors. Six patients with metastatic breast cancer were adopted TIL therapy in a Phase II Pilot Clinical Trial, half of whom experienced measurable tumor shrinkage [42]. Further researches for TIL immunotherapy in TNBC patients are needed, which could bring hope to cancer patients. Overall, high-risk patients may benefit from CTLA-4 inhibitors and TIL therapy. However, further understanding of the m7G-related miRNAs and immune activity is needed to improve the immunotherapy strategies for TNBC patients.

Nevertheless, the limitations of our study are that we were unable to gather our own data to validate the model. In addition, further verified experiments on the expression, function, and mechanism of action of these miRNAs are needed.

5. Conclusion

Genomics and clinical data from the public database using bioinformatics and medical statistical analysis were gathered. Six m7G-related prognostic miRNAs and established prognostic risk signature for TNBC patients were identified. Findings of the current study will give an insight towards the role of miRNA m7G modification mechanisms in TNBC. Moreover, this will also help in the early diagnosis of this cancer.

Data Availability

The data used to support the findings of this study are included within the article.

Conflicts of Interest

The authors declare that they have no competing interest.

Authors' Contributions

Wei Zhang and Ming Qiu designed and supervised the study. Jing Xu performed data collection and original manuscript writing. Xiaoxia Cen and Yu Yao contributed to the manuscript revision and data interpretation. Suo Zhao and Wei Li provided the help of R software. Jing Xu, Xiaoxia Cen, and Yu Yao contributed equally to this work.

Acknowledgments

This study was supported by the National Natural Science Foundation of China (No. 81370984).

References

[1] F. Rastelli, S. Biancanelli, A. Falzetta et al., "Triple-negative breast cancer: current state of the art," *Tumori*, vol. 96, no. 6, pp. 875–888, 2010.

[2] B. D. Lehmann, J. A. Bauer, X. Chen et al., "Identification of human triple-negative breast cancer subtypes and preclinical models for selection of targeted therapies," *The Journal of Clinical Investigation*, vol. 121, no. 7, pp. 2750–2767, 2011.

[3] G. Bianchini, J. M. Balko, I. A. Mayer, M. E. Sanders, and L. Gianni, "Triple-negative breast cancer: challenges and opportunities of a heterogeneous disease," *Nature Reviews Clinical Oncology*, vol. 13, no. 11, pp. 674–690, 2016.

[4] Z. Sporikova, V. Koudelakova, R. Trojanec, and M. Hajduch, "Genetic markers in triple-negative breast cancer," *Clinical Breast Cancer*, vol. 18, no. 5, pp. e841–e850, 2018.

[5] R. Dent, M. Trudeau, K. I. Pritchard et al., "Triple-negative breast cancer: clinical features and patterns of recurrence," *Clinical Cancer Research*, vol. 13, no. 15, pp. 4429–4434, 2007.

[6] C. Bao, Y. Lu, J. Chen et al., "Exploring specific prognostic biomarkers in triple-negative breast cancer," *Cell Death & Disease*, vol. 10, no. 11, p. 807, 2019.

[7] A. J. Shatkin, "Capping of eucaryotic mRNAs," *Cell*, vol. 9, no. 4, pp. 645–653, 1976.

[8] C. Tomikawa, "7-Methylguanosine modifications in transfer RNA (tRNA)," *International Journal of Molecular Sciences*, vol. 19, no. 12, p. 4080, 2018.

[9] C. Enroth, L. D. Poulsen, S. Iversen, F. Kirpekar, A. Albrechtsen, and J. Vinther, "Detection of internal N7-methylguanosine (m7G) RNA modifications by mutational profiling sequencing," *Nucleic Acids Research*, vol. 47, no. 20, article e126, 2019.

[10] K. Shimotohno, Y. Kodama, J. Hashimoto, and K. I. Miura, "Importance of 5'-terminal blocking structure to stabilize mRNA in eukaryotic protein synthesis," *Proceedings of the National Academy of Sciences of the United States of America*, vol. 74, no. 7, pp. 2734–2738, 1977.

[11] A. Alexandrov, M. R. Martzen, and E. M. Phizicky, "Two proteins that form a complex are required for 7-methylguanosine modification of yeast tRNA," *RNA*, vol. 8, no. 10, pp. 1253–1266, 2002.

[12] Z. Dai, H. Liu, J. Liao et al., "N^7-Methylguanosine tRNA modification enhances oncogenic mRNA translation and promotes intrahepatic cholangiocarcinoma progression," *Molecular Cell*, vol. 81, no. 16, pp. 3339–3355.e8, 2021.

[13] H. Han, C. Yang, J. Ma et al., "N^7-methylguanosine tRNA modification promotes esophageal squamous cell carcinoma tumorigenesis via the RPTOR/ULK1/autophagy axis," *Nature Communications*, vol. 13, no. 1, 2022.

[14] J. Chen, K. Li, J. Chen et al., "Aberrant translation regulated by METTL1/WDR4-mediated tRNA N7-methylguanosine

modification drives head and neck squamous cell carcinoma progression," *Cancer Communications*, vol. 42, no. 3, pp. 223–244, 2022.

[15] E. A. Orellana, Q. Liu, E. Yankova et al., "METTL1-mediated m^7G modification of Arg-TCT tRNA drives oncogenic transformation," *Molecular Cell*, vol. 81, no. 16, pp. 3323–3338.e14, 2021.

[16] S. Haag, J. Kretschmer, and M. T. Bohnsack, "WBSCR22/Merm1 is required for late nuclear pre-ribosomal RNA processing and mediates N7-methylation of G1639 in human 18S rRNA," *RNA*, vol. 21, no. 2, pp. 180–187, 2015.

[17] Y. Chi, Z. Liang, Y. Guo et al., "WBSCR22 confers cell survival and predicts poor prognosis in glioma," *Brain Research Bulletin*, vol. 161, pp. 1–12, 2020.

[18] D. Yan, L. Tu, H. Yuan et al., "*WBSCR22* confers oxaliplatin resistance in human colorectal cancer," *Scientific Reports*, vol. 7, no. 1, article 15443, 2017.

[19] A. A. Khan, H. Huang, Y. Zhao et al., "WBSCR22 and TRMT112 synergistically suppress cell proliferation, invasion and tumorigenesis in pancreatic cancer via transcriptional regulation of ISG15," *International Journal of Oncology*, vol. 60, no. 3, 2022.

[20] I. J. Campeanu, Y. Jiang, L. Liu et al., "Multi-omics integration of methyltransferase-like protein family reveals clinical outcomes and functional signatures in human cancer," *Scientific Reports*, vol. 11, no. 1, article 14784, 2021.

[21] J. Krol, I. Loedige, and W. Filipowicz, "The widespread regulation of microRNA biogenesis, function and decay," *Nature Reviews Genetics*, vol. 11, no. 9, pp. 597–610, 2010.

[22] T. G. McDaneld, "MicroRNA: mechanism of gene regulation and application to livestock1," *Journal of Animal Science*, vol. 87, Supplement 14, pp. E21–E28, 2009.

[23] H. Sabit, E. Cevik, H. Tombuloglu, S. Abdel-Ghany, G. Tombuloglu, and M. Esteller, "Triple negative breast cancer in the era of miRNA," *Critical Reviews in Oncology/Hematology*, vol. 157, article 103196, 2021.

[24] H. Huang, H. Weng, and J. Chen, "The biogenesis and precise control of RNA m^6A methylation," *Trends in Genetics*, vol. 36, no. 1, pp. 44–52, 2020.

[25] L. Pandolfini, I. Barbieri, A. J. Bannister et al., "METTL1 Promotes *let-7* MicroRNA Processing via m7G Methylation," *Molecular Cell*, vol. 74, no. 6, pp. 1278–1290.e9, 2019.

[26] L. Yin, J. J. Duan, X. W. Bian, and S. C. Yu, "Triple-negative breast cancer molecular subtyping and treatment progress," *Breast Cancer Research*, vol. 22, no. 1, p. 61, 2020.

[27] J. Vinther, "No evidence for *N*7 -methylation of guanosine (m^7G) in human let-7e," *Molecular Cell*, vol. 79, no. 2, pp. 199-200, 2020.

[28] S. Zhou, B. Wang, J. Hu et al., "miR-421 is a diagnostic and prognostic marker in patients with osteosarcoma," *Tumour Biology*, vol. 37, no. 7, pp. 9001–9007, 2016.

[29] A. Shopit, X. Li, Z. Tang et al., "miR-421 up-regulation by the oleanolic acid derivative K73-03 regulates epigenetically SPINK1 transcription in pancreatic cancer cells leading to metabolic changes and enhanced apoptosis," *Pharmacological Research*, vol. 161, article 105130, 2020.

[30] Z. Ren, M. He, T. Shen et al., "miR-421 promotes the development of osteosarcoma by regulating MCPIP1 expression," *Cancer Biology & Therapy*, vol. 21, no. 3, pp. 231–240, 2020.

[31] R. Li, T. Wan, J. Qu, Y. Yu, and R. Zheng, "Long non-coding RNA DLEUI promotes papillary thyroid carcinoma progression by sponging miR-421 and increasing ROCK1 expression," *Aging*, vol. 12, no. 20, pp. 20127–20138, 2020.

[32] W. Xiao, S. Zheng, Y. Zou et al., "CircAHNAK1 inhibits proliferation and metastasis of triple-negative breast cancer by modulating miR-421 and RASA1," *Aging*, vol. 11, no. 24, pp. 12043–12056, 2019.

[33] G. Xu, Z. Zhang, L. Zhang et al., "miR-4326 promotes lung cancer cell proliferation through targeting tumor suppressor APC2," *Molecular and Cellular Biochemistry*, vol. 443, no. 1-2, pp. 151–157, 2018.

[34] H. W. Cui, W. Y. Han, L. N. Hou, L. Yang, X. Li, and X. L. Su, "miR-1915-3p inhibits Bcl-2 expression in the development of gastric cancer," *Bioscience Reports*, vol. 39, no. 5, 2019.

[35] N. Borrelli, M. Denaro, C. Ugolini et al., "miRNA expression profiling of 'noninvasive follicular thyroid neoplasms with papillary-like nuclear features' compared with adenomas and infiltrative follicular variants of papillary thyroid carcinomas," *Modern Pathology*, vol. 30, no. 1, pp. 39–51, 2017.

[36] Y. Wan, R. Cui, J. Gu et al., "Identification of four oxidative stress-responsive microRNAs, miR-34a-5p, miR-1915-3p, miR-638, and miR-150-3p, in hepatocellular carcinoma," *Oxidative Medicine and Cellular Longevity*, vol. 2017, Article ID 5189138, 12 pages, 2017.

[37] L. Kilpinen, A. Parmar, D. Greco et al., "Expansion induced microRNA changes in bone marrow mesenchymal stromal cells reveals interplay between immune regulation and cell cycle," *Aging*, vol. 8, no. 11, pp. 2799–2813, 2016.

[38] S. Sakaguchi, M. Miyara, C. M. Costantino, and D. A. Hafler, "$FOXP3^+$ regulatory T cells in the human immune system," *Nature Reviews. Immunology*, vol. 10, no. 7, pp. 490–500, 2010.

[39] N. Sobhani, D. R. Tardiel-Cyril, A. Davtyan, D. Generali, R. Roudi, and Y. Li, "CTLA-4 in regulatory T cells for cancer immunotherapy," *Cancers*, vol. 13, no. 6, p. 1440, 2021.

[40] S. Loi, S. Michiels, S. Adams et al., "The journey of tumor-infiltrating lymphocytes as a biomarker in breast cancer: clinical utility in an era of checkpoint inhibition," *Annals of Oncology*, vol. 32, no. 10, pp. 1236–1244, 2021.

[41] C. Denkert, G. von Minckwitz, S. Darb-Esfahani et al., "Tumour-infiltrating lymphocytes and prognosis in different subtypes of breast cancer: a pooled analysis of 3771 patients treated with neoadjuvant therapy," *The Lancet Oncology*, vol. 19, no. 1, pp. 40–50, 2018.

[42] N. Zacharakis, L. M. Huq, S. J. Seitter et al., "Breast cancers are immunogenic: immunologic analyses and a phase II pilot clinical trial using mutation-reactive autologous lymphocytes," *Journal of Clinical Oncology*, vol. 40, no. 16, pp. 1741–1754, 2022.

Hindawi
Journal of Oncology
Volume 2022, Article ID 7340266, 7 pages
https://doi.org/10.1155/2022/7340266

Review Article

ICU and Sepsis: Role of Myeloid and Lymphocyte Immune Cells

Anxiu Wang,[1] Su Zhang,[1] Guangming Peng,[2] Yuanxu Tang,[2] and Yaopeng Yang[2]

[1]*Geriatrics Department, People's Hospital of Yuxi City, Yuxi 653100, China*
[2]*Emergency Medicine Department, People's Hospital of Yuxi City, Yuxi 653100, China*

Correspondence should be addressed to Yaopeng Yang; yaopeng_yang@126.com

Received 2 August 2022; Revised 31 August 2022; Accepted 14 September 2022; Published 25 September 2022

Academic Editor: Muhammad Muddassir Ali

Sepsis is a severe immune system reaction to infection and a major cause of ICU-related fatalities. Because of the high mortality, high cost of treatment, and complex aetiology of sepsis, sepsis has a huge impact on healthcare. Some of the health complications in sepsis are abnormal cardiac functions, hypoperfusion, hypotension, tissue damage, multiple organ failure, and ultimately death. Individuals with weak immune systems and chronic medical conditions are highly vulnerable to sepsis. In sepsis, a patient shows the extreme immune response in the initial stage while prolonged immunosuppression in the later stages. Sepsis-driven immunosuppression ushers in death because sepsis cases develop secondary infections postrecovery. The later immunocompromised state in sepsis is attributed myeloid-derived suppressor cell upregulation and reduced immune activity displayed by lymphocytes (lymphocyte anergy). As a result, it is currently suggested that regulating the immune response is a better therapeutic approach than focusing on inflammation to improve the immune system's capacity to fight infections. Moreover, finding novel and accurate prognostic biomarkers that can help in rapid sepsis diagnoses and deciding better therapeutic strategies will significantly lower clinical case mortality rates.

1. Introduction

Sepsis reflects a mortality-driving clinical status identified through immunological dysregulation during an infection. Annually, 31,500,000 patients and 5,300,000 mortalities due to sepsis are reported. Septic shock describes a clinical scenario, whereby patient develops vascular-circulatory dysfunction together with profound immune response (IR) against an infection leading to a high mortality. Such IRs are characterized through systemic hyperinflammation early stage, called systemic inflammatory response syndrome (SIRS), together with prolonged immunosuppression during late-phase, termed compensatory anti-inflammatory response syndrome (CARS) [1–4]. Sepsis represents a major mortality driver within severely affected cases residing within intensive care units (ICUs) but degrees of septicemia vary among individuals and depend on the age, overall nutritional status, preexisting medical condition, immune response, and the virulence displayed by the invading pathogen [5]. Sepsis increases the duration of hospital stay, and sepsis patients show 8 times higher mortality than others. According to some estimates, >50% mortality in ICUs are attributed to sepsis [6]. The IR mounted against the infectious agent involves all host immune system components [7]. According to the "host theory" of sepsis, the "cytokine storm," or unchecked host production of proinflammatory cytokines, is what causes the clinical signs of sepsis [8]. Recent research, however, demonstrates that unchecked production of pro- and anti-inflammatory cytokines is present in this situation. Moreover, cytokine-class also varies among individuals with certain individuals who show increased synthesis of proinflammatory cytokines whereas others show higher production of anti-inflammatory cytokines [8]. The availability of better treatment options has certainly reduced the mortality associated with sepsis, but unfortunately, sepsis survivors are burdened with life-long health complications such as immune dysfunction, increased susceptibility for secondary infections, and poor quality of life [9, 10]. The "postsepsis syndrome" is a relatively new term and indicates a consistent compromised life at cognitive, psychological, physical, and medical level after aggravated sepsis [10]. Several common symptoms of sepsis are tachycardia,

tachypnea, body temperature > 38°C or <36°C, WBC-count of $>12 \times 10^{9}$/L or $<4 \times 10^{9}$/L, and hypotension [11]. Septic condition was found to drastically downregulate circulating numbers of CD4+/CD8+ lymphocytes leading to impaired host IR [7].

The present review is focused on the role of myeloid and lymphocyte cells within immunity issues identified in such cases and several potential biobiomarkers that can be used in improved prognosis and prediction of adverse outcomes during the hospital/ICU admission.

2. Etiology of Sepsis

The nonhomeostatic, systemic, and damaging IR that sepsis imposes on the host against infection/s leads to organ failure. Through aberrant stimulation of immune cell components and release of proinflammatory cytokines, the innate immune system supports systemic inflammatory-based responses. The duration and intensity of the inflammatory response have a significant role in sepsis prognosis, and a hyperinflammatory environment is typically associated with negative outcomes [12]. The early IRs in sepsis are mediated by various pattern recognition receptors (PRRs) and pathogen-associated molecular patterns (PAMPs), whereby most share complementary and overlapping functions. PRRs and PAMPs activate host-IR against invading pathogen/s [13]. As per the latest definition of sepsis, the International Consensus for Sepsis and Septic Shock describes it to be a life-threatening condition of organ dysfunction caused by a dysregulated IR to an infection [14]. The diagnosis of sepsis depends upon inflammation-based response-strength within the patient. In sepsis, both overexuberant inflammation and immunosuppression develops simultaneously in a patient. During the initial stages, a sepsis patient generates an inflammatory response against the infection. It progresses towards severe sepsis, a clinical situation in which sepsis is accompanied with organ dysfunction. The final stage is septic shock where a patient develops sepsis with tissue hypoperfusion [15]. The outcome of sepsis cases largely depends on the type of microorganism responsible for sepsis. The European Prevalence of Infection in Intensive Care (EPIC II) investigation reported Gram-negative bacteria are more common in sepsis than Gram-positive species (62.2% vs. 46.8%). The study also noted that the duration of ICU stay increased the risk for sepsis by drug-resistant strains of *Staphylococci*, *Acinetobacter*, *Pseudomonas*, and *Candida* species [16]. Of note, Gram-negative bacteria caused increased mortality in sepsis patients than Gram-positive bacteria [17]. It was observed that *Staphylococcus*/*E. coli* were linked to lower deaths (20% and 19%) than *Candida* (43%) or *Acinetobacter* (40%). The highest mortality (73%) was observed in *Pseudomonas aeruginosa* infections [18]. The lungs are the most frequently colonized site of bacterial colonization, and pulmonary sepsis is more common than abdominal sepsis (56.3% vs. 37.3%), and pulmonary sepsis was more common in old age patients. Both ICU mortality and one-year mortality associated with pulmonary-sepsis prevailed over abdominal sepsis (31.7% vs. 12.6 and 45.4% vs. 24.4%) [19]. One of the major causes for mortality is sepsis which is a multiorgan failure contributed by abnormal activation of blood platelets and immune cells.

An essential mediator in the body's overall response to sepsis is blood platelets. In fact, the main causes of sepsis-induced organ failures are activated platelets and immune system cells. However, a low platelet count is an independent and more potent predictor of poor outcomes in sepsis; therefore, routine platelet testing can aid in accurate risk assessment and the use of alternative therapeutic approaches in the management of sepsis [20]. Sepsis is also more common in individuals with preexisting health complications. For instance, a population level study in the US showed that 16% patients of acute myeloid leukemia (AML) developed sepsis in contrast to 4% patients without AML. The mortality rate of AML patients with sepsis was 30% compared to 21% observed in non-AML patients [21]. Of note, the heightened inflammatory phase in sepsis is followed by an immunosuppression. Recent trends have demonstrated that the immunosuppressive stage of sepsis is the major cause for mortality due to increased risk for secondary infections attributed to "immune paralysis" within a few weeks or month after recovery [22]. This is one of the possible reasons that adjunctive therapy targeted to dampen the inflammatory situation does not yield conclusive results, and the scientific community is of the view that restoration of normal immune functions by utilizing immunostimulants is more promising than anti-inflammatory agents. However, personalized decisions regarding the sepsis therapy must be taken to target inflammation, immunosuppression, or any other metabolism [23].

3. Prognostic Biomarkers for Sepsis

A common occurrence in patients with sepsis, trauma, burns, or serious traumas is lymphocyte anergy. Additionally, loss of delayed-type hypersensitivity, which increases the risk of sepsis and death [24], is linked to lymphocyte anergy. The neutrophil-to-lymphocyte ratio (NLR) is an important indicator for sepsis prognosis. A significantly higher ratio of NLR is observed in sepsis nonsurvivors together with exacerbated NLR linked to poor prognoses in septic cases [25]. Additionally, a higher NLR ratio was observed within acute kidney injury (AKI) patients in sepsis and acted as an independent indicator for AKI within sepsis/septic-shock cases [26]. Statistically validated variations within salivary C-reactive protein levels within septic neonates were denoted, in comparison to control cohort (12.0 ± 4.6 ng/L versus 2.8 ± 1.2 ng/L). Moreover, the salivary CRP levels were also a good indicator of subsequent rise in the serum CRP levels within such cases. Furthermore, the mean platelet volume and NLR were also markedly exacerbated within such cases in comparison to control cohort [27]. Recently, neutrophils-to-lymphocytes-and-platelets (N/LP) ratio was also suggested as proxy prognostic biomarker for inflammatory stati in sepsis. In patients with AKI, an exacerbated ratio of N/LP indicated aggravated danger of death and a separate prediction biomarker for death within septic-AKI cases admitted to ICUs [28]. The soluble triggering receptor expressed on myeloid cells-1 (sTREM-

1) represent valuable biomarkers for understanding sepsis/septic shock intensities. Additionally, it helps distinguish between septic and nonseptic illnesses. Compared to CRP and procalcitonin, sTREM-1 is thought to have improved sensitivity and specificity, making it a viable biomarker for the quick identification of infectious illnesses [29]. Saldir et al. reported septic neonates showed markedly exacerbated levels of IL-6, sTREM-1, endocan, and immature/total neutrophil ratio (I/T ratio) than nonseptic neonates. The measurement of these biomarkers can help in early identification of sepsis in neonates. The study showed that IL-6 was the most accurate biomarker for sepsis followed by sTREM-1 [30]. Plasma levels of sTREM-1 were markedly exacerbated within sepsis, compared to SIRS. Moreover, plasma sTREM-1 levels varied within (severe) sepsis/septic shock cases. This indicates that sTREM-1 is a functional biomarker for sepsis progression and a direct indicator of disease severity [31]. Another useful biomarker for sepsis is myeloid-related protein complex 8/14 because MRP8/14 expression levels increase with sepsis severity. The nonsurvivors had an exacerbated level of MRP8/14 than survivors in a 28 day follow-up. Moreover, AKI-carrying sepsis cases showed upregulated MRP8/14 than patients without AKI. This indicated that MRP8/14 acts as a functional biomarker for sepsis diagnoses/progression in ICU cases exhibiting AKI [32]. Recent observations have shown that the ratio of platelet-to-lymphocyte (PLR) is an important prognosis biomarker regarding inflammation in sepsis. A PLR > 200 indicated markedly exacerbated mortality, and a ratio of PLRs ≤ 200 was not significant [33].

4. Myeloid Cells in Sepsis

Myeloid-derived suppressor cells represent $Gr1^+$ $CD11b^+$ immune components defined through reduced expression of several characteristic biomarkers used to classify mature myeloid cells. They are also known as null cells, myeloid suppressor cells, or immature myeloid cells. These elements are the granulocyte and monocyte progenitors, and they may suppress the T cell response during an inflammatory state. To avoid any confusion, such immunological components were given the generic designation myeloid-derived suppressor cells (MDSCs) in 2007 [34, 35]. MDSCs express Gr1 and CD11b, two myeloid differentiation biomarkers, and first identified their crucial role in antitumor and immune surveillance. The heterogeneous population of MDSCs comprises the precursor of immune components including dendritic cells, macrophages, together with granulocytes, strongly inhibiting T cell function by exacerbating nitric oxide and reactive oxygen species generation [36]. Apart from their central role in immunosuppression, MDSCs also play certain nonimmunological roles in tumor angiogenesis and tumor metastasis [37, 38]. MDSCs are immunosuppressive, and their number increases in medical conditions characterized by acute or chronic inflammatory milieu such as cancer. Recent studies have linked MDSCs to the pathogenesis of sepsis. Strikingly, an increased number of MDSCs were responsible for nosocomial infections, adverse outcomes in sepsis patients, and exacerbated mortality in ICU admitted sepsis patients. Since MDSCs are present in very low numbers in healthy subjects, such could be employed as biomarkers and drug-action sites in sepsis therapy [39]. Primary function of MDSCs is immunosuppression by controlling the inflammation in sepsis. The role that this MDSC function plays in sepsis is dual. The host immune system mounts a potent IR during the early stages of septic shock, which causes hyperinflammation. Immunosuppression brought on by MDSCs during this phase prevents organ malfunction and restricts the harmful effects of hyperinflammation. In contrast, persistent inflammation-immunosuppression and catabolism syndrome (PICS) and chronic critical illness (CCC) are both brought on by long-term immunosuppression brought on by MDSCs [40]. During the first three days of the septic phase, MDSCs were produced. These cells enhanced proinflammatory cytokine populations, released nitric oxide, and raised mortality. However, MDSCs in the late phase of sepsis (12 day) are anti-inflammation, expressing IL-10/TGF-beta. Late MDSCs showed more immature phenotype than early MDSCs and created less macrophages/dendritic cells in comparison to primordial MDSCs when treated with GM-CSF. This suggests that as septic inflammation developed, MDSCs skew towards a more immature phenotype and change their nature from proinflammatory to anti-inflammatory immune cells [35]. MDSCs suppress the activity of both adaptive and innate immune systems and promote chronic immunosuppression observed across late septic phases [41]. MDSCs were upregulated during several health complications where acute or chronic inflammatory conditions are a common underlying cause. For instance, sepsis, autoimmune disorders, burns, cancer, and trauma are certain clinical conditions where MDSC numbers increase. MDSCs are powerful immunosuppressive immune-system components stemming from their ability to reduce the suppress CD8(+) and CD4(+) T cell activation [42]. MDSC-induced immunosuppression is attributed to degradation of L-arginine, discharging anti-inflammatory/immunosuppressive cytokines such as IL-10 and TGF-β, activating immunosuppressive T regulatory cells (T_{regs}) and exacerbated generation of reactive oxygen and reactive nitrogen species (ROS, RNS) [39]. Xu et al. reported that 95% of esophageal tumor cases displayed upregulated granulocyte derived-MDSCs (G-MDSCs), correlating with elevated postsurgical morbidities. Moreover, an exacerbated number of monocyte-derived MDSCs indicated poor prognosis in cancer-related sepsis [43]. At molecular level, generation of MDSCs is linked with miR-21 and miR-181b expressions. The CCAAT enhancer-binding protein (C/EBPβ) upregulated miR-21 and miR-181b, leading onto transcription factor NFI-A upregulation and promoting MDSCs within spleen/bone marrow within a murine model for sepsis. However, C/EBPβ-deficient myeloid progenitors showed reduced NFI-A and consequently reduced generation of MDSCs in septic mice. This suggests that reducing the expression of C/EBPβ can be used as a therapeutic strategy to reduce immunosuppression in sepsis treatment [44]. In mouse model of $Gram^+$ sepsis, a massive upregulation in $Gr1^+$ $CD11b^+$ MDSC populations was observed. Both G-MDSCs ($Ly6G^-$ $CD11b^+$) and M-MDSCs ($Ly6C^+Ly6G^-CD11b^+$) were increased but M-MDSCs showed a stronger increase in the numbers for longer duration than G-MDSCs. At molecular level, the postseptic

immunosuppression is mediated by IL-6-dependent MyD88 and TLR signaling [45].

5. Lymphocytes in Sepsis

The adaptive immune system's B and T lymphocytes are crucial parts because they trigger an antigen-specific immune response to an invading disease. B (humoral immunity) and T cells are required for the initial antigen recognition and subsequent IR to eliminate the foreign antigen (cell-based immunity). While B cells differentiate into plasma cells and generate bespoke antibodies to clear infections, T cells are responsible for cell-mediated clearance of the invading pathogen [46]. Sepsis is characterized by reduced numbers of both B and T lymphocytes, a clinical condition called B and T lymphopenia, which causes immunosuppression in the patient. The B and T lymphopenia in sepsis is attributed to extensive apoptosis of lymphocytes, and preventing lymphocyte apoptosis by using caspase inhibitors markedly reduced the mortality in sepsis [7]. Anergy is a tolerance mechanism in immune cells where the cells do not mount a normal IR against an antigen. The cells remain in an inactivated but live stage for a prolonged duration in a hyporesponsive state [47]. Anergy of T lymphocytes is associated with immunodepression and indicates loss of activation through TCR signaling or $Ca^{(2+)}$ mobilization [48]. $CD4^+$, $CD8^+$, and total T lymphocyte downregulations were reported within sepsis cases. Lymphocyte downregulation was, however, induced by the type of bacterial infection, and Gram-negative bacteria more severely suppress the immune system than Gram-positive bacteria. For instance, sepsis induced by Gram-positive bacteria *Streptococcus pneumoniae* and *Staphylococcus aureus* caused an extended reduction (≥14 days) for $CD4^+$, $CD8^+$, total T lymphocyte, and NK cellular populations. Conversely, sepsis by Gram-negative pathogens, *Neisseria meningitidis* and *Enterobacteria*, caused reduction for a smaller duration, and the patients fully recovered in 3 days. Moreover, B cell/$CD3^+$/DR^+ and $CD4^+$ T lymphocyte populations within *Neisseria meningitidis* and *Enterobacteria*-infected patients were rapidly and markedly increased during the recovery phase compared to Gram-positive septic cases [49]. Population statistics for total T lymphocytes and CD4+ T lymphocytes were markedly reduced within septic patients than normal controls. Moreover, septic patients also showed lower numbers of NK cells, CD3+/DR + lymphocytes and CD4/CD8 ratio than healthy controls. However, the number of B lymphocytes was increased [50]. Treatment with Rg1 markedly increased the survival rate by suppressing systemic inflammatory response and enhancing the bacterial clearance. Moreover, Rg1 also inhibited lymphocyte apoptosis and attenuated lung and liver injury in septic mice which suggests that Ginsenoside Rg1 is protective in CLP-induced polymicrobial sepsis due to its anti-inflammatory and immunomodulatory activities [51]. Sepsis-induced lymphopenia was observed in patients during a 28-day follow-up. Sepsis nonsurvivors lowered degrees of CD19+ CD23+ across a one-week follow-up compared to sepsis survivors and a CD19+CD23+ value of 64.6% on receiver-operating characteristic curve was able to discriminate between sepsis nonsurvivors and sepsis survivors. Moreover, sepsis nonsurvivors showed an exacerbated percentage of CD80+ and CD95+ B cells than survivors. This suggests that a lower percentage of CD23+ and exacerbated CD80+ and CD95+ B cell percentages were linked to exacerbated death incidences during ICU admission in septic shock patients [52].

Recently, a "lymphocyte apoptosis model" is proposed to stratify risks together with improving prognoses within septic cases. The model is based on the biomarkers for lymphocyte apoptosis/immune-function and have potential in predicting survival in septic cases. The study observed that on the day 1 of admission, sepsis perishers showed markedly exacerbated levels of lymphocyte apoptosis and plasma cytochrome C, together with markedly reduced lymphocytes, Th1/Th2 ratios, and HLA-DR expression than sepsis survivors [53].

It has been observed that ICU-admitted septic cases showed reduction in all major lymphocytes: B, T, and NK cells. Moreover, critically ill patients also showed downregulated T cells together with a markedly reduced ICU mortality was observed in patients which showed an exacerbated total T cell count (>0.36/nL) on ICU presentation, independent of the patient's age. Also, sepsis survivors showed restoration of lymphocytes, and T cells and sepsis perishers were failed to overcome lymphopenia and T cell depletion [54].

6. Therapeutic Approach to Combat Sepsis

For many years, an uncontrolled inflammation was considered as the major cause for sepsis-associated symptoms including pyrexia and respiratory distress, together with shock. Further supporting our belief that targeting inflammatory pathways to minimise cytokine storm is the key to combating sepsis and lowering sepsis-related mortality is the finding that proinflammation cytokines like TNF- and IL-1 become elevated within sepsis. Alternative therapeutic approaches are required to treat septic cases, as shown by clinical trials targeting inflammatory pathways that either failed or even reduced the survival rate in septic patients. In actuality, immunoparalysis—which is a direct result of elevated lymphocyte apoptosis—causes the majority of sepsis individuals to pass away [55]. This suggests that preventing immunosuppression by reducing lymphocyte apoptosis is a promising strategy to reduce late phase complications in sepsis. Several studies have been undertaken to study the therapeutic potential of natural products and supplements. For instance, genipin treatment reduced late-phase lymphocyte apoptosis by reducing the expression of FADD, caspase-8, and caspase-3 and consequently increased the survival rate of mice in the CLP model of sepsis. Moreover, genipin prevented a reduction in the numbers of $CD4^+$ and $CD8^+$ T cell population and reduced the number of immunosuppressive regulatory T cell (Treg). Genipin also reduced immunosuppression by increasing the splenic expression of interferon-γ and interleukin (IL)-2 and reducing the levels of IL-4 and IL-10 [56]. In a related study, ASI-IV therapy enhanced overall survival in septic mice, decreased pathological damage to the lung and spleen, suppressed NF-B

and ERK1/2 signalling pathways, decreased bacterial load, and decreased levels of proinflammatory cytokines. These biological effects of ASI-IV protected mice against sepsis [3]. Glutamine also protected against sepsis-induced inflammatory reactions by increasing the numbers of CD8$\alpha\alpha^+$ TCR$\alpha\beta^+$ IELs and reducing the apoptosis in these cells. Glutamine also reduced the expression of proinflammatory cytokines from CD8$\alpha\alpha^+$ TCR$\alpha\beta^+$ IELs and mitigated intestinal epithelial injury during sepsis [57]. Martire-Greco et al. reported reduced lymphocytes and increased MDSCs in the lymph nodes of immunocompromised mice along with abnormal T cell proliferation. However, treatment with all-trans-retinoic acid (ATRA) restored the immunocompetence by increasing the numbers of $CD4^+$ and $CD8^+$ T cells which consequently improved the humoral immunity indicating that ATRA administration can be a promising strategy to ameliorate the immunosuppressive state in septic cases [58].

7. Conclusion

An early inflammatory condition and a subsequent yet lingering immunosuppressive condition define sepsis, an inflammatory clinical condition. The biochemical pathways and immunological cells involved in the genesis of sepsis make up a very complex network. Because of its complicated origin, high death rate, and dearth of effective treatments, sepsis places a heavy burden on healthcare systems. The advanced stages of sepsis can cause organ dysfunction and ultimately death. In sepsis, a cytokine storm is followed by a compromise immunity called immunoparalysis which increases the chances of secondary infection and associated mortality. Sepsis remains a main driver for mortalities within ICU-admitted cases, and early diagnosis and appropriate treatment options can improve prognosis and reduced mortality. Moreover, early prognosis also helps in choosing appropriate antibiotics which can improve treatment outcomes. In recent years, it has been established that a majority of septic patients succumb to their illness due to immunocompromised state and not due to hyperinflammation. MDSCs are a mixed combination of myeloid cells and reduce the IR by inhibiting T cell-based immunity. The severely immunocompromised state in sepsis is attributed to increased numbers of MDSCs and lower levels of various types of lymphocytes. In contrast, some studies have even suggested that absence of MDSCs remains a main driver for mortalities within sepsis. This suggests that the role and immune functions of MDSCs want further exploration due to their controversial role in sepsis. Although treating infections and other sepsis-related complications continues to be the mainstay of treating sepsis, recent developments in the study of immune cells, such as MDSCs and lymphocytes, have opened the door for newer therapeutic approaches to combat the condition's immunosuppressive state. Numerous studies have demonstrated that one method for overcoming reduced IR in septic infections is to reduce lymphocyte apoptosis. Additionally, the strategies are aimed at reducing secondary infections in septic cases postrecovery which must also be explored for lowering mortality and enhancing quality-of-life in septic cases postrecovery.

Data Availability

Data will be provided upon request.

Conflicts of Interest

The authors declare that they have no conflicts of interest.

Authors' Contributions

Anxiu Wang and Su Zhang make equal contributions to the study.

References

[1] T. Ogura, Y. Nakamura, K. Takahashi, K. Nishida, D. Kobashi, and S. Matsui, "Treatment of patients with sepsis in a closed intensive care unit is associated with improved survival: a nationwide observational study in Japan," *Journal Intensive Care*, vol. 6, no. 1, pp. 1–10, 2018.

[2] C. Fleischmann, A. Scherag, N. K. Adhikari et al., "Assessment of global incidence and mortality of hospital-treated sepsis. Current estimates and limitations," *American Journal of Respiratory and Critical Care Medicine*, vol. 193, no. 3, pp. 259–272, 2016.

[3] R. Liu, H. Jiang, Y. Tian, W. Zhao, and X. Wu, "Astragaloside IV protects against polymicrobial sepsis through inhibiting inflammatory response and apoptosis of lymphocytes," *The Journal of Surgical Research*, vol. 200, no. 1, pp. 315–323, 2016.

[4] N. J. Shubin, S. F. Monaghan, and A. Ayala, "Anti-inflammatory mechanisms of sepsis," *Contributions to Microbiology*, vol. 17, pp. 108–124, 2011.

[5] R. S. Hotchkiss and I. E. Karl, "The pathophysiology and treatment of sepsis," *The New England Journal of Medicine*, vol. 348, no. 2, pp. 138–150, 2003.

[6] J. Hajj, N. Blaine, J. Salavaci, and D. Jacoby, "The "centrality of sepsis": a review on incidence, mortality, and cost of care," *Healthcare (Basel)*, vol. 6, no. 3, p. 90, 2018.

[7] R. de Pablo, J. Monserrat, A. Prieto, and M. Alvarez-Mon, "Role of circulating lymphocytes in patients with sepsis," *BioMed Research International*, vol. 2014, Article ID 671087, 11 pages, 2014.

[8] B. Cheng, A. H. Hoeft, M. Book, Q. Shu, and S. M. Pastores, "Sepsis: pathogenesis, biomarkers, and treatment," *BioMed Research International*, vol. 2015, Article ID 846935, 2 pages, 2015.

[9] K. R. Genga and J. A. Russell, "Update of sepsis in the intensive care unit," *Journal of Innate Immunity*, vol. 9, no. 5, pp. 441–455, 2017.

[10] Z. Mostel, A. Perl, M. Marck et al., "Post-sepsis syndrome - an evolving entity that afflicts survivors of sepsis," *Molecular Medicine*, vol. 26, no. 1, pp. 1–14, 2019.

[11] G. Polat, R. A. Ugan, E. Cadirci, and Z. Halici, "Sepsis and septic shock: current treatment strategies and new approaches," *The Eurasian Journal of Medicine*, vol. 49, no. 1, pp. 53–58, 2017.

[12] A. Dewitte, S. Lepreux, J. Villeneuve et al., "Blood platelets and sepsis pathophysiology: a new therapeutic prospect in critically

ill patients," *Annals of Intensive Care*, vol. 7, no. 1, pp. 1–18, 2017.

[13] S. L. Raymond, D. C. Holden, J. C. Mira et al., "Microbial recognition and danger signals in sepsis and trauma," *Biochimica et Biophysica Acta (BBA)-Molecular Basis of Disease*, vol. 1863, no. 10, pp. 2564–2573, 2017.

[14] M. Singer, C. S. Deutschman, C. W. Seymour et al., "The third international consensus definitions for sepsis and septic shock (sepsis-3)," *Journal of the American Medical Association*, vol. 315, no. 8, pp. 801–810, 2016.

[15] R. S. Hotchkiss, L. L. Moldawer, S. M. Opal, K. Reinhart, I. R. Turnbull, and J. L. Vincent, "Sepsis and septic shock," *Nature Reviews Disease Primers*, vol. 2, pp. 1–21, 2016.

[16] J. L. Vincent, J. Rello, J. Marshall et al., "International study of the prevalence and outcomes of infection in intensive care units," *Journal of the American Medical Association*, vol. 302, no. 21, pp. 2323–2329, 2009.

[17] J. Cohen, P. Cristofaro, J. Carlet, and S. Opal, "New method of classifying infections in critically ill patients," *Critical Care Medicine*, vol. 32, no. 7, pp. 1510–1526, 2004.

[18] M. S. Rangel-Frausto, "The epidemiology of bacterial sepsis," *Infectious Disease Clinics of North America*, vol. 13, no. 2, pp. 299–312, 1999.

[19] X. L. He, X. L. Liao, Z. C. Xie, L. Han, X. L. Yang, and Y. Kang, "Pulmonary infection is an independent risk factor for long-term mortality and quality of life for sepsis patients," *BioMed Research International*, vol. 2016, Article ID 4213712, 10 pages, 2016.

[20] M. Levi, "Platelets in critical illness," *Seminars in Thrombosis and Hemostasis*, vol. 42, no. 3, pp. 252–257, 2016.

[21] I. A. Malik, M. Cardenas-Turanzas, S. Gaeta et al., "Sepsis and acute myeloid leukemia: a population-level study of comparative outcomes of patients discharged from Texas hospitals," *Clinical Lymphoma, Myeloma & Leukemia*, vol. 17, no. 12, pp. e27–e32, 2017.

[22] C. Cao, M. Yu, and Y. Chai, "Pathological alteration and therapeutic implications of sepsis-induced immune cell apoptosis," *Cell Death & Disease*, vol. 10, no. 10, p. 782, 2019.

[23] A. M. Peters van Ton, M. Kox, W. F. Abdo, and P. Pickkers, "Precision immunotherapy for sepsis," *Frontiers in Immunology*, vol. 9, p. 1926, 2018.

[24] G. Monneret, F. Venet, A. Pachot, and A. Lepape, "Monitoring immune dysfunctions in the septic patient: a new skin for the old ceremony," *Molecular Medicine*, vol. 14, no. 1-2, pp. 64–78, 2008.

[25] Z. Huang, Z. Fu, W. Huang, and K. Huang, "Prognostic value of neutrophil-to-lymphocyte ratio in sepsis: a meta-analysis," *The American Journal of Emergency Medicine*, vol. 38, no. 3, pp. 641–647, 2020.

[26] X. Bu, L. Zhang, P. Chen, and X. Wu, "Relation of neutrophil-to-lymphocyte ratio to acute kidney injury in patients with sepsis and septic shock: a retrospective study," *International Immunopharmacology*, vol. 70, pp. 372–377, 2019.

[27] A. Omran, M. Ali, M. H. Saleh, and O. Zekry, "Salivary C-reactive protein and mean platelet volume in diagnosis of late-onset neonatal pneumonia," *The Clinical Respiratory Journal*, vol. 12, no. 4, pp. 1644–1650, 2018.

[28] J. Gameiro, J. A. Fonseca, S. Jorge, J. Gouveia, and J. A. Lopes, "Relacion entre neutrofilos, linfocitos y plaquetas como factor pronostico de mortalidad en pacientes con lesion renal aguda por sepsis," *Nefrología*, vol. 40, no. 4, p. 461, 2020.

[29] C. Cao, J. Gu, and J. Zhang, "Soluble triggering receptor expressed on myeloid cell-1 (sTREM-1): a potential biomarker for the diagnosis of infectious diseases," *Frontiers in Medicine*, vol. 11, no. 2, pp. 169–177, 2017.

[30] M. Saldir, T. Tunc, F. Cekmez et al., "Endocan and soluble triggering receptor expressed on myeloid cells-1 as novel markers for neonatal sepsis," *Pediatrics and Neonatology*, vol. 56, no. 6, pp. 415–421, 2015.

[31] L. Li, Z. Zhu, J. Chen, B. Ouyang, M. Chen, and X. Guan, "Diagnostic value of soluble triggering receptor expressed on myeloid cells-1 in critically-ill, postoperative patients with suspected sepsis," *The American Journal of the Medical Sciences*, vol. 345, no. 3, pp. 178–184, 2013.

[32] S. Gao, Y. Yang, Y. Fu, W. Guo, and G. Liu, "Diagnostic and prognostic value of myeloid-related protein complex 8/14 for sepsis," *The American Journal of Emergency Medicine*, vol. 33, no. 9, pp. 1278–1282, 2015.

[33] Y. Shen, X. Huang, and W. Zhang, "Platelet-to-lymphocyte ratio as a prognostic predictor of mortality for sepsis: interaction effect with disease severity—a retrospective study," *BMJ Open*, vol. 9, no. 1, p. e022896, 2019.

[34] J. E. Talmadge and D. I. Gabrilovich, "History of myeloid-derived suppressor cells," *Nature Reviews. Cancer*, vol. 13, no. 10, pp. 739–752, 2013.

[35] L. Brudecki, D. A. Ferguson, C. E. McCall, and M. El Gazzar, "Myeloid-derived suppressor cells evolve during sepsis and can enhance or attenuate the systemic inflammatory response," *Infection and Immunity*, vol. 80, no. 6, pp. 2026–2034, 2012.

[36] D. I. Gabrilovich and S. Nagaraj, "Myeloid-derived suppressor cells as regulators of the immune system," *Nature Reviews. Immunology*, vol. 9, no. 3, pp. 162–174, 2009.

[37] C. Murdoch, M. Muthana, S. B. Coffelt, and C. E. Lewis, "The role of myeloid cells in the promotion of tumour angiogenesis," *Nature Reviews. Cancer*, vol. 8, no. 8, pp. 618–631, 2008.

[38] S. Ostrand-Rosenberg and P. Sinha, "Myeloid-derived suppressor cells: linking inflammation and cancer," *Journal of Immunology*, vol. 182, no. 8, pp. 4499–4506, 2009.

[39] I. T. Schrijver, C. Théroude, and T. Roger, "Myeloid-derived suppressor cells in sepsis," *Frontiers in Immunology*, vol. 10, p. 327, 2019.

[40] J. C. Mira, L. F. Gentile, B. J. Mathias et al., "Sepsis pathophysiology, chronic critical illness, and persistent inflammation-immunosuppression and catabolism syndrome," *Critical Care Medicine*, vol. 45, no. 2, pp. 253–262, 2017.

[41] T. Alkhateeb, A. Kumbhare, I. Bah et al., "S100A9 maintains myeloid-derived suppressor cells in chronic sepsis by inducing miR-21 and miR-181b," *Molecular Immunology*, vol. 112, pp. 72–81, 2019.

[42] A. G. Cuenca, M. J. Delano, K. M. Kelly-Scumpia et al., "A paradoxical role for myeloid-derived suppressor cells in sepsis and trauma," *Molecular Medicine*, vol. 17, no. 3-4, pp. 281–292, 2011.

[43] J. Xu, Y. Peng, M. Yang et al., "Increased levels of myeloid-derived suppressor cells in esophageal cancer patients is associated with the complication of sepsis," *Biomedicine & Pharmacotherapy*, vol. 125, p. 109864, 2020.

[44] J. Dai, A. Kumbhare, D. Youssef, Z. Q. Yao, C. E. McCall, and M. El Gazzar, "Expression of C/EBPβ in myeloid progenitors during sepsis promotes immunosuppression," *Molecular Immunology*, vol. 91, pp. 165–172, 2017.

[45] M. Koeberle, T. Biedermann, and Y. Skabytska, "444 Post-septic immune-suppression following Gram positive sepsis is mediated by TLR dependent induction of myeloid derived suppressor cells," *Journal of Investigative Dermatology*, vol. 136, no. 9, p. S236, 2016.

[46] R. L. E. Cano and H. D. E. Lopera, "Chapter 5: Introduction to T and B lymphocytes," in *Autoimmunity: From Bench to Bedside*, J. M. Anaya, Y. Shoenfeld, A. Rojas-Villarraga, R. L. E. Cano, and H. D. E. Lopera, Eds., El Rosario University Press, Bogota (Colombia), 2013, https://www.ncbi.nlm.nih.gov/books/NBK459471/.

[47] R. H. Schwartz, "T cell anergy," *Annual Review of Immunology*, vol. 21, no. 1, pp. 305–334, 2003.

[48] A. K. De, K. M. Kodys, J. Pellegrini et al., "Induction of global anergy rather than inhibitory Th2 lymphokines mediates post-trauma T cell immunodepression," *Clinical Immunology*, vol. 96, no. 1, pp. 52–66, 2000.

[49] M. Holub, Z. Klucková, M. Helcl, J. Príhodov, R. Rokyta, and O. Beran, "Lymphocyte subset numbers depend on the bacterial origin of sepsis," *Clinical Microbiology and Infection*, vol. 9, no. 3, pp. 202–211, 2003.

[50] M. Holub, Z. Klučková, B. Beneda et al., "Changes in lymphocyte subpopulations and CD3+/DR + expression in sepsis," *Clinical Microbiology and Infection*, vol. 6, no. 12, pp. 657–660, 2000.

[51] Y. Zou, T. Tao, Y. Tian et al., "Ginsenoside Rg1 improves survival in a murine model of polymicrobial sepsis by suppressing the inflammatory response and apoptosis of lymphocytes," *The Journal of Surgical Research*, vol. 183, no. 2, pp. 760–766, 2013.

[52] J. Monserrat, R. de Pablo, D. Diaz-Martín et al., "Early alterations of B cells in patients with septic shock," *Critical Care*, vol. 17, no. 3, p. R105, 2013.

[53] W. Jiang, W. Zhong, Y. Deng et al., "Evaluation of a combination "lymphocyte apoptosis model" to predict survival of sepsis patients in an intensive care unit," *BMC Anesthesiology*, vol. 18, no. 1, p. 89, 2018.

[54] P. Hohlstein, H. Gussen, M. Bartneck et al., "Prognostic relevance of altered lymphocyte subpopulations in critical illness and sepsis," *Journal of Clinical Medicine*, vol. 8, no. 3, p. 353, 2019.

[55] P. Weber, P. Wang, S. Maddens et al., "VX-166: a novel potent small molecule caspase inhibitor as a potential therapy for sepsis," *Critical Care*, vol. 13, no. 5, p. R146, 2009.

[56] J. S. Kim, S. J. Kim, and S. M. Lee, "Genipin attenuates sepsis-induced immunosuppression through inhibition of T lymphocyte apoptosis," *International Immunopharmacology*, vol. 27, no. 1, pp. 15–23, 2015.

[57] J. N. Tung, W. Y. Lee, M. H. Pai, W. J. Chen, C. L. Yeh, and S. L. Yeh, "Glutamine modulates CD8$\alpha\alpha^+$ TCR$\alpha\beta^+$ intestinal intraepithelial lymphocyte expression in mice with polymicrobial sepsis," *Nutrition*, vol. 29, no. 6, pp. 911–917, 2013.

[58] D. Martire-Greco, V. I. Landoni, P. Chiarella et al., "All-trans-retinoic acid improves immunocompetence in a murine model of lipopolysaccharide-induced immunosuppression," *Clinical Science*, vol. 126, no. 5, pp. 355–365, 2014.

Hindawi
Journal of Oncology
Volume 2022, Article ID 1022580, 25 pages
https://doi.org/10.1155/2022/1022580

Research Article

Prognostic Modeling of Lung Adenocarcinoma Based on Hypoxia and Ferroptosis-Related Genes

Chang Liu,[1,2] Yan-Qin Ruan,[3] Lai-Hao Qu,[1,2] Zhen-Hua Li,[1,2] Chao Xie,[1,2] Ya-Qiang Pan,[1,2] Hao-Fei Li,[4] and Ding-Biao Li [1,2]

[1]*Thoracic Surgery, Yan'an Affiliated Hospital of Kunming Medical University, Kunming Medical University, Kunming 650000, Yunnan Province, China*
[2]*Key Laboratory of Tumor Immunological Prevention and Treatment of Yunnan Province, Yan'an Affiliated Hospital of Kunming Medical University, Kunming Medical University, Kunming 650000, Yunnan Province, China*
[3]*Guizhou Center for Disease Control and Prevention, Guiyang, Guizhou Province 550001, China*
[4]*The First Clinical College of Xinxiang Medical University, Xinxiang, Henan Province 453003, China*

Correspondence should be addressed to Ding-Biao Li; lidb88@163.com

Received 27 July 2022; Revised 10 August 2022; Accepted 16 August 2022; Published 19 September 2022

Academic Editor: Ibrahim Hakki Cigerci

Background. It is well known that hypoxia and ferroptosis are intimately connected with tumor development. The purpose of this investigation was to identify whether they have a prognostic signature. To this end, genes related to hypoxia and ferroptosis scores were investigated using bioinformatics analysis to stratify the risk of lung adenocarcinoma. *Methods*. Hypoxia and ferroptosis scores were estimated using The Cancer Genome Atlas (TCGA) database-derived cohort transcriptome profiles via the single sample gene set enrichment analysis (ssGSEA) algorithm. The candidate genes associated with hypoxia and ferroptosis scores were identified using weighted correlation network analysis (WGCNA) and differential expression analysis. The prognostic genes in this study were discovered using the Cox regression (CR) model in conjunction with the LASSO method, which was then utilized to create a prognostic signature. The efficacy, accuracy, and clinical value of the prognostic model were evaluated using an independent validation cohort, Receiver Operator Characteristic (ROC) curve, and nomogram. The analysis of function and immune cell infiltration was also carried out. *Results*. Here, we appraised 152 candidate genes expressed not the same, which were related to hypoxia and ferroptosis for prognostic modeling in The Cancer Genome Atlas Lung Adenocarcinoma (TCGA-LUAD) cohort, and these genes were further validated in the GSE31210 cohort. We found that the 14-gene-based prognostic model, utilizing *MAPK4*, *TNS4*, *WFDC2*, *FSTL3*, *ITGA2*, *KLK11*, *PHLDB2*, *VGLL3*, *SNX30*, *KCNQ3*, *SMAD9*, *ANGPTL4*, *LAMA3*, and *STK32A*, performed well in predicting the prognosis in lung adenocarcinoma. ROC and nomogram analyses showed that risk scores based on prognostic signatures provided desirable predictive accuracy and clinical utility. Moreover, gene set variance analysis showed differential enrichment of 33 hallmark gene sets between different risk groups. Additionally, our results indicated that a higher risk score will lead to more fibroblasts and activated CD4 *T* cells but fewer myeloid dendritic cells, endothelial cells, eosinophils, immature dendritic cells, and neutrophils. *Conclusion*. Our research found a 14-gene signature and established a nomogram that accurately predicted the prognosis in patients with lung adenocarcinoma. Clinical decision-making and therapeutic customization may benefit from these results, which may serve as a valuable reference in the future.

1. Introduction

Lung cancer is one of the most frequent malignancies with high mortality and poor prognosis [1, 2]; 80% of lung malignancies diagnosed were NSCLC [3]. LUAD accounts for nearly 40% of NSCLC cases [4, 5], and its incidence is continually increasing [6]. In recent years, several therapeutic advances have been made, including targeted therapies and emerging immunotherapy [7, 8]. Although both methods are effective in a restricted range of lung cancer

subtypes, the rate of survival for LUAD is still poor [9]. According to statistics, LUAD has a poor prognosis that only 18% could survive longer than 5 years [10]. As a result, the search for valid biomarkers might lead to the establishment of individualized diagnosis and therapy for LUAD patients [11]. The cancer tissue has many specific characteristics, including accelerated cell cycle, alterations of the genome, increase in cell mobility and invasive growth of the cells, incapable of going through normal apoptosis process, and depletion of normal cell functions. Because of these physiological and pathological characteristics, it is difficult for tumors to be treated.

Recently, it has been studied that ferroptosis is a relatively new type of cell death. This process is often accompanied by significant iron buildup and lipid peroxidation in dying cells [12]. It can be distinguished from apoptosis, necrosis, and autophagy by certain key characteristics. Firstly, it is iron-dependent and is induced by the buildup of harmful lipid reactive oxygen species. In addition, polyunsaturated fatty acids are consumed during the process [12]. With the rapid development of the role of iron ions in cancer, new prospects have emerged for their use in cancer therapy [13]. The expression of the S100 calcium-binding protein A4 (FSP1) in lung cancer cell lines is related to resistance to ferroptosis, suggesting that overexpression of FSP1 may be a method for ferroptosis escape [14]. In addition, MAPK pathway activation is associated with the susceptibility to ferroptosis triggered by cystine deprivation in NSCLC cell lines [15]. Alvarez et al. [16] recently found that inhibiting the iron-sulfur cluster biosynthesis enzyme NFS1 induced ferroptosis in vitro and slowed tumor development in LUAD. Additionally, Liu et al. [17] discovered that brusatol, an inhibitor of NRF2, increased the response rate of cystine deprivation-triggered ferroptosis through the FOCAD-FAK signaling pathway in NSCLC cell lines. What is more surprising is that the merger of brusatol and erastin demonstrated a superior therapeutic effect on NSCLC. The findings in these prior studies suggest that ferroptosis is quite important for lung cancer treatment. Based on the above research, we made the following hypothesis that ferroptosis is connected with the prognosis of LUAD, and thus ferroptosis-related genes may function as prognostic biomarkers.

Hypoxia or oxygen deprivation is a feature of most solid tumors because the growth of a tumor requires a large amount of oxygen. As the rapid tumor growth outstrips the supply of oxygen, an imbalance between decreased oxygen supply and increased oxygen demand was formed. This is a typical feature observed in the tumor microenvironment (TME) that increases the aggressiveness of many tumors and also causes abnormal blood vessel formation due to impaired blood supply, leading to poorer clinical outcomes [18–20]. Many transcription factors are active in tumor cells when the environment is hypoxic, and these transcription factors regulate cell proliferation, motility, and apoptosis via a variety of downstream signaling mechanisms [21]. This leads to an immunosuppressive TME that reduces the effectiveness of immunotherapy [22] and upregulates the expression of PD-L1, further supporting cancer escape [23, 24]. Although several studies have shown that intratumoral hypoxia and HIF1A expression affect overall survival (OS) in LUAD [25–27], hypoxia-based cannot be used to estimate who are at a high risk very early.

According to recent research, HIF1A may influence lipid metabolism and cause lipids to be stored in droplets, which reduces peroxidation-mediated endosomal damage and limits cellular ferroptosis [28]. Additionally, HIF-2α has been reported to activate hypoxia-inducible lipid droplet-associated (HILPDA) expression and selectively enrich polyunsaturated lipids, thus promoting cellular ferroptosis [29]. Furthermore, increased ferritin heavy chains under hypoxic conditions can protect HT1080 tumor cells from ferroptosis [30]. These findings suggest a potential relationship between ferroptosis and hypoxia. But more research is needed to further investigate how ferroptosis and hypoxia interact with each other and how they can affect LUAD patients' prognosis.

A variety of models have been created to predict the prognostication in LUAD according to the TME [31], ferroptosis [32], hypoxia [33], and tumor immunology [34]. However, to our knowledge, there is no reported prognostic role of hypoxia and ferroptosis-interrelated features in LUAD. To fill the gap and broaden the diagnostic and therapeutic potential of LUAD, we performed a comprehensive analysis using TCGA and Gene Expression Omnibus (GEO), aiming to endorse the least prognostic genes for LUAD. Finally, a signature on hypoxia- and ferroptosis-interrelated genes was constructed to know the prognostic value in LUAD patients.

2. Materials and Methods

2.1. Data Source. Transcriptomic data from 593 samples, composed of 59 normal and 534 LUAD, from TCGA database were used in this study. A total of 476 LUAD samples had available survival data. The GSE31210 dataset [35, 36] (https://www.ncbi.nlm.nih.gov/geo/query/acc.cgi?acc=GSE31210), containing transcriptomic data and survival information for 226 LUAD patients, was obtained from the GEO database to validate the established model.

2.2. Single Sample Gene Set Enrichment Analysis. The MSigDB (https://www.gsea-msigdb.org/gsea/msigdb/) was performed to acquire the hallmark gene sets of hypoxias, which consisted of 200 genes. The results show that there are 259 genes related to ferroptosis in total, which were gathered from the FerrDb database (https://www.zhounan.org/ferrdb/). The TCGA-LUAD database matched the expression patterns of the aforementioned genes. The ssGSEA method (from the *R* package GSVA) was performed to analyze all samples, and the hypoxia and ferroptosis scores for each sample were then calculated [37].

2.3. Coexpression Network Construction. The TCGA-LUAD transcriptome data were selected for the establishment of gene coexpression networks using the *R* package WGCNA [38]. Hypoxia and ferroptosis scores were used as

phenotypic characteristics. To assess the correlation of all samples in the TCGA-LUAD database, we performed a cluster analysis to ensure the completeness of the samples. As shown in Supplementary Figure 1(a), TCGA-44-3917-01A-01R-A278-07 was identified as an outlier and therefore was not included in this section of the subsequent analysis. During the network construction phase, the soft thresholding power β was obtained above 0.90, with the fit index of the scale-free topology. A dendrogram of all genes was established using the dissimilarity measure to group them together (1-TOM) (Supplementary Figure 1(b)). We set 30 as the minimum module size, and modules with similar gene expressions were clustered and displayed in a tree diagram with color assignments according to the dynamic tree-cutting algorithm. To identify the modules associated with hypoxia and ferroptosis scores, a heatmap of module-feature relationships with correlation coefficients and *P*-values was drawn. Modules that had a strong dependency on both scores were identified as modules of interest, and the genes in these modules of interest were defined as hub genes.

2.4. Analysis of Differentially Expressed Genes (DEGs). Transcriptome data from 53 normal and 539 LUAD samples were used as the foundation for comparison to analyze genes expressed differently. DEGs were analyzed using the *R* package limma, with significance criteria of $|\log_2 \text{fold change (FC)}| > 1$ and $P < 0.05$ as significance thresholds.

2.5. Overlap Analysis. Overlap analysis was used to identify common genes between the identified hub genes and DEGs, which were defined as DE-hypoxia and ferroptosis score-related genes for the subsequent analysis.

2.6. Functional Enrichment. Using Metascape (https://metascape.org) [39], the researchers were able to confirm the functional enrichment of DE-hypoxia and ferroptosis score-related genes in this investigation. $P < 0.05$ was the significant threshold.

The active signaling was analyzed using gene set variation analysis (GSVA) [37], which could compute sample gene set enrichment using a Kolmogorov–Smirnov-like rank statistical analysis. In the present study, a GSVA assessment was used to establish the *t* score and to allocate 50 hallmark gene signature activity conditions to the groups with high or low risk. At last, we compared the values. The cutoff value was set to $|t| > 2$.

2.7. Identification and Establishment of the Gene Signature. TCGA's 476 LUAD cases were randomly separated into two groups by using a 7 : 3 split ratio. One group was used for training and another one for testing. The DE-hypoxia and ferroptosis score-interrelated genes that are related to OS were discovered using the TCGA training dataset. The characteristics related to LUAD prognosis were determined by using univariate Cox regression (UCR) analysis. $P < 0.05$ was considered as significant. After the LASSO-penalized Cox regression (LCR) analysis of the proposed predictive panels, 10-fold cross-validation was used. Risk scores can be generated by using prognostic gene signature. In accordance with the appropriate cutoff of the risk score, patients from the TCGA training and TCGA test sets, as well as GSE31210, were split into two groups. The AUC of the ROC curve and Kaplan–Meier (KM) analyses were applied. External validation was performed using the GSE31210 dataset.

2.8. Nomogram Construction and Validation. To identify whether the risk model can be influenced by clinical factors, UCR and MCR analysis together with the survival *R* package were performed. Following those analyses, a nomogram was obtained using MCR coefficients of the risk score and clinical variables in the TCGA cohort, which was then analyzed. It was necessary to create calibration curves to determine whether OS for one, three, or five years were consistent with the actual findings (bootstrap-based 1000 iterations resampling validations). We developed these analyses based on the *R* package rms.

2.9. Immune Cells Infiltration (ICI). The ICI into two groups was determined using the ssGSEA method and the *R* software [40]. The analysis considered only values with a $P < 0.05$. The violin diagrams used to illustrate the changes in ICI between separate categories were drawn with the ggplot2 package.

2.10. Patients and Tissue Samples. We performed experimental validation on specimens from five LUAD patients who underwent surgery at Yan'an Affiliated Hospital, Kunming Medical University, to validate 14 hypoxia and ferroptosis score-related signature expression status in LUAD and adjacent normal tissues (ANT). ANTs were used as controls. The institutional and national research committees were followed in the conduct of all procedures, as well as the Helsinki Declaration. The hospital's Ethics Committee gave its approval before any of the operations could be carried out (Permit No. 2017-014-01). All of the patients who took part in the trial gave their informed permission before participation.

2.11. RNA Isolation and qRT-PCR. The 20 tissues were dissociated using TRIzol Reagent (Life Technologies); then, total RNA was collected and determined the concentration using NanoDrop 2000FC-3100 (Thermo Fisher Scientific). Prior to performing qRT-PCR, the SureScript-First-strand-cDNA-synthesis kit (GeneCopoeia) was used to reverse transcription reaction. The qRT-PCR reaction was as follows: 4 μL of reverse transcription product, 2 μL of 5 × BlazeTaq qPCR Mix (GeneCopoeia, Guangzhou, China), 0.5 μL primers, and 3 μL of ddH_2O. A BIO-RAD CFX96 TouchTM PCR detection system (Bio-Rad Laboratories, Inc., USA) was utilized to perform the PCR reaction as follows: 95°C for 30 s, 40 cycles of incubation at 95°C for 10 s, 60°C for 20 s, and 72°C for 30 s. In this study, the primers used were synthesized by Servicebio (Servicebio Co., Ltd., Guangzhou, China) as follows: for KLK11:5′-

AGGGCTTGTAGGGGGAGA-3′, 5′-TGGGGAGGCTGTT GTTGA-3′; for MAPK4: 5′-TCAAGATTGGGGATTTCG-3′, 5′-TATGGGCTCATGTAGGGG-3′; for ITGA2: 5′-ATC AGGCGTCTCTCAGTTTC-3′, 5′-GTTTTCTTCTTGGCT TTCAC-3′; for WFDC2: 5′-CAGGCACAGGAGCAGAGA AG-3′, 5′-TCATTGGGCAGAGAGCAGAA-3′; for TNS4: 5′-GGGGCTTTTGTCATAAGGG-3′, 5′-TTTGAAGTGG ACCACGGTG-3′; for LAMA3: 5′-GGTTTTGGTCCGT GTTCT-3′, 5′-ACTGCCCCGTCATCTCTT-3′; for SMAD 9: 5′-GGAGATGAAGAGGAAAAGTGG-3′, 5′-GAAAGA GTCAGGATAGGTGGC-3′. GAPDH was chosen to be an internal control, and the $2^{-\Delta\Delta Ct}$ method was used to calculate the hub genes' relative expression level [41]. The experiment was repeated in triplicate on independent occasions.

2.12. Statistical Analysis. Statistical analysis was performed using *R* 3.4.3 and GraphPad Prism V9. *P*-value <0.05 means significant difference. To evaluate survival, both UCR and MCR analyzes were used. Both hazard ratios (HRs) and 95 percent CIs were reckoned to identify genes that were related to OS. Paired *t*-tests were performed for statistical differences in this study using GraphPad Prism V9.

3. Results

3.1. Filtering for Hypoxia Score- and Ferroptosis Score-Related Genes in TCGA-LUAD Database. A total of 200 hypoxia-interrelated and 259 ferroptosis-interrelated genes were gained from MSigDB and FerrDB, respectively. The expression conditions of these genes in 593 samples (normal: 59, LUAD: 534) were then matched and utilized as the basis for ssGSEA, which aimed to derive the hypoxia and ferroptosis scores in TCGA database. The ssGSEA outputs for the detailed score results are shown in Supplementary Table 1.

WGCNA was performed by applying the obtained hypoxia and ferroptosis scores as phenotypic data. After excluding the outlier samples, we constructed a sample-clustering tree (Figure 1(a)). Herein, a scale-free network was built when $\beta = 3$, which was defined as a soft threshold parameter (Figure 1(b)). Finally, 23 modules were identified according to the dynamic tree-cutting algorithm and were labeled with different colors (Figure 1(c)). The turquoise module was most irrelevant to ferroptosis score (cor = −0.69, $P = 3e - 10$) and hypoxia score (cor = −0.63, $P = 8e - 68$), whereas the red module correlated more strongly with both ferroptosis score (cor of −0.47, $P = 6e - 34$) and hypoxia score (cor = −0.49, $P = 2e - 36$) (Figure 1(d)). Therefore, these two models were identified as the modules of interest. Collectively, 8314 genes (Supplementary Table 2) and 660 genes (Supplementary Table 3) were identified as hub genes and considered as hypoxia and ferroptosis score-related genes for subsequent analysis.

3.2. Identification of LUAD-Related DEGs. Differential expression analysis was used to acquire transcriptome data from TCGA (59 normal and 534 LUAD samples), which was produced using the *R* program limma. When LUAD samples were compared to normal samples, a total of 1,969 eligible DEGs were obtained, among which 906 were significantly increased in LUAD samples, and 1,063 were significantly decreased (Figure 2(a); Supplementary Table 4).

3.3. Analysis of DE-Hypoxia and Ferroptosis Score-Related Genes. Based on the overlap analysis, we identified 152 common genes from the list of 8,974 hypoxia and ferroptosis score-related genes and the list of 1,969 LUAD-related DEGs, which were defined as DE-hypoxia and ferroptosis score-related genes (Figure 2(b)). In LUAD, 86 of these genes were upregulated, while 66 were inversed. The expression patterns of DE-hypoxia and ferroptosis score-related genes in the TCGA-LUAD database are described in Supplementary Table 5.

Functional annotations obtained from Metascape indicated that DE-hypoxia and ferroptosis score-related genes were mainly augmented in "transcriptional misregulation in cancer," "spermatogenesis," and "positive regulation of cell projection organization" (Figures 2(c) and 2(d)).

3.4. Establishment of the Hypoxia and Ferroptosis Score-Related Signature. In the TCGA training set ($n = 334$), the association of the 152 identified DE-hypoxia and ferroptosis score-related genes with survival in LUAD patients was analyzed using UCR. As shown in Table 1, only 17 of the 152 genes met the set significance threshold of $P < 0.05$. The HRs of *SMAD9*, *SNX30*, *STK32A*, *WFDC2*, *KLK11*, and *CTD.2589M5.4* were all <1, indicating that they were potential protective factors for LUAD. In contrast, *ANGPTL4*, *LAMA3*, *VGLL3*, *ITGA2*, *TNS4*, *KCNQ3*, *PHLDB2*, *FAM83A.AS1*, *SLC16A3*, *FSTL3*, and *MAPK4*, all with HR >1, were possible oncogenes. We performed LLR analysis based on 17 variables in the TCGA training set (Figures 3(a) and 3(b)) to obtain the best genes for constructing the prognostic signature. Ultimately, the hypoxia and ferroptosis score-related signature involved 14 genes: *MAPK4*, *TNS4*, *WFDC2*, *FSTL3*, *ITGA2*, *KLK11*, *PHLDB2*, *VGLL3*, *SNX30*, *KCNQ3*, *SMAD9*, *ANGPTL4*, *LAMA3*, and *STK32A*. We estimated the risk score of each individual in TCGA set based on the coefficient of each gene (Figure 3(c); Supplementary Table 6).

The patients with LUAD in the TCGA training set were separated into two groups with the cutoff value at 1.0803 (Supplementary Table 7). The allocation of risk scores is shown in Figure 3(d). Association analyses revealed a significant correlation ($P < 0.05$) between the *T* stage and various risk groups in the TCGA training set (Table 2). A significant association between a high-risk score and a poor outcome ($P < 0.0001$; Figure 3(e)) was shown in the Kaplan–Meier survival curves. ROC curves indicated that hypoxia and ferroptosis score-related signature could be used to predict OS in the TCGA training group (Figure 3(f)). Additionally, the heatmap indicated that the expression levels of *KCNQ3*, *ITGA2*, *ANGPTL4*, *TNS4*, *FSTL3*, *LAMA3*, *MAPK4*, *PHLDB2*, and *VGLL3* were upregulated with enhancing risk score, but the expression levels of *KLK11*,

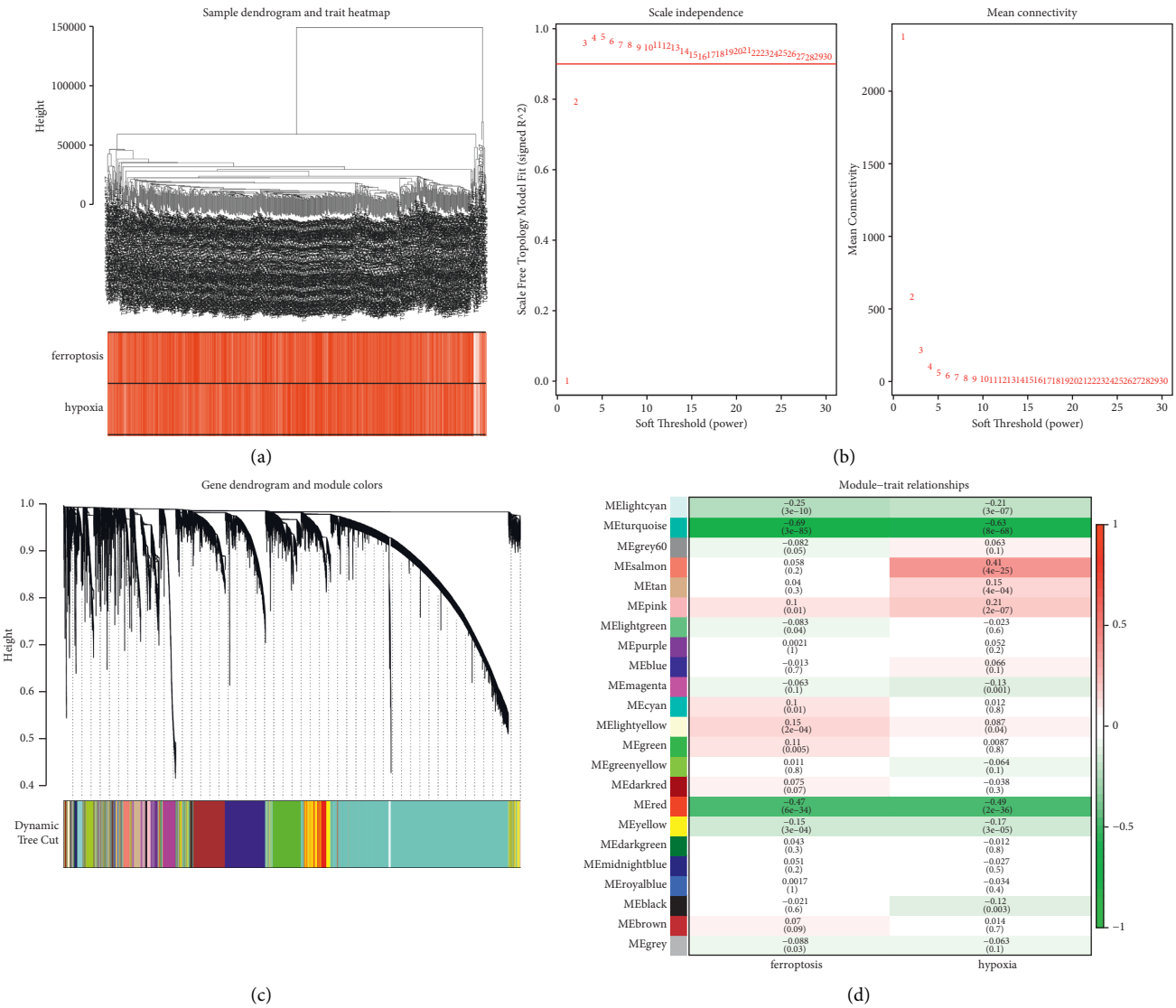

Figure 1: (a) Sample-clustering dendrogram with feature heatmap. (b) Network topology analysis with different soft threshold power. (c) Cluster dendrograms of genes based on topological overlap of dissimilarities, and module colors were assigned. (d) Heatmap showing the relationship between gene modules and phenotypic traits. Each row and column correspond to a module *e*-gene and a trait. The correlation coefficient in each cell represents the same relationship with heatmap in decreasing magnitude from red to green. The number in parentheses in each cell represents the correlation *P*-value.

SMAD9, *WFDC2*, *SNX30*, and *STK32A* were reduced. Additionally, in individuals with LUAD, *T* stages are also relevant to these genes expression (Figure 4).

3.5. Validation Prognostic Signature with 14 Genes. We used the same algorithm to compute the risk scores for the patients in the TCGA test cohort ($n = 142$; Supplementary Table 8) and the GSE31210 dataset ($n = 226$; Supplementary Table 9). According to cutoff values determined for each dataset, patients were separated into two risk groups. The results corroborated those from the TCGA training set. Figures 5(a) and 5(d) indicated that mortality status was more concentrated in the domain of high-risk scores. In both validation datasets, Figures 5(b) and 5(e) showed that high-risk patients had a considerably poorer outcome. In both datasets, the 14-gene prognostic signature performed well. The risk scores of AUCs for 1-, 3-, and 5-year OS predictions were 0.666, 0.652, and 0.637 in the TCGA test set, respectively (Figure 5(c)), while the AUCs of the 14-gene signature were 0.741, 0.648, and 0.677 for the three kinds of OS predictions, respectively, using the GSE31210 dataset (Figure 5(f)). The distribution of LUAD patients with different groups according to each clinical feature in the TCGA test set is shown in Table 3. Association studies revealed a significant ($P < 0.01$) correlation between the clinical stage and different risk groups in the GSE31210 dataset (Table 4).

3.6. Correlation Analysis of Risk Score with Clinical Characteristics of LUAD. We observed the allocation of patient risk scores according to different clinical characteristics.

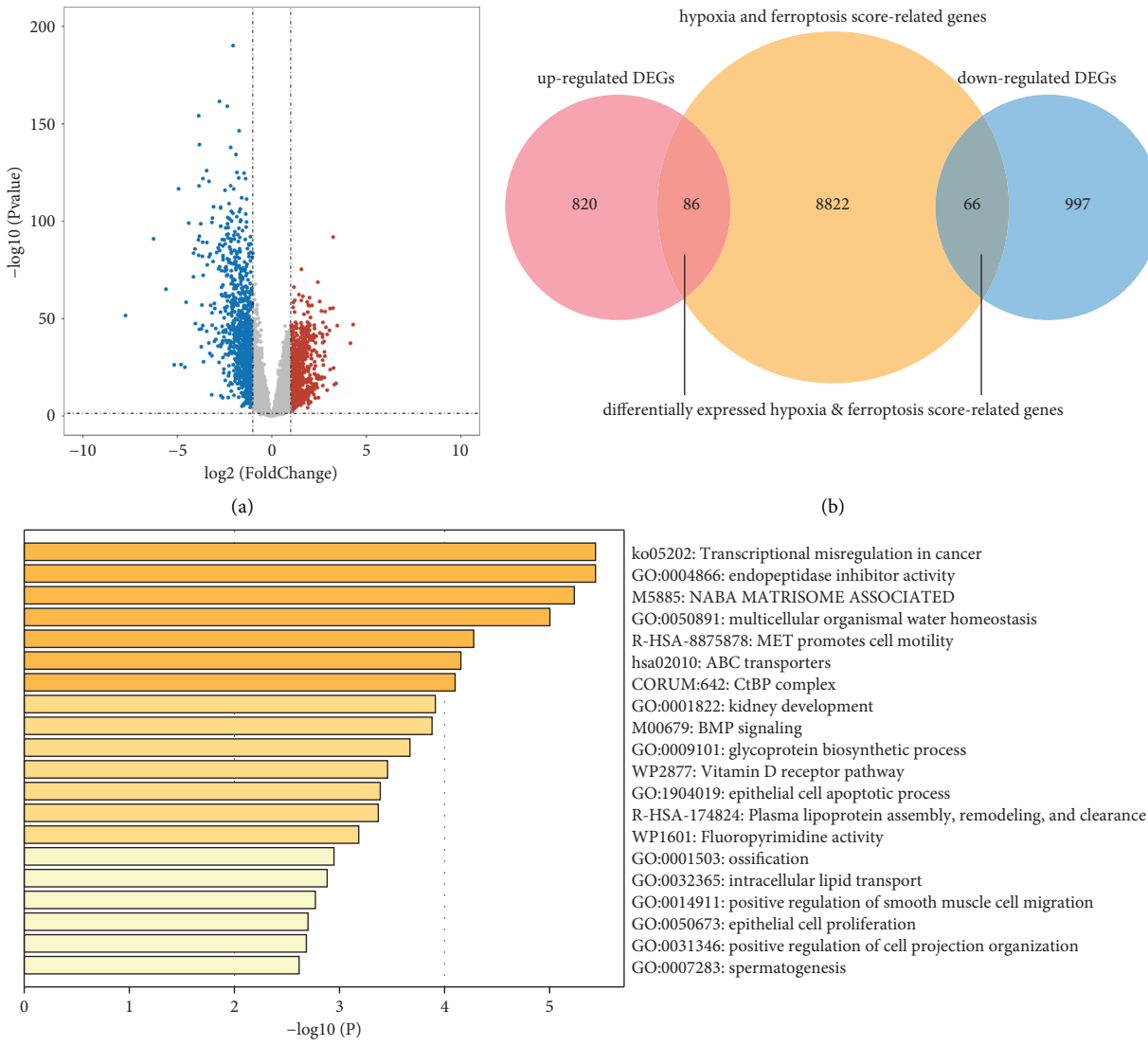

Figure 2: Continued.

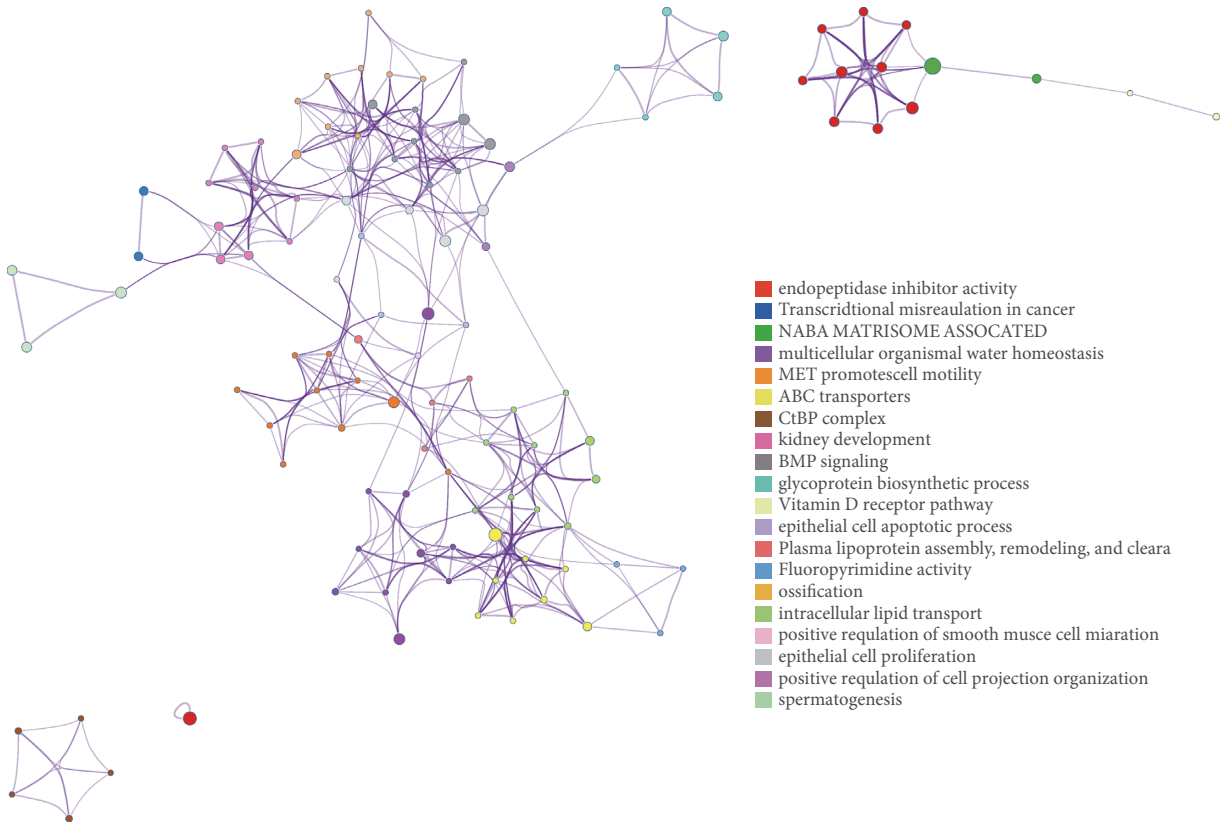

(d)

Figure 2: (a) Volcano map of significant DEGs. Red spots: upregulated genes; blue spots: downregulated genes; gray: genes with no change in expression. (b) Venn diagram showing the repetitious genes of DEGs and WGCNA. (c, d) Function analysis of DE-hypoxia and ferroptosis score-related genes using Metascape.

Table 1: UCR analysis of the 152 identified DE-hypoxia and ferroptosis score-related genes explores 17 genes associated with LUAD patient survival.

ID	z	HR	HR. 95L	HR. 95H	P-value
MAPK4	4.21113029756985	1.46745295679297	1.22755540646437	1.75423298130611	$2.54E-05$
TNS4	4.02119788604733	1.29938376610491	1.14367045280752	1.47629779843681	$5.79E-05$
WFDC2	−3.79860720374219	0.811653740106402	0.728800938850636	0.903925555951741	0.000145511488661
FSTL3	3.68304906615447	1.40517139515741	1.17250302799022	1.68400985126077	0.000230460779083
FAM83A.AS1	3.19219681770566	1.38043585405413	1.13252613465791	1.68261295597717	0.00141195086371
ITGA2	3.1297146270081	1.26268315773328	1.0910870928145	1.46126626125743	0.001749761967554
KLK11	−2.89081539413551	0.817085437051864	0.712500352475736	0.937022149003037	0.003842437575419
SLC16A3	2.69059352882516	1.38307857948644	1.09206101692107	1.75164778259545	0.007132503883482
PHLDB2	2.67561048467087	1.36825660397289	1.08747876280116	1.72152891472853	0.007459328240577
VGLL3	2.48631904817044	1.24621454130366	1.04770025500438	1.48234256462046	0.012907219145633
SNX30	−2.41280356238469	0.718205289102291	0.548879152164541	0.939767588658339	0.015830348860021
KCNQ3	2.23280002150132	1.34420966442955	1.03680712106375	1.74275386929437	0.025562134874828
SMAD9	−2.20299987655253	0.660110772189965	0.456177215306126	0.955212616809054	0.02759475734267
ANGPTL4	2.17133207596654	1.15838922218355	1.01441557907091	1.32279670951033	0.029906079314469
LAMA3	2.05948665187877	1.18322521780815	1.00816336324203	1.38868557130958	0.039447642418345
CTD.2589M5.4	−1.98163055774902	0.831910477060721	0.693468992502609	0.997989887544674	0.047520604494006
STK32A	−1.97258211072512	0.789000052327525	0.623465515365524	0.998485188403512	0.048543192818321

Interestingly, the distribution of patient risk scores was highly related to the stages of the patients. Risk scores in patients in stage III were increased compared to those in stage I ($P < 0.05$; Figure 6(a)). In terms of the T stage (Figure 6(b)), patients with LUAD in $T4$ had the highest risk scores, which have a significant difference in $T1$ and $T2$, but comparable to $T3$. Patients with LUAD in the $T3$ stage had slightly higher risk scores than those in the $T1$ stage ($P < 0.01$); in the N stage (Figure 6(c)), patients in the $N2$ stage had higher risk scores than those in the $N0$ stage

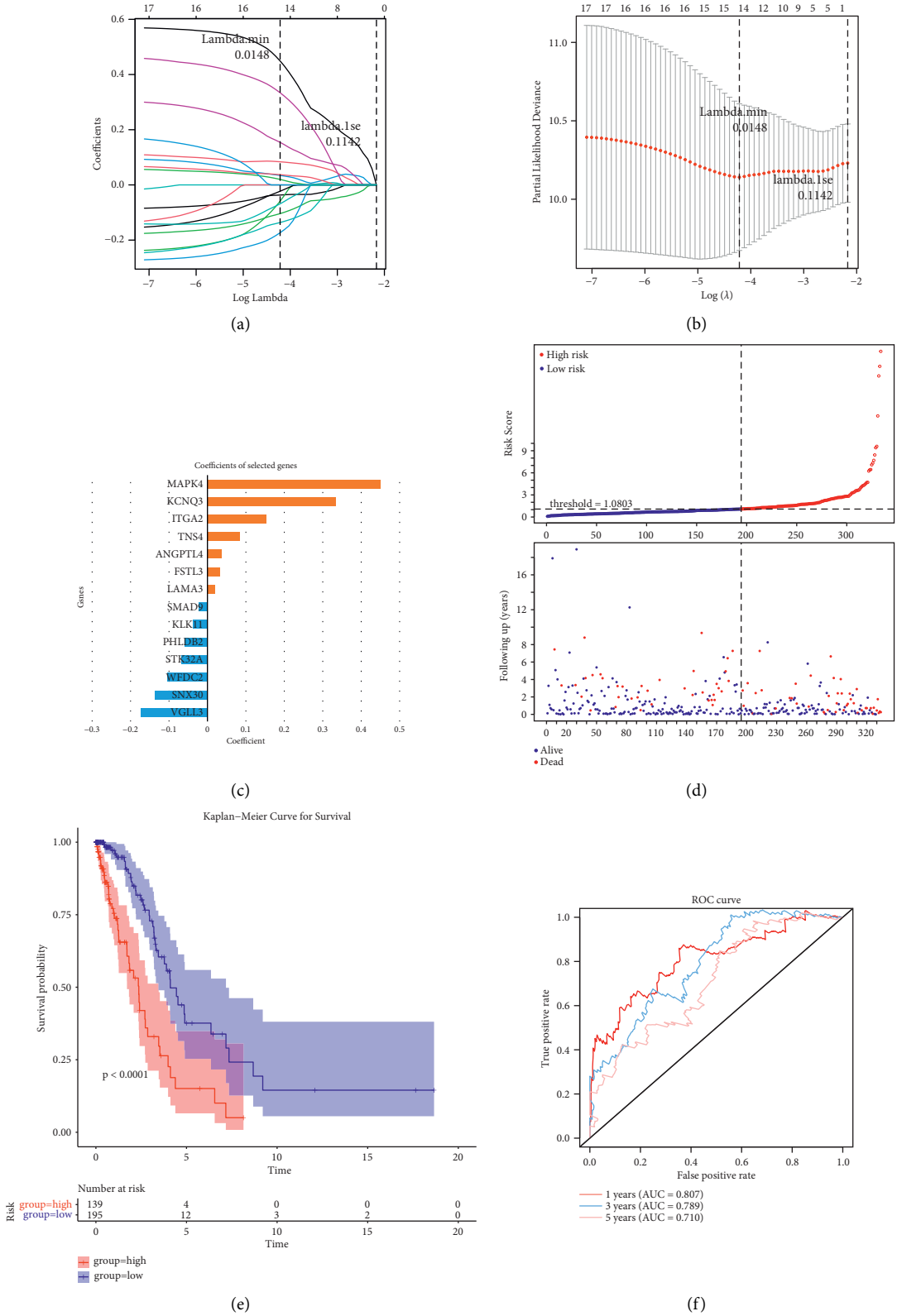

Figure 3: (a–c) The LCR was used to figure out the lowest criteria (a, b) and coefficients (c). (d) Allocations of risk scores (based on the hypoxia and ferroptosis score-related prognostic signature); (e) *K-M* survival curves. (f) Hypoxia and ferroptosis score-related signature can be utilized to predict OS in the TCGA training set according to ROC curves.

Table 2: Association analysis shows that clinical characteristics correlate results with different risk groups in the TCGA training set.

		Expression		
	Total ($N = 309$)	High ($N = 129$)	Low ($N = 180$)	P-value
Gender				
Female	165 (53.4%)	66 (51.2%)	99 (55.0%)	0.582
Male	144 (46.6%)	63 (48.8%)	81 (45.0%)	
Age (years)				
≥60	229 (74.1%)	95 (73.6%)	134 (74.4%)	0.979
<60	80 (25.9%)	34 (26.4%)	46 (25.6%)	
Pathologic stage				
Stage I	168 (54.4%)	62 (48.1%)	106 (58.9%)	0.0815
Stage II	74 (23.9%)	30 (23.3%)	44 (24.4%)	
Stage III	50 (16.2%)	28 (21.7%)	22 (12.2%)	
Stage IV	17 (5.5%)	9 (7.0%)	8 (4.4%)	
T stage				
*T*1	102 (33.0%)	31 (24.0%)	71 (39.4%)	0.0128
*T*2	166 (53.7%)	76 (58.9%)	90 (50.0%)	
*T*3	29 (9.4%)	13 (10.1%)	16 (8.9%)	
*T*4	10 (3.2%)	8 (6.2%)	2 (1.1%)	
*T*X	2 (0.6%)	1 (0.8%)	1 (0.6%)	
M stage				
*M*0	198 (64.1%)	82 (63.6%)	116 (64.4%)	0.47
*M*1	16 (5.2%)	9 (7.0%)	7 (3.9%)	
*M*X	95 (30.7%)	38 (29.5%)	57 (31.7%)	
N stage				
*N*0	202 (65.4%)	75 (58.1%)	127 (70.6%)	0.16
*N*1	54 (17.5%)	26 (20.2%)	28 (15.6%)	
*N*2	46 (14.9%)	25 (19.4%)	21 (11.7%)	
*N*3	1 (0.3%)	0 (0%)	1 (0.6%)	
*N*X	6 (1.9%)	3 (2.3%)	3 (1.7%)	

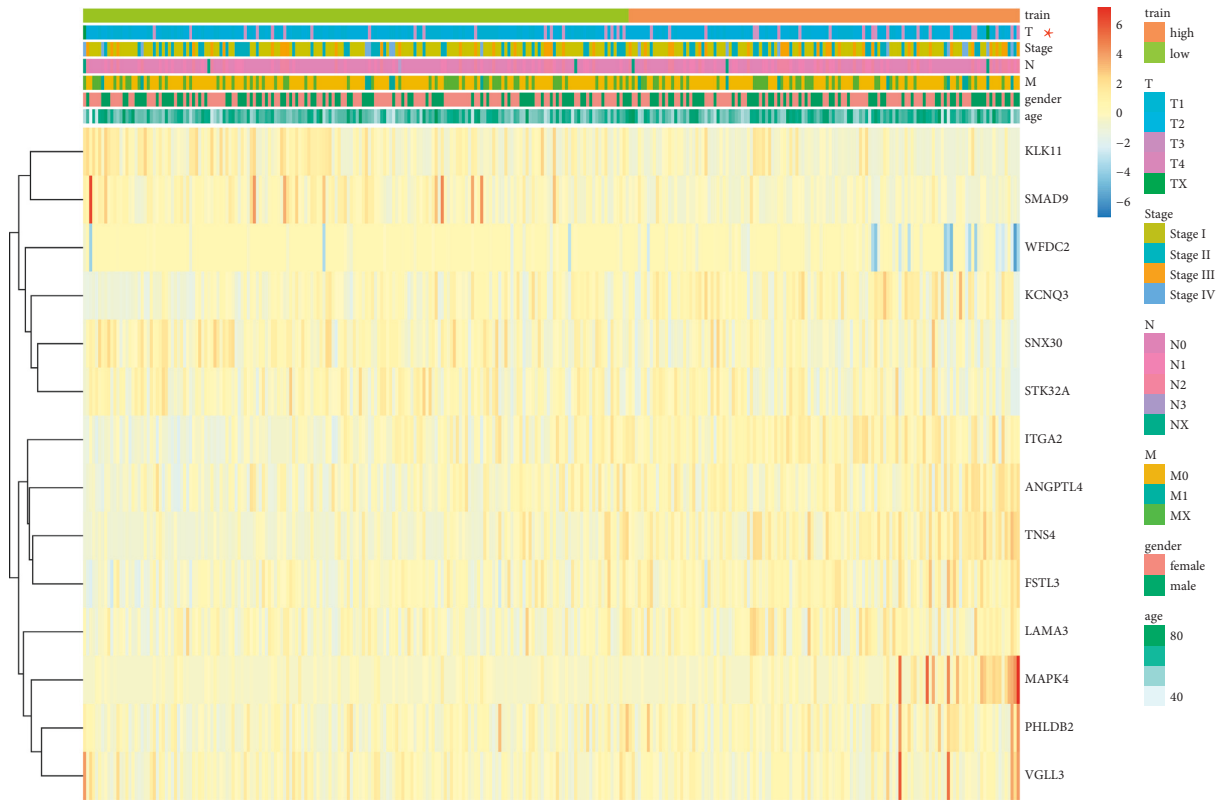

(a)

Figure 4: Continued.

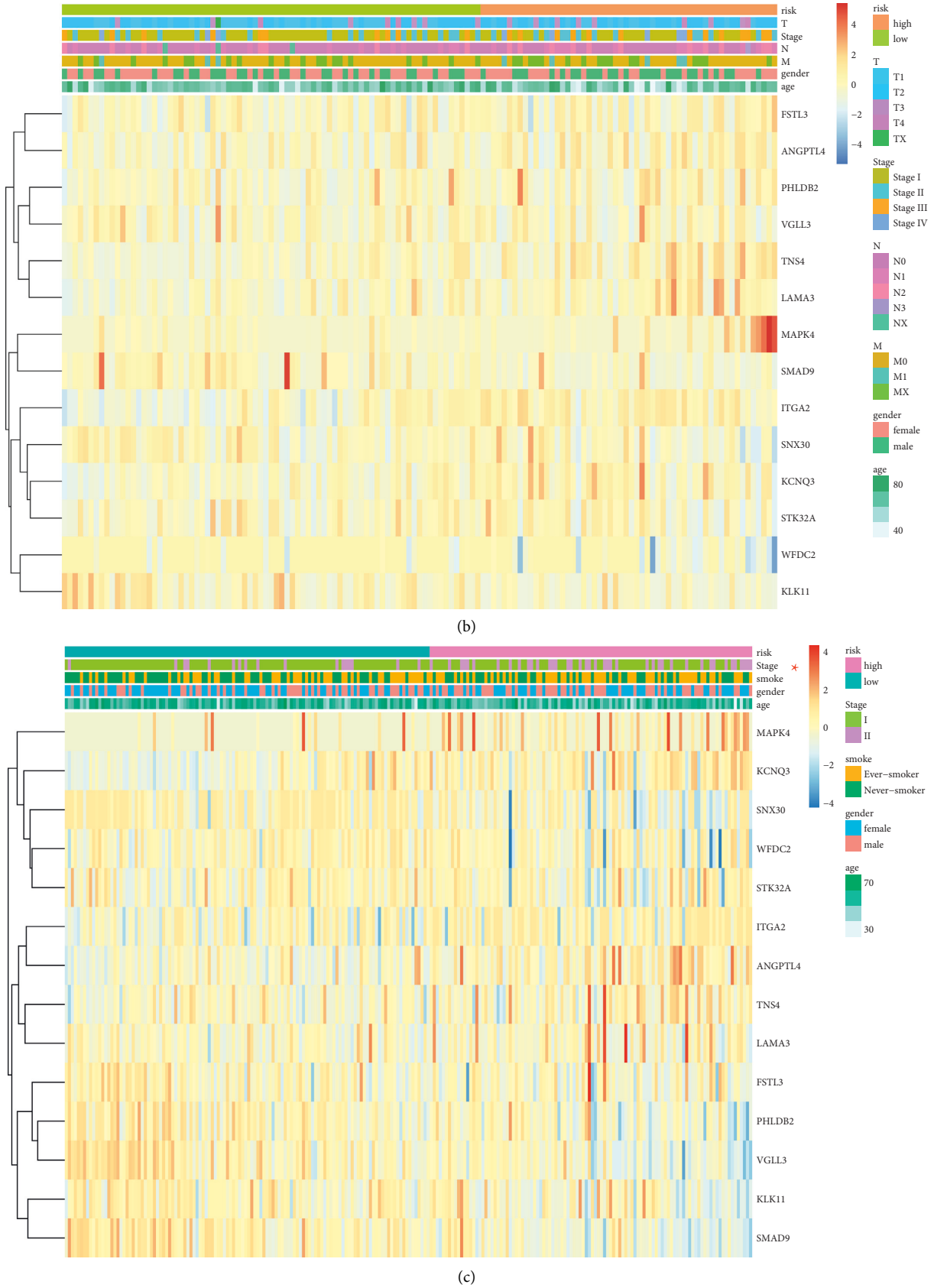

Figure 4: Heatmap of the relationship between the expression of 14 genes associated with hypoxia and ferroptosis scores and clinicopathological features in the (a) TCGA training, (b) TCGA test, and (c) GSE31210 dataset.

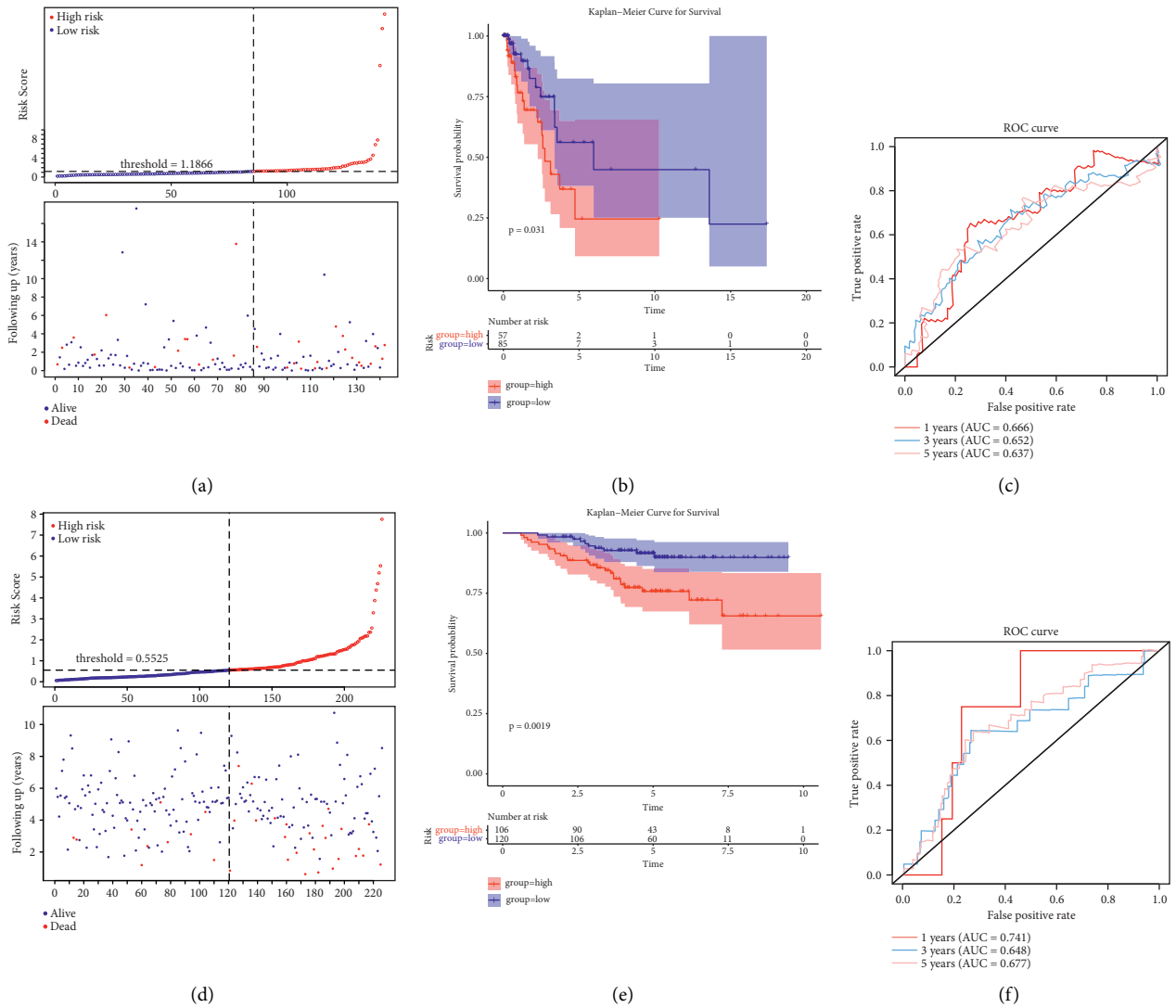

FIGURE 5: (a, d) Allocations of risk scores. (b), (e) The *K-M* survival curves showed that a high-risk score was related to less OS. Hypoxia and ferroptosis score-related signature can be utilized to predict OS in the (c) TCGA test and (d) GSE31210 dataset according to ROC curves.

($P < 0.01$). Although the risk score in stage *N*3 was lower than in stage *N*2 ($P < 0.05$), the sample size in stage *N*3 was too small to be considered valid. Subsequently, the impact of clinical characteristics on the OS in LUAD patients was investigated using KM survival analysis. Specifically, in the stratified analysis of stage (Figure 6(d)), patients with a lower stage are more likely to have a better prognosis, which showed the same trend with distribution of risk score levels. In the stratified analysis of the *T* stage (Figure 6(e)), the *T*1 stage had a better OS, whereas *T*3 and *T*4 stages exhibited a poor prognosis. The worst prognosis in LUAD patients in the *T*4 stage was consistent with the previous result that patients with *T*4 stage had the highest risk score. In terms of the *N* stage (Figure 6(f)), the *N*3 stage contained only one LUAD sample, and therefore, its impact on patient prognosis was ignored. Patients with the *N*0 stage had the longest survival time compared with those with the *N*2 stage who had the shortest survival time. The allocation of risk scores and stratified prognosis according to other clinical characteristics, including age, sex, and *M* stage, are detailed in Supplementary Figure 2.

3.7. Subgroup Analysis of the Prognostic Signature. After establishing a correlation between hypoxia and ferroptosis score-related gene signatures and the aforementioned clinicopathological traits, we aimed to measure whether our model's prognostic efficacy can be utilized for clinical factors. Five patients were separated according to the indicated subgroups, and then data stratification was executed according to age, sex, pathological tumor stage, pathological *T* stage, pathological *N* stage, and pathological *M* stage. The hypoxia and ferroptosis score-related gene signature was able to differentiate between prognoses in all subgroups except for *T*3-*T*4 and *M*1 features, implying a clinically and statistically significant prognostic value (Figure 7).

Table 3: Association analysis shows that clinical characteristics correlate results with different risk groups in the TCGA test set.

	Expression			
	Total ($N = 135$)	High ($N = 56$)	Low ($N = 79$)	P-value
Gender				
Female	73 (54.1%)	28 (50.0%)	45 (57.0%)	0.532
Male	62 (45.9%)	28 (50.0%)	34 (43.0%)	
Age (years)				
≥60	97 (71.9%)	35 (62.5%)	62 (78.5%)	0.0658
<60	38 (28.1%)	21 (37.5%)	17 (21.5%)	
Pathologic stage				
Stage I	73 (54.1%)	25 (44.6%)	48 (60.8%)	0.159
Stage II	31 (23.0%)	13 (23.2%)	18 (22.8%)	
Stage III	23 (17.0%)	13 (23.2%)	10 (12.7%)	
Stage IV	8 (5.9%)	5 (8.9%)	3 (3.8%)	
T stage				
*T*1	48 (35.6%)	16 (28.6%)	32 (40.5%)	0.506
*T*2	68 (50.4%)	31 (55.4%)	37 (46.8%)	
*T*3	13 (9.6%)	7 (12.5%)	6 (7.6%)	
*T*4	5 (3.7%)	2 (3.6%)	3 (3.8%)	
*T*X	1 (0.7%)	0 (0%)	1 (1.3%)	
M stage				
*M*0	91 (67.4%)	35 (62.5%)	56 (70.9%)	0.381
*M*1	8 (5.9%)	5 (8.9%)	3 (3.8%)	
*M*X	36 (26.7%)	16 (28.6%)	20 (25.3%)	
N stage				
*N*0	86 (63.7%)	31 (55.4%)	55 (69.6%)	0.094
*N*1	27 (20.0%)	13 (23.2%)	14 (17.7%)	
*N*2	18 (13.3%)	11 (19.6%)	7 (8.9%)	
*N*3	1 (0.7%)	1 (1.8%)	0 (0%)	
*N*X	3 (2.2%)	0 (0%)	3 (3.8%)	

Table 4: Association analysis shows that clinical characteristics correlate results with different risk groups in the GSE31210 dataset.

	Expression			
	Total ($N = 226$)	High ($N = 106$)	Low ($N = 120$)	P-value
Gender				
Female	121 (53.5%)	53 (50.0%)	68 (56.7%)	0.385
Male	105 (46.5%)	53 (50.0%)	52 (43.3%)	
Age (years)				
≥60	130 (57.5%)	58 (54.7%)	72 (60.0%)	0.505
<60	96 (42.5%)	48 (45.3%)	48 (40.0%)	
Pathologic stage				
I	168 (74.3%)	65 (61.3%)	103 (85.8%)	<0.001
II	58 (25.7%)	41 (38.7%)	17 (14.2%)	
Smoke				
Ever-smoker	111 (49.1%)	58 (54.7%)	53 (44.2%)	0.147
Never-smoker	115 (50.9%)	48 (45.3%)	67 (55.8%)	

3.8. Independent Prognostic Role of Risk Scores. We investigated whether the risk score could be the only prognostic factor in LUAD patients using UCR and MCR. Based on the data from in TCGA set, UCR analyses showed that the risk score, stage, *T* stage, and *N* stage were significantly related to LUAD prognosis (Figure 8(a)). Subsequently, the above-mentioned variables ($P < 0.05$) were subjected to MCR analysis. The results identified hypoxia and ferroptosis score-related gene signature (risk score) and stage as two independent prognostic factors predicting prognosis in LUAD patients (Figure 8(b)).

LUAD patients' OS were predicted using a compound nomogram incorporating the risk score and stage. This approach was developed to provide a more accurate prediction tool for clinical practice (Figure 8(c)). It was evident from the calibration plots that the prognostic nomogram model accurately predicted patient survival with only a slight divergence from the actual outcomes (Figure 8(d)).

3.9. Differences in Hallmark Gene Sets between Two Group Patients. According to the results of the analysis of signature gene sets, signaling pathways converging in numerous biological processes were found to vary in two groups. Notably, hypoxia, TNFα signaling via NF-κB, mitotic spindle, and glycolysis were decreased in the low-risk group. On the other hand, the other group was preferentially associated with bile acid metabolism, pancreatic beta cells, and KRAS signaling (Figure 9 and Supplementary Table 10).

3.10. TME Infiltration Pattern of LUAD Based on Risk Score. The ssGSEA algorithms were used on the data to investigate how risk scores affect TME components. As the results of heatmaps and Wilcoxon tests performed on TCGA-LUAD datasets, the infiltration of several TME contents, such as

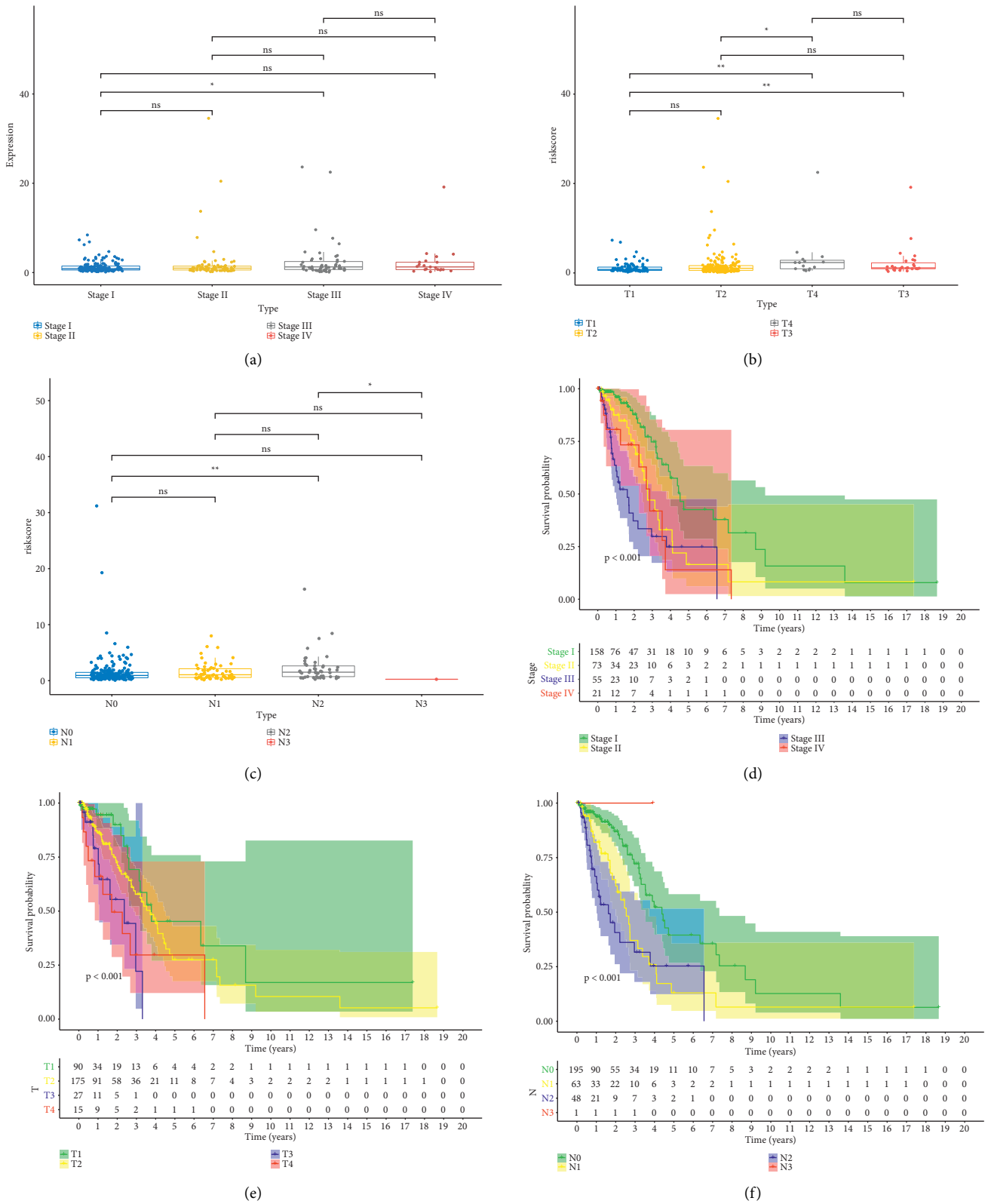

FIGURE 6: Wilcoxon analysis of the differing risk score distributions among various (a) stages, (b) *T* stages, and (c) *N* stages in the TCGA-LUAD cohort. The *K-M* survival curves of patients with different (d) stages, (e) *T* stages, and (f) *N* stages. $^{*}P < 0.05$, $^{**}P < 0.01$, and $^{***}P < 0.001$.

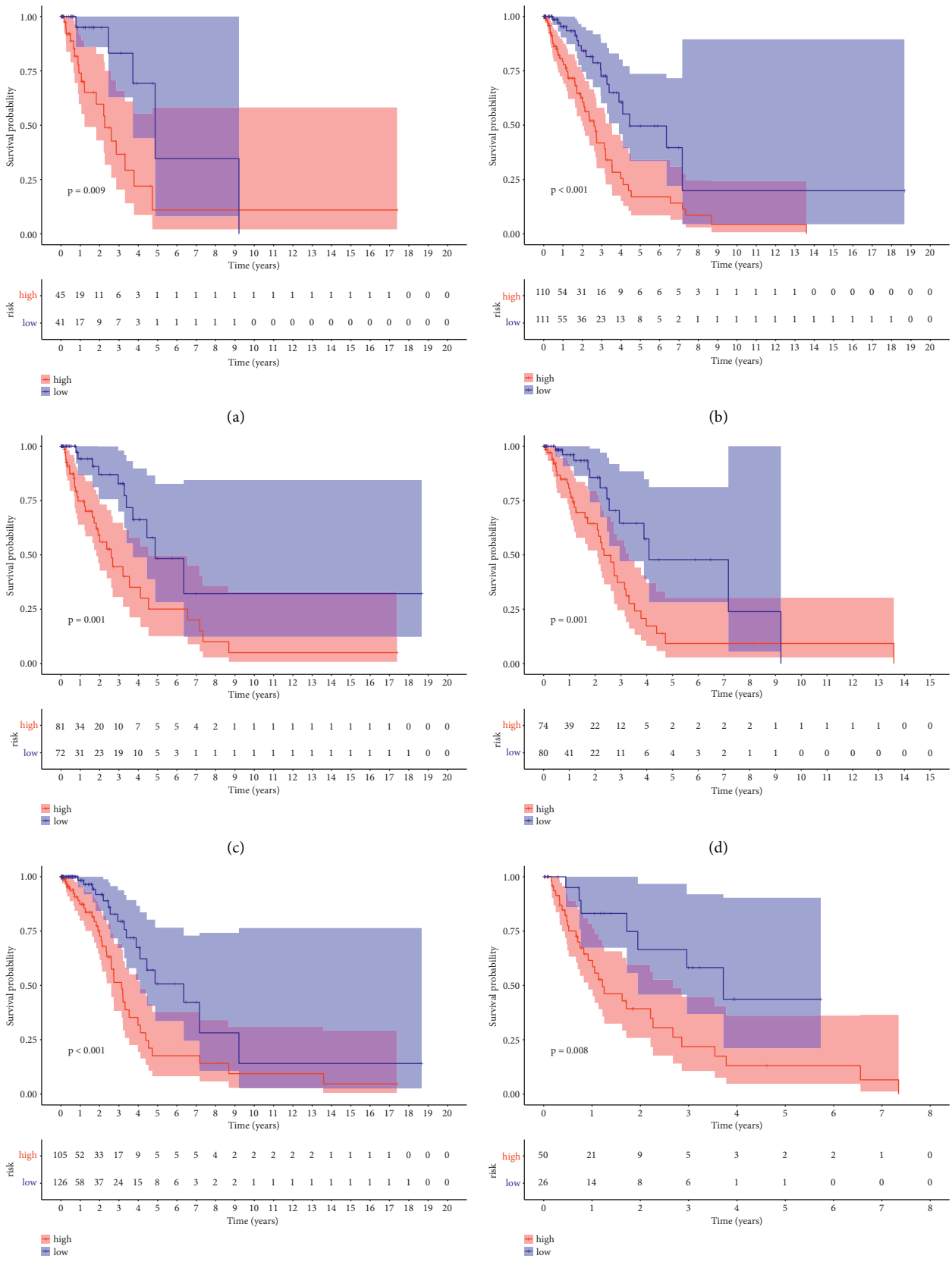

Figure 7: Continued.

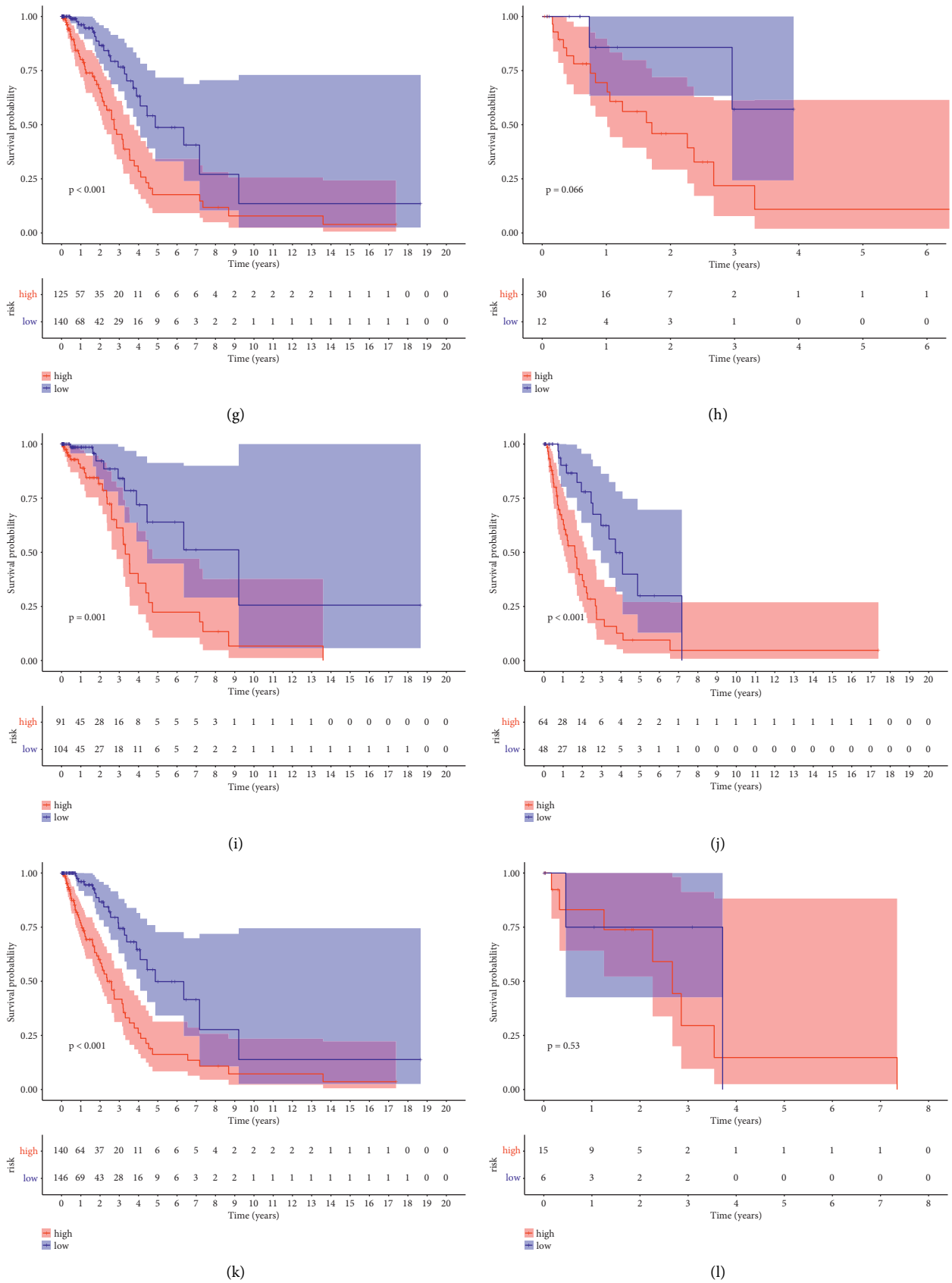

FIGURE 7: *K-M* survival analysis of the fourteen-gene risk score level in subgroups: (a) younger than 60 years old and older than 60 years old, (b) male and female, (c) stages I-II and stages III-IV, (d) T1 2 stage and T3-4 stage, (e) *N*0 stage and *N*+ stage, and (f) *M*0 stage and *M*1 stage.

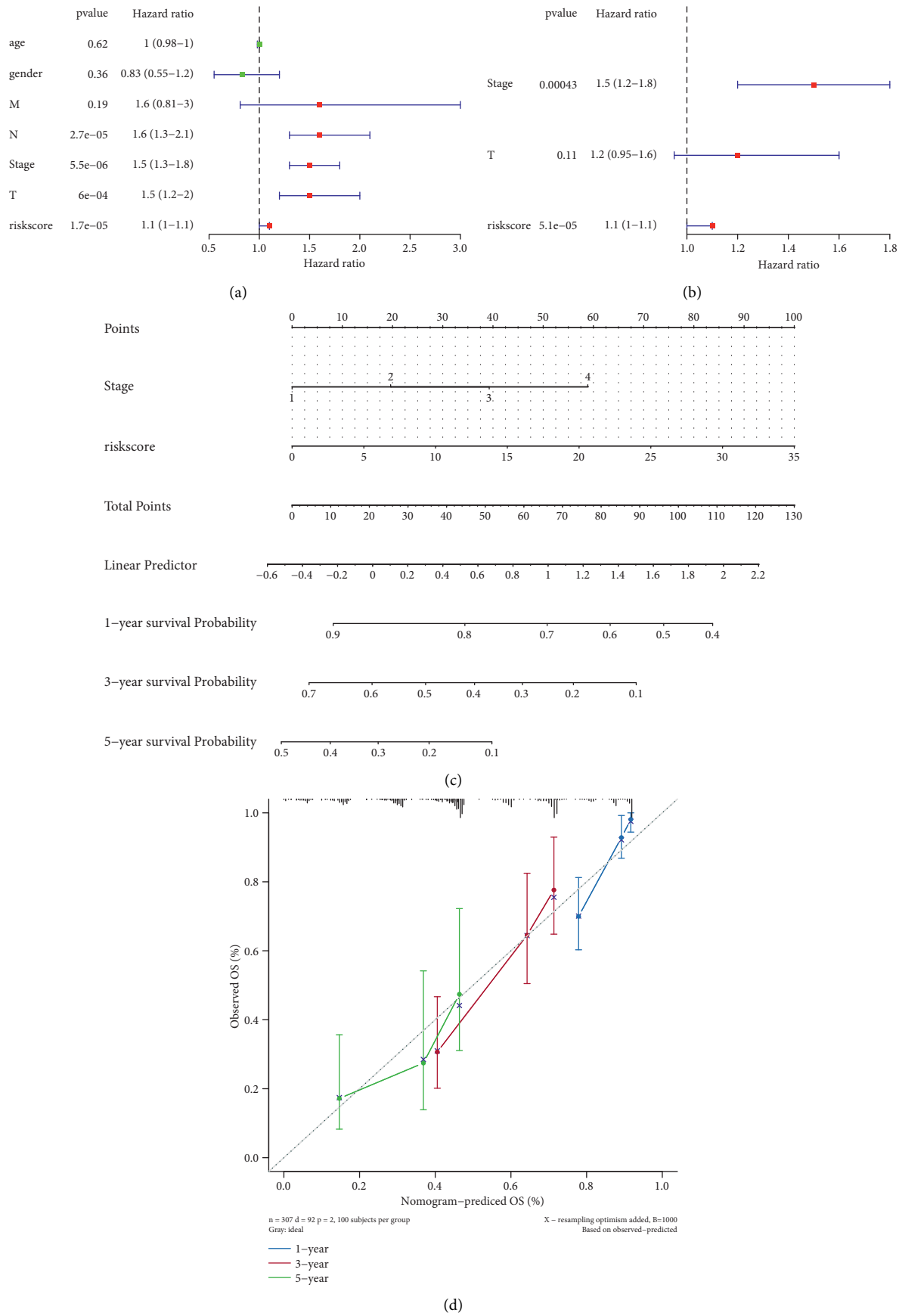

Figure 8: (a) Forrest plot of UCR analysis in LUAD. (b) Forrest plot of MCR analysis in LUAD. (c) A prognostic nomogram predicting OS of LUAD. (d) Calibration plots of the nomogram for predicting the OS in the TCGA-LUAD dataset.

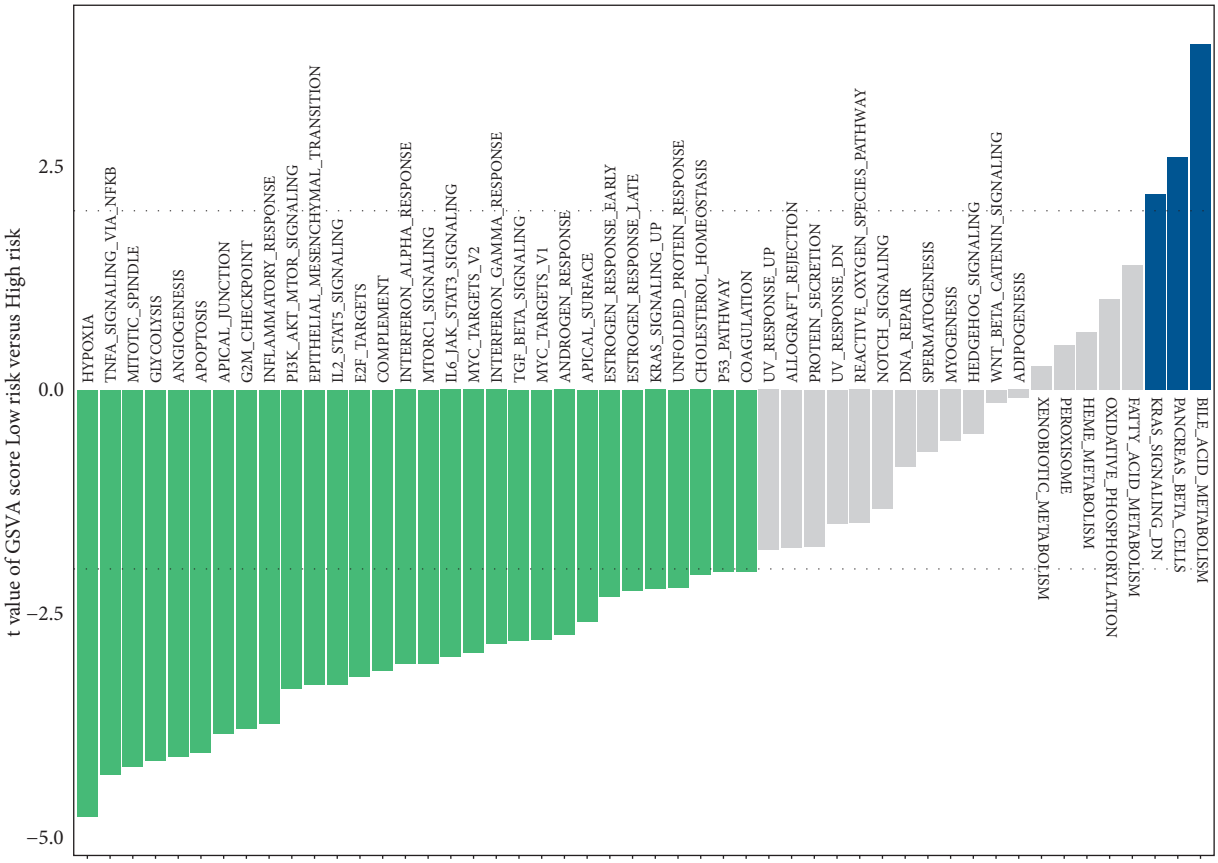

Figure 9: Gene set variation analysis. Differences in hallmark gene set activities scored by GSVA between two groups. T values are figured out using a linear model and the $|t| > 2$ as a cutoff value.

eosinophils and immature dendritic cells, was increased in the less-risk group, whereas the ICI of activated CD4 T cells and others was more in the other group, as depicted in Figure 10.

3.11. Validation of Seven Selected Prognostic Genes Based on qRT-PCR. According to the expression profiles of the identified DEGs (Supplementary Table 5), *TNS4*, *WFDC2*, and *ITGA2* were revealed to be all highly expressed, while *MAPK4*, *SMAD9*, *KLK11*, and *LAMA3* were all down-regulated in LUAD samples from the TCGA dataset. As shown in Figure 11, the high expression of *TNS4*, *WFDC2*, and *ITGA2* and the low expression of *MAPK4*, *SMAD9*, *KLK11*, and *LAMA3* in LUAD tissues ($n = 10$) were confirmed compared with the expression levels in the ANTs ($n = 10$).

4. Discussion

As well known, lung cancer is one of the general forms of malignancy globally. Nearly 80% of lung cancer patients have NSCLC, and nearly 50% have LUAD [42]. LUAD is a malignant tumor that affects the lungs and has a poor prognosis [43]. Although there have been breakthroughs in the treatment of patients with LUAD, the OS rate in these individuals remains low.

Ferroptosis is a particular kind of programmed cell death [17]. Ferroptosis-related research on lung cancer has mostly focused on the identification of related biomarkers that could induce ferroptosis [16, 44–46]. Hypoxia is also related to high proliferation rates in tumor cells [47]. Tumor hypoxia has a broad range of consequences, affecting a variety of biological systems, including metabolic changes, angiogenesis, and metastasis [48–50]. Numerous hypoxia-associated genes are associated with lung adenocarcinoma [51, 52]. However, no high-throughput research has been conducted to date to explore the possible prognostic value of them in LUAD.

Here, the ferroptosis and hypoxia Z-scores of each sample were estimated as clinical features based on the expression of ferroptosis and hypoxia-related genes identified in each sample, respectively. We obtained 23 modules, and the turquoise module showed no relationship with ferroptosis scores ($\text{cor} = -0.69$, $P = 3e - 10$) and hypoxia scores ($\text{cor} = -0.63$, $P = 8e - 68$), while the red module correlated more strongly with both scoring phenotypes, with ferroptosis score and hypoxia score. We then identified 152 common genes from the list of 8,974 hypoxia and ferroptosis

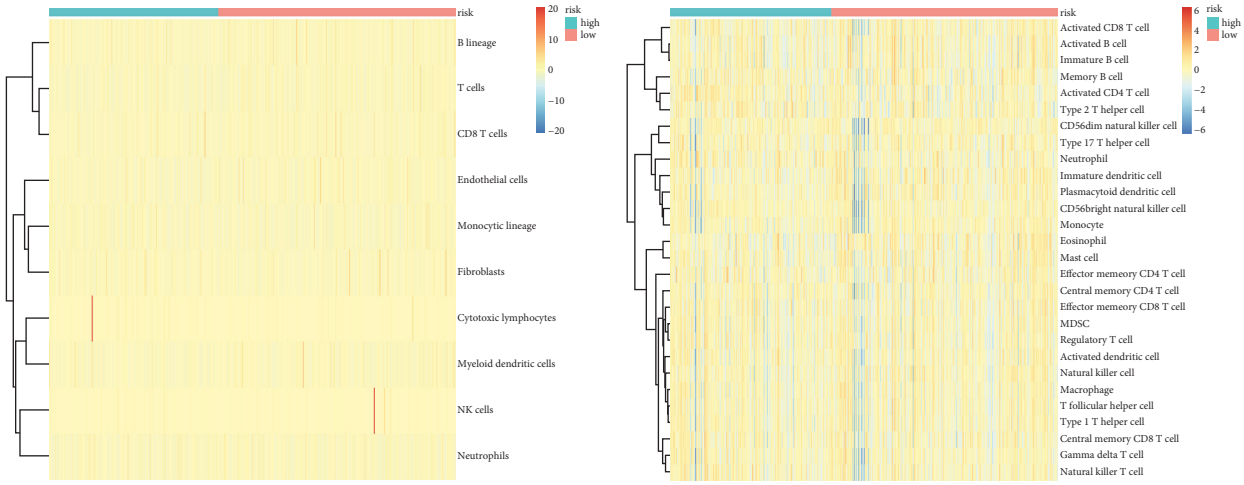

(a) (b)

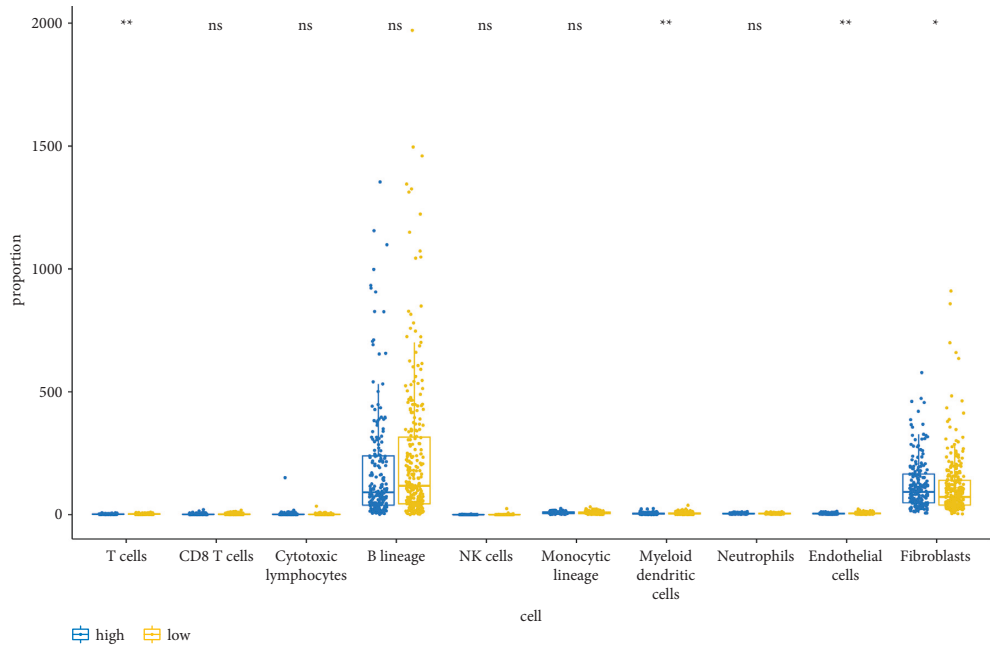

(c)

Figure 10: Continued.

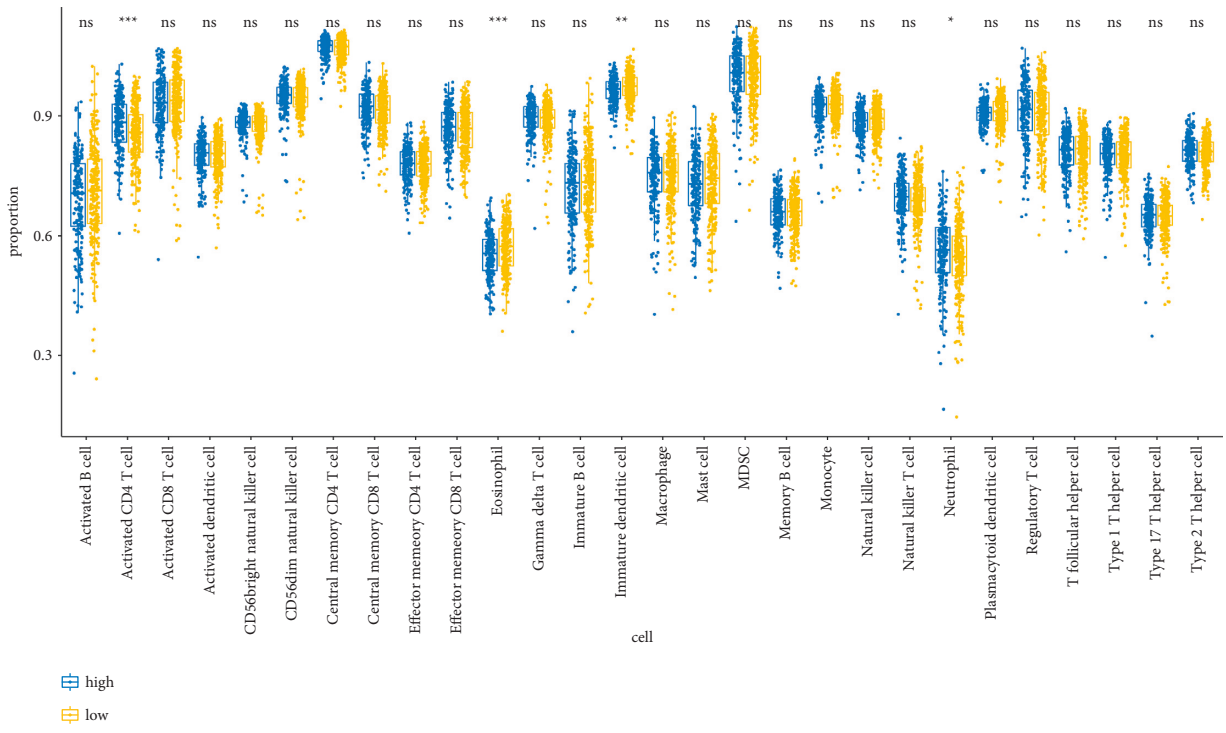

(d)

FIGURE 10: (a, b) Heatmap illustrating the distributions of immune cell subsets, fibroblasts, and endothelial cells assessed via MCP-counter (a) and ssGSEA (b) algorithms in the TCGA-LUAD cohort. (c, d) Wilcoxon analysis of the differing TME subtype distributions between two groups in the TCGA-LUAD cohort. $^{*}P < 0.05$, $^{**}P < 0.01$, and $^{***}P < 0.001$.

score-related genes and 1,969 LUAD-related DEGs, which were defined as DE-hypoxia and ferroptosis score-related genes, respectively.

Functional annotations obtained from Metascape indicated that DE-hypoxia and ferroptosis score-related genes were mainly enriched in "transcriptional misregulation in cancer," "endopeptidase inhibitor activity," and "positive regulation of cell projection organization." Overexpression of oncogenic transcription factors has been proven in recent research to change cells' core autoregulatory circuitry, which has long been recognized to induce tumorigenesis due to mutations in transcription factor genes [53]. Therefore, it is possible to intervene in this pathway to prevent the development of LUAD.

Of the 152 DE-hypoxia and ferroptosis score-related genes, 7.3% (17/152) were associated with prognosis in univariate Cox analysis. In addition, univariate Cox analysis identified six genes as protective markers and 11 genes as risk factors for patients with LUAD. Fourteen genes were identified using LASSO Cox regression (*MAPK4*, *TNS4*, *WFDC2*, *FSTL3*, *ITGA2*, *KLK11*, *PHLDB2*, *VGLL3*, *SNX30*, *KCNQ3*, *SMAD9*, *ANGPTL4*, *LAMA3*, and *STK32A*) to construct prognostic-related gene signatures and develop prognostic models to classify LUAD patients into two groups with various risks. Herein, we suggested that lower-risk patients seem to live longer. Additionally, we built a nomogram using MCR analysis and proved its predictive ability using ROC curves, calibration plots, and decision curves.

MAPK4 overexpression promotes LUAD progression [54]. Tensin 4 (*TNS4*) is involved in MET-induced cell motility and is connected to the GPCR signaling pathway. According to one study, increased *TNS4* expression leads to poor treatment outcomes in gastric cancer patients [55]. *WFDC2* is upregulated in lung cancer [56–58] and has thus recognized the clinical application of *WFDC2* as a serum tumor marker in the early diagnosis and efficacy monitoring of lung cancer [59]. In addition, in a study of individuals with LUAD, Song et al. [34] reported that *WFDC2* was substantially related to the TNM stage of LUAD and prognosis of patients. Recent studies have reported substantial overexpression of *FSTL3* in a subset of cancers [60–62]. Additionally, in patients with NSCLC and thyroid carcinoma, *FSLT3* expression is substantially linked to lymph node metastasis and poor prognosis [60, 61]. *ITGA2* overexpression is essential for tumor development, metastasis, and motility, and this molecule triggers the overexpression of the STAT3 signaling pathway, thus promoting tumor progression [63]. KLK11 protein is expressed more in NSCLC serum, although *KLK11* mRNA levels are lower in cancerous lung tissues than in ANTs [64]. Leakage of these secreted proteins into the systemic circulation due to disruption of lung structure during angiogenesis or development may be the reason for this discrepancy between low mRNA levels and elevated serum protein levels in lung cancer [65]. It has been well studied that PHLDB2 is linked to a variety of malignancies

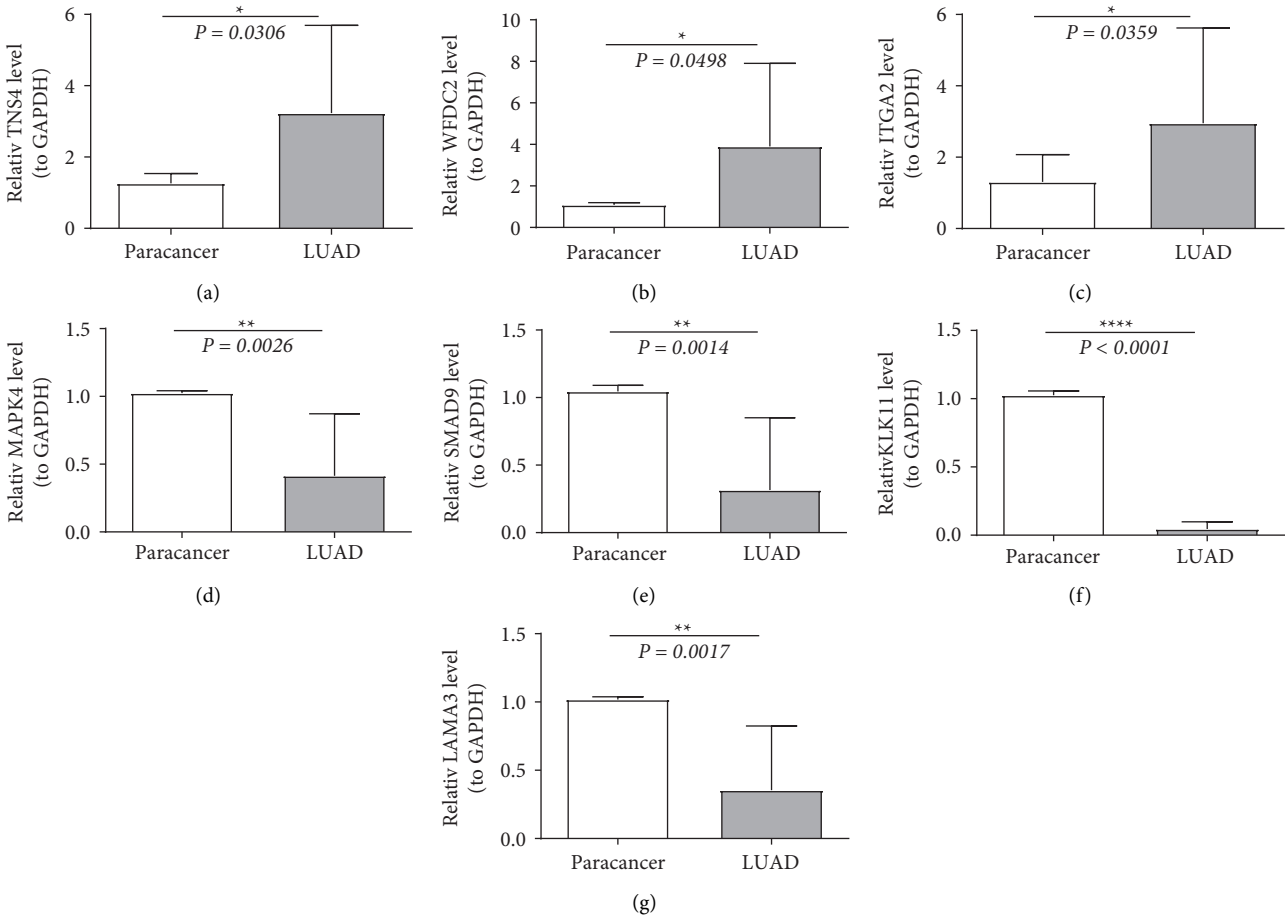

Figure 11: The high expression of TNS4 (a), WFDC2 (b), and ITGA2 (c) and the low expression of MAPK4 (d), SMAD9 (e), KLK11 (f), and LAMA3 (g) in LUAD tissues were confirmed compared to the paracancerous tissues.

[66, 67]. PHLDB2's primary role is to control migration through interacting with the transcription factors CLASPS, prickle 1, and liprin 1 [68, 69]. According to Ge et al., patients with lower PHLDB2 expression have a better prognosis [70]. VGLL3 is a unique Ets1 interacting partner that inhibits adipocyte differentiation and controls trigeminal nerve development [71]. VGLL3 acts as a coactivator of mammalian toxicity equivalency factors and is implicated in many kinds of cancers, including breast, colon, and lung cancers [72, 73]. Methylation, phosphorylation [74], and dephosphorylation of SMAD9 may function in the progression of lung cancer [75]. Tumor cell-derived human angiopoietin-like protein 4 (ANGPTL4) has been shown to disrupt vascular endothelial cell connections, enhance pulmonary capillary permeability, and facilitate tumor cell protrusion through the vascular endothelium, which is involved in lung cancer [76]. Through the synergistic action of AP-1 binding sites [77], the epithelial enhancer mediates the production of laminin subunit alpha 3 (LAMA3), which is associated with tumor progression. Xu et al. [78] reported that it was discovered that the inhibition of *LINC00628* decreased LUAD cell proliferation and drug resistance by lowering the methylation of the *LAMA3* promoter. STK32A is important in cellular balance and transcription factor phosphorylation, together with cell cycle regulation, and its overexpression leads to enhanced NSCLC cell progression, as well as enhanced NF-κB p65 phosphorylation and inhibition of apoptosis [79]. *SNX30* encodes sorted nexin-30 protein, a member of the sorted nexin, which a large class of proteins localized in the cytoplasm with membrane-bound potential via a phospholipid-binding domain [80]. *KCNQ3* encodes a protein that regulates neuronal excitability, and *GCSH* encodes a mitochondrial protein that forms the glycine cleavage system [81]. However, there is a lack of research on the mechanisms of action of these two genes in cancer.

Following this assessment, KM survival studies demonstrated that the 14 prognosis-associated genes may have a contribution to the initiation and development of LUAD in certain individuals. It came as a surprise to observe that risk scores for the 14-gene prognostic profile were shown to be strongly correlated with the OS in LUAD patients in two cohorts split by the TCGA and one GEO validation cohort. We discovered that modulation of the prognostic gene profile was linked with the LUAD survival models (*T*, *N*, *M*, stage, sex, and age) in our study. Furthermore, the nomogram of independent risk factors, which included risk score models, had a good predictive value and might assist clinicians in making optimum treatment choices to enhance

the OS rates of patients with LUAD in the future. These results suggest that hypoxia- and ferroptosis-related genes were indispensable in the construction of prognostic models for LUAD development and that they may have the potential to act as OS biomarkers.

Our findings suggested that the signaling pathways that converge in various biological processes differ between two groups, and the hypoxia, TNFα, signaling via NF-κB, mitotic spindle, and glycolysis were significantly down-regulated in the less-risk group. Additionally, 14 prognosis-related genes in LUAD, including one hypoxia-related gene, *ANGPTL4*, were significantly expressed in the tumor tissues. This finding reflects the dependence of LUAD on hypoxia and the heterogeneity of hypoxia responses in the low- and high-risk groups. Hypoxia heterogeneity indicates its involvement in promoting a phenotypic variety of cancer cells in the TME, which promotes metastasis and therapeutic resistance. Li et al. [82] demonstrated that suppressing NLRP2 boosted cell proliferation through NF-κB signaling activation, thus resulting in an EMT phenotype in LUAD cells. Therefore, the regulatory pathways involved in NF-κB also function in the progression of LUAD. The evidence implies that LUAD pathogenesis is a complicated biological process involving multiple genes. Apart from that, dysregulation of multiple genes may contribute to the progression of LUAD by a variety of distinct processes. The differences in GSVA signatures and prognostic genes between the two groups have the potential to be explored in a more in-depth study. These discoveries may, in general, open new avenues of investigation of additional molecular mechanisms of LUAD for academics and physicians.

Significant differences in immune infiltrating cell types between two groups were shown in this study. Interestingly, the enrichment fraction of activated CD4 *T* cells and neutrophils was enhanced in the high-risk group, whereas the enrichment fraction of eosinophil and immature dendritic cells was found in the low-risk group. Immune cells, neutrophils that infiltrate tumor tissue, called TANs, also play a role in antitumor immunity. TANs stimulate *T* cell responses in lung cancer rather than have an immunosuppressive effect [83]. In LUAD, overexpression of bridging granule genes is associated with a significant enhancement in infiltration of activated CD4 and CD8 *T* cells [84]. We hypothesize that the inflammatory response induced by immune cells may function in accelerating tumor cell mutations, which in turn may affect patient prognosis. The specific mechanisms by which the tumor immune microenvironment affects prognosis remain to be explored.

Here, a prognostic model of LUAD with general applicability was successfully developed and validated based on hypoxia and ferroptosis. In addition, we performed experiments to validate the 14 molecules in the model. Of these, seven molecules were validated by qRT-PCR to be significantly different between tumor and paracancerous tissues. However, our study has some limitations. Due to the lack of studies on hypoxia and ferroptosis in tumors, the information provided by MSigDB and FerrDB websites may be inaccurate, as the references were manually obtained from previous studies. More studies will do to validate the roles of these fundamental prognostic genes' hypoxia- and ferroptosis regulation roles in LUAD [3]. Both cohorts (TCGA-LUAD and 1 GEO cohort) were used to construct predictive signature. This hypoxia- and ferroptosis-predictive signal may be more reliable if examined in our research center's prospective clinical trial cohort.

5. Conclusion

Hypoxia and ferroptosis are two major mechanisms associated with lung adenocarcinoma development. In this research, the candidate genes associated with hypoxia and ferroptosis scores were identified; as a result, we have found a 14-gene signature and developed a predictive nomogram that could accurately predict OS in individuals with LUAD. These results may be useful in facilitating the making of medical decisions and personalizing therapeutic interventions.

Abbreviations

LUAD:	Lung adenocarcinoma
TCGA:	The Cancer Genome Atlas
ssGSEA:	Single sample gene set enrichment analysis
WGCNA:	Weighted gene coexpression network analysis
LASSO:	Least absolute shrinkage and selection operator
ROC:	Receiver operating characteristic
MAPK4:	Mitogen-activated protein kinase 4
TNS4:Tensin 4WFDC2:	Tensin 4WFDC2:WAP four-disulfide core domain 2
FSTL3:	Follistatin-like 3
ITGA2:	Integrin subunit alpha 2
KLK11:	Kallikrein-related peptidase 11
PHLDB2:	Pleckstrin homology like domain family *B* member 2
VGLL3:	Vestigial like family member 3
SNX30:	Sorting nexin family member 30
KCNQ3:	Potassium voltage-gated channel subfamily *Q* member 3
SMAD9:	SMAD family member 9
ANGPTL4:	Angiopoietin-like 4
LAMA3:	Laminin subunit alpha 3
STK32A:	Serine/threonine kinase 32A
GSVA:	Gene set variance analysis
NSCLC:	Non-small-cell lung cancer
FSP1:	S100 calcium-binding protein A4
MAPK:	Mitogen-activated kinase-like protein
NRF2:	Nuclear factor erythroid 2-like 2
TME:	Tumor microenvironment
HIF1A:Hypoxia-inducible factor 1-αHILPDA:	Hypoxia-inducible factor 1-αHILPDA:Hypoxia-inducible lipid droplet-associated

DEGs:	Differentially expressed genes
GSVA:	Gene set variation analysis
K-M:	Kaplan–Meier
AUC:	Area under the curve
OS:	Overall survival
HR:	Hazard ratio
CI:	Confidence interval
TANs:	Tumor-associated neutrophils.

Data Availability

The datasets used and/or analyzed during the current study are available from the corresponding author upon reasonable request.

Disclosure

Chang Liu, Yan-Qin Ruan, and Lai-Hao Qu are the co-first authors.

Conflicts of Interest

The authors declared no potential conflicts of interest with respect to the research, authorship, and/or publication of this article.

Authors' Contributions

Chang Liu contributed to conception; Yan-Qin Ruan, Lai-Hao Qu and Zhen-Hua Li contributed to methodology; Chao Xie, Ya-Qiang Pan, and Hao-Fei Li contributed to software; Chang Liu contributed to writing and original draft production; and Ding-Biao Li contributed to writing, reviewing, and editing. The final version was reviewed and approved by all authors. Chang Liu, Yan-Qin Ruan, and Lai-Hao Qu have the same contribution to this work, and they are the co-first authors.

Acknowledgments

The authors would like to acknowledge the GEO and TCGA network for sharing data. This study was sponsored by the Key Projects of Science and Technology Department of Yunnan Province (2018FA044) and the Key Laboratory of Tumor Immunological Prevention and Treatment of Yunnan Province (2017DG004).

Supplementary Materials

Supplementary Figure 1. Hypoxia and ferroptosis scores were used as phenotypic characteristics. To assess the correlation of all samples in the TCGA-LUAD database, we performed a cluster analysis to ensure the completeness of the samples. Supplementary Figure 2. The allocation of risk scores and stratified prognosis according to other clinical characteristics, including age, sex, and *M* stage, are detailed. Supplementary Table 1. The ssGSEA outputs for the detailed score results. Supplementary Table 2. 8314 genes. Supplementary Table 3. 660 genes. Supplementary Table 4. Significant increase in LUAD samples, and 1,063 were significantly decreased. Supplementary Table 5. The expression profiles of the identified DEGs. Supplementary Table 6. The risk score of each individual in the TCGA set. Supplementary Table 7. The patients with LUAD in the TCGA training set were separated into two groups with the cutoff value at 1.0803. Supplementary Table 8. We used the same algorithm to compute risk scores for the patients in the TCGA test cohort ($n = 142$). Supplementary Table 9. The GSE31210 dataset. Supplementary Table 10. The other group was preferentially associated with bile acid metabolism, pancreatic beta cells, and KRAS signaling. (*Supplementary Materials*)

References

[1] C. E. DeSantis, K. D. Miller, A. Goding Sauer, A. Jemal, and R. L. Siegel, "Cancer statistics for African Americans, 2019," *CA: A Cancer Journal for Clinicians*, vol. 69, no. 3, pp. 211–233, 2019.

[2] Q. Li, W. Ma, S. Chen et al., "High integrin $\alpha 3$ expression is associated with poor prognosis in patients with non-small cell lung cancer," *Translational Lung Cancer Research*, vol. 9, no. 4, pp. 1361–1378, 2020.

[3] R. S. Herbst, D. Morgensztern, and C. Boshoff, "The biology and management of non-small cell lung cancer," *Nature*, vol. 553, no. 7689, pp. 446–454, 2018.

[4] E. Bender, "Epidemiology: the dominant malignancy," *Nature*, vol. 513, no. 7517, pp. S2–S3, 2014.

[5] S. Shukla, J. R. Evans, R. Malik et al., "Development of a RNA-seq based prognostic signature in lung adenocarcinoma," *Journal of the National Cancer Institute*, vol. 109, no. 1, Article ID djw200, 2017.

[6] R. L. Siegel, K. D. Miller, and A. Jemal, "Cancer statistics, 2020," *CA: A Cancer Journal for Clinicians*, vol. 70, no. 1, pp. 7–30, 2020.

[7] X. T. Li, J. J. Yang, Y. L. Wu, and J. Hou, "Toward innovative combinational immunotherapy: a systems biology perspective," *Cancer Treatment Reviews*, vol. 68, pp. 1–8, 2018.

[8] J. L. Low, R. J. Walsh, Y. Ang, G. Chan, and R. A. Soo, "The evolving immuno-oncology landscape in advanced lung cancer: first-line treatment of non-small cell lung cancer," *Ther Adv Med Oncol*, vol. 11, 2019.

[9] B. Wang, T. Jing, W. Jin et al., "KIAA1522 potentiates TNFα-NFκB signaling to antagonize platinum-based chemotherapy in lung adenocarcinoma," *Journal of Experimental & Clinical Cancer Research*, vol. 39, no. 1, p. 170, 2020.

[10] M. Imielinski, A. H. Berger, P. S. Hammerman et al., "Mapping the hallmarks of lung adenocarcinoma with massively parallel sequencing," *Cell*, vol. 150, no. 6, pp. 1107–1120, 2012.

[11] M. Santarpia, A. Aguilar, I. Chaib et al., "Non-small-cell lung cancer signaling pathways, metabolism, and PD-1/PD-L1 antibodies," *Cancers*, vol. 12, no. 6, p. 1475, 2020.

[12] J. Li, F. Cao, H. L. Yin et al., "Ferroptosis: past, present and future," *Cell Death & Disease*, vol. 11, no. 2, p. 88, 2020.

[13] Y. Mou, J. Wang, J. Wu et al., "Ferroptosis, a new form of cell death: opportunities and challenges in cancer," *Journal of Hematology & Oncology*, vol. 12, no. 1, p. 34, 2019.

[14] S. Doll, F. P. Freitas, R. Shah et al., "FSP1 is a glutathione-independent ferroptosis suppressor," *Nature*, vol. 575, no. 7784, pp. 693–698, 2019.

[15] I. Poursaitidis, X. Wang, T. Crighton et al., "Oncogene-Selective sensitivity to Synchronous cell death following modulation of the Amino acid Nutrient cystine," *Cell Reports*, vol. 18, no. 11, pp. 2547–2556, 2017.

[16] S. W. Alvarez, V. O. Sviderskiy, E. M. Terzi et al., "NFS1 undergoes positive selection in lung tumours and protects cells from ferroptosis," *Nature*, vol. 551, no. 7682, pp. 639–643, 2017.

[17] P. Liu, D. Wu, J. Duan et al., "NRF2 regulates the sensitivity of human NSCLC cells to cystine deprivation-induced ferroptosis via FOCAD-FAK signaling pathway," *Redox Biology*, vol. 37, Article ID 101702, 2020.

[18] D. Kung-Chun Chiu, A. Pui-Wah Tse, C. T. Law et al., "Hypoxia regulates the mitochondrial activity of hepatocellular carcinoma cells through HIF/HEY1/PINK1 pathway," *Cell Death & Disease*, vol. 10, no. 12, p. 934, 2019.

[19] J. C. Walsh, A. Lebedev, E. Aten, K. Madsen, L. Marciano, and H. C. Kolb, "The clinical importance of assessing tumor hypoxia: relationship of tumor hypoxia to prognosis and therapeutic opportunities," *Antioxidants and Redox Signaling*, vol. 21, no. 10, pp. 1516–1554, 2014.

[20] B. Muz, P. de la Puente, F. Azab, and A. K. Azab, "The role of hypoxia in cancer progression, angiogenesis, metastasis, and resistance to therapy," *Hypoxia*, vol. 3, pp. 83–92, 2015.

[21] G. L. Semenza, "Hypoxia-inducible factors: mediators of cancer progression and targets for cancer therapy," *Trends in Pharmacological Sciences*, vol. 33, no. 4, pp. 207–214, 2012.

[22] D. Fukumura, J. Kloepper, Z. Amoozgar, D. G. Duda, and R. K. Jain, "Enhancing cancer immunotherapy using antiangiogenics: opportunities and challenges," *Nature Reviews Clinical Oncology*, vol. 15, no. 5, pp. 325–340, 2018.

[23] J. Koh, J. Y. Jang, B. Keam et al., "EML4-ALK enhances programmed cell death-ligand 1 expression in pulmonary adenocarcinoma via hypoxia-inducible factor (HIF)-1α and STAT3," *OncoImmunology*, vol. 5, no. 3, Article ID e1108514, 2016.

[24] M. Ruf, H. Moch, and P. Schraml, "PD-L1 expression is regulated by hypoxia inducible factor in clear cell renal cell carcinoma," *International Journal of Cancer*, vol. 139, no. 2, pp. 396–403, 2016.

[25] S. Terry, S. Buart, T. Z. Tan et al., "Acquisition of tumor cell phenotypic diversity along the EMT spectrum under hypoxic pressure: consequences on susceptibility to cell-mediated cytotoxicity," *OncoImmunology*, vol. 6, no. 2, Article ID e1271858, 2017.

[26] M. Zhao, Y. Zhang, H. Zhang et al., "Hypoxia-induced cell stemness leads to drug resistance and poor prognosis in lung adenocarcinoma," *Lung Cancer*, vol. 87, no. 2, pp. 98–106, 2015.

[27] A. C. Putra, K. Tanimoto, M. Arifin, and K. Hiyama, "Hypoxia-inducible factor-1α polymorphisms are associated with genetic aberrations in lung cancer," *Respirology*, vol. 16, no. 5, pp. 796–802, 2011.

[28] M. Yang, P. Chen, J. Liu et al., "Clockophagy is a novel selective autophagy process favoring ferroptosis," *Science Advances*, vol. 5, no. 7, Article ID eaaw2238, 2019.

[29] Y. Zou, M. J. Palte, A. A. Deik et al., "A GPX4-dependent cancer cell state underlies the clear-cell morphology and confers sensitivity to ferroptosis," *Nature Communications*, vol. 10, no. 1, p. 1617, 2019.

[30] D. C. Fuhrmann, A. Mondorf, J. Beifuß, M. Jung, and B. Brune, "Hypoxia inhibits ferritinophagy, increases mitochondrial ferritin, and protects from ferroptosis," *Redox Biology*, vol. 36, Article ID 101670, 2020.

[31] C. Ma, H. Luo, J. Cao et al., "Identification of a novel tumor microenvironment-associated eight-gene signature for prognosis prediction in lung adenocarcinoma," *Frontiers in Molecular Biosciences*, vol. 7, Article ID 571641, 2020.

[32] A. Zhang, J. Yang, C. Ma, F. Li, and H. Luo, "Development and validation of a Robust ferroptosis-related prognostic signature in lung adenocarcinoma," *Frontiers in Cell and Developmental Biology*, vol. 9, Article ID 616271, 2021.

[33] Z. Dai, T. Liu, G. Liu et al., "Identification of clinical and tumor microenvironment characteristics of hypoxia-related risk signature in lung adenocarcinoma," *Frontiers in Molecular Biosciences*, vol. 8, Article ID 757421, 2021.

[34] C. Song, Z. Guo, D. Yu et al., "A prognostic nomogram Combining immune-related gene signature and clinical factors predicts survival in patients with lung adenocarcinoma," *Front Oncol*, vol. 10, p. 1300, 2020.

[35] H. Okayama, T. Kohno, Y. Ishii et al., "Identification of genes upregulated in ALK-positive and EGFR/KRAS/ALK-negative lung adenocarcinomas," *Cancer Research*, vol. 72, no. 1, pp. 100–111, 2012.

[36] M. Yamauchi, R. Yamaguchi, A. Nakata et al., "Epidermal growth factor receptor tyrosine kinase defines critical prognostic genes of stage I lung adenocarcinoma," *PLoS One*, vol. 7, no. 9, Article ID e43923, 2012.

[37] S. Hanzelmann, R. Castelo, and J. Guinney, "GSVA: gene set variation analysis for microarray and RNA-seq data," *BMC Bioinformatics*, vol. 14, no. 1, p. 7, 2013.

[38] J. D. Wang, H. S. Zhou, X. X. Tu et al., "Prediction of competing endogenous RNA coexpression network as prognostic markers in AML," *Aging (Albany NY)*, vol. 11, no. 10, pp. 3333–3347, 2019.

[39] Y. Zhou, B. Zhou, L. Pache et al., "Metascape provides a biologist-oriented resource for the analysis of systems-level datasets," *Nature Communications*, vol. 10, no. 1, p. 1523, 2019.

[40] A. Subramanian, P. Tamayo, V. K. Mootha et al., "Gene set enrichment analysis: a knowledge-based approach for interpreting genome-wide expression profiles," *Proc Natl Acad Sci U S A*, vol. 102, no. 43, pp. 15545–15550, 2005.

[41] K. J. Livak and T. D. Schmittgen, "Analysis of relative gene expression data using Real-time Quantitative PCR and the 2−ΔΔCT method," *Methods*, vol. 25, no. 4, pp. 402–408, 2001.

[42] H. X. Dong, R. Wang, X. Y. Jin, J. Zeng, and J. Pan, "LncRNA DGCR5 promotes lung adenocarcinoma (LUAD) progression via inhibiting hsa-mir-22-3p," *Journal of Cellular Physiology*, vol. 233, no. 5, pp. 4126–4136, 2018.

[43] S. Devarakonda, D. Morgensztern, and R. Govindan, "Genomic alterations in lung adenocarcinoma," *The Lancet Oncology*, vol. 16, no. 7, pp. e342–51, 2015.

[44] Y. J. Chen, T. I. Roumeliotis, Y. H. Chang et al., "Proteogenomics of non-smoking lung cancer in East Asia Delineates molecular signatures of pathogenesis and progression," *Cell*, vol. 182, no. 1, pp. 226–244.e17, 2020.

[45] O. S. Kwon, E. J. Kwon, H. J. Kong et al., "Systematic identification of a nuclear receptor-enriched predictive signature for erastin-induced ferroptosis," *Redox Biology*, vol. 37, Article ID 101719, 2020.

[46] J. S. Lou, L. P. Zhao, Z. H. Huang et al., "Ginkgetin derived from Ginkgo biloba leaves enhances the therapeutic effect of cisplatin via ferroptosis-mediated disruption of the Nrf2/HO-1 axis in EGFR wild-type non-small-cell lung cancer," *Phytomedicine*, vol. 80, Article ID 153370, 2021.

[47] M. C. Brahimi-Horn, J. Chiche, and J. Pouyssegur, "Hypoxia and cancer," *Journal of Molecular Medicine (Berlin)*, vol. 85, no. 12, pp. 1301–1307, 2007.

[48] K. L. Eales, K. E. R. Hollinshead, and D. A. Tennant, "Hypoxia and metabolic adaptation of cancer cells," *Oncogenesis*, vol. 5, no. 1, Article ID e190, 2016.

[49] D. M. Gilkes, G. L. Semenza, and D. Wirtz, "Hypoxia and the extracellular matrix: drivers of tumour metastasis," *Nature Reviews Cancer*, vol. 14, no. 6, pp. 430–439, 2014.

[50] B. L. Krock, N. Skuli, and M. C. Simon, "Hypoxia-induced angiogenesis: good and evil," *Genes & Cancer*, vol. 2, no. 12, pp. 1117–1133, 2011.

[51] L. Moreno Leon, M. Gautier, R. Allan et al., "The nuclear hypoxia-regulated NLUCAT1 long non-coding RNA contributes to an aggressive phenotype in lung adenocarcinoma through regulation of oxidative stress," *Oncogene*, vol. 38, no. 46, pp. 7146–7165, 2019.

[52] X. Cao, X. Fang, W. S. Malik et al., "TRB3 interacts with ERK and JNK and contributes to the proliferation, apoptosis, and migration of lung adenocarcinoma cells," *Journal of Cellular Physiology*, vol. 235, no. 1, pp. 538–547, 2020.

[53] T. I. Lee and R. A. Young, "Transcriptional regulation and its misregulation in disease," *Cell*, vol. 152, no. 6, pp. 1237–1251, 2013.

[54] W. Wang, T. Shen, B. Dong et al., "MAPK4 overexpression promotes tumor progression via noncanonical activation of AKT/mTOR signaling," *Journal of Clinical Investigation*, vol. 129, no. 3, pp. 1015–1029, 2019.

[55] K. Sakashita, K. Mimori, F. Tanaka et al., "Prognostic relevance of Tensin4 expression in human gastric cancer," *Annals of Surgical Oncology*, vol. 15, no. 9, pp. 2606–2613, 2008.

[56] E. Wojcik, J. Tarapacz, U. Rychlik et al., "Human epididymis protein 4 (HE4) in patients with small-cell lung cancer," *Clin Lab*, vol. 62, no. 9, pp. 1625–1632, 2016.

[57] S. I. Choi, M. A. Jang, B. R. Jeon, H. B. Shin, Y. K. Lee, and Y. W. Lee, "Clinical usefulness of human epididymis protein 4 in lung cancer," *Ann Lab Med*, vol. 37, no. 6, pp. 526–530, 2017.

[58] W. Huang, S. Wu, Z. Lin, P. Chen, and G. Wu, "Evaluation of HE4 in the diagnosis and follow up of non-small cell lung cancers," *Clin Lab*, vol. 63, no. 3, pp. 461–467, 2017.

[59] Q. Zeng, M. Liu, N. Zhou, L. Liu, and X. Song, "Serum human epididymis protein 4 (HE4) may be a better tumor marker in early lung cancer," *Clinica Chimica Acta*, vol. 455, pp. 102–106, 2016.

[60] L. Gao, X. Chen, Y. Wang, and J. Zhang, "Up-regulation of FSTL3, regulated by lncRNA DSCAM-AS1/miR-122-5p Axis, promotes proliferation and migration of non-small cell lung cancer cells," *OncoTargets and Therapy*, vol. 13, pp. 2725–2738, 2020.

[61] G. Panagiotou, W. Ghaly, J. Upadhyay, K. Pazaitou-Panayiotou, and C. S. Mantzoros, "Serum follistatin is increased in thyroid cancer and is associated with Adverse tumor characteristics in humans," *The Journal of Clinical Endocrinology & Metabolism*, vol. 106, no. 5, pp. e2137–e2150, 2021.

[62] J. Du, X. Yan, S. Mi et al., "Identification of prognostic model and biomarkers for cancer Stem cell characteristics in glioblastoma by network analysis of Multi-Omics data and stemness Indices," *Frontiers in Cell and Developmental Biology*, vol. 8, Article ID 558961, 2020.

[63] D. Ren, J. Zhao, Y. Sun et al., "Overexpressed ITGA2 promotes malignant tumor aggression by up-regulating PD-L1 expression through the activation of the STAT3 signaling pathway," *Journal of Experimental & Clinical Cancer Research*, vol. 38, no. 1, p. 485, 2019.

[64] H. Sasaki, O. Kawano, K. Endo et al., "Decreased kallikrein 11 messenger RNA expression in lung cancer," *Clinical Lung Cancer*, vol. 8, no. 1, pp. 45–48, 2006.

[65] C. Planque, L. Li, Y. Zheng et al., "A multiparametric serum kallikrein panel for diagnosis of non-small cell lung carcinoma," *Clinical Cancer Research*, vol. 14, no. 5, pp. 1355–1362, 2008.

[66] G. Chen, T. Zhou, Y. Li, Z. Yu, and L. Sun, "p53 target miR-29c-3p suppresses colon cancer cell invasion and migration through inhibition of PHLDB2," *Biochemical and Biophysical Research Communications*, vol. 487, no. 1, pp. 90–95, 2017.

[67] S. J. Stehbens, M. Paszek, H. Pemble, A. Ettinger, S. Gierke, and T. Wittmann, "CLASPs link focal-adhesion-associated microtubule capture to localized exocytosis and adhesion site turnover," *Nature Cell Biology*, vol. 16, no. 6, pp. 558–570, 2014.

[68] B. C. Lim, S. Matsumoto, H. Yamamoto et al., *Journal of Cell Science*, vol. 129, no. 16, pp. 3115–3129, 2016.

[69] V. Astro, S. Chiaretti, E. Magistrati, M. Fivaz, and I. de Curtis, *Journal of Cell Science*, vol. 127, no. Pt 17, pp. 3862–3876, 2014.

[70] D. Ge, Y. Shao, M. Wang, H. Tao, M. Mu, and X. Tao, "RNA-seq-Based Screening in coal Dust-treated cells identified PHLDB2 as a novel lung cancer-related molecular marker," *BioMed Research International*, vol. 2021, pp. 1–8, 2021.

[71] E. Simon, N. Theze, S. Fedou, P. Thiebaud, and C. Faucheux, "Vestigial-like 3 is a novel Ets1 interacting partner and regulates trigeminal nerve formation and cranial neural crest migration," *Biol Open*, vol. 6, no. 10, pp. 1528–1540, 2017.

[72] K. Gambaro, M. C. Quinn, P. M. Wojnarowicz et al., "VGLL3 expression is associated with a tumor suppressor phenotype in epithelial ovarian cancer," *Molecular Oncology*, vol. 7, no. 3, pp. 513–530, 2013.

[73] Z. Helias-Rodzewicz, G. Perot, F. Chibon et al., "YAP1 and VGLL3, encoding two cofactors of TEAD transcription factors, are amplified and overexpressed in a subset of soft tissue sarcomas," *Genes, Chromosomes and Cancer*, vol. 49, no. 12, pp. 1161–1171, 2010.

[74] V. Dexheimer, J. Gabler, K. Bomans, T. Sims, G. Omlor, and W. Richter, "Differential expression of TGF-beta superfamily members and role of Smad1/5/9-signalling in chondral versus endochondral chondrocyte differentiation," *Scientific Reports*, vol. 6, no. 1, Article ID 36655, 2016.

[75] L. Gao, Q. Tian, T. Wu et al., "Reduction of miR-744 delivered by NSCLC cell-derived extracellular vesicles upregulates SUV39H1 to promote NSCLC progression via activation of the Smad9/BMP9 axis," *Journal of Translational Medicine*, vol. 19, no. 1, p. 37, 2021.

[76] X. Zhu, X. Guo, S. Wu, and L. Wei, "ANGPTL4 correlates with NSCLC progression and regulates epithelial-Mesenchymal Transition via ERK pathway," *Lung*, vol. 194, no. 4, pp. 637–646, 2016.

[77] T. Virolle, C. Coraux, O. Ferrigno, L. Cailleteau, J. P. Ortonne, and P. Pognonec, "Binding of USF to a non-canonical E-box following stress results in a cell-specific derepression of the

lama3 gene," *Nucleic Acids Research*, vol. 30, no. 8, pp. 1789–1798, 2002.

[78] S. F. Xu, Y. Zheng, L. Zhang et al., "Long non-coding RNA LINC00628 interacts epigenetically with the LAMA3 promoter and contributes to lung adenocarcinoma," *Molecular Therapy - Nucleic Acids*, vol. 18, pp. 166–182, 2019.

[79] F. Ma, Y. Xie, Y. Lei, Z. Kuang, and X. Liu, "The microRNA-130a-5p/RUNX2/STK32A network modulates tumor invasive and metastatic potential in non-small cell lung cancer," *BMC Cancer*, vol. 20, no. 1, p. 580, 2020.

[80] K. Haberg, R. Lundmark, and S. R. Carlsson, "SNX18 is an SNX9 paralog that acts as a membrane tubulator in AP-1-positive endosomal trafficking," *Journal of Cell Science*, vol. 121, no. 9, pp. 1495–1505, 2008.

[81] T. T. Sands, F. Miceli, G. Lesca et al., "Autism and developmental disability caused by KCNQ3 gain-of-function variants," *Annals of Neurology*, vol. 86, no. 2, pp. 181–192, 2019.

[82] T. Li, X. Li, R. Mao et al., "NLRP2 inhibits cell proliferation and migration by regulating EMT in lung adenocarcinoma cells," *Cell Biology International*, vol. 46, no. 4, pp. 588–598, 2022.

[83] E. B. Eruslanov, P. S. Bhojnagarwala, J. G. Quatromoni et al., "Tumor-associated neutrophils stimulate T cell responses in early-stage human lung cancer," *Journal of Clinical Investigation*, vol. 124, no. 12, pp. 5466–5480, 2014.

[84] Y. K. Chae, W. M. Choi, W. H. Bae et al., "Overexpression of adhesion molecules and barrier molecules is associated with differential infiltration of immune cells in non-small cell lung cancer," *Scientific Reports*, vol. 8, no. 1, p. 1023, 2018.

Hindawi
Journal of Oncology
Volume 2022, Article ID 7973726, 12 pages
https://doi.org/10.1155/2022/7973726

Research Article

The Clinical and Genetic Characteristics in Children with Idiopathic Hypogonadotropin Hypogonadism

Qiong Zhou,[1] Wenbin Sheng,[1] Suhong Yang,[1] and Chaochun Zou[2]

[1]*Hangzhou Children's Hospital, Hangzhou 310005, China*
[2]*Children's Hospital of Zhejiang University School of Medicine, Hangzhou 310052, China*

Correspondence should be addressed to Chaochun Zou; zcc14@zju.edu.cn

Received 18 July 2022; Revised 24 August 2022; Accepted 26 August 2022; Published 19 September 2022

Academic Editor: Muhammad Muddassir Ali

Background. Idiopathic hypogonadotropin hypogonadism (IHH) is caused by hypothalamic-pituitary-gonadal axis dysfunction. This is divided into Kallmann syndrome which has an impaired sense of smell and hypogonadotropin hypogonadism with normal olfactory (nIHH sense. Approximately 60% of patients are associated with Kallmann syndrome, whereas there are approximately 40% with hypogonadotropin hypogonadism (nIHH). This disease is associated with various variants in genes along with different phenotypic characteristics, and even those gene variations could also lead to the cancer formation in patients. So, current study has been designed to investigate and to better understand the characteristics of various IHH-associated genes and the correlation between IHH genes and phenotype. *Methods*. The cohort included 14 children with IHH (6 patients of KS and 8 patients of IHH), including 13 boys and 1 girl. Exclusion criteria are as follows: diagnosis of secondary hypogonadotropin hypogonadism due to tumor, trauma, drugs, or other systemic diseases. Clinical data and genetic results were analyzed. *Results*. Almost all male patients showed micropenis (12/13, 92.3%), and few of them had cryptorchidism (5/13, 41.7%). A total of 6 genes, CHD7, PROKR2, ANOS1, FGFR1, SEMA3A, and NDNF, were detected. CHD7 was the most common (11/17, 64.7%), and the main mutation type was missense mutation (14/16, 87.5%). Six reported variants and 10 new variants (5 genes, including entire ANSO1 duplicates) were found. Neonatal variation was detected in 3 patients with IHH. Eight patients inherited the variation from their father, while five patients inherited it from their mother. One patient had both FGFR1 and SEMA3A gene variants, while the other had two different CHD7 gene variants and entire ANSO1 repeats. According to ACMG criteria, 4 variants were pathogenic (P), 2 were possibly pathogenic (LP), and 8 had uncertain significance (US). In patients with P or LP (5/6, 83.3%), we found that extragonadal symptoms were more common. *Conclusions*. It was concluded that variations in the studied genes could lead to the IHH. Ten new variants have been reported which may lead to different symptoms of IHH. For CHD7 variants, the rare sequencing variants (RSVs) of P or LP showed commonly associated with CHARGE syndrome. Findings of the current study may help for the better diagnosis and treatment of IHH.

1. Introduction

Idiopathic hypogonadotropin hypogonadism (IHH) is due to the hypothalamic gonadotropin-releasing hormone (GnRH) neuron damage. This damage leads to impair secretion, or insufficient action, or decrease in pituitary gonadotropic hormone secretion which results in lack of sex gland function [1]. Its incidence is 1-10/100,000 with a male to female ratio of about 3.6 : 1 [1]. According to the presence of olfactory abnormalities, it can be divided into Kallmann syndrome (KS) and idiopathic hypogonadotropin hypogonadism of normal olfactory (nIHH). IHH has genetic heterogeneity and more than 40 genes have been confirmed to be associated with IHH, which accounts for more than 50% of all patients [2, 3]. In fact, the list of uncommon genes and candidate genes continues to grow [4]. Anosmin-1 gene (ANOS1), also named KAL1, is dominated by X-linked inheritance, and CHD7, FGFR1, FGF8, PROKR2, and SOX10 are dominated by autosomal dominant inheritance. In addition, autosomal recessive FEZF1 and PROK2 are mainly inherited in families with high

suspicion of KS. In recent years, IL17RD, SEMA3A, SEMA3E, NDNF, and ANOS1 genes have been found to be closely related to olfactory sense. In addition to hypothalamic gonadotropin-releasing hormone (GnRH) neurons and olfactory damage, several gene mutations have also been found to be associated with other physical abnormalities. ANOS1 may present unilateral renal hypoplasia [5], CHD7 may be associated with tooth development, hearing abnormality, short stature, and intellectual impairment, and FGF8 may be associated with hearing loss and cleft lip and palate, while FGFR1 may be associated with tooth development and cleft lip and palate [5]. Nevertheless, the association between the characteristic IHH phenotype and genotype has not been fully established. The purpose of this study was to better understand the characteristics of IHH genes and the correlation between IHH genes and phenotype, so as to help make better treatment plans for IHH patients and lay the foundation for further research.

2. Materials and Methods

2.1. Sampling and Study Plans. We reviewed all IHH patients with genetic diagnosis in the Children's Hospital of Zhejiang University School of Medicine and the Hangzhou Children's Hospital from 2017 to 2022. Their family history, clinical features, biochemical indicators including sexual hormone, imaging (bone age, sexual gonad, olfactory bulb, and pituitary), and genetic testing were collected.

Inclusion criteria are as follows: for children > 13 years of age in females or >14 years of age in males: (1) no spontaneous pubertal development or pubertal development arrest, (2) the level of sex hormones showed prepuberty (lower than normal, i.e., male serum androgen level ≤ 1 ng/mL and female serum estrogen level ≤20 pg/mL) [6], (3) there were no space-occupying lesions in imaging of hypothalamus and pituitary region, and (4) chromosome karyotype is normal and for female < 13 years old or male < 14 years old, (1) KS was diagnosed by MRI olfactory bulb, (2) the absence of minipuberty and , low levels of gonadotropins and sex hormones, and (3) genetic tests that may support diagnosis. Exclusion criteria are as follows: diagnosis of secondary hypogonadotropin hypogonadism due to tumor, trauma, drugs, or other systemic diseases.

This study was approved by the Ethics Committee of Children's Hospital of Zhejiang University School of Medicine and Hangzhou Children's Hospital.

2.2. Gene Analysis. In general, gonadal panel and whole exon sequencing (WES) were used for detection, and the genes contained were all IHH gene pointed out in the consensus [2]. Through ClinVar (http://www.ncbi.nlm.nih.gov/clinvar), pathogenic mutations were checked. Data interpretation rules were followed as per ACMG guidelines. For the variable names, refer to the rules of HGVS (http://www.hgvs.org/mutnomen/).

2.3. Annotation for Variants. Various database searches, general population database search, disease database search, literature search, mutation type specificity analysis, and computational prediction were performed. Allele frequencies in the gnomAD database were used to calculate OR and define RSV (MAF < 0.0001). Computational prediction consists of three parts: pathogenicity prediction in computer tools, alignment conservative analysis, and 3D visualization in 3D modeling software. Six computer tools (SIFT [7], Polyphen-2 [8], PROVEAN [9], Mutation Taster [10], CADD [11], and MetaSVM [12]) are used for predicting the pathogenicity of missense or code shifter, and two (Splice Site Score calculation and SpliceAI [13]) are used for splicing sites. We used Clustal W to align each human gene sequence with homolog of 25 other related species in UniProt database to judge the evolutionary conservation of each amino acid site. The more conserved the site, the more important it is for protein function, which indirectly reveals its pathogenicity. Amino acid changes were visualized using 3D modeling software ChimeraX. Using these spatial models, we compare the nature changes of wild and mutant amino acids and their contact relationships with other amino acids to predict the potential pathogenic effects of specific mutations on proteins.

2.4. Statistical Analysis. SPSS version 23 software package was used to check the normal distribution of continuous variables. Normal distribution variables are described by mean ± standard deviation, and nonnormal distribution variables were described by median and quartile distance. Category variables were expressed as percentages.

3. Results and Discussion

3.1. Clinical Features and Auxiliary Examination. The age of diagnosed children ranged from 2.1 to 18.7 years with a mean age of 12.44 ± 4.98 years. There were 13 males and 1 female. Among the 13 male children, 11 (84.6%) were 7.9 to 18.7 years old, and 6 (46.2%) were ≥14 years old. The female patient was diagnosed at 16.2 years old. There were 6 patients (42.9%) of KS and 8 patients (57.1%) of nIHH. In terms of genital characteristics, among the 13 male children, 12 patients (92.3%) had micropenis or (and) cryptorchidism, including 6 (50.0%) of simple micropenis and 5 (41.7%) of micropenis and cryptorchidism. There was no simple cryptorchidism, but one (nIHH3) had micropenis combined with penis descent and scrotal division. Of the 14 patients, 2 (14.3%) had normal genitalia.

In other clinical manifestations, 4 patients (28.6%) were obese or overweight, of which nIHH1, nIHH5, and nIHH7 were obese and nIHH2 was overweight. Three patients (21.4%), including KS1, KS2, and nIHH5, had short stature. Two patients (14.3%), KS5 and nIHH8, had slurred speech and mental retardation. One (7.1%, KS1) had psychomental abnormalities and gradually developed depression after diagnosis. One (7.1%, KS5) had hearing damage (mainly left ear), male breast development, and hypopigmentation in addition to pronunciation and intelligence defects. One (nIHH1) had a history of nephrotic syndrome at the age of 3 and had received glucocorticoids for 2 years with stable controlling. The only female patient (nIHH8) had a history of ovarian teratoma in addition to slurred speech and mental retardation. nIHH5 is not only short stature and obesity but also diabetes and fatty liver caused by obesity. In the family history, 3 (21.4%) had fathers or mothers with delayed pubertal development, with KS3 and nIHH7 as fathers and nIHH6 as mothers.

In laboratory tests, except for one male infant, the luteinizing hormone (LH), follicle-stimulating hormone (FSH), and testosterone (T) measured at 6 months were 0.28 mIU/mL, 0.91 mIU/mL, and 0.2 ng/mL, respectively. The levels of LH, FSH, and T in 1 infant and 3 school-age boys were all lower than the normal level in this age group. T of 8 male children ≥ 12 years old were all lower than 0.5 ng/mL, and their LH and FSH levels were normal or lower than normal [14, 15]. In one female child, LH, FSH and estradiol (E2) were far below the normal low limit [14, 15]. Five of the 13 boys underwent human chorionic gonadotropin (HCG) stimulation test to assess testicular function, of which only one was normal (testosterone > 1 ng/mL), and the other four did not reach 1 ng/mL, nor increased by more than 3 times compared with the baseline value. Five patients underwent gonadotropin-releasing hormone (GnRH) stimulation test. The statistics of the post-LH and -FSH levels ranged from 0.44 mIU/mL to 6.16 mIU/mL and 1.11 mIU/mL to 6.3 mIU/mL, respectively. B ultrasound of testis in 13 boys showed that testis was significantly smaller than normal range. All of the above can be seen in Tables 1 and 2. In the imaging examination, the girl's uterus and ovary B ultrasound indicated that she was in the state of puberty. The pituitary MR of 14 patients showed no space occupying or organic lesions, MRI examination of olfactory bulb was completed in 10 boys, and absence or dysplasia of olfactory bulb, olfactory groove, and olfactory bundle was found in 6 boys (Figure 1).

3.2. Molecular Genetic Analysis. A total of 7 genes associated with IHH were identified in 14 patients, including 10 of CHD7, one of NDNF, one of ANOS1, one of FGFR1, one of SEMA3A, one of FGF8, and one of PROKR2, respectively. There were 16 variants in 14 patients. Copy number variation of ANOS1 was found in one patient. The remains were all point mutations, including 2 splicing site mutations of CHD7 gene (KS1 and KS4), one coding mutation (insertion) of PROKR2 gene (nIHH7), and 12 missense mutations. nIHH1 has two missense mutations of CHD7 and ANOS1 repeat. nIHH5 had a missense mutation in FGFR1 and SEMA3A, respectively. Neonatal variation was found in 2 patients with IHH; 9 of the patients inherited the variation from their father and 5 from their mother, both of whose parents carried the heterozygous variation. There were 2 patients with c.1565G>T(p.G522V) variant.

Among the 15 point mutations, there were 9 novel variants including 2 splice site mutations and 1 frameshift mutation. The amino acid sites of 5 CHD7 variants were retrieved from ExAC database: c.409T>G(p.S137A), c.749G>A(p.R250H), c.1565G>T(p.G522V), c.59G>A(p.G20D), and c.2182G>A (p.D728N). However, in each gene variation database, CHD7 retrieved c.2182G>A(p.D728N), NDNF, FGFR1, FGF8, and SEMA3A but did not retrieve the mutations in this cohort. CHD7 c.1565G>T(p.G522V) in ClinVar database was reported in CHARGE syndrome, primary ovarian insufficiency, KS, and other diseases, and in MASTERMIND database notes 2007-2022, this variant was reported in as many as 10 studies. The mutation frequency was significantly higher than that of other mutations and was classified as hot spot mutation and currently classified as benign or likely benign. CHD7 c.409T>G(p.S137A) in the ClinVar database was also reported to be benign or likely benign, with no specific disease description. Other studies reported c.2182G>A(p.D728N) of CHD7 in IHH or CHARGE syndrome [16–18], c.1369A>G(p.T457A) of SEMA3A [19], and c.749G>A(p.R250H) of CHD7 in abnormal sexual development [20]. At the same time, no focal duplication of ANOS1 gene has been reported, and only multiple abnormal patients with multiple gene duplication have been reported [21]. After ClinGen and ClinVar data retrieval, at present, only prompt ANOS1 has sufficient evidence for haploinsufficiency, but no evidence for triplosensitivity; hence, it is currently considered to be uncertain significance.

We calculated pathogenicity predictions for all variants except copy number duplicates. First, the prediction results of c.409T>G(p.S137A) and c.1565G>T(p.G522V) of CHD7 in the three missense mutation software were consistent with the benign or likely benign conclusion suggested in the database (none of which was defined as pathogenicity). The remaining 10 missense mutations and 7 variants were predicted to have obvious pathogenicity. The c.59G>A(p.G20D) and c.2182G>A (p.D728N) amino acid sites of CHD were predicted to be pathogenic in only one of the three software. The R424H variant of FGFR1 was positive for all three predictors, but its predictive value was close to normal (Table 3). Then, 10 missense mutations (except c.409T>G(p.S137A) and c.1565G>T(p.G522V) of CHD7) were calculated again with three software of predictable coding and noncoding regions. The pathogenicity of the two splicing sites was predicted. Results suggested pathogenicity in all (at least 2 out of 3) (Table 4). Second, using all 12 missense mutations as subjects, the results showed that in c.59G>A(p.G20D), c.749G>A(p.R250H), c.2724G>T(p.W908C), c.2744A>G(p.D915G), and c.4153G>C(p.D1385H) of CHD7, c.1369A>G(p.T457A) of SEMA3A, and c.368G>A(p.G123E) of FGF8, wild-type residues at these seven specific sites were highly conserved in 25 different species (Figures 2 and 3). Third, since 3D models of Trp908Cys, Asp915Gly, and Asp1385His for CHD7, Thr457Ala for SEMA3A, Ile480Asn for NDNF, and Arg298Thrfs∗2 for PROKR2 (manufactured by Swiss Model) are available, we can see macroscopic changes in protein structure as well as the direct effects of individual amino acid changes. For all six variants, the residue size, charge, and hydrophobicity varied at specific sites. In addition, the Arg298Thrfs∗2 of PROKR2, due to frameshift variation, leads to the premature termination of protein synthesis and the disappearance of long sequences of amino acids on the structure. In CHD7, for Trp908Cys, 16 contacts disappeared, forming a new hydrogen bond (H-bond). For Asp915Gly, it changed from acidic amino acid to nonpolar hydrophobic amino acid. One old contact broke. For Asp1385His, from acidic amino acid to alkaline amino acid, 4 old contacts and 2 H-bonds broke; meanwhile, 6 new contacts and 1 clashes formed. For NDNF Ile480Asn, nonpolar hydrophobic amino acids became acidic, changing from 6 old contacts to 8 new contacts, and 1 clash formed. For Thr457Ala of SEMA3A, the polar neutral amino acid becomes nonpolar hydrophobic, and 2 new contacts and 1 H-bonded formed. For Arg298Thrfs∗2 of PROKR2, in addition to the disappearance of amino acid sequence, there was also a great change at the termination codon, from alkaline amino acid to polar neutral amino acid, 7 contacts lost, and 1 new H-

Table 1: Clinical characteristics of 6 patients with KS.

No.	Gender	Diagnosis age (y)	Puberty	Height (cm)	Micropenis/ cryptorchidism	Specific disease history/associated phenotypes	Family history	TV (mL)	HCG test: basal/post T (ng/mL)	LHRH test: basal/post LH (mIU/mL)	LHRH test: basal/post FSH (mIU/mL)	Olfaction/OB on MRI
KS1	M	13.0	Absent	145.0	+/+	Depressive disorder, short stature		L0.5, R0.4	<0.02/-	<0.1/-	0.4/-	Hyposmia/abnormal
KS2	M	15.6	Absent	152.5	+/-	Short stature		L0.3, R0.5	0.40/0.86	<0.07/1.77	0.61/5.34	Hyposmia/abnormal
KS3	M	13.2	Absent	150.0	+/+		CDGP (father), younger bother with same mutation	L0.95, R0.5	0/0.26	<0.07/-	3.62/-	Normal/abnormal
KS4	M	15.7	Absent	164.8	+/+			L0.53, R0.76	0.13/-	<0.07/6.16	1.92/5.22	Normal/abnormal
KS5	M	18.7	Partial*	170.0	-/-	Left ear hearing impairment, inarticulate, gynecomastia, depigmentation, intellectual defect		L2.5, R3.0	0.44/-	1.3/-	2.6/-	Hyposmia/abnormal
KS6	M	11.7	Absent	141.0	+/-			L0.17, R0.17	0.13/-	0.07/-	1.06/-	Hyposmia/abnormal

*His testicles may have developed in Tanner stage 2 by the age of 15, but there was no progress for the next 3 years. TV, . CDGP: constitutionally delayed growth and development.

Table 2: Clinical characteristics of 8 patients with nIHH.

No.	Gender	Diagnosis age (years)	Puberty	Height (cm)	Micropenis/ cryptorchidism	Specific disease history/associated phenotypes	Family history	TV (mL)	HCG test: basal/post	LHRH test: basal/post		Olfaction/OB on MRI
									T (ng/mL)	LH (mIU/mL)	FSH (mIU/mL)	
nIHH1	M	7.9	Absent	132.0	+/-	Nephrotic syndrome (2 years of cortisol therapy since age 3), obesity		NA	0.23/-	<0.07/-	0.82/-	Normal/normal
nIHH2	M	10.1	Absent	143.0	+/-	Overweight		NA	0.11/1.47	0.39/-	3.56/-	Normal/normal
nIHH3[a]	M	2.4	NA	94.0	+/-	Congenital penis curvature, scrotal division		NA	0.2/-	0.28/-	0.91/-	NA/normal
nIHH4	M	2.1	NA	91.0	+/+			NA	0.12/-	0.04/-	0.55/-	Normal/NA
nIHH5	M	16.7	Absent	140.0	+/+	Short stature, obesity, diabetes, fatty liver		L0.36,R0.63	0.21/0.38	0.3/1.91	1.23/4.8	Normal/normal
nIHH6	M	14.4	Absent	156.5	+/-		CDGP (mother)	L0.54, R0.6	0.1/0.62	0.31/6.53	0.59/6.3	Normal/NA
nIHH7	M	16.5	Absent	165.7	+/-	Obesity	CDGP (father)	L2.0, R2.5	0.17/0.29	0.2/4.4	1.7/4.6	Normal/NA
nIHH8	F	16.2	Partial[b]	158.5		Ovarian cystic teratoma, inarticulate, intellectual defect			E2:14.9 pg/mL	<0.1/0.44	0.31/1.11	Normal/NA

a: He was only tested for sex hormones when he was six months old. b :She had Tanner stage 2 breast development at 13 years of age and it did not progress for the next 3 years NA, not available. CDGP: Constitutionally delayed growth and development.

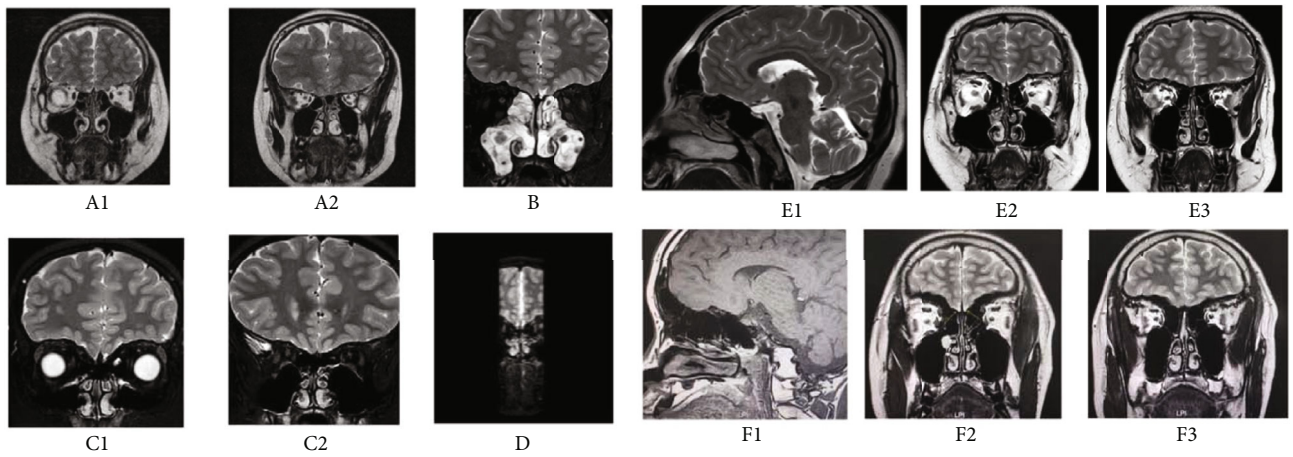

Figure 1: MR abnormalities of olfactory bulb in 6 boys with IHH.

Table 3: Genetic analysis of 14 children with IHH.

Case	Gene	Variant	Novel	Amino acid	Pathogenicity[b]	Inheritance	Source of variant	MAF (%)	Polyphen-2	SIFT	PROVEAN
KS1	CHD7	c.2442+1G>A	Yes	/	Likely pathogenic	AD, Het	De novo	No	/	/	/
KS2	CHD7	c.2744A>G	Yes	p.D915G	Uncertain	AD, Het	Paternal	No	0.991	0.001	5.7
KS3	CHD7	c.409T>G	No	p.S137A	Likely benign	AD, Het	Paternal	0.020	0.002	0.19	0.62
KS4	CHD7	c.2698-1G>T	Yes	/	Pathogenic	AD, Het	Paternal	No	/	/	/
KS5	CHD7	c.2724G>T	Yes	p.W908C	Uncertain	AD, Het	Maternal	No	1	0.00	12.43
KS6	NDNF	c.1439T>A	Yes	p.I480N	Uncertain	AD, Het	Paternal	No	0.963	0.002	5.23
nIHH1	CHD7	c.749G>A	No	p.R250H	Uncertain	AD, Het	Paternal	0.006471	0.999	0.011	0.76
		c.1565G>T	No	p.G522V	Likely benign	AD, Het	Paternal	0.619	0.099	0.05	0.47
	ANOS1[a]	GRCh38/hg38:chrX: (8528874-8732137)dup			Uncertain	XLR	De novo	No			
nIHH2	CHD7	c.1565G>T	No	p.G522V	Likely benign	AD, Het	Maternal	0.619	0.099	0.05	0.47
nIHH3	CHD7	c.59G>A	No	p.G20D	Uncertain	AD, Het	Maternal	0.001057	0.916	0.285	0.44
nIHH4	CHD7	c.2182G>A	No	p.D728N	Uncertain	AD, Het	Paternal	0.01164	0.155	0.011	2.34
nIHH5	FGFR1	c.1271G>A	Yes	p.R424H	Uncertain	AD, Het	Paternal	No	0.060	0.041	2.51
	SEMA3A	c.1369A>G	No	p.T457A	Uncertain	AD, Het	Maternal	No	0.789	0.005	3.58
nIHH6	FGF8	c.368G>A	Yes	p.G123E	Uncertain	AD, Het	Maternal	No	0.974	0.000	4.99
nIHH7	PROKR2	c.891-892insA	Yes	p.R298Tfs∗2	Likely pathogenic	AD, Het	Paternal	No	/	/	/
nIHH8	CHD7	c.4153G>C	Yes	p.D1385H	Uncertain	AD, Het	De novo	No	1	0.000	6.71

a: represents copy number variation, and represents variant if no hint is given. Uncertain is recorded after checking two databases; b: records after checking according to hospital laboratory report and multiple databases. SIFT score: Less than 0.05 is expected to be Deleterious, greater than or equal to 0.05 is expected to be Tolerated. Polyphen-2 score: If the score is between 0.909 and 1, it is Probably damaging;Scores between 0.447 and 0.908 are "potentially Damaging", while 0 and 0.447 are Benign. PROVEAN score: Less than -2.5 is expected to be Deleterious, more than -2.5 is expected to be Neutral AD: autosomal dominant,Het: heterozygous, XLR: X-linked recessive.

bond formed (Figure 4). According to the above findings, combined with classification according to the guidelines of ACMG, 4/16 (25%) variants were classified as pathogenic, 2/16 (12.5%) as likely pathogenic, and 8/16 (50%) as uncertain (Table 4).

IHH is an inherited and clinically heterogeneous disease. Different pathogenic genes produce similar clinical phenotypes, and the same pathogenic genes have different clinical characteristics. KS patients are more likely to have abnormal olfactory function, but it is also common for patients with abnormal olfactory bulb to have normal olfactory function. In this study cohort, most male patients had reproductive system abnormalities with a high incidence, such as micropenis (92.3%), cryptorchidism (41.7%), penis retraction (7.7%), and scrotal division (7.7%), which were consistent with literature reports [16–19]. These findings suggest the possibility and necessity of early diagnosis of IHH. Abnormal male gonadal development may indicate defects in the HPG axis during

Table 4: Further genetic pathogenicity analysis of 12 children with IHH (excluding benign or likely benign variants).

Case	Gene	Variant	Amino acid	Source of variant	Mutation taster	CADD_ raw	CADD_ phred	MetaSVM_ score	Classification (ACMG)
KS1*	CHD7	c.2442+1G>A	/	De novo	1	/	/	/	P (PVS1, PS2, PM2, PP3, PP4)
KS2	CHD7	c.2744A>G	p.D915G	Paternal	0.999	4.436	32	0.31	LP (PM1, PM2, PP3, PP4)
KS4*	CHD7	c.2698-1G>T	/	Paternal	1	/	/	/	P (PVS1, PM2, PP3)
KS5	CHD7	c.2724G>T	p.W908C	Maternal	1	4.566	32	1.068	LP (PM1, PM2, PP3, PP4)
KS6	NDNF	c.1439T>A	p.I480N	Paternal	0.999	4.094	28.5	0.508	US (PM2, PP2, PP3)
nHH1	CHD7	c.749G>A	p.R250H	Paternal	0.999	3.505	25	0.08	US (PP3, PP4)
nHH3	CHD7	c.59G>A	p.G20D	Maternal	0.986	2.865	23.3	1.045	US (PP3, PP4)
nHH4	CHD7	c.2182G>A	p.D728N	Paternal	0.999	2.819	23.2	0.488	US (PP3, PP4)
nHH5	FGFR1	c.1271G>A	p.R424H	Paternal	0.999	3.489	24.9	0.062	US (PM2, PP3, PP4)
	SEMA3A	c.1369A>G	p.T457A	Maternal	0.999	3.672	25.6	1.111	US (PM2, PP2, PP3, PP5, PP6)
nHH6	FGF8	c.368G>A	p.G123E	Maternal	0.999	3.812	26.3	1.017	US (PM2, PP3, PP6)
nHH7	PROKR2	c.891_892insA	p.R298Tfs∗2	Paternal	/	/	/	/	P (PVS1, PM2, PM4, PP4)
nHH8	CHD7	c.4153G>C	p.D1385H	De novo	0.999	4.305	31	1.004	P (PS2, PM1, PM2, PP3, PP4)

*: Splice Site Score Calculation and SpliceAI for Splicing Sites: Test positive. The 12 variants predicted by MutationTaster are all classified as "pathogenic". CADD_raw is the initial score, and CADD_phred is the converted score. The higher the score, the greater the harmful effect.The CADD_phred score is recommended to be greater than 15. MetaSVM fractional cut value is 0.0 (higher score indicates greater harmful effects). ACMG: American College of Medical Genetics Laboratory Practice Committee Working Group, Described as P:pathogenic; LP:likely pathogenic; US: uncertain significance. B: benign ;LB: likely benign. PVS: pathogenic very strong, PS: pathogenic strong, PM: pathogenic moderate,PP: pathogenic supporting.

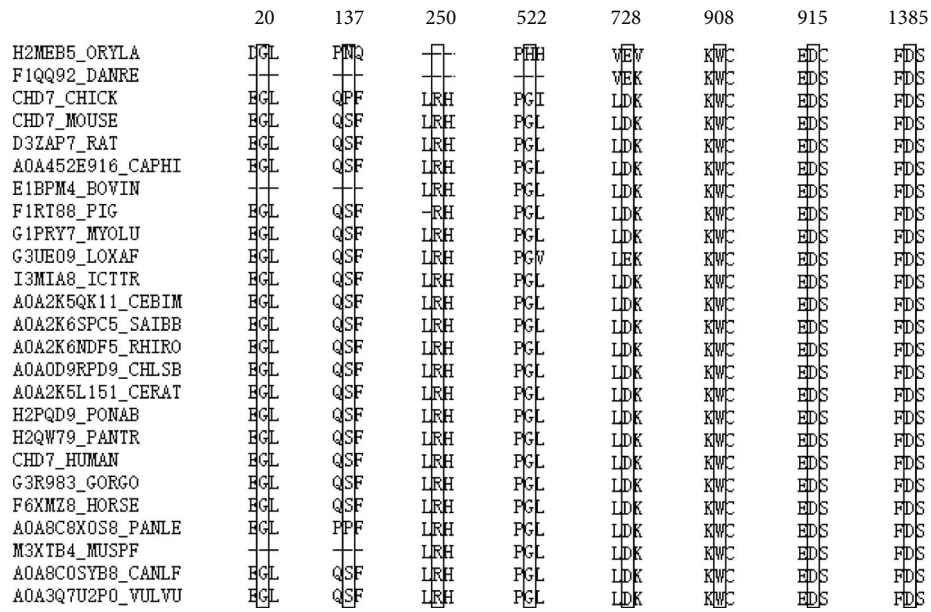

Figure 2: Sequence alignment of CHD7 protein from 25 different species.

embryonic development [22]. Therefore, for male children with the above abnormalities found in the neonatal period, based on existing and ongoing studies on the reference range of sex hormones and other endocrine hormones in children of all ages [14, 15], the sex hormone profile of 4-8 weeks can be used to diagnose IHH [23–25]. There were very few female patients, only 1 case, and indeed no abnormal manifestations of secondary sexual characteristics. This is similar to previous reports [26, 27]. After entering puberty, the female patient delayed menarche and was found to have ovarian teratoma, which has since been diagnosed. This woman also had a number of nonreproductive abnormalities, and other IHH patients in the cohort also had various types of extragonadal abnormalities, including overweight or obesity, short stature, hearing impairment, mental retardation, pronunciation impairment, hypopigmentation, and mental abnormalities. This laid a foundation for us to study the relationship between IHH gene type and clinical phenotype.

The sex hormone levels of the IHH group were generally low in the study. IHH is caused by decreased GnRH secretion in the hypothalamus or by dysregulation of its receptor. Testis function is normally normal. In this study, 4/5 male

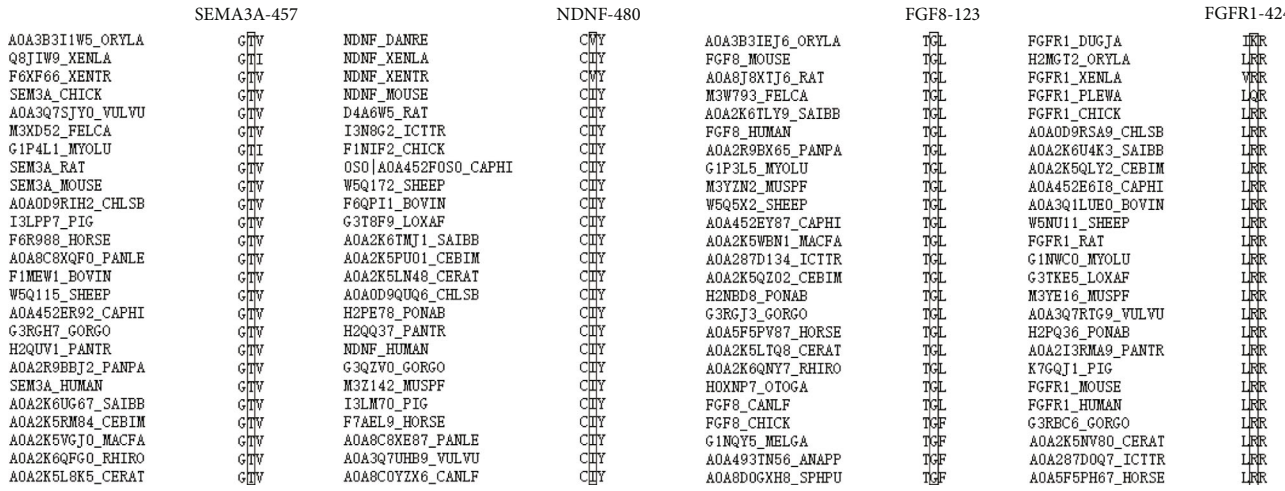

Figure 3: Sequence alignment of four other proteins from 25 different species.

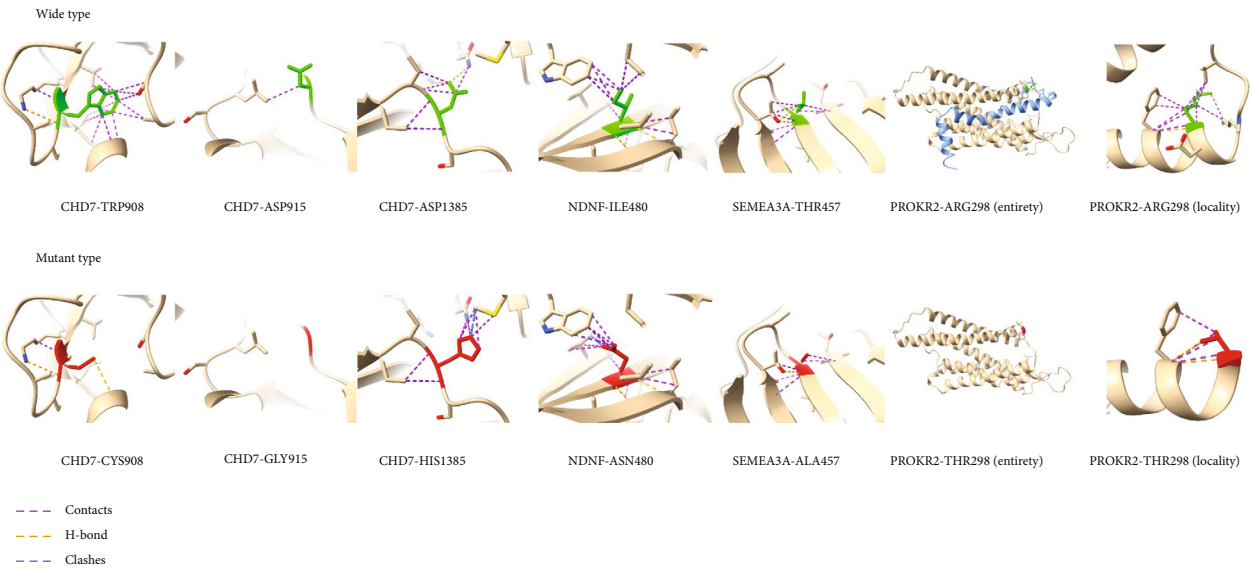

Figure 4: 3D structural modeling of wild and mutant proteins.

children had poor response to the standard HCG test. Unfortunately, no prolonged test was conducted to confirm this. The GnRH test does not determine whether gonadotropin deficiency is caused by hypothalamus or pituitary gland and may be negative in patients with hypothalamic gonadotropin deficiency and positive in some patients with pituitary deficiency. In this cohort, 3/6 children had LH peak value < 4 mIU/mL, and some studies believed that gonadotropin-releasing hormone stimulation test was suggestive for the differential diagnosis of IHH and CDGP, and LH peak value < 4 mIU/mL was meaningful for the diagnosis of IHH [28]. However, there were also 3/6 patients with LH peak value > 4 mIU/mL, of which 2/6 patients > 5 mIU/mL. KS5 and nIHH8 genitalia showed no obvious abnormalities and entered the Tanner stage 2. This may be because gonadotropin pulsating patterns in IHH patients have a fairly wide range of abnormal developmental patterns, from the complete absence of GnRH-induced LH impulses to sleep-induced GnRH release, indistinguished from early adolescence [29–31]. This broad spectrum of neuroendocrine activity explains the various reproductive phenotypes observed in patients with IHH [32]. Olfactory function examination and MRI examination of olfactory organs in 286 patients with IHH and 2183 normal controls found that IHH patients' self-evaluation of olfactory far underestimated the proportion of true olfactory defects. The results of olfactory function examination showed that all the patients who complained of olfactory abnormalities had olfactory abnormalities, so the chief complaint of anosmia was reliable. In this study, olfactory function was mainly evaluated by children and parents during consultation, which may underestimate the proportion of olfactory abnormalities, but it is still reliable for patients with olfactory defects with clear complaints.

The main gene detected in our cohort was CHD7: 11/17 (64.7%). Among the 6 variants assessed as pathogenic or possibly pathogenic, 5 were CHD7 genes (83.3%), which was significantly different from many study cohorts. CHD7

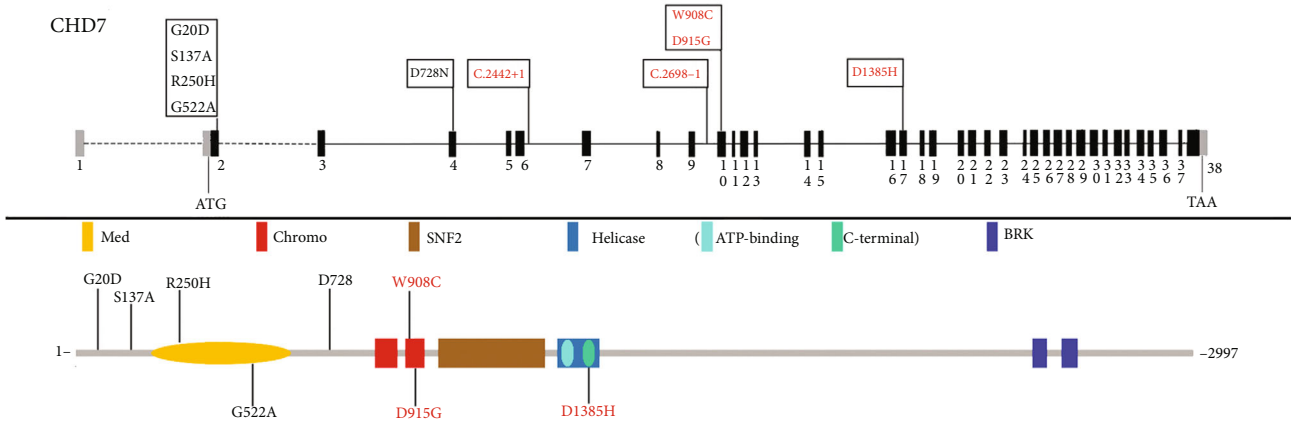

Figure 5: Schematic diagram of CHD7 gene and protein.

accounted for 4% [33], 8.2% [34], and 26.7% [26, 27] of the detected genes in multiple cohorts. CHD7 is a large nucleoprotein containing two N-terminal chromosomal domains, a central Snf2-like ATPASE and helicase domain, a histone/DNA binding SANT domain, and two C-terminal BRK domains. Our variation distribution in the first half, CHD7 gene and protein area tend to gather at the genetic model of exon 2 and 10 around, protein model on the distribution regularity, no known protein model function domain, and of pathogenic or possibly pathogenic variation is not show the inclination "hot spots" (see Figure 5). To further explore unknown protein regions, we looked them up on the InterPro website and found no conservative areas. This may be hypothetical evidence that rare CHD7 variants in humans may cause various phenotypes of IHH, which is only a milder manifestation of CHARGE syndrome and is also reported to be supported by Kim et al. [35] and Bergman et al. [36]. In their patients with CHARGE syndrome, pathogenic missense mutations mainly occurred in the functional domain aggregation region of CHD7 gene. Clinical features that have been reported that may be associated with CHD7 gene are high palatal arch or cleft palate, dental hypoplasia, auricle dysplasia, perceptual deafness and semicircular canal hypoplasia, short stature, mental retardation, eye defect, or coloboma [35, 37, 38]. These may be monogenic or oligogenic inheritance. Anosmia is not absolutely related to CHD7.

Therefore, both KS and nIHH have CHD7 variants detected in the queue. The presence or absence of anosmia depends on penetrance of the gene, especially in the case of penetrance, especially in the heterozygous state. With the exception of KS3 and nIHH2 (variants classified as benign and possibly benign), 5 of the 8 children with CHD7 variants detected had extragonadal abnormalities (62.5%). Both KS1 (C.2442+1G>A of CHD7) and KS2 (C.2744A>G of CHD7) showed short stature, with olfactory abnormalities and olfactory bulb abnormalities. Both KS5 (C.2724G>T of CHD7) and nIHH8 (C.4153G>C of CHD7) had mental retardation. KS5 found a hearing deficit. These are consistent with known reports. In addition, KS5 and nIHH8 also have pronunciation defects, which may also be related to CHD7 gene, and more sample studies are needed. However, the variants assessed as P or LP (4/5, 80%) were more common to have extragonadal manifestations than the single-gene variants assessed as US (0/2, 0%), which was consistent with the report by Sun et al. [16]. nIHH1 detected 3 gene variants, and on the condition that the pathogenicity of each variant (including the CHD7 variant classified as US) was not clear, the link between gene and phenotype does not allow the possibility of a linear correlation. Similarly, detailed phenotypic analysis of 17 patients reported by Xu et al. [39] showed that 80% (4/5) of patients with P or LP variants showed multiple CHARGE features (mostly extragonadal abnormalities), compared with 8% (1/12) of patients with nonpathogenic (US, B, and LB) variants. The B or LB variants assessed in this group also showed no extragonadal abnormalities (0/2, 0%).However, in Jongmans et al. [40] and Bergman et al. [41], there was no association between genotype and phenotype in CHARGE syndrome patients. However, the sample size of patients with P and LP variants was small, so US variants need to be further confirmed by functional tests or/and reclassified with additional evidence. Therefore, variations in specific clinical manifestations that may provide information related to genetic types need to be carefully interpreted.

Another variant evaluated as P in our cohort was C. 891_892insA of PROKR2, which not only resulted in a change in a single amino acid but also resulted in the termination of all nucleotide encoding after the mutation site due to frameshift mutation and the disappearance of amino acid sequence. Prokineticin-2 (PROK2) is a protein that plays an important role in olfactory nerve development. Human regulation of GnRH neurons and physiology requires its receptor PROKR2. PROKR2 was first reported in 2006 to be associated with syndromic hypogonadotropin with/without anosmia [42]. RSV in PROKR2 is always heterozygous, as reported by this patient (nIHH7) and others [38]. Combined with the fact that the father of the child has a history of CDGP, the child may have a reversal of reproductive defects. Some heterozygous variations in PROKR2 may act in a dominant inhibitory manner [43]. PROKR2-associated hypogonadotropin hypogonadism has been hypothesized to be caused by the interaction of other gene products, since the overexpression of the variant allele does not inhibit the function of the coexpressed wild-type protein [44]. Larger queues are needed to validate the results. The

extragonadal manifestations of the children were only obesity, without synkinesia, and other manifestations, but there were few nonreproductive manifestations similar to those reported previously [38]. SEMA3A is a key signaling protein for axon development and plays an important role in many physiological processes. It is involved in axon rejection, dendrite branching, synaptic formation, and neuronal migration by binding NRP1, NRP2, and PLXNA complex receptors. nIHH5 has both SEMA3A c.1369A>G and FGFR1 c.1271G>A variants. Here, the focus is on the SEMA3A variant recently reported by Dai et al. [19], which is not a new variant. This study provides strong evidence to support its pathogenic role in patients with nIHH. The study identified families with the mutation in 196 patients with IHH. Interestingly, the child carried 5 variants of 5 genes (including this variant), the mother carried 4 variants of the other 4 genes, and both the father and one sister carried only c.1369A>G (SEMA3A).

The other sister had one of the five genes and the corresponding variant (not c.1369A>G of SEMA3A), and only the child had IHH manifestations, while the other four had normal phenotypes. At the same time, the researchers completed functional tests of the variant. The results suggest that the SEMA3A variant (c.1369A>G(p.T457A)) leads to defects in FAK phosphorylation and GN11 cell migration and supports its pathogenic role in nIHH patients. However, as it is a single experimental evidence, according to ACMG genetic classification, this experiment has not been reported and verified so far, so it cannot be classified as reproducible and confirmed as stable and effective. Therefore, it cannot be applied to PS3 evidence and can only be evaluated as PP5 evidence. Moreover, PP6 was temporarily classified as US because the evidence came from the conserved judgment sites of homologous alignment of other species and the prediction of protein model software of computer. We need to validate the changes in protein function caused by this variant and further strengthen the experimental evidence to support the hypothesis of its pathogenicity. The FGFR1 protein is a member of the receptor tyrosine kinase (RTK) superfamily. FGFR1 signaling has been shown to play critical roles in the development of the olfactory system, as well as normal GnRH neuronal migration, differentiation, and survival within the hypothalamus. The pathogenesis of nIHH5 follows the oligogenic pattern of disease development, suggesting that these mutations act synergistically to bring about the IHH phenotype. The nongonadal abnormalities in this child are short stature, obesity, and obesity-related complications, which are not synkinesia, cleft lip, and/or palate; hypoplasia of teeth was mentioned in the literature. Digit malformations [6, 38, 45] and others require a summary of more samples. Another possible oligogenic genetic pattern is nIHH1, which has both c.749G>A and c.1565G>T of CHD7 and whole repeats of ANOS1. Having looked at CHD7 in detail, let us expand on ANOS1. ANOS1, also known as Kallmann syndrome 1 (KAL1) gene, is one of the most common genes involved in IHH and is responsible for the X-linked recessive form of KS. ANOS1 is located on chromosome Xp22.31 and consists of 14 exons encoding an extracellular cell adhesion protein anosmin-1 with 680 amino acids, which is essential for olfactory guidance and migration of olfactory and GnRH neurons from the nasal cavity to their final destination [46]. Because the deletion and variation of this gene has clear pathogenic evidence, it is highly correlated with anosmia or hypoxia, digital synkinesia, high-arched palate, unilateral renal agenesis, and other clinical phenotypes [5]. However, the child in this case only had the duplication of this gene, and in addition to sexual dysplasia, he only had a 2-year history of nephropathy without renal structural abnormalities. At present, there is no clear support for the variation of these genes to cause the IHH phenotype of the child. The last gene to discuss is NDNF. NDNF is a secreted neurotrophic factor that promotes neuronal migration, growth, and survival, as well as the growth of neural processes. A recent study demonstrated statistical enrichment of PTV in NDNF, which encodes glycosylated disulfide proteins in the FN3 domain, by studying 240 IHH-independent precursor bands [47]. The enrichment of PTV in NDNF suggests that deletions in NDNF may explain some patients of IHH. NDNF is expressed in the nasal region after formation of the olfactory placode in mice and humans [47]. The positive effects of recombinant NDNF on GnRH neuronal migration in vitro and the migration defects of GnRH neurons in zebrafish injected with z-ndnf MO and ndnf-null mice provide strong evidence for the role of NDNF in GnRH neuronal migration [47]. Even though c.1439T>A (NDNF) mutation of KS6 is currently classified as US, we should keep an eye on it and complete functional tests to supplement more clinical data of patients associated with this variant.

We believe that more support will be provided in the future.

4. Conclusion

Abnormalities in CHD7, PROKR2, ANOS1, FGFR1, SEMA3A, or NDNF genes can lead to IHH, with or without extragenital manifestations. IHH should be highly suspected in males with small penises and/or cryptorchidism. New 6 reported variants and 10 new variants (5 genes, including entire duplicates of ANSO1) were identified in IHH with different symptoms. A small proportion of patients may be affected by oligogenic inheritance. For CHD7 variants, the RSV of P or LP is more commonly associated with CHARGE syndrome. These findings provide more references and suggestions for the diagnosis and research of IHH.

Abbreviations

IHH: Idiopathic hypogonadotropin hypogonadism
nIHH: Hypogonadotropin hypogonadism with a normal sense of smell
KS: Kallmann syndrome
ACMG: American College of Medical Genetics Laboratory Practice Committee Working Group
WES: Whole exon sequencing
P: Pathogenic
LP: Likely pathogenic
US: Uncertain significance
B: Benign
LB: Likely benign
RSV: Rare sequencing variant
MAF: Maximum allele frequency

LH: Luteinizing hormone
FSH: Follicle-stimulating hormone
T: Testosterone
H-bod: Hydrogen bond
GnRH: Gonadotropin-releasing hormone
CDGP: Constitutionally delayed growth and development.

Data Availability

The data supported the research are included in the article.

Ethical Approval

The study design and protocol were approved by the Ethics Committee of Children's Hospital of Zhejiang University School of Medicine and the Hangzhou Children's Hospital.

Consent

Consent is not applicable. This manuscript contains no individual person's data in any form (including any individual details, images, or videos).

Conflicts of Interest

No benefits in any form have been received or will be received from a commercial party related directly or indirectly to the subject of this article.

Authors' Contributions

All authors have participated in revising the manuscript critically and gave their final approval of the version to be submitted.

Acknowledgments

We thank all children with IHH and their parents for supporting our study. This work is supported by the Medical and Health Science and Technology Project of Zhejiang Province (2020KY230) and Key R&D Projects of Zhejiang Provincial Department of Science and Technology (2021 C03094).

References

[1] S. D. Bianco and U. B. Kaiser, "The genetic and molecular basis of idiopathic hypogonadotropic hypogonadism," *Nature Reviews. Endocrinology*, vol. 5, no. 10, pp. 569–576, 2009.

[2] U. Boehm, P. M. Bouloux, M. T. Dattani et al., "European consensus statement on congenital hypogonadotropic hypogonadism– pathogenesis, diagnosis and treatment," *Nature Reviews. Endocrinology*, vol. 11, no. 9, pp. 547–564, 2015.

[3] H. Miraoui, A. A. Dwyer, G. P. Sykiotis et al., "Mutations in FGF17, IL17RD, DUSP6, SPRY4, and FLRT3 are identified in individuals with congenital hypogonadotropic hypogonadism," *American Journal of Human Genetics*, vol. 92, no. 5, pp. 725–743, 2013.

[4] S. D. Quaynor, M. E. Bosley, C. G. Duckworth et al., "Targeted next generation sequencing approach identifies eighteen new candidate genes in normosmic hypogonadotropic hypogonadism and Kallmann syndrome," *Molecular and Cellular Endocrinology*, vol. 437, pp. 86–96, 2016.

[5] R. Balasubramanian and W. F. Crowley Jr., *Isolated Gonadotropin-Releasing Hormone (GnRH) Deficiency*, University of Washington, Seattle, Seattle (WA), 2007.

[6] N. Pitteloud, A. Meysing, R. Quinton et al., "Mutations in fibroblast growth factor receptor 1 cause Kallmann syndrome with a wide spectrum of reproductive phenotypes," *Molecular and Cellular Endocrinology*, vol. 254-255, pp. 60–69, 2006.

[7] N. L. Sim, P. Kumar, J. Hu, S. Henikoff, G. Schneider, and P. C. Ng, "SIFT web server: predicting effects of amino acid substitutions on proteins," *Nucleic Acids Research*, vol. 40, no. W1, pp. W452–W457, 2012.

[8] I. A. Adzhubei, S. Schmidt, L. Peshkin et al., "A method and server for predicting damaging missense mutations," *Nature Methods*, vol. 7, no. 4, pp. 248-249, 2010.

[9] Y. Choi, G. E. Sims, S. Murphy, J. R. Miller, and A. P. Chan, "Predicting the functional effect of amino acid substitutions and indels," *PLoS One*, vol. 7, no. 10, article e46688, 2012.

[10] J. M. Schwarz, C. Rodelsperger, M. Schuelke, and D. Seelow, "MutationTaster evaluates disease-causing potential of sequence alterations," *Nature Methods*, vol. 7, no. 8, pp. 575-576, 2010.

[11] P. Rentzsch, D. Witten, G. M. Cooper, J. Shendure, and M. Kircher, "CADD: predicting the deleteriousness of variants throughout the human genome," *Nucleic Acids Research*, vol. 47, no. D1, pp. D886–D894, 2019.

[12] M. Mohiyuddin, J. C. Mu, J. Li et al., "MetaSV: an accurate and integrative structural-variant caller for next generation sequencing," *Bioinformatics*, vol. 31, no. 16, pp. 2741–2744, 2015.

[13] K. Jaganathan, S. Kyriazopoulou Panagiotopoulou, J. F. McRae et al., "Predicting splicing from primary sequence with deep learning," *Cell*, vol. 176, no. 3, pp. 535–548.e24, 2019.

[14] L. F. Sun, Y. Y. Li, B. X. Huang et al., "Establishment of reference ranges of sex hormones for healthy children in Shenzhen, China based on chemiluminescence," *Chinese Journal of Contemporary Pediatrics*, vol. 19, no. 12, pp. 1257–1262, 2017.

[15] M. K. Bohn, P. Horn, D. League, P. Steele, A. Hall, and K. Adeli, "Pediatric reference intervals for endocrine markers and fertility hormones in healthy children and adolescents on the Siemens Healthineers Atellica immunoassay system," *Clinical Chemistry and Laboratory Medicine*, vol. 59, no. 8, pp. 1421–1430, 2021.

[16] B. Sun, X. Wang, J. Mao et al., "Classification of CHD7 rare variants in Chinese congenital hypogonadotropic hypogonadism patients and analysis of their clinical characteristics," *Frontiers in Genetics*, vol. 12, article 770680, 2022.

[17] J. D. Li, J. Wu, Y. Zhao et al., "Phenotypic spectrum of idiopathic hypogonadotropic hypogonadism patients With *CHD7* Variants from a large Chinese cohort," *The Journal of Clinical Endocrinology & Metabolism*, vol. 105, no. 5, pp. 1515–1526, 2020.

[18] B. Zhang, Y. Song, W. Li, and C. Gong, "Variant analysis of the chromodomain helicase DNA-binding protein 7 in pediatric disorders of sex development," *Pediatric Investigation*, vol. 3, no. 1, pp. 31–38, 2019.

[19] W. Dai, J. D. Li, X. Wang, W. Zeng, F. Jiang, and R. Zheng, "Discovery of a novel variant of SEMA3A in a Chinese patient with isolated hypogonadotropic hypogonadism,"

International Journal of Endocrinology, vol. 2021, Article ID 7752526, 7 pages, 2021.

[20] S. Eggers, S. Sadedin, J. A. van den Bergen et al., "Disorders of sex development: insights from targeted gene sequencing of a large international patient cohort," *Genome Biology*, vol. 17, no. 1, p. 243, 2016.

[21] M. A. Mencarelli, E. Katzaki, F. T. Papa et al., "Private inherited microdeletion/microduplications: implications in clinical practice," *European Journal of Medical Genetics*, vol. 51, no. 5, pp. 409–416, 2008.

[22] M. Bonomi, D. V. Libri, F. Guizzardi et al., "New understandings of the genetic basis of isolated idiopathic central hypogonadism," *Asian Journal of Andrology*, vol. 14, no. 1, pp. 49–56, 2012.

[23] M. M. Grumbach, "A window of opportunity: the diagnosis of gonadotropin deficiency in the male infant," *The Journal of Clinical Endocrinology and Metabolism*, vol. 90, no. 5, pp. 3122–3127, 2005.

[24] M. G. Forest and A. M. Cathiard, "Pattern of plasma testosterone and delta4-androstenedione in normal newborns: evidence for testicular activity at birth," *The Journal of Clinical Endocrinology and Metabolism*, vol. 41, no. 5, pp. 977–980, 1975.

[25] C. Milani, L. Andreone, M. G. Ropelato, S. Gottlieb, S. Campo, and R. A. Rey, "Time course of the serum gonadotropin surge, inhibins, and anti-Müllerian hormone in normal newborn males during the first month of life," *The Journal of Clinical Endocrinology and Metabolism*, vol. 91, no. 10, pp. 4092–4098, 2006.

[26] C. Y. Cho, W. Y. Tsai, C. T. Lee et al., "Clinical and molecular features of idiopathic hypogonadotropic hypogonadism in Taiwan: a single center experience," *Journal of the Formosan Medical Association*, vol. 121, no. 1, pp. 218–226, 2022.

[27] K. Aoyama, H. Mizuno, T. Tanaka et al., "Molecular genetic and clinical delineation of 22 patients with congenital hypogonadotropic hypogonadism," *Journal of Pediatric Endocrinology & Metabolism*, vol. 30, no. 10, pp. 1111–1118, 2017.

[28] J. F. Mao, X. Y. Wu, S. Y. Lu, and M. Nie, "Clinical values of single or repeated triptorelin stimulating test in the differential diagnosis between idiopathic hypogonadotropic hypogonadism and constitutional delayed puberty," *Zhongguo Yi Xue Ke Xue Yuan Xue Bao*, vol. 33, no. 5, pp. 566–570, 2011, Chinese.

[29] D. I. Spratt, D. B. Carr, G. R. Merriam, R. E. Scully, P. N. Rao, and W. F. Crowley Jr., "The spectrum of abnormal patterns of gonadotropin releasing hormone secretion in men with idiopathic hypogonadotropic hypogonadism: clinical and laboratory correlations," *The Journal of Clinical Endocrinology and Metabolism*, vol. 64, no. 2, pp. 283–291, 1987.

[30] L. B. Nachtigall, P. A. Boepple, F. P. Pralong, and W. F. Crowley Jr., "Adult-onset idiopathic hypogonadotropic hypogonadism–a treatable form of male infertility," *The New England Journal of Medicine*, vol. 336, no. 6, pp. 410–415, 1997.

[31] T. Raivio, J. Falardeau, A. Dwyer et al., "Reversal of idiopathic hypogonadotropic hypogonadism," *The New England Journal of Medicine*, vol. 357, no. 9, pp. 863–873, 2007.

[32] H. M. Lewkowitz-Shpuntoff, V. A. Hughes, L. Plummer et al., "Olfactory phenotypic spectrum in idiopathic hypogonadotropic hypogonadism: pathophysiological and genetic implications," *The Journal of Clinical Endocrinology and Metabolism*, vol. 97, no. 1, pp. E136–E144, 2012.

[33] Q. Liu, X. Yin, and P. Li, "Clinical, hormonal, and genetic characteristics of 25 Chinese patients with idiopathic hypogonadotropic hypogonadism," *BMC Endocrine Disorders*, vol. 22, no. 1, p. 30, 2022.

[34] Y. Wang, C. Gong, M. Qin, Y. Liu, and Y. Tian, "Clinical and genetic features of 64 young male paediatric patients with congenital hypogonadotropic hypogonadism," *Clinical Endocrinology*, vol. 87, no. 6, pp. 757–766, 2017.

[35] H. G. Kim, I. Kurth, F. Lan et al., "Mutations in CHD7, encoding a chromatin-remodeling protein, cause idiopathic hypogonadotropic hypogonadism and Kallmann syndrome," *American Journal of Human Genetics*, vol. 83, no. 4, pp. 511–519, 2008.

[36] J. E. Bergman, N. Janssen, A. M. van der Sloot et al., "A novel classification system to predict the pathogenic effects of CHD7 missense variants in CHARGE syndrome," *Human Mutation*, vol. 33, no. 8, pp. 1251–1260, 2012.

[37] M. C. Jongmans, C. M. van Ravenswaaij-Arts, N. Pitteloud et al., "CHD7 mutations in patients initially diagnosed with Kallmann syndrome–the clinical overlap with CHARGE syndrome," *Clinical Genetics*, vol. 75, no. 1, pp. 65–71, 2009.

[38] F. A. Costa-Barbosa, R. Balasubramanian, K. W. Keefe et al., "Prioritizing genetic testing in patients with Kallmann syndrome using clinical phenotypes," *The Journal of Clinical Endocrinology and Metabolism*, vol. 98, no. 5, pp. E943–E953, 2013.

[39] C. Xu, D. Cassatella, A. M. van der Sloot et al., "Evaluating CHARGE syndrome in congenital hypogonadotropic hypogonadism patients harboring CHD7 variants," *Genetics in Medicine*, vol. 20, no. 8, pp. 872–881, 2018.

[40] M. C. Jongmans, R. J. Admiraal, K. P. Van Der Donk et al., "CHARGE syndrome: the phenotypic spectrum of mutations in the CHD7 gene," *Journal of Medical Genetics*, vol. 43, no. 4, pp. 306–314, 2006.

[41] J. E. Bergman, N. Janssen, L. H. Hoefsloot, M. C. Jongmans, R. M. W. Hofstra, and C. M. A. van Ravenswaaij-Arts, "CHD7 mutations and CHARGE syndrome: the clinical implications of an expanding phenotype," *Journal of Medical Genetics*, vol. 48, no. 5, pp. 334–342, 2011.

[42] C. Dodé, L. Teixeira, J. Levilliers et al., "Kallmann syndrome: mutations in the genes encoding prokineticin-2 and prokineticin receptor-2," *PLoS Genetics*, vol. 2, no. 10, article e175, 2006.

[43] A. P. Abreu, S. D. Noel, S. Xu, R. S. Carroll, A. C. Latronico, and U. B. Kaiser, "Evidence of the importance of the first intracellular loop of prokineticin receptor 2 in receptor function," *Molecular Endocrinology*, vol. 26, no. 8, pp. 1417–1427, 2012.

[44] C. Monnier, C. Dodé, L. Fabre et al., "*PROKR2* missense mutations associated with Kallmann syndrome impair receptor signalling activity," *Human Molecular Genetics*, vol. 18, no. 1, pp. 75–81, 2009.

[45] C. Dodé, J. Levilliers, J. M. Dupont et al., "Loss-of-function mutations in *FGFR1* cause autosomal dominant Kallmann syndrome," *Nature Genetics*, vol. 33, no. 4, pp. 463–465, 2003.

[46] Y. Hu and P. M. Bouloux, "X-linked GnRH deficiency: role of KAL-1 mutations in GnRH deficiency," *Molecular and Cellular Endocrinology*, vol. 346, no. 1-2, pp. 13–20, 2011.

[47] A. Messina, K. Pulli, S. Santini et al., "Neuron-derived neurotrophic factor is mutated in congenital hypogonadotropic hypogonadism," *American Journal of Human Genetics*, vol. 106, no. 1, pp. 58–70, 2020.

Hindawi
Journal of Oncology
Volume 2022, Article ID 1892459, 10 pages
https://doi.org/10.1155/2022/1892459

Research Article

B-Cell Translocation Gene 2 Upregulation Is Associated with Favorable Prognosis in Lung Adenocarcinoma and Prolonged Patient Survival

Junting Liang,[1] Linna Cheng,[2] Haiyan Gao,[3] Wanying Fu,[4] Xiulei Zhang,[5] Jianhua Zhang,[6] Jinming Li,[7] and Chuanliang Chen[1]

[1]*Clinical Bioinformatics Experimental Center, Henan Provincial People's Hospital, People's Hospital of Zhengzhou University, Zhengzhou, 450003 Henan, China*
[2]*Institute of Hematology, Henan Key Laboratory of Stem Cell Differentiation and Modification, Henan Provincial People's Hospital, Zhengzhou University People's Hospital, Henan University People's Hospital, Zhengzhou, 450003 Henan, China*
[3]*Henan Key Laboratory of Neurological Imaging, Henan Provincial People's Hospital, People's Hospital of Zhengzhou University, Zhengzhou University, Zhengzhou, 450003 Henan, China*
[4]*School of Basic Medicine, Xinxiang Medical University, Xinxiang, 453003 Henan, China*
[5]*Department of Microbiome Laboratory, Henan Provincial People's Hospital, People's Hospital of Zhengzhou University, Zhengzhou, 450003 Henan, China*
[6]*Medical Engineering Technology and Data Mining Institute of Zhengzhou University, Zhengzhou, 450000 Henan, China*
[7]*The Translational Research Institute, Henan Provincial People's Hospital, School of Medicine, Zhengzhou University, Zhengzhou, 450003 Henan, China*

Correspondence should be addressed to Jinming Li; jmli@smu.edu.cn and Chuanliang Chen; henanccl@163.com

Received 30 July 2022; Revised 26 August 2022; Accepted 30 August 2022; Published 14 September 2022

Academic Editor: İbrahim Hakkı Cigerci

The tumor suppressor protein B-cell translocation gene 2 (BTG2) is downexpressed in lung adenocarcinoma (LUAD); however, its role in LUAD survival remains unknown. This investigation is aimed at exploring the activity of BTG2 in LUAD. We analyzed BTG2 expression in LUAD datasets of the TCGA database and examined that BTG2 was markedly downregulated in comparison with adjacent normal tissues. The prognostic analysis suggested that higher expression of BTG2 protein correlates with prolonged survival in patients. Vectors expressing BTG2 were stably transduced into lung adenocarcinoma A549 cells. The overexpression of BTG2 in A549 cells causes cellular G1 phase arrest but did not affect cell proliferation, accompanied by increased activation of NF-κB. Our data indicate that BTG2 overexpression may trigger an autoregulatory prosurvival NF-κB pathway, which is resistant to environmental intervention owing to an increased level of BTG2.

1. Introduction

Among the most frequently occurring cancers is that associated with the lungs. It is one of the major causes of mortality worldwide [1, 2]. Lung adenocarcinoma (LUAD) is one of the most frequently occurring non-small-cell cancer [3]. Early disease diagnosis and new treatment methods need further investigation to determine the underlying molecular mechanisms responsible for the incidence and development of LUAD.

Tumor suppressor genes (TSGs) generally regulate cell cycle arrest, apoptosis, or protein ubiquitination [4–9]. Despite the importance of TSGs in tumorigenesis, the underlying molecular mechanisms of TSGs in lung cancer progression are still unclear. Therefore, more studies are required to understand the roles of TSGs in LUAD.

B-cell translocation gene-2 (BTG2) is a BTG/TOB gene family member [10]. Studies have shown that overexpression of BTG2 can repress in vitro cellular growth [11] and BTG2 serves as a tumor suppressor gene in various types of malignant

tumors [12–14]. Previous reports suggest that BTG2 is downregulated in various malignant tumors, including prostate cancer [15], lung cancer [16], and hepatic cell carcinoma [17]. It has been discovered that the downregulation of BTG2 is linked with substandard breast carcinoma prognosis [18, 19]. Many investigations have indicated that BTG2 overexpression could stimulate cellular apoptosis and restrain cell invasion in prostate cancer [20], medulloblastoma [21], and breast cancer [22]. However, the underlying molecular mechanisms of BTG2 in LUAD remained unclear.

The current study is aimed at using the TCGA database to locate the gene BTG2 as a downregulated gene and predict prognosis and survival in LUAD patients, developing the human lung adenocarcinoma A549 cell line with BTG2 overexpression, and investigating its function experiments to assess its role in tumor progression.

2. Materials and Methods

2.1. Identification of Differentially Expressed Genes (DEGs). The expression data of RNA was acquired from The Cancer Genome Atlas (TCGA, https://cancergenome.nih.gov/). Log2 fold change > 1 and adjusted $P < 0.05$ were set as the cutoff values to screen for DEGs. Data analysis was done via R package *limma* 3.38.3.

2.2. Overall Survival Analysis. R packages *survival* 2.43.3 and *survminer* 0.4.3 were used to sketch the Kaplan-Meier curve and perform a log-rank test to detect the effect of the BTG2 gene on prognosis.

2.3. Plasmid Construction and Cell Transfection. The BTG2 sequence was synthesized and cloned into the vector pCDNA3.1+ (Invitrogen, USA), and Sanger sequencing was then carried out for verifying the final construct. Plasmids were purified with the help of DNA Midiprep Kits (Qiagen, Germany) and transfected into lung adenocarcinoma A549 cells through lipofectamine 2000 transfection reagent (Invitrogen, USA). For establishing controls, cells were transfected with blank plasmid and then screened (1.2 mg/mL G418) after 48 h transfection. Clones were selected by the limiting dilution method to obtain the stable clones with BTG2 overexpression.

2.4. Western Blot Analysis. The BTG2 overexpression efficiency in A549 and H1299 was detected by western blot according to standard methods. For internal control, GAPDH was used.

2.5. Flow Cytometry and Cell Cycle. A549 cells were grown at a concentration of 1×10^6 cells per 10 cm flask, in 1640 medium with 10% FBS for 24 h, followed by harvestation for cell cycle analysis. Briefly, cells were fixed at 4°C. Prior to incubation with 50 μg/mL of propidium iodide (PI), cells were collected. Finally, the stained cells were proceeded to flow cytometry analysis.

2.6. RNA Sequencing. Triplicate samples of vector A549 cells and BTG2 overexpressed cells were delivered to the company GENEWIZ for RNA sequencing. Using the list of DEGs identified above, GO and KEGG pathway analyses were conducted using Metascape. Metascape was also utilized for visualizing the network of protein-protein interaction (PPI). Modular analysis was carried out via Metascape.

2.7. Statistical Analysis. GraphPad Prism 8.3.0 was utilized for statistical calculations. Intergroup comparisons were done via an independent sample t-test. A P value of < 0.05 was deemed statistically significant.

3. Results

3.1. BTG2 is Downregulated in LUAD and Correlates with a Poor Prognosis. The mRNA expression data of 594 lung adenocarcinoma patients were downloaded from the LUAD dataset collected from TCGA. The BTG2 expression in LUAD was assessed by R package *limma* 3.38.3. Our study demonstrated that BTG2 is downregulated in LUAD than in nondiseased tissues (Figure 1(a)). The lower BTG2 levels in LUAD than the normal tissues were further validated in the Gene Expression Profiling Interactive Analysis database (GEPIA, http://gepia.cancer-pku.cn/) (Figure 1(b)). Furthermore, the association between the expression BTG2 and overall survival was assessed by the Kaplan-Meier survival curve with a log-rank comparison. LUAD patients expressing lower BTG2 showed poorer survival than those with higher BTG2 levels (Figure 2). Aforementioned results indicate that BTG2 is downregulated in LUAD, and the low expression of BTG2 predicts poor prognosis. Thus, it seems that BTG2 is a tumor suppressor in LUAD.

3.2. Construction of BTG2 Eukaryotic Expression Vector and A549-BTG2 Cell Clone. To generate the BTG2 eukaryotic expression vector, the BTG2 DNA fragment was amplified and digested. The 548 bp BTG2 fragment was inserted into the plasmid pDNA3.1+ resulting in the pcDNA-BTG2 vector construct. The result of Sanger sequencing confirmed that the BTG2 coding sequence was successfully cloned into pcDNA3.1 (+) vectors. Meanwhile, the Sanger recombinant plasmid sequence was proved correct (data not shown).

To explore the functional role of BTG2 at the cellular level, we established stably pcDNA-BTG2-transfected A549 cell clones in vitro. G418 was used to select the stably transfected cell clones. It turned out that 5 cell clones survived in G418. Western blotting results showed that the five cell clones express BTG2, while the cells without BTG2 transfection had no significant product. The cell clone A549-BTG2-1 expressed BTG2 and was considered the cell model for further experiments (Figure 3(a)).

3.3. Cell Function Experiments of A549 Cells. Cell proliferation and apoptosis analysis were studied by CCK-8 assay and flow cytometry analysis, respectively, to determine the effects of BTG2 overexpression on A549 cells. The data revealed that overexpression of BTG2 did not inhibit cell proliferation and apoptosis (Figures 3(b) and 3(c)). Later on, the effect of BTG2 overexpression was examined for the cell cycle. It revealed a significant increase in the sub-G1 phase in the BTG2 overexpressed cells compared with wild-type A549 (Figure 3(d)), which suggests that BTG2 induced cell cycle arrest. All these

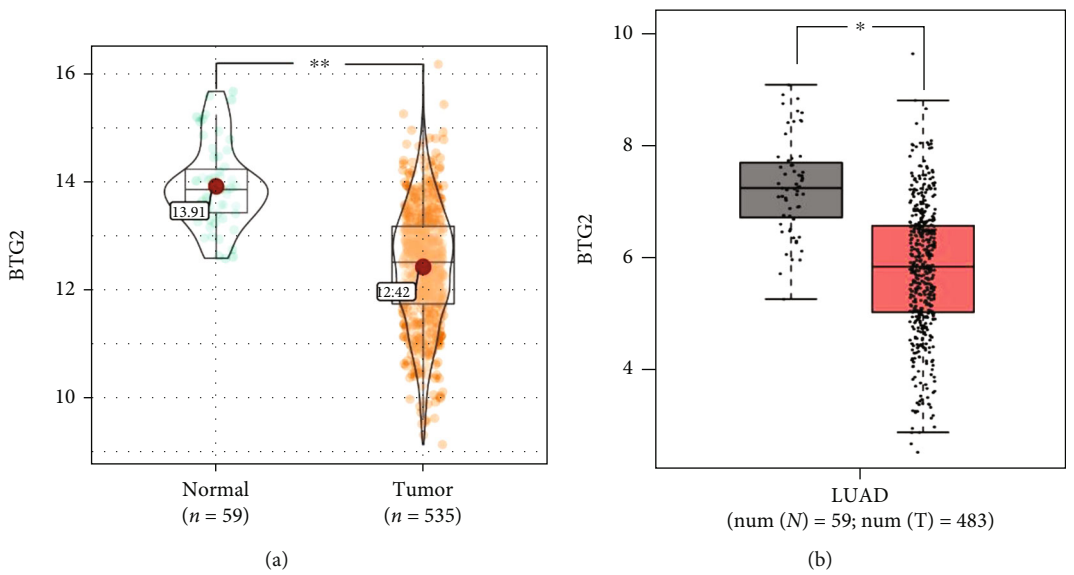

Figure 1: BTG2 was downregulated in LUAD tissues. BTG2 expression levels in LUAD cancer patients compared to normal samples from TCGA through R package limma 3.38.3 (a) and GEPIA online analysis (b).

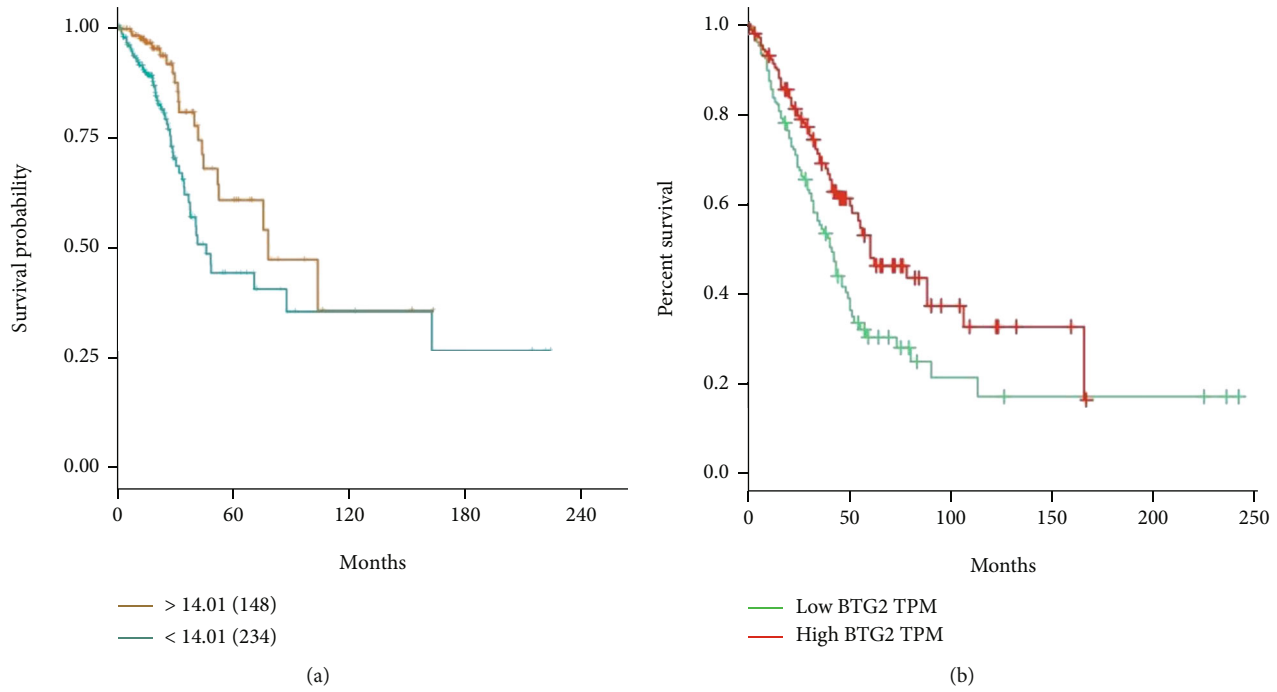

Figure 2: Kaplan-Meier plot showing the association between BTG2 expression and survival. (a) Analysis performed from TCGA in R package limma 3.38.3 and (b) GEPIA online database.

indicate that BTG2 induces cell cycle arrest but has no apparent effects on tumor cell growth.

3.4. BTG2 Downregulates the Cell Cycle-Related Genes and Activates the NF-κB Pathway. To further determine the underlying mechanisms, we performed RNA sequencing of A549 cells after overexpressing BTG2 to evaluate the effects of BTG2 on the transcriptome.

All text samples were compared with the entire control sample group for obtaining differentially expressed genes (DEGs). 1040 genes were found to have significantly altered expression, including 601 upregulated and 439 downregulated genes.

Gene Ontology (GO) and Kyoto Encyclopedia of Genes and Genomes (KEGG) analyses were carried out to evaluate if DEGs are up- or downregulated to predict mRNA functions and molecular interactions among these genes. The top 20 enriched GO and KEGG terms are shown in Figure 4.

The GO analysis indicated that downexpressed genes were significantly enriched in the functional categories associated with protein acylation, cellular response to hormone

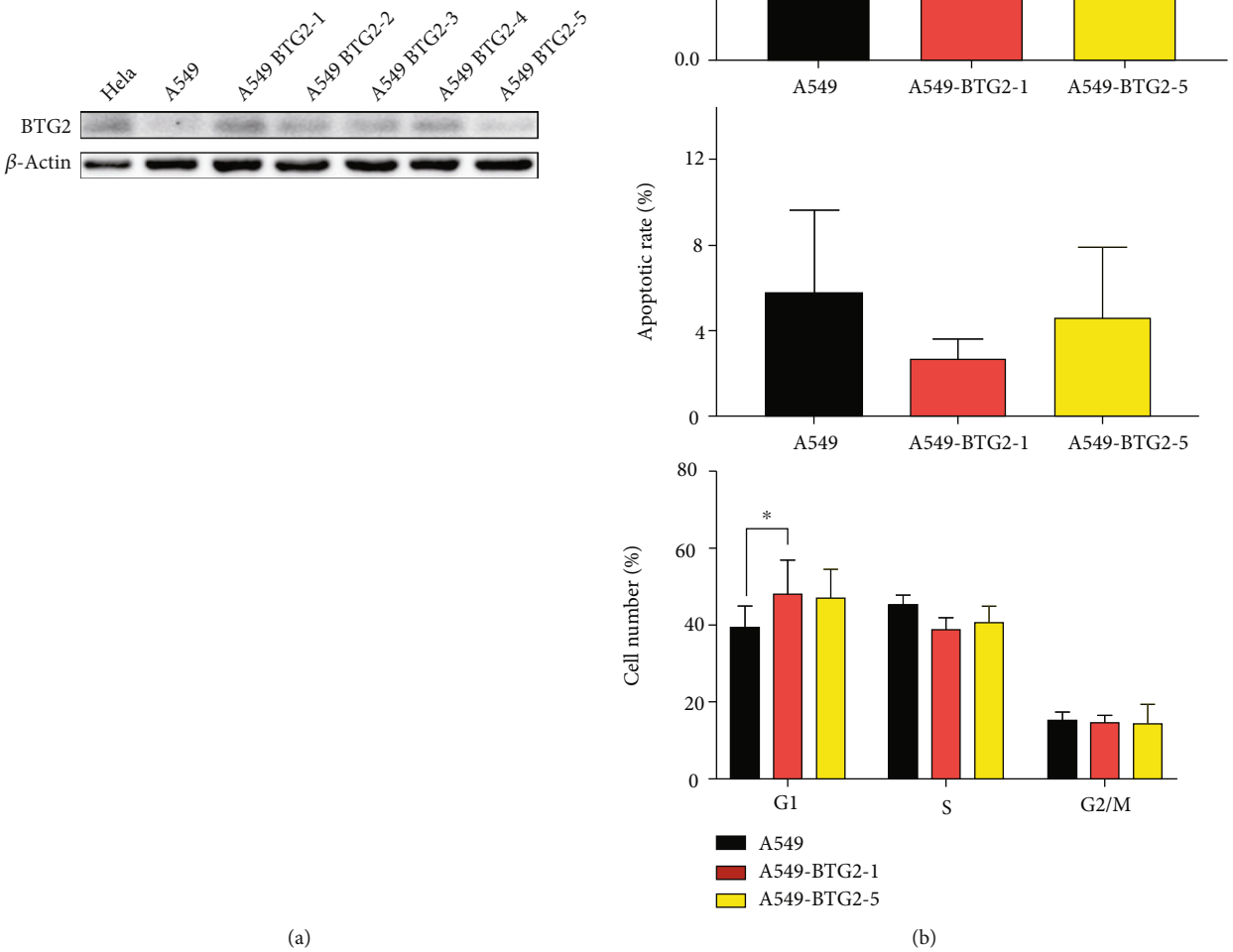

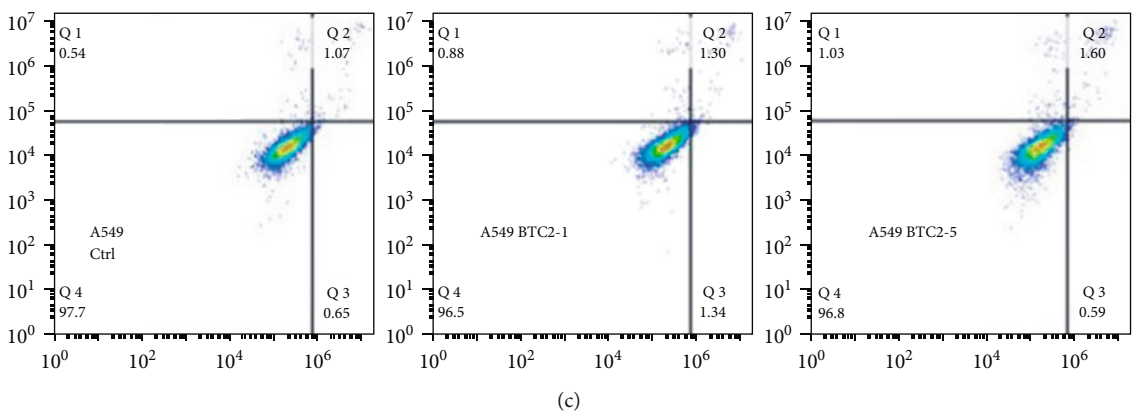

Figure 3: Continued.

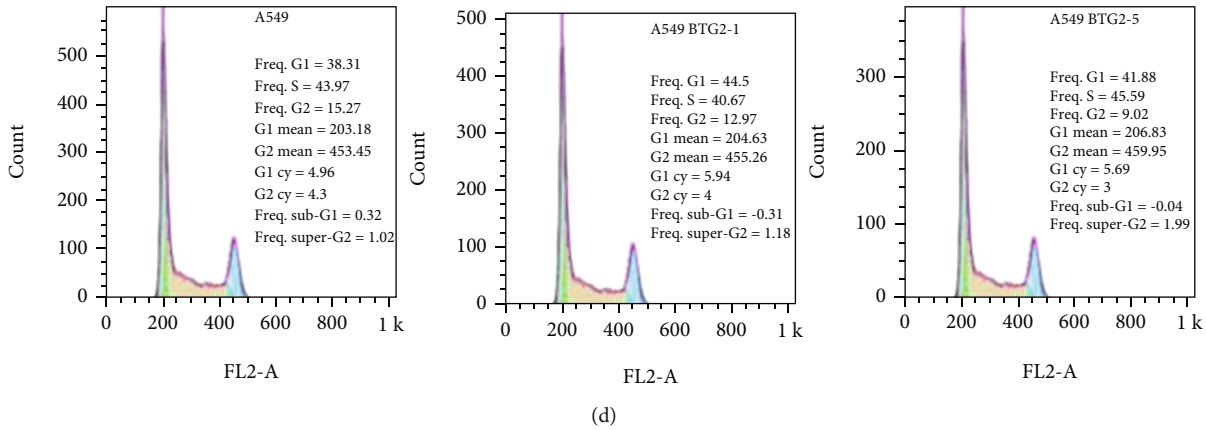

(d)

Figure 3: (a) The Western blot of BTG2 expression in selected clones of parental and BTG2 overexpressed cells. BTG2 expression level in HeLa cells served as a positive control and β-actin level as an internal control. (b) Cell growth determined by CCK-8 assays in BTG2- or vector-transfected A549 cells. (c) Representative cell cycle and flow cytometry data. (d) Cellular apoptosis was assessed via flow cytometry analysis using Annexin V-FITC and PI double staining. Data are presented as the mean ± SD and represent three independent experiments. $^{*}P < 0.05$ by Student's t-test.

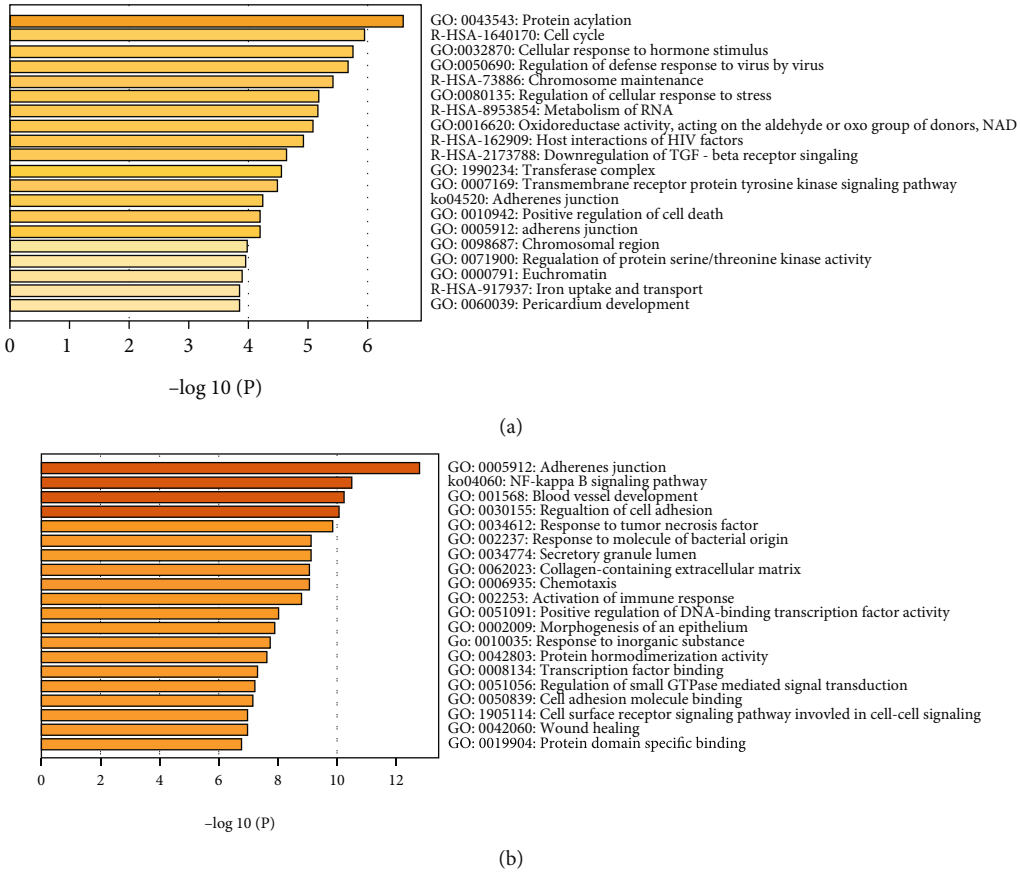

(a)

(b)

Figure 4: Analysis of GO and KEGG pathways of downregulated genes (a) and upregulated genes (b).

stimulus, and regulation of defense response to the virus. The pathway analysis demonstrated that cell cycle, chromosome maintenance, metabolism of RNA, host interactions of HIV factors, TGF-beta receptor signaling, and iron uptake and transport were significantly enriched (Figure 4(a)). The protein-protein interaction (PPI) analysis identified in the downregulated genes is shown in Figure 5. The most significant molecular complex detection (MCODE) components

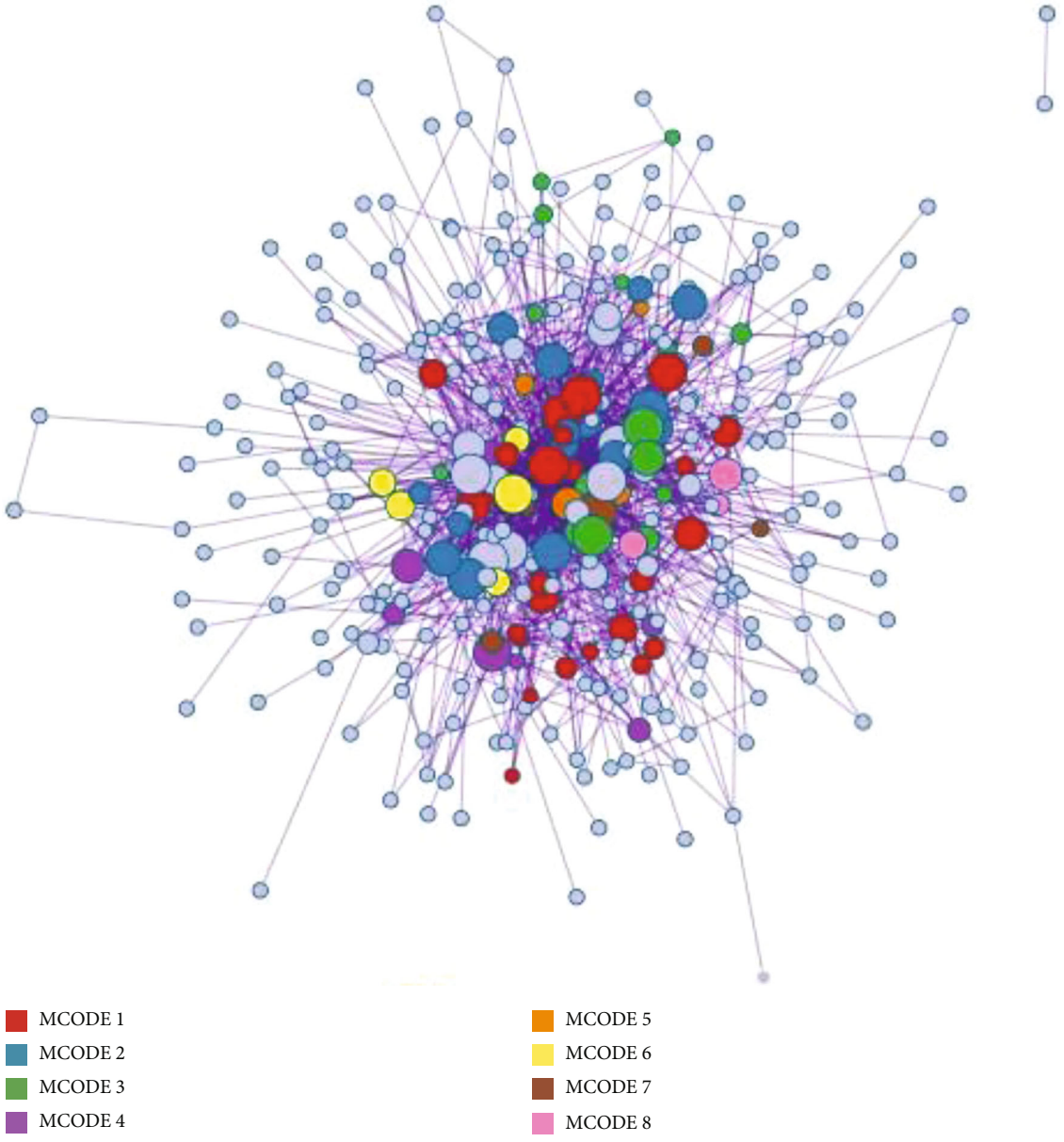

(a)

Figure 5: Continued.

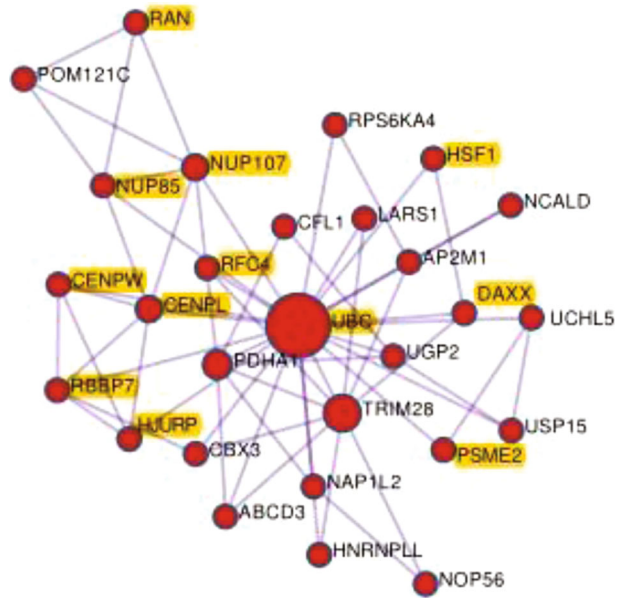

(b)

Figure 5: PPI network and MCODE components identified in downregulated genes. (a) PPI network of proteins. (b) MCODE1 was selected from the PPI network. Genes associated with the cell cycle are colored in yellow.

were extracted from the PPI network. Twelve genes, DAXX, PSME2, RAN, RBBP7, RFC4, UBC, HJURP, NUP107, NUP85, CENPL, CENPW, and HSF1, were highlighted in MCODE 1 including cell cycle pathway (Figure 5).

The most significantly enriched GO terms of upregulated genes were a response to adhesion junction, blood vessel development, and regulation of cell adhesion, respectively. KEGG enrichment analysis revealed that highly expressed genes participated in the NF-κB signaling pathway (Figure 4(b)). The PPI enrichment analysis of upregulated genes identified eight MCODE components. Three genes, NFKBIA, RELB, and ERC1, were enriched in the MCODE5 containing NF-κB signaling pathway and NIK/NF-κB signaling (Figure 6).

BTG2 overexpression led to significant downregulation of genes involved in cell cycle progression, consistent with findings in the flow cytometry analysis. Conversely, genes involved in the NF-κB signaling pathway were significantly upregulated, indicating activation of the survival pathway upon BTG2 overexpression.

4. Discussion

We investigated the BTG2 function in LUAD. First, we evaluated the mRNA expression level of BTG2 and its effect on prognosis in LUAD. For further determining BTG2 gene activity, we used A549 cells with low BTG2 expression as our target cells. Then, the cell strain with BTG2 stable expression was analyzed through *in vitro* studies. Our results might provide some clues on the functional role of this gene in adenocarcinoma cancer.

Previous studies showed that BTG2 was significantly downregulated and linked with poor lung cancer patient prognosis. In line with these findings, our present data indicated that the BTG2 expression level was decreased considerably compared to normal lung tissues, and low BTG2 expression tended to have poor survival in LUAD. All these findings indicated that BTG2 is a potential lung cancer tumor suppressor.

To understand the activity of BTG2 in lung cancer, we transfected BTG2 into A549 cells. We found that BTG2 significantly induced a G1 phase cell cycle arrest, whereas cell proliferation was not influenced after BTG2 overexpression. To reveal the potential molecular mechanism, we performed RNA sequencing of BTG2 overexpressed A549 cells, and the data were then checked for DEGs. 1040 DEGs were identified; these included 601 upregulated and 439 downregulated genes. These genes may provide insight into what processes, mechanisms, and pathways are affected by BTG2.

GO enrichment analysis revealed that highly expressed genes were involved in adhesion junction response, blood vessel development, and regulation of cell adhesion. According to the KEGG pathway analysis, upregulated genes, such as NFκB1, NFκBIA, PLAU, PTGS2, RELB, TNFAIP3, TRAF1, ERC1, BIRC3, ATM, CD14, CD40, CXCL2, ICAM1, CXCL8, and LTB, were involved in NF-κB signal pathway. NF-κB transcription factors are dimers that comprise RELA, c-REL, NF-κB1 (p105/p50), RELB, and NF-κB2. The NF-κB signaling pathway is one of the most important survival-signaling cascades after extracellular stimuli. In our study, the CCK-8 assay revealed that cell growth was not markedly decreased in overexpressed BTG2 A549 cells. On the other hand, we noted that downregulated genes affected the cell cycle pathways, which supports the outcome of FACS analysis. Such findings revealed that the NF-κB activation weakens BTG2 overexpression's effect on the cell cycle. Therefore, the NF-κB signaling pathway may be involved in rescuing from apoptosis in BTG2 overexpression A549 cells and helping tumor cells survive.

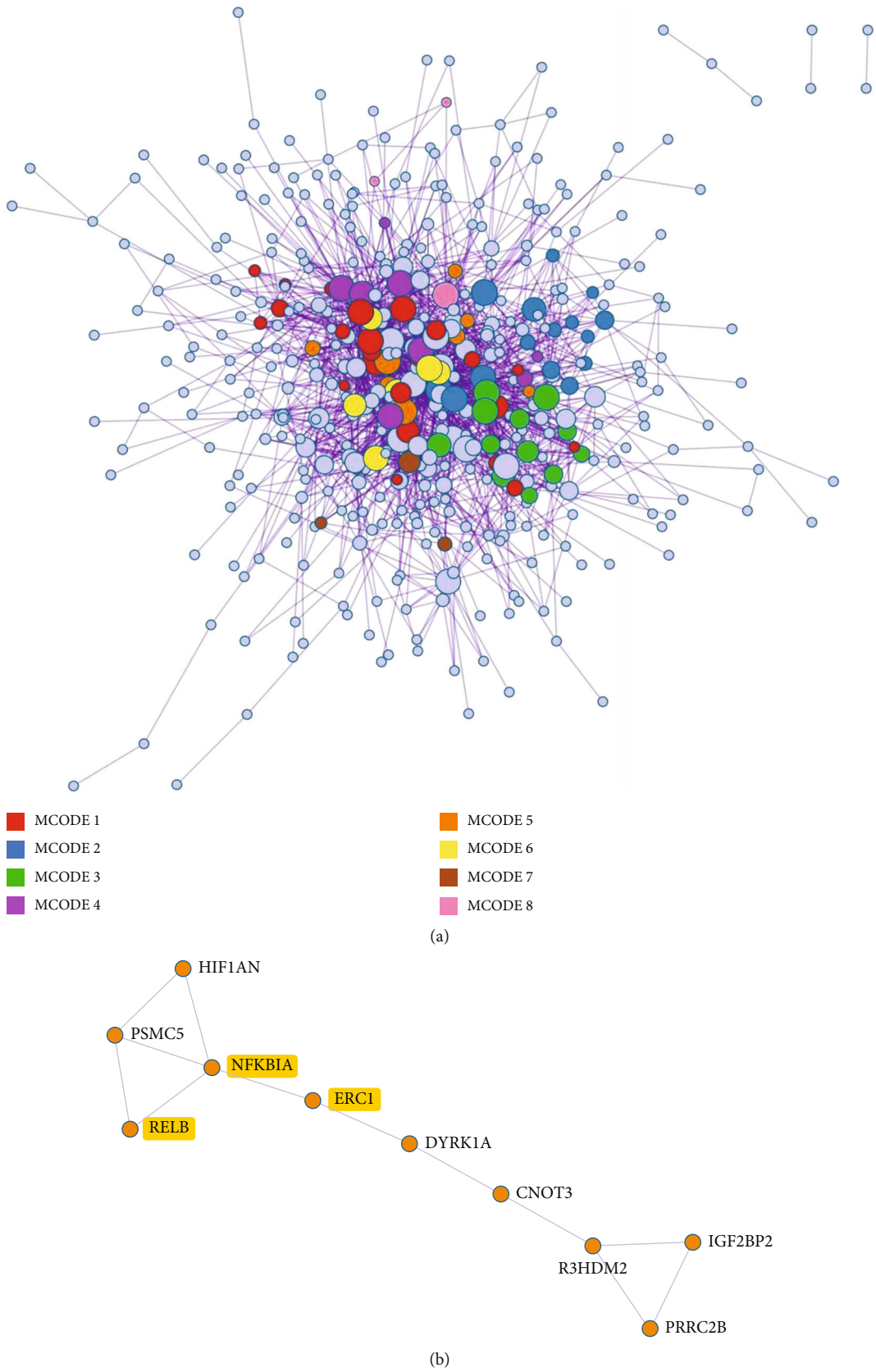

Figure 6: PPI network and MCODE components identified related to upregulated genes. (a) PPI network of proteins. (b) MCODE5 was selected from the PPI network. Genes involved in the signaling pathway of NF-κB are colored in yellow.

The TGA database assessment of the TCGA database for LUAD patients revealed that individuals with elevated levels of endogenous BTG2 expression (in tumor tissues) tend to have better clinical outcomes. Differences were also observed for the BTG2 overexpression in LUAD A549 cells. Exogenous BTG2 gene expression did not affect cell proliferation or apoptosis of A549 cells, as revealed by CCK8 and flow cytometry analyses. BTG2, as a foreign gene, randomly integrates into the host genome and will have a high expression level when inserted at a favorable position.

5. Conclusion

In conclusion, our results demonstrated that the overexpression of BTG2 in A549 cells might trigger survival-signaling pathways. And the p105: p50 NF-κB signaling has been revealed to participate in response to BTG2 exogenous overexpression. Therefore, a potential therapeutic approach for LUAD may involve targeting BTG2 by disrupting the NF-κB pathway.

Data Availability

All the data and materials are available.

Conflicts of Interest

The authors have no conflicts to declare.

Authors' Contributions

All the authors wrote and review the paper and agreed to the submission. Junting Liang and Linna Cheng have contributed equally to this work and share first authorship.

Acknowledgments

This study was supported by the Science and Technology Research in Henan Province (Grant No. 202102310463), Natural Science Foundation of Henan Province (Grant No. 202300410447 and Grant No. 222300420362 to L.C.), Provincial and Ministerial Joint Construction Project of Henan Provincial Health Commission (Grant No. SBGJ202003003 to L.C.), and Key Project of Henan Province Medical Science and Technology Project (LHGJ20190602 to L.C.).

References

[1] W. Cao, H. D. Chen, Y. W. Yu, N. Li, and W. Q. Chen, "Changing profiles of cancer burden worldwide and in China: a secondary analysis of the global cancer statistics 2020," *Chinese Medical Journal*, vol. 134, no. 7, pp. 783–791, 2021.

[2] R. L. Siegel, K. D. Miller, H. E. Fuchs, and A. Jemal, "Cancer statistics, 2021," *CA: a Cancer Journal for Clinicians*, vol. 71, no. 1, pp. 7–33, 2021.

[3] H. Nakamura and H. Saji, "Worldwide trend of increasing primary adenocarcinoma of the lung," *Surgery Today*, vol. 44, no. 6, pp. 1004–1012, 2014.

[4] J. Lipsick, "A history of cancer research: tumor suppressor genes," *Cold Spring Harbor Perspectives in Biology*, vol. 12, no. 2, 2020.

[5] Z. Mohamadzade, B. M. Soltani, Z. Ghaemi, and P. Hoseinpour, "Cell specific tumor suppressor effect of Hsa-miR-1226-3p through downregulation of *HER2*, *PIK3R2*, and *AKT1* genes," *The International Journal of Biochemistry & Cell Biology*, vol. 134, p. 105965, 2021.

[6] S. R. Ng, W. M. Rideout 3rd, E. H. Akama-Garren et al., "CRISPR-mediated modeling and functional validation of candidate tumor suppressor genes in small cell lung cancer," *Proceedings of the National Academy of Sciences of the United States of America*, vol. 117, no. 1, pp. 513–521, 2020.

[7] A. K. Virmani and A. F. Gazdar, "Tumor suppressor genes in lung cancer," *Methods in Molecular Biology*, vol. 222, pp. 97–115, 2003.

[8] L. Yang, F. Lin, Z. Gao, X. Chen, H. Zhang, and K. Dong, "Anti-tumor peptide SA12 inhibits metastasis of MDA-MB-231 and MCF-7 breast cancer cells via increasing expression of the tumor metastasis suppressor genes, CDH1, nm23-H1 and BRMS1," *Experimental and Therapeutic Medicine*, vol. 20, no. 2, pp. 1758–1763, 2020.

[9] C. Zhang, M. Jiang, N. Zhou et al., "Use tumor suppressor genes as biomarkers for diagnosis of non-small cell lung cancer," *Scientific Reports*, vol. 11, no. 1, p. 3596, 2021.

[10] P. Buanne, G. Corrente, L. Micheli et al., "Cloning of PC3B, a novel member of the PC3/BTG/TOB family of growth inhibitory genes, highly expressed in the olfactory epithelium," *Genomics*, vol. 68, no. 3, pp. 253–263, 2000.

[11] S. Matsuda, J. Rouault, J. Magaud, and C. Berthet, "In search of a function for the TIS21/PC3/BTG1/TOB family," *FEBS Letters*, vol. 497, no. 2-3, pp. 67–72, 2001.

[12] B. Mao, Z. Zhang, and G. Wang, "BTG2: a rising star of tumor suppressors (review)," *International Journal of Oncology*, vol. 46, no. 2, pp. 459–464, 2015.

[13] R. Terra, H. Luo, X. Qiao, and J. Wu, "Tissue-specific expression of B-cell translocation gene 2 (BTG2) and its function in T-cell immune responses in a transgenic mouse model," *International Immunology*, vol. 20, no. 3, pp. 317–326, 2008.

[14] L. Zhang, H. Huang, K. Wu, M. Wang, and B. Wu, "Impact of BTG2 expression on proliferation and invasion of gastric cancer cells in vitro," *Molecular Biology Reports*, vol. 37, no. 6, pp. 2579–2586, 2010.

[15] M. A. Ficazzola, M. Fraiman, J. Gitlin et al., "Antiproliferative B cell translocation gene 2 protein is down-regulated post-transcriptionally as an early event in prostate carcinogenesis," *Carcinogenesis*, vol. 22, no. 8, pp. 1271–1279, 2001.

[16] P. Wang, Y. Cai, D. Lin, and Y. Jiang, "Gamma irradiation upregulates B-cell translocation gene 2 to attenuate cell proliferation of lung cancer cells through the JNK and NF-B pathways," *Oncology Research*, vol. 25, no. 7, pp. 1199–1205, 2017.

[17] Y. Chen, C. Chen, Z. Zhang et al., "Expression of B-cell translocation gene 2 is associated with favorable prognosis in hepatocellular carcinoma patients and sensitizes irradiation-induced hepatocellular carcinoma cell apoptosis in vitro and in nude mice," *Oncology Letters*, vol. 13, no. 4, pp. 2366–2372, 2017.

[18] H. Kawakubo, E. Brachtel, T. Hayashida et al., "Loss of B-cell translocation gene-2 in estrogen receptor-positive breast carcinoma is associated with tumor grade and overexpression of cyclin d1 protein," *Cancer Research*, vol. 66, no. 14, pp. 7075–7082, 2006.

[19] L. Yuniati, B. Scheijen, L. T. Van Der Meer, and F. N. Van Leeuwen, "Tumor suppressors BTG1 and BTG2: beyond

growth control," *Journal of Cellular Physiology*, vol. 234, no. 5, pp. 5379–5389, 2019.

[20] V. Coppola, M. Musumeci, M. Patrizii et al., "BTG2 loss and miR-21 upregulation contribute to prostate cell transformation by inducing luminal markers expression and epithelial-mesenchymal transition," *Oncogene*, vol. 32, no. 14, pp. 1843–1853, 2013.

[21] S. Farioli-Vecchioli, M. Tanori, L. Micheli et al., "Inhibition of medulloblastoma tumorigenesis by the antiproliferative and pro-differentiative gene PC3," *The FASEB Journal*, vol. 21, no. 9, pp. 2215–2225, 2007.

[22] H. Chen, H. Pan, Y. Qian, W. Zhou, and X. Liu, "MiR-25-3p promotes the proliferation of triple negative breast cancer by targeting BTG2," *Molecular Cancer*, vol. 17, no. 1, p. 4, 2018.

Hindawi
Journal of Oncology
Volume 2022, Article ID 4662874, 10 pages
https://doi.org/10.1155/2022/4662874

Research Article

Immune Effect of T Lymphocytes Infiltrated by Tumors on Non-Small-Cell Lung Cancer

Siyuan Sheng,[1] **Chuangang Lu**,[2] **Jianhui Guo**,[3] **Minjing Liu**,[1] **and Yongdong Wu**[1]

[1]*Department of Basic Medicine, Xiangnan University, Chenzhou 423000, Hunan, China*
[2]*Sanya Central Hospital, Sanya 572000, Hainan, China*
[3]*Spine Surgery of Changde Second People's Hospital, Changde 415000, Hunan, China*

Correspondence should be addressed to Siyuan Sheng; shengsiyuan@xnu.edu.cn

Received 18 July 2022; Revised 10 August 2022; Accepted 17 August 2022; Published 10 September 2022

Academic Editor: İbrahim Hakkı Cigerci

Lung cancer is increasing every year and it has high morbidity and mortality. Antitumor immunotherapy is a new method for the treatment of lung cancer. Currently, tumor immunotherapy mainly includes classical immunotherapy and immune-targeted therapy To explore the influence of tumor T-lymphocyte (T-cell) infiltration in non-small-cell lung cancer (NSCLC) patients, 100 NSCLC patients diagnosed and treated in Changde Second People's hospital were recruited. Patients were followed up for 3 years. The subjects were divided into a survival group (group S) and a death group (group D). The patient's pathological tissue sections were made, and the degree of T-cell infiltration was counted by H&E (Hematoxylin and eosin) staining. The infiltration degree was graded, and the positive rate of T-cell subsets was calculated by immunohistochemical staining. The 3-year positive rate was 48%, with 48 cases in group S and 52 cases in group D. The positive rate of H&E staining of group S was 100%, including 0 cases of grade 0, 5 cases of grade 1 (10.42%), 16 cases of grade 2 (33.33%), and 27 cases of grade 3 (56.25%). The positive rate of group D was 86.54%, including 4 cases of grade 0 (8.89%), 10 cases of grade 1 (22.22%), 25 cases of grade 2 (55.56%), and 6 cases of grade 3 (13.33%). The total number of T-cell infiltrates in group S was much higher than that in group D ($P < 0.05$). Immunohistochemical results showed that the mean positive rate of $CD8^+$ T-cell infiltration was 72.1% in group S and 47.6% in group D, with a considerable difference ($P < 0.05$). No remarkable difference was found in $CD4^+$ and $CD25^+$ ($P < 0.05$). $CD8^+ + CD4^+$, $CD8^+/CD4^+$, $CD25^+/CD8^+$, $CD25^+/CD4^+$, and $CD25^+/(CD8^+ + CD4^+)$ positive rates were calculated, and the difference between group S and group D was substantial in $CD8^+ + CD4^+$ ($P < 0.05$). The results showed that T cells infiltrated by tumors had an immunosuppressive effect on tumor cells.

1. Introduction

Lung cancer is a malignant tumor with high morbidity and mortality that occurs in the upper bronchial mucosa, and its morbidity and mortality are increasing every year [1–3]. In 2020, the morbidity and mortality of lung cancer patients in China were 37.0% and 39.8%, respectively, worldwide, with 816,000 new cases, accounting for 17.9% of new cancers in China [4]. The number of deaths were 715,000, accounting for 23.8% of the total deaths due to malignant tumors in China. Among them, 80%–85% of lung cancer patients have non-small-cell lung cancer (NSCLC). NSCLC includes adenocarcinoma, squamous cell carcinoma, and large cell carcinoma, and treatment is generally carried out according to clinical stage [5–7]. The survival time of lung cancer patients is closely related to clinical stage. Early screening and diagnosis can improve the positive rate of NSCLC patients and reduce mortality. Since 2005, China has carried out malignant tumor screening programs, including lung cancer, in rural and urban areas. It aims to improve the medical level and strengthen the publicity of tumor knowledge (including the symptoms of different tumors, examination methods, and prevention measures), improve the national lung cancer screening rate, and achieve early detection and early treatment. Despite the continuous progress of medical technology and the increasing number of treatment methods in recent years, the positive rate of NSCLC patients is still not high. Some studies have found

that the 5-year positive rate is less than 20%, and local recurrence and distant metastasis are the two main reasons leading to the high mortality of patients [8, 9].

At present, the main treatments include surgery, radiotherapy, chemotherapy, and immunotherapy. The tumor immune microenvironment is closely related to the occurrence and development of tumors. Immune cells, especially the T lymphocyte subpopulation, maintain normal immune function and monitor the body's immune function. Immune suppression lead to the tumors formation. The factors that affect mutant cells to avoid immune surveillance mainly include tumor immunosuppression and tolerance. The first kind is tumor immunosuppression. Tumors induce the body to produce immunosuppressive cells and factors, such as regulatory T cells (Treg) and myeloid-derived suppressor cells (MDSCs). Tregs are produced by $CD4^+$ and $CD25^+$ T-cell subsets in the thymus to maintain the immune function and stability of the internal environment. These cells account for 2%–5% of peripheral T cells. Tregs inhibit T-cell function and secrete immunosuppressive factors to promote tumors. Bone marrow cells are derived from MDSCs, a population of cells that can accumulate gradually in cancer patients and suppress immune function. The second is tumor immune tolerance. Due to the lack of one or more components to stimulate the body's immune system, tumor cells have low immunogenicity and even induce the death of immune functional cells [10–14].

Antitumor immunotherapy is a new method for the treatment of lung cancer. Currently, tumor immunotherapy mainly includes classical immunotherapy and immune targeted therapy [15–20]. Classical immunotherapy generally includes three strategies, namely, active, passive, and supportive immunotherapy. The first is active immunotherapy. By injecting a tumor vaccine, $CD4^+$ and $CD8^+$ effector T cells can be induced to clear tumor cells in the patient and enable host cells to avoid attack. At present, many tumor vaccines have been developed in the clinic, including antigen specific, tumor cell, and DC cell vaccines [21]. The second is passive immunotherapy. The immune effector is produced outside the body and delivered into the tumor patient. The most common forms are injections of recombinant cytokines, immune effector cells, and monoclonal antibodies [22]. The efficacy of immunotherapy generally does not decrease with advanced age, but the efficacy generally decreases in patients with autoimmune diseases and long-term use of hormone-based drugs [23].

The parameter, which is used commonly for evaluating anti-tumor efficacy, is the Response Evaluation Criteria in Solid Tumors (RECIST) for solid tumors [24]. Patients were graded into complete response (CR), partial response (PR), progressive disease (PD), and stable disease (SD) rates. However, it is now evaluated that this standard evaluation is not a good evaluation of the efficacy of immunotherapy for tumor treatment. For example, RECIST can be evaluated as PD after immunotherapy, which may change to CR, PR, or SD. Therefore, researchers have proposed a new efficacy evaluation criterion, the immune-related Response Criteria (IRRC), which can more accurately and objectively evaluate the efficacy of tumor immunotherapy [25]. Tumor-infiltrating T cells have been proven to be a predictor of the efficacy of immunotherapy by many studies. Anti-PD-1 mainly inhibits tumor proliferation by inducing tumor infiltration of $CD8^+$ T cells, while anti-CTLA-4 plays an immunotherapy role by inducing $CD8^+$ effector T cells and $CD8^+$ T-cell proliferation. The content of CTLA-4 +PD-1+ tumor-infiltrating cells is correlated with the therapeutic effect of PD-1, and the higher the content is, the stronger the effect [26].

Studies have shown that approximately two-third of the infiltrated cells in the stroma of NSCLC tumors are lymphocytes, and approximately 80% of the lymphocytes are T cells [27]. Tumor-infiltrating lymphocytes (TILs) refer to T cells that mainly exist in the local part of the tumor. Lymphocytes are immersed in the tumor microenvironment to participate in tumor immunity, and TILs can suppress tumor growth to a certain extent, which represents the body's anti-tumor immune response. TILs with different densities have different prognostic effects on tumors. Studies have confirmed that certain types of TILs, such as $CD4^+$ T and $CD8^+$ T cells, can inhibit tumor growth and have immune effects on tumor patients. It was found that the total number of tumor-infiltrating T cells was related to the prognosis of the tumor due to the immune effect on the tumor, and the tumor-infiltrating T-cell subpopulation also had a strong relationship with the prognosis. Abnormal immune function will weaken the body's ability to defend against tumors and cause abnormal proliferation and diffusion of tumor cells, so the immune function of most patients with malignant tumors will have problems. Studies have confirmed that T-cell dysfunction can occur and fail to inhibit tumor growth, even with a high degree of tumor invasion [28]. Tumor-infiltrating T cells are populations containing many different subsets of cells, which can be divided into different subsets according to different differentiated antigens, including five types, namely, $CD3^+$, $CD4^+$, $CD8^+$, $CD16^+$, and $CD25^+$. Under normal circumstances, the ratios of TILs and T-cell subsets from different tumor sources are different, but the ratios remain constant and cooperate and restrict each other to maintain the normal immune function of the body. Higher or lower ratios of either of them will lead to immune disorders. For example, $CD8^+$ T cells increased and the $CD4^+/CD8^+$ ratio decreased in infiltrating lymphocytes of oral squamous cell carcinoma. The lower the degree of differentiation, the lower the ratio. The content of $CD25^+$ T cells in freshly isolated tumor-infiltrating T cells was low, and the percentage of $CD25^+$ T-cells increased with increasing $CD25^+$ T cells In Vitro. $CD3^+$ subsets represent the immune function of T cells in the body and are mainly composed of $CD4^+$ and $CD8^+$ cells. $CD4^+$ T cells represent helper T cells (Th), which can assist cellular immunity, while $CD8^+$ cells represent inhibitory T cells (Ts), which can inhibit humoral immunity. $CD8^+$ cells are proposed to be the effector cells of the body's immune cells that directly kill the tumor, and the more $CD8^+$ cells there are, the better the prognosis of the tumor. Observing the status of tumor-infiltrating T cells in NSCLC patients can analyze their immune effect on tumors and analyze the development of tumors [29–35].

2. Materials and Methods

2.1. The Research Objective. One hundred NSCLC patients diagnosed and treated in Changde Second People's hospital from December 2017 to December 2018 were recruited. Patients were followed up for 3 years. The inclusion criteria for patients is as follows: (i) patients aged ≥18 years; (ii) patients diagnosed with NSCLC by pathological examination and imaging examination; and (iii) patients without preoperative chemoradiotherapy. The exclusion criteria for patients is (i) patients with other malignant tumors; (ii) patients with heart, liver, kidney, and other life-threatening diseases; (iii) patients with certain mental diseases who could not cooperate with the experiment on their own; and (iv) patients with incomplete or lost clinical data. All subjects signed informed consent forms, and the study was approved by the ethics committee of Changde Second People's hospital.

2.2. Main Instruments and Reagents. Table 1 shows the reagents used for the detection of various CD T cells.

Table 1: Main reagents used in the experiment.

Reagent	Detection	Company
CD8 monoclonal antibody (McAb)	$CD8^+$ T cell	
CD4 McAb	$CD4^+$ T cell	BD, USA
CD25 McAb	$CD25^+$ T cell	

2.3. The Experimental Methods. The survival of patients was followed up by telephone or letter. The total follow-up time was 3 years, and the survival of patients over 3 years was recorded. The study subjects were divided into group S and group D, and the positive rate of patients was counted.

Three years later, pathological specimens of the patients were collected, and tissue sections were made. H&E staining was performed to calculate the degree of T-cell infiltration and grade the infiltration degree. Specific indicators are shown in Table 2. The positive rates of $CD8^+$, $CD4^+$, and $CD25^+$ lymphocyte subsets were calculated by immunohistochemical staining.

(i) Section dewaxing. Paraffin was removed from tissue sections by xylene and placed in ethanol gradient concentration solution (80%, 70%, 50%) and distilled water for 1 min each.

(ii) H&E staining. After section dewaxing process, the staining of nucleus was done by placing section in hematoxylin dye solution for 10 min and then washed with water for 5 min. In the separation, 1.0% hydrochloric acid + ethanol solution was used for 30 s, and then washed with water for 30 s. Blue staining was done by dilute lithium carbonate solution for 1 min. After staining, samples were washed with water. Cytoplasm staining was done with 0.5% eosin solution for 1 min, followed by washing. 50%, 70%, 80%, and 95% gradient concentration ethanol solution was used for gradual dehydration for 1 min, xylene was used to make the section transparent (neutral gum seal). After that microscopic observations were done.

(iii) Immunohistochemical staining. Section dewaxing was performed and sections were incubated with 3% H_2O_2 at room temperature for 10 min and then rinsed with distilled water, Sections were immersed with PBS for 5 min (repeated twice). Primary antibody working solution (anti-CD4, CD8, CD25 mAb) was added and incubated at 37°C for 1.5 h. After that, sections were rinsed with PBS for 2 min (repeat rinsing 3 times), secondary antibody working solution was added and incubated at 37°C for 30 min. Rinsing with PBS for 2 min (repeat rinsing 3 times) was done and chromogenic agent for 10 min (DAB solution) added, which was followed by rinsing with tap water, redye, transparent, and sealed. At the end, microscope observation was performed.

$$\begin{aligned}
\text{Accumulate survival rate} &= \frac{\text{Number of survivors}}{\text{Total number}} * 100\%,\\
\text{Positive rate of HE staining} &= \frac{\text{Number of cases with lymphocyte infiltration}}{\text{Total number of this group}} * 100\%,\\
\text{Immunohistochemical staining positive rate} &= \frac{\text{Number of positive cells in 1000 lymphocytes/number of random number}}{\text{1000 lymphocytes in field of vision}} * 100\%.
\end{aligned} \tag{1}$$

2.4. The Counting Methods. H&E staining was used to display the counts of $CD8^+$ T cells, $CD4^+$ T cells, and $CD25^+$ T cells. T-cell-positive cells were stained tan-yellow. Staining numbers of $CD8^+$ T cells, $CD4^+$ T cells, and $CD25^+$ T cells in each field were counted. The three visual fields were selected, and the count was averaged. The colored cells were pressed, the upper line and the right line were counted, and the lower line and the left line were discarded.

The method used to determine the immunohistochemical results is as follows. Pathological sections were observed under a high-power microscope (×400). The field with more tumor cells and fewer tumor stroma and normal cells was selected, and the field with more tumor stroma and fewer tumor cells was selected. Three fields were randomly selected, each field was counted three times, and the average value was taken.

Table 2: Grade indicators of lymphocyte infiltration.

Level	Indicator
0	No lymphocyte
1	A small amount, approximately 1/3 of the field of vision
2	Distributed in clusters, accounting for approximately 1/3 to 2/3 of the field of vision
3	A lot, more than 2/3 of the field of view

The technical route followed in this study is shown in Figure 1.

2.5. Statistical Methods. All the data were analyzed by SPSS 26.0. The counting data were indicated with a percentage (%), tested using the χ^2(Chi-squared) test. $P < 0.05$ was considered statistically significant.

3. Results

3.1. Statistical Results of Patient Survival. There were 100 patients with TNM stages as follows. There were 16 patients in stage I, 15 in stage II, 32 in stage III, and 37 in stage IV. There were 59 male patients and 41 female patients. The average age was 59.2 ± 4.51 years (Figure 2). Forty-eight patients (26 males and 22 females) survived, and 52 patients (33 males and 19 females) died at 3 years, with an SR of 48% (48/100). The 100 patients were divided into group S and group D according to 3-year survival (Figure 3).

3.2. Relationship between Total T-Cell Infiltration and the Postoperative Survival Rate of NSCLC Patients. Patients in group S (48 cases) had lymphocyte infiltration in pathological tissue sections, with a positive rate of 100%, including 0 cases of grade 0, 5 cases of grade 1 (10.42%), 16 cases of grade 2 (33.33%), and 27 cases of grade 3 (56.25%). In patients in group D (52 cases), 7 cases did not have lymphocytic infiltration, and 45 cases had lymphocytic infiltration, with a positive rate of 86.54%, including 4 cases of grade 0 (8.89%), 10 cases of grade 1 (22.22%), 25 cases of grade 2 (55.56%), and 6 cases of grade 3 (13.33%). The total number of T-cell infiltrates in group S was notably higher than that in group D ($P < 0.05$) (Figures 4 and 5).

3.3. Relationship between $CD8^+$, $CD4^+$, $CD25^+$ T-Cell Infiltration and the Postoperative Survival Rate of NSCLC Patients. Immunohistochemistry was performed on pathological sections of all patients with $CD8^+$ monoclonal antibody, and the positive cells were brown-yellow. In Figure 6(a), the average positive rate of patients in group S (48 cases) was 72.1% and that of patients in group D (52 cases) was 47.6%. The average positive rate of the $CD8^+$ subgroup in group S was obviously superior to that in group D ($P < 0.05$). Immunohistochemistry was performed on pathological sections of all patients with CD4 mAbs, and the positive cells were brown-yellow. The results showed that the average positive rate of group S (48 cases) was 15.3%, and the average positive rate of group D (52 cases) was 11.7%. The average positive rate of $CD4^+$ subsets in group S was higher than that in group D, and the difference was not remarkable ($P > 0.05$) (Figure 6(b)). Immunohistochemistry was performed on pathological sections of all patients with CD25 mAbs, and the positive cells were brownish yellow. The results in Figure 6(c) show that the average positive rate of group S (48 cases) was 13.2%, and the average positive rate of group D (52 cases) was 8.9%. The average positive rate of the $CD25^+$ subgroup in group S was superior to that in group D, but the difference was not substantial ($P > 0.05$).

3.4. Relationship between $CD8^+ + CD4^+$ and $CD8^+/CD4^+$ and the Postoperative Survival Rate of NSCLC Patients. The sum of $CD8^+$ T cells and the positive percentage of $CD4^+$ T cells ($CD8^+ + CD4^+$) represents the degree of T-cell infiltration. Figure 7(a) shows that the average degree of T-cell infiltration in group S (48 cases) was 87.4% and that in group D (52 cases) was 59.3%. The degree of T-cell infiltration in group S was evidently higher than that in group D ($P < 0.05$). Figure 7(b) shows that the ratio of the $CD8^+/CD4^+$ T-cell positive percentage in group S (48 cases) was 4.71 on average and that in group D (52 cases) was 4.07 on average. Group S was higher than group D ($P < 0.05$).

3.5. Relationship between $(CD25^+/CD8^+)$ $(CD25^+/CD4^+)$ $(CD25^+/(CD8^+ + CD4^+))$ and Postoperative Survival Rate of NSCLC Patients. In Figure 8(a), the average $CD25^+/CD8^+$ T-cell ratio of group S (48 cases) was 0.183, and the average $CD25^+/CD8^+$ T-cell ratio of group D (52 cases) was 0.187, showing no significant difference ($P > 0.05$). In Figure 8(b), the average $CD25^+/CD4^+$ T-cell ratio of group S (48 cases) was 0.863, and the average $CD25^+/CD4^+$T-cell ratio of group D (52 cases) was 0.761, showing no significance ($P > 0.05$). Figure 8(c) shows that the average $CD25^+/(CD8^+ + CD4^+)$ T-cell ratio of group S (48 cases) was 0.151, and the average $CD25^+/CD8^+$ T-cell ratio of group D (52 cases) was 0.150, showing no significance ($P > 0.05$).

4. Discussion

Lung cancer is a malignant tumor with high morbidity and mortality, among which 80%–85% of lung cancer patients have NSCLC. Despite the continuous progress of medical technology in recent years, the positive rate of NSCLC patients is still not high, and some studies have found that the 5-year SR is less than 20%. The immune system of the body, especially T cells, is closely related to the occurrence and development of tumors. Zylbermann et al. speculated

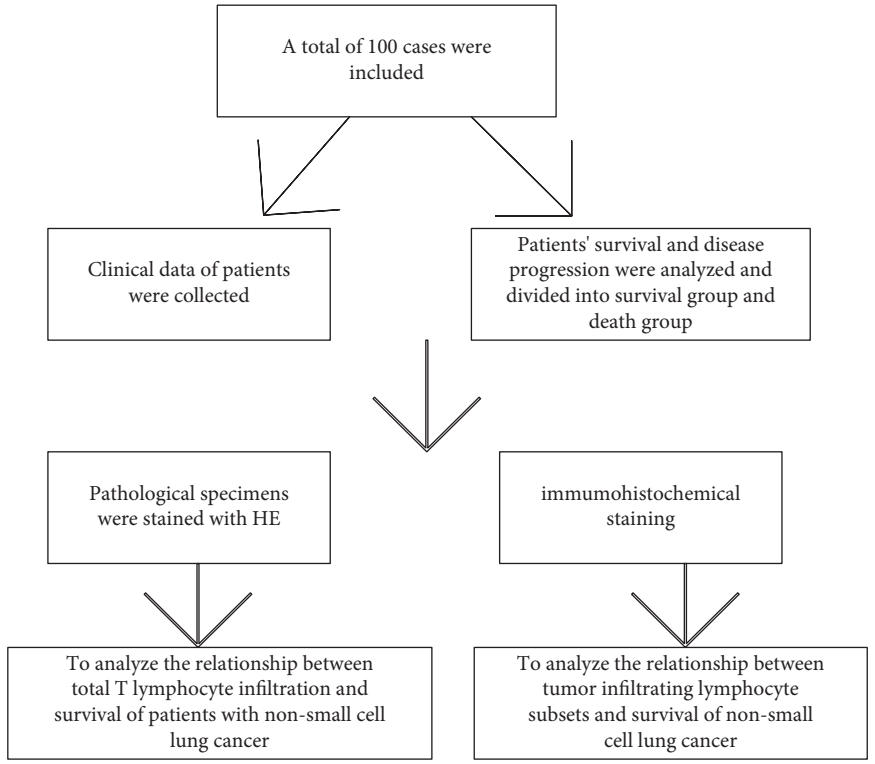

Figure 1: Technical flowchart to analyze the relationship between T-cell infiltration and survival of S and D group.

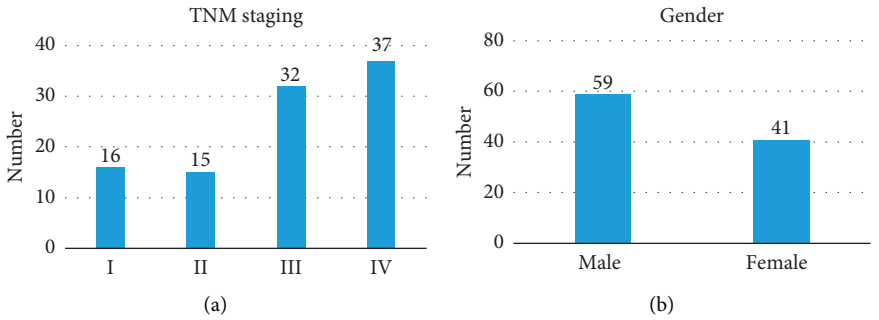

Figure 2: Patient general data statistical results. (a) TNM staging of patients; (b) the sex distribution of patients.

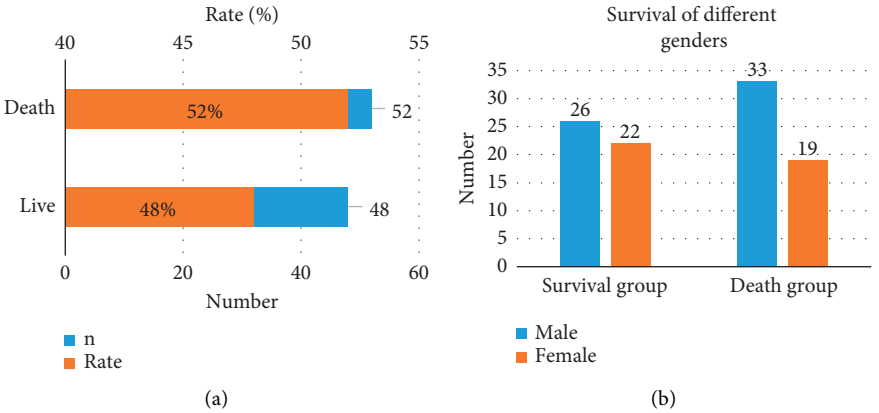

Figure 3: Statistical results of the 3-year survival of patients. Note: (a) represents the overall survival situation; (b) represents the survival of patients of both sexes.

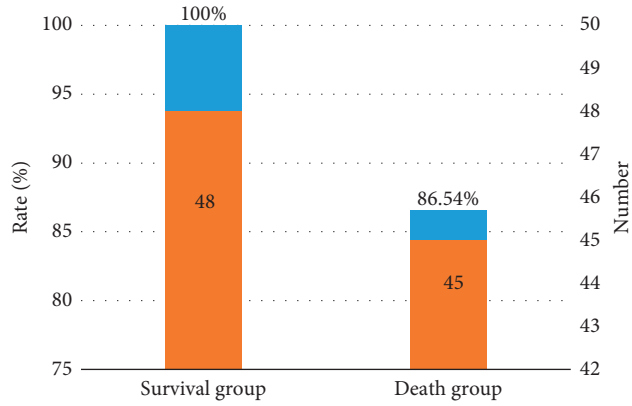

Figure 4: Comparison of the total number and positive rate of infiltrating lymphocytes between group S and group D.

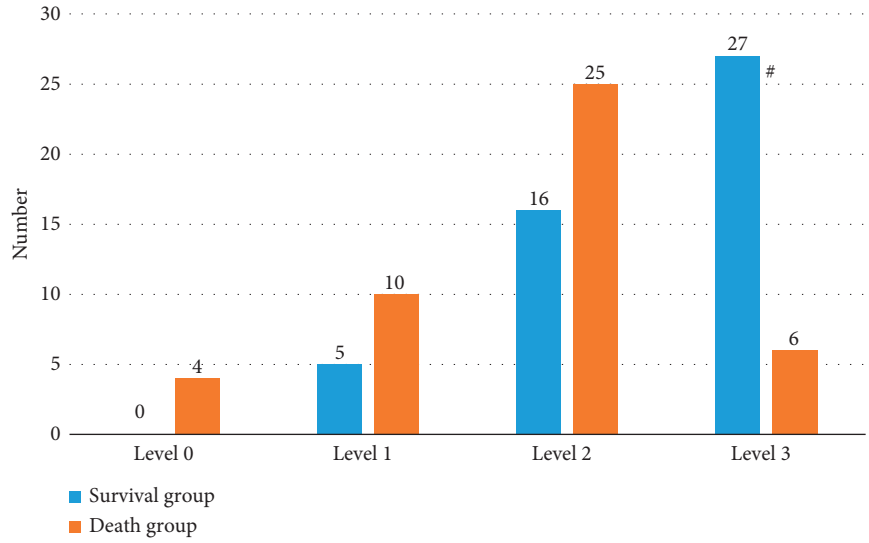

Figure 5: Comparison of lymphocyte infiltration grade between group S and group D. Note: #indicates that the total number of T-cell infiltrates in group S was considerably higher than that in group D, $P < 0.05$.

that tumor-infiltrating lymphocytes can defend against tumors [36]. Tumor-infiltrating T cells are lymphocytes dominated by T cells that exist locally in tumors and can inhibit tumor growth, representing the body's anti-tumor immune response [37]. TILs with different densities have different prognostic effects on tumors. Studies have confirmed that certain types of $CD3^+$ T and $CD8^+$ T cells in TILs can inhibit tumor growth and have immune effects on tumor patients [38]. It was found that the total number of tumor-infiltrating T cells was related to the prognosis of the tumor due to the immune effect on the tumor, and the tumor-infiltrating T-cell subpopulation also had a strong relationship with the prognosis [39]. Tumor-infiltrating T cells are populations containing many different subsets of cells, which can be divided into different subsets according to different differentiated antigens, including 5 types, namely, $CD3^+$, $CD4^+$, $CD8^+$, $CD16^+$, and $CD25^+$ [40]. Under normal circumstances, the ratios of TILs and T-cell subsets from different tumor sources are different, but the ratios remain constant and cooperate and restrict each other to maintain the normal immune function of the body. Higher or lower ratios of either of them will lead to immune disorders. Observing the status of tumor-infiltrating T cells in NSCLC patients can analyze their immune effect on tumors and analyze the development of tumors.

The results showed that 48 patients (26 males and 22 females) survived and 52 patients (33 males and 19 females) died at 3 years, with an positive rate of 48% (48/100). The 100 patients were divided into group S ($n = 48$) and group D ($n = 52$) according to 3-year survival. No great difference was indicated in age or sex between group S and group D, $P > 0.05$, which was comparable. HE staining of the pathological sections of 48 patients in group S showed lymphocyte infiltration, with a positive rate of 100%, including 0 cases of grade 0, 5 cases of grade 1 (10.42%), 16 cases of grade 2 (33.33%), and 27 cases of grade 3 (56.25%). In group D (52 cases), 7 cases did not have lymphocytic infiltration, and 45 cases had lymphocytic infiltration, with a positive rate of 86.54%, including 4 cases of grade 0 (8.89%), 10 cases of grade 1 (22.22%), 25 cases of grade 2 (55.56%), and 6 cases of grade 3 (13.33%). The total number of T-cell infiltrates in group S was higher than that in group D ($P < 0.05$). This finding indicates that tumor-infiltrating T cells have

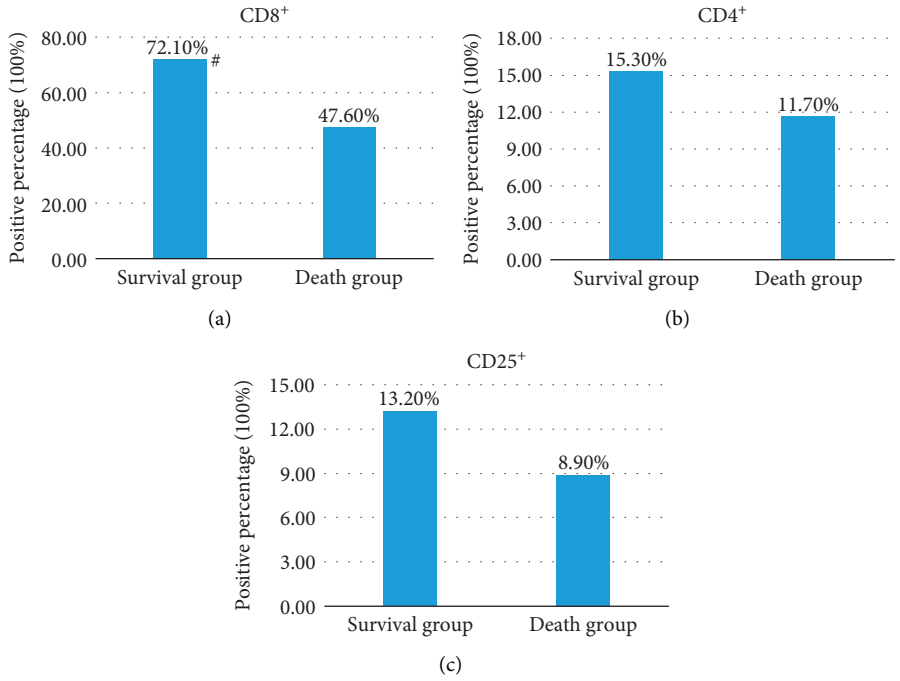

Figure 6: Relationship between $CD8^+$, $CD4^+$, and $CD25^+$ cell infiltration and postoperative positive rate in NSCLC patients. (a) The relationship between $CD8^+$ cell infiltration and postoperative positive rate of NSCLC patients; (b) the relationship between $CD4^+$ cell infiltration and postoperative positive rate of NSCLC patients; (c) the relationship between $CD25^+$ cell infiltration and postoperative positive rate NSCLC patients. #indicates that the average positive rate of the $CD8^+$ subgroup in group S was substantially higher than that in group D ($P < 0.05$).

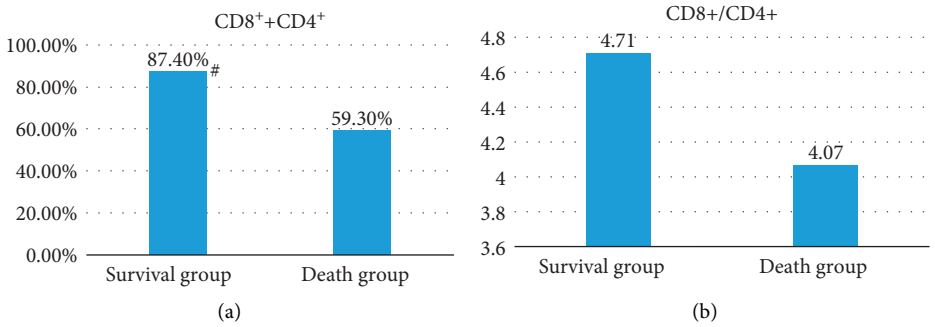

Figure 7: Relationship between $CD8^+$ +$CD4^+$, $CD8^+/CD4^+$ and postoperative positive rate in NSCLC patients. (a) The sum of the positive percentages of $CD8^+$ T cells and $CD4^+$ T cells; (b) the ratio of $CD8^+$ T cells to $CD4^+$ T cells. #indicates that the degree of T-cell infiltration in group S was higher than that in group D, and the difference was statistically significant ($P < 0.05$).

a certain immune effect on NSCLC patients. The higher the total number of T-cell infiltrates, the slower the tumor development and the higher the survival rate of patients.

Immunohistochemical staining of pathological sections of all patients with CD8, CD4, and CD25 mAbs showed that the average positive rate of $CD8^+$ T-cell infiltration in group S (48 cases) was 72.1%, and in group D (52 cases), it was 47.6%. The average positive rate of the $CD8^+$ subgroup in group S was higher than that in group D ($P < 0.05$). The average positive rate of $CD4^+$ T-cell infiltration in group S (48 cases) was 15.3%, and in group D (52 cases), it was 11.7%. The average positive rate of $CD4^+$ subsets in group S was superior to that in group D, and the difference was not substantial ($P > 0.05$). The average positive rate of $CD25^+$ T-cell infiltration in group S (48 cases) was 13.2% and that in group D (52 cases) was 8.9%. The average positive rate of the $CD25^+$ subgroup in group S was slightly higher than that in group D ($P > 0.05$). This finding indicates that the postoperative survival rate of NSCLC patients is related to T-cell infiltration, especially $CD8^+$ cell infiltration, which has an immunosuppressive effect on local tumors. $CD4^+$ and $CD25^+$ also have certain immune effects on tumors, but the inhibitory activity is not strong, which may be related to the TNM stage of the disease, and the activity gradually increases with the development of the disease. However, it was

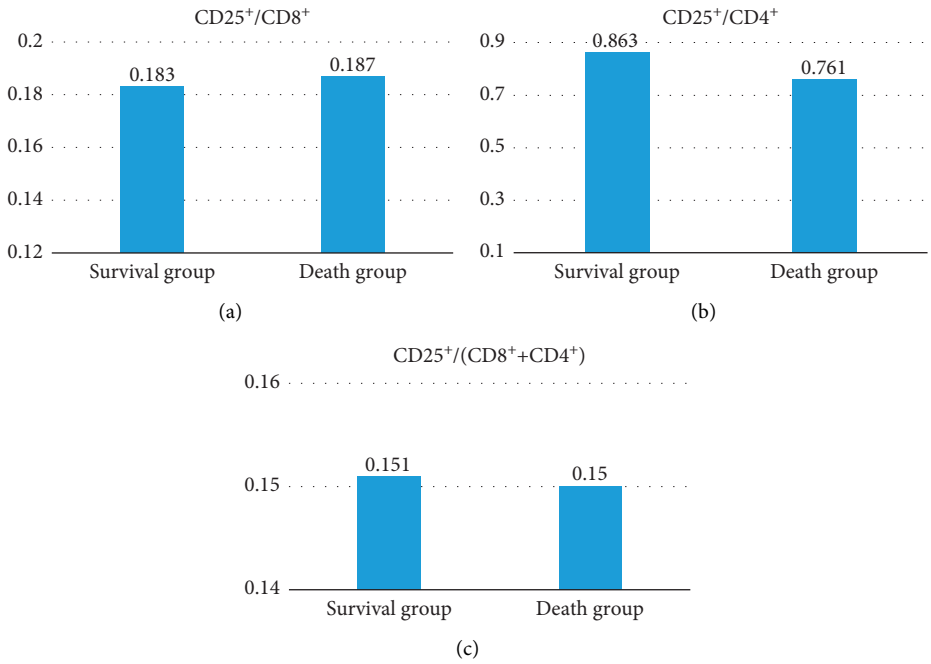

Figure 8: Relationship between ($CD25^+/CD8^+$), ($CD25^+/CD4^+$), ($CD25^+/(CD8^+ + CD4^+)$ and postoperative positive rate in NSCLC patients. (a) The relationship between $CD25^+/CD8^+$ and the postoperative positive rate of NSCLC patients; (b) the relationship between $CD25^{+/}CD4^+$ and the postoperative positive rate of NSCLC patients; (c) the relationship between $CD25^+/(CD8^+ + CD4^+)$ and the postoperative positive rate of NSCLC patients.

found that the number of $CD4^+$ cells is closely related to tumor growth [41], which was not found in this study and may be related to TNM stage and the differentiation degree of patients.

The percentages of $CD8^+$ and $CD4^+$ cells were 87.4% in group S (48 cases) and 59.3% in group D (52 cases), respectively ($P < 0.05$). The ratio of the $CD8^+$ to $CD4^+$ T-cell-positive percentage in group S (48 cases) was 4.71 on average. In group D (52 cases), the average was 4.07, and group S was higher than group D, with no notable difference ($P > 0.05$). The results showed that the sum of the $CD8^+$ and $CD4^+$ percentages was related to the postoperative survival of patients, which may be related to the immune effect of $CD8^+$; the higher the $CD8^+$ $CD4^+$ value is, the stronger the immune effect of the tumor, and the higher the SR. Some studies have shown that the $CD8^+/CD4^+$ ratio can evaluate the balance of the immune system and reflect regulatory ability, but there was no evident difference between the two groups of patients in this study, which may still need to be confirmed by many studies [42]. The average ratio of $CD25^+$ to $CD8^+$ T cells in group S (48 cases) was 0.183, and in group D (52 cases), it was 0.187, showing no statistical significance ($P > 0.05$). The average ratio of $CD25^+$ to $CD4^+$ T cells was 0.863 in group S (48 cases) and 0.761 in group D (52 cases) ($P > 0.05$). The average ratio of $CD25^+$ to $(CD8^+ + CD4^+)$ T cells in group S (48 cases) was 0.151 and that in group D (52 cases) was 0.150 ($P > 0.05$). The results showed that there was no obvious relationship between $CD25^+/CD8^+$, $CD25^+/CD4^+$, $CD25^+/(CD8^+$ $CD4^+)$ and the SR of NSCLC patients. Nevertheless, there are still some limitations in this study. First, the sample size was small and single, requiring larger samples to verify the results. Second, the follow-up period was 3 years, and patients were not followed up for 5 years or longer. All these factors will lead to errors in exploring the tumor immunity effect of tumor-infiltrating T cells on NSCLC.

5. Conclusion

In summary, the postoperative survival rate of NSCLC patients was related to T-cell infiltration, especially $CD8^+$ cell infiltration, which had an immunosuppressive effect on local tumors. In addition, it was also related to the sum of the $CD8^+$ and $CD4^+$ percentages. The higher the $CD8^+ + CD4^+$ value, the stronger the immune effect on the tumor, and the higher the SR of patients. Therefore, tumor-infiltrating T cells can inhibit tumor growth, which is related to the postoperative SR of NSCLC patients. In conclusion, tumor-infiltrating T cells had an immunosuppressive effect on tumor cells, and the total number and subsets of tumor-infiltrating T cells had a great impact on the survival rate of patients.

Data Availability

The data set used in this paper can be obtained from the corresponding author upon request.

Conflicts of Interest

The authors declared that they have no conflicts of interest regarding this work.

Acknowledgments

This work was supported by Hunan Science Foundation of China, the anti-tumor activities of CABYR-specific stem cell-like memory T cell in non-small cell lung cancer (project no. 2019JJ50566), Outstanding Youth Project of Hunan Provincial Department of Education, research on the mechanism of TCF-1 on non-small-cell Lung Cancer (Project no. 20B544), and High-level talent program of Xiangnan University.

References

[1] F. Wu, L. Wang, and C. Zhou, "Lung cancer in China: current and prospect," *Current Opinion in Oncology*, vol. 33, no. 1, pp. 40–46, 2021.

[2] J. Rodriguez-Canales, E. Parra-Cuentas, and II. Wistuba, "Diagnosis and molecular classification of lung cancer," *Cancer Treat Res*, vol. 170, pp. 25–46, 2016.

[3] I. Maghfoor and M. C. Perry, "Lung cancer," *Annals of Saudi Medicine*, vol. 25, no. 1, pp. 1–12, 2005.

[4] H. Sung, J. Ferlay, R. L. Siegel et al., "Global cancer statistics 2020: GLOBOCAN estimates of incidence and mortality worldwide for 36 cancers in 185 countries," *CA: A Cancer Journal for Clinicians*, vol. 71, no. 3, pp. 209–249, 2021.

[5] T. Akhurst, "Staging of non-small-cell lung cancer," *PET Clinics*, vol. 13, no. 1, pp. 1–10, 2018.

[6] E. C. Naylor, J. K. Desani, and P. K. Chung, "Targeted therapy and immunotherapy for lung cancer," *Surgical Oncology Clinics of North America*, vol. 25, no. 3, pp. 601–609, 2016.

[7] S. Tsim, C. A. O'Dowd, R. Milroy, and S. Davidson, "Staging of non-small cell lung cancer (NSCLC): a review," *Respiratory Medicine*, vol. 104, no. 12, pp. 1767–1774, 2010.

[8] C. M. Haskell and E. C. Holmes, "Non-small cell lung cancer," *Current Problems in Cancer*, vol. 11, no. 1, pp. 1–52, 1987.

[9] F. A. Shepherd, J. Rodrigues Pereira, T. Ciuleanu et al., "Erlotinib in previously treated non-small-cell lung cancer," *N Engl J Med*, vol. 353, no. 2, pp. 123–132, 2005.

[10] K. Kuribayashi, N. Funaguchi, and T. Nakano, "Chemotherapy for advanced non-small cell lung cancer with a focus on squamous cell carcinoma," *Journal of Cancer Research and Therapeutics*, vol. 12, no. 2, pp. 528–534, 2016.

[11] B. J. Laidlaw, J. E. Craft, and S. M. Kaech, "The multifaceted role of CD4(+) T cells in CD8(+) T cell memory," *Nat Rev Immunol*, vol. 16, no. 2, pp. 102–111, 2016.

[12] R. S. Herbst, D. Morgensztern, and C. Boshoff, "The biology and management of non-small cell lung cancer," *Nature*, vol. 553, no. 7689, pp. 446–454, 2018.

[13] M. L. Hsu and J. Naidoo, "Principles of immunotherapy in non-small cell lung cancer," *Thoracic Surgery Clinics*, vol. 30, no. 2, pp. 187–198, 2020.

[14] S. A. Patel and J. Weiss, "Advances in the treatment of non-small cell lung cancer: immunotherapy," *Clinics in Chest Medicine*, vol. 41, no. 2, pp. 237–247, 2020 Jun.

[15] A. Steven, S. A. Fisher, and B. W. Robinson, "Immunotherapy for lung cancer," *Respirology*, vol. 21, no. 5, pp. 821–833, 2016.

[16] M. Abbott and Y. Ustoyev, "Cancer and the immune system: the history and background of immunotherapy," *Seminars in Oncology Nursing*, vol. 35, no. 5, Article ID 150923, 2019 Oct.

[17] Y. Zhang and Z. Zhang, "The history and advances in cancer immunotherapy: understanding the characteristics of tumor-infiltrating immune cells and their therapeutic implications," *Cell Mol Immunol*, vol. 17, no. 8, pp. 807–821, 2020.

[18] J. Inthagard, J. Edwards, and A. K. Roseweir, "Immunotherapy: enhancing the efficacy of this promising therapeutic in multiple cancers," *Clinical Science*, vol. 133, no. 2, pp. 181–193, 2019.

[19] Á. Rodríguez Pérez, D. Campillo-Davo, V. F. I. Van Tendeloo, and D. Benitez-Ribas, "Cellular immunotherapy: a clinical state-of-the-art of a new paradigm for cancer treatment," *Clin Transl Oncol*, vol. 22, no. 11, pp. 1923–1937, 2020.

[20] E. H. Castellanos and L. Horn, "Immunotherapy in lung cancer," *Cancer Treat Res*, pp. 203–223, 2016.

[21] T. Chodon, R. C. Koya, and K. Odunsi, "Active immunotherapy of cancer," *Immunological Investigations*, vol. 44, no. 8, pp. 817–836, 2015.

[22] T. Schlake, A. Thess, M. Thran, and I. Jordan, "mRNA as novel technology for passive immunotherapy," *Cell Mol Life Sci*, vol. 76, no. 2, pp. 301–328, 2019.

[23] G. Galli, A. De Toma, F. Pagani et al., "Efficacy and safety of immunotherapy in elderly patients with non-small cell lung cancer," *Lung Cancer*, vol. 137, pp. 38–42, 2019.

[24] J. D. Wolchok, A. Hoos, S. O'Day et al., "Guidelines for the evaluation of immune therapy activity in solid tumors: immune-related response criteria," *Clinical Cancer Research*, vol. 15, no. 23, pp. 7412–7420, 2009.

[25] E. A. Eisenhauer, P. Therasse, J. Bogaerts et al., "New response evaluation criteria in solid tumours: revised RECIST guideline (version 1.1)," *European Journal of Cancer*, vol. 45, no. 2, pp. 228–247, 2009.

[26] Y. Zhao, C. K. Lee, C. H. Lin et al., "PD-L1:CD80 Cis-Heterodimer triggers the Co-stimulatory receptor CD28 while repressing the inhibitory PD-1 and CTLA-4 pathways," *Immunity*, vol. 51, no. 6, pp. 1059–1073.e9, 2019.

[27] A. Kataki, P. Scheid, M. Piet et al., "Tumor infiltrating lymphocytes and macrophages have a potential dual role in lung cancer by supporting both host-defense and tumor progression," *Journal of Laboratory and Clinical Medicine*, vol. 140, no. 5, pp. 320–328, 2002.

[28] P. Jiang, S. Gu, D. Pan et al., "Signatures of T cell dysfunction and exclusion predict cancer immunotherapy response," *Nat Med*, vol. 24, no. 10, pp. 1550–1558, 2018.

[29] S. Wang, J. Sun, K. Chen et al., "Perspectives of tumor-infiltrating lymphocyte treatment in solid tumors," *BMC Med*, vol. 19, no. 1, p. 140, 2021.

[30] S. Su, J. Liao, J. Liu et al., "Blocking the recruitment of naive $CD4^+$ T cells reverses immunosuppression in breast cancer," *Cell Res*, vol. 27, no. 4, pp. 461–482, 2017.

[31] J. Sehouli, C. Loddenkemper, T. Cornu et al., "Epigenetic quantification of tumor-infiltrating T-lymphocytes," *Epigenetics*, vol. 6, no. 2, pp. 236–246, 2011.

[32] N. P. Iurchenko, N. M. Glushchenko, and L. G. Buchynska, "Comprehensive analysis of intratumoral lymphocytes and FOXP3 expression in tumor cells of endometrial cancer," *Exp Oncol*, vol. 36, no. 4, pp. 262–266, 2014.

[33] P. Domingues, M. González-Tablas, Á. Otero et al., "Tumor infiltrating immune cells in gliomas and meningiomas," *Brain, Behavior, and Immunity*, vol. 53, pp. 1–15, 2016.

[34] Q. Wang, W. Lou, W. Di, and X. Wu, "Prognostic value of tumor PD-L1 expression combined with $CD8^+$ tumor infiltrating lymphocytes in high grade serous ovarian cancer," *International Immunopharmacology*, vol. 52, pp. 7–14, 2017.

[35] G. Romagnoli, M. Wiedermann, F. Hübner et al., "Morphological evaluation of tumor-infiltrating lymphocytes (TILs) to investigate invasive breast cancer immunogenicity, reveal lymphocytic networks and help relapse prediction:

a retrospective study," *International Journal of Molecular Sciences*, vol. 18, no. 9, p. 1936, 2017.

[36] R. Zylbermann, D. Landau, and D. Berson, "The influence of study habits on myopia in Jewish teenagers," *J Pediatr Ophthalmol Strabismus*, vol. 30, no. 5, pp. 319–322, 1993.

[37] S. Kurtulus, A. Madi, G. Escobar et al., "Checkpoint blockade immunotherapy induces dynamic changes in PD-1– CD8+ tumor-infiltrating T cells," *Immunity*, vol. 50, no. 1, pp. 181–194.e6, 2019.

[38] Z. Sun, Z. Ren, K. Yang et al., "A next-generation tumor-targeting IL-2 preferentially promotes tumor-infiltrating CD8+ T-cell response and effective tumor control," *Nature Communications*, vol. 10, no. 1, pp. 3874–3912, 2019.

[39] A. M. Dahlin, M. L. Henriksson, B. Van Guelpen et al., "Colorectal cancer prognosis depends on T-cell infiltration and molecular characteristics of the tumor," *Modern Pathology*, vol. 24, no. 5, pp. 671–682, 2011.

[40] D. R. Kroeger, K. Milne, and B. H. Nelson, "Tumor-infiltrating plasma cells are associated with tertiary lymphoid structures, cytolytic T-cell responses, and superior prognosis in ovarian cancer," *Clinical Cancer Research*, vol. 22, no. 12, pp. 3005–3015, 2016.

[41] B. C. Sheu, S. M. Hsu, H. N. Ho, R. H. Lin, P. L. Torng, and S. C. Huang, "Reversed CD4/CD8 ratios of tumor-infiltrating lymphocytes are correlated with the progression of human cervical carcinoma," *Cancer*, vol. 86, no. 8, pp. 1537–1543, 1999.

[42] A. Pera, C. Campos, N. López et al., "Immunosenescence: implications for response to infection and vaccination in older people," *Maturitas*, vol. 82, no. 1, pp. 50–55, 2015.

Hindawi
Journal of Oncology
Volume 2022, Article ID 1488165, 15 pages
https://doi.org/10.1155/2022/1488165

Research Article

Immunotherapeutic Value of Transcription Factor 19 (TCF19) Associated with Renal Clear Cell Carcinoma: A Comprehensive Analysis of 33 Human Cancer Cases

Xiaobao Cheng, Jian Hou, Xiangyang Wen, Runan Dong, Zhenquan Lu, Yi Jiang, Guoqing Wu, and Yuan Yuan

Department of Urology, The University of Hongkong-Shenzhen Hospital, Shenzhen, China

Correspondence should be addressed to Xiaobao Cheng; chengxb@hku-szh.org

Received 19 June 2022; Revised 30 June 2022; Accepted 6 July 2022; Published 6 September 2022

Academic Editor: Recep Liman

Background. We aimed to study the relationship between transcription factor 19 (TCF19) and cancer immunotherapy in the 33 types of human cancers. *Methods*. The Cancer Genome Atlas database was analyzed to obtain the gene expression data and clinical characteristics for the cases of 33 types of cancers. GSE67501, GSE78220, and IMvigor 210 were included in the immunotherapy cohorts. Relevant data were obtained by analyzing the gene expression database. The prognostic value of TCF19 was determined by analyzing various clinical parameters, such as survival duration, age, the stage of the tumor, and sex of the patients. The single-sample gene set enrichment analysis method was used to determine the activity of TCF19 and the method was also used to assess the differences between the TCF19 transcriptome and protein levels. The correlation between TCF19 and various immune processes and elements such as immunosuppressants, stimulants, and major histocompatibility complexes were analyzed to gain insights into the role of TCF19. The coherent paths associated with the process of TCF19 signal transduction and the influence of TCF19 on immunotherapy biomarkers have also been discussed herein. Finally, three independent immunotherapy methods were used to understand the relationship between TCF19 and immunotherapy response. *Results*. It was observed that TCF19 was not significantly influenced by the age (5/33), sex (3/33), or tumor stage (3/21) of cancer patients. But the results revealed that TCF19 exhibited a potential prognostic value and could predict the survival rate of the patients. In some cases of this study, the activity and expression of TCF19 were taken at the same level (7/33). *Conclusion*. TCF19 is strongly related to immune cell infiltration, immunomodulators, and immunotherapy markers. Our study demonstrated that high expression levels of TCF19 are strongly linked with the immune-related pathways. Nevertheless, it is noteworthy that TCF19 is not significantly associated with immunotherapy response.

1. Introduction

The renal tumor is one of the most common tumors in urology. Results from the statistical analysis conducted with the data associated with cancer revealed that renal tumors ranked second in terms of incidence of urinary system malignant tumors in China [1]. Clear cell renal cell carcinoma (ccRCC) is the major pathological type of renal cancer, which accounts for 70–80% of the cancers in urology. The annual percentage of increase in the rate of incidence is 3% in Europe and in the United States [2]. CcRCC is characterized as an aggressive tumor and approximately one-third of the patients suffering from ccRCC were diagnosed while tumor metastasis already occurred [3]. Cellular molecular-targeted therapy is the most effective method of treating metastatic ccRCC as patients suffering from kidney cancer do not respond to radiotherapy and chemotherapy. The European Urology Association (EUA) and the United States National Comprehensive Cancer Network (NCCN) recommended the molecular-targeted drugs as the first and second-line medicine for metastatic ccRCC [4, 5]. The prognostic factors of ccRCC include

histological factors, tumor anatomical factors, molecular factors, and clinical factors. Among these, currently known molecular markers such as carbonic anhydrase 9, CRP [6, 7] , and cabozantinib [8] are not of high prognostic value and accuracy, and these have not been recommended for clinical application. At present, there are no universally accepted and reliable standard predictors for the diagnosis and prognosis of ccRCC at an early stage. The exploration of abnormally expressed genes in ccRCC tissues can potentially help identify new molecular biomarkers for the diagnosis and prognosis of ccRCC.

Transcription Factor 19 (TCF19) is a protein-coding gene that encodes a protein with a PHD-type zinc finger domain that is involved in transcriptional regulations [9]. At first, TCF19 was isolated from human, mouse, and hamster cells and it acts as a growth regulatory molecule [10]. TCF19 is associated with cell growth and regulation by affecting the G1S phase of the cell cycle. The genetic coding region of TCF19 is located on the short arm 6P21.3 of autochromosome 6, with a total length of 5.60 KB [11]. TCF19 is present in almost all human tissues, and its levels of expression are high in various tumor tissues [12–15]. Although current studies indicate that TCF19 may be associated with the progression of various tumors, few mechanisms have been reported for the role of TCF19 in carcinogenesis and immune regulation.

The processes of carcinogenesis and immune regulation are significantly affected by the physiological effects of TCF19 activation. Since TCF19 is chronically activated, it is highly expressed in various solid tumors [12–15] and chronic inflammatory tissues [16–18]. The presence of highly expressed TCF19 has been found not only in invasive tumor tissues but also in malignant tumor cell lines. This potentially indicates that TCF19 is correlated to the responses of inflammation and cell cycle progression [11, 16]. The genes associated with the TCF family regulate innate immunity and adaptive immunity [19, 20]. It has been previously reported that TCF1 helps achieve a balance between the CD8+ T cells by regulating the internal IL-10 signaling pathway which in turn influences immunotherapy [21]. Macrophages, a substantial component of the innate immune system, are related to the antitumor immune response in various cancers. It was stated that the M2 tumor-associated macrophages (TAMs) promote the processes of tumor progression, recurrence, and distal metastasis [22]. Macrophages are polarized by the stimulation of transcription factors in the tumor microenvironment by controlling their antitumor activity and by affecting their immunotherapy [23, 24]. Our previous study also confirmed that changes in macrophage polarization play substantial activities to regulate the inflammatory traumatic urethral stricture [25] and resistance to chemotherapy and endocrine therapy in advanced prostate cancer [26]. In general, TCF family genes significantly influence the immune system and the state of tumor tissue. Nevertheless, the immunotherapeutic value of TCF19 in the cases of human cancer has been rarely studied.

Herein, we described the expression profile of TCF19 in 33 different cancers and studied the potential regulatory roles of TCF19 for controlling the ccRCC immune microenvironment. Also, we studied the microsatellite instability (MSI) and tumor mutation burden (TMB) in ccRCC. Moreover, the association of the expression level of TCF19 with immune checkpoint blocking therapy was also investigated. In brief, this research provides data that help understand the immunotherapeutic role of TCF19 in ccRCC which may potentially help design various functional experiments.

2. Methods

(See Figure 1) shows the flowchart of this research.

2.1. Data Collection. The TCGA database (https://portal.gdc.cancer.gov/), a robust database, provides information on cancer genes. The database includes information on gene expression profiles, copy number variation (CNV), and single nucleotide polymorphism (SNP). We downloaded the mRNA expression and SNP data of 33 tumors for this study. Also, we downloaded the data from the GTEX database (https://commonfund.nih.gov/GTEx). Following the merging with the TCGA data and correction, we identified the differential expressions for various types of cancers. Moreover, we downloaded the corresponding tumor cell lines data from the CCLE database (https://portals.broadinstitute.org/ccle/), and we investigated the expression level of the gene in these tumor tissues. Furthermore, we investigated the significant correlation of this gene with the stages of tumor progression.

2.2. Association of TCF19 Expression with Clinical Characteristics of 33 Cancers. We downloaded the progression-free survival (PFS) and overall survival (OS) TCGA data of patients from the Xena database to evaluate the association of this gene with the prognosis of the patients. We utilized the Kaplan–Meier (K-M) method to analyze the survival curve ($P < 0.05$) for every cancer type. We employed "survival" and "SurvMiner" *R* packages for the survival analysis. Also, we used "survival" and "forest-plot"*R* packages for the Cox analysis to evaluate the interrelation of gene expression with the magnitude of survival of the patients.

2.3. TCF19 Enrichment Analysis

2.3.1. Gene Set Variation Analysis (GSVA) Enrichment Analysis. GSVA, a package for the R program, was used to identify the enrichment of transcriptomic gene sets. GSVA identifies the changes from the level of the gene to the level of the pathway. This is achieved by using the specific gene sets of biological function. We utilized the Molecular Signatures Database (v7.0) for downloading the gene sets. GSVA algorithm identified the score of each gene set to determine the ability of changes in biological function within the different samples.

2.3.2. Gene Set Enrichment Analysis (GSEA) Enrichment Analysis. In the GSEA analysis, we used predefined gene sets and sequencing gene sets (based on the differential

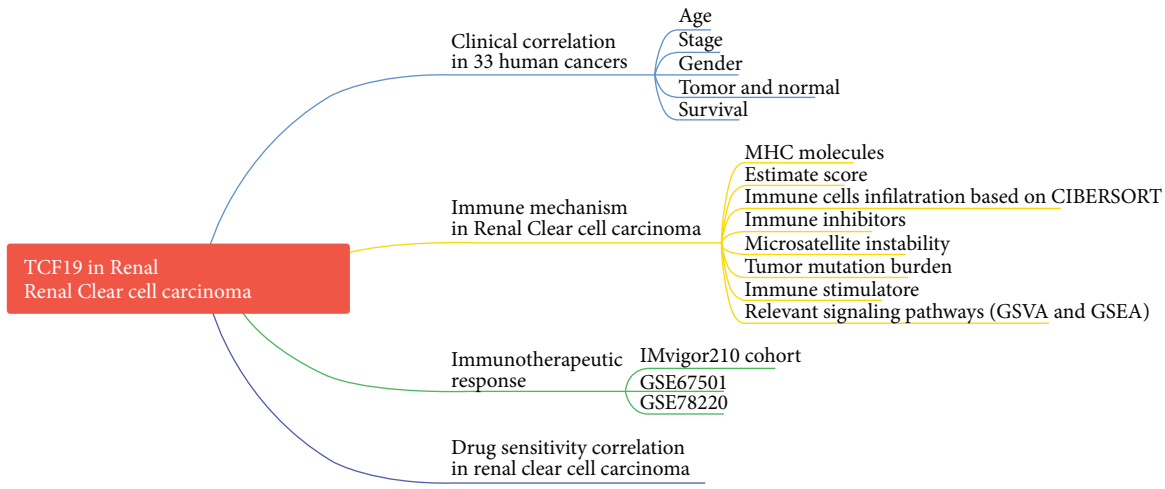

Figure 1: The flowchart of the study. Firstly, the expression of TCF19 is investigated within the different ages, stages, genders, and tissues, then the GSEA is utilized to explore the relevant immune signaling pathways based on the expression level of TCF19. Secondly, we apply the univariate Cox regression model and the Wilcoxon test between the nonresponder and responder groups of the immunotherapeutic response cohort to identify the survival association. Finally, we perform the drug sensitivity correlation with TCF19 expression in renal clear cell carcinoma.

expression level between the two types of samples). This method identifies whether the predefined gene sets were significantly enriched in the sequencing table. The "cluster profiler" and the "enrich-Plot" packages were used for the GSEA analysis and for exploring the imaginable mechanisms at the molecular level for the differential prognosis of different patients with different tumors. The differences in the signaling pathways associated with the high and low gene expression groups were studied, and the findings were compared.

2.3.3. The Expression Level of TCF19 Is Correlated with Immune-Related Factors. RNA-seq data from patients with different subgroups of 33 cancers were analyzed by using the CIBERSORT algorithm to understand the content of infiltrating immune cells. This method also identifies the relation of gene expression with the content of immune cells. Moreover, we used the TISIDB website to identify the relation of gene expression with various immune factors, including chemokines, immune-stimulators, immune-suppressants, and MHC molecules.

2.3.4. Correlation Analysis of TCF19 Expression and Tumor Mutation. The total number of mutations, including base substitutions, deletions, and insertions in tumor cells is called TMB. The frequency and number of variation/exon lengths were calculated for every sample tumor, and TMB was calculated by dividing the nonsynonymous mutation sites by the total length of the protein-coding region. The MSI of every TCGA sample was obtained from the data presented in previously published reports [27].

2.3.5. Correlation Analysis of TCF19 Expression with Drug Sensitivity and Immunotherapy Response. The National Cancer Institute (NCI) listed the Cellminer database which contains the information on 60 cancer cells [1]. At present, the widely used database is the NCI-60 cell line with a broad range of cancer cell samples and it is used to investigate the anticancer drugs. In our study, we downloaded the NCI-60 drug sensitivity data and the RNA-seq gene expression data to evaluate the relations of gene expression with the sensitivity of antitumor drugs. The correlation analysis method was utilized to achieve the results. We considered a *P*value <0.05 for the statistical threshold.

We analyzed the immunotherapeutic response according to the previous method [2]. We used three independent immunotherapeutic cohorts in our present study. Usually, immunotherapeutic ways provided four outcomes, including complete response (CR), partial response (PR), progressive disease (PD), and stable disease (SD). We divided the patients into responders and nonresponders. Patients who had CR or PR signs were categorized as responders compared to the nonresponders, who had signs of SD or PD. We utilized the Wilcoxon rank-sum test to investigate the expression differences of TCF19 between the responder and the nonresponder groups.

2.3.6. Statistical Analyses. R (version 4.0) was used for all statistical analyses. We calculated the hazard ratios (HRs) and 95% confidence intervals followed by applying the univariate survival analysis model. We applied the K-M survival analysis to investigate patient survival time. We divided the patients into the high gene expression level and the low gene expression level to arrive at the appropriate results. The statistical tests were bilateral, and we considered a *P*value <0.05 for the statistical threshold.

3. Results

3.1. Results of the Analysis of TCF19 Expression and Clinical Correlation in 33 Cancers. We analyzed the expression level of TCF19 in 33 types of human cancers using the data

presented in the TCGA and GTEX datasets. Table 1 presented the full names of the 33 cancer types utilized in this comprehensive study. The high levels of expression of the gene were observed in 27 types of carcinomas, including ACC, BLCA, BRCA, CHOL, CESC, COAD, ESCA, GBM, HNSC, KIRC, LAML, LGG, LIHC, LUAD, LUSC, OV, PCPG, PAAD, PRAD, READ, SARC, SKCM, STAD, TCGT, THCA, UCEC, and UCS (Figure 2(a)). TCF19 expression levels in most normal tissues were lower than that in cancer cells. In the CCLE expression profile of various cell lines, the expression level of TCF19 is illustrated in figure 2(b). Moreover, we found that TCF19 expression was related to the stages of various tumors, such as ACC, BRCA, TGCT, KICH, KIRC, and LIHC (Figure 3). This work studied the correlation between the expression levels of TCF19 and survival prognosis in patients suffering from cancer. We found that the expression level of TCF19 was closely associated with the OS of patients in 14 different types of cancers (such as KIRC, ACC, KICH, KIRP, LAML, THYM, LGG, HNSC, LIHC, MESO, PRAD, SKCM, UVM, and PAAD; Figure 4(a)). In addition, the results from the KM-curve survival analysis suggested that the highly expressed TCF19 was correlated with poor OS in 13 types of malignant cancers, including ACC, BRCA, KICH, LIHC, GBM, SKCM, KIRC, KIRP, LGG, LUAD, PAAD, PCPG, and MESO (Supplementary Figure 1). The expression level of TCF19 was closely linked with PFI in 12 cancer types, including PAAD, ACC, MESO, KICH, LIHC, PCPG, PRAD, LGG, SARC, THCA, KIRC, UCEC, and other tumors (Figure 4(b)). The K-M curve analysis for survival prognosis suggested that a highly expressed group of TCF19 was associated with a shorter PFI in 10 kinds of malignant cancers (such as UCEC, ACC, KICH, PAAD, KIRC, LGG, LIHC, PCPG, PRAD, and THCA; Supplementary Figure 2).

A nomogram prediction model was constructed using the TCF19 expression level and the clinical features. The results obtained from regression analysis were displayed in the form of alignment charts. Variables such as gender, age, tumor stage, and grade were analyzed, and the results were presented. The gene correlation column diagram model of TCF19 of the constructed TCGA-KIRC sample is shown in Figure 5(a). Correction curves corresponding to the two periods were generated in the fifth and seventh years. The model effect was quite consistent (Figure 5(b)).

3.2. The TCF19 Expression Is Potentially Associated with Immune-Associated Factors. Tumor-associated fibroblasts, extracellular matrix, immune cells, various growth factors, inflammatory factors (characterized by special physicochemical characteristics), cancer cells, etc., are present in the tumor microenvironment. The microenvironment significantly affects the diagnosis of tumors, survival outcome, and degree of the response generated toward clinical treatment. Our findings indicated that the TCF19 expression level was substantially correlated with the infiltration of immune factors. TCF19 expression level was significantly related to the CD4 memory-activated cells in 14 kinds of cancers. In 15 kinds of cancers, the TCF19 expression level was significantly related to the follicular helper cells, and in the other 14 kinds of cancers the TCF19 expression level were correlated significantly with the macrophages M1 cell (Figure 6). Further analysis of the tumor microenvironment in kidney carcinoma (KIRC) revealed that TCF19 expression level was significantly related to the various gene set scores including the CD_8_T effector, TME score A, TME score, DNA damage response, base excision repair, immune checkpoint, antigen processing machinery, mismatch repair, nucleotide excision repair, DNA replication, Pan F TBRs, EMT1, and EMT2 in kidney carcinoma ().

3.3. GSVA/GSEA Correlation Analysis of TCF19. The GSVA scores were determined for all tumors to elucidate the molecular mechanism associated with the TCF19 gene associated with pan-cancer. We divided the tumor samples into two groups based on the higher expression level and the lower expression levels. The median value of the gene expression level in each tumor was utilized for comparison. It was observed that in the case of kidney carcinoma, highly

Table 1: 33 types of human cancer studied in this research.

Abbreviation	Full name
ACC	Adrenocortical carcinoma
BLCA	Bladder urothelial carcinoma
BRCA	Breast invasive carcinoma
CESC	Cervical squamous cell carcinoma and endocervical adenocarcinoma
CHOL	Cholangiocarcinoma
COAD	Colon adenocarcinoma
DLBC	Lymphoid neoplasm diffuse large B-cell lymphoma
ESCA	Esophageal carcinoma
GBM	Glioblastoma multiforme
HNSC	Head and neck squamous cell carcinoma
KICH	Kidney chromophobe
KIPAN	Pan-kidney cohort (KICH + KIRC + KIRP)
KIRC	Kidney renal clear cell carcinoma
KIRP	Kidney renal papillary cell carcinoma
LAML	Acute myeloid leukemia
LGG	Brain lower grade glioma
LIHC	Liver hepatocellular carcinoma
LUAD	Lung adenocarcinoma
LUSC	Lung squamous cell carcinoma
MESO	Mesothelioma
OV	Ovarian serous cystadenocarcinoma
PAAD	Pancreatic adenocarcinoma
PCPG	Pheochromocytoma and paraganglioma
PRAD	Prostate adenocarcinoma
READ	Rectum adenocarcinoma
SARC	Sarcoma
STAD	Stomach adenocarcinoma
SKCM	Skin cutaneous melanoma
STES	Stomach and esophageal carcinoma
TGCT	Testicular germ cell tumors
THCA	Thyroid carcinoma
THYM	Thymoma
UCEC	Uterine corpus endometrial carcinoma
UCS	Uterine carcinosarcoma
UVM	Uveal melanoma

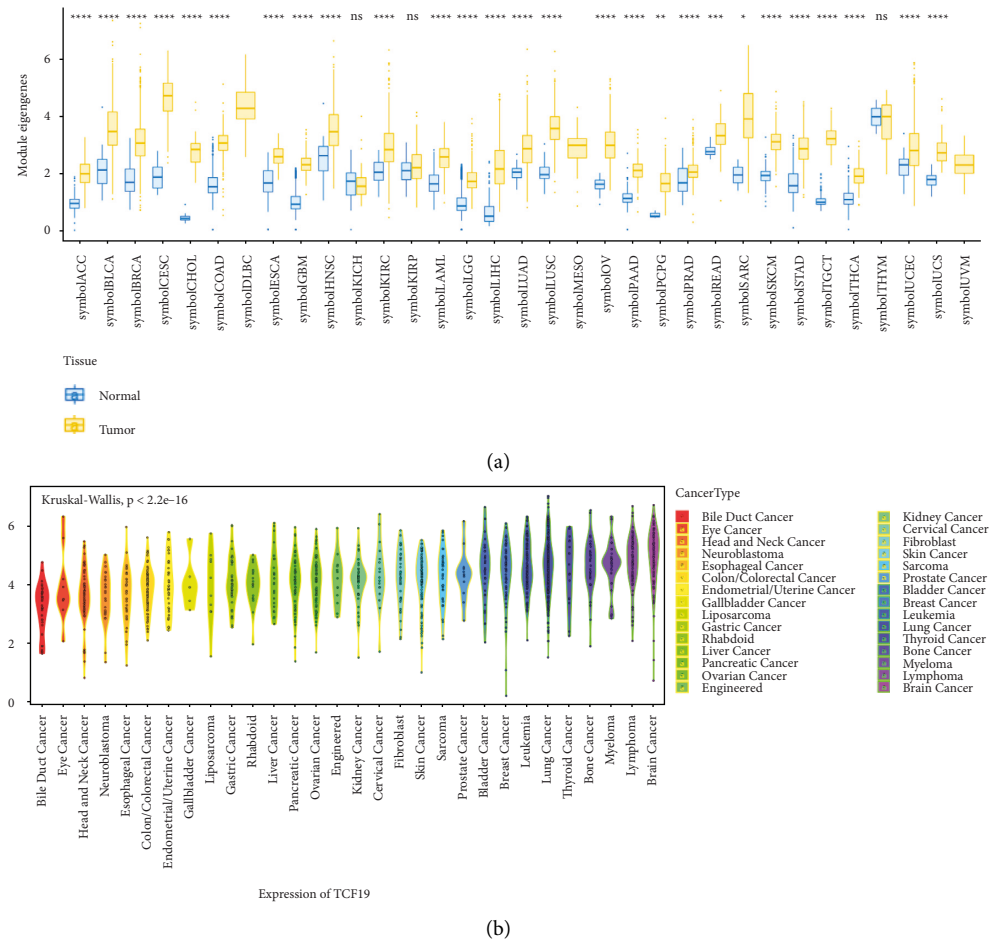

Figure 2: The expression of TCF19. (a) The TCF19 expression level in 33 human cancers using the TCGA combined with GTEx datasets and (b) the CCLE expression profile revealed that TCF19 is expressed in different tumor cell lines.

expressed TCF19 genes were primarily associated with some specific pathways such as interferon alpha response, E2F targets, allograft rejection, IL-6-JAK-STAT3 signaling, interferon gamma response, and G2M checkpoint (Figure 8(a)–8(c)). Results from the GSEA analyses of TCF19 and kidney carcinoma are presented in Figures 8(d)–8(f).

3.4. Correlation Analysis of TCF19 Expression with Tumor Mutations and Gene Regulation. The study further constructed the WGCNA net based on the KIRC expression profile for exploring the coexpression network linked with TCF19 in pan-cancer. The clustering chart of patients is shown in Supplementary Figure 3. We utilized the "soft power Estimate" function in the WGCNA package to identify the soft threshold β value and the value of β is set to 12. We detected 17 gene modules using the Tom matrix. These are black (298), blue (519), brown (446), cyan (357), green (354), green yellow (489), grey (3788), grey60 (82), light cyan (129), light green (74), light yellow (57), night blue (155), pink (449), purple (230), red (308), turquoise (1822), and yellow (443) (Supplementary Figure 3). The modules and traits were further analyzed, and it was found that the maximum correlation was observed for the ME green yellow module (COR = 0.35, P = (5E-19)) (Supplementary Figure 3). The coexpression analysis method was further used to explore the relationship between the level of TCF19 expression and 33 tumor immune-related genes. The analyzed genes included genes associated with MHC, immune activator, chemokine receptor proteins, immunosuppressor, and chemokine. It was observed that TCF19 was significantly associated with most of the immune-related genes (Supplementary Figure 4). Moreover, TCF19 was significantly associated with the crucial tumor-related marker genes that controlled the various biological processes, including the TGF beta signaling pathway, TNFA signaling, hypoxia, coking death, repair of DNA, autophagy, and ferroptosis (Supplementary Figure 5).

The immunotherapy response was crucially associated with some biomarkers, including TMB and MSI. We investigated the relation of TCF19 expression level with TMB in this study. We revealed that the TCF19 expression level was significantly correlated with TMB in all tumors, including P ACC, CPG, UCEC, SKCM, COAD, PRAD, STAD, KICH, LIHC, LUAD, and THCA (Figure 9(a)). A significant difference was observed for MSI in various cancers,

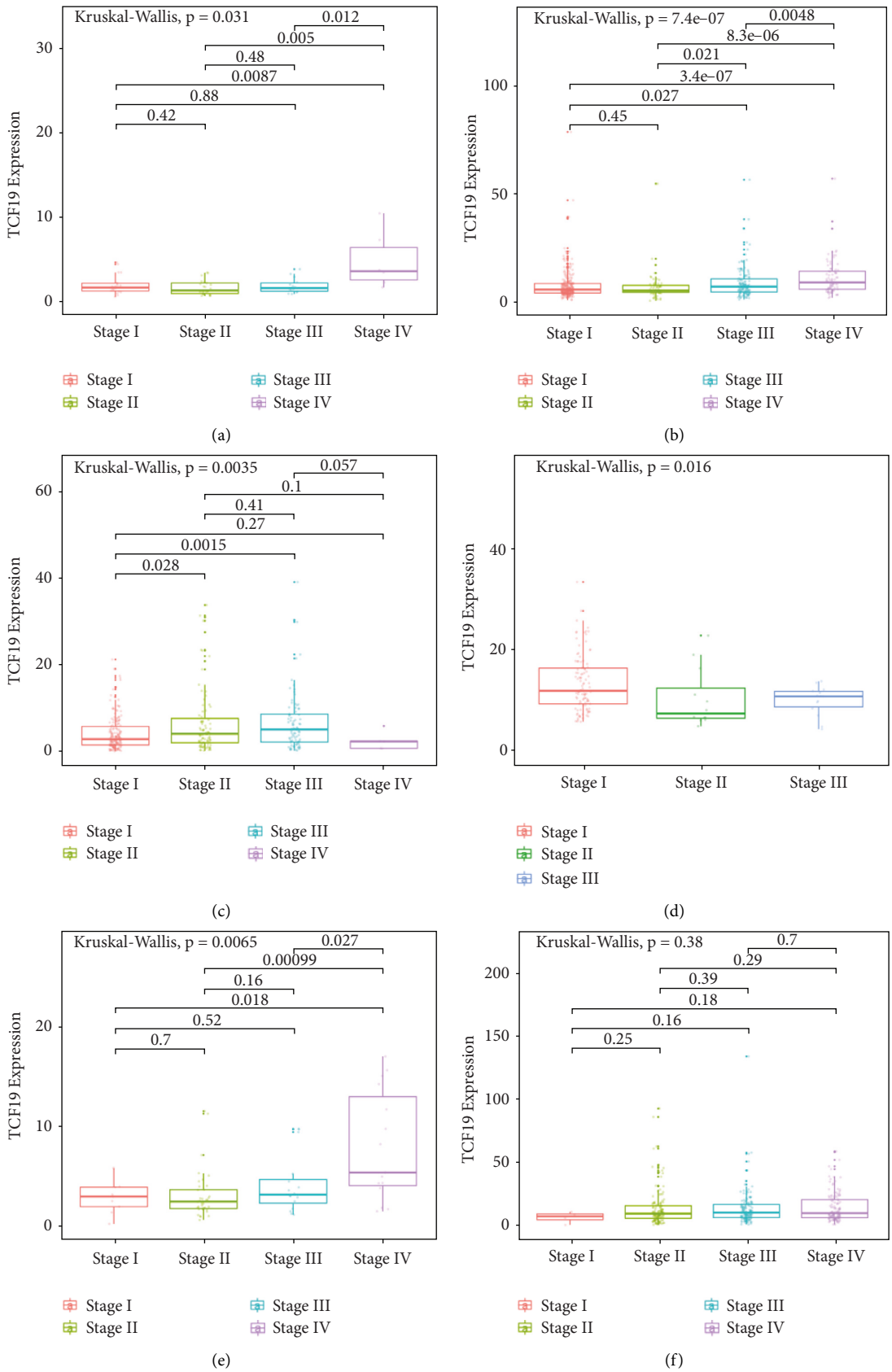

Figure 3: The correlation analysis of TCF19 with the stage of multiple tumors.

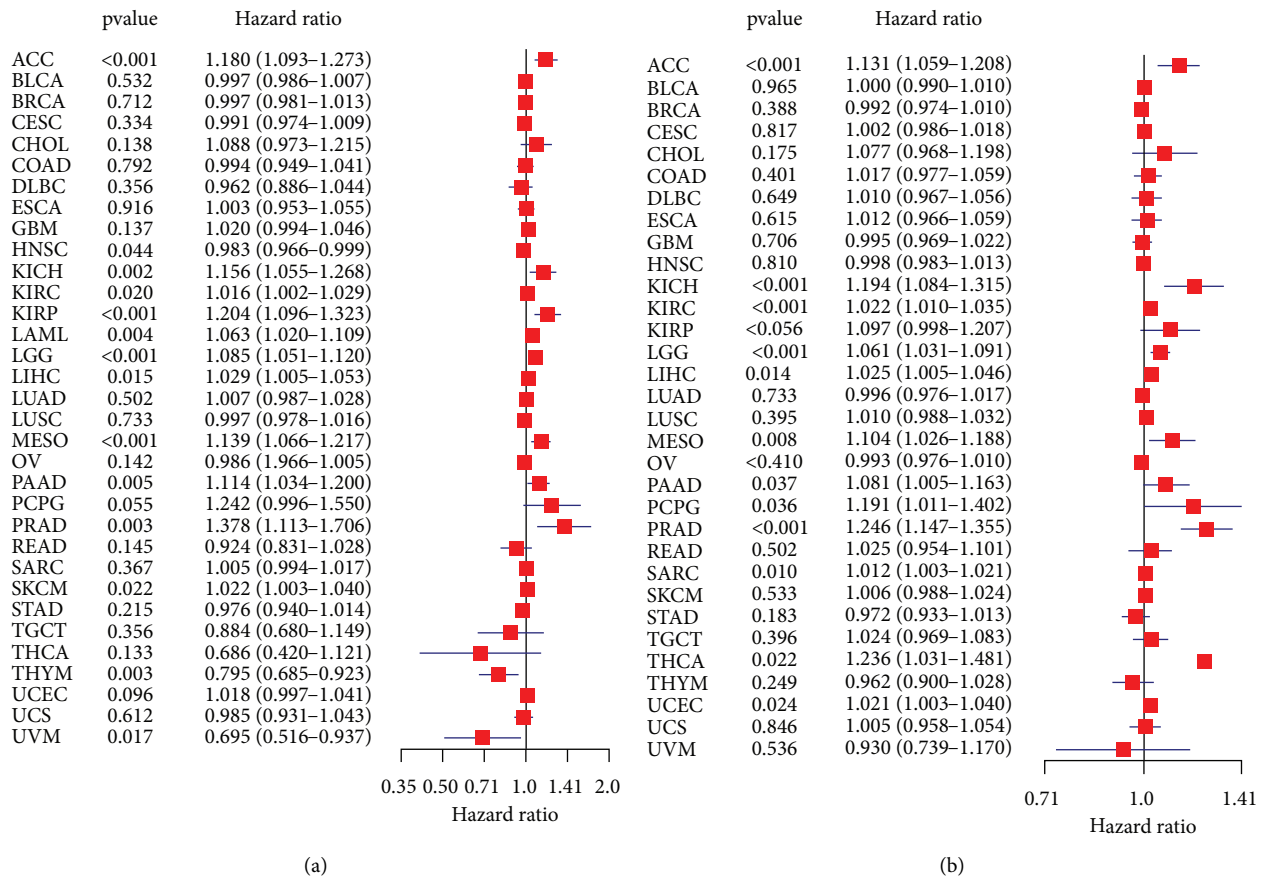

FIGURE 4: The association between TCF19 expression and prognosis of patients with multiple cancers. (a) The univariate regression model identifies the association of TCF19 expression with the overall survival (OS) rate in multiple cancer patients and (b) the univariate regression model identifies the association of TCF19 expression with the progression-free interval (PFI) of patients with multiple cancers.

including UCEC, KIRC, GBM, COAD, BRCA, STAD, PRAD, and DLBC (Figure 9(b)).

3.5. Correlation Analysis of TCF19 Expression with Drug Sensitivity and Immunotherapeutic Response. The effect of surgery and chemotherapy on the conditions of early-stage tumors had been widely explored. We investigated the cell miner database to identify the association of TCF19 expression level with IC50 values of antitumor drugs. We revealed that the higher expression level of TCF19 was correlated with the tolerance level of multiple antitumor drugs (Supplementary Figure 6). It was observed that TCF19 correlated positively with fludarabine, 6-mercaptopurine, dexamethasone decadron, nelarabine, and fenretinide. The gene negatively correlated with AFP464, trametinib, aminoflavone, cobimetinib (isomer 1), palbociclib, and lificguat.

The dataset corresponding to IMvigor 210 tumor immunotherapy was downloaded and 348 patients subjected to the conditions of PD-L1 therapy (and presenting complete survival information) were enrolled. The K-M survival analysis was used for the studies, and the results revealed that high TCF19 expression levels reflected the poor prognosis of patients (figure 5(c)).

4. Discussion

In China, kidney carcinoma is the second-highest malignant tumor in urology [1]. Approximately 1/3rd of the patients developed metastatic carcinoma before diagnosis [5]. Advanced renal clear cell carcinoma showed resistance to the treatment strategies including radiotherapy and chemotherapy. Hence, the cellular and molecular-targeted treatment method is widely used to treat ccRCC. Multiple guidelines recommend molecular-targeted therapy as the first and second choice of treatment for metastatic ccRCC [6, 7]. Therefore, it is important to explore new therapeutic targets for advanced ccRCC.

At the beginning of the research, we identified the expression differences of TCF19 in tumor tissues relative to the normal samples. The results helped identify the potential immunotherapeutic value of TCF19. TCF19 is a gene that is associated with cell growth regulation which primarily regulates the cell cycle and the process of apoptosis. TCF19 was first isolated from mouse, human, and hamster cells. The previous report indicated that the TCF19 expression level was higher in various cancerous tissues, including the liver, colon, rectum, head and neck, lung, and gastrointestinal tract [12–15]. In this work, TCF19 was

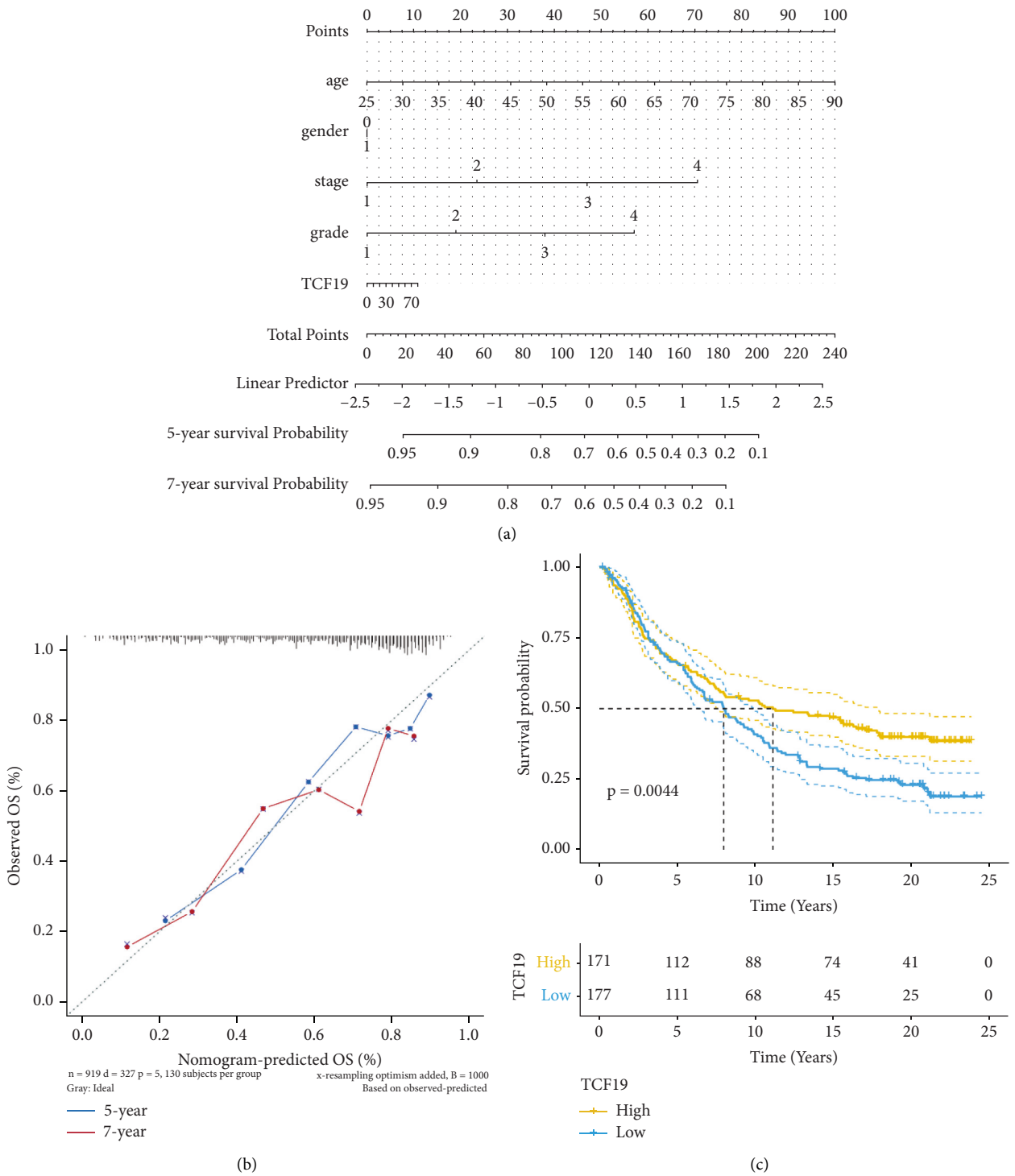

Figure 5: The TCF19 expression level is associated with the risk and prognosis of patients. (a) It shows the gene correlation column line graph model for TCF1, (b) it shows the correction curves plotted for two periods of five and seven years, and (c) it shows the Kaplan–Meier survival analysis plots of TCF19 expression versus patients treated with PD-L1.

highly expressed in ACC, BLCA, KIRC, PRAD, TCGT, and other urinary system tumors which were under previous findings. In addition, the results from the K-M survival investigation suggested that a higher expression level of TCF19 is significantly associated with a shorter prognosis of various tumors in both OS and PFI. These studies might suggest that TCF19 is crucially linked with a shorter prognosis of multiple tumors.

Since TCF19 significantly affects the tumor immune microenvironment, more studies need to be conducted on the immune cells, tumor microenvironment, immunomodulators, and immunotherapy responses to gain in-depth

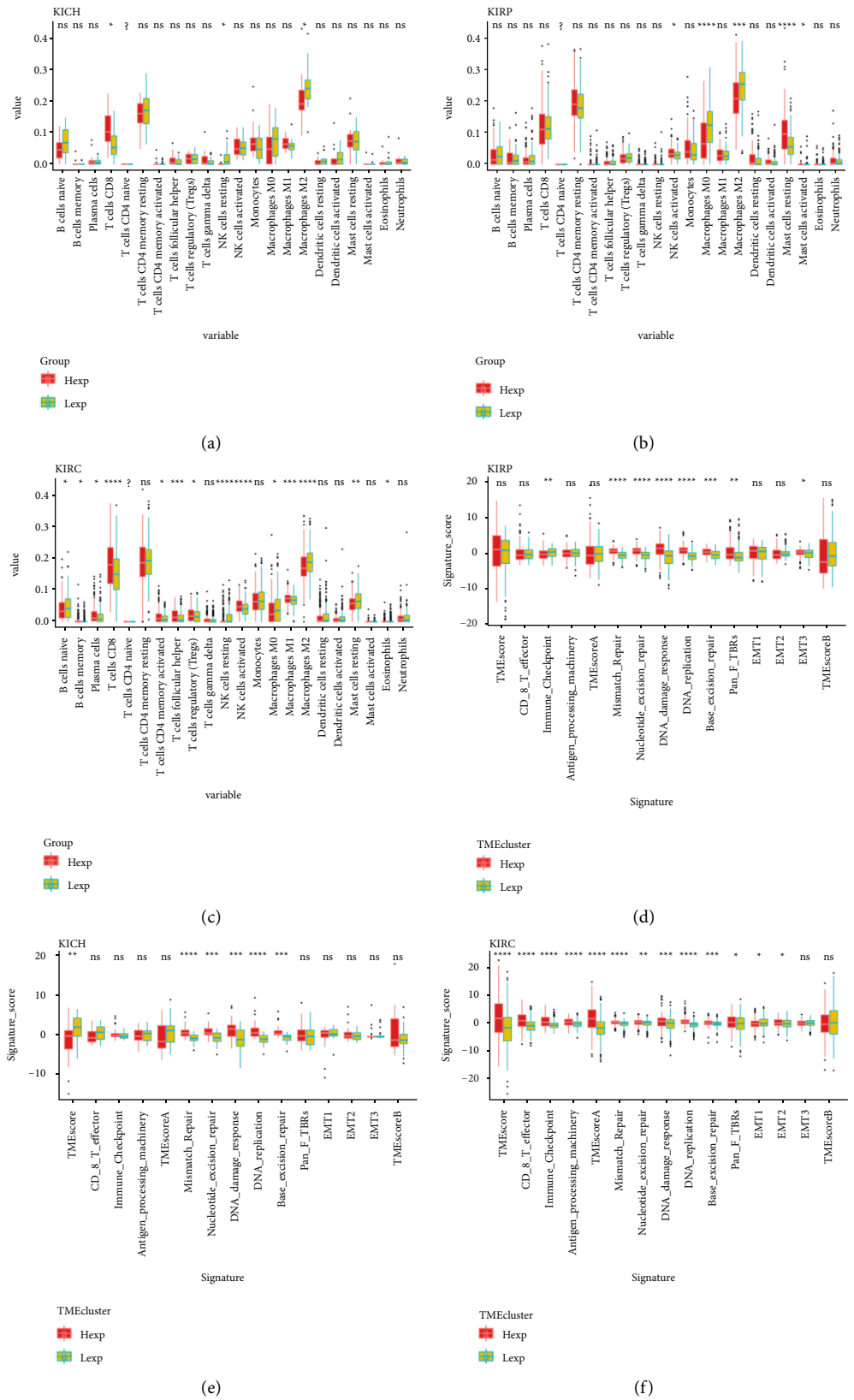

Figure 6: Continued.

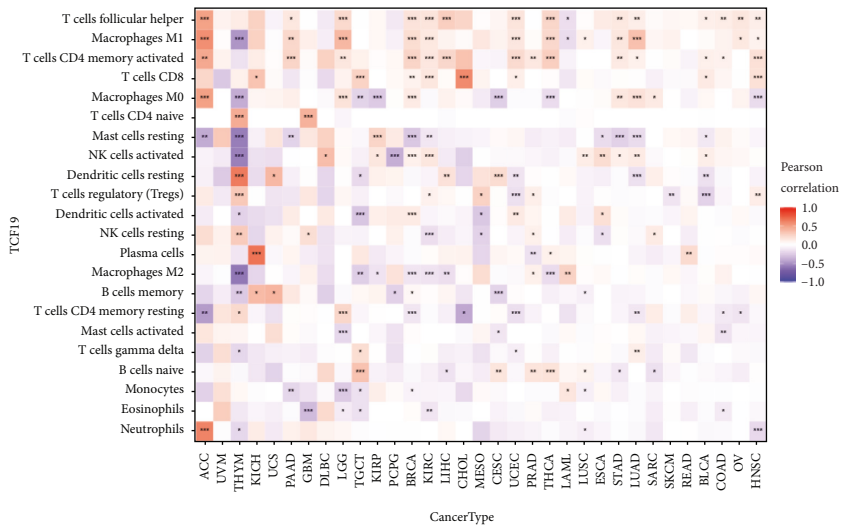

(g)

Figure 6: The TCF19 is correlated with the immune infiltration in pan-cancer. (a–f) The expression level of TCF19 is significantly correlated with the infiltration of immune cells in multiple cancers and (g) it indicates the correlation analysis of TCF19 expression with multiple tumors.

knowledge. This study aimed to gain insights into the underlying mechanisms associated with the TCF19 gene that was associated with immune-related factors. 33 types of human cancers were studied to obtain relevant information. This work also aimed to explore the immune-related mechanisms associated with urinary tumors. The expression of TCF19 and clinical characteristics was analyzed, and the results obtained from COX regression analysis revealed that TCF19 was a prognostic factor of ccRCC. Correction curves were generated for the ccRCC patients in the fifth and seventh years and the consistent model effects were observed. Daniela Ruggiero reported the increased level of expression of the TCF19 gene in two major histological subtypes (squamous cell carcinoma (SCC) and lung adenocarcinoma) and revealed that TCF19 promoted the progression of the cell cycle in NSCLC cells. This validated the fact that TCF19 was a therapeutic target [28]. Du WB reported that TCF19 was significantly upregulated in colorectal cancer and TCF19 was closely related to the progression of malignancy, distant metastasis, and poor prognosis of colorectal cancer. So, he speculated that TCF19 could aggravate the malignant progression of CRC [29]. Ji, Xu, and Miao further reported that TCF19 was highly expressed in cancer cells associated with head and neck SCC, liver cancer, and gastric cancer. They reported that TCF19 could be potentially correlated with tumor prognosis by conducting gene assays, K–M survival analysis, and western-blot tests [12, 13, 15]. It is worth noting that the results of our research reflected the association of the gene with a substantial prognosis of these tumors and confirmed the reliability of the analytical results obtained. Moreover, the correlation between TCF19 and the prognosis of ccRCC was also reported. But now the mechanism involving TCF19 in the occurrence of ccRCC has not been clearly described. We may infer that the modulation of the TCF19 activity associated with ccRCC could potentially help obtain results that can help improve the therapeutic techniques.

Conventional surgical treatment and radiotherapy and chemotherapy cannot be effective to treat patients suffering from late-stage ccRCC. Maybe more research should be conducted on the gene targets and immune checkpoint inhibitors associated with pan-cancer as the results can potentially help predict the prognosis of antitumor immunotherapy. This research studied the relation of TCF19 with the process of immune cell infiltration for further investigating the crucial immunotherapeutic potential of TCF19. The results revealed that the expression level of TCF19 significantly correlated with the infiltration of the immune cells, including CD4 memory T cells, T follicular helper cells, and M1 macrophages. Analysis of the relationship between tumor microenvironment and KIRC revealed that KIRC was significantly correlated with some scores such as TMEscoreA, TMEscore, mismatch repair, $CD8^+$ T effector, immune checkpoint, antigen processing machinery, nucleotide excision repair, and DNA damage. The scores of the responses, Pan F TBRs, DNA replication, base excision repair, EMT1, and EMT2 significantly correlated with KIRC. And this study further investigated the relations of TCF19 with the immune-related genes, including genes associated with MHC, immune activator, immuno-suppressive markers, chemokine, and their receptor protein. Interestingly, we found that immune-associated factors were significantly correlated with the expression level of the TCF19 gene. Our previous study reported that several immune-prognostic genes influenced the process of immunotherapy associated with urinary bladder cancer [30]. Besides, it has been reported that the regulation of macrophage polarization attenuated the inflammatory traumatic urethral stricture in New Zealand rabbits [25]. Another study recently reported that M2-

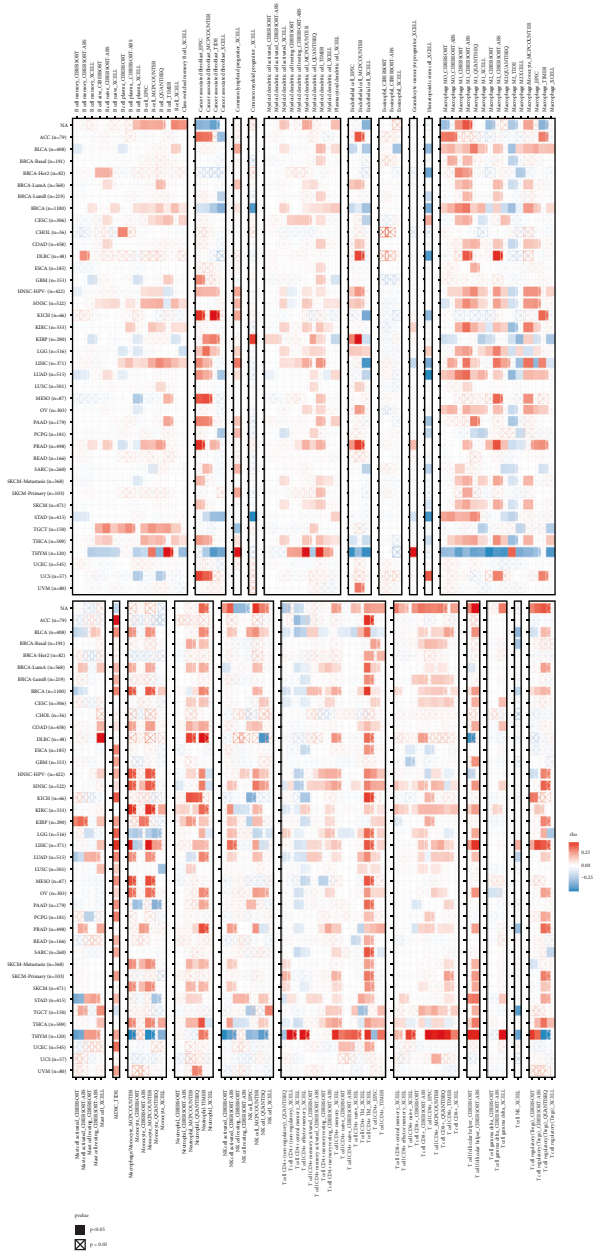

Figure 7: The analysis of TCF19 expression and the tumor microenvironment in the ccRCC.

tumor-associated macrophages (TAMs) were able to promote the process of bone metastasis and were able to influence the chemotherapy and drug resistance ability of the cells of prostate cancer. The regulation of the process of macrophage polarization can influence the effect of immunotherapy in patients suffering from prostate cancer [26]. Sen, Yang GH, and Mondal reported that TCF19, a novel pancreatic islet regulator, regulated the processes of energy metabolism and stress adaptation associated with the tumor cells by regulating gluconeogenesis. It was associated with the inflammatory responses in the beta cells of the pancreas and the DNA damage response network. The occurrence and progression of pan-cancer were also affected [16–18]. It has been reported recently that TCF19 influences the effect of immunotherapy in lung cancer through nanotechnology by regulating the polarity of the tumor-associated macrophages [31]. Those results revealed that TCF19 might influence the process of immunotherapy by regulating the immune-related genes and the inflammatory cells such as macrophages associated with tumor cell immunotherapy.

Furthermore, we observed that two immunotherapy biomarkers (TMB and MSI) were associated with TCF19 in various tumors. In general, as the number of somatic mutations in a tumor increase, the ability to generate neoantigens increases. It was also observed that the tumor neoantigen load could be efficiently determined by analyzing the TMB [32]. MSI is a robust mutant factor phenotype, the generation of which can be attributed to the presence of defects in mismatch repairing of DNA. MSI is a crucial predictor for immunotherapy responses [33]. This study showed that TMB and MSI were significantly associated with the TCF19 expression level in various tumors. However, the TCF19 expression level was not significantly associated with immunotherapy responses. Despite all 3 cohorts responded to antiPD1 therapy. We hypothesized that TCF19 might influence the extent of the response generated toward immunotherapy by targeting the various immune checkpoints. Also, our study only analyzed 3 relevant cohorts, which makes it difficult to elucidate the actual immunotherapy response of TCF19. More relevant immunotherapy cohort studies should be conducted in the future.

And finally, we followed the gene enrichment analysis to arrive at the result which revealed that the highly expressed TCF19 gene was primarily associated with specific pathways such as E2F, IL6, and G2M. The E2F and IL6 families are classical tumor signaling pathways. It has been reported that they exhibit unique and overlapping properties during the processes of transcription, proliferation, and apoptosis of tumor cells [34, 35]. The results might indicate that TCF19 potentially affects the extent of proliferation, infiltration, and metastasis realized by regulating multiple classical signaling pathways.Also, this specific mechanism associated with the processes needs to be explored further. The Cellminer database was analyzed to determine the relationship between TCF19 and IC_{50} to explore the correlation between TCF19 and antitumor drug sensitivity. The results revealed that the high level of expression of TCF19 reflected the tolerance level toward multiple antitumor drugs. The factors and mechanisms affecting the sensitivity of antitumor drugs are complex and diverse but results from the analysis of the K-M survival plot revealed that the higher expression group of TCF19 was significantly linked with a shorter prognosis for cancer patients. It was also observed that TCF19 negatively correlated with the effect of immunotherapy. The results indicated that TCF19 can be used as a potential indicator of the extent of the response generated toward renal cancer immunotherapy. Cancer immunotherapy based on TCF19 can also be explored and the results can potentially open a new avenue for the

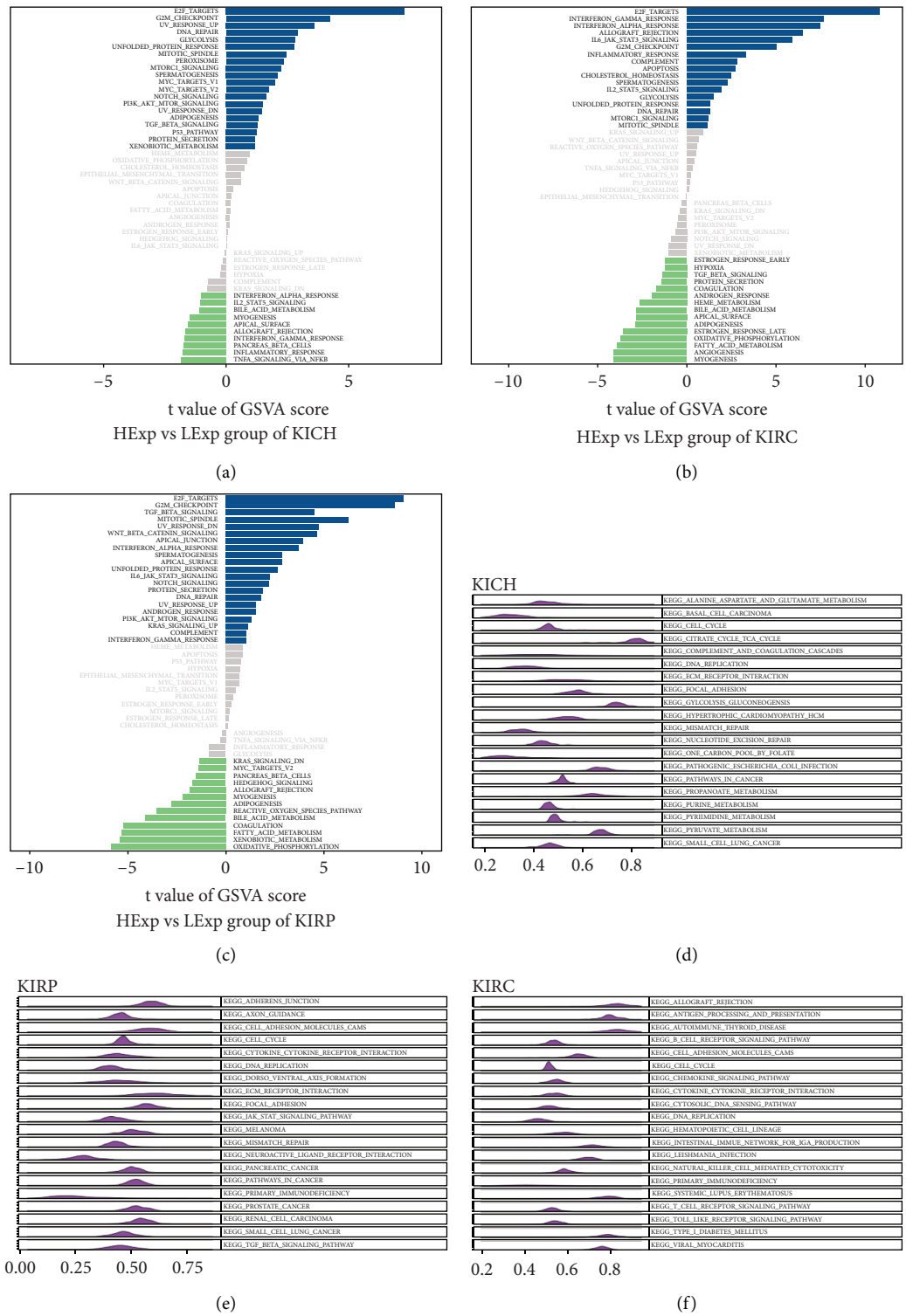

Figure 8: The results of GSVA analysis of TCF19. (a–c) It shows the GSVA analysis of TCF19 in KIRC, KIRP, and KICH, and (d–f) represents the GSEA analysis of TCF19 in KIRC, KIRP, and KICH.

development of tumor immunotherapy strategies. For example, Han [36] predicted the clinical outcome when patients suffering from lung adenocarcinoma were subjected to conditions of radiotherapy and immunotherapy by analyzing the genetic characteristics of the B cells. Dai [37] constructed an immune-related gene

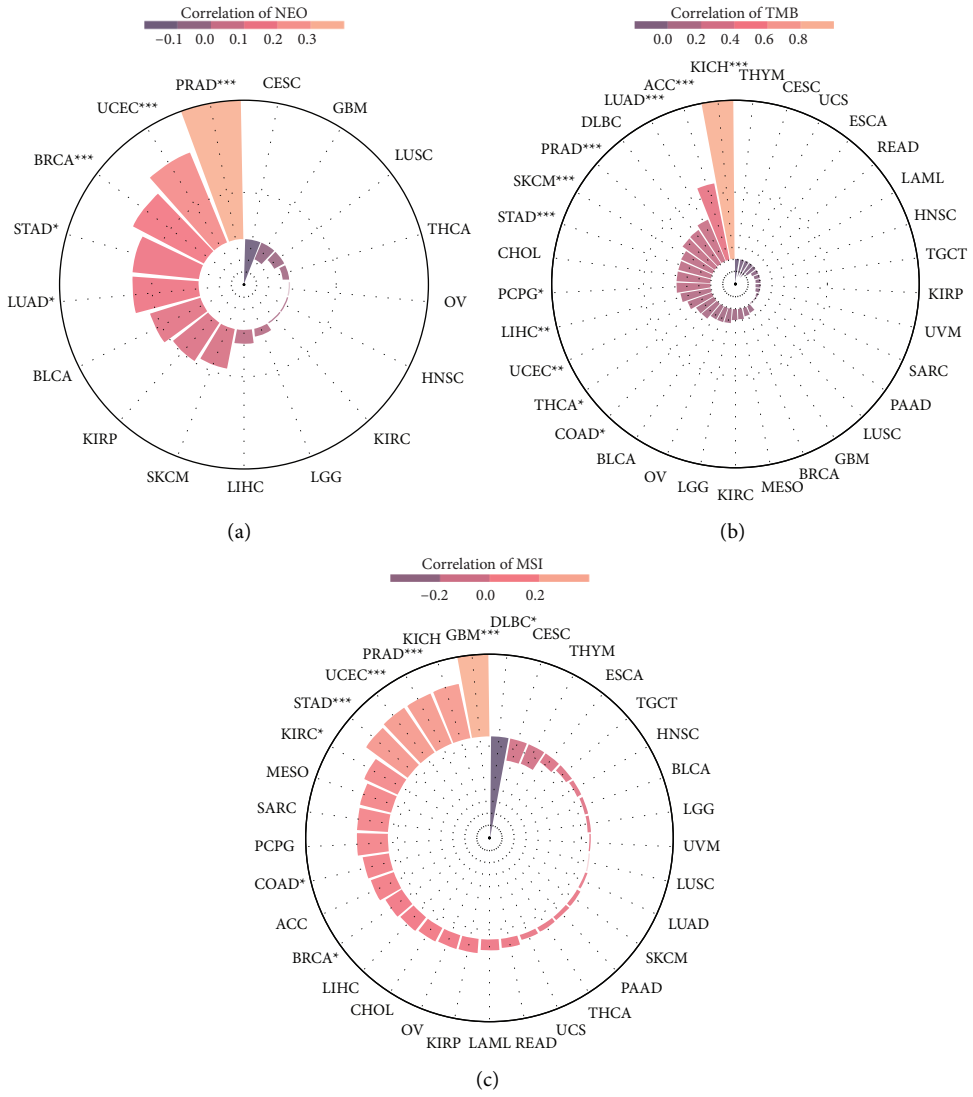

FIGURE 9: The relationship of TMB and MSI with the TCF19 expression in cancers. (a) Shows the relationship between TCF19 expression and TMB, (b) indicates the relations of TCF19 expression with MSI, and (c) represents the correlations of TCF19 expression with Neoantigen.

prognostic index (IRGPI) based on 11 immune-related genes, which can accurately forecast the immune cell infiltrations in the tumor microenvironment of hepatocellular carcinoma and the response generated toward immunotherapy. Feng Xu [38] studied lung adenocarcinoma cases and reported that immune-related genes were independently predicting the poor survival rate of patients.

As per we know, there is a minor number of relevant researches currently available to explain the functions of TCF19 in ccRCC. This study provided valuable information on how the TCF19 gene participated in cancer immunotherapy. The results also revealed the relationship between TCF19 and various immune indicators (such as the infiltration process of immune cells, immune-modulatory factors, and the biomarkers of the immune system). The obtained data can potentially help understand the underlying mechanisms associated with TCF19 and the immune system. Although the correlation between tumor immune microenvironment and TCF19 cannot be applied to all kinds of tumors, our work revealed the immune effects of TCF19 on the microenvironment of specific cancer cells which may potentially help improve the processes of TCRCC targeting therapy. However, preliminary results have been reported using various bioinformatics methods. Therefore, further research should be conducted to understand how TCF19 influences cancer immunotherapy. In our next step, we need to extend the existing analysis database and mutually authenticate with the existing database. Authentication should be realized at the molecular, cytological, and animal levels by conducting experiments to investigate the relationship between the prognosis of the patients and the properties of the clinical tumor tissue

samples. We believe that the results can potentially help for improving the efficiency of diagnosis, treatment methods, and survival prognosis of cancer patients.

5. Conclusion

This is one of the few studies that focus on the immunotherapeutic value of TCF19 associated with ccRCC. We believe that the results reported herein can potentially help design functional experiments that can help develop the field of clinical treatment.

Abbreviations

BCa:	Bladder cancer
TCGA:	The cancer genome atlas
diff-LncRNAs:	Differentially expressed LncRNAs
DEGs:	Differentially expressed genes
GO:	Gene ontology
KEGG:	Kyoto encyclopedia of genes and genomes
CC:	Cellular component
MF:	Molecular function
BP:	Biological process
FC:	Fold-change
GSEA:	Gene set enrichment analysis
DAVID:	The database for annotation Visualization and Integrated Discovery
OS:	Overall survival
ssGSEA:	Single-sample gene set enrichment analysis.

Data Availability

The original data are provided by the corresponding author upon request without any hesitation.

Conflicts of Interest

The authors have no conflicts of interest.

Authors' Contributions

Jian Hou and Xiangyang Wen designed the manuscript. Jian Hou, Xiangyang Wen, Xiaobao Cheng, and Runan Dong transcribed the whole article. Zhenquan Lu, Yi Jiang, Guoqing Wu, and Yuan Yuan downloaded the data for comprehensive analysis. All authors read and approved the final version of the submitted manuscript.

Acknowledgments

The High Level-Hospital Program, Health Commission of Guangdong Province (HKUSZH201901042).

Supplementary Materials

Supplementary figure 1: the relationship between TCF19 expression and prognosis (OS) of cancer patients. Supplementary Figure 2: the relationship between TCF19 expression and prognosis of cancer patients (PFI). Supplementary Figure 3: the WGCNA analysis of TCF19 in pan-cancer. Supplementary figure 4(a–f): the relationship between TCF19 expression and 33 tumor immune-related genes (genes analyzed include MHC, immune activators, immune suppressors, chemokines, and chemokine receptor proteins). Supplementary Figures 5(a–g): the association between TCF19 and common tumor-associated regulatory genes (such as TGF beta signaling, TNFA signaling, hypoxia, scorch death, DNA repair, autophagy genes, and iron death-related genes). Supplementary figure 6: the analysis of the relationship between TCF19 and the sensitivity of common antitumor drugs. (*Supplementary Materials*)

References

[1] R. L. Siegel, K. D. Miller, and A. Jemal, "Cancer statistics, 2018," *CA: a Cancer Journal for Clinicians*, vol. 68, no. 1, pp. 7–30, 2018.

[2] S. Chevrier, J. H. Levine, V. R. T. Zanotelli et al., "An immune atlas of clear cell renal cell carcinoma," *Cell*, vol. 169, no. 4, pp. 736–749.e18, 2017.

[3] H. Girgis, O. Masui, N. M. A. White et al., "Lactate Dehydrogenase A is a potential prognostic marker in clear cell renal cell carcinoma," *Molecular Cancer*, vol. 13, no. 1, p. 101, 2014.

[4] B. Ljungberg, L. Albiges, Y. Abu-Ghanem et al., "European association of urology guidelines on renal cell carcinoma: the 2019 update," *European Urology*, vol. 75, no. 5, pp. 799–810, 2019.

[5] R. J. Motzer, E. Jonasch, M. D. Michaelson et al.

[6] M. R. Harrison, E. R. Plimack, J. Sosman et al.

[7] R. J. Motzer, E. Jonasch, M. D. Michaelson et al., "NCCN guidelines insights: kidney cancer, version 2.2020," *Journal of the National Comprehensive Cancer Network*, vol. 17, no. 11, pp. 1278–1285, 2019.

[8] S. H. Sim, M. P. Messenger, W. M. Gregory et al.

[9] S. H. Sim, M. P. Messenger, W. M. Gregory et al., "Prognostic utility of pre-operative circulating osteopontin, carbonic anhydrase IX and CRP in renal cell carcinoma," *British Journal of Cancer*, vol. 107, no. 7, pp. 1131–1137, 2012.

[10] T. K. Choueiri, B. Escudier, T. Powles et al., "Cabozantinib versus everolimus in advanced renal-cell carcinoma," *New England Journal of Medicine*, vol. 373, no. 19, pp. 1814–1823, 2015.

[11] G. R. Li, G. Feng, A. Gentil-Perret, C. Genin, and J. Tostain, "Serum carbonic anhydrase 9 level is associated with post-operative recurrence of conventional renal cell cancer," *The Journal of Urology*, vol. 180, no. 2, pp. 510–514, 2008.

[12] K. A. Krautkramer, A. K. Linnemann, D. A. Fontaine et al., "Tcf19 is a novel islet factor necessary for proliferation and survival in the INS-1beta-cell line," *American Journal of Physiology - Endocrinology And Metabolism*, vol. 305, no. 5, pp. E600–E610, 2013.

[13] C. X. Zeng, S. B. Fu, W. S. Feng, J. Y. Zhao, F. X. Li, and P. Gao, "TCF19 enhances cell proliferation in hepatocellular carcinoma by activating the ATK/FOXO1 signaling pathway," *Neoplasma*, vol. 66, no. 01, pp. 46–53, 2019.

[14] R. B. Krishnan, I. Jamry, and D. D. Chaplin, "Feature mapping of the HLA class I region: localization of the POU5F1 and TCF19 genes," *Genomics*, vol. 30, no. 1, pp. 53–58, 1995.

[15] R. Z. Miao, X. B. Guo, Q. M. Zhi et al., "VEZT, a novel putative tumor suppressor, suppresses the growth and tumorigenicity of gastric cancer," *PLoS One*, vol. 8, no. 9, p. e74409, 2013.

[16] Z. H. Zhou, G. Chen, C. Deng et al., "TCF19 contributes to cell proliferation of non-small cell lung cancer by inhibiting FOXO1," *Cell Biology International*, vol. 43, no. 12, pp. 1416–1424, 2019.

[17] G. P. Xu, Y. G. Zhu, H. J. Liu, Y. Y. Liu, and X. N. Zhang, "LncRNA mir194-2HG promotes cell proliferation and metastasis via regulation of miR-1207-5p/TCF19/Wnt/β-Catenin signaling in liver cancer," *OncoTargets and Therapy*, vol. 13, pp. 9887–9899, 2020.

[18] P. Ji, J. Chang, X. Y. Wei et al., "Genetic variants associated with expression of TCF19 contribute to the risk of head and neck cancer in Chinese population," *Journal of Medical Genetics*, vol. 59, no. 4, pp. 335–345, 2021.

[19] S. Sen, S. Sanyal, D. K. Srivastava, D. Dasgupta, S. Roy, and C. Das, "Transcription factor 19 interacts with histone 3 lysine 4 trimethylation and controls gluconeogenesis via the nucleosome-remodeling-deacetylase complex," *Journal of Biological Chemistry*, vol. 292, no. 50, pp. 20362–20378, 2017.

[20] P. Mondal, S. S. Gadad, S. Adhikari et al., "TCF19 and p53 regulate transcription of TIGAR and SCO2 in HCC for mitochondrial energy metabolism and stress adaptation," *The FASEB Journal: Official Publication of the Federation of American Societies for Experimental Biology*, vol. 35, no. 9, Article ID e21814, 2021.

[21] G. Yang, D. Fontaine, S. Lodh, J. Blumer, A. Roopra, and D. Davis, "TCF19 impacts a network of inflammatory and DNA damage response genes in the pancreatic beta-cell," *Metabolites*, vol. 11, no. 8, p. 513, 2021.

[22] D. Raghu, H. H. Xue, and L. A. Mielke, "Control of lymphocyte fate, infection, and tumor immunity by TCF-1," *Trends in Immunology*, vol. 40, no. 12, pp. 1149–1162, 2019.

[23] S. Wen, H. Lu, D. Wang, J. Guo, W. Dai, and Z. Wang, "TCF-1 maintains CD8(+) T cell stemness in tumor microenvironment," *Journal of Leukocyte Biology*, vol. 110, no. 3, pp. 585–590, 2021.

[24] B. S. Hanna, L. Llao-Cid, M. Iskar et al.

[25] B. S. Hanna, L. Llaó-Cid, M. Iskar et al., "Interleukin-10 receptor signaling promotes the maintenance of a PD-1(int) TCF-1(+) CD8(+) T cell population that sustains anti-tumor immunity," *Immunity*, vol. 54, no. 12, pp. 2825–2841.e10, 2021.

[26] Y. Liu, W. Shang, H. Liu et al., "Biomimetic manganese-eumelanin nanocomposites for combined hyperthermia-immunotherapy against prostate cancer," *Journal of Nanobiotechnology*, vol. 20, no. 1, p. 48, 2022.

[27] L. Lu, Y. J. Liu, P. Q. Cheng, H. Dan, H. C. Xu, and G. Ji, "Macrophages play a role in inflammatory transformation of colorectal cancer," *World Journal of Gastrointestinal Oncology*, vol. 13, no. 12, pp. 2013–2028, 2021.

[28] H. Wang, Q. Cheng, K. Chang, L. Bao, and X. Yi, "Integrated analysis of ferroptosis-related biomarker Signatures to improve the diagnosis and prognosis prediction of ovarian cancer," *Frontiers in Cell and Developmental Biology*, vol. 9, Article ID 807862, 2021.

[29] Y. H. Chen, R. N. Dong, J. Hou et al.

[30] Y. H. Chen, R. N. Dong, J. Hou et al., "Mesenchymal stem cell-derived exosomes induced by IL-1β attenuate urethral stricture through let-7c/PAK1/NF-κB-Regulated macrophage M2 polarization," *Journal of Inflammation Research*, vol. 14, pp. 3217–3229, 2021.

[31] N. Xu, R. N. Dong, T. T. Lin et al.

[32] N. Xu, R. N. Dong, T. T. Lin et al., "Development and validation of novel biomarkers related to M2 macrophages infiltration by weighted gene Co-expression network analysis in prostate cancer," *Frontiers in Oncology*, vol. 11, Article ID 634075, 2021.

[33] R. Bonneville, M. A. Krook, E. A. Kautto et al., "Landscape of microsatellite instability across 39 cancer types," *JCO Precision Oncology*, no. 1, pp. 1–15, 2017.

[34] D. Ruggiero, T. Nutile, S. Nappo et al., "Genetics of PlGF plasma levels highlights a role of its receptors and supports the link between angiogenesis and immunity," *Scientific Reports*, vol. 11, no. 1, Article ID 16821, 2021.

[35] W. B. Du, Z. Huang, L. Luo et al., "TCF19 aggravates the malignant progression of colorectal cancer by negatively regulating WWC1," *European Review for Medical and Pharmacological Sciences*, vol. 24, no. 2, pp. 655–663, 2020.

[36] N. Xu, Z. B. Ke, X. D. Lin et al., "Development and validation of a molecular prognostic index of bladder cancer based on immunogenomic landscape analysis," *Cancer Cell International*, vol. 20, no. 1, p. 302, 2020.

[37] Y. Wang, B. Chen, Z. He et al., "Nanotherapeutic macrophage-based immunotherapy for the peritoneal carcinomatosis of lung cancer," *Nanoscale*, vol. 14, no. 6, pp. 2304–2315, 2022.

[38] T. A. Chan, M. Yarchoan, E. Jaffee et al., "Development of tumor mutation burden as an immunotherapy biomarker: utility for the oncology clinic," *Annals of Oncology*, vol. 30, no. 1, pp. 44–56, 2019.

[39] H. Yamamoto and K. Imai, "An updated review of microsatellite instability in the era of next-generation sequencing and precision medicine," *Seminars in Oncology*, vol. 46, no. 3, pp. 261–270, 2019.

[40] J. DeGregori and D. G. Johnson, "Distinct and overlapping roles for E2F family members in transcription, proliferation and apoptosis," *Current Molecular Medicine*, vol. 6, no. 7, pp. 739–748, 2006.

[41] Q. Chang, E. Bournazou, P. Sansone et al.

[42] Q. Chang, E. Bournazou, P. Sansone et al., "The IL-6/JAK/Stat3 feed-forward loop drives tumorigenesis and metastasis," *Neoplasia*, vol. 15, no. 7, pp. 848–IN45, 2013.

[43] L. Han, H. Shi, Y. Luo et al., "Gene signature based on B cell predicts clinical outcome of radiotherapy and immunotherapy for patients with lung adenocarcinoma," *Cancer Medicine*, vol. 9, no. 24, pp. 9581–9594, 2020.

[44] Y. Dai, W. Qiang, K. Lin, Y. Gui, X. Lan, and D. Wang, "An immune-related gene signature for predicting survival and immunotherapy efficacy in hepatocellular carcinoma," *Cancer Immunology Immunotherapy*, vol. 70, no. 4, pp. 967–979, 2021.

[45] F. Xu, X. Zhan, X. Zheng et al., "A signature of immune-related gene pairs predicts oncologic outcomes and response to immunotherapy in lung adenocarcinoma," *Genomics*, vol. 112, no. 6, pp. 4675–4683, 2020.

Hindawi
Journal of Oncology
Volume 2022, Article ID 5632744, 11 pages
https://doi.org/10.1155/2022/5632744

Research Article

Anlotinib Inhibits Tumor Angiogenesis and Promotes the Anticancer Effect of Radiotherapy on Esophageal Cancer through Inhibiting EphA2

Zhenlin Gu,[1] Weiguo Zhu,[2] Wanwei Wang,[2] Yingying Xu,[2] Lei Jiang,[2] Jiasheng Huang,[3] and Jing Huang[2]

[1]*Department of Vascular Surgery, The Affiliated Huaian No. 1 People's Hospital of Nanjing Medical University, Huaian 223300, Jiangsu, China*
[2]*Department of Radiation Oncology, The Affiliated Huaian No. 1 People's Hospital of Nanjing Medical University, Huaian 223300, Jiangsu, China*
[3]*Department of Interventional Radiology, The Affiliated Huaian No. 1 People's Hospital of Nanjing Medical University, Huaian 223300, Jiangsu, China*

Correspondence should be addressed to Jing Huang; hayyhj@njmu.edu.cn

Received 14 July 2022; Revised 10 August 2022; Accepted 17 August 2022; Published 31 August 2022

Academic Editor: Muhammad Muddassir Ali

Background. Anlotinib is a novel multitarget tyrosine kinase inhibitor for tumor angiogenesis and has antitumor activity in a variety of solid tumors. Given that, our study was designed to unearth the mechanism of anlotinib in radioresistant esophageal cancer (EC) cells. *Methods*. Radioresistant EC cell lines TE-1R and KYSE-150R were established by multiple fractionated irradiation. Detection of cell proliferation was governed by the MTT assay, angiogenesis by the tube formation assay, and cell migration and invasion by the transwell assay. Lastly, RT-qPCR Western blotting was employed to detect the expression of related genes. Cancerous cells showing tumor growth were then detected by tumor xenografts in mice. *Results*. Radioresistant EC cell lines TE-1R and KYSE-150R were successfully established. Anlotinib downregulated EphA2 inhibited proliferation, angiogenesis, migration, and invasion of radioresistant EC cells *in vitro*. The up-regulated expression of EphA2 in both EC cell lines and radioresistant EC cells, along with anlotinib, in turn, inhibited the expression of EphA2 in radioresistant EC cells. Inhibiting EphA2 also enhanced anlotinib-mediated effects on radioresistant EC cells, so as to restrain cell proliferation, angiogenesis, migration, and invasion. Correspondingly, overexpression of EphA2 is capable of reversing the therapeutic effect of anlotinib on radioresistant EC cells. Also, anlotinib enhances the inhibitory effect of irradiation on mice. *Conclusion*. It is concluded that anlotinib inhibits EphA2 expression, thereby suppressing angiogenesis and resensitizing EC cells to radiotherapy, providing another perspective to overcome radioresistance in EC.

1. Introduction

As a heterogeneous malignancy, esophageal cancer (EC) is mostly diagnosed in advanced stages and esophageal squamous cell carcinoma (ESCC) and accounts for most cases of the disease [1]. Smoking, alcohol consumption, gastroesophageal reflux disease, obesity, and diet are common risk factors for EC [2]. EC is usually asymptomatic in the early stages, and in advanced disease one may complain of heartburn unresponsive to medication, unconscious weight loss, progressive dysphagia, signs of blood loss, chest pain, and odynophagia [3]. Multimodality approaches such as endoscopic mucosal resection and endoscopic submucosal dissection, surgical treatment, neoadjuvant and adjuvant chemotherapy, as well as concurrent chemoradiotherapy have been developed for the treatment of EC [4]. However, tumor-associated microenvironmental factors and cellular mechanisms may somehow lead to radioresistance [5]. Thus, dealing with radioresistance may be a practical approach to manage EC. Blood vessel

normalization in tumors could reduce tumor uptake. Intratumoral accumulation, [6] tumor blood vessel normalization, and ES radiotherapy need further research studies.

Anlotinib is an orally administered tyrosine kinase inhibitor that is designed to inhibit angiogenesis and growth of tumors [7]. Anlotinib could reduce blood vessel sprout and microvessel density (MVD), and restrain migration and tube formation in tumors [8]. In fact, anlotinib has great therapeutic efficacy in treating cancers, such as advanced nonsmall cell lung cancer (NSCLC), advanced soft tissue sarcoma, and metastatic renal cell carcinoma [9]. In ESCC, it has been reported that anlotinib combined with radiotherapy and chemotherapy has strong antitumor effects on patient-derivedxenografts-bearing mice [10]. In a clinical trial, it has been found that anlotinib combined with chemotherapy could improve the survival of patients with advanced ESCC [11]. Considering the essence of anlotinib, tyrosine kinase receptors attracted our attention to determine the mechanism of anlotinib in EC. Belonging to the tyrosine kinase receptor group, EphA2 is abundantly produced in tumors and the regulation of EphA2 confers a potential in managing tumors [12]. EphA2 is a tumor-associated surface antigen of chimeric antigen receptor used in the treatment of ESCC [13]. It has been further analyzed that regulating EphA2 expression mediates vasculogenic mimicry of EC cells [14]. In ESCC samples after radiotherapy, the genomic profile of EphA2 is altered and the absence of mutation of EphA2 confers radioresistance [15]. In endometrial cancer, EphA2 overexpression is positively correlated with high VEGF expression, which is associated with angiogenesis and disease-specific survival of patients [16]. Referring to these reports, we assumed that anlotinib suppresses radioresistance and tumor angiogenesis of EC cells through inhibiting EphA2, and it may renew the mechanism underlying radioresistance in EC and provide for therapeutic reference.

2. Materials and Methods

2.1. Ethics Statement. Animal experiments were reviewed and approved by the animal ethics committee of "The Affiliated Huaian No.1 People's Hospital of Nanjing Medical University."

2.2. Cell Culture. Human normal esophageal epithelial cells (THEECs) and EC cell lines TE-1 and KYSE-150 (ATCC, VA, USA) were kept in Roswell Park Memorial Institute (RPMI)-1640 (10% fetal bovine serum [FBS], 100 unit/mL penicillin, and 100 mg/mL streptomycin). The media were all provided by Gibco (NY, USA).

2.3. Induction of Radioresistance in EC Cells. Radioresistant EC cell lines (TE-1R and KYSE-150R) were induced through multiple fractionated irradiation [17]. TE-1 and KYSE-150 cells (1.5×10^6 cells) in a culture flask (25 cm^2) were irradiated with 1 Gy X-ray, immediately supplemented with a fresh medium, and were grown to 90% confluence. Then, cells were cultured in a new culture flask to 50% confluence and treated with a second irradiation. Totally, cells were irradiated at 1 Gy three times, 2 Gy three times, and 4 Gy three times.

2.4. Colony Formation Assay. A colony formation assay was utilized to assess the radioresistance of parental and resistant EC cells. Parental and resistant EC cells in the log phase were trypsinized and seeded into 100-mm petri dishes. Upon cell adherence, cells were irradiated with 0, 2, 4, 6, 8, and 10 Gy X-ray, respectively, and were continuously cultured for 12 days to form cell colonies.

2.5. Cell Transfection. Cells in the log phase were cultured on a 6-well plate containing RPMI-1640 (2×10^5 cells/well). Cells at 90% confluence were transfected with EphA2-negative control (CTRL), siRNA-EphA2, or overexpression (OE)-EphA2 (GenePharma, Shanghai, China) via Lipofection™ (InivoGene, CA, USA). Three replicate wells were set.

2.6. Anlotinib Treatment. Cells were treated with anlotinib (CTTQ, Jiangsu, China) at 2, 4, and 8 μmol/L, respectively, for 48 h. A control was established with cells treated with normal saline [18].

2.7. 3-(4, 5-Dimethylthiazol-2-yl)-2,5-diphenyltetrazolium Bromide (MTT) Assay. Cells were placed in a 96-well plate at 3×10^3 cells/well. After 48 h, cells were combined with MTT solution at 20 μL/well (Beyotime, Shanghai, China) for 4 h, and treated with dimethyl sulfoxide at 100 μL/well. The D value at 490 nm was recorded on an automatic microplate reader (Tecan M200, TECAN, Switzerland).

2.8. Tube Formation Assay. Cells were cultured in a serum-free medium for 24 h and then in a medium containing 10% FBS. Then, the supernatant was centrifuged at 1000 r/min and filtered through a filter (0.22 μm) to obtain the conditioned medium (CM), which was preserved at 4 °C. A mixture (40 μL) made by the CM and Matrigel (1 : 1) was spread on a 96-well plate overnight and incubated with human umbilical vein endothelial cell suspension (1×10^5 cells/mL) at 200 μL/well. The formed tubes were observed and counted in 4 fields of view under a microscope (Olympus, Tokyo, Japan) [18].

2.9. Transwell Assay. Cells were prepared into a single cell suspension with serum-free Dulbecco's Modified Eagle Medium (DMEM). The cell suspension (100 μL, 3×10^5 cells/mL) was added to the upper side of the Transwell chamber (Corning, N.Y., USA). Matrigel (BD Company, NJ, USA) was used for the invasion assay but not for the migration assay. The bottom chamber was supplemented with 10% FBS-DMEM (600 μL). After 24 h, cells were fixed with 95% ethanol, stained with crystal violet, and counted under a microscope.

2.10. Tumor Xenografts in Nude Mice. Male and female BALB/c(nu/nu) nude mice (4–6 weeks old; 15–18 g) were provided by Beijing Vital River Laboratory Animal Technology Co., Ltd. (Beijing, China). Mice were housed in specific pathogen-free-level animal barriers (18–23°C, humidity 50–60%, 12 h day/night alternate, disinfected food and water). A week later, the skin on the left back of the mice was sterilized with ethanol, and the mice were subcutaneously injected with 100 μL of cell suspension (1×10^6 cells/mL) into the back. In the following 2 weeks, the general condition of the mice and the local condition of the injection site were observed. The mice were divided into three groups: KYSE-150R group, KYSE-150R + X-ray group, and KYSE-150R + Anlotinib + X-ray group. The mice in the KYSE-150R + Anlotinib + X-ray group were given anlotinib at 1.5 mg/kg by intragastric administration for 2 weeks. The mice in the KYSE-150R + X-ray group and KYSE-150R + Anlotinib + X-ray group were irradiated with 6 Gy X-rays every week. At 4 weeks postinjection, the mice were euthanized, the excised tumors were weighed, and tumor volume was measured [18].

2.11. Reverse Transcription Quantitative Polymerase Chain Reaction (RT-qPCR). After extraction of total RNA in tissues and cells by Trizol (Invitrogen, CA, USA), RNA concentration was determined with Nanodrop 2000 (Thermo Fisher Scientific, MA, USA). RNA was reverse-transcribed to cDNA using the PrimeScript RT kit (Takara, Kyoto, Japan). Using the SYBR Premix Ex Taq kit (Tli RNase H Plus) kit (Takara), real-time PCR was performed on an ABI7500 (Thermo Fisher Scientific). EphA2 expression was calculated by the $2^{-\triangle\triangle Ct}$ method [16] and normalized to glyceraldehyde-3-phosphate dehydrogenase (GAPDH). The primers (GenePharma) are shown in Table 1.

2.12. Western Blot Assay. After extraction of protein from tissues and cells, protein concentration was measured by the bicinchoninic acid method. The protein was mixed with loading buffer at 2 : 1 and denatured. After separation by sodium dodecyl sulfate-polyacrylamide gel electrophoresis, the protein was transferred to a polyvinylidene fluoride membrane and combined with primary antibodies EphA2 (1 : 2000, Thermo Fisher Scientific), VEGF (1 : 2000, Abcam), basic fibroblast growth factor (bFGF; 1 : 1000, Abcam), and GAPDH (1 : 1000, Millipore, MA, USA). Afterward, an HRP-labeled secondary antibody (1 : 5,000, Abcam) reacted with the membrane which was then developed by enhanced chemiluminescence. GAPDH was referred to as an internal control. Target protein expression was calculated by the gray analysis software.

2.13. Statistical Analysis. Data were assessed with SPSS 21.0 (IBM, NY, USA) and measurement data were expressed as mean ± standard deviation. Measurement data in normal distribution were compared by the *t*-test between the two groups. One-way analysis of variance (ANOVA), followed by Tukey's multiple comparisons test was applied to analyze data among multiple groups. At $P < 0.05$, statistical significance was established.

3. Results

3.1. Induction of Radioresistance in EC Cells. Colony formation assay was applied to assess the radioresistance of parental and radioresistant EC cells. The outcomes indicated that after irradiation at 0, 2, 4, 6, 8, and 10 Gy, respectively, for 12 days, the number of formed colonies decreased with the increase in the irradiation dose. Also, when irradiated at the same dose, the number of colonies of radioresistant EC cells increased as compared to parental EC cells. Since the results indicated that radioresistant EC cells had stronger radioresistance and colony-forming ability, it was confirmed that radioresistant EC cell lines TE-1R and KYSE-150R were successfully established (Figures 1(a)–1(d)).

3.2. Anlotinib Inhibits Proliferation, Angiogenesis, Migration, and Invasion of Radioresistant EC Cells. Anlotinib has antitumor activity in various solid tumors, however, its effect on the anticancer effect of radiotherapy in EC was unclear at times. To further explore this issue, we established TE-1R and KYSE-150R cell lines and treated the cells with different concentrations of anlotinib (2, 4, and 8 μmol/L). It was found from the MTT assay that after anlotinib treatment, the proliferation of TE-1R and KYSE-150R cells was impaired in a concentration-dependent manner (Figure 2(a)). The inhibitory effect of anlotinib on proliferation was more effective at 4 μmol/L; therefore, anlotinib at 4 μmol/L was used for later experiments.

In tube formation and transwell assays, along with the Western blot assay, we disclosed that after anlotinib treatment, tumor angiogenesis, migration, and invasion of TE-1R and KYSE-150R cells were inhibited, and protein expression of angiogenesis-related factors VEGF and bFGF was reduced (Figures 2(b)–2(e)).

3.3. EphA2 Expression Is Raised in Radioresistant EC Cells. EphA2, a tyrosine kinase receptor, has been reported to be upregulated in ESCC [13]. In the present study, we applied RT-qPCR and Western blot to measure EphA2 expression in cells. The outcome reflected that EphA2 expression was higher in TE-1 and KYSE-150 cells than in THEECs, and was higher in TE-1R and KYSE-150R cells than in TE-1 and KYSE-150 cells (Figures 3(a) and 3(b)). In addition, we also found that EphA2 was upregulated in EC on the Starbase website (Figure 3(c)).

3.4. Inhibiting EphA2 Enhances Anlotinib-Mediated Effects on Radioresistant EC Cells. We utilized RT-qPCR and Western blot to test EphA2 expression in TE-1R and KYSE-150R cells and revealed that anlotinib treatment reduced EphA2 expression (Figure 4(a)). Then, we applied siRNA-EphA2 or OE-EphA2 to downregulate or upregulate EphA2 expression in TE-1R and KYSE-150R cells, and we treated these cells

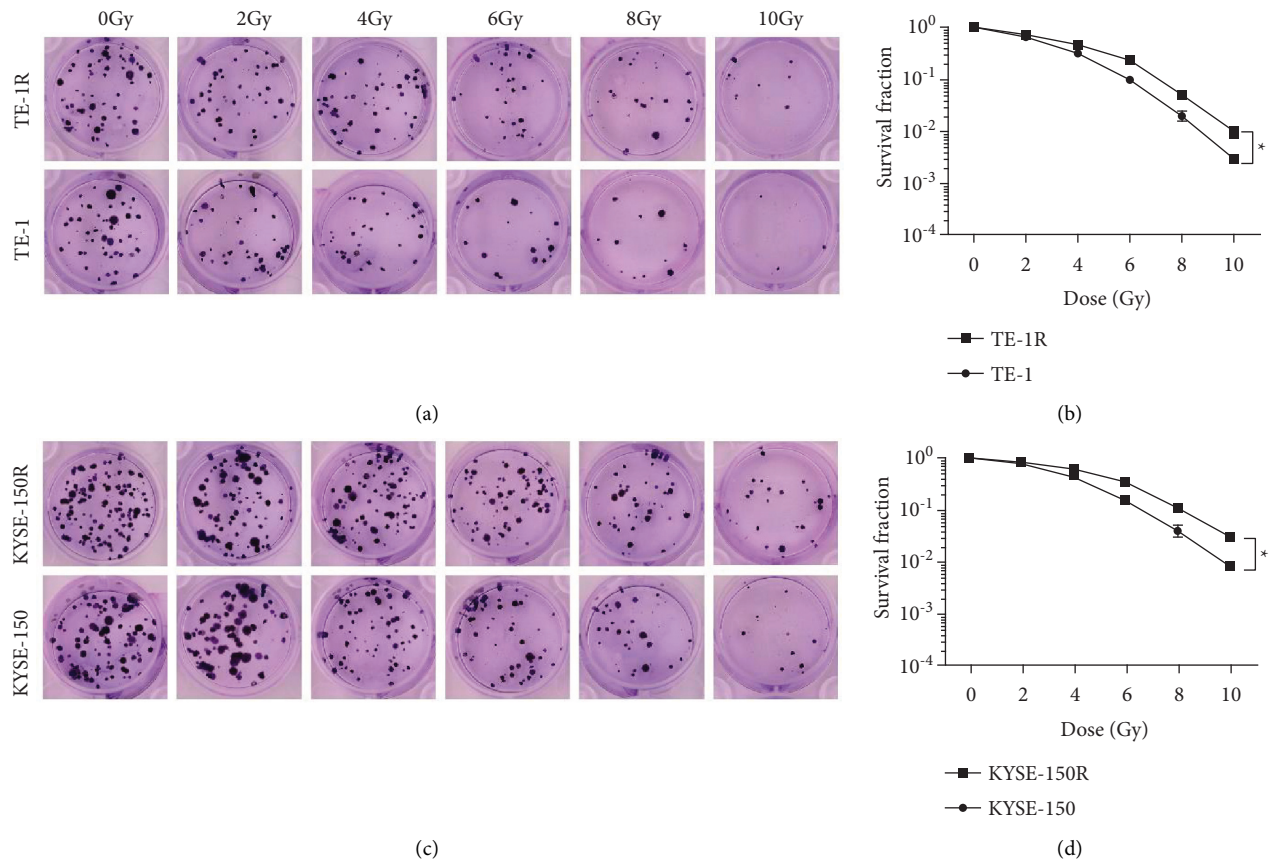

Figure 1: Induction of radioresistance in EC cells. (a) Colony-forming ability of TE-1 and TE-1R cells irradiated with different doses, (b) survival curve of TE-1 and TE-1R cells irradiated with different doses, (c) colony-forming ability of KYSE-150 and KYSE-150R cells irradiated with different doses, and (d) survival curve of KYSE-150 and KYSE-150R cells irradiated with different doses. $^{*}P < 0.05$ and $^{**}P < 0.01$; repetition = 3; the data were expressed in the form of mean ± standard deviation and were compared by the *t*-test.

with anlotinib at 4 μmol/L. Subsequently, the experimental data from *in vitro* cell function experiments indicated that OE-EphA2-mediated the upregulation of EphA2 and reversed the inhibitory effect of anlotinib on VEGF and bFGF protein expression, as well as on proliferation, tumor angiogenesis, and migration, and on invasion abilities of TE-1R and KYSE-150R cells. By contrast, siRNA-EphA2-induced downregulation of EphA2 which further enhanced anlotinib-mediated effects on TE-1R and KYSE-150R cells (Figures 4(b)–4(f)).

3.5. Downregulating EphA2 Depresses Proliferation, Angiogenesis, Migration, and Invasion of Radioresistant EC Cells. Next, we further explored the effect of EphA2 on cells and transfected siRNA-EphA2 or OE-EphA2 into TE-1R and KYSE-150R cells. At first, RT-qPCR and Western blot were employed to verify that EphA2 expression in cells was successfully downregulated or upregulated by siRNA-EphA2 or OE-EphA2 (Figure 5(a)). Next, through *in vitro* cell function experiments, we noticed that silencing EphA2 reduced proliferation, tumor angiogenesis, migration, and invasion, as well as VEGF and bFGF protein expression in cells, while restoring EphA2 had opposite effects (Figure 5(b)–5(f)).

3.6. Anlotinib Suppresses Growth of Radioresistant EC Cells In Vivo. The tumor formation rate of 24 nude mice was 100%, and no natural death occurred during the experiment. For mice exposed to irradiation, it was recognized that tumor volume, weight, and EphA2 expression were all suppressed. Then, further treatment with anlotinib was found to enhance the inhibitory effects of irradiation on mice (Figures 6(a)–6(d)).

4. Discussion

Radiation has an established role in definitive, palliative, and neoadjuvant environments, having a vital effect on the treatment of local EC [19]. Multiple drugs have been introduced to overcome radioresistance in EC, including anlotinib. In our research, we have recognized the therapeutic efficacy of anlotinib and further disclosed the underlying mechanism of anlotinib by regulating EphA2 in EC. Collectively, anlotinib inhibited tumor angiogenesis of radioresistant EC cells by inhibiting EphA2.

To specify the action of anlotinib in radioresistance of EC, we administrated anlotinib at 4 μmol/L to treat radioresistant EC cells and observed its inhibitory impacts on cellular proliferation, angiogenesis, migration, and invasion, as well as tumor growth. In a case report, it has been

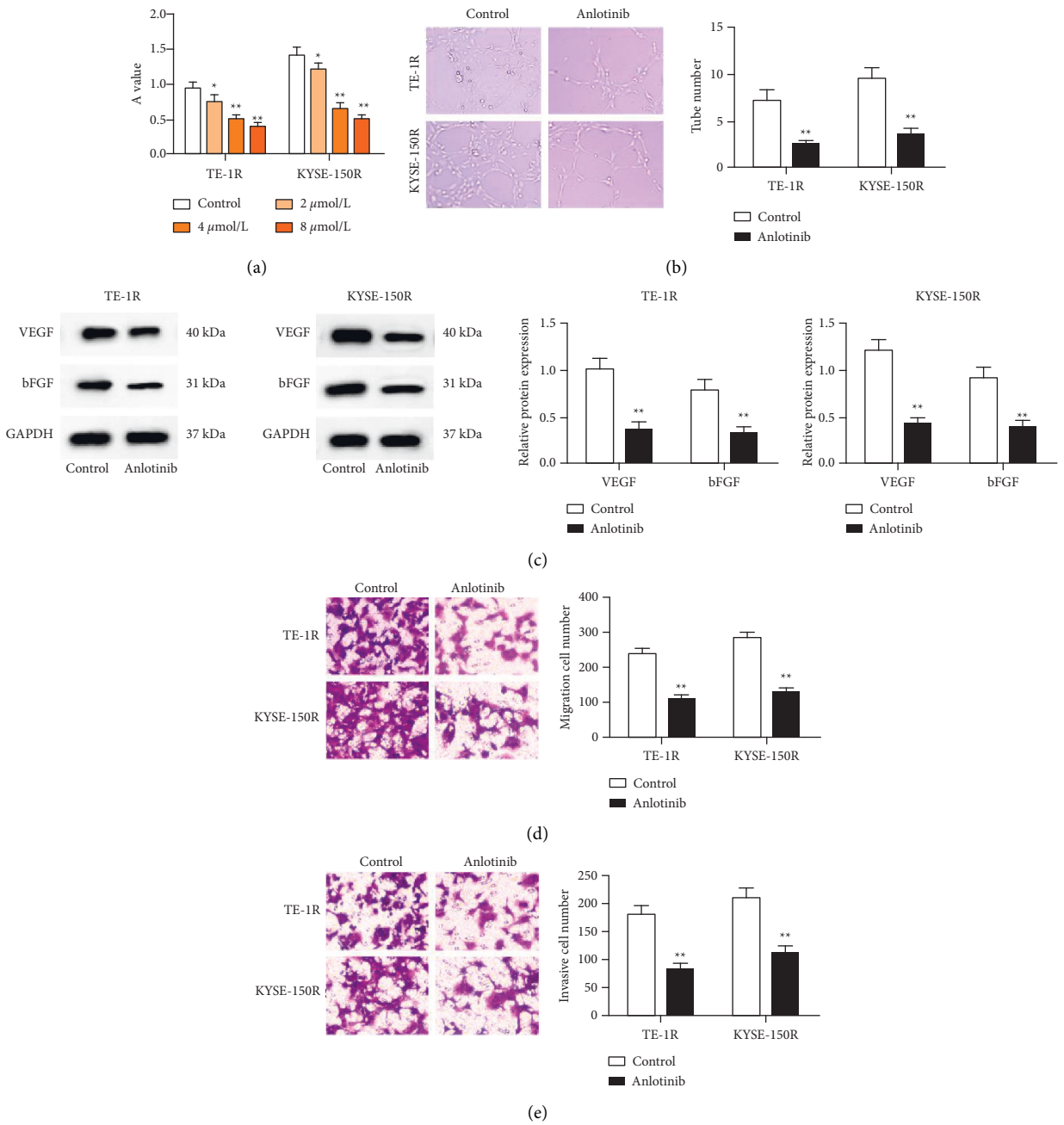

FIGURE 2: Anlotinib inhibits proliferation, angiogenesis, migration, and invasion of radioresistant EC cells. (a) The MTT assay detected cell proliferation, (b) the tube formation assay detected cell angiogenesis, (c) Western blot detected VEGF and bFGF expression in cells, (d) the transwell assay detected cell migration, and (e) the transwell assay detected cell invasion. $^{*}P < 0.05$ and $^{**}P < 0.01$; repetition *, $^{**} = 3$; the data were expressed in the form of mean ± standard deviation. Data were compared by the t-test (two groups), or one-way ANOVA (multiple groups) and Tukey's multiple comparisons test (pairwise comparison).

observed that administration of anlotinib has a better response for the fourth-line therapy and prolongs the overall survival time of patients with ESCC [11]. In another clinical trial, it has been noticed that combined administration of nivolumab and anlotinib as a second-line therapy could improve the physical condition of the patient with advanced ESCC [20]. In addition to that, a recent report has highlighted that anlotinib and chemoradiotherapy in combination have the ideal antitumor effect to suppress the process of ESCC in mice [10]. Besides, a double-blind randomized phase 2 trial has mentioned that the use of anlotinib has a great advantage in improving progression-free survival (PFS) of patients within recurrent and metastatic ESCC [21]. A case report has observed that for ESCC patients with failed immunotherapy course, their survival is greater than 19 months, and the overall patient survival is greater than 32 months after a fourth-line therapy (anlotinib combined with chemotherapy) [11]. Anlotinib combined with

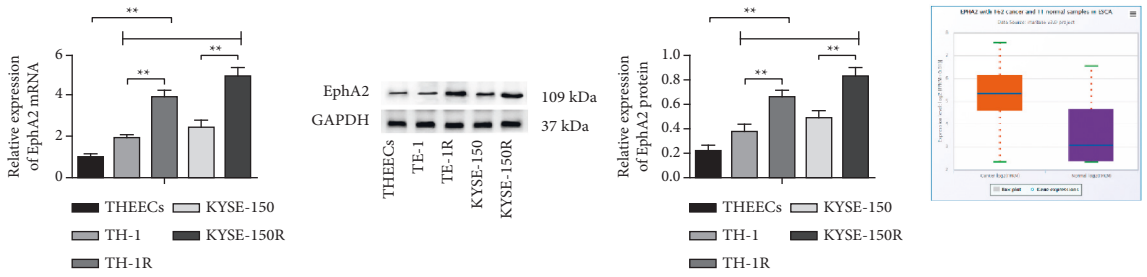

(a) (b) (c)

Figure 3: EphA2 expression is raised in radioresistant EC cells. (a) RT-qPCR detected EphA2 expression in THEECs, EC cell lines (TE-1 and KYSE-150), and radioresistant EC cells (TE-1R and KYSE-150R), (b) Western blot detected EphA2 expression in THEECs, EC cell lines (TE-1 and KYSE-150), and radioresistant EC cells (TE-1R and KYSE-150R), and (c) Starbase predicted that EphA2 was upregulated in EC. $^{*}P < 0.05$ and $^{**}P < 0.01$; repetition *, $^{**} = 3$; the data were expressed in the form of mean ± standard deviation and compared by one-way ANOVA and Tukey's multiple comparisons tests.

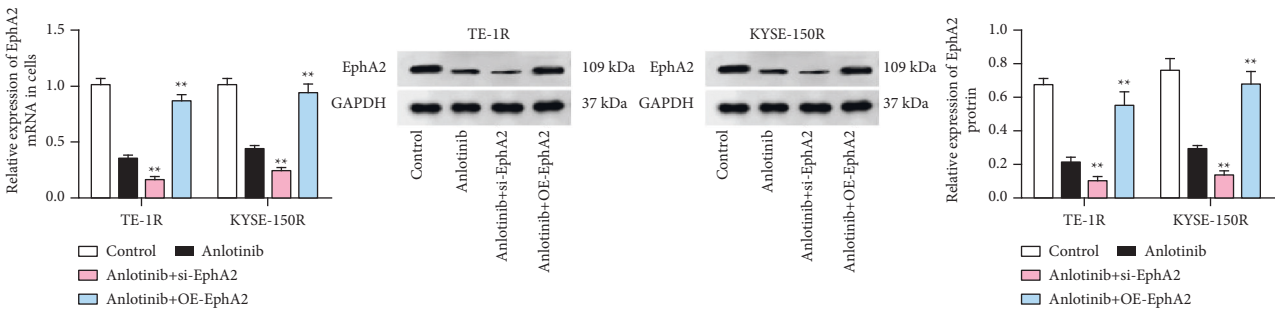

(a)

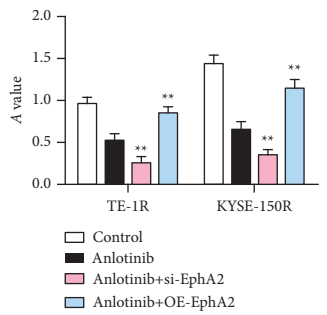

(b)

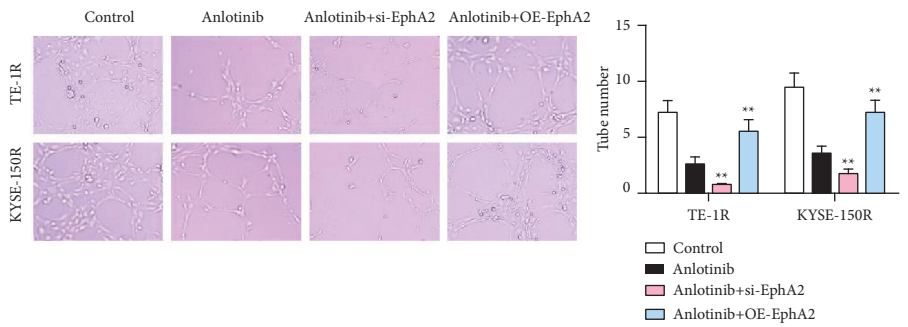

(c)

Figure 4: Continued.

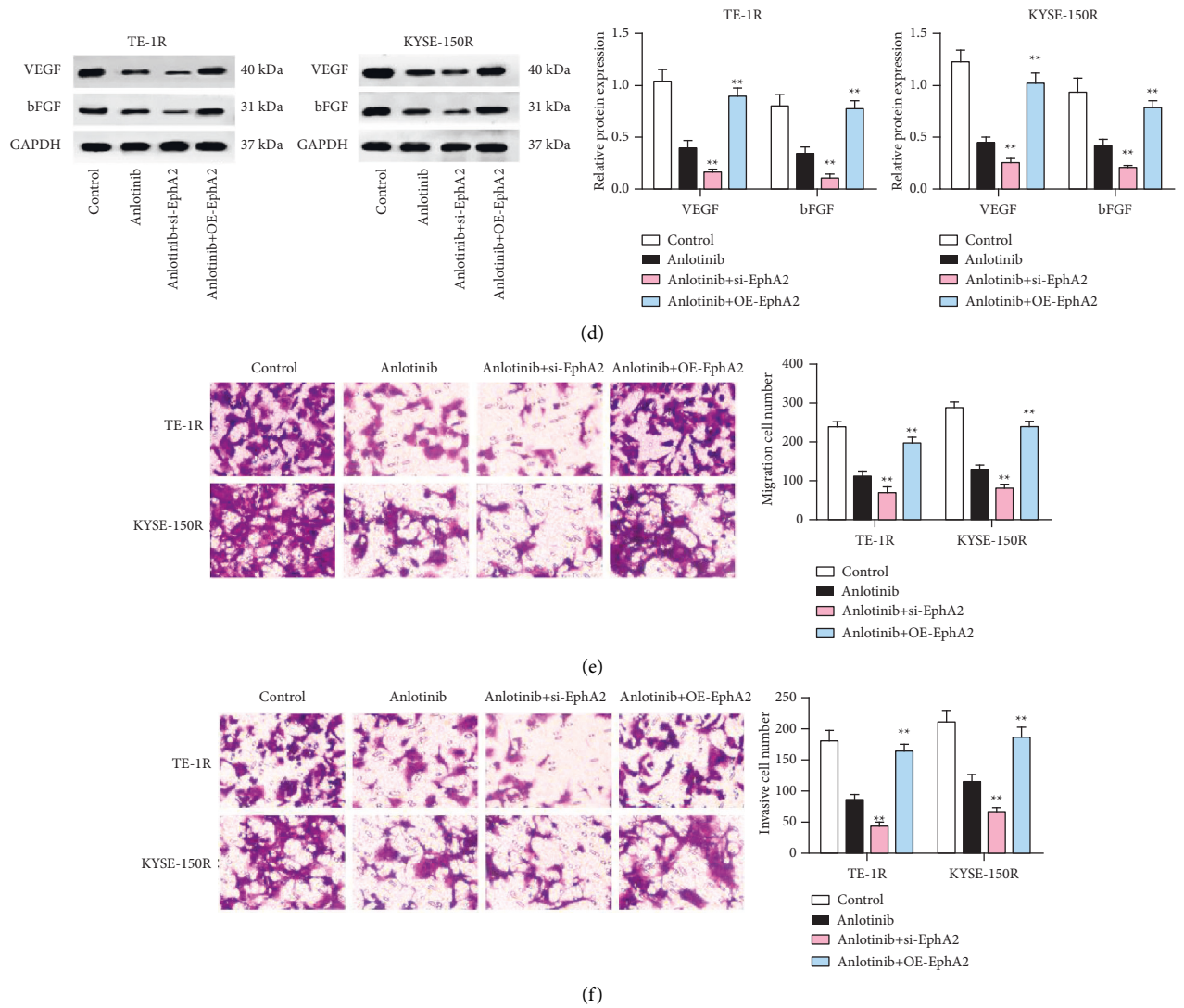

FIGURE 4: Inhibiting EphA2 enhances anlotinib-mediated effects on radioresistant EC cells. (a) RT-qPCR and Western blot detected EphA2 expression in cells, (b) the MTT assay detected cell proliferation, (c) the tube formation assay detected cell angiogenesis, (d) Western blot detected VEGF and bFGF expression in cells, (e) the transwell assay detected cell migration, and (f) the transwell assay detected cell invasion. $^{*}P < 0.05$ and $^{**}P < 0.01$; repetition *, $^{**} = 3$; the data were expressed in the form of mean ± standard deviation and compared by one-way ANOVA and Tukey's multiple comparisons tests.

concurrent chemoradiotherapy improves the clinical efficacy and safety of locally advanced ESCC patients [22]. Not only limited to EC but treatment with anlotinib works actively in other cancer types. For instance, treatment with anlotinib in thyroid cancer cells causes impairments in cell viability and migration *in vitro* and tumor growth *in vivo* [23]. Moreover, some studies have emerged on the regulatory mechanism of anlotinib in suppressing tumorigenesis. It is revealed that anlotinib could limit lung cancer cells to proliferate, invade, and migrate and can limit tumor growth by blocking the mitogen-activated protein kinase/extracellular signal-regulated kinase (ERK) pathway [24]. Other than that, anlotinib-induced inhibition of proliferation, migration, invasion, and tube formation, as well as tumorigenicity *in vivo* is recognized in colorectal cancer through suppressing the AKT/ERK pathway [18]. Our study also mentioned that anlotinib also exhibited great effects on promoting the efficacy of radiotherapy in EC. Consistently, it is noted that in the setting of lung cancer, the synergism of radiotherapy and anlotinib is more effective to suppress cell proliferation and tumor cell growth than the administration of anlotinib alone [25]. Overall, anlotinib is a promising drug for managing the process of cancer and improving the survival of cancer patients; moreover, anlotinib and radiotherapy synergistically function to control the tumorigenic activities of malignant cells.

Next, we studied that EphA2 was upregulated in EC cell lines and radioresistant EC cells, and further validated that anlotinib suppressed EphA2 expression in radioresistant EC cells. Subsequently, we performed cell function assays and finally uncovered that upregulating EphA2 enhanced the proliferation, invasion, migration, and angiogenesis of

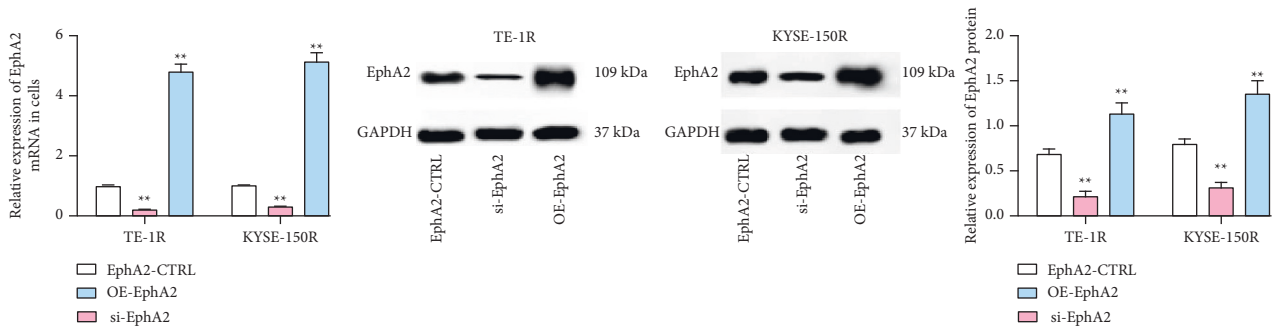

(a)

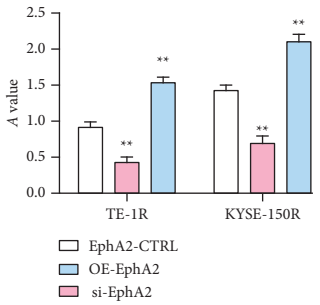

(b)

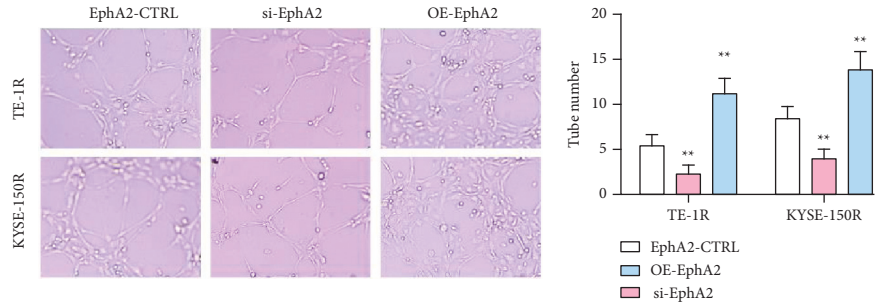

(c)

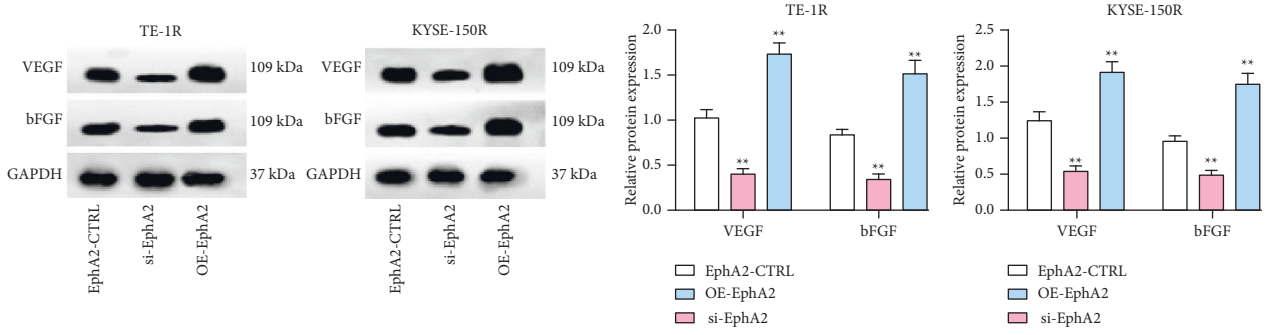

(d)

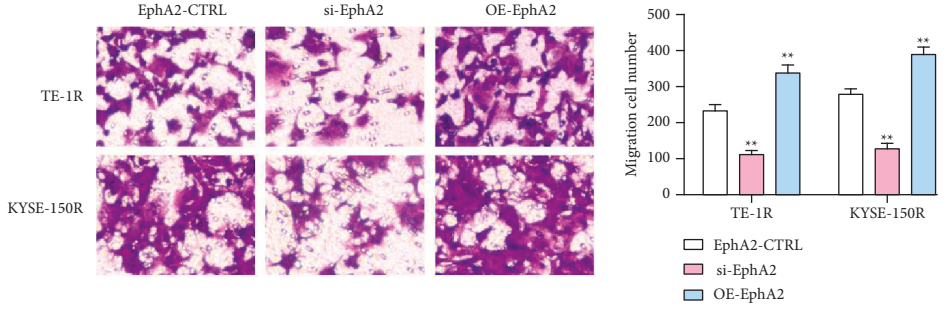

(e)

Figure 5: Continued.

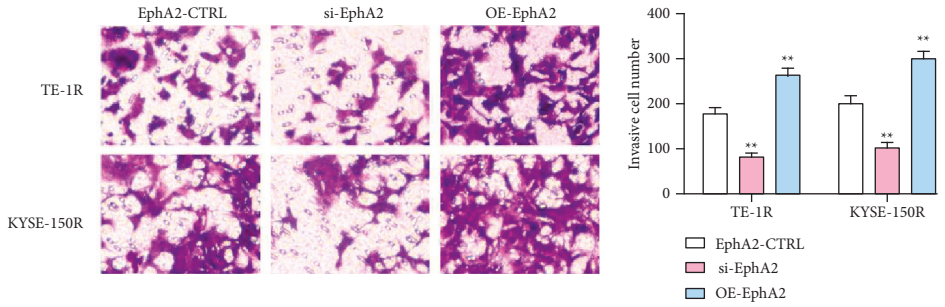

Figure 5: Downregulating EphA2 depresses proliferation, angiogenesis, migration, and invasion of radioresistant EC cells. (a) RT-qPCR and Western blot detected EphA2 expression in cells, (b) the MTT assay detected cell proliferation, (c) the tube formation assay detected cell angiogenesis, (d) Western blot detected VEGF and bFGF expression in cells, (e) the transwell assay detected cell migration, and (f) the transwell assay detected cell invasion. $^{*}P < 0.05$ and $^{**}P < 0.01$; *, **repetition = 3; the data were expressed in the form of mean ± standard deviation and compared by one-way ANOVA and Tukey's multiple comparisons tests.

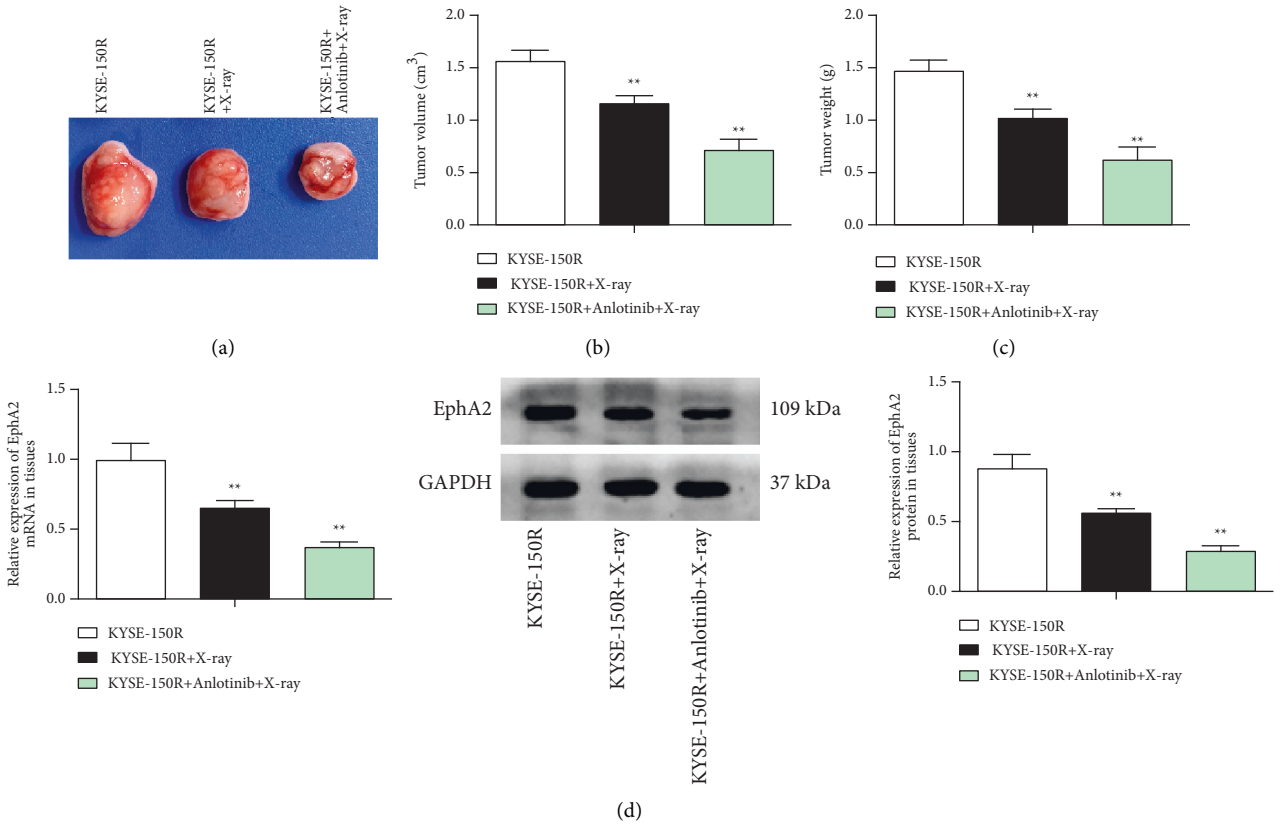

Figure 6: Anlotinib suppresses the growth of radioresistant EC cells *in vivo*. (a) Representative images of tumors, (b) tumor volume in nude mice, (c) tumor weight in nude mice, and (d) RT-qPCR and Western blot detected EphA2 expression in tumors of nude mice. $^{*}P < 0.05$ and $^{**}P < 0.01$; *, $^{**}n = 5$; the data were expressed in the form of mean ± standard deviation and compared by one-way ANOVA and Tukey's multiple comparisons tests.

radioresistant EC cells. On the contrary, downregulating EphA2 had opposite effects. Deeply, we analyzed the synergism of EphA2 and anlotinib and revealed that inhibiting EphA2 strengthened the effects of anlotinib on radioresistant EC cells. In fact, phosphotyrosine profiling has indicated that EphA2 expression is raised in ESCC, and knocking down EphA2 could decrease the proliferation and invasion of malignant cells [26]. Other researchers have also identified the role of EphA2 in various tumors. For example, EphA2 expression is elevated in small-cell lung cancer, and suppression of EphA2 has the ability to restrain cell proliferation [27]. Concerning the regulatory role of EphA2 in cancer radioresistance, it has been described that blocking EphA2 could suppress the radioresistance of NSCLC cells, as

well as the migration, proliferation, and invasion of malignant cells [28]. It is known that miR-200c-induced radiosensitivity, as well as invasion, migration, and tube formation reduction, is associated with EphA2 downregulation in human cancer cells [29]. VEGF and bFGF are both proangiogenic factors [30]. Regarding the molecular mechanism of VEGF and bFGF inhibition by EphA2, there are studies explaining that EphA2 is involved in the p38 MAPK/VEGF pathway [31, 32] and EphA2 promotes bFGF expression by activating the AKT signaling pathway [33], suggesting that EphA2 may positively regulate the expression of VEGF and bFGF through the p38 MAPK and AKT pathways.

5. Conclusion

The research concludes in a manner that it provides a novel perspective on the regulatory mechanism of anlotinib in EC, and delineates that anlotinib could circumstantially inhibit EphA2 expression, thus suppressing angiogenesis and resensitizing EC cells to radiotherapy. However, our study is at the preclinical level, and many efforts are required to develop the results in clinics. [34].

Data Availability

The data used to support the findings of this study are included within this article.

Ethical Approval

Animal experiments have been reviewed and approved by the animal ethics committee of " The Affiliated Huaian No.1 People's Hospital of Nanjing Medical University."

Disclosure

This manuscript was previously preprinted on a third-party platform. The link is anlotinib induces tumor blood vessel normalization to strengthen the anticancer effect of radiotherapy on esophageal cancer by inhibiting EphA2 (Research Square). All authors have approved this manuscript.

Conflicts of Interest

The authors declare that they have no conflicts of interest.

Authors' Contributions

Weiguo Zhu finished the study design; Jing Huang, Jiasheng Huang, and Yingying Xu finished the experimental studies; Zhenlin Gu and Wanwei Wang finished data analysis; and Jing Huang and Zhenlin Gu finished the manuscript editing. All authors read and approved the final manuscript.

Acknowledgments

The study was funded by Huai 'an Natural Science Research Program (No.HAB202026) and the Science Development Foundation of Nanjing Medical University (No. NMUB2020153).

References

[1] S. Krug and P. Michl, "Esophageal cancer: new Insights into a heterogenous disease," *Digestion*, vol. 95, no. 4, pp. 253–261, 2017.

[2] F. L. Huang and S. J. Yu, "Esophageal cancer: risk factors, genetic association, and treatment," *Asian Journal of Surgery*, vol. 41, no. 3, pp. 210–215, 2018.

[3] M. W. Short, K. G. Burgers, and V. T. Fry, "Esophageal cancer," *American Family Physician*, vol. 95, no. 1, pp. 22–28, 2017.

[4] H. Kato and M. Nakajima, "Treatments for esophageal cancer: a review," *Gen Thorac Cardiovasc Surg*, vol. 61, no. 6, pp. 330–335, 2013.

[5] G. Z. Chen, H. C. Zhu, W. S. Dai, X. N. Zeng, J. H. Luo, and X. C. Sun, "The mechanisms of radioresistance in esophageal squamous cell carcinoma and current strategies in radiosensitivity," *Journal of Thoracic Disease*, vol. 9, no. 3, pp. 849–859, 2017.

[6] M. Arjaans, T. H. Oude Munnink, S. F. Oosting et al., "Bevacizumab-induced normalization of blood vessels in tumors hampers antibody uptake," *Cancer Research*, vol. 73, no. 11, pp. 3347–3355, 2013.

[7] S. Y. Y. Anlotinib, "First Global approval," *Drugs*, vol. 78, no. 10, pp. 1057–1062, 2018.

[8] B. Lin, X. Song, D. Yang, D. Bai, Y. Yao, and N. Lu, "Anlotinib inhibits angiogenesis via suppressing the activation of VEGFR2, PDGFRβ and FGFR1," *Gene*, vol. 654, pp. 77–86, 2018.

[9] G. Shen, F. Zheng, D. Ren et al., "Anlotinib: a novel multitargeting tyrosine kinase inhibitor in clinical development," *Journal of Hematology & Oncology*, vol. 11, no. 1, p. 120, 2018.

[10] J. Shi, Y. Zhang, J. Wang, J. Li, and Z. Li, "Anlotinib combined with chemoradiotherapy Exhibits significant therapeutic efficacy in esophageal squamous cell carcinoma," *Front Oncol*, vol. 10, p. 995, 2020.

[11] D. Yang, F. Xu, X. Lai et al., "Combined treatment with anlotinib and chemotherapy for advanced esophageal squamous cell carcinoma improved patient survival: a case report," *Am J Transl Res*, vol. 12, no. 10, pp. 6578–6583, 2020.

[12] T. Xiao, Y. Xiao, W. Wang, Y. Y. Tang, Z. Xiao, and M. Su, "Targeting EphA2 in cancer," *Journal of Hematology & Oncology*, vol. 13, no. 1, p. 114, 2020.

[13] H. Shi, F. Yu, Y. Mao et al., "EphA2 chimeric antigen receptor-modified T cells for the immunotherapy of esophageal squamous cell carcinoma," *Journal of Thoracic Disease*, vol. 10, no. 5, pp. 2779–2788, 2018.

[14] J. Zhang, G. Deng, L. Qiao et al., "Effect of galectin-3 on vasculogenic mimicry in esophageal cancer cells," *Oncology Letters*, vol. 15, no. 4, pp. 4907–4911, 2018.

[15] G. Weng, W. Zhao, Y. Yin et al., "Genomic alterations of whole exome sequencing in esophageal squamous cell carcinoma before and after radiotherapy," *Journal of Thoracic Disease*, vol. 12, no. 10, pp. 5945–5957, 2020.

[16] W. M. Merritt, A. A. Kamat, J. Y. Hwang et al., "Clinical and biological impact of EphA2 overexpression and angiogenesis in endometrial cancer," *Cancer Biology & Therapy*, vol. 10, no. 12, pp. 1306–1314, 2010.

[17] Z. Jing, L. Gong, C. Y. Xie et al., "Reverse resistance to radiation in KYSE-150R esophageal carcinoma cell after epidermal growth factor receptor signal pathway inhibition by

cetuximab," *Radiotherapy & Oncology*, vol. 93, no. 3, pp. 468–473, 2009.

[18] Q. Yang, L. Ni, S. Imani et al., "Anlotinib suppresses colorectal cancer proliferation and angiogenesis via inhibition of AKT/ERK signaling Cascade," *Cancer Management and Research*, vol. 12, pp. 4937–4948, 2020.

[19] M. Zhang and A. J. Wu, "Radiation techniques for esophageal cancer," *Chinese Clinical Oncology*, vol. 6, no. 5, p. 45, 2017.

[20] Y. Tang, Z. Ou, Z. Yao, and G. Qiao, "A case report of immune checkpoint inhibitor nivolumab combined with anti-angiogenesis agent anlotinib for advanced esophageal squamous cell carcinoma," *Medicine (Baltimore)*, vol. 98, no. 40, Article ID e17164, 2019.

[21] J. Huang, J. Xiao, W. Fang et al., "Anlotinib for previously treated advanced or metastatic esophageal squamous cell carcinoma: a double-blind randomized phase 2 trial," *Cancer Medicine*, vol. 10, no. 5, pp. 1681–1689, 2021.

[22] G. Wang, N. M. Beeraka, W. Xiao et al., "Comparative clinical efficacy of 'concurrent chemoradiotherapy (CCRT) and anlotinib' than CCRT in patients with locally advanced ESCC," *Technology in Cancer Research and Treatment*, vol. 21, Article ID 153303382210809, 2022.

[23] X. Ruan, X. Shi, Q. Dong et al., "Antitumor effects of anlotinib in thyroid cancer," *Endocrine-Related Cancer*, vol. 26, no. 1, pp. 153–164, 2019.

[24] H. Hu, Y. Liu, S. Tan et al., "Anlotinib Exerts anti-cancer effects on KRAS-Mutated lung cancer cell through suppressing the MEK/ERK pathway," *Cancer Management and Research*, vol. 12, pp. 3579–3587, 2020.

[25] L. Guo, L. Zhang, Y. Guan, Y. Li, C. Zhang, and Q. Guo, "*In vitro* studies of H520 cell cycle and apoptosis by anlotinib combined with radiotherapy," *Thorac Cancer*, vol. 12, no. 5, pp. 593–602, 2021.

[26] N. Syed, M. A. Barbhuiya, S. M. Pinto et al., "Phosphotyrosine profiling identifies ephrin receptor A2 as a potential therapeutic target in esophageal squamous-cell carcinoma," *Proteomics*, vol. 15, no. 2-3, pp. 374–382, 2015.

[27] H. Ishigaki, T. Minami, O. Morimura et al., "EphA2 inhibition suppresses proliferation of small-cell lung cancer cells through inducing cell cycle arrest," *Biochemical and Biophysical Research Communications*, vol. 519, no. 4, pp. 846–853, 2019.

[28] S. Gong, Y. Li, L. Lv, and W. Men, "Restored microRNA-519a enhances the radiosensitivity of non-small cell lung cancer via suppressing EphA2," *Gene Therapy*, 2021.

[29] T. Koo, B. J. Cho, D. H. Kim et al., "MicroRNA-200c increases radiosensitivity of human cancer cells with activated EGFR-associated signaling," *Oncotarget*, vol. 8, no. 39, pp. 65457–65468, 2017.

[30] F. T. Zahra, M. S. Sajib, and C. M. Mikelis, "Role of bFGF in Acquired resistance upon anti-VEGF therapy in cancer," *Cancers*, vol. 13, no. 6, p. 1422, 2021.

[31] K. Zuo, K. Zhi, X. Zhang et al., "A dysregulated microRNA-26a/EphA2 axis impairs endothelial progenitor cell function via the p38 MAPK/VEGF pathway," *Cellular Physiology and Biochemistry*, vol. 35, no. 2, pp. 477–488, 2015.

[32] Y. Liu, H. L. Tan, G. Li, C. Y. Yu, Z. W. Su, and S. L. Ren, "EphA2 mediated vascular endothelial growth factor expression via the p38 MAPK signaling pathway in squamous cell carcinoma of the head and neck," *Zhonghua er bi yan hou tou jing wai ke za zhi*, vol. 48, no. 3, pp. 229–233, 2013.

[33] M. Sainz-Jaspeado, J. Huertas-Martinez, L. Lagares-Tena et al., "EphA2-induced angiogenesis in ewing sarcoma cells works through bFGF production and is dependent on caveolin-1," *PLoS One*, vol. 8, no. 8, Article ID e71449, 2013.

[34] W. H. J. Zhu, Z. Gu, J. Huang, Y. Xu, and W. Wang, "Anlotinib induces tumor blood vessel normalization to strengthen the anticancer effect of radiotherapy on esophageal cancer by inhibiting EphA2," *Research Square Platform LLC*, 2021.

Hindawi
Journal of Oncology
Volume 2023, Article ID 9832716, 1 page
https://doi.org/10.1155/2023/9832716

Retraction

Retracted: Analysis of Clinical Characteristics and Risk Factors of Postoperative Recurrence and Malignant Transformation of Low-Grade Glioma

Journal of Oncology

Received 11 July 2023; Accepted 11 July 2023; Published 12 July 2023

This article has been retracted by Hindawi following an investigation undertaken by the publisher [1]. This investigation has uncovered evidence of one or more of the following indicators of systematic manipulation of the publication process:

(1) Discrepancies in scope
(2) Discrepancies in the description of the research reported
(3) Discrepancies between the availability of data and the research described
(4) Inappropriate citations
(5) Incoherent, meaningless and/or irrelevant content included in the article
(6) Peer-review manipulation

The presence of these indicators undermines our confidence in the integrity of the article's content and we cannot, therefore, vouch for its reliability. Please note that this notice is intended solely to alert readers that the content of this article is unreliable. We have not investigated whether authors were aware of or involved in the systematic manipulation of the publication process.

Wiley and Hindawi regrets that the usual quality checks did not identify these issues before publication and have since put additional measures in place to safeguard research integrity.

We wish to credit our own Research Integrity and Research Publishing teams and anonymous and named external researchers and research integrity experts for contributing to this investigation.

The corresponding author, as the representative of all authors, has been given the opportunity to register their agreement or disagreement to this retraction. We have kept a record of any response received.

References

[1] C. Luo, Q. Luo, Y. Xu et al., "Analysis of Clinical Characteristics and Risk Factors of Postoperative Recurrence and Malignant Transformation of Low-Grade Glioma," *Journal of Oncology*, vol. 2022, Article ID 4948943, 11 pages, 2022.

Hindawi
Journal of Oncology
Volume 2022, Article ID 4948943, 11 pages
https://doi.org/10.1155/2022/4948943

Research Article

Analysis of Clinical Characteristics and Risk Factors of Postoperative Recurrence and Malignant Transformation of Low-Grade Glioma

Cheng Luo,[1] Qian Luo,[1] Yaoduan Xu,[2] Jiushan Song,[3] Yi Liu,[1] Laizang Wang,[1] Zhuoqi Dong,[2] Wei Huang,[1] Hualin Yu,[1] and Jinghui Li[1]

[1]*The Second Department of Neurosurgery, First Affiliated Hospital of Kunming Medical University, Kunming 650000, Yunan, China*
[2]*The Department of Neurosurgery, Third People's Hospital of Honghe Prefecture, Gejiu 661000, Yunnan, China*
[3]*The Pediatric Department, First Affiliated Hospital of Kunming Medical University, Kunming 650000, Yunnan, China*

Correspondence should be addressed to Hualin Yu; yuhualin6@kmmu.edu.cn and Jinghui Li; lijinghui@kmmu.edu.cn

Received 14 June 2022; Revised 6 July 2022; Accepted 8 July 2022; Published 31 August 2022

Academic Editor: Muhammad Muddassir Ali

This research was developed to explore the clinical characteristics and related risk factors of postoperative recurrence and malignant transformation of low-grade glioma (LGG). The subjects were rolled into observation group (19 cases) and control group (51 cases) according to recurrence and malignant transformation during the follow-up period. The clinical data of the two groups were compared, and the risk factors of recurrence and malignant transformation were analyzed with the time of recurrence and malignant transformation as independent variables. The experimental results showed that the proportion of patients aged over 45 years in the observation group (63.16%) was higher than that in the control group (50.98%). The proportion of preoperative functional status score (KPS) ≥80 in the observation group (68.42%) was lower than that in the control group (78.43%). The proportion of patients with tumor over 5 cm in the control group (27.45%) was lower than that in the observation group (52.63%), and the proportion of total resection of tumor in the control group (47.06%) was higher than that in the observation group (21.05%). Furthermore, the multivariate analysis showed that preoperative KPS score, preoperative duration of disease, resection scope, postoperative treatment, oncotesticular antigen (OY-TES-1) mRNA, P53, mouse double microbody amplification gene (MDM2), vascular endothelial growth factor (VEGF), and epidermal growth factor receptor (EGFR) were independent risk factors (all $P < 0.05$). In summary, patients with postoperative recurrence and malignant transformation had poorer physical condition and higher degree of malignancy before surgery. Preoperative KPS score, duration of disease, surgical resection scope, postoperative treatment, OY-TES-1 mRNA, P53, MDM2, VEGF, and EGFR were the risk factors.

1. Introduction

Intracranial tumors are classified into primary and secondary types according to their specific causes. Tumor types are also different in different age groups. For younger children, intracranial tumors mainly occur in the posterior fossa and midline. For adults, it is mainly a glioma of the cerebral hemisphere [1]. The cerebral hemisphere is part of the brain that controls movement, language, and emotion. Gliomas occur in the cerebral hemisphere and can cause headaches, nausea, vomiting, seizures, and limb movement disorders. Glioma, as a primary intracranial tumor, has a high recurrence rate and fatality rate [2]. At present, the main clinical diagnosis methods are skull CT and nuclear magnetic examination. Existing studies suggested that glioma, as a malignant tumor, is mainly formed by intermutations between astrocytes, oligodendrocytes, ependymal cells, and neurons [3]. According to statistics, there are more male patients than female patients, and the age of patients is generally younger. The growth of mesenchymal tumors is usually slow, and the time from onset of symptoms to medical treatment is usually several weeks to several months

and a few years. In addition, glioma has the possibility of metastasizing to other parts of the body [4], and the metastasis path generally occurs through the subarachnoid space, blood, and lymphatic system. The first is through the subarachnoid space. Medulloblastoma among gliomas is easily transplanted along the subarachnoid space and may induce tube meningiomas and intraorbital tumors. To avoid this kind of metastasis, it is necessary to have whole-brain or spinal cord radiation therapy after surgery. The second path of metastasizing the tumor is blood transfer. The most common way gliomas metastasize is through blood, through which patients can develop lung, breast, and skin cancers, and this route of metastasis is very difficult to prevent. The third way is metastasis through the lymphatic system. Glioma can also metastasize through the lymphatic system, and tumors may enter specific organs or parts of the body along the lymphatic space around spinal nerves or cranial nerves to induce diseases [5]. Because all parts of the body are lymphatic, this metastasis is very harmful to the body. To prevent lymphatic system metastasis, patients must actively take countermeasures after the occurrence of disease.

Gliomas include low-grade glioma (LGG) and high-grade glioma (HGG) according to their clinical characteristics and degree of malignancy [6]. LGG patients have slow disease progression and good postoperative prognosis. Although there is a possibility of recurrence, the overall chances of recurrence are less. HGGs develop rapidly, and relapse occurs in a short period of time after surgery [7]. Clinically, both intraoperative and postoperative images accurately showed that the tumor was removed, and then the tumor grew at the original site again, which was called recurrence [8]. However, recurrence is rare for LGG, and the main clinical findings are incomplete surgical resection and a small amount of residual tissue. Intraoperative neglect and postoperative image reflection are not obvious, with a small residual site, and continued growth leads to a second operation [9]. The tumor has an indistinct border with the surrounding brain tissue or is located in important functional areas. This tumor was conservatively excised for fear of damaging the surrounding functional areas. Some tumors are deep and have a poor surgical field of vision, resulting in residue. There are also large tumors that are left intraoperatively for different reasons, and these residues can also cause recurrence. Therefore, regular follow-up and even chemotherapy and radiotherapy are recommended to reduce the risk of recurrence. In addition, even though the postoperative prognosis of ground-based glioma is good, malignant transformation (MTF) also occurs in some patients [10]. MTF refers to LGG progression to World Health Organization (WHO) grade III or IV tumor [11]. According to the literature, the incidence of LGG MTF is 23–72%, and the median time of MTF is 2.7–5.4 years [12]. For patients with LGG, craniotomy under general anesthesia is often used for treatment. According to the patient's situation, maximum tumor resection or total tumor resection can be selected. However, due to the characteristics of diffuse growth, recurrence may occur after surgery, so postoperative radiotherapy and chemotherapy are generally used [13]. In addition, after surgical treatment, physical therapy, speech therapy, and other rehabilitation treatments can be carried out to avoid disease recurrence and prolong the survival time of patients. Since LGG can also be a high-grade glioma with MTF grade III or IV in the course of disease, regular dynamic follow-up observation is required even after surgery [14, 15].

Although LGG has a relatively good prognosis after surgery, there will be a certain possibility of recurrence and MTF if it is not prevented after surgery. If advanced glioma develops, it will pose a serious threat to the survival of patients. Therefore, understanding the postoperative recurrence of LGG and the clinical characteristics of MTF and grasping the related factors causing recurrence and MTF can prejudge the postoperative situation of patients to avoid the occurrence of such phenomena. In this experiment, the patients with LGG were followed up after surgery, the recurrence and MTF time of patients with recurrence and MTF were recorded, and the basic information of patients without progression of the disease was compared to obtain the clinical characteristics of patients with recurrence and MTF. The existing research data were reviewed to determine the relevant factors affecting the progression of the patient's disease and were included in the study scope to explore the risk factors related to relapse and MTF among the relevant factors. The above experiments are expected to provide a reference for the clinical prevention of postoperative recurrence and MTF in LGG patients.

2. Materials and Methods

2.1. Research Objects. Seventy patients who received LGG surgery in the Neurosurgery Department of the First Affiliated Hospital of Kunming Medical University from 2019 to 2021 were selected as the study subjects. There were 49 males and 21 females, ranging from 30 to 70 years old, with an average age of 42.7 ± 11.5 years. According to the diagnostic criteria of recurrence and malignant transformation, a total of 19 patients showed recurrence and malignant transformation, and the rate of recurrence and malignant transformation was 27.14%. According to the progress of postoperative disease, patients without postoperative disease changes were set as the control group, and patients with postoperative recurrence and malignant transformation were set as the observation group. This study had been approved by the Medical Ethics Committee of the First Affiliated Hospital of Kunming Medical University. Patients and their families understood the research content and methods and agreed to sign corresponding informed consent forms.

Inclusion criteria were as follows: (i) pathological diagnosis of LGG; (ii) patients aged ≥18 years; (iii) patients with complete clinical data.

Exclusion criteria were as follows: (i) patients with other tumors; (ii) patients with liver and kidney dysfunction; (iii) patients unwilling to cooperate with the whole follow-up process.

2.2. Research Methods. General information (sex, age, and preoperative physical status score), preoperative epilepsy and preoperative duration, tumor status (tumor size and tumor location), and related surgical treatment information (resection scope) of 70 patients who met the criteria were collected before surgery. Related protein levels after the operation, including proliferating cell nuclear antigen (PCNA), matrix metalloproteinase 9 (MMP-9), cancer testicular antigen OY-TES-1 protein, OY-TES-mRNA protein expression, P53, mouse double microsomal amplified gene MDM2, vascular endothelial growth factor (VEGF), and epidermal growth factor receptor (EGFR), were detected. Methods of treatment (chemotherapy, radiotherapy, and radiotherapy + chemotherapy), postoperative Karnofsky Performance Scale (KPS) score, epilepsy, and other conditions were analyzed. After that, patients were followed up. During the follow-up, patients' postoperative recovery was known by phone or text message, and the recurrence time of patients with recurrence and MTF was counted. Based on the above information, the clinical characteristics of patients with recurrence and MTF were analyzed, and the risk factors for recurrence and MTF were analyzed with the time of recurrence and MTF as independent variables. The related technical route or data collection of the research participants and concluding reports is shown in Figure 1.

2.3. Relative Protein Detection. The immunohistochemical streptomycin biotin-peroxidase method (SP) and polymerase chain reaction (PCR) were used to determine the expression of related proteins (Figure 2).

2.4. Observation Indicators. General data of the patients, including sex, age, preoperative KPS score, preoperative duration of disease, postoperative KPS score, and postoperative epilepsy, were collected.

Tumor conditions, such as tumor size and tumor location, were recorded.

Surgical treatment information, such as surgical resection scope and postoperative treatment, was collected.

Protein levels, including PCNA, MMP-9, OY-TES-1, OY-TES-mRNA, P53, MDM2, VEGF, and EGFR, were detected.

2.5. Statistical Methods. SPSS 22.0 was used for statistical analysis of the study. Measurement data were indicated as the mean ± standard deviation. The X^2 (Chi-square) test was used for comparisons between groups, the Kaplan–Meier method was used for univariate analysis, and Cox regression analysis was used for multivariate analysis. $P < 0.05$ was considered statistically significant.

3. Results

3.1. General Information. The comparison of general data between the observation group and the control group showed that there were statistically significant differences in age, preoperative KPS score, and preoperative epilepsy between the two groups, $P < 0.05$. The proportion of patients aged over 45 years in the observation group was 63.16%, and that in the control group was 50.98%. The proportion of patients aged over 45 years in the observation group was higher than that in the control group. Of those with a preoperative KPS score ≥80, the observation group accounted for 68.42%, the control group accounted for 78.43%, and that of the observation group was less than that of the control group. The proportion of patients with epilepsy before surgery was 15.79% in the observation group and 35.29% in the control group, which was smaller in the observation group than that in the control group. The details are shown in Table 1.

3.2. Tumor Size and Location. The tumor size difference between the observation group and the control group was statistically significant, $P < 0.05$. The proportion of patients with tumor over 5 cm was 27.45% in the control group and 52.63% in the observation group, which was larger in the observation group than that in the control group. The details are shown in Table 2.

3.3. Comparison of Surgical Resection Range and Postoperative Treatment. The surgical resection range and postoperative treatment were compared between the two groups, and the differences were remarkable, $P < 0.05$. Total resection accounted for 47.06% in the Ctrl group and 21.05% in the Obs group, which was smaller in the Obs group than that in the Ctrl group. The proportion of patients receiving radiotherapy plus chemotherapy after surgery in the Ctrl group was 41.18%, and that in the Obs group was 15.79%, which was smaller in the Obs group than that in the Ctrl group (Table 3).

3.4. Relative Protein Expression. The positive expression of each protein was compared between the observation group and the control group, and the difference was statistically significant (all $P < 0.05$). The proportion of patients with positive PCNA expression was 37.25% in the control group and 94.74% in the observation group, which was smaller in the control group than that in the observation group. The proportion of MMP-9 positive patients was 15.69% in the control group and 100% in the observation group, which was smaller in the control group than that in the observation group. The proportion of patients with positive OY-TES-1 expression was 29.41% in the control group and 42.11% in the observation group, which was smaller in the control group than that in the observation group. The proportion of patients with positive OY-TES-mRNA expression was 33.33% in the control group and 47.37% in the observation group, which was smaller in the control group than that in the observation group. The proportion of patients with positive P53 expression was 49.02% in the control group and 89.47% in the observation group, which was smaller in the control group than that in the observation group. The proportion of MDM2 positive patients was 52.94% in the

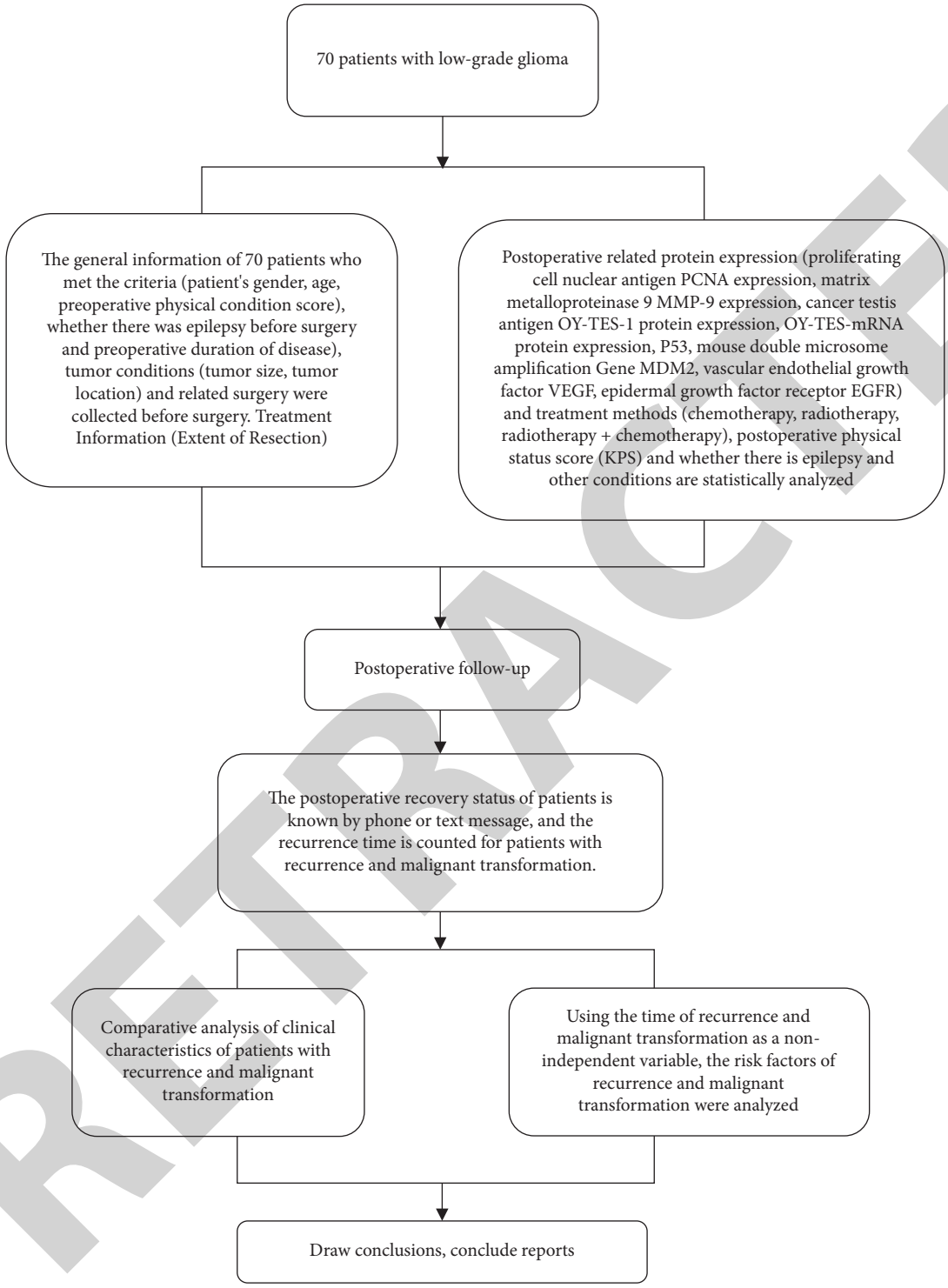

Figure 1: Technical route for data collection of the research participants and concluding reports.

control group and 78.95% in the observation group, which was smaller in the control group than that in the observation group. The proportion of patients with positive VEGF expression was 33.33% in the control group and 57.89% in the observation group, which was smaller in the control group than that in the observation group. The proportion of patients with positive EGFR expression was 60.78% in the control group and 89.47% in the observation group, which was smaller in the control group than that in the observation group. The details are shown in Table 4 and Figure 3.

3.5. Risk Factor Analysis. Univariate analysis showed that preoperative KPS score, preoperative duration of disease, surgical resection scope, postoperative treatment, and expression of PCNA, OY-TES-1, OY-TES-mRNA, P53, MDM2, VEGF, and EGFR proteins were all related to

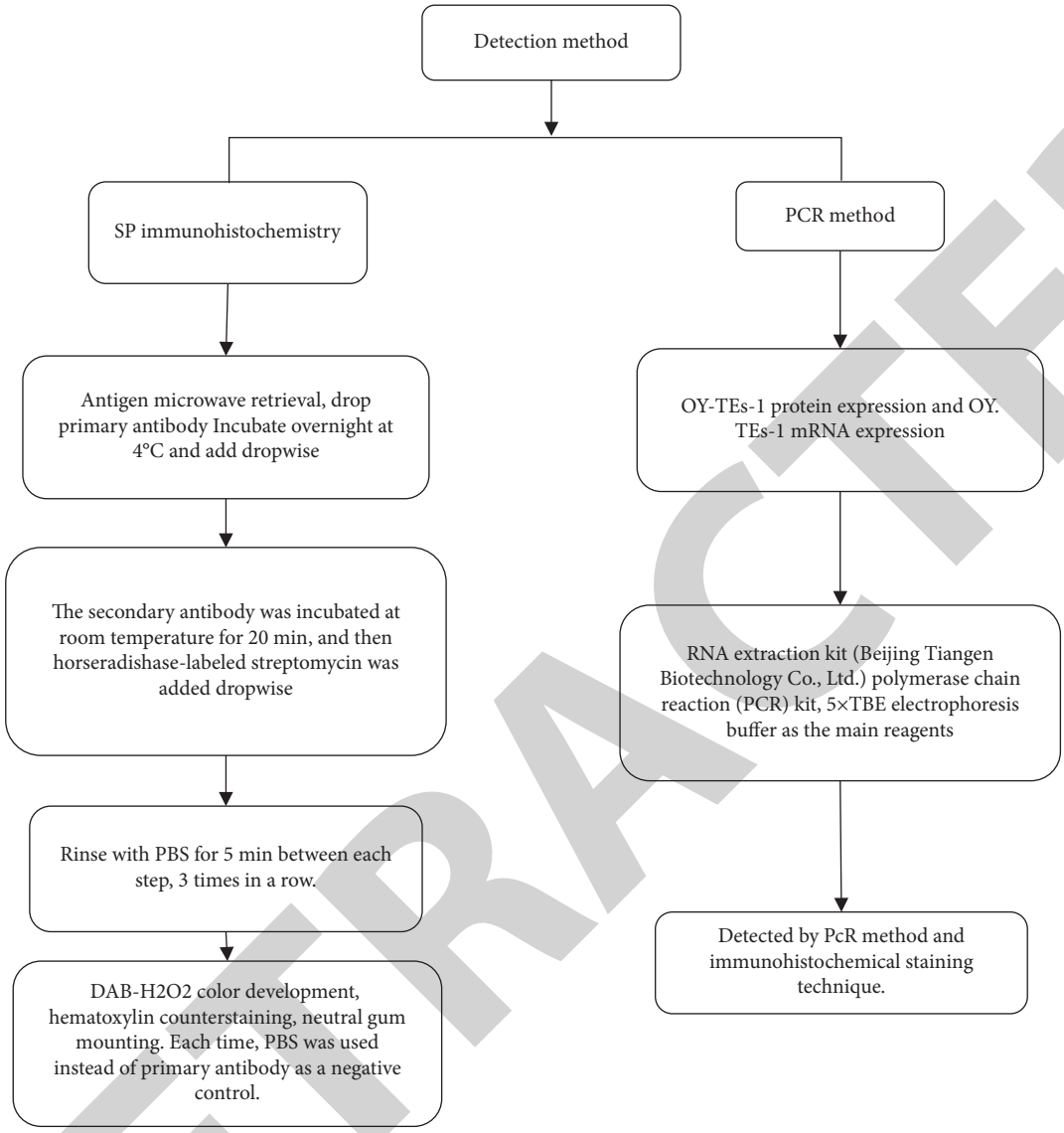

Figure 2: Related protein expression detection process through PCR and SP immunohistochemistry methods.

Table 1: Comparison of general data between the two groups.

Information	Ctrl group ($n = 51$)	Obs group ($n = 19$)	X^2	P
Sex				
Male	35	14	0.098	0.867
Female	16	5		
Age				
≤45	25	7	5.465	0.026
>45	26	12		
Preoperative KPS score				
<80	11	6	7.836	0.013
≥80	40	13		
Preoperative epilepsy				
Yes	18	3	4	0.024
No	33	16		
Preoperative duration of disease (month)				
≤3	14	5	0.113	0.076
3–6	27	7		
>6	10	7		

Table 2: Comparison of tumor-related conditions between the two groups.

Type	Group		X^2	P
	Ctrl group	Obs group		
Tumor site				
Cerebral hemisphere	38	13	0.223	0.572
Others	13	6		
Tumor size (cm)				
≤5	37	9	5.184	0.037
>5	14	10		

Table 3: Surgical resection range and postoperative treatment comparison between the two groups.

Type	Group		X^2	P
	Ctrl group	Obs group		
Surgical resection range				
Total resection	24	4		
Subtotal resection	15	7	6.962	0.021
Local total resection	12	8		
Postoperative treatment				
Radiation therapy	14	9		
Chemotherapy	16	7	5.134	0.028
Radiotherapy + chemotherapy	21	3		

Table 4: Positive comparison of related protein expression between the two groups.

Type	Group		X^2	P
	Ctrl group ($n = 51$)	Obs group ($n = 19$)		
PCNA	19 (37.25%)	18 (94.74%)	4.596	0.035
MMP-9	8 (15.69%)	19 (100%)	6.812	0.005
OY-TES-1	15 (29.41%)	8 (42.11%)	3.563	0.041
OY-TES-1 mRNA	17 (33.33%)	9 (47.37%)	5.977	0.022
P53	25 (49.02%)	17 (89.47%)	9.856	0.001
MDM2	27 (52.94%)	15 (78.95%)	7.263	0.030
VEGF	17 (33.33%)	11 (57.89%)	5.160	0.017
EGFR	31 (60.78%)	17 (89.47%)	4.035	0.039

recurrence and MTF in Obs group, all $P < 0.05$. Sex, age, tumor site, tumor size, postoperative KPS score, and postoperative epilepsy were not associated with recurrence or MTF ($P > 0.05$). The details of single factor analysis in the observation group are shown in Table 5. Cox regression analysis of $P < 0.05$ in univariate analysis showed that preoperative KPS score, preoperative duration of disease, surgical resection scope, postoperative treatment, and expression of OY-TES-mRNA, P53, MDM2, VEGF, and EGFR proteins were independent risk factors affecting recurrence and MTF, all $P < 0.05$. The details of the multifactor analysis of relapse and malignant transformation are shown in Table 6.

4. Discussion

Glioma is a tumor disease in neurosurgery. The most common clinical manifestation is tumor growth to a certain extent. It can cause obvious symptoms of high cranial pressure, which mainly manifest as headache, vomiting, and blurred vision. Other manifestations and secondary glioma growth areas have very large relations. If glioma grows in the motor area, it can cause contralateral limb activity obstacles. If glioma grows in the optic nerve, it can cause vision problems, tending to develop glioma in the cortex. If it involves the cortex, it can cause epilepsy [16]. The survival time of a patient with glioma mainly depends on the treatment, degree of malignancy of the tumor, and patient constitution. LGG refers to malignant LGG of the brain [17]. Generally, astrocytoma and oligodendroglioma have a good prognosis for LGG [18]. For LGG patients, craniotomy under general anesthesia is often used for treatment, and maximum tumor resection or total tumor resection is selected according to the patient's situation. Due to its characteristics of diffuse growth, there is a possibility of recurrence and MTF after surgery, so postoperative radiotherapy and chemotherapy are generally used [16]. In addition, after surgical treatment, physical therapy, speech therapy, and other rehabilitation treatments can be carried out to avoid disease recurrence and prolong the survival time of patients. LGG usually includes grade I gliomas and grade II gliomas. Grade I gliomas have low proliferative potential, are relatively confined, and can be cured by surgical resection. Grade II gliomas generally refer to invasive growth, which is characterized by low proliferative activity and a low degree of malignancy. However, if the degree of resection is insufficient, residual lesions will relapse and even develop into high-grade lesions, thus affecting life [6, 19]. Generally, LGG is more commonly seen in well-differentiated diffuse astrocytoma, also known as low-grade diffuse astrocytoma. The onset age is 30–40 years, and there are more males than females. In addition, CT neuroimaging examination shows low-density lesions with unclear inner edges of the brain, obvious enhancement, or cystic changes. MRI will display a relatively low signal in T1 and a relatively high space-occupying lesion in T2 [20]. Patients with LGG receive comprehensive treatment based on surgical resection, thus providing the possibility of long-term and high-quality survival. For some cases of relapse and MTF after treatment of glioma, this consideration is due to the following reasons. The first is environmental. If patients continue to go to places with high radiation levels after glioma treatment, the tumor cells will mutate again, and the disease will recede. The second is improper postcare. Care after glioma treatment is critical, and if the care is not appropriate, it is very easy to cause disease recurrence and malignant change. The third is that the operation excision is not clean. The postoperative progression of glioma may be caused by unclean surgical resection. The shape and location of glioma vary from person to person. The tumor location of some patients is special, and there may be many tissues or blood vessels around it. In this case, it is difficult to remove the tumor, and only part of the tumor may be removed, but not completely.

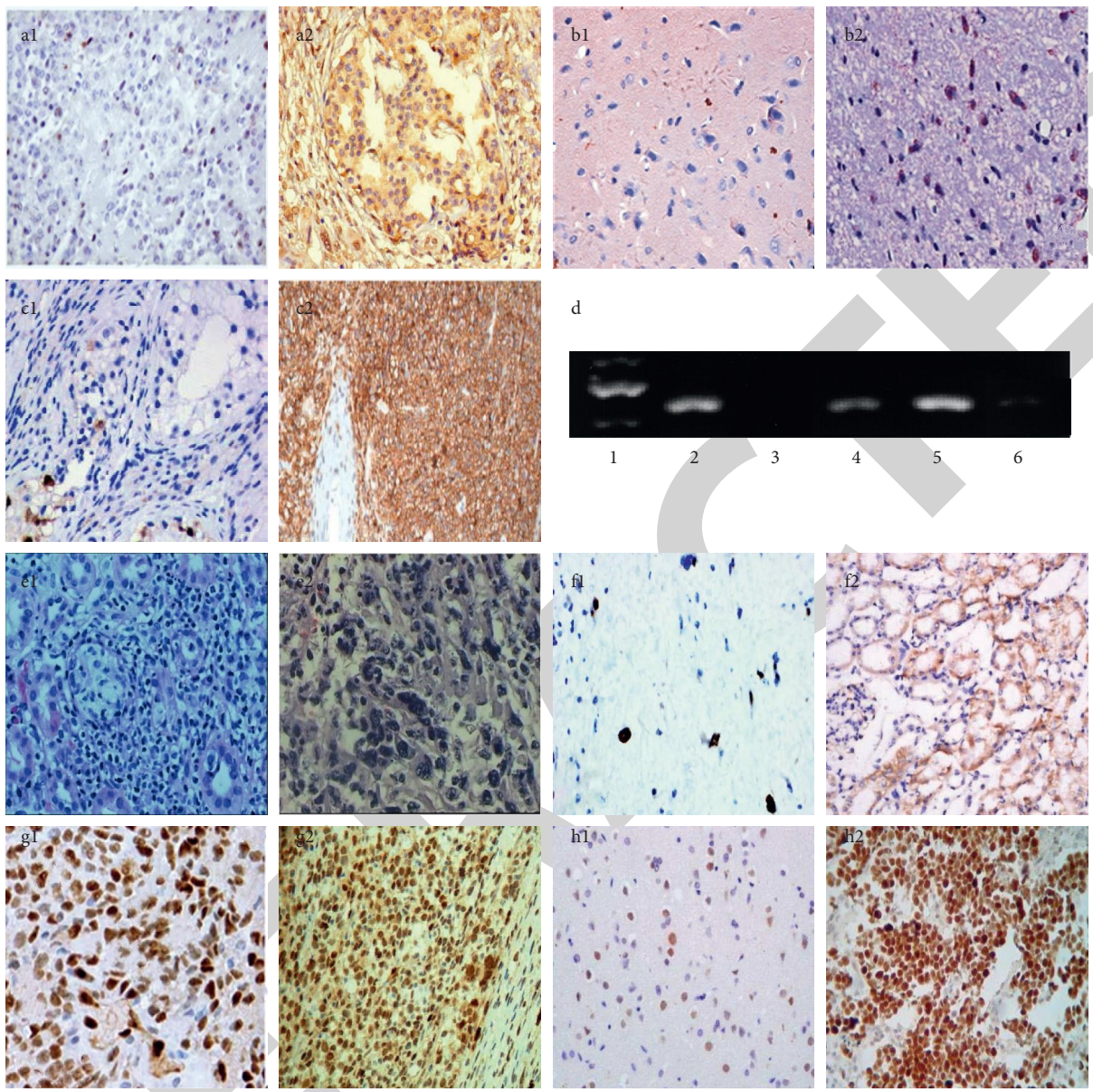

Figure 3: Expression of related proteins in primary, recurrent, and malignant transformed gliomas (SP400×). Note: a1, a2, b1, b2, c1, c2, e1, e2, f1, f2, g1, g2, and h1, h2 are the levels of PCNA, MMP-9, OY-TES-1, P53, MDM2, VEGF, and EGFR in primary and malignant transforming gliomas, respectively. d is the positive expression of OY-TES-1 mRNA, where 1 is DNA marker, 2 is testicular cDNA (positive control), 3 is positive expression of OY-TES-1 mRNA in primary glioma tissues, and 4–6 are positive expression of OY-TES-1 mRNA in recurrent and MTF glioma tissues.

This kind of glioma that is not completely resected needs adjuvant therapy after surgery to control tumor regrowth [21, 22]. If there is no postoperative adjuvant therapy, then the probability of glioma recurrence and MTF is very large. People who are susceptible to this disease in daily life are mainly the following: (i) people who have been infected with cytomegalovirus are more likely to suffer from this disease, but there is no conclusion at present; (ii) people with familial genetic factors are more prone to this disease; and (iii) people with long-term exposure to ionizing radiation are more likely to experience glioma. For example, they often use mobile phones and computers for a long time [23].

LGG patients can live up to 30 years if treated promptly. However, according to the current overall treatment results, it is still difficult to cure. According to statistics, the 5-year and 10-year survival rates of LGG patients are 60% and 35%, respectively, while the median survival period of LGG is between 8 and 10 years [24]. Therefore, understanding the clinical characteristics of postoperative recurrence and malignant transformation of LGG and grasping the related factors causing recurrence and malignant transformation can prejudge the postoperative situation of patients so as to avoid the occurrence of disease progression and reduce the survival time of patients. In this experiment, LGG patients

Table 5: Single factor analysis of recurrence and malignant transformation in the Obs group.

Type	Cases of recurrence and malignant transformation	Mean time to recurrence and malignant transformation (months)	t	P
Sex				
Male	14	21.69 ± 2.13	−0.081c	0.987
Female	5	23.56 ± 1.58		
Age				
≤45	7	24.23 ± 2.54	−0.795	0.524
>45	12	21.77 ± 2.36		
Preoperative KPS score				
<80	6	15.02 ± 2.13	4.846	0.046
≥80	13	22.67 ± 2.61		
Preoperative duration of disease (month)				
≤3	5	15.13 ± 1.54		
3–6	7	13.61 ± 2.99	4.563	0.003
>6	7	9.75 ± 3.32		
Tumor site				
Half of the brain	13	19.86 ± 2.31	0.522	0.087
Others	6	14.12 ± 2.04		
Tumor size (cm)				
≤5	9	23.75 ± 3.46	0.565	0.325
>5	10	20.91 ± 2.78		
Surgical resection range				
Total resection	4	20.05 ± 2.06		
Subtotal resection	7	18.47 ± 2.35	11.042	0.036
Local total resection	8	13.32 ± 2.89		
Postoperative KPS score				
<80	8	10.02 ± 2.54	0.786	0.261
≥80	11	12.58 ± 2.96		
Preoperative epilepsy				
Yes	3	12.35 ± 1.86	0.092	0.872
No	16	10.78 ± 2.05		
Postoperative treatment				
Radiation therapy	9	9.56 ± 2.16		
Chemotherapy	7	10.48 ± 1.88	3.746	0.023
Radiotherapy + chemotherapy	3	13.59 ± 2.04		
PCNA expression				
Negative	1	14.12 ± 2.84		
Positive	11	11.04 ± 3.10	3.976	0.031
Strong positive	7	8.67 ± 2.55		
MMP-9 expression				
Positive	8	12.83 ± 3.56	0.495	0.043
Strong positive	11	9.86 ± 3.28		
OY-TES-1 protein expression				
Negative	11	20.62 ± 2.43	3.562	<0.001
Positive	8	27.54 ± 2.61		
OY-TES-1 mRNA protein expression				
Negative	10	19.85 ± 2.79	3.336	<0.001
Positive	9	26.93 ± 3.15		
P53				
Negative	2	23.41 ± 2.09	2.875	0.003
Positive	17	11.26 ± 2.54		
MDM2				
Negative	4	22.43 ± 3.24	3.594	0.026
Positive	15	16.68 ± 3.38		
VEGF				
Negative	8	19.64 ± 3.08	3.119	0.009
Positive	11	15.44 ± 2.61		

Table 5: Continued.

Type	Cases of recurrence and malignant transformation	Mean time to recurrence and malignant transformation (months)	t	P
EGFR				
Negative	2	20.15 ± 2.87	2.967	0.043
Positive	17	13.47 ± 2.64		

Table 6: Multifactor analysis of relapse and malignant transformation.

Item	Parameter estimates	The standard deviation	Wald X^2	P
Preoperative KPS score	0.650	0.361	6.489	0.032
Preoperative duration of disease	1.269	0.359	5.419	0.027
Surgical resection range	0.631	0.204	9.206	0.003
Postoperative treatment	0.725	0.435	4.086	0.041
PCNA	1.123	0.608	3.564	0.065
OY-TES-1	1.232	0.713	3.385	0.078
OY-TES-1 mRNA	0.657	0.579	4.513	0.034
P53	0.656	0.198	7.897	0.006
MDM2	0.631	0.294	6.261	0.003
VEGF	1.104	0.328	4.266	0.020
EGFR	0.827	0.211	9.581	0.004

were followed up after surgery, and the time of recurrence and malignant transformation of patients with recurrence and malignant transformation was recorded. Moreover, the basic information of patients without progression of disease was compared so as to obtain the clinical characteristics of patients with recurrence and malignant transformation. By referring to existing research data, the relevant factors affecting the progression of patients' disease were determined and included in the research scope, and the risk factors related to relapse and malignant transformation among the relevant factors were explored. The experimental results showed that the proportion of patients aged over 45 years in the observation group was 63.16%, and that in the control group was 50.98%. The proportion of patients aged over 45 years in the observation group was larger than that in the control group. It indicates that older patients are vulnerable to disease recurrence and malignant transformation due to the decline of autoimmune function and metabolic ability after surgery. KPS score is also known as the tumor patient quality of life score. Patients with a score greater than 80 performed well in all physical indicators [25]. In this experiment, the proportion of patients with preoperative KPS score ≥80 in the observation group was 68.42%, and that in the control group was 78.43%, which was smaller in the control group than that in the observation group. It indicates that patients with malignant progression of postoperative disease are mostly patients with poor physical condition before surgery. The proportion of patients with epilepsy before surgery was 15.79% in the observation group and 35.29% in the control group, which was smaller in the observation group than that in the control group. It was found that the mechanism of epilepsy induced by glioma may be that the invasive tumor cells change the excitability of the surrounding normal neurons, making them the pacemakers of seizures. However, the destructive effect of malignant tumors on peripheral neurons and their axons obstructs the occurrence and transmission of epilepsy [26, 27]. In addition, patients with tumor over 5 cm accounted for 27.45% in the control group and 52.63% in the observation group, which was larger in the observation group than that in the control group. The malignant degree of disease was higher in patients with disease progression after operation. The total resection accounted for 47.06% in the control group and 21.05% in the observation group, which was smaller in the observation group than that in the control group. Meanwhile, the postoperative radiotherapy plus chemotherapy accounted for 41.18% in the control group and 15.79% in the observation group, which was smaller in the observation group than that in the control group. These results indicate that the patients with disease progression after surgery were mostly patients with incomplete surgical resection and single postoperative adjuvant therapy. Tumor markers can indicate the existence and growth of tumors, and monitoring tumor markers can help judge the treatment effect, prognosis, recurrence, and metastasis [28]. Proliferating cell nuclear antigen (PCNA) was first identified and named by Miyachi in 1978 in sera from patients with systemic lupus erythematosus (SLE). In the scholar's study, PCNA was found to be closely related to cell DNA synthesis and played an important role in the initiation of cell proliferation, which was a good indicator of cell proliferation status. Therefore, PCNA research has been very hot in recent years, especially in the field of cancer. In this experiment, the proportion of patients with positive PCNA expression was 37.25% in the control group and 94.74% in the observation group, which was smaller in the control group than that in the observation group. MMP-9 is an enzyme belonging to the zinc-metalloproteinase family. In this study, the proportion of MMP-9 positive patients was 15.69% in the control group and 100% in the observation group, which was

smaller in the control group than that in the observation group. As a tumor marker, the expression of cancer testicular antigen OY-TES-1 mRNA was generally low in normal tissues and high in cancer lesion tissues. In this study, the proportion of patients with positive OY-TES-mRNA expression was 33.33% in the control group and 47.37% in the observation group, which was smaller in the control group than that in the observation group. Since its discovery in 1979, P53 has been a focus of oncology research. P53 is a tumor suppressor gene, and P53 mutations occur in many tumors, so it is common to see reports of immunohistochemical staining of P53 in tumors. In this study, the proportion of patients with positive P53 expression was 49.02% in the control group and 89.47% in the observation group, which was smaller in the control group than that in the observation group. MDM2 has been found to be amplified and expressed in a variety of tumors and can coadjust with P53 tumor suppressor gene to promote tumor formation and development. In this study, the proportion of MDM2-positive patients was 52.94% in the control group and 78.95% in the observation group, which was smaller in the control group than that in the observation group. EGFR, which plays an important role in physiological processes such as cell growth, proliferation, and differentiation, is overexpressed in a variety of solid tumors. VEGF plays an important role in angiogenesis, invasion, and metastasis of various tumors. In this study, the proportion of patients with positive VEGF expression was 33.33% in the control group and 57.89% in the observation group, which was smaller in the control group than that in the observation group. The proportion of patients with positive EGFR expression was 60.78% in the control group and 89.47% in the observation group, which was smaller in the control group than that in the observation group. The above protein expression results indicate that patients with postoperative recurrence and malignant transformation also have a higher positive rate of related tumor markers. Furthermore, the single factor analysis of the related factors causing the progression of postoperative disease showed that preoperative KPS score, preoperative duration of disease, surgical resection scope, postoperative treatment, and PCNA, OY-TES-1, OY-TES-mRNA, P53, MDM2, VEGF, and EGFR protein expression were all related to recurrence and malignant transformation (all $P < 0.05$). Multivariate analysis showed that preoperative KPS score, preoperative duration of disease, surgical resection scope, postoperative treatment, and expression of OY-TES-mRNA, P53, MDM2, VEGF, and EGFR proteins were independent risk factors affecting recurrence and malignant transformation (all $P < 0.05$).

5. Conclusion

The clinical characteristics of postoperative recurrence and MTF in LGG patients were older patients, lower preoperative KPS score, larger tumor, incomplete surgical resection, single postoperative treatment, and higher preoperative malignancy. Independent risk factors included preoperative KPS score, preoperative duration of disease, surgical resection scope, postoperative treatment, and expression of OY-TES-mRNA, P53, MDM2, VEGF, and EGFR proteins.

Data Availability

The data used to support the findings of the study can be obtained from the corresponding author upon request.

Disclosure

Cheng Luo and Qian Luo are the co-first authors of this paper.

Conflicts of Interest

The authors declare no conflicts of interest regarding the publication of this paper.

Authors' Contributions

Cheng Luo and Qian Luo contributed equally.

Acknowledgments

This work was supported by Yunnan Provincial Department of Science and Technology Applied Basic Research Youth Project, Research on Cinnamaldehyde Regulates Autophagy through AMPK/mTOR to Improve the Mechanism of Neuronal Energy Metabolism after Ischemic Stroke (Project no. 202101AU070118), and Reserve Talents Project for Young and Middle-aged Academic and Technical Leaders in Yunnan Province, Research on Mechanism Basis and Clinical Brain Network of Drug-Resistant Epilepsy Induced Epilepsy (Project no. 202105AC160029).

References

[1] M. C. Tom, D. P. Cahill, J. C. Buckner, J. Dietrich, M. W. Parsons, and J. S. Yu, "Management for different glioma subtypes: are all low-grade gliomas created equal?" *American Society of Clinical Oncology. Annual Meeting*, vol. 39, pp. 133–145, 2019.

[2] T. M. Malta, C. F. de Souza, T. S. Sabedot et al., "Glioma CpG island methylator phenotype (G-CIMP): biological and clinical implications," *Neuro-Oncology*, vol. 20, no. 5, pp. 608–620, 2018.

[3] C. J. Przybylowski, S. L. Hervey-Jumper, and N. Sanai, "Surgical strategy for insular glioma," *Journal of neuro-oncology*, vol. 151, no. 3, pp. 491–497, 2021.

[4] M. De Pardieu, S. Boucebci, G. Herpe et al., "Glioma-grade diagnosis using in-phase and out-of-phaseT1-weighted magnetic resonance imaging: a prospective study," *Diagnostic and interventional imaging*, vol. 101, no. 7-8, pp. 451–456, 2020.

[5] H. Wang, M. Yin, L. Ye et al., "S100A11 promotes glioma cell proliferation and predicts grade-correlated unfavorable prognosis," *Technology in Cancer Research and Treatment*, vol. 20, Article ID 153303382110119, 2021.

[6] S. Choi, Y. Yu, M. R. Grimmer, M. Wahl, S. M. Chang, and J. F. Costello, "Temozolomide-associated hypermutation in gliomas," *Neuro-Oncology*, vol. 20, no. 10, pp. 1300–1309, 2018.

Hindawi
Journal of Oncology
Volume 2022, Article ID 8915503, 17 pages
https://doi.org/10.1155/2022/8915503

Research Article

The Biomarker Like the Correlation between Vasculogenic Mimicry, Vascular Endothelial Cadherin, Sex-Determining Region on Y-Box Transcription Factor 17, and Cyclin D1 in Oesophageal Squamous Cell Carcinoma

Yanzi Qin,[1] **Wenjun Zhao**,[2] **Zhaogeng Cai**,[1] **Qi Wang**,[1] **Jin Gao**,[1] **Hongfei Ci**,[1] **Zhenzhong Feng**,[3] **and Li Ma**[1]

[1]*Department of Pathology, The First Affiliated Hospital of Bengbu Medical College, Changhuai Road 287#, Bengbu, Anhui 233000, China*
[2]*Department of Emergency Internal Medicine, The Third the People's Hospital of Bengbu, Bengbu, Anhui 233000, China*
[3]*Department of Pathology, The Second Affiliated Hospital of Anhui Medical University, Furong Road 678#, Hefei, Anhui 233000, China*

Correspondence should be addressed to Zhaogeng Cai; 0100131@bbmc.edu.cn and Li Ma; 0100117@bbmc.edu.cn

Received 7 July 2022; Accepted 22 July 2022; Published 29 August 2022

Academic Editor: Muhammad Muddassir Ali

Background. This study aimed to explore the relationships between the sex-determining region on Y (SRY) box transcription factor 17 (SOX17), Cyclin D1, vascular endothelial cadherin (VE-cadherin), and vasculogenic mimicry (VM) in the occurrence and development of esophageal squamous cell carcinoma (ESCC). *Methods*. The expressions of SOX17, Cyclin D1, and VE-cadherin, as well as VM, in tissues, were determined using immunohistochemistry. SOX17, Cyclin D1, and VE-cadherin mRNA in ESCC and their corresponding adjacent normal tissues were quantified using quantitative reverse transcription polymerase chain reaction analysis. Cell invasion, migration, and proliferation were determined after the silencing of VE-cadherin. SOX17, Cyclin D1, and VE-cadherin protein were quantified using Western blotting. *Results*. The expression levels of SOX17, Cyclin D1, and VE-cadherin significantly correlated with the clinical characteristics of ESCC. After the VE-cadherin silencing, cell invasion, migration, and proliferation decreased, along with the Cyclin D1 levels, while the SOX17 levels increased. *Conclusion*. SOX17, Cyclin D1, and VE-cadherin are involved in the development of ESCC.

1. Introduction

The incidence of esophageal cancer (EC) has been steadily increasing year by year, making EC the sixth most common cause of cancer-related death in the world [1]. The incidence and mortality of EC in China remain high [2], with 90% of cases being esophageal squamous cell carcinoma (ESCC) [3]. However, the process of tumorigenesis in EC remains unclear.

The growth of a solid tumor depends on its vascularity [4]. Anti-angiogenic therapies are designed to target vascular endothelial cells and prevent the formation of tumor blood vessels [4]. VM is a recently identified tumor microcirculation model that is independent of the organism's endothelial cells; its growth model is completely different from the classical tumor vascular growth model [5]. VE-cadherin is a specific transmembrane adhesion protein found on the surface of vascular endothelial cells. It maintains the integrity of vessels and promotes adhesion between the adjacent endothelial cells [6, 7]. Recent studies have shown that the overexpression of VE-cadherin may be an important regulatory mechanism for VM [4, 8].

In the early 1990s, the discovery of the sex-determining region of the Y (SRY) gene led to the identification of the

SRY-related box (SOX) transcription factors [9, 10]. These factors often have pleiotropic functions that can lead to the activation of alternate transcriptional programs [11–13]. SOX17, first cloned from cDNA libraries of mouse testicular tissue, was found to have a stage-specific function in spermatogenesis [14]. Later, SOX17 was found to have antiproliferative effects in endometrial cancer by suppressing the transcription of Notch effector mastermind-like 3, a coactivator of β-catenin [15]. In a colonic carcinoma model, SOX17 antagonizes β-catenin signaling by redirecting β-catenin away from Wnt target genes and by depleting its protein levels via the glycogen synthase kinase-3β (GSK3β) independent promotion of its proteasomal degradation [16]. In structure-function analysis, SOX17 was found to be inactivated in colon cancer [17], lung cancer [18], and hepatocellular carcinoma.

Cyclin D1 protein is a type of cyclin encoded by a gene located on human chromosome 11q13. It has a molecular weight of approximately 120 kDa and contains 295 amino acids [19]. Cyclin D1 forms cyclin D1-CDK4 or cyclin D1-CDK6 complexes by binding to CDK4 or CDK6. These complexes phosphorylate the key substrate Rb gene, which leads to the release of the transcription factor E2F bound to Rb, thereby regulating and accelerating the process of G1 to S phase transition. This transition enhances deoxyribonucleic acid (DNA) transcription, shortens the cell cycle, and promotes cell proliferation [20]. Studies have reported that cells overexpressing Cyclin D1 continue to proliferate even in the absence of a growth factor, indicating that Cyclin D1 is a proto-oncogene [21]. Multiple studies have shown that the abnormal expression of Cyclin D1 protein is the first stage in the development of a number of malignant tumors [22, 23].

We previously reported the involvement of VE-cadherin in VM formation. In addition, tumor cells with a VM structure were found to be separated from the lumen by only one layer of periodic acid-Schiff (PAS) positive substance [24]. However, the exact mechanism in ESCC remains unclear. Whether SOX17 participates in the formation of VM in ESCC is not yet known. The aim of this experimental study was to observe the effect of VE-cadherin silencing via small interfering ribonucleic acid (siRNA) interference on the expression of SOX17 and Cyclin D1 in ESCC and the corresponding impact on the invasion and metastasis of ESCC.

2. Materials and Methods

In this study, tissue samples from 210 patients with ESCC, 60 patients with normal esophageal mucosa, and 60 patients with esophageal squamous epithelial dysplasia or squamous cell carcinoma (SCC) in situ were collected from the First Affiliated Hospital of Bengbu Medical College between January 2014 and December 2015 (Anhui, China). The tissue samples of ESCC were obtained from surgical specimens. None of the patients with ESCC included in this study had received chemotherapy or radiotherapy before the surgery. Among the specimens of ESCC, 169 were obtained from males, and 41 were obtained from females; there were 86 ulcer types, 89 cases medullary types, 22 mushroom types, and 13 constricted types; 28 cases were well differentiated; 139 cases were moderately differentiated; and 43 cases were poorly differentiated; with regard to tumor location, 19 cases were in the upper segment, 97 cases in the middle segment, and 94 cases in the lower segment; in terms of tumor diameter, there were 110 cases of <3.5 cm and 100 cases of ≥3.5 cm; with respect to infiltration depth, 132 cases broke through the serosal layer, while 78 cases did not; 80 cases had lymph node metastasis, while 130 cases had none; and regarding the pathological tumor, node, and metastasis (pTNM) stage, 145 cases were in stages I and II, while 65 cases were in stages III and IV. Additionally, fresh saline tissue samples of ESCC and adjacent normal tissues were collected from 10 patients between August 2019 and December 2019 from our hospital (Anhui, China). These samples were immediately placed in liquid nitrogen for later use in western blot analysis. For detection of mRNA levels, the fresh tissues were immersed in RNA store solution (TIANGEN, Beijing, China) in the ratio of 1:10 and stored in liquid nitrogen at 4°C overnight.

2.1. Immunohistochemistry. The paraffin-embedded samples were sectioned into 3 μm-thick slices. After dewaxing and debenzenization, limonic acid high-pressure antigen repair, anti-SOX17 antibody (dilution ratio 1:150, AB224637, Abcam, USA), anti-Cyclin D1 antibody (dilution ratio 1:300, ab40754, Abcam, USA), anti-VE-cadherin antibody (dilution ratio 1:200, AF6265, Affinity Biosciences, USA), and CD34 (dilution ratio 1:250, AB110643, Abcam, USA) were added one by one. Diaminobenzidine (DAB) color was added to the treated slices.

In the SOX17- and Cyclin D1-positive cells, granular brownish yellow staining was seen in the nucleus, while the VE-cadherin-positive cells showed granular brownish yellow staining of the cell membrane and cytoplasm. The staining results included the proportion of positive cells and staining intensity [25]. The proportion of positive cells refers to the percentage of positive cells among the total observed cells of the same species: 0 (≤10%), 1 point (11–25%), 2 points (26–50%), 3 points (51–75%), and 4 points (>75%). Staining intensity was graded as 0, 1, 2, and 3 points for no staining, light yellow, brownish yellow, and tan yellow staining, respectively. The points for the percentage of positive cells and the staining intensity were multiplied, and the mean value was calculated to decide the staining results as follows: 0–3 was considered negative, and 4–12 was taken as positive.

For all CD34-stained immunohistochemical sections, DAB color development was performed, and the color development reaction was stopped by washing with flowing water for 1 min. The cells were rinsed with water for 2 min and then stained with PAS for 15–30 min. The cells were rinsed with distilled water three times, for 1 min each time. VM was detected by the presence of tumor cells around the PAS-positive and CD34-negative tubes with few necrotic tumor cells and inflammatory cells infiltrating the surrounding tissues and the absence of red blood cells in the

lumen of the tubes. Endothelium-lined normal vessels were identified by the presence of CD34-positive endothelial cells in their wall.

2.2. Cell Lines and Cell Culture. The human ESCC cell lines EC9706 and Eca109 were grown in Dulbecco's Modified Eagle's Medium (Hyclone, USA), supplemented with 10% fetal bovine serum (FBS; Gibco, USA) in 5% CO_2 at 37°C. The cell lines were divided into three groups: the untransfected group, the control siRNA group, and the VE-cadherin siRNA group. In the control group, the EC9706 and Eca109 cells were not treated, and in the control siRNA group, the EC9706 and Eca109 cells were infected with an empty plasmid. In the VE-cadherin siRNA group, the EC9706 and Eca109 cells were infected with a lentivirus encoding precursor VE-cadherin or vector and treated with puromycin for two weeks to obtain stably-transfected cells.

2.3. siRNA Transfection. The EC9706 and Eca109 cells were seeded into six-well plates and transfected with VE-cadherin siRNA and negative control (NC, GenePharma, China) using Lipofectamine 2000 (Invitrogen, USA), in accordance with the manufacturer's instructions. The VE-cadherin siRNA was as follows: forward: CCAUUGUGCAAGUCC ACACAUTT and reverse: AUGUGGACUUGCACAAUG GTT. The cells were subjected to analysis, as described in the "Results" section.

2.4. Western Blotting. An appropriate amount (250–500 mg) of fresh tissue was immersed in 1 ml of strong radioimmunoprecipitation assay (RIPA) buffer containing phenylmethylsulfonyl fluoride (PMSF). An electric homogenizer was used to produce the homogenate. The samples were collected after the addition of lysis buffer and placed on ice for cracking for 20–30 min. Then centrifugation was performed at 12,000 rpm for 10 min. The ESCC cells were lysed in RIPA buffer with proteinase inhibitors. The protein concentrations were quantified using a bicinchoninic acid assay kit (Beyotime Biotechnology, China). Subsequently, the proteins were isolated by sodium.

Dodecyl sulfate-polyacrylamide gel electrophoresis and transferred onto polyvinylidene fluoride membranes (Millipore, USA). The membranes were incubated in 5% nonfat milk and immunoblotted with the following antibodies: anti-SOX17 antibody (diluted 1:500, AB224637, Abcam, USA), anti-Cyclin D1 antibody (diluted 1:1,000, ab40754, Abcam, USA), anti-VE-cadherin antibody (diluted 1:1,000, AF6265, Affinity Biosciences, USA), and anti-β-actin antibody (Cell Signaling Technology, USA).

2.5. Quantitative Real-Time PCR. Trizol (Invitrogen, USA) was used to extract mRNA from the ESCC tissues or cells, and the extracted mRNA samples were reversely transcribed into cDNA templates. Quantitative real-time PCR was performed using an ABI7900 System with SYBR Green (SG; TaKaRa, China). The primers were as follows: Cyclin D1 forward: TGTGCATCTACACCGACAACTC, Cyclin D1 reverse: TGGAAATGAACTTCACATCTGTG; SOX17 forward: GGTTTTTGTTGCTGTTG, SOX17 reverse AACTTG GAAATAGGGTTTTGAC;VE-cadherin forward: TAC-CAGCCAAGTTGTGA, VE-cadherin reverse: GCCGTG TTATCGTGATTATCC; and β-actin forward: 5′-CTGGGC TACACTGAGCACC,β-actin reverse: AAGTGGTCGTTG AGGGCAATG.

2.6. Wound Healing Assays. Two cell lines were seeded overnight in six-well plates followed by transfection with VE-cadherin siRNA or negative control (NC) siRNA. When the cells reached greater than 90% confluency, the tip of a pipette was used to make a wound, and the detached cells were rinsed away with phosphate-buffered saline (PBS). Images of the scratches were taken at 0 h and 24 h.

2.7. MTT Assay. The ESCC cell lines were seeded overnight into 96-well plates at 5×10^3 cells per well. Subsequently, the cells were transfected with VE-cadherin siRNA for 72 h. Cell viability was measured by MTT assay, as described previously [26].

2.8. Transwell Migration and Invasion Assay. Cell migration and invasion were evaluated by transwell assay, as previously described [27]. Briefly, the transfected ESCC cells were seeded in 24-well plates with 8 μm-pore-size chamber inserts (Corning, USA). The upper chambers were coated with Matrigel (BD Biosciences, USA) before cell seeding. After incubation for 48 h, the invading and migrating cells on the bottom surface of each chamber were stained with Giemsa solution and photographed. The migrating cells were then counted into5random fields for quantification.

2.9. Statistical Analyses. The continuous and categorical data are presented as mean ± standard deviation and frequency (percentage). Comparisons of quantitative data between two and multiple groups were conducted with a Student's t-test and one-way analysis of variance, respectively, using GraphPad Prism 8.0. Kaplan–Meier curves with log-rank tests were used for univariate overall survival (OS) analysis. Cox regression models were used for multivariate OS analysis. The differences were considered to be statistically significant if $P < 0.05$.

3. Results

3.1. The Association of SOX17, Cyclin D1, VE-Cadherin Expression, and VM with the Clinical Characteristics of ESCC. The positivity rates for SOX17 expression in the normal esophageal mucosa, esophageal squamous epithelial dysplasia, or SCC in situ and ESCC samples were 83.3% (50/60), 60% (36/60), and 41.4% (87/210), respectively, and the difference was statistically significant ($P < 0.05$). There was no significant correlation between SOX17 protein expression and clinicopathological characteristics such as gender, age, or tumor location ($P > 0.05$). SOX17 protein expression showed inverse correlations with tumor size, grade of

differentiation, depth of invasion, and pTNM stage. The rate of SOX17 expression was lower among cases with lymph node metastasis than among those without lymph node metastasis ($P < 0.05$). The positivity rates for Cyclin D1 expression in the normal esophageal mucosa, esophageal squamous epithelial dysplasia or SCC in situ, and ESCC samples were 25.0% (15/60), 50.0% (30/60), and 67.6% (68/210), respectively, and the difference was statistically significant ($P < 0.05$). The Cyclin D1 expression rate showed positive correlations with the tumor size, depth of infiltration, lymph node metastasis, and pTNM stage of the ESCC ($P < 0.05$). The positivity rates for VE-cadherin expression in the normal esophageal mucosa, esophageal squamous epithelial dysplasia or SCC in situ, and ESCC samples were 3.3% (2/60), 16.7% (10/60), and 51.9% (109/210), respectively, and the difference was statistically significant ($P < 0.05$). The rate of VE-cadherin protein expression in the ESCC was significantly higher than in the normal esophageal mucosa (51.9% vs. 3.3%, $P < 0.05$). Moreover, VE-cadherin protein expression showed no correlation with patient age and gender. VE-cadherin protein expression was positively correlated with tumor size, grade of differentiation, lymph node metastasis, pTNM stage, and depth of infiltration of the ESCC ($P < 0.05$). And the endothelium-lined normal vessels were identified by the presence of CD34-positive endothelial cells in their wall; the results showed positive staining of normal blood vessels. The positive rate of VM in the ESCC was 50% (105/210), while no VM was found in the esophageal squamous epithelial dysplasia, SCC in situ, or the normal esophageal mucosa. VM positivity was not correlated with gender, age, tumor location, or histological grade ($P < 0.05$), but it did correlate with tumor size, gross type, infiltration depth, LNM, and pTNM stage ($P < 0.05$). The above results are summarized in Table 1 and Figures 1(a)–1(h).

3.2. Correlation Analysis. On the one hand, Spearman correlation analysis revealed that SOX17 expression in the ESCC was negatively correlated with Cyclin D1 expression ($rs = -0.451$), VE-cadherin expression ($rs = -0.487$), and VM ($rs = -0.609$, all $P < 0.001$; Table 2). On the other hand, Cyclin D1 expression was positively correlated with VE-cadherin expression ($rs = 0.556$) and VM ($rs = 0.448$, $P < 0.001$; Table 2). VE-cadherin expression also showed a positive correlation with VM ($rs = 0.715$, $P < 0.001$; Table 2).

3.3. Survival Analysis. The five-year OS rate in the ESCC group was 37.1% (78/210). The OS of patients with SOX17 expression was significantly better than that of patients without SOX17 expression ($P < 0.001$; Table 3, Figure 2(a)). The OS of patients with Cyclin D1 expression, VE-cadherin expression, and VM was, however, significantly lower than that of patients negative for these factors ($P < 0.001$; Table 3, Figures 2(b)–2(d)).

On Cox regression model analysis, various factors, such as gender, age, tumor type, tumor location, tumor diameter, histological grade, lymph node metastasis, depth of invasion, pTNM stage, VM, SOX17 expression, Cyclin D1 expression, and VE-cadherin expression, were identified as prognostic factors. It was found that the expression of SOX17, Cyclin D1, VE-cadherin, and VM were independent risk factors affecting the long-term prognosis of ESCC patients (Table 4).

3.4. The Comparison of SOX17, Cyclin D1, and VE-Cadherin Protein Levels and mRNA Levels in Fresh ESCC and Adjacent Tissue Samples. In fresh samples from 10 ESCC patients, the mean SOX17 protein (0.826 ± 0.212 vs. 1.196 ± 0.483, $P < 0.05$) and mRNA (0.223 ± 0.373 vs. 1.611 ± 1.978, $P < 0.05$) expression levels in the ESCC tissues were significantly lower than the corresponding levels in the adjacent tissues (>5 cm away from the tumor). However, the mean Cyclin D1 protein (0.914 ± 0.537 vs. 0.684 ± 0.381, $P < 0.05$) and mRNA (1.980 ± 0.592 vs. 0.442 ± 0.317, $P < 0.05$) expression levels in the ESCC tissues were higher than the corresponding levels in the adjacent tissues. The mean VE-cadherin protein (0.683 ± 0.295 vs. 0.414 ± 0.087, $P < 0.055$) and mRNA (0.350 ± 0.293 vs. 0.092 ± 0.071, $P < 0.05$) expression levels were also significantly higher in the ESCC tissues than in the adjacent tissues. The results are shown in Figure 3.

3.5. The Inhibition of the Invasion and Migration of EC Cells due to the Silencing of VE-Cadherin. The transwell experiments demonstrated that the migration and invasion abilities of the EC9706 and Eca109 cell lines were significantly lower in the VE-cadherin siRNA group than in the corresponding control groups ($P < 0.05$). No difference was observed between the untransfected group and the control siRNA group (Figures 4(a)–4(d)). In addition, the wound healing speed of the cells in the VE-cadherin siRNA group was significantly slower than that of the corresponding control groups (Figures 5(a)–5(c)).

3.6. The Reduction of EC Cell Proliferation due to the Silencing of VE-Cadherin. The proliferative abilities of the EC9706 and Eca109 cells were significantly weakened after the silencing of VE-cadherin ($P < 0.05$) (Figure 5(d)). No significant difference was observed between the untransfected group and the control siRNA group (Figure 5(d)).

3.7. The Increase in SOX17 Expression and Decrease in Cyclin D1 Expression due to the Silencing of VE-Cadherin. After transfection, VE-cadherin protein expression was significantly lower in the VE-cadherin siRNA group than in the control groups ($P < 0.05$). Moreover, SOX17 protein expression was significantly upregulated, and Cyclin D1 protein expression was downregulated in the VE-cadherin siRNA group (Figure 6).

4. Discussion

The formation of VM can provide a blood supply for the rapid proliferation of tumors, relieve the ischemic and hypoxic microenvironment around tumors, and further

Table 1: Relationships of SOX17 expression, Cyclin D1 expression, VE-cadherin expression, and VM with the clinicopathological characteristics of ESCC.

Variable	SOX17		χ^2	P	Cyclin D1		χ^2	P	VE-cadherin		χ^2	P	VM		χ^2	P
	Positive	Negative			Positive	Negative			Positive	Negative			Positive	Negative		
Gender			0.507	0.477			0.011	0.918			0.632	0.427			0.758	0.384
Male	68	101			114	55			90	79			87	82		
Female	19	22			28	13			19	22			18	23		
Age (years)			0.001	0.971			0.003	0.957			0.798	0.372			0.488	0.485
<65	37	52			60	29			43	46			42	47		
≥65	50	71			82	39			6	55			63	58		
Gross type			8.605	0.035			7.228	0.065			10.932	0.012				
Ulcerative	31	55			60	26			53	33			51	35	7.910	0.048
Medullary	35	54			65	24			46	43			43	46		
Mushroom	11	11			11	11			6	16			7	15		
Constrictive	10	3			6	7			4	9			4	9		
Location			0.796	0.672			4.116	0.128			8.207	0.017			2.364	0.307
Upper	9	10			15	4			9	10			10	9		
Middle	42	55			59	38			41	56			43	54		
Lower	36	58			68	26			59	35			52	42		
Differentiation			7.473	0.024			5.424	0.066			5.284	0.071			1.489	0.475
Well	16	12			16	12			9	19			11	17		
Moderate	60	79			91	48			75	64			72	67		
Poor	11	32			35	8			25	18			22	21		
Diameter (cm)			26.719	≤0.001			20.627	≤0.001			11.188	0.001			12.905	≤0.001
<3.5	64	46			59	51			45	65			42	68		
≥3.5	23	77			83	17			64	36			63	37		
Serous infiltration			9.598	0.002			26.113	≤0.001			27.920	≤0.001			9.872	0.002
Yes	44	88			106	26			87	45			77	55		
No	43	35			36	42			22	56			28	50		
Lymph node metastasis			37.199	≤0.001			40.301	≤0.001			90.646	≤0.001			58.881	≤0.001
Yes	12	68			75	5			75	5			67	13		
No	75	55			67	63			34	96			38	92		
pTNM stage			23.297	≤0.001			33.145	≤0.001			56.959	≤0.001			37.455	≤0.001
I + II	76	69			80	65			50	95			52	93		
III + IV	11	54			62	3			59	6			53	12		

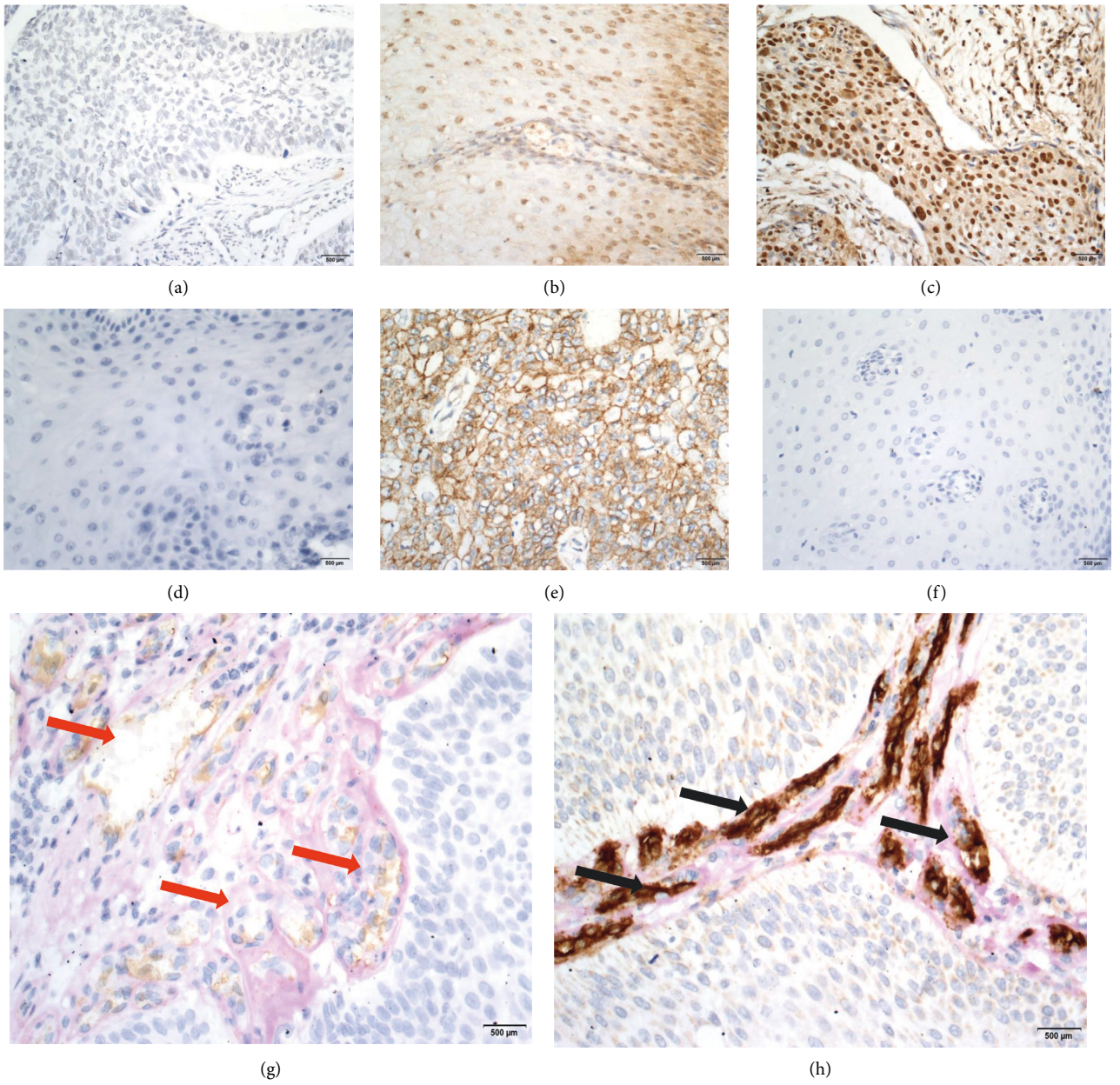

Figure 1: Immunohistochemical analysis of SOX17, Cyclin D1, and VE-cadherin expression and VM in ESCC and normal esophageal tissues (×400 magnification): negative staining of SOX17 in ESCC (a), positive staining of SOX17 in the nucleus of normal esophageal tissue (b), positive staining of cyclin D1 in the nucleus of ESCC (c), negative staining of Cyclin D1 in the normal esophageal tissue (d), positive staining of VE-cadherin in the cell membrane and plasma of ESCC (e), negative staining of VE-cadherin in the normal esophageal tissue (f), VM in ESCC (g) (red arrow), and positive staining of normal blood vessels with CD34 (h) (black arrow).

accelerate the invasion and metastasis of tumors, which influences the clinical stage and long-term prognosis of cancer patients [5, 28]. This study confirmed the existence of VM in ESCC by carrying out an immunohistochemical analysis of tumor tissues. At the same time, it was found that VM is closely associated with the depth of invasion, pTNM stage, and lymph node metastasis. The above findings are consistent with those of previous studies [6]. In survival analysis, the presence of VM is an independent poor prognostic factor in ESCC patients.

VE-cadherin, as an adhesion protein, can mediate the adhesion of cells to each other and maintain the further formation of tumor blood vessels. In the present study, VE-cadherin was found to be highly expressed in ESCC, and its positive expression was directly related to the depth of invasion, the occurrence of lymph node metastasis, and pTNM stage of ESCC. VE-cadherin expression was also found to be an independent poor prognostic factor for ESCC patients. In vitro experiments suggested that the high expression of VE-cadherin can accelerate ESCC invasion and metastasis,

Table 2: Correlation of SOX17, Cyclin D1, and VE-cadherin expression and VM in ESCC ($n = 210$).

Variable	SOX17		*rs*	*P*	Cyclin D1		*rs*	*P*	VE-cadherin		*rs*	*P*
	Positive	Negative			Positive	Negative			Positive	Negative		
CyclinD1			−0.451	≤0.001								
Positive	37	105										
Negative	50	18										
VE-cadherin			−0.487	≤0.001			0.556	≤0.001				
Positive	20	89			101	8						
Negative	67	34			41	60						
VM			−0.609	≤0.001			0.448	≤0.001			0.715	≤0.001
Positive	12	93			93	12			96	13		
Negative	75	30			49	56			17	88		

Table 3: Mean and median overall survival (OS; $n = 210$).

	Mean[a]				Median					
	Estimate	Std. error	95% Confidence interval		Estimate	Std. error	95% Confidence interval		Log rank (Mantel–Cox)	p
			Lower bound	Upper bound			Lower bound	Upper bound		
SOX17									61.200	≤0.001
Positive	62.621	2.533	57.657	67.584						
Negative	34.432	1.913	30.683	38.181	27.000	2.773	21.566	32.434		
Overall	46.174	1.816	42.616	49.732	37.000	3.150	30.827	43.173		
Cyclin D1									55.022	≤0.001
Positive	36.415	1.881	32.730	40.101	28.000	2.553	22.996	33.004		
Negative	66.172	2.617	61.042	71.302						
Overall	46.174	1.816	42.616	49.732	37.000	3.150	30.827	43.173		
VE-cadherin									111.011	≤0.001
Positive	28.927	1.541	25.906	31.947	25.000	1.115	22.815	27.185		
Negative	64.518	2.194	60.219	68.818						
Overall	46.174	1.816	42.616	49.732	37.000	3.150	30.827	43.173		
VM									92.811	≤0.001
Positive	29.581	1.719	26.212	32.950	25.000	1.394	22.267	27.733		
Negative	62.422	2.213	58.084	66.760						
Overall	46.174	1.816	42.616	49.732	37.000	3.150	30.827	43.173		

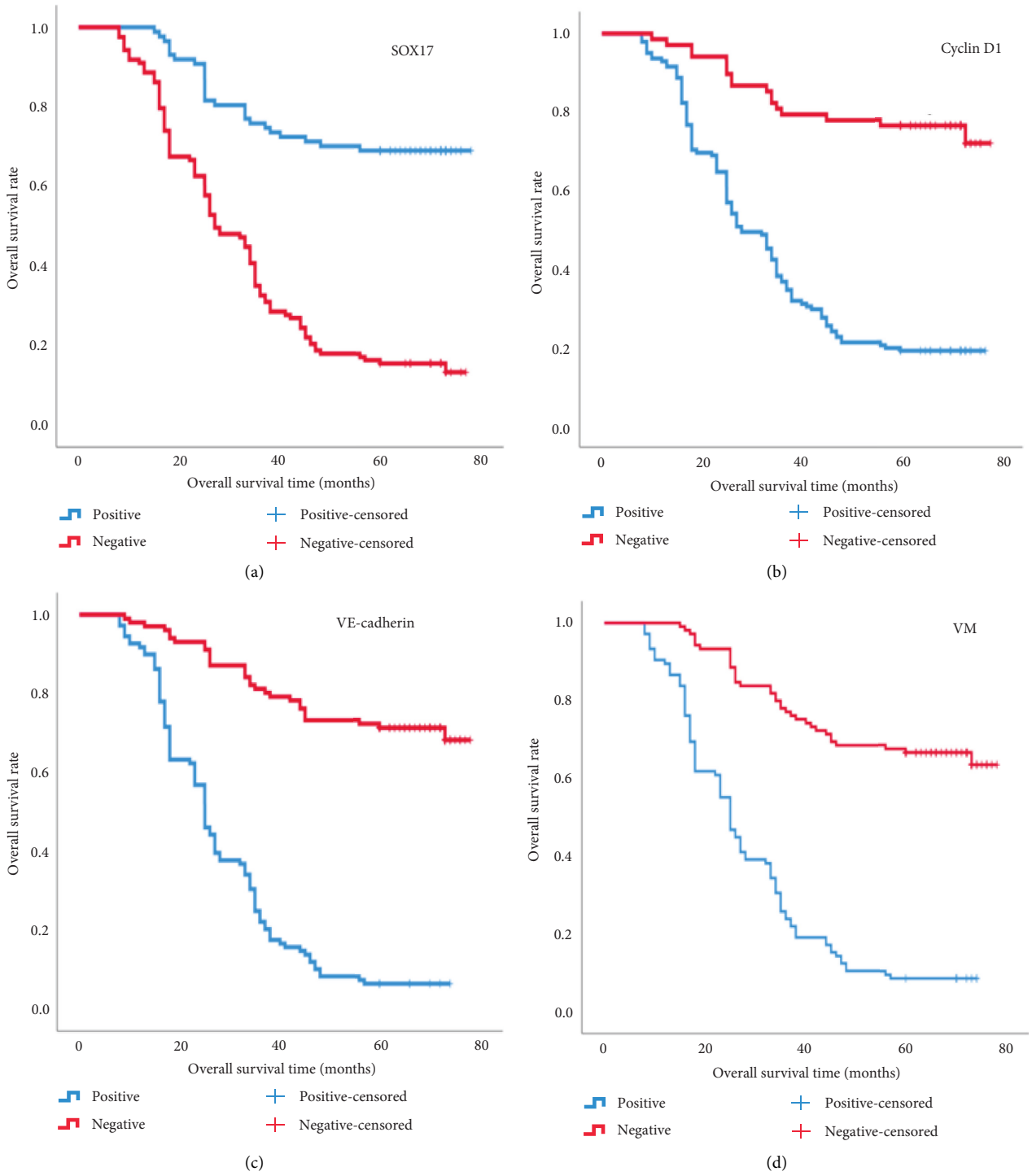

Figure 2: Kaplan–Meier analysis of the survival rates of patients with ESCC: higher overall survival of patients with positive SOX17 expression (a), log rank = 61.200 ($P < 0.001$); lower overall survival of patients with positive Cyclin D1 expression (b), log-rank = 70.109 ($P < 0.001$); overall survival of patients in relation to VE-cadherin (c); log-rank = 32.174 ($P < 0.001$); and lower overall survival of patients with presence of VM (d) log-rank = 92.811 ($P < 0.001$). Blue lines: cases positive for SOX17, Cyclin D1, VE-cadherin expression and VM and red lines: cases negative for SOX17, Cyclin D1, and VE-cadherin expression and VM.

which was similar to the findings of previous reports [6]. Notably, after siRNA-mediated interference of bcl-2 expression in EC9706 cells under hypoxic conditions, the expression of VM-related molecules, such as VE-cadherin and matrix metalloproteinase (MMP) -2, was significantly inhibited, and VM generation was significantly reduced [29]. Moreover, VE-cadherin downregulation in melanoma is associated with the loss of VM formation [30]. Heinolainen et al. [31] and Han et al. [32] speculated that VE-cadherin might be an important determinant of VM in EC. Based on

Table 4: Results of multivariate logistic regression analyses of OS ($n = 210$).

	B	*SE*	*Wald*	*df*	*p*	Exp *(B)*	95% CI for Exp*(B)*	
							Lower	Upper
Age (years)	0.948	0.192	24.378	1	≤0.001	2.579	1.771	3.757
Sex	−0.195	0.234	0.693	1	0.405	0.823	0.520	1.302
General type	0.035	0.117	0.091	1	0.764	1.036	0.823	1.304
Location	0.138	0.155	0.796	1	0.372	1.148	0.848	1.555
Diameter (cm)	−0.301	0.200	2.269	1	0.132	0.740	0.500	1.095
Differentiation	0.107	0.155	0.477	1	0.490	1.113	0.822	1.507
Infiltration depth	−0.512	0.248	4.258	1	0.039	0.599	0.368	0.975
Lymph node metastasis	−0.553	0.348	2.531	1	0.112	0.575	0.291	1.137
pTNM	−0.287	0.314	0.836	1	0.361	0.750	0.406	1.389
SOX17	0.571	0.290	3.884	1	0.049	1.771	1.003	3.125
Cyclin D1	−0.873	0.313	7.787	1	0.005	0.418	0.226	0.771
VE-cadherin	−0.774	0.346	4.996	1	0.025	0.461	0.234	0.909
VM	−0.691	0.300	5.297	1	0.021	0.501	0.278	0.903

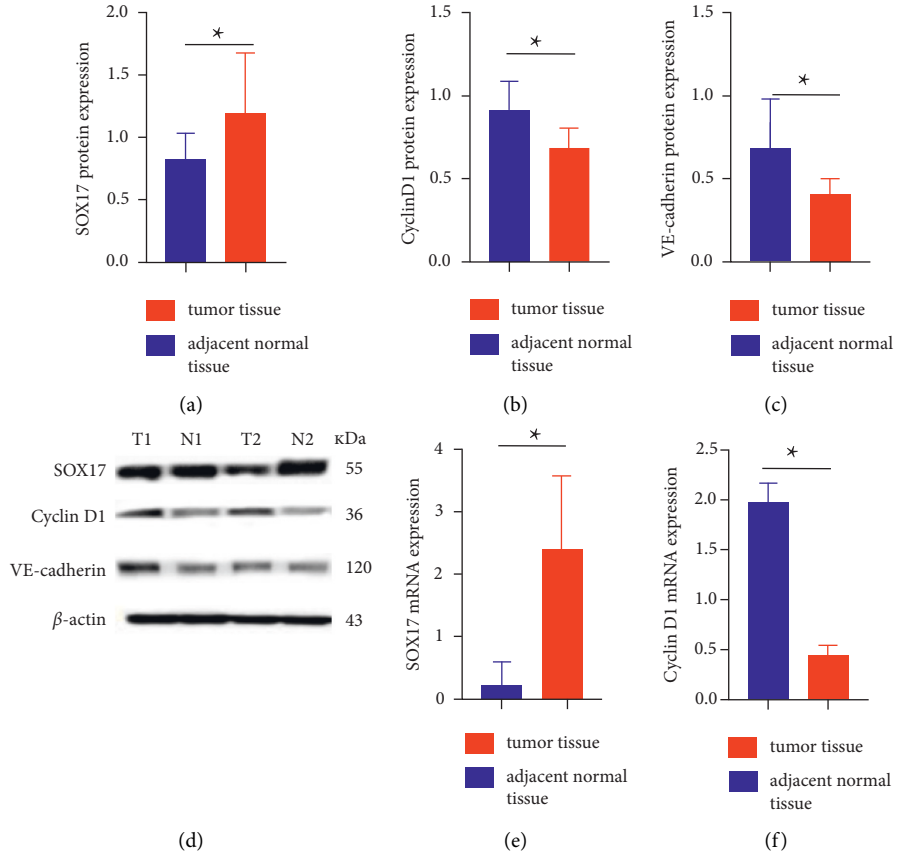

Figure 3: Continued.

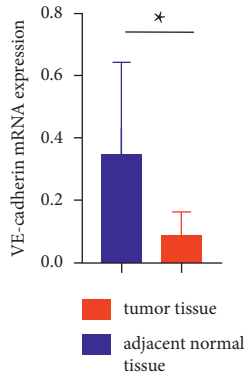

(g)

Figure 3: SOX17, Cyclin D1, and VE-cadherin protein and mRNA expression: (a)–(c) Graphical representation of SOX17, Cyclin D1, and VE-cadherin protein expression, respectively ($^*P < 0.05$); (d) Western blot analysis of SOX17, Cyclin D1, and VE-cadherin protein levels in ESCC tissues and nontumor tissues (T1 and T2 correspond to ESCC tissues; N1 and N2 correspond to normal mucosal tissues); and (e)–(g) Graphical representation of SOX17, Cyclin D1, and VE-cadherin mRNA expression, respectively ($^*P < 0.05$ vs. adjacent normal tissues).

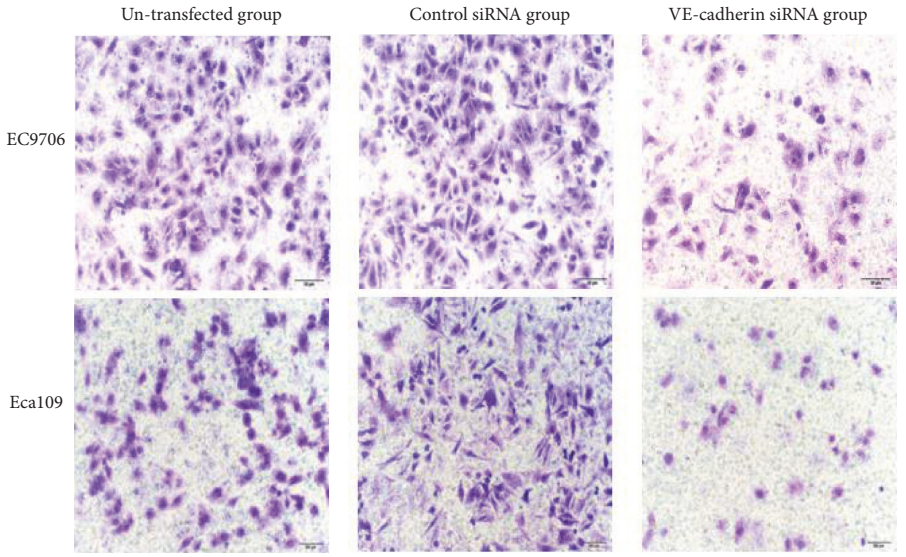

(a)

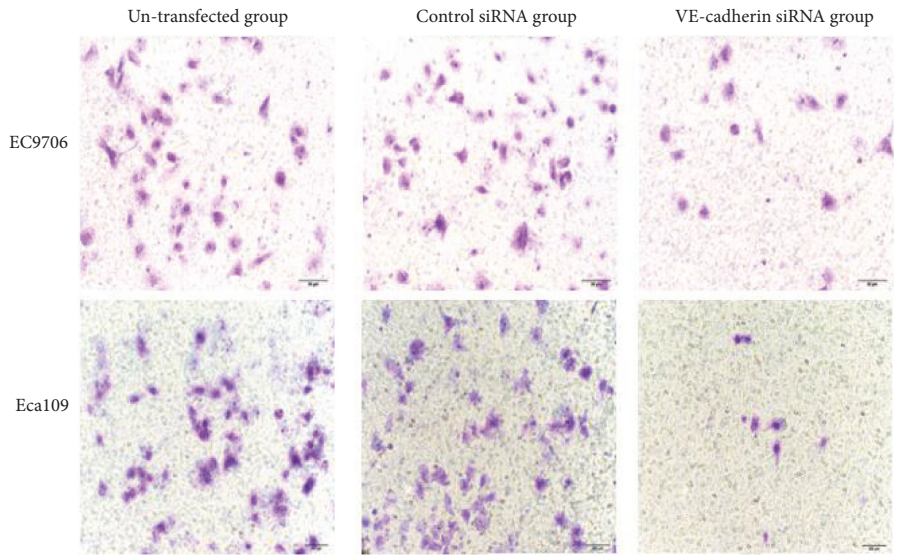

(b)

Figure 4: Continued.

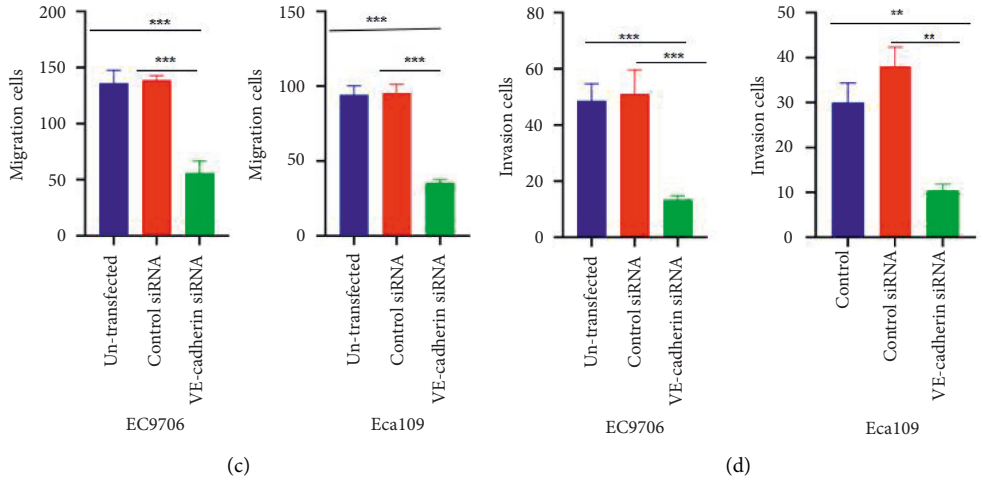

Figure 4: (a)–(d). Migration and invasion abilities of EC cells after VE-cadherin silencing. Transwell assay showing the migration of the EC9706 and Eca109 cells (a); transwell assay showing the invasion of EC9706 and Eca109 cells (b); and graphical representation of migration and invasion among EC9706 and Eca109 cells (c) and (d), respectively. $^{**}P < 0.01$ and $^{***}P < 0.01$ vs. untransfected group or control siRNA.

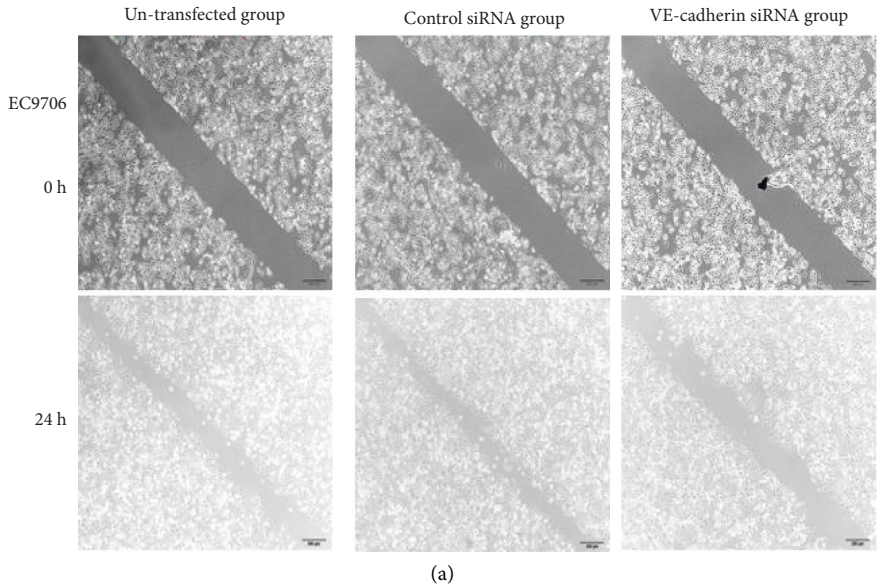

Figure 5: Continued.

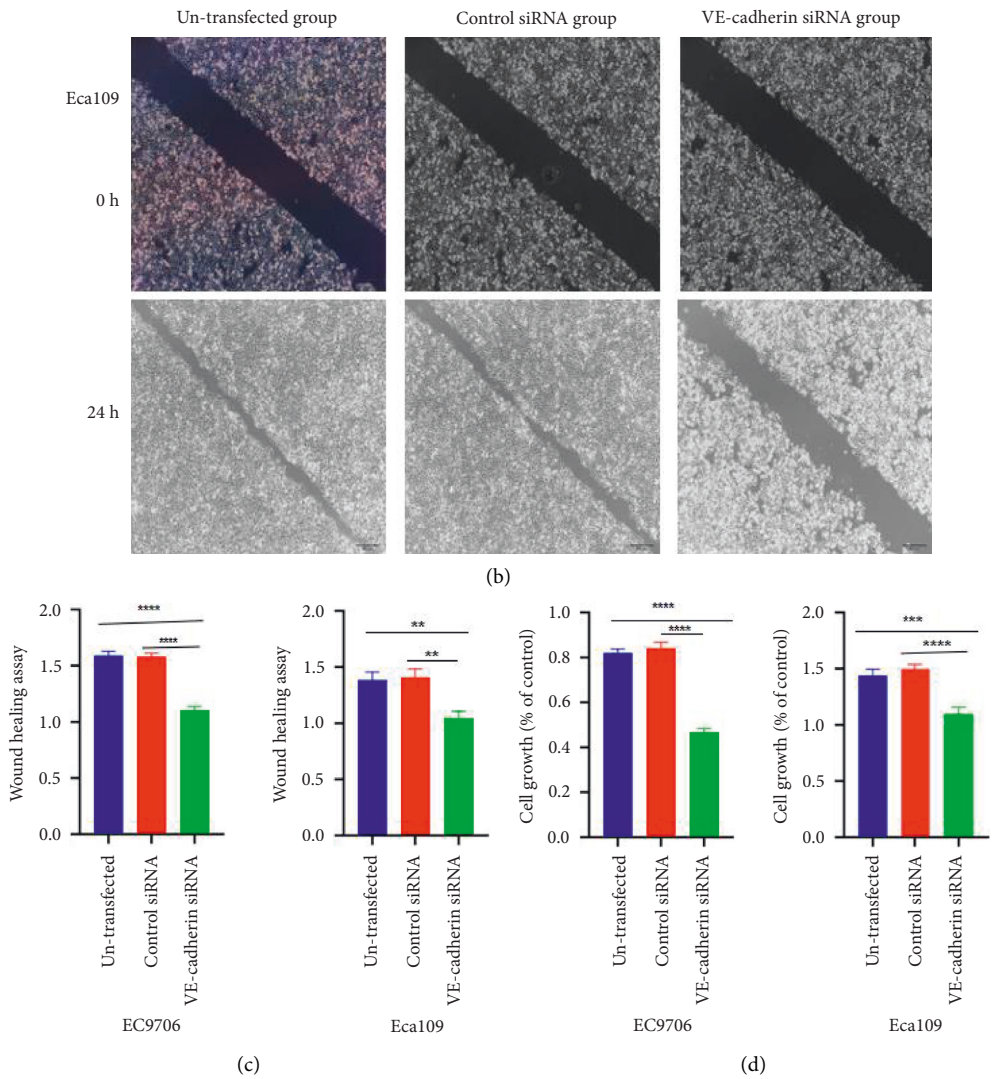

Figure 5: The wound healing experiment showed the effect of silencing VE-cadherin on the migration and healing ability of EC9706 and Eca109 cells (a) and (b), respectively. Comparison of in vitro proliferation of EC9706 and Eca109 cells (c) and (d). $^{**}P < 0.01$, $^{***}P < 0.001$, and $^{****}P < 0.0001$ vs. untransfected group or control siRNA.

the findings of the present study, we firmly believe that VE-cadherin promotes the formation of VM in ESCC.

SOX17 overexpression suppresses colony formation and cell migration/invasion in ESCC cell lines. In addition, SOX17 overexpression was found to inhibit tumor growth and metastasis in an ESCC xenograft model [17, 33, 34]. The SOX17 transcription factor has been known to have tumor suppressive function in ESCC [34–36]. In the present study, a significantly lower SOX17 expression was found in ESCC compared to the normal esophageal epithelium, confirming the tumor suppressive function of SOX17. A previous study demonstrated that hypermethylation of the promoter of the SOX17 gene leads to the silencing of SOX17 protein expression in >50% of ESCC patients [33]. In this study, the low expression of SOX17 was significantly correlated with tumor differentiation, depth of invasion, lymph node metastasis, and pTNM stage, suggesting that SOX17 acts as a tumor suppressor gene in ESCC. Moreover, SOX17 expression was an independent predictor of prognosis in this study.

The present study found that Cyclin D1 protein and mRNA expression levels were significantly increased in ESCC. Moreover, the high expression of Cyclin D1 promoted the invasion of ESCC. Cyclin D1, an important regulator of the cell cycle, participates in the transition from G0/G1 to the S phase and is commonly expressed at abnormally high levels in cancers. It participates in tumor progression and is used as a cancer biomarker phenotype [37]. Studies have shown that upregulation of Cyclin D1 can promote the progression of various tumors, including endometrial cancer [38], liver cancer [42], and colorectal cancer [43]. Yang et al. found that the Cancer Genome Atlas data showed a trend between higher Cyclin D1 levels and shorter survival time, indicating the importance of Cyclin D1 in the development of colon cancer [44]. This study also confirmed that the high expression of Cyclin D1 was related

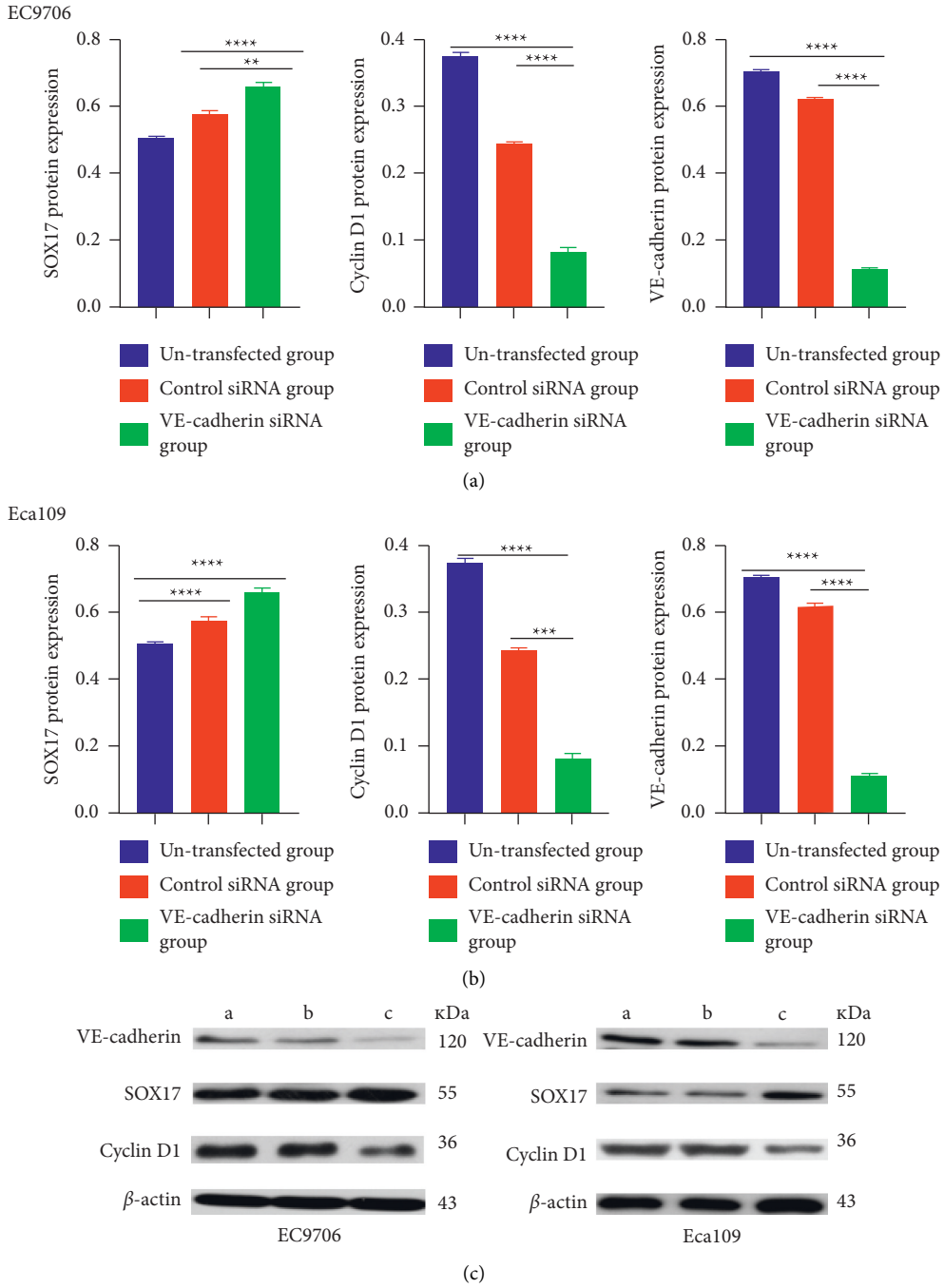

Figure 6: Top panel: Western blot analysis to detect the expression of SOX17, Cyclin D1, and VE-cadherin in the three groups of EC9706 and Eca109 cells after VE-cadherin silencing (A, B). Quantitative western blot data (C, D). (a indicates the control group; b indicates the control siRNA group; and c indicates the VE-cadherin siRNA group). B indicates the control siRNA group; and c indicates the VE-cadherin siRNA group). $^{*}P < 0.05$, $^{**}P < 0.01$, $^{***}P < 0.001$, and $^{****}P < 0.0001$ versus un-transfected group or control siRNA.

to a poor prognosis of ESCC and can be used as an independent prognostic factor for evaluating patients with ESCC. Some researchers have pointed out that tumor inhibition can be achieved by inhibiting Cyclin D1 expression. Liang et al. reported that oncogenic Cyclin D1 is a novel target gene of tumor suppressor molecule miR-520e in breast cancer. MiR-520e is capable of directly binding to the 3′ untranslated region of Cyclin D1 mRNA to promote the degradation of Cyclin D1 mRNA, leading to the inhibition of cyclin D1 in breast cancer [45]. Jiang et al. predicted that mesenchymal-epithelial transition (MET), Cyclin D1, and CDK4 of the hepatocyte growth factor/MET signaling pathway form a regulatory network around miR-1, which is then involved in the regulation of ESCC development [46].

Li et al. proved that SOX17 can inhibit the formation of tumors by inhibiting the proliferation of cervical cancer cells

in vivo and in vitro [39]. The specific mechanism of inhibition is the induction of cell cycle arrest by transinhibiting the Wnt/β-catenin pathway in cervical cancer cells and blocking the transition from G0/G1 phase to the S phase [39]. Ye [40] noted that by downregulating SOX17 expression, the expression levels of cyclin D1 and P27 were upregulated, thereby shortening the cell cycle and promoting the proliferation and invasion of MKN45 gastric cancer cells. Accordingly, SOX17 may participate in cell proliferation and cell cycle regulation by inhibiting the Wnt signaling pathway.

VM is closely related to tumor growth, invasion, metastasis, and the long-term prognosis of cancer patients [41–43]. The present study confirmed that VM formation in ESCC was positively correlated with high Cyclin D1 expression and low SOX17 expression. These findings indicate that VE-cadherin may promote the formation of VM in ESCC by affecting the expression levels of Cyclin D1 and SOX17. In a previous study, we confirmed that SOX4 may promote the formation of VM by promoting EMT in ESCC [24]. Studies have shown that in a hypoxic environment, hypoxia-inducible factor-2α, a VM-initiating factor, is activated, which increases VE-cadherin transcription. VE-cadherin, in turn, induces the repositioning of ephrin type-A receptor 2 (EphA2) to the cell membrane. Furthermore, PI3K is activated by VE-cadherin and EphA2 simultaneously. The activated PI3K regulates the activation of the pre-gene of membrane type 1-matrix metalloproteinase (MT1-MMP). The combination of MT1-MMP and MMP2 promotes the fragmentation of laminin 5γ25γ2 chains into fragments (5γ2 and 5γ2χ), and increased levels of these two fragments in the extracellular microenvironment eventually lead to the formation of a VM net-like structure [44].

Research has shown that HT29 colon cancer cells with high Wnt3a expression have a stronger ability to form tubular structures in three-dimensional culture, and the expression of endothelial phenotype-related proteins, such as vascular endothelial growth factor 2 (VEGFR2) and VE-cadherin, are increased [45]. A mouse xenograft model showed that high Wnt3a expression led to larger tumor masses and more VM. In addition, the Wnt/β-catenin signal antagonist Dickkopf-1 can reverse the ability of Wnt3a-overexpressing cells to form tubular structures and reduce the expression of VEGFR2 and VE-cadherin. Therefore, it has been speculated that Wnt/β-catenin signal transduction is involved in the formation of VM in colon cancer [45].

The results of the present study revealed that the high expression of VE-cadherin, low expression of SOX17, and high expression of Cyclin D1 are closely related to ESCC. The interaction of these three factors promotes the formation of VM. However, the silencing of VE-cadherin expression significantly inhibits Cyclin D1 expression and enhances SOX17 expression, which can inhibit tumor progression. Given that VE-cadherin directly regulates SOX17 and Cyclin D1, as found in this study, it is hypothesized that VE-cadherin regulates cell proliferation and promotes VM in two ways: (i) by regulating Wnt signaling molecule expression, thereby affecting the expression of the upstream molecule SOX17 and the downstream molecule Cyclin D1, and (ii) by targeting SOX17 and Cyclin D1 directly through other signals. Further research is required to validate the findings of this study.

In conclusion, the present study found low SOX17 expression, high Cyclin D1 expression, and high VE-cadherin expression in ESCC. Moreover, the expression of these proteins was closely associated with VM in ESCC. We believe that the development of targeted therapies to suppress Cyclin D1 expression or enhance SOX17 expression may impair the formation of VM, thereby prolonging the survival of ESCC patients. Further studies are required to determine the exact pathophysiological mechanism linking Cyclin D1, SOX17, VE-cadherin, and VM [46–48].

Abbreviations

ESCC:	Esophageal squamous cell carcinoma
VM:	Vasculogenic mimicry
EMT:	Epithelial-mesenchymal transition
EC:	Esophageal cancer
LNM:	Lymph node metastasis
pTNM:	Pathological tumor-node-metastasis
VE-cadherin:	Vascular endothelial cadherin
SRY:	Sex-determining region on Y
HMG box:	High mobility group box
SOX17:	Sex-determining region of Y chromosome box 17
PBS:	Phosphate-buffered saline
ANOVA:	One-way analysis of variance
OS:	Overall survival
FAK:	Focal adhesion kinase
ERK1/2:	Extracellular signal-regulated kinase 1 and 2
DAB:	3,3-N-Diaminobenzidine tetrahydrochloride
FBS:	Fetal bovine serum
RIPA:	Radioimmunoprecipitation assay
PMSF:	Phenylmethylsulfonyl fluoride
SDS-PAGE:	Sodium dodecyl sulfate-polyacrylamide gel electrophoresis
PVDF:	Polyvinylidene fluoride
HGF:	Hepatocyte growth factor
HIF-2α:	Hypoxia-inducible factor-2α
(MET):	Mesenchymal-epithelial transition
MT1-MMP:	Membrane type 1 matrix metalloproteinase
Dkk1:	Dickkopf-1

Data Availability

All data generated or analyzed during this study are included in this article.

Ethical Approval

This study was conducted in accordance with the Declaration of Helsinki. This study was conducted with approval from the Ethics Committee of Bengbu Medical College (No. 055).

Consent

Written informed consent was obtained from all participants.

Disclosure

This paper is present as a preprint in Research Square: https://www.researchsquare.com/article/rs-166570/v2.

Conflicts of Interest

The authors declare that they have no conflicts of interest.

Authors' Contributions

Yanzi Qin, Wenjun Zhao, and Zhaogeng Cai contributed equally to this work. Yanzi Qin and Li Ma participated in the research design. Yanzi Qin, Wenjun Zhao, Qi Wang, Jin Gao, and Hongfei Ci performed the research and wrote the manuscript. Zhaogeng Cai, Li Ma, and Zhenzhong Feng contributed towards critically revising the manuscript.

Acknowledgments

This work was funded by the Natural Science Key Project of the Anhui Provincial Department of Education (KJ2019A0344), the 512 Talent Cultivation Plan of the Bengbu Medical College (by51201305), and the Natural Science Key Project of the Bengbu Medical College (BYKY1817ZD). This paper is present as a preprint in Research Square: https://www.researchsquare.com/article/rs-166570/v2.

References

[1] F. Bray, J. Ferlay, I. Soerjomataram, R. L. Siegel, L. A. Torre, and A. Jemal, "Global cancer statistics 2018: GLOBOCAN estimates of incidence and mortality worldwide for 36 cancers in 185 countries," *CA Cancer J Clin*, vol. 68, no. 6, pp. 394–424, 2018.

[2] W. Chen, R. Zheng, and P. D. Baade, "Cancer statistics in China, 2015," *CA Cancer J Clin*, vol. 66, no. 2, pp. 115–132, 2016.

[3] J. A. Ajani, T. A. D'Amico, K. Almhanna et al., "Esophageal and esophagogastric junction cancers, version 1.2015," *Journal of the National Comprehensive Cancer Network*, vol. 13, no. 2, pp. 194–227, 2015.

[4] D. Delgado-Bellido, M. Fernández-Cortés, M. I. Rodríguez et al., "VE-cadherin promotes vasculogenic mimicry by modulating kaiso-dependent gene expression," *Cell Death & Differentiation*, vol. 26, no. 2, pp. 348–361, 2019.

[5] J. Zhang, G. Zhang, P. Hu et al., "Vasculogenic mimicry is associated with increased tumor-infiltrating neutrophil and poor outcome in esophageal squamous cell carcinoma," *OncoTargets and Therapy*, vol. 10, pp. 2923–2930, 2017.

[6] H. C. Cappelli, A. K. Kanugula, R. K. Adapala et al., "Mechanosensitive TRPV4 channels stabilize VE-cadherin junctions to regulate tumor vascular integrity and metastasis," *Cancer Letters*, vol. 442, pp. 15–20, 2019.

[7] I. Paatero, L. Sauteur, M. Lee et al., "Junction-based lamellipodia drive endothelial cell rearrangements in vivo via a VE-cadherin-F-actin based oscillatory cell-cell interaction," *Nature Communications*, vol. 9, no. 1, p. 3545, 2018.

[8] C. Yeo, H. J. Lee, and E. O. Lee, "Serum promotes vasculogenic mimicry through the EphA2/VE-cadherin/AKT pathway in PC-3 human prostate cancer cells," *Life Sciences*, vol. 221, pp. 267–273, 2019.

[9] J. Gubbay, J. Collignon, P. Koopman et al., "A gene mapping to the sex-determining region of the mouse Y chromosome is a member of a novel family of embryonically expressed genes," *Nature*, vol. 346, no. 6281, pp. 245–250, 1990.

[10] R. Lovell-Badge, "The early history of the Sox genes," *The International Journal of Biochemistry & Cell Biology*, vol. 42, no. 3, pp. 378–380, 2010.

[11] L. Hou, Y. Srivastava, and R. Jauch, "Molecular basis for the genome engagement by Sox proteins," *Seminars in Cell & Developmental Biology*, vol. 63, pp. 2–12, 2017.

[12] Y. Kamachi and H. Kondoh, "Sox proteins: regulators of cell fate specification and differentiation," *Development*, vol. 140, no. 20, pp. 4129–4144, 2013.

[13] V. Lefebvre, B. Dumitriu, A. Penzo-Méndez, Y. Han, and B. Pallavi, "Control of cell fate and differentiation by Sry-related high-mobility-group box (Sox) transcription factors," *The International Journal of Biochemistry & Cell Biology*, vol. 39, no. 12, pp. 2195–2214, 2007.

[14] Y. Kanai, M. Kanai-Azuma, T. Noce et al., "Identification of two Sox17 messenger RNA isoforms, with and without the high mobility group box region, and their differential expression in mouse spermatogenesis," *Journal of Cell Biology*, vol. 133, no. 3, pp. 667–681, 1996.

[15] Y. Zhang, W. Bao, K. Wang et al., "SOX17 is a tumor suppressor in endometrial cancer," *Oncotarget*, vol. 7, no. 46, pp. 76036–76046, 2016.

[16] D. Sinner, J. J. Kordich, J. R. Spence et al., "Sox17 and Sox4 differentially regulate β-catenin/T-cell factor Activity and proliferation of colon carcinoma cells," *Molecular and Cellular Biology*, vol. 27, no. 22, pp. 7802–7815, 2007.

[17] W. Zhang, S. C. Glöckner, M. Guo et al., "Epigenetic inactivation of the canonical Wnt antagonist SRY-box containing gene 17 in colorectal cancer," *Cancer Research*, vol. 68, no. 8, pp. 2764–2772, 2008.

[18] D. Yin, Y. Jia, Y. Yu et al., "SOX17 methylation inhibits its antagonism of Wnt signaling pathway in lung cancer," *Discovery Medicine*, vol. 14, no. 74, pp. 33–40, 2012.

[19] T. Jiang, J. Liu, and J. Mu, "Downregulation of microRNA-449a-5p promotes esophageal squamous cell carcinoma cell proliferation via cyclin D1 regulation," *Molecular Medicine Reports*, vol. 18, no. 1, pp. 848–854, 2018.

[20] W. Liu, T. Yin, J. Ren et al., "Activation of the EGFR/Akt/NF-κB/cyclinD1 survival signaling pathway in human cholesteatoma epithelium," *European Archives of Oto-Rhino-Laryngology*, vol. 271, no. 2, pp. 265–273, 2014.

[21] J. G. Howe, J. Crouch, D. Cooper, and B. R. Smith, "Real-time quantitative reverse transcription-PCR for cyclin D1 mRNA in blood, marrow, and tissue specimens for diagnosis of mantle cell lymphoma," *Clinical Chemistry*, vol. 50, no. 1, pp. 80–87, 2004.

[22] Y. Ru, X. J. Chen, Z. W. Zhao et al., "CyclinD1 and p57kip2 as biomarkers in differentiation, metastasis and prognosis of gastric cardia adenocarcinoma," *Oncotarget*, vol. 8, no. 43, pp. 73860–73870, 2017.

[23] L. Cinque, A. Sparaneo, F. Cetani et al., "Novel association of MEN1 gene mutations with parathyroid carcinoma," *Oncology Letters*, vol. 14, no. 1, pp. 23–30, 2017.

[24] Y. Qin, W. Zhao, and Z. Cai, "Correlation of SOX4, SOX17, VE-Cadherin and Vasculogenic Mimicry with Prognosis in Esophageal Squamous Cell Carcinoma," 2021, https://www.researchgate.net/publication/349123546_Correlation_of_SOX4_SOX17_VE-cadherin_and_vasculogenic_mimicry_with_prognosis_in_esophageal_squamous_cell_carcinoma.

[25] J. Xia, L. Cheng, C. Mei et al., "Genistein inhibits cell growth and invasion through regulation of miR-27a in pancreatic cancer cells," *Current Pharmaceutical Design*, vol. 20, no. 33, pp. 5348–5353, 2014.

[26] J. Xia, Q. Duan, A. Ahmad et al., "Genistein inhibits cell growth and induces apoptosis through up-regulation of miR-34a in pancreatic cancer cells," *Current Drug Targets*, vol. 13, no. 14, pp. 1750–1756, 2012.

[27] Q. Yang, J. Huang, Q. Wu et al., "Acquisition of epithelial-mesenchymal transition is associated with Skp2 expression in paclitaxel-resistant breast cancer cells," *British Journal of Cancer*, vol. 110, no. 8, pp. 1958–1967, 2014.

[28] N. N. Tang, H. Zhu, H. J. Zhang et al., "HIF-1α induces VE-cadherin expression and modulates vasculogenic mimicry in esophageal carcinoma cells," *World Journal of Gastroenterology*, vol. 20, no. 47, pp. 17894–17904, 2014.

[29] J. Zhang, L. Qiao, N. Liang et al., "Vasculogenic mimicry and tumor metastasis," *J BUON*, vol. 21, no. 3, pp. 533–541, 2016.

[30] M. J. C. Hendrix, E. A. Seftor, P. S. Meltzer et al., "Expression and functional significance of VE-cadherin in aggressive human melanoma cells: role in vasculogenic mimicry," in*Proceedings of the National Academy of Sciences of the United States of America*, vol. 98, no. 14, pp. 8018–8023, 2001.

[31] K. Heinolainen, S. Karaman, G. D'Amico et al., "VEGFR3 modulates vascular permeability by controlling VEGF/VEGFR2 signaling," *Circulation Research*, vol. 120, no. 9, pp. 1414–1425, 2017.

[32] H. Han, L. Du, Z. Cao, B. Zhang, and Q. Zhou, "Triptonide potently suppresses pancreatic cancer cell-mediated vasculogenic mimicry by inhibiting expression of VE-cadherin and chemokine ligand 2 genes," *European Journal of Pharmacology*, vol. 818, pp. 593–603, 2018.

[33] I. Y. Kuo, C. C. Wu, J. M. Chang et al., "Low SOX17 expression is a prognostic factor and drives transcriptional dysregulation and esophageal cancer progression," *International Journal of Cancer*, vol. 135, no. 3, pp. 563–573, 2014.

[34] I. Y. Kuo, Y. L. Huang, C. Y. Lin et al., "SOX17 overexpression sensitizes chemoradiation response in esophageal cancer by transcriptional down-regulation of DNA repair and damage response genes," *J Biomed Sci*, vol. 26, no. 1, p. 20, 2019.

[35] M. W. Schilham, M. A. Oosterwegel, P. Moerer et al., "Defects in cardiac outflow tract formation and pro-B-lymphocyte expansion in mice lacking Sox-4," *Nature*, vol. 380, no. 6576, pp. 711–714, 1996.

[36] Z. Wu, B. Yu, and L. Jiang, "MiR-212-3p mediates apoptosis and invasion of esophageal squamous cell carcinoma through inhibition of the Wnt/β-catenin signaling pathway by targeting SOX4," *Journal of Thoracic Disease*, vol. 12, no. 8, pp. 4357–4367, 2020.

[37] G. Tchakarska and B. Sola, "The double dealing of cyclin D1," *Cell Cycle*, vol. 19, no. 2, pp. 163–178, Jan 2020.

[38] Y. M. Liao, Y. Song, Y. K. Li, J. H. Du, and Y. Zhou, "SOX17, β-catenin and CyclinD1 expression in the endometrioid adenocarcinoma and influence of 5-AZA on expression," *Cancer Gene Therapy*, vol. 27, no. 3-4, pp. 256–263, 2020.

[39] L. Li, W. T. Yang, P. S. Zheng, and X. F. Liu, "SOX17 restrains proliferation and tumor formation by down-regulating activity of the Wnt/β-catenin signaling pathway via trans-suppressingβ-catenin in cervical cancer," *Cell Death & Disease*, vol. 9, no. 7, p. 741, Jul 3 2018.

[40] Y. W. Ye, J. H. Wu, C. M. Wang et al., "Sox17 regulates proliferation and cell cycle during gastric cancer progression," *Cancer Letters*, vol. 307, no. 2, pp. 124–131, 2011.

[41] J. A. Hulin, S. Tommasi, D. Elliot, and A. A. Mangoni, "Small molecule inhibition of DDAH1 significantly attenuates triple negative breast cancer cell vasculogenic mimicry in vitro," *Biomedicine & Pharmacotherapy*, vol. 111, pp. 602–612, 2019.

[42] J. Bai, S. Yeh, X. Qiu et al., "TR4 nuclear receptor promotes clear cell renal cell carcinoma (ccRCC) vasculogenic mimicry (VM) formation and metastasis via altering the miR490-3p/vimentin signals," *Oncogene*, vol. 37, no. 44, pp. 5901–5912, 2018.

[43] R. Kawahara, Y. Niwa, and S. Simizu, "Integrin β1 is an essential factor in vasculogenic mimicry of human cancer cells," *Cancer Science*, vol. 109, no. 8, pp. 2490–2496, 2018.

[44] H. Ge and H. Luo, "Overview of advances in vasculogenic mimicry – a potential target for tumor therapy," *Cancer Management and Research*, vol. 10, pp. 2429–2437, 2018.

[45] J. C. Lissitzky, D. Parriaux, E. Ristorcelli, A. Vérine, D. Lombardo, and P. Verrando, "Cyclic AMP signaling as a mediator of vasculogenic mimicry in aggressive human melanoma cells in vitro," *Cancer Research*, vol. 69, no. 3, pp. 802–809, 2009.

[46] W. Yan, L. Cheng, and D. Zhang, "Ultrasound-targeted microbubble destruction mediated si-CyclinD1 inhibits the development of hepatocellular carcinoma via suppression of PI3K/AKT signaling pathway," *Cancer Management and Research*, vol. 12, pp. 10829–10839, 2020.

[47] L. Cao, Y. Liu, D. Wang et al., "MiR-760 suppresses human colorectal cancer growth by targeting BATF3/AP-1/cyclinD1 signaling," *Journal of Experimental & Clinical Cancer Research*, vol. 37, no. 1, p. 83, 2018.

[48] H. Yang, J. Lin, J. Jiang, J. Ji, C. Wang, and J. Zhang, "miR-20b-5p functions as tumor suppressor microRNA by targeting cyclinD1 in colon cancer," *Cell Cycle*, vol. 19, no. 21, pp. 2939–2954, 2020.

Hindawi
Journal of Oncology
Volume 2022, Article ID 9975838, 10 pages
https://doi.org/10.1155/2022/9975838

Research Article

Bioinformatics Analysis of Inflammation Gene Signature in Indicating Cholangiocarcinoma Prognosis

Yanting Wang,[1] Shi Chen,[2] and Song He[3]

[1]*Department of Gastroenterology and Hepatology, The Second Affiliated Hospital of Zhejiang University School of Medicine, Hangzhou, Zhejiang, China*
[2]*Department of Oncology, Chengdu Jinniu District People's Hospital, Chengdu, Sichuan, China*
[3]*Department of Hepatobiliary Surgery, The Affiliated Hospital of Xiangnan University, Chenzhou, Hunan, China*

Correspondence should be addressed to Song He; hesong1115@163.com

Received 16 June 2022; Accepted 6 July 2022; Published 27 August 2022

Academic Editor: İbrahim Hakkı Cigerci

Aim. We studied inflammatory response-related genes in cholangiocarcinoma by bioinformatics analysis. *Methods*. The expression profiles and clinical information of cholangiocarcinoma patients were downloaded from the TCGA cohort and the Gene Expression Omnibus. The greatest absolute shrinking and selecting operator Cox analyses were utilized to build a multigene predictive signature. *Results*. An inflammation response-related gene profile was generated using LASSO-Cox regression analysis of Homo sapiens bestrophin 1 (BEST1), Chemokine (C–C motif) ligand 2 (CCL2), and plasminogen activator, urokinase receptor (PLAUR). Individuals in the highest category had a significantly lower overall survival time than those from the low-risk group. A receiver operating curve analysis was used to demonstrate the predictive ability of the predictive gene signature. Through multivariate Cox analysis, the risk score was discovered to be a predictor of overall survival (OS). According to functional assessments, the immunological state and milieu of the two risk areas were significantly different. The expression levels of predictive genes were found to be strongly linked to the sensitivity of cancer cells to antitumor therapy. *Conclusion*. A new signature made up of three respective response-relevant genes is found to be a promising indicator of prognosis by influencing the immune condition and tumor microenvironment.

1. Introduction

Hepatocellular carcinoma and cholangiocarcinoma are common primary cancers of the liver responsible for an increasing number of cancer-related deaths [1]. Cholangiocarcinoma has become more commonly diagnosed across the world in recent decades [2, 3]. Despite numerous improvements in recent decades to better comprehend the pathology of cholangiocarcinoma, its prognosis remains poor [4, 5]. Surgery is the optimal method for patients with limited, resectable cholangiocarcinoma. Yet, the prognosis for these patients remained poor, with a median overall survival (OS) ranging from 12 to 31 months [6]. With the well-established correlation between inflammation and cancer, the inflammatory role in the onset and progression of cancer has long been the subject of current studies. Inflammation can both promote and prevent cancer growth [7]. Scientists can investigate the association between cancer and inflammatory indicators by assessing parameters that are typically available in the blood [8, 9]. The Glasgow Prognostic Score, which includes C-reactive protein and albumin, exhibits independent predictive significance in cancer patients [10]. A growing number of studies utilize various acute-phase proteins to create comprehensive predictive scores for malignancies based on inflammation. Some inflammatory response-related genes, in addition to serum indicators, were employed to predict the metastatic potential and prognosis of hepatocellular carcinoma [10]. However, the link between inflammatory response-related genes and the prognosis of cholangiocarcinoma remains unstudied.

The use of 3D bioprinting to reconstruct tumor microenvironments could be exploited to develop novel antitumor medications. [11] Inflammatory response genes are associated with tumor microenvironments and antitumor drug sensitivity and thus could be exploited in the 3D

bioprinting of new antitumor therapies. In this study, we investigated the predictive significance of inflammatory response-related genes in cholangiocarcinoma and generated an inflammatory response-related gene signature. Our study assessed the relationship between the signature and immunological state along with the microenvironment in cholangiocarcinoma.

2. Methods

2.1. Data Collection. The TCGA cohort and the Gene Expression Omnibus were used to acquire mRNA expression data and clinical information of individuals with cholangiocarcinoma (GEO). GSE107943 was chosen for further analysis after being screened from the GEO database. The fragments per kilobase of exon model per million mapped fragments (FPKM) format were used to acquire data from the GSE107943 dataset. The TCGA RNA-seq transcriptome data were converted to FPKM values. Data from the TCGA and GSE107943 datasets were transformed to normalized counts.

2.2. Inflammatory Response-Related Gene Signature. A sample size of 200 genes associated with the inflammatory response was identified, along with their expression profiles. In the TCGA and GEO cohorts, the differentially expressed genes (DEGs) between tumor and nontumor tissues were identified using the R package "limma" with a fold change greater than 2 and a false discovery rate of 0.05. After Bonferroni correction, univariate Cox analysis was utilized to screen for predictive significance in inflammatory response-related genes. To reduce overfitting, our study used LASSO-penalized Cox regression analysis to build a prognostic model. [12, 13] The "glmnet" R package was used to select and reduce variables using the LASSO technique. Using tenfold cross-validation, the penalty parameter of the prognostic model was defined using the minimum criterion (i.e., the value corresponding to the lowest partial likelihood deviation). The risk ratings of patients were calculated using the expression of each inflammatory reaction gene or its corresponding regression coefficient. Based on their median risk scores, patients were divided into high-risk and low-risk groups. By using the R packages "Rtsne" and "ggplot2," PCA and t-SNE analysis were used to explore the distribution of distinct groups in terms of gene expression levels in the created model. Survival studies of the OS of high and low-risk groups were performed using the R tool "survminer." The "survival" R package and the "time ROC" R package were used to perform the time-dependent ROC curve method in order to assess the predictive power of the prognosis signature. Univariate and multivariate Cox analyses were used to explore the signature's independent prognostic relevance.

2.3. Immune Status and Tumor Microenvironment Analysis. The "GSVA" R package was used to evaluate the invasion scores of 16 immune cells and the activity of 13 immune-related pathways between both the high-risk and low-risk groups using single-sample gene set enrichment analysis (ssGSEA). The levels of immune and stromal malignant cells in various malignant cells were measured using the immune and stromal scores. To investigate whether there exists a link between the risk rating and other scores, the Spearman correlation was applied. [14] To examine if there was a link between the risk score and the immune infiltration subtype, we utilized a two-way ANOVA analysis. Tumor stem cell characteristics were assessed utilizing information extracted from the transcriptome and epigenetics of tumor samples. [15] The Spearman correlation test was used to investigate the relationship between tumor stemness and the risk score.

2.4. Chemotherapy Sensitivity Analysis. The NCI-60 database contains 60 distinct cancer cell lines from 9 different types of tumors, including Cholangiocarcinoma, Bladder Cancer, Colorectal Cancer, Esophageal Cancer, Melanoma, Ovarian Cancer, Pancreatic Cancer, Prostate Cancer, and Small Cell Lung Cancer, and was accessed using the CellMiner interface (https://discover.nci.nih.gov/cellminer). Pearson correlation analysis was used to explore the relationship between prognostic gene expression and drug sensitivity. Correlation analysis was used to examine the efficacy of 263 drugs approved by the FDA or in clinical studies.

2.5. Statistical Analysis. To compare DEGs between the tumor and adjacent tissues, the Wilcoxon test was performed. The chi-square test was used to compare different proportions. The ssGSEA scores of immune cells and immunological pathways were compared between high-risk groups using the Mann–Whitney test. The Kaplan–Meier analysis was used to compare the differences in OS across subgroups. Univariate and multivariate Cox analyses were used to screen the different factors for OS. The correlations of the prognostic model risk score and the prognostic gene expression level with stemness score, stromal score, immune score, and drug sensitivity were investigated using Spearman or Pearson correlation analysis. R software (version 4.0.3) was used to create the plots, which included the utility, venn, igraph, ggplot2, pheatmap, ggpubr, corrplot, and survminer. In all statistical outcomes, a two-tailed P value less than 0.05 indicated statistical significance.

3. Results

3.1. Prognostic Inflammation-Related DEGs Identification. Samples of this study consisted of 45 cholangiocarcinoma patients (45 cancer samples) from the TCGA cohort and 30 patients (30 cancer samples and 27 nontumorous samples) from the GSE107943 cohort (See Table 1). These samples have complete clinical and transcriptomic data. Results showed that 59 genes were associated with inflammatory responses expressed in tumor and nontumorous tissues (Figure 1(a)). In a univariate Cox analysis, inflammation response-related genes were found to be linked to OS (Figure 1(b)). Among the analyzed genes, 5 overlapping inflammatory response-related genes were selected for further analysis (Figures 1(c) and 1(d)).

Table 1: The characteristics of patients from various cohorts at the start of their treatment.

Characteristics	TCGA cohort $N = 45$	GSE107943 cohort $N = 30$
Age		
≤65	21 (46.7%)	16 (53.3%)
>65	24 (53.3%)	14 (46.7%)
Gender		
Female	25 (55.6%)	6 (20.0%)
Male	20 (44.4%)	24 (80.0%)
Grade		
Grades 1-2	23 (51.1%)	23 (76.7%)
Grades 3-4	22 (48.9%)	7 (23.3%)
AJCC stage		
Stages I-II	31 (68.9%)	21 (70.0%)
Stages III-IV	14 (31.1%)	9 (30.0%)

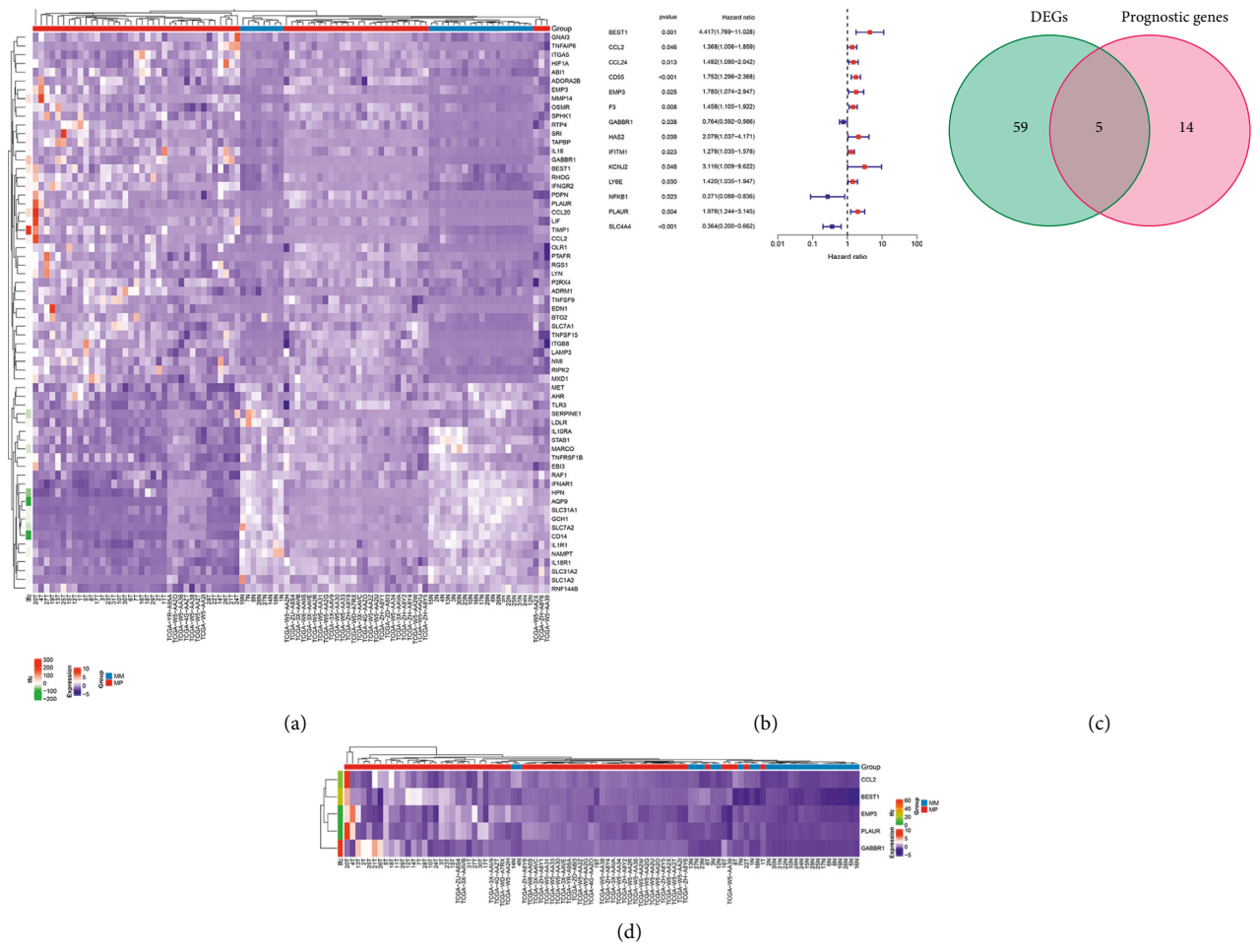

Figure 1: Genes involved in the inflammatory response have been identified as potential candidates. (a) Genes that differ between tumor and nontumor tissues in terms of expression. (b) Forest plots demonstrating 14 genes that linked to patient survival. (c) A Venn diagram was used to determine which genes were differentially expressed and which ones were predictive. (d) Prognostic and differentially expressed genes in tumor and nontumor regions.

3.2. Construction of a Prognostic Model. The expression profiles of the above 5 genes were assessed using LASSO-Cox regression analysis and a prognostic model was built (Figure 2(a)). A three-gene marker was created using the best value of λ (Figure 2(b)). Score = 0.899 ∗ BEST1 expression level + 0.169 ∗ CCL2 expression level + 0.395 ∗ PLAUR expression level. Patients were divided into low-risk and high-risk groups based on the median cut-off value (Figure 3(a)). Confounding factors such as age, gender, and tumor stage were evenly distributed between low-risk and high-risk

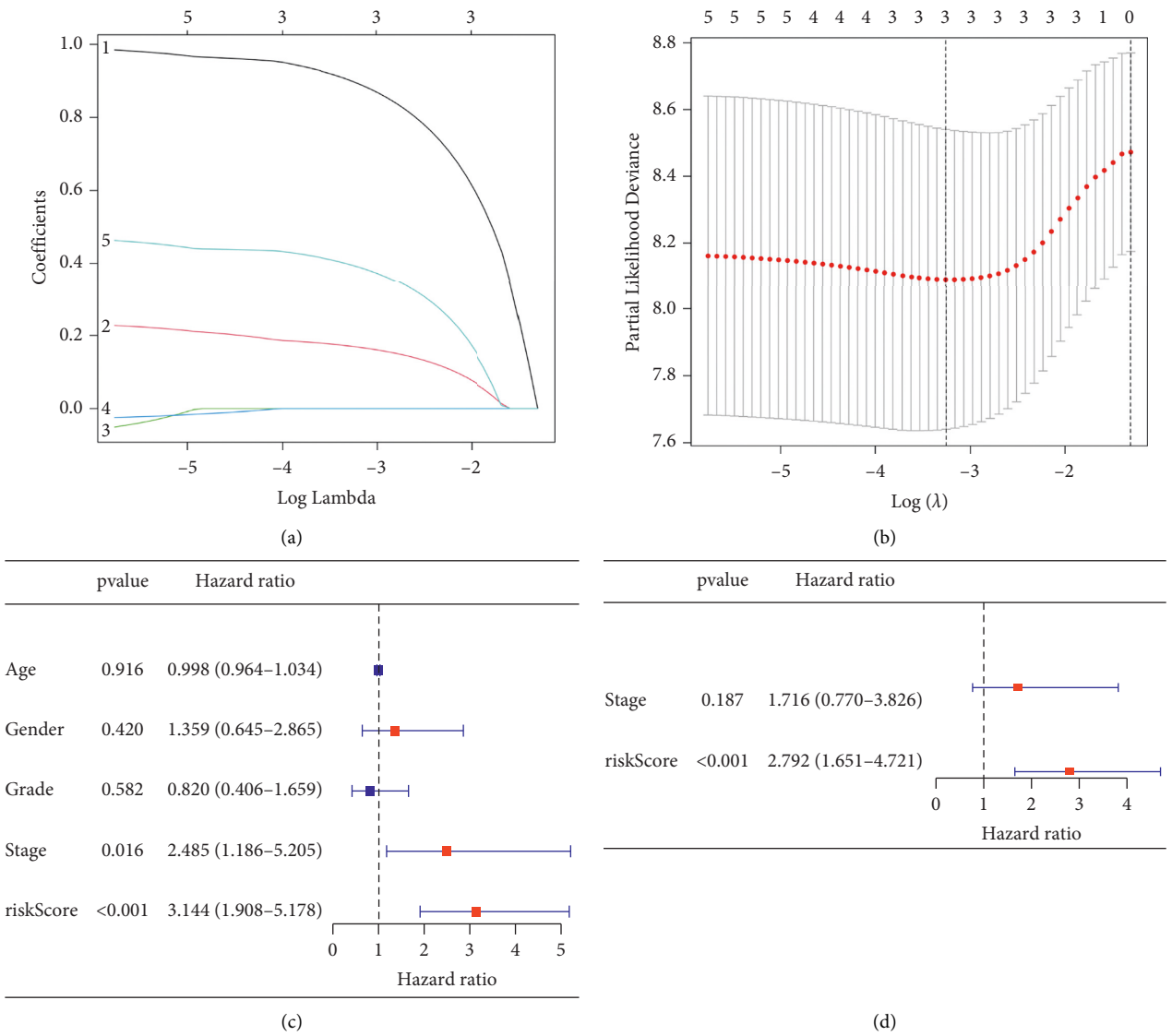

Figure 2: A gene signature that is associated with inflammation was generated. (a) LASSO-Cox regression analysis of possible inflammatory response-related genes. (b) The optimal value of the LASSO-Cox regression analysis. (c) Prognosis-related factors were screened using univariate Cox regression analysis. (d) Prognosis-related factors were screened using multivariate Cox regression analysis.

groups (Table 2). According to the scatter chart, individuals at high-risk are more likely to die from cancer than those at low-risk (Figure 3(b)). According to PCA and t-SNE analysis, individuals in different risk categories were scattered in two directions (Figures 3(c) and 3(d)). Patients at high-risk had a significantly shorter OS than those at low-risk, according to the Kaplan–Meier curve (Figure 3(e), P0.001). Time-dependent ROC curves were produced to investigate survival prediction using the prognostic model, with the area under the curve (AUC) reaching 0.730 at 1 year, 0.683 at 2 years, and 0.779 at 3 years (Figure 3(f)).

3.3. Independent Prognostic Value of the 3-Gene Signature and Association with Clinical Features. We conducted both univariate and multivariate Cox analyses of covariates to evaluate if the risk score was an independent predictor of OS. In a univariate Cox analysis, the risk score in the total population was significantly related to OS (HR = 3.144, 95% CI = 1.908–5.178, $P < 0.001$) (Figure 2(c)). Multivariate Cox analysis demonstrated that the risk score remained an independent predictor of OS after controlling for additional confounding variables (HR = 2.792, 95% CI = 1.651–4.721, $P < 0.001$) (Figure 2(d)). No meaningful association between the risk rating and clinical characteristics of cholangiocarcinoma patients, including age, gender, tumor grade, and stage, was found (Figures 4(a) and 4(d)).

3.4. Immune Status and Tumor Microenvironment Analysis. To study the relationship between risk score and immunological condition, ssGSEA was used to calculate the enriched scores of various immune cell subpopulations, associated components, and pathways. In the high-risk

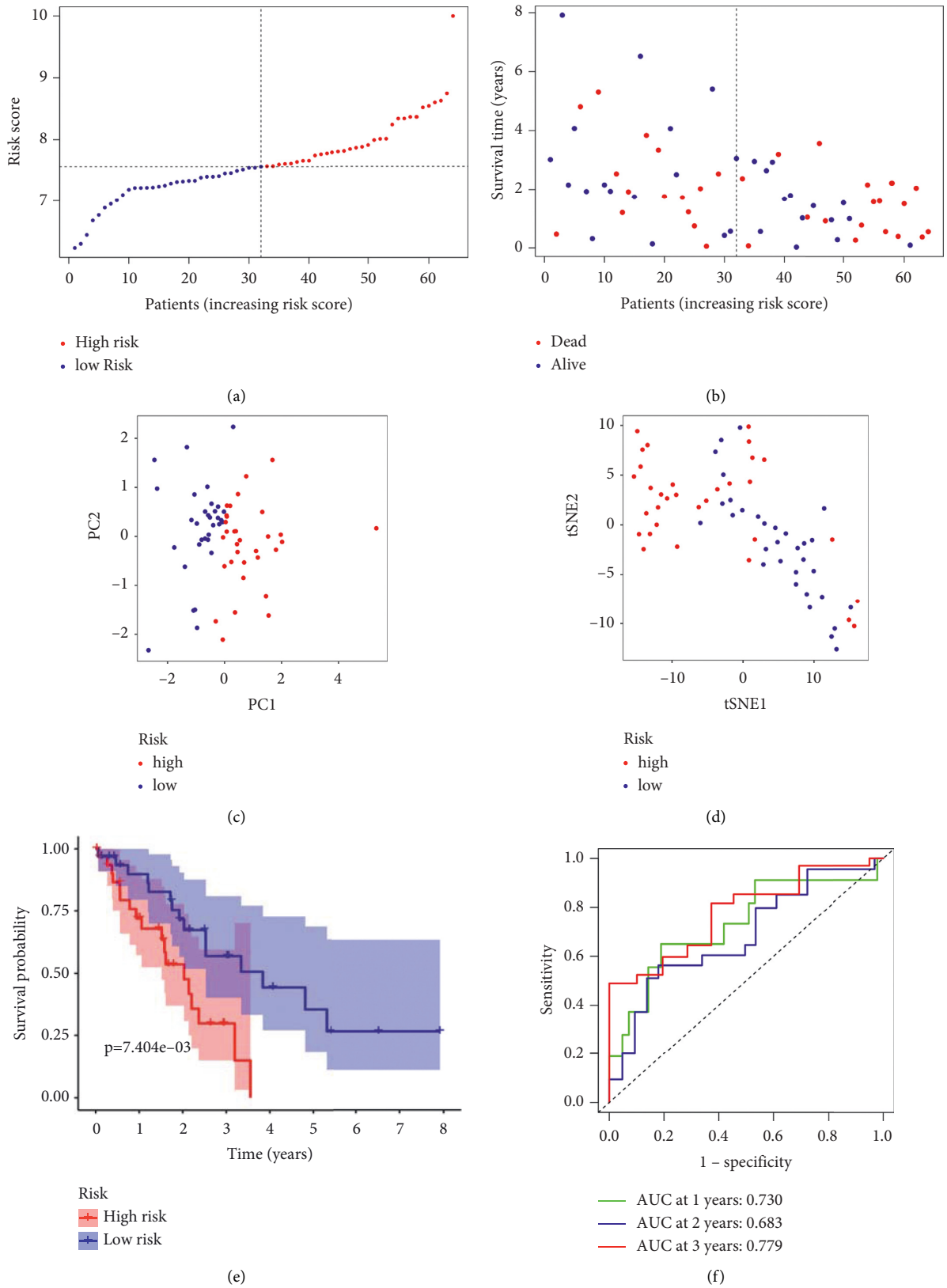

Figure 3: The prognostic analysis of the 3-gene signature model. (a) The median value and distribution of risk scores. (b) The prognosis status distribution. (c) PCA plot (Plotted Correlation Analysis). (d) Analysis using the t-SNE method. (e) The Kaplan–Meier curves for overall survival in high-risk and low-risk groups. (f) Overall survival AUC time-dependent ROC curves.

Table 2: Patients in various risk groups have varied characteristics.

Characteristics	Low-risk cohort $N = 32$	High-risk cohort $N = 32$
Age		
≤65	17 (53.1%)	16 (50.0%)
>65	15 (46.8%)	16 (50.0%)
Gender		
Female	15 (46.8%)	9 (28.1%)
Male	17 (53.1%)	23 (71.8%)
Grade		
Grades 1-2	16 (50.0%)	22 (68.7%)
Grades 3-4	16 (50.0%)	10 (31.2%)
AJCC stage		
Stages I-II	25 (78.1%)	22 (68.7%)
Stages III-IV	7 (21.8%)	10 (31.2%)

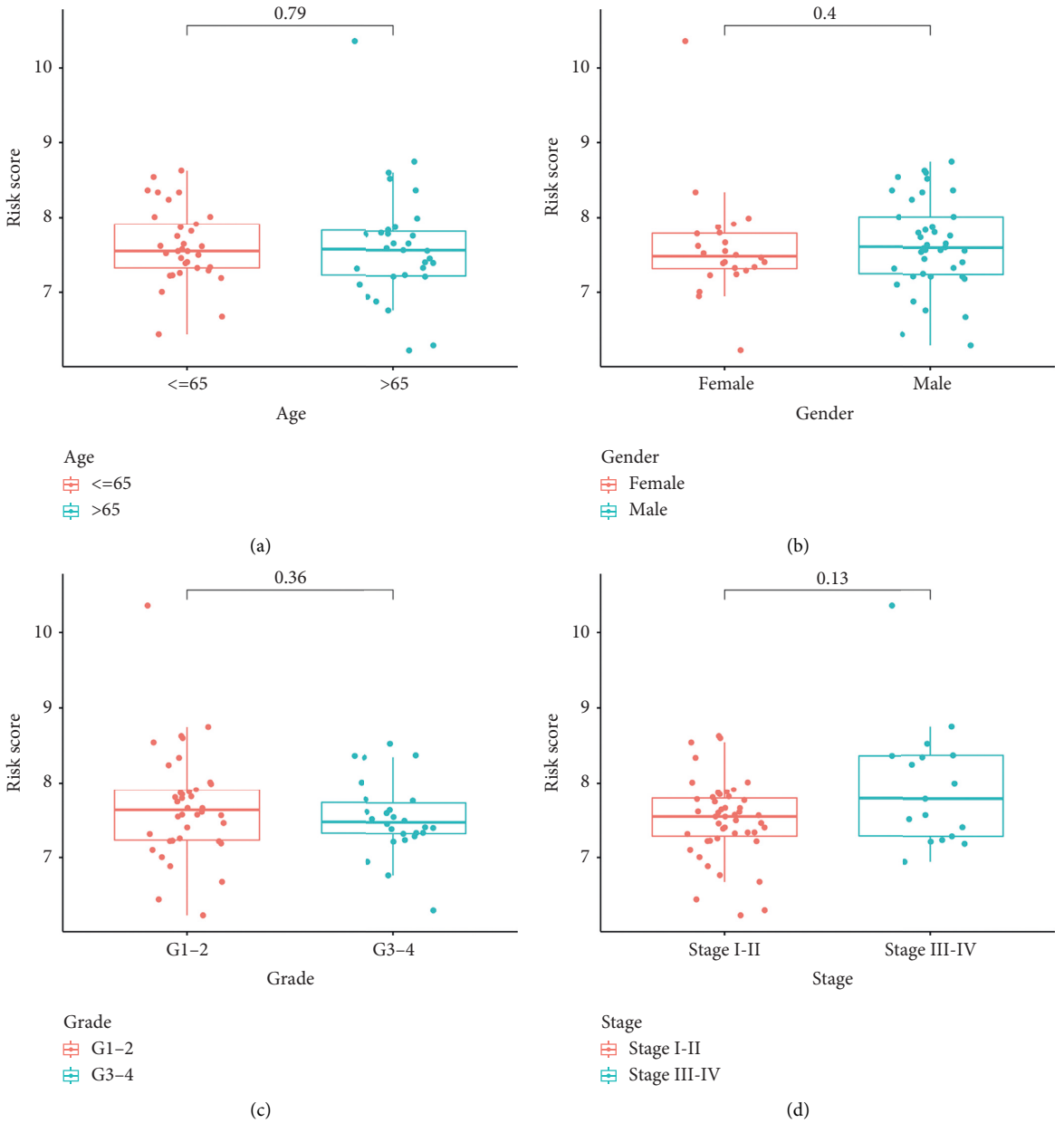

Figure 4: (a) Age, (b) gender, (c) tumor grade, and (d) tumor stage were used to split the risk score into various groups.

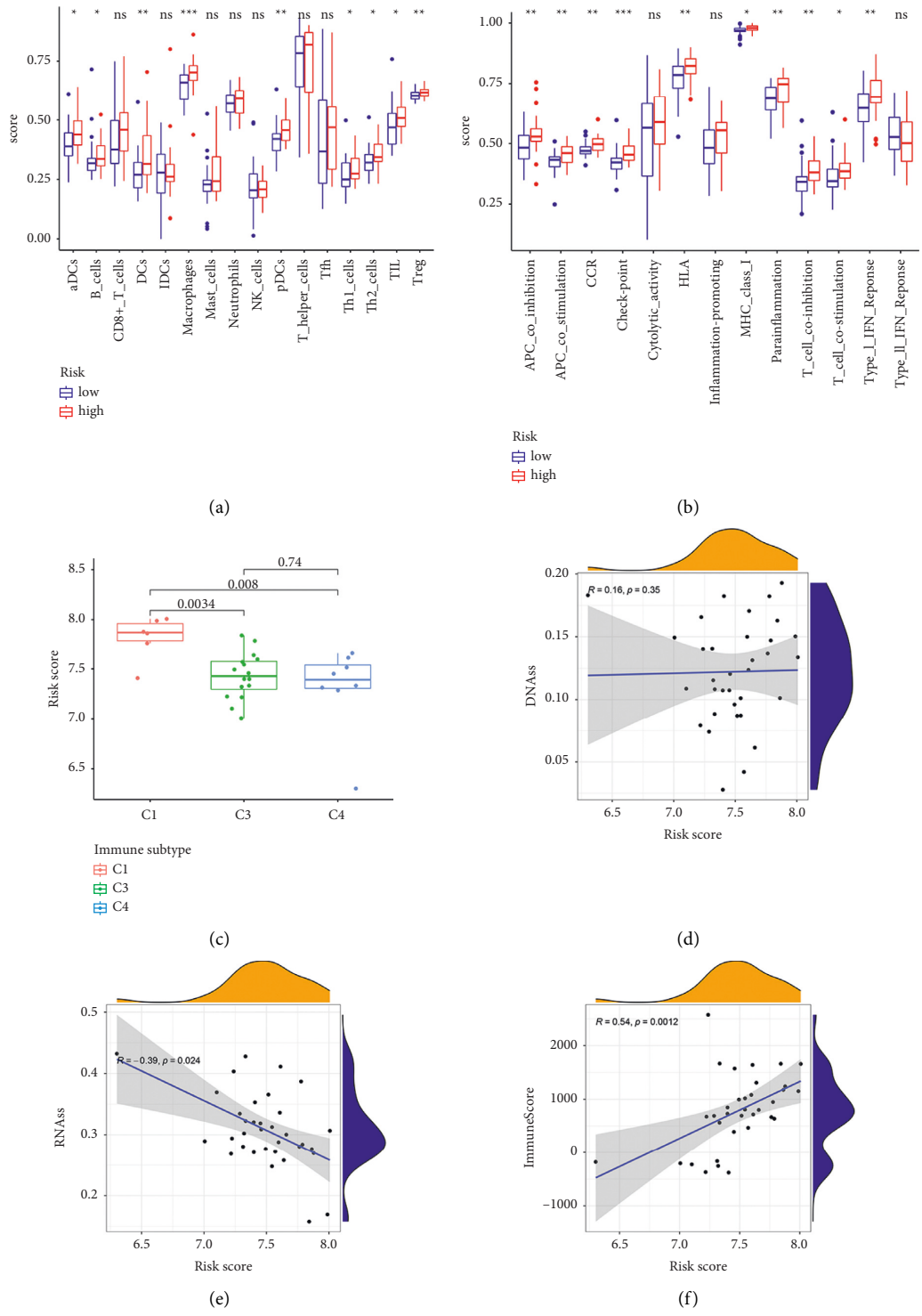

Figure 5: Continued.

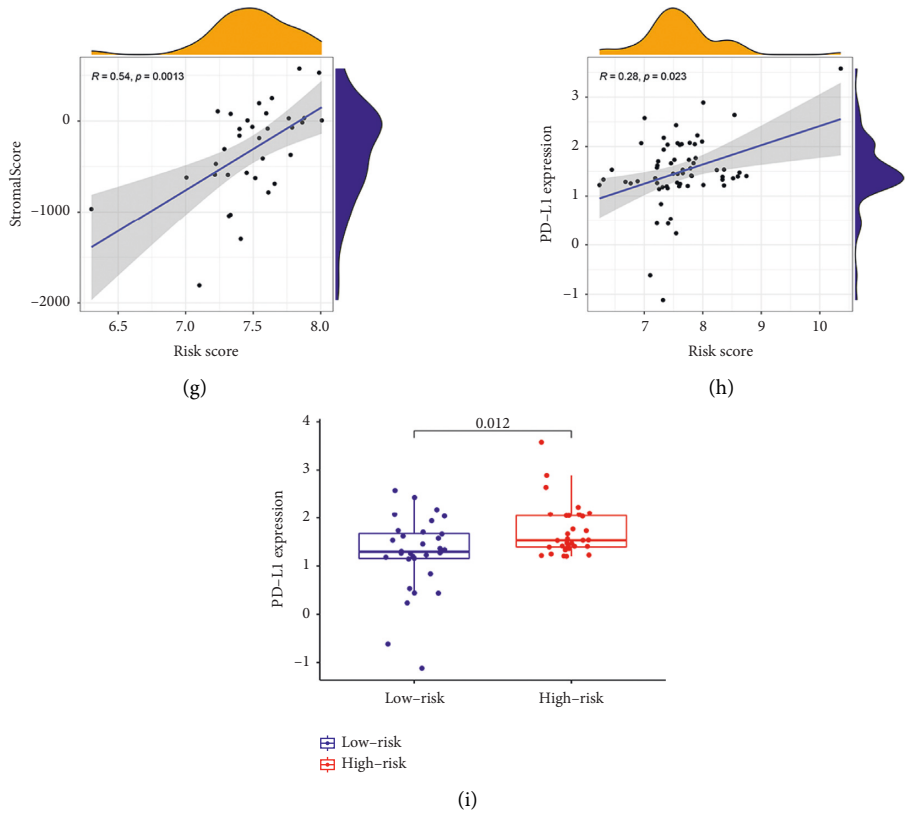

Figure 5: (a) The immunological status of different risk groups and the association between risk score and surrounding tissue. (b) The ratings of 16 immune cells and 13 immune-related functions were displayed using boxplots. (c) An assessment of prediction models for different subtypes of immune infiltration. Correlation among PD-L1 expression and RNAss, DNAss, stromal score, immunologic scoring system, and risk score. (d–i) The levels of PD-L1 expression in various risk groups were compared.

group, the antigen presentation pathways, including aDCs, pDCs, APC co-inhibition, APC co-stimulation, HLA, and MHC class I, were significantly higher (all adjusted $P < 0.05$, Figures 5(a) and 5(b)). Furthermore, the high-risk group had larger proportions of Th1 cells, Th2 cells, TIL cells, Treg cells, T cell co-stimulation, and T cell co-inhibition compared to the low-risk group, indicating differences in T cell regulation between the two groups.

To investigate how the risk score was linked to immunological components, the association between the risk score and immune infiltrates was studied. C1 (wound healing), C2 (INF-g dominating), C3 (inflammatory), C4 (lymphocyte deficient), C5 (immunologically silent), and C6 (tumor-suppressing) immune infiltrates were observed in human malignancies, ranging from tumor-promoting to tumor-suppressing (TGF-b dominant). The C5 and C6 immune subtypes were eliminated from the study because no patient specimens in HCC belonged to the C5 immune subtype and that merely one sample belonged to the C6 immunological subtype. The correlation between the immune infiltrate of cholangiocarcinoma in the cohort and the risk score was investigated. Results showed that high-risk scores highly associated with C1, while low-risk scores were strongly correlated with C3 and C4 (Figure 5(c)).

The RNA stemness score (RNAss) and DNA stemness score (DNAss) based on DNA methylation patterns were used to ascertain cancer stemness. Stromal and immune scores were used to estimate the tumor immune microenvironment. The correlation study was performed to investigate whether the risk score was linked to cancer stem cells and the immune microenvironment. Results revealed that the risk score was highly associated with RNAss rather than DNAss, and it was positively correlated with both immunologic and stromal ratings (Figure 5(d)–5(g)). The PD-1/PD-L1 pathway plays a crucial role in the immune evasion of cancer. The degree of expression of the immunological checkpoint PD-L1 was a vital indicator for specific targeting. The expression level of PD-L1 was considerably higher in the highest quintile than in the lowest quartile (Figure 5(i)), and immune checkpoint expression levels were positively correlated with risk assessment (Figure 5(h)).

3.5. Prognostic Gene Expression and Cancer Cell Sensitivity to Chemotherapy. The expressions of prognostic genes in NCI-60 cell lines were compared to drug sensitivity and it was found that all prognostic alleles were linked to chemotherapeutic treatment sensitivity ($P < 0.01$) (Figure 6).

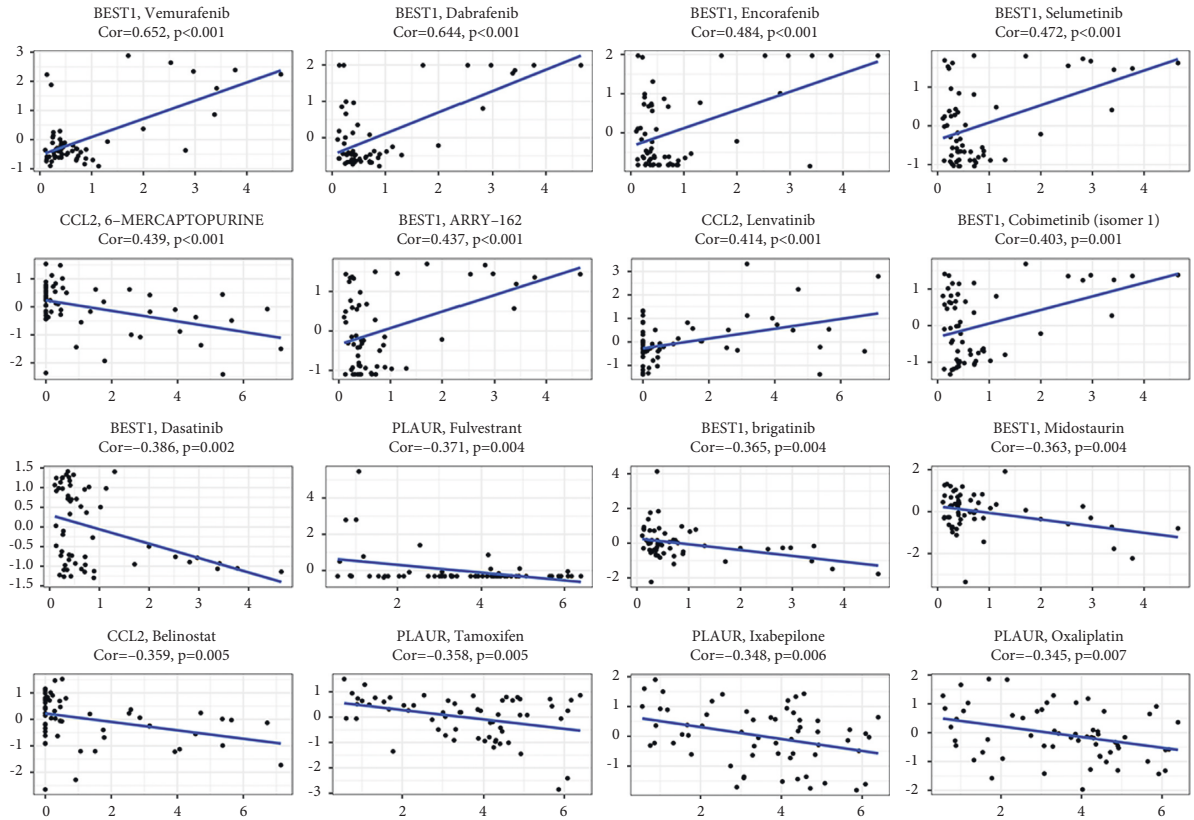

Figure 6: The relationship between prognostic gene expression and medication sensitivity as a scatter plot.

4. Discussion

In this study, we investigated the expression of 200 inflammatory response-related genes in cholangiocarcinoma tissues and analyzed their correlation to the prognosis. 49 DEGs were eliminated from the TCGA and GEO cohorts. In a univariate Cox analysis, five of the DEGs were associated with overall survival. Three inflammatory response-related genes were incorporated into a predictive model using LASSO regression analysis, namely Homo sapiens bestrophin 1 (BEST1), Chemokine (C–C motif) ligand 2 (CCL2), and plasminogen activator, urokinase receptor (PLAUR). Depending on their median risk score, patients were categorized into high-risk and low-risk groups. In a multivariate Cox regression analysis, the risk score was demonstrated to be an independent predictor of OS. The relationships between the risk score and immunological status and microenvironment were then investigated. Three inflammatory response-related genes were shown to have a high relationship with cancer cell susceptibility to antitumor drugs.

CCL2, also known as the inflammation-associated expression signature, was mostly derived from cancer-associated fibroblasts, which were components of the cholangiocarcinoma tumor microenvironment. [16, 17] Its risk score in the total population was significantly related to OS (HR = 3.144, 95% CI = 1.908–5.178, $P < 0.001$). Multivariate Cox analysis demonstrated that the risk score remained an independent predictor of OS after controlling for additional confounding variables (HR = 2.792, 95% CI = 1.651–4.721, $P < 0.001$). By stimulating the STAT3-CCL2 signaling pathway, the FAP induces immunosuppression by cancer-associated fibroblasts in the tumor microenvironment. The TWEAK/Fn14 signaling pathway may also increase the development and progression of cholangiocarcinoma niches through the downstream target CCL2. [18] Due to the lack of investigations on these genes, it remains unclear if BEST1 and PLAUR affect the prognosis of cholangiocarcinoma through inflammatory response and tumor microenvironment.

To gain a better knowledge of the connection between the risk score and immunological elements, a study on the role of risk rating in immune infiltration type was conducted. We observed that a higher risk score was substantially linked to C1, whereas a lower score was clearly connected to C3 and C4, meaning that C1 encourages cancer initiation and development while C3 and C4 are good preventative factors [19]. Furthermore, macrophages and regulatory T cells (Treg cells) presented more in the high-risk group than in the low-risk group. Because of their roles in the immunological invasion, scientists have associated a higher number of tumor-associated macrophages and Treg cells with a worse prognosis. When utilized as tumor immunotherapies, anti-PD-L1 antibodies, for example, have shown clinical activity in a variety of cancer types. Increased immune checkpoint suppressed antitumor immune responses from T cells by increasing the expression of PD-1 and CTLA4 receptors. In this study, immune checkpoint scores were greater in the high-risk group than in the low-

risk group, and the risk score was strongly linked to PD-L1 expression. As a result, the prognostic model can forecast immune checkpoint expression levels and may be used to guide treatment decisions. Our research also has a few drawbacks. The predictive results in the study will need further supportive data from experiments, and the regulatory mechanism of inflammation response-related gene profile regulators on tumor growth as well as the immune microenvironment is unknown, necessitating additional research to gain a better understanding.

In conclusion, our research identified three genes involved in the inflammatory response as a new predictive signature. The signature was found to be associated independently with overall survival and to have played a role in functional analysis, tumor microenvironment, and treatment compassion, providing insights into cholangiocarcinoma prognosis. The mechanism underlying the association between inflammatory response-related genes with tumor immunity in cholangiocarcinoma remains unclear. Furthermore, these genes could be exploited to develop new antitumor medications as therapeutic alternatives.

Data Availability

The data used to support this study are available from the corresponding author upon request.

Conflicts of Interest

The authors declare that they have no conflicts of interest.

Authors' Contributions

Yanting Wang and Shi Chen equally contributed to the study.

References

[1] A. Shiani, S. Narayanan, L. Pena, and M. Friedman, "The role of diagnosis and treatment of underlying liver disease for the prognosis of primary liver cancerole," *Cancer Control*, vol. 24, no. 3, 2017.

[2] X. Xiang, D. Hu, Z. Jin, P. Liu, and H. Lin, "Radiofrequency ablation vs. surgical resection for small early-stage primary intrahepatic cholangiocarcinoma.esection for small early-stage primary intrahepatic cholangiocarcinoma," *Frontiers in Oncology*, vol. 10, Article ID 540662, 2020.

[3] P. J. Brindley, M. Bachini, S. I. Ilyas et al., "Cholangiocarcinoma," *Nature Reviews Disease Primers*, vol. 7, no. 1, p. 65, 2021.

[4] Y. Bang, J. Lim, H J. Choi, and H. J. Choi, "Recent advances in the pathology of prodromal non-motor symptoms olfactory deficit and depression in Parkinson's disease: clues to early diagnosis and effective treatment," *Archives of Pharmacal Research*, vol. 44, no. 6, pp. 588–604, 2021.

[5] S. Rizvi, S. A. Khan, C. L. Hallemeier et al., "Cholangiocarcinoma—evolving concepts and therapeutic strategies," *Nature Reviews Clinical Oncology*, vol. 15, no. 2, pp. 95–111, 2018.

[6] H. Lin, Y. S. Wu, Z. Li, Y. S. Jiang, Z. Li, and Y. Jiang, "Prognostic value of retrieved lymph node counts in patients with node-negative perihilar cholangiocarcinomas," *ANZ Journal of Surgery*, vol. 88, no. 12, pp. E829–e834, 2018.

[7] F. R. Greten, S. I. R. Grivennikov, and S. I. Grivennikov, "Inflammation and inflammation and cancer: triggers, mechanisms, and consequencesancer: triggers, mechanisms, and consequences," *Immunity*, vol. 51, no. 1, pp. 27–41, 2019.

[8] D. S. Chen, I. S. Mellman, and I. Mellman, "Elements of cancer immunity and the cancer-immune set point," *Nature*, vol. 541, no. 7637, pp. 321–330, 2017.

[9] J. I. Yu, H. C. Park, S. W. Paik et al., "Clinical Clinical Significance of systemic inflammation markers in newly diagnosed, previously untreated hepatocellular carcinoma," *Cancers*, vol. 12, no. 5, Article ID 1300, 2020.

[10] D C. C. McMillan, "The systemic inflammation-based Glasgow Prognostic Score: a decade of experience in patients with cancer," *Cancer Treatment Reviews*, vol. 39, no. 5, pp. 534–540, 2013.

[11] F. Meng, C. M. Meyer, D. Joung, D. A. Vallera, M. C. McAlpine, and A. Panoskaltsis-Mortari, "3D bioprintedin vitro metastatic models via reconstruction of tumor microenvironments," *Advanced Materials*, vol. 31, no. 10, Article ID e1806899, 2019.

[12] N. Simon, J. Friedman, T. Hastie, and R. Tibshirani, "Regularization paths for cox's proportional hazards model via coordinate descent," *Journal of Statistical Software*, vol. 39, no. 5, pp. 1–13, 2011.

[13] R. Tibshirani, "The lasso method for variable selection in the Cox model," *Statistics in Medicine*, vol. 16, no. 4, pp. 385–395, 1997.

[14] K. Yoshihara, M. Shahmoradgoli, E. Martínez et al., "Inferring tumour purity and stromal and immune cell admixture from expression data," *Nature Communications*, vol. 4, no. 1, Article ID 2612, 2013.

[15] L. Dib, L. San-Jose, A. L. Ducrest, N. Salamin, and A. Roulin, "Selection on the major color gene melanocortin-1-receptor shaped the evolution of the melanocortin system genes," *International Journal of Molecular Sciences*, vol. 18, no. 12, Article ID 2618, 2017.

[16] Y. Lin, B. Li, W. Liu et al., "Fibroblastic FAP promotes intrahepatic cholangiocarcinoma growth via MDSCs recruitment," *Neoplasia*, vol. 21, no. 12, pp. 1133–1142, 2019.

[17] L. Wu, Y. Zhou, Y. Guan et al., "Seven genes associated with lymphatic metastasis in thyroid cancer that is linked to tumor immune cell infiltration," *Frontiers in Oncology*, vol. 24, no. 11, Article ID 756246, 2022.

[18] B. J. Dwyer, E. J. Jarman, A. M. Kilpatrick et al., "TWEAK/Fn14 signalling promotes cholangiocarcinoma niche formation and progression," *Journal of Hepatology*, vol. 74, no. 4, pp. 860–872, 2021.

[19] Z. Lin, Q. Xu, D. Miao, and F. Yu, "An inflammatory response-related gene signature can impact the immune status and predict the prognosis of hepatocellular carcinoma," *Frontiers in Oncology*, vol. 11, Article ID 644416, 2021.